
ADVANCES IN COMPOSITE MATERIALS - ECODESIGN AND ANALYSIS

Edited by **Brahim Attaf**

INTECHWEB.ORG

Advances in Composite Materials - Ecodesign and Analysis

Edited by Brahim Attaf

Published by InTech

Janeza Trdine 9, 51000 Rijeka, Croatia

Copyright © 2011 InTech

All chapters are Open Access articles distributed under the Creative Commons Non Commercial Share Alike Attribution 3.0 license, which permits to copy, distribute, transmit, and adapt the work in any medium, so long as the original work is properly cited. After this work has been published by InTech, authors have the right to republish it, in whole or part, in any publication of which they are the author, and to make other personal use of the work. Any republication, referencing or personal use of the work must explicitly identify the original source.

Statements and opinions expressed in the chapters are these of the individual contributors and not necessarily those of the editors or publisher. No responsibility is accepted for the accuracy of information contained in the published articles. The publisher assumes no responsibility for any damage or injury to persons or property arising out of the use of any materials, instructions, methods or ideas contained in the book.

Publishing Process Manager Ivana Lorkovic

Technical Editor Teodora Smiljanic

Cover Designer Martina Sirotic

Image Copyright Hadrian, 2010. Used under license from Shutterstock.com

First published March, 2011

Printed in India

A free online edition of this book is available at www.intechopen.com

Additional hard copies can be obtained from orders@intechweb.org

Advances in Composite Materials - Ecodesign and Analysis,

Edited by Brahim Attaf

p. cm.

ISBN 978-953-307-150-3

INTECH OPEN ACCESS
PUBLISHER

INTECH open

free online editions of InTech
Books and Journals can be found at
www.intechopen.com

Contents

Preface IX

Part 1 Sustainable Materials and Ecodesign Aspects 1

- Chapter 1 **Generation of New Eco-friendly Composite Materials via the Integration of Ecodesign Coefficients 3**
Brahim Attaf
- Chapter 2 **Design, Manufacture and Performance Evaluation of Non-Asbestos Sealing Composites 21**
Boqin Gu, Ye Chen and Jianfeng Zhou
- Chapter 3 **Thermoplastic Polymer based Modified Red Mud Composites Materials 55**
A.H. Bhat, H.P.S. Abdul Khalil and A. K. Banthia
- Chapter 4 **Biopolymer as Reinforcement into Natural Matrices: a New Route to Bio-Composite Materials 87**
Marion Noël, Emmanuel Fredon, Eric Mougel, Eric Masson and Daniel Masson
- Chapter 5 **Properties of Polymer Composites with Cellulose Microfibrils 103**
Denis Mihaela Panaitescu, Adriana Nicoleta Frone, Marius Ghiurea, Catalin Ilie Spataru, Constantin Radovici and Michaela Doina Iorga

Part 2 Composite Materials and Curing Processes 123

- Chapter 6 **Radiation Curing of Thermosetting-Thermoplastic Blends as Matrices for Structural Carbon Fibre Composites 125**
Sabina Alessi, Clelia Dispenza, Giuseppe Pitarresi and Giuseppe Spadaro
- Chapter 7 **Optimization of Curing Cycles for Thick-wall Products of the Polymeric Composite Materials 141**
Oleg Dmitriev and Sergey Mischenko

- Chapter 8 **Development of 3D Knitted Fabrics
for Advanced Composite Materials 161**
Luminita Ciobanu

Part 3 Modelling and Testing of Composites 193

- Chapter 9 **To Carry Out Tolerance Analysis
of an Aeronautic Assembly Involving
Free Form Surfaces in Composite Material 195**
Wilma Polini
- Chapter 10 **Application of Optical Fibre Sensors
to Measuring the Mechanical Properties
of Composite Materials and Structures 221**
Wojciech Błażejowski, Paweł Gąsior and Jerzy Kaleta
- Chapter 11 **Cost Effective Computational Approach
for Generation of Polymeric Composite Material
Allowables for Reduced Testing 247**
G. Abumeri, F. Abdi, K.S. Raju,
J. Housner, R. Bohner and A. McCloskey
- Chapter 12 **Elaboration and Properties of Carbon Fibre
Reinforced Copper Matrix Composites 271**
Pierre-Marie Geffroy, Jean-François Silvain and Jean-Marc Heintz
- Chapter 13 **Engineering, Modeling and Testing
of Composite Absorbing Materials
for EMC Applications 291**
Marina Koledintseva, Konstantin N. Rozanov and James Drewniak
- Chapter 14 **Radioactivity Control of Composite Materials
Using Low Energy Photon Radiation 317**
Konstantinos N. Athanassiadis
- Chapter 15 **Dynamic Responses of Composite Structures
with Fluid-Structure Interaction 337**
Young W. Kwon and Angela C. Owens
- Chapter 16 **Experimental Investigation
of Dynamic Compression and Damage Kinetics
of Glass/Epoxy Laminated Composites
under High Strain Rate Compression 359**
Tarfaoui Mostapha
- Chapter 17 **Buckling and Post-buckling Analysis
of Composite Plates 383**
Elena-Felicia Beznea and Ionel Chirica

- Chapter 18 **Finite Element Analysis of Delamination Growth in Composite Materials using LS-DYNA: Formulation and Implementation of New Cohesive Elements** 409
Ahmed Elmarakbi
- Chapter 19 **Finite Element Analysis of Progressive Degradation versus Failure Stress Criteria on Composite Damage Mechanics** 429
J.L. Curiel Sosa
- Chapter 20 **Bonded Composite Patch Repairs on Cracked Aluminum Plates: Theory, Modeling and Experiments** 445
Fabrizio Ricci, Francesco Franco and Nicola Montefusco
- Part 4 Stress-strength Analysis of Adhesive Joints** 465
- Chapter 21 **Strength of Composite Scarf Joints** 467
Young W. Kwon
- Chapter 22 **Design and use of a Fatigue Test Machine in Plane Bending for Composite Specimens and Bonded Joints** 491
G. Di Franco, G. Marannano, A. Pasta and G. Virzi Mariotti
- Chapter 23 **On the Behavior of FRP-to-concrete Adhesive Interface: Theoretical Models and Experimental Results** 517
Enzo Martinelli, Antonio Bilotta, Ciro Faella and Emidio Nigro
- Part 5 Characterization and Thermal Behaviour** 547
- Chapter 24 **Estimation of the Degree of Anisotropy and Overall Elastic Stiffness of Advanced Anisotropic Materials** 549
Mohamed S. Gaith and Imad Alhayek
- Chapter 25 **Lightweight Unfolded Composite Materials Acquiring Stability of the Shape due to Factors of Space Environment** 577
Laricheva V.P.
- Chapter 26 **G40-800/5260 Carbon Fiber/Bismaleimide Composite Material: High Temperature Characteristics of Static and Fatigue Strengths** 587
Toshiyuki Shimokawa, Yoshiaki Kakuta and Takenori Aiyama
- Chapter 27 **Self-Consistent Micromechanical Enhancement of Continuous Fiber Composites** 607
Andrew Ritchey, Joshua Dustin, Jonathan Gosse and R. Byron Pipes
- Chapter 28 **The Effective Thermal Transport in Composite Materials** 625
Bashir M. Suleiman

Preface

Studies and research activities conducted in the field of high-technology materials show that advanced composite materials are successfully used in key components for many fields of applications, from aerospace & automobile industries, marine construction, renewable energy, modern medicine to micro-/nano-material technologies, including other more complex civil and mechanical engineering assemblies. In addition to this variety of applications, the considerable increase in demand of these smart materials will open up many opportunities to design and manufacture new products for the future. However, these products have to satisfy sustainable development requirements, which can be achieved by a balanced equation that simultaneously guarantees economic growth and environmental protection.

According to these ecological considerations, researchers and industrials involved with high-technology composite materials are strongly encouraged to integrate ecodesign aspects into the composite product lifecycle, providing then a better assessment of environmental and health performances. Furthermore, “going green” can also contribute to the world’s socio-economic well-being and living conditions for present and future generations.

By adopting these principles of sustainable design, I am pleased to have this opportunity to edit this new book, which opens a new challenge in the world of composite materials and explores the achieved advancements of specialists in their respective areas of research and innovation.

The scientific and technological research contributions coming from both spaces of academia and industry were so diversified that the 28 chapters composing the book have been grouped into the following main parts:

- *Sustainable materials and ecodesign aspects*: research was focused on the integration of environmental aspects in the different stages of the design process, development of eco-friendly, non-asbestos and fully biodegradable macro-/micro-/nano-composite materials exhibiting less pollution and waste.
- *Composite materials and curing processes*: investigations were undertaken on some technologies of fabrication and on the simulation of the curing process with a reduction of VOC emissions and energy consumption.
- *Modelling and testing of composites*: studies were conducted on mechanical characterization, tolerance analysis, fluid-structure interaction, buckling phenomenon,

delamination growth and stress analysis using in one hand numerical approaches, such as finite element method and on the other hand experimental investigations.

- *Stress-strength analysis of adhesive joints*: experimental testing, design formulas and FE codes were used to predict the failure strength of the joint and evaluate the structural behaviour of the damaged elements that were repaired and reinforced with adhesive layers.
- *Characterization and thermal behaviour*: properties of composite material devices for high demanding applications were investigated experimentally and numerically.

The results achieved from theoretical, numerical and experimental investigations can help designers, manufacturers and suppliers involved with high-tech composite materials to boost competitiveness and innovation productivity. Specific recommendations are to give much more focus and attention to (i) the chemical substances used in the manufacturing process, (ii) the amount of VOC emissions, (iii) the enhancement of quality-health-environment performance, (iv) the amount of waste produced, expired materials and ways of recycling, (v) the classification of companies and firms with regard to the new regulations and eco-standards, and more...

The editor would like to thank all Chapter Authors for their remarkable contributions coming from all around the world and appreciate the resulting synergy between academia and industry. Without this rich variety of contributions, the existence of the Book "*Advances in Composite Materials- Ecodesign and Analysis*" would not have been possible.

I also wish to acknowledge the help given by InTech Open Access Publisher staff, in particular Ivana Lorković for her assistance and support.

January 2011

Dr. Brahim Attaf
Marseille
France

Part 1

Sustainable Materials and Ecodesign Aspects

Generation of New Eco-friendly Composite Materials via the Integration of Ecodesign Coefficients

Brahim Attaf

*Expert in Composite Materials & Structures
France*

1. Introduction

Thanks to their excellent formability, their mass-saving advantage, their high stiffness-to-density and strength-to-density ratios, *i.e.*, E/ρ and σ/ρ and the greater freedom to tailor these high properties in the desired orientation and position, fibre-reinforced polymer (FRP) composites are used in many fields of engineering, from architectural structures, ship superstructures, automobiles, bridge decks, machine parts, dams and reservoirs, to the high technology of the modern aerospace industries (Attaf & Hollaway, 1990a,b). Furthermore, these lightweight materials have some precise objectives, which cannot be reached with some other conventional materials. These attractive advantages coupled with economic design have lead to open up many opportunities to design and manufacture new composite materials and structures for future applications. However, these materials have to satisfy ecodesign requirements, which are based on new standards for designing environmentally-friendly composite products. Within this context, the industrial designers, manufacturers and suppliers who work in the field of composites are having to factor in the impacts of their products on the environment and find new feasible alternatives. Typically, these alternatives are based on a set of equations, called “ecodesign function” (Attaf, 2007). This function must guarantee quality assurance, health protection and environmental preservation all at the same time, making it necessary to come up with ecodesign strategies that include cleaner production, so as to be in compliance with new regulations and still make the product more competitive in the worldwide market.

With this approach as an objective, codes and standards for future composite materials and structures should integrate, at each stage of the designing process, three balanced key criteria characterised mainly by quality assurance (Q for short), health protection (H for short) and environmental preservation (E for short). To achieve these requirements, we have defined and developed new criteria in the form of coefficients. Taking into account the previously specified ecological considerations, these coefficients are now called “eco-coefficients”. To assess these eco-coefficients, probability approach (Attaf, 2009) and optimisation procedures based on additive colours technique are undertaken in this analysis. And once these eco-coefficients are determined and approved by ecodesign standards, they can then be integrated into the formulations of design and analysis, in characterisation tests; they can also be implemented into future finite-element computer

programs, etc. In addition, by simply undertaking a comparison of eco-results with classical ones, which do not take into account eco-coefficients, designers and analysts can make better use of ecodesign aspects to assess environmental and health performances.

The aim of this investigation is regarded as: (i) a stimulation for innovation, sustainability and research activities within the field of ecodesign of composite materials and structures; and (ii) an encouragement for designers and engineers involved with high-technology composite materials to have more motivation towards the integration of *Q-H-E* aspects into the development process of FRP products.

2. Ecodesign of composite materials and structures

2.1 Position of ecodesign approach within sustainable development concept

According to most scientific results related to the protection of biodiversity, global warming and climate change may have severe effects on human health and the environment. To improve the well-being and living conditions of present and future generations, it is important that the negative impacts generated from human and industrial activities should be seriously considered in all design phases of a new development. To this end, the sustainable development concept is a strong key issue aiming to achieve the previously discussed objective, which is obviously based on three main criteria or “pillars”; these are: (i) environmental sustainability, (ii) economic sustainability and (iii) social sustainability. As the concept of sustainable design or simply ecodesign is inseparable from the sustainable development concept, it is therefore an undissociable part of it, where quality assurance, health protection and environmental preservation aspects are considered to be important branches belonging to the previously described main pillars. Figure 1 illustrates the specific ecodesign situation in relation to the sustainable development concept.

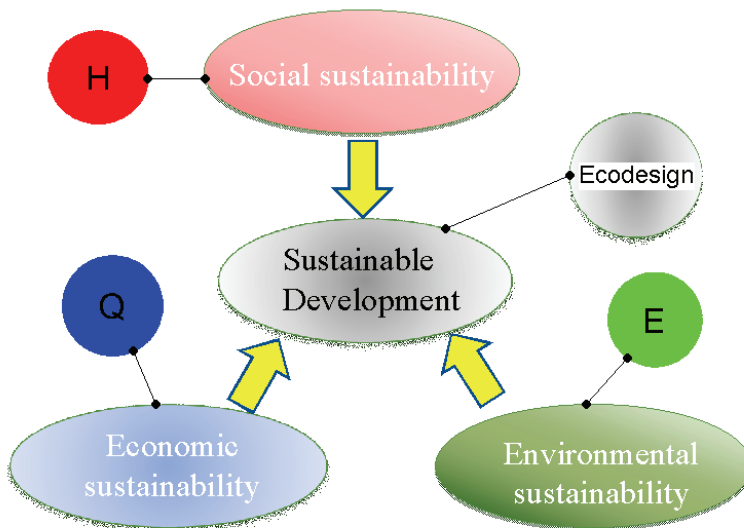


Fig. 1. Ecodesign approach *vs.* sustainable development concept

2.2 Evolution of the interaction between Q-H-E aspects

The main condition of ecodesign can be reached when the interaction between Q , H , E aspects yields a common area of intersection between these aspects, i.e., $Q \cap H \cap E$. The original diagram (Figure 2a) shows health, quality and environment as three separate aspects that operate independently from each other. Joining the Q , H , E aspects gives rise to a new diagram fulfilling the ecodesign condition (Attaf, 2007) that is characterised by the

subset $\dot{\dot{F}}$ resulting from this intersection (Figure 2b). The three dots ($\dot{\dot{}}$) above the character F are only a brief description of the diagram illustrated in Figure 2a, showing interaction between health, quality and environment aspects. In other terms, the three dots represent the three pillars that characterise the basic elements of the sustainable development concept, as discussed above (Figure 1).

Depending on the resultant area of interaction, an optimisation process can be applied to subset $\dot{\dot{F}}$ to maximise this area. If optimisation is highly improved ($\dot{\dot{F}} = \dot{\dot{F}}_{\max}$), then the future diagram illustrated in Figure 1c is achieved and the searched objective is reached, however.

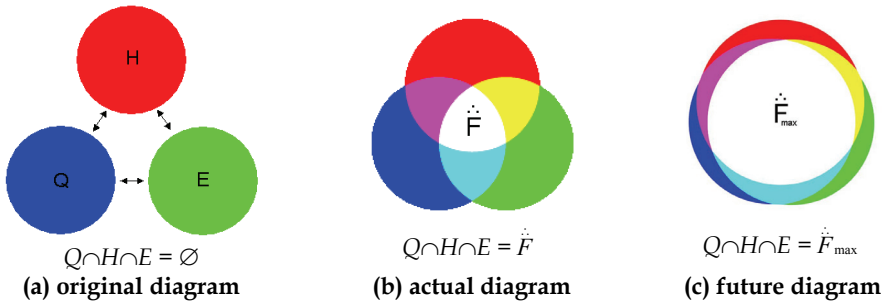


Fig. 2. Evolution of the interaction between Q , H , and E aspects

2.3 Ecodesign model and sample space

As it was shown in Figure 2c, the interaction between the three Q - H - E aspects yields the apparition of a certain number of events, which are illustrated in Figure 3. Each event is assumed to accomplish one or several functions that are defined by the following subsets (Attaf, 2007)

- Subset A (■): characterized by an assured quality, a non-protected health and a non-preserved environment.
- Subset B (■): characterized by an assured quality, a protected health and a non-preserved environment.
- Subset C (■): characterized by a non-assured quality, a protected health and a non-preserved environment.
- Subset D (■): characterized by a non-assured quality, a protected health and a preserved environment.
- Subset S (■): characterized by an assured quality, a non-protected health and a preserved environment.
- Subset $\dot{\dot{F}}$ (□): characterized by an assured quality, a protected health and a preserved environment.

- Subset G (■): characterized by an assured quality, a non-protected health and a preserved environment.

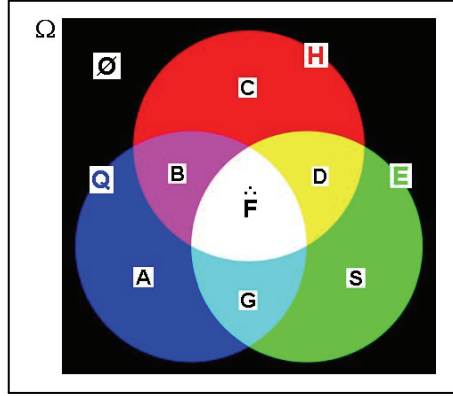


Fig. 3. Diagram showing the ecodesign model and the outcome subsets

The possible outcome sets and subsets can be expressed by the universal sample space as (Attaf, 2007)

$$\Omega = \{ Q, H, E, A, B, C, D, S, G, \dot{F}, \emptyset \} \quad (1)$$

in which,

$$\begin{aligned} A &= Q \cap \bar{H} \cap \bar{E} & B &= Q \cap H \cap \bar{E} & C &= \bar{Q} \cap H \cap \bar{E} \\ D &= \bar{Q} \cap H \cap E & S &= \bar{Q} \cap \bar{H} \cap E & G &= Q \cap \bar{H} \cap E \\ \dot{F} &= Q \cap H \cap E & \emptyset &= \bar{Q} \cap \bar{H} \cap \bar{E} \end{aligned}$$

where, \cap denotes intersection symbol, and \bar{Q} , \bar{H} , \bar{E} are the complement of Q , H , E and indicate that “Quality non-realizable”, “Health non-realizable” and “Environment non-realizable”, respectively.

The subsequent analysis will concentrate only on the subset \dot{F} , a unique searched subset that characterises the event: “intersection between Q , H and E does exist all the time”.

3. Application of probability principles to ecodesign function

3.1 Probability approach

To illustrate the model-set probability, let us consider the sample space Ω that contains all the possible subsets (events) defined by Equation (1) and illustrated in Figure 3. Since the three key sets Q , H and E are composed of several variable elements associated to the different stages involved in the design process where each key set is assumed to fulfil a specific function; it can therefore be written that (Attaf, 2007):

$$\begin{aligned} Q &= \{ x_1, x_2, x_3, \dots, x_m \} \\ H &= \{ y_1, y_2, y_3, \dots, y_n \} \\ E &= \{ z_1, z_2, z_3, \dots, z_p \} \end{aligned} \quad (2)$$

For better visualisation of different issues and calculation of the possible outcome probabilities, it is convenient to construct the probability tree diagram providing simple

probabilistic measure. Figure 4 illustrates the different branches representing the possible events (Attaf, 2009).

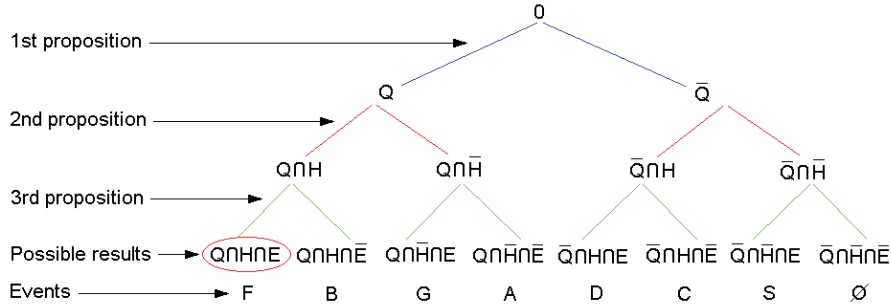


Fig. 4. Probability tree diagram and possible events

The probability theory will be applied to investigate the behaviour of the subset $\dot{\bar{F}}$, identified by the encircled area in Figure 4. As a result, the corresponding event and its associated probability can respectively be written as (Attaf, 2007 & 2009)

$$\dot{\bar{F}} = Q \cap H \cap E \quad (3)$$

$$P(\dot{\bar{F}}) = P(Q \cap H \cap E) \quad (4)$$

3.2 Ecodesign function

The probability $P(\dot{\bar{F}})$ represents the searched eco design function; a function that has multiple variables and lies between the values of 0 and 1, and is defined by $f(Q=x_i, H=y_i, E=z_i)$. However, according to the nature of sets Q , H and E (independent or dependent) and the rules of multiplication in the probability theory, two possible cases (Figures 2a and 2b) may be presented; these are:

- The sets Q , H , E are independent (Figure 2a): a condition which does not satisfy the searched objective because the probability of the intersection is an empty set. Thus, it may be expressed by the following equation:

$$f(Q=x_i, H=y_i, E=z_i) = P(\dot{\bar{F}}) = P(\emptyset) = 0 \quad (5)$$

- The sets Q , H , E are dependent (Figure 2b and/or 2c): a condition that does satisfy the searched objective. Thus, the probability of the occurred intersection can be written as:

$$f(Q=x_i, H=y_i, E=z_i) = P(\dot{\bar{F}}) = P(Q) \times P_Q(H) \times P_{Q \cap H}(E) \quad (6)$$

where, $P(Q)$ represents the probability of an achievable quality;

$P_Q(H)$ represents the probability of an achievable health, knowing that quality has been achieved; and

$P_{Q \cap H}(E)$ represents the probability of an achievable environment, knowing that quality and health have been achieved.

The following probability notations may be of some use in a certain literature reviews:

$$P_Q(H) = P(H|Q) = P(Q \cap H) / P(Q) \quad (7a)$$

$$P_{Q \cap H}(E) = P(E|Q \cap H) = P(Q \cap H \cap E) / P(Q \cap H) \quad (7b)$$

Equations (7a) and (7b) are only valid when $P(Q)$ and $P(Q \cap H)$ are strictly greater than zero. On the other hand and according to the probability analysis, the realization of the event \ddot{F} can take several values as a final result. This latter can be recapitulated by the following possible events (Attaf, 2007):

- If probability value is null ($P(\ddot{F}) = 0$), then the event is impossible.
- If probability value is equal to 1 ($P(\ddot{F}) = 1$), then the event is certain.
- If probability value is located between the two extreme values ($0 < P(\ddot{F}) < 1$), then it does exist a series of probable events.

3.3 Practical descriptions of the variable probability elements

To be familiar with the probability variable elements expressed by Equation (2), let us consider for example the statement “*quality-assurance aspect is achievable and sustainable for the mould polymerisation process*” and we let the letter “ x ” denotes the property named “*quality-assurance aspect is achievable and sustainable*” and the subscript “ k ” refers to the stage number involved in the design process, which corresponds here to “*mould polymerisation process*”, we can then characterise the above statement as “ x_k ”. For instance, if the subscript $k=4$, then the statement can be represented as “ x_4 ”. The circular limit line labelled “ Q ” shown in Figure 3 encompasses the region that contains all the members that have the same property “*quality-assurance aspect is achievable and sustainable*” (x_1, x_2, \dots, x_m).

Proceeding in the same manner as previously, we may characterise the statement “*environment-protection aspect is achievable and sustainable for resin type*” as “ z_k ”, where the letter “ z ” denotes the property named “*environment-protection aspect is achievable and sustainable*” and the subscript “ k ” denotes the stage number involved in the design process which corresponds here to “*resin type*”. For instance, if the subscript $k=2$, then the previous statement will be symbolised as “ z_2 ”. The circular limit line called “ H ” shown in Figure 3 encompasses the region that contains all the members that have the same property “*environment-protection aspect is achievable and sustainable*” (z_1, z_2, \dots, z_p).

According to this representation for modelling, the property is always symbolised with a letter x , y or z associated to quality, health or environment, respectively. Whereas the stage number involved in the design process is symbolised with a subscript k ($k=1,2,\dots, N$). The statement is denoted by “ x_k ”, “ y_k ” or “ z_k ”.

4. Ecodesign coefficients

4.1 Identification of the eco-coefficients

As there are N successive stages in the design process, we found it convenient to assign to each of Q , H and E aspects a specific coefficient representing the probability of approval. When ecological considerations are taken into account, these coefficients are now called “eco-coefficients”. From this standpoint, it may for stage (k) be assumed that:

- $\alpha = P(Q = x_k)$ is an eco-coefficient representing the probability of approval in terms of quality assurance,

- $\beta = P(H = y_k | Q = x_k)$ is an eco-coefficient representing the probability of approval with regard to health protection and known that quality is achieved; and
- $\gamma = P(E = z_k | Q = x_k \cap H = y_k)$ is an eco-coefficient representing the probability of approval with regard to environmental preservation, known that health and quality are achieved.

When the so-called “eco-coefficients” are taken into account during analysis and design of composite materials and structures, the terms “eco-analysis”, “eco-formulation”, “ecodesign”, etc. can be considered to apply.

4.2 Assessment of the eco-coefficients using code colours

To further facilitate the understanding of the ecodesign modelling and the approach allowing the calculation of different eco-coefficients, we think that it will be easy to formulate the problem by simply referring to Figure 3, which illustrates the synthesis of additive colours between the three primary RGB ones. For instance, the red colour characterises the set H (Health), the blue colour characterises the set Q (Quality) and the green colour characterises the set E (Environment). Moreover, combining these three primary colours in equal amount yields white that characterises the subset \bar{F} . Furthermore, superposing in equal amounts one of the primary colours with another colour gives a secondary colour; among them: yellow = red + green (subset D), magenta = red + blue (subset B) and cyan = blue + green (subset G). The total absence of colours yields the black, an empty subset, symbolised by \emptyset .

The eco-coefficients α , β , γ may be located between α_s and 1, β_s and 1, γ_s and 1, respectively (i.e., $\alpha_s \leq \alpha \leq 1$; $\beta_s \leq \beta \leq 1$; $\gamma_s \leq \gamma \leq 1$). The subscript “s” refers to sustainability, whereas α_s , β_s , γ_s are sustainable coefficients, and their satisfaction measures are defined and established by sustainability requirements and eco-standards.

Table 1, shows in separate cases a rating satisfaction measure in the form of colour gauges when the events Q , H and E are independent and the values of α , β and γ are varying separately.

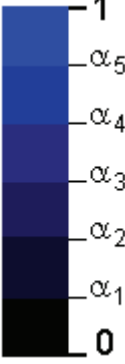
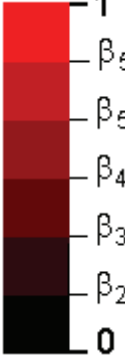
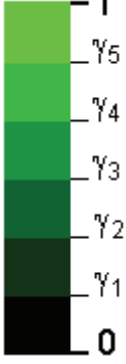















Interval	Assessment	Colour gauges		
		Quality ($q = \alpha$)	Health ($q = \beta$)	Environment ($q = \gamma$)
$q_5 \leq q \leq 1$	Excellent			
$q_4 \leq q < q_5$	Very good			
$q_3 \leq q < q_4$	Good			
$q_2 \leq q < q_3$	Fair			
$q_1 \leq q < q_2$	Poor			
$0 \leq q < q_1$	Very poor			

Table 1. Probability colour gauges for different values of α , β and γ when Q - H - E aspects are independent

On the other hand, Table 2 illustrates an example in which the Q - H - E aspects are dependent, α is fixed while β and γ are varying simultaneously.

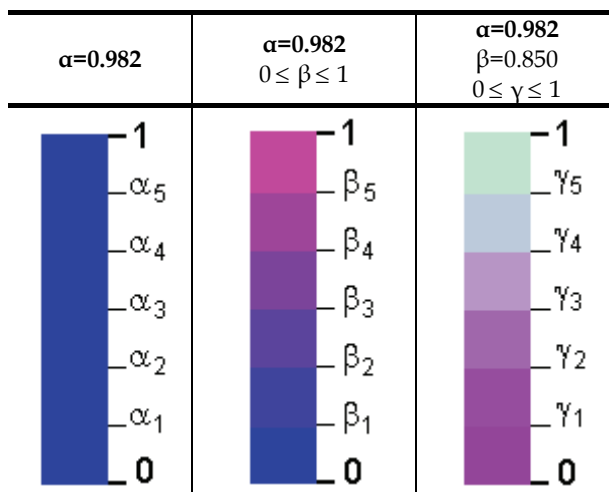


Table 2. Probability gauge for the eco-coefficients α , β and γ when Q - H - E aspects are dependent

From this primary analysis, it would be advantageous to exploit interesting results through the mixing additive colours technique when using the analogy between probability theory and code colours (Attaf, 2009). This technique can help designers and analysts involved with high-technology composite materials to easily understand the ecodesign approach and provide them with a strategic vision to reduce the negative impacts and assess the Q - H - E performances during the composite product life-cycle.

5. Ecodesign optimisation

5.1 Ecodesign flow-chart

The objective is characterised by an optimisation of the ecodesign function, in which the Q - H - E aspects all interact together (probability of the event \dot{F}). The optimisation process is represented by a flow-chart and illustrated in Figure 6. The analysis of data after each loop for the stage $k=1$ will be iterated for the other stages involved in the design process ($k=2, \dots, N$). For instance, if the final probability output results are close to unity, then the objective previously outlined in Figure 2c is fully reached! However, if the output results are not close to the objective required by the ecodesign standards, we need to search for possible new alternatives. These alternatives can be provided by practical variation of the elements x_k , y_k and z_k .

5.2 Example of alternative solution

To illustrate the procedure of optimisation, let us consider for example stage k involved in the design process and let the subscript $k=4$ characterising for instance the sentence “open-mould polymerisation process” for which we assume that the “quality assurance aspect” and the

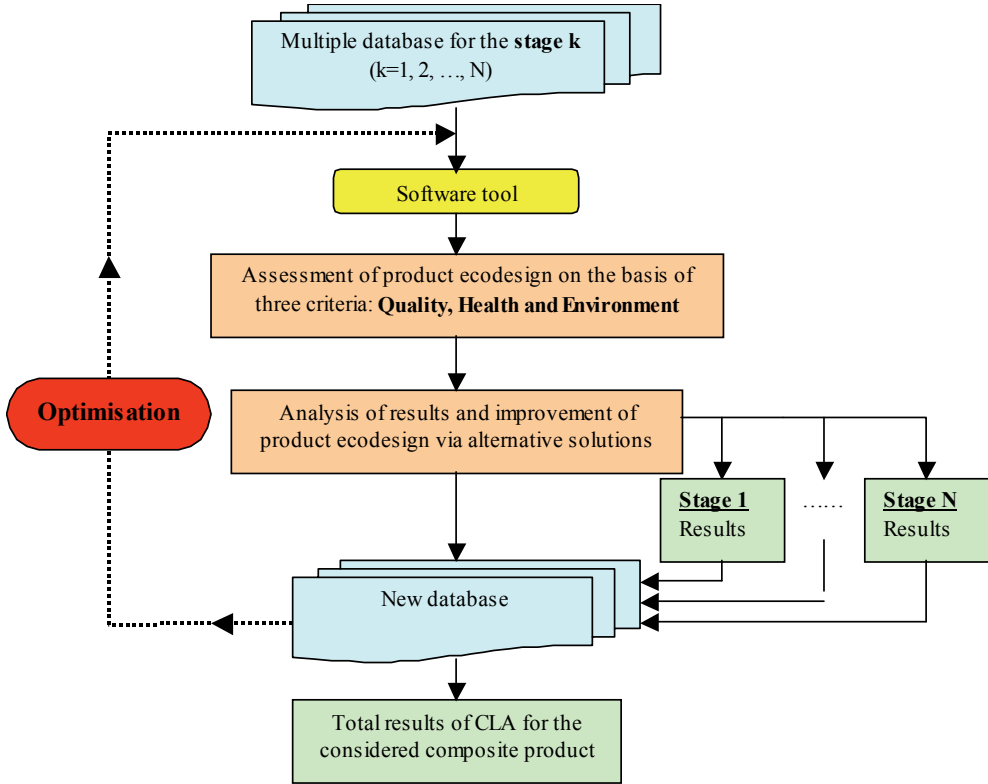


Fig. 5. Process flowchart for ecodesign of FRP composite product

"health protection aspect" symbolised respectively by " x_4 " and " y_4 " are achievable and sustainable; whereas the "environmental preservation aspect", symbolised by " z_4 " is unachievable for such a manufacturing process (open-mould). This means that the elements x_4 and y_4 belong simultaneously to both sets Q and H ; and therefore they belong to subset B ($x_4 \in B$ and $y_4 \in B$) as illustrated in Figure 6. However, the element z_4 does not belong to sets Q and H ($z_4 \notin Q$ and $z_4 \notin H$) but it belongs to set E ; so it belongs to subset S . In order to

realise the event \dot{F} , the element z_4 must be altered in practice to become a new element satisfying the following statement "environmental preservation aspect is achievable and sustainable for closed-mould polymerisation process". With this alternative solution, achieved by a modification of the moulding process from *open-mould* to *closed-mould*, the three elements x_4 , y_4 and z_4 related to stage 4 now belong to subset \dot{F} (Figure 6). Further alterations of these elements are possible in practice to reach the maximum limit target and to fully satisfy the ecodesign requirements.

As discussed previously, if we let " z_1 " denotes the statement "environmental preservation aspect is unachievable for polyester resin with high-styrene-content", this can be practically changed to yield a new element satisfying the statement "environmental preservation aspect is achievable for polyester resin with low-styrene-content". By replacing "high-styrene-content" with "low-styrene-content", this gives a new " z_1 " that satisfies the ecodesign requirements.

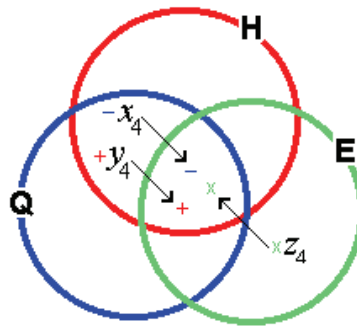


Fig. 6. Example of alternative solution related to stage 4

5.3 Multidimensional optimisation software tool

Given the complexity of the optimisation process, which has to be applied in each phase involved in the design of a FRP composite product whilst taking into account the three key criteria Q , H & E , it is important to develop a software tool capable to solve the probability problem and provide a high technique that can optimise the eco-design function.

In this software tool, the optimisation process is composed of three steps which are recapitulated as follows: the first step defines the stage involved in the design process ($k=1,2,..$), collects the associated data and specifies the target value of probability to be reached; the second step assesses and analyses results on the basis of the three main criteria (Q , H & E) and then applies if necessary the optimisation procedure to achieve the required value of probability; and the third step reports in the form of a specification sheet the final eco-results and provides a comparison with classical ones.

The analysis of the eco-design function will be made systematically by phase and according to the type of data collected, the assessment may be done using qualitative and/or quantitative method. Among the main phases subjected to an assessment procedure for FRP composite products are included:

- Phase 1: Definition of the FRP composite product functions and the design objectives.
- Phase 2: Choice of the constituents and the manufacturing processes
- Phase 3: Characterisation of the different materials and definition of thicknesses
- Phase 4: Correlation between tests and calculations
- Phase 5: Manufacture and inspection of the first FRP composite article (FAI)
- Phase 6: Qualification and certification of the FRP composite product
- Phase 7: Launch of the FRP composite product manufacturing on the Supply Chain
- Phase 8: Marketing of the FRP composite product (distribution and transport)
- Phase 9: Use, repair and maintenance of the FRP composite product
- Phase 10: End of life of the FRP composite product, waste management and recycling
- Phase 11: Evolution of lifecycle FRP composite product

For better interpretation and visualisation of results, the global eco-design assessment of the FRP composite product may be given in the form of a spider graph showing the location of eco-coefficients values with regards to the limiting envelop of the eco-design function. In addition, the other constraints such as: hygiene & security, risk, energy, cost, time factor, etc.. may be included in one of the three aspects that best matches the study.

6. Material eco-characterisation and advanced eco-formulations

Throughout the design process, it is considered that the condition of intersection between Q , H & E is always performed, so the product of the associated eco-coefficients. For notation simplicity, this product expressed by $\alpha \times \beta \times \gamma$ may be reduced and replaced by a single factor called “eco-efficiency factor”, denoted for example by the Greek letter λ . This factor will be inserted into each step involved in the design process and its measured value may be different from one stage to another. For the stage (k), the ecodesign performance is evaluated in relation to the measurement results of the factor $\lambda^{(k)}$ equals to $\alpha^{(k)} \times \beta^{(k)} \times \gamma^{(k)}$. For instance, if this factor reaches the sustainable factor *i.e.*, $\lambda^{(k)} = \lambda_s^{(k)}$, the objective required is then attained and the ecodesign condition is fully accomplished for that stage. However, if the factor $\lambda^{(k)}$ fails in stage (k), this will cause a systematic rejection of the material, the process, the method or the service used in that stage. An alternative solution is absolutely necessary before performing the next stage ($k+1$).

6.1 Eco-characterisation of composite materials

To further explain this approach, let us consider a simple standard material characterisation test under uniaxial mechanical tension, chosen because it is the easiest and most convenient mechanical test (Attaf, 2008). For better understanding and more explicit interpretation, the results are presented in the form of conventional stress-strain diagram, where the x -axis represents strain ϵ and the y -axis represents stress σ , but to clearly illustrate the different successive stages of material behaviour, we consider a ductile elastic-plastic material. As a result, the stress-strain curve in Figure 7 illustrates the linear and non-linear elastic domains, the plastic domain, and the corresponding failure point. However, no information on the material behaviour with respect to the environment and health protection is given. Since our approach is essentially based on this argument, we consider that the absence of such information in the final results may cause serious problems for human health and the environment in the short or long term (*e.g.*, asbestos). To overcome these inconveniences and achieve ecodesign approach, it is imperative to consider the environmental and health constraints in more detail and integrate them into the output results of test.

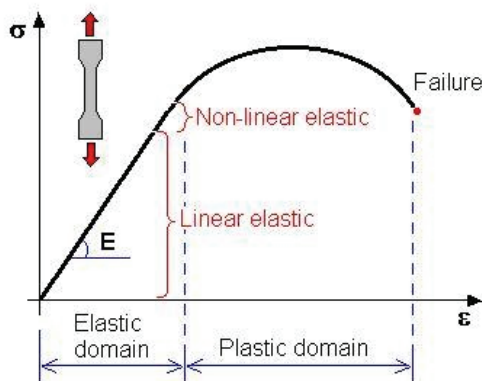


Fig. 7. Stress-strain relationship with no information on the material behaviour in relation to health and environmental aspects

This approach allows deciding very early on in the material selection process whether to approve or reject a proposed material.

In the stage of material characterisation, the environmental and health impacts are taken into account by considering the eco-efficiency factor λ . This factor will be inserted into the standard mechanical characterisation formulae of materials. Hence, Young's modulus of elasticity, determined by Hooke's law and derived from experimental results must be adapted to the actual situation by integrating health and environmental considerations into characterisation tests. Thus, the new Young's modulus of elasticity will become $\dot{\bar{E}}$ "Young's eco-modulus". The three dots ($\dot{\cdot}$) above the character E are only a brief description of the interaction between Q , H & E as discussed previously in Section 2.2.

In relation to this orientation, the modulus eco-efficiency may be evaluated by measuring the elasticity eco-efficiency factor, defined by the following ratio (Attaf, 2008):

$$\frac{\dot{\bar{E}}}{E} = \lambda \quad (8)$$

The numerator value of $\dot{\bar{E}}$ approaches the denominator value $E \neq 0$, when λ tends towards unity. As it was discussed earlier, if this value does not meet ecodesign requirements, a search for possible new alternatives can be provided to maximise the eco-coefficients until sufficient agreement is achieved. Further investigations on the optimisation of these eco-coefficients are still necessary, however.

6.2 Generalized Hooke's eco-law for unidirectional ply

In high-performance composite structures, structural components are manufactured mainly from unidirectional fibre-reinforced plies, where the ply axes are identified in the principal coordinate system with numbers 1, 2 and 3. Whereas, the laminate axes are identified in the global coordinate system (Cartesian coordinates) with letters x , y and z (Jones, 1999 & Saarela, 1994). The 1-axis and z-axis are combined into a single axis (Figure 8).

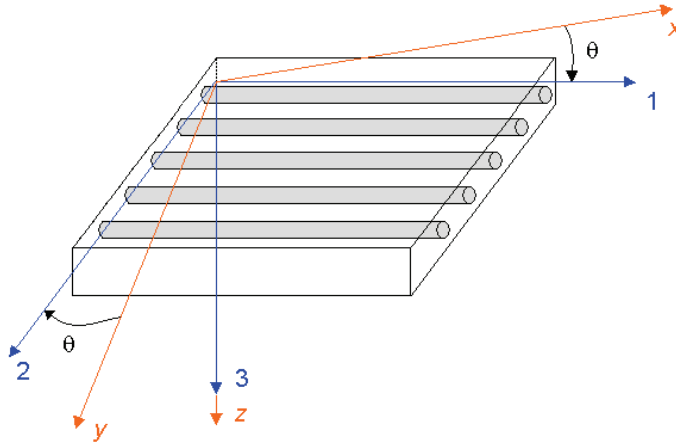


Fig. 8. Principal coordinate system (1, 2, 3) vs. global coordinate system (x , y , z) for unidirectional ply

The Young's moduli E_1, E_2, E_3 and the shear moduli G_{12}, G_{23}, G_{13} of the unidirectional ply determined from experimental tests will become $\dot{E}_1, \dot{E}_2, \dot{E}_3, \dot{G}_{12}, \dot{G}_{23}, \dot{G}_{13}$, respectively. In relation to this orientation and for a unidirectional fibre-reinforced ply, the eco-efficiency factors related to the engineering constants for the linear-elastic mechanical behaviour may be defined in the principal coordinate system as (Attaf, 2008):

$$\lambda_i = \frac{\dot{E}_i}{E_i}, \quad \lambda_{ij} = \frac{\dot{G}_{ij}}{G_{ij}} \quad \text{with} \quad \frac{\dot{E}_i}{\nu_{ij}} = \frac{\dot{E}_j}{\nu_{ji}} \quad (i,j=1,2,3 \text{ and } i \neq j) \quad (9)$$

where E_i, \dot{E}_i are classical and sustainable Young's moduli in i -direction ($i=1, 2$ and 3),

G_{ij}, \dot{G}_{ij} are classical and sustainable shear moduli in the i - j plane (i - $j=2$ - $3, 3$ - 1 and 1 - 2),

λ_i, λ_{ij} are the eco-efficiency factors of Young's and shear moduli, respectively and,

ν_{ij} is the Poisson's ratio for transverse strain in the j -direction when stressed in the i -direction. For this value, it is important to note that no attempt was made to investigate the sustainability of Poisson's ratios. Their influence is beyond the scope of this analysis. According to these assumptions and generalized Hooke's law, the strain-stress eco-relations for an orthotropic material in the principal coordinate system (1,2,3) may be written in compact matrix form as:

$$\{\varepsilon\}_{123} = \left[\dot{S}_{ij} \right]_{123} \{\sigma\}_{123} \quad (i,j=1,2,\dots,6) \quad (10)$$

where $\{\varepsilon\}_{123} = \{\varepsilon_1 \ \varepsilon_2 \ \varepsilon_3 \ \gamma_{23} \ \gamma_{31} \ \gamma_{12}\}^T$, $\{\sigma\}_{123} = \{\sigma_1 \ \sigma_2 \ \sigma_3 \ \tau_{23} \ \tau_{31} \ \tau_{12}\}^T$ are the transpose of the strain and stress vectors, and $\left[\dot{S}_{ij} \right]_{123}$ is the eco-compliance matrix of order

6×6 (6 rows by 6 columns). The components $\dot{S}_{ij} = \dot{S}_{ji}$ are defined as:

$$\begin{array}{cccccc} \dot{S}_{11} = 1/\dot{E}_1 & \dot{S}_{12} = -\nu_{12}/\dot{E}_1 & \dot{S}_{13} = -\nu_{13}/\dot{E}_1 & \dot{S}_{14} = 0 & \dot{S}_{15} = 0 & \dot{S}_{16} = 0 \\ \dot{S}_{21} = -\nu_{21}/\dot{E}_2 & \dot{S}_{22} = 1/\dot{E}_2 & \dot{S}_{23} = -\nu_{23}/\dot{E}_2 & \dot{S}_{24} = 0 & \dot{S}_{25} = 0 & \dot{S}_{26} = 0 \\ \dot{S}_{31} = -\nu_{31}/\dot{E}_3 & \dot{S}_{32} = -\nu_{32}/\dot{E}_3 & \dot{S}_{33} = 1/\dot{E}_3 & \dot{S}_{34} = 0 & \dot{S}_{35} = 0 & \dot{S}_{36} = 0 \\ \dot{S}_{41} = 0 & \dot{S}_{42} = 0 & \dot{S}_{43} = 0 & \dot{S}_{44} = 1/\dot{G}_{23} & \dot{S}_{45} = 0 & \dot{S}_{46} = 0 \\ \dot{S}_{51} = 0 & \dot{S}_{52} = 0 & \dot{S}_{53} = 0 & \dot{S}_{54} = 0 & \dot{S}_{55} = 1/\dot{G}_{13} & \dot{S}_{56} = 0 \\ \dot{S}_{61} = 0 & \dot{S}_{62} = 0 & \dot{S}_{63} = 0 & \dot{S}_{64} = 0 & \dot{S}_{65} = 0 & \dot{S}_{66} = 1/\dot{G}_{13} \end{array}$$

Also, the eco-stiffness matrix of the ply may be obtained by the inverse of the eco-compliance matrix. Thus, we can write:

$$\left[\dot{Q}_{ij} \right]_{123} = \left[\dot{S}_{ij} \right]_{123}^{-1} \quad (i,j= 1,2,...,6) \quad (11)$$

When using the eco-stiffness matrix, the stress-strain relations can be obtained by the inverse of Equation (10). Thus, we obtain:

$$\{\sigma\}_{123} = \left[\dot{Q}_{ij} \right]_{123} \{\varepsilon\}_{123} \quad (i,j= 1,2,...,6) \quad (12a)$$

Since orthotropic fibres have almost the same characteristics along 2- and 3-axis, the 2-3 plane is considered to be a plane of symmetry and the three-dimensional 123-coordinate system will be reduced to two-dimensional 12-coordinate system. Thus, Equation (12a) becomes:

$$\{\sigma\}_{12} = \left[\dot{Q}_{ij} \right]_{12} \{\varepsilon\}_{12} \quad (i,j= 1,2,6) \quad (12b)$$

where $\{\sigma\}_{12} = \{\sigma_1 \ \sigma_2 \ \tau_{12}\}^T$, $\{\varepsilon\}_{12} = \{\varepsilon_1 \ \varepsilon_2 \ \gamma_{12}\}^T$ are the stress and strain vectors in 12-coordinate system, and $\left[\dot{Q}_{ij} \right]_{12}$ is the eco-stiffness matrix of order 3×3 (3 rows by 3 columns).

Using the transformation matrix, Equation (12b) may be written, after some rearrangements, in the global xy -coordinate system as:

$$\{\sigma\}_{x,y} = \left[\overline{\dot{Q}_{ij}} \right]_{x,y} \{\varepsilon\}_{x,y} \quad (i,j=1,2,6) \quad (13)$$

where $\{\sigma\}_{x,y} = \{\sigma_x \ \sigma_y \ \tau_{xy}\}^T$, $\{\varepsilon\}_{x,y} = \{\varepsilon_x \ \varepsilon_y \ \gamma_{xy}\}^T$ are the stress and strain vector in the

global xy -coordinate system, and $\left[\overline{\dot{Q}_{ij}} \right]_{x,y}$ is the eco-stiffness matrix of order 3×3 (3 rows

by 3 columns). The components $\overline{\dot{Q}_{ij}} = \overline{\dot{Q}_{ji}}$ ($i, j = 1, 2, 6$) are functions of the fibre orientation angle, θ and the orthotropic elastic eco-moduli of the ply. By letting $C=\cos \theta$ and $S=\sin \theta$, the eco-stiffness components are defined in the global xy -coordinate system as:

$$\begin{aligned} \overline{\dot{Q}_{11}} &= \dot{Q}_{11} C^4 + 2(\dot{Q}_{12} + 2\dot{Q}_{66}) S^2 C^2 + \dot{Q}_{22} S^4 & \overline{\dot{Q}_{16}} &= (\dot{Q}_{11} - \dot{Q}_{12} - 2\dot{Q}_{66}) S C^3 + (\dot{Q}_{12} - \dot{Q}_{22} + 2\dot{Q}_{66}) S^3 C \\ \overline{\dot{Q}_{12}} &= (\dot{Q}_{11} + \dot{Q}_{22} - 4\dot{Q}_{66}) S^2 C^2 + \dot{Q}_{12} (S^4 + C^4) & \overline{\dot{Q}_{26}} &= (\dot{Q}_{11} - \dot{Q}_{12} - 2\dot{Q}_{66}) S^3 C + (\dot{Q}_{12} - \dot{Q}_{22} + 2\dot{Q}_{66}) S C^3 \\ \overline{\dot{Q}_{22}} &= \dot{Q}_{11} S^4 + 2(\dot{Q}_{12} + 2\dot{Q}_{66}) S^2 C^2 + \dot{Q}_{22} C^4 & \overline{\dot{Q}_{66}} &= (\dot{Q}_{11} + \dot{Q}_{22} - 2\dot{Q}_{12} - 2\dot{Q}_{66}) S^2 C^2 + \dot{Q}_{66} (S^4 + C^4) \end{aligned}$$

With these ecological considerations, the constituent equations for laminated composite structures can be derived using the classical lamination theory (Jones, 1999).

6.3 Constitutive eco-equations of laminates

When the environment and health impacts besides quality are taken into consideration in the structural analysis, the constitutive relations for an unsymmetrically n -layered laminated composite plate ($k=1,2,..n$), and without transverse shear deformations can, after integration through each ply thickness and summation, be written in matrix form as:

$$\begin{Bmatrix} N_x \\ N_y \\ N_{xy} \\ M_x \\ M_y \\ M_{xy} \end{Bmatrix} = \sum_{k=1}^n \int_{z_{k-1}}^{z_k} \begin{Bmatrix} \sigma_x \\ \sigma_y \\ \tau_{xy} \\ z\sigma_x \\ z\sigma_y \\ z\tau_{xy} \end{Bmatrix} dz = \begin{bmatrix} \dot{A}_{11} & \dot{A}_{12} & \dot{A}_{16} & \dot{B}_{11} & \dot{B}_{12} & \dot{B}_{16} \\ & \dot{A}_{22} & \dot{A}_{26} & \dot{B}_{12} & \dot{B}_{22} & \dot{B}_{26} \\ & & \dot{A}_{66} & \dot{B}_{16} & \dot{B}_{26} & \dot{B}_{66} \\ & & & \dot{D}_{11} & \dot{D}_{12} & \dot{D}_{16} \\ & & & & \dot{D}_{22} & \dot{D}_{26} \\ & & & & & \dot{D}_{66} \end{bmatrix} \begin{Bmatrix} \epsilon_{0x} \\ \epsilon_{0y} \\ \gamma_{0xy} \\ \kappa_x \\ \kappa_y \\ \kappa_{xy} \end{Bmatrix} \quad (14a)$$

Or in compacted matrix form:

$$\begin{Bmatrix} N \\ M \end{Bmatrix}_{xy} = \sum_{k=1}^n \int_{z_{k-1}}^{z_k} \begin{Bmatrix} \{\sigma\}_{xy} \\ z \{\sigma\}_{xy} \end{Bmatrix} dz = \begin{bmatrix} \dot{A} & \dot{B} \\ \dot{B} & \dot{D} \end{bmatrix} \begin{Bmatrix} \epsilon^0 \\ \kappa \end{Bmatrix}_{xy} \quad (14b)$$

where N and M are the resultant in-plane forces and bending/torsional moments, respectively. Whereas, ϵ^0 and κ are the associated strains and curvatures.

The eco-components of the sub-matrices \dot{A}_{ij} (extensional eco-stiffnesses), \dot{B}_{ij} (coupling eco-stiffnesses) and \dot{D}_{ij} (bending eco-stiffnesses) are expressed as:

$$(\dot{A}_{ij}, \dot{B}_{ij}, \dot{D}_{ij}) = \sum_{k=1}^n \int_{z_{k-1}}^{z_k} (\bar{Q}_{ij})_k (1, z, z^2) dz \quad (i, j = 1, 2, 6) \quad (15)$$

These sub-matrices may be assembled in a single matrix $\begin{bmatrix} \dot{C} \end{bmatrix}$ called extensional-coupling-bending eco-stiffness matrix. Thus,

$$\begin{bmatrix} \dot{C} \end{bmatrix} = \begin{bmatrix} \dot{A} & \dot{B} \\ \dot{B} & \dot{D} \end{bmatrix} \quad (16)$$

and Equation (14b) may be written as:

$$\begin{Bmatrix} N \\ M \end{Bmatrix}_{xy} = \begin{bmatrix} \dot{C} \end{bmatrix} \begin{Bmatrix} \epsilon^0 \\ \kappa \end{Bmatrix}_{xy} \quad (17)$$

6.4 Finite element eco-approach

When the analytical or mathematical solution does not exist, numerical methods such as finite element method (Jones, 1999 and Zienkiewicz et al, 2005) may be used to yield an approached solution. However, to achieve sustainable structural performance that is also based on an assessment of environmental and health performances, it is imperative to consider these constraints in more detail and integrate them into the finite element analysis. In such situation, the finite element eco-approach for dynamic analysis will first consist in resolving for one element type (e) the system of the following equations:

$$[M_e] \{\ddot{q}_e(t)\} + [\dot{K}_e] \{q_e(t)\} = \{f_e(t)\} \quad (18)$$

where $\{q_e(t)\}$ is the vector of nodal displacements and rotations, $\{\ddot{q}_e(t)\}$ is the vector of accelerations, and $\{f_e(t)\}$ is the vector of forcing functions (external loads). Whereas $[M_e]$ and $[\dot{K}_e]$ are the mass matrix and eco-stiffness matrix, respectively. These are defined by the following expressions:

$$[M_e] = \int_{\Omega_e} [E]^T [\bar{m}] [E] d\Omega_e \quad (19)$$

$$[\dot{K}_e] = \int_{\Omega_e} [S]^T [\dot{C}] [S] d\Omega_e \quad (20)$$

in which Ω_e is the surface of an element; $[\bar{m}]$ is the inertia matrix, $[E]$ is the displacement function matrix, $[S]$ is the strain interpolation matrix, and $[\dot{C}]$ is the elastic extensional-coupling-bending eco-stiffness matrix. The Jacobian matrix $[J]$ is used to allow the passage from Cartesian coordinates (x, y, z) to natural coordinates (ξ, η, ζ).

For static analysis, the acceleration vector vanishes and Equation (18) is independent of time and becomes as follows:

$$[\dot{K}_e] \{q_e\} = \{f_e\} \quad (21)$$

Assembling eco-stiffness and mass matrices, and forcing functions vector of each element involved into the generation of the whole structure yields the global system of equations:

- For dynamic eco-analysis: $[M] \{\ddot{q}(t)\} + [\dot{K}] \{q(t)\} = \{F(t)\} \quad (22)$

- For static eco-analysis: $[\dot{K}] \{q\} = \{F\} \quad (23)$

where $\{q\}$ is the vector of global displacements, $\{\ddot{q}\}$ is the vector of global accelerations, $\{F\}$ is the vector of external loads (vanishes for free vibration analysis), $[M]$ is the global mass matrix, and $[\dot{K}]$ is the global eco-stiffness matrix.

By comparing the eco-results with the classical ones that do not take into account environmental and health considerations, we can yield an estimate difference value called "eco-deviation", which may be calculated using the following relation:

$$\text{Eco-deviation (\%)} = \left| \frac{\dot{V} - V}{V} \right| \times 100 \quad (24)$$

where \dot{V} is the eco-result corresponding to $\lambda = \lambda_i$ ($0 < \lambda_i < 1$) and V is the classical result corresponding to $\lambda = 1$, generally.

For better comment and understanding of this eco-approach, the final results may be presented in the form of graphs with normalized axes. A dimensionless quantity named "eco-efficiency ratio", representing the ratio between eco-results and classical ones, can be chosen for the y -axis and denoted for example by the Greek letter $\Lambda = \dot{V}/V$. When performing stress analysis of composite materials and structures, Λ can for instance be equal to $\dot{\sigma}/\sigma$ or $\dot{\tau}/\tau$. The discrepancy between classical and sustainable results can help designers and analysts to evaluate easily environmental and health performances. Moreover, this discrepancy can be minimised via alternative solutions to reach the appropriate value required by eco-design standards.

7. Conclusion

Based on mathematical formulations, scientific, industrial and technological know-how in the field of FRP composite materials and structures, this contribution aims to innovate and develop a new approach providing the integration at each stage of the designing process three balanced key criteria characterised mainly by Quality assurance, Health protection and Environmental preservation (Q , H & E). To achieve these requirements, new criteria in the form of eco-coefficients were defined and developed. However, greater depth of study is still required to establish the rating satisfaction measure that yields the appropriate values of sustainable coefficients, which are considered as an important source of reference for comparison survey. To approach sustainability values of these coefficients, probability analysis of eco-design function and some optimisation procedures based on a new technique of additive colours were undertaken in accordance with the three balanced key criteria. When these eco-coefficients are approved by sustainability standards, they can then be integrated into formulations of design and analysis, in characterisation tests; they can also be implemented into future finite-element computer programs, etc. Designers, analysts and engineers can make better use of eco-design aspects to assess environmental and health performances when comparing eco-results with classical ones.

This investigation could be integrated in the international standards, codes and guidelines for sustainability research actions, and contribute to new orientations in the design of eco-friendly composite materials and structures. It may also be regarded as a stimulation of eco-innovation, sustainability and research activities in the field of FRP composite products eco-design and as an encouragement for designers and engineers to have a great motivation towards the integration of health and environmental aspects into the designing process. In addition, new eco-design recommendations could be developed via this innovative survey. These recommendations will, however, increase the design space of future composite materials and their products. This will offer a new data to use in evaluating the different stages of a material/process/product life-cycle.

This type of "eco-action" constitutes a multidisciplinary approach that can involve specialists in mechanical/civil/structural and process engineering, mathematics, physics,

chemistry, health, environment and sociology. In addition, the impacts that may be investigated including: (1) the undesirable substances entering in the manufacturing process, (2) the amount of emissions of greenhouse gases, (3) the level of $Q-H-E$ interaction, (4) the quantity of the waste production and expired materials, (5) the classification of the company with regard to the authorized regulations, etc. Then, alternative solutions leading to new methods of eco-design are suggested. The approved eco-coefficients may become a source of normative coefficients used for validating the different manufacturing stages and qualifying & certifying the new developed eco-composite materials and structures.

8. References

- Attaf, B. & Hollaway, L. (1990a). Vibrational analyses of stiffened and unstiffened composite plates subjected to in-plane loads. *Composites* Vol.21, No.2, (March 1990) pp.117-126, ISSN 0010-4361
- Attaf, B. & Hollaway, L. (1990b). Vibrational analyses of glass reinforced polyester composite plates reinforced by a minimum mass central stiffener. *Composites* Vol.21, No.5, (Sept.1990) pp.425-430, ISSN 0010-4361
- Attaf, B. (2007). Towards the optimisation of the eco-design function for composites. *JEC Composites*. No.34, (July-August 2007) pp.58-60, ISSN 1639-965X
- Attaf, B. (2008). Eco-characterisation of composite materials. *JEC Composites*. No.42, (July-August 2008) pp.58-60, ISSN 1639-965X
- Attaf, B. (2009). Probability approach in eco-design of fibre-reinforced composite structures. *Proceedings of CAM'2009 Conference*, Algeria, November 2009, Biskra
- Hollaway, L. & Attaf, B. (1989). On the vibration of glass/polyester composite stiffened and unstiffened rectangular plates. *Proceedings of the Seventh Int. Conf. on Composite Materials*, pp. 435-444, China, October 1989, Chinese Society of Aeronautics, Beijing
- Jones, R.M. (1999). *Mechanics of composite materials*. Taylor & Francis, Inc., ISBN 1-56032-712-X, Philadelphia
- Saarela, O. (1994). Computer programs for mechanical analysis and design of polymer matrix composites. *Prog. Polym. Sci.* Vol.19, pp 58-60, ISSN 0079-6700
- Yang, T.Y. (1986). *Finite element structural analysis*. Prentice-Hall, Inc., ISBN 0-13-317116-7, New Jersey
- Zienkiewicz, O.C., Taylor, R.L. & Zhu, J.Z. (2005). *The finite element method: its bases and fundamentals*. Elsevier Butterworth-Heinemann, ISBN 0 7506 6320 0, Oxford

Design, Manufacture and Performance Evaluation of Non-Asbestos Sealing Composites

Boqin Gu, Ye Chen and Jianfeng Zhou
*Nanjing University of Technology,
China*

1. Introduction

Asbestos was once considered to be a "miracle mineral". This naturally occurring silicate has many desirable characteristics, including resistance to fire, heat, and corrosion. It is strong, durable and flexible. Asbestos is inexpensive because it is available in abundant quantities. Its versatility has led to its use as a component of a variety of products in numerous industries (American Academy of Actuaries, 2007). The development of fiber-reinforced elastomer gaskets began in the 1880s and led to the patent application for Klingerit in 1904 (Piringer & Rustemeyer, 2004). Since more than one hundred years ago, these kinds of non-metallic gaskets, which were made of compressed asbestos fibers (CAF) materials, have been the most widely used sealing elements with a maximal yield.

Up till the 1970s, the health hazards of asbestos were recognized. Several diseases have been linked to asbestos exposure, including mesothelioma, lung cancer, other cancers, asbestosis, and pleural changes (American Academy of Actuaries, 2007). Due to the restriction on the use of asbestos, the pressure was on scientists and engineers to develop non-asbestos gasket material replacements, and asbestos was replaced by alternative fibers and fillers. These alternatives were employed in an attempt to replicate the product properties of the former CAF materials. These substitutes were developed using reinforcing fibers like aramid, glass and carbon fibers to achieve high strength, and additives like inorganic materials (e.g., clays, precipitated silica, graphite etc.). Since the 1990s, a great number of worldwide famous sealing materials manufacturers have put significant efforts onto the development of a variety of novel non-asbestos sealing composites (NASC), such as Garlock in USA, Klinger in Austria, Kempchen in Germany, and Valqua and Pilar in Japan. Collaborating with some international organizations and research institutions, they conducted a series of experimental and application researches, and obtained many valuable results (Payne & Bazergui, 1990). These investigations have laid a foundation for further studies on performance evaluations and industrial applications.

Aramid was used as reinforcing fibers in the earliest non-asbestos gasket materials, because it provided processing advantages, especially during calendaring. However, it is very expensive and has poor thermal stability. Most commonly used fibers and fillers in non-asbestos gasket materials do not achieve the outstanding stability as CAF materials do when the binding elastomers become aged. More recently, novel formulations and manufacturing

processes have been developed based on cheap reinforcing fibers, the hybrid effect of different reinforcing fibers or an adapted material structure. These non-asbestos gasket materials not only are significantly cheaper but also have a better performance at high temperatures. Gu & Chen developed two kinds of sealing composite materials. One was reinforced with aramid and pre-oxidized hybrid fibers and prepared by molding preparation method and the other was reinforced with carbon and glass hybrid fibers and manufactured by using calendar preparation method. The effect of different surface treatment methods of the fibers on the heat resistance of the composite materials was studied. The optimum prescriptions of the composites were obtained by regression design method (Gu & Chen, 2007; Chen & Gu, 2008). Gao & Chen carried out explorative investigations on the preparation method of nanometer calcium carbonate filled modifications of rubber-based sealing composite materials and on the influence of nanometer filled modifications on the mechanical properties of the prepared gasket materials (Gao & Chen, 2009). A novel material concept for compressed fiber materials was proposed to significantly decelerate the ageing of elastomer bound gasket materials by the use of special elastomers and an adapted material structure, i.e., the multi-layer structure. The steam testing, as opposed to the standard gasket testing, has been used to demonstrate this improvement (Piringer & Rustemeyer, 2004).

It is essential that gasket materials possess good mechanical performances and sealability. Mechanical performances include compressibility, resilience and stress relaxation property. They are usually used to evaluate abilities to cause gasket material deformation into flange face irregularities under assembly condition, to hold sealing surfaces of joints contacted tightly under internal pressures, and of stress retention at high temperatures, respectively. Sealability is a comprehensive performance of gaskets and indicates the ability to prevent the sealed fluid from leakage through the joints. Sealability can also be called tightness and can be measured quantitatively by the leakage rate.

In the mid 1980s, the American Pressure Vessel Research Committee (PVRC) set up "Room-temperature Mechanical Test Procedure" and "Hot Mechanical Test Procedure" for estimating the probable long-term performance and potential fire survivability of non-asbestos gaskets to guide the qualification and selection of non-asbestos spiral wound, jacketed and sheet gaskets for petroleum and petrochemical plant services in the range of 423-866K. Procedures, test fixtures, and typical test results for several process plant gaskets were discussed. An aged exposure parameter was introduced that correlates cumulative damage with exposure time and temperature for materials that degrade over time (Payne et al., 1989a; Payne et al., 1989b; Payne & Bazergui, 1990). The change in properties of some compressed sheet gasket materials subjected to temperature exposure for periods of up to one year was investigated by Marchand & Derenne. This resulted in a better understanding of the long term effect of thermal degradation on the properties of elastomeric sheet gasket materials. An improved qualification protocol based on the obtainment of the thermal endurance graph of a sheet gasket material was proposed for the extrapolation of the long term service temperature (Marchand & Derenne, 1996). Tsuji et al. researched experimentally the effect of aging time on sealing performance of non-asbestos spiral wound gaskets at elevated temperatures under either the stress controlled condition or the strain controlled condition. The tightness parameter T_p at different elevated temperatures was obtained. The results indicated that the non-asbestos spiral wound gasket had the same sealing performance as the substitute for the asbestos spiral wound gasket between 483 and

693 K (Tsuji et al., 2004). Xie et al. investigated the compressive and resilient performances and relaxation property of the developed compressed non-asbestos fiber reinforced rubber sheet gasket materials, and discussed in detail the effect of the non-asbestos fiber on the properties of the sheet gasket materials (Xie & Cai, 2002; Xie & Xie, 2004).

Systematic researches on gasket performances and their characterizations have been carried out in the Fluid Engineering and Sealing Technology Laboratory at Nanjing University of Technology since the 1980s. The compressive-resilient performance, creep and stress relaxation properties, and leakage behaviour of some types of gaskets were investigated. The representation of gasket performances was put forward, and the formulae for expressing gasket performances were obtained by means of the proposed models and regression analysis of experimental data (Gu et al., 1999; Gu et al., 2000; Gu et al., 2001; Gu, 2002; Zhu et al., 2007; Zhu et al., 2008; Gu et al., 2010). A novel tightness concept was presented, and the tightness analysis and design methods of gasket sealing joints based on the criterion of the maximum allowable leakage rate were developed. Relatively accurate predictions of leakage rates of some gasket sealing connections were also obtained (Gu & Zhu, 1988; Gu & Huang, 1997; Gu et al., 2004; Gu & Chen, 2006; Gu et al., 2007a; Gu et al., 2007b).

Up to now, much work has been fulfilled on the development, performance evaluation and engineering applications of the sealing composites reinforced with non-asbestos fibers, and many results have been achieved. However, relatively comprehensive and systematic reports on design, manufacture and performance evaluation of NASC are still very scarce, especially on the characterization of micro structural parameters, and the mechanical analysis and macro performance prediction of these materials according to the theories of micromechanics and viscoelastic mechanics.

In this chapter, manufacturing technology, surface treatment methods for reinforcing fibers, and formulation design methods of NASC are introduced. Measurements and characterizations of some micro structural parameters of fibers including their aspect ratio, orientation and distribution are investigated. A micromechanical model of single fiber cylindrical cell and a model of compressive type single-fiber cell are established, on the basis of which the methods are proposed for evaluating macro-mechanical performances of NASC, such as tension, compression, and stress relaxation. A leakage model for predicting non-asbestos gasket leakage rates is presented and verified experimentally. Furthermore, the performances of some developed NASC are also evaluated.

2. Manufacturing technology of NASC

2.1 Molding process

The molding process of NASC is similar to that of the traditional rubber based composites, as shown in Fig. 1. The plastication should be carried out using a mill mixer or an internal mixer, to improve plasticity of raw rubber. Before this step, raw rubber may be roasted in a hot chamber within 333-343 K to decrease its hardness and improve manufacturability. The roll temperature of the mill mixer should be controlled below 343 K, and the roller space is about 0.5-1 mm.

The gross rubber is obtained in the mixing step where all accessory ingredients and filling materials are evenly dispersed in broken-down rubber by extrusion and shearing actions of rollers repeatedly.

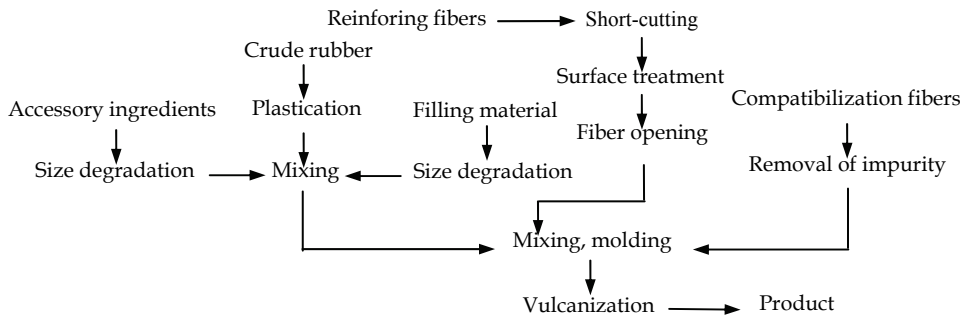


Fig. 1. A molding process of NASC

The mixing step can also be carried out in a mill mixer or an internal mixer. During mixing, the reinforcing fibers can be evenly dispersed in gross rubber, and the aspect ratio of the fibers is reduced to an appropriate value. In the vulcanization step, the rubber and a vulcanizing agent will chemically crosslink at sulfurizing pressures and temperatures. The effect of sulfurization parameters on the transverse tensile strength of aramid fiber reinforced NASC is illustrated in Fig. 2.

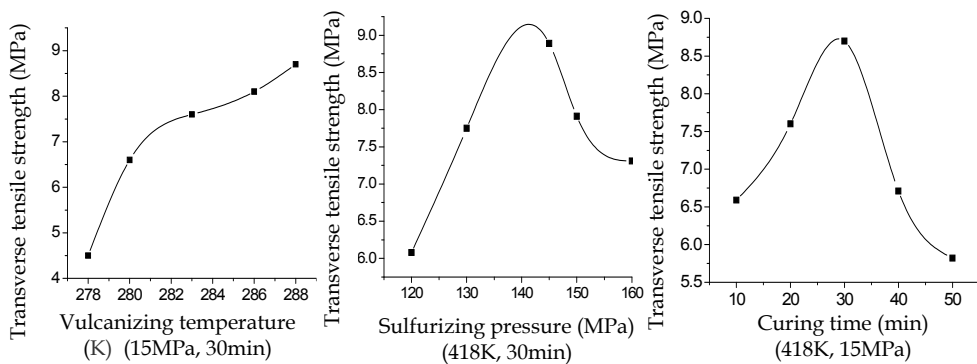


Fig. 2. The effect of sulfurization parameters on transverse tensile strength of aramid fiber reinforced NASC

2.2 Calender process

A calender process flow diagram is illustrated in Fig. 3. In this process, rubber is dissolved by an organic solvent and then mixed with other constituents. The NASC sheet is molded in a roller-type calender.

Preparation of rubber paste is fulfilled in three steps including plasticizing, mixing and dissolving. The mixing and plasticizing steps are the same as those in the molding process. The gross rubber should be separated into small pieces, and then dissolved into the rubber paste by organic solvents, such as gasoline, benzene, methylbenzene and ethyl acetate.

In the mixing step, rubber paste, filling material and reinforcing fibers are mixed, and good quality gross rubber particles with suitable diameter, humidity and hardness are prepared.

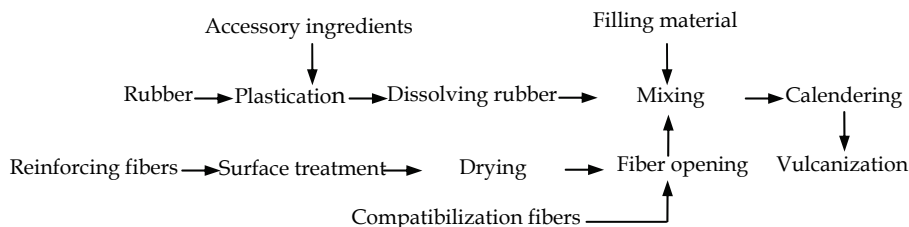


Fig. 3. A calender process of NASC

The calender process is carried out with two rollers rotating in the opposite directions. Gross rubber particles are fed into the clearance between rollers, and manufactured into NASC sheets. The operating principle of a roller-type calender is shown in Fig. 4.

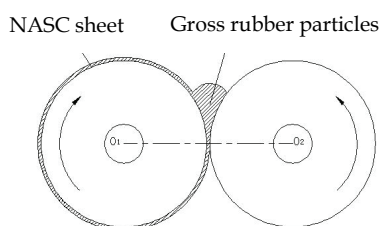


Fig. 4. The operating principle of a roller-type calender

The operating parameters of the calender process mainly include speed ratio of rollers, calender speed (roller surface speed), roller temperature, feed speed, roller clearance and extrusion pressure.

The two rollers are usually thermally stabilized by steam and cool water, respectively. Accordingly, they are called hot roller and cold roller. The appropriate speed ratio of two rollers is in the range of 1.04-1.06.

2.3 Surface treatment of non-asbestos reinforcing short fibers

The surface activity of most non-asbestos fibers is very poor, which leads to the lower wettability between fibers and rubbers. Therefore, in order to obtain a good interface bonding strength, the reinforcing fibers must be pretreated by suitable surface treatment methods. The commonly used surface treatment methods include surface activating treatment and dipping treatment.

Some NASC were developed by the molding process with aramid short fiber as reinforcing fiber, and NBR and NR as elastic binding material. Three surface treatment methods were adopted to pretreat aramid fiber; they are RFL latex dipping, HRH binding agent treatment and silane coupling agent dipping. The results of SEM observation of the developed NASC are shown in Fig. 5.

It can be seen that the surfaces of the aramid fibers without treatment are very smooth, and there are only a few rubber particles adhering on the fiber surfaces. After surface treatments, the adhesion effect between fiber and rubber matrix was obviously improved.

Carbon short fiber can be treated by coupling agent dipping process or epoxide resin coating process after pretreating by air oxidation process or low temperature plasma process. The transverse tensile strength of NASC developed by the calender process was

tested after aging treatment at 623 K, and the results are shown in Fig. 6. It can be seen that surface treatments have improved the reinforcing effects of carbon fiber.

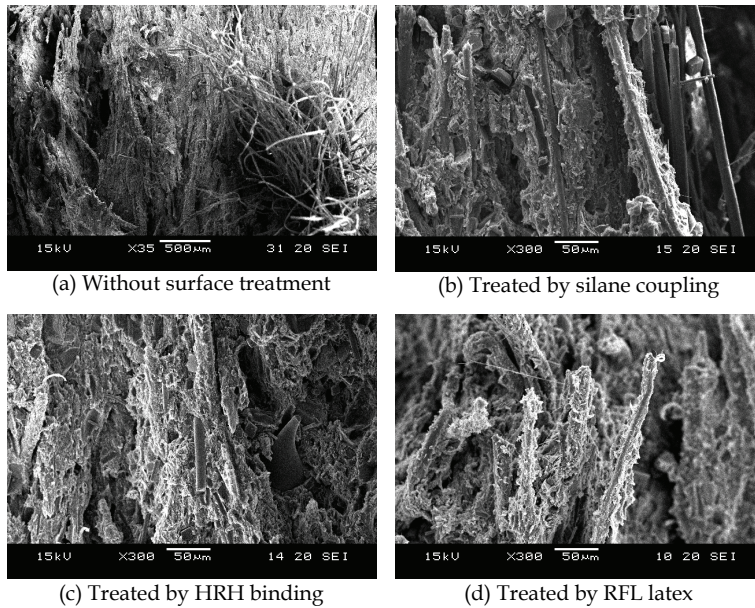


Fig. 5. SEM photos of transverse tensile fracture sections of aramid fiber reinforced NASC

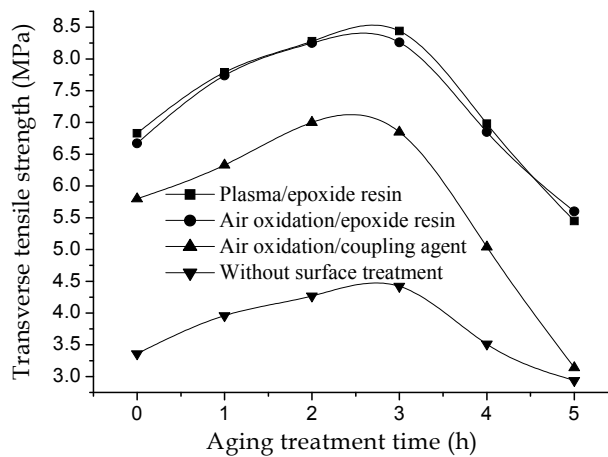


Fig. 6. Transverse tensile strength of carbon fiber reinforced NASC after aging at 623 K

The treatment effect of glass fiber by coupling agent is also distinctive, as illustrated in Fig. 7. The glass fiber should be firstly dipped in a silicon coupling agent water solution for pre-treatment, and then immersed into an epoxide resin methylbenzene solution (2wt%) for further coating treatment. Finally, they must be dried at 423 K to solidify impregnated layer.

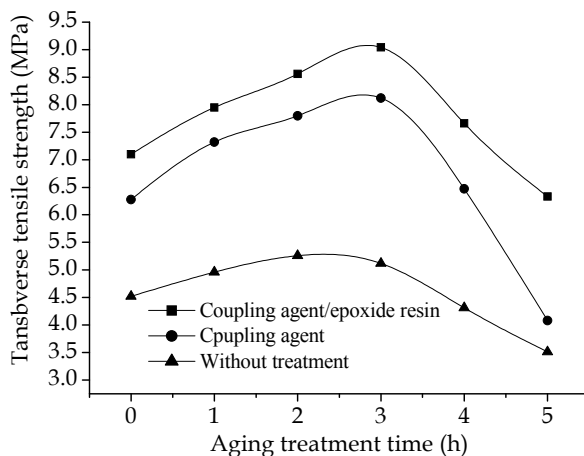
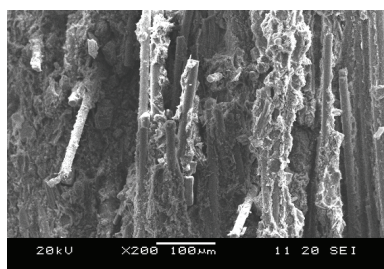
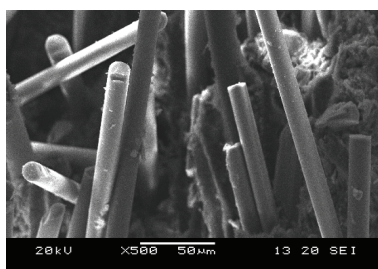


Fig. 7. Transverse tensile strength of glass fiber reinforced NASC after aging at 623 K

The SEM photos of transverse tensile fracture sections of carbon/glass hybrid fiber reinforced NASC aged at 623 K for 5 hours are shown in Fig. 8. It can be seen that the intertwined and the rubber coating conditions of fibres are obviously improved after the surface treatment of the fibers by the coupling agent/epoxide resin coating process.



(a) Treated by coupling agent/epoxide resin coating process



(b) Without surface treatment

Fig. 8. SEM photos of transverse tensile fracture sections of carbon/glass hybrid fiber reinforced NASC

3. Formulation design of NASC

3.1 Selection of raw materials for NASC

The main constituents of NASC are non-asbestos reinforcing fibers, elastic binding materials, filling materials and chemical additives. There are great differences of the physicochemical properties between non-asbestos fibers and asbestos fibers. Therefore, in the design of NASC, the effects of the properties and the content of the non-asbestos reinforcing fibers on the performances and manufacturability of the NASC should be paid more attention.

The suitable non-asbestos reinforcing fibers are usually selected according to the performance requirements of NASC. Heat resistance, aspect ratio, medium-resistance, compatibility with rubber, performance-price ratio and source of the reinforcing fibers

should be considered, too. The commonly used non-asbestos reinforcing fibers include carbon fiber, aramid fiber, glass fiber, mineral wool, plant fiber, and so on.

Elastic binding material binds reinforcing fibers and other filling materials together, makes up elastic network structure, and provides compression-resilience and medium-resistance performances of NASC. Natural rubber, nitrile rubber, styrene-butadiene rubber, neoprene rubber, ethylene propylene rubber, fluorine rubber and silicone rubber can all be used as the elastic binding materials of NASC. In consideration of the product performances and price, natural rubber and nitrile rubber are preferably selected.

The filling materials of rubber products include compatibilization filler, reinforcing filler and functional filler. Commonly used filling materials include brucite fiber or sepiolite fiber, carbon black, carbonate, sulphate, metallic oxides, and silicon oxides. In NASC, large grained filler must pair up with short grained filler to maintain proper inter space among rubber bulk material, fibers and filler particles, and ensure sufficient combination between rubber and filler particles.

The selectable accessory ingredients include vulcanizing agents, vulcanization accelerators, vulcanizing activators, anti-aging agents, plasticizing agents and colouring agents etc.. The mixture of dibenzothiazyl disulfide (40 wt%) and tetramethylthiuram disulfide (60 wt%) can be used as a vulcanization accelerator. Zinc oxide (3-5 wt%) and stearic acid (0.5-2 wt%) can be selected as a vulcanizing activator. N-phenyl-n-isopropyl ursol (4010NA) is usually used as the anti-aging agent of rubbers, and the amount is about 1-4wt% (related to rubber weight). Plasticizing agents, colouring agents, solvent, blowing agents, dusting agents and reinforcing resins etc. can also be adopted as accessory ingredients.

3.2 Formulation design of NASC

The uniform design method can be used to further decrease test number in formulation optimization. The approximate formulation of composites can be obtained by uniform design, but the principal and subordinate factors which affect material performances cannot be analyzed by the design table. Furthermore, the regression design can also be adopted to optimize the formulation of NASC. In the mixing regression design, a small quantity of test points will be selected to obtain enough experimental data. According to these data, the regression equation can be derived from the relationship between the test index and the different constituent contents. Finally, the optimization point can be obtained.

3.2.1 Formulation design of aramid fiber reinforced NASC

The formulation design of the aramid fiber reinforced NASC can be defined as the design problem with three components which include reinforcing fiber (aramid fiber), elastic binding material (NBR/NR) and filling material (compatibilization fiber). In consideration of the attribute for processing of the material, the content of components in NASC is limited by Eq. (1).

$$7\% \leq x_1 \leq 22\%, \quad 40\% \leq x_2 \leq 55\%, \quad 10\% \leq x_3 \leq 25\% \quad (1)$$

where x_1 , x_2 and x_3 are the weight contents of aramid fiber, compatibilization fiber (brucite fiber or sepiolite fiber) and elastic binding material, respectively.

The contents of other ingredients, such as accessory ingredient, can be determined according to the contents of three components mentioned above. By selecting 5 factor levels for each component, the uniform design scheme for test points is listed in Table 1.

Test points	x_1 (wt%)	x_2 (wt%)	x_3 (wt%)
①	7	43	19
②	10	49	25
③	13	55	17
④	16	40	23
⑤	19	46	15
⑥	22	52	21

Table 1. Experiment scheme according to the uniform design method

According to the test points in Table 1, aramid fiber reinforced materials were developed by the molding process. It can be seen in Table 2 that the transverse tensile strength of the materials developed according to ①, ② and ③ test points meets the strength requirement (≥ 7.0 MPa). The strength of the materials prepared according to ④ and ⑤ test points are obviously higher than that of scheme ①. Too much reinforcing fiber in the material of formulation ⑥ led to the poor processing manufacturability and low production efficiency, and therefore, formulation ① was chosen to be the preliminary scheme.

Test points	Transverse tensile strength (MPa)
①	3.55
②	5.26
③	8.81
④	6.75
⑤	10.69
⑥	10.87

Table 2. Transverse tensile strength of aramid fiber reinforced NASC

Results of the single factor experiment about the usage of elastic binding material and aramid fiber are given in Tables 3 and 4, respectively. The aramid fiber and the rubber contents are suggested to be 13 wt% and 20 wt%, respectively.

Performances	Rubber content (wt%)				
	15%	17%	20%	23%	26%
Transverse tensile strength (MPa)	9.22	8.89	8.7	6.87	6.54
Compression rate (%)	4.75	10.06	11.2	13.66	11.4
Resilience rate (%)	43.20	52.15	52.23	51.04	45.7
Stress relaxation rate (%)	28.9	29.4	32.35	37.06	36.15

Table 3. The effect of rubber content on performances of NASC (The amount of aramid fiber is 13 wt%)

Performances	Aramid fiber content (wt%)			
	7%	10%	13%	15%
Transverse tensile strength (MPa)	6.57	7.77	8.70	8.86
Compression rate (%)	15.40	11.36	11.20	9.08
Resilience rate (%)	37.78	48.48	52.23	50.36
Stress relaxation rate (%)	41.42	37.80	32.35	29.42

Table 4. The effect of aramid fiber content on performances of NASC (The amount of elastic binding material is 20 wt%)

The optimization formulation of aramid fiber reinforced NASC is listed in Table 5.

Gradient	Weight content (wt%)	Gradient		Weight content (wt%)
NBR-26	13.0	Filling materials	Calcium carbonate	7.9
NR	7.0		Kaolin clay	3.4
Aramid fiber	13.0		White carbon black	3.4
Compatibilization fiber	45.3		Soap stone powder	2.3
Vulcanizing agent	2.5	Other accessory ingredients		1.8
Curing catalyst	0.4			

Table 5. Formulation of aramid fiber reinforced NASC

3.2.2 Formulation design of carbon/glass hybrid fiber reinforced NASC

The regression design of carbon/glass hybrid fiber reinforced NASC can be defined as the design problem with three components which include reinforcing hybrid fiber (carbon/glass hybrid fiber), elastic binding material (NBR) and filling material (compatibilization fiber and other stuffings). In consideration of the attribute for processing of the material, the component contents in NASC are in the following ranges:

$$0.12 \leq X_1 \leq 0.25, 0.4 \leq X_2 \leq 0.8, 0.1 \leq X_3 \leq 0.5 \quad (2)$$

where X_1 , X_2 and X_3 are the contents of the elastic binding material, the reinforcing fiber and the filling material, respectively.

The stress relaxation rate y of NASC after ageing treatment at 573 K is used as an evaluating indicator, and the regression design of NASC is to obtain the regression equation by the experiments under the following conditions:

$$a_i \leq X_i \leq b_i, (i = 1, 2, 3) \quad \text{and} \quad X_1 + X_2 + X_3 = 1 \quad (3)$$

where a_i and b_i are the constraint conditions described in Eq. (2).

A symmetrical complex Z is established. The coordinate system $x_1x_2x_3$ represents the actual design space of the components of NASC, and the coordinate system $z_1z_2z_3$ represents the encoding space. Accordingly, the relationship between Z and X can be expressed by:

$$X_1 = a_1 + (b_1 - a_1)z_1/B, \quad X_2 = a_1 + (b_2 - a_2)z_2/B, \quad X_3 = 1 - (X_1 + X_2) \quad (4)$$

where $B = \max(z_{ij})$, i is the test number, and j the variable number. The coordinates of the actual test points are listed in Table 6, where the stress relaxation rates of the materials after ageing treatment at 573 K are also listed.

The stress relaxation rate of NASC after ageing at 573 K can be expressed by the coordinates of the encoding point, and the regression equation holds:

$$\hat{y} = 63z_1 + 77z_2 + 120.8z_3 - 137.6z_1z_2 + 0.49z_1z_3 - 261.6z_2z_3 \quad (5)$$

where \hat{y} is the predicted value of the stress relaxation rate of the material, and z_1 , z_2 and z_3 are the coordinates of the encoding point.

NO.	Encoding content of components			Actual content of components			Relaxation rate y (%)
	z_1	z_2	z_3	X_1	X_2	X_3	
1	0	1/2	1/2	0.12	0.667	0.213	51.6
2	1/2	0	1/2	0.207	0.4	0.393	32.9
3	1/2	1/2	0	0.207	0.667	0.127	43.9
4	1/4	1/4	1/2	0.163	0.533	0.303	34.6
5	1/4	1/2	1/4	0.163	0.667	0.17	42.3
6	1/2	1/4	1/4	0.207	0.533	0.26	31.3
7	3/4	1/8	1/8	0.25	0.467	0.283	58.4
8	1/8	3/4	1/8	0.142	0.8	0.058	52.4
9	1/8	1/8	3/4	0.142	0.467	0.392	43.1

Table 6. Experimental scheme and test results

The purpose of prescription optimization is to improve the heat resistance and the attribute for processing of NASC, to reduce the self-cost of the raw materials of the product, and to ensure the stress relaxation rate of the material satisfying the index prescribed in the product standard. The prescription optimization of NASC is to obtain the optimal values of z_1 , z_2 and z_3 under the following conditions:

$$z_i \geq 0, \sum_{i=1}^3 z_i = 1, z_1 = z_{1\min}, z_2 = z_{2\min}, \hat{y} \leq 35 \quad (i = 1, 2, 3) \quad (6)$$

According to Eq. (5), the coordinates of the best theoretic design point of the contents of the components in NASC can be obtained, as $z_1=0.38$, $z_2=0$ and $z_3=0.63$. From Eq. (4), the formulation is $x_1=0.186$, $x_2=0.4$ and $x_3=0.414$.

Some NASC were prepared when the weight ratio (carbon fiber to glass fiber) equalled to 4:0, 3:1, 2:2, 1:2, 1:3 and 0:4 respectively. The experimental results of the transverse tensile strength and the stress relaxation rate of these materials after ageing treatment at 573 K for 5 hours are shown in Fig. 9. It can be found that the strength of the material is the highest and the relaxation rate is relatively low when the weight ratio is 2:3 (weight content of carbon fiber in hybrid fibers is 40%).

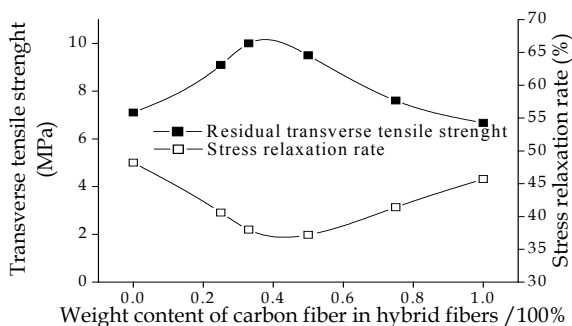


Fig. 9. The effect of carbon fiber content in hybrid fibers on transverse tensile strength and stress relaxation rate of NAFC

Therefore, the optimization formulation of the NASC reinforced with carbon/glass hybrid fibers was obtained, as listed in Table 7.

Component	Content (wt%)	Component		Content (wt%)
NBR	18.6	Accelerating agent		0.22
Carbon fiber	16.0	Zinc white		0.48
Glass fiber	24.0	Stearinic acid		0.18
Sepiolite fiber	10.3	Antiaging protective		0.6
Phenolic resin	8.38	Filling material	Lime carbonate	6.31
Hyperfine graphite powder	7.44		Kaolin clay	3.2
Vulcanized agent	0.35		Soap stone powder	1.6
			Carbon black	2.34

Table 7. Formulation of carbon/glass hybrid fibers reinforced NASC

4. Measurement and characterization of micro structures of NASC

4.1 Measurement and characterization of aspect ratio

The aspect ratio of short fiber determines the transfer and distribution of stress in material, and its distribution regularity can be obtained by measuring the radius and the length of fibers in the NASC products. Some samples of NASC were prepared. Using organic solvents, such as gasoline or toluene, to dissolve the matrix rubber, the short fibers different in size are left and dried. Considering the fiber radius is about micron, a digital camera with high-resolution is used to take pictures of fibers, and the length and radius of each short fiber are obtained by numerically analyzing the pictures. Then the distribution of aspect ratios can be obtained by counting the aspect ratios of 500 to 1000 fibers. The typical histograms of aspect ratios of aramid fibers can be seen in Fig. 10.

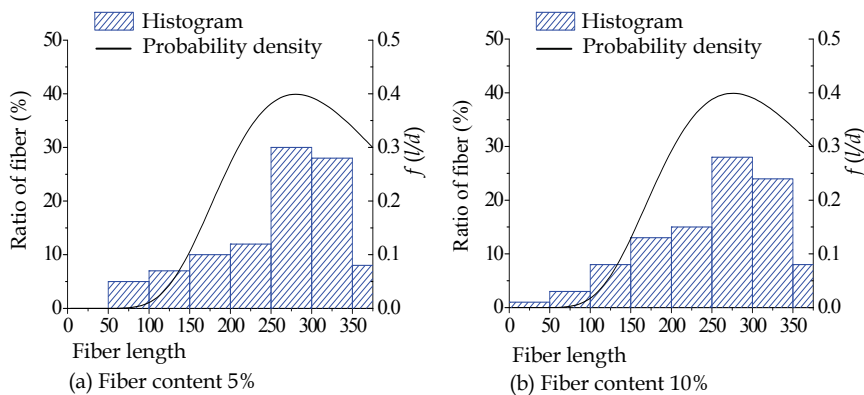


Fig. 10. Aspect ratio distribution of aramid fibers with the initial length of 4-6 mm

The distribution of aspect ratios in NASC is influenced by the initial aspect ratio, the rupture characteristic and the content of fibers, the matrix characteristic and the preparation process.

If the aspect ratio varies in a relatively small range, it can be characterized by the mean aspect ratio. If it distributes dispersedly, however, the characterization with a distribution function is appropriate. Furthermore, a histogram can also be used to express the distribution of aspect ratios without considering the dispersity of aspect ratios.

The log-normal density function is usually used to characterize the aspect ratios, as Eq. (7) expresses.

$$f(l/d) = \frac{1}{\sqrt{2\pi}} \exp \left[-\frac{[\ln(l/d) - a]^2}{2b^2} \right] \quad (7)$$

where $a = \sqrt{2[\ln(\bar{l}/d) - \ln(l_{\text{mod}}/d)]}/3$, $b = [2\ln(\bar{l}/d) + \ln(l_{\text{mod}}/d)]/3$, \bar{l}/d is the mean aspect ratio and l_{mod}/d the maximum probability density of the aspect ratio.

The arithmetical mean of aspect ratios can be calculated by Eq. (8).

$$\bar{l}_s/d = \frac{1}{m} \sum_{n=1}^m (l_n/d) \quad (8)$$

where \bar{l}_s/d is the average value of aspect ratios, m is the number of short fibers and l_n/d is the aspect ratio of the number n short fiber. The arithmetical mean aspect ratio can also be calculated by Eq. (9) if the histogram of aspect ratios is known.

$$\bar{l}_s/d = \sum p_i (l_i/d) / \sum p_i \quad (9)$$

where l_i/d is the aspect ratio of fibers in the interval i , and p_i is the ratio of the number of fibers whose aspect ratios are in the interval i to the total number of fibers.

4.2 Measurement and characterization of fiber orientation

Investigating the orientation of fibers in matrix will provide both theoretical explanations for the reinforcing mechanism of short fibers and the basis for prediction and optimization of mechanical properties of NASC.

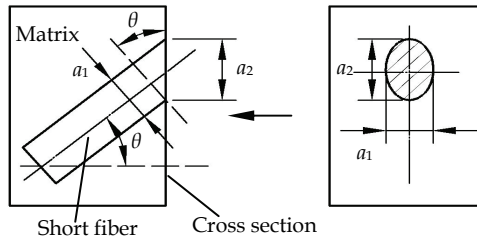


Fig. 11. A schematic diagram of the section-analysis method

A proprietary technology was developed to obtain the fiber orientation in matrix. Four steps are involved. Firstly, cut a rectangular block of material and hold it in position by a clamp in the slicer. Secondly, slice the cross section of the material block at -423 K using the slicer

knife to machine a smooth end face, of which the normal direction should be along the rolling direction. Thirdly, visually observe the end face using a microscope associated with a high-resolution digital camera. Finally, analyze the photos and find out the configuration of the elliptical cross section of fibers. The orientation angle can be determined from the long axis and the short axis of the ellipse, as illustrated in Fig. 11.

The normal direction of the cross section is in accordance with the reference direction, and the orientation angle θ is the separation angle between the axial direction of a fiber and the reference direction. The relationship among θ and the long axis length a_1 and the short axis length a_2 is in the form

$$\theta = \arccos(a_1/a_2) \quad (10)$$

The orientation of a fiber can be characterized by a histogram, a distribution function or modified coefficients. The orientation expressed by an exponential density function $f(\theta)$ is

$$f(\theta) = \xi \exp(-\lambda\theta) / (1 - \exp(-\pi\lambda/2)) \quad (11)$$

where ξ is the fiber orientation parameter. In order to utilize the results of the fiber orientation characterization to predict the macro mechanical properties of NASC, the modified coefficients are introduced. The longitudinal modified coefficient $f_{\theta 1}$ can be calculated by Eq. (12) based on the distribution function.

$$f_{\theta 1} = \int_0^{\pi/2} f(\theta) \cos^2 \theta d\theta \quad (12)$$

$f_{\theta 1}$ is employed to evaluate the influence of fiber orientations on longitudinal mechanical property. The transversal mechanical property is evaluated by the transverse orientation coefficient $f_{\theta 2}$ which can also be obtained based on a distribution function or a histogram given by Eqs. (13) and (14), respectively.

$$f_{\theta 2} = \int_0^{\pi/2} f(\theta) \sin \theta \cos \theta d\theta \quad (13)$$

$$f_{\theta 2} = \sum_{n=1}^{m_0} f_{\theta}(\theta_n) \sin \theta_n \cos \theta_n \quad (14)$$

4.3 Fiber distribution in matrix

Theoretical work on NASC is usually based on the assumption that fibers are stiff and straight in matrix. The real fibers, however, bend and wind together. With the reduce of fiber contents or the increase of fiber lengths, fiber bending and winding are enhanced. Due to the forming process, the bending, winding and uneven distribution of fibers always exist randomly and are very difficult to be characterized.

4.4 Thickness of interface

For most fiber reinforced composites, the thickness of interface between a fiber and the matrix is very small and hence is usually not considered. For NASC, however, to enhance

the reinforcing effect of fibers and to optimize the bonding capability of fiber surface, short fibers should be pretreated using surface conditioning agents before mixing, and the interface has great influence on mechanical properties of NASC. The interface thickness can be easily determined by calculating the change in the fiber radius before and after pretreatment.

4.5 Porosity

Some pores will occur during the preparation process of NASC, especially in the sulfuration process. Most of these pores exist in the interface and they will change the stress transfer mode. The porosity p , which is the ratio of the total volume of all pores to the volume of the composite, can be used to evaluate the volume fraction of pores in the composite.

5. A micromechanical model and prediction of macro performances

Loads exerting on NASC will be transferred to fibers through matrix, and the mechanism relates to constitutive equations and mechanical behaviors of fibers, matrix and interface phase. According to the thermo-viscoelastic theory and the shear-lag theory of fibrous composites, a micromechanical model of a single fiber cylindrical cell, which includes a fiber, the matrix and their interphase, is established.

5.1 A micromechanical model of NASC

Fig. 12 illustrates a micromechanical model of NASC, where l is the fiber length, L the matrix length and $L \approx l$. The volume content of fiber is V_f .

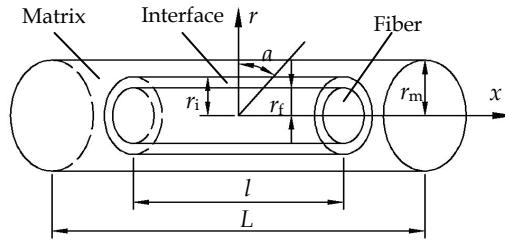


Fig. 12. A micromechanical model of NASC

The stress transfer procedure can be seen in Fig. 13.

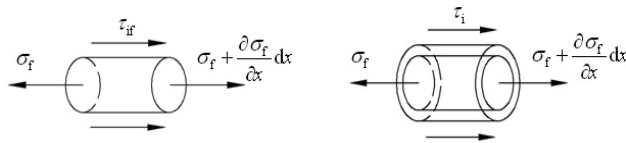


Fig. 13. Micromechanical stress transfer in NASC

When the single fiber cylindrical cell is only subjected to the tension load along the x axis, the circumferential and the radial stresses in the model are much less than the axial stress, and they can be neglected.

The equilibrium relationship of the stresses shown in Fig. 13 can be expressed by

$$\frac{\partial \sigma_f(x)}{\partial x} = -\frac{2\tau_{if}(x)}{r_f} \quad (15)$$

where $\sigma(x)$ is the axial stress in fiber and $\tau_{if}(x)$ is the shear stress on fiber surface. The axial shear stress in matrix $\tau_m(r, x)$ can be expressed by

$$\tau_m(r, x) = \frac{(r_m^2 - r^2)r_i}{(r_m^2 - r_i^2)r} \tau_{im}(x) \quad (16)$$

where $\tau_{im}(x)$ is the shear stress at the interface boundary near the matrix.

The shear stress in the matrix is a time dependent physical quantity, and it holds the following relationship with the shear strain.

$$\frac{\partial u_m(r, x, t)}{\partial r} = \int_0^t J_{tm}(t-s) d\tau_m(r, x, t) \quad (17)$$

where $u_m(r, x, t)$ is the axial displacements of the matrix, and $J_{tm}(t-s)$ is the creep function. If the bond of both the matrix and the fiber with interface ideally, the axial displacement of the matrix can be expressed by

$$u_m(r, x, t) = u_i(r_i, x, t) + \frac{r_f}{\mu_i} \ln\left(\frac{r_i}{r_f}\right) \tau_{if}(x, t) + \frac{[2r_m^2 \ln(r/r_i) - (r^2 - r_i^2)]r_i}{2(r_m^2 - r_i^2)} \int_0^t J_{tm}(t-s) d\tau_{im}(x, t) \quad (18)$$

The strain of the matrix $\varepsilon_m(r, x, t)$ holds

$$\begin{aligned} \varepsilon_m(r, x, t) = \frac{\partial u_m(r, x, t)}{\partial x} = \frac{\sigma_f(x)}{E_f} + \alpha_f \Delta T - \frac{r_f^2}{2\mu_i} \ln\left(\frac{r_i}{r_f}\right) \frac{\partial^2 \sigma_f(x, 0)}{\partial x^2} \\ - \frac{[2r_m^2 \ln(r/r_i) - (r^2 - r_i^2)]r_i^2}{4(r_m^2 - r_i^2)} \left[J_{tm}(t) \frac{\partial^2 \sigma_f(x, 0)}{\partial x^2} - \int_0^t J_{tm}(t-s) \frac{\partial^2 \dot{\sigma}_f(x, s)}{\partial x^2} ds \right] \end{aligned} \quad (19)$$

According to the viscoelastic theory, the shear stress of the matrix $\tau_{if}(x, t)$ holds

$$\tau_{if}(x, t) = \frac{u_m(r_m, x, t) - u_i(r_i, x, t) - \frac{r_f}{\mu_i} \ln\left(\frac{r_i}{r_f}\right) \tau_{if}(x, t)}{[2r_m^2 \ln(r_m/r_i) - (r_m^2 - r_i^2)]r_f / [2(r_m^2 - r_i^2)]} dG_{rm} \quad (20)$$

where G_{rm} is the relaxation function of $\tau_{if}(x, t)$. Differentiating $\sigma_f(x, t)$ by x gives

$$\frac{\partial^2 \sigma_f(x, t)}{\partial x^2} = -\frac{2 \left[\frac{\partial u_m(r_m, x, t)}{\partial x} - \frac{\partial u_i(r_i, x, t)}{\partial x} + \frac{r_f^2}{2\mu_i} \ln\left(\frac{r_i}{r_f}\right) \frac{\partial^2 \sigma_f(x, t)}{\partial x^2} \right]}{[2r_m^2 \ln(r_m/r_i) - (r_m^2 - r_i^2)]r_f^2 / [2(r_m^2 - r_i^2)]} dG_{rm} \quad (21)$$

Considering $u_i(r_f, x, t) = u_f(r_f, x, t)$, $\frac{\partial u_i(r_f, x, t)}{\partial x} = \frac{\partial u_f(r_f, x, t)}{\partial x} = \varepsilon_f = \frac{\sigma_f(x, t)}{E_f} + a_f \Delta T$ and $\frac{\partial u_m(r_m, x, t)}{\partial x} = \varepsilon_m(r_m, t)$, Eq. (22) is obtained.

$$\begin{aligned} \frac{\partial^2 \sigma_f(x, t)}{\partial x^2} + \frac{2 \frac{r_f^2}{2\mu_i} \ln\left(\frac{r_i}{r_f}\right)}{\left[2r_m^2 \ln(r_m/r_i) - (r_m^2 - r_i^2)\right] r_f^2 / \left[2(r_m^2 - r_i^2)\right]} \left[\frac{\partial^2 \sigma_f(x, t)}{\partial x^2} G_m(0) + \int_0^t \frac{\partial^2 \sigma_f(x, s)}{\partial x^2} \dot{G}_m(t-s) ds \right] \\ - \frac{2}{\left[2r_m^2 \ln(r_m/r_i) - (r_m^2 - r_i^2)\right] r_f^2 E_f / \left[2(r_m^2 - r_i^2)\right]} \left[\sigma_f(x, t) G_m(0) + \int_0^t \sigma_f(x, s) \dot{G}_m(t-s) ds \right] \\ + \frac{2[\varepsilon_m(r_m, t) - a_f \Delta T]}{\left[2r_m^2 \ln(r_m/r_i) - (r_m^2 - r_i^2)\right] r_f^2 / \left[2(r_m^2 - r_i^2)\right]} dG_m = 0 \end{aligned} \quad (22)$$

Eq. (22) is the micromechanical model of NASC which expresses the stress transfer regularity among the matrix, the fiber and their interface.

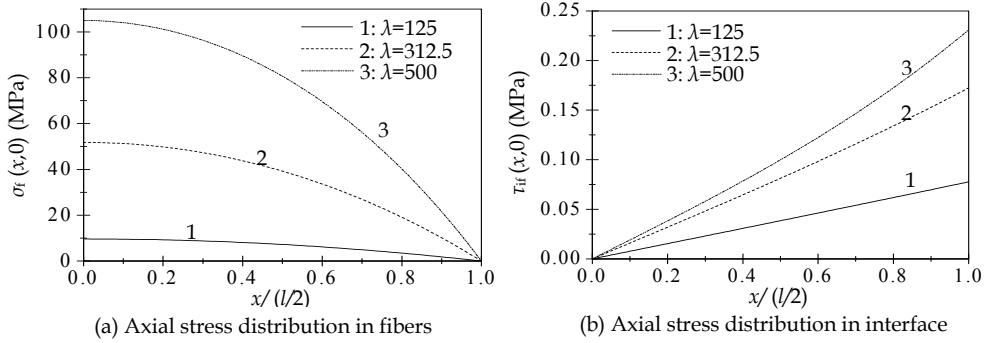


Fig. 14. Influence of the fiber aspect ratio on the stress distribution

The stresses in fibers and interface are illustrated in Fig. 14, where the coordinate x represents the axial distance from the midst ($x=0$) to the end ($x=l/2$) of the fibers. Fig. 14(a) reveals that the axial stress in the fibers σ_f reduces from the midst to the end, and with the increasing aspect ratio λ , σ_f at the fiber end increases. Fig. 14(b) illustrates the shear stress distribution in interface at the fiber side, and the shear stress increases from the midst to the end.

5.2 Prediction of mechanical performances of NASC

5.2.1 Prediction of the stress-strain relationship

Since the module of interface is much smaller than that of fibers and the interface thickness is much smaller than the matrix, the load is borne mainly by the fibers and the matrix. When the aspect ratio of the fiber is no larger than a critical value, the stress-strain relationship can be expressed by

$$\sigma_c(\varepsilon_c) = f_{\theta 1} f_i f_f V_f \bar{\sigma}_f(\varepsilon_c) + V_m \bar{\sigma}_m(\varepsilon_c) \quad (23)$$

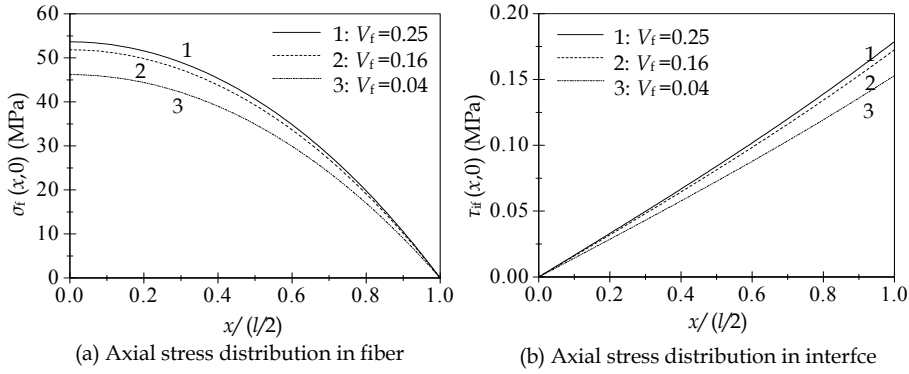


Fig. 15. Influence of the fiber volume fraction on the stress distribution

where $f_{\theta 1}=1$ when all fibers are parallel to the load direction, otherwise $f_{\theta 1}=0.5$; f_i is the correction coefficient for interface performance obtained by experiments; $f_i = (1 - V_f^2)$ and

$$\bar{\sigma}_f(\epsilon_c) = \left[1 - \frac{\tanh(\beta_0 \lambda / a_0)}{\beta_0 \lambda / a_0} \right] E_f (\epsilon_c - a_f \Delta T), \quad \bar{\sigma}_m(\epsilon_c) = E_m \epsilon_c \quad (24)$$

When the aspect ratio of the fibers is larger than the critical value, the relationship between stress and strain can be expressed by

$$\sigma_c(\epsilon_c) = \begin{cases} f_{\theta 1} f_i f_f V_f \bar{\sigma}_f(\epsilon_c, \bar{\lambda}) + V_m \bar{\sigma}_m(\epsilon_c, \bar{\lambda}) & \epsilon_c \leq \epsilon_{cf} \\ f_{\theta 1} f_i f_f V_f \bar{\sigma}_f(\epsilon_c, \bar{\lambda}/2) + V_m \bar{\sigma}_m(\epsilon_c, \bar{\lambda}/2) & \epsilon_c > \epsilon_{cf} \end{cases} \quad (25)$$

where ϵ_{cf} is the tensile strain of the fibers at the time it breaks, which holds

$$\epsilon_{cf} = \sigma_{fu}^T / \left\{ E_f \left[1 - \frac{1}{\cosh(\beta_0 \lambda / a_0)} \right] \right\} + a_f \Delta T \quad (26)$$

5.2.2 Prediction of the tensile module

Due to the effect of fibers, the maximum permissible deformation of NASC is only about 10% of that of rubber and the bearing capacity of NASC is greatly improved. The tensile module can be used to characterize the bearing capacity of NASC. The longitudinal tensile module E_{cL} can be calculated by Eq. (27) if the aspect ratios of fibers are relatively concentrated, otherwise it can be calculated by Eq. (28).

$$E_{cL} = f_p \left(f_{\theta 1} f_i f_f V_f \frac{\bar{\sigma}_f}{\epsilon_c} + V_m E_m \right) \quad (27)$$

$$E_{cL} = f_p \left(\sum_{n=1}^m f_{\theta 1} f_i f_f V_{fn} \frac{\bar{\sigma}_{fn}}{\epsilon_c} + f_m V_m E_m \right) \quad (28)$$

where $\bar{\sigma}_{fn}$ can be calculated according to Eq. (29).

$$\bar{\sigma}_{fn} = \left[1 - \frac{\tanh(\beta_0 \bar{\lambda}_n / \alpha_0)}{\beta_0 \lambda / \alpha_0} \right] E_f (\varepsilon_c - \alpha_f \Delta T) \quad (29)$$

where $\bar{\lambda}_n$ is the mean aspect ratio of fibers with the length l_n , V_{fn} is the volume content of fibers with the length l_n , and $f_p = 1 - 1.9p + 0.9p^2$. The Halpin-Tsai equation is employed to predict the transverse tensile module of NASC E_{cH} with single orientation.

$$E_{cH} = \frac{1 + 2\eta V_f}{1 - \eta V_f} E_m \quad (30)$$

where

$$\eta = \frac{E_f/E_m - 1}{E_f/E_m + 2} \quad (31)$$

In consideration of the effect of fiber length and orientation and porosity of material on the transverse tensile module, Eq. (32) is established.

$$E_{cH} = f_p \left(\frac{1 + 2V_f}{1 - V_f} E_m + f_{\theta 2} f_i f_f V_f \frac{\bar{\sigma}_f}{\varepsilon_c} \right) \quad (32)$$

5.2.3 Prediction of the longitudinal tensile strength

The temperature-related longitudinal tensile strength σ_{cl}^T of NASC can be calculated by Eq. (33).

$$\sigma_{cl}^T = f_{\theta 1} f_i f_f V_f \bar{\sigma}_f^T + f_d V_m \bar{\sigma}_m^T \quad (33)$$

where $f_d = (1 - V_f)$, $\bar{\sigma}_f^T$ is the mean stress in fibers when tensile failure occurs and it can be obtained from the micromechanical model of NASC, $\bar{\sigma}_m^T$ is the mean stress in the matrix when tensile failure occurs and $\bar{\sigma}_m^T = E_m^T \varepsilon_{cu}^T$, and f_d is the weakening coefficient of rubber induced by fibers.

When the aspect ratio λ is smaller than the critical value λ_c , the debonding between fibers and the matrix will occur. However, when $\lambda > \lambda_c$, the fiber breaks. Therefore, the temperature-related longitudinal tensile strength can be calculated according to Eq. (34).

$$\sigma_{cl}^T = f_{\theta 1} f_i f_f V_f \left[\int_{\lambda_{min}}^{\lambda_c} f(\lambda) \lambda (\tau_s^T - \Delta \tau_i^T) d\lambda + \int_{\lambda_c}^{\lambda_{max}} f(\lambda) (1 - 0.5\lambda_c/\lambda) (\sigma_{fu}^T - \Delta \sigma_f^T) d\lambda \right] + f_d V_m \bar{\sigma}_{mm}^T \quad (34)$$

where $\Delta \sigma_f^T$ is the stress in fibers induced by temperature change and $\Delta \tau_i^T$ is the shear stress

in fibers, $\Delta \sigma_f^T = \left[1 - \frac{\tanh(\beta_0 \lambda / \alpha_0)}{\beta_0 \lambda / \alpha_0} \right] E_f \alpha_f \Delta T$ and $\Delta \tau_i^T = \frac{E_f \alpha_f \Delta T}{\lambda}$.

5.2.4 Prediction of the transverse tensile strength

The transverse tensile strength is a main evaluating indicator for NASC in engineering, and its prediction may be performed according to 3 cases, as follows.

1. Debonding of interface from fiber

In this case, the transverse tensile strength σ_{ch}^T can be calculated by

$$\sigma_{\text{ch}}^T = \sqrt{\Pi V_f} t_{\text{if}}^T + 2 \frac{t_i}{r_f} \sqrt{\frac{V_f}{\Pi}} \sigma_{\text{ih}}^T + \left(1 - 2 \frac{t_i + r_f}{r_f} \sqrt{\frac{V_f}{\Pi}} \right) \sigma_{\text{mh}}^T \quad (35)$$

Eq. (35) can be used to predict the transverse tensile strength assuming that all fibers orientate in the same direction at the moment the matrix debonds from the fibers. If the fibers orientate in different directions, some will bear the longitudinal load. In this case, the transverse tensile strength is larger than that calculated by Eq. (35), and it can be calculated by Eq. (36).

$$\sigma_{\text{ch}}^T = f_{\theta 3} \left(\sqrt{V_f \Pi} t_{\text{if}}^T + 2 \frac{t_i}{r_f} \sqrt{\frac{V_f}{\Pi}} \sigma_{\text{ih}}^T \right) + f_{\theta 2} f_i f_f V_f \overline{\sigma_f^T} + \left(1 - 2 \frac{t_i + r_f}{r_f} \sqrt{\frac{V_f}{\Pi}} \right) \sigma_{\text{mh}}^T \quad (36)$$

2. Debonding of interface from matrix

If all fibers orientate in the same direction at the moment the interface debonds from the matrix, the transverse tensile strength σ_{ch}^T can be calculated by Eq. (37).

$$\sigma_{\text{ch}}^T = \frac{t_i + r_f}{r_f} \sqrt{V_f \Pi} t_{\text{im}}^T + \left(1 - 2 \frac{t_i + r_f}{r_f} \sqrt{\frac{V_f}{\Pi}} \right) \sigma_{\text{mh}}^T \quad (37)$$

If fibers orientate in different directions, σ_{ch}^T can be calculated by Eq. (38).

$$\sigma_{\text{ch}}^T = f_{\theta 3} \frac{t_i + r_f}{r_f} \sqrt{\Pi V_f} t_{\text{im}}^T + f_{\theta 2} f_i f_f V_f \overline{\sigma_f^T} + \left(1 - 2 \frac{t_i + r_f}{r_f} \sqrt{\frac{V_f}{\Pi}} \right) \sigma_{\text{mh}}^T \quad (38)$$

3. Damage of interface

The transverse tensile strength can be calculated by

$$\sigma_{\text{ch}}^T = \frac{F_H}{WL} = \sqrt{V_f \Pi} t_{\text{is}}^T + 2 \frac{t_i}{r_f} \sqrt{\frac{V_f}{\Pi}} \sigma_{\text{ih}}^T + \left(1 - 2 \frac{t_i + r_f}{r_f} \sqrt{\frac{V_f}{\Pi}} \right) \sigma_{\text{mh}}^T \quad (39)$$

Using Eq. (39), the transverse tensile strength σ_{ch}^T can be predicted assuming that all fibers orientate in the same direction at the moment the interface is damaged. If fibers orientate in different directions, σ_{ch}^T can be calculated by Eq. (40).

$$\sigma_{\text{ch}}^T = f_{\theta 3} \left(\sqrt{V_f \Pi} t_{\text{is}}^T + 2 \frac{t_i}{r_f} \sqrt{\frac{V_f}{\Pi}} \sigma_{\text{ih}}^T \right) + f_{\theta 2} f_i f_f V_f \overline{\sigma_f^T} + \left(1 - 2 \frac{t_i + r_f}{r_f} \sqrt{\frac{V_f}{\Pi}} \right) \sigma_{\text{mh}}^T \quad (40)$$

5.2.5 Prediction of compression-resilience performances

NASC is used to make gaskets, and the direction of compressive loads acting on it is normal to the orientation direction of fibers. The model of a compressive type single-fiber cell (Fig.

16) is established to derive the compression-creep constitutive equation of NASC with the assumption $L \approx l$. The cell model is divided into three parts along compression-resilience direction; the first part consists of matrix, interface and fiber (0-1), the second part consists of matrix and interface (1-2), and the third part includes only matrix (2-3).

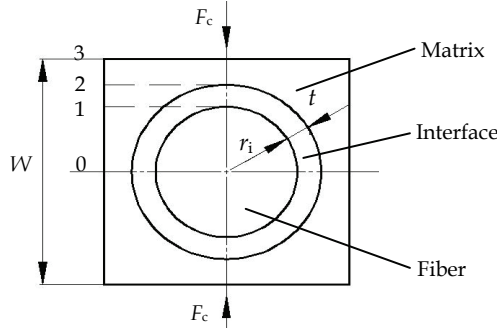


Fig. 16. A model of a compressive type single-fiber cell

The total strain of the material ε_{cc} under the load F_c holds

$$\varepsilon_{cc} = \frac{2}{W} \left[\varepsilon_{c0-1} r_f + \varepsilon_{c1-2} t_i + \varepsilon_{c2-3} \left(\frac{W}{2} - t_i - r_f \right) \right] \quad (41)$$

The compressive stress and strain of material relate to time. The compression-creep constitutive equation of NASC is in the form

$$\begin{aligned} \varepsilon_{cc}(t) = & \left(\frac{2}{\sqrt{2}E_f} + \frac{2t_i}{\sqrt{t_i^2 + 2t_i r_f E_i}} \right) \sigma_{cc}(t) + 2 \left[\sigma_{cc}(0) J_{cm}^T(t) + \int_0^t J_{cm}^T(t-\varsigma) \frac{d\sigma_{cc}(\varsigma)}{d\varsigma} d\varsigma \right] \\ & \times \left(\frac{1}{2} - \frac{t_i \sqrt{V_f/\Pi}}{r_f} - \sqrt{V_f/\Pi} \right) - \left[2\alpha_f \sqrt{V_f/\Pi} + \frac{2\alpha_i t_i}{r_f} \sqrt{V_f/\Pi} + 2\alpha_m \left(\frac{1}{2} - \frac{t_i \sqrt{V_f/\Pi}}{r_f} - \sqrt{V_f/\Pi} \right) \right] \Delta T \end{aligned} \quad (42)$$

The compression rate of NASC can be calculated by

$$\begin{aligned} R_c = & \left(\frac{2}{\sqrt{2}E_f} + \frac{2t_i}{\sqrt{t_i^2 + 2t_i r_f E_i}} \right) \sigma_{cc}(t) + 2 \int_0^t J_{cm}^T(t-\varsigma) d\varsigma \left(\frac{1}{2} - \frac{t_i \sqrt{V_f/\Pi}}{r_f} - \sqrt{V_f/\Pi} \right) \frac{\Delta \sigma_{cc}(t)}{\Delta t} \\ & - \left[2\alpha_f \sqrt{V_f/\Pi} + \frac{2\alpha_i t_i}{r_f} \sqrt{V_f/\Pi} + 2\alpha_m \left(\frac{1}{2} - \frac{t_i \sqrt{V_f/\Pi}}{r_f} - \sqrt{V_f/\Pi} \right) \right] \Delta T \end{aligned} \quad (43)$$

Substituting $\Delta T=0$ into Eq. (43) gives the compressive rate of NASC at room temperature.

The compressive strain can be calculated by

$$\varepsilon_{cc} = \left(\frac{2}{\sqrt{2}E_f} + \frac{2t_i}{\sqrt{t_i^2 + 2t_i r_f E_i}} \right) \sigma_{cc}(t) + [X + Y(t)] \left(1 - \frac{2t_i \sqrt{V_f/\Pi}}{r_f} - 2\sqrt{V_f/\Pi} \right) \frac{\Delta \sigma_{cc}(t)}{\Delta t} \quad (44a)$$

$$- \left[2\alpha_f \sqrt{V_f/\Pi} + \frac{2\alpha_i t_i}{r_f} \sqrt{V_f/\Pi} + 2\alpha_m \left(\frac{1}{2} - \frac{t_i \sqrt{V_f/\Pi}}{r_f} - \sqrt{V_f/\Pi} \right) \right] \Delta T \quad (44b)$$

where $X = \int_{0^+}^t J_{cm}^T(t-\zeta) d\zeta$ and $Y(t) = \int_{0^+}^t J_{cm}^T(t-\zeta) d\zeta$.

After unloading the compressive load, the residual compressive strain is

$$\varepsilon_{cb} = Y(t) \left(1 - \frac{2t_i \sqrt{V_f/\Pi}}{r_f} - 2\sqrt{V_f/\Pi} \right) \frac{\sigma_{cc}(t)}{t} \quad (45)$$

The resilient rate of NASC can be obtained by

$$R_c = \frac{\varepsilon_{bb}}{\varepsilon_{cc}} \quad (46)$$

where

$$\begin{aligned} \varepsilon_{bb} = & \left(\frac{2}{\sqrt{2}E_f} + \frac{2t_i}{\sqrt{t_i^2 + 2t_i r_f E_i}} \right) \sigma_{cc}(t) + X \left(1 - \frac{2t_i \sqrt{V_f/\Pi}}{r_f} - 2\sqrt{V_f/\Pi} \right) \frac{\Delta \sigma_{cc}(t)}{\Delta t} \\ & - \left[2\alpha_f \sqrt{V_f/\Pi} + \frac{2\alpha_i t_i}{r_f} \sqrt{V_f/\Pi} + 2\alpha_m \left(\frac{1}{2} - \frac{t_i \sqrt{V_f/\Pi}}{r_f} - \sqrt{V_f/\Pi} \right) \right] \Delta T \end{aligned} \quad (47)$$

Substituting $\Delta T=0$ into Eq. (46) gives the resilient rate of NASC at room temperature.

5.2.6 Prediction of creep behavior

The creep behavior equation of NASC can be expressed by Eq. (48).

$$\begin{aligned} \varepsilon_{cc}(t) = & \left(\frac{2}{\sqrt{2}E_f} + \frac{2t_i}{\sqrt{t_i^2 + 2t_i r_f E_i}} \right) \sigma_{cc}(t) + 2\sigma_{cc}(0) J_{cm}^T(t) \left(\frac{1}{2} - \frac{t_i \sqrt{V_f/\Pi}}{r_f} - \sqrt{V_f/\Pi} \right) \\ & - \left[2\alpha_f \sqrt{V_f/\Pi} + \frac{2\alpha_i t_i}{r_f} \sqrt{V_f/\Pi} + 2\alpha_m \left(\frac{1}{2} - \frac{t_i \sqrt{V_f/\Pi}}{r_f} - \sqrt{V_f/\Pi} \right) \right] \Delta T \end{aligned} \quad (48)$$

Because the strain in both fiber and interface is much smaller than that in matrix, only the strain in matrix is considered under compressive load. Then the stress-strain relationship of the third part in Fig.6 resulted from the resilience constitutive equation is in the form

$$\sigma_{cm}(t) = \varepsilon_{c2-3}(0) G_{cm}^T(t) + \int_{0^+}^t G_{cm}^T(t-\zeta) \left[\frac{d\varepsilon_{c2-3}(\zeta)}{d\zeta} + \alpha_m \frac{dT(\zeta)}{d\zeta} \right] d\zeta \quad (49)$$

If the compressive strain ε_{cc} is constant during the course of stress-resilience, Eq. (50) is obtained.

$$\sigma_{cm}(t) = \varepsilon_{c2-3}(0) G_{cm}^T(t) + \int_{0^+}^t G_{cm}^T(t-V) \alpha_m \frac{dT(V)}{dV} dV \quad (50)$$

The stress-resilience equation of NASC is in the form

$$\sigma_{cc}(t) = \frac{\varepsilon_{cc}(0)G_{cm}^T(t)}{1 - \frac{2t_i\sqrt{V_f/\Pi}}{r_i} - 2\sqrt{V_f/\Pi}} + \int_0^t G_{cm}^T(t-\varsigma)\alpha_m \frac{dT(\varsigma)}{d\varsigma} d\varsigma \quad (51)$$

The detailed derivation of Eqs. (7)-(51) can be found elsewhere (Zhu, 2008).

6. Performance evaluation of NASC

6.1 Mechanical performances of non-asbestos sealing composites

The properties of NASC specified in current standards include mainly density, transverse tensile strength, plasticity, oil resistance, and so on. The performances of non-asbestos sealing gaskets can be divided into two types. One is related to the performance indexes of gasket products, which are the main items of product inspection prescribed in gasket product standards. These performance indexes are the important basis for evaluating the quality of gasket products. They involve compressibility, resilient rate, stress relaxation rate and leakage rate (AQSIQ, 2003; AQSIQ, 2008). The other is correlated with the gasket constants in current code design guidelines, such as gasket yield factor y which is defined as the minimum gasket stress required to cause the gasket material to deform into the flange face irregularities and gasket factor m which is defined as the ratio of the minimum gasket stress needed to hold the joint sealed under the operating conditions to the internal pressure p (ASME, 2007). In this section, the theoretic prediction and experimental evaluation of some performances of NASC and gasket products are presented.

6.1.1 Test apparatus and procedure

A series of tests for tensile property, compressibility, resilient rate, and stress relaxation property were conducted on an INSTRON 3367 universal testing machine. Samples were made of the developed NASC reinforced with aramid fiber, as mentioned in section 3.2.

For tensile tests, the dumbbell-shaped samples were adopted, and the tests were performed according to the Chinese standard GB/T 1447-2005 "Fiber-reinforced plastics composites/determination of tensile properties". The test conditions are listed in Table 8.

Sample Quantity	Sample Dimension (mm)	Fiber Length (mm)	Fiber Content (wt%)	Tensile speed (mm/min)	Temperature (K)
36	20×10×2.5	1-3, 4-6, 7-9	5, 10, 15, 20, 30, 40	200	293, 373, 423

Table 8. The conditions for tensile tests

The compressibility and resilient rate tests were carried out according to the Chinese standard GB/T 12622-2008 "Standard test method for compressibility and recovery of gaskets for pipe flanges". The test conditions are listed in Table 9.

Sample Quantity	Sample Dimension (mm)	Fiber Content (wt%)	Loading Speed (mm/min)	The Maximum Stress (MPa)	Temperature (K)
8	10×10×2.5	20, 40	200	10, 20	293

Table 9. The conditions for compressibility and resilient rate tests

For the tests of the stress relaxation property, the samples were placed in the chamber of the testing machine and heated to the desired test temperatures. After the temperature remained constant for about 5 minutes, the compressive loads were applied to the samples. The change in compressive stress of the samples was measured over time under the constant sample deformation. The test conditions are listed in Table 10.

Sample Quantity	Sample Dimension (mm)	Fiber Content (wt%)	Loading Speed (mm/min)	The Maximum Stress (MPa)	Temperature (K)
8	10×10×2.5	20, 40	200	10, 20	293, 423

Table 10. The conditions for stress relaxation tests

6.1.2 Results and discussions

Figs. 17 and 18 show the stress-strain curves of the samples at room temperature with different fiber mean aspect ratios $\bar{\lambda}$ and fiber volume contents V_f , respectively.

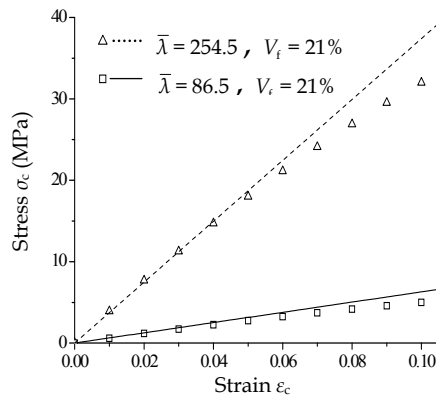


Fig. 17. Stress-strain curves of NASC with different fiber aspect ratios

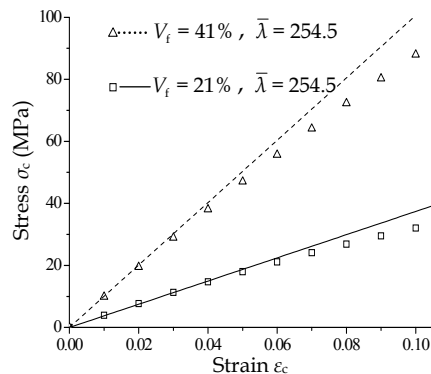


Fig. 18. Stress-strain curves of NASC with different fiber volume contents

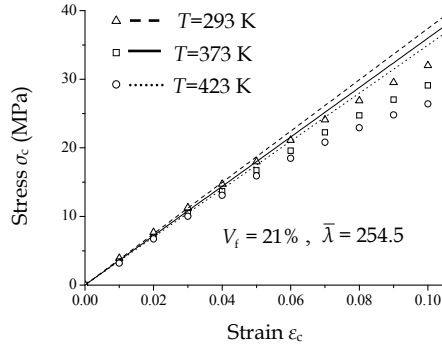


Fig. 19. Stress-strain curves of NASC at different test temperatures

Fig. 19 illustrates the stress-strain relationships of the samples at different test temperatures with a known fiber mean aspect ratio and a given fiber volume content. In these figures, symbols “ Δ , \square , \circ ” represent experimental data, and the curves are plotted according to the prediction formulae proposed in section 5.2. It can be seen from the Figs. 17-19 that the slope of stress-strain curves of NASC increases with the increase of fiber mean aspect ratio and fiber volume content. Aramid fiber has a good reinforcing effect on elastomer matrix composites. The larger the fiber mean aspect ratio, the more obvious is the reinforcing effect. Because the modulus of aramid fiber is much larger than those of elastomer matrix material and compatibilization fiber like sepiolite fiber, the increase in the aramid fiber content results in the significant augment of the strength of NASC.

The error between the experimental data and values predicted using the derived constitutive equation increases with increasing strains, and all the predicted stresses are larger than those obtained by experiments. The essential reason for the error of prediction is that the difference between the aspect ratios of various fibers was neglected. The changes in the transverse tensile strength of NASC with fiber mean aspect ratio and fiber volume content are shown in Figs. 20-21.

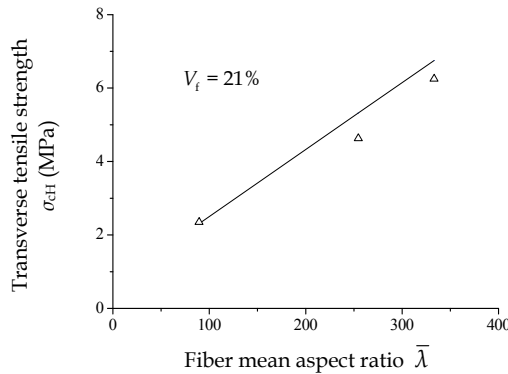


Fig. 20. Relationship between transverse tensile strength and fiber mean aspect ratio

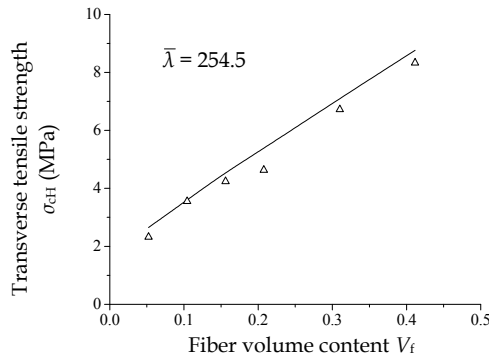


Fig. 21. Relationship between transverse tensile strength and fiber volume content

Fig. 22 illustrates the effect of test temperature on the transverse tensile strength. In these Figures, symbol "Δ" represents experimental data, and the curves represent the prediction results. The transverse tensile strength increases with the increase in the fiber mean aspect ratio and the fiber volume content. The transverse tensile strength of NASC is interrelated with temperature, and it decreases with increasing temperature. The temperature induces thermal stresses in the fiber, matrix and fiber-matrix interface, which affect the temperature-dependent tensile strength of the composite finally. Because the coefficient of thermal expansion of the elastomer matrix is much larger than that of the fiber, big thermal stresses both in the fiber and in the matrix will be generated with variation of temperature, and a small shear stress in the fiber-matrix interface is produced as well (Zhu et al., 2008). These factors result in the decrease of transverse tensile strength with increasing temperature.

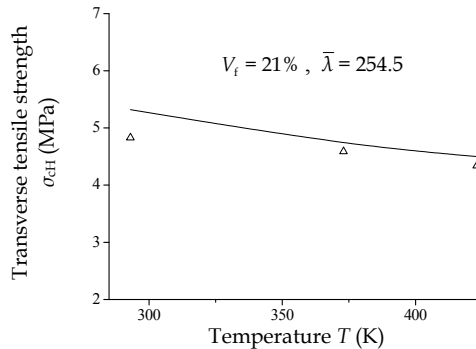


Fig. 22. Effect of temperature on transverse tensile strength

The compressibility and resilient rate of NASC obtained by tests and those predicted using Eqs. (43) and (46) are listed in Table 11. It can be found that the compressibility of NASC increases with increasing the maximum compressive stress and decreasing the fiber volume content, while the resilient rate decreases with the increase in the maximum compressive stress and the fiber volume content.

Fiber Content (wt%)	The Maximum Compressive Stress (MPa)	Compressibility (%)			Resilient Rate (%)		
		Test Data	Prediction Result	Relative Error (%)	Test Data	Prediction Result	Relative Error (%)
21	10	31.1	30.1	3.3	69.3	62.5	10.3
21	20	36.2	33.8	6.9	62.7	55.3	12.5
41	10	23.1	21.6	6.7	54.8	48.0	13.2
41	20	28.3	25.9	8.9	51.2	46.6	9.4

Table 11. Compressibility and resilient rate of NASC

Figs. 23-25 present the test and prediction results of stress relaxation property of NASC, in which symbols " Δ ", " \square " represent experimental results, and the curves are plotted according to the prediction values of stress relaxation property using Eq. (51). The stress relaxation rate increases with increasing initial stress and temperature and decreasing fiber volume content. The fiber mean aspect ratio and orientation have less evident influence on the stress relaxation property of NASC. The experimental and prediction results are basically identical, and the maximum error is about 8.5%.

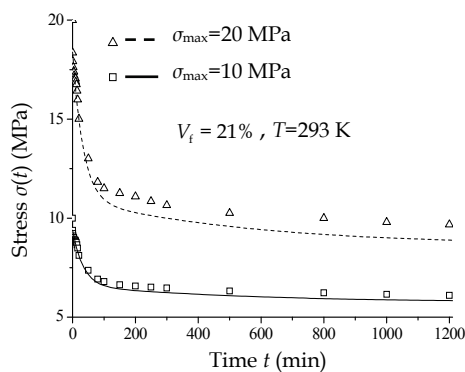


Fig. 23. Stress relaxation curves of NASC under different maximum stresses

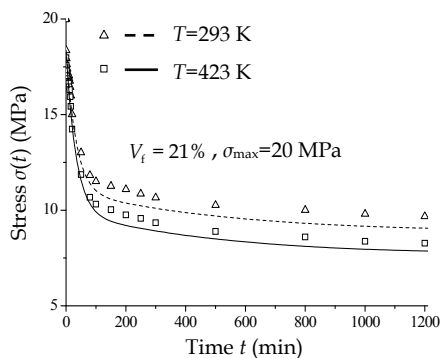


Fig. 24. Stress relaxation curves of NASC at different temperatures

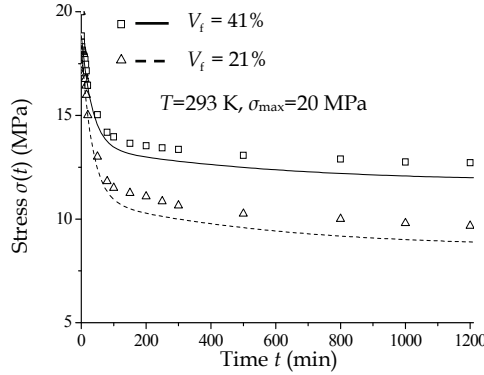


Fig. 25. Stress relaxation curves of NASC with different fiber contents

6.2 Sealing behaviour of non-asbestos sealing composites

6.2.1 Leakage model of non-asbestos gasket sealing

NASC can be assumed to be a kind of porous media. The flow of gas through porous media includes molecular transfer and convection transfer. The leakage rate L of gases flowing through porous media can be calculated using the capillary model (Gu et al., 2007b).

$$L = \sum_{i=1}^k \left(\frac{\pi r_i^4}{8\eta c l_m} p_m + \frac{4r_i^3}{3cl_m} \sqrt{\frac{2\pi RT}{M}} \right) (p_1 - p_2) \quad (52)$$

where r_i and l_m are the radius and the average length of capillaries, respectively, c is the bending coefficient of capillaries, η the dynamic viscosity of gases, T the Kelvin temperature of gases, M the gas molecular weight, R the gas constant, p_m the average pressure, $p_m = (p_1 + p_2)/2$, and p_1 and p_2 are the pressures at the entrance and exit of capillaries, respectively.

There exists the following relationship between the number k and the radius r_i of leakage paths and the gasket compressive stress σ :

$$k = f_1(\sigma^{-m}) \quad (53)$$

$$r_i = f_2(\sigma^{-n}) \quad (54)$$

According to Eqs.(52)-(54), the leakage rate of gas through gasket sealing joints L can be calculated by the following formula:

$$L = \left[A_L \frac{1}{\eta} \left(\frac{\sigma}{\sigma_0} \right)^{-n_L} p_m + A_M \sqrt{\frac{T}{M}} \left(\frac{\sigma}{\sigma_0} \right)^{-n_M} \right] \frac{(p_1 - p_2)}{l} \quad (55)$$

where l is the gasket effective width, A_L , A_M , n_L and n_M are regression coefficients which can be obtained from experimental data, and σ_0 is the gasket seating stress prescribed in the corresponding gasket standards (AQSIQ,2003, AQSIQ,2008).

6.2.2 Test verification and leakage rate prediction method

Tests were performed on a fully automatic testing machine for gasket performances, and the specific details on the test machine and test procedure can be found in the reference (Gu et al., 2007b). The test conditions are listed in Table 12.

Sample Quantity	Sample Dimension (mm)	Test Medium	Gasket Seating Stress (MPa)	Gas Pressure Difference (106 Pa)	Test Temperature (K)
3	$\phi 109 \times \phi 61 \times 2$	99.9% nitrogen	20, 30, 40, 50, 60	1, 2, 3, 4.5, 6	293

Table 12. Conditions for the leakage test

The relationship between medium pressure difference $p_1 - p_2$ and leakage rate L under different gasket seating stresses σ_s is shown in Fig. 26, in which symbols represent experimental data, and curves are plotted according to the leakage model. The experimental results show that the leakage rate increases obviously with the increase of the test medium pressure when the gasket seating stresses are smaller. On the contrary, when the gasket seating stresses are larger, this tendency is not obvious. The variation of leakage rates with pressure difference across gasket width follows precisely the curves represented by the leakage model, as indicated by the high value of the correlation coefficient R which is nearly equal to unity.

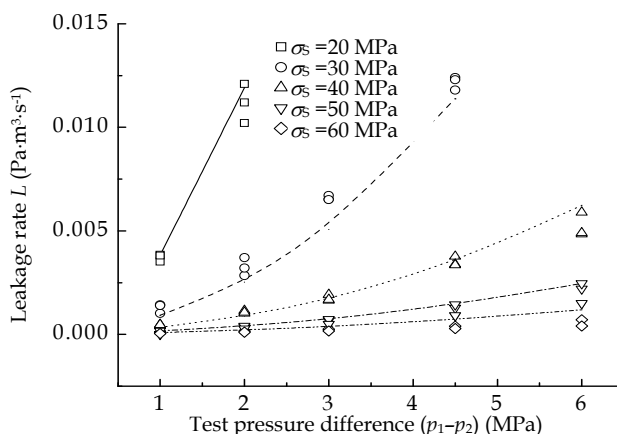


Fig. 26. Relationship between leakage rate and test pressure difference under different seating stresses

The coefficients A_L , A_M , n_L and n_M in Eq. (55) can be obtained by regression analysis of the experimental data, and they are listed in Table 13. According to Eq. (55) and the regression coefficients, the relationships between the pressure difference and the leakage rate under different gasket compressive stresses are obtained, and they are also illustrated in Fig. 26.

A_L	A_M	n_L	n_M	R
8.52×10^{-23}	2.79×10^{-12}	4.08	3.06	0.984

Table 13. Regression coefficients in Eq. (55)

According to Eq. (55) and the regression coefficients in Table 13, the leakage rates of other gases leaking through non-asbestos gaskets with different sizes and used under various working conditions can also be predicted. It can be assumed that the leakage paths in gaskets are distributed uniformly in the circumferential direction. The larger the gasket perimeter, the more the leakage paths are. Therefore, when the leakage rate prediction is performed for the gaskets with different sizes, the correction of Eq. (56) is necessary, and hence, the leakage prediction formula holds:

$$L = \left[A_L \frac{1}{\eta} \left(\frac{\sigma}{\sigma_0} \right)^{-n_L} p_m + A_M \sqrt{\frac{T}{M}} \left(\frac{\sigma}{\sigma_0} \right)^{-n_M} \right] \frac{(p_1 - p_2) D_2}{l D_1} \quad (56)$$

where D_1 and D_2 are diameters of the tested gasket and the gasket on which the leakage rate will be predicted, respectively.

It can be seen from Eq. (55) and Eq. (56) as well that the total leakage rate of gases through non-asbestos gaskets is the sum of the laminar flow rate and the molecular flow rate. The leakage is mainly the molecular flow when the gasket seating stress is large and the gas pressure is low, and the leakage rate is directly proportional to the pressure difference ($p_1 - p_2$). On the contrary, when the gasket seating stress is small and the gas pressure high, the leakage is predominantly the laminar flow. In this case, the leakage rate is in direct proportion to the square difference of pressures ($p_1^2 - p_2^2$), and the influence of the molecular flow can be ignored. The latter situation represents the leakage state of gasket sealing joints in most pressure vessels and piping.

7. Conclusions

Two kinds of non-asbestos sealing composites were developed by using aramid, glass, and pre-oxidized carbon fibers as reinforcing fibers, and nitrile rubber and natural rubber as binders. Design of these composites as well as preparation techniques were discussed. The surface treatment effects of fibers by using such methods as immersion coating, surface oxidation and plasma treatments were investigated. The results of the transverse tensile test and the SEM analysis reveal that the surface pretreatment can largely enhance the associative strength of the interface between fiber and matrix.

Both the molding and the calendaring preparation processes of NASC were presented. Contents of main compositions of two kinds of NASC were determined by uniform design and regression design methods in which the transverse tensile strength, compressibility, resilient rate and stress relaxation rate of the composites were used as evaluation indexes. According to the data resulted from mixing regression design experiments, the regression equation was obtained.

Methods for measuring and characterizing the micro structural parameters including the aspect ratio, orientation, distribution of short fibers, interphase thickness, and porosity of NASC were discussed. The short fiber aspect ratio can be obtained by measuring the dimensions of the fibers that were separated from the composite, and results can be evaluated by the mean aspect ratio method, the histogram method and the distribution function method. The short fiber orientation can be tested by the section-analysis method and the plane-observation method, and results can be evaluated by the distribution function method, the histogram method and the modified coefficient method.

The micromechanical model of a single fiber cylindrical cell, which includes fiber, matrix and their interphase, was established. The stress transfer mode among the fiber, the matrix and the interphase was investigated, and the stress distributions in them were obtained. A model of a compressive type single-fiber cell was established, and the prediction methods for the stress-strain relationship, the tensile module, the longitudinal tensile strength, the transverse tensile strength, the compression-resilience performance and the creep behavior were proposed.

A series of tests for tensile property, compressibility, resilient rate, and stress relaxation property of NASC were conducted. The experimental results were compared with the predicted values. The predicted stress-strain relationship of NASC is in good agreement with the experimental result when the strain of the composite is relatively small, while the error is obvious when the strain is relatively large. The transverse tensile strength increases with the increase of the fiber volume content and the mean aspect ratio and decreases with the increase in the test temperature. All the experimental results are smaller than those predicted, and the maximum error between them is about 13%. The compressibility increases with increasing the maximum compressive stress and decreasing the fiber volume content, while the resilient rate decreases with the increase in the maximum compressive stress and the fiber volume content. They are nearly irrelevant to the fiber mean aspect ratio and orientation. The errors both between the predicted compressive rates and experimental data and between the predicted resilient rates and the experimental results are less than 15%. At the beginning of the stress relaxation, the stress in the composite decreases quickly, the stress relaxation speed decreases essentially after 80 to 100 minutes, and the stress relaxation curve trends to be a straight line. The stress relaxation rate increases with increasing initial stress and temperature and decreasing fiber volume content. Such microstructure parameters as fiber mean aspect ratio and orientation have less evident influence on the stress relaxation property of NASC. The experimental and predicted results are basically identical, and the maximum error is about 8.5%, which indicates that the stress relaxation property of NASC can be well evaluated by the stress relaxation equation presented in this chapter.

A leakage model was developed to predict non-asbestos gasket leakage rates with different gasket sizes and various gases under different working conditions. The model is constructed on the base of the gasket leakage tests conducted over a nitrogen pressure range of 1 to 6 MPa and a gasket seating stress range of 20 to 60 MPa. The established model gives relatively accurate predictions, but it is necessary to conduct additional tests before predicting leakage rate of other types of gaskets. High temperature will cause the deterioration of sealing materials and result in the increase of leakage rates, which has not been taken into consideration in the present model, and this subject should be studied.

8. Acknowledgement

This work was supported by the National Natural Science Foundation of China (Grant No. 10872088) and the Doctoral Foundation of the Ministry of Education of China (Grant No. 20070291004 and No. 20093221120009). The authors of this chapter gratefully acknowledge the corresponding government organizations for the funds that made this project possible. We would also like to thank those postgraduate students who participated in our previous work throughout these years and made the contribution in the aspect of material preparation, performance test, data processing, and so on.

9. References

- American Academy of Actuaries (2007). *Overview of Asbestos Claims Issues and Trends*, Mass Torts Subcommittee of the American Academy of Actuaries, Washington, USA
- AQSIQ (2003). The General Administration of Quality Supervision, Inspection and Quarantine of the People's Republic of China, GB/T 9129-2003, *Specifications of Non-metallic Flat Gaskets for Pipe Flanges*. Standards Press of China, ISBN 155066.1-19884, Beijing, China (in Chinese)
- AQSIQ (2008). The General Administration of Quality Supervision, Inspection and Quarantine of the People's Republic of China, GB/T 17727-2008, *Nonmetal material gaskets for marine flange*. Standards Press of China, ISBN 750665591, Beijing, China (in Chinese)
- ASME (2007). The American Society of Mechanical Engineers, *ASME Boiler and Pressure Vessel Code 2007, Sec VIII, Division 1, Rules for construction of Pressure Vessels*. New York, USA
- Chen, Y. & Gu B.Q. (2008). Development of a new kind of sealing composite material reinforced with carbon and glass hybrid fibers. *Advanced Materials Research*, Vols. 44-46, 651-658, ISSN 1022-6680
- Gao, P. & Chen Y. (2009). The effect of nanometer modification on the performances of short fiber reinforced rubber-based sealing composite material. *Lubrication Engineering*, Vol.34, No.8, 66-69, ISSN 0254-0150 (in Chinese)
- Gu B. Q. & Chen, Y. (2007). Development of a new kind of sealing composite material reinforced with aramid and pre-oxidized fibers. *Key Engineering Materials*. Vols. 353-358, 1243-1246, ISSN 1013-9826
- Gu, B. Q. (1999). Application of model of gases flowing through porous media to gasket sealing. *Journal of Nanjing University of Chemical Technology*, Vol. 21, No. 1, 19-22, ISSN 1007-7537 (in Chinese)
- Gu, B. Q., Shi, L. X. & Lu, X. F. (2000). Investigation of high temperature performances of spiral wound gaskets with flexible graphite filler. *China Petroleum Machinery*, Vol. 28, No. 2, 13-16, ISSN 1001-4578 (in Chinese)
- Gu, B. Q., Lu, X. F. & Xu, G. P. (2001). Determination of performance indexes of non-asbestos fiber-reinforced elastomer gasket. *Proceedings of the 5th National Conference on Pressure Vessel Technology*, 116-120, ISSN 1007-7472.0.2000-05-023, Nanjing, China, September, 2001, Subcommittee on Pressure Vessels, Chinese Society of Mechanical Engineers, Hefei, China (in Chinese)
- Gu, B. Q. (2002). Performances and application of non-asbestos gaskets. *Process Equipment & Piping*, Vol. 39, No. 1, 5-9, ISSN 1009-3281 (in Chinese)
- Gu, B. Q., Li, Y. Y., Sun, Z. G., Huang, X. L., Zhou, J. F. & Shao, C. L. (2010). Study on time-correlated leakage model of nonmetallic gaskets. *Advanced Materials Research*, Vols. 97-101, 629-633, ISSN 10226680
- Gu, B. Q. & Zhu, H. S. (1988). Tightness analysis of bolted flanged connections. *Petrochemical Equipment*, Vol. 17, No. 1, 16-20, ISSN 1000-7466 (in Chinese)
- Gu, B. Q. & Huang, X. L. (1997). Dichtheitsklassen und entsprechende Leckratenmeßverfahren. *3R international*, 1997, Vol.36, No.4/5,198-201, ISSN 0340-3386

- Gu, B. Q., Li, X. H. & Tian, Z. (2004). *Static seal design Technology*. Standards Press of China, ISBN 7-5066-3430-9, Beijing, China (in Chinese)
- Gu, B. Q. & Chen, Y. (2006). Tightness assessment method of bolted flanged connections at elevated temperature. *Lubrication Engineering*, Vol. 178, No. 6, 39-41, ISSN 0254-0150 (in Chinese)
- Gu, B. Q., Chen, Y., Zhang, Y. & Zhu, R. S. (2007a). Tightness prediction of flanged joints with elastic washers. *Proceedings of the Ninth International Conference on Engineering Structural Integrity Assessment*, 1512-1515, ISBN 978-7-111-05002-5, Beijing, China, October, 2007, China Machine Press, Beijing, China
- Gu, B. Q., Chen, Y. & Zhu, D. S. (2007b). Prediction of leakage rates through sealing connections with nonmetallic gaskets. *Chinese Journal of Chemical Engineering*, Vol. 15, No. 6, 837-841, ISSN 1004-9541
- Marchand, L., Derenne, M. (1996). Long term performance of elastomeric sheet gasket materials subjected to temperature exposure. *Proceedings of the International Conference on Pressure Vessel Technology*, 107-123, ISBN 079181789X, Montreal, Can, July, 1996, ASME, New York, NY, USA
- Payne, J. & Bazergui, A. (1990). *Summary Report on Elevated Temperature Tests for Asbestos-free Gasket Materials*, NACE for MTL, ISBN 1-877914-10-X
- Payne, J. R., Mueller, R. T., Bazergui, A. (1989a). Gasket qualification test scheme for petrochemical plants. Part I. Test methods and application results. *Application of Modal Analysis Techniques to Seismic and Dynamic Loadings*, Vol. 158, 53-58, ISSN 0277027X, Honolulu, HI, USA, July, 1989, ASME, New York, NY, USA; JSME, Tokyo, Jpn
- Payne, J. R., Mueller, R. T., Bazergui, A. (1989b). Gasket qualification test scheme for petrochemical plants. Part II. Quality criteria and evaluation schemes. *Application of Modal Analysis Techniques to Seismic and Dynamic Loadings*, Vol. 158, 59-69, ISSN 0277027X, Honolulu, HI, USA, July, 1989, ASME, New York, NY, USA; JSME, Tokyo, Jpn
- Piringer, S. & Rustemeyer U. (2004). Improving performance of fiber-based gaskets at elevated temperatures-the sandwich approach. *Sealing Technology*, Vol. 2004, No. 3, 6-11, ISSN 1350-4789
- Tsuji, H., Kitagawa, H., Kodaira, N. (2004). Effect of aging time on sealing performance of non-asbestos gasket at elevated temperature. *Analysis of Bolted Joints*, 209-214, ISBN 0791846814, San Diego, CA, United States, July, 2004, ASME, New York, NY, USA
- Xie, S. J. & Cai R. L. (2002). Research on mechanical behaviour of the compressed nonasbestos fiber reinforced rubber sheet. *Fluid Machinery*, Vol. 30, No. 12, 4-6, ISSN 1005-0329 (in Chinese)
- Xie, S. J. & Xie, J. M. (2004). Investigation into the effect of nonasbestos fibers on the performances of compressed nonasbestos sealing sheets. *Non-Metallic Mines*, Vol. 27, No. 1, 50-52, ISSN 1000-8098 (in Chinese)
- Zhu, D. S., Gu, B. Q. & Chen, Y. (2007). Study on Tensile Strength of Short-fiber-reinforced elastomer matrix composites. *Proceedings of the Ninth International Conference on Engineering Structural Integrity Assessment*, 803-807, ISBN 978-7-111-05002-5, Beijing, China, October, 2007, China Machine Press, Beijing, China

- Zhu, D. S., Gu, B. Q. & Chen, Y. (2008). Study on Temperature-Dependent Tensile Strength of Short-Fiber-Reinforced Elastomer Matrix Composites. *Advanced Materials Research*, Vols. 44-46, 97-104, ISSN 1022-6680
- Zhu, D. S. (2008). Prediction of Mechanical Performances of Short Fiber Rubber Matrix Composite. A dissertation for the doctoral degree at Nanjing University of Technology (in Chinese)

Thermoplastic Polymer based Modified Red Mud Composites Materials

A.H. Bhat¹, H.P.S. Abdul Khalil and A. K. Banthia²

¹*School of Industrial Technology, Universiti Sains Malaysia, Penang-11800,*

²*Materials Science Centre, Indian Institute of Technology Kharagpur-721302,*

¹*Malaysia*

²*India*

1. Introduction

Soaring prices are a reminder of the essential role that affordable products play in sustainable economic growth and higher human development. Utilization of waste materials has become more pressing than ever. Red mud is accumulating at a rate of 30 million ton annually throughout the world. Under normal conditions when 1 ton of alumina is produced from bauxite, an equal amount of red mud is generated as a waste. A further aspect is their reuse as starting materials for other products (Grjotheim & Welch, 1998; Kasliwal, & Sai, 1999). Red mud has been suggested as filler for polymer reinforcement or as a cheap adsorbent for removal of toxic metals or an acid by several researchers. Chand and Hashmi, 1999, tried to improve the mechanical properties and abrasive wear properties of polymer blend filled with red mud. Pradhan et al. 1999 had reported that activated red mud as a good adsorbent was used for adsorption of phosphate or chromium. In addition, the mechanical and thermal properties of polymers are generally improved by the addition of inorganic fillers. The challenges in this area of high-performance organic-inorganic hybrid materials are to obtain significant improvements in the interfacial adhesion between the polymer matrix and the reinforcing material since the organic matrix is relatively incompatible with the inorganic phase. Generally, a better interfacial bonding will impart better properties to a polymer composite such as high modulus, strength, and stiffness (Agag et al., 2001; Jang, 1992). This reinforcement of polymer filled with inorganic material is largely dependent on the physical interfacial phenomenon between the filler and matrix. This can be determining the degree of adhesion by physical interaction, such as active functional groups, hydrogen bonding, Lewis acid-base interactions, surface energy, and crystallite faces of filler surface at the interface (Park & Kim, 2000; Park & Cho, 2000). To increase physical interaction, various surface treatment techniques are applied, such as oxidation in acid solutions, (Donnet & Bansal, 1990) dry oxidation in oxygen, (Yuan et al., 1991) anodic oxidation, (Ishikawa & Matsumoto, 2001; Park, S. J.; Kim) and plasma treatments (Dilsiz et al., 1995). Surface modification leads to development of surface functional activity on a filler surface, resulting in modification to achieve good interfacial adhesion between the reinforcement and the matrix.

In materials research, the development of polymer nanocomposites is rapidly emerging as a multidisciplinary research activity whose results could broaden the applications of

polymers to the great benefit of many different industries. The details about worldwide generation of Red Mud, country wise and region wise is shown in fig. 1.

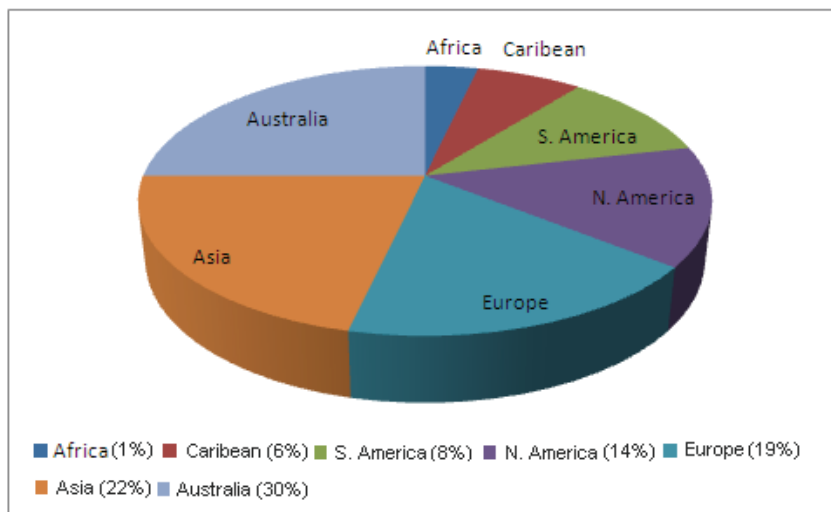


Fig. 1. Red Mud generation Continent/Region wise

The use of layered inorganic fillers has been a common practice in the plastics industry to improve the properties of thermoplastics. The effects of filler on the material properties of composite materials depend strongly on its particle size, shape, aggregate size, surface characteristics, and degree of dispersion. Polymer composites prepared in combination with an organic component as a matrix and an inorganic component as filler on the nanoscale (Huang et al., 1987; Suriyet et al., 1992; Novak & Ellsworth, 1993; Hajji et al., 1999) have additional advantages, such as the possibility of obtaining a material that has the advantages of both organic materials (e.g., light weight, flexibility, good moldability) and inorganic materials (e.g., high strength, heat stability, and chemical resistance)(Shao et al, 2003).

Low volume additions ($\leq 5\%$) of nanoparticles of layered red mud provide property enhancements with respect to the neat resin that are comparable to those achieved by conventional loadings (15-40%) of traditional fillers. Red mud (nanofiller) is a major waste material obtained during the production of alumina from bauxite by the Bayer's process. It comprises of silicates and oxides of iron, aluminum, sodium, calcium and titanium, along with some other minor constituents. Based on economics as well as environmental related issues, enormous efforts have been directed worldwide towards red mud management issues i.e. of utilization, storage and disposal. Different avenues of red mud utilization are more or less known but none of them have so far proved to be economically viable or commercially feasible.

Thermoplastics have a big potential for applications in the industry as well as in construction, electrical applications and food packagings. One of the few disadvantages associated with the use of nanofillers, is their high cost. The present research work has been undertaken with an objective to explore the use of red mud as a reinforcing material as a low cost option. This is due to the fact that red mud alone contains all these reinforcement elements and is plentifully available.

In mechanical reinforcement major issues are the homogeneous dispersion of nanofillers in the polymeric matrix and the developments of chemical bonding or strong interaction at the nanofiller-matrix interface. In this study we have used acid modified and organically modified red mud for better homogeneous dispersion as well as enhanced material properties. The focus of this research was to experimentally characterize the two polymer nanocomposite systems and investigate the role of modification of filler in their behavior. Modified Red mud nanoparticles were dispersed in poly (vinyl alcohol) (PVA) and poly hydroxy ether of bisphenol-A (Ph) matrices.

The conventional solvent casting technique was employed to generate polymer nanocomposites. Red mud was treated with boric acid and phosphomolybdic acid to develop the acidic functional groups or active oxygen, resulting in the better dispersion of the red mud into the polymer matrices. Red mud was also organically modified with the oligomers of aniline formaldehyde, for better interaction between the filler and the polymer matrices. The particle size of the modified red mud was determined by field emission scanning electron microscopy (FESEM). The as-synthesized composite films were typically characterized by FTIR spectroscopy and X-Ray Diffraction. The morphological image of the composite materials was studied by scanning electron microscopy (SEM) and the dispersion of the modified fillers within the matrix was studied by transmission electron microscopy (TEM). The thermal properties measured by thermogravimetric analysis (TGA) showed enhanced thermal stability of a series of composite materials. The differential scanning calorimetry (DSC) showed increase in glass transition temperature and crystallization of the composite films.

The physical topography of the composite materials was studied by Atomic Force Microscopy (AFM).

Polyvinyl alcohol (PVA) is commercially available in dry granular or powdered form. It is a water-soluble and fully biodegradable polymer (Chen et al., 2000; Bachtisi & Kiparissides, 1996). PVA is having planar zigzag structure like polyethylene (Horii et al., 1992). All PVA grades are readily soluble in water. As a hydrophilic polymer, PVA exhibits excellent water retention properties. Conditions for dissolution are governed primarily by degree of hydrolysis, but they are influenced by other factors such as molecular weight, particle size distribution and particle crystallinity [Peppas & Merrill 1977]. Optimum solubility occurs at 87-89% hydrolysis. The partially hydrolyzed grades in this range exhibit a high degree of cold-water solubility. For total dissolution, however, they require water temperatures of about 185°F (85°C) with a hold time of 30 minutes. It is, in fact, a refinement of PVAcetate since the most common manufacturing process is to replace by hydrolysis (or alcoholysis) the acetate groups with hydroxyl groups. This is commonly achieved using the presence of catalytic quantities of alkali such as sodium hydroxide (which, since it acts only as a catalyst, should not in theory remain in the final product). The extent of hydrolysis will determine the amount of residual acetyl groups and this in turn apparently affect the viscosity characteristics. [Ray & Bousmina, 2005] PVA exists only as a polymer; a monomer has not yet been isolated, so the chemical structure is described in Fig.2.

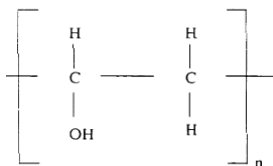


Fig. 2. Chemical formula of PVA

The PVA concentration in an aqueous solution is determined by the type of application. However, at concentrations greater than 10 wt%, the viscosity of the aqueous solution at room temperature is such that pouring becomes difficult. In addition to its solubility, PVA is also appreciated for its good mechanical properties in the dry state, resistance to common solvents, barrier effect in dry atmospheres, possibility of food contact for suitable grades, biodegradability. Some of the physical properties of PVA are as presented in table 1.

Properties	Values
Appearance	White to cream granular powder
Density	1.23-1.30 g/cm ³
Thermal stability	Gradual discoloration above 100 °C; darkens rapidly above 150 °C; rapid decomposition above 200 °C.
Coefficients of thermal expansion	7-8 × 10 ⁻⁵ / °C
Thermal conductivity	0.2 W/m.k
Yield Stress	40-50 MPa
Elongation at break	100-200%
Melting point	230 °C for fully hydrolysed grades 180-190 for partially hydrolysed grades.
Glass transition temperature	75-85 °C

Table 1. Physical properties of PVA

PVA can be plasticized and processed by casting, dipping, injection and extrusion. (Biron, 2007).

The main engineering applications, possibly in combination with other polymers, are:

- Films for packing chemicals, fertilizers, herbicides, disinfectants, dyes, colorants, scalers, cosmetics etc.
- Release films for composite moulding.
- Solvent resistant tubes and pipes.
- Membranes for pumps carrying petroleum or chemical products

Trade names: Elvanol, Polyviol, Mowiol, Rhodoviol.

The commercial name of poly (hydroxy ether) of bisphenol A is Phenoxy, and as a thermoplastic polymer it possesses many excellent properties such as (Zhang et al., 2002)

- Good chemical stability
- Excellent matrix material for producing polymer nanocomposites
- Thermal stability
- Tractability
- Transparency

The poly (hydroxy ether of bisphenol A) (phenoxy (Ph)) has been revealed as a polymeric matrix able to intercalate in, and partially exfoliate a commercial organically modified montmorillonite. Dispersion was attributed to chemical interactions between the Ph and the inorganic clay (Fornes et al., 2004).

Poly (hydroxy ether of bisphenol A) (Ph) based polymer nanocomposites (PN) reinforced with a layered red mud with acidic and organic modifications were prepared by conventional solvent casting technique. The best dispersion occurred in the PN where the interactions between the functional groups of the polymer matrix and those of the organic substitution of the red mud appeared to be the highest. The modulus increase is an indirect but quantitative measurement of the attained dispersion level.

The structure of Poly (hydroxy ether) of bisphenol A is shown in fig.3.

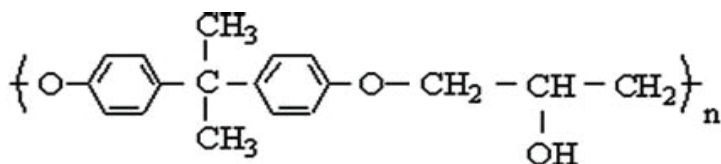


Fig. 3. Poly (hydroxy ether) of bisphenol A

2. Modification of red mud

2.1 Preparation of boric/phosphomolybdic acid modified-red mud

A known amount of raw red mud was first washed with distilled water two to three times and then dried in an oven. When the red mud dried completely; it was treated with a 5 M solution of boric acid/ phosphomolybdic acid for 24 hours. Then it was being filtered, dried, weighed and grinded in order to get its powdered form. The weight of the red mud increased by 24 %. The powder was then sieved through 53-micron mesh to remove the larger particles. The powder so obtained was fine and acidically modified. Thus, Layered silicates and double layered hydroxides, $\text{Al}_2(\text{OH})_7(\text{AH})$ and $\text{MgAl}(\text{OH})_5(\text{MAH})$, of red mud were modified with inorganic acids. The inorganic acid modifier compatibilizes the silicate and hydroxide surface to polymer matrices and spaces the crystalline layers apart to minimize the energy needed for exfoliation process.

2.2 Preparation of organically modified-red mud

The organic modification of red mud was done by the following two steps:

- i. Freshly prepared Aniline Hydrochloride is mixed with red mud with a magnetic stirrer.
 - ii. Formaldehyde is then added drop by drop to the mixture with intense stirring action.
- The addition of aniline hydrochloride to red mud replaces the cation present in the octahedral sites of the silicate with aniline occupying the same. The formaldehyde added would form a condensation oligomer as the product with the pendent group as formaldehyde which is compatible with the polymer. The ratio of Aniline to formaldehyde is kept 1:1 so as to stop any further condensation of the aniline and formaldehyde as this could lead to the polymer blend type nanocomposite, which could have the problems associated with miscibility of polymer blends and this filler would not be universal filler for the polymer matrix. The figure 4 depicts the experimental setup for the organic modification of red mud.

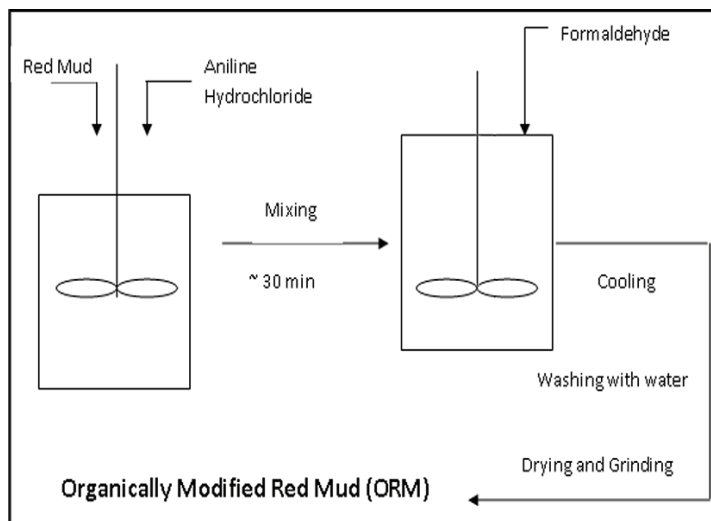
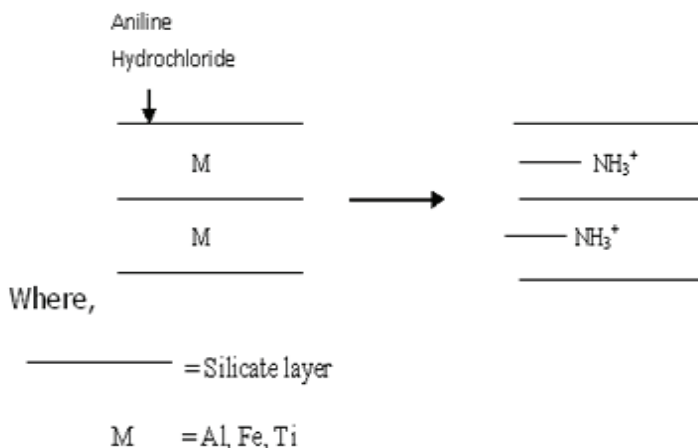


Fig. 4. Experimental setup of organic modification of red mud

2.3 Mechanism:

Figure 5 showed the mechanism and condensation reaction between substituted aniline and formaldehyde. After substitution of the metal cation, condensation reaction occurs between the substituted amine group with extra hydrogen and the formaldehyde molecule to form water as a byproduct. Thus the organic entity enters the space between the silicate layers thus providing a suitable site for binding the polymer. When this filler is mixed with the polymer, the polymer chains are attracted due to the presence of the organic species at the interlayer spaces, and thus get intercalated in between the layers, which have about nanometer size openings.

The reaction mechanism can be best depicted by the following sequence



Mechanism for organic modification of red mud

Condensation reaction between substituted aniline and formaldehyde

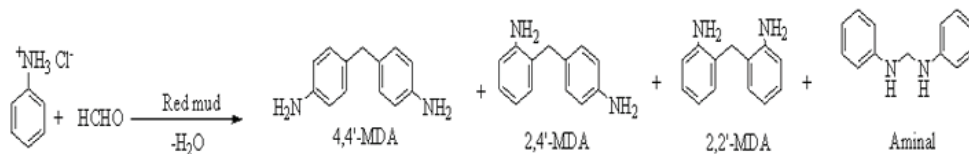


Fig. 5. Mechanism and Condensation reaction showing Organic Modification of Red Mud

3. Experimental

3.1 Preparation of PVA-acid red mud nanocomposite materials and organically modified red mud nanocomposite materials

10% (w/v) aqueous solution of PVA was prepared by dissolving 10g of dried powdered PVA in 100ml of distilled water at a temperature of 100 °C with continuous stirring. Polymer modified red mud nanocomposite (PRM) films were made by mixing different loading percentage of acid modified red mud and organically modified red mud into the virgin PVA solution. The PVA-red mud solution thus obtained was sonicated for better dispersion and removal of any air bubble present in the solution. The solution was cast on the plane glass surface and dried at room temperature. The composition of the PRM materials was varied from 0 to 5 wt % of RM with respect to the PVA content.

3.2 Red mud loading levels

Sample index	PVA	SP1	SP2	SP3	SP4	SP5	SP6	SP7
% Loading of boric acid mod. red mud	0	0.5	1.0	1.5	2.0	3.0	4.0	5.0

Sample index	PVA	CP1	CP2	CP3	CP4	CP5	CP6	CP7
% Loading of organically mod. red mud	0	0.5	1.0	1.5	2.0	3.0	4.0	5.0

Sample index	PVA	PRM1	PRM2	PRM3	PRM4	PRM5	PRM6	PRM7
% Loading of Phosphomolybdic acid mod. red mud	0	1.0	1.5	2.0	2.5	3.0	4.0	5.0

Table 2. Sample Designation

3.3 FTIR spectroscopy

The nature of the chemical bonds in raw red mud and the modified red mud were characterized by FTIR spectroscopy. The FTIR spectra of raw red mud and acid modified red mud are shown in Fig. 5 and it clearly depicts the main characteristic peaks associated with them. The characteristic vibration band of raw red mud for hydroxyl stretching vibration (O-H) was found at 3417 cm^{-1} while for boric acid modified red mud, the hydroxyl stretching occurred at 3379 cm^{-1} and the same characteristic peak for phosphomolybdic acid was observed at 3129 cm^{-1} . A red shift in the hydroxyl stretching vibration (O-H) at 3379 cm^{-1}

¹ in the boric acid modified red mud (BRM) and 3129 cm⁻¹ in the phosphomolybdic acid modified red mud (PRM) arises due to disappearance of the hydroxyl groups upon cross linking reaction with the boric acid and the phosphomolybdic acid respectively. The peak at $\nu = 993$ cm⁻¹ in case of raw red mud could be attributed to Si-O stretching vibration and the same peak for BRM and PRM were observed at 1000 cm⁻¹ and 996 cm⁻¹ respectively. The blue shift observed in the peak position of Si-O occurred due to the interaction of red mud with the inorganic acids.

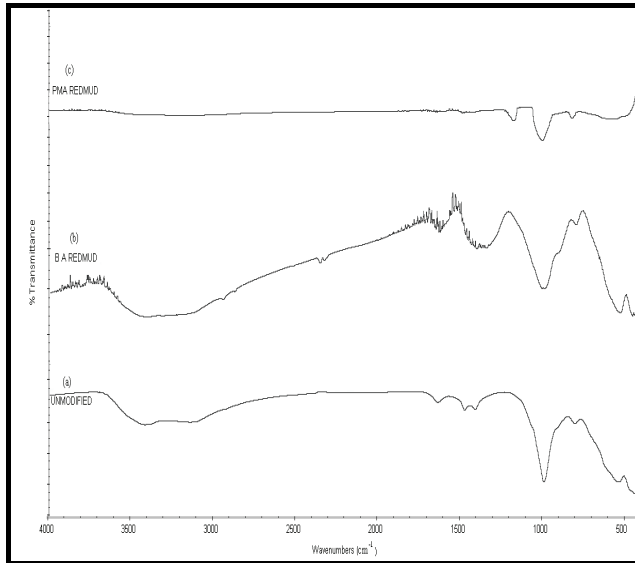


Fig. 5. FTIR Spectra of (a) Raw red mud (b) Boric acid modified red mud (BRM) (c) Phosphomolybdic acid modified red mud (PRM)

According to the Rocchiccioli - Deltcheff et al. [80], the four absorption bands in the spectrum of pure phosphomolybdic acid (PMA) shows the typical features of Keggin anions and the peak frequencies at 1064, 961, 868, 780 cm⁻¹ are assigned to the ν (P-O), ν (Mo-O_t) (O_t refers to the terminal oxygen), ν (Mo-O_c-Mo) (O_c refers to the corner oxygen) and ν (Mo-O_e-Mo) (O_e refers to the edge oxygen) respectively. All these characteristic bands of PMA are not present in the spectra of the PRM, indicating that there is specific interaction between the keggin structure and red mud.

Groups	Raw red mud (cm ⁻¹)	BRM (cm ⁻¹)	PRM (cm ⁻¹)
OH	3417	3379	3129
OH bend.	1636	1631	-
B-O	-	1368	-
Si-O	993	1000	996
P-O	-	-	1074
Mo-O _c -Mo			872

Table 3. Assignment of FTIR spectral bands for raw red mud and the acid modified red mud

An upward shift was observed for the ν (P-O) and ν (Mo-O_c-Mo) stretching vibrations, whereas bands ascribed to the stretching vibration ν (Mo-O_t) does not appear in the PRM.

The major vibration bands for organically modified red mud as shown in Fig. 6 occurs at OH/NH stretching (3320 cm^{-1}), NH_3^+ (1598 cm^{-1}) and Ar-N (1512 cm^{-1}). A red shift in the hydroxyl peak at 3320 cm^{-1} for modified red mud arises due to the interaction of red mud platelets with the aniline hydrochloride moiety through physical interactions. The characteristic Si-O stretching vibration is not found in case of ORM due to formation of a coating of organic moiety around the silicate galleries.

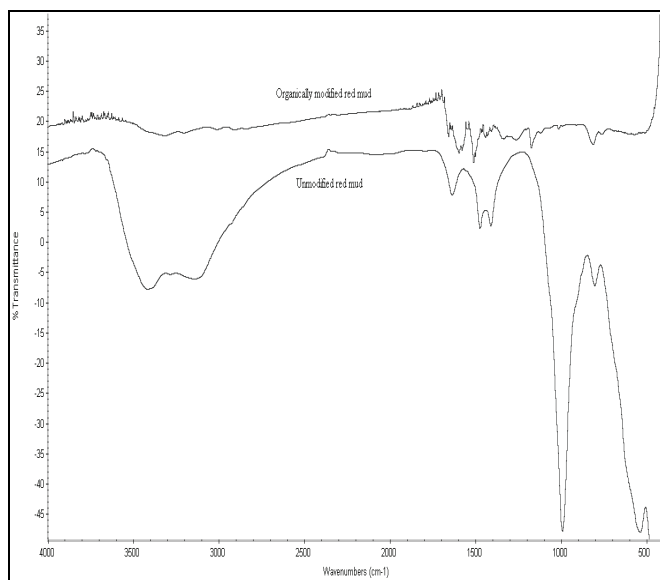


Fig. 6. FTIR Spectra of Raw red mud and organically modified red mud (ORM)

Groups	Raw red mud (cm^{-1})	ORM (cm^{-1})
OH	3417	3320
OH (bending)	1636	-
NH_3^+	-	1598
Ar-N	-	1512
Si-O	993	-

Table 4. Assignment of FTIR spectral bands for raw red mud and organically modified red mud

The representative FTIR spectra of the pure PVA and various polymer nanocomposite materials are shown in Fig.7. The characteristic vibration band of PVA for hydroxyl stretching vibration (O-H) having polymeric association is shown at 3292 cm^{-1} . While the alkyl stretching band of C-H is shown at 2942 cm^{-1} . The peak at $\nu=1736\text{ cm}^{-1}$ is due to C=O

stretching of saturated aliphatic esters (acetate), 1042cm^{-1} (O-H Bending), and 1424 cm^{-1} (C-H Bending).

The FTIR spectrum in Fig. 3.6 also shows the spectra associated with PRM2, SP2 and CP2. The intensity of the O-H stretching vibration peak ($\nu = 3200\text{-}3400\text{ cm}^{-1}$) decreased and peak frequency shifted from 3292 to 3250 cm^{-1} , i.e. to a lower frequency as compared to that of pure PVA. The red shift in the hydroxyl stretching frequency occurs due to the various degree of hydrogen bonding between the polymer and the filler which lengthens and weakens the O-H bond and hence lowers the vibrational frequency. Also, the peak frequency of C-H for PRM2, SP2 and CP2 occurs at 2916 cm^{-1} , 2945 cm^{-1} and 2960 cm^{-1} respectively as tabulated in Table 5.

By loading 1% ORM (CP2) in the polymer matrix, the alkyl stretching vibration of C-H increases from $2942\text{-}2960\text{ cm}^{-1}$ and occurs due to the interaction of polymer matrix with the organic moiety of the filler.

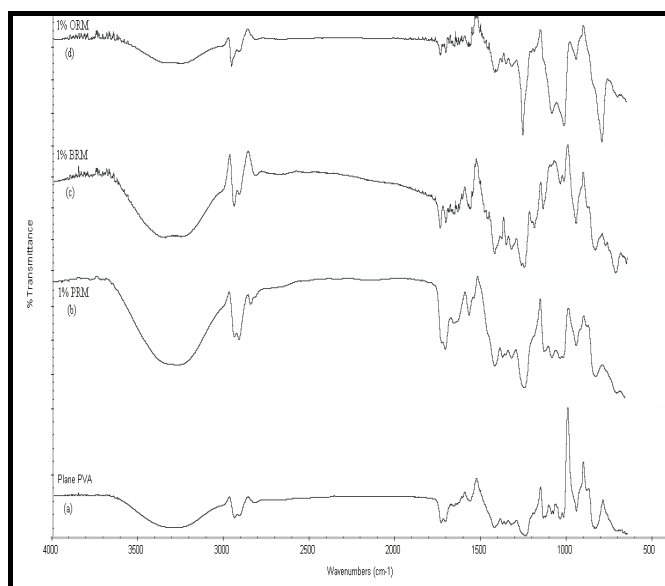


Fig. 7. FTIR Spectra of (a) Pure PVA (b) PRM2 (c) SP2 (d) CP2

Groups	PVA (cm^{-1})	PRM2 (cm^{-1})	SP2 (cm^{-1})	CP2 (cm^{-1})
OH	3292	3268	3267	3250
C-H	2942	2916	2945	2960
C=O	1736	1712	1743	1742
O-H (bending)	1042	1043	1041	1019
CH ₂ (bending)	1424	1423	1424	1414

Table 5. Assignment of FTIR spectral bands for Pure PVA and the PVA/modified red mud nanocomposite membranes

The FTIR spectra in Fig. 8 shows the spectra associated with PRM4, CP4 and SP4. The intensity of the O-H stretching vibration peak ($\nu = 3200\text{--}3400\text{ cm}^{-1}$) decreased and the peak frequency shifted from 3292 in case of pure PVA to 3278 cm^{-1} , 3245 cm^{-1} and 3230 cm^{-1} for PRM4, CP4 and SP4 respectively i.e. to a lower frequency as compared to that of pure PVA. This is again due to the intermolecular hydrogen bond formation, thereby decreasing the O-H stretching frequency with the increase in the percent loading of the modified filler. The other characteristic peaks are given in table 6.

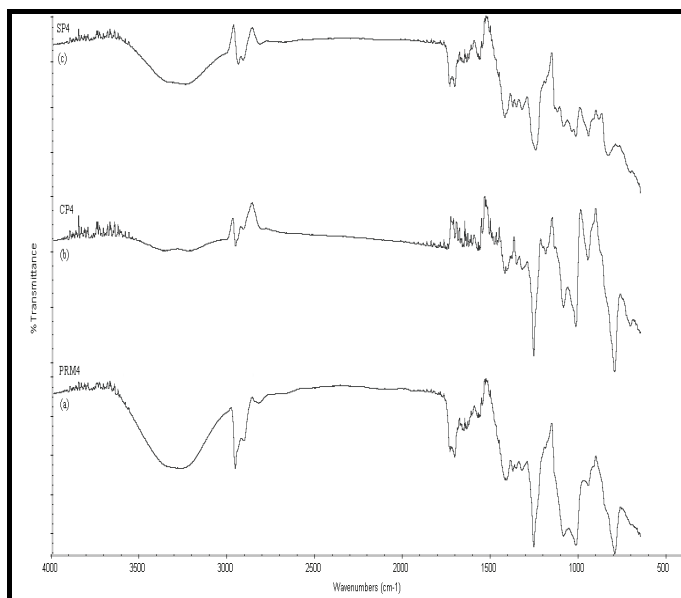


Fig. 8. FTIR Spectra of (a) PRM4 (b) CP4 (c) SP4

Groups	PRM4 (cm^{-1})	SP4	CP4
OH	3278	3245	3230
C-H	2961	2943	2959
C=O	1711	1737	1754
O-H (bending)	1020	1021	1020
CH ₂ (bending)	1414	1424	1424

Table 6. Assignment of FTIR spectral bands for PVA/modified red mud nanocomposite membranes with different loading percentage of filler

3.4 X - ray diffraction study

Wide angle X-ray diffraction studies were performed on raw red mud and the modified red mud as shown in Fig. 9.

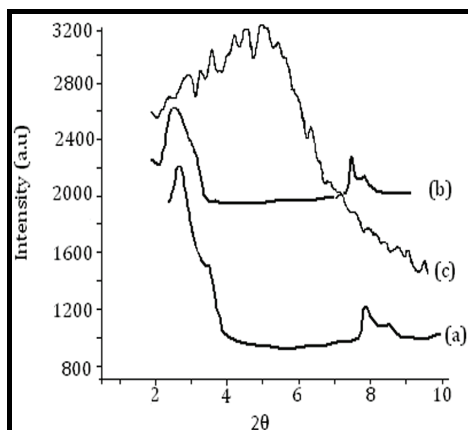


Fig. 9. Xrd pattern of (a) Raw red mud (b) Phosphomolybdic acid modified red mud (c) Organically modified red mud

The spacing, d_{001} , of the (001) basal reflections of the Raw red mud and PRM were measured and are shown in table 7. It was found that the basal spacing of the PRM is larger than the raw red mud.

Sample	2 θ	d-spacing (\AA)
Raw red mud	2.71	32.76
PRM	2.46	36.72

Table 7. XRD basal spacing results of raw red mud, and acid modified red mud

In the ORM, the case appears to be slightly different with the peak being lost. Thus, we could infer that the silicate layers undergo exfoliation or random dispersion at the modification stage itself. This suggests that the aniline formaldehyde type precursor have formed a coating on the partially exfoliated silicate layers leading to random dispersion thus rendering the absence of peaks in the XRD micrograph (Alexandre & Dubois, 2000).

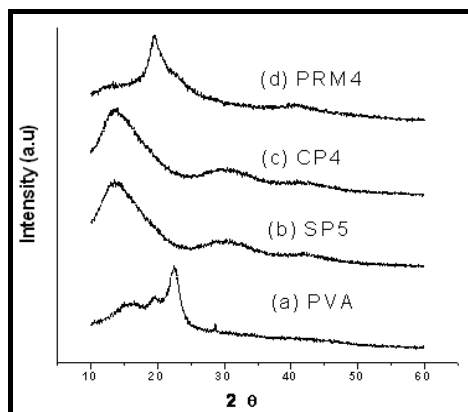


Fig. 10. X-ray Diffraction pattern of (a) PVA (b) SP5 (c) CP4 (d) PRM4 film

The XRD patterns for the Virgin PVA and the PVA nanocomposite films with different critical loading percentage of modified red mud were depicted in Fig. 10. The crystallinity of the nanocomposite membranes was found to be mainly due to PVA. The characteristic diffraction peak for pure PVA was observed at 2θ value of 22.56° . While the diffraction peak of the nanocomposite films were considerably broadened and displaced to lower 2θ values as shown in table 8, indicating reduction in the crystallinity of the nanocomposites.

The spacing, d_{001} , of the (001) basal reflections of the silicate galleries of the PVA nanocomposite films were measured as shown in table 3.9. It was found that the basal spacing for CP4 is larger than other nanocomposites materials, thereby giving evidence of more exfoliation in CP4 than the rest nanocomposites. Hence, it can be concluded that the interlayer spacing got increased by intercalation of polymer matrix. So, a lot of surface area of modified red mud is now available to the polymer for bonding.

Sample	2θ	d_{001} -spacing (\AA)
SP5	13.47	6.56
CP4	13.11	6.74
PRM4	19.15	4.63

Table 8. XRD d_{001} -spacing Results

The change of crystalline behavior was further evidenced by the studies of the morphological image of as-synthesized materials. Individual silicate layers, along with two, three and four layer stacks, were found to intercalate and partially exfoliate in the PVA matrix.

3.5 SEM

On higher magnification (10,000 X) viewing of morphology of pristine PVA SP4 and SP5 type of nanocomposite films in Figure 11 (a) , (b) and (c) respectively, it was found that the morphology of polymer nanocomposite films becomes much smooth than pure PVA.

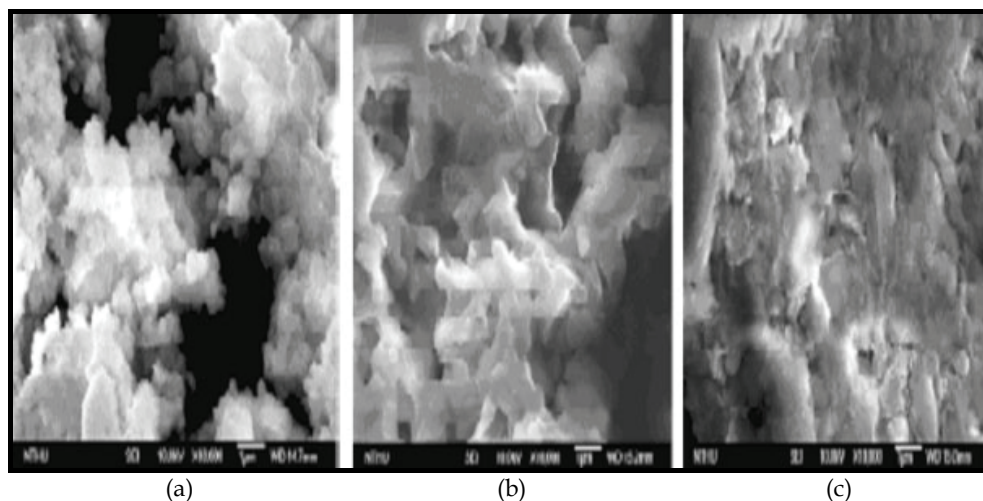


Fig. 11. SEM micrographs of (a) PVA (b) SP4 (c) SP5

The granules shape of PVA indicates some crystalline behavior occurring in pure polymer. The incorporation of red mud seems to destroy the orientation of semicrystalline polymer and to convert the polymer morphology approaching to amorphous state. [Bhat & Banthia, 2007] The SP5 showed much smooth morphology that is different to crystallites of PVA observation. This result is consistent with the wide-angle powder XRD patterns as described previously.

3.6 Transmission Electron Microscopy (TEM)

TEM complements XRD by observing a very small section of the material for the possibility of intercalation or exfoliation. It also provides information about the particle size and nanodispersion of particles. It however, supplies information on a very local scale. However, it is a valuable tool because it enables us to see the polymer and the filler on a nanometer scale.

The images, in Fig.12, 13 and Fig. 14, provide information regarding likely sizes of particles present in the matrix. Figure shows each of the polymer nanocomposite systems with critical loading of modified red mud. In Fig. 12 the silicate galleries of the organically modified red mud showed partial exfoliation and intercalation as depicted by the ridges in the image. While SP5 and PRM4 showed completely intercalated system. Nanoparticles showed agglomeration in some parts of the composite films due to the conformation of the polymer chains adhered to the nanoparticles.

Particle sizes on the TEM images are worth noting. In Figure 12, several ORM particles in PVA are ~ 8 nm, in Figure 13, BRM in PVA are as small as ~ 12 nm, and in Fig. 14, PRM in PVA ranges to a size of ~ 23 nm. Thus, it could be inferred, that there were numerous platelets that were expanded by the penetration of polymer chains.

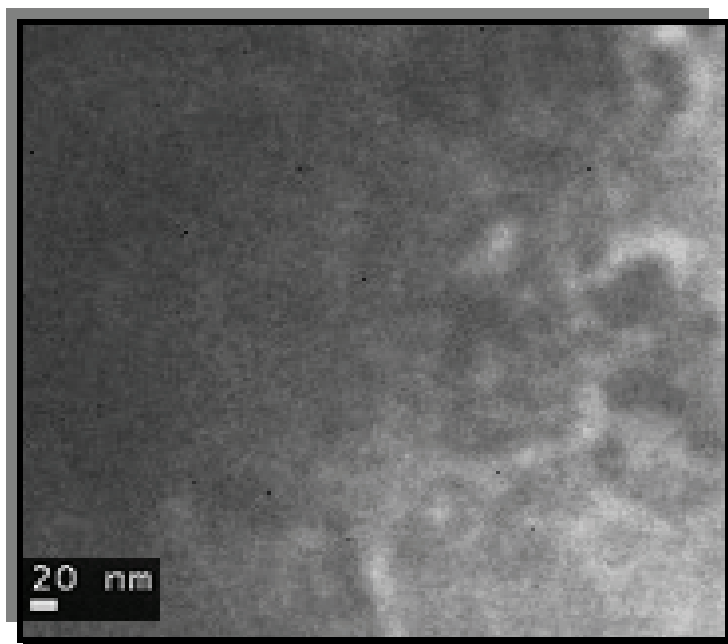


Fig. 12. TEM micrographs of CP4

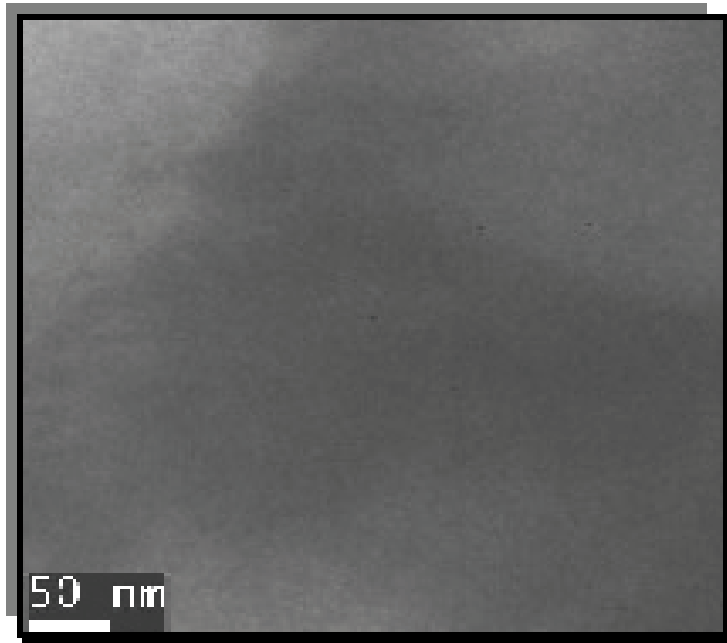


Fig. 13. TEM micrographs of SP5

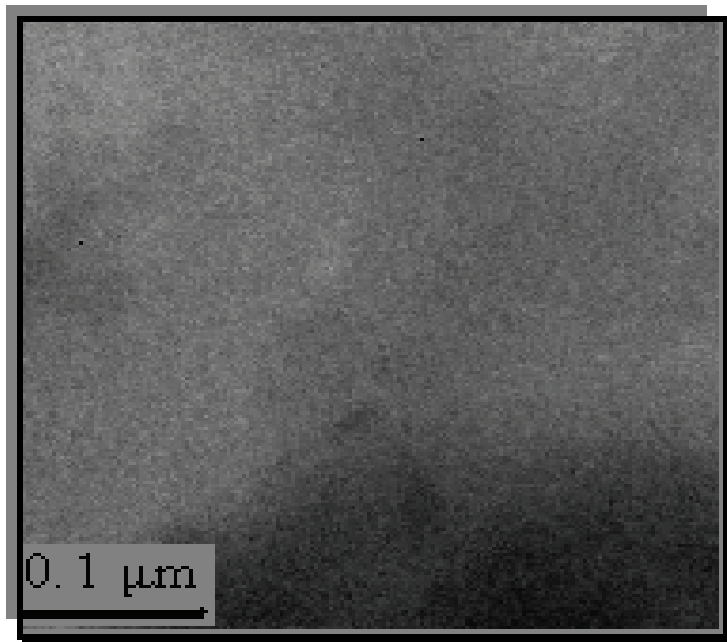


Fig. 14. TEM micrographs of PRM4

3.7 Atomic Force Microscopy (AFM)

The surface morphology of the pure PVA membrane and the PVA-modified nanocomposite membranes were analyzed by Tapping Mode - Atomic Force Microscopy (TM-AFM). Quantitatively, the differences in the morphology can be expressed in terms of various roughness parameters such as the mean roughness R_a , the root mean square (rms) of vertical data R_q , and the maximum height R_{max} . Here, the mean roughness is the mean value of surface relative to the center plane, the plane for which the volume enclosed by the image above and below this plane are equal; R_{max} the height difference between the highest and lowest points on the surface relative to the mean plane and R_q is the standard deviation of the Z values within the given area. The roughness parameters were calculated for pure PVA and PVA nanocomposite membrane surfaces with critical loading of filler and have been summarized in tabular format.

The TM-AFM images of the Pure PVA membrane is depicted in Fig. 15. The AFM images of PVA membrane shows randomly distributed hard crystalline regions (crystallites) of 100 – 250 nm in dimension on the membrane surface as evident from the observed morphology.

The pure PVA membrane surface has a mean roughness of 1.026 nm.

The nanocomposite membrane with critical loading percentage of 3 wt. % BRM content (Fig. 16) shows a homogeneous and non-porous morphology. The mean roughness for the surface topography of the membrane was found to be 6.595nm. This shows that there is a good compatibility between the filler (BRM) and the PVA matrix. While critical loading surface topography of CP4 and PRM4 as shown in Fig. 17 and 18 respectively again showed homogenous and non-porous morphology. The mean roughness of CP4 and PRM4 were observed to be 2.016 nm and 9.22 nm respectively as shown in table 9.

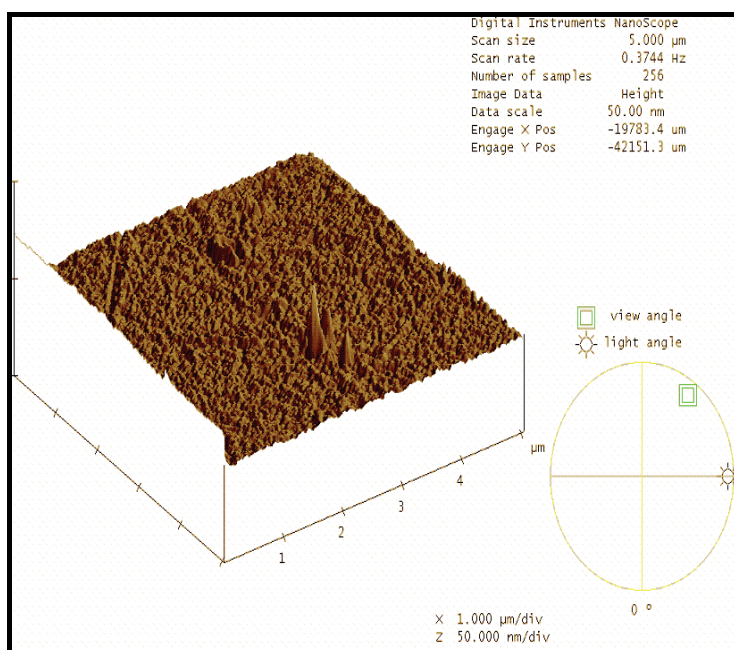


Fig. 15. Tapping Mode (3D) AFM images of Pure PVA membrane

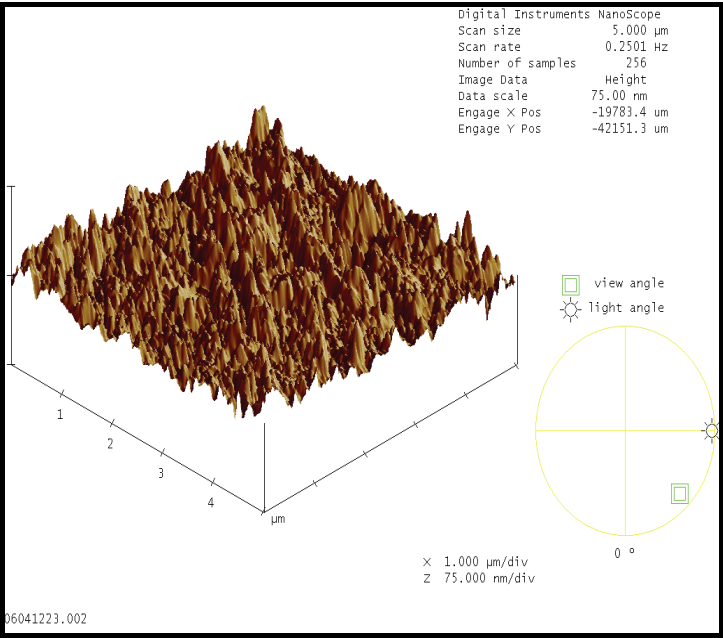


Fig. 16. Tapping Mode (3D) AFM images of SP5

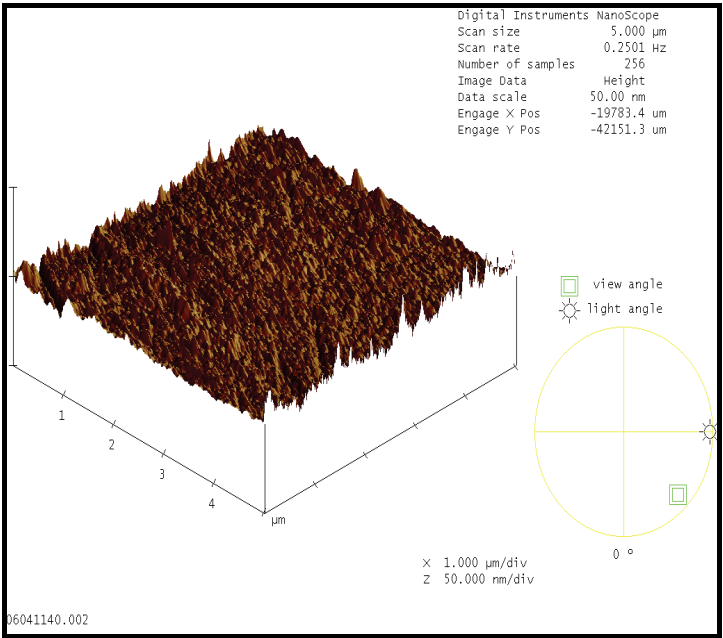


Fig. 17. Tapping Mode (3D) AFM images of CP4

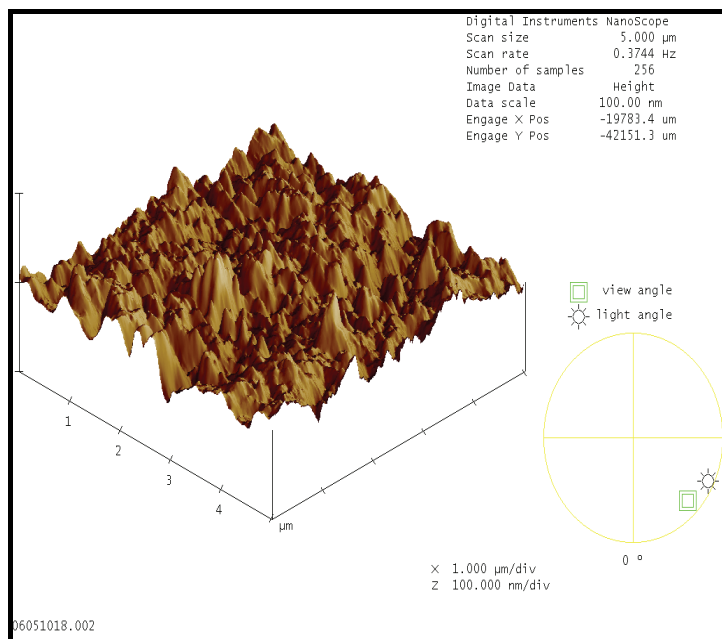


Fig. 18. Tapping Mode (3D) AFM images of PRM4

Membrane Details	R_a (nm)	R_{max} (nm)	R_q (nm)
Pure PVA	1.026	47.829	1.953
CP4	2.167	38.766	2.846
SP5	6.595	107.72	8.731
PRM4	9.22	89.803	11.572

Table 9. Roughness parameters for Pristine PVA and the PVA nanocomposite membrane surfaces

3.8 Thermogravimetric properties

The thermal stability of the raw red mud, ORM, pure PVA and PVA nanocomposite membranes with different filler content was investigated by thermogravimetric analysis. The TGA thermograms of the raw red mud, ORM, and PVA- nanocomposite films are shown in Fig. 19, Fig.20 and Fig. 21 respectively. The raw red mud is thermally stable up to 267 °C while ORM is stable upto 243 °C. Although ORM has 37% residue at 600°C, raw red mud is more stable, with 88% residue at 600°C. Raw red mud suffers an 11% weight loss at 600°C because of the probable loss of volatile impurities.

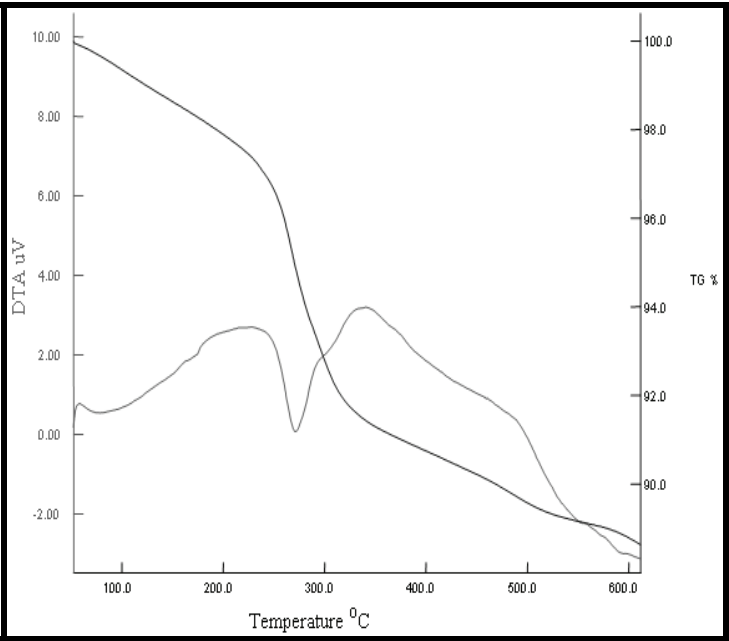


Fig. 19. DTA-TG Analysis of Raw red mud

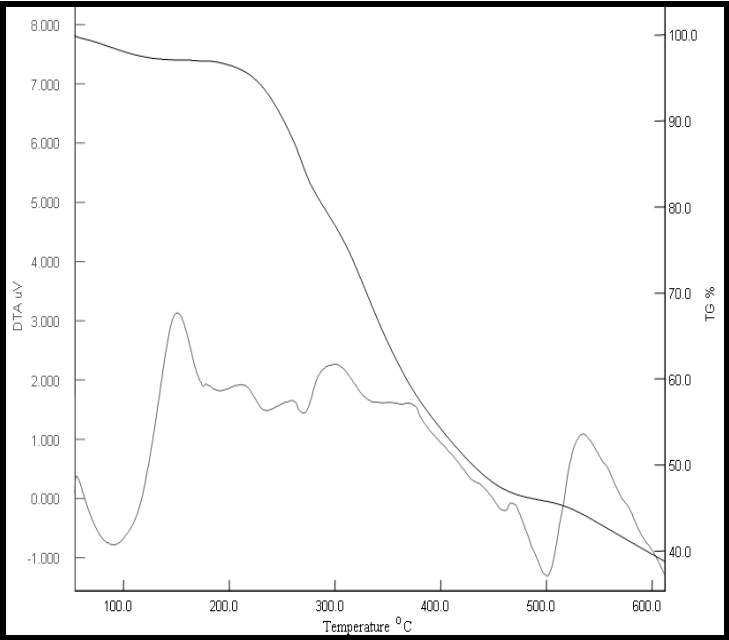


Fig. 20. DTA-TG Analysis of ORM

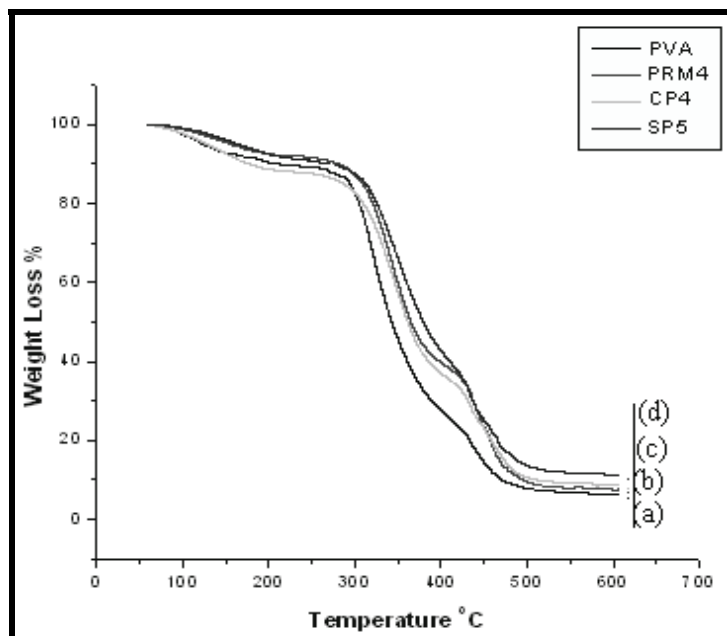


Fig. 21. Shows thermograms of (a) PVA (b) PRM4 (c) CP4 (d) SP5 film

Sample	T_i (°C)	T_f (°C)	Ash (%)
Raw red mud	267	356	88
ORM	243	482	37
Pure PVA	252	442	4.12
PRM4	274	462	7.23
CP4	277	467	10.13
SP5	281	474	12.43

Table 10. Degradation temperatures and ash content of the raw red mud, ORM, Pristine PVA and the PVA-nanocomposite membranes

The pristine PVA is thermally stable up to 250 °C. The PVA nanocomposite membranes show enhanced thermal stability; the thermal degradation of the PVA nanocomposites generally showed two major weight loss steps. The first weight loss of 15-20 wt % is centered on 150 °C and corresponds to weight loss of absorbed water and structural water of the polymer nanocomposite membranes. The weight losses in the temperature ranges of 353–483°C can be attributed mainly to the subsequent structural decomposition of the polymer backbones at higher temperatures. Evidently, the thermal decomposition of the polymer nanocomposite materials shift slightly towards the higher temperature range than that of pure PVA, which confirms the enhancement of thermal stability of intercalated polymer [Lee & Jang, 1996]. The Polymer nanocomposite membrane with critical loading of SP5, showed better thermal stability as compared to CP4 and PRM4. This could be due to better intercalation of polymer matrix within the silicate galleries of SP5 while in case of

CP4, inspite of partial exfoliation and intercalation, thermal stability is considerably lesser than SP5. This could be due to presence of organic moiety in CP4 which causes a decrease in its thermal stability. After, 500°C, the curve all became flat and mainly the inorganic residue (i.e. Al₂O₃, MgO, and SiO₂) remained.

3.9 Differential scanning calorimetry

DSC traces of PVA and polymer nanocomposite materials are shown in Fig.22. PVA exhibited an endotherm at 52.°C corresponding to the glass transition temperature (T_g) of PVA [90]. All the nanocomposite materials with different critical loading percentage of modified red mud were found to have a high T_g compared to the bulk PVA. This could tentatively be attributed to the confinement of the intercalated polymer chains within the red mud galleries that prevents the segmental motions of the polymer chains, thereby enhancing the glass transition temperature of the polymer matrix. The nanocomposite membrane SP5 showed maximum T_g and melting temperature (T_m) of 68 °C and 207 °C respectively. Thereby, revealing efficient dispersion of BRM within the polymer matrix.. The glass transition temperature (T_g) and melting temperature (T_m) of pure PVA and PVA nanocomposite membranes have been tabulated in table 11.

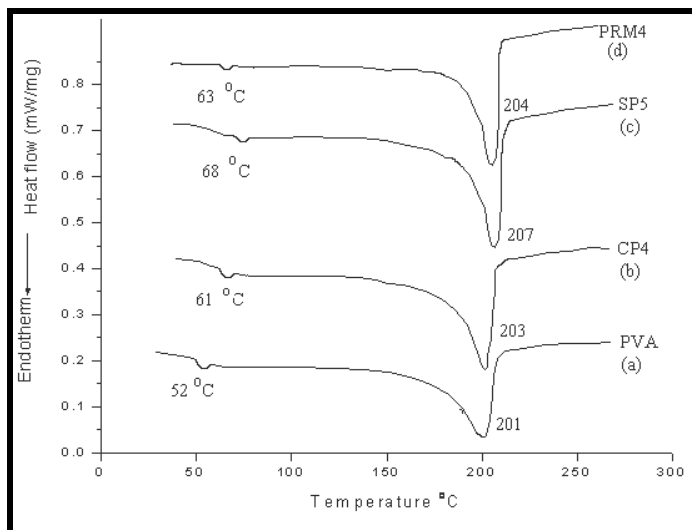


Fig. 22. DSC thermograms of (a) PVA (b) CP4 (c) SP5 (d) PRM4

Sample	T_g (°C)	T_m (°C)
Pure PVA	52	201
CP4	61	203
SP5	68	207
PRM4	63	204

Table 11. Glass Transition temperature (T_g) and melting temperature of pure PVA and the PVA- nanocomposite membranes

4. Preparation of Phe-phosphomolybdic acid modified red mud nanocomposite materials (PRC) and Phe-organically modified red mud nanocomposite materials (PNC)

10% (w/v) solution of Phe was prepared by dissolving dried Phe in THF with continuous stirring at 50 °C. Polymer nanocomposite (PN) films were made by mixing different loading percentage of phosphomolybdic acid modified red mud (PRM) and organically modified red mud (ORM) into the virgin Phe solution, stirred constantly and sonicated for half an hour for better dispersion. The composition of the PN materials was varied from 0 to 3wt % of modified RM with respect to the Phe content. The samples were designated as shown in Table 12.

Sample index	% Loading of filler
*Phe	0
**PRC1	1.0
PRC2	2.0
PRC3	3.0
***PNC1	1.0
PNC2	2.0
PNC3	3.0

*Phe: Phenoxy or poly (hydroxy ether) of Bisphenol A

** PRC: Phe-phosphomolybdic acid modified red mud nanocomposites

*** PNC: Phe-organically modified red mud nanocomposites

Table 12. Sample Designation

4.1 FTIR spectroscopy

The FTIR spectra in Figure 23 showed the presence of characteristic peaks of poly (hydroxy ether) of bisphenol A. The characteristic vibration band of Phe for hydroxyl stretching vibration (O-H) having polymeric association was observed at 3394 cm⁻¹, While the alkyl stretching band of C-H was shown at 2974 cm⁻¹ and aryl stretching band of C-H at 3037 cm⁻¹. The peak at $\nu = 1183$ cm⁻¹ is due to C-O stretching of phenyl ether linkage. Further, the peak at $\nu = 1607$ cm⁻¹ could be attributed to the aromatic ring.

Figure 23 also showed the spectra of Phe-modified red mud nanocomposite membranes with different loading percentage of the filler. The characteristic vibration band of PRC3 for hydroxyl stretching vibration (O-H) was observed at 3270 cm⁻¹. The intensity of the O-H stretching vibration peak decreased and peak frequency shifted from 3394 to 3270 cm⁻¹, i.e. to a lower frequency as compared to that of pure phenoxy. The red shift in the hydroxyl stretching frequency occurs due to the various degree of hydrogen bonding between the polymer and the filler which lengthens and weakens the O-H bond and hence lowers the vibrational frequency. The alkyl stretching band of C-H in case of PRC3 also showed red shift from 2974 to 2861 cm⁻¹ due to the interaction of modified red mud with the polymer matrix. Similarly, peak at $\nu = 3036$ cm⁻¹, was attributed to the stretching vibration of aryl C-H band, slightly lower frequency than the pure phenoxy. The other characteristic vibrational frequencies of PRC3 are presented in table 13.

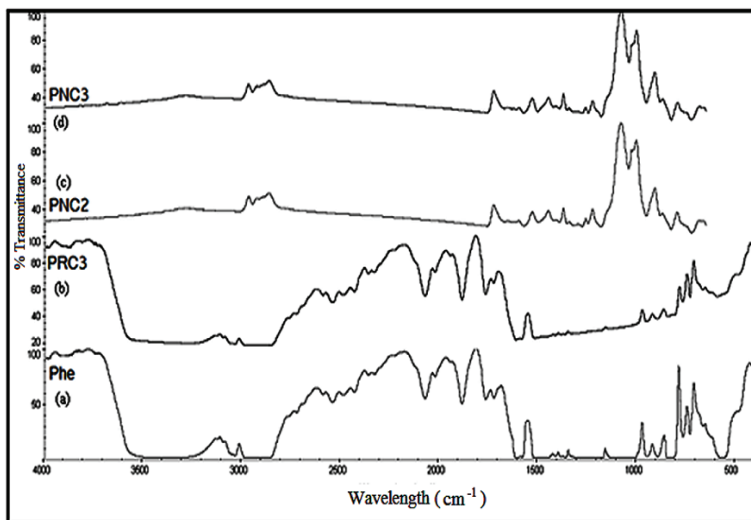


Fig. 23. FTIR Spectrum of (a) Pure Phe (b) PRC3 (c) PNC2 (d) PNC3

Groups	PHE (cm ⁻¹)	PRC3 (cm ⁻¹)	PNC2 (cm ⁻¹)	PNC3 (cm ⁻¹)
OH	3394	3270	-	-
C-H	2974	2861	2948	2947
C-H (Ar)	3037	3036	3016	3020
NH ₃ ⁺	-	-	1571	1572
C-O	1183	1168	1182	1180
C=O	-	1766	1760	1760
Ar	1607	1613	1499	1503
Si-O	-	953	952	951
Mo-O _c -Mo	-	896	-	-

Table 13. Assignment of FTIR spectral bands for Pure Phenoxy and the Ph/modified red mud nanocomposite membranes

The spectra of PNC2 and PNC3 as shown in fig. 23, showed the disappearance of the hydroxyl stretching frequency (O-H). The disappearance of the hydroxyl peak depicted complete physical interaction of the O-H group with different groups of the organically modified red mud, thereby not leaving any free hydroxyl group. However, alkyl stretching band of C-H for PNC2 and PNC3 were observed at 2948 and 2947 cm⁻¹ respectively. The red shift in the alkyl stretching frequency C-H of PNC2 and PNC3 as compared to the pure phenoxy showed interaction of the filler with the polymer matrix.

The characteristic vibrational frequencies of PNC2 and PNC3 at $\nu = 1571$ and 1572 cm⁻¹ respectively, was attributed to the stretching frequency of ammonium ion (NH₃⁺), thereby

depicting formation of zwitter ion. The other vibrational frequencies associated with PNC2 and PNC3 have been tabulated in table 13. The organically modified red mud(ORM) showed better interaction with the poly (hydroxy ether) of bisphenol A matrix as compared to phosphomolybdic acid modified red mud (PRM), therefore, it can be inferred that ORM will show better dispersion into the polymer matrix as compared to PRM.

4.2 X - ray diffraction study

The wide angle diffraction pattern of PRC2 and PRC3 films are shown in Fig. 5. The crystallinity of the composite membranes is mainly due to Phe. The characteristic diffraction peak for PRC2 and PRC3 were observed at a 2θ value of 2.36° and 2.26° . The diffraction peak at $2\theta = 2.26^\circ$ is considerably broadened and the interplanar distance has also widened compared to the raw red mud and PRC2 nanocomposite, indicating intercalation of the phenoxy matrix within the nanofiller of the nanocomposite membranes.

The polymer nanocomposite films showed decrease in the intensity of the crystalline peak as the loading percentage of organically modified red mud increased. The decrease in the intensity of crystalline peaks showed an increase in the disorderness of the interlayers of modified red mud.

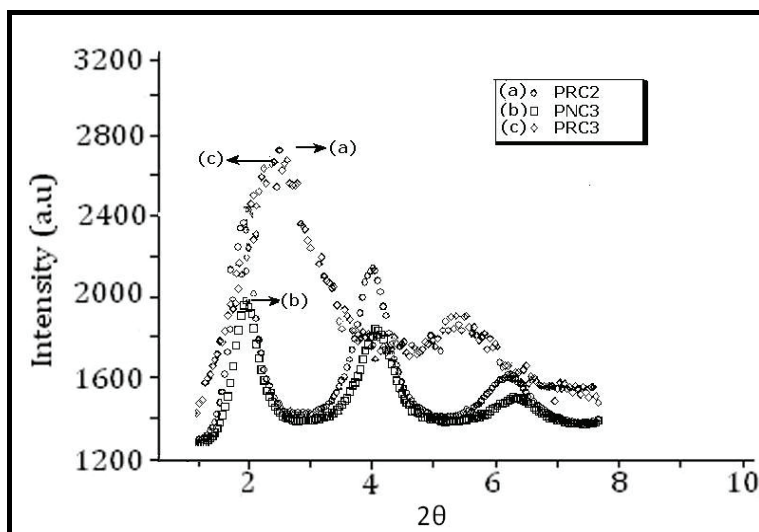


Fig. 24. XRD pattern of (a) PRC2 (b) PNC3 (c) PRC3 nanocomposites

From table 14, it is clear that the basal spacing for PRC3 is larger than the other PRM based nanocomposites materials, thereby giving evidence of better intercalation of polymer matrix within the silicate galleries of filler in case of PRC3 than the rest of nanocomposites.

Sample	2θ	d-spacing (\AA°)
PRC2	2.36	37.56
PRC3	2.26	39.48
PNC3	2.11	41.62

Table 14. XRD results of Phe-PRM and Phe-ORM based nanocomposite membranes

The X-ray diffraction pattern of phenoxy-organically modified red mud nanocomposite membranes are shown in fig. 24. The characteristic diffraction band of PNC3 was observed at $2\theta = 2.11^\circ$. The increase in the interlayer distance of silicate galleries of the organically modified red mud indicated that Phe has successfully intercalated into the silicate layers.

4.3 Field Emission Scanning electron microscopy (FESEM)

Field emission scanning electron microscope has evolved in which the electron beam cross section has become smaller and smaller increasing magnification several fold. Raw red mud and modified red mud were characterized by Field Emission Scanning Electron Microscopy (FESEM), as shown in Figure 25. The FESEM analysis showed that the raw red mud consisted of aggregates, including particles of different dimensions. The FESEM image of the PRM and ORM showed a very fine distribution of particles with a size of 64 and 71 nm respectively as shown in Fig. 7. While ORM showed a homogenous distribution of particles than raw red mud with particle size larger than PRM due to formation of organic coating around the particles.

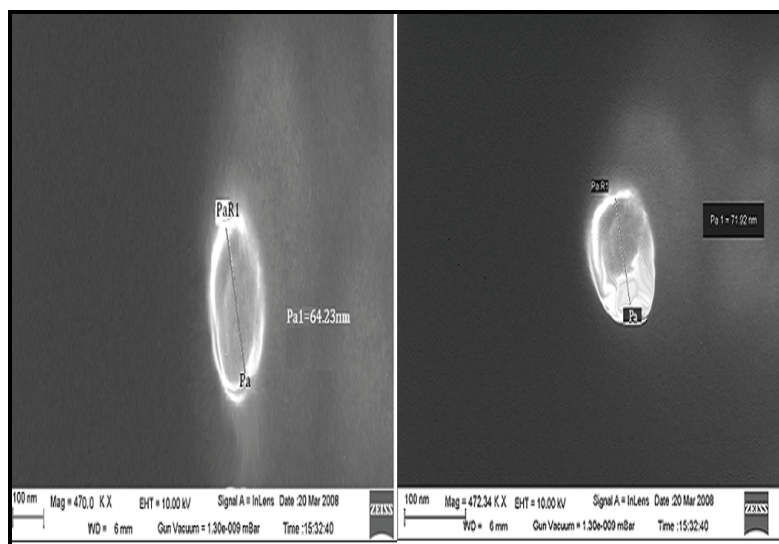


Fig. 25. FESEM images depicting size of a single red mud particle (a) Phosphomolybdic acid modified red mud (PRM), (b) Organically modified red mud (ORM)

4.4 Transmission Electron Microscopy (TEM)

TEM complements XRD by observing a very small section of the material for the possibility of intercalation or exfoliation. It also provides information about the particle size and nanodispersion of particles. It however, supplies information on a very local scale. However, it is a valuable tool because it enables us to see the polymer and the filler on a nanometer scale.

Fig. 8 (a) showed a representative TEM image of the PNC3 with a 3 wt% loading percentage of organically modified red mud in the phenoxy matrix, while fig. 8(b) showed a representative TEM image of PRC3. As seen in fig. 8(a), a rather good dispersion of the

organically modified red mud is achieved. It is clear that the area covered by the red mud in fig.8 (a) is larger than in fig. 8(b) indicating a more extended platelet separation and an overall best nanodispersion of the critical loading of 3 wt% ORM in the phenoxy matrix.

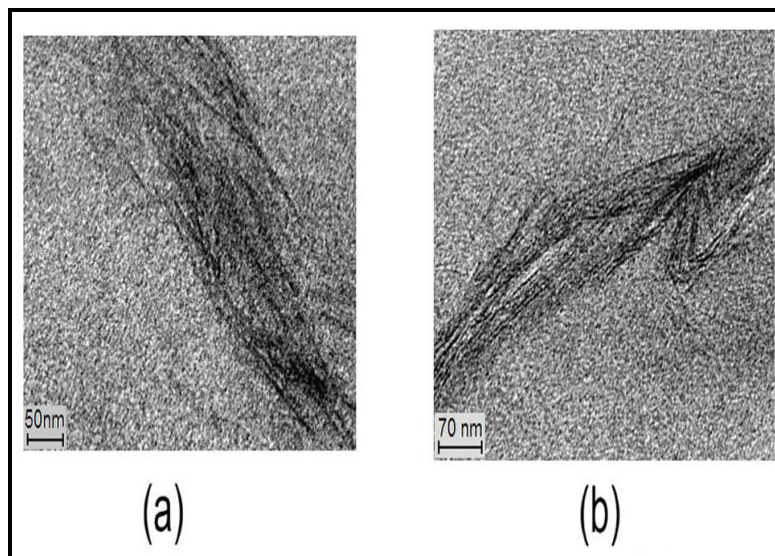


Fig. 26. TEM micrographs of (a) PNC3 (b) PRC3

The average particle size was found as 14 nm in case of PNC3 as shown in fig. 26(a), while the size of the particles in PRC3 was found to be 19 nm as shown in fig. 26(b). In fig. 26(b), the nanoparticles showed certain extent of agglomeration and formation of interconnected aggregates or tactoids of silicates.

There may be several fundamental problems that affect the polymer particle interactions in solution, resulting in disordered nanoparticle aggregates. These problems may arise from competing interactions between solvent, polymer chains and filler particles. The conformation of the polymer chains adhered to the nanoparticles also influences the ordered dispersion of the particles.

The presence of the organically modified red mud and phosphomolybdic acid modified red mud with different loading percentage and dispersing capabilities, may help us to identify the main structural driving force for dispersion in these Phe based PNs. It has been reported that the interaction between the polymer chains and the inorganic surface of the clay (Fornes et al., 2004) is crucial in polar polymers, and therefore it could also exist between the polar Phe and the modified red mud surface. Good dispersion of modified red mud in the polymer matrix will have a significant effect on the properties of the nanocomposites.

4.5 Thermogravimetric properties

The thermal stability of the pure Phe and Phe nanocomposite membranes with different filler content was investigated by thermogravimetric analysis. The TGA thermograms corresponding to the thermal decomposition of pure Phenoxy and Phe- nanocomposite films are shown in fig. 27 and fig. 28.

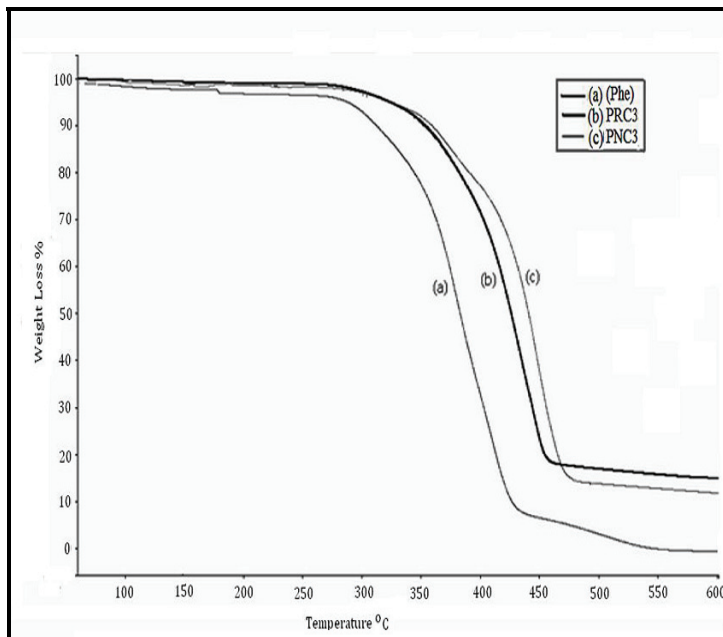


Fig. 27. Thermograms of (a) Phe (b) PRC3 (c) PNC3

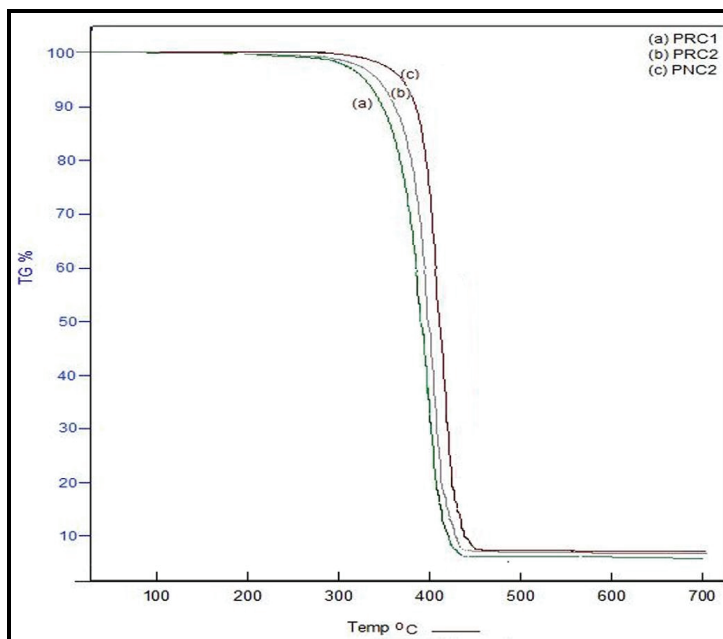


Fig. 28. Shows typical TGA thermograms of (a) PRC1 (b) PRC2 (c) PNC2

As can be observed, both pure polymer and nanocomposite materials decompose in a single stage. If we compare the thermal stability of the polymer and the critical loading percentage nanocomposite membranes of PNC3 and PRC3, it is clear that PNC3 is more stable than pure Phenoxo and PRC3. The pristine Phe is thermally stable up to 275 °C. Since, the Phe nanocomposite membranes show enhanced thermal stability, the initial decomposition temperature (T_i) of phenoxo occurred at 276 °C while in case of PNC3 and PRC3, T_i was found at 318 and 298 °C respectively as shown in table 15. Similarly, final decomposition temperature (T_f) of phenoxo, PNC3 and PRC3 were observed at 433, 479 and 458 °C respectively. The enhancement in the thermal stability of PNC3 could be attributed to the better compatibility and intercalation of polymer matrix within the silicate galleries of 3 wt% organically modified red mud. Similarly, from fig.28 and table 15, it was observed that PNC2 showed higher T_i and T_f as compared to the PRC1 and PRC2, thereby showing higher thermal stability comparatively.

In general, major weight losses were observed in the range of 275–500 °C for Phe and polymer nanocomposite films, which may be correspondent to the structural decomposition of the polymer backbones at higher temperatures. After 500°C, all the curves became flat and mainly the inorganic residue (i.e. Al_2O_3 , MgO, and SiO_2 etc.) remained.

Sample	T_i (°C)	T_f (°C)	Ash (%)
Pure Phe	276	433	3.2
PRC1	287	439	6.33
PRC2	293	443	7.97
PNC2	312	454	8.23
PNC3	318	479	11.30
PRC3	298	458	14.15

Table 15. Degradation temperature and ash content of Pristine Phe and the Phe-nanocomposite membranes

4.6 Atomic Force Microscopy (AFM)

The surface morphology of the pure Phenoxo membrane and the Ph-modified nanocomposite membranes were analyzed by Tapping Mode - Atomic Force Microscopy (TM-AFM). Quantitatively, the differences in the morphology can be expressed in terms of various roughness parameters such as the mean roughness R_a , the root mean square (rms) of vertical data R_q , and the maximum height R_{max} . Here, the mean roughness is the mean value of surface relative to the center plane, the plane for which the volume enclosed by the image above and below this plane are equal; R_{max} the height difference between the highest and lowest points on the surface relative to the mean plane and R_q is the standard deviation of the Z values within the given area. The roughness parameters were calculated for pure Ph and Ph nanocomposite membrane surfaces with critical loading of filler and have been summarized in tabular format. The TM-AFM images of the Pure Phe membrane is depicted in Fig. 29. The AFM images of Phe membrane showed randomly distributed hard crystalline regions (crystallites) of 50 – 200 nm in dimension on the membrane surface as evident from the observed morphology. The pure Phe membrane surface has a mean roughness of 3.297 nm.

The nanocomposite membrane with critical loading percentage of 3 wt. % ORM (i.e., PNC3) content (Fig. 29) showed a homogeneous and non-porous morphology. The mean roughness for the surface topography of the membrane was found to be 4.045 nm.

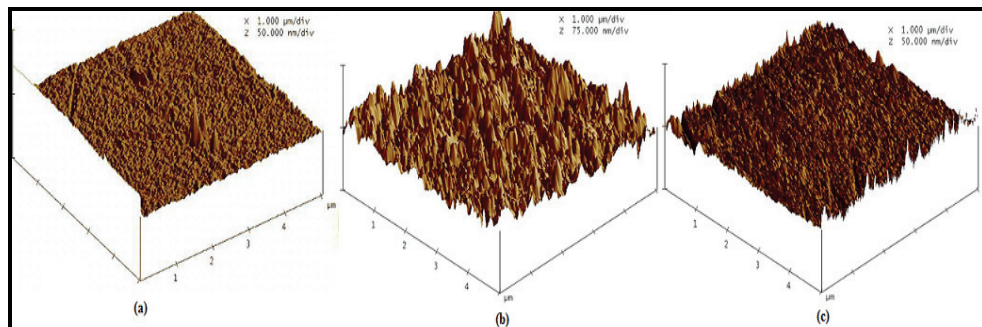


Fig. 29. Tapping mode (3D) AFM images of (a) Phe (b) PRC3 (c) PRC2

This shows that there is a good compatibility between the filler (ORM) and the Ph matrix. This is in consistent with the results of SEM studies. While critical loading surface topography of PRC3 showed some non-uniform regions with non-porous morphology. The mean roughness of PRC3 was observed to be 4.562 nm as shown in table 16. This showed that the phosphomolybdic acid modified red mud with 3 wt% loading percentage tends to form some aggregated particles within the polymer matrix leading to higher roughness values as compared to the PNC3.

Sample	R_a (nm)	R_{max} (nm)	R_q (nm)
Pure Ph	3.297	27.668	4.173
PNC3	4.045	57.648	5.497
PRC3	4.562	116.65	7.003

Table 16. Roughness parameters for Pristine Ph and the Ph nanocomposite membrane surfaces

4.7 Differential Scanning Calorimetry (DSC)

DSC traces of pure Phenoxo and polymer nanocomposite materials are shown in Fig.30. Ph exhibited a shallow endotherm at 61°C corresponding to the glass transition temperature (T_g) of Ph. All the nanocomposite materials with different critical loading percentage of modified red mud were found to have a high T_g as compared to the pristine Phe. This could be attributed to the confinement of the intercalated polymer chains within the red mud galleries that prevents the segmental motions of the polymer chains, thereby enhancing the glass transition temperature of the polymer matrix. The PNC3 nanocomposite membrane showed maximum T_g and melting temperature (T_m) of 66 °C and 220 °C respectively. This depicted that PNC3 is thermally more stable than PRC3 nanocomposite membrane on account of better dispersion and adhesion of the ORM within the polymer matrix. The glass transition temperature (T_g) and melting temperature (T_m) of pure phenoxo and Ph nanocomposite membranes have been tabulated in table 17.

Sample	T_g (°C)	T_m (°C)
Pure Phe	61	206
PNC3	64	211
PRC3	66	220

Table 17. Glass Transition temperature (T_g) and melting temperature of pure Phe and Phe-nanocomposite membranes

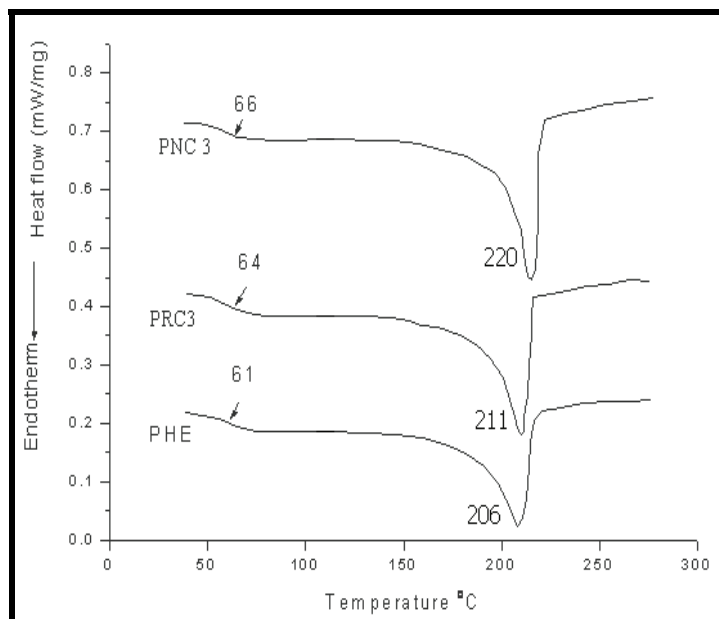


Fig. 30. DSC thermograms of (a) Ph (b) PRC3 (c) PNC3

4.8 Conclusion

- Red mud was successfully modified with the inorganic acids and organic moiety (aniline formaldehyde). The modification ameliorates both the dispersion level and the material properties of the polymer nanocomposites.
- The PVA- boric acid modified red mud nanocomposite films showed better glass transition temperature T_g and thermal stability at a filler concentration of 3.0wt percentage.
- In PVA/ORM nanocomposite systems, 2.0wt% modified red mud (CP4) based nanocomposite film exhibited relatively good dispersion with increase in the thermal stability, glass transition temperature.
- In PVA/PRM nanocomposite systems, 2.5wt% modified red mud (PRM4) based nanocomposite film exhibited relatively good dispersion with increase in the material properties as compared to the pristine poly (vinyl alcohol).
- PVA based nanocomposites showed an increase in the roughness values with the increase in the filler content but the 3.0wt% of boric acid modified red mud nanocomposite membrane showed lower roughness values as compared to the critical loading percentage of ORM and PRM based nanocomposites.
- On comparing the material properties of all the three nanocomposite systems, it was found that the critical loading percentage of BRM based nanocomposite system (i.e., SP5) showed better enhancement as compared to the critical loading percentage of ORM and PRM based nanocomposite systems.
- The TEM images of the PVA-modified red mud nanocomposite membranes showed homogeneous nano phase dispersion of the modified red mud in the PVA polymer matrices at a scale of 8- 23 nm particle size.

- In the poly(hydroxy ether of bisphenol A) (Phe) based nanocomposites as reported in this work, mostly intercalated structures were produced in the acid modified red mud modifications, but modification by organic moiety (ORM) resulted in a mixed intercalated-exfoliated structure.
- Thermal stability of polymer also increases after nanocomposites preparation, because red mud acts as a heat barrier, which enhances the overall thermal stability of the system, as well as assist in the formation of char after thermal decomposition.
- Phe based nanocomposites showed an increase in the roughness values with the increase in the filler content but the 3.0wt% of organically modified red mud nanocomposite membrane showed lower roughness values as compared to the critical loading percentage of PRM based nanocomposites. Thus, PNC3 showed homogenous and non-porous morphology as compared to the coarse morphology of PRC3 type of nanocomposites.
- The average particle size in case of PNC3 is 14 nm while the particle size of PRC3 is 19 nm as revealed by TEM studies.

5. References

- Agag, T.; Koga, T.; Takeichi, T. (2001). Studies on thermal and mechanical properties of polyimide-clay nanocomposites, *Polymer*, 42, 3399.
- Alexandre, M.; Dubois P. (2000). Polymer-layered silicate nanocomposites: preparation, properties and uses of a new class of materials. *Materials Science & Engineering, R: Reports*, R28 (1-2), 1-63.
- Bachtsi, A.R; Kiparissides, C. (1996). Synthesis and release studies of oil containing poly (vinyl alcohol) microcapsules prepared by coacervation, *Journal of Controlled Release*, 38 (1), 49-58.
- Bhat, A.H, Banthia, A.K, (2007). Preparation and Characterization of Poly (vinyl alcohol)-Modified red mud composite materials, *Journal of Applied Polymer Science*, 103 (1), pp. 238-243.
- Biron, M., (2007). Thermoplastics and Thermoplastic Composites. Elsevier Ltd., Jordan Hill, Oxford.
- Chand, N.; Hashmi, S. A. R. (1999). Effect of Red Mud Addition on Abrasive Wear Rate of Isotactic Polypropylene/Low Density Polyethylene Blend under Low Stress Conditions, *J Sci Ind Res*, 58, 795.
- Chand, N.; Hashmi, S. A. R. (1999). Effect of addition of polycarbonate on sheared flow of red mud-filled isotactic polypropylene *Bull Mater Sci*, 22, 801.
- Chen, H.L. Wu, L.G; Tan, J; Zhu, C.L.; (2000). PVA membrane filled β -cyclodextrin for separation of isomeric xylenes by pervaporation. *Chemical Engineering Journal*, 78 (2-3), 159-164.
- Dilsiz, N.; Ebert, E.; Weisweiler, W.; Akovali, G. (1995). Effect of plasma Polymerization on Carbon Fibers Used for Fiber/Epoxy Composites *J Colloid Interface Sci*, 170, 241.
- Donnet, J. B.; Bansal, R. C. Carbon Fibers, 2nd ed.; Dekker: New York, 1990.
- Fornes TD, Hunter DL, Paul DR. (2004) Nylon - 6 nanocomposites from alkylammonium - modified clay: the role of alkyl tails on exfoliation. *Macromolecules*, 37(5), pp. 1793-1798.
- Grjotheim, K.; Welch, B. J. Aluminium Smelter Technology: A Pure and Applied Approach, 2nd ed.; Verlag: Dusseldorf, 1998.

- Hajji, P.; David, L.; Gerard, J. F; Pascault, J. P; Vigier, G. (1999). Synthesis, structure, and morphology of polymer-silica hybrid nanocomposites based on hydroxyethyl methacrylate, *Journal of Polymer Science, Part B: Polymer Physics*, 37(22), 3172-3187.
- Horii, F; Hu, S; Ito, T; Odani, H; Kitamaru, R. (1992). Cross-polarization/magic-angle-spinning carbon-13 NMR study of solid structure and hydrogen bonding of poly(vinyl alcohol) films with different tacticities, *Polymer*, 33(11), 2299-2306.
- Huang, H H.; Orler, B.; Wilkes, G L. (1987). Structure-property behavior of new hybrid materials incorporating oligomeric species into sol-gel glasses. 3. Effect of acid content, tetraethoxysilane content, and molecular weight of poly(dimethylsiloxane), *Macromolecules*, 20, 1322.
- Ishikawa, Y.; Matsumoto, Y. (2001). Electrodeposition of TiO₂ photocatalyst into nano-pores of hard alumina, *Electrochim Acta*, 46, 2819.
- Jang, B. Z. (1992). Control of interfacial adhesion in continuous carbon and kevlar fiber reinforced polymer composites, *Compos Sci Technol*, 44, 333.
- Kasliwal, P.; Sai, P. S. T. (1999). Enrichment of titanium dioxide in red mud: a kinetic study *Hydrometallurgy*, 53, 73.
- Lee, D. C.; Jang, L. W. (1996). Preparation and characterization of PMMA-clay hybrid composite by emulsion polymerization. *Journal of Applied Polymer Science*, 61(7), pp. 1117-1122.
- Novak, B. M; Ellsworth, M. W. (1993). "Inverse" organic-inorganic composite materials: high glass content non-shrinking sol-gel composites, *Materials Science & Engineering, A: Structural Materials: Properties, Microstructure and Processing*, A162(1-2), 257- 64.
- Park, S. J.; Cho, M. S. (2000). Effect of anti-oxidative filler on the interfacial mechanical properties of carbon-carbon composites measured at high temperature. *Carbon*, 38, 1053.
- Park, S. J.; Kim, M. H. (2000). Effect of acidic anode treatment on carbon fibers for increasing fiber - matrix adhesion and its relationship to interlaminar shear strength of composites *J Mater Sci*, 35, 1901.
- Park, S. J.; Kim, J. S. (2001). Influence of Plasma Treatment on Microstructures and Acid - Base Surface Energetics of Nanostructured Carbon Blacks: N₂ Plasma Environment, *J Colloid Interface Sci*, 232, 311.
- Peppas, N.A; Merrill, E.W. (1977). Development of semicrystalline poly(vinyl alcohol) hydrogels for biomedical applications, *Journal of Biomedical Materials Research*, 11(3), 423-34.
- Pradhan, J.; Das, S. N.; Thakur, R. S. (1999). Adsorption of Hexavalent Chromium from Aqueous Solution by Usin Activated Red Mud, *J Colloid Interface Sci*, 217, 137.
- Ray S. S and Bousmina M, (2005). Biodegradable polymers and their layered silicate nanocomposites: In *greening the 21st century materials world*, *Progress in Materials Science*, 50(8), 962-1079.
- Shao, C.; Kim, H-Y; Gong, J.; Ding, B.; Lee, D-R.; Park, S-J. (2003). Fiber mats of poly(vinyl alcohol)/silica composite via electrospinning, *Materials Letters*, 57(9-10), 1579-1584.
- Surivet, F.; Lam, T. M ; Pascault, J. P; Pham, Q. T. (1992). Organic-inorganic hybrid materials. 1. Hydrolysis and condensation mechanisms involved in alkoxysilane-terminated macromonomers, *Macromolecules*, 25(17), 4309-20.
- Yuan, L. T.; Shyu, S. S.; Lai, J. Y. (1991). Plasma surface treatments on carbon filbers. II. Mechanical property and interfacial shear strength *J Appl Polym Sci*, 42, 2525.
- Zhang H, Ma H, Hongtu Li and Wang (2002). J, Synthesis and characterization of a polymer- metal complex from bisphenol A polyhydroxy ether with sulfur-bearing side-groups, *Polym Int.*, 51, pp.1129-1134.

Biopolymer as Reinforcement into Natural Matrices: a New Route to Bio-Composite Materials

Marion Noël^{1,2}, Emmanuel Fredon¹, Eric Mougel¹,
Eric Masson² and Daniel Masson¹

¹LERMAB INRA 1093, UHP Nancy I, ENSTIB,

²Cribois

^{1,2}France

1. Introduction

In order to design a new, efficient and competitive material, no process is better than combining several components, and their own performance. Such composite materials are designed to meet specific technical expectations. They mostly consist in an organic, ceramic or metallic reinforced matrix, where reinforcement can be long or divided fibres, divided particles, filling dust... Reinforcement is expected to confer to the material its mechanical properties. The matrix binds the reinforcement parts together and guaranties the forces transmission.

Within the composite materials widely manufactured in mass industrial production, an attractive and well-known, tremendously emerging composite category is the WPC, or Wood Plastic Composites category. This material is composed of a polymeric matrix, preferably thermoplast resin as polyvinylchloride or polyethylene, even if thermoset resins as epoxies or phenolics can be, or have been, used (phenol-formaldehyde mixed with wood flour known as Bakelite, for instance). The reinforcement has to be a natural compound as wood or possibly other fibrous biomass. The addition of fillers leads to two major improvements. First the material is lightened, as fillers density is lower than the matrix density. Second, the mechanical properties are expected to be improved.

Literature content is abundant as the combinations potential is huge. Most of times, the admixtures encounter a poor interfacial adhesion between natural hydrophilic polar fillers and synthetic hydrophobic nonpolar matrix. To reach a better interfacial cohesion, chemical treatment of the surface of reinforcing components has to be carried out to allow creating bridge of chemical bonds between matrix and reinforcement. Bledzki & Gassan, 1999 and George et al., 2001 provide a list of possible cellulosic fibers treatments from esterification or acetylation of cellulose to treatment with isocyanates or silanes or use of triazine or organosilanes as coupling agents.

The use of cellulosic fibres instead of synthetic reinforcements allows to reduce production cost but also to involve natural compounds within the material conception. In the same guideline, biobased polymers have been more recently considered as matrices. Those biopolymers come from bioresources and/or can be degraded at the end of their life cycle. Bio-

sourced bio-polymers can come from animals (chitin, protein, ...), microorganisms (poly(lactic acid), poly(hydroxyalkanoates), ...), or plants (starch, cellulose, lignin, ...). Fossile bio-polymers are mostly composed of polycaprolactone, poly(lactic acid), poly(glycolic acid), polyvinylalcohol and polyesteramide. Bio-polymers are competitive with standard polymers in terms of performance, even if their producing cost and involved energy consumption are still high.

In the environmental point of view, entirely biobased composites are obviously promising. Reinforcement of biopolymer matrices with natural fibres or fillers has been reported. Fink & Ganster, 2006 witnessed a good compatibility between cellulosic fibres with poly(lactic acid) without coupling, while polyethylene, polypropylene and polystyrene had to be grafted or copolymerised with maleic acid anhydride. Gatenholm et al., 1992 noticed also an excellent dispersibility of cellulose fibres in polyhydroxybutyrate (PHB) matrix compared with synthetic matrices.

Bio-based, natural materials are often sensitive to their environment. It is the case of wood, used since centuries in the building, furniture, artistic fields for its excellent properties. Constituted of cellulose reinforcement in a ligneous matrix, wood is itself a natural composite. But its high hydrophilic character and sensitivity to biological attacks are its most limiting disadvantages. Indeed, wood exposed outdoor has to be protected either by surface coatings or preservation chemicals. Coatings have the advantage to be more or less innocuous to the environment, but a mechanical crack in the coating layer leads to unavoidable and irreversible wood degradation. Chemical treatments penetrate the wood structure in a higher thickness, but a major concern is the releasing of preservative chemical in the environment. That's why grafting or in-situ polymerization of chemical compounds is expected. Rowell, 2005 described the chemical modification of wood. As hydroxyl groups in wood are responsible of the hydrophilic property, their esterification with acid anhydrides is a possibility to reduce moisture affinity with wood. Different epoxydes or isocyanates are also susceptible to react with wood. Wood impregnation by polyethylene glycol, polyglycerols, formaldehyde resins, styrens or methyl methacrylate have been widely reported (Ibach & Rowell, 2001; Zhang et al., 2006).

A different way to produce an entirely biobased composite is to reinforce a natural matrix, as wood, with natural or biodegradable polymers, as polymerized lactic acid. This association has not been much reported to date (Noël et al., 2009). The affinity between both materials should lead to interesting chemical reaction providing wood protection. Grafting of carboxylic end groups of poly(lactic acid) onto hydroxyl groups of wood, and in-situ polymerization should avoid any chemical release in the environment. What is looked for is an increase in wood dimensional stability and biological resistance. Simultaneously, the density increase due to the treatment is expected to induce gainful property variation.

2. Composite material manufacturing

2.1 Method

Poly(lactic acid) (PLA) is one of the most produced and processed bio-polymers. It is produced from lactic acid monomers polycondensation. Lactic acid can be synthesized from fossile resources or extracted from corn and produced by biotechnological means, which gives the natural origin of PLA. Polycondensation of aqueous lactic acid into PLA is mostly achieved by Ring Opening Polymerization (ROP): the first step is a direct polycondensation leading to oligomers. This step is limited by a complicated elimination of the water produced. In the second step, the oligomers are depolymerized into lactide cycles. The last

step consists in opening the cycles to build long PLA polymer chains. Residual monomers which did not react are then recycled and reused. The only first step of direct polycondensation has been considered to prepare the wood treatment product.

Solid wood impregnation can be achieved in two steps. The first step consists in making the acid treatment penetrate the cells. This is achieved under vacuum. The second step consists in making the acid mono- and/or oligomers polymerize into the wood matrix.

To help polymerization, aqueous acid dilution must be first dehydrated and oligomerized. Indeed, water would be an obstacle to the in-situ polymerization step. On the other side, if oligomerization can help the in-situ polymerization step, attention must be paid to the oligomers viscosity, as the perfect case would be to achieve not only the lumen but also the cell wall penetration. It has been shown that an oligomerization of aqueous lactic acid (88% in water), leading to a mean polymerization degree of 2 to 3, is a good compromise. Such a product possesses a viscosity of 750 cP, and can be obtained by vacuum dehydration at 120°C for 1 hour. This gives stable oligomers, which can be stored in close flasks at room temperature for several weeks.

Wood matrix must be dried until anhydrous state before the impregnation step. Removing as much water molecules as possible is also necessary to free the hydroxyle grafting sites. Samples of pine sapwood (*Pinus sylvestris*) and beech (*Fagus sylvatica*) are used as reference species.

The impregnation process begins with a vacuum step where most of the air contained in wood is extracted. Then, lactic acid oligomers are introduced in the container until covering wood samples. The container stays some hours in low pressure. Alternation of low and atmospheric pressure is conducted for one day. This process is expected to allow most of the air contained in wood to be replaced by oligomers. The chemical affinity between oligomers and wood constituents in the cell walls leads then to the wall penetration.

Following this protocol, high impregnation yields can be reached. Indeed, up to 70 % of mass uptake is noticed on beech and 120 % on pine sapwood. According to wood and lignocellulosics mean densities, and following the simplified formula (1), it seems that up to 80 % of wood cellular vacuum (beech and pine sapwood respectively) can be filled with oligomers. This is information of a quite good affinity between lactic acid oligomers and solid wood.

$$P(\%) = \left(1 - \frac{\rho_0}{\rho_{lcm}} \right) \times 100 \quad (1)$$

with P : wood porosity

ρ_0 : anhydrous wood density

ρ_{lcm} lignocellulosic material density $\approx 1530 \text{ kg.m}^{-3}$

Lactic acid oligomers final polymerization is then achieved by oven-heating. Checking the impregnation yield evolution along heating time gives valuable information about the in-situ polymerization rate. Indeed, water is the polycondensation by-product gradually eliminated.

2.2 Alternatives

The role of lactic acid polymers into wood is to reinforce the lignocellulosic matrix. Therefore, the favourite polymerization protocol is the one which leads to the highest in-situ polymerization degree.

In the polymers manufacturing industry, especially PLA manufacturing, designing a polymer with a significant polymerization degree in an efficient process makes the use of chemical catalysts unavoidable.

As care must be taken not to expose wood to severe temperature, catalyst addition is a possibility to help polymerization in soft conditions. A lot of well suited chemical catalysts can be found in the literature. The assumption of their efficiency is done by dispersing them separately into the oligomers, without being impregnated into the wood matrix. The as-prepared mixtures are vacuum heated and their polymerization degree assessed. Sulfuric acid and Tin (II) ethyloxanoate have proved themselves to be the most efficient catalysts. Indeed, starting from the oligomers product, a second heating step leads to a polymerization degree of 40 with 0.6% sulphuric acid (120°C / 1h) and 24 with 5% Tin (II) ethyloxanoate (150°C / 1h).

A commercially available PLA shows a density of around 70'000 g.mol⁻¹. Because of physical restrictions, this is obviously not achievable into the lignocellulosic matrix. All the more that polymerization conditions have to be soft enough to avoid wood degradation.

Following the in-situ polymerization by mean of Thermo-Mechanical Analysis (TMA) gives valuable information about the influence of the components the ones on the others. Impregnated beech samples (20mm longitudinal x 0.6mm radial x 5mm tangential) have sustained a three points bending test within a temperature increase of 200 °C (from 25 to 225°C with a rate of 2°C.mn⁻¹). As can be seen in Figures 1 and 2, a critical temperature of about 112°C induces a significant decrease of the Young Modulus.

In the same temperature range (from around 60°C to around 112°C), the Young Modulus decrease is related to a strong deformation. This is due to the oligomers viscosity decrease, which leads to a deeper penetration in the matrix. This is translated by a noticeable wood softening. From 112°C to around 180°C, Young Modulus increases, while deformation is reduced. This is due to the oligomers polymerization which reinforces the structure.

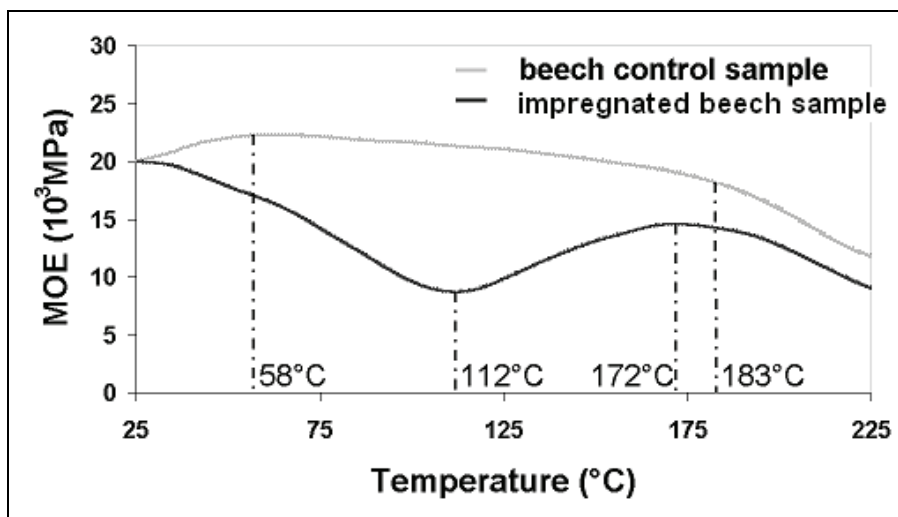


Fig. 1. Young's modulus behaviour of impregnated beech veneer sample compared to beech control sample

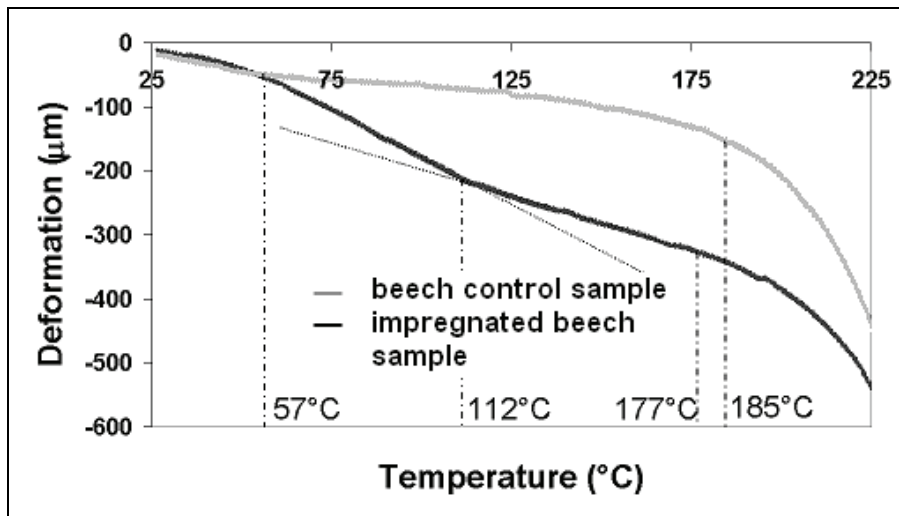


Fig. 2. Deformation of impregnated beech veneer sample compared to beech control sample
To focus on the softening temperature, TMA bending tests have been carried out under five isothermal conditions (Figure 3). This reveals that from 120°C, the first Young Modulus strong decrease step is followed by a compensating increase step.

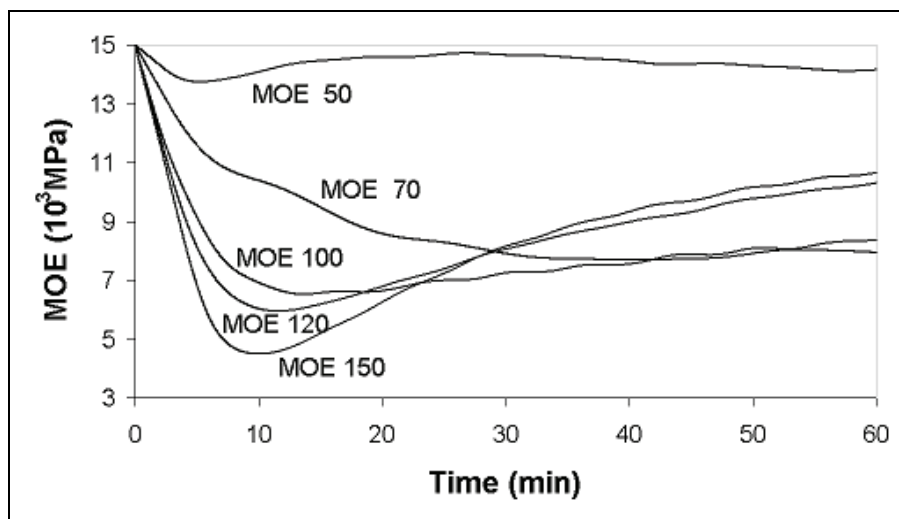


Fig. 3. Young's modulus behaviour of impregnated beech veneer samples subjected to isothermal conditions at 50, 70, 100, 120 and 150 °C

On the basis of these observations, the treatment process has been set up (Figure 4).

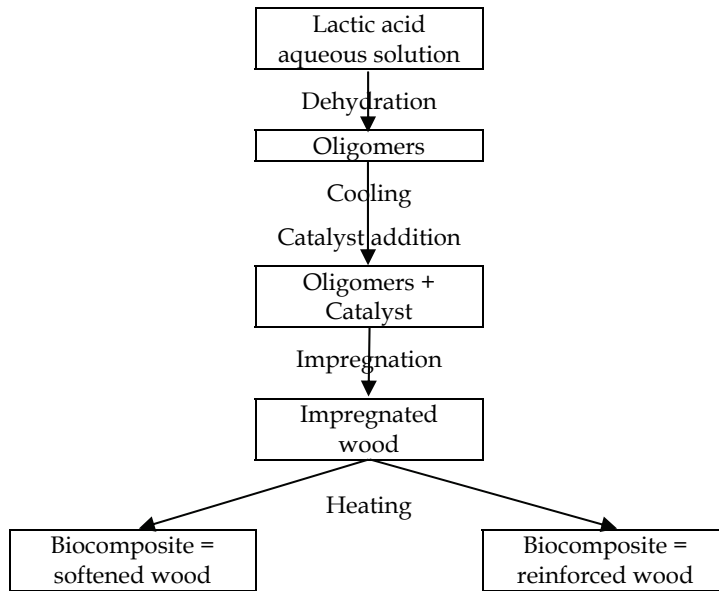


Fig. 4. Composite manufacture processing

2.3 Physical observation

Treatment has been conducted on samples in a macroscopic scale. A strong interaction between wood and the polymerized oligomers can be attested.

The composite material obtained by mean of the short treatment without catalyst consists in impregnated wood, partially dry. No grafting or strong polymerization seems to have occurred. The long treatment induces a complete drying.

Obtained by mean of catalyzed short treatment, the material obtained is strongly softened, partially dry and highly darkened. Completely dry after the long treatment, the composite appears hard and brittle.

A strong swelling is noticed after heating step: up to 30%. As oligomers impregnation induces only 2% swelling, this indicates that oligomers inside wood lumens penetrate the cell walls during heating step. Figure 5 shows a transverse section of long treated pine where lumens appear empty.

Chemical catalysis causes another physical reaction: a strong darkening of wood during heating step. According to Formula (2), figure 6 shows the ΔE^* of pine sapwood and beech samples due to heating.

$$\Delta E^* = \sqrt{(L_f^* - L_i^*)^2 + (a_f^* - a_i^*)^2 + (b_f^* - b_i^*)^2} \quad (2)$$

with L^* , a^* and b^* the three colour coordinates in the CIELab system of samples before (i=initial) and after (f=final) treatment.

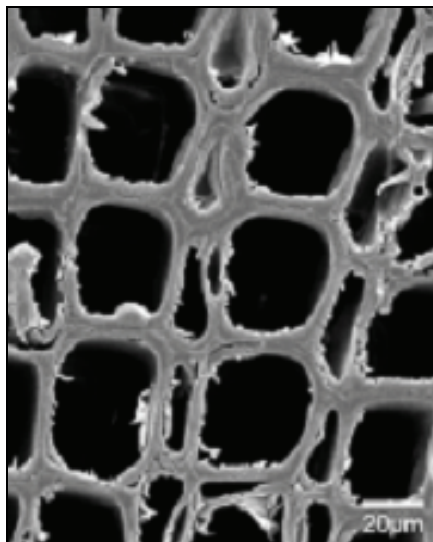


Fig. 5. SEM micrographs of treated pine sapwood sample

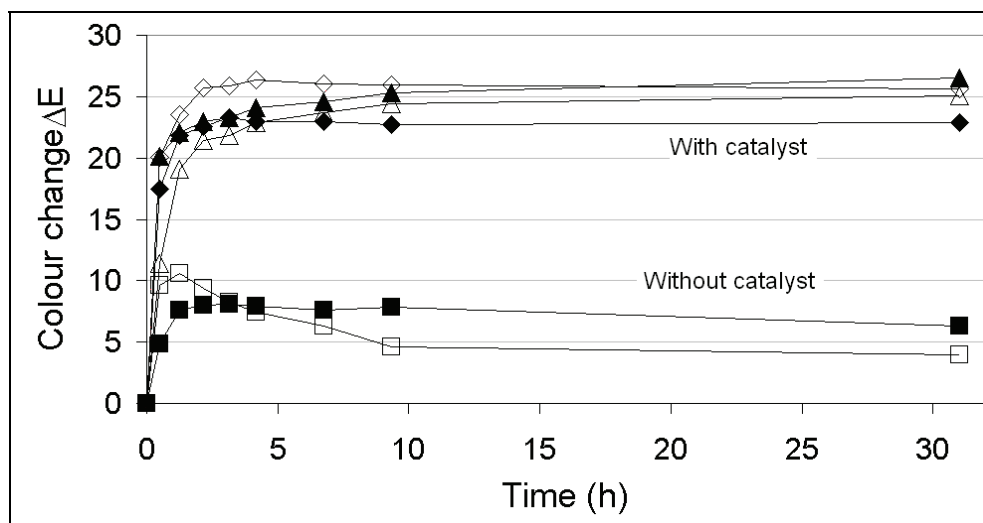


Fig. 6. Colour change of treated samples during the heating period

Colour change of samples treated without catalyst is in the range of classical colour changes due to heat treatment on wood. With catalyst, darkening is strong enough to modified wood appearance.

PLA darkening while processing is often reported in the literature. PLA purity, related to the L-isomers content is considered as one possible reason of coloration. But interactions between oligomers and lignocellulosic compounds could also lead to such a darkening. Every constituent of the composite has been subjected to short and long heating: oligomers,

wood, cellulose, extracted wood, extractives, and lignin sulfonate powder. Darkening is observed on wood subjected to short and long catalysed treatment, on low purity oligomers subjected to sulphuric acid catalysed long treatment, on cellulose subjected to catalysed long treatment, on extractives subjected to sulphuric acid catalysed treatment. Lignin sulfonate powder, already brown, is strongly darkened in every case.

Wood softening is translated by the wood structure disintegration into single fibres. Middle lamella, mostly composed of lignin, seems to be destroyed by the chemical treatment and do not fix cells anymore. Figure 7 attests this observation.

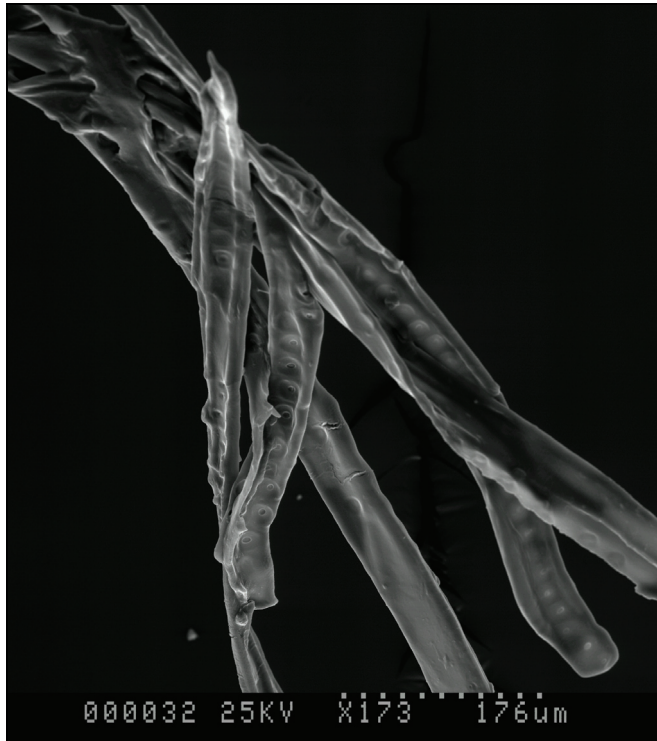


Fig. 7. Treated pine sapwood whose tracheids are easily manually disjointed. Softening and darkening are strongly related and both phenomenons imply a lignin modification.

3. Product performance

3.1 Physico-chemical properties

In-situ polymerization of lactic acid oligomers has been analysed by FTIR spectroscopy and gel permeation chromatography.

Infra-red spectroscopy attests the occurrence of polymerised lactic acid into wood structure (Figure 8). Indeed, PLA characteristic peaks at 875 cm^{-1} and 765 cm^{-1} are superimposed on wood spectra, and the shift of carbonyl absorption band from 1746 to 1764 cm^{-1} during heating indicates a higher ester linkage content.

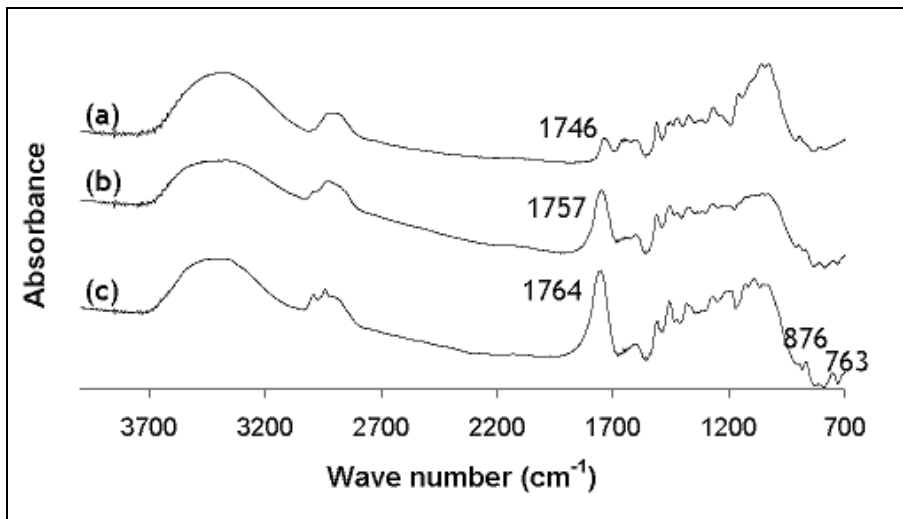


Fig. 8. FTIR spectra of pine control sample (a), pine after catalysed short (b) and long (c) treatment

Polymer extracted from treated samples by chloroform show a noticeable increase and a strong enlargement in molecular weight distribution (Figure 9).

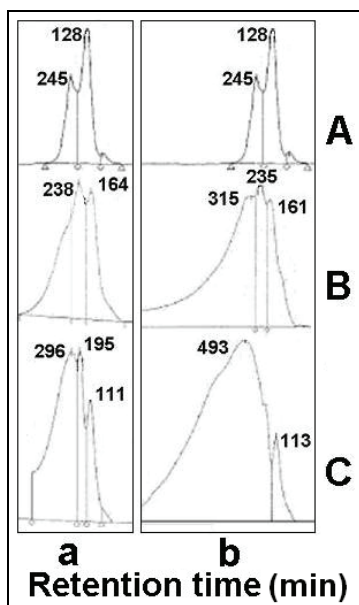


Fig. 9. GPC chromatograms of impregnated oligomers (A), oligomers extracted from short (B) non catalysed (a) and catalysed (b) treatment, and oligomers extracted from long (C) non catalysed (a) and catalysed (b) treatment

After short treatment, oligomers are not durably linked to the wood structure as around 90% weight loss by chloroform extraction is noticed. No characteristic oligomer peaks is noticed in the FTIR spectra neither. After long treatment, around 50% weight loss indicates that half the amount of oligomers remained in wood, either due to physical trapping of the molecules or hydrogen bondings.

3.2 Physical performance

Expected to be used outside, wood has to reach a suitable performance according to swelling. The anti-swelling efficiency of long treated samples has been evaluated around 70%. Even samples subjected to water leaching, which is susceptible to occur in the environment, show the same anti-swelling efficiency values. This is due to the occurrence of oligomers into the cell walls, around cellulose microfibrils where water uptake takes usually place, and promises a good outside stability.

Water leaching has been quantified as around 16% oligomers weight loss on the oligomer content basis, after one week of leaching. It has been found that acid concentration of removed water increases in time along with the gradual hydrolysis of lactic acid chains in the wood cell walls.

3.3 Mechanical performance

Mechanical performance have been assessed in terms of bending strength (σ_B), compression strength (σ_C), shearing strength (f_V), and hardness (Brinell HB and Monnin N normalized methods). Table 1 summarizes densified samples strengths.

Specimen	σ_B (MPa)	σ_C (MPa)	f_V (MPa)	N
Beech control	120	72		11.9
Non catalysed treatment	142	97		15.3
Sulfuric acid catalysed treatment	50	107		19.4
Tin octoate catalysed treatment	86	92		19.3
Pine sapwood control	170	47	2.7	3.7
Non catalysed treatment	146	66	2.2	3.3
Sulfuric acid catalysed treatment	172	64	1.1	7.8
Tin octoate catalysed treatment	181	54	1.2	5.2

Table 1. Mechanical properties of densified composite

Densified composite shows a different mechanical behaviour according to the species and treatment.

Pine samples bending strength is not affected by catalysed or non catalysed treatment. Contrariwise, catalysed treatments strongly affect beech samples. With every treatment on both species, the bending deflection is decreased, which translates the brittleness of the material. This is not necessarily a limitation. Especially in the case of pine samples, where the same bending force leads to break but with less deformation.

Compression strength parallel to the grain is increased by every treatment on both species, with reduced deflection as well.

Shearing strength test performed on pine samples confirms a strong embrittlement of middle lamella. Indeed, shearing strength is strongly decreased by catalysed treatments.

Monnin hardness is strongly increased by catalysed treatment.

Densified composite obtained by non catalysed treatment shows improved or at least unchanged mechanical properties.

Densified composite obtained by catalysed treatment shows improved compression strength and Monnin hardness, but an obvious degradation of fibres cohesion has occurred.

Mechanical assessment of softened composite has been used to quantify the structural degradation. Table 2 summarizes softened samples strengths.

Specimen	σ_B (MPa)	f_v (MPa)	N
Beech control	120		11.9
Non catalysed treatment	77		2.7
Sulfuric acid catalysed treatment	15		5.3
Tin octoate catalysed treatment	6		1.5
Pine sapwood control	170	2.7	3.7
Non catalysed treatment	75	2.3	0.3
Sulfuric acid catalysed treatment	14	1.1	1.8
Tin octoate catalysed treatment	28	101	1.3

Table 2. Mechanical properties of softened composite

Compression strength cannot be assessed on softened samples because no breaking point is ever reached (Figure 10). Instead, crushing happens progressively along the test. Bending strength, shearing strength and hardness are strongly decreased by every treatment, even more by catalysed treatments.

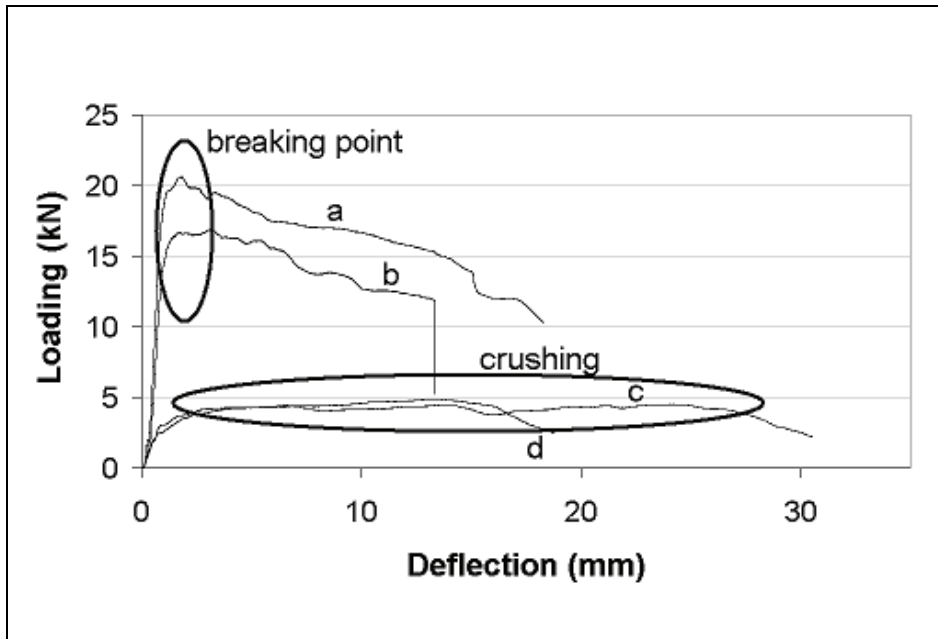


Fig. 10. Compression-breaking curves of pine control specimens (a and b) and specimen subjected to short catalysed treatment (c and d)

3.4 Biological performance

Composites have been subjected to a decay resistance test of 8 weeks against *Gloeophyllum trabeum* and *Coriolus versicolor* for beech samples and *Gloeophyllum trabeum* and *Poria placenta* for pine samples. At the end, control samples have been recognized as nutritive material. Due to their surface acidity, treated samples succeed in repelling the fungi.

4. Industrial application promises

4.1 Perspectives

According to the former sections, a heating catalysed treatment of impregnated wood led under soft conditions leads to a strongly softened material. This softened character remains even under ambient temperature which offers the advantage of a possible moulding in ambient conditions. Then, after a second step of heating, the material recovers its initial stiffness.

Figure 11 gives an overview of some possible applications:

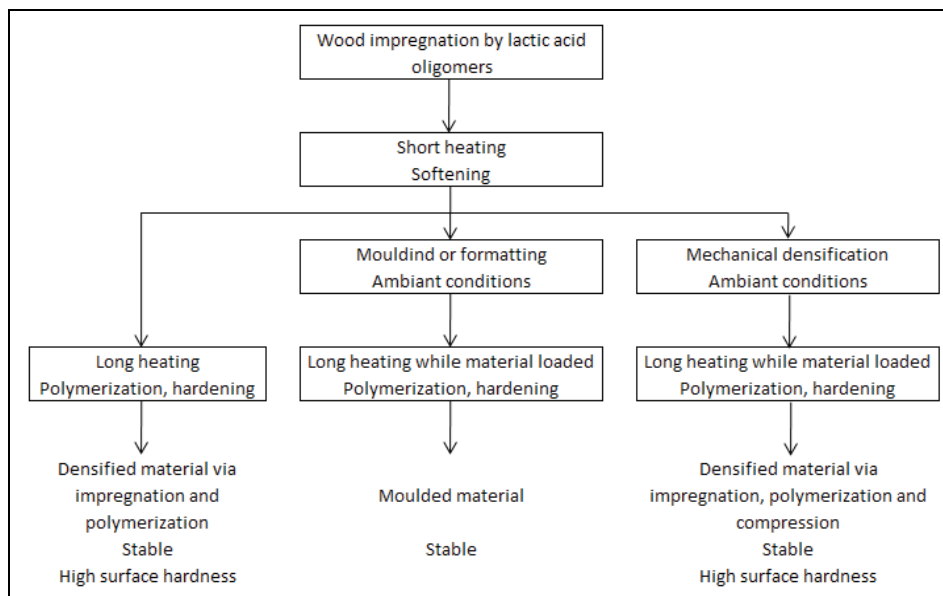


Fig. 11. Applications suggestions

4.2 Wood densification

Wood densification via impregnation and polymerization leads to a competitive material, resistant to biological attack, with high surface hardness and satisfying mechanical properties.

Use of the softened composite to manufacture densified material via impregnation, polymerization and compression would be of high interest in industrial fields as flooring, for instance. Cylindric impregnated samples have been subjected to heating, under loading in a metallic mold. Load has been settled to compress the samples enough to extract the air contained in wood lumens. Compressed and polymerized material consists in cellulose and lactic acid oligomers only.

Brinell hardness of such composites has been assessed and is summarized in Table 3.

Specimen	HB (MPa)
Beech control	3.9
Compressed beech control	19.9
Non catalysed treated beech sample	5.2
Compressed non catalysed treated beech sample	16.4
Catalysed treated beech sample	4.6
Compressed catalysed treated beech sample	7.8

Table 3. Brinell hardness of compressed composites

A strong increase in surface hardness is noticed when samples are compressed. The increase is even more obvious on control non treated wood. But once subjected to moisture, non treated samples are unstable whereas treated samples shape is fixed.

4.3 Wood moulding

To achieve non treated wood moulding, high temperature and air moisture content are necessary to obtain a plastic behaviour. The advantage of softened composite is its ability to be moulded with low loads, under ambient conditions. Figure 12 shows some radius of curvature applied on softened composite during the next long heating step. Shape is fixed, and the limitation is the fibres decohesion in the radial direction, which could be avoided by use of a suitable mold.

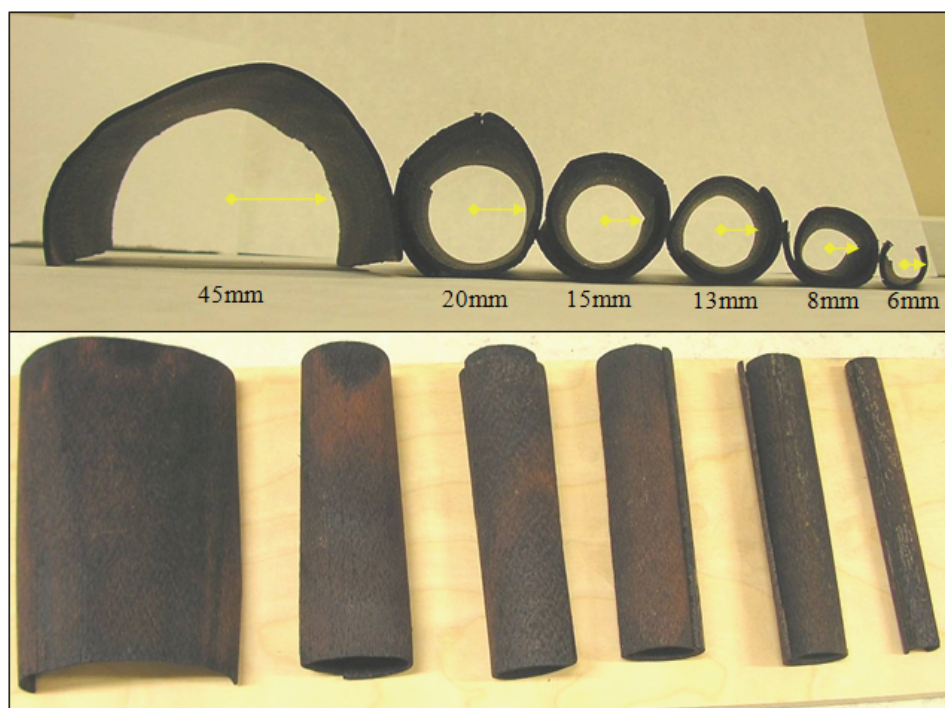


Fig. 12. Moulded and fixed samples

4.4 Further processing

To suppose an industrial development of softened or densified composites, any possible further processing has to be evaluated.

Two polyurethane coatings systems (primer + top-coat), aqueous and solvent based, have been applied on densified composite. Visual inspection is satisfying. Cross-cut (Figure 13) and impact normalized tests show comparable results as those obtained with the same coating systems applied on wood.



Fig. 13. Cross-cut testing carried out on aqueous based coating applied on densified composite

Tools wearing during machining has to be considered as well. Sanding paper is already been recognized as easily spotted when used to sand densified composite samples. Attention must be paid to blades, since surface acidity of densified samples is around pH 3 (wood surface acidity being around pH 6 to 7).

5. Conclusion

Lactic acid oligomers have been used as reinforcement into the lignocellulosic matrix. Without any polymerization catalyst, the densified composite obtained is stable, biologically resistant and mechanically competitive: high density and good hardness results make it suitable for flooring application for instance.

When a polymerization catalyst is added to the oligomers, wood components are damaged. The softened composite obtained can however be hardened again since an extended heating leads to a stable and biologically resistance material. The middle lamella degradation provokes mechanical properties decrease which suggests applications as decorative moulded objects or covering panels rather indoor than outdoor, for instance.

Manufacturing conditions can obviously be optimized to lead to a better composite material: temperature, duration, chemical catalysts, etc.

Another field of interest would be either to reinforce wood structure with other bio-polymer molecules, or to use lactic acid oligomers mixture to reinforce other natural matrices as bamboo for instance.

6. References

- Bledzki, A.K.; Gassa, J. (1999). Composites reinforced with cellulose based fibres *Progress in polymer science*, 24, 221-274
- Ganster, J.; Fink, H.-P. (2006). Novel cellulose fibre reinforced thermoplastic materials *Cellulose*, 13, 271-280

- Gatenholm, P.; Kubát, J.; Mathiasson, A. (1992). Biodegradable natural composites. I. Processing and properties *Journal of applied science*, 45, 9, 1667-1677
- George, J.; Sreekala, M.S.; Thomas, S. (2001). A review on interface modification and characterization of natural fiber reinforced plastic composites *Polymer engineering and science*, 24, 41, 1471-1485
- Ibach, R.E.; Rowell, R.M. (2001). Wood preservation based on in situ polymerization of bioactive monomers. *Holzforschung*, 55, 358-372
- Noël, M.; Fredon, E.; Mougél, E.; Masson, D.; Masson, E.; Delmotte, L. (2009) Lactic acid/wood-based composite material. Part 1: Synthesis and characterization *Bioresource Technology*, 100, 4711-4716
- Noël, M.; Mougél, E.; Fredon, E. ; Masson, D. ; Masson, E. (2009) Lactic acid/wood-based composite material. Part 2: Physical and mechanical performance *Bioresource Technology*, 100, 4717-4722
- Rowell, R.M. (2005). Chemical modification of wood, In: *Handbook of wood chemistry and wood composites*, Vol. 14, Ed. Taylor and Francis, 381-420
- Zhang, Y.; Zhang, S.Y.; Yang, D.Q. ; Wan, H. (2006). Dimensional stability of wood-polymer composites. *Journal of applied polymer science*, 102, 5085-5094

Properties of Polymer Composites with Cellulose Microfibrils

Denis Mihaela Panaitescu, Adriana Nicoleta Frone, Marius Ghiurea,
Catalin Ilie Spataru, Constantin Radovici and Michaela Doina Iorga
*National Institute of Research and Development in Chemistry and Petrochemistry
Romania*

1. Introduction

Plastic materials are indispensable in our lives but they are an important source of environmental pollution. In order to reduce the environmental load generated from the disposal of used plastic materials, a growing interest has been focused on biodegradable polymers based materials. These polymers can be completely converted into water and carbon dioxide by the action of microorganisms after disposal.

Owing to their good mechanical properties, polymer composites with micro or nano cellulose fibers are promising substitutes for glass-fiber-containing composites in many industrial fields like automotive, construction, electronics, biomedicine, cosmetics, and last but not least, the packaging industry. Among the advantages of using cellulose fibers as reinforcements in polymer composites renewability, low cost, low density, low energy consumption, high specific strength and modulus, high sound attenuation, low abrasivity and relatively reactive surface are the most important. Cellulose fibers modified at nanometer size induce much higher mechanical properties to polymer matrices as regard to common cellulose fibers because of their higher crystallinity and mechanical properties combined with higher surface area and better interfaces.

The production of nano-scale cellulose fibers and their application in composite materials has gained increasing attention in the past two decades (Hubbe et al., 2008). Two main methods have been used to generate nano-scale cellulose fibers: the chemical way, mainly by strong acid hydrolysis, which removes the amorphous regions of cellulose fiber and produces nano-size fibrils and the mechanical method, by high pressure refiner treatment (Chakraborty et al., 2005), grinder treatment (Taniguchi and Okamura, 1998), microfluidizer (Zimmermann et al., 2004), and high-pressure homogenizer treatment (Istvan and Plackett, 2010).

In this chapter the discussion is focused on the physical and mechanical properties of polyvinyl alcohol (PVA) as a biodegradable matrix reinforced with three types of cellulose fibers prepared by different methods. This chapter will first discuss the most used methods for cellulose nanofibers preparation and the reinforcing effect of these cellulose fibers in different polymer matrices. This will be followed by the experimental results obtained in our laboratory on PVA composites prepared with cellulose fibers isolated by mechanical treatment, acid hydrolysis and ultrasound treatment. The isolated cellulose fibers were

characterized by scanning electron microscopy (SEM) and X-ray diffraction (XRD) and PVA composites, prepared through film casting method, by XRD, thermal analysis and mechanical characterization.

2. State of the art

Cellulose was rediscovered at the end of the last century due to nanoscience and improved technologies available for the disintegration of cellulose in submicron and nanosize fibers. The native cellulose molecule consists of linear glucan chains with repeating (1-4)- β -glucopyranose units. The supramolecular structure of cellulose is very complex and it has been the subject of many studies (Eichhorn et al., 2010).

In living plants cellulose occurs in fibers, the cell wall of wood fibers consisting of repeated crystalline structures resulted from the aggregation of cellulose chains, termed microfibrils. These microfibrils, with high aspect ratio, are surrounded by an amorphous matrix of hemicelluloses and lignin. Besides wood, bast fibers (Cao et al., 2008; Li and Pickering, 2008; Shaikh et al. 2009; Belhassen et al., 2009), agricultural residues (El-Sakhawy and Hassan, 2007; Fama et al., 2009), leaf fibers (de Rodriguez et al., 2006; Zuluaga et al., 2009), bacterial cellulose (Nakagaito et al., 2005; Yano et al., 2008), the shell of some fruits and vegetables (Chen et al., 2009; Rosa et al., 2010) or tunicates (Petersson and Oksman, 2006) were used as sources for cellulose nanofibers preparation. Among the methods of nanofiber isolation, the most used are: mechanical disintegration, acid hydrolysis and biological treatments. Mechanical treatments involve conventional refining procedures (Hubbe et al., 2008), crushing and cryocrushing (Bhatnagar and Sain, 2005; Panaitescu et al., 2007a; Alemdar and Sain, 2008) or high pressure homogenization of cellulose source suspended in water (Lee et al., 2009a). Chakraborty isolated cellulose fibers with submicron diameters by combining the severe shearing in a refiner with high-impact crushing under liquid nitrogen (Chakraborty et al., 2005).

Mechanical treatments have some disadvantages related to the high energy required in the process and to the high degree of inhomogeneity, the resulted material containing larger fibrils in addition to microfibrils (Nakagaito and Yano, 2004; Nakagaito and Yano, 2005; Andresen et al., 2006; Andresen and Stenius, 2007; Stenstad et al. 2008).

Chemical treatments involve mainly acid and alkaline hydrolysis. Acid hydrolysis leads to the isolation of micro and nanofibers with a high degree of crystallinity by removing the amorphous regions of the raw cellulosic material. Using sulfuric acid, a negatively charged surface of the cellulose fibers can be obtained, through the esterification of hydroxyl groups by the sulfate ions, which prevents the agglomeration of fibers.

Many researchers have successfully used this method, alone or in combination with others methods, to obtain cellulose nanofibers (Zhang et al., 2007; El-Sakhawy et al., 2007; Moran et al., 2008; Chen et al., 2009): Bondenson et al. (2006) treated microcrystalline cellulose (MCC) with sulfuric acid in concentration of 63.5% (w/w) and isolated cellulose whiskers with an aspect ratio between 20 and 40, Lee et al. (2009b) obtained nanocellulose fibers by hydrobromic acid hydrolysis of MCC, an increasing in MCC crystallinity being reported, Rosa et al. (2010) obtained cellulose whiskers with diameters as low as 5 nm and aspect ratio of up to 60 by sulfuric acid hydrolysis of coconut husk fibers.

Degradation of the cellulosic substrate may also occur in the presence of microorganisms (fungi, bacteria) or, directly, with enzymes. Enzymatic treatment of cellulose was performed by Henriksson et al. (2007) who reported the obtaining of cellulose nanofibers from two

different commercial bleached wood sulphite pulps. Li et al. (2008) reported that removal of non-cellulosic components from cellulose fibers by enzyme treatment can increase the crystallinity, thermal stability and the amount of -OH groups of the treated fibers.

New and environmental friendly methods for cellulose nanofibers isolation were also tested in laboratory conditions. Ultrasonication had been used alone or in combination with other methods (e.g. acid hydrolysis) to obtain cellulose fibers. Filson and Dawson-Andoh (2009) obtained nanofibers with an average diameter between 21 and 23 nm applying this method. Application of cellulose nanofibers in polymer reinforcement is a relatively new research field. Two directions could be detected: research studies which explore the development of nano-bio-plastics as fully biodegradable nanocomposites and studies aimed at dispersing cellulose nanofibers in non-biodegradable, petroleum derived polymers. Polymer composites containing cellulose nanofibers were prepared with polyvinyl alcohol (PVA), polylactide (PLA), starch and polycaprolactone but also with polyethylene or polypropylene. Improvement in term of brittleness, thermal stability or barrier properties were signaled in case of biodegradable polymers reinforced with cellulose nanofibers (Iwatake et al., 2008; Chen et al., 2009; Fama et al., 2009; Pandey et al., 2009; Suryanegara et al., 2009; Bledzki et al., 2009; Chang et al., 2010). Cellulose fibers reinforcement could be a good solution for starch, which is a low cost source of biodegradable composites but a material with very poor mechanical properties. Dufresne and Vignon (1998, 2000) reported an improvement by a factor of 3.5 of the tensile modulus of starch at 50 wt% cellulose fibers addition. PLA is a commercially available biopolymer with similar properties to petroleum derived thermoplastics. Some drawbacks like brittleness and low thermal stability restrict its applications. Using cellulose fibers (10 wt%) and a solvent exchange method, Iwatake et al. (2008) succeeded in fabricating a composite sheet with uniform filler distribution showing an increase of Young's modulus and tensile strength of 40 and 25% respectively. Chemical modification of cellulose has been explored as a route for improving filler dispersion in hydrophobic polymers such as polyethylene or polypropylene (Panaitescu et al., 2007b; Rahman et al., 2009; Yanjun et al., 2010).

PVA is a water-soluble and biodegradable polymer with excellent chemical resistance and an interesting material for biomedical applications. PVA has no toxic action on the human body being used to manufacture medicines cachets, yarn for surgery, controlled drug delivery systems (Tang et al., 2009). New fields of application regard cardiovascular devices (Millon and Wan, 2006), dialysis membrane, artificial cartilage, tissue engineering scaffold (Zhou et al., 2010). Development of ecofriendly packaging materials is still a challenging area and many studies are focused on the improvement of PVA mechanical and barrier properties by combination with other polymers or fillers in order to use it in the packaging industry (Sedlarik et al., 2006). For many other applications, mechanical properties of PVA should be substantially improved without damaging its valuable properties. Low cellulose fibers addition could be an appropriate solution. Many studies emphasized the effectiveness of large amount of cellulose fibers in improving mechanical properties of PVA. Zimmermann et al. (2004) reported an improvement of the elastic modulus and tensile strength of up to five times and three times, respectively, in the case of dispersing 20 wt% cellulose fibers in PVA. An increase of about five times of the tensile strength relative to the reference polymer was reported by Bruce et al. (2005) at 50 wt% cellulose fibers in PVA and an increase by a factor of 3.5 at the same concentration of fibers in the work of Leitner et al. (2007). Nevertheless, no increase in tensile strength and modulus was observed by Lu et al. (2008) above 10 wt% cellulose fibers in PVA.

Despite the important publication activity dealing with cellulose nanofibers and related nanocomposites the application of such materials is quite limited. There are several reasons for this situation. One of them is the difficulty of the separation of plant fibers into smaller constituents with uniform and reproducible characteristics. Another reason is the high energy demands for most isolation processes. Problems concerning interfacial adhesion and uniform dispersion of the cellulose fibers in the polymer matrix delayed also the wide application of these materials.

Moreover, results obtained in different laboratories on polymer composite containing cellulose fibers are often contradictory because of many factors controlling the process like filler size and content, interface adhesion, fiber aspect ratio and orientation, fiber dispersion in the matrix and stress transfer efficiency through the interface (Dufresne et al., 2003). However, the role of nanofiber characteristics and aggregation in influencing macroscale properties of polymer matrix is not yet well understood.

Important research work was focused on studying the changes induced in PVA characteristics by high concentration of cellulose fibers prepared by different processes. These results were obtained in different laboratories and different conditions were applied in order to prepare PVA composite films. PVA is a polymer sensitive to preparation conditions so that significant changes may occur depending on the working atmosphere and heat treatments applied. Knowing the high influence of preparing and characterization conditions on PVA properties, it is difficult to select the proper system PVA/cellulose fibers for a target application based on existing information. Moreover, achieving improved mechanical properties with the less concentration of cellulose fibers is desirable for preserving transparency and flexibility of PVA films. For these reasons, we further describe research results obtained in our laboratory for monitoring the influence of cellulose fibers obtained by different treatments on the microscopic and macroscopic properties of PVA, all the samples being prepared in the same conditions. PVA composites were prepared by solution casting using low concentration (≤ 5 wt.%) of cellulose fibers obtained by mechanical treatment (L), acid hydrolysis (H) and ultrasound treatment (U). The isolated cellulose fibers were characterized by scanning electron microscopy (SEM) and X-ray diffraction (XRD). PVA composites containing these fibers were characterized with the aim of determining thermal and mechanical behavior.

3. Experimental part

3.1 Materials

Polyvinyl alcohol, PVA 120-99, 1200 polymerization degree and 99% hydrolysis degree was used as matrix. Microcrystalline cellulose (MCC) with a mean particle size of 20 μm and an aspect ratio of 2 - 4, from Sigma-Aldrich, was used as raw material for the preparation of nanofibers and cellulose microfibers obtained from regenerated wood fibers (L) through mechanical treatment were donated by National Institute of Wood.

3.2 Nanofibers isolation

(a) By ultrasonic treatment

MCC with a mean particle size of 20 μm , as revealed by SEM image (Fig. 1), was dispersed under continuous stirring in distilled water (1/500) and sonicated at 80% power for 20 minutes using an ultrasonicator type Vibra Cell VC505 (500 W, 20 KHz). In order to control

the process temperature, the beaker with the cellulose suspension was put in a water bath with controlled temperature. The appearance of turbidity in the supernatant was a definite indication of the presence of cellulose nanofibers. Cellulose fibers suspension was obtained by decanting the supernatant into other vessel. Cellulose fibers - sample U was characterized by X ray diffraction after drying 4 hours at 40°C.

(b) By acid treatment

MCC was dispersed in distilled water (1/10). The resulted suspension was placed in an ice bath and stirred while concentrated sulfuric acid was added by drop until the desired acid concentration of 63% was reached. The suspension was heated at 40°C while stirred for 5 h. The obtained mixture was washed with distilled water using repeated centrifuge cycles (20 min at 7000 rpm, Universal 320R Ultracentrifuge) until a pH of 4 was reached. Further, the obtained sample of cellulose fibers (H) was ultrasonicated (Elmasonic S40H, Elma) for five hours in an ice bath in order to avoid the sample overheating. Cellulose fibers - sample H was characterized by X ray diffraction after drying 4 hours at 40°C.

(c) Cellulose fibers obtained through mechanical treatment (L) were used as received.

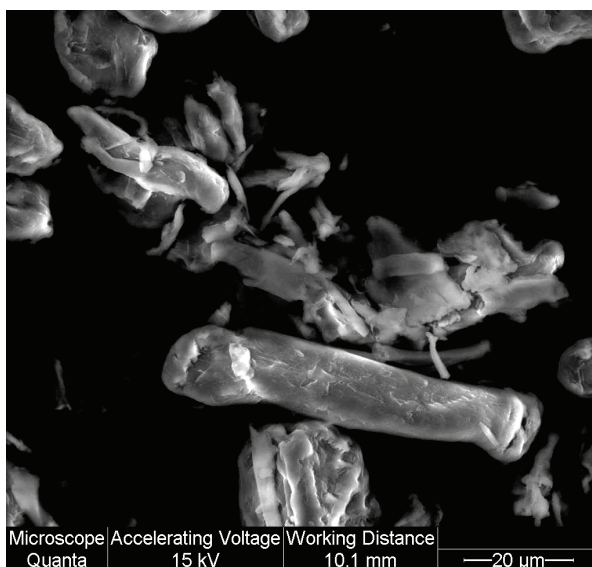


Fig. 1. SEM image of commercial microcrystalline cellulose (MCC)

3.3 Nanocomposite films preparation

In order to obtain PVA/cellulose fibers composite films with different filler concentrations, the required amount of PVA corresponding to a final concentration of 10% in the aqueous medium and the calculated amount of L, U and H cellulose fibers suspensions to achieve 1, 3 and 5 wt% filler concentration in the final composite were mixed using a high speed stirrer (500 min⁻¹). The stirring was performed at 80°C for 3 hours, and the resulting mixture was degassed for approximately 15 minutes in an Elmasonic S40 H ultrasonic bath. The films were cast on a PET plate and were kept at room temperature for 2 days until they were completely dried and then removed from the PET plates and placed in a desiccator for two

weeks before mechanical characterization. Neat PVA films were obtained under similar conditions.

3.4 Characterization methods

SEM micrographs of cellulose fibers were obtained with an environmental Quanta Scanning Electron Microscope 200, with a tungsten electron source in the following conditions: accelerating voltage 10 – 30 kV, no coating. The crystalline structure of cellulose fibers was determined by XRD with a DRON-UM diffractometer (horizontal goniometer Bragg-Brentano) using Co K α radiation (wavelength $\lambda = 1.79021 \text{ \AA}$), scanning from the 2θ value of 5° to 36° at a scanning rate of $0.05^\circ/5 \text{ sec}$. Samples were analyzed in reflection mode.

Mechanical behavior of composite films at room temperature was tested in tensile mode according to ISO 527-1:1993 Part 1 and ISO 527-3:1995 Part 3 by an Instron 3382. The Universal Testing Machine was equipped with a video extensometer for strain measurement and with a load cell of 1 kN capacity. The following data: video axial strain at break (elongation at break), tensile stress at break (tensile strength), Young's modulus (tensile modulus) and other optional features were automatically display using the software of Instron 3382, Bluehill 2. Young's modulus on the strain channel with a start value of 0.05% and an end value of 0.25% was calculated by the system applying the least square fit algorithm to each region between the start and end value selecting the highest slope. The load cell of 1 kN capacity, used for PVA composites tensile properties measurements has a sensitivity of 0.001 N. Test specimens were cut to 110 mm (length) \times 10 mm (width) \times 0.035-0.045 mm (thickness) from the films maintained in desiccators, 7 specimens being tested for each sample. Tensile modulus was determined at a crosshead speed of 2 mm/min and tensile strength and elongation at 10 mm/min. Lower crosshead speed was necessary for correct determination of tensile modulus as stipulated by ISO 527 Part 1. Differential scanning calorimetry (DSC) and thermogravimetric analysis (TGA) were performed on a SDT Q600 V20.9 from TA Instruments under Helium flow (100 mL/min). The samples weighing between 5 and 10 mg were packed in aluminium pans and placed in the DSC cell. The samples were tested from the ambient temperature to 600°C at a heating rate of $10^\circ\text{C}/\text{min}$. The DSC glass transition temperature (T_g) was taken at the onset of the glass transition region. The PVA composite samples were conditioned for 24 h at 40°C in a vacuum oven prior to thermal analysis.

4. Results

4.1 Cellulose fibers characterization

The three samples of cellulose fibers, L, H and U, were investigated by scanning electron microscopy (Fig. 2, 3a-c and 4). SEM image obtained for sample L (Fig. 2) revealed the distribution of fiber diameters ranging from 5 to $20 \mu\text{m}$. The surface of L is smoother and the aspect ratio l/d of 4 to 14, greater than the l/d of MCC sample, ranging from 2 to 4.

The acid hydrolysis of MCC is a heterogeneous process which involves the diffusion of acid into the cellulose fibers, and the subsequent cleavage of glycosidic bonds. Figures 3a-c are SEM micrograph of acid treated MCC after different time of acid hydrolysis (2, 4 and 5 hours). Fig. 3a shows how the acid broke the MCC particle, attacking amorphous areas and releasing aggregates of cellulose microfibrils. Fig. 3b shows that a big fraction of amorphous areas were entirely destroyed and cellulose crystallites in needle form released. Portions with agglomerated microfibrils could also be observed.

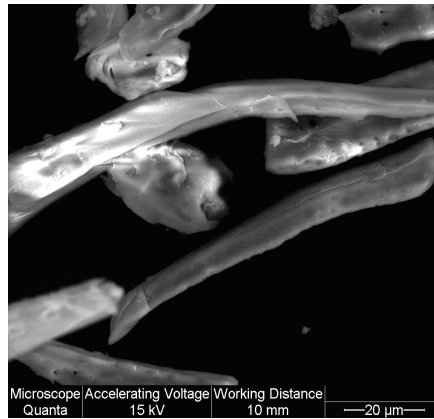
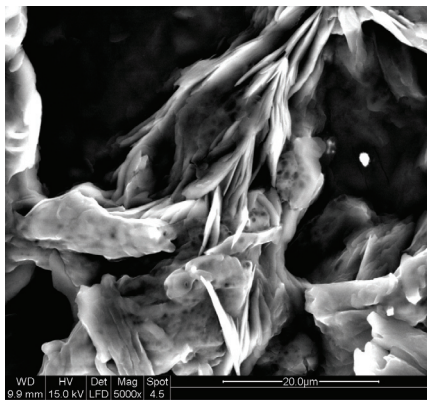
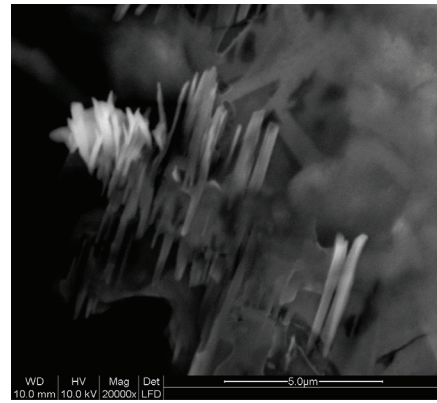


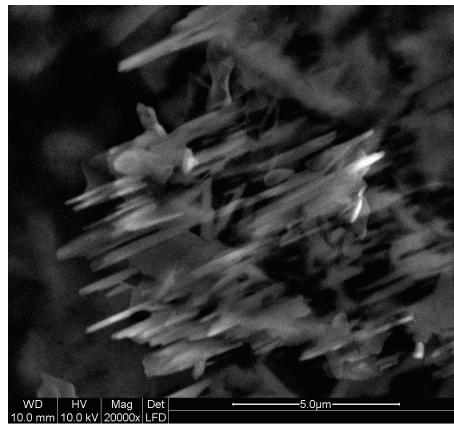
Fig. 2. SEM image of L type cellulose fibers



(a)



(b)



(c)

Fig. 3. SEM micrographs of (a) the first stages of acid attack of MCC, (b) releasing of cellulose microfibril aggregates and (c) cellulose fibers type H

In Fig. 3c rod like cellulose microfibrils with diameter of 100 – 400 nm and aspect ratio of 10 to 20 are observed. Cellulose fibers with smaller diameters can not be detected in SEM images, at this magnitude. It is presumed that the further ultrasonic treatment destroyed the agglomerates.

SEM micrograph of U type cellulose fibers (Fig. 4) shows that MCC particles are entirely disintegrated into fragments with different shapes and size by sonication treatment. The effectiveness of MCC defibrillation process is very high, particles and fibers with a diameter of 20 – 800 nm being observed. Individual particles but also large aggregates of cellulose fragments can be easily observed. It is possible that a re-aggregation to take place, promoted by the strong hydrogen bonding between the individual cellulose whiskers prepared by ultrasonication. The heterogeneity of shapes and size is very great in this sample because of the high energy involved in ultrasonication, so that a separation process was imperative for removing higher size aggregates of cellulose fibers.

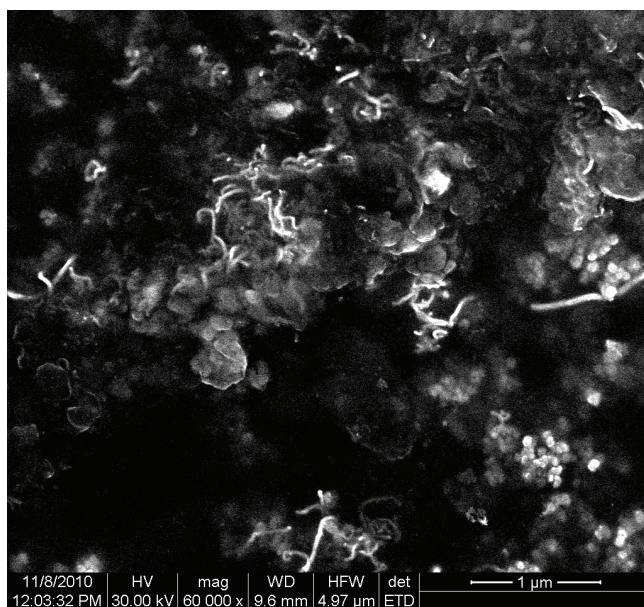


Fig. 4. SEM image of cellulose fibers prepared by ultrasonication

X-ray diffraction patterns of MCC and cellulose fibers (L, H and U) are shown in Fig. 5. The characteristics peaks originated from cellulose I are visible for all the samples at the same values of 2θ (17.3° , 18.9° , 26.2°). These values correspond to the interplanar spacings of the three principal planes (101), $(10\bar{1})$ and (002) of the monoclinic unit cell of cellulose: $d_{101} = 5.99 \text{ \AA}$, $d_{10\bar{1}} = 5.40 \text{ \AA}$ and $d_{002} = 3.95 \text{ \AA}$, respectively. Very close values for 2θ were reported by Lee et al. (2009b) taking into account the different wavelength of CuK α radiation used. In the case of sample L the two first peaks are not separated forming a broad peak, probably because of the more complex structure of sample L which contain beside celluloses, hemicelluloses and lignin.

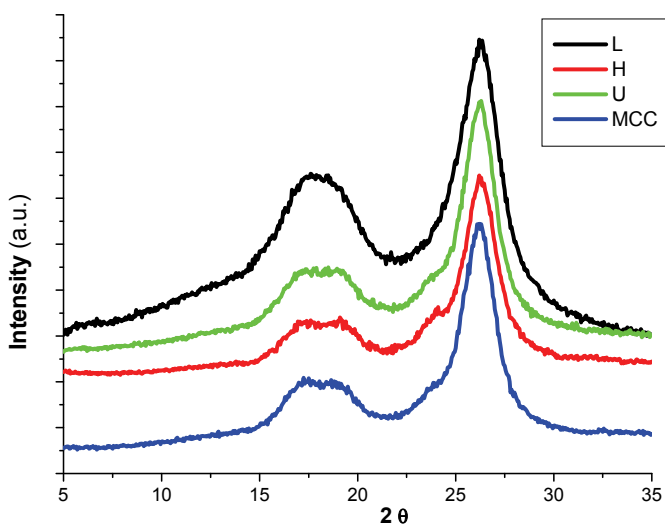


Fig. 5. X-ray diffraction patterns of MCC and cellulose fibers (samples L, H and U)

4.2 Polymer composites characterization

a. Mechanical characterization

The tensile strength, elongation at break, and elastic modulus of the PVA/cellulose fibers composites compared with those of unreinforced PVA are shown in Figs. 6 - 8.

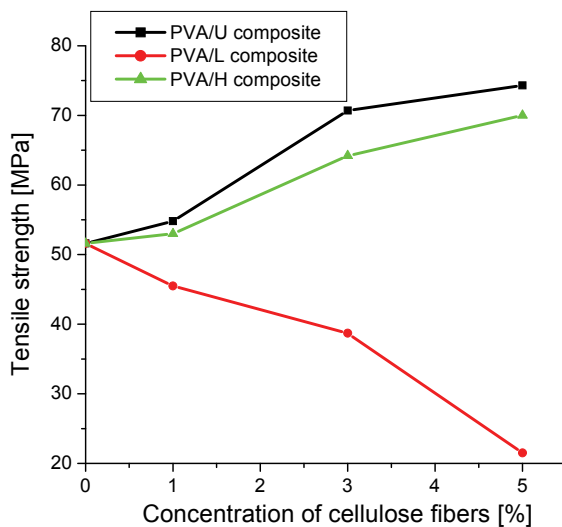


Fig. 6. Tensile strength of neat PVA and PVA reinforced with cellulose fibers U, L and H

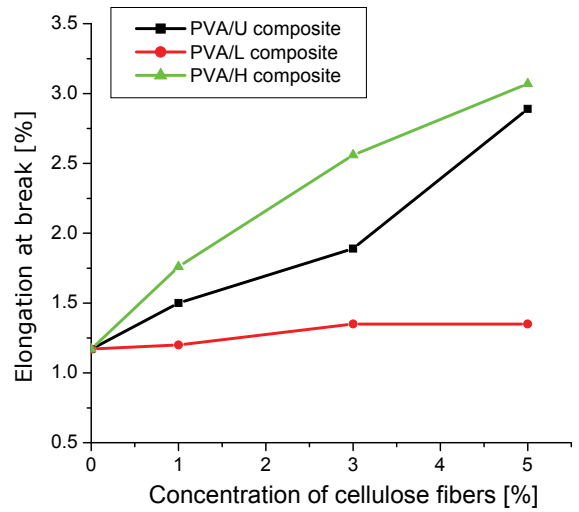


Fig. 7. Elongation at break of neat PVA and PVA reinforced with cellulose fibers U, L and H

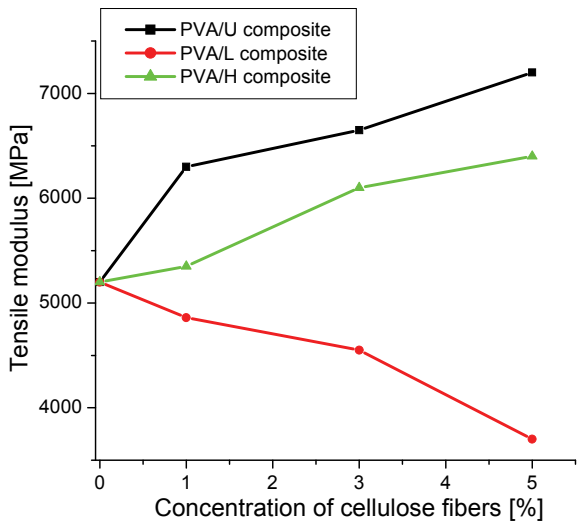


Fig. 8. Tensile modulus of neat PVA and PVA reinforced with cellulose fibers U, L and H

It is apparent that the three types of fibers differently influence the mechanical properties of PVA matrix. U and H fibers lead to an improvement of mechanical properties, both the strength and modulus and elongation at break being enhanced and the type L to a decrease in strength and stiffness. The observed differences are mainly due to the different size of fibers, U and H fibers having diameters on the nanoscale while L being micron sized fibers.

It is known that an important increase in strength and stiffness of polymer matrix can be obtained at concentrations above 30% of micron sized cellulose fibers, lower concentration of 20 – 25% being effective only in the case of a good treatment of fibers or coupling agent adding. In these composites, elongation at break knows significant decreases, polymer matrix ductility being severely altered by micron sized fibers (Bledzki et al., 2003; Ganster et al., 2006). Hence, it was not expected that the low concentration of L fibers could improve PVA mechanical properties.

In contrast to conventional filled polymer systems where the increase of strength and stiffness is accompanied by an important decrease of ductility, in nanocomposites a simultaneous increase of Young's modulus, tensile strength and elongation could appear, especially in the case of strong filler/matrix interface (Lin et al., 2009). Therefore, the incorporation of U and H fibers in PVA which provide a significant improvement of all mechanical properties (strength, stiffness and ductility) is a proof of a good interfacial adhesion in our composites.

The highest improvement of tensile strength and modulus in regard to PVA (Fig. 6 and 8) was obtained for PVA/U composites, 5 wt% U in PVA: almost 50% and 40%, respectively. The different behavior of U and H fibers as reinforcements in PVA could be a result of their different size (in the case of U fibers, the nanosized fraction were separated from the coarse fraction) and the higher tendency to form agglomerates in the case of higher aspect ratio fibers (H). The enhancement of mechanical properties of PVA/U and PVA/H composite films by comparison with neat PVA resulted from the good adhesion at the filler/matrix interface, favored by the small size of fibers and, accordingly, their high surface area. The hydrogen bonding between the OH groups of cellulose fibers and similar group of PVA matrix led to improved adhesion between phases which resulted in improved mechanical properties. Lee et al. (2009b) explained an increase of about 70% of the elastic modulus and up to 55% of the tensile strength by the intermolecular forces between cellulose fibers and PVA matrix.

b. Thermal characterization

The thermal properties of cellulose fibers reinforced PVA were determined from DSC and DTG thermograms. The main thermal transitions, glass transition temperature (T_g) and melting point (T_m), were evaluated and compared with those of the neat PVA. DSC results of PVA composites containing 5wt% of cellulose fibers, L, H and U types, are shown in Fig. 9.

PVA exhibits an endotherm close by 57°C (57.2°C) corresponding to the glass transition temperature of PVA. The appearance of one T_g in the nanocomposite samples highlights the good interaction of cellulose fibers and PVA in the amorphous phase. No significant changes in T_g value are observed in the case of PVA composites containing 5 wt% U or H fibers as shown in Table 1, but a decrease with four degrees is detected in PVA filled with 5 wt% L fibers as regard to neat PVA. This behavior is caused by the decrease of the cohesive energy density in the amorphous phase of the PVA/L composites in comparison with neat PVA and can be explained by the rupture of the hydrogen bonds in PVA because of larger

size of L type fibers (tens of microns in diameter and hundred of microns in length). As a result, the rubbery properties and the increase of the mobility of the macromolecules will appear from lower temperatures. Nanometer sized fibers, H and U, will not cause massive breaks of hydrogen bonds in PVA and, the expected interactions between these cellulose fibers and PVA will not alter the supramolecular structure of the amorphous phase. Nevertheless it seemed that these new formed interactions are not strong enough to slow the chain mobility associated with glass transition since the Tg values measured on PVA/H and PVA/U composite samples are close to that of neat PVA.

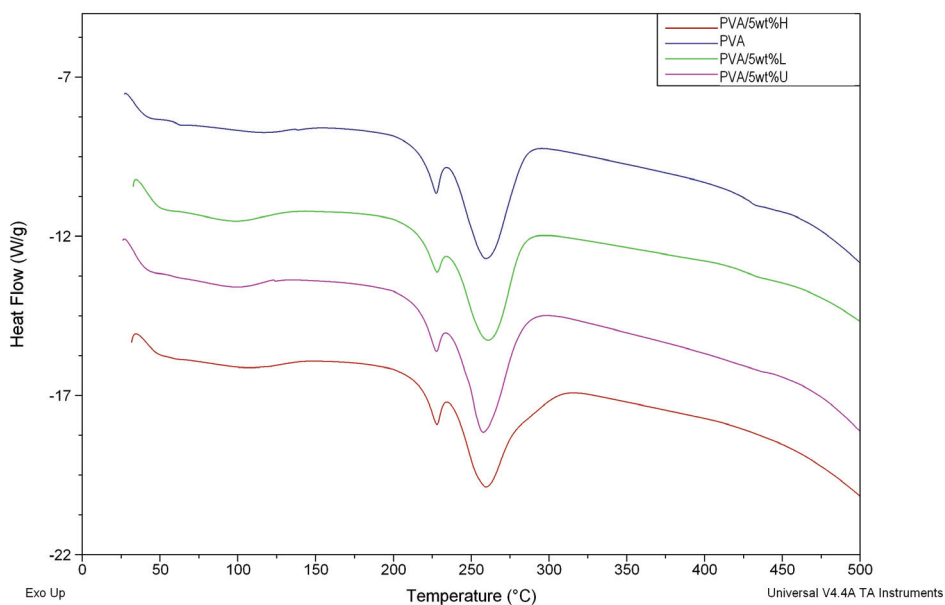


Fig. 9. DSC diagrams of neat PVA and PVA composites containing U, L and H fibers

Samples	Tg °C	Tm °C	ΔH_m J/g	Xc %
PVA	57.2	227.1	79.3	48.7
PVA/5%U	56.8	226.9	70.5	45.5
PVA/5%L	53.0	227.2	60.0	38.7
PVA/5%H	57.0	227.3	78.1	50.4

Table 1. DSC data of neat PVA and PVA composites containing 5 wt.% fibers

PVA exhibits a sharp endothermic curve with a peak at 227.1°C, as shown in Fig. 9, corresponding to the melting of the crystalline phase of PVA. T_m values remains roughly constant for all PVA composites whatever the type of fiber used but the heat of fusion is different depending on the filler characteristics. The degree of crystallinity (X_c) of the PVA component in the composite was obtained as follows:

$$X_c = \frac{\Delta H_f}{w * \Delta H_0} * 100 \quad (1)$$

where ΔH_f and ΔH_0 are the heats of fusion for PVA and 100% crystalline PVA, respectively and w is the mass fraction of PVA in the composite. ΔH_0 was taken 163 J/g (Ramaraj et al., 2010).

A highest degree of crystallinity is observed in PVA/H composite and the lowest in PVA/L composite. PVA filled with H type fibers show higher crystallinity than neat PVA. This could be ascribed to stronger interactions between cellulose fiber surface and adjacent PVA chains. The nucleating effect of cellulose fibers could also explain this increase of crystallinity. PVA/H composite shows a higher crystallinity as regard to PVA/U composite but the mechanical behavior of the latter is better. This is due to the fact that, besides the matrix crystallinity, other factors influence the tensile properties of the composite. The nanoscale dispersion of the filler and its orientation in the matrix are among these factors.

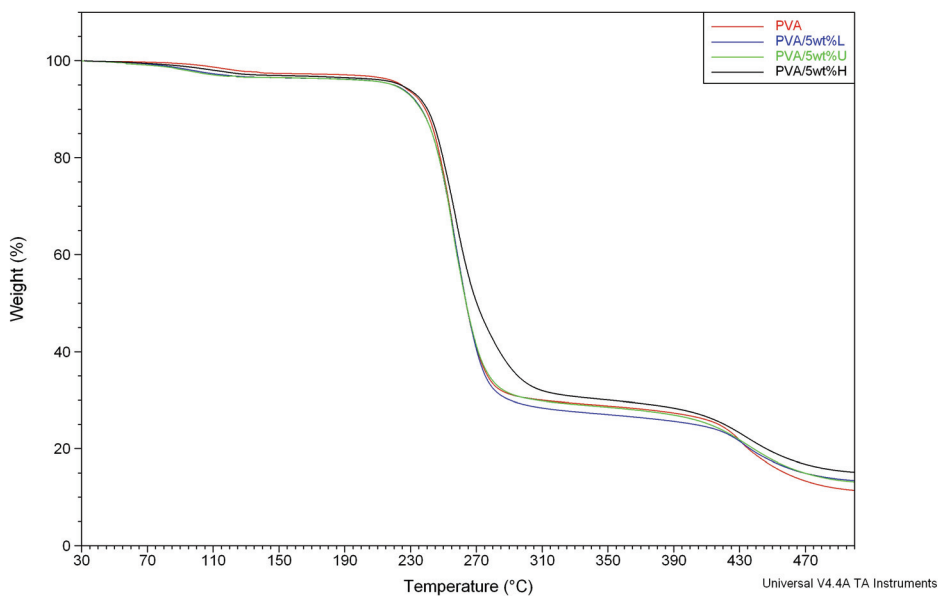


Fig. 10. TGA thermograms of neat PVA and PVA composites containing U, L and H fibers

Thermogravimetric analysis (TGA) was used to investigate the effect of cellulose fibers on the thermal stability of the composites. In the obtained PVA thermograms (Fig. 10) three

main weight loss regions can be observed (Lee et al., 2009b; Qua et al., 2009). All the samples show an initial weight loss in the region 75 - 150 °C caused by the evaporation of water. Between 2.5 and 3.5 wt.% physically and chemically bound water was detected in neat PVA and PVA composites thermograms. Figure shows that the second degradation region is located between 220 and 300 °C and is due to the pyrolysis of cellulose fibers and to the degradation of PVA films, the weight loss being around 70% for all the samples. As reported by Qua et al. (2009), the second stage of degradation mainly involves dehydration reactions and the formation of volatile products.

The third stage weight loss occurs above 400 °C and consists of decomposition of carbonaceous matter (Lee et al., 2009b).

It can be observed in Fig. 10 that the differences in TGA curves are negligible for neat PVA and PVA composites. However, some differences can be detected in the case of PVA/H composite. TGA's first order derivative (Fig. 11) show a broadening of the main decomposition peak and a shift of the onset temperature for the third decomposition stage to higher temperatures. This can be due to sulfonic groups bound to the cellulose fibers by acid hydrolysis which influence the degradation process.

The onset degradation temperature (T_d) and enthalpy (ΔH_d) could be easily determined from DTG curves (Table 2). Slightly higher onset degradation temperatures were obtained for PVA composites as regard to neat PVA, showing a marginal increase of the thermal stability caused by the cellulose fibers. Lee showed that the thermal stability of PVA composites was improved with the increase of the nanocellulose loading (Lee et al., 2009b).

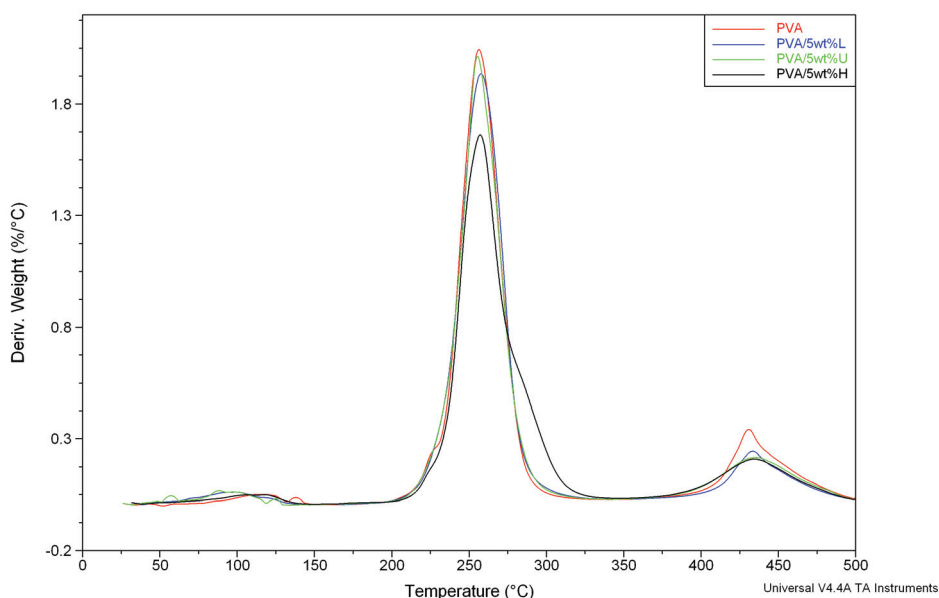


Fig. 11. DTG thermograms of neat PVA and PVA composites containing U, L and H fibers

Samples	Td °C	ΔHd J/g
PVA	238.7	513.8
PVA/5%U	242.9	509.2
PVA/5%L	239.7	480.5
PVA/5%H	239.8	525.3

Table 2. DSC data of neat PVA and PVA composites containing 5 wt.% fibers

The lowered PVA/L decomposition enthalpy was thought to be related to the more complex structure of these fibers containing beside cellulose, hemicellulose and lignin and to the more porous fiber structure.

5. Conclusion

The application of cellulose nanofibers in polymer reinforcement is a relatively new research field. The development of fully biodegradable nanocomposites is still a challenging area.

In this chapter discussion is focused on the physical and mechanical properties of polyvinyl alcohol as a biodegradable matrix reinforced with cellulose fibers prepared by different methods. Three types of fibers with different characteristics in terms of composition, size and aspect ratio were tested as reinforcements in PVA: L fibers of micron size and high aspect ratio contain beside cellulose, hemicellulose and lignin, H fibers with a nanosize dimension and high aspect ratio and U fibers with a nanosize dimension and low aspect ratio contain only cellulose.

These cellulose fibers were obtained by mechanical treatment, acid hydrolysis and ultrasound treatment, respectively. The isolated cellulose fibers were characterized by scanning electron microscopy (SEM) and X-ray diffraction (XRD).

Our work was focused on studying the changes induced in PVA characteristics by low concentration of these cellulose fibers. Similar conditions were applied in order to prepare PVA composite films, knowing the high influence of preparing and characterization conditions on PVA properties, in order to select the proper system PVA/cellulose fibers for a target application.

The obtained composites with low concentration of cellulose fibers (1 – 5 wt.%) showed improved mechanical properties, preserving the transparency and flexibility of the original films. The highest improvement of the tensile strength and modulus in regard to PVA was obtained for PVA composite containing 5 wt% cellulose fibers prepared by ultrasound treatment: almost 50% and 40%, respectively. Favorable interfacial properties and the lack of agglomerations at low fibers concentration in PVA were supposed to explain the high values of the mechanical properties.

PVA filled with acid treated cellulose fibers showed higher crystallinity than neat PVA, as resulted from DSC analysis. Stronger interactions between cellulose fiber surface and adjacent PVA chains and the nucleating effect of cellulose fibers were proposed to explain

this increase of crystallinity. Slightly higher onset degradation temperatures were obtained for PVA composites as regard to neat PVA, showing an increase of the thermal stability caused by the addition of cellulose fibers.

The biocomposites presented in this chapter are advanced materials with improved mechanical and thermal properties, high transparency and flexibility and large possibilities of application in packaging and other fields.

Future work will be focus on the study concerning the processing behavior of these materials and on achieving new preparation methods with industrial application.

6. References

- Alemдар, A., and Sain, M. (2008). Biocomposites from wheat straw nanofibers: Morphology, thermal and mechanical properties. *Composites Sci. Technol*, Vol. 68, No. 2, pp. 557-565
- Andresen, M., Johansson, L. S., Tanem, B. S., and Stenius P (2006). Properties and characterization of hydrophobized microfibrillated cellulose. *Cellulose*, Vol. 13, pp. 665-677
- Andresen, M., and Stenius, P. (2007). Water-in-oil emulsions stabilized by hydrophobized microfibrillated cellulose. *J Dispers Sci Technol*, Vol. 28, pp. 837-844
- Belhassen, R., Mendez, J. A., Boufi, S., Lopez, J. P., Puig, J., Pelach, A., and Mutje, P. (2009). Preparation and Properties of Biocomposites Based on Jute Fibers and Blend of Plasticized Starch and Poly(*b*-hydroxybutyrate). *Journal of Applied Polymer Science*, Vol. 114, pp. 313-321
- Bhatnagar, A., and Sain, M. (2005). Processing of cellulose nanofiber-reinforced composites. *J Reinforced Plastics Composites*, Vol. 24, No. 12, pp. 1259-1268
- Bledzki, A. K., and Faruk, O. (2003). Wood Fibre Reinforced Polypropylene Composites: Effect of Fibre Geometry and Coupling Agent on Physico-Mechanical Properties. *Applied Composite Materials*, Vol. 10, pp. 365-379
- Bledzki, A. K., Jazskiewicz A., and Scherzer, D. (2009). Mechanical properties of PLA composites with man-made cellulose and abaca fibres. *Applied Science and Manufacturing*, Vol. 40, pp. 404-412
- Bondeson, D., Mathew, A., and Oksman, K. (2006). Optimization of the isolation of nanocrystals from microcrystalline cellulose by acid hydrolysis. *Cellulose*, Vol.13, No.2, pp. 171-180
- Bruce, D. M., Hobson, R. N., Farrent, J. W., Hepworth, and D. G. (2005). High-performance composites from low-cost plant primary cell walls. *Appl Sci Manufact*, Vol. 36, pp. 1486-1493
- Cao, X., Chen, Y., Chang, P. R., Stumborg M. and Huneault, M. A. (2008). Green Composites Reinforced with Hemp Nanocrystals in Plasticized Starch. *J. of Appl. Polym. Sci.*, Vol. 109, No. 6, pp. 3804-3810
- Chakraborty, A., Sain, M. and Kortschot, M (2005). Cellulose microfibrils: A novel method of preparation using high shear refining and cryocrushing *Holzforschung*, Vol. 59, pp. 102-107

- Chang, P. R., Jian, R., Zheng, P., Yu, J., and Ma, X. (2010). Preparation and properties of glycerol plasticized-starch (GPS)/cellulose nanoparticle (CN) composites. *Carbohydrate Polymers*, Vol. 79, pp. 301-305
- Chen, Y., Liu, C., Chang, P. R., Cao, X., and Anderson, D. P. (2009). Bionanocomposites based on pea starch and cellulose nanowhiskers hydrolyzed from pea hull fiber: Effect of hydrolysis time. *Carbohydrate Polymers*, Vol. 76, No. 4, pp. 607-615
- de Rodriguez, N. L. G., Thielemans, W., and Dufresne, A. (2006). Sisal cellulose whiskers reinforced polyvinyl acetate nanocomposites. *Cellulose*, Vol. 13, No. 3, pp. 261-270
- Dufresne, A. and Vignon, M. R. (1998). Improvement of starch film performances using cellulose microfibrils. *Macromolecules*, Vol. 31, pp. 2693-2696
- Dufresne, A., Dupeyre, D., and Vignon M. R. (2000). Cellulose microfibrils from potato tuber cells: processing and characterization of starch-cellulose microfibril composites. *J Appl Polym Sci*, Vol. 76, pp. 2080-2092
- Dufresne, A., Dupeyre, D., and Paillet, M. (2003). Lignocellulosic flour-reinforced poly(hydroxybutyrate-co-valerate) composites. *J Appl Polym Sci*, vol. 87, pp. 1302-1315
- Eichhorn, S. J., Dufresne, A., Aranguren, M., Marcovich, N. E., Capadona, J. R., Rowan, S. J., Weder, C., Thielemans, W., Roman, M., Renneckar, S., Gindl, W., Veigel, S., Keckes, J., Yano, H., Abe, K., Nogi, M., Nakagaito, A. N., Mangalam, A., Simonsen, J., Benight, A. S., Bismarck, A., Berglund L. A., and Peijs, T. (2010). Review: current international research into cellulose nanofibres and nanocomposites. *Journal of Materials Science*, Vol. 45, No. 1., pp. 1-33
- El-Sakhawy, M., and Hassan, M. L. (2007). Physical and mechanical properties of microcrystalline cellulose prepared from agricultural residues. *Carbohydrate Polymers*, Vol. 67, pp. 1-10
- Famá, L., Gerschenson, L., and Goyanes, S. (2009). Starch-vegetable fiber composites to protect food products. *Carbohydrate Polymers*, Vol. 75, No. 2, pp. 230-235
- Filson, P. B., and Dawson-Andoh, B. E. (2009). Sono-chemical preparation of cellulose nanocrystals from lignocellulose derived materials. *Bioresource Technology*, Vol. 100, pp. 2259-2264
- Ganster, J., and Fink, H. P. (2006). Novel cellulose fibre reinforced thermoplastic materials. *Cellulose*, Vol. 13, pp. 271 -280
- Henriksson, M., Henriksson, G., Berglund, L.A., and Lindstrom, T. (2007). An environmentally friendly method for enzyme-assisted preparation of microfibrillated cellulose (MFC) nanofibers. *European Polymer Journal*, Vol. 43, No. 8, pp. 3434-3441
- Hubbe, M. A., Rojas, O. J., Lucia, L. A. and Sain, M. (2008). Cellulosic Nanocomposites: A review. *BioResources*, Vol. 3, No. 3, pp. 929-980
- Iwatake, A., Nogi, M., and Yano, H. (2008). Cellulose nanofiber-reinforced polylactic acid. *Composites Science and Technology*, Vol. 68, pp. 2103-2106
- Lee, S. Y., Chun, S. J., Kang, I. A., and Park, J. Y. (2009a). Preparation of cellulose nanofibers by high-pressure homogenizer and cellulose-based composite films. *Journal of Industrial and Engineering Chemistry*, Vol. 15, pp. 50-55

- Lee, S. Y., Mohan, D. J., Kang, I. A., Doh, G. H., Lee, S., and Han, S. O. (2009b). Nanocellulose reinforced PVA composite films: Effects of acid treatment and filler loading. *Fibers and Polymers*, Vol. 10, No. 1, pp. 77-82
- Leitner, J., Hinterstoisser, B., Wastyn, M., Keckes, J., and Gindl, W. (2007). Sugar beet cellulose nanofibril-reinforced composites. *Cellulose*, Vol. 14, pp. 419-425
- Li, Y. and Pickering, K.L. (2008). Hemp fibre reinforced composites using chelator and enzyme treatments. *Composites Science and Technology*, Vol. 68, No. 15/16, pp. 3293-3298
- Lin, N., Chen, G., Huang, J., Dufresne, A., and Chang, P. R. (2009). Effects of Polymer-Grafted Natural Nanocrystals on the Structure and Mechanical Properties of Poly(lactic acid): A Case of Cellulose Whisker-graft-Polycaprolactone. *J Appl Polym Sci*, Vol. 113, pp. 3417-3425
- Lu, J., Wang, T., and Drzal, L. T. (2008). Preparation and properties of microfibrillated cellulose polyvinyl alcohol composite materials. *Appl Sci Manufact*, Vol. 39, pp. 738-746
- Millon, L. E., and Wan, W. K. (2006). The Polyvinyl Alcohol-Bacterial Cellulose System As A New Nanocomposite for Biomedical Applications. *J Biomed Mater Res Part B: Appl Biomater*, Vol. 79B, pp. 245-253
- Moran, J. I., Alvarez, V. A., Cyrus, V. P., and Vazquez, A. (2008). Extraction of cellulose and preparation of nanocellulose from sisal fibers. *Cellulose*, Vol. 15, No. 1, pp. 149-159
- Nakagaito, A. N., and Yano, H. (2004). The effect of morphological changes from pulp fibers towards nano-scale fibrillated cellulose on the mechanical properties of high strength plant fiber based composites. *Applied Physics A*, Vol. 78, No. 4, pp. 547-552
- Nakagaito, A.N., Iwamoto, S. and Yano, H. (2005). Bacterial cellulose: the ultimate nano-scalar cellulose morphology for the production of high-strength composites. *Appl. Phys A*, Vol. 80, No. 1, pp. 93-97
- Nakagaito, A. N., and Yano, H. (2006). Novel high-strength biocomposites based on microfibrillated cellulose having nano-order-unit web-like network structure. *Appl. Phys. A*, Vol. 80, pp. 155-159
- Panaiteescu, D. M., Matasaru, I., Iovu, H., Ghiurea, M., Iorga, M. D., and Stanescu, P. (2007a). Thermoplastic Composites with Cellulose Microfibrils Obtained by Mechanical Treatments. *Materiale Plastice*, Vol. 44, No. 2, pp. 144-147
- Panaiteescu, D. M., Donescu, D., Bercu, C., Vuluga, D. M., Iorga, M. and Ghiurea, M. (2007b). Polymer Composites with Cellulose Microfibrils. *Polymer Eng. Sci.*, Vol. 47, No. 8, pp. 1228-1234
- Pandey, J. K., Chu, W. S., Kim, C.S., Lee, C. S., and Ahn, S.H. (2009). Bio-nano reinforcement of environmentally degradable polymer matrix by cellulose whiskers from grass. *Composites: Part B*, Vol. 40, pp. 676-680
- Petersson, L., and Oksman, K. (2006). Biopolymer based nanocomposites: Comparing layered silicates and microcrystalline cellulose as nanoreinforcement. *Composites Science and Technology*, Vol. 66, pp. 2187-2196

- Qua, E. H., Hornsby, P. R., Sharma, H. S., Lyons, G. and McCall, R. D. (2009). Preparation and Characterization of Poly(vinyl alcohol) Nanocomposites Made from Cellulose Nanofibers. *Journal of Applied Polymer Science*, Vol. 113, pp. 2238–2247
- Rahman, W.A.W. A., Adenan, N., Rasit Ali, R. and Sulaiman, H. (2009). Effect of Silane Crosslinker on the Thermal Properties of Rice Straw/HDPE Biocomposite. *Journal of Applied Polymer Science*, Vol. 9, pp. 3041–3047
- Ramaraj, B., Nayak, S. K., and Yoon, K. R. (2010). Poly(vinyl alcohol) and Layered Double Hydroxide Composites: Thermal and Mechanical Properties. *J Appl Polym Sci*, Vol. 116, No. 3, pp. 1671–1677
- Rosa, M. F., Medeiros, E.S., Malmonge, J. A., Gregorski, K. S., Wood, D. F., Mattoso L. H. C., Glenn, G., Orts, W. J., and Imam, S. H. (2010). Cellulose nanowhiskers from coconut husk fibers: Effect of preparation conditions on their thermal and morphological behavior. *Carbohydrate Polymers*, Vol. 81, pp. 83–92
- Sedlarik, V., Saha, N., Kuritka, I., and Saha, P. (2006). Characterization of Polymeric Biocomposite Based on Poly(vinyl alcohol) and Poly(vinyl pyrrolidone). *Polym Compos*, Vol. 27, pp. 147–152
- Shaikh, H., Pandare, M. K. V., Nair, G., and Varma, A. J. (2009). Utilization of sugarcane bagasse cellulose for producing cellulose acetates: Novel use of residual hemicellulose as plasticizer. *Carbohydrate Polymers*, Vol. 76, No. 1, pp. 23–29
- Siro, I., and Plackett, D. (2010). Microfibrillated cellulose and new nanocomposite materials: a review. *Cellulose*, Vol. 17, pp. 459–494
- Stenstad P, Andresen M, Tanem BS, Stenius P (2008) Chemical surface modifications of microfibrillated cellulose. *Cellulose*, Vol. 15, pp. 35–45
- Suryanegara, L., Nakagaito, A. N., and Yano, H. (2009). The effect of crysattlization of PLA on the thermal and mechanical properties of microfibrillated cellulose-reinforced PLA composites. *Composites Science and Technology*, Vol. 69, pp. 1187–1192
- Tang, Y., Du, Y., Li, Y., Wang, X., and Hu, X. (2009). A thermosensitive chitosan/poly(vinyl alcohol) hydrogel containing hydroxyapatite for protein delivery. *J Biomed Mater Res*, Vol. 91A, pp. 953–963
- Taniguchi, T. and Okamura, K. (1998). New films produced from microfibrillated natural fibres. *Polym Int*, Vol. 47, pp. 291–294
- YanJun, X., Hill, C. A. S., Xiao, Z., Militz, H., and Mai, C. (2010). Silane coupling agents used for natural fiber/polymer composites: A review. *Applied Science and Manufacturing*, Vol. 41, pp. 806–819
- Yano, S., Maeda, H., Nakajima, M., Hagiwara, T., and Sawaguchi, T. (2008). Preparation and mechanical properties of bacterial cellulose nanocomposites loaded with silica nanoparticles. *Cellulose*, Vol. 15, No. 1, pp. 111–120
- Zhang, J., Elder, T. J., Pu, Y., and Ragauskas, A. J. (2007). Facile synthesis of spherical cellulose nanoparticles. *Carbohydrate Polymers*, Vol. 69, pp. 607–611
- Zhou, W. Y., Guo, B., Liu, M., Liao, B., Rabie, B. A. M., and Jia, D. (2010). Poly(vinyl alcohol)/Halloysite nanotubes bionanocomposite films: Properties and in vitro osteoblasts and fibroblasts response. *J Biomed Mater Res*, Poly(vinyl

- alcohol)/Halloysite nanotubes bionanocomposite films: Properties and in vitro osteoblasts and fibroblasts response , Vol. 93A, pp. 1574–1587
- Zimmermann, T., Pöhler, E. and Geiger, T. (2004). Cellulose Fibrils for Polymer Reinforcement. *Advanced Engineering materials*, Vol. 6, no. 9, pp. 754-761
- Zuluaga, R., Putaux, J. L., Cruz, J., Vélez, J., Mondragon, I., and Gañán, P. (2009). Cellulose microfibrils from banana rachis: Effect of alkaline treatments on structural and morphological features. *Carbohydrate Polymers*, Vol. 76, pp. 51–59

Part 2

Composite Materials and Curing Processes

Radiation Curing of Thermosetting-Thermoplastic Blends as Matrices for Structural Carbon Fibre Composites

Sabina Alessi¹, Clelia Dispenza¹,

Giuseppe Pitarresi² and Giuseppe Spadaro¹

¹*Dipartimento di Ingegneria Chimica dei Processi e dei Materiali, Università di Palermo*

²*Dipartimento di Ingegneria Meccanica, Università di Palermo*

Viale delle Scienze 90128, Palermo

Italy

1. Introduction

Radiation processing indicates all the processes based on the use of ionizing radiation that cause chemical changes in the matter. Practical application of radiation processing have been evolved since the introduction of this technology nearly fifty years ago. The earliest developments are represented by the sterilization of disposable medical products, preservation of food and crosslinking of plastic materials, while the curing of monomeric coatings was developed somewhat later (Woods, 2000; Cleland et al. 2003). In the last years the use of these and other processes has grown more and more and they are widely practiced today to produce heat-shrinkable plastic films for packaging foods or insulation on electrical wires and jackets on multi-conductor cables in order to increase heat tolerance and to improve the resistance to abrasion and solvents. Other important applications include the reduction of the molecular weight by scissoring of polymers, the grafting of monomers into polymers in order to modify their surface properties and the curing of fibre-reinforced polymer composite materials, whose main applications are in automotive and aeronautic/aerospace industries (Clough, 2001; Singh et al. 1996; Lopata et al. 1999; Goodman & Palmese, 2002; Jhonson, 2006; Berejka, 2010). Due to its behaviour regarding the possibility to involve very small particles, like electrons or heavy ions, radiation processing is the ideal way to produce nano-structured systems. Different examples are reported in literature, such as nano-lithography devices (Woods, 2000) and nano-hydrogels especially in the biomedical area (Singh & Kuma, 2008; Chmielewski, 2010).

The radiation sources generally used in radiation processing applications can be divided into two main groups, that one regarding the use of natural or artificial isotopes and the other one in which particle accelerators are employed. In the first group artificial radioisotopes, like Cobalt-60 and Cesium-137, are included and the second group comprises electron accelerators, accelerators for the production of positive ions and x-ray generators (Woods & Pikaev, 1990; Spinks & Woods, 1990).

Currently the most widely used sources of ionizing radiations in the industrial processes are Cobalt-60 and electron accelerators.

Cobalt-60 produces γ photons of two discrete energy values, 1.332 and 1.173 MeV. Since γ photons tend to lose the greater part of their energy through a single interaction, during irradiation a fraction of them are completely absorbed, but the remaining photons are transmitted with their full initial energy.

Electron beams produced by accelerators are mono-energetic and they may be pulsed or continuous. Unlike γ photons, electrons lose their energy gradually, through a number of small energy transfers, so that they are slowed down by thin absorbers.

The use of γ or e-beam radiations depends upon different considerations, such as the nature and size of the objects to irradiate, the penetration to be realized and the productivity required. For a fixed material and for a fixed distance from the radiation source, the radiation is characterized by the penetration in the material and the rate by which the energy is absorbed by the material. The first parameter depends on the nature and energy of radiation and can be related to the absorbed dose, i.e. the energy absorbed by the unit of weight of the material, measured in Gray (Gy), or more commonly in kGy ($1 \text{ J/Kg} = 1 \text{ Gy}$). The second parameter is the dose rate that is the energy absorbed by the unit of weight of the material per unit of time, measured in Gy/s or more commonly in kGy/h.

In particular gamma rays are more penetrating than electron beams, but generally they are characterized by a lower dose rate. On the other hand γ sources offer the advantage of a very simple process, but they suffer from a low flexibility of the plant and from degradation during the time owing to the decrease of the activity of the source. Due to all these considerations γ radiation is normally used when high penetration is required without any productivity problems, while for low penetration and high productivity e-beam process is advisable.

The interaction of electromagnetic and particle radiations with matter occurs by means of different processes, even if it always produces fast charged particles, which generate a mixture of ionized and excited species. The overall effect of both types of ionizing radiation is qualitatively similar, since the same types of ionized and excited species are formed in both cases.

When a moving charged particle interacts with the matter, its energy loss gives rise to a trail of excited and ionized atoms and molecules in the same path of the particles. The same effect is caused by an electromagnetic radiation since the energy absorbed is transferred to electrons and positrons and then dissipated along the paths of these particles. In this way the overall result of the absorption of any type of ionizing radiation by matter is the formation of excited and ionized species, giving rise to similar chemical effects.

As already observed, radiation processing finds several applications in different fields. In particular it has been subjected to a very marked interest for the synthesis and modifications of polymeric materials. In fact, the interaction of ionizing radiation with apt monomers can give rise to radical or ionic (mainly cationic) polymerizations.

Radical polymerization of vinyl monomers is easily performed, while cationic process is more difficult due to the possibility that the cationic species can be neutralised by even very small amount of basic impurities (Chapiro, 1962; Crivello, 1999).

Also the modification of polymers by ionizing radiation has been subject of studies and several industrial applications. The interaction of ionizing radiation with polymeric materials causes the formation of free radicals that further evolve towards chain scission, with molecular degradation, chain branching and cross-linking with molecular weight increase (Woods & Pikaev, 1990). All these effects coexist, their extent depending on many factors, such as the molecular structure of the irradiated polymer, the presence of air or

other gases during irradiation and the operating conditions (temperature, dose rate, etc.). The molecular modifications induced by irradiation can strongly modify the mechanical, electrical and thermal properties of the polymers. Crosslinking for the production of electrical insulating materials or tubes for both high thermal and mechanical resistance are among the most important applications (Jansen & Brocardo Machado, 2005).

Among the ionising radiation induced polymerization processes, one the most stimulating and studied application is the radiation curing of epoxy resins in order to produce polymeric matrices for carbon fibre structural composites, in both aerospace and advanced automotive industries. Compared to thermal curing, the main advantages lie in the reduced curing time, the ambient curing temperature, the greater design flexibility and the higher materials shelf life (Singh et al., 1996; Lopata et al. 1999; Jhonson, 2006). In particular the possibility to carry out the process at mild temperature derives from the fact that it does not need thermal activation. This behaviour makes the process environmentally friendly, energy saving and induces positive effects on the properties of the synthesised materials. In fact the significant reduction of thermally induced mechanical stresses derived from the use of mild process temperature leads to an improvement of the mechanical properties of the cured materials.

The use of polymeric composite materials for transport applications has considerably increased in the last few decades for their favourable strength/weight ratio, with respect to low weight metallic materials traditionally employed in such structures. Other advantages coming from the use of polymeric composites are the improvement of the resistance to both corrosion and chemicals.

The standard thermal cure process induces high quality and performance in these materials and it has been extensively studied and optimized for each specific application (Ellis, 1994; Di Pasquale et al., 1997; Mimura et al., 2000). On the other hand radiation processing has become more and more promising for advanced structures for the several advantages offered. Lopata, Saunders and Singh widely discussed the benefits of electron beam curing for the manufacture of high performance composites and in particular Lopata suggested the importance of this process also for the repairing of such structures (Lopata et al., 1999; Singh et al., 1996; Lopata & Sidwell, 2003).

The first successful attempts of radiation curing were developed on acrylic derivative epoxies, which undergo to polymerization via radical mechanism, but the obtained materials did not meet the required thermal (high glass transition temperature, T_g) and mechanical properties (high elastic modulus and high fracture energy) for aerospace and advanced automotive applications (Woods & Pikaev, 1990).

Materials with enhanced thermal and mechanical behaviours, similar to that of the materials realized via thermal curing, were obtained when the cationic polymerization of epoxy resins was performed through the use of suitable onium salts, already successfully used in the UV induced epoxy curing (Lopata et al. 1999; Crivello, 1999; Crivello, 2002; Crivello, 2005; Bulut & Crivello, 2005). Due to the presence of strongly electronegative groups, onium salts are very acid and make possible the epoxy ring opening and the further cationic attack to the other epoxy monomers with the increase of the chain length.

Most of the commercially available initiators are diaryliodonium or triarylsulfonium salts of weak bases. Several mechanisms for polymerization of epoxies have been suggested (Decker & Moussa, 1991; Crivello, 1999, 2002 and 2005; Bulut & Crivello, 2005) and probably radiation induced polymerization of epoxies can proceed via different mechanisms whose relative contributions might vary from one formulation to another.

During radiation curing, several parameters can greatly influence the final properties of the cured materials. In particular parameters such as the composition of the epoxy resin system (including the catalyst species, the chemical structure of the epoxy, other modification agents etc.), and those related to the process such as irradiation dose, dose rate and curing temperature have a key role in determining the properties of these materials (Fengmei et al. 2002; Degrand et al., 2003 ; Nho et al., 2004; Raghavan, 2009).

A general problem for epoxy cured systems, either thermally or by irradiation, is that both high glass transition temperature and high elastic modulus are accompanied by a brittle behaviour and by a decrease of the toughness, with a poor resistance of the material to crack initiation and growth and with a low fracture energy value (Ellis, 1994; Broek, 1986; Riew & Kinloch, 1993).

The basic goal in toughening crosslinked epoxy resins is to improve their crack resistance and toughness without a significant decreasing of the other important inherent properties, such as the flexural modulus and the thermo-mechanical properties (T_g) of the original epoxy resins. A way to improve the toughness is the incorporation in the monomer of a second component. This has been successfully done for thermally cured systems, incorporating in the monomer a second component into the continuous matrix of epoxy resins through physical blending or chemical reactions (Kim et al., 1999; Mimura et al., 2000).

Unmodified epoxy resins are usually single-phase materials, while the addition of modifiers can turn the toughened epoxy resins into multiphase systems. When modifier domains are correctly dispersed in discrete forms throughout the epoxy matrix, the fracture energy or toughness can be greatly improved.

Among the toughening agents studied for thermally cured systems, the best improvement of toughness, without losing thermal and mechanical properties, has been obtained by engineering thermoplastics, like poly(ether sulfone), poly(ether imide), poly(aryl ether ketone), poly(phenylene oxide), polyamide etc. (Unnikrishnan & Thachil, 2006; Mimura et al., 2000; Blanco et al. 2003, Park & Jin, 2007). The thermoplastic toughened epoxies form homogeneous blends in the uncured state and can lead to phase separation on curing. The curing and phase separation processes were studied in many papers (Gan et al., 2003; Giannotti et al., 2003; Montserrat et al., 2003; Swier & Van Mele, 1999 and 2003; Tang et al., 2004; Xu et al., 2004; Li et al., 2004; Wang et al., 2004).

In particular the phase diagrams temperature/compositions for epoxy/toughening agent systems as function of the epoxy curing degree are of fundamental importance. In fact, the use of engineering thermoplastics as a method for toughening high performance, thermally curable epoxies, can cause different morphologies (Inoue, 1995; Mimura et al., 2000; Swier & Van Mele, 1999 and 2003). The "homogeneous" morphology results from a single phase that requires the dissolution of the thermoplastic into the epoxy with a curing process without phase separation. This method effectively reduces the crosslinking density of the epoxies, but it provides only modest improvement of the toughness in thermally cured systems. Another kind of morphology that can be obtained is the "second phase" morphology, resulting from two phases formed. In a first type the thermoplastic is the discontinuous phase (thermoplastic particles) and the epoxy the continuous phase. It generally occurs at thermoplastic loadings of about 15% or less, and it provides only modest improvement of toughness in thermally cured systems. A second type of the particulate consists of the epoxy which forms a discontinuous phase (epoxy particles) distributed in a thermoplastic continuous phase (phase inversion) and it generally occurs with a thermoplastic loadings of

more than 15-20%. Also in this case there is only modest improvement of toughness in thermally cured systems.

The preferred morphology which allows to realize high fracture toughness in epoxy based systems is the "co-continuous" morphology, which consists of an epoxy continuous phase and a thermoplastic continuous phase. These phases have nanometer or micrometer dimensions and require thermoplastic loading exceeding 15-20%, while the phase size and the toughness are controlled by the thermoplastic backbone, by its reactive end groups, its molecular weight and obviously by the epoxy nature (Mimura et al., 2000).

Up to 2000 the majority of studies and programs focused on the development of ionising radiation curable resin systems that could match the performance of thermally cured matrices for structural composites, while the understanding of how radiation curing takes place and its dependence on both system and process parameters was limited (Singh et al. 1996; Berejka & Eberl, 2002; Singh, 2001; Decker, 1999). On the contrary in the latest years many research efforts have been done toward other directions, in particular investigating the influencing factors of this process in order to provide a careful foundation of radiation curable epoxy based systems. In particular the influence of the catalyst (type and content), the effect of the nature of epoxy resins and of the processing parameters, such as dose and temperature, on the curing degree of the systems, the EB curing mechanism, the role of the onium salt and the influence of the monomer conversion on the glass transition temperature have been investigated (Fengmei et al. 2002; Gang et al., 2002; Degrand et al., 2003; Nho et al., 2004; Raghavan, 2009; Coqueret et al. 2010).

A very important work has been performed by the "Cooperative Research and Development Agreement" (CRADA) sponsored by the Department of Energy Office of Science, NASA Langley Research Center, U.S. Air Force Research Laboratory, U.S. Army Research Laboratory, and several industrial partners. Several epoxy resins systems in the presence or not of toughening agents and cured by electron beam irradiation have been realised. These resin systems showed mechanical, thermal, and physical properties that are significantly better than earlier electron beam curable resins, and are comparable to many thermally cured, high performance, toughened and untoughened epoxies (Janke et al., 2001). This review presents the results obtained by the authors in the study of e-beam curing of epoxy resin systems in order to produce polymeric matrices for carbon fibre composites (Alessi et al., 2005, 2007, a,b and 2010).

The influence of the processing parameters on both the curing reactions and the properties of the obtained materials is presented. In particular the possibility to really perform the process at mild temperature is critically discussed and the consequences of the low-temperature process on the final structures and properties of the cured materials are evidenced.

Also the influence of engineering thermoplastics in the toughening of the cured matrices is illustrated.

2. Radiation curing of epoxies as matrices for advanced composites

The occurrence of curing reactions has been checked by the monitoring of the temperature during samples irradiation. The temperature of the irradiated samples depends on different thermal events, whose rate depends on the processing parameters. The temperature increase is due to both the absorption of radiation energy and the heat developed by the exothermic curing reactions, while the temperature decrease is due to heat releasing from the irradiated samples to the environment. The balance of these phenomena determines the temperature of

the epoxy resin during irradiation. The heat production rate is low when both the concentration of iodonium salt and the dose rate are low, while the heat released to the environment is mainly related to the surface/volume ratio.

2.1 Untoughened epoxies

E-beam curing of blends of various epoxies/iodonium salts has been carried out.

One example is reported in Fig 1, where the temperature as function of the absorbed dose for Bis(4diglycidiloxy-phenil) methane (DGEBF)/iodonium salt samples (Alessi et al., 2005) is reported. The iodonium salt concentration is constant (0.1 phr) and the experiments have been performed at different dose rates (84, 420 and 840 kGy/h). At low dose rate (84 kGy/h) the temperature curve has a very slight increase and tends to a plateau value of about 50°C. On the contrary at high dose rates (420 and 840 kGy/h) the temperature increases up to 180°C and after decreases, but toward higher values than that reached during the correspondent irradiation at low dose rate.

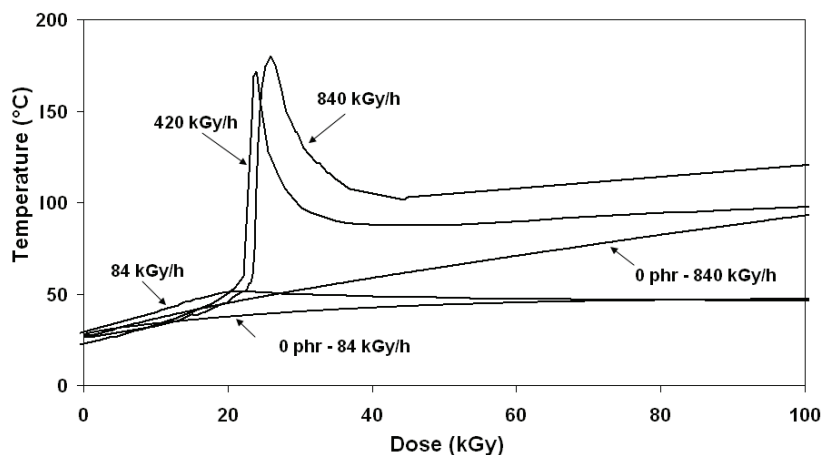


Fig. 1. Temperature as a function of irradiation dose at different dose rates.

“Reprinted from *Nuclear Instruments and Methods in Physics Research B*, 236, Alessi, S., Calderaro, E., Parlato, A., Fuochi, P., Lavallo, M., Corda, U., Dispenza, C., Spadaro, G. Ionizing radiation induced curing of epoxy resin for advanced composites matrices, 55-60, Copyright (2005), with the permission from Elsevier”

In the same figure the thermal profiles of the system without initiator, i.e. without polymerization reactions, are reported for two dose rates conditions, revealing that the major contribution to the plateau value is essentially due to the heat evolved by the radiation absorption. Since during curing very different temperature profiles can be obtained, the production of materials with marked different properties is realized. In fact, in conditions apt to produce marked temperature increase, the epoxy monomer undergoes to a simultaneous radiation and thermal curing, while when the irradiation is performed at low temperature the systems undergoes only to radiation curing.

Dynamic mechanical thermal analysis (DMTA) tests, carried out on samples cured in different processing conditions, and at different dose temperature profiles, evidence the different

structure and properties of the synthesised materials. In Fig. 2 elastic modulus, E' , and loss factor, $\tan\delta$, as function of the temperature for the materials cured in the conditions of Fig. 1 are reported. The sample cured at low temperature presents two broad relaxation peaks. This is an indication of a not uniform structure with networks of different cross linking degrees. This phenomenon can be related to vitrification phenomena during irradiation. In fact polymerization reactions cause the increase of the glass transition temperature of the irradiated system, which soon reaches the low processing temperature. In these conditions the structure becomes rigid and further curing reactions are controlled by the diffusion of the reactive species in the bulk of the polymerising system. Furthermore the storage modulus/temperature curve reported in the same figure presents an increase between the two relaxation temperatures. This can be attributed to post-irradiation thermal curing due to the heating during the DMTA test itself. We can conclude that the low temperature radiation curing is not complete and that the second relaxation peak can be considered the result of the combined effect of radiation and post-irradiation thermal curing. DMTA tests relative to the sample cured at high temperature presents only one relaxation peak, due to the high temperature reached during irradiation, which allows to overcome the vitrification phenomena, giving rise to the formation of a more "uniform" structure. In these conditions a simultaneous radiation and thermal curing is performed. It is interesting to note that the relaxation temperature is significantly lower than the second relaxation temperature of the material cured at low temperature. This can be explained with the more efficient thermal treatment (due to the test itself) when the structure is less rigid.

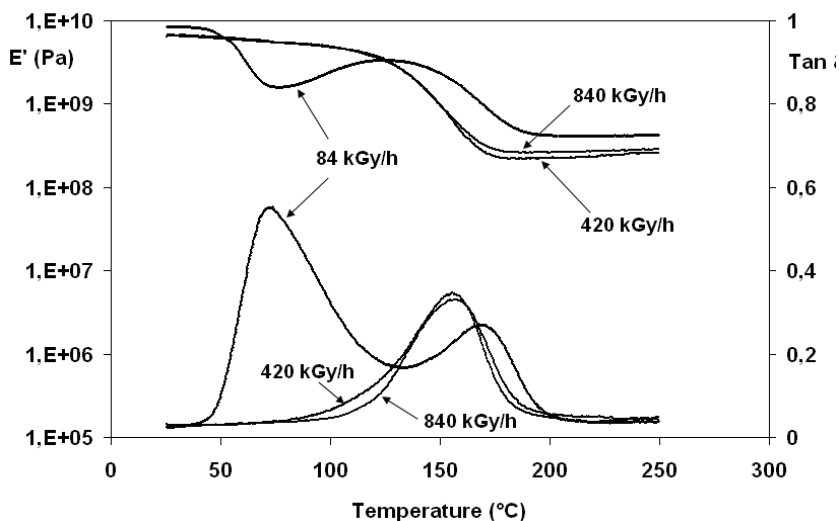


Fig. 2. Dynamical mechanical thermal curves at an irradiation dose of 150 kGy and at different dose rates.

"Reprinted from *Nuclear Instruments and Methods in Physics Research B*, 236, Alessi, S., Calderaro, E., Parlato, A., Fuochi, P., Lavalle, M., Corda, U., Dispenza, C., Spadaro, G. Ionizing radiation induced curing of epoxy resin for advanced composites matrices, 55-60, Copyright (2005) with the permission from Elsevier"

As the results indicate that not always radiation process allows to complete curing reactions, in order to check their completeness, samples radiation cured in various conditions have been subjected to post-irradiation thermal treatments.

In Fig. 3 DMTA curves of the sample cured at 150 kGy - 84 kGy/h and of the sample also subjected to a post-irradiation thermal treatment at 175°C for 2 hours are reported. In the last case a single relaxation peak is observed, thus indicating the formation of an uniform structure. Comparing the two curves reported in Fig.3, it is possible to note that the sample post cured after irradiation at low temperature presents a relaxation temperature very close to that of the second relaxation peak related to the only irradiation process, while not significant increase of T_g after thermal curing has been observed for sample irradiated at high temperature, whose correspondent comparison is not here reported. It is possible to conclude that the way to optimise the curing degree and the thermal properties of the radiation cured materials is a suitable combination of radiation curing at low temperature and a post-irradiation thermal treatment. It is important to consider that the post-irradiation thermal curing is performed on already polymerised solid materials, in an oven and out of the mould. In these conditions thermal treatment does not create environmental problems (no volatile emission) and the obtained materials do not present thermally induced mechanical stresses.

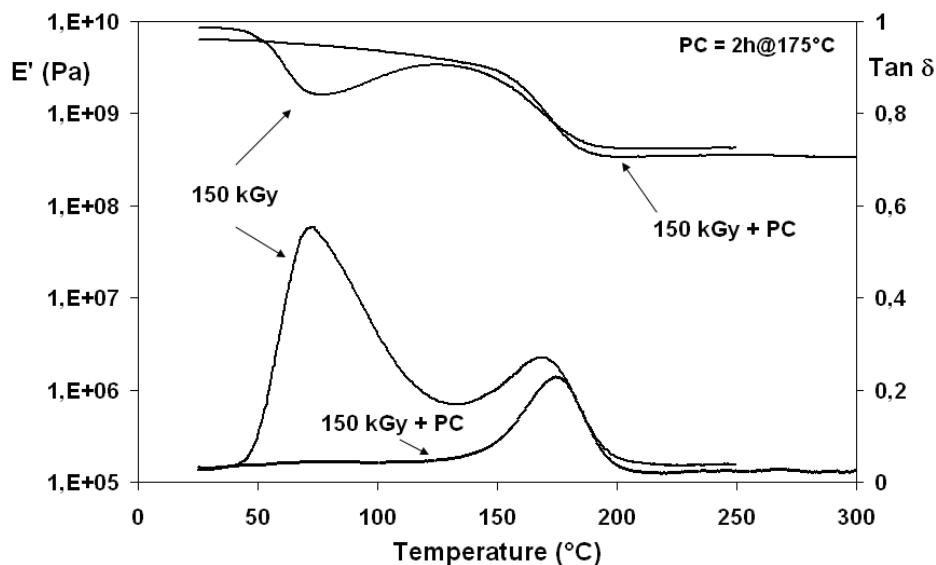


Fig. 3. Dynamical mechanical thermal curves for blends cured at 150 kGy and 84 kGy/h with and without post irradiation thermal curing. Iodonium salt concentration: 0.1phr (per hundred of resin).

"Reprinted from *Nuclear Instruments and Methods in Physics Research B*, 236, Alessi, S., Calderaro, E., Parlato, A., Fuochi, P., Lavallo, M., Corda, U., Dispenza, C., Spadaro, G. Ionizing radiation induced curing of epoxy resin for advanced composites matrices, 55-60, Copyright (2005), with the permission from Elsevier"

As already cited in the introduction, the polymer matrices for structural carbon fibre composites for advanced automotive and aerospace applications need to meet severe requirements in terms of thermal and mechanical properties. The optimal combination of a “dual curing” process, radiation curing at moderate temperature, followed by a post-irradiation thermal treatment at high temperature, allows to obtain materials with high thermal performances, indicated by glass transition temperatures higher than 170°C.

An alternative way to increase the T_g of the polymer matrix is to use epoxy resins with higher degrees of functionalities. Blends of difunctional DGEBF and trifunctional Tris(4-glycidiloxyphenyl) methane (Tactix) resins have been cured by ionizing radiation in the presence of an iodonium salt (Alessi et al., 2007, a).

In table 1, for difunctional/trifunctional blends at different composition, glass transition temperatures, elastic modulus in the rubbery state (at $T=T_g+30^\circ\text{C}$) and $\tan\delta$ maximum are reported. With respect to the 100% DGEBF system, the presence of a trifunctional monomer allows to perform T_g increase up to about 70°C. This effect is related to a strong increase of cross-linking degree, as confirmed by the values of the elastic moduli in the rubbery state and of the maximum of $\tan\delta$, also reported in the same table.

System	T_g (°C)	$E_{\text{rubbery state}}^*$ (MPa)	$\tan\delta_{\text{max}}$
100D	157	70	0.35
80D-20T	175	600	0.20
60D-40T	230	800	0.11
90D-10t.a.	139	50	0.45
54D-36T-10t.a.	212	800	0.13

Table 1. Relaxation temperatures (T_g), elastic modulus in the rubbery state (* at $T=T_g+30^\circ\text{C}$) and $\tan\delta$ maximum for epoxy based systems at different difunctional/trifunctional ratios, e-beam cured at 150 kGy and 840 kGy/h. D: difunctional epoxy resin (DGEBF); T: trifunctional epoxy resin (Tactix); t.a.: toughening agent (Polyethersulfone based).

“Alessi, S., Dispenza, C., Spadaro, G.. Thermal Properties of E-beam Cured Epoxy/Thermoplastic Matrices for Advanced Composite Materials. Macromolecular Symposia. 2007. 247. 238-243. Copyright Wiley_VCH Verlag GmbH & Co. KGaA. Reproduced with permission”

2.2 Toughened epoxies

The increase of crosslinking degree obtained by either the combination of radiation and thermal curing or by the mixing of epoxy monomers at different functionalities, causes improvement of thermal properties and significant increase of the elastic modulus. Unfortunately such molecular behaviour can give rise to very brittle materials. As discussed in the introduction the toughness can be increased by the use of apt toughening agents, like high modulus and high T_g thermoplastics.

This has been done in Alessi et al., 2007b, where blends of difunctional DGEBF, polyethersulphone (PES) and iodonium salts have been e-beam cured by ionizing radiation.

First of all it is shown that the presence of PES does not interfere with radiation curing process and that similar results with respect to systems without thermoplastic are obtained. In particular a similar effect of the processing parameters and more specifically of the irradiation dose rate on the temperature during irradiation is observed, with the obtaining of mild temperature profiles at low dose rates and a dramatic temperature increase at high dose rates. Similar comments can be made also for the molecular structure and thermal properties of the cured materials, as shown in Fig. 4 by DMTA curves, where data relative to a DGEBF/PES blends cured at different dose and dose rates are reported. Also in this case, a post irradiation thermal curing allows to uniform the structure and to obtain a sufficiently high value of glass transition temperature.

In the same table 1 glass transition temperatures, elastic modulus in the rubbery state and $\tan\delta$ maximum are reported, for difunctional/trifunctional blends toughened by a PES based thermoplastic. Also in this case the introduction of the trifunctional epoxy monomer causes a marked increase of T_g value, indicating an increase of the cross linking degree, confirmed by the correspondent values of $\tan\delta$ maximum and of the elastic modulus in the rubbery state.

The presence of the thermoplastic can induce a marked effect in the mechanical properties. The presence of PES does not significantly affect the tensile elastic modulus. Our experiments give for difunctional epoxy formulations containing 10PES, e-beam cured at 80 kGy-90kGy/h, a value of the elastic modulus of about 3.6 GPa, very close to the values of

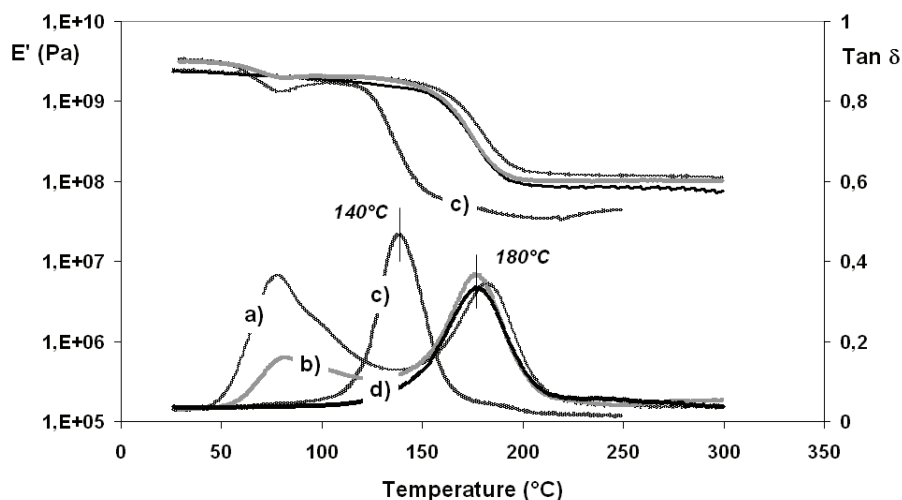


Fig. 4. Dynamical mechanical thermal curves for blends, toughened by PES, cured at different process conditions: a) 80 kGy, 84 kGy/h; b) 150 kGy and 84 kGy/h; c) 150 kGy and 840 kGy/h; d) 80 kGy and 84 kGy/h and thermally post-cured for 2 h @ 100°C. Iodonium salt concentration: 1phr (per hundred of resin).

"Reprinted from *Radiation Physics and Chemistry*, 76, Alessi, S., Dispenza, C., Fuochi, P.G., Corda, U., Lavalle, M., Spadaro, G. E-beam curing of epoxy-based blends in order to produce high-performance composites, 1308-1311, Copyright (2007), with the permission from Elsevier"

similar untoughened epoxy resins (Janke et al., 2001). On the contrary a marked toughness increase is observed. In table 2 the results of the fracture toughness test in terms of the critical intensity factor K_{IC} (Broeck, 1986; ASTM D 695-02a., 2002), for both DGEBF neat resin and DGEBF/PES blends, are reported (Alessi et al. 2010). Passing from neat epoxy resin systems to blends, a general K_{IC} increase is observed. It is worth to note that the K_{IC} values relative to the toughened materials are not very far from the best results obtained by thermally cured systems (Janke et al., 2001).

In Fig. 5a-b the images of the specimens tested on tensile and three point bending testing machines are shown.

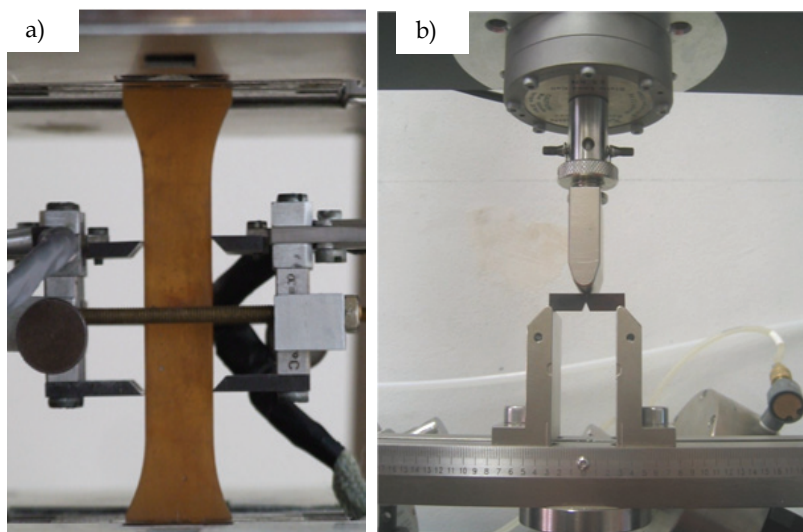


Fig. 5. Mechanical tests. a) Tensile: specimen gripped on a testing machine.; b) Fracture toughness: SENB (Single Edged Notched Bending) specimen in a three point bending configuration.

System	K_{IC} (MPa*m ^{1/2})
0 PES	0.6 ± 0.1
10 PES	1.5 ± 0.2
20 PES	1.2 ± 0.1

Table 2. K_{IC} values for different epoxy resin based systems irradiated at 80kGy and 70kGy/h.

“Polymer Degradation and Stability, 95, Alessi, S., Conduruta, D., Pitarresi, G., Dispenza, C., Spadaro, G. Hydrothermal ageing of radiation cured epoxy resin-polyether sulfone blends as matrices for structural composites, 677-683, Copyright (2009), with the permission from Elsevier”.

As discussed in the introduction the toughness is strongly related to the blend morphology. In Fig 6 the SEM micrographs of the toughened materials, on fractured surfaces of the tested specimens (table 2), are shown (Alessi et al., 2010). It can be observed that in both cases a co-continuous morphology is obtained, where two phases, one epoxy-rich and the second one PES-rich, are interconnected each other.

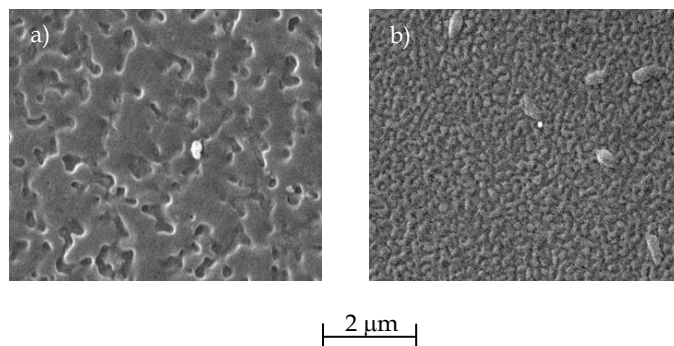


Fig. 6. SEM micrographs for epoxy resin based systems toughened by PES irradiated at 80 kGy and 70 kGy/h. a) PES content : 10 phr; b) PES content : 20 phr.

“Reprinted from *Polymer Degradation and Stability*, 95, Alessi, S., Conduruta, D., Pitarresi, G., Dispenza, C., Spadaro, G. Hydrothermal ageing of radiation cured epoxy resin-polyether sulfone blends as matrices for structural composites. 677-683, Copyright (2009), with the permission from Elsevier”

3. Conclusions

In this review the application of radiation processing to the synthesis of epoxy based polymeric matrices for carbon fibre composites is presented.

In the introduction the general fundamentals of radiation processing, with reference to its use in the science and technology of polymer materials and in particular to radiation curing of epoxy resin systems, are discussed.

The most important results obtained by our research group are reviewed. The aim of our research is to improve both thermal and mechanical properties of the e-beam cured materials, relating them to the processing parameters for a full scale production in the aerospace and automotive industries.

It is shown that strong differences can be observed in the temperature of the epoxy systems during irradiation. The temperature depends on several parameters, such as the system formulation, the dose rate and the geometry of the irradiated sample. Varying these parameters, the temperature ranges from low to very high values. In these last conditions simultaneous thermal and radiation curing is performed. DMTA analyses evidence that the different temperature profiles during irradiation cause the formation of very different network structures with consequent different thermal behaviour. It is concluded that the best thermal performances are obtained by a combined “dual cure” process, consisting in e-beam irradiation at moderate dose rates and temperatures, followed by an “out of mould” post-irradiation thermal curing on already solid materials. It is very important to note that the heat released from the irradiated systems toward the environment, which is one of the

parameters which affects the temperature profile during irradiation, depends, among others, on the geometry of the irradiated system and in particular on the surface/volume ratio. This means that the irradiation of samples with the same formulation and at the same dose rate, but with different geometry, can have different temperature profiles and the cured materials can have different properties. This is a very important point in the scale up from laboratory to full scale industrial production. The reference parameter can be the temperature profile during irradiation which must be kept constant in the scaling up.

Regarding the mechanical properties, it is shown that blends of epoxy resins with engineering thermoplastics, similar to that used for thermally cured formulations, can be successfully cured by e-beam irradiation and the fracture energy values are not far from the best performances obtained through the more traditional thermal curing.

Finally SEM analysis shows that the toughness improvement is strictly related to the formation of co-continuous morphologies.

Figs. 1, 2, 3 reprinted from:

"Nuclear Instruments and Methods in Physics Research B, 236, Alessi, S., Calderaro, E., Parlato, A., Fuochi, P., Lavalle, M., Corda, U., Dispenza, C., Spadaro, G. Ionizing radiation induced curing of epoxy resin for advanced composites matrices, 55-60, Copyright (2005), with the permission from Elsevier"

Fig. 4 reprinted from:

"Radiation Physics and Chemistry, 76, Alessi, S., Dispenza, C., Fuochi, P.G., Corda, U., Lavalle, M., Spadaro, G. E-beam curing of epoxy-based blends in order to produce high-performance composites, 1308-1311, Copyright (2007), with the permission from Elsevier"

Fig. 6 reprinted from:

"Polymer Degradation and Stability, 95, Alessi, S., Conduruta, D., Pitarresi, G., Dispenza, C., Spadaro, G. Hydrothermal ageing of radiation cured epoxy resin-polyether sulfone blends as matrices for structural composites, 677-683, Copyright (2009), with the permission from Elsevier".

Data of Table 1 derived from:

"Alessi, S., Dispenza, C., Spadaro, G.. Thermal Properties of E-beam CuredEpoxy/Thermoplastic Matrices for Advanced Composite Materials. Macromolecular Symposia. 2007. 247. 238-243. Copyright Wiley_VCH Verlag GmbH & Co. KGaA. Reproduced with permission"

Data of Table 2 derived from:

"Polymer Degradation and Stability, 95, Alessi, S., Conduruta, D., Pitarresi, G., Dispenza, C., Spadaro, G. Hydrothermal ageing of radiation cured epoxy resin-polyether sulfone blends as matrices for structural composites, 677-683, Copyright (2009), with the permission from Elsevier".

4. References

Alessi, S., Calderaro, E., Parlato, A., Fuochi, P., Lavalle, M., Corda, U., Dispenza, C., Spadaro, G. (2005). Ionizing radiation induced curing of epoxy resin for advanced

- composites matrices. *Nuclear Instruments and Methods in Physics Research B*, 236, 55-60, 0168-583X.
- Alessi, S., Dispenza, C., Spadaro, G. (2007). Thermal Properties of E-beam Cured Epoxy/Thermoplastic Matrices for Advanced Composite Materials. *Macromolecular Symposia*, 247, 238-243, 1521-3900. a
- Alessi, S., Dispenza, C., Fuochi, P.G., Corda, U., Lavalle, M., Spadaro, G. (2007). E-beam curing of epoxy-based blends in order to produce high-performance composites. *Radiation Physics and Chemistry*, 76, 1308-1311, 0969-806X. b
- Alessi, S., Conduruta, D., Pitarresi, G., Dispenza, C., Spadaro, G. (2010). Hydrothermal ageing of radiation cured epoxy resin-polyether sulfone blends as matrices for structural composites. *Polymer Degradation and Stability*, 95, 677-683, 0141-3910.
- ASTM D 695-02a. (2002). Standard Test Methods for Compressive Properties of Rigid Plastics, 10 Aug. 2002.
- Berejka, A.J. & Eberl, C. (2002). Electron beam curing of composites in North America. *Radiation Physics and Chemistry*, 63, 551-556, 0969-806X.
- Berejka, A.J. (2010). Radiation curing: coatings and composites. *Nucleonika*, 55, 1, 97-106, 0029-5922.
- Blanco, I., Cicala, G., Faro, C.L., Recca, A. (2003). Development of a toughened DGEBS/DDS system toward improved thermal and mechanical properties by the addition of a tetrafunctional epoxy resin and a novel thermoplastic. *Journal of Applied Polymer Science*, 89, 268-273, 0021-8995.
- Broek, D. (1986). *Elementary Engineering Fracture Mechanics*. Kluwer Academic Publishers (4th revised edition), 90-247-2580-1, Hingham, MA 02043, USA
- Bulut, U. and Crivello, J.V. (2005). Investigation of the Reactivity of Epoxide Monomers in Photoinitiated Cationic Polymerization. *Macromolecules*, 38, 3584-3595, 0024-9297.
- Chapiro, A. (1962). *Radiation Chemistry of Polymeric Systems*, Interscience, New York.
- Chmielewski, A. G. (2010). Chitosan and radiation chemistry. *Radiation Physics and Chemistry*, 79, 272-275, 0969-806X.
- Cleland, M.R., Parks, L.A., Cheng, S. (2003). Applications for radiation processing of materials. *Nuclear Instruments and Methods in Physics Research B*, 208, 66-73, 0168-583X.
- Clough, R.L. (2001). High-energy radiation and polymers: A review of commercial processes and emerging applications. *Nuclear Instruments and Methods in Physics Research B*, 185, 8-33, 0168-583X.
- Coqueret, X., Krzeminski, M., Ponsaud, P., Defoort, B. (2009). Recent advances in electron-beam curing of carbon fiber-reinforced composites. *Radiation Physics and Chemistry*, 78, 557-561, 0969-806X.
- Crivello, J.V. (1999). UV and electron beam-induced cationic polymerization. *Nuclear Instruments and Methods in Physics Research B*, 151, 8-21.
- Crivello, J. V. (2002). Advanced curing technologies using photo-and electron beam induced cationic polymerization. *Radiation Physics and Chemistry*, 63, 21-27, 0969-806X.
- Crivello, J.V. (2005). Investigation of the photoactivated frontal polymerization of oxetanes using optical pyrometry. *Polymer*, 46, 12109-12117, 0032-3861.
- Decker, C. & Moussa, K. (1991). A new class of highly reactive acrylic monomers, Light-Induced copolymerization with difunctional oligomers. *Macromolecular Chemistry and Physics*, 192, 507-522, 1521-3935.
- Decker, C. (1999). High-speed curing by laser irradiation. *Nuclear Instruments and Methods in Physics Research B*, 151, 22-28, 0168-583X.

- Degradand, H., Cazaux, F., Coqueret, X., Defoort, B., Boursereau, F., Larnac, G.. (2003). Thermal effects on the network structure of diglycidylether of bisphenol-A polymerized by electron-beam in the presence of an iodonium salt. *Radiation Physics and Chemistry*, 68, 885-891, 0969-806X.
- Di Pasquale, G., Motta, O., Recca, A., Carter, J.T., McGrail, P.T., Acierno, D. (1997). New high-performance thermoplastic toughened epoxy thermosets. *Polymer*, 38, No.17, 4345-4348, 0032-3861.
- Ellis, B. (1994). *Chemistry and technology of epoxy resins*. Blackie Academic & Professional, Chapman & Hall, Glasgow.
- Fengmei, L., Jianwen, B., Xiangbao, C., Huaying, B., Huiliang, W. Factors influencing EB curing of epoxy matrix. *Radiation Physics and Chemistry*, 63 (2002) 557-561, 0969-806X
- Gan, W., Yu Y., Wang, M., Tao, Q., Li, S. (2003). Morphology Evolution during the Phase Separation of Polyetherimide/Epoxy Blends. *Macromolecular Rapid Communications*, 24, 952-956, 1521-3927.
- Gang, S., Zhang, Z.G., Chen, C.Q., Zhong, W.H.. (2002). Analyses on during process of electron beam radiation in epoxy resins. *Materials Chemistry and Physics*, 78, 349-357, 0254-0584.
- Giannotti, M.I., Solsona, M.S., Galante, M.J., Oyanguren, P.A. (2003). Morphology control in polysulfone-modified epoxy resins by demixing behaviour. *Journal of Applied Polymer Science*, 89 405-412, 0021-8995.
- Goodman, D. L. & Palmese, G. R. (2002). Curing and Bonding of Composites using Electron Beam, In: *Handbook of polymer blends & composites*, Kulshreshtha, A. K. and Vasile, C. vol. 1, ch. 11, RAPRA Technology Ltd, 978-1-85957-309-6, Shropshire, UK.
- Inoue, T. (1995). Reaction-induced phase decomposition in polymer blends. *Progress in Polymer Science*, Vol.20, 119-153, 0079-6700.
- Janke, C. J., Lomax, R. D., Robitaille, S., Duggan, S., Serranzana, R. C., Lopata, V. J. (2001). Improved Epoxy Resins Cured by Electron Beam Irradiation. *Proceedings of 46th International SAMPE Symposium*, Long Beach, CA, May 2001, 46, 2115-2126
- Jansen, J.U. & Brocardo Machado, L.D. (2005). A new resin for photocurable electrical insulating varnishes. *Nuclear Instruments and Methods in Physics Research B*, 236, 546-551, 0168-583X.
- Jhonson, M.A. (2006). *Electron Beam Processing for Advanced Composites*. Radtech Report July-August, 37-42.
- Kim, S., Kim, J., Lin, S.H., Jo, W.H., Choe, C.R. (1999). Effects of mixing temperatures on the morphology and toughness of epoxy/polyamide blends. *Journal of Applied Polymer Science*, 72, 1055-1063, 0021-8995.
- Li, L., Liu, M.J., Li, S. (2004). Morphology effect on water sorption behaviour in a thermoplastic modified epoxy resin system. *Polymer*, 45, 2837-2842, 0032-3861.
- Lopata, V.J. & Sidwell, D.R. (2003). Electron Beam Processing for Composite Manufacturing and Repair. Radtech Report September-October.
- Lopata, V., Saunders, C.B., Singh, A., Janke J.C., Wrenn, G.E., Havens, S.J. (1999). Electron-beam-curable epoxy resins for the manufacture of high-performance composites. *Radiation Physics and Chemistry*, 56, 405-415, 0969-806X.
- Mimura, K., Ito, H., Fujioka, H. (2000). Improvement of thermal and mechanical properties by control of morphologies in PES-modified epoxy resins. *Polymer*, 41, 4451-4459, 0032-3861.
- Montserrat, S., Roman, F., Basany, M., Colomer, P. (2003). Phase separation in a poly(ether sulfone) modified epoxy-amine system studied by temperature modulated

- differential scanning calorimetry and dielectric relaxation spectroscopy. *Macromolecular Symposia.*, 198, 399-410, 1521-3900.
- Nho, Y. C., Kang, P. H., Park, J. S. (2004). The characteristics of epoxy resin cured by γ -ray and E-beam. *Radiation Physics and Chemistry*, 71, 241-244, 0969-806X.
- Park, S.J. & Jin, F.L. (2007). Improvement in fracture behaviors of epoxy resins toughened with sulfonated poly(ether sulfone). *Polymer Degradation and Stability*, 92, 509-514, 0141-3910.
- Raghavan, J. (2009). Evolution of cure, mechanical properties, and residual stress during electron beam curing of a polymer composite. *Composites: Part A*, 40, 300-308, 1359-835X.
- Riew, C.K., Kinloch, A.J. (1993). *Toughened Plastics I, Science and Engineering.*, *Advances in Chemistry Series* 233, American Chemical Society, Washington, D.C.
- Singh, A., Saunders, C., , Barnard, J.W., Lopata, V.J, Kremers, W., McDougall, T. E., Chung, M., Tateishi, M. (1996). Electron processing of fibre-reinforced advanced composites. *Radiation Physics and Chemistry*, 48, 153-170, 0969-806X.
- Singh, A. (2001). Radiation processing of carbon fibre-reinforced advanced composites. *Nuclear Instruments and Methods in Physics Research B*, 185, 50-54, 0168-583X.
- Singh, B. and Kuma, S. (2008). Synthesis and characterization of psyllium-NVP based drug delivery system through radiation crosslinking polymerization. *Nuclear Instruments and Methods in Physics Research B*, 266, 3417-3430, 0168-583X.
- Spinks, J.W.T. & Woods, R.J. (1990). *An Introduction to Radiation Chemistry*, Third Edition, John-Wiley and Sons, Inc., New York, Toronto 1990. ISBN 0-471-61403-3.
- Swier S. & Van Mele B., (1999). Reaction-induced phase separation in polyethersulfone-modified epoxy-amine systems studied by temperature modulated differential scanning calorimetry. *Thermochimica Acta*, 330, 175-187, 0040-6031.
- Swier S. & Van Mele B., (2003). In situ monitoring of reaction-induced phase separation with modulated temperature DSC: comparison between high-Tg and low-Tg modifiers, *Polymer*, 44, 2689-2699, 0032-3861.
- Tang, X., Zhang, L., Wang, T., Yu, Y., Gan, W., Li, S. (2004). Hydrodynamic effect on secondary phase separation in an epoxy resin modified with polyethersulfone. *Macromol. Rapid Commun.*, 25, 1419-1424, 1521-3927.
- Unnikrishnan, K.P. & Thachil, E.T. (2006). Toughening of epoxy resins. *Designed Monomers & Polymers*, 9 129-152, 1385-772X.
- Wang, M., Yu, Y., Wu, X., Li, S. (2004) Polymerization induced phase separation in poly(ether imide)-modified epoxy resin cured with imidazole. *Polymer*, 45, 1253-1259, 0032-3861.
- Woods, R.J. (2000). Radiation Processing: Current Status and Future Possibilities. *Journal of Radioanalytical and Nuclear Chemistry*, Vol.243, No.1, 255-260, 0236-5731.
- Woods, R.J. & Pikaev, A.K. (1990). *Applied radiation chemistry. Radiation Processing*, John-Wiley and Sons, Inc., New York, NY, 0-471-54452-3.
- Xu, G., Shi, W., Shen, S. J. (2004). Curing kinetics of epoxy resins with hyperbranched polyesters as toughening agents. *Polymer Science Part B: Polymer Physics*, 42, 2649-2656, 1099-0488.

Optimization of Curing Cycles for Thick-wall Products of the Polymeric Composite Materials

Oleg Dmitriev and Sergey Mischenko
Tambov State Technical University
Russia

1. Introduction

Production of composites is a complex, energy-intensive, relatively time-consuming chemical-technological process. Therefore, the issue of increasing intensity of production of composite products is largely linked to the performance of technological operations for composites, such as forming, curing, heat treatment and cooling (Balakirev et al., 1990).

The quality of the thermoset composite products is an integral part of increasing the intensity of the process their of obtaining, which is mainly determined by the properties of the cured material, its macro-and microstructure and geometrical parameters of the finished product. Dependence of the quality of products from the processing parameters is determined mainly by the curing cycle, temperature - conversion of homogeneity, achieved the degree of cure, the degree of thermal degradation of the resin, as well as residual stresses.

The process of curing of thermosetting products of composites accompanied, as a rule, exothermic reaction. Due to the low thermal conductivity of the composites during their curing a significant heterogeneity of the temperature-conversion field perpendicular to layers of prepregs occurs and increases with the thickness of the product. If not optimal temperature-time cycle, this leads to significant overheating of internal layers of material products, the deviation curing degree of polymeric resin from optimal, the destruction of resin, the accumulation of internal stresses that cause the reduction of strength properties of the material, warping of finished product, etc. To remove these deficiencies and thereby improve the product quality indicators can be achieved through optimal assignment of temperature-time cycle of $U(t)$ on the surface of the product (Balakirev et al., 1990).

The principal terms of the optimal technology curing thermoset composites, which provide high quality products on the physical and mechanical properties and greater stability of these properties with respect to time, are as follows (Wu & Joseph, 1990):

- products should be cured on a strictly defined temperature-time cycle;
- compaction pressure should provide the desired resin content and density of the material in the product, as well as of a given thickness;
- in the process of molding products should be provided with the necessary degree of curing resin in the composite;
- product after compaction shall not contain residual stresses greater than the number corresponding to the dynamic equilibrium in the range of operating temperatures and ensures greater stability over time dimensions and mechanical properties of products.

The main parameters of the curing process of composite products are: temperature-time cycle, compaction pressure, the time of its application and duration of the process (Balakirev et al., 1990). Properties of cured polymer composite material depend strongly on the correct choice of these parameters and, consequently, the character of the curing process in time, especially at the initial stage, which lays the desired structure. Therefore, the problem of determining optimal curing cycle of composites is an important and responsible.

The main tasks that must be addressed in the selection of optimal curing of composite, that guaranteed high quality and low unit cost, are (Rosenberg & Enikolopyan, 1978):

- reducing the temperature-conversion of inhomogeneities in the composite;
- reducing the duration of the curing cycle and energy consumption;
- complete curing resin in prepregs;
- compacting of the composite up to the desired thickness of the product.

Until recently, for the choice of curing cycles used empirical methods and curing cycles selected according to the results of lengthy experiments. For example, the authors of works (Rosenberg & Enikolopyan, 1978) selected curing cycles on the basis of the conditions for obtaining maximum strength, finding the dependence of breaking stress in the bending strength of the temperature or pressure. In (Kulichikhin & Astakhov, 1991) curing cycles of products was determined by rheological and dielectric measurements. The author of (Botelho et al., 2001) hold time during the curing thermosetting resins determined by change the viscoelastic properties. In (Stern, 1992), (Aleksashin & Antyufeyev, 2005) curing cycle of products based on epoxy and phenol-formaldehyde epoxy resin was determined by time gelation studied using differential thermal analysis and differential scanning calorimetry. A significant shortcoming of these and many other methods is the need to use samples of small diameter and small thickness, the inability to exert the necessary pressure molding, the absence of rheological characteristics of polymeric binder, etc. Therefore, the results obtained using these methods do not fully correspond to the processes proceeding during cure of materials in real constructions.

The disadvantage of the methods of curing cycles choice is that they basically can be applied to thin-walled products (thickness 1-3 mm), which is implemented a uniform setting of cure on thickness of material, and absolutely can not be applied to thick-walled products (more than 3-5 mm), in which the entire course of the curing process is determined by speed of withdrawal of heat (by thermal conductivity) to be allocated in the exothermic reaction of curing. The curing cycles of thick-walled products usually obtained on base of the curing cycles of thin plates that was obtained empirically. In doing so, the temperature of isothermal hold did not change, and hold time in the press were set to form a linear dependence on the thickness of the product (Dedyukhin & Stavrov, 1976). This method is built without taking into account heat transfer, curing kinetics and processes that related to changes viscosity of resin, which leads to large errors.

The use for this purpose of simple calculation methods, based on the theory of similarity, allowing extrapolate the curing process parameters, found in the same conditions to other conditions of curing. For example, in (Dedyukhin & Stavrov, 1976) obtained a formula for calculation, allowing determine of the hold time of the cure in one-step cycle, depending on temperature molds, taking into account the heating rate and activation energy of resin. However, these formulas do not contain connection the temperature curing cycle and the mechanical characteristics of the material (residual stresses) and do not take into account the possible overheating of internal layers of the product as a result of exothermic effect. Nevertheless, they used to calculate the curing cycles of thick-walled products.

Thus, an analysis of previously used empirical and simple calculation methods revealed the following deficiencies:

- a. to determine of the curing cycles of composite required a broad program of experiments;
- b. the curing cycles, found to be satisfactory for this material in some conditions, may not be appropriate in other conditions, in particular, when need other thickness of material;
- c. these techniques do not guarantee complete and high-quality curing of material by the selected temperature-time curing cycle.

The most complete problem of selection of curing cycle products can be solved through the combined use of optimization methods with the use of mathematical models of thermo-kinetic curing process and define of mathematical model parameters. This method consists in setting and solving the problem of minimizing a certain criterion of optimality (Afanasyev, 1985). It can help to determine the curing cycle of composite products for any geometrical sizes and shapes.

The first attempts for solving the problem of finding optimal curing of thick-walled products cycle of thermosetting composites were made by the authors of works (Wu & Joseph, 1990), (Frank et al., 1991) and further developed in (Balakirev et al., 1990), (Dmitriev et al., 2009). As a mathematical model in most of these works was used a simplified system of linear differential equations of heat conduction and kinetics without the mass transfer, which limited its use and accuracy of solutions. Strict theory of solutions of such problems are currently not, therefore, in these works have used the approximate methods.

Thus, one can conclude that if there is a large diversity of methods for selecting the curing cycles the majority of them were built on the basis of empirical approaches. In a small number of mathematical methods was used the simplified set of optimization problems, based on a simple linear mathematical models, without taking into account the many phenomena of the process, for example, currents of resin under the pressure, dependence of thermophysical properties on temperature, degree of curing and filling ratio (fraction factor). In addition, almost entirely absent in the tasks of optimizing the recording of pressure forming, determining its magnitude and duration of application.

The aim is to head the prospects of using the method for calculating the optimal curing cycles of large-scale products of polymer composite materials based on mathematical modeling and numerical search of the temperature-time cycle, ensuring the creation of high-quality finished product in the minimal possible time, with minimal power consumption, or with minimal residual stresses.

2. Mathematical model and identification of its parameters

In the mathematical description of any phenomenon or process, we solve two conflicting objectives. On the one hand it is necessary to obtain a simple model with a small number of parameters and we have research equipment for determine it. On the other hand the model should be adequate to the real process with acceptable accuracy. Use for this purpose of simple linear mathematical models without taking into account the many phenomena of the process, such as, for example, outflow the resin under the pressure, dependence of thermophysical properties on temperature, degree of cure and the filling factor leads to large modeling errors and uncertainty of the solutions.

Technologies for obtaining large-size thick-walled products have the greatest interest. Examples of such technologies include the hot pressing in mold, autoclave vacuum forming and winding on the mandrel (Balakirev et al., 1990). Products that produced by these technologies tend to have a flat shape or a small curvature, which allows to consider such products as the unlimited plate and to use one-dimensional mathematical model of the process, although there are no obstacles to the use of more complex models. A mathematical model for each technology has its own characteristics, but at the same time, a unified framework (Dmitriev & Shapovalov, 2001). Typically, a mathematical model of a hot curing of composites when regulating the temperature of the forming tooling $U(t)$ is a system of differential equations of heat and mass transfer, kinetics of curing, leaking (extrusion) of resin, compacting the material in the process of forming and rheological equations of state. As an example, the method of calculating the optimum curing cycles of composites for the thick-walled products or panels, produced by autoclave vacuum molding is considered. For the autoclave vacuum molding the dominant processes in the material are heat-mass transfer and curing. A mathematical model of the autoclave molding and curing of products made of thermosetting composites in multi-layer $i = 1, \dots, 5$ technology package, taking into account the outflow of resin is a system of differential equations of the following:

- heat-mass transfer:

$$C_i \left(\frac{\partial T}{\partial t} + \gamma_i w_{x_i} \frac{\partial T}{\partial x} \right) = \frac{\partial}{\partial x} \left(\lambda_i \frac{\partial T}{\partial x} \right) + \gamma_i Q_{f_i} \frac{\partial \beta_i}{\partial t}, \quad (1)$$

$$T \equiv T(x, t), \quad L_{i-1} \leq x < L_i, \quad L_0 = 0, \quad 0 < t \leq t_f, \quad i = 1, \dots, 5,$$

$$C_i \equiv C_i(T), \quad \lambda_i \equiv \lambda_i(T), \quad w_{x_i} = 0, \quad Q_{f_i} = 0, \quad L_i \equiv \text{const}, \quad \text{at } i = 1, 4, 5,$$

$$C_2 \equiv C_2(T, \beta_2, \gamma_2), \quad \lambda_2 \equiv \lambda_2(T, \beta_2, \gamma_2), \quad w_{x_2} \neq 0, \quad Q_{f_2} \neq 0, \quad L_1 \leq x < L_2(t), \quad i = 2,$$

$$C_3 \equiv C_3(T, \beta_3, \gamma_3), \quad \lambda_3 \equiv \lambda_3(T, \beta_3, \gamma_3), \quad w_{x_3} \neq 0, \quad Q_{f_3} \neq 0, \quad L_2(t) \leq x < l_{bl}(t), \quad i = 3,$$

$$C_3 \equiv C_3(T), \quad \lambda_3 \equiv \lambda_3(T), \quad w_{x_3} = 0, \quad Q_{f_3} = 0, \quad l_{bl}(t) \leq x < L_3, \quad i = 3,$$

$$\text{with boundary conditions:} \quad T(x, 0) = f(x), \quad 0 \leq x \leq L_5, \quad (2)$$

$$-\lambda_1 \frac{\partial T}{\partial x} \Big|_{x=0} = \alpha [T_a(t) - T(0, t)], \quad 0 < t \leq t_f, \quad (3)$$

$$-\lambda_5 \frac{\partial T}{\partial x} \Big|_{x=L_5} = \alpha [T_a(t) - T(L_5, t)], \quad 0 < t \leq t_f, \quad (4)$$

$$\lambda_i \frac{\partial T}{\partial x} \Big|_{x=L_i-0} = \lambda_{i+1} \frac{\partial T}{\partial x} \Big|_{x=L_i+0}, \quad 0 < t \leq t_f, \quad i=1, \dots, 4,$$

$$T(x, t) \Big|_{x=L_i-0} = T(x, t) \Big|_{x=L_i+0}, \quad 0 < t \leq t_f, \quad i=1, \dots, 4,$$

$$\text{control parameters} \quad U(t) = T(L_1, t) \quad \text{or} \quad U(t) = T_a(t),$$

- kinetics of cure

$$\frac{\partial \beta_i}{\partial t} = \begin{cases} \varphi_i(\beta) \exp[-E_i(\beta)/RT], & \beta < 1, \\ 0, & \beta = 1, \end{cases} \quad (5)$$

$$\beta_i \equiv \beta_i(x, t), \quad L_{i-1} \leq x < L_i, \quad 0 < t \leq t_f,$$

$$\beta_i(x, 0) = \beta_{0i}(x) \geq 0, \quad i=2, 3,$$

- outflow resin and compacting material

$$w_{x_2}(t) = \begin{cases} \frac{dL_{re}(t)}{dt}, & L_2(t) - \ell_{fl}(t) \leq x \leq L_2(t), \\ 0, & 0 < x < L_2(t) - \ell_{fl}(t), \end{cases} \quad (6)$$

$$w_{x_3}(t) = \begin{cases} \frac{d\ell_{re}(t)}{dt}, & L_2(t) \leq x \leq L_2(t) + \ell_{bl}(t), \\ 0, & L_2(t) + \ell_{bl}(t) < x < L_3, \end{cases} \quad (7)$$

$$L_2(t) = L_2(0) \frac{1 - \gamma_s}{1 - \gamma_f} + L_{re}(t), \quad L_2(0) = L_{pr.min} \frac{1 - \gamma_f}{1 - \gamma_s},$$

$$\frac{dL_{re}(t)}{dt} = - \frac{P_a + P_0 - \rho_{re} g \cdot [\ell_{fl}(t) + \ell_{bl}(t)]}{\frac{1}{k_{fl}} \int_{L_2(t) - \ell_{fl}(t)}^{L_2(t)} \mu(x, t) dx + \frac{1}{k_{bl}} \int_{L_2(t)}^{L_2(t) + \ell_{bl}(t)} \mu(x, t) dx}, \quad 0 < t \leq t_f, \quad (8)$$

$$L_{re}(0) = L_2(0) \frac{\gamma_s - \gamma_f}{1 - \gamma_f}, \quad (9)$$

$$\mu(x, t) = \tilde{\mu}(\beta) \exp\left(\frac{E_\mu}{RT}\right), \quad \gamma(t) = \frac{L_2(t) - L_2(0)(1 - \gamma_s)}{L_2(t)}, \quad (10)$$

$$\ell_{fl}(t) = \frac{L_2(0)(1 - \gamma_s)}{n} \left[1 + \frac{(n-1)(\gamma_s - \gamma(t))}{\gamma_s - \gamma_f} \right],$$

$$\ell_{bl}(t) = \frac{L_2(0)\gamma_s - L_{re}(t)}{\xi}, \quad \xi = V_{por}/V_{bl},$$

$$\gamma_s = \frac{\rho_{pr}(0) M_{re}(0)}{\rho_{re} M_{pr}(0)}, \quad \gamma_f = \frac{\rho_{pr.min} M_{re.min}}{\rho_{re} M_{pr.min}},$$

where C - volumetric heat capacity, $J/(m^3 \cdot K)$; E - activation energy of curing, J/mol ; E_μ - activation energy of viscous flow, J/mol ; f - initial distribution of temperature, K ; Q_f - full heat of the reaction, J/m^3 ; k - permeability, m^2 ; L - thickness of the product, m ; ℓ_{bl} - the depth of penetration of the resin in the bleeder, m ; ℓ_{fl} - the thickness of the tightly compressed layers of filler, m ; M - mass, kg ; n - number of layers of prepreg in the product; P_0, P_a - the pressure in the autoclave and vacuum bag, Pa ; R - universal gas constant, $J/(mol \cdot K)$; T - temperature, K ; T_a - the temperature of heating air, K ; t - time, s ; x - spatial coordinate, m ; V - volume, m^3 ; w - speed of the current resin, m/s ; α - heat-removing factor, $W/(m^2 \cdot K)$; β - the degree of curing; γ - the mass contents of the resin in the prepreg; φ - kinetic function, $1/s$; λ - thermal conductivity, $W/(m \cdot K)$; μ - dynamic viscosity of the resin, $Pa \cdot s$; ρ - density, kg/m^3 ; ξ - porosity bleeder;

indexes: re - resin; fl - fabric filler; bl - bleeder; pr - prepreg; s - start; f - final; a - the air.

Moreover, $x = 0$ corresponds to the lower surface of the metal tool plate, $x = L_5$ - corresponds to the upper surface of the airweave breather layer; $i=1, 2, \dots, 5$ - correspond to each layer of a technological package: $i = 1$ - metal tool plate, $i = 2$ - laminate prepreg, $i = 3$ - bleeder, $i = 4$ - perforated metal sheet, $i = 5$ - airweave breather layer.

In autoclave vacuum molding the temperature of heating air $T_a(t)$ or the temperature of the forming tooling $T(L_1, t)$ are control parameters $U(t)$.

The proposed model describes only the changes in the size of the composite products, which are caused by changes in the content of the resin. Shrinkage caused by changes of molecular structure of the resin during curing is not considered.

No	Model parameters	Designation
<i>Determined experimentally in the CMS</i>		
1	Volumetric heat capacity	$C(T, \beta, \gamma)$
2	Thermal conductivity	$\lambda(T, \beta, \gamma)$
3	Full heat of the reaction	Q_f
4	Activation energy of curing	$E(\beta)$
5	Kinetic function of curing	$\varphi(\beta)$
6	Activation energy of viscous flow	E_μ
7	Dynamic viscosity of the resin during cure	$\tilde{\mu}(\beta)$
8	Permeability of filler	k_{fl}
9	Permeability of bleeder	k_{bl}
<i>Determine additional</i>		
10	Porosity of bleeder	ξ
11	Thickness of the tightly compressed layers of filler	$L_{pr, min}$
12	Initial thickness of the product	L_o
13	Initial prepreg degree of curing	β_o
14	Initial mass contents of the resin in the prepreg	γ_s

Table 1. Determined experimentally parameters of the mathematical model

The forming often occurs without the outflow of resin from the prepreg in the technological package or in a closed mold by direct hot pressing. Then the mathematical model is simplified to two differential equations, this equation of heat conduction and kinetics. Accordingly, the number needed to identify the characteristics of the material decreases.

One of key parameters of the mathematical model of curing process are the characteristics of a material, both in the cured a state and in the uncured state, and also during curing. They are not constant, but are a function of temperature T , the degree of curing β , resin content γ or time t , which are subject to identification by experimental data (see table 1).

Typically, these parameters are determined from experiments using special techniques and devices. For their definitions are used: differential scanning calorimeter (DSC) for studying the thermal processes occurring in the prepreg on heating, thermomechanical analyzer (TMA), dynamic mechanical analyzer (DMA), thermal conductivity meters, etc.

However, currently available experimental devices and apparatus are intended primarily to study the properties of solid materials or cured composites or curing kinetics of the small size of samples in the absence of process pressure. Devices for the determination of rheological characteristics of thermosetting resins, typically built on traditional classical rheology and can measure the characteristics of the pure resin without the structural features of composite and production process (Kulichikhin & Astakhov, 1991). This restricts the use of standard methods and devices for studying the curing of composites, because they do not fully possible to determine all the parameters of a mathematical model of the curing process with all the relationships and features. Thus, to solve this problem it is necessary to use special methods and measuring devices that allow to determine the characteristics of composites in conditions close to conditions for the production of composites in the process. This path will allow more finely into account all the circumstances connected with the study of properties of composites and to obtain more precise parameters of the mathematical model.

Characteristics that are determined in conditions close to technological process are in some sense effective, that correspond to the peculiarities of the process and bear in itself factors and effects that not considered at the mathematical description and simulation. So promising are the methods and experimental devices that allow to study materials for the real designs using special samples and reproduce in the study of process conditions, that are process pressure, heating rate, peculiarities laying prepreg, study filled composite to replace the study of pure resin, etc. These requirements relate to the presence of interphase interactions occurring at the interface of resin-filler and influencing the kinetics of curing, as well as the influence of process pressure and laying on the thermal conductivity of the composite. An important condition for developing such devices, along with the ability to simulate technological modes of cure, is the ability to create special boundary conditions are necessary to simplify the algorithms for processing the experimental data and the desired accuracy of determine parameters.

Given the fact that the process of curing and polymer composites are highly information-intensive objects, their properties are often complicated functions, to solve the problem of determining the parameters of the mathematical model is necessary to use automation and computer equipment.

To determine the material characteristics and other parameters of the mathematical model we have developed a number of methods and the computer-measuring system (CMS) research of the curing of composites (Dmitriev et al., 2010). CMS allows to explore in the process of curing all the characteristics needed to solve the equations of the mathematical model of curing composites (1)-(10): thermophysical characteristics of composites $C(T, \beta, \gamma)$, $\lambda(T, \beta, \gamma)$ depending on the temperature T , the degree of curing β and resin content γ , the rate of evolved heat of cure reaction $W(t)$, full heat of the reaction Q_f , kinetic characteristics, that

are activation energy of curing $E(\beta)$, the kinetic function $\varphi(\beta)$, which includes the speed and order of chemical reactions, rheological characteristics, that are activation energy of viscous flow E_μ and effective viscosity of resin $\tilde{\mu}(\beta)$ in the curing. Permeability fiber filler k is determined by CMS in conjunction with the effective viscosity as a complex $\tilde{\mu}(\beta)/k$ and does not require additional study, but if necessary it can be determined with the help of special equipment. Other parameters of the material and products, such as the density ρ , the thickness of the product L , mass M , the number of layers of prepreg in the product n is determined by standard methods or set.

The research composites by CMS produced in the measuring cell in the range of temperatures from room to 270 °C.

The object of the experimental study is a specially prepared sample, which is a package thickness of 5...20 mm, assembled from several sections of the researched prepreps cut to a square with side 100 mm. Stacking layers of prepreps and orientation fiber of the sample performed similarly to industrial products: unidirectional, cross or cross-bias, etc. Samples of materials prepared on these conditions and their size allows to take into account in studied effective characteristics the rheological processes taking place during curing, the especial of stacking layers of prepreg in the product, to average a local inhomogeneity of the structure of materials and factor content of resin, which does not allow to perform other standard methods and devices, including scanning calorimetry method.

By means CMS in the measuring cell is organized the process of heating the studied sample, described by the (1) - (10), and measured over time following values: the time t , voltage of the heater $u(t)$, the temperature in the 2...5 points on the thickness of the sample $T(x,t)$, the thickness sample $L(t)$, the force pressing the sample $F(t)$, dielectric permittivity $\varepsilon(t)$ and dielectric losses $\tan\delta(t)$.

Research carried out for each sample in two phases: heating to cure and re-heating after cooling. During the first phase studied the kinetics of the cure, the flux of resin and the effective thermophysical characteristics of $C_w(t(T))$, $\lambda_w(t(T))$, including the rate of evolved heat of cure reaction $W(t)$. In the second phase studied the properties of cured material $C_{cd}(t(T))$, $\lambda_{cd}(t(T))$. On the basis of these data are calculated $C(T,\beta,\gamma)$ and $\lambda(T,\beta,\gamma)$. To research the kinetic and rheological characteristics conducted experiments on the cure at least for two samples with different rates of heating. The conditions of the experiment, ie voltage of core heater u , which determines the heating rate and the force F on the sample, are chosen to reproduce the technology modes and to ensure the minimum error of the desired characteristics. Dielectric characteristics of $\varepsilon(t)$ and $\tan\delta(t)$ are needed to determine the moment of pressure application and the completion of curing.

In the experiment CMS performs the primary processing of data and recording it to the hard disk, as well as testing and monitoring of the system. At the end of the experiment is performed calculations researched characteristics.

As a method of determining the thermophysical characteristics of $C(T,\beta,\gamma)$, $\lambda(T,\beta,\gamma)$ used the method of integral characteristics (Dmitriev et al., 2010). Kinetic characteristics of $E(\beta)$ and $\varphi(\beta)$ that are part of the equation of kinetics are determined by the rate of evolved heat of cure reaction $W(t)$, measured in the curing of two or more samples heated at different temperature-time modes $T_{av}(t)$. By measuring the thickness $L(t)$ of curing sample at squeezing-out of resin are determined the rheological characteristics E_μ and $\tilde{\mu}(\beta)$.

Calculated formulas and algorithms for processing of the experimental data obtained on the basis of established methods are the core software of CMS. Researched characteristics of composites and other parameters of the mathematical model are entered into a database of CMS and are the information basis for the automated calculation of the optimal curing cycles of the composite products for any thickness and configuration.

The results of experimental studies of the curing process and subsequent heating of the samples made of fiberglass plastic, as well as calculations of its characteristics are presented in Fig. 1-3.

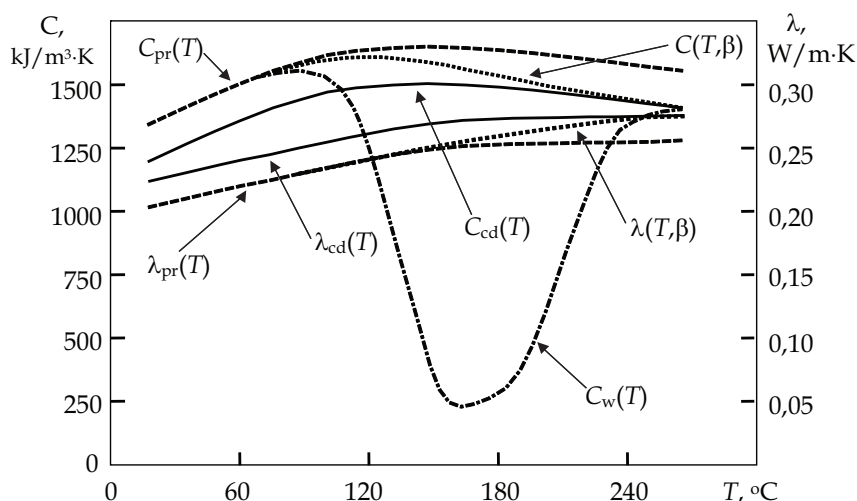


Fig. 1. Thermophysical characteristics of fiberglass plastic at $\gamma_s=0,51$

The initial part of effective thermophysical characteristics $C_w(T)$, $\lambda_w(T)$ (Fig. 1) before the beginning of intensive curing reaction characterizes thermophysical characteristics uncured prepreg $C_{pr}(T)$, $\lambda_{pr}(T)$. The beginning of intensive curing reaction (on the figure is 110...120 °C) corresponds to a rapid decrease in the effective volume heat capacity $C_w(T)$, because it includes the rate of evolved heat of cure reaction $W(t)$ and it is in this part of the effective exothermic heat capacity. Effective thermophysical characteristics $C_w(T)$, $\lambda_w(T)$ in the final stage of the experiment at a high degree of curing β merge with thermophysical characteristics cured material $C_{cd}(T)$, $\lambda_{cd}(T)$, which corresponds to the transition of composite in the cured state. As seen from Fig. 1 the dependence of thermophysical characteristics of cured composite $C_{cd}(T)$, $\lambda_{cd}(T)$ and uncured prepreg $C_{pr}(T)$, $\lambda_{pr}(T)$ are equidistant curves. This allows the difference between the thermophysical characteristics cured composite and uncured prepreg ΔC and $\Delta \lambda$ at the time of the beginning of the curing reaction, used for the calculation of thermophysical characteristics in the process of curing $C(T, \beta)$, $\lambda(T, \beta)$. They are determined by thermophysical characteristics prepreg $C_{pr}(T)$, $\lambda_{pr}(T)$ in the range from room temperature to the temperature of the beginning of the curing reaction, and above the temperature of the beginning of the curing reaction are determined by $C_{cd}(T)$, $\lambda_{cd}(T)$ and ΔC , $\Delta \lambda$.

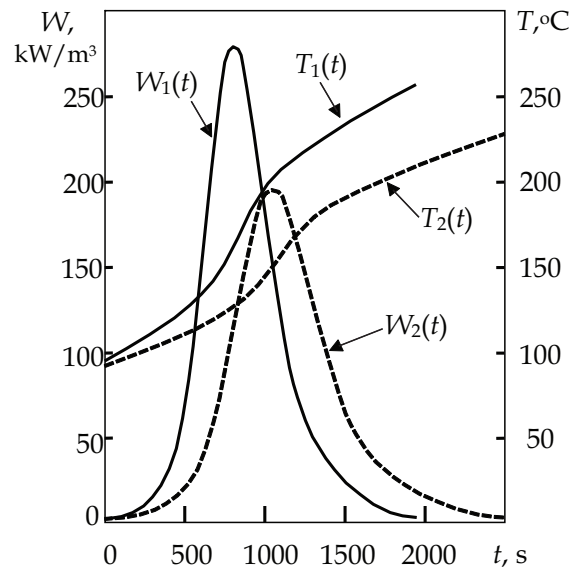


Fig. 2. Evolved heat of cure reaction of fiberglass plastic

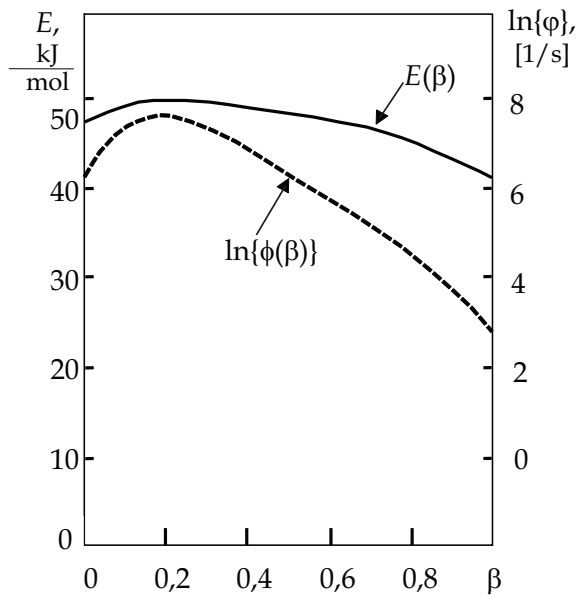


Fig. 3. Kinetic characteristics of fiberglass plastic

The rate of evolved heat of cure reaction $W(t)$ (Fig. 2) has a pronounced extremum, corresponding to the transition from a liquid resin to the viscous-flow state (gel point). With the increase in the rate of heating the extreme of evolved heat of cure reaction $W(t)$ shifts toward higher temperatures. At the same time, the duration of heat generation and gelation time with increasing heating rate decreases. The area under the curve of the rate of evolved heat of cure reaction $W(t)$ characterizes the full heat of the reaction Q_f of curing reaction of the resin, and the ratio of the thermal effect Q to the full thermal effect of Q_f corresponds to the degree of completeness of the process of curing or calorimetric degree of curing β .

Kinetic characteristics $E(\beta)$ and $\phi(\beta)$ (Fig. 3) of the curing process are calculated from the rate of evolved heat of cure reaction $W(t)$, at least of two temperature–time cycles. Rheological characteristics E_μ and $\tilde{\mu}(\beta)$ are calculated by the change in the thickness of the samples $L(t)$ under flowing out of the resin under pressure during curing.

Thermophysical, kinetic, rheological and dielectric characteristics of composites obtained in the experiment will be automatically recorded in the database of CMS. The dielectric characteristics $\varepsilon(t)$ and $\tan\delta(t)$ is then used to calculate the correlation dependence or the function of relationship $\Psi(\beta)$ between the calorimetric and dielectric degree of cure, which is necessary for control of the manufacturing product process of composites in real time by controlling the degree of cure as well as to determine when to activate the pressure and completion of curing process (Dmitriev et al., 2010). The obtained parameters of the mathematical models are the basis for computer simulations of different situations in the curing process and calculate the optimal curing cycles of composite products of any thickness.

3. Numerical analysis of curing cycles

Using the once studied properties of the composite, the software of CMS allows multiple to simulate the curing process on the computer under different conditions, thus calculate the temperature-conversion field during curing of composite, as well as represent them in the form of graphs and 3D surfaces, thereby, to analyze the uneven curing of the material for the manufacture, quickly assess the advantages and disadvantages of the used curing cycle for the material and choose the right strategy to optimize the cycle.

Similar numerical studies were performed on a computer for fiberglass plastic and made a numerical analysis of the existing standard cure cycles, designed for the production of plates with thickness up to 10 mm, we evaluated their suitability for the production of thicker plates, for example 30 mm thick, and we calculated the optimal curing cycles. The temperature-conversion field, ie the temperature at the surface of the plate T_0 and in the middle $T_{L/2}$, respectively, the degree of curing β , the rate of evolved heat of cure reaction W and the maximum module temperature gradient G on the thickness L in the process of curing fiberglass plastic on the two-step cycle thickness $L = 10$ and 30 mm are shown in Fig. 4-5.

Based on the analysis of numerical calculations of temperature-conversion fields (Fig. 4-5) can do the following conclusions:

1. In general, the standard cycle is suitable for the manufacture of plates with thickness up to 10 mm. Here there are small temperature gradients G , and drops in temperature $T_0 - T_{L/2} = \Delta T$, that is overheating of the inner layers due to the exothermic effect.

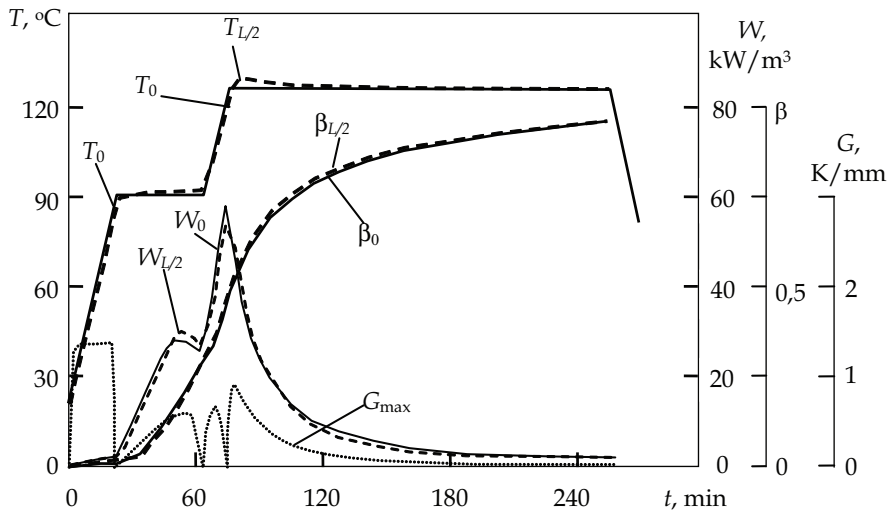


Fig. 4. Standard temperature cycle used for curing fiberglass plastic thickness $L = 10$ mm

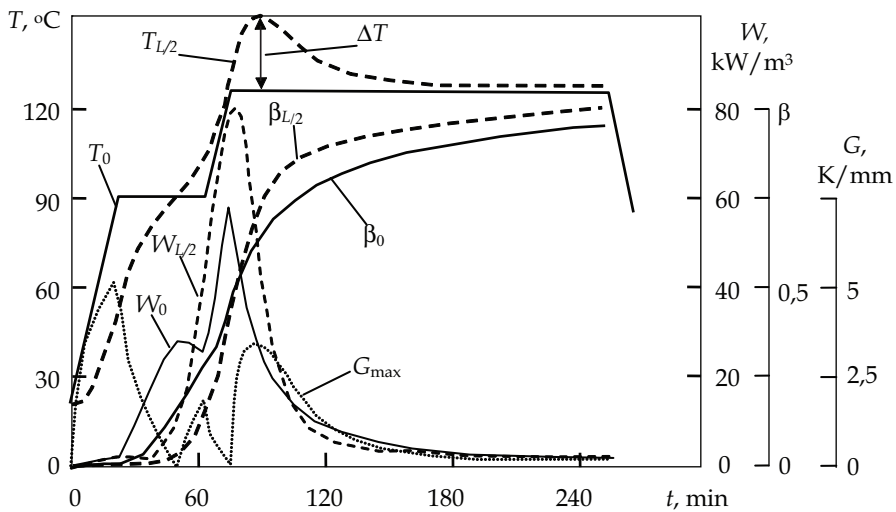


Fig. 5. Standard temperature cycle used for curing fiberglass plastic thickness $L = 30$ mm

- When curing the material thickness $L = 30$ mm at the standard cycle in the first step the temperature drops are $\Delta T_1 = 12,0$ K, the temperature gradients are $G_1 = 1,52$ K/mm, in the second step, when there is formation of the structure of the material the maximum overheating ΔT_2 and the maximum module temperature gradient G_2 reach respectively $\Delta T_2 = 25,1$ K, $G_2 = 2,59$ K/mm. With such a temperature drop over the thickness and overheating of the inner layers of the material begin to occur the destruction processes of the resin, increasing the porosity of the composite, residual stresses accumulate. All

this causes a decrease in the strength properties of the material, and in the manufacture of large-sized products appears to warping. Also, be aware that the large structures made of composite materials, such as elements of the wing, tail and fuselage are structures with different thickness, so the flow of polymerization processes in these zones of the composite are significantly different. In this case, the molding cycle should be chosen so as to obtain the necessary strength characteristics in most of the large area of intense construction.

These results demonstrate that the use of temperature-time curing cycle, as defined in laboratory conditions and is recommended for thin samples can not be used in the curing product of a thickness exceeding 10 mm. In these cases, to obtain high quality products require regular technical correction cycle, or its optimization.

4. Optimization of the curing cycles of composites

Solution of the optimization task of the curing process of composite products is as follows: necessary to find the temperature-time cycle U , which is a control parameter

$$U(t;t_f), U(t;Q^*), U(t;\sigma) = \{T_0(t), T_L(t)\}, \quad j = 1, 2, \dots, k_{st}, \quad (11)$$

that delivers minimum for one of the optimality criteria I and provides a high quality finished product:

- with a minimum possible duration of curing t_f :

$$I_{t_f} = \min_{U(t;t_f)} \int_0^{t_f} d\tau, \quad (12)$$

- with minimal power consumption Q^* :

$$I_{Q^*} = \min_{U(t;Q^*)} \int_0^{t_f} T_a(\tau) d\tau, \quad (13)$$

- or with minimal residual stresses σ :

$$I_\sigma = \min_{U(t;\sigma)} \int_0^L \left(\int_{\beta_s}^{\beta_f} p(\beta) \frac{\partial T(x, t(\beta))}{\partial x} d\beta \right)^2 dx, \quad (14)$$

in solving the equations of the mathematical model (1)-(10) or mathematical models (Wu & Joseph, 1990), (Dmitriev & Shapovalov, 2001), corresponding to the current technique of forming products

$$\Re(C, \lambda, Q_f, E_\beta, \varphi, E_\mu, \tilde{\mu}, P, \rho, k, n) = 0, \quad j = 1, 2, \dots, k_{st}, \quad (15)$$

as well as restrictions in the form of inequalities imposed on process

$$\max_{\substack{0 \leq x \leq L \\ t_0 < t \leq t_f}} T(x, t) \leq T_{\max}, \quad \max_{\substack{0 \leq x \leq L \\ t_0 \leq t \leq t_f}} \left| \frac{\partial T}{\partial x} \right| \leq \bar{\chi}, \quad \max_{t_0 \leq t \leq t_f} \left\{ \max_{0 \leq x \leq L} T(x, t) - \min_{0 \leq x \leq L} T(x, t) \right\} \leq \bar{\theta}, \quad (16)$$

taking into account the allowable for equipment temperature-time cycles

$$U_{j_{\min}}(t) \leq U_j(t) \leq U_{j_{\max}}(t), \quad j = 1, 2, \dots, k_{st}, \quad (17)$$

where $p(\beta)$ – weighting function that determines the dependence of residual stresses σ of the temperature gradient (chosen empirically); T_a – working temperature autoclave, K; T_{\max} – maximum allowable temperature inside the material during the curing product, K; $\bar{\chi}$ – maximum allowable temperature gradient during curing that does not cause the accumulation of domestic stresses the material, K/m; $\bar{\theta}$ – the maximum allowable temperature difference on the thickness of the product that does not cause the heterogeneity of the curing material, °C; $U_{j_{\max}}(t)$, $U_{j_{\min}}(t)$ – upper and lower limits of rate of heating the surface of the product at the j -th step, defined on the basis of the appropriateness of reference of the curing process, favorable conditions for the formation of curing resin structure and parameters of equipment.

Seeking a temperature-time cycle is calculated as

$$U_j(t) = \begin{cases} \tilde{T}_{j-1} + \tilde{K}_j t, & t_{j-1} < t < t_{n_j} \\ \tilde{T}_j, & t_{n_j} \leq t \leq t_j \end{cases}, \quad j = 1, 2, \dots, k_{st}, \quad (18)$$

where \tilde{K} – heating rate of surface product, K/s; k_{st} – number of steps heating; \tilde{T} – temperature of isothermal hold on the j -th step of heating, K; t_{n_j} – moment of transition from the stage of linear heating to the isothermal hold \tilde{T} , s.

A condition for the finish of the j -th step of heating and the transition to a $j+1$ step are:

$$\max_{\substack{0 \leq x \leq L \\ t_{j-1} < t < t_j}} \frac{\partial \beta_j}{\partial t} - \max_{0 \leq x \leq L} \frac{\partial \beta_j}{\partial t} \geq \eta_j, \quad \max_{\substack{0 \leq x \leq L \\ t_{j-1} < t < t_j}} T_j(x, t) - \max_{0 \leq x \leq L} T_j(x, t) \geq \vartheta_j, \quad j = 1, 2, \dots, k_{st}. \quad (19)$$

A condition for the finish of solving the problem (11)-(19) is to achieve a given degree of cure of β_f throughout the thickness of the product:

$$\min_{\substack{0 \leq x \leq L \\ t_0 < t < t_f}} \beta(x, t) \geq \beta_f. \quad (20)$$

Conditions (19) associated with the requirement of intensive curing process, so if the speed of curing decreased on the value of η_j and maximum temperature on the thickness of the product reduced on the value of ϑ_j , then execute the transition to $j+1$ step of heating and isothermal hold. Compliance with (20) guarantees the attainment by all points of the product specified value degree of finality to the process of curing β_f .

The main criterion for the quality of the finished product is its solidity, the lack of delaminating and buckling. Developing common criteria for monolithic reinforced composites is associated with large experimental difficulties and the lack of reliable experimental data on the study of strength and deformation properties of composites at elevated temperatures, especially in the curing process. Usually the monolithic criterion is given in the form of an inequality, which limits the residual and thermal stresses within the

transverse compressive strength and stretching. However, such an assignment criterion of quality products also requires a simulation of the stress-strain state of curing composite and, hence, the definition of a large number of temperature - and conversion - dependent anisotropic mechanical properties such as modules of the elastic, Poisson's coefficients, modules of shear, coefficients of thermal expansion, etc. Therefore, the criterion of the quality of the finished product useful to associate with a temperature-conversion parameters of cure and values of the restrictions (16), which define the relationship with the mechanical properties of the composite, to determine experimentally.

From an examination of the physical essence of the physico-chemical transformations implies that the curing process should be limited to a maximum temperature T_{\max} , which are beginning to take place in connection undesirable side reactions associated with the destruction of resin, resulting in deteriorating the mechanical properties of cured products. This temperature is determined by the chemical composition of resin and this T_{\max} has a certain value for each resin.

In the curing process is usually part of the evolved exothermic reaction heat is transferred into the environment, so when curing product in it there is a temperature gradient in the direction of the cooling surface. The appearance of the temperature-conversion irregularities in the product leads to residual stresses that exceed the limit of long-term strength of the material, resulting in possible cracks, delaminating and violation of a monolithic product. For practical purposes, a comprehensive description of the inhomogeneity of the temperature-conversion field is a temperature gradient, which is directly related to the gradient of the degree of completion of the curing process.

Effects of temperature gradients in the physical and mechanical properties that arise in the curing on the thickness of the material studied with the help of special experiments, consisting in testing the mechanical properties of thin samples cured in the CMS in the context of an artificially-created temperature gradients. Setting limits damaging stresses in the bending was set temperature gradient $\bar{\chi}$, which for fiberglass and carbon are in the 0,2-1 K/mm.

In the curing of thick-walled products, one of the most undesirable modes is the curing in conditions of the front exothermic reaction because it is the most favorable conditions for the formation of residual stresses. To prevent the spread of the reaction front with the optimization process of cure can be limiting the maximum temperature difference on the thickness of the product. In addition, the large difference of temperatures on the thickness of the product contribute to the formation of various structures on the segments of the material and increase the residual stress. Limit values for the temperature difference on the thickness of products $\bar{\theta}$ for fiberglass plastics and carbon plastics derived from the testing of mechanical properties specially cured specimen is $5 \sim 8^{\circ} \text{C}$.

The choice of optimality criterion is the most subtle and responsible step in solving the problem of optimization. Based on the needs of the production of large thick-walled products made of thermosetting polymer composites, there are three main areas in the selection objective. The first - the creation of the finished products meet certain quality criteria for the minimum possible time. The second trend - the creation of high-quality finished product with minimal power consumption. Finally, the third area concerns the creation of structures products free of residual stresses, or with minimal residual stresses in a balanced state. Depending on the purposes of this decision is selected the corresponding optimality criterion (12), (13) or (14). If necessary, can be solved also the multi-criteria task of search for optimal curing cycle.

From the chemical and technological considerations the most reasonable are step curing cycles. Therefore, we can assume that in our case, the kind of a required temperature-time cycle (18) is already set, it is necessary to find only optimum speeds of heating of a product surfaces \tilde{K}_j on everyone $j=1,2,\dots,k$ steps, the temperature of isothermal holds \tilde{T}_j , their durations t_j and the number of steps heating k_{st} . As a result of solution of the optimization problem defines the optimal boundary temperature-time cycles of the curing product of composites, in which the curing time t_f or energy Q^* or the residual stress σ will be minimal. Meeting the challenge of finding the best treatment based on an incremental optimization of each of the j -th step of heating. For the optimization of the curing cycles of composite material products promising to use the penalty function method in conjunction with the algorithm of sequential quadratic programming, which is the core system software. On the basis of studying the characteristics of fiberglass plastic by the developed CMS, we calculated the optimal curing cycles flat products of thickness 10 and 30 mm. The calculated optimal curing cycles plates shown in Fig. 6-7, and Table. 2.

The calculations of the optimal curing cycles performed with the following restrictions: in the first step of heating the allowable on thickness the temperature gradient is $G = 1$ K/mm and permissible overheating of the inner layers of $\Delta T = 8^\circ\text{C}$, in the second and third steps of heating allowable the temperature gradient is $G = 0,4$ K/mm and the permissible overheating of the inner layers of $\Delta T = 5^\circ\text{C}$ (see Fig. 6-7 and Table 2). Increased temperature gradient in the first step of heating caused by reason of reducing the duration of the first hold, because degree of cure is not reached the point of gelation and the unevenness of the temperature-conversion field does not affect the accumulation of residual stresses.

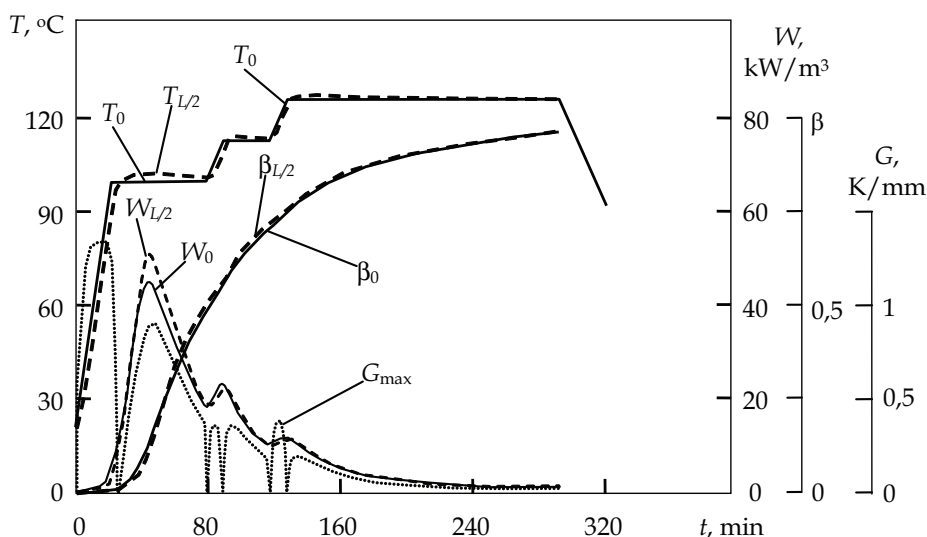


Fig. 6. Optimal temperature cycle of curing fiberglass plastic thickness $L = 10$ mm

Often to removing the solvent, which is present in the resin, in the first step operates a low-temperature hold at $80\ldots 90^\circ\text{C}$. In this case, if the temperature is calculated by the

optimization exceeds the specified value, then the temperature of the first hold is not selected, but rigidly defined, and its minimum duration is determined by the time required for evaporation of the solvent.

As a result of calculations, the obtained curing cycles differ from the standard cycle of smaller drops in temperature over the thickness, much smaller temperature gradients and gradual increase in the degree of curing.

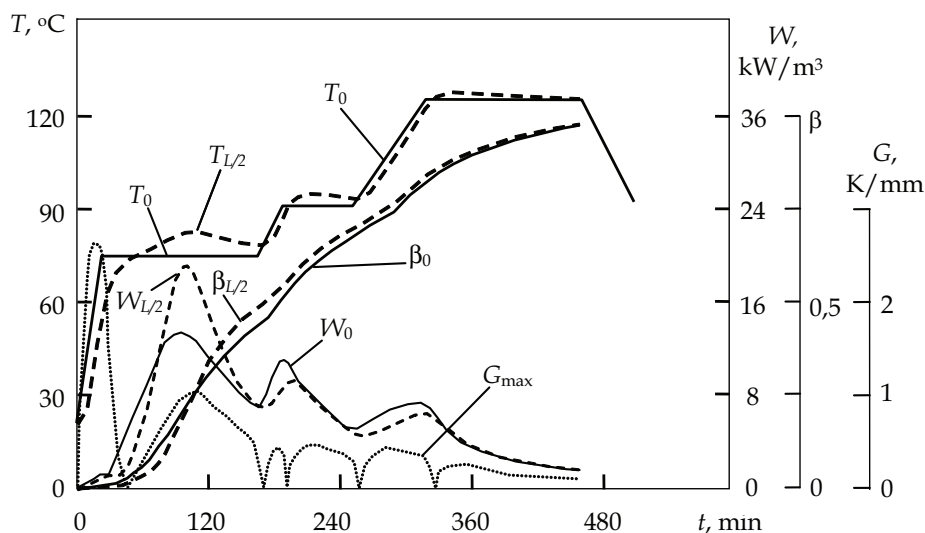


Fig. 7. Optimal temperature cycle of curing fiberglass plastic thickness $L = 30$ mm

Thickness of the product L , mm	Step heating j	Curing cycle parameters						
		Rate of heating \tilde{K}_j , K/min	Heating time t_{js} , min	Curing temperature \tilde{T}_j , °C	Curing time t_{jh} , min	Duration of curing t_j , min	Max. gradient G , K/mm	Max. overheating ΔT , K
10	1	3,0	36,7	100,0	44,5		0,9	2,4
	2	1,7	7,1	112,3	29,1	292	0,4	1
	3	1,3	9,7	125,0	180,3		0,3	0,5
30	1	2,4	22,5	74,1	144,0		1,0	7,8
	2	0,8	21,7	90,5	66,8	460	0,4	3,4
	3	0,5	66,1	125,0	106,4		0,3	2,0

Table 2. Optimal temperature cycles of curing fiberglass plastic

For comparison, Fig. 8 shows the existing standard cycle for $L = 5$ mm, and calculated the optimal cycles for $L = 10, 20, 30$ and 40 mm. As can be seen from the graphs (Fig. 6-8), at the increase in thickness of the product duration of curing process significantly increases and the temperature of the first and subsequent isothermal holding markedly decreased, while the evolved heat of cure reaction in the early stages of the process also reduced. This reduces the heterogeneity of the temperature and conversion fields to the specified levels $\bar{\chi}$, $\bar{\theta}$ and leads to qualitative improvements of products. Due to reduction of the isothermal holding temperature levels and increase their duration reduced the intensity of the process, and the total duration of isothermal holding for thick-walled products increases. With increasing thickness of the product increases the number of steps heating k_{st} , which is associated with the desire of optimization algorithm to intensify the curing process while satisfying the restrictions (16). These curing cycles are optimal in terms of strength characteristics and minimal residual stress, ensure high quality and low cost products due to the minimum duration and power consumption. They had no sudden changes in temperature and degree of cure in thickness, which contributes to the formation of relaxed homogeneous structure of the composite.

Similar properties have been studied and calculated the optimal curing cycles flat products in thicknesses from 5 to 50 mm made of several types of materials such as fiberglass plastics, organic plastics, carbon fiber reinforced plastics and rubbers. As an example, Fig. 9 also shows the temperature-time cycles of curing carbon fiber reinforced plastic thickness to 30 mm.

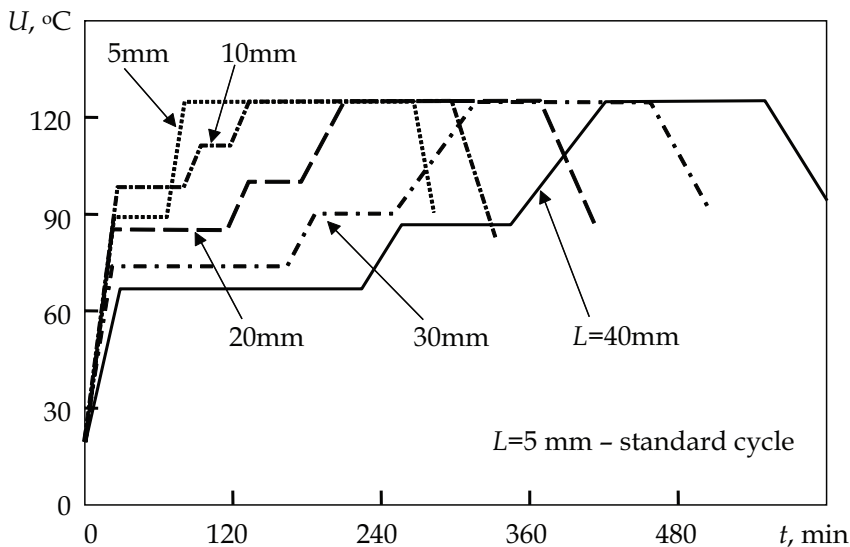


Fig. 8. Optimal cure cycles of flat products of various thickness L of fiberglass plastic

The criterion for the end of the curing process is to achieve of dielectric permittivity to ended maximum allowable values and stabilize the dielectric loss.

The analysis and comparison of the calculated curing cycles flat products made of composites with existing cycles designed for thin products demonstrated the feasibility of

widespread use of the method of mathematical modeling and optimization for testing of existing and calculation of the curing cycles of new composite materials, as well as the further development of the method.

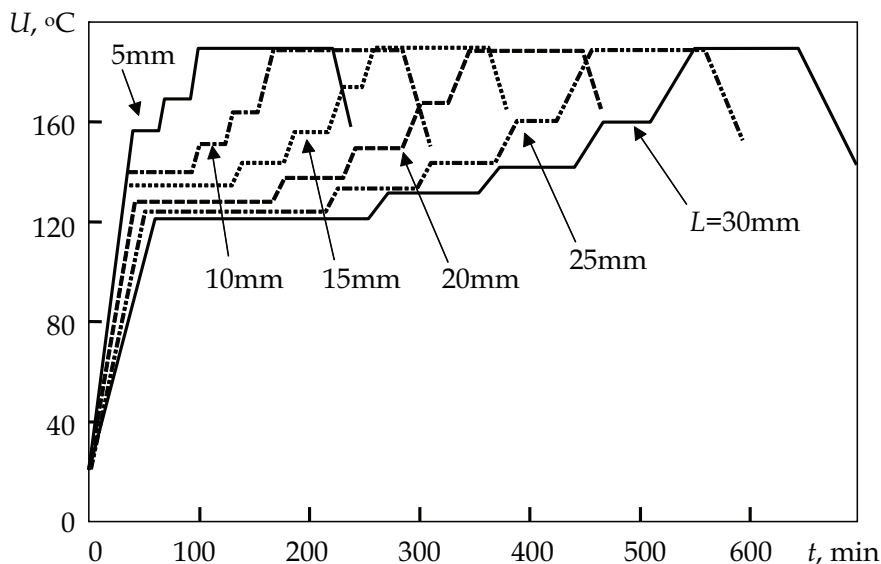


Fig. 9. Optimal cure cycles of flat products of various thickness L of carbon plastic

5. Conclusion

Presented an example of determining the optimal curing cycles of plates of different thickness of the composites based on thermosetting resins demonstrates the need to implement in practice when determining the curing cycles of the method of mathematical simulation and optimization. The method allows to repeatedly under different conditions to simulate the curing process on the computer, that is calculate the temperature-conversion field during curing of composites, as well as represent them in the form of graphs and 3D surfaces, thereby analyze uneven curing and quickly assess the advantages and disadvantages of the curing cycle for the material and choose the correct strategy for optimizing the production cycle, thus obtain high quality finished products with minimal energy consumption, or with minimal residual stresses.

6. References

- Afanasyev, Y.A. (1985) The criterion of optimization in optimal control of technological processes of heat treatment of products made of composite polymer materials. *Mekhanika kompozitnykh materialov*, No. 6 (December 1985) pp. 1066-1073
- Aleksashin, V.M. & Antyufeyev, N.V. (2005) Application of thermal analysis to research the adhesive compositions. *Klei. Germetiki. Tekhnologii*, No. 12 (December 2005) pp. 28-31

- Balakirev, V. S., et al. (1990). *Automated Production of Composite Material Items*, Khimiya, Moscow
- Botelho, E.C., Rezende, M.C. & Scherbakoff, N. (2001) Rheological Studies Applied in the Processing and Characterization of Carbon/Carbon Composites. *Journal of Composite Materials*, Vol. 4, (2001) pp. 359-369.
- Dedyukhin, V.G. & Stavrov, V.P. (1976) *Pressed fiberglass plastics*, Khimiya, Moscow
- Dmitriev, O.S. & Shapovalov, A.V. (2001) Mathematical modeling of curing products of polymer composite materials in an autoclave by vacuum forming in a multilayered technological package, *Proc. of the Intern. Conf. on Theory and Practice of Technology of Article Production from Composite Materials and New Metal Alloys, 21 Century*, pp. 568-574, Russia, January, 2001, MSU, Moscow
- Dmitriev, O.S., Kirillov, V.N., Mischenko, S.V. & Dmitriev, S.O. (2009) Optimization of Curing Cycles Products of the Polymer Composite Materials on Base of Glutinous Prepregs. *Polymer Science, Series D. Glues and Sealing Materials*, Vol. 2, No. 4, (2009) pp. 223-229, ISSN 1995-4212
- Dmitriev, O.S., Kirillov, V.N., Mischenko, S.V. & Dmitriev, A.O. (2010) Computer-Measuring System for Research into Properties of Glutinous Prepregs and Calculation of Curing Cycles of the Polymer Composite Materials on Their Base. *Polymer Science, Series D. Glues and Sealing Materials*, Vol. 3, No. 1, (2010) pp. 20-25, ISSN 1995_4212
- Frank, D., Laananen, D., Bogucki, G. et al (1991) Cure Optimization for Thin-Skinned Sandwich Structures, *Proceedings of 36th International SAMPE Symposium*, Vol. 36, pp. 999-1013, April, 1991, SAMPE
- Kulichikhin, S.G. & Astakhov, P.A. (1991) Optimization of forming cycles of fiberglass plastics based reokinetics analysis. *Plast. mass.*, No. 11, (November 1991) pp. 36-38
- Rosenberg, B.A. & Enikolopyan, N.S. (1978) Problems of technological monolithic products of composite materials. *Zhurn. Vsesoyuz. khim. obschestva*, Vol. 23, No. 3, (March 1978) pp. 298-304
- Stern, W.E. (1992) A Practical Method for the Cure Cycle Optimization of Epoxy Resins Via Differential Scanning Calorimetry, *Proceedings of 37th International SAMPE Symposium*, Vol. 37, pp. 231-239, March, 1992, SAMPE
- Wu, H.T. & Joseph, B. (1990). Knowledge Based Control of Autoclave Curing of Composites. *SAMPE Journal*, Vol. 26, No. 6, (June 1990) pp. 39-54

Development of 3D Knitted Fabrics for Advanced Composite Materials

Luminita Ciobanu, Ph.D., Eng.
 „Gheorghe Asachi” Technical University of Iasi
 Romania

1. Introduction

Generally, a composite material is made of distinct materials, that together act in a different way than when considered separately. There are a lot of examples of composite materials, both natural and synthetic, from the human body, to buildings, airplanes and so on.

Most comprehensive definition of the composite materials that characterises their nature is given by P. Mallick. According to Mallick (1997), a composite is a combination of two or more chemically different materials, with an interface between them. The constituent materials maintain their identity in the composite material (at least at macroscopic level), but their combination gives the system properties and characteristics different from those of each component. One material is called matrix and is defined as the continuous phase. The other element is called reinforcement and is added to the matrix in order to improve or modify its properties. The reinforcement represents the discontinuous phase, distributed evenly in the matrix volume.

There are several options for reinforcement and matrix, as illustrated in Fig.1, that are taken into consideration based on the mechanical requirements specific to the application.

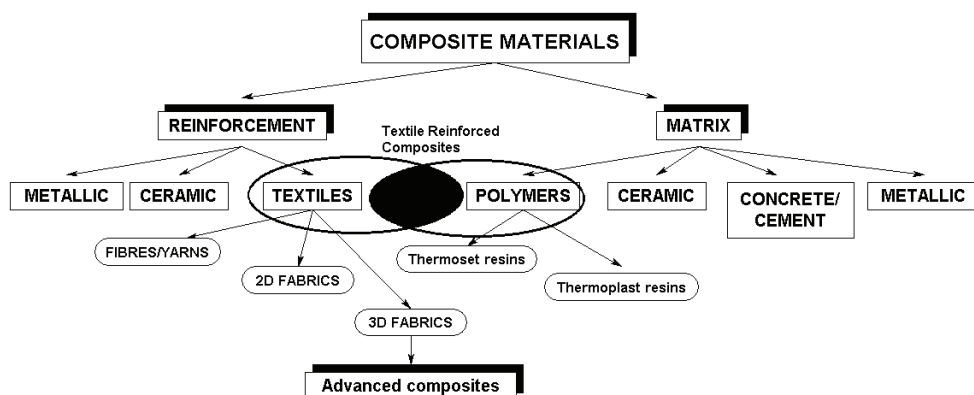


Fig. 1. Structure of composite materials

The development of textile reinforced composites (TRCs) with resin matrix is based on the desire to produce improved materials, with tailored properties. The textile material gives the

ensemble strength, while the matrix ensures the composite unity and transmits the strains. The advantages of the textile reinforced composites are:

- controlled anisotropy of the textiles which means that their structure materials can be designed so that the fibres are placed on preferential directions, according to the maximum strain;
- the use of textile reinforcements allows to obtain a better weigh/strength ratio compared with the classic materials, such as steel;
- textile materials maintain their integrity and behaviour under extreme conditions – for example, they do not corrode in an outdoor environment, nor vary their dimensions when there are significant temperature variations, nor are they sensible to electro-magnetic fields;
- TRCs present an improved fatigue life.

The aeronautic industry was the first that used TRCs for airplanes. Currently, there is a high diversity of TRCs applications, with high economic impact (Mouritz, 1999). Composite materials can be found in all fields of technical textiles. Industrial applications of the composites include tanks, storage structures, pipes, hoses, etc. The automotive industry uses TRCs for car frames and other machine parts (manifold, wheels), while in aeronautics the composites developed from 1st level applications to 2nd level that refers to resistance elements in an airplane structure and the future trend is building one exclusively with composites. The composite materials also replaced traditional ones for the rotor blades of helicopters, increasing their life span and their resistance to wear (Mallick, 1997). One field of great interest for textile reinforced composites is the wind energy management – these materials are used to build wind mills. The TRCs are also used to produce sport equipment – tennis rackets, bicycles and motorcycles, etc.

An interesting application is in buildings, where composites (the so called Textile Reinforced Concrete) are used to reinforce walls (cement/concrete matrix), increasing their strength and reducing their thickness and subsequently production costs.

Classification of textile reinforced composites

Two main criteria can be used to characterise the textile reinforcements: the material structure/geometry and the technological process (Hu, 2008).

Fukuta et al. (1984) gives a classification of the textile reinforcement based on the significant dimensions of the textile material and its specific geometry. Fukuta considers not only the 3 dimensions, but also the preset fibres directions used in the material structure.

According to Scardino (1989), the textile reinforcements can be divided into 4 groups, depending on their architecture: discrete, continuous, with plane geometry and with spatial geometry, as illustrated in Table 1.

When considering the technological process, all textile processes can be used to produce reinforcement for composite materials, but the specifics of each type of process and the resultant material geometry lead to differences in possibilities and behaviour. The main processes employed in the production of textile reinforcements are: weaving, braiding, knitting and non-woven. Also there are other processes, such as filament winding and poltrusion, which process filaments. Most used reinforcements are woven fabrics (2D and 3D) and nonwovens (fibre mats), but the knitted fabrics, especially warp knitted structures, present a good development potential.

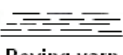


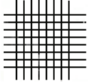
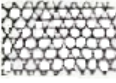
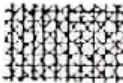





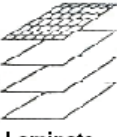

Axis Dimens.		0 Monoaxial	1 Nonaxial	2 Biaxial	3 Triaxial	4 Multiaxial
1D			 Roving yarn			
2D		 Chopped strand mat	 Preimpregnation sheet	 Plain weave	 Triaxial weave	 Multiaxial
3D	Linear element	 3D solid braiding	 Multiply weave	 Triaxial 3D weave	 Multiaxial 3D weave	
	Plane element	 Laminate	 Beams	 Honeycomb		

Fig. 2. Textile reinforcement systems, classification according to Fukuta et al.

Level	Reinforcement	Textile construction	Fibre length	Fibre orientation	Fibre entanglement
I	Discreet	Short fibres	Discontinuous	Uncontrolled	none
II	Linear	Filaments	Continuous	Linear	none
III	Plane	2D materials	Continuous	Planar	Planar
IV	Integrated	Advanced materials	Continuous	3D	3D

Table 1. Constructive classification of the textile reinforcements

The selection of a certain process is based on the architectural possibilities, the material characteristics and behaviour (dimensional stability, mechanic strength, drape and formability, etc) and its suitability with regard to the composite processing and its application.

Potential of knitted fabrics for composite reinforcement

The main advantages of knitted fabrics for composite reinforcement are:

- the possibility of producing knitted fabrics with 3D complex shapes
- improvement of fabric handling and matrix injection during composite processing
- acceptable processability of high performance fibres (glass, aramid, PES HT or HM)
- rapid manufacturing of knitted fabrics for reinforcements
- controlled anisotropy (yarn in-laid under preferential angles).

When considered in reference to other types of textile materials, knitted fabrics are not as well developed, mainly due to their lower mechanical properties (Leong et al., 2000). According to Verpoest et al. (1997), knitted fabrics present lower in-plane strength and stiffness in comparison to materials such as woven, braiding, non-crimps. Another problem limiting the use of knitted fabrics for composite reinforcement is the low value for volume fraction, due to the specific geometry of knitted stitches, characterised by areas without yarns.

The reduced mechanical behaviour is determined by the specific bending of fibres in the knitted stitches. Mechanical properties are controlled through fabric structure, structural parameters, yarn characteristics and process parameters. Structure is an effective way of improving properties by the use of float stitches and in-laid straight yarns placed under certain angles. Stitch density also affects the tensile behaviour and fabric stiffness,

Yarns are also important, their properties being transferred to the fabric level. The specifics of the knitting process make bending strength and rigidity the most important characteristics. This situation is essential, considering that high performance fibres are rigid and therefore must be processed carefully. Apart from carbon fibres, all other high performance yarns can be bent around a needle hook and transformed into stitches. The problems related to their processing are the fibre destruction and the modifications brought by the strains during knitting that lead to reduced mechanical characteristics of the fabric. The use of in-laid straight yarns eliminates the problem of fibre damage and also increases the volume fraction.

The multiaxial warp knitted fabrics, presented in part 3 of this chapter, are the most used for the production of composites. They have a laminar structure, with layers of yarns under preset angles, according to the application. The layers are connected and the risk of delamination is reduced.

Another development direction is the production of preforms with complex shapes for advanced composite materials. This is an interesting development direction, considering the complexity of the fabric architecture that can be achieved through knitting. The literature presents a significant amount of references concerning the development, characterisation and mechanical behaviour of these 3D fabrics.

2. Raw materials used for the production of knitted fabrics for advanced composite materials

Textile reinforcements are produced using high performance fibres, like glass, carbon/graphite, Kevlar, PES HM and HT, ceramic fibres, boron and silicon carbide fibres, etc. These yarns have superior mechanical behaviour that can meet the specific demands of composite applications that are illustrated in Table 2. They also have high bending rigidity that affects the knitting process and other characteristics that must be taken into consideration when designing a knitted reinforcement for composite materials (Miller, 1989).

Glass fibres (yarns, rovings) are the most common high performance fibres used to reinforce composite materials. They are characterised by hardness, resistance to chemical agents, stability and inertness, low weight and processability (Muckhopadhyay, 1994). There are more types of glass fibres depending on their chemical composition: E-glass, with good strength and high electrical resistivity, most common in composite materials; S-glass, with high tensile strength, most common in military applications; and C-glass, characterised by chemical stability and corrosion resistance.

	Fibre	Relative density [g/cm ³]	Young's Modulus [GPa]	Tensile strength [GPa]
1	Carbon (PAN)	2.0	400	2.0-2.5
2	Boron	2.6	400	3.4
3	E-glass	2.5	70	1.5-2.0
4	S-glass	2.6	84	4.6
5	Kevlar 29	1.44	60	2.7
6	Kevlar 49	1.45	60	2.7

Table 2. Main characteristics for some high performance fibres

Mechanically, the glass fibres are characterised by high strength, low elongation, high bending rigidity and brittleness. Law and Dias (1994) and Savci et al. (2001) showed that the glass fibres can resist when bent around the needle hook and therefore can be processed through knitting. Due to their brittleness and their low resistance to friction, the glass yarns damage easily, thus affecting the knitting process and subsequently the real strength of the reinforcement. Knitting glass fibre therefore requires a preliminary stage to determine the optimum technological conditions that ensure minimum fibre damage while maintaining the fabric quality. The fabric density, essential for the fibre fraction volume of the composite reinforcement gives this quality, together with the amount of fibre damage. High fibre fraction volume is a sine-qua-non requisite for the performance of the composite materials.

Experimental work

The experimental work is based on the direct study of the yarn after knitting, in order to identify the damage degree of the glass fibres inflicted by the knitting process. All models for the mechanical behaviour of the glass knitted fabric are based on the Young's modulus for the glass yarns. During the knitting process the filaments are damaged in a significant proportion, therefore altering the initial value of Young's modulus and altering the fabric properties. No previous study indicated the relation between technological parameters and the final value of the Young's modulus.

Two types of glass fibre were considered for the experiment: EC 11 408 Z28 T6 - Vetrotex and EC 13 136 Z30 P 100. The yarns are knitted using single jersey, as being the simplest possible structure.

The fabrics were produced on a CMS 320 TC (Stoll) flat machine with the following characteristics: gauge 10 E, negative feeding - IRO NOVA (Fig. 3) and holding down sinkers and presser foot (Fig. 4).

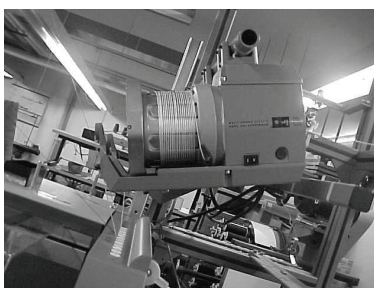


Fig. 3. IRO NOVA negative feeding

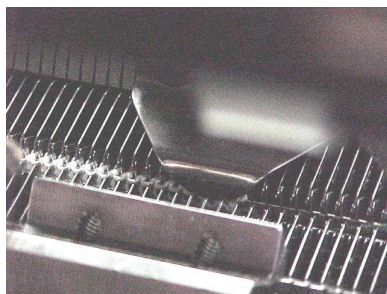


Fig. 4. Holding down sinkers and presser foot

In order to adapt to the yarn count, the fabrics are knitted with different values for the stitch quality cam, presented in Table 3. Each sample had 100 wales and 100 courses. The fabrics were relaxed until they presented no dimensional variation. The structural parameters (horizontal and vertical stitch density and stitch length) are illustrated in Table 4.

Yarn count [tex]	Quality stitch cam (NP)					Take down (WM)
	NP 1	NP 2	NP 3	NP 4	NP 5	
408	10.0	10.5	11.0	11.5	12.0	20
136	9.5	10.0	10.5	11.0	11.5	18

Table 3. Technological parameters used for knitting the samples

Yarn count [tex]	NP 2			NP 3			NP 4			NP 5		
	D _w [w/10 cm]	D _r [r/10 cm]	I _s [mm]	D _w [w/10 cm]	D _r [r/10 cm]	I _s [mm]	D _w [w/10 cm]	D _r [r/10 cm]	I _s [mm]	D _w [w/10 cm]	D _r [r/10 cm]	I _s [mm]
408	48	69	7.28	46	64	7.8	48	61	8.25	42	57	8.85
136	56	88	6.00	50	84	6.51	44	78	7.17	40	70	7.52

Table 4. Values for the structural parameters, in relaxed state

After relaxation 10 yarn lengths were drawn from the fabrics in order to determine their tensile properties, avoiding the edges, visibly more damaged than the rest. The tensile strength was tested on a HOUSENFELD H10K-S (Tinius Olsen), according to ASTM 2256. According to previous studies, the glass yarns break in less than the minimum 20 seconds indicated by the standard. Therefore, the testing speed selected was the minimum value of 50 mm/minute. The data confirmed the breaking of the glass yarns less than 7 seconds.

Experimental results

Knitting conditions

Fig. 5 presents the aspect of a 408 tex glass fibre jersey fabric produced with the quality stitch cams in the limit position, in this case NP = 10.5. The destroyed filaments are placed more at the level of the sinkers loops and not at the level of the needle loops, as Law and Dias pointed out in their study. This situation sustains the idea of other cause for yarn damage than the tension peaks in the knitting point. Furthermore, the significant filament breakage repeats at every two courses, corresponding to the reverse carriage displacement when the needles

receive less yarn. If the stitch length is even lower, the yarn gets out of the needle hooks and it can not be knitted. This situation is exemplified in Fig. 6, for a jersey fabric made of 136 tex glass fibres. The filaments appear to be completely destroyed, creating a plush effect.

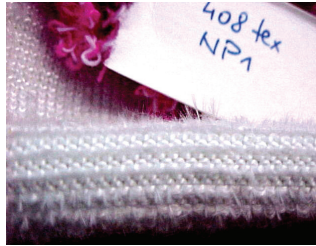


Fig. 5. Aspect of the jersey fabric (408 tex) knitted with NP1=10.5

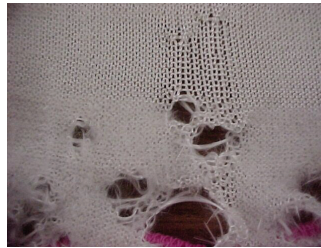


Fig. 6. Aspect of the jersey fabric (136 tex) knitted with NP1=10.5

Test results

The experimental results were calculated based on the raw data from the testing machine, according to the established methodology (ASTM D 2256), to obtain the following values: breaking strength, breaking tenacity, Young's modulus E , breaking elongation, breaking toughness and time to break. The results are centralised in Table 5. Yarn variant called Normal is the witness yarn, while the other variants are yarns knitted with a certain position for the stitch quality cam, defined in Table 3.

Yarn count [tex]	Yarn variant	Breaking force [N]	Breaking tenacity [cN/tex]	E modulus [N/tex]	Breaking elongation [%]	Breaking toughness [J/g]	Time to break [sec]
136	Normal	75.67	55.59	27.37	2.2	6.64	6.89
	NP 3	23.59	17.27	14.79	1.38	1.45	4.14
	NP 4	30.92	22.73	18.26	1.42	1.93	4.24
	NP 5	37.51	27.58	21.24	1.55	2.47	4.66
408	Normal	229.87	56.34	84.65	2.46	6.86	6.76
	NP 2	118.73	29.10	61.18	1.87	3.01	5.60
	NP 3	156.59	38.37	69.52	2.00	4.29	6.01
	NP 4	165.05	40.45	70.08	2.12	4.86	6.38
	NP 5	167.83	41.14	71.66	2.15	4.87	6.44

Table 5. Experimental results for tensile testing

Discussions

Contrary to Law and Dias, the experience of knitting on flat electronic machines showed that the needle could be pulled inside its channel without restrictions for the lowest point. The relation filament breaking – stitch length was found to be opposite to the one presented by Law and Dias. For each yarn count there is an inferior limit for the stitch length, guaranteeing the quality of the fabric. For this limit the degree of filament breaking is so high the yarn is almost completely destroyed and will break when unravelled from the fabric. It is the case of the 136 tex yarn knitted with NP2 stitch cam position. No tensile tests were performed for this variant and therefore it was not included in the experimental data.

The differences in strength and tenacity, compared to the normal values, show that the knitting process has a negative influence on the tensile properties. Furthermore, the decrease in strength is in a direct correlation with the stitch length – the lower the stitch length, the lower the tensile properties. Figs. 7 and 8 present the representative graphics for each type of yarns, illustrating the variation of the breaking force with the elongation.

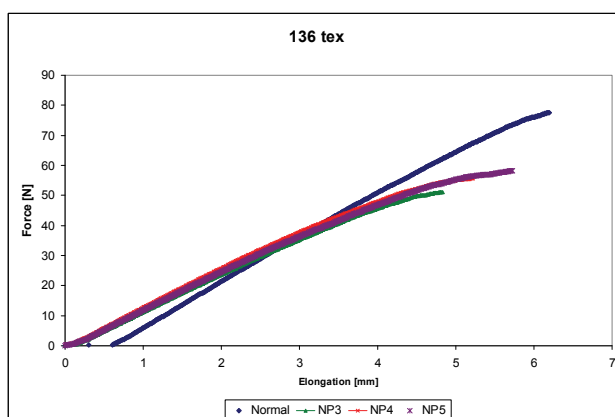


Fig. 7. Force-elongation curves for the EC 13 136 Z30 P 100 glass yarn

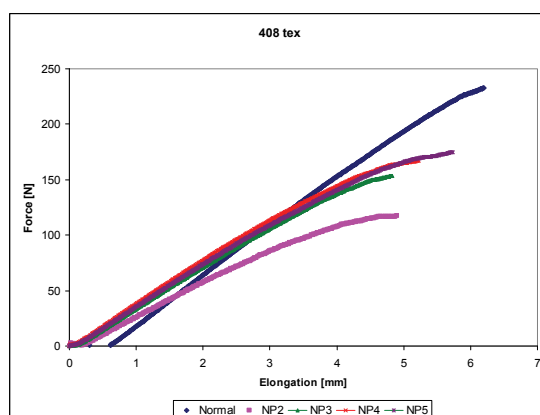


Fig. 8. Force-elongation curves for the EC 11 408 Z28 T6 glass yarn

The experimental data and the graphics are showing a contradiction with Law and Dias, concerning the cause of filament breakage during knitting. If the tension occurring in the looping point is responsible for the filament damage, then higher stitch length should present higher values for the breaking force, but the experimental results contradict this. One answer for this different opinion could be the feeding mechanism. In this case, the yarn was fed using an IRO NOVA feeding device, ensuring the proper quantity of yarn for the process. Without it, knitting proved impossible.

The breaking phenomenon appears due to the friction between the yarns and the knitting elements, especially the knock-over plates that can act like knives during rob back stage. The longer the stitch length, the smaller the tension in yarns and there is less filament damage.

The differences between the normal values and the ones for the knitted yarns 136 tex are varying from - 71% in case of the smallest stitch length and - 55% for the highest stitch length. In the case the 408 tex yarn, the difference interval is - 48.34% to - 26.99%.

The decrease in breaking toughness is more significant, as illustrated in Fig. 9. The toughness value for the 136 tex NP2 variant was introduced and was considered 0 only for comparison purposes. When compared, the initial toughness values for the two yarns are similar, but the 136 tex yarn shows a much higher decrease in breaking toughness then the other yarn. The decrease interval for 136 tex is extremely high 78-63%, while for 408 tex the decrease is in the interval 56-29%.

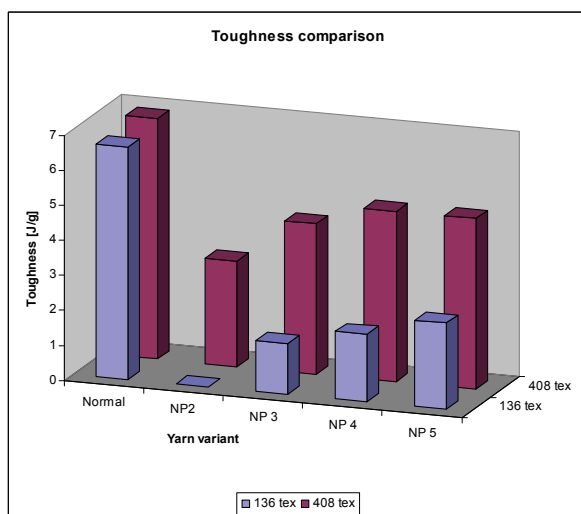


Fig. 9. Influence of yarn count and filament damage on breaking toughness

This situation suggests the influence of the number of filaments in the yarn, and also the fact that the amount of filament damage on the knitting machine is the same, regardless of the yarn count. A superior number of filaments ensure a better knittability, the yarn maintaining better tensile properties.

The breaking force and toughness values determined for the yarns knitted with NP4 and NP5 stitch cam positions are similar indicating that filament damage amount is the same. Even if the best properties are obtained for the highest stitch length – corresponding to NP5 value for the quality cams, this must be balanced with the fabric density, essential for the

overall performance of the fabric in the composite material. Therefore, the optimum technological parameters appear to be those for the fourth situation, with NP4 value for the stitch quality cam. In practice, even if the strength level is lower, value NP3 can also be used, due to the higher fabric density.

3. 3D knitted structures

In the case of knitted fabrics, the 3D architecture is facilitated by their high extensibility and formability that allow the production of complex shapes. This is the reason why the knitted fabrics are regarded as a viable option for preforms for advanced composite materials.

The main advantages of the 3D knitted fabrics are:

- a. the high formability of the fabrics, especially due to their drape characteristics
- b. the high complexity of the shapes that can be produced;
- c. the use of existing technology, without major adaptations;
- d. knitted fabrics exhibit good impact behaviour.

Knitted three dimensional performs are less studied and used, mostly because the following problems related to their production and their properties:

- a. the development of these fabrics is still at laboratory stage;
- b. the mechanical characteristics of the resulting composites are at a lower level and require improvement;
- c. the specific properties and their prediction are not yet well developed, mainly because of the complexity of the knitted fabrics;
- d. the pretension of the perform before its impregnation with resin determines a uneven behaviour for the final composite due to fibre migration in the stitches.

The 3D knitted fabrics can be divided into three main groups: multiaxial fabrics (multilayer), sandwich/spacer fabrics and knitted fabrics with spatial geometry (spatial fashioned).

Multiaxial fabrics

The multiaxial fabrics are characterised by the presence of multiple layers of yarns disposed at preferential angles that are assembled in the knitted fabrics. These fabrics are produced on special warp knitting machines using glass fibre or carbon fibre for the layers. The warp knitting technology is best suited for this kind of structures with in-laid yarns. Multiaxial fabrics are used mostly for the reinforcement of composite materials.

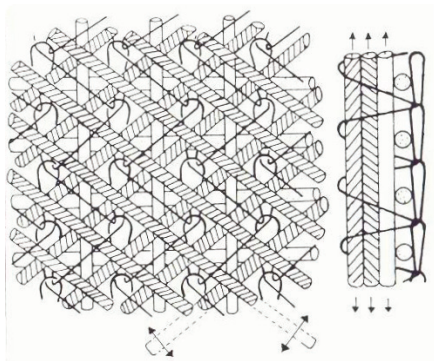


Fig. 10. Structure of the multiaxial knitted fabrics

The different layers of yarns in the multiaxial warp knitted fabrics are independent and the yarns fed under preset angles: 0° (weft yarns), 90° (warp yarns) and any value between these, like $\pm 30^\circ$ and $\pm 45^\circ$. The layers are united by the actual knitted fabric, using pillar or tricot stitches, as exemplified in Fig. 10 (Raz, 1989).

The preset angles correspond to the directions requiring higher strength during use and are imposed by the application. Currently, there are two main technologies adapted for the production of multiaxial fabrics: the Karl Mayer technology and the Liba technology.

a. Karl Mayer technology

The Karl Mayer machine uses four yarn systems – one to produce the ground fabric, one to insert the warp yarns, one for the weft yarns and the fourth for the yarns disposed under a preset angle. The inclined yarns are fed with two guide bars that have a rotational movement of 1 pitch every row. The guides are shogged in only one direction, passing from one bar to the other, changing the yarn direction within the fabric structure, as illustrated in Fig. 11.

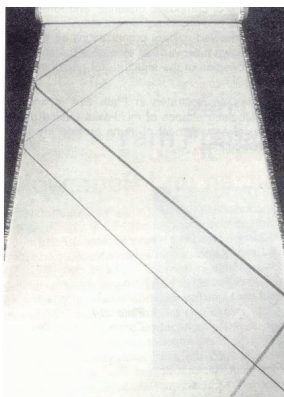


Fig. 11. The modified angle when changing direction in a Karl Mayer multiaxial fabric

The advantages of the Karl Mayer system are: the accuracy of the inclined yarns position, the fact that the needles do not destroy these yarns and the high productivity. Still, the fabrics are less compact affecting the fabric mechanical behaviour.

b. LIBA technology

The Liba technology is by far the best adapted to produce multiaxial fabrics. The MAX 3 CNC machines use a Copcentra machine that is preceded by a number of 3 zones where the layers are formed with the help of carriers feeding the yarns under the desired angle along the table: 0° for the weft yarns and 26° to 60° for the rest. The warp yarns (90°) are introduced in the knitting zone, using special guides. The layers are brought to the knitting zone and connected using pillar or tricot stitches. A non-woven mat (chopped glass fibres) can also be inserted, if the application requires it.

Fig. 12 illustrates the Liba system (source: www.liba.de). Liba also developed such a system also for carbon fibres (Copcentra MAX 5 CNC), where the carrier course is modified in order to reduce fibre waste.

The system allows obtaining fabrics with different degrees of compactness, made of different raw materials, as exemplified in Fig. 12 (source www.liba.de). The risk of fibre

destruction caused by the needles penetrating the layers is eliminated through the walking needle technique, where the needle bed is moved together with the layers.

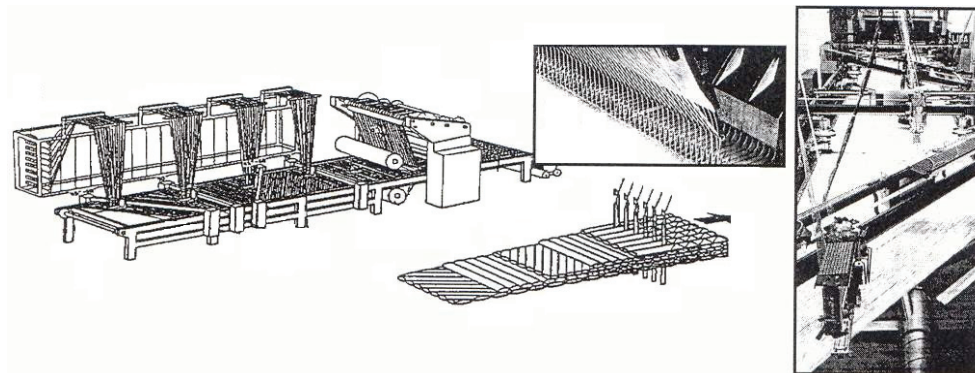
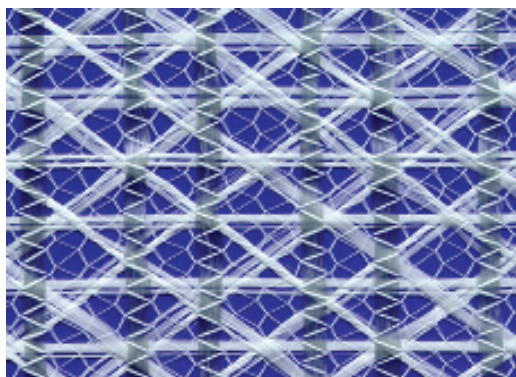
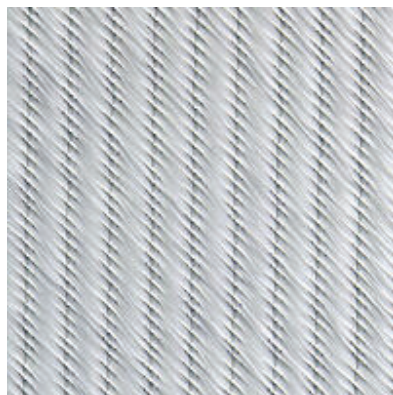


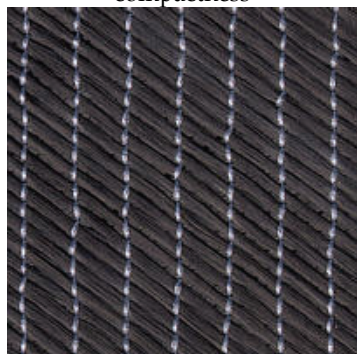
Fig. 12. Liba CNC machine for multiaxial fabrics



Glass fibre multiaxial fabric with low degree of compactness



Glass fibre multiaxial fabric with high degree of compactness



Multiaxial fabric made of carbon fibre



Multiaxial fabric made of Kevlar fibre

Fig. 13. Examples of multiaxial fabrics

Spatial fashioned knitted fabrics

The 3D knitted performs started to be developed in the '90, mainly based on the development of electronic flat knitting machines and CAD/CAM systems. Even if there is significant progress in this domain, there are a lot of aspects that need addressed in order for the spatial knitted fabrics to become industrially feasible.

The spatial fashioning of the knitted fabrics is based on the need to produce fabrics with complex shapes that are similar to the shape of the final product. Even if a certain degree of spatial geometry can be obtained by using modules of structures with different patterns or by dynamic stitch length, the technique of spatial fashioning is the only one that has no limitations with regard to the shape complexity and dimensions. This technique (also known as 'flechage') is based on knitting courses on all working needles and courses on a variable number of needles, determining zones with different amount of stitches. The zones with the highest amount of stitches will have in the end a spatial geometry.

A classification of the spatial fashioned fabrics must take into consideration the 3D shape of the product, defined geometrically as a 3D body. These bodies can be divided in solids of revolution, such as tubes (cylinders), spheres and hemispheres, cones and frustum of cones, ellipsoids, hyperboloids, and polyhedrons, such as tetrahedrons, pyramids, parallelepipeds, etc. Apart from these simple bodies, other bodies can be considered: bodies obtained from composing simple bodies or bodies with irregular shape.

The fabric 2D plan is a rectangular area where are positioned fashioning lines that define the final 3D shape of the product. Such a 3D fabric is obtained by placing more fashioning lines with certain characteristics, forming repeating geometric basic forms within the plan or not (as is the case for parallelepiped forms).

The **fashioning lines** can be defined as the zones where the knitting will be carried out on a variable number of needles, these zones generating the spatial geometry. The lines have two components, corresponding to decreasing the number of working needles and the other to increasing them. In the fabric, these two lines become one, the actual fashioning line, as presented in Fig. 14.

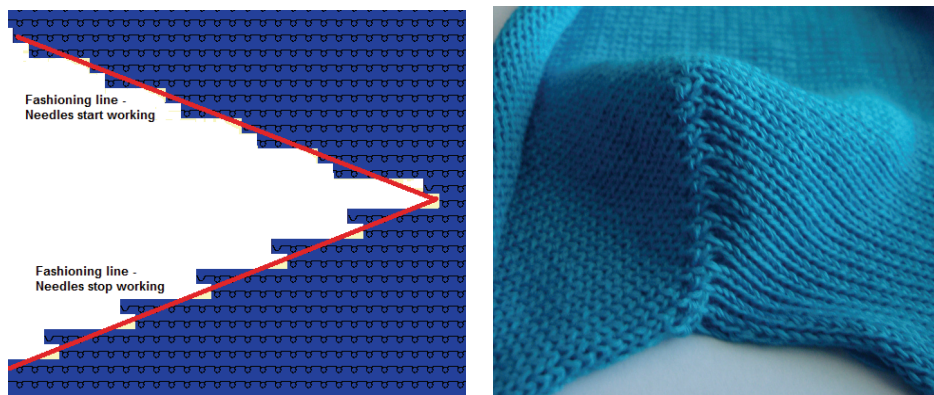


Fig. 14. Fashioning line - in the knitting programme and in the fabric

Fig. 15 illustrates the correlation between the 3D shape of the product and the 2D plan of the fabric, emphasising the most significant elements for the knitting process design. The evolute of the 3D body is obtained using sectioning lines and is the same with the 2D plan of the fabric that contains the fashioning lines. The knitting direction is very important when designing a

3D fabric. Knitting along the transversal or longitudinal direction of the final shape determines the knitting programme, the plan aspect and furthermore the specific behaviour of the fabric in the product. In some cases, only one knitting direction with regard to the product shape is possible, the other option being technologically not feasible. Other limitations concern the positioning of the fashioning lines within the fabric and their dimensions.

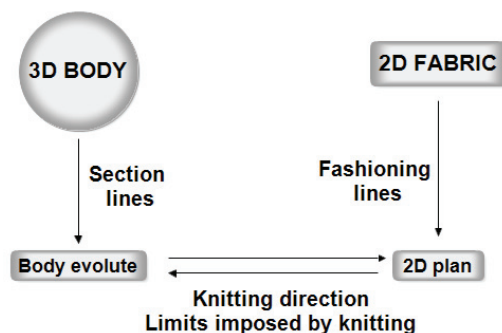


Fig. 15. Correlation between the 3D body and the knitted 2D fabric

Some of the most representative examples are illustrated in Figs. 16 to 20, presenting the 3D shape and the fabric 2D plan.

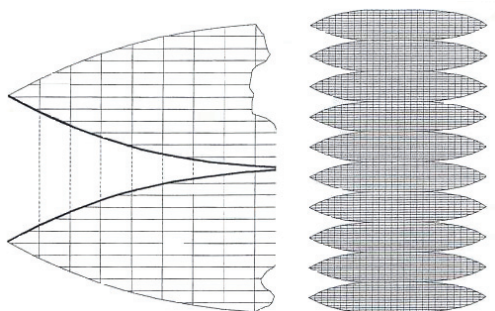


Fig. 16. (Hemi)spherical shape (Cebulla et al., 2000)

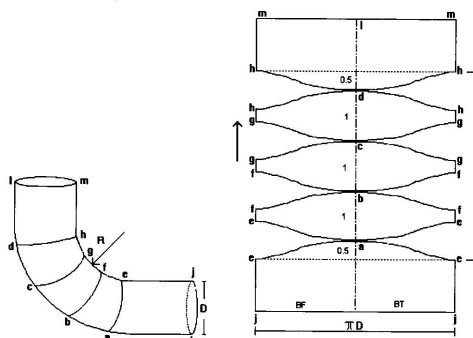


Fig. 17. Bent tubular shape (Song et al.)

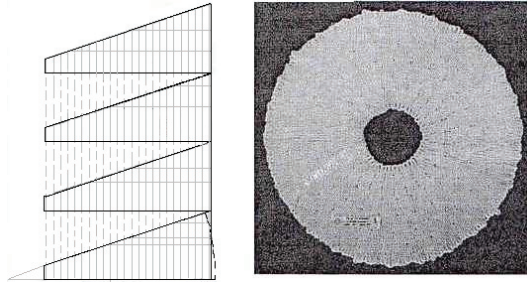


Fig. 18. Discoid shape (Cebulla et al., 2000)

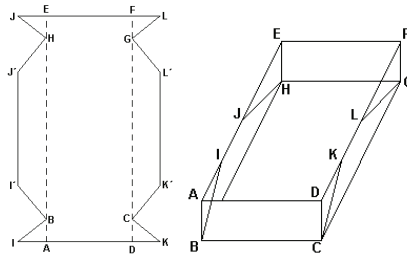


Fig. 19. Parallelepiped shape (Dias, 2000)

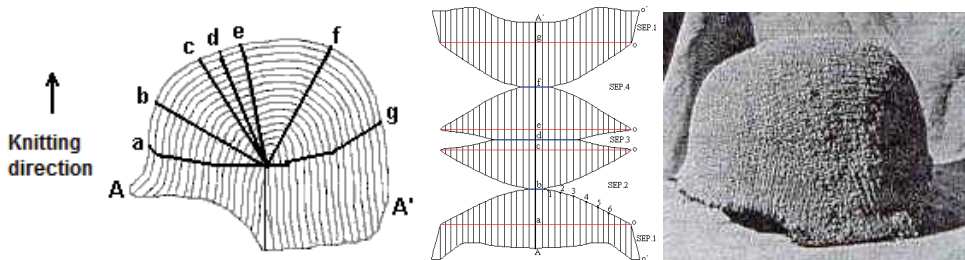


Fig. 20. Helmet made of aramid fibres – theoretical form, 2D fabric and final preform (Araujo et al., 2000)

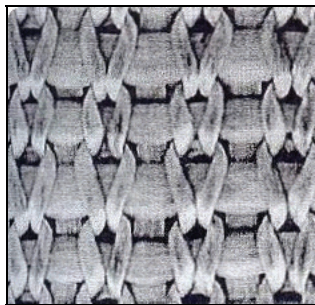


Fig. 21. Jersey fabric reinforced with weft and warp yarns (Cebulla et al., 2000)

There are some issues related to the fashioned fabrics used as preforms. One is the fabric strength, considering that the weft knitted materials exhibit limited mechanical characteristics. The solution to this problem is to insert warp and weft yarns within the structure. Fig. 21 presents a jersey fabric with warp and weft yarns, produced on a flat machine with adapted yarn feeder for the warp yarns (Cebulla et al., 2000). Apart from giving the fabric strength, it also improves the volume fraction of the reinforcement, increasing the quality of the composite materials.

Sandwich/spacer fabrics

A sandwich/spacer fabric is a 3D construction made of two separate fabrics, connected in between by yarns or knitted layers (Ciobanu, 2003). The fabric thickness determined by length of the connecting yarns/layers.

When produced on warp machines, these fabrics are known as spacers. They are obtained on double needle bar machines, with 4 to 6 guide bars – 1 or 2 guide bars produce the independent fabrics by knitting only on one bed and the middle bars create the connection by working on both beds (forming stitches or being in-laid). The fabric thickness depends on the distance between the two beds (spacer distance).

Fig. 22 exemplifies a spacer fabric made of glass fibre. An interesting application for spacer fabrics are the so called textile reinforced concrete that is used in buildings. Liba designed a double needle bar Raschel machine model DG 506-30-2HS that produces spacer fabrics with net structure, as illustrated in Fig. 23. The fabrics present weft and warp in-lays that form the net geometry and give the fabric strength on both directions (source: www.liba.de).



Fig. 22. Spacer fabric made of glass fibre

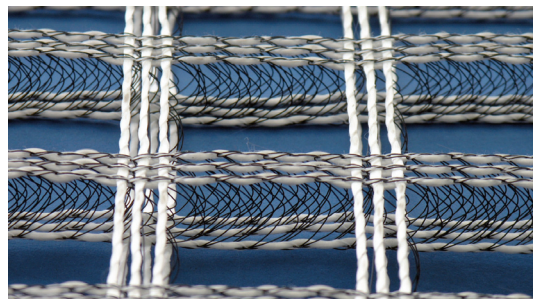


Fig. 23. Net spacer used for textile reinforced concrete

In the case of weft knitted fabrics, they are known as sandwich fabrics. Even if they can be produced also on circular machines (connection with yarns), they are mainly produced on electronic flat knitting machines that offer the required technical conditions and the development possibilities.

The connection can be generated through yarns fed on both beds or by knitted layers. The first solution is limited with regard to shape complexity and fabric thickness. The second connecting principle requires knitting separately on the two beds and at a certain point to stop and knit the connection layer on selected needles, usually 1x1. These needles can work also for the separate fabrics (if the length of the layer is small enough), or can be used exclusively to produce the connection, if the length and/or the shape complexity require (Fig. 24).



Fig. 24. Sandwich fabric with connecting knitted layers

There are two types of connecting layers (Araujo et al., 2000):

- Single layers (Fig. 25.a) – the layer is produced on one bed (jersey) or on both beds (rib, interlock) and can have a perpendicular or an inclined disposition between the separate fabrics.
- Double layers (Fig. 25.b) - two layers are knitted separately on the beds, connected at a certain point with a rib evolution; if a specified amount of rib courses will be produced also in the exterior fabrics, then the connection will be "X" shaped, with possibilities to extend more the rib dimensions or to alternate the disposition of the two layers.

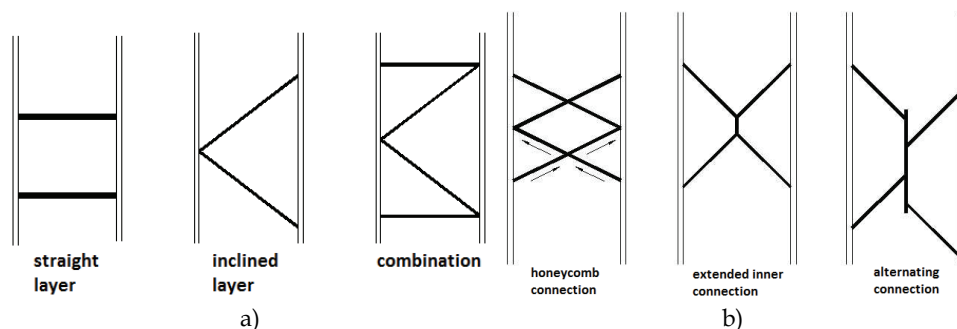


Fig. 25. Types of connecting layers

The sandwich fabrics presented are characterised by constant thickness and rectangular form in cross section. There are three major ways to diversify these fabrics and to obtain structures with complex shape (Ciobanu, 2003):

- The use of connection layers with different length
- The use of connection layers with variable form (the fashioning/flechage technique)
- The use of exterior fashioned separate fabrics

Sandwich fabrics with connecting layers of different length

The simple variation of the layer length will modify the cross-section of the fabric. The shape is created by the specific position of the separate fabrics between the consecutive layers. Two possibilities can be mentioned. One takes into consideration a specified sequence of layers with different length, as illustrated in Fig. 26. The different length of the layers will determine an inclined geometry for the exterior fabrics.

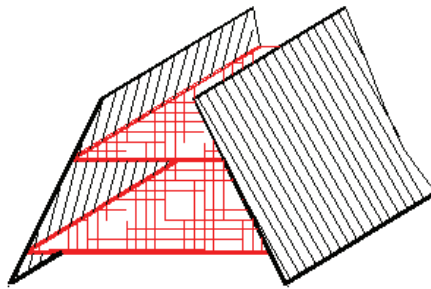


Fig. 26. Sandwich fabric with connecting layers of variable length

The other possibility refers to a sequence of two layers with predetermined (different) length, combined with an according number of courses in the separate fabric(s) that generates a corner effect (position at 90°). It is the case of fabrics with L and T shapes, presented in Fig. 27 and Fig. 28.

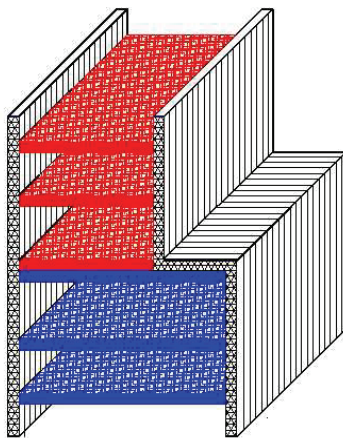


Fig. 27. Sandwich fabric with L shape

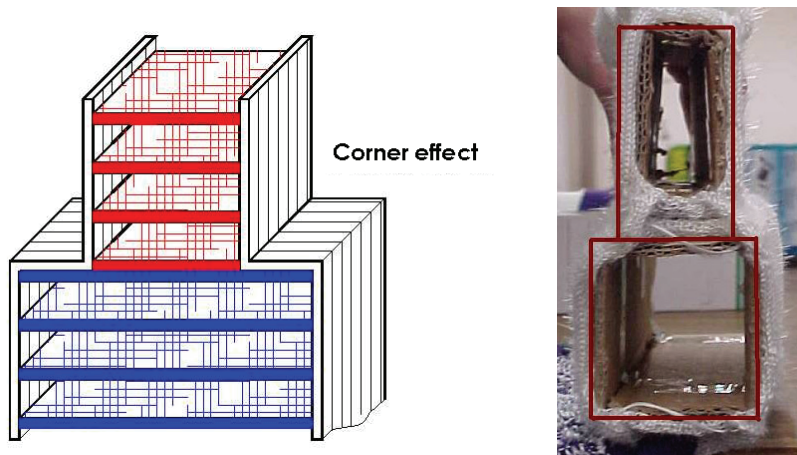


Fig. 28. Sandwich fabric with T shape

Sandwich fabrics with shaped layers (variable courses technique)

In this case the shape is determined directly by the shape of the layers, obtained through the variable courses technique. The technique is based on knitting on only a part of the needles producing the layer, in certain rows, while the others are missing. One example (knitting programme, Sirix) is presented in Fig. 29.

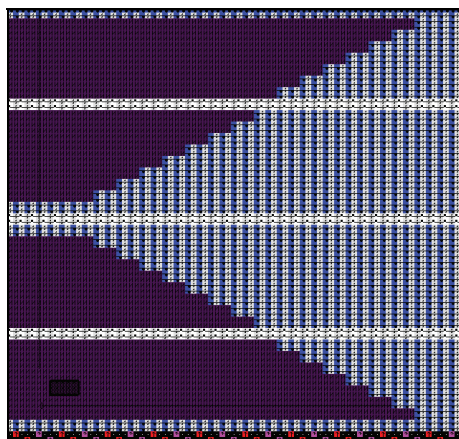


Fig. 29. Knitting sequence for a shaped layer (SIRIX, Stoll)

The fabric cross section given by the connecting layers is controlled through these layers. Different shapes can be therefore produced, as exemplified in Fig. 30. The layers are emphasised in red, while the separate fabrics are lined; the arrows are indicating the knitting direction. Two main types of shaped layers can be identified: with integral shape (the yarn guide is feeding continuously, even if on only a variable number of needles), as in Fig. 30.a. and b. and with divided shape (the evolution is split on distinct groups of needles, requiring separate feeding), as in the case of the fabric presented in Fig. 30.c.

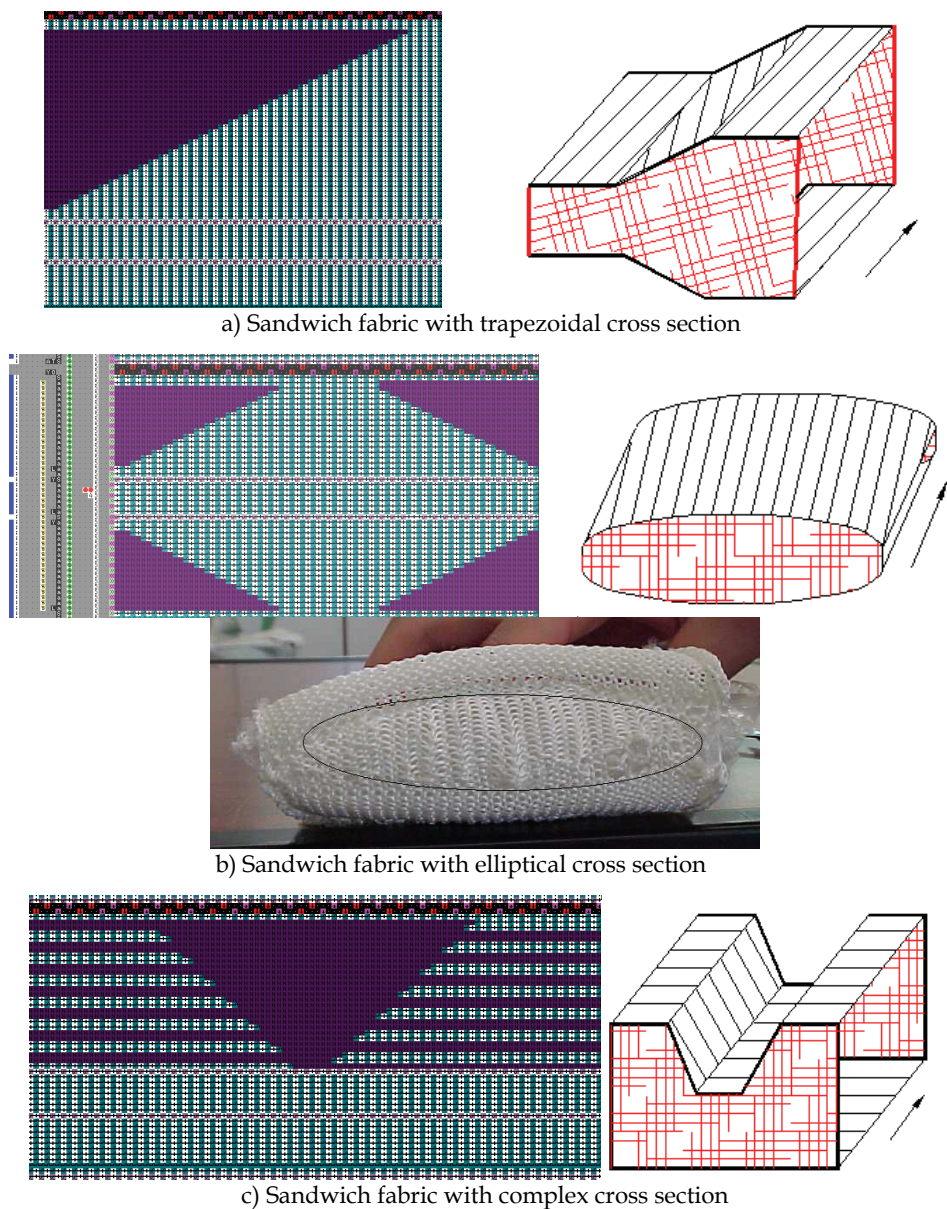


Fig. 30. Examples of sandwich fabrics with shaped connecting layers

Sandwich fabrics with fashioned exterior fabric

The fully-fashioning of the separate fabrics is obtained by narrowing and enlargement technique the number of working needles of the fabrics, using stitch transfer and racking. Fig. 31 illustrates one such possibility.

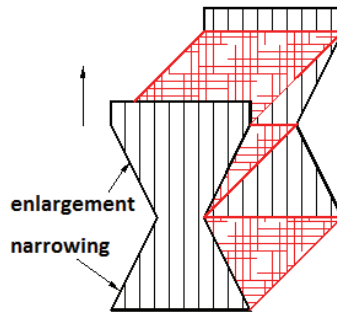


Fig. 31. Sandwich fabric with fashioned exterior fabrics

4. Application example – knitted preform for airplane wing

The application presented in the paper refers to a knitted preform for an airplane wing (glider). It was intended to knit a 3D shape identical to the wing. The preform was used to produce the composite material (through RTM).

Type and geometry of the knitted preform

The airplane wing prototype was defined using NACA 4 digital profile, according to specifications. Fig. 32 presents the geometry and dimensions of the chosen profile.

The wing is characterised by the following aspects:

- A difference in width between the beginning and the end of the wing – that requires successive narrowing;
- The difference between the two extremities is 60 mm, determining the narrowing slope;
- The fabric thickness for the outer layer is 5 mm;
- There are two interior walls with 5 mm thickness and different heights, according to the wing cross section: 79 mm – for the higher wall, and 64 mm – for the smaller wall.

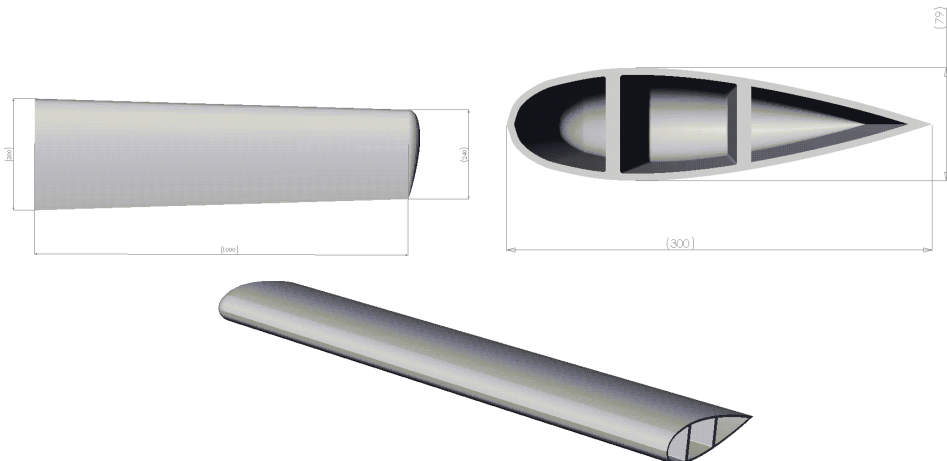


Fig. 32. Wing geometry and dimensions

Constructive, structural and technological characterisation of the preform

The complexity of the wing shape required the production of the knitted preform on a flat weft knitting machine, due to their advantages mentioned before.

The preform was knitted on a CMS 320 TC Stoll machine, using EC 11 408 Z28 T6 (Vetrotex) glass fibre. The yarn was tested on a Housenfield (Tinius Olsen) testing machine model H100 KS in order to determine its mechanical properties. The yarn is characterised in chapter 2 of this work.

The production of a preform that includes the inner walls requires a sandwich structure with connection through single knitted layers, according to the dimensions defined above. A very important aspect is the knitting direction that is determined in this case by the position of the inner walls. In the preform, the inner walls are created by the connecting knitted layers. Choosing another knitting direction, perpendicular to the one considered is not a viable solution due to the fact that this way the inner walls (connecting layers) are impossible to knit. Fig. 33 illustrates the architecture of the knitted preform. The zones marked on the drawing represent:

- border – 1 x 1 rib on selected needles;
- initial zone – 1 x 1 rib – this is the part where the rib evolution is produced on all needles and the feeder for the glass yarn is not yet working; it is subsequently removed, together with the border;
- beginning zone – first zone in the preform, corresponding to its inclined inferior extremity;
- zone I – zone made only of the outer fabrics up to the first inner wall (connecting layer);
- zone II – zone of the outer fabrics between the inner walls;
- zone III – zone of the outer fabrics up to the beginning of the inclined superior extremity;
- ending zone – zone corresponding to the superior extremity.

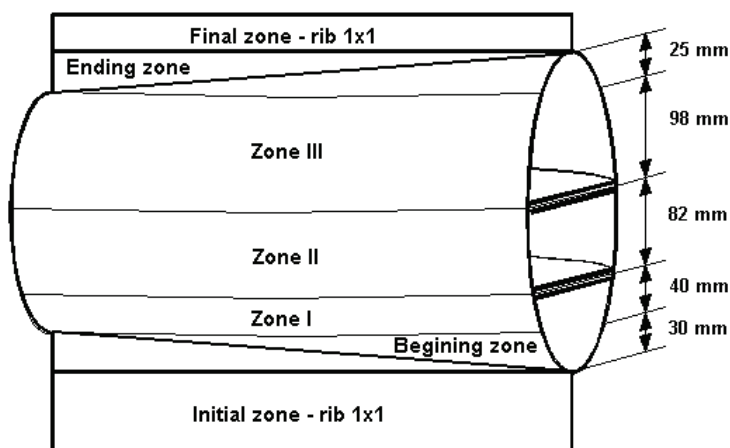


Fig. 33. Architecture of the knitted preform

The lateral edges of the preform must also be characterised, the lower edge being closed and shaped, while the wider edge is open and straight.

In the case of the considered knitted sandwich structure, both the outer fabrics and the inner walls are knitted on selected needles (1x1). A tubular evolution on selected needles with fleece yarns can be used in order to increase the fabric compactness (see Fig. 34). The main problem with last structure is the positioning outside the fabric of the floating fleece yarns that generates an irregular plush aspect, and also increases the snagging. Still, the simple pretension of the fabric, specific to the production of the composite material eliminates this situation.

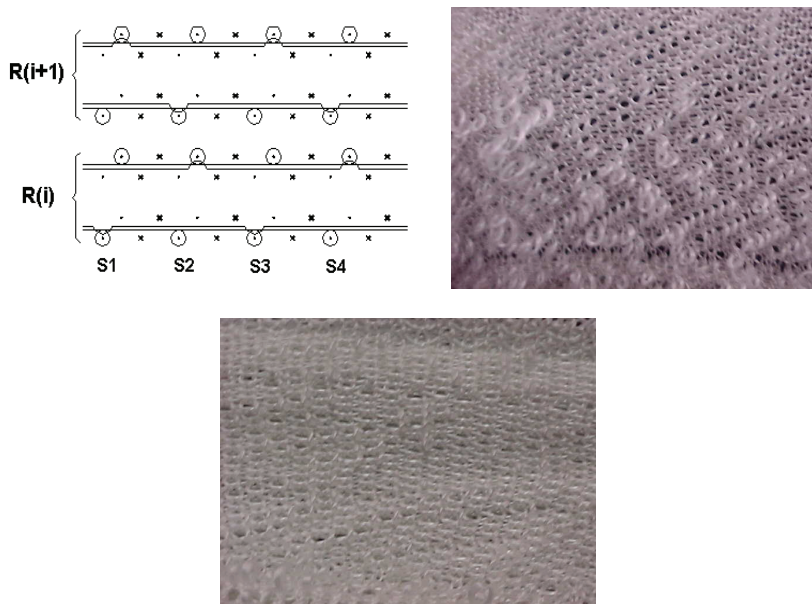


Fig. 34. Tubular evolution on selected needles with fleece in-lay – fabric aspect relaxed and stretched

Table 6 presents the values of the main structural parameters for the two structures (simple tubular on selected needles and tubular on selected needles with fleece yarns).

Structure	Stitch density		Stitch pitch A, [mm]	Stitch height B, [mm]	Stitch length l_{stitch} , [mm]		Weight M/m^2 , [g]
	D_w [wales/50mm]	D_r [rows/50mm]					
Tubular, on selected needles	16	26	3.12	1.92	9.6		842
Tubular, on selected needles, with fleece yarns	12	25	4.17	1.92	10.3	4.7	950

Table 6. The values of the main structural parameters for the knitted fabrics

Beginning and ending zones of the preform

The difference in width between the two extremities can be obtained through more knitting sequences. One possibility is to produce some zones that will be subsequently removed. In these zones the evolution is successively changed from 1x1 rib to tubular jersey, specific to the sandwich structure. The use of two feeders for the tubular fabric (row 2) requires 1x1 rib evolutions on selected needles that present the disadvantage of larger floats. To avoid this situation, the 1x1 rib evolutions on selected needles can be maintained only for small zones, the rest of the working needles producing tubular evolutions (see Fig. 35). Such a variant presents the advantage of simplifying the knitting sequence and the process.

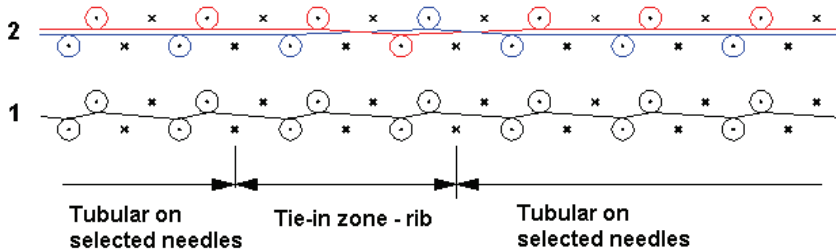


Fig. 35. Tie-in zone – from tubular to rib on selected needles (beginning zone)

Fig. 36 illustrates a fashioning solution for the beginning and ending zones. In this case, a number of incomplete rows are knitted with tubular evolution, using one yarn feeder. The groups of needles are successively introduced to work until all active needles are working. This way, the supplementary zones to be subsequently eliminated are cut out.

The number of incomplete rows will determine the slope of the inferior extremity. The slope of the superior extremity will be determined the same way, but the knitting sequence will be reversed. Regardless of the chosen variant, the number of rows knitted in the beginning zone is calculated with relation (1):

$$N_r = \frac{L}{B} \quad (1)$$

Where:

N_r - number of rows for the beginning and ending zones;

L - height of the beginning or ending zone, mm;

B - stitch height, mm.

The height of the beginning/ending zone is determined in the design stage, according to the specific dimensions of the wing; in this case 30 mm for the beginning zone and 25 mm for the ending zone. The calculated value is used to determine the groups of needles that will pass successively from one evolution to the other, or will successively start to work (2).

$$l_{\text{group}} = \frac{N_{\text{needles}}}{N_r} \quad (2)$$

Where:

l_{group} - width of a group of needles;

N_{needles} - total number of needles working in each bed;

N_r - number of rows in the beginning/ending zone.

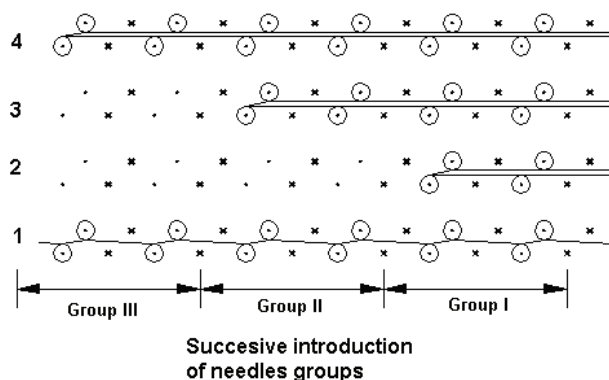


Fig. 36. Knitting sequence for the beginning zone

The inner walls of the preform

The inner walls of the preform are produced as single connecting layers of the sandwich fabric. The layer length is 80 mm, respectively 64 mm. In order to satisfy the required 5 mm thickness for the inner walls, two successive connecting layers with the same length will be knitted. After the introduction of the resin the two neighbouring connecting layers will generate an inner wall. Apart from knitting connecting layers of such high length, the production of two layers one after the other represented another problem.

During the knitting of the single connecting layer, some rows of the outer fabric are produced on the opposite bed in order to reduce the tension generated by the long period in which the needles making the outer independent fabrics miss. These supplementary rows must be taken into consideration when calculating the number of rows between the two connecting layers so that they are horizontal.

Presentation of the preform made of glass fibre

The general aspect of the preform is presented in Fig. 37. The beginning and ending zones of the outer fabrics can be observed, as well as the zones where the connecting layers were produced (see Fig. 38). One connecting zone is encircled in Fig. 37.



Fig. 37. Preform with jersey evolution on selected needles



Fig. 38. Preform with jersey evolution on selected needles and fleece in-lays

The successive connecting layers are exemplified in Fig. 39 where the preform is presented in cross section, showing the two connecting layers of 80 mm length.



Fig. 39. Connection layers – cross section view and aspect of the first connection layer

Production of a supplementary exterior layer for the wing

In order to increase the fabric compactness, as well as to improve the mechanical behaviour of the preform, a supplementary exterior layer is added, covering the preform. The tubular fabric is knitted perpendicularly in relation to the direction used to knit the preform (see Fig. 40).

The fabric dimensions correspond to the ones presented in Fig. 32. The conical shape is obtained with successive, symmetrical narrowing. The tubular fabric is closed, giving a rounding effect in N_1 and N_2 zones. The closing can be done using the bind-off technique, though it is preferably to avoid its use for fabrics made of glass fabric. The repeated transfers lead to a significant amount of broken filaments, affecting the mechanical behaviour and even destroying the stitches during the introduction of the fabrics in/on the moulds before the RTM process.

Considering that there are no restrictions regarding the structure and its tensioning, the evolution chosen for the tubular fabric can be jersey, 1x1 jersey or even jersey fleece (see Fig. 41).

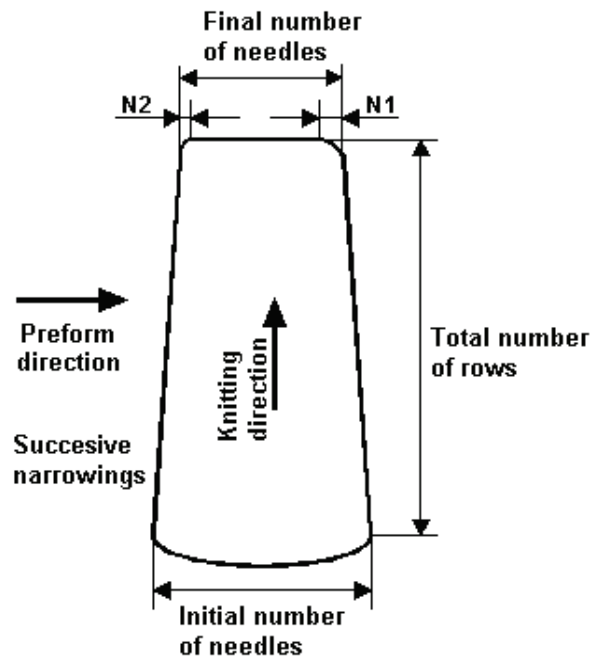


Fig. 40. Production of the supplementary layer

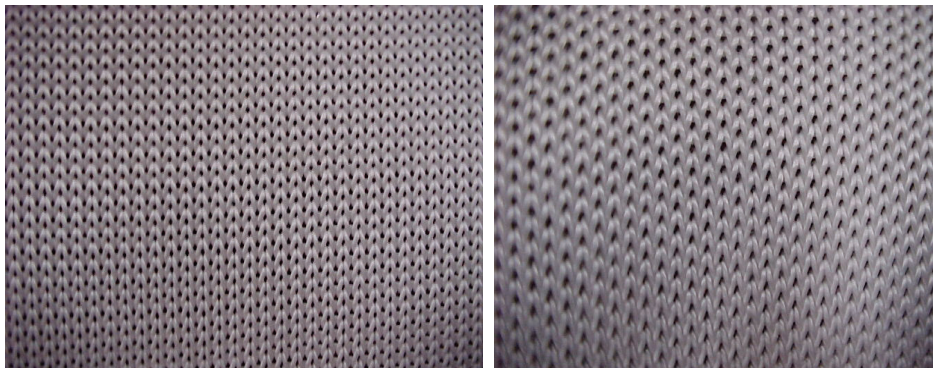


Fig. 41. Front aspect of a jersey and 1x1 miss jersey fabrics made with glass fibre count 408 tex

Production of a glider wing made of composite material using a knitted preform

The composite material glider wing was produced using an injection process RTM (Nicolau et al., 2002). The resin used was unsaturated polyester orthophtalic resin, S226E (Neste), characterised by reduced viscosity, 150 mPa s. The pre-acceleration was obtained with a 0.15% solution of cobalt 6%. The catalyst used was Trigonox TX 44B. This recipe formula avoids resin curing during the injection process.

Moulds production

The complexity of the preform shape required exterior and interior moulds that would generate the desired shape for the composite. The exterior mould (see Fig. 42) is made of a composite material reinforced with two layers of glass fibre matt. The three interior moulds (Fig. 43) that are to be introduced in the preform, are produced with polyurethane foam and have a protective layer.

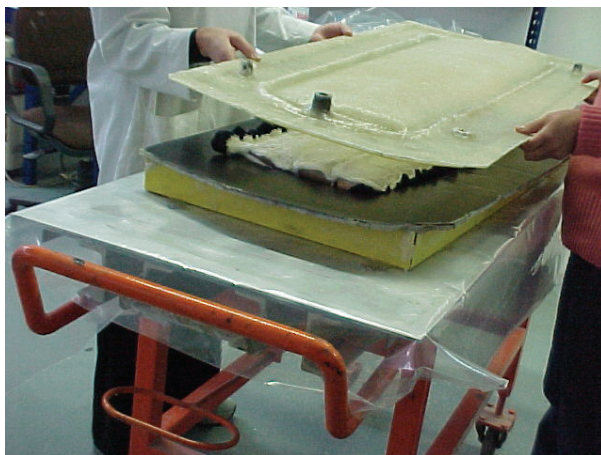


Fig. 42. Exterior mould – inferior and superior components



Fig. 43. Internal moulds – front view

Description of the RTM process

The injection process included the following stages (Nicolau et al., 2002):

- mould cleaning and application of the separation liquid;

- introduction of the interior moulds in the preform (Fig. 44) and covering with the supplementary tubular fabric;
- positioning in the exterior mould;
- mould vacuum closing;
- connecting the mould to the devices for resin injection and vacuum;
- vacuum formation inside the mould;
- resin preparation and catalyst introduction inside the bowl under 1 bar pressure;
- starting the injection process (Fig. 45).



Fig. 44. Introduction of the interior moulds in the preform



Fig. 45. Resin injection process

The polyester resin was injected inside the exterior mould at low pressure ($1,5 \cdot 10^5$ Pa) using the vacuum device. The injection process took approximately 30 minutes. After injection the

composite material was subjected to a thermal treatment in order to complete the curing process. The composite wing is presented in Figure 46.



Fig. 46. Composite wing – aspect before and after resin injection

5. Conclusions

Knitted fabrics are well used in the field of technical textiles, including composite materials with plastic matrix. As composite reinforcement, knitted fabrics have some negative points with regard to their mechanical behaviour, but this can be improved through structure (especially the use of in-laid yarns) and structural parameters.

Other issues concern the knittability of high performance fibres (volume of fibre damage during processing) and there are ways of limiting the filament breaking phenomenon – the modification of knitting elements, lower yarn tension, etc. The study presented in this chapter identifies as main cause of destruction the rob-back stage in the knitting process, when the yarns are pulled over the trick plate under high tension. The best approach to knitting high performance fibres seems to be a case by case approach, when the knitting conditions can be determined in order to obtain good quality fabrics.

Both weft and warp knitting technologies can be used to produce composite reinforcement. Warp knitting is best suited for structures with in-laid straight yarns (multiaxial fabrics), while weft knitting allows obtaining fabrics with three dimensional architecture, used as preforms for advanced composite materials. The examples of 3D knitted fabrics presented in

this chapter illustrate the idea that knitting is a viable option when considering the production of complex shapes. Further studies should explore diversification possibilities. Other directions for future development are: the design of knitted fabric in relation to 3D bodies, the simulation of fabric spatial geometry and properties prediction.

6. References

- Araujo, M.D., Hong H. & Fangueiro, R. (2000) *Têxteis Técnicos: Materiais do Novo Milénio*, vol. I *Visão Geral*, Williams Lda, ISBN 972 98468 0 4, Braga (in Portuguese)
- Araujo, M. D.; Hong, H. & Fangueiro, R. (2000). *Têxteis Técnicos: Materiais do Novo Milénio*, Vol. III, *Aplicações, Novos Processos e Novos produtos*. Williams Lda, ISBN 972 98468 2 0, Braga (in Portuguese)
- ASTM (2008). ASTM D2256 Standard Test Method for Tensile Properties of Yarns by the Single-Strand Method, *ASTM Standards on Disc*, section 7 Textiles (I)
- Cebulla, H.; Diestel, O. & Offerman, P. (2001). *Modelling and Production of Fully Fashioned Biaxial Weft Knitted Fabrics*, *TECNITEX 2001, AUTEX, Technical Textiles: Designing Textiles for Technical Applications*, vol. I, editor Araujo, M.D., Portugal, pp. 263-269, ISBN 972-98468-3-9, Povia de Varzim, Portugal, Williams Lda, Braga
- Ciobanu, L. (2003). *Contributions to the production and development of technical knitted fabrics*, PhD thesis, „Gheorghe Asachi” Technical University, Iași (in Romanian)
- Dias, T. et al. (2000). Knitting Seamless Three-Dimensional Shell Structures on Modern Electronic Flat Bed Knitting Machines, *Proceedings of the International Conference, 24&25 August, Bolton, UK*, pp. 36-43, ISBN 1 85573 494 X, Woodhead Publishing, UK
- Fukuta et al., in 15th Textile Research Symposium, the Textile Machinery Society of Japan, Osaka, 1984, p. 36-38
- Hu, J. (2008). Introduction to three-dimensional fibrous assemblies, in *3-D fibrous assemblies Properties, applications and modelling of three-dimensional textile structures*, Woodhead Publishing, ISBN 978-1-84569-377-0, Cambridge, UK
- Lau, K.W. & Dias, T. (1994) *Knittability of High – Modulus Yarns*, JTI, vol. 85, nr. 2, , pp. 173-190, Woodhead Publishing, ISSN 0040 5000, Cambridge, UK
- Leong, K.H. et al. (2000). The potential of knitting for engineering composites – a review, *Composites Part A: applied science and manufacturing*, 31, p. 197-220
- Mallick, P. (1997). *Composites Engineering Handbook*, Marcel Dekker, USA
- Miller, D.M. (1989). Glass Fibers, in *Engineered Material Handbook*, ASM International Handbook Committee, Vol. I – Composites, p. 45-48, ISBN 0 87170 279 7
- Mouritz, A.P., et al. (2000). Review of applications for advanced three-dimensional fibre textile composites, *Composites Part A: applied science and manufacturing*, vol. 30, , issue 3, p. 1445-1461, ISSN 135-835X
- Muckhopadhyay, S.K. (1994). High-performance Fibres, *Textile Progress*, vol. 25, nr. 3/4, Textile Institute, ISSN 0040 5167, ISBN 1870812662
- Nicolau, A. et al. (2002). Structural Composite Parts Production from Textile Preforms, *Materiais 2001, 1st International Materials Symposium*, Pos M5, Porto, Portugal
- Raz, S. (1989). *Warp Knitting Production*, Verlag Melliand Textilberichte, Heidelberg, ISBN 3-87529-022-4
- Savci, S.; Curiskis, J.I. & Pailthorpe, M.T. (2001). Knittability of Glass Fiber Weft – Knitted Preforms for Composites, *TRJ*, vol. 71, 1, pp. 15-21, ISSN 0040-5175

- Scardino, F. (1989). An Introduction to Textile Structures and their Behaviour, in *Textile Structural Composites*, Composite Materials Series, vol. 3, editors Tsu-Wei Chou, Ko, F.K., p. 1-24, ISBN 0-444-42992-1, Elsevier Science Publishers B.V., Amsterdam
- Song, G.; Wu, J. & Wei, Y. Computer Aided-Design of Three Dimensional Knitwear, *JOTI*, vol. 97, no. 6, pp. 549-552
- Verpoest, I. et al. (1997). The potential of knitted fabrics as a reinforcement for composites, *Proceedings Volume of the 11th International Conference on Composite Materials*, Gold Coast, Australia, 14-18 July, 1997, 1:108-33
- www.liba.de

Part 3

Modelling and Testing of Composites

To Carry Out Tolerance Analysis of an Aeronautic Assembly Involving Free Form Surfaces in Composite Material

Wilma Polini

*Dipartimento di Meccanica, Strutture, Ambiente e Territorio,
Università degli Studi di Cassino, Cassino
Italy*

1. Introduction

The increasing competition in aerospace industries has brought to cutting programs in manufacturing, design and assembly of aircraft structural frame. An aircraft is made of several assemblies including 3D complex shapes and the different functional requirements from design and manufacturing that these assemblies should respect are various. Nowadays the most important policy is the “Concurrent Engineering” which rule is to lead in a parallel way, design and manufacturing, making them communicate with the aim of reducing reworking times and discard products; such requirements are strongly felt in the aerospace industries.

Tolerance analysis has a considerable weight in the Concurrent Engineering and represents the best way to solve assembly problems in order to ensure higher quality and lower costs. It is a critical step to design and to build a product and its importance has grown in the past years. In fact, the need to assign dimensional and geometric tolerances to assembly components is due to the standardization of the production and to the correct working of the assembly. The appropriate allocation of tolerances among the different parts of an assembly can result in lower costs per assembly and higher probability of fit, reducing the number of rejects or the amount of rework required on components.

A product is designed and manufactured to perform a task, and its issue depends on one or more parameters of the assembly that are commonly called “project functions”. A project function is a dimension or a geometric variable of the assembly whose value depends by the dimensions, the geometry and the tolerances assigned to the components constituting the assembly. The nominal value and the tolerance range of the project function allow us to guarantee the assembly functionality. Practically, the dimensions and the tolerances of the assembly components combine, according to the assembly sequences, and generate the tolerance stack-up functions. Solving a tolerance stack-up function means to determine the nominal value and the tolerance range of a project function by combining the nominal values and the tolerance ranges assigned to the assembly components.

Tolerance analysis may consider alternative assembly cycles in order to identify that one allowing to obtain the assembly functionality with the maximum value of the tolerance range assigned to the components. Huge problems may present during the assembly

process if the tolerance study on a sub-component was not carried out or was ineffectual (Whitney, 2004). It is even possible that the product design may have to be subsequently changed because of unforeseen tolerance problems not detected prior to actual assembly took place. In this case costs to the business will be high. It was estimated that 40%-60% of the production cost is due to the assembly process (Delchambre, 1996).

The study of the tolerance stack-up functions, during the design stage, is very critical for aeronautic field whereas the complexity of the structures, to which high performances are required; so advanced material, design techniques and assembly technologies are needed. In fact, the aeronautic structures involve free-form surfaces, which are often made in composite material. They may be considered as non-rigid parts that could be subjected to significant distortion after the removal of manufacturing forces. This condition, known as free-state variation, is principally due to weight and flexibility of the part and the release of internal stresses resulting from fabrication.

Many well-known approaches exist in the literature to tolerance analysis (Hong & Chang, 2002; Shen et al., 2004). However, these methods are not easy to apply, especially for complex aerospace assemblies, since they were born to deal with elementary features, such as plane, hole, pin and so on. So the aid of computer is called for. In the recent years, the development of efficient and robust design tools has allowed to foresee manufacturing or assembly problems during the first steps of product modeling by adopting a concurrent engineering approach. Today Computer Aided Tolerance (CAT) Software is readily available, but even if these tools provide good results they have not been widely used. Commercial CATs are not completely true to the GD&T standards and need improvement after a better mathematical understanding of the geometric variations. The user needs expertise and great experience combined with a thorough understanding of the packages' theoretical base plus modeling principles to build a valid model and obtain relatively accurate results. Computer Aided Tolerance software efficiently deals with mechanical assemblies where the feature to align are planes, hole-pin, but it hardly treats of free-form surfaces to connect.

The present work deals with the tolerance analysis of freeform surfaces belonging to parts in composite material and that may be non-rigid. The aim of this chapter is to present the steps to carry out the tolerance analysis of an assembly involving free-form surfaces in composite material by using a commercial CAT software. The great effort of the present work is overcome the limits of the CAT software to deal with dimensional and geometric tolerances applied to free form surfaces in composite material. This paper tries to answer to some questions on tolerance analysis without clear answer: What are the functions of the product, how do we flow down these key product functions through into its detail parts? How to model a free-form surface for a tolerance analysis? How to deal with a composite material for a tolerance analysis? How to improve the assembly process in order to reduce the tolerance impacts on these functions?

An aeronautic component is considered as case study. This is an internal frame of a winch arm mounted on an helicopter. The part addressed in this paper is the after internal frame that allows to mount the fairing covers of the head of the winch arm directly on its structural beam. It is made in carbon fiber composite material. The frame is made with five layer of carbon fiber imbued in a matrix of epoxy resin for a total stack thickness of 1.65 mm. After the stratification process, a curing process is carried out by autoclave with a control of temperature and pressure. The weight of the part is about 350 g. Assembly operation among the parts are done by using special grub screws that are inserted in the holes of each

component. No adhesives or resins are used to secure the surfaces, since a perfect adhesion is not required.

The paper is organized as follows: In Sec. 2, the mean of tolerance analysis is deeply discussed. In Sec. 3, the main models found in the literature for tolerance analysis are presented. In Sec. 4, the main functions of the commercial CAT softwares are shown. In Sec. 5, the steps of the proposed method for tolerance analysis of an assembly involving free-form surfaces in composite material are shown. In Sec. 6, the application of the proposed steps to an aeronautic case study is deeply discussed.

2. Tolerance analysis

The aim of a tolerance analysis of an assembly is to evaluate the cumulative effect due to the tolerances, that are assigned to the assembly components, on the functional requirements of the whole assembly. Each functional requirement is schematized through an equation, that is usually called stack-up function, whose variables are the model parameters that are function of the dimensions and the tolerances assigned to the assembly components. It looks like

$$FR = f(p_1, p_2, \dots, p_n) \quad (1)$$

where FR is the considered functional requirement, p_1, \dots, p_n are the model parameters and $f(p)$ is the stack-up function, that is usually not linear.

A functional requirement is usually a characteristic that relates two features. Its analytical expression is obtained by applying the equations of the *Euclidean geometry* to the features that define the functional requirement or to the points of the features that define the functional requirement.

A stack-up function has to model two possible assembly variations. The first variation is due to the tolerances assigned to the features of the assembly components. The obtained model (that is called "*local model*") has to be able to schematize all the tolerance kinds, i.e. dimensional, form, and so on, but in the same time it has to be able to represent the Envelope Principle (Rule # 1 of ASME standard) or the Independence Principle (according with ISO 8015 standard) applied to different dimensions of the same part. The *local model* has to define the range of variation of the model's parameters from the assigned tolerances and it has to schematize the interaction among the assigned tolerance zones. The second variation is due to the contact among the assembly components. The variability of the coupled features, by which the link among the parts is made, gives a deviation in the location of the coupled parts. The resulting model (that is called "*global model*") has to be able to schematize the joints with contact and the joints with clearance between the coupled features.

Once modeled the stack-up functions, they may be solved by means of a worst case or a statistical approach (Creveling, 1997). To carry out a worst case approach, it is needed to define the worst configurations of the assembly (i.e. those configurations due to the cumulative effect of the smallest and the highest values of the tolerances assigned to the assembly components) that satisfy its assigned tolerances. This means to solve a problem of optimization (maximization and/or minimization) under constraints due to the assigned tolerances. Many are the methods developed by the literature to carry out a worst case approach (see Luenberger, 2003). To carry out a statistical approach, it is needed to translate

each tolerance assigned to an assembly component into one or more parameters of the stack-up function. Therefore, a Probability Density Function (PDF), that is function of both the manufacturing and the assembly processes, is assigned to each parameter. Being the definition of the relationship among the production and assembly processes and the probability density function of the tolerance of the component strongly hard to estimate, the commonly used assumption is to adopt a Gaussian probability density function. Moreover, a further assumption is to consider independent the parameters used to represent the variability of the features delimiting each dimensional tolerance. The variation of the FR is obtained by means of a Monte Carlo simulation technique (Nigam & Turner, 1995; Nassef & ElMaraghy, 1996) it is usually calculated as \pm three times the estimated standard deviation (three sigma paradigm of (Creveling, 1997)).

3. Literature review

The foremost works on the tolerance modeling problem are found in (Requicha, 1983; Requicha, 1993) that introduced the mathematical definition of the tolerance's semantic. He focused on constructing semantically correct tolerance zones and he proposed a solid offset approach for this purpose. Since then, a lot of models are proposed by the literature to perform the tolerance analysis of an assembly whose components may be considered as rigid parts (Hong & Chang, 2002).

The *vector loop* model uses vectors to represent relevant dimensions in an assembly (Chase et al., 1995; Chase et al., 1996; Chase et al., 1997a). Each vector represents either a component dimension or an assembly dimension. Vectors are arranged in chains or loops to reproduce the effects of those dimensions that stack together to determine the resultant assembly dimensions. Three types of variations are modelled in the vector loop model: *dimensional variations*, *kinematic variations* and *geometric variations*. Dimensional variations defined by dimensional tolerances are incorporated as \pm variations in the length of the vector. Kinematic variations describe the relative motions among mating parts, i.e. small adjustments that occur at assembly time in response to the dimensional and geometric variations of the components. Geometric variations capture those variations that are imputable to geometric tolerances.

The *variational solid modelling* approach involves applying variations to a computer model of a part or an assembly of parts (Martino & Gabriele, 1989; Boyer & Stewart, 1991; Gupta & Turner, 1993). To create an assembly, the designer identifies the relevant features of each component and assigns dimensional and geometrical tolerances to them. In real conditions (i.e. manufactured part), the feature has been characterized by a roto-translational displacement with respect to its nominal position. This displacement is modelled to summarize the complete effects of the dimensional and geometric variations affecting the part by means of a differential homogeneous transformation matrix. Once the variabilities of the parts are modelled, they must be assembled together. Another set of differential homogeneous transformation matrices is introduced to handle the roto-translational deviations introduced by each assembly mating relation.

The *matrix* model aims at deriving an explicit mathematical representation of the boundary of the entire spatial region that encloses all possible displacements due to one or more variability sources. In order to do that, homogenous transformation matrices are considered as the foundation of the mathematical representation. A displacement matrix is used to describe any roto-translational variation a feature may be subjected to. The *matrix* model is

based on the positional tolerancing and the Technologically and Topologically Related Surfaces (TTRS) criteria (Clément et al., 1998); by classifying the surfaces into several classes, each characterized by some kind of invariance with respect to specific displacement kinds (e.g. a cylinder is invariant to any rotation about its axis) the resulting displacement matrix can be simplified (Clément et al., 1994).

In the terminology adopted by the *jacobian model* approach, any relevant surface involved in the tolerance stack-up is referred to as *functional element* (FE). In the tolerance chain, FEs are considered in pairs: the two paired surfaces may belong to the same part (internal pair), or to two different parts, and paired since they interact as mating elements (kinematic pair, also referred to as external pair). The parts should be in contact to be modelled by this model. Transformation matrices may be used to locate a FE of a pair with respect to the other: these matrices can be used to model the nominal displacement between the two FEs, but also additional small displacements due to the variabilities modelled by the tolerances. The main peculiar aspect of the *jacobian* approach is how such matrices are formulated, i.e. by means of an approach derived from the description of kinematic chains in robotics (Laperrière & Lafond, 1999; Laperrière & Kabore, 2001).

The *torsor* model uses screw parameters to model three dimensional tolerance zones (Chase et al., 1996). Screw parameters are a common approach adopted in kinematics to describe motion; they are used to describe a tolerance zone, since a tolerance zone is the region where a surface is allowed to move. The screw parameters are arranged in a particular mathematical operator called *torsor*, hence the name of the approach. To model the interactions between the parts of an assembly, three types of torsors (or Small Displacement Torsor SDT) are defined (Ballot & Bourdet, 1997): a *part SDT* for each part of the assembly to model the displacement of the part; a *deviation SDT* for each surface of each part to model the geometrical deviations from nominal; a *gap SDT* between two surfaces linking two parts to model the mating relation.

The *Tolerance Maps* model is being developed at the Arizona State University (Davidson et al., 2002; Mujezinovic et al., 2004; Ameta et al., 2007). It is based on a two-levels model: the *local model*, that models part variations in order to consider the interactions of the geometric controls applied to a feature of interest and the *global model* that interrelates all control frames on a part or assembly. A Tolerance-Map (T-Map) is a hypothetical solid of points in n-dimensions which represent all possible variations of a feature or an assembly. Overlaying the coordinates of the T-Map the stack-up equations to perform the tolerance analysis are obtained.

However, these methods are not easy to apply, especially for complex aerospace assemblies, since they were born to deal with elementary features, such as plane, hole, pin and so on. So the aid of computer is called for. In the recent years, the development of efficient and robust design tools has allowed to foresee manufacturing or assembly problems during the first steps of product modeling by adopting a concurrent engineering approach.

Efforts to deal with the tolerance analysis in aeronautic field were carried out. Sellakh proposed an assisted method for tolerance analysis of aircraft structures through assembly graphs and TTRS theory (Sellakh et al., 2003). Marguet presented a methodology to analyse and optimise the assembly sequence of simple shape assemblies (Marguet & Mathieu, 1998; Marguet et Mathieu, 1999). Ody showed a comparison among Error Budgeting techniques and 3D Tolerance Software Packages (Ody et al., 2001). Those papers present solutions of typical mechanical assemblies that involve the alignment of plane, holes and pins, but the aeronautic surfaces have a free form generally.

Some are the works found in the literature to deal with the tolerance analysis of compliant assemblies, i.e. assemblies that contain deformable parts, such as sheet-metal, plastics, composites and glass. Some of the first research related to this area was done by (Gordis & Flannely, 1994). They used frequency domain analysis to predict in-plane loads and displacements from misalignment of fastener holes in flexible components. Liu and Hu have used simple finite element models to predict assembly variation of flexible sheet metal assemblies (Liu & Hu, 1995; Liu & Hu, 1997). Their work was focused on the effect of part fixturing and order of assembly.

Merkley uses the assumptions of Francavilla and Zienkiewicz (Francavilla & Zienkiewicz, 1975) to linearize the elastic contact problem between mating flexible parts (Merkley, 1998). Merkley derived a method for predicting the mean and the variance of assembly forces and deformations due to assembling two flexible parts having surface variations. He describes the need for a covariance matrix representing the interrelation of variations at neighboring nodes in the finite element model. The interrelation is due to both surface continuity, which Merkley calls geometric covariance, and elastic coupling, which he calls material covariance. Merkley used random Bezièr curves to describe surface variations and to calculate geometric covariance. Bihlmaier presents a new method for deriving the covariance matrix using spectral analysis techniques (Bihlmaier, 1999). The new method, called the Flexible Assembly Spectral Tolerance Analysis method, or FASTA, also includes the effect of surface variation wavelength on assemblies.

4. Computer Aided Tolerancing software

Today Computer Aided Tolerance (CAT) software is readily available for tolerance analysis of rigid part assemblies, but even if these tools provide good results they have not been widely used (Turner & Gangoiiti, 1991; Chase et al., 1997b; Salomons et al., 1998; Prisco & Giorleo, 2002). The CAT system known as CE/TOL[®] is based on the *vector loop* model. Many commercial CAT software packages are based on the *variational* model, such as eM-TolMate of UGS[®], 3-DCS of Dimensional Control Systems[®], VisVSA of UGS[®]. Commercial CATs are not completely true to the GD&T standards and need improvement after a better mathematical understanding of the geometric variations. The user needs expertise and great experience combined with a thorough understanding of the packages' theoretical base plus modeling principles to build a valid model and obtain relatively accurate results. Computer Aided Tolerance software efficiently deals with mechanical assemblies where the feature to align are planes, hole-pin, but it hardly treats of free-form surfaces to connect.

A CAT software shares the same user interface and the same database of a CAD package; the CAT information is stored within the CAD model with no need of translation.

The CAT software used in the following of this work is eM-TolMate of UGS[®] and, therefore, further information about this package has been discussed in the following. EM-TolMate involves the building of the model through the feature definition, the tolerance specification, the assembly and the measurement definitions.

The feature definition process must be performed for each component of the final assembly (there must be a separate CAD model for each component); it uses the existing CAD geometry of the model to create its own features. Therefore, full associativity with CAD entities is assured. The basic features supported in eM-TolMate are plane, pin (cylindrical, tapered, threaded), hole, point, tab, slot, constant profile surface, constant cross section, sphere, surface of revolution, general 3D surface. Edge features (for thin-walled parts) are

also available. In many cases, the user needs to mathematically derive some feature from existing features (e.g. line of intersection between a plane and a parallel cylinder, centroid of several points or best fit line between several points).

The tolerance specification allows the user to define the dimensional or geometric tolerances supported by the existing international standards of GD&T (ASME and ISO). There is no limit on the number of tolerances applied to a feature. Diameter modifier and material modifier (MMC and LMC) may be added to tolerances applied to a feature of size. Available statistical distributions are normal (default), uniform, triangular, exponential, gamma, Weibull, Laplace or Pearson distribution.

The assembly definition creates an empty CAD model which represents the assembly. The sequence of assembly, represented by a tree structure, has to be defined by using the source components into the correct position of the assembly tree. Afterwards the assembly operations have to be specified by the selection of the mating features that are involved in each operation. Except for the first component of the assembly, the assembly operation has to be defined for each component which will be constrained to the target features of the components inserted before it in the tree. The constraint scheme can be isostatic, but also under or overconstrained.

The measurement definition specifies the geometric relationship that is to be put under control in the assembly or in the single part. EM-TolMate supports various types of measurements: linear distance, angle, clearance, virtual size.

The built model is simulated according to Monte Carlo technique in a statistical approach. EM-TolMate determines simulation order for each feature on each component, the tolerance priority order and the tolerance degree of control (i.e. the degrees of freedom constrained by the tolerance on a feature). The system warns the user about any lack of completeness or ambiguity in tolerancing scheme (e.g. loops, unreferenced datums). Based on this information, eM-TolMate uses random numbers to create several sets of feature variations from nominal geometry, according to the specified tolerances. The simulations (one for each set of variations) proceed based on the mating features specified by the user and components are assembled into position relative to each other. Finally, measurements of the actual assembly are performed and the results are stored in memory. Worst-case limits can be estimated when the sample size of simulations are big enough and setting the estimated limits to "Actual". To assure a high level of accuracy, a large number of simulations has to be carried out.

The user performs the results analysis phase interactively after the simulations are finished. There are two kinds of results: the variation analysis, which computes statistical parameters and reports the overall variation range for each measurement, and the contributors analysis, which determines the sources of variation and presents this information in a sorted list. The user may view the results analysis on the screen or output the information to a file in various file formats.

5. The proposed method

Concurrent Engineering imposes that the design of the manufacturing and the assembly jigs, of the manufacturing and assembly cycles, be in the same time of the product design. In fact, only the concurrent design of the final product, of the single components, of the manufacturing processes and jigs, of the assembly cycle and jigs and of the inspection procedures assures to achieve a high quality with the smallest costs.

The proposed method adapts the steps of the tolerance analysis process suggested by the eM-TolMate® package and described in the previous paragraph to the case of an assembly involving non-rigid freeform surfaces in composite material. It is constituted by the following 7 steps:

- a. *Verify the stiffness of the assembly components.* Non-rigid parts may be subjected to significant distortion after the removal of manufacturing forces. This condition, known as free state variation, is principally due to weight and flexibility of the parts and the release of internal stresses resulting from fabrication. This distortion is acceptable if the part surfaces remain within the indicated tolerances, once the part is coupled to another part of the final product by applying reasonable forces. Therefore, the first step of the proposed method is to analyse the internal stress and the relative strain of each assembly components due to the assembly sequence, since those components have freeform surfaces of a small thickness in composite material. This means to simulate the assembly configuration of each assembly components through a fixturing equipment on a coordinate measuring machine and, then to measure the displacements from the nominal configuration represented by the CAD model through an inspection process. This is true if the effect of the inspection process on the measured deviation is indeed non significant and this hypothesis needs to be verified. The displacements between the real part and the nominal one, obtained in the inspection process, may be used as input values for a structural numerical analysis with the objective to obtain the stress and strain fields induced in the material when the part is assembled in the final product. The numerical analysis may be carried out with a Finite Element Method®, but before implementing the real case simulation, an assessment of the software capability on composite material is required through a simple 2D case study. If the results of the numerical analysis demonstrate that the deformations induced by the assembly sequence are at least of an order of magnitude smaller than the applied tolerances, the part may be considered rigid and the models or software of the traditional tolerance analysis literature may be applied. In this way the complexity to consider the compliant of the assembly components may be avoided.
- b. *Design the measurements of the assembly.* A first analysis of the assembly working allows to identify all the functional requirements that the product should perform. This means translating the functionality of the design assembly in all the couplings or kinematic constraints among assembly components that are needed for the assembly to work correctly. Then, the pairs of assembly components involved in each functional requirements are defined. The features of each pair of components, that are involved in each functional requirement, are identified and are generally assigned to them a set of tolerances. Therefore, the functional requirements and the assembly constraints are translated into measurement of the assembly, while the coupling parts and their feature are passed to the following step of the method. A widespread measurement in aeronautic field is the distribution of the minimum distances along two faced freeform surfaces, e.g. when the adhesive thickness between the faced parts to connect should be as constant as possible in order to obtain an efficient structural connection and to avoid local compressions at the interface of faced parts due to strong reduction of thickness. In this case it has been demonstrated that the minimum distance among the two patterns of points, belonging to the two faced surfaces, calculated by projecting the point to point distance along the direction perpendicular to the nominal surfaces is very

- near to the minimum distance and it is easy to calculate by eM-TolMate® (Polini et al., 2007).
- c. *Define the features of the assembly components, specify the tolerances and the related statistical distribution.* The features of the coupling parts of the assembly may be free-form surfaces or basic surfaces. The free-form surfaces of each assembly components have to be schematically represented by a set of control points. The number and distribution of the control points depends by the slope of the free form surface. If two freeform surfaces are faced, the pattern of control points of the second surface may be obtained by intersecting the second surface with the pattern of vectors, that are normal to the first surface in each control point. The tolerances applied to the freeform surface should be applied to each control point defined on the surface. The basic surfaces are plane, pin, hole, point, tab, slot, constant profile surface, constant cross section, sphere, surface of revolution, general 3D surface, edge features and derived features. Dimensional tolerancing is supported as +/- tolerances (symmetric or not, sizes or distance from an origin feature) and for size tolerances of pins, holes, slots and tabs. Tolerance attributes can be freely modified to reflect effectively the parameters of actual features. The most common attribute is the tolerance probability density function for each tolerance applied to each feature of the assembly component. The probability density function depends by the manufacturing process of the feature and it is generally hardly to estimate. Therefore, the default distribution is assumed to be the Gaussian, since it is symmetric, it is simply to use and it is well known by the literature. However, it is always to change it. Finally, it is needed to verify the datum reference frames (DRFs), the assembly should have its DRF, that is generally considered "global"; while each component should have its DRF, that is considered "local". Moreover, the elements (planes, axes and so on) that constitute a local DRF should be easily identified, manufactured with the design specifications and accessible for verification. The elements of the local DRFs should be qualified by tolerances. The elements of the local DRFs should be used to manufacture, to assembly and to control the assembly components. These simple rules on the definition of the DRFs allow to obtain whose components may be manufactured, assembled and controlled. Obviously, they have to be applied by means of a concurrent approach that is implemented by a designer of product, by a planner of manufacturing processes, by a designer of assembly cycles and by a designer of inspection processes.
- d. *Design the assembly cycle and jigs.* If required, the assembly jigs should be designed at first. The assembly jigs should have a plane and two pins in order to locate and fix the coupling component. The tooling hole (TH) system is the assembly system that is widespread in aeronautic field and consists in jigs mated with the assembly components by means of pins that are inserted into tooling holes (TH) located on the assembly components. The tolerances of the TH are very critical, since they influence the location and orientation among the different components of the assembly and, therefore, the functional requirements of the assembly. Some suggestions to choice the tolerances of a TH may be found in (Marziale & Polini, 2007). The positioning of a component on its jig is made by the contact of two planar surfaces (one on the part and one on the assembly jig) and the clearance fit between two Tooling Holes (positioned on the part) with the corresponding pins (positioned on the assembly jig), as shown in Fig. 1. The position of the THs has an important role in order to limit the flag waving effect

of the component as regards its assembly jig, since a small change in THs position cause a great variation in the location and the orientation of the part on the corresponding jig due to the large dimensions of the parts. Therefore, the distance among the tooling holes must be as larger as the dimensions of the part increases, but this condition is difficult to achieve in some practical cases. Another important consideration is that it is preferred to position the THs out of the part shape, on appendixes that will be trimmed once the part is assembled, in order to have lower production costs. Through these considerations an assembly jig has to be designed for each part. Each assembly jig has a set of tolerances, since it is realised by manufacturing processes.

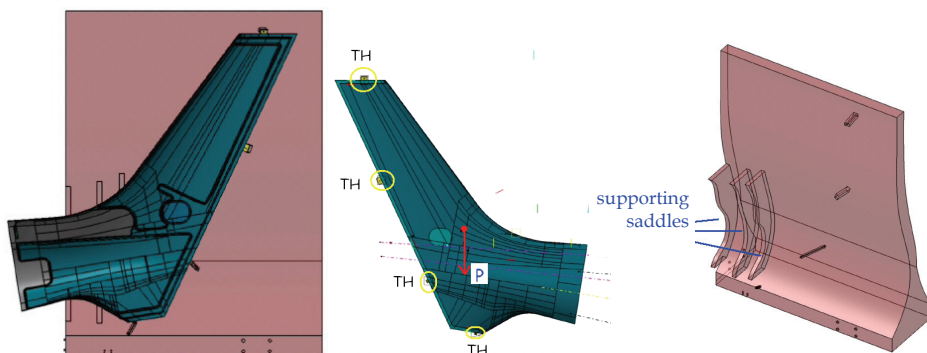


Fig. 1. Aircraft skin's jig with tooling hole system

The design of the assembly cycle foresees as first step the location of each component on its designed jig. Each component has micro-movements respect to its jig due to the tolerances of the jig and of the component applied to the coupling system, i.e. to the TH system. These micro-movements influence the positioning of the part and, therefore, they have to be characterized by means of probability density function, such as done for tolerances of the parts. The probability density function depends by the manufacturing process of the jig and the component and by the assembly constraints. It is generally hardly to estimate, since it should involve many experimental tests. The default probability density function is the Gaussian. Therefore, each couple of components is assembled by moving near the related jigs and, then, by putting the constrain elements, such as adhesive, bolts or screws. In this way a sub-assembly more and more complex is generated up to obtain the final product. The positioning of the components and, therefore, the accuracy of the final product, depends by the stack-up function of dimensions and tolerances belonging to the components and to the jigs.

- e. *Choose the simulation runs and carry out simulations.* Monte Carlo simulation has been used to reproduce the combined effect of all the assigned tolerances and the component degrees of freedom respect the assembly jigs on the assembly functional requirements. The assigned tolerances and the component degrees of freedom have been simulated by means of the probability density functions assigned in the previous steps. The number of runs of simulation has been fixed at the value for which the estimated mean and standard deviation of the obtained probability density function of each functional requirement achieve an asymptotic trend. A step by step procedure has been adopted to evaluate the simulation runs, the starting value has been 10000 runs.

- f. *Analyse the results.* During the assembly simulation, the results of the measurement calculations are stored in memory. When the assembly simulation is finished, a table containing all the measurement results remains in memory. These results may be exported to make statistical analysis. It is possible to evaluate the distribution of the results of each measurement and, therefore, to calculate the percentage of parts outside the tolerance ranges. Another possibility is to evaluate the reasonable tolerance range to assign to each measuring by starting from its estimated distribution in order to satisfy the tolerance analysis. Finally, a sensitivity analysis may be carried out in order to identify the tolerances mainly affecting each gap trend. The percentage weight of each tolerance has been calculated by evaluating the variance of a measurement σ_{TOT} , when all the tolerances are applied to assembly's components, and the variance of the same measurement σ_{TOT-Ti} once i -th tolerance is not applied to the assembly's components:

$$C_i = \frac{\sigma_{TOT}^2 - \sigma_{TOT-Ti}^2}{\sigma_{TOT}^2} [\%] \quad (2)$$

6. Application example

6.1 Case study

The proposed approach has been carried out considering as case study an aeronautical component. This is a winch arm mounted on an helicopter (see Fig. 2). The winch arm is the external unit that allows the helicopter to rescue people or things where it is impossible to land through a rope lowered by an electrical motor.

The winch arm have a main arm and a head covered by three thin fairings.

On the main arm (the part with number 1 in Fig. 3a) are assembled two frames (the yellow parts 5 and 6 in Fig. 3a) that are two cambered elements connecting and supporting all the structure. The parts with number 5 and 6 in Fig. 3a are the forward and the after internal frames that allow to mount the fairing covers of the head (parts 3 and 4 in Fig. 3a) of the winch arm directly on its structural beam. Finally, the Mid Cowling (part 2 in Fig. 3a) is the central exterior fairing that covers the head of the winch arm. The part 7 in Fig. 3a is a cover for the overhaul of the winch arm. All the components of the winch arm assembly are made in carbon fiber composite material. Both of the frames are made with five layers of carbon fibers imbued in a matrix of epoxy resin for a total stack thickness of 1,65 mm. The carbon fibers are oriented in a $\pm 45^\circ$ alternated arrangement within a steel cast which reproduces the part. After the stratification process, a curing process is carried out by autoclave with a control of temperature and pressure. The obtained part has size of 300 mm x 400 mm x 500 mm.

The weight of each part is about 350g. Assembly operations among the parts are done using of special grub screws that are inserted in the holes of each component. No adhesives or resins are used to secure the surfaces, since a perfect adhesion is not required.

Even if the form of the frame may appear simple, the shapes of its surfaces aren't regular. The After Frame is coupled to a metallic part, called Box Support, that allows to fix the engine of the winch arm (see Fig. 3b).

Each part has three datum planes as component references. Those planes are external to the part geometry, as shown in Fig. 4 for the Mid Cowling (dimensions and tolerances are not

reported in this chapter, since they are reserved). The nominal location and tolerances of coupling holes are defined as regards to this external reference frame. Profile tolerances are defined as general requirements for the whole assembly by the manufacturer. The value declared is ± 0.75 mm. In this case form errors may have effect on the airflow around the head of the winch arm.

Furthermore, the parts may have a significant geometric distortion after removal of the forces applied during fabrication. This is a characteristic of composite laminates and occurs as soon as the stratification cast is removed. This is due to its low thickness, weight, flexibility and to the release of internal stresses resulting from the manufacturing processes. When the manufacturing process is completed all the references to the nominal configuration are lost. In order to re-obtain the nominal shape it is necessary to apply forces able to win the elastic recovery of the part. This problem is present during the assembly of the Mid Cowling with its mating components.

Further applications of the proposed method may be found in (Polini et al., 2007; Marziale & Polini, 2008).



Fig. 2. a) winch arm mounted on the helicopter, b) 3D model of winch arm

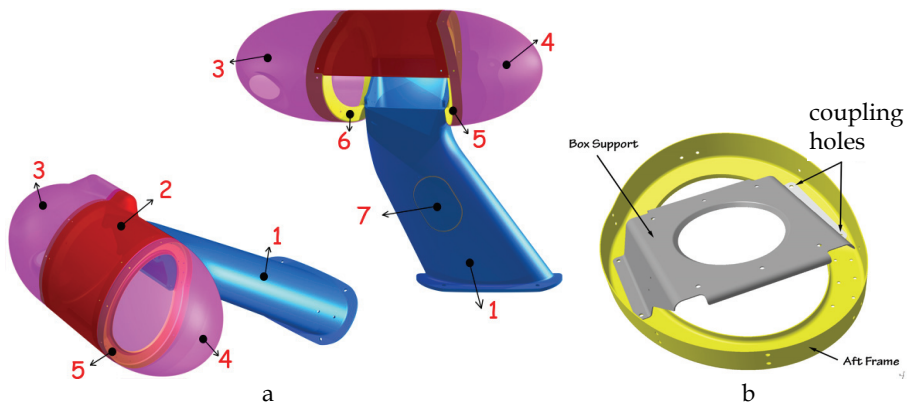


Fig. 3. a) Components of winch arm: 1-Hoist Mount, 2-Mid Cowling, 3-After Cowling, 4-Forward Cowling, 5-Forward Frame, 6-After Frame, 7-Cover; b) Coupling of the After Frame with the Box Support

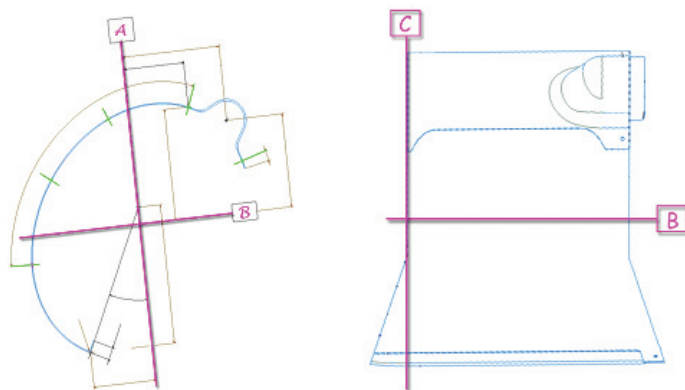


Fig. 4. Datum planes of the Mid Cowling

6.2 Verify the stiffness of the assembly components

For example the procedure has been applied to the Mid Cowling, but the same should be applied to all the components of the winch arm. To be inspected, the Mid Cowling has to be mounted on a fixturing equipment that reproduces its assembly positions, see Fig. 5. Because it is joined to after and forward frames by means of special grub screws that are inserted in each component holes, the fixturing equipment has to reproduce the position of these coupling holes. Therefore, the fixturing equipment has to reproduce the three reference planes A, B and C in Fig. 4. The part may be connected to the equipment through pins with cone-shape heads that couple with the part holes and through blocking elements such as c-shaped clamps and springs. The pins allow to accurately locate the part holes inside the CMM working volume. Finally, to spatially orientate the elements of the equipment, ball-and-socket joints may be used. All the details on the design of the fixturing equipment may be found in (Ascione & Polini, 2010).

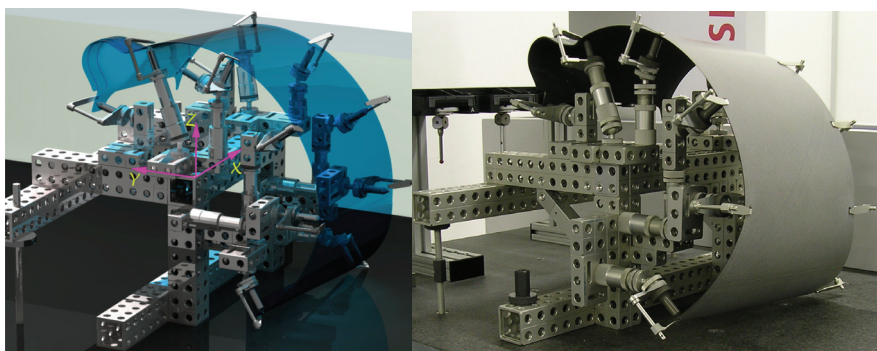


Fig. 5. Fixturing equipment of the Mid Cowling

Five different patches have been defined on the Mid Cowling (see Fig. 6). Each has been measured by continuous scanning along path $\pi/4$ rad tilted. The distance between two following scanning lines was set to 2 mm; thus, involving 10000 points acquired on each patch.

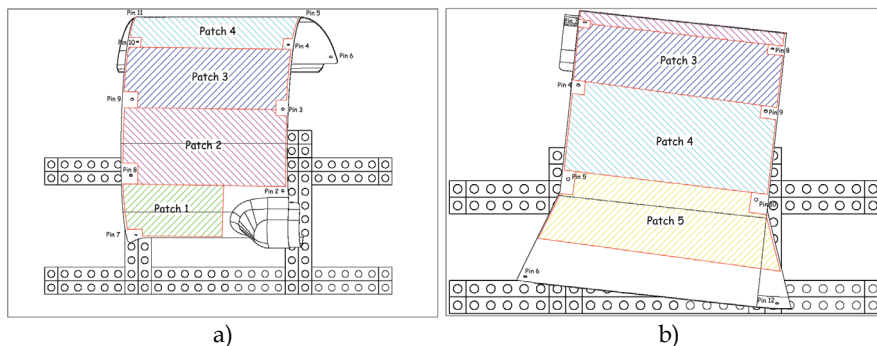


Fig. 6. Detected scan patches; a) top view; b) front view

The force of 0.1N applied by CMM probe to the non-rigid freeform surface of the Mid Cowling does not produce a significant deformation. In fact, the maximum deviation is equal to $0.35\text{ }\mu\text{m}$ as shown in (Moroni et al., 2007), while typical value of profile tolerance in this kind of application is around $50\text{ }\mu\text{m}$.

The deviation along the normal curvature of the surface of the part was calculated for each acquired point. The distribution of the deviations on the surface represents the overall error of shape. Such a value may be seen as the sum of three different contributions; the first due to component production process; the second due to the assemblage of the part and the third due to the measuring procedure. The deviation was calculated for each acquired point with Holos® measuring software.

The data analysis has been performed on each patch extracted from the Mid Cowling. From the analysis of distance colour maps it is possible to observe that no systematic behaviour of the deviations is present (see Fig. 7).

To estimate the repeatability of the measuring procedure, the scanning on the 5 patches was repeated 5 times, maintaining the same Mid Cowling coupling position on the equipment. Therefore, the inspecting procedure may be considered the only responsible of variability of the measuring results. Then, the average deviation was calculated for each of the 50000 measuring points. Finally, the difference between each measurement point and the average deviation was calculated. The values thus calculated were distributed according to a Gaussian probability density function, as verified with the Anderson-Darling statistic test ($p\text{-value} > 0.1$).

The value of the overall repeatability of the measuring process, that has been calculated as the standard deviation of the sample of 250000 values, is equal to $8.5\text{ }\mu\text{m}$. This value is very small; this means to say that the effect of the inspection process on the measured deviation is indeed non significant.

The idea introduced in this work is that the displacement between the real part and the nominal one, obtained in the inspection process, may be used as input values for a structural numerical analysis with the objective to obtain the stress and strain fields induced in the material when the part is assembled in the final product. That is possible because the measured field of displacement represent the real configuration of the component in its assembly state. The inspection process simulate the assembly configuration of the real part; therefore, the measured displacements are the differences from the real part, assembled on the winch arm, and its nominal configuration represented by the CAD model. The measured displacements have been used as loads applied on the components in its nominal

configuration for the numerical simulation. In this way the results of the structural analysis are characteristic values of the assembled parts, since the assembly process locks the components of the assembly in the same way the assembly is bounded in the inspection process and in the numerical simulation. The numerical analysis has been carried out with the MSC_Patran/Nastran® software but, before implementing the real case simulation, an assessment of its capability on composite material has been required to obtain a validation of the results for our case. In this sense a matching procedure between experimental results and numerical results on the same material in the same configuration has been necessary.

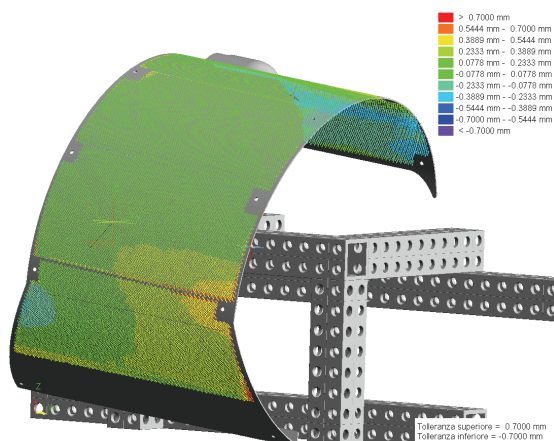


Fig. 7. Chromatic mapping of the deviations between measured points and nominal geometry

Having available experimental results for a tensile test on the composite material constituting the Mid Cowling, the matching procedure has been carried out by simulating the same test mean the numerical software and then comparing the obtained values with the correspondents of experimental test. All the details of the tensile test are reported in (Ascione & Polini, 2010). Fig. 8 shows in blue the stress-strain curve obtained from the analysis for the first node of the mesh (the node at the intersection of the two plane of symmetry) and in green the stress-strain curve for the experimental test. It is possible to see that the results obtainable with the used numerical software on the considered material are reliable.

The same procedure used to simulate the tensile test has been performed to model the Mid Cowling. In Fig. 9 it is possible to see the finite element representation of the Mid Cowling, where triangular shell elements have been used to replace the continuous geometry. In this case triangular elements have been used, since this kind of elements is the best approximation of the distribution of the displacements measured through the inspection process. In Fig. 9 there are green and light blue elements, since the green elements represent the part's geometry, while the light blue elements represent the points where the displacement has been applied. Further details on the setting of the numerical analysis are deeply described in (Ascione & Polini, 2010).

The results of this simulation have been the stress and strain fields induced in the Mid Cowling subjected to the loads explained above. The strain field is showed in Fig. 10. The values of the strain showed in these results are congruent as magnitude with those ones of

the tensile test and with the values of the displacements imposed as loads. Therefore, it is possible to consider the obtained values representative of the real state of the component in its real configuration of assembly. The maximum value of the strain field is about $7.28 \mu\text{m}$ that is very smaller than the applied tolerances. Therefore, the Mid Cowling may be considered as a rigid part for the tolerance analysis.

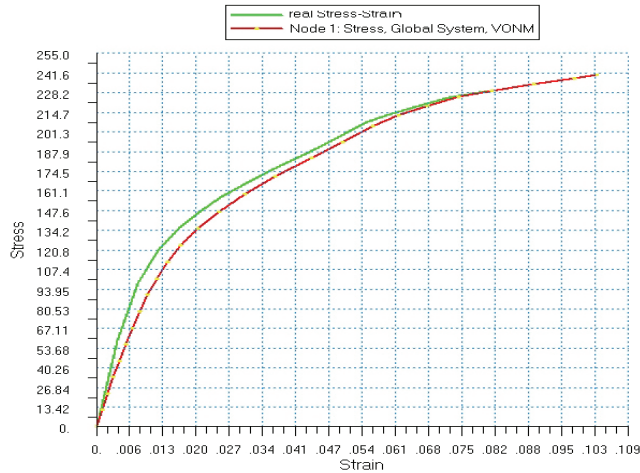


Fig. 8. Stress-strain diagram with green curve for the experimental test and with red curve for the numerical results

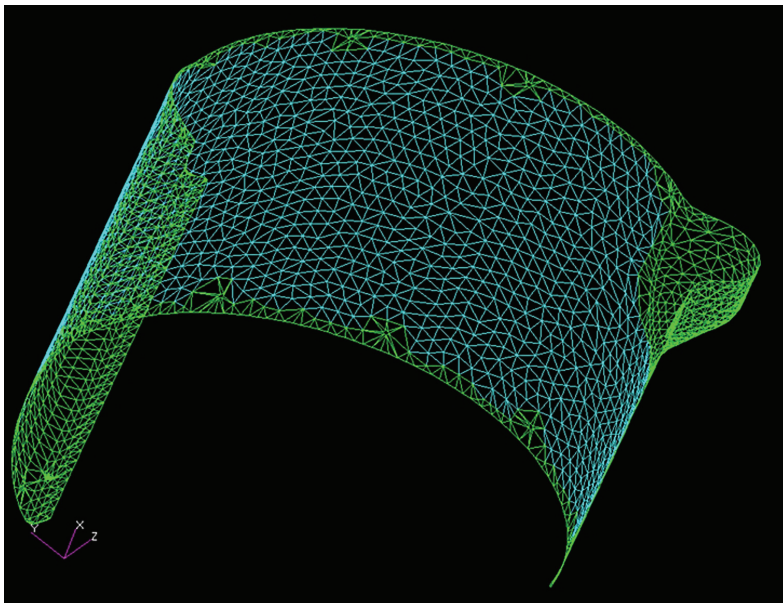


Fig. 9. FEM model used to simulate the Mid Cowling

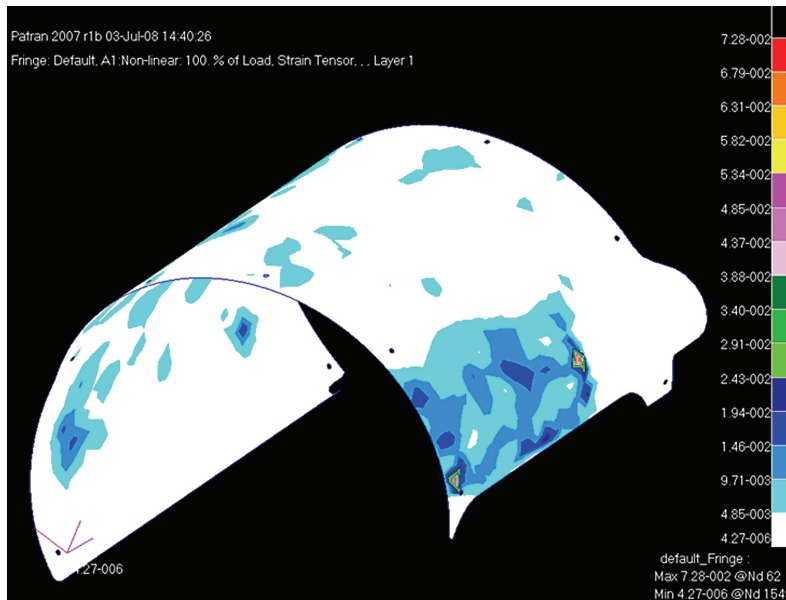


Fig. 10. Strain field resulting from the FEM Analysis of the Mid-Cowling.

6.3 Design the measurements of the assembly

The effect of the deviations when the After Frame is positioned on the Hoist Mount and the Box Support is positioned on the After Frame cause a change in the position of the Box Support as regards the nominal one. Therefore, the axis of the engine of the winch arm, that is positioned at the centre of the hole of the Box Support, may deviate from the nominal position and this deviation may invalidate the right working of the engine. The evaluation of the deviation of the axis of the engine from the nominal position is the first measurement of the assembly. It has been evaluated on the plane of the coupling of the engine with the Box Support along the two axes of the Datum Reference Frame of the Box Support (see Fig. 11).

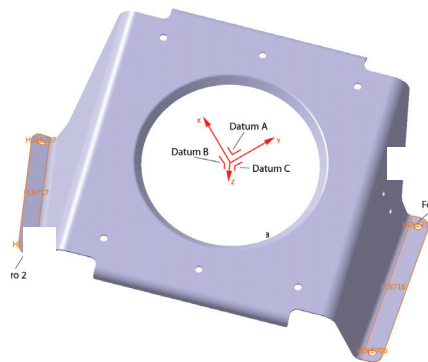


Fig. 11. Datum Reference Frame of the Box Support

The effect of the deviations, when the After Frame is positioned on the Hoist Mount and the After Cowling is positioned on the After Frame, cause a change in the orientation of the After Cowling as regards the nominal one. The aerodynamic drag of the After Cowling depends by the angle of incidence the air rush on the Cowling itself. Therefore, the deviation in the orientation of the After Cowling may invalidate the right working of the winch arm. The evaluation of the deviation of the orientation of the After Cowling from the nominal is the second measurement of the assembly. It has been evaluated as the two translational motions of the centre of the ellipse along the two axis of the Datum Reference Frame of the After Cowling and the three rotations of the axis of the Cowling as regards the nominal position measured in the Datum Reference Frame of the After Cowling. The same reasoning may be repeated for the Forward Cowling.

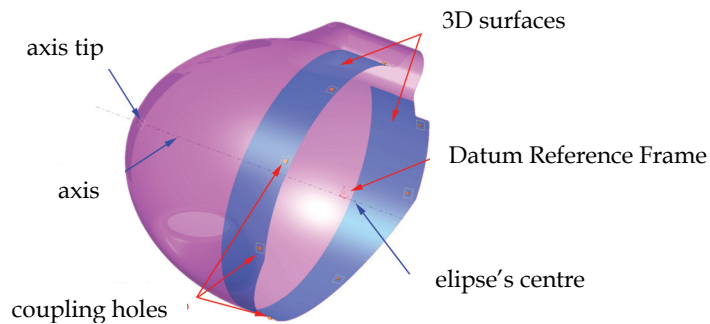


Fig. 12. Features and Datum Reference Frame of the After Cowling

6.4 Define the features of the assembly components, specify the tolerances and the related statistical distribution

The features of the Hoist Mount are the two planes and the two patterns of six holes that allow to couple the part with the After and Forward Frame. The holes have a dimensional tolerance of ± 0.25 mm. The Y-axis of the Datum Reference Frame passes from the centre of the holes 1 and 2 of the pattern that allows to couple the After Frame, as shown in Fig. 13 on the left. The Z-axis is perpendicular to the coupling plane with the After Frame and the X-axis is perpendicular to ZY plane. The origin is in the centre of the hole 2 of the pattern projected on the coupling plane.

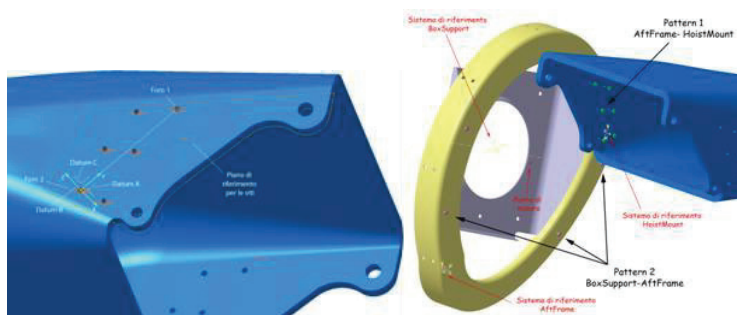


Fig. 13. Features and Datum Reference Frame of the Hoist Mount

The features of the After Frame are the pattern 1 of six holes that couples the part with the Hoist Mount and the pattern 2 of four holes that couples the part with the Box Support, as shown in Fig. 14. The X-axis of the Datum Reference Frames is due to the intersection of the two planes containing the two patterns. The Z-axis is perpendicular to the plane that contains the pattern 1 and that mates the Hoist Mount. The Y-axis is perpendicular to ZY plane. The origin is due to the intersection of the X-axis with the cylindrical surface on the side of the After Frame. Moreover, there are two further patterns of six and eight holes on the lateral cylindrical surface for the coupling with the Mid Cowling and the After Cowling (see Fig. 15). All the holes have a dimensional tolerance of ± 0.25 mm. To the lateral cylindrical surface a profile tolerance of 0.076 mm and a dimensional tolerance to the thickness of ± 0.10 mm are applied, as shown in Fig. 16.

The same features and the same datum reference frame may be found in the Forward Frame.

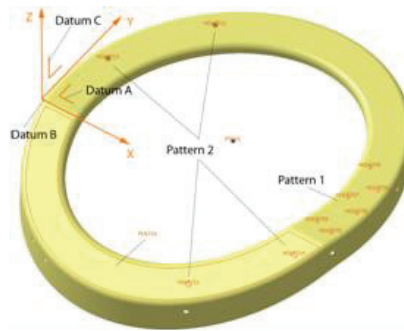


Fig. 14. Features and Datum Reference Frame of the After Frame

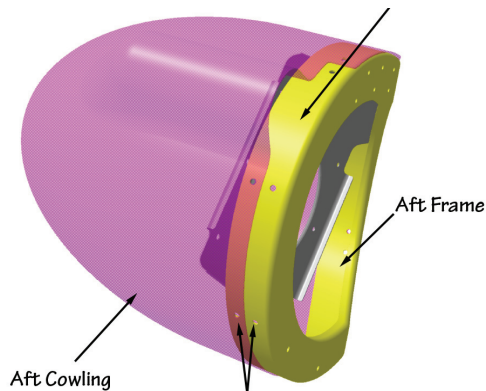


Fig. 15. Coupling of the After Frame with the After Cowling

The features of the Box Support are constituted by a pattern of four holes that allows to couple the After Frame, the central hole where the axis of the engine of the winch arm is fitted and the pattern of six holes that allows to fix the engine (see Fig. 11). The central hole and the pattern of six holes lie on the same plane. The pattern of four holes lies on a plane

that mates with the plane of the After Frame. The Z-axis of the Datum Reference Frame is perpendicular to the plane where the central hole lies. The origin is the centre of the hole to fit the engine. The X-axis connects the origin with the centre of one hole of the pattern to fix the engine. The holes of the patterns have a dimensional tolerance of ± 0.25 mm.

The After Cowling is constituted by a cylindrical surface, that is signed in blue in Fig. 12, where there is a pattern of eight holes for coupling it to the After Frame. To this surface a profile tolerance of 0.076 mm is applied, while its thickness has a dimensional tolerance of ± 0.10 mm (see Fig. 16). Moreover, it has an elliptical surface, that is signed in pink in Fig. 12, with aerodynamic properties. The Datum Reference Frame is located in the centre of the ellipse that generates the cylindrical surface for coupling with the After Frame. The Y-axis is parallel to the largest axis and the X-axis is parallel to the smallest axis of the ellipse. The Z-axis is perpendicular to YX plane with a positive orientation outside the material. The origin is in the centre of the ellipse.

The same features and the same datum reference frame may be found in the Forward Cowling.

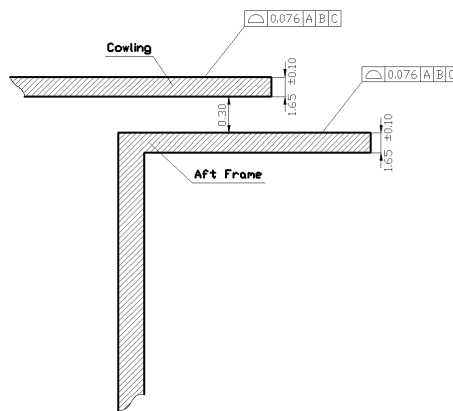


Fig. 16. Tolerances applied to the coupling surfaces of the After Frame and the After Cowling

The applied tolerances have been considered distributed as a Gaussian probability density function, whose parameters (mean and standard deviation) have been estimated as the nominal value of the surface property and one third of the applied tolerance range respectively.

6.5 Design the assembly cycle and jigs

After the curing process, the patterns of holes are manually made by means of a brace and bit with the help of a mask that is placed on the part as guide. Therefore, the After Frame is coupled with the Host Mount by means of special grub screws that are inserted in the holes of each component, as shown in Fig. 17 on the left. No adhesives or resins are used to secure the surfaces, since a perfect adhesion is not required. The Box Support is coupled to the obtained sub-assembly, as shown in Figure 17 in the middle. Finally, the Frames (Forward and Cowlings) are coupled, as shown in Fig. 17 in the middle and on the right. No jigs have been used, since the assembly is small and it is manually caught.

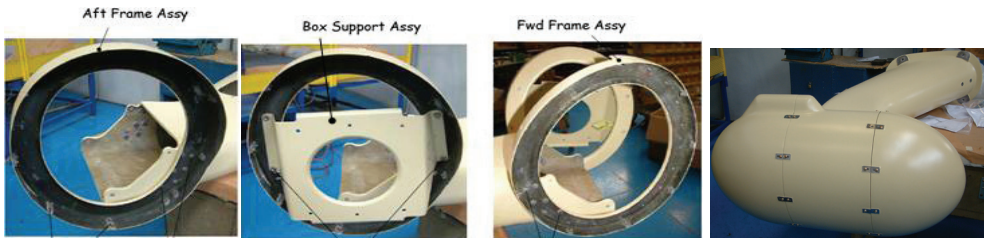


Fig. 17. Assembly cycle of the winch arm

6.6 Choose the simulation runs, carry out simulations and analyze the results

Monte Carlo simulation has allowed to perturb dimensions and geometry of the winch arm components inside the tolerance ranges in order to give the statistical distribution of the deviations of the axis of the engine and of the orientation of the After Cowling. Monte Carlo simulation has been carried out by a well-known Computer Aided Tolerance software, eM-Tolmate of UGS®. The number of runs of simulation has been fixed at 200000, once many tests have been carried out, since this value guarantees a stable estimation of the mean and the standard deviation of the probability distribution characterising the two measurements.

The deviation of the axis of the engine follows an estimated probability density function near to Gaussian along the considered X and Y-axes, as shown in Fig. 18 and Fig. 19. The estimated mean is equal to -0.0005 mm along the X-axis and 0.000 mm along the Y-axis, while the estimated standard deviation is equal to 0.251 mm along the X-axis and 0.294 mm along the Y-axis. Therefore, the axis of the engine may range between -0.88 mm and +0.88 mm (i.e. $\pm 3\sigma$) that include 99.73% of the obtained Gaussian distribution. This range does not significantly influence the right working of the engine.

The deviation of the orientation of the After Cowling has been evaluated as the three translational motions (ΔX , ΔY and ΔZ) of the centre of the ellipse along the three axis of the DRF of the After Cowling and the three rotations ($\Delta\alpha$, $\Delta\beta$ and $\Delta\gamma$) of the axis of the Cowling around the three axes of the DRF of the After Cowling. The three translations and the three rotations follow an estimated probability density function that may be considered Gaussian, as shown in Fig. 20 and in Fig. 21. Table 1 shows the mean and standard deviation that have been estimated for the obtained probability density functions.

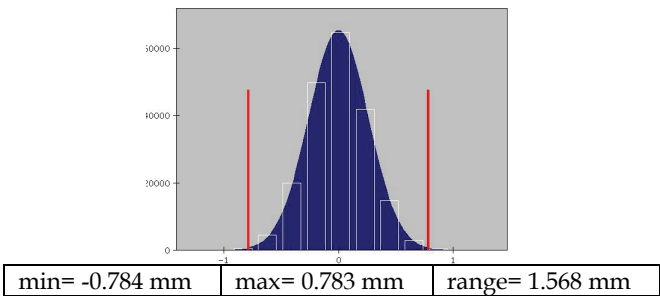


Fig. 18. Probability density function of the deviation of the axis of the engine along the X-axis of the DRF belonging to the Box Support

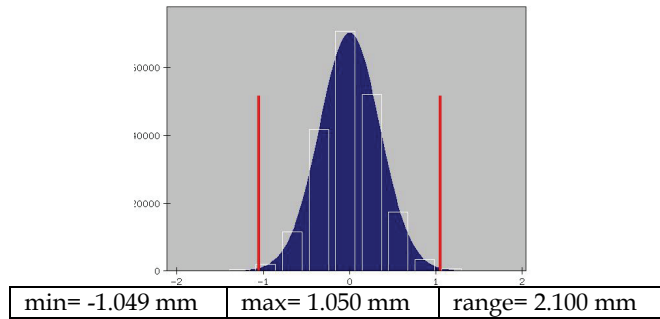


Fig. 19. Probability density function of the deviation of the axis of the engine along the Y-axis of the DRF belonging to the Box Support

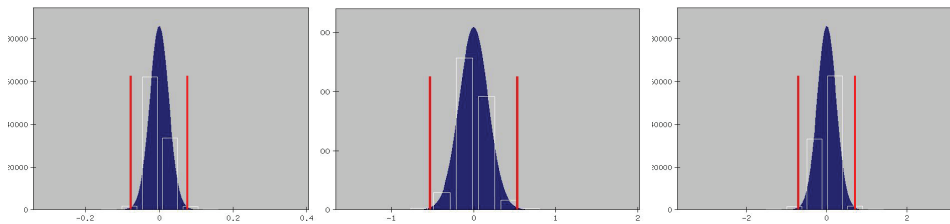


Fig. 20. Probability density function of the three translations motions of the centre of the ellipse of the After Cowling along the three axes of its DRF: X-axis on the left, Y-axis in the middle and z-axis on the right

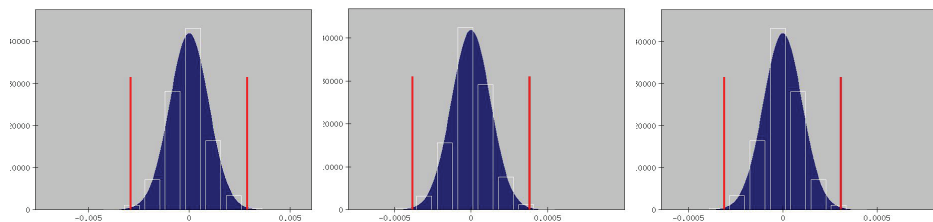


Fig. 21. Probability density function of the three rotations of the axis of the After Cowling around the three axes of its DRF: X-axis on the left, Y-axis in the middle and Z-axis on the right

The obtained results underline that the After Cowling may significantly translate along the largest axis of the ellipse (Y-axis) of about ± 0.531 mm and along the axis perpendicular to the plane of coupling of the After Cowling with the After Frame (Z-axis) of about ± 0.709 mm, while the translation along the X-axis is negligible. Moreover, the After Cowling may significantly rotate around the Z of about ± 0.724 radians, while the rotations around X and Y axes are negligible. This is due to the coupling of the After Cowling with the After Frame by means of the screws that get into the holes of the parts with a certain clearance.

Measurements of the After Cowling	nominal value	mean	standard deviation (σ)	3σ
ΔX [mm]	0.0000	0.0001	0.0256	0.0768
ΔY [mm]	0.0000	-0.0007	0.1771	0.5313
ΔZ [mm]	0.0000	-0.0005	0.2364	0.7092
$\Delta\alpha$ [rad]	0.0000	0.0000	0.0010	0.0030
$\Delta\beta$ [rad]	0.0000	0.0000	0.0010	0.0030
$\Delta\gamma$ [rad]	0.0000	-0.0005	0.2414	0.7242

Table 1. Estimated parameters of the probability density function of the After Cowling

7. Conclusion

The present work deals with the tolerance analysis of freeform surfaces belonging to parts in composite material and that may be non-rigid. This chapter presents a method to carry out the tolerance analysis of an assembly involving free-form surfaces in composite material by using a commercial CAT software. The great effort of the present work is overcome the limits of the CAT software to deal with dimensional and geometric tolerances applied to free form surfaces in composite material. The proposed method is constituted by seven steps. The first one verifies the stiffness of the assembly components by means of Finite Element Method® in order to evaluate the possibility to apply the tolerance analysis models developed for rigid assemblies. The second step designs the measurements of the assembly; the third defines the features of the assembly components; the fourth specifies the tolerances and the related statistical distribution; the fifth designs the assembly cycle and jigs; the sixth chooses the simulation runs and carry out simulations and the seventh analyses the results. The method has been applied to the winch arm mounted on an helicopter. All the components of the winch arm assembly are made in carbon fiber composite material. Assembly operations among the parts are done through special screws that are inserted in the holes of each component. No adhesives or resins are used to secure the surfaces, since a perfect adhesion is not required. The method has allowed to verify some functional requirements of the winch arm. In particular, it has verified that the applied tolerances do not compromise significantly the assembly of the engine to rescue people or things. Moreover, it has underlined the possible changes in the Cowlings' orientation and location that may modify the aerodynamic performances of the winch arm.

8. References

- Ameta, G., Davidson, J.K. & Shah, J.J. (2007). Influence of form on Frequency Distribution for 1-D clearance which is generated from Tolerance-Maps, *Proceedings of 10th CIRP Conference on Computer Aided Tolerancing*, ISBN/ISSN: 978-3-8322-6036-1, Erlangen, Germany, March 21st-23rd
- Ascione, R. & Polini, W. (2010). Measurement of nonrigid freeform surfaces by coordinate measuring machine, *The International Journal of Advanced Manufacturing Technology*, Vol. 51, No. 10, 1055-1067, doi: 10.1007/s00170-010-2684-5

- ASME Standard. (1994). *Dimensioning and tolerancing*, ASME Y14.5M, American Society of Mechanical Engineering, New York.
- Ballot, E. & Bourdet, P. (1997). A computational method for the consequences of geometric errors in mechanisms, *Proceedings of the 5th CIRP Seminar on Computer Aided Tolerancing*, April 27-29, Toronto, Canada.
- Bihlmaier, B.F. (1999). *Tolerance Analysis of Flexible Assemblies using Finite Element and Spectral Analysis*, MS Thesis, Brigham Young University, Provo, Utah
- Boyer, M. & Stewart, N.F. (1991). Modeling spaces for toleranced objects, *Int. Journal of Robotics Research*, Vol.10, No.5, 470-582.
- Chase, K.W., Gao, J. & Magleby, S.P. (1995). General 2-D tolerance analysis of mechanical assemblies with small kinematic adjustments, *J Des Manuf*, Vol. 5, 263-274
- Chase, K.W., Gao, J., Magleby, S.P. & Sorensen, C.P. (1996). Including geometric feature variations in tolerance analysis of mechanical assemblies, *IIE Trans*, Vol. 28, 795-807
- Chase, K.W., Gao, J. & Magleby, S.P. (1997a). Tolerance analysis of 2-and 3D mechanical assemblies with small kinematic adjustments, In: *Advanced Tolerancing Techniques*, Zhang H.C., (Ed.), 103-138, Wiley, ISBN 978-0-471-14594-3, New York
- Chase, K.W., Magleby, S.P. & Glancy, C.G. (1997b). A compressive system for Computer-Aided Tolerance Analysis of 2-D and 3-D Mechanical Assemblies, *Proc. of the 5th Int. CIRP Seminar on Computer-Aided Tolerancing*, April 27-29, Toronto, Canada.
- Clément, A., Rivière, A. & Temmerman, M. (1994). *Cotation tridimensionnelle des systèmes mécaniques, théorie & pratique*, PYS, ISBN 2-85330-132-X, Ivry-Sur-Seine, France.
- Clément, A., Rivière, A., Serré, P. & Valade, C. (1998). The TTRSs: 13 Constraints for Dimensioning and Tolerancing, In: *Geometric design tolerancing: theories, standards and applications*, ElMaraghy H.A., (Ed.), 122-131, ISBN 978-0-412-83000-6, Chapman & Hall, London.
- Creveling, C.M. (1997). *Tolerance Design*, Addison-Wesley, ISBN 0201634732, Boston.
- Davidson, J.K., Mujezinovic, A. & Shah, J.J. (2002). A new mathematical model for geometric tolerances as applied to round faces, *ASME Trans, J Mech Des*, Vol. 124, 609-622
- Delchambre, A. (1996). *CAD Method for Industrial Assembly. Concurrent Design of Product, Equipment and Control Systems*, Wiley, ISBN 978-0-471-96261-8, New York
- Francavilla, A. & Zienkiewicz, O. (1975). A Note on Numerical Computation of Elastic Contact Problems, *Int. Journal for Numerical Methods in Engineering*, Vol. 9, 913-924
- Gordis, J. & Flannelly, W. (1994). Analysis of stress due to fastener tolerance in assembled components, *AIAA Journal*, Vol. 32, No. 12, 2440-2446
- Gupta S. & Turner, J.U. (1993). Variational solid modelling for tolerance analysis; *IEEE Computer Graphics and Applications*, Vol.13, 64-74.
- Hong, Y.S. & Chang, T.C. (2002). A comprehensive review of tolerancing research. *Int. J. Prod. Res.*, Vol. 40, No. 11, (July 2002) 2425-2459
- ISO Standard, (1985). *ISO 8015: Fundamental Tolerancing Principle*
- Laperrière, L. & Lafond, P. (1999). Modelling tolerances and dispersions of mechanical assemblies using virtual joints, *Proceedings of ASME Design Engineering Technical Conferences*, ISBN 0791819671, September 12-15, Las Vegas, Nevada, USA.
- Laperrière, L. & Kabore, T. (2001). Monte Carlo simulation of tolerance synthesis equations, *Int. J. Prod. Res*, Vol. 39, 2395-2406

- Liu, S. & Hu, S. (1995). An Offset Finite Element Model and Its Applications In Predicting Sheet Metal Assembly Variation, *Int. Journal of Machine Tools and Manufacture*, Vol. 35, No. 11, 1545-1557
- Liu, S. & Hu, S. (1997). Variation Simulation for Deformable Sheet Metal Assemblies using Finite Element Methods, *Journal of Manufacturing Science and Engineering, Transactions of the ASME*, Vol. 119, No. 3, 368-374
- Luenberger, D.G. (2003). *Linear and Nonlinear Programming*, Addison-Wesley, ISBN 020115794, Boston
- Marguet, B. & Mathieu, L. (1998). Tolerancing problems for aircraft industries, In: *Geometric Design Tolerancing: Theories, Standards and Applications*, ElMaraghy H.A., (Ed.), 419-427, ISBN 978-0-412-83000-6, Chapman & Hall
- Marguet, B. & Mathieu, L. (1999). Aircraft Assembly analysis method taking into account part geometric variations, In: *Global Consistency of Tolerances*, Van Houten F. and Kals H., (Eds.), 365-374, ISBN 0-7923-5654-3, Kluwer Academic Publishers
- Martino, P.M. & Gabriele, G.A. (1989). Application of variational geometry to the analysis of mechanical tolerances, *Failure Prevention and Reliability, ASME Paper n.DE - Vol.16*, 19-27.
- Marziale, M. & Polini, W. (2007). Tooling Hole Tolerance Analysis in Aeronautic Field, *Proceedings of 10th CIRP International Seminar on CAT*, ISBN 978-3-8322-6036-1, March 21st-23rd, Erlangen, Germany
- Marziale, M. & Polini, W. (2008). Tolerance Analysis of an Aircraft Tail Beam, *Proceedings of 18th FAIM International Seminar on Flexible Automation and Intelligent Manufacturing*, 30 June - 2 July, Skovde, Sweden.
- Merkley, K. (1998). *Tolerance Analysis of Compliant Assemblies*. Ph.D Thesis, Brigham Young University, Provo, Utah
- Moroni, G., Polini, W., & Rasella, M. (2007). Non-Rigid Free Form Surface Inspection: an aeronautical composite component case study, *Proceedings of the 10th CIRP Conference on Computer Aided Tolerancing*, Erlangen, Germany, March 21-23.
- Mujezinovic, A., Davidson, J.K. & Shah, J.J. (2004). A new mathematical model for geometric tolerances as applied to polygonal faces, *ASME Trans, J Mech Des*, Vol. 126, 504-518
- Nassef, A.O. & ElMaraghy, H.A. (1996). Probabilistic Analysis of geometric tolerances. In: *Computer Aided Tolerancing*. Kimura F., (Ed.), 187-203, Chapman & Hall, London
- Nigam, S.D. & Turner, J.U. (1995). Review of statistical approaches to tolerance analysis. *Computer Aided Design*. Vol. 27, 6-15
- Ody, R., Burley, G., Naing, S. & Corbett, J. (2001). Geometric and Dimensioning Tolerances in error budgeting for assembly-centric design of aero-structures, *Proceedings of the 7th CIRP Int. Seminar on Computer Aided Tolerancing*, pp. 111-120, ENS de Cachan, France, April 24-25.
- Polini, W., Marrocu, M. & D'Ambrosio, L. (2007). Tolerance Analysis of Free-Form Surfaces in Composite Material, *Journal of Computing and Information Science in Engineering*, Vol. 7, (March 2007) 31-43
- Prisco, U. & Giorleo, G. (2002). Overview of Current CAT Systems, *Integrated Computer Aided Engineering*, Vol. 9, No. 4, 373-387
- Requicha, A.A.A. (1983). Toward a theory of geometric tolerancing, *Int J Rob Res*, Vol. 2, No. 4, 45-60

- Requicha, A.A.A. (1993). Mathematical definitions of tolerance specifications, *Manuf Rev*, Vol. 6, No. 4, 269-274
- Salomons, O.W., van Houten, F.J.A.M. & Kals, H.J.J. (1998). Current status of CAT Systems, In: *Geometric Design Tolerancing: Theories, Standards and Applications*, ElMaraghy H.A., (Ed.), 438-452, Chapman & Hall, London.
- Sellakh, R., Rivière, A., Chevassus, N. & Falgarone H. (2003). An assisted method for tolerancing applied to aircraft structures, *Proc. of 8th CIRP Int. Seminar on Computer Aided Tolerancing*, pp. 187-198, Charlotte, North Carolina
- Shen, Z.; Ameta, G.; Shah, J.J. & Davidson, J.K. (2004). A Comparative Study of Tolerance Analysis Methods, *Proceedings of ASME 2004 Design Engineering Technical Conferences and Computers and Information in Engineering Conference*, Paper No. DETC2004-57699, Salt Lake City, Utah, September 28-October 2
- Turner, J. & Gangoiti, A.B. (1991). Tolerance Analysis Approaches in commercial software, *Concurrent Engineering*, Vol. 1/2, 11-23
- Whitney, D.E. (2004). *Mechanical Assemblies. Their Design, Manufacture and Role in Production Development*, Oxford University Press Inc., ISBN 0-19-565782-6, New York

Application of Optical Fibre Sensors to Measuring the Mechanical Properties of Composite Materials and Structures

Wojciech Błażejowski, Paweł Gąsior and Jerzy Kaleta
*Wrocław University of Technology
Poland*

1. Introduction

The role of polymer composites in mechanical structures has been steadily increasing. The key factor here is the coefficient of specific strength, i.e. a ratio of tensile strength to specific gravity. As compared with metals, this coefficient assumes a high value for composites, including the polymer ones. Other major factors determining the choice of materials are: the product price, mass manufacturability, high strength and durability, corrosion resistance, material production and machining energy consumption and a few more. Also the latter criteria increasingly favour composites. Materials engineering as applied to composites offers the possibility of creating entirely new materials and modifying the traditional materials, which in both cases better meet designers' expectations.

The ever increasing popularity of composite structures is first of all due to the considerable reduction in weight in comparison with metal structures, at a sufficiently high mechanical durability. Nevertheless, the safety requirements require that the stress-strain state of composite structure be monitored. Standard NDE methods such as radiography, interferometric holography, ultrasonic scanning or visual inspection are usually not effective in on-line monitoring. Even if they were used for periodic checks, they would not be able to detect promptly defects critical to the condition of the monitored structure. Moreover, conventional measurement devices, such as electrical resistance strain gauges, often get damaged in adverse environmental conditions.

State-of-the-art measuring methods based on optical fibre technology are increasingly often used to monitor the structural health of industrial objects. Optical fibre sensors have many advantages over the conventional devices. The obvious one is that they can work at high levels of electromagnetic interference and in other adverse conditions (high dust concentration, high temperature, high pressure, significant deformations). Moreover, such sensors are characterized by high (deformation and temperature) measuring sensitivity in a wide measuring range. Owing to their small geometric dimensions and a relatively small weight they can be installed inside a structure (e.g. by embedding them in the composite material) or on its surface. Thanks to their high potential for multiplexing it is possible to create a nervous system of the object being monitored, enabling health and damage assessment. In addition, optical fibre based sensors ensure spark-proof safety which is an important consideration for inflammable applications.

Because of the wide range of problems connected with the measurement of mechanical quantities in composites by means of optical fibre sensors it becomes necessary to concentrate on major problems. The authors decided to focus on the structural health monitoring (SHM) aspects for all kinds of composite structures. Solutions being mainly the result of the authors' own research, with reference to the literature on the subject, will be highlighted.

Considering the above, the objective is to present the fundamentals of the measurement method based on optical fibre sensors as applied to:

- monitoring the behaviour of, among others, laminates and pultruded composites used as reinforcement in building structures and aeronautical structures;
- measuring (static and cyclic) strains in Smart composites where strong magnetic fields limit or exclude the use of other measuring techniques;
- monitoring the structural health of composite structures subjected to extreme strain, such as composite pressure vessels for storing compressed hydrogen and methane car fuels.

The focus is on the experimental aspect of measurements, and the numerical modelling of composite materials and structures is deliberately neglected. However, one should note that modelling plays an important role in many measurement situations (e.g. it is used to determine the number and location of sensors, the theoretical state of strain on a meso- and macroscale, the distribution of temperature, etc.).

2. Composite materials and importance of SHM

Currently most of the research and applications are concerned with composites whose matrix is made of polymers, ceramic materials or metals (e.g. aluminium, titanium, nickel and other alloys) and which are reinforced with glass or carbon fibres. Such composites have found wide application in the manufacturing of fuselages and other structural components of planes, gliders, space shuttles and rockets, car body components, fuel tanks, yacht hulls and masts, wind turbine blades and domestic appliances components, in medicine and in many other fields. Moreover, composites are used to reinforce the existing building structures, including the historic ones (e.g. to preserve bridges, churches, etc., or to increase their load-bearing capacity).

The percentage of composite materials used in high-tech applications increases every year, causing a rise in the production of reinforcing fibres. It is estimated that the demand for carbon fibres in 2018 will increase by about 275% (from 41240 to 113500 tons) as compared with that in 2010, (Sloan, 2010). The highest increase in demand is forecasted for applications connected with the wind power industry (700%), the storage of compressed fuels (~410%) and the broadly understood aerospace industry (~220%).

The interest in composite materials is due to their very good mechanical (strength) parameters and low specific gravity. Highly valuable is the possibility of creating a composite with strictly defined parameters for a given structure. Moreover, increasingly often various (mainly optical fibre based) sensors are incorporated into the structure of composite materials. Thanks to this, different parameters (e.g. strain and temperature) can be measured directly in the structure's material. Another major advantage of optical fibre sensors (OFS) is that they can be used to detect defects and their accumulations and to determine the safe life of the material during its service. In recent years most of the research

on OFS has been devoted to their use for the continuous monitoring of the structural health of composite elements.

Novel structural health monitoring (SHM) systems for composite structures are currently developed. Thanks to the use of measuring systems integrated with the structure the latter can be optimally managed. Continuous monitoring enables the detection of hazards in the structure, undetected by inspections or modelling. Consequently, the damaged components can be promptly replaced whereby the safe service life can be extended. Moreover, thanks to SHM systems the knowledge about structures and their behaviour in real conditions can be improved whereby the next generation of such structures will be better designed. Ultimately, the costs connected with building new structures will be lower and the safety, reliability and life of the latter will increase (Glisic & Inaudi, 2007).

3. Optical fibre sensors and measuring technique fundamentals

Currently optical fibre sensors (OFS) are increasingly widely used to monitor the mechanical properties of composite materials and structures in their operating conditions where the reliability and safety of the structures (often working under extreme strains) is critical. Typical applications of various OFS to condition monitoring are presented below. Strain (displacement) and temperature are the main parameters which can be measured by such techniques. On the basis of the measured strain and temperature one can estimate other mechanical parameters, such as stress/strain distribution, force, pressure, curvature, leakage and so on.

3.1 Fibre bragg gratings

Fibre Bragg gratings (FBG) are the most popular fibre based sensors. A Bragg grating is a structure made inside the core of a single-mode optical fibre, characterized by periodical changes in the value of the refractive index (Fig. 1). Due to the presence of such a modulated

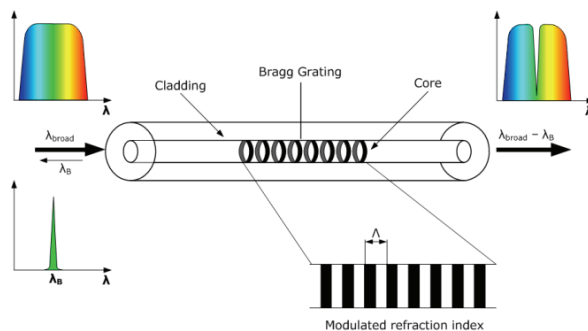


Fig. 1. Scheme of fibre Bragg grating principle of operation

structure inside the core of the optical fibre some of the optical radiation transmitted through the latter is reflected from the grating structure while the remainder is propagated without any loss (Yu & Yin, 2002). The wavelength reflected from the Bragg grating, the so-called Bragg wave (λ_B), is described by the relation:

$$\lambda_B = 2 \cdot n_{\text{eff}} \cdot \Lambda \quad (1)$$

where: n_{eff} – the effective refractive index of the optical fibre core, Λ – a Bragg grating constant.

Sensors bonded to the external surface of the monitored structure or located inside the material are subject to deformations causing changes in the Bragg wavelength, which becomes the touchstone for the measured deformations. It should be noted, however, that a change in λ_B in real measuring systems is the result of the simultaneous influence of temperature and deformations, which can be measured in ranges: $-270^\circ\text{C} \div 800^\circ\text{C}$ and $-3\% \div 3\%$, respectively.

3.2 Interferometric SOFO® sensors

Another type of OFS applicable to composite structures are interferometric sensors (i.e. SOFO® sensors with long measuring arms). Interferometric optical fibre sensors are characterized by the modulation of the light signal phase propagated in the measuring system (Glisic & Inaudi, 2007). The measuring heads of SOFO® sensors, in the form of a single-mode optical fibre, may attain from a few centimetres to a dozen or so meters and are either integrated with the surface of the monitored object (e.g. by means of special tape – SMARTape®) or located inside the monitored structure (e.g. in the case of tested vessels they are buried in the composite). The sensors are designed to measure displacements (deformations). The measurement consists in analyzing the difference in the phases of the optical signals propagating in the two arms (the measuring arm and the reference arm) of the Michelson interferometer (Fig. 2).

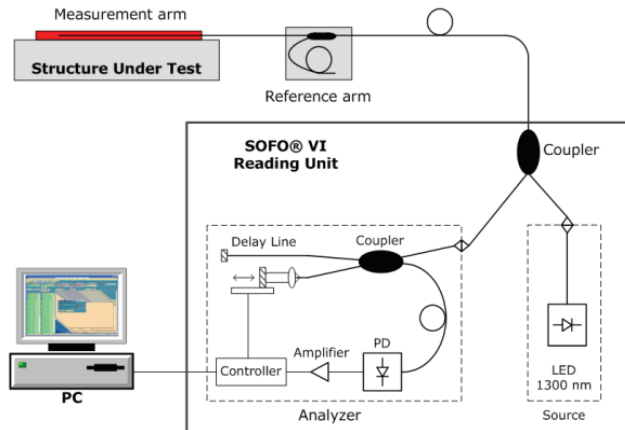


Fig. 2. Scheme of Smartec SOFO® interferometric measuring system (Glisic & Inaudi, 2007)

The measuring arm is in direct contact with the examined structure. The reference arm is separated mechanically from the monitored object, but it is still close enough for the temperature of both arms to be the same. Thanks to this the influence of temperature fluctuations on the measurement results is eliminated. The change in the phase of the light wave is a result of the change in the length of the optical fibre constituting the measuring head. Because of the interference of the two beams it is possible – through an analysis of interference fringes – to quantitatively determine the deformation of the sensors and consequently, the deformation of the monitored structure (Glisic & Inaudi, 2007). Since

interferometric sensors belong to a group of sensors with long measuring arms (long-gage sensors), the measured deformations are averages for the whole length of the sensor.

3.3 EFPI sensors

Extrinsic Fabry-Perot interferometric (EFPI) sensors are built from two optical fibres facing each other, but with a small air gap (in the order of micrometers) between them, inside a capillary. The working principle of EFPI sensors is based on multi-reflection Fabry-Perot interference between optical signals reflected from air-glass interface mirrors (Leng & Asundi, 2003). The scheme of the EFPI principle of operation is shown in Fig. 3.

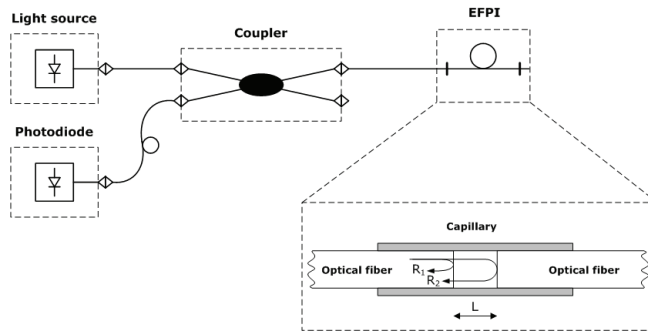


Fig. 3. Scheme of system based on extrinsic Fabry-Perot interferometric sensors

Changes in air gap length (L), which in fact are changes in sensor length, correspond to the variation in the applied mechanical strain. They can be measured by demodulating the interference signal, i.e. by means of coherent or low-coherent techniques (Glisic & Inaudi, 2007).

4. Selected applications of OFS to composite elements

There is a great variety of fibre-optic measuring methods which are used in the monitoring of composite structures. Therefore in the literature survey the authors decided to focus on the areas in which they have considerable achievements and experience. Among others, the monitoring of laminates and pultruded composites, structural aircraft components, SMART magnetic composites and composite pressure vessels for storing CH₂ and CNG is discussed.

4.1 Reinforcing laminates and pultruded composites

Optical fibre sensors have found the widest application in the measurement of deformations of all kinds of laminates and pultruded composites. This is owing to several advantages which OFS have, such as:

- similar material properties of the sensor and the reinforcing material in the composite,
- OFS, even the ones complicated in shape, can be located directly in the material (sensor small size and weight and measuring head flexibility),
- resistance to electromagnetic interference (the sensor is a dielectric),
- a wide range of measured physical quantities and simultaneous measurement in many points,
- resistance to environmental conditions.

OFS, usually in the form of bare-fibre Bragg gratings or interferometric sensors, are located directly between the successive layers of the laminate or are interwoven with reinforcement bundles in the case of woven/drawn elements. Depending on the method of manufacturing the composite and its end use, the sensor may be impregnated with resin during the production of the material ("wet" methods such as pultrusion and winding) or later using the vacuum method.

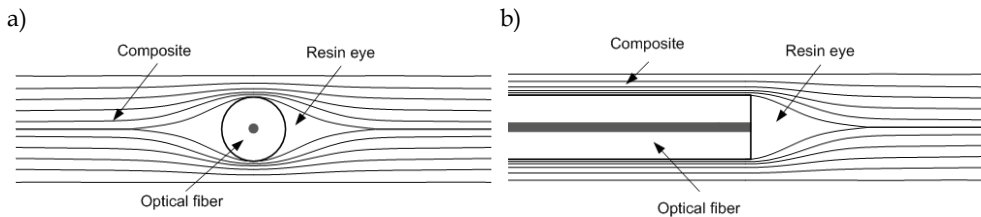


Fig. 4. Scheme showing how local defects arise in composite laminates with embedded optical fibre sensors (Balageas et al., 2006)

Nevertheless, one should also note potentially negative aspects which need to be taken into account or eliminated (or their effect minimized). One of the drawbacks is the sensor size. Even though the optical fibre diameter is relatively small (typically 125 μm), it is quite considerable in comparison with that of the fibres used to reinforce the composite (amounting to $\sim 16 \mu\text{m}$ for glass fibres and $\sim 8 \mu\text{m}$ for carbon fibres) and with the thickness of a single laminate layer. Thus by locating the optical fibre inside the composite one may introduce areas of reinforcement discontinuity (Lee et al., 1995). These areas are excessively filled with resin and are referred to as resin pockets or resin eyes (Fig. 4). The disturbances in stress field distribution in the material may initiate delamination of the latter (Balageas et al., 2006; Udd et al., 2005).

The size and shape of a local defect in the form of a resin pocket depend on the orientation of the optical fibre relative to the reinforcement fibres. The laminate's mechanical parameters are least affected when the sensor is laid along the direction of the reinforcement and most affected when it is laid perpendicularly to the latter. If the sensor is laid parallel to the reinforcing fibres and the two ends of the optical fibre are led outside the area of the sample, the size of the additional defect in the laminate is close to zero (Balageas et al., 2000).

Another aspect which needs to be considered is the effect of the process of manufacture of composite laminate on the measuring properties of the FBG sensors located inside it. In (Kuang et al., 2001) the authors analyzed the spectrum reflected from the fibre Bragg grating in the reference environment (outside the composite before installation), comparing it with the response of a sensor embedded directly between the layers of the laminate. For some test samples they found the spectrum reflected from the sensor to be distorted and widened. This was due to the locally strong nonuniformity of the load acting on the sensor along its whole length (7 mm). Such local nonuniformities in the distribution of the strain field resulted mainly in an increase or decrease of the Bragg grating constant (Λ), which manifested itself in the splitting of the single Bragg wave peak into several peaks. This behaviour of the sensor was observed mainly for laminates consisting of several composite layers laid at different angles relative to each other. In the case of unidirectional composites, only a shift of the reflection (Bragg wave) spectrum towards lower values, due to the local

compression or tension of the sensor as a result of the manufacturing process (e.g. resin curing in elevated pressure and temperature conditions), was observed. The possibility of fibre-optic monitoring of resin curing during the manufacture of high-strength laminates was described by, among others, Leng in (Leng & Asundi, 2003). Thanks to the use of FBG and EFPI sensors residual strains during curing can be determined and local material defects in the form of delaminations can be detected. The quoted authors prepared samples made up of 16 layers of carbon prepreps, between which optical fibre sensors were installed along the direction in which the reinforcement had been laid. In addition, a Teflon disk 300 mm in diameter was placed in one of the samples to simulate a local delamination. In order to harden them the samples were annealed at a temperature of up to 120°C. By analyzing the signals received from the sensors installed in the samples with and without the defect one could detect the local damage already during the curing process. It was also found that residual strains after the curing of the samples are greater along the direction of compression for the flawed sample. The difference between the signals received from the EFPI and FBG sensors for the samples during curing amounted to 5-10% (Leng & Asundi, 2003). Then in order to determine their bending strength the samples were subjected to the three-point bending test. The test results confirmed that the strength of the samples with the designed flaw was lower than that of the samples without the flaw and that the artificially introduced delamination reduced the stiffness of the structure (Leng & Asundi, 2003).

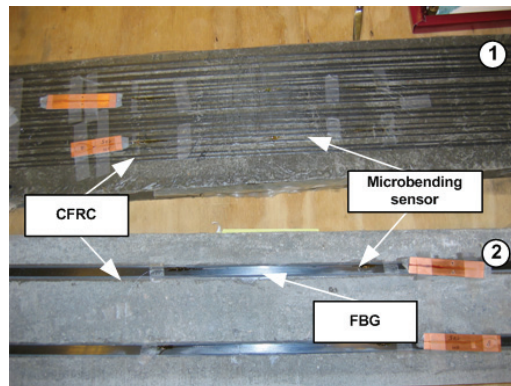
One of the main uses of laminates and pultruded composites is the reinforcement of the existing structures or structures under construction. The strength and load-bearing capacity of such structures as bridges, viaducts and buildings are commonly increased by introducing (through bonding) additional reinforcement made of materials characterized by high tensile strength and stiffness (e.g. laminates or pultruded composites in the form of strip or mat) glued to the surface of the structure being reinforced. Thanks to its relatively little weight the reinforcement does not additionally weight down the structure.

But composite reinforcements have drawbacks – they tend to creep and are brittle. For this reason research is underway aimed at the detection and control of internal material defects at the early stage in their development (Majumder et al., 2008). For example, a method of manufacturing glass fibre reinforced composites (GFRC) and carbon fibre reinforced composites (CFRC) through pultrusion with FBG and EFPI sensors located inside is presented in (Kalamkarov et al., 1999). The quasi-static and cyclic test measurement results received from the optical fibre sensors for the tested samples were in agreement with the results obtained from extensometric measurements. Moreover, it was shown that optical fibres with polymer cladding are characterized by better parameters of the sensor/material bond. Sensors in acrylic cladding tended to separate from the laminate and could not be used in composites which required manufacturing processes conducted at a temperature of above 85°C. In the case of the sensors in the polymer cladding the allowable temperatures were as high as 385°C (Kalamkarov et al., 1999).

The use FBG sensors located in pultruded epoxy-glass (GFRP-OFBG) and epoxy-carbon CFRP-OFBG) composites designed for reinforcing concrete beams is described in (Zhou et al., 2003). The composite elements prepared in this way were cast in concrete, cured and subjected to three-point bending. The FBG sensors registered the strains of the composite rods in a range of up to 200 microstrains (with an accuracy of $1\pm 2 \mu\epsilon$), registered the cracking of the concrete layer and informed about the slipping out of the reinforcements from the concrete. The authors showed that pultruded composite rods (with incorporated

sensors) can be used both as elements increasing the load-bearing capacity of a structure (reinforcing the latter) and as measuring heads integrated directly with the monitored element.

a)



b)

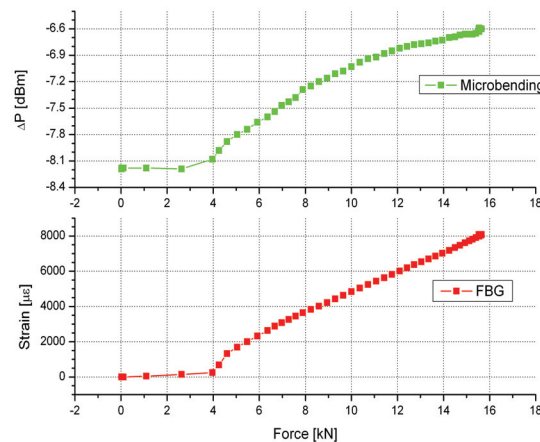


Fig. 5. Tested beams with composite reinforcements: (a) laboratory made in IMSAM (1) and by Polish Bridges company (2), and (b) characteristics registered by respectively microbending sensor and FBG sensor for beam with commercial composite reinforcement (Błażejowski et al., 2007)

Above one can find exemplary results of investigations into the monitoring of composite reinforcements of engineering structures, carried out by the present authors. Composite reinforcements, in the form of pultruded CFRC and GFRC strips, were glued to the tested concrete beams. Besides the reinforcements, two types of optical fibre sensors, i.e. FBG sensors and amplitude microbending measuring heads, were employed. Figure 5a shows two tested concrete beams with composite reinforcements (made in the laboratory in the Institute of Materials Science and Applied Mechanics (IMSAM) at Wrocław University of Technology and by the Polish Bridges (PB) company) and embedded optical fibre sensors.

During three-point bending in an MTS810 strength tester the following were registered as a function of time: the force, the strain (measured by the FBG sensors) and the change in optical power (registered by the microbending head).

a)



b)

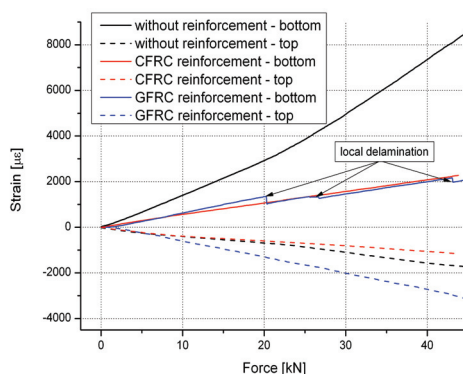


Fig. 6. Four-point bending of steel beam reinforced with unidirectional carbon-epoxy composite with integrated FBG sensors (a) and comparison of measurement results for different reinforcements (b)

Figure 5b shows exemplary measurement results for the microbending sensor and the FBG sensor, as a function of the force applied to the tested concrete beam with the Polish Bridges reinforcements. Similar measurements were carried out for concrete beams without reinforcement and with the laboratory made glass composite and carbon composite reinforcements. On this basis the effect of the type of reinforcement on the strength of the concrete beams was determined. The tests confirmed the suitability of optical fibre sensors for the testing of engineering structures reinforced with elements made of composite materials (Błażejowski et al., 2007).

Then tests were carried out for two types of reinforcement (pultruded carbon/glass reinforcement) with integrated FBG sensors, designed to increase the load-bearing capacity of steel frame structures. The reinforcement together with the sensor was glued to the

beam's (tensioned) bottom. An additional reference (FBG) sensor was installed on the top (compressed) side. The reinforced beams were subjected to the static four-point bending test during which the force and the strain in two areas were registered.

The measurement results are presented in Fig. 6b. An additional measurement was performed on a steel beam without any reinforcements to determine the effect of the composite of the structure. It was found that the reinforcements applied made the beam stiffer whereby its load-bearing capacity increased as manifested by lower strains in comparison the beam without reinforcements under the same static load. Thanks to the reinforcement the elastic range of the whole beam increased (up to about 20 kN). In the strain-force diagram for the beam with glass reinforcement one can see local jumps in the registered strain values (at ~20.2 kN, 26.4 kN and 43 kN), indicating that the reinforcement locally gets unstuck from the structure. In the sample, this manifested itself in local whitening of the composite.

4.2 Aerospace structural components

Owing to their excellent mechanical properties, particularly high strength and stiffness, composite components are increasingly used in aerospace structures. Modern planes (e.g. Boeing B787) include many subassemblies made from composite materials, especially carbon fibre reinforced composites (CFRC). Their (volumetric) percentage in the total aircraft parts is as high as 80%, which amounts to 50% of the ready aircraft weight. However, the development of defects in composite materials is much more complicated than in metallic materials and it is still not fully explored (Diamanti et al., 2002). For this reason, in recent years much research has been devoted to structural health monitoring (SHM), also of aerospace structural components, by means of fibre-optic measuring techniques. The research projects are aimed at developing systems for monitoring aerospace structures not only during their everyday operation, but also during the processes of production (e.g. pressure and vacuum forming, resin impregnation and curing, machining, assembly, etc.) of the particular composite components.

In (Takahashi et al., 2010) the authors describe a method of developing a system for the continuous monitoring of the composite parts of the plane's fuselage (a partition with reinforcements) through a system controlling the state (distribution) of strain on its surface during the entire production stage and service life. The developed system was based on Bragg gratings integrated with the structure of a CFRC reinforced composite. Through the measurement of local strains the system can detect and locate defects and other damage arising in the structure's material. The authors also showed that it was possible to measure the strain of composite samples in the course of the whole process of pressure forming and described its effect on the tested object. In order to determine the optimum location of point FBG sensors on the reinforced composite partition a numerical FE model was created and loaded on its outer surface with a pressure corresponding to the maximum design pressure.

Two types of defects: reinforcement separation and local impact into the partition resulting in the delamination of the composite were implemented in the virtual model. Thanks to this it became possible to determine the optimum distance between FBG sensors, ensuring detection of defects in any area of the investigated object. It was estimated that the intersensor distance for sensors with a sensitivity of 10 $\mu\epsilon$, installed on the reinforcements should not exceed 100 mm. In the case of the sensors controlling the surface of the partition, one FBG grating is capable of detecting a defect within an area 300 mm in diameter.

A major problem which designers of systems for continuous structural health monitoring encounter is the location of measuring transducers and their optimization with regard to the number of measuring points. The constraints put on the number of sensors are aimed at reducing the measuring system costs (e.g. costs of sensors, instrumentation, measuring units, system installation). They are also dictated by difficulties with the on-line processing of large quantities of measurement information. A large number of sensors does not always guarantee system reliability. Proper software with implemented data processing algorithms, capable of keeping the user informed about potential risks, is also needed.

Besides research on optimizing the arrangement and number of sensors (e.g. through numerical modelling and the hybrid (model + experiment) approach), purely experimental research on implementing the very wide networks of sensors (comprising a few thousand and more sensors) is being conducted. The aim is to create SHM systems which, similarly as the human nervous system (nerves/sensors, the brain/the information processing unit), enable the monitoring of entire engineering structures (Balageas et al., 2001).

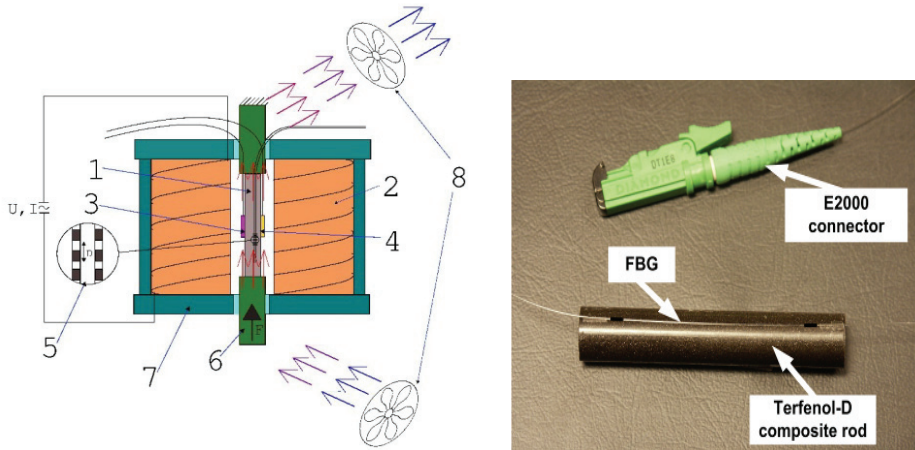
Exemplary research on implementing an SHM system comprising a large number of sensors is presented in the paper (Childers et al., 2001). The authors describe a measuring system consisting of 3000 measuring points based on fibre Bragg gratings, for monitoring the strain of a transport plane wing. Static tests on 12 m long composite wing made of carbon-epoxy composite with Kevlar inserts were carried out. A system consisting of 466 foil strain gauges was used as the reference. A novel system for handling many FBG sensors in a single fibre had been specially designed for the tests. The system is based on the optical frequency domain technique (OFDR) and is capable of simultaneously reading signals from 4 measuring heads. Each of the heads is 8 m long and contains 800 sensors spaced at every 10 mm.

The results obtained from the two different measuring systems were very similar. Moreover, it was found that thanks to the use of the fibre-optic system the total weight of the measuring system could be considerably reduced and at the same time the number of measuring points could be increased. As a result, the behaviour of the structure under real loads could be more accurately represented. In addition, owing to the small number of cables the system based on Bragg gratings turned out to be much easier to install than the strain gauge system (Childers et al., 2001).

4.3 SMART magnetic composite elements

SMART magnetic materials (SMM) are active materials which in recent years have been increasingly often and wider used in the aerospace industry, the navy, the car industry, civil engineering and in many other fields (Schwartz, 2002). The so-called giant magnetostrictive materials (GMMs) form a major subgroup in SMM. They enable the conversion of magnetic energy into mechanical energy and vice versa with high efficiency. A typical representative of GMMs is Terfenol-D which offers many advantages but its low tensile strength and the occurrence of high eddy currents detract from them. Attempts are made to eliminate the drawbacks by creating composites. For several years now research projects, e.g. (Kaleta et al., 2009; Gąsior et al., 2009; Yin Lo et al., 2006), targeted at creating magnetostrictive materials capable of assuming the form of, e.g., rods or laminates and effectively replacing solid Terfenol-D, have been conducted. Such composites offer the possibility of new applications, in e.g. SHM (tagging).

a)



b)

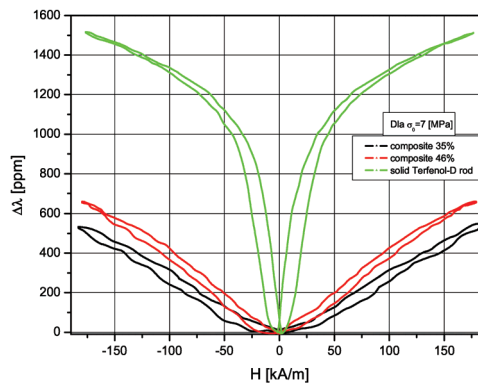


Fig. 7. Composite sample containing powdered Terfenol-D, with installed fibre-optic sensor and test stand for magnetostrictive composites (a) and exemplary change in longitudinal magnetostriction under influence of applied magnetic field for different composite and solid samples, registered by FBG sensor (b) (Kaleta et al., 2009)

Monolithic (solid) GMMs and composites incorporating them are tested mainly with regard to their magnetic properties. The parameters describing these properties are magnetostriction (the deformation of a ferromagnetic under the influence of an external magnetic field) or the opposite effect (the Villary effect). In both cases, the conventional methods of measuring strains (e.g. by means of extensometers or strain gauges) are practically inapplicable since GMMs are inside coils (or even constitute their core) and the sharp fluctuations in E-M fields there disturb the measurement.

For this reason, optical fibre sensors are an ideal solution for measuring the mechanical parameters of magnetic materials (including GMMs). Owing to their dielectric nature they are resistant to all electromagnetic interferences and in addition, enable strain registration with an accuracy as high as $1 \mu\epsilon$.

In (Kaleta et al., 2009; Gąsior et al., 2009) the authors used FBG sensors to measure the deformation of solid Terfenol-D rods and composite rods based on epoxy resin and powdered Terfenol-D. The fibre-optic sensors were installed on the surface of the samples (Fig. 7a) in the longitudinal and circumferential directions whereby magnetostriction could be measured in two directions. During the bonding of the sensors to the samples the latter were prestressed. As a result, strains could be measured under both compression and tension. This is important since in order to obtain optimum operating conditions for these composites they need to be prestressed (Kaleta et al., 2009).

The aim of the static tests described in the above papers was to determine the magneto-mechanical properties of rods made of GMM composites and solid Terfenol-D. Their magnetostriction was determined depending on the percentage of the magnetic phase in the material (Fig. 7b). The test results showed that although the magnetostriction is three times lower in comparison with that of the solid material, it is about 30 times higher than that of nickel (the reference material). But the influence of eddy currents was eliminated and the tensile strength increased (Kaleta et al., 2009).

4.4 Composite pressure vessels

Today composite pressure vessels are used in many fields, such as: the car industry, the aerospace industry, rescue services, etc. They owe their popularity to the considerable reduction in the weight of the vessel in comparison with steel vessels, and to their high mechanical strength. Also their excellent resistance to corrosion is not without significance. In order to illustrate the subject, a case of a composite hydrogen vessels is presented below. The use of hydrogen to feed fuel cells and for combustion in conventional engines requires a safe and expensive fuelling method. Storing hydrogen in pressure vessels of the CH₂ (compressed hydrogen) type has become the predominant technology, especially in cars. The latest (4th generation) designs are pressure vessels with a nominal working pressure (NWP) of 70 MPa. The weight of the vessel itself should be low enough in order for the latter to be installed in a car without the necessity to reduce the boot space. For this reason, wholly composite vessels (Fig. 8) must be installed. The load-bearing wrapping of such a vessel is made from high-strength carbon fibres (CFRC) while the liner (ensuring tightness) is made of high-quality plastics. The burst test pressure (BTP) at a safety factor of 2.35 (for CFRC) has to be above 164.5 MPa. In the case of glass composites (GFRC) the safety factor increases to 3.65 whereby BTP is higher.

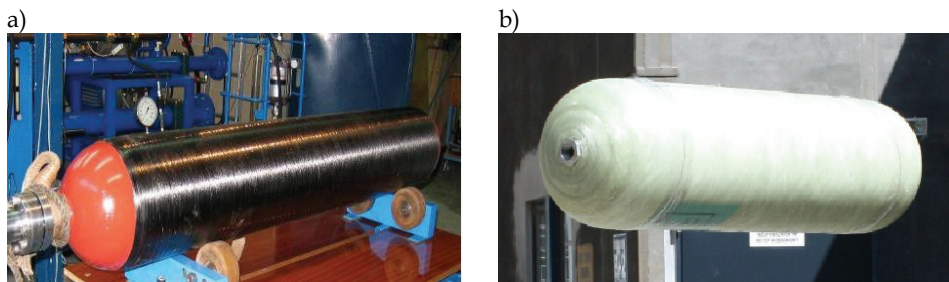


Fig. 8. Examples of pressure vessels for storing CNG and CH₂: of type 2 (a) and type 4 (b), (Błażejowski et al., 2007)

Because of the stringent requirements the CH2 vessel is an integrated high-tech product which can withstand extreme strains, and all its building components, i.e. the materials, the calculations, the design, the lining and wrapping technologies and the test methods, represent the cutting edge of research and engineering. The problem of SHM for such a vessel is discussed below. The discussion is based on the present authors' experience gained in carrying out research projects, among others, within the 6th EU Framework Program (Storage of Hydrogen – StorHy) and the 7th UE FP (Integrated GAS Powertrain – InGas).

The combination of the highly-strained composite load-bearing structure of the vessel and the hazardous substance (which compressed hydrogen fuel is) necessitates the monitoring of the structural health of such objects. It is estimated that the danger area in the case of explosion of a full car methane tank is 250 m large in diameter and in the case of hydrogen it may be as large as 1000 m in diameter (Mair, 2007). Therefore it is of critical importance to ensure operational safety over the entire ten-year service life.

At the moment the standards require that pressure vessels be subjected to routine tests certifying them fit for further use, but it is not necessary to permanently install SHM systems. Because of such regulations pressure vessel manufacturers prefer to increase the amount of the material reinforcing the structure to increase its safety than to optimize the the vessel design. This leads to higher production costs and a higher final product price. However, currently efforts are made, e.g. (Sulatisky et al., 2010), to exert pressure on the legislative bodies to introduce regulations reducing the current high safety factors for the manufacture of pressure vessels when a continuous structural health monitoring is employed. As already mentioned, standard NDE methods are not suitable for the on-line monitoring of such objects and can be used only for periodic inspections (Foedinger et al., 1999; Degrieck et al., 2001). A system of sensors should ensure the assessment of the technical condition of the high-pressure cylinder during both its production and (above all) its long use.

The research in this field, e.g. (Foedinger et al., 1999; Degrieck et al., 2001; Kang et al., 2006; Hernández-Moreno et al., 2009; Sulatisky et al., 2010; Błażejowski et al., 2010; Glisic & Inaudi, 2004; Frias et al., 2010), shows that the best of the offered solutions is to use optical fibre sensors for this purpose, since they are characterized by resistance to electromagnetic interference, non-sparking safety, ease of integration with the structure of the composite material and high sensitivity in a wide measuring range. Such sensors, permanently installed on the surface of the vessel or incorporated into the structure of the composite material, enable the continuous monitoring of the structure's technical condition over its whole service life.

In one of the first works (Foedinger et al., 1999) dealing with the application of optical fibre sensors to the monitoring of the structural health of standard testing and evaluation bottles (STEBs), the authors used FBG sensors which were integrated with the composite load-bearing layer as it was being wound during its manufacturing. The sensors were to measure the strain and temperature of the vessel during the curing of the epoxy resin and quasi-static pressure tests. A micrographic analysis of the cross sections of the composite load-bearing shell containing the optical fibre was carried out and showed good interaction between the two as well as no defects in the areas incorporating the sensors. The latter were located in several areas of the pressure vessel, e.g. in its cylindrical part and in its bottoms. Each time they were positioned in the direction consistent with the direction of the reinforcement, which means that they were wound at different angles to the principal axis of the vessel. In addition, resistance strain gauges and thermocouples were employed as the reference

sensors. The strain gauges were installed on the vessel's outer surface (after resin curing) in the neighbourhood of the fibre Bragg gratings. The investigations showed good agreement between the sensor measurement results and the strain gauge measurement results (depending on the winding direction and the location, the difference between the FBG sensor results and the strain gauge results ranged from 1.2% to 24%) and the numerical FE model results.

In (Degrieck et al., 2001), the authors investigated the possibility of using fibre Bragg gratings to monitor the strains of components made of composite materials, including laminates and pressure vessels made by winding. The research was carried out in several stages. First tensile tests and temperature tests were carried out on a bare optical fibre with an FBG sensor. Then carbon-epoxy laminate with a fibre Bragg grating placed between the layers was made. The laminate was subjected to the static three-point bending test. Finally, a pressure vessel was made by winding a glass fibre, in which an optical fibre together with a Bragg grating was wound (in the circumferential direction) with the final reinforcement layer, parallel to the latter. The vessel was then subjected to tests. In the first test it was statically loaded with an internal pressure of 0-16 bar and then cyclically with 0-3 bar. In both tests a change in pressure resulted in a shift of the Bragg wave reflected from the sensor incorporated into the structure of the composite load-bearing layer. It was found that being located directly in the material structure, FBG sensors are ideal for measuring strains in composite materials and in addition, they represent a promising technique for nondestructive testing and evaluating the structural health of composite elements (Degrieck et al., 2001).

The suitability of optical fibre (FBG) sensors for monitoring composite pressure vessels, especially taking into account the possibility of integrating such sensors with the load-bearing layer during the manufacture of vessels by winding, is the subject of the paper (Kang et al., 2006). The authors describe the difficulties they encountered while embedding measuring heads (made by welding FBG sensor together) in a composite material. Only one of the four measuring heads in a pressure vessel with the sensors prepared in this way survived the manufacturing process (winding and high-temperature curing). It turned out that because of their low resistance to lateral stresses in the weld, the welded fibres are poorly resistant to the conditions prevailing during vessel manufacturing whereby the risk of optical fibre damage during reinforcement winding increases considerably. Measuring heads consisting of several sensors produced directly in one optical fibre segment additionally coated with a thin protective layer proved to be much better. In the latter case, the percentage of sensors which after the vessel manufacturing process were still fit for measurements increased to ~79% (11 out of the 14 sensors were available). By comparing the reflection spectrum for the pressure vessel before annealing with the spectrum for the ready vessel one could determine the local residual strain. In all the measuring points local compression amounting to several hundred microstrains ($\mu\epsilon$) was registered, but the strains at the vessel bottoms were relatively larger (Kang et al., 2006).

Then the vessel was subjected to the pressure test until failure. For reference purposes, strain gauges were installed on the vessel's surface. The gauges were damaged before the vessel burst. The maximum registered strains amounted to 0.95% for the pressure of 2900 psi (~200 bar). Also the splitting of the Bragg wave into several peaks was observed – probably due to the displacement of a sensor relative to its optimal position fixed during winding (the sensor was not situated parallel to the reinforcement fibres), (Kang et al., 2006).

The reliability and safety of composite vessels with an integrated SHM system is also the subject of the research conducted by Hao and others (Hao et al., 2007). They proposed to create a system which would monitor the circumferential and longitudinal strain of a tested vessel made of glass-epoxy composite, by means of three FBG sensors installed on its surface. In addition the authors used two strain gauges to locally measure strains in the circumferential and longitudinal directions. The tested vessel (with a 3.2 mm thick load-bearing wall) was statically loaded with a pressure of 0-200 bar. The obtained measurement results showed good convergence for the strains registered in the longitudinal direction, particularly in a low pressure range (up to 8 bars), and large scatters for the circumferential strains. The differences between the FBG sensors and the strain gauges amounted to as much as 60%, even though they were separated by a distance of maximum 12 mm. According to the quoted authors this is due to the different distances of the sensors from the defect around which the vessel burst (Hao et al., 2007).

The use of fibre Bragg gratings for the monitoring of the state of stress of a composite pressure vessel was also the subject of research carried out by Frias and others (Frias et al., 2010). In their paper the authors describe a measuring system based on six FBG sensors and two piezoelectric polyvinylidene fluoride (PVTF) sensors, integrated with the composite vessel structure. The sensors were located between the steel liner and the load-bearing layer made of glass fibre in thermoplastic resin. The liner was made by welding the two bottoms and the circumferential FBG sensors were located in the direct vicinity of the weld. The other sensors (two Bragg gratings and two piezoelectric sensors) were located in the cylindrical part, and registered longitudinal strains. The vessel was subjected to cyclic testing within which 9 test series with 30 cycles in each were carried out. The upper cycling pressure amounted to 5-40 bar with a 5 bar step in the successive series. The test results showed good convergence for the different measuring systems. Moreover, the liner in the weld region was found to plasticize quickly under the cyclic loading, as indicated by the circumferential FBG sensors. The latter showed that the vessel behaved nonlinearly in the circumferential direction in the weld area and linearly in the longitudinal direction outside this area (Frias et al., 2010).

Glisic and his co-workers in (Glisic & Inaudi, 2004) presented the application possibilities of a system for monitoring the structural health of 4th-type composite (the so-called full composite, a polymer liner and carbon-epoxy reinforcement) pressure vessels for storing compressed methane in cars, with a nominal working pressure of 350 bar. The proposed measuring system is based on interferometric SOFO® sensors. The latter are characterized by relatively long measuring arms which average the measured strain over their length. The aim of the research carried out within the EU ZEM Project (the 5th EU Framework Program) was to develop a topology of sensors distribution on a vessel, and a proper algorithm analyzing the measurement data, enabling the detection of local defects which could endanger the safety of the users (Glisic & Inaudi, 2004).

SMARTape® sensors were integrated with the vessel structure and located between the last carbon fibre layer and the first glass fibre layer. The interferometric SOFO® sensors measured strains in the longitudinal direction (four sensors spaced at every 90° on the circumference) and in the circumferential (helical) direction (2 sensors with opposite lead angles).

Glisic and Inaudi proposed an algorithm (a monitoring strategy) for measurement data analysis which made it possible to detect different anomalous behaviours of the vessel and defects arising in its structure. It was assumed that in the case of damage the vessel would

become more deformable (under a constant pressure), which meant that the slope of the strain-pressure line would change. It was also assumed that a local defect could result in local deformations (e.g. ovalization, bending) of the vessel, which would be registered by pairs of SOFO® sensors distributed symmetrically on its surface. Thanks to the latter assumption the correlation of measurements between selected sensors could be analyzed. In the case of a defect, the linear dependence between the strains registered by one sensor and the ones registered by another sensor will be disturbed and will change (Glisic & Inaudi, 2004).

In order to prove the above assumptions a series of static and quasi-static tests were carried out on new pressure vessels and vessels with designed flaws (cuts differing in their geometrical dimensions and delaminations), subjected to a pressure of 0-350 bar. The authors of (Glisic & Inaudi, 2004) show that an increase in such parameters as deformability or the relative compliance coefficient and a change in the reciprocal linear dependence between the particular sensors are indications of vessel damage.

5. Structural health monitoring of composite pressure vessels

5.1 Concept of composite pressure vessel monitoring system

The on-line monitoring of a pressure vessel is not limited to only the measurement of the mechanical parameters (e.g. strain fields) of its composite load-bearing layer. In order to determine the vessel's structural health and to detect critical defects which may pose a risk to the safety of the users it is necessary to employ proper algorithms to analyze the acquired measurement data. An ideal solution to this problem is a hybrid method in which the acquired measurement data are compared with the numerical model of the monitored object. Moreover, a good numerical model should indicate the primary sensor locations to be taken into account when installing sensors. However, this approach is not always possible, usually due to the lack of sufficient information needed to create a reliable numerical model of the investigated object. In addition, the use of the hybrid method necessitates the use of separate numerical models for each type of vessel. Any change in the design must be properly taken into account in the modelling process.

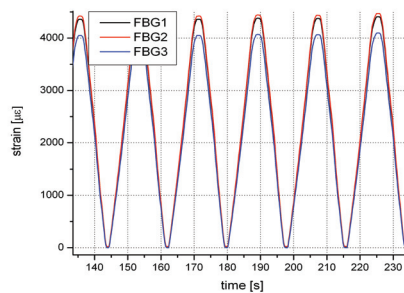
In the case of pressure vessels for which there is no precise information on the geometry of the load-bearing wrapping or the materials used, the present authors proposed to use a method consisting in analyzing local changes in the strain field (measured in many places) during the service life of the vessel and comparing them for particular pressure values. Any deviations from the assumed uniform strain field distribution in the vessel's cylindrical part indicate its potential damage (Błażejowski et al., 2008).

In order to create a fully functional system of monitoring the structural health of composite pressure vessels a special coefficient called ABS (absolute value) was calculated and compared with the threshold value. The ABS coefficient value was calculated as the absolute value of the difference between the coefficients of the directional strain-pressure lines for the successive vessel stress cycles. In addition, in order to locate possible defects the ABS coefficient values were compared between the particular measuring points (sensors). For a pressure vessel with no defects the dependencies between the particular sensors should be the same or very similar (considering the uniform state of stress in the load-bearing layer). When damage (e.g. a delamination or a crack) arises, the strain field is no longer uniform and the dependencies between the sensors are disturbed (Błażejowski et al., 2010).

5.2 Cyclic tests of pressure vessels

A pressure vessel with a steel liner, for storing hydrogen was subjected to cyclic tests at room temperature in accordance with the Draft ECE Compressed Gaseous Hydrogen Regulation, 2003. The vessel was loaded with pressures in the maximum range of 20-875 bar on a test rig in the Institute of Materials Science and Applied Mechanics at Wrocław University of Technology.

a)



b)

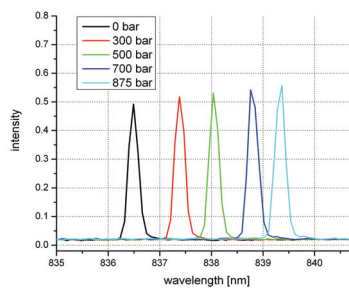


Fig. 9. Hoop strain characteristic registered by fibre Bragg gratings in different places of vessel (a) and Bragg wave shift registered by sensor FBG1 for different internal pressures (b) (Błażejowski et al., 2007)

Optical fibre sensors (FBG) for local strain measurement were used for the monitoring of the structural health of the vessel. In addition, acoustic emission sensors were employed for reference measurement purposes (Błażejowski et al., 2007). In the course of the basic tests (20-875 bar) about 700 cycles simulating vessel operation (filling-emptying) were carried out. The diagram in Fig. 9 shows exemplary vessel hoop strains registered by sensors: FBG1, FBG2 and FBG3 during cycle loading and the variation in the length of the Bragg wave registered by the FBG1 sensor in a pressure range of 0-875 bar. It should be noted that the vessel's circumferential strains for the pressure of 875 bar are relatively high (ranging from ~4000 to 4500 $\mu\epsilon$ depending on the type of sensor), (Gašior et al., 2007).

Figure 10 shows the maximum strains (at internal pressure $P_{\max}=875$ bar) registered by the FBG sensors installed in the circumferential direction, versus the number of vessel loading cycles. It should be noted that an increase in the number of cycles results in a local increase

in registered strain values (enlarged fragment A in Fig. 10) leading to the failure of the vessel. This is due to the fatigue (cyclic softening) of the steel from which the liner was made. The bursting of the vessel was preceded by rapid increase in locally registered circumferential strains (enlarged fragment B in Fig. 10). By analyzing the slope of the strain-number of cycles curve in its linear region one can determine how long the vessel can safely remain in service, i.e. predict its life. This is particularly important in the case when pressure vessels are to stay in service for many years.

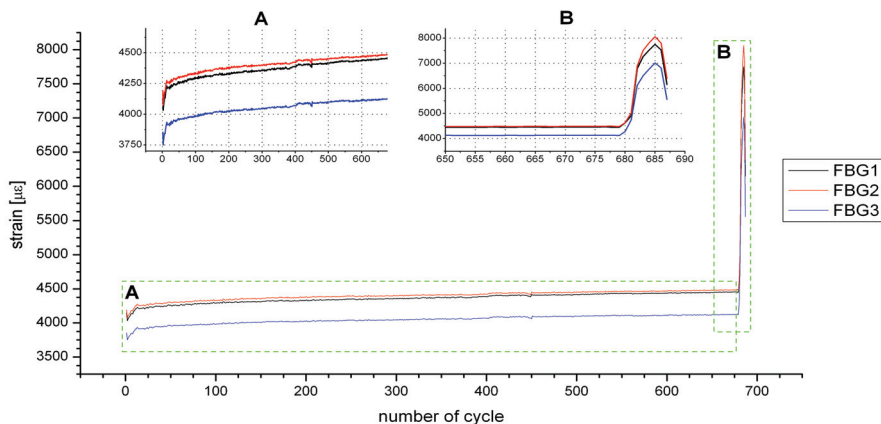


Fig. 10. Maximum circumferential strain (for $P = 875$ bar) versus number of vessel loading cycles and close-ups of marked areas, (Błażejowski et al., 2007)

Figure 11 shows signals registered by the particular sensors (the circumferential FBG sensors, the strain gauges and the acoustic emission sensors) at the moment of failure of the vessel (the broken line in Fig. 11). It is apparent that the failure was preceded by the previously mentioned rapid increase in strains (in the order of $1500 \div 3000 \mu\epsilon$ depending on the sensor and its distance from the defect) registered in the circumferential direction. Moreover, there is good correlation between the measured changes in the strain field on the vessel's outer surface and the acoustic signals registered by the AE sensors. At the moment of failure a considerable increase in the root mean square (RMS) acoustic emission signal occurs, which indicates a high degree of damage to the composite layer (Gąsior et al., 2007). Figure 12 shows an analysis of local circumferential strains for the last 8 cycles of the tests to which the pressure vessel was subjected. The analysis was carried out in accordance with the procedure described in sect. 5.2, consisting in the determination of the ABS coefficient. Its value was calculated as the difference between the directional coefficients for the strain-pressure lines obtained from the reference measurement and the next measurements. The first of the measurements was adopted as the reference point. Figure 12 shows a marked jump in ABS coefficient values between cycles 3 and 4 for all the analyzed measuring points. Moreover, the differences between the particular ABS coefficient values increase, which is a symptom of nonuniformity of the strain field distribution on the external surface of the vessel. This situation is indicative of the strong development of defects in the load-bearing structure of the composite pressure vessel (Błażejowski et al., 2008).

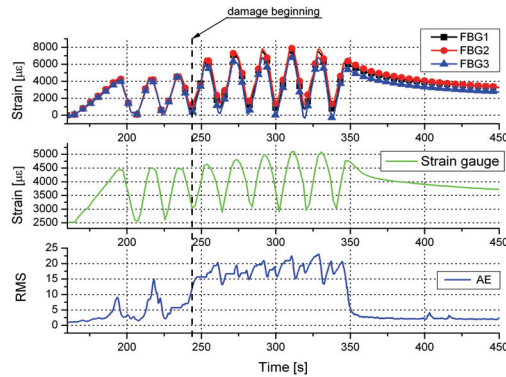


Fig. 11. Local circumferential vessel strains registered by FBG sensors (upper diagram) and strain gauges (middle diagram), and acoustic emission signal (bottom diagram) at instant of vessel failure (Gašior et al., 2007)

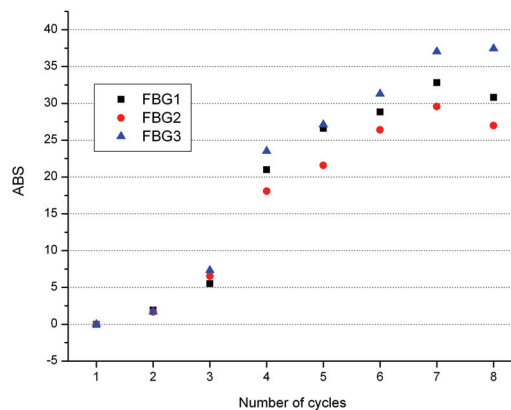


Fig. 12. Analysis of measurement results for final vessel loading cycles (detection of defects in structure of pressure vessel), (Gašior et al., 2007)

5.3 Cyclic tests of pressure vessels with designed flaws

A major problem in the monitoring of extremely strained composite structures is the early detection and identification of defects arising in the structure of the material. The defects can be the result of material fatigue under cyclic loads (e.g. filling and emptying of the vessel) or other events, e.g. external impacts or the exceedance of the allowable stress (pressure) and working temperature.

The standards relating to the testing of pressure vessels for storing high-pressure fuels (ECE Regulation No. 110, 2008; ISO/DIS15869.3, 2008) distinguish two main types of defects: flaws and delaminations. According to the cited regulations, a vessel with a flaw should meet the requirements of, among others, the cyclic tests at room temperature for a vessel without visible flaws.

Tests of vessels with flaws are referred to in the standards as composite flaw tolerance tests. Depending on the standard, the size of a flaw can be defined as “larger than the limit for the visual inspection, specified by the vessel manufacturer” and so no smaller than:

- length 25mm x depth 1.25mm,
- length 200mm x 0.75mm depth.

The flaws are made (by cutting) in the vessel’s composite shell in the direction parallel to its principal axis (Fig. 13). As already mentioned, after the flaws are made the vessel is subjected to the standard cyclic test whose result is deemed positive if the vessel does not fail (loss of airtightness or burst).

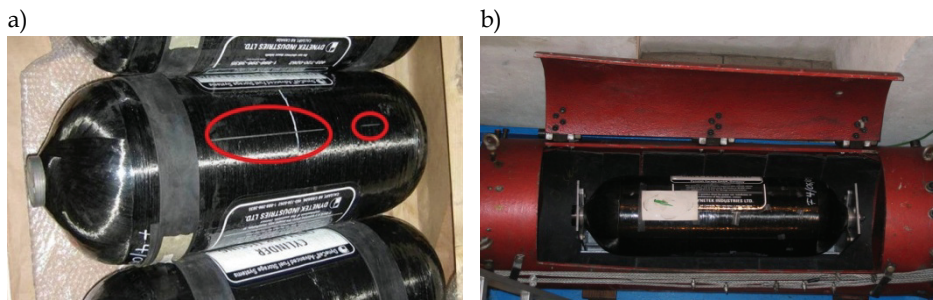


Fig. 13. Composite pressure vessels with designed flaws (cuts) (Błażejowski et al., 2008)

A pressure vessel for storing hydrogen at NWP = 207 bar (3000 psi) with 12 fibre Bragg gratings installed and two designed flaws in the form of cuts (Fig. 14) was subjected to a cyclic test at room temperature. The test consisted of over 4050 cycles in a pressure range of 20-258.5 bar (1,25 x NWP).

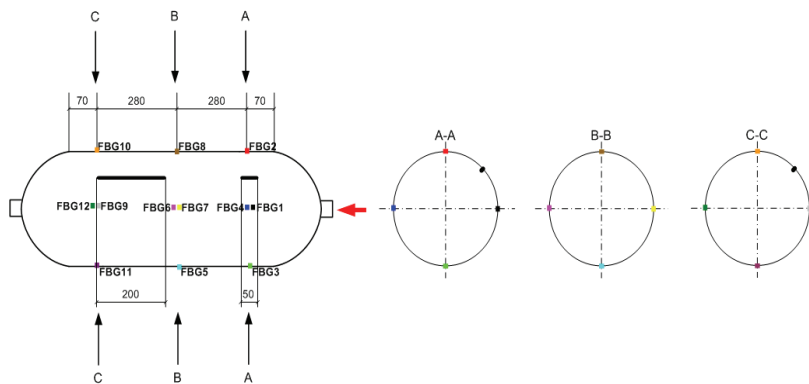
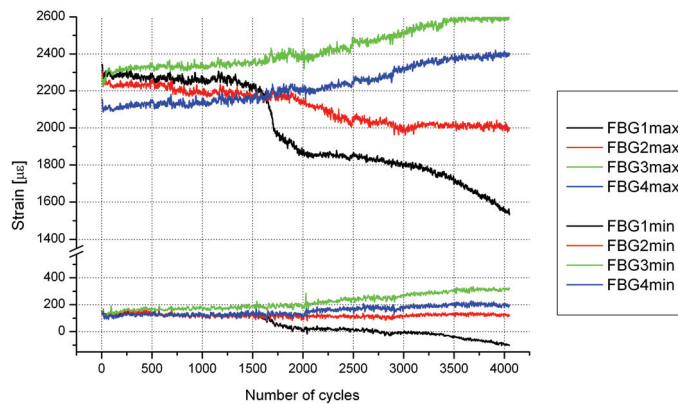


Fig. 14. Arrangement of designed flaws and sensors on tested pressure vessel (Błażejowski et al., 2008)

The measured local strains in a cross section with the shorter flaws (cross section A-A) are shown in Fig. 15. Figure 15a shows the minimum (ϵ_{\min}) and maximum (ϵ_{\max}) strains registered by sensors FBG1-FBG4 for pressures 20 and 285.bar. Fig. 15b shows the variation in strain amplitude ($\epsilon_{\max} - \epsilon_{\min}$) versus vessel load cycles. It should be noted that in the

analyzed cross section as the number of load cycles decreases so does the strain values registered by sensors FBG1 and FBG2 located closest to the flaw. At the same time the amplitude of the strains registered by the other sensors increases. This is evidence of local defects accumulation in the load-bearing shell of the composite vessel and of the growth of the designed flaw.

a)



b)

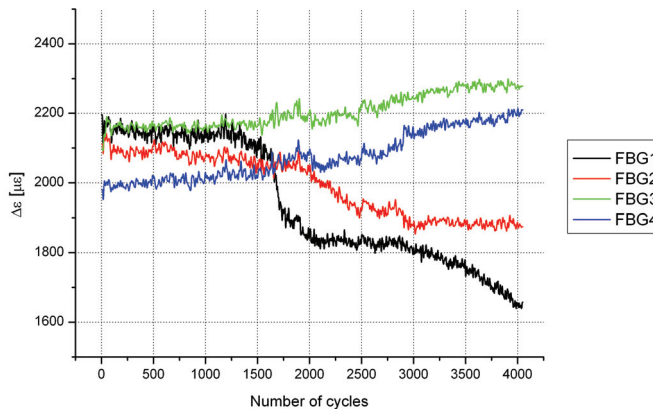


Fig. 15. Local strains of pressure vessel with designed flaws, measured by fibre Bragg gratings in cross section A-A (a) for pressure of 20 bar (min) and 258.5 bar (max), and amplitude of locally measured strains (b) versus number of vessel load (20-285.5 bar) cycles (Błażejowski et al., 2008)

The fluctuations of the maximum and minimum strain values are due to the specific character of the cyclic tests, i.e. due to the actual fluctuations of the maximum and minimum internal pressure around the fixed value (the switching pressure).

Figure 16 shows an analysis of the ABS coefficients for each of the FBG sensors installed on the tested pressure vessel, carried out in accordance with the description in sect. 5.2. It should be noted that as the number of pressure cycles increases so does the value of each of

the analyzed ABS coefficients. This indicates the growth (accumulation) of defects in the tested vessel.

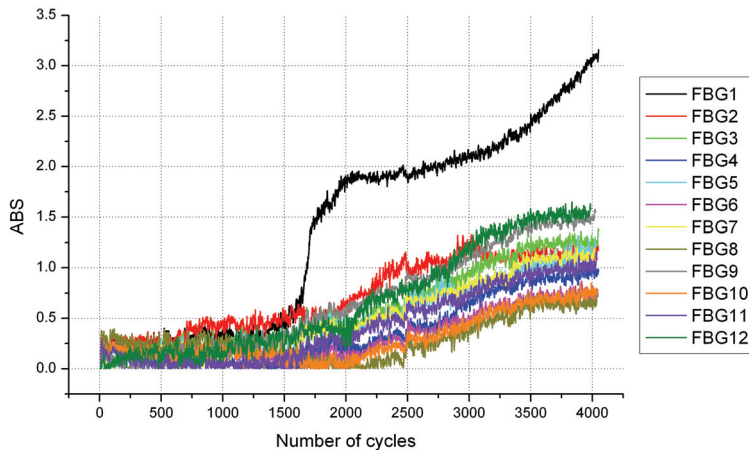


Fig. 16. Analysis of ABS coefficients versus number of pressure cycles for all FBG sensors installed on tested vessel with designed flaws (Błażejowski et al., 2008)

The largest changes were registered by sensors FBG1, FBG2, FBG11 and FBG 12, i.e. the sensors located closest to the introduced designed flaws. Moreover, one can see that the variation of the ABS coefficient, registered by sensor FBG1 after about 1600 cycles sharply increased during the next cycles. This indicates intensive local accumulation of defects, whose increase slowed down in the interval from ~2000 to ~3000 cycles, and then began to sharply increase again.

6. Conclusions

- The increasing use of polymer composites in various engineering structures necessitates the application of novel effective techniques of measuring mechanical quantities. Preferred are nondestructive techniques which would be inexpensive, reliable over the long service life of engineering structures and resistant to external influences. Measuring techniques are also expected to satisfy the requirements which structural health monitoring (SHM) systems have to meet. Systems based on optical fibre sensors (OFS) satisfy most of the requirements.
- The OFS technology offers the possibility of implementing “nervous systems” for infrastructure elements that allow health and damage assessment. Provided proper procedures are followed, optical fibre sensors can be located between the reinforcement fibres inside the composite material without affecting the mechanical properties of the composite element. Optical fibre based sensors can be used for measurements in adverse conditions (e.g. strong electromagnetic interference, high temperature and humidity) in which conventional methods cannot be used. Measuring heads based on fibre Bragg gratings have proved to be particularly suitable for composite structures. Also interferometric sensors (e.g. EFPI, SOFO®) can be used to some extent for this purpose.

- The increased interest in the novel measuring methods is also due to the many advantages of OFS over the conventional measuring methods. In practical applications measuring heads based on fibre Bragg gratings have been used most often.
- A major advantage of optical fibre sensors is that they can be used to build SHM systems comprising several thousand measuring points. This is particularly valuable when the object to be monitored is large or when it is not possible to determine the weak (critical) points in its structure. Thanks to the installation of many sensors the calculation methods can be simplified and the possibility that important information concerning the operational safety will be overlooked can be reduced. In addition, such systems are lightweight (in comparison with, e.g., strain gauge systems) and require little cabling.
- OFS can be used for on-line structural health monitoring. A major field of their application are extremely strained pressure vessels for fuel gas (methane, hydrogen). It was demonstrated that the OFS system is capable of detecting and controlling the growth of defects arising in the structure of composite materials whereby the safe service life of pressure vessels can be determined. Thanks to the way in which optical fibre sensors are installed it is possible to diagnose the health of structures during both their manufacture and long service life.
- Exemplary applications to building elements (reinforced concrete beams), composite aerospace structures and new generation of composites stimulated with a magnetic field (SGMM composites) were described.

7. References

- Balageas, D., Fritzen, C. i Guemes, A. (2006). *Structural Health Monitoring*. London/Newport Beach, Great Britain/USA: ISTE.
- Błażejowski, W., Czulak, A., Gasior, P., Kaleta, J. i Mech, R. (2010). SMART composite high pressure vessels with integrated optical fiber sensors. *Sensors and Smart Structures Technologies for Civil, Mechanical, and Aerospace Systems 2010, Proc. of SPIE Vol. 7647* 764712-1. San Diego.
- Błażejowski, W., Gasior, P., Kaleta, J. i Sankowska, A. (2007). Optical fiber sensors integrated with composite material based constructions. *Lightguides and Their Applications III, Proc. of SPIE 66081L-1-66081L-10*.
- Błażejowski, W., Gasior, P., Kaleta, J. i Sankowska, A. (2008). Optical Fiber Sensors as NDT methods for strain state monitoring of high pressure composites vessels. Comparison of different types of OFS. *8th International Conference on Durability of Composite Systems - Duracosys*. Porto.
- Childers, B., M.E., F., Allison, S., Moore, T., Hare, D., Batten, C. i inni. (2001). Use of 3000 Bragg grating strain sensors distributed on four eight-meter optical fibers during static load tests of a composite structure. *Smart Structures and Materials 2001, Proceedings of the SPIE Conference*. San Diego.
- Degrieck, J., De Waele, W. i Verleysen, P. (2001). Monitoring of fibre reinforced composites with embedded optical fibre Bragg sensors, with application to filament wound pressure vessels. *NDT&E International*, 34, pp. 289-296.
- Diamanti, K., Hodgkinson, J. i Soutis, C. (2002). Damage detection of composite laminates using PZT generated Lamb waves. *Proc. of the First European Workshop on Structural Health Monitoring*, (pp. 398-405). Paris.

- Draft ECE Compressed Gaseous Hydrogen Regulation, R. 1. (2003).
- Foedinger, R., Rea, D., Sirkis, J., Baldwin, C., Troll, J., Grande, R. i inni. (1999). Embedded fiber optic sensor arrays for structural health monitoring of filament wound composite pressure vessels. *Smart Structures and Materials 1999: Sensory Phenomena and Measurement Instrumentation for Smart Structures and Materials, Proc.of SPIE Vol. 3670*, (pp. 289-301). Newport Beach.
- Frias, C., Faria, H., Frazão, O., Vieira, P. i Marques, A. (2010). Manufacturing and testing composite overwrapped pressure vessels with embedded sensors. *Materials and Design* (31), pp. 4016-4022.
- Gąsior, P., Kaleta, J. i Sankowska, A. (2007). Optical fiber sensors in health monitoring of composite high pressure vessels for hydrogen. *Optical Measurement Systems for Industrial Inspection V, Proc. of SPIE 66163G-1-66163G-10*, 6616. Munich.
- Gąsior, P., Kaleta, J., Lewandowski, D. i Mech, R. (2009). Fiber Bragg gratings application for strain measurements of Terfenol-D based composites. *SMART'09: Proceedings of the IV ECCOMAS thematic conference on Smart Structures and Materials*. Porto.
- Glisic, B. i Inaudi, D. (2004). Health monitoring of a full composite CNG tanks using long-gage fiber optic sensors. *11th SPIE's Annual International Symposium on Smart Structures and Materials, Proc. of Spie Vol. 5384-7*. San Diego.
- Glisic, B. i Inaudi, D. (2007). *Fibre Optic Methods for Structural Health Monitoring*. John Wiley and Sons Ltd.
- Hao, J., Leng, J. i Wei, Z. (2007). Non-destructive Evaluation of Composite Pressure Vessel by Using FBG Sensors. *Chinese Journal of Aeronautics*, 20(2), pp. 120-123.
- Hernández-Moreno, H., Collombet, F., Douchin, B., Choqueuse, D. i Davies, P. (2009). Entire Life Time Monitoring of Filament Wound Composite Cylinders Using Bragg Grating Sensors III In-Service External Pressure Loading. *Appl Compos Mater*(16), pp. 135-147.
- ISO/DIS15869.3. (2008). *Gaseous hydrogen and hydrogen blends – Land vehicle fuel tanks*.
- Kalamkarov, A. L., Fitzgerald, S., MacDonald, D. i Georgiade, A. (1999). On the processing and evaluation of pultruded smart composites. *Composites*, B(30), pp. 753-763.
- Kaleta, J., Lewandowski, D., Mech, R. i Gąsior, P. (2009). Magnetomechanical properties of Terfenol-D powder composites. *Solid State Phenomena*, 154, pp. 35-40.
- Kang, D., Kim, C. i Kim, C. (2006). The embedment of fiber Bragg grating sensors into filament wound pressure tanks considering multiplexing. *NDT&E International*, 39, pp. 109-116.
- Kuang, K., Kenny, R., Whelan, M., Cantwell, W. i Chalker, P. (2001). Embedded fibre Bragg grating sensors in advanced composite materials. *Composites Science and Technology*(61), pp. 1379-1387.
- Lee, D., Lee, J. i Yun, S. (1995). The mechnaical characterristics of smart composite structures with embedded optical fiber sensors. *Composite Structure*(32), pp. 39-50.
- Leng, J. i Asundi, A. (2003, November). Structural health monitoring of smart composite materials by using EFPI and FBG sensors. *Sensors and Actuators*, A(103), pp. 330-340
- Mair, G. (2007). *Potentials and Procedures of the Probabilistic Approach*. Available at: http://www.storhy.net/pdf/PotentialProbabilisticApproach_Mair.pdf
- Majumder, M., Gangopadhyay, T., Chakraborty, A., Dasgupta, K. i Bhattacharya, D. (2008). Fibre Bragg gratings in structural health monitoring - Present status and applications. *Sensors and Actuators*, A(147), pp. 150-164.

- ECE Regulation No. 110 (2008).
- Schwartz, M. (2002). *Encyclopedia of Smart Materials*. John Wiley & Sons Ltd.
- Sloan, J. (2010, March). *Carbon Fiber: UP!* Available at: <http://www.compositesworld.com/articles/carbon-fiber-up>
- Sulatisky, M., Hay, B. i Mourre, D. (2010). Damage Detection in High-Pressure Cylinders. *18th World Hydrogen Energy Conference (WHEC 2010)*. Essen.
- Takahashi, I., Sekine, K., Takeya, H., Iwahori, Y., Takeda, N. i Koshioka, Y. (2010). Life cycle structural health monitoring of airframe structures by strain mapping using FBG sensors. *Sensors and Smart Structures Technologies for Civil, Mechanical, and Aerospace Systems 2010, Proc. of SPIE Vol. 7647 764723-1*. San Diego.
- Udd, E., Winz, M., Kreger, S. i Heider, D. (2005). Failure Mechanisms of Fiber Optic Sensors Placed in Composite Materials. *Smart Structures and Materials 2005: Smart Sensor Technology and Measurement Systems, Proc. of Spie Proceedings Vol. 5758*, (pp. 409-416). San Diego.
- Yin Lo, C., Wing Or, S. i Lai Wa Chan, H. (2006). Large Magnetostriction in Epoxy-Bonded Terfenol-D Continuous-Fiber Composite With [112] Crystallographic Orientation. *IEEE Transactions on Magnetics*, 42(10), pp. 3111-3113.
- Yu, F. i Yin, S. (2002). *Fiber Optic Sensors*. New York: Marcel Dekker Inc.
- Zhou, Z., Ou, J. P. i Wang, B. (2003). Smart FRP-OFGB bars and their application in reinforced concrete beams. *Proceedings of 1st International Conference on Structural Health Monitoring and Intelligent Infrastructure*, (pp. 861-866). Tokyo.

Cost Effective Computational Approach for Generation of Polymeric Composite Material Allowables for Reduced Testing

G. Abumeri¹, F. Abdi¹, K.S. Raju², J. Housner¹,
R. Bohner³ and A. McCloskey³

¹Alpha STAR Corp., Long Beach, CA

²National Institute for Aviation Research, Wichita State University, KS

³Northrop Grumman Corporation, El Segundo CA
USA

1. Introduction

The objective of this work is to provide the aerospace community with a robust computational capability to determine composite material strength allowables. The technical approach presented in this document serves two purposes: (1) reduce laminate level testing for determination of allowables; and (2) estimate allowables with some level of reliability when such data are difficult to obtain. A- and B-basis strength values are essential for reducing risk in aircraft structural components made from fiber reinforced polymer composite materials. Risk reduction is achieved by lowering the probability of failure of critical aircraft structures through the use of A- and B-basis design values. Generating strength allowables solely by means of testing is costly and time consuming as large number of composite coupons must be tested under various environments: cold, ambient and elevated temperatures (with and without moisture). The aerospace community is challenged by the following: (1) tests must be conducted on many types of coupons to determine allowables for in-plane and out-of-plane properties (un-notched and notched); and (2) new composite materials are introduced to the market at a rapid rate amplifying the need for timely cost effective approach. The tests must be carried out in accordance to standards set by ASTM (American Society for Testing and Materials).

Current practices for determining allowables follow procedures recommended by FAA and working draft of the composite materials handbook CMH-17 Rev G (formerly military handbook Mil-HDBK-17-1F) [1&2]. **Table 1** lists the robust and reduced test sampling requirements set forth by CMH-17. Determination of A-basis values requires more test samples than those needed to determine B-basis values as A-basis strength are applied to single members within an assembly whose failure would result in loss of structural integrity. For A-basis, at least 99% of the population of material strength values is expected to equal or exceed this tolerance bound with 95% confidence. B-basis values are applied to redundant structures where failure would result in safe load redistribution. For B-basis, 90% of the population of material strength values is expected to equal or exceed that strength value with 95% confidence. **Figure 1** illustrates the statistical definition of 0.01 and 0.10 probabilistic

strength for A-basis and B-basis, respectively. The physical definition of A- and B-basis is presented in Figure 2. A-basis strength value [2] is traditionally calculated using equation $(\bar{x} - (K_A) \cdot S)$; similarly B-basis strength value is computed using equation $(\bar{x} - (K_B) \cdot S)$; where \bar{x} is the mean strength of the test samples, S is sample standard deviation, and K_A and K_B are tolerance factors. The higher the tolerance factor, the lower the allowable; the higher the number of test replicates the more stable the allowable. CMH-17 provides tables of tolerance factors for various distributions as function of the sample size. The same procedures and standards require checking for outliers, distribution types if non-normality is observed, and batch variability. Details on numerical and test procedures for standard practice for determination of allowables can be found in [1 & 2].

Category	# of Batches	# of Samples	Category	# of Batches	# of Samples
A-basis - Robust Sampling	10	75	B-basis - Robust Sampling	10	55
A-basis - Reduced Sampling	5	55	B-basis - Reduced Sampling	3	18

Table 1. FAA Guidelines for Robust and Reduced Sampling

The proposed approach for determination of strength allowables builds on existing accepted standards and practices [1&2]. It uses statistics from lamina level testing to reverse engineer uncertainties in fiber and matrix material properties and manufacturing variables. These uncertainties are subsequently used in generating virtual test samples for laminated notched and un-notched specimens. The virtual samples are then used in lieu of actual test samples with resulting savings in cost and time. The methodology combines probabilistic methods with advanced multi-scale multi-physics progressive failure analysis (MS-PFA) [4] to reduce the number of tests needed for determination of A- and B-basis strength values. Details of the technical approach are provided next and the viability of the approach is demonstrated through application to four composite materials.

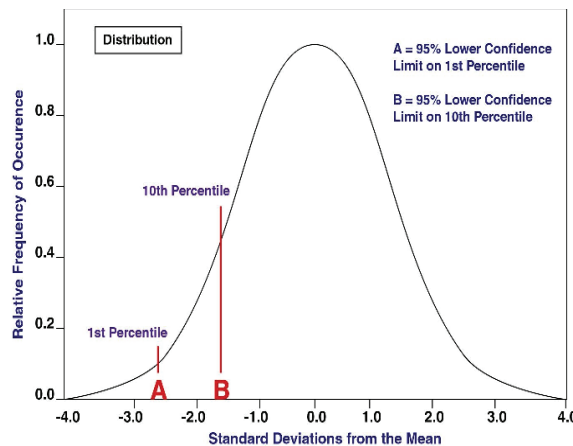


Fig. 1. Statistical Definition of A-and B-basis Strength [3]

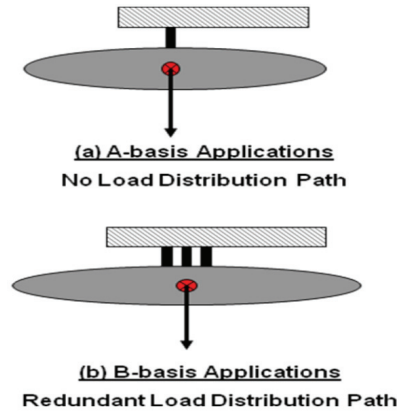


Fig. 2. Physical Definition of A-and B-Basis Strength

2. Nomenclature

E_{11}	Lamina extensional modulus in fiber direction
E_{22}	Lamina extensional modulus perpendicular to fiber direction
E_{f11}	Fiber extensional modulus in fiber direction
E_{f22}	Fiber extensional modulus perpendicular to fiber direction
E_m	Matrix extensional modulus
Eps11C	Lamina compressive strain limit parallel to fiber
Eps11T	Lamina tensile strain limit parallel to fiber
Eps12S	Lamina in-plane strain limit
Eps22C	Lamina compressive strain limit perpendicular to fiber
Eps22T	Lamina tensile strain limit perpendicular to fiber
FVR	Fiber volume ratio
VVR	Void volume ratio
MVR	Matrix volume ratio
G_{12}	Lamina in-plane shear modulus
G_{f12}	Fiber shear modulus – In-plane
G_{f23}	Fiber shear modulus – Out-of-plane
GUI	Graphical user interface
IPS	In-plane shear
LC	Longitudinal compression
LT	Longitudinal tension
S11C	Lamina compressive strength in fiber direction
S11T	Lamina tensile strength in fiber direction
S12S	Lamina in-plane shear strength
S22C	Lamina compressive strength perpendicular to fiber direction
S22T	Lamina tensile strength perpendicular to fiber direction
Sf11 C	Fiber compressive strength
Sf11T	Fiber tensile strength
SmC	Matrix compressive strength
SmS	Matrix shear strength

SmT	Matrix tensile strength
TT	Transverse tension
TC	Transverse compression
CDF	Cumulative distribution function
PDF	Probability density function
COV	Coefficient of variation

3. Description of technical approach

Methodology and computational procedure is described as an integrated MS-PFA and probabilistic analysis capability. It is comprised of the following:

- determination of scatter and sensitivity of in-situ material properties and fabrication parameters (e.g., fiber tensile strength, and fiber volume ratio);
- reproducing the test measured scatter/distribution in lamina using MS-PFA, and probabilistic analysis;
- generate random samples using lamina level uncertainties;
- update scatter from simulation to match lamina CDF and PDF curves using Bayesian statistics followed by determination of allowables with the desired confidence levels;

Scatter in strength data obtained from unidirectional lamina testing is used in predicting allowables for notched and un-notched laminates. The variability is generally caused by: (1) scatter in micro-scale mechanical properties of the fiber, matrix, and interface; (2) variability in composite manufacturing parameters; and (3) manufacturing defects such as void, waviness, and gaps. Lamina level testing is carried out to determine ply in-plane and out-of-plane mechanical properties. **Table 2** lists the measured ply properties obtained from in-plane testing of composite specimens made from unidirectional laminates. The same table also lists the physical parameters influencing the measured ply response. For example, variation in ply longitudinal strength collected from test is a function of scatter of fiber strength and fiber content. MS-PFA [4] is used in conjunction with probabilistic methods [5] to reproduce scatter in strength obtained from lamina level testing. **Figure 3** shows the lamina level testing performed per ASTM standards to generate in-plane ply properties. **Figure 4** shows the process for reproducing the scatter from lamina level testing. Micro-scale random variables consisting of fiber and matrix mechanical properties combined with fabrication parameters are perturbed to reproduce the scatter from lamina level testing. This process results in a unique set of coefficient of variations for various random variables that can be used in random sampling of test specimens for higher order ASTM tests (laminate level).

The use of lamina level uncertainties to predict allowables for laminate level building block tests is the added value of the work presented in this paper. The work reported in [6] confirms that lamina uncertainties are adequate for use in generation of scatter in laminate level response. The uncertainties causing scatter in strength of a composite laminate are: (1) variability in fiber and matrix properties and composite fabrication parameters; (2) manufacturing defects ("as designed" versus "as built" and "as is"); and (3) human error encountered during testing. A flow chart of the technical approach for determination of A- and B-basis allowables is presented in **Figure 5**. The basis for the computation is the reproduction of scatter in ply strength caused by variability of constituent material properties and manufacturing defects. The approach was validated by comparing its A- and B-basis predictions with values obtained from standard methods [1&2] using test data from robust or reduced sampling.

Measured Ply Property	Physical Variables Influencing Measured Property
Longitudinal tension strength (S11T)	Fiber tensile strength (Sf11T) and fiber volume ratio (FVR)
Longitudinal tension modulus (E11T)	Fiber longitudinal tensile stiffness (Ef11) and fiber volume ratio (FVR)
Longitudinal compression strength (S11C)	Fiber compressive strength (Sf11C) and fiber volume ratio (FVR), fiber micro-buckling
Longitudinal compression modulus (E11C)	Fiber longitudinal compressive stiffness (Ef11) and fiber volume ratio (FVR)
Transverse tension strength (S22T)	Matrix tensile strength (SmT) and matrix volume ratio (MVR)
Transverse tension modulus (E22T)	Matrix modulus (Em), fiber transverse modulus and matrix volume ratio (MVR)
Transverse compression strength (S22C)	Matrix compressive strength (SmC) and matrix volume ratio (MVR)
Transverse compression modulus (E22C)	Matrix modulus (Em) and matrix volume ratio (MVR)
In-Plane shear strength at 0.2% Offset (IPS)	Matrix shear strength (SmS) and matrix volume ratio (MVR)
In-Plane shear strength at 5% Strain (IPS)	Matrix shear strength (SmS) and matrix volume ratio (MVR) and nonlinear properties of the matrix
In plane shear modulus (G12)	Matrix modulus (Em), matrix Poisson's ratio, Fiber Shear Modulus (Gf12) and matrix volume ratio (MVR)

Table 2. Stiffness and Strength Properties Obtained by Physical Testing of Composite Specimens (in-plane loading)

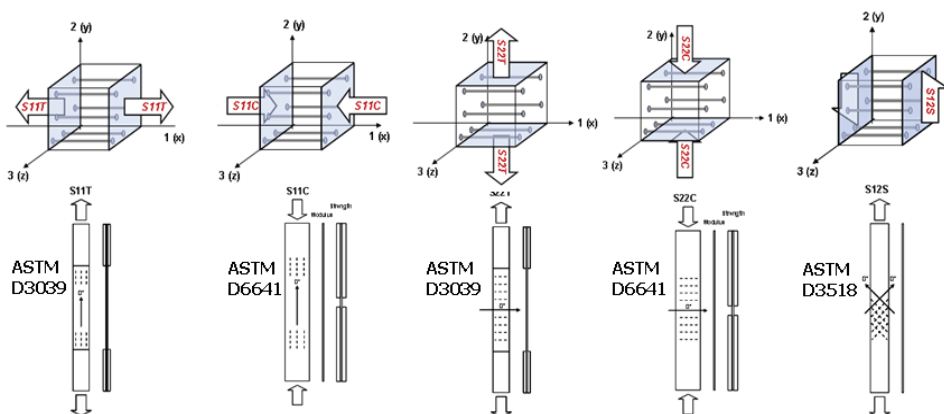


Fig. 3. Five Basic ASTM Tests are Needed at the Lamina Level to Characterize Fiber and Matrix Constituent Material Properties

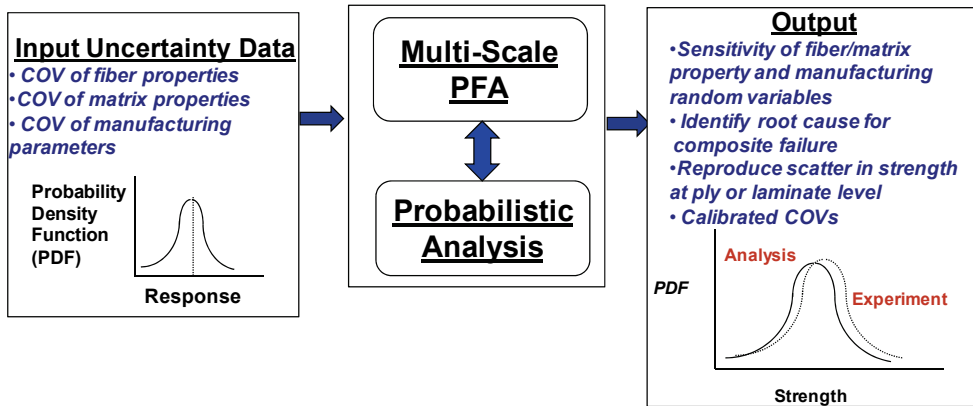


Fig. 4. Process for Reproducing Scatter from Ply or Laminate Level Testing

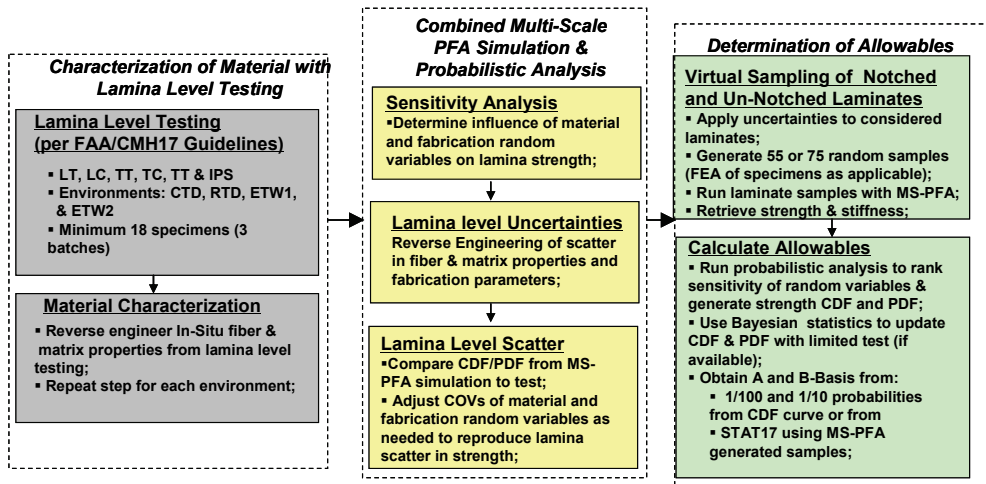


Fig. 5. Technical Approach for Determination of A- and B-Basis with Reduced Testing

4. Validation of technical approach

The computational capability described herein is validated for polymer composite materials typically used in aerospace applications. Data for MTM45-1 145 AS4, IM7/MTM45 graphite/epoxy and T300/PPS material are used to demonstrate the effectiveness of the methodology. Additionally, the capability of obtaining A-basis starting from B-basis is demonstrated.

Strength Allowables for MTM45-1 145 AS4 (Lamina Level)

Ply properties from lamina level testing at room temperature dry condition, obtained from [7], are used to characterize the MTM45-1 145 AS4 tape composite material. This is achieved by deriving its in-situ fiber and matrix properties. **Table 3** lists the AS4 fiber in-situ

mechanical properties while **Table 4** lists similar properties for the MTM45 matrix. The derived constituent properties combined with ply manufacturing parameters of 61% fiber volume fraction and 2% void volume fraction reproduced accurately the average ply properties reported from test in [7]. A comparison of calculated ply properties by MS-PFA simulation and test is presented in **Table 5**. With accurate determination of average ply properties starting from in-situ fiber matrix properties, random variables statistics for micro-scale mechanical properties are obtained directly from lamina level testing published in [7]. **Table 6** lists the derived random variables statistics for use in determination of strength allowables for MTM45-1 145 AS4. The COVs of strength and stiffness properties were obtained from lamina level tests published in reference [7] while the COVs of other random variables were iterated on to ensure proper simulation of lamina level scatter. The considered random variables included fiber and matrix stiffness and strength and fiber and

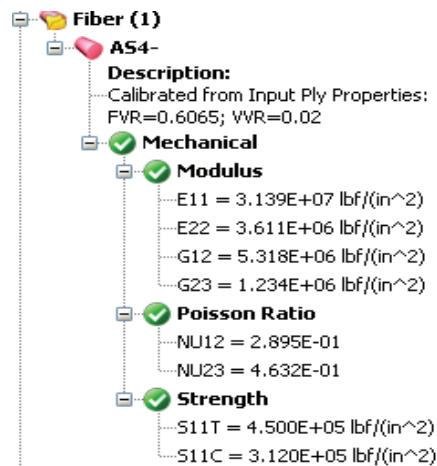


Table 3. AS4 Fiber In-Situ Properties

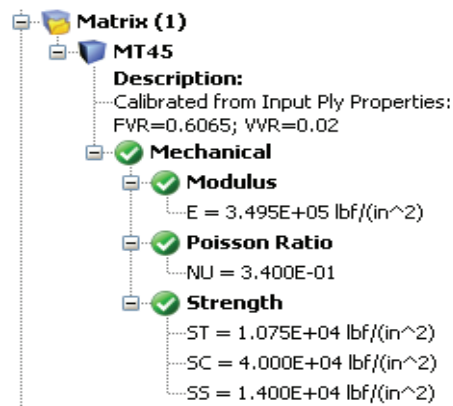


Table 4. MTM45 Matrix In-Situ Properties

AS4/12K (Tape): FVR=60.65%; VVR=2%			
Property	RTD		
	Test [msi]	Simulation [msi]	Error [%]
E11	17.925	18.79	4.83
E22	1.2	1.15	-4.17
G12	0.53	0.53	0.00
	[ksi]	[ksi]	[%]
S11T	274.78	271.6	-1.16
S11C	203.53	200.9	-1.29
S22T	6.92	6.84	-1.16
S22C	26.81	25.18	-6.08
S12S	9.36	8.68	-7.26

Table 5. Comparison of Average Ply Properties Obtained from Test to those from Simulation for MTM45-1 145 AS4

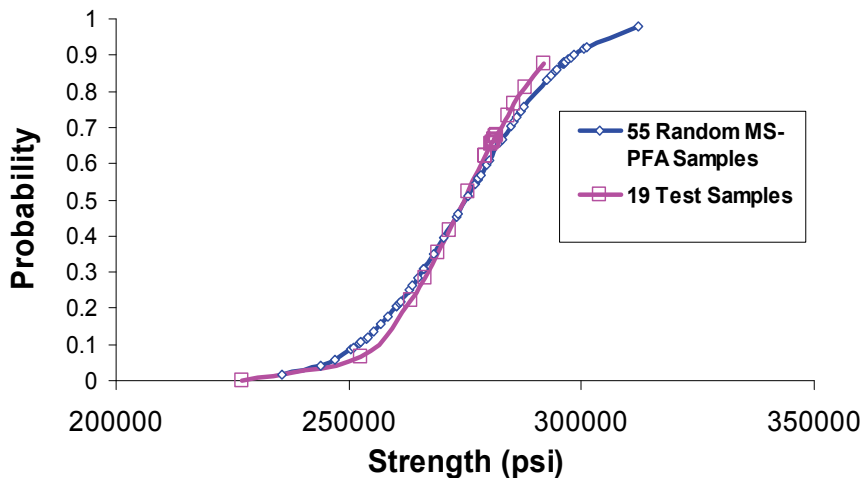
Fiber-Matrix Properties Random Variables	Mean Value	COV	Standard Deviation	Distribution Type
Fiber Ef11 – Longitudinal modulus (msi)	31.39	3.0%	0.9417	Normal
Fiber Sf11T- Longitudinal tension strength (ksi)	450	5.5%	24.75	Normal
Fiber S11C – Longitudinal compression strength (ksi)	312	5.0%	15.6	Normal
Matrix Em – Normal modulus (msi)	0.3495	3.1%	0.018345	Normal
Matrix SmT – Matrix tension strength (ksi)	10.75	17.5%	1.881	Normal
Matrix SmC – Matrix compression strength (ksi)	40	5.0%	2	Normal
Matrix SmS – Matrix shear strength (ksi)	14	4.0%	0.56	Normal
Manufacturing Parameters Random Variables	Mean Value	COV	Standard Deviation	Distribution Type
Fiber content (%)	60.65	4%	2.426	Normal
Void content (%)	2	2.5%	0.05	Normal

Table 6. Random Variables Statistics for Use in Determining Allowables for MTM45-1 145 AS4 Composite

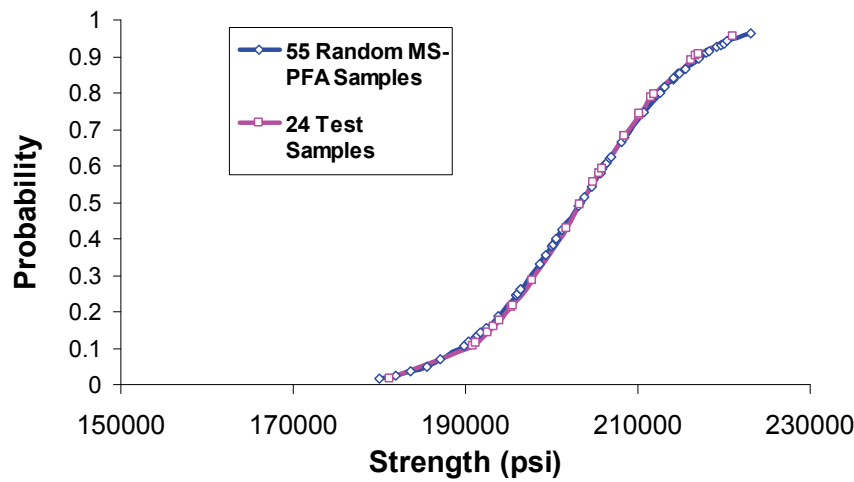
void contents. The COVs for the mechanical properties were obtained from lamina level testing published in reference [7] using the correlation between measured ply property and micro-scale properties of **Table 2**. The COVs for the manufacturing variables were obtained by iterating on the scatter produced by combined MS-PFA and probabilistic analysis to match the one from lamina level testing of the five in-plane ASTM tests of **Figure 3**.

Figure 6 shows the lamina level cumulative distribution functions (CDFs) for the 5 in-plane ASTM tests LT, LC, TT, TC, and IPS generated from virtual test data using MS-PFA simulation and from actual test. The data from test and simulation are fitted to a normal distribution in the plots (a) through (e) for the various ASTM tests. The amount of data reported in reference [7] for each ASTM type varied. For example, for the LT test, 19 samples were reported while for LC a total of 24 samples were reported. The CDF from simulation was generated for each test using the random variables statistics listed in **Table 6**. A total of 55 samples were randomly generated with MS-PFA considering simultaneous uncertainties in material and manufacturing random variables. That means MS-PFA was run 55 times for each ASTM test to predict failure stress for each sample. All variables listed in **Table 6** took on random values for each analysis sample by MS-PFA. As illustrated in **Figures 6-a** through **6-c**, the distribution (scatter) and mean strength generated by the simulation matched perfectly the ones from test for LC, LT, and TT tests.

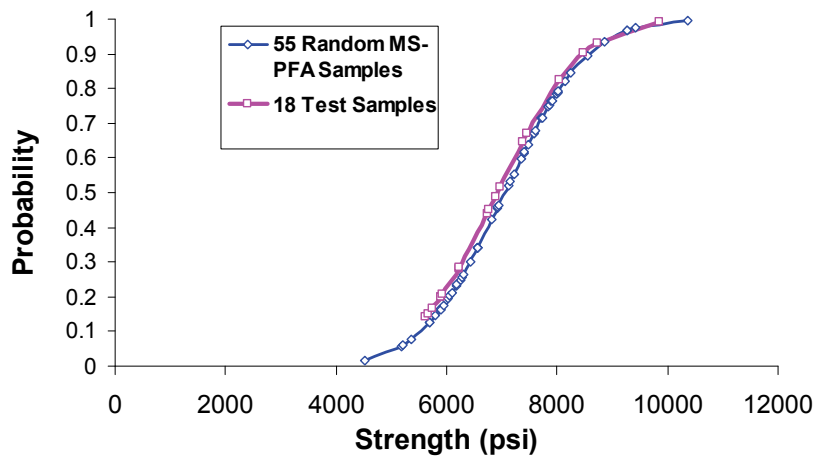
The data generated for TC and IPS are shown in **Figures 6-d** and **6-e**. The CDFs from simulation are updated for TC and IPS per the procedure outlined in **Figure 5** for fine tuning the COV variables. Initial predictions for mean strength from simulation were 5.5% and 6.3% lower than average from test for TC and IPS. The updates, although not necessary, are done to ensure that the mean strength from simulation matches exactly the mean from test. This process allows the analyst to correlate data from test with simulation and update the simulation results with test data regardless how limited the data is. The difference between mean predicted and test strengths for TC and IPS specimens could have been reduced to a negligible value by adjusting the calibrated in-situ properties. However, the authors intended to illustrate that the difference in mean strength between simulation and test depicts a realistic situation.



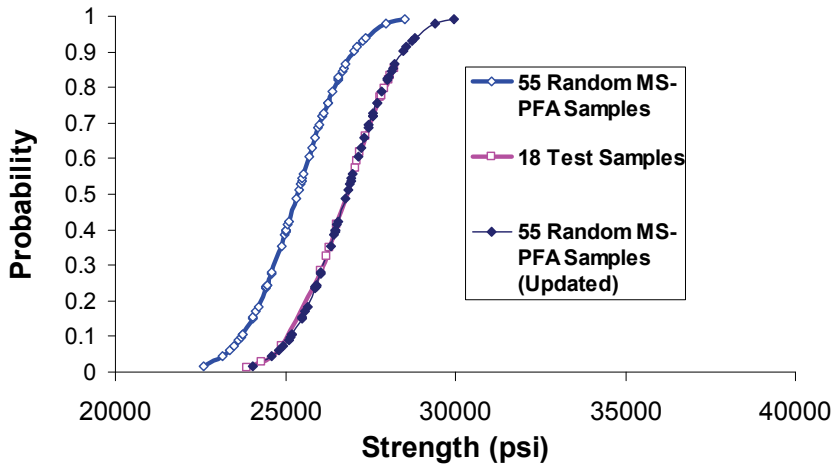
(a) MS-PFA Samples Compared to Test for MTM45-1 145 AS4 Longitudinal Tension (LT)



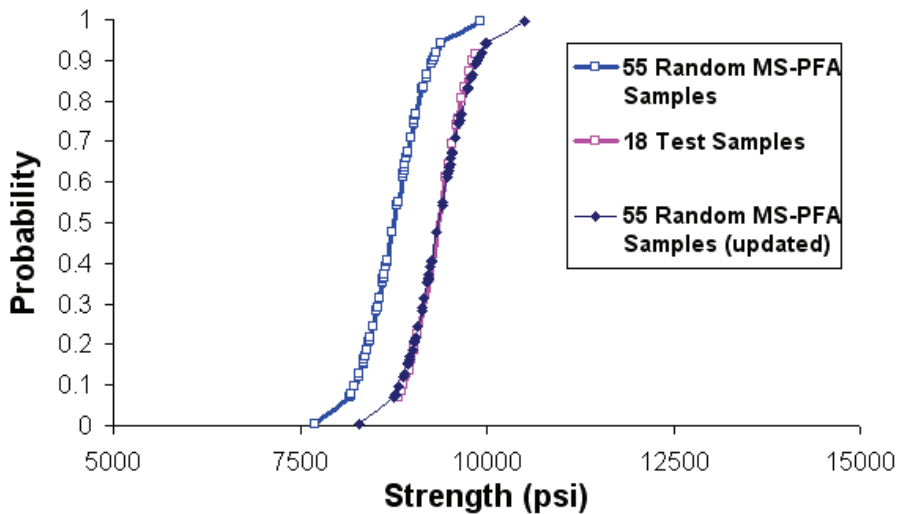
(b) MS-PFA Samples Compared to Test for MTM45-1 145 AS4 Longitudinal Compression (LC)



(c) MS-PFA Samples Compared to Test for MTM45-1 145 AS4 Transverse Tension (TT)



(d) MS-PFA Samples Compared to Test for MTM45-1 145 AS4 Transverse Compression (TC)



(e) MS-PFA Samples Compared to Test for MTM45-1 145 AS4 In-Plane Shear (IPS)

Fig. 6. Scatter in Failure stress for LT, LC, TT, TC, and IPS Generated by MS-PFA Simulation for MTM45-1 145 AS4 Compared to Lamina Level Test Data [7]

Based on accurate reproduction of strength scatter with MS-PFA from test, one concludes that the uncertainties defined are valid for use in laminate level simulation of notched or unnotched specimens. If the scatter produced from simulation is not accurate, other physical random variables can be included in the analysis while iterating on the COV to match the scatter at the lamina level.

The virtual test samples data produced by MS-PFA are run with STAT-17 [2] to determine A- and B-basis values. **Table 7** compares the A- and B-basis values from the 55 samples generated

by MS-PFA to those reported in reference [7]. The samples generated virtually by MS-PFA are analyzed using STAT-17 to determine A- and B-basis values. The results obtained from STAT-17 for MS-PFA samples met the normality criterion. Note that the allowables reported in [7] for TT and IPS tests were obtained using ANOVA method (a very conservative criterion). The advantage of simulation lies in its capability of providing alternate approach to avoid unreasonable allowable strength values when CMH-17 criteria are not met.

Lamina	Test Mean	MS-PFA Mean	Test Report [7]	MS-PFA*	% Diff
Test	Strength (ksi)	Strength (ksi)	A-Basis (ksi)	A-Basis (ksi)	w.r. [7]
LT	274.78	275.18	234.76	224.01	-4.58%
LC	203.53	203.38	168.23	172.55	2.57%
TT	6.92	7.05	0.48**	3.68	N/A
TC	26.81	25.36	21.61	21.71	0.46%
IPS	9.36	8.76	4.97**	7.61	N/A
Lamina	Test Report [7]	MS-PFA	% Diff		
Test	B-Basis (ksi)	B-Basis (ksi)	w.r. [7]		
LT	250.71	245.80	-1.96%		
LC	182.47	185.68	1.76%		
TT	0**	5.12	N/A		
TC	24.26	23.27	-4.08%		
IPS	6.8**	8.10	N/A		

* Randomly generated with MS-PFA then used as input to STAT-17 (Normal)

**Reference [7] used ANOVA method to report allowables

Table 7. Validation of MTM45-1 145 AS4 Lamina Level Allowables Obtained Using Virtual Test Samples by MS-PFA (Simulated Samples are Inputed to STAT-17)

Table 8 lists lamina level allowables obtained from simulated CDF at 0.01 probability for A-basis and at 0.10 probability for B-basis are compared to those reported in reference [7]. Overall, generating samples randomly with MS-PFA and processed with STAT-17 produce similar allowables to those obtained from a CDF for the given ASTM test. However, the CDF curve would depict more stable allowables as it is not dependent on tolerance factors. Next, results obtained for laminate level allowables are presented and discussed.

Lamina	Test Mean	MS-PFA Mean	Test [7]	MS-PFA*	Difference
Test	Strength (ksi)	Strength (ksi)	A-Basis (ksi)	A-Basis (ksi)	w.r.t [7]
LT	274.78	275.18	234.76	229.91	-2.07%
LC	203.53	203.38	168.23	175.17	4.13%
TT	6.92	7.05	0.48**	4.04	N/A
TC	26.81	25.36	21.61	22.32	3.29%
IPS	9.36	8.76	4.97**	7.93	N/A
Lamina	Test [7]	MS-PFA	Difference		
Test	B-Basis (ksi)	B-Basis (ksi)	w.r.t [7]		
LT	250.71	249.91	-0.32%		
LC	182.47	187.11	2.54%		
TT	0**	5.28	N/A		
TC	24.26	23.27	-4.08%		
IPS	6.8**	8.29	N/A		

* Obtained from CDF of Probabilistic Strength (A-basis at 0.10 Probability; B-basis at 0.1 Probability)

**Reference [7] reported use of ANOVA for this prediction

Table 8. Validation of MTM45-1 145 AS4 Lamina Level Allowables Obtained Using Virtual Test Samples by MS-PFA (A- and B-Basis Values are Obtained from CDF Curve at 0.01 and 0.1 Probabilities)

Strength Allowables for MTM45-1 145 AS4 (Laminate Level without use of Test Data)

A major contribution of the work presented here is the ability to use lamina level uncertainties to predict uncertainties for any laminate. Micro-scale uncertainties are infused to higher level structures of the FAA building block of **Figure 7**. The uncertainties derived in **Table 6** are used to determine A- and B-basis allowables for un-notched laminate specimens for two layups: $[0/90]_s$ and quasi-isotropic (25% 0° plies, 50% $\pm 45^\circ$ plies, and 25% 90° plies). The allowables were obtained with MS-PFA for tension and for compression loading conditions. **Figure 8** shows plots of the CDF of strength determined using the same uncertainties used in the lamina level simulation. **Table 9** lists the values for A- and B-basis obtained from MS-PFA simulation and from reference [7] using standard methods.

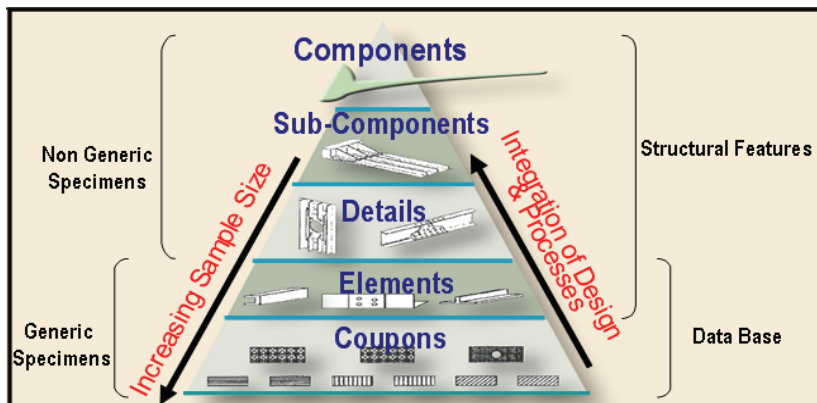
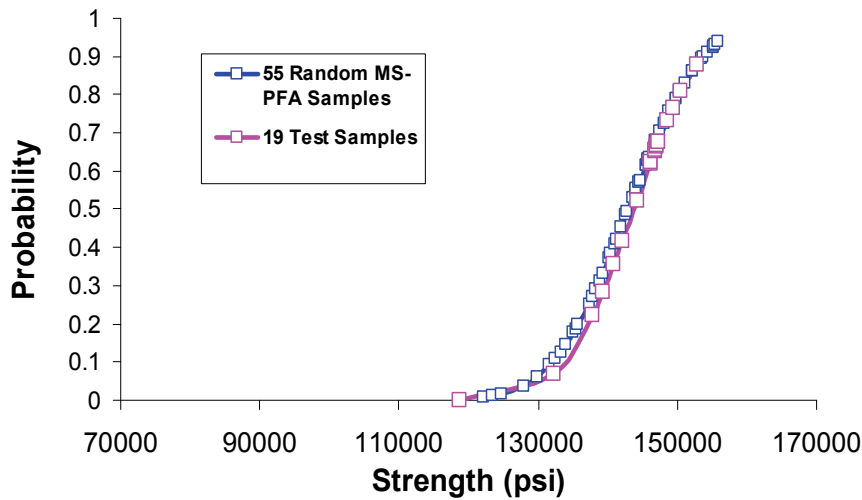
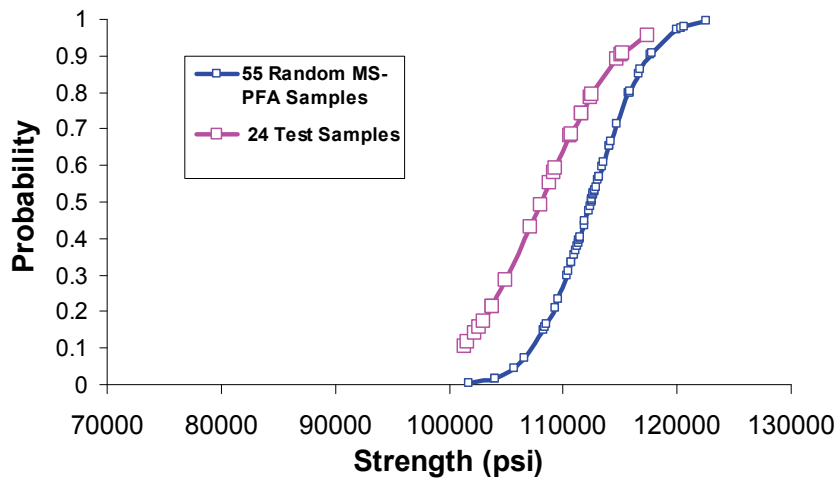


Fig. 7. FAA Building Block Validation with Generic and Non-Generic Specimens Depicting Multi-Scale and Multi-Level Integration of Structural Parts

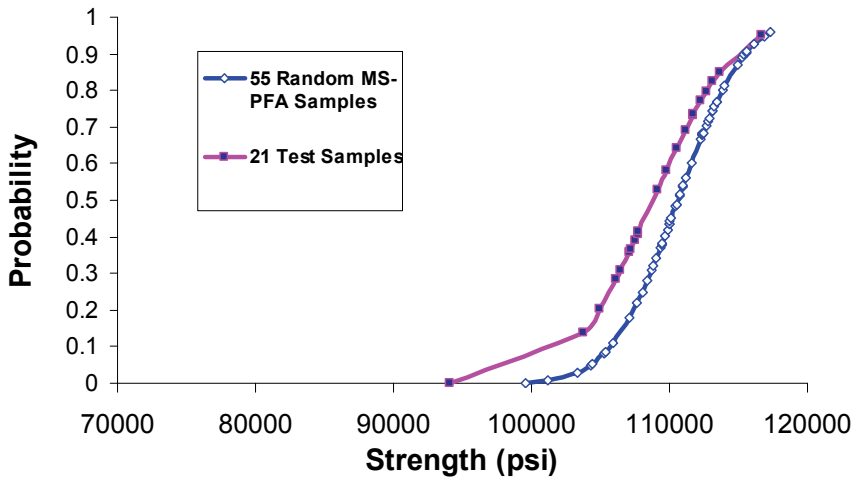
In **Figure 8**, strengths from physical testing are plotted alongside the strengths generated with MS-PFA. This is done to illustrate the degree of fitness of simulated data compared to test. The allowables values listed in **Table 9** are obtained from simulation using the uncertainties of **Table 6** and assuming data from physical testing are not available. **Figure 9** shows the probabilistic sensitivities of random variables for the quasi-isotropic laminate. The sensitivity analysis ranks the random variables by order of influence on the laminate strength response. This is done by identifying the “root cause” for composite damage and failure. Controlling variability in the influential random variables reduces scatter in laminate strength response. As can be concluded from **Figure 9**, the transverse tensile strain EPS22T is the most predominant uncertainty followed by fiber volume ratio, FVR. Note that for laminate level specimens, a strain failure criteria is used for ply failure analysis in MS-PFA while for lamina level specimens, strength based criteria were used. The random variable statistics remain unchanged as the evaluation moved from lamina level to laminate level. Strain limits used as fracture criteria for laminate analysis are derived from lamina analysis and the reverse engineering process of fiber and matrix properties discussed earlier (**Table 3** and **Table 4**).



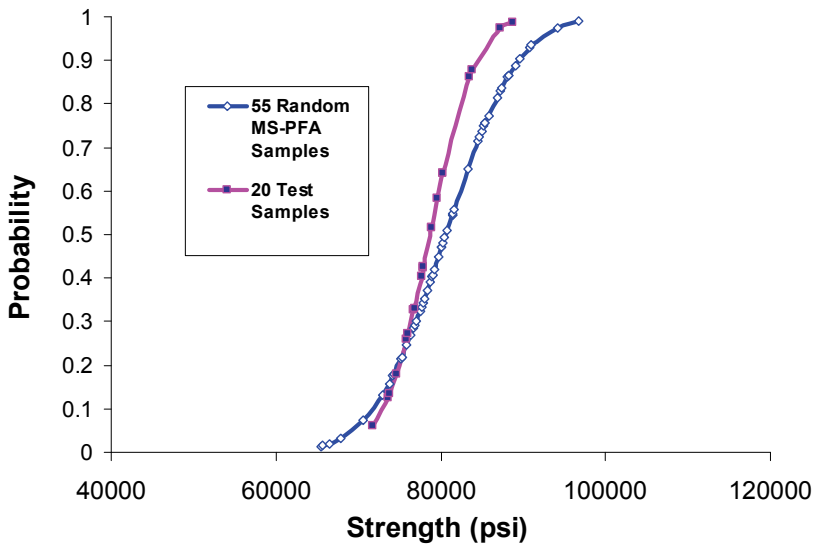
(a) MS-PFA Samples Compared to Test for 0/90 MTM45-1 145 AS4 Un-notched Tension



(b) MS-PFA Samples Compared to Test for 0/90 MTM45-1 145 AS4 Un-notched Compression



(c) MS-PFA Samples Compared to Test for MTM45-1 145 AS4 Quasi Isotropic Un-notched Tension



(d) MS-PFA Samples Compared to Test for MTM45-1 145 AS4 Quasi Isotropic Un-notched Compression

Fig. 8. Scatter in Laminate Level Failure Stress for MTM45-1 145 AS4 0/90 and Quasi Un-notched Specimens Generated by MS-PFA Simulation Compared to Test Data [7]

Test Type	Test Mean	MS-PFA Mean	Test [7]	MS-PFA*	Difference
Un-Notched	Strength (ksi)	Strength (ksi)	A-Basis (ksi)	A-Basis (ksi)	w.r.t [7]
0/90 Tensile	143.74	142.96	122.82	125.87	2.48%
0/90 Compressive	108.07	112.47	89.71	91.30	1.77%
Quasi Tensile	108.82	110.62	95.35	99.80	4.67%
Quasi Compressive	78.81	80.62	68.51	61.15	-10.74%
Test Type	Test[7]	MS-PFA	Difference		
Un-Notched	B-Basis (ksi)	B-Basis (ksi)	w.r.t [7]		
0/90 Tensile	131.16	129.20	-1.49%		
0/90 Compressive	97.09	104.02	7.14%		
Quasi Tensile	100.83	104.41	3.55%		
Quasi Compressive	72.63	69.44	-4.39%		

* Randomly generated then used as input to STAT-17 (Normal)

Table 9. Validation of MTM45-1 145 AS4 Laminate Level Allowables Obtained Using Virtual Test Samples by MS-PFA (Simulated Samples are Input to STAT-17)

The effect of sample size on A- and B-basis predictions is presented in **Figure 10** for the quasi-isotropic laminate under tension loading. MS-PFA was used to generate 55, 100 and 1000 samples. The predictions improved with the use of increased number of samples as compared to the 21 physical tests reported in reference [7]. The A and B- basis values for different random sample size are listed in **Table 10**. The randomly generated samples were fitted to normal distribution. Evaluating these virtual samples with STAT-17 yielded the A- and B-basis values presented in **Table 10**. As more virtual samples were generated, the mean value approached the real mean from the 21 physical tests. Data presented in **Table 10** establishes confidence in the computational approach, especially to the stability of data obtained from virtual simulation. Next, validation of allowables for IM7/MTM45-1 with reduced testing is presented and discussed.

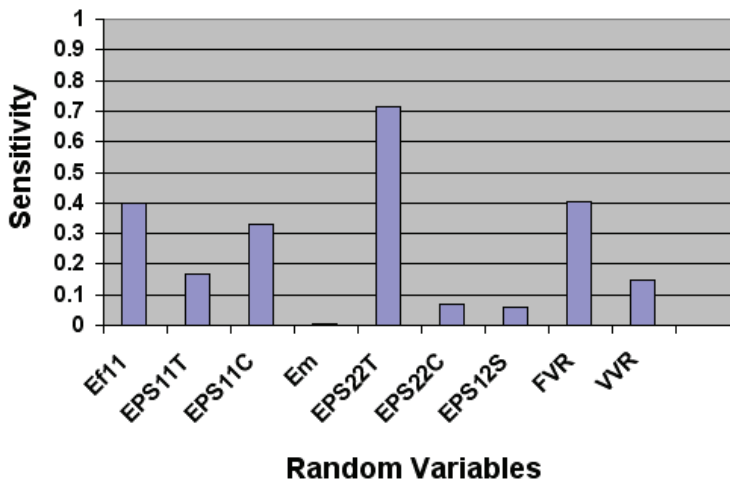


Fig. 9. Sensitivity of Random Variables for MTM45-1 145 AS4 Quasi Un-notched Laminate (Tension Loading)

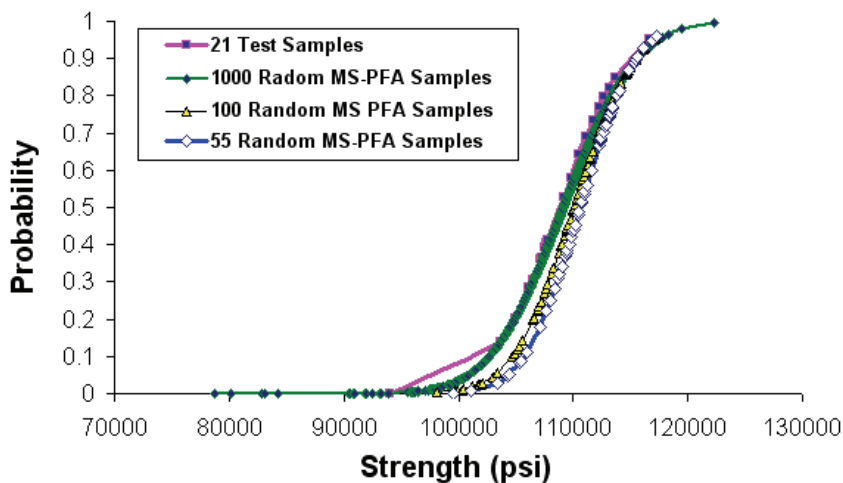


Fig. 10. Effect of Number of Virtual Samples on Strength of MTM45-1 145 AS4 Quasi Un-notched Laminate (Tension Loading)

Test Type Un-Notched	Mean	A-Basis	B-Basis
	Strength (ksi)	Strength (ksi)	A-Basis (ksi)
21 Test Samples [7]	108.82	95.34	100.83
55 Virtual Samples	110.62	99.80	104.41
100 Virtual Samples	110.09	98.85	103.66
1000 Virtual Samples	109.15	96.90	102.32
Difference w.r.t. tests [6]			
55 Virtual Samples	1.65%	4.68%	3.55%
100 Virtual Samples	1.16%	3.68%	2.81%
1000 Virtual Samples	0.31%	1.64%	1.48%

Table 10. Effect of Number of Virtual Samples on Determination of A- and B-Basis for MTM45-1 145 AS4 Quasi Un-Notched Laminate (Tension Loading)

B-Basis Strength Allowables for IM7/MTM45-1 (Sealed Envelope Prediction)

To further affirm the validity of the approach for generating allowables with reduced testing, Northrop Grumman Corporation (NGC) provided data for IM7/MTM45 composite for use in a “sealed envelope” process [8]. Using statistics provided by NGC for lamina level testing, B-basis values were calculated for notched and un-notched laminates using the approach proposed in this document to reduce laminate level testing. NGC provided one third of the laminate level test data usually used in the generation of allowables. Independent of full test results, predictions were made and handed to NGC for comparison against a “sealed envelope” of real test data. B-basis tensile strength values for un-notched and notched IM7/MTM45-1 coupons were predicted (using a reduced number of test replicates) and provided to NGC. Predicted results were compared to those obtained using standard military specification practices and the standard number of test replicates. The

difference in the B-basis results obtained from prediction and those from current practices ranged from -5.31% and 5.34%. **Figure 11** shows the steps followed to compute B-basis values for the various coupons starting with a reduced number of test replicates. The number of replicates varied from 3 to 6 as listed in **Table 11**. The same table compares MS-PFA B-basis predictions to those obtained using traditional methods and all available replicates [9-10]. The B-basis values from the references were not made available until after computational allowables were derived. The B-basis predictions were obtained with MS-PFA using a unique set of prescribed uncertainties of the following random variables: fiber tensile strength, matrix tensile strength, matrix shear strength, fiber volume ratio, and void volume ratio. The uncertainties were derived from the lamina level testing for IM7/MTM45 Open hole tension (OHT) coupon simulations showed errors in predicted mean tensile strength ranging from -12.7% to 8.88% compared to true average from test. The difference

Coupon Type	Lamina	B-basis (ksi)	B-basis (ksi)	Difference
Un-Notched Tension RTD	Proportions	MS-PFA	CMH17 [2]	w.r.t. [2]
	[50-0-50]	156.22	158.54	-1.46%
	[25-50-25]	112.98	119.32	-5.31%
	[10-80-10]	69.09	65.59	5.34%
Un-Notched Compression RTD	[50-40-10]	173.41	178.4	-2.80%
	[25-50-25]	59.4	62.15	-4.42%
	[10-80-10]	41.59	41.67	-0.19%
	[50-40-10]	98.13	100.63	-2.48%

Table 11. Un-Notched and Notched B-Basis Strength Predictions for IM7/MTM45 (Tension Loading)

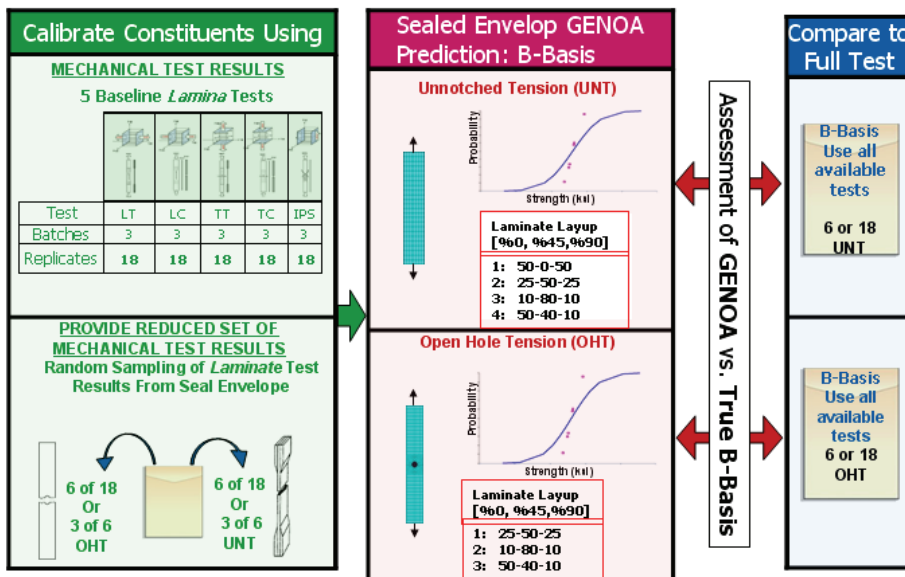


Fig. 11. Process Used for Computing B-Basis Values for Various IM7/MTM45 Coupons Starting with a Reduced Number of Test Replicates

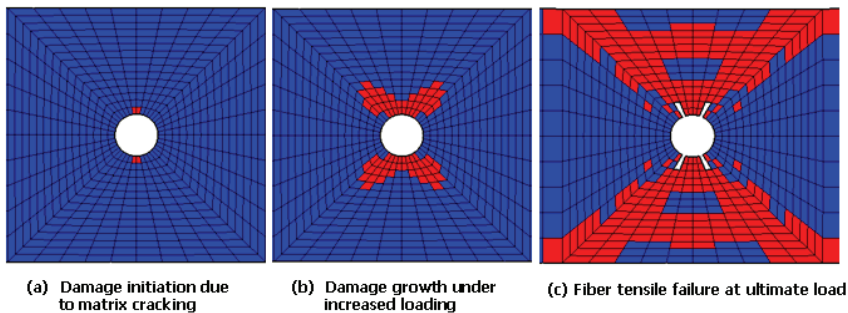


Fig. 12. Damage Initiation, Damage Growth and Fracture in Quasi OHT Made from IM7/MTM45 (Red Indicates Material Damage)

between simulation and test averages were addressed using Bayesian statistics update where CDF from simulation was corrected with the 6 few tests that were available. Animation of damage at the initiation stage and progression up to ultimate failure for the quasi open hole coupon under tension loading is presented in **Figure 12**. MS-PFA [4] identified critical damage evolution events isolating plies and elements contributing to the failure.

A- and B-Basis Validation for Open Hole Tension (OHT) T300/PPS Thermoplastic

To further demonstrate the validity of the MS-PFA approach for determination of allowables with reduced testing, A- and B-basis predictions were made for an open hole specimen under tension loading [11,12]. The specimen was fabricated from T300 carbon PPS thermoplastic composite material in a woven configuration with $[\pm 45/(0/90)]_{3S}$ layup. First, MS-PFA was used to reverse engineer the constituent properties from lamina level LT, LC, TT, TC and IPS tests. Second, uncertainties in fiber and matrix properties and fabrication parameters were assumed since lamina level statistics for the T300/PPS material were not available. Unknown COV's can be obtained from existing databases of comparable or similar materials or from experience based on anticipated scatter. **Table 12** lists the

Test #	Failure Load	Test #	Failure Load
1	0.9218	16	1.0008
2	0.9507	17	1.0027
3	0.9593	18	1.0027
4	0.9690	19	1.0065
5	0.9709	20	1.0065
6	0.9728	21	1.0065
7	0.9853	22	1.0143
8	0.9853	23	1.0143
9	0.9892	24	1.0268
10	0.9950	25	1.0287
11	0.9950	26	1.0335
12	0.9960	27	1.0335
13	0.9979	28	1.0393
14	0.9979	29	1.0470
15	0.9998	30	1.0510

Table 12. Normalized Tensile Failure Load for T300/PPS Open Hole Composite Coupon

Property	COV
Fiber longitudinal modulus	5%
Fiber longitudinal tensile strength	5%
Matrix modulus	5%
Matrix tensile strength	5%
Matrix shear strength	5%
Fiber volume fraction	5%
Void volume fraction	5%

Table 13. Random Variables Used in Predicting A- and B-Basis Allowables for T300/PPS

normalized failure load from the test for the OHT case. The range of the failure load varied from 0.9218 to 1.051 with a standard deviation of 0.028. **Table 13** lists the assumed random variables for use in the prediction of allowables. Initial COV of 5% was assumed for all random variables.

MS-PFA was used in conjunction with probabilistic analysis to replicate the scatter in the failure strength for the OHT coupon. The random variables were selectively perturbed by the analysis engine to populate enough data to predict the cumulative distribution of the failure stress. As indicated in **Figure 13**, the scatter from simulation did not agree with that from test when a coefficient of 5% was applied uniformly to all random variables. However, reducing the coefficient of variation to 1% for the fiber and matrix stiffness and strength and the fabrication variables, yielded an excellent agreement with test (**Figure 14**). If test data did not exist to calibrate the COV's of the constituent properties and fabrication parameters, one can assume a 5% value as a starting point. Sensitivity analysis can also be used to reduce the list of random variables to include those that are very influential (those with sensitivity higher than 10%).

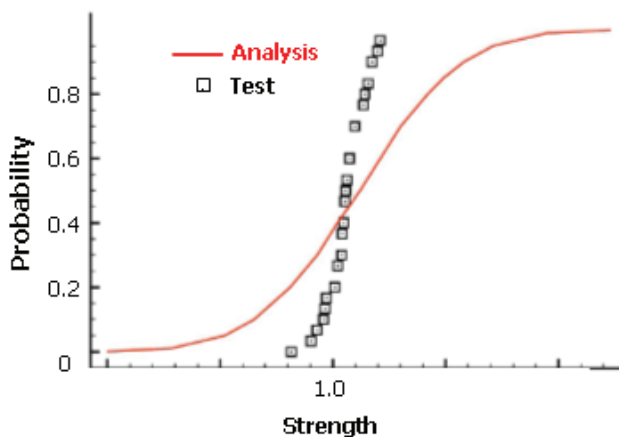


Fig. 13. Comparison of Scatter from Simulation and Test for T300/PPS OHT Strength With a Coefficient of Variation of 5%

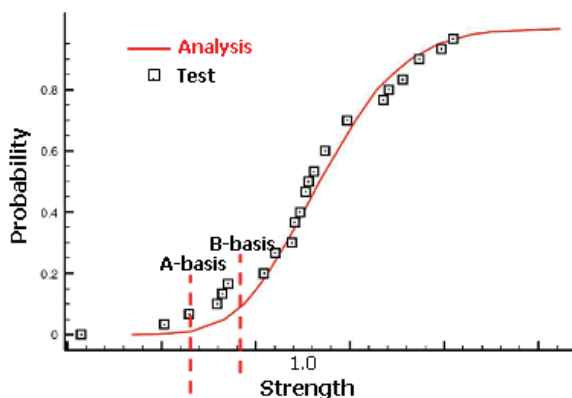


Fig. 14. Comparison of Scatter from Simulation and Test for T300/PPS OHT Strength With a Coefficient of Variation of 1%

Processing the 30 test data through STAT17 resulted in an A-basis value of 0.92 and a B-basis value of 0.9486 with respect to a mean normalized strength of 1.0. The CDF obtained from MS-PFA resulted in A-basis value of 0.9104 and a B-basis value of 0.959 when the strengths were retrieved at the 1/100 and 1/10 probabilities. The maximum error from the prediction with respect to test was 1.1% as shown in **Table 14**.

	Test (Mil-HDBK)	Analysis	% Error
A-Basis	0.92	0.9104	1.04%
B-Basis	0.9486	0.959	-1.10%

Table 14. Open Hole Tension Case Comparison of A- and B-Basis Values from Test and Analysis

Determination of A-Basis Values from B-Basis

As discussed earlier, accepted standards for determination of A-basis require physical testing of 55 specimens from 10 batches (as a minimum). Reference [13] listed strength data from testing of 145 specimens for 90° tension laminate made from T700 fibers and 2510 epoxy matrix. The MS-PFA approach was used to generate random samples to determine A-basis for the transverse tension laminate assuming only 18 test samples existed. Note that the 18 specimens is the minimum accepted standard [1,2] for B-basis determination. The 18 test specimens were obtained from a total 3 batches from [13], the data extracted were the first 18 test points reported in reference [13]. MS-PFA was then used to simulate the scatter for the 18 specimens and used to generate additional samples (55 and 145 random samples). The virtual test samples generated by MS-PFA used the statistics listed in **Table 15**.

Figure 15 shows a plot of the 18 test samples, 145 test samples, and 55 and 145 MS-PFA virtually generated test samples. The MS-PFA virtual samples fitted the 145 samples from physical test with great accuracy. The technical approach in MS-PFA can be used to generate virtual test samples not available thru physical testing. This is evident by the goodness of fit between simulated and test data and with the accurate calculation of A- basis as presented in **Table 16**.

Property	Mean	COV	Distribution
Ef11 (msi)	34.80	5.00%	Normal
Sf11T (ksi)	604.50	7.56%	Normal
Sf11C (ksi)	366.90	6.15%	Normal
Em (msi)	0.53	5.00%	Normal
SmT (ksi)	11.62	8.39%	Normal
SmC (ksi)	46.00	4.73%	Normal
SmS (ksi)	37.82	2.82%	Normal
FVR	0.53	2.50%	Normal
VVR	0.03	2.50%	Normal

Table 15. Random Variable Statistics for Determining A-Basis Strength from B-Basis for T700/2510 90° Tension Laminate

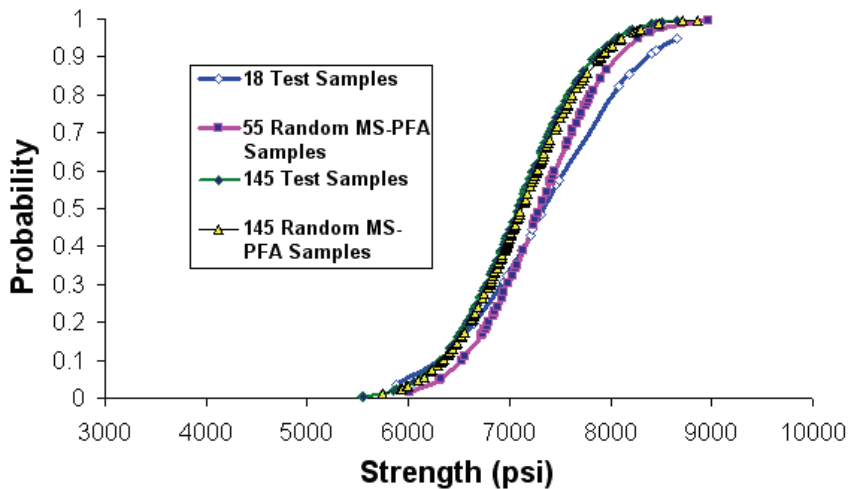


Fig. 15. Comparison of 18 and 145 tests to 55 and 145 MS-PFA Virtual Samples Used in Determining A-Basis Strength from B-Basis for T700/2510 90° Tension Laminate

Test Type	Mean	A-Basis	B-Basis
Un-Notched 90 Deg Tension	Strength (ksi)	Strength (ksi)	Strength (ksi)
18 Test Samples [12]	7341	4610	5741
145 Test Samples [12]	7083	5523	6200
55 Virtual Samples	7302	5603	6326
145 Virtual Samples	7121	5684	6258
Difference w.r.t. 145 Test Samples [13]			
55 Virtual Samples	3.09%	1.45%	2.03%
145 Virtual Samples	0.53%	2.92%	0.94%

Table 16. Determining A-Basis Strength from B-Basis for T700/2510 90° Tension Laminate

The referenced table lists A- and B-basis calculations obtained using the data from test and simulation after running STAT-17 with the generated virtual test samples. For each random sample generated, MS-PFA is executed to determine sample failure stress. **Table 16** also lists the mean strength from test and simulation. The mean strength value from 145 MS-PFA simulations was within about 0.5% of that from 145 physical test samples. The accuracy in predicting mean strength and A- basis values demonstrates the effectiveness of the devised methodology for determination of allowables with reduced testing.

5. Summary

A computational method has been presented for determining A and B-basis composite strength allowables with a significant reduction in testing over standard FAA and CMH-17 methods. The method combines multi-scale multi-physics progressive failure analysis (MS-PFA) with probabilistic methods and Bayesian updates. It was demonstrated for typical aerospace composite materials such as MTM45-1 145 AS4, IM7/MTM45-1, T300/PPS and T700/2510. Starting from lamina level coupon test data, root cause fiber and matrix properties, fabrication variables, and associated uncertainties are reverse engineered with MS-PFA for use in generation of strength allowables. MS-PFA is then used to virtually generate random laminate level test samples. In turn, the virtual test data are used to calculate allowable values for notched and un-notched composite laminate specimens. The methodology is robust and can be easily inserted into material characterization and qualification programs to yield a significant reduction in the number of physical tests at the laminate level. Additionally, the approach can be relied on to generate allowables for configurations (layouts) that were not initially included in a test plan as long as the simulation results are verified with few tests that are representative of the over-all design envelope. Very importantly, the methodology was validated for typical aerospace composite laminates and calculated A and B-basis values compared very well with test.

6. References

- [1] Material Qualification and Equivalency for Polymer Matrix Composite Material Systems: Updated Procedure. DOT/FAA/AR-03/19, Office of Aviation Research, Washington, D.C. 20591, September 2003.
- [2] The Composite Materials Handbook CMH-17, <http://www.cmh17.org/>
- [3] R. Rice, R. Goode, J. Bakuckas, and S. Thompson, "Development of MMPDS Handbook Aircraft Design Allowables". 7th Joint DOD/FAA/NASA Conference on Aging Aircraft, September 2003, New Orleans, LA.
- [4] M. Garg, G. Abumeri and D. Huang, "Predicting Failure Design Envelop for Composite Material System Using Finite Element and Progressive Failure Analysis Approach". SAMPE 2008.
- [5] G. Abumeri, F. Abdi, M. Baker, M. Triplet and, J. Griffin, "Reliability Based Design of Composite Over-Wrapped Tanks". SAE World Congress, 2007, 07M-312, Detroit MI, April 2007.
- [6] J. Tomblin, and W. Seneviartne, "Laminate Statistical Allowable Generation for Fiber-Reinforced Composite Materials: Lamina Variability Method". Report number DOT/FAA/AR-06/53, January 2009. US Department of Transportation, Federal

- Aviation Administration (Office of Aviation Research and Development), Washington, DC.
- [7] E. Clarkson, "Advanced Composites Group MTM45-1 145 AS4 Unidirectional Tape Qualification Statistical Analysis Report", National Institute for Aviation Research, Wichita State University, 2009.
 - [8] G. Abumeri, M. Garg, F. Abdi, A. McCloskey and R. Bohner, "Validation of a Computational Approach for Composite Material Allowables Using Sealed Envelope Predictions for Reduced Testing," *Sampe Journal*, Sep/Oct 2009.
 - [9] A. Crocket, "Advanced Composites Group MTM45-1 IM7-145 32%RW 12K IM7 Unidirectional, 145 gsm Qualification Material Property Data Report", National Institute for Aviation Research, Wichita State University, December 4, 2008.
 - [10] E. Clarkson, Y. Ng, and J. Tomblin, "B-Basis Values and Estimates for ACG Material MTM45-1/IM7-145gsm-32R%W", National Institute for Aviation Research/NCAMOP, Wichita State University, October 2008.
 - [11] M. Talagani, F. Abdi, and S. Verhoef, "Obtaining A-basis and B-basis Values for Open Hole Specimens Using Virtual Testing", 4th Ankara International Aerospace Conference, September 2007-METU, AIAC,-2007-127, Ankara, Turkey.
 - [12] G. Abumeri and M. Garg, and M. Talagani, "A Computational Approach For Predicting A- And B-Basis Allowables For Polymer Composites", *SAMPE 40th ISTC - Memphis, TN - Sep 2008*.
 - [13] J. Tomblin, J. Sherraden, W. Seneviratne, and K. S. Raju, "A-Basis and B-Basis Design Allowables for Epoxy - Based Prepreg, TORAY T700GC-12K-31E/#2510 Unidirectional Tape AGATE-WP3.3-033051-132", NIAR, Wichita State University, Wichita, KS, Nov 2002.

Elaboration and Properties of Carbon Fibre Reinforced Copper Matrix Composites

Pierre-Marie Geffroy¹, Jean-François Silvain² and Jean-Marc Heintz²

¹CNRS, Science des procédés céramiques et de traitements de surface, Limoges

²CNRS, Institut de la Chimie et de la Matière Condensée de Bordeaux
France

1. Introduction

Carbon fibres reinforced copper matrix composites (Cu/C composites) offer an excellent thermal conductivity and a low coefficient of thermal expansion. Then, these composites are compromising heat dissipation materials for electronic application.

The modern electronic devices consist of a variety of metallic, ceramic, plastic or composite components. The large difference of coefficient of thermal expansion (CTE) between ceramic substrates, such as Al_2O_3 and AlN , and heat dissipation materials, such as Cu and Al, and Si and GaAs semiconductors, induces thermal stresses resulting in failures at the interfaces between the different layers of the devices (fig. 1). In high power dissipation packages, thermal management is an important issue to prevent thermal damage of sensitive components on the silicon chip, especially for high density electronic packaging. Thermal management is thus one of the critical aspects in design of multichip modules to ensure reliability of electronic devices with high packing and power densities. In this context, there is an increasing demand of new heat dissipation materials having low CTE combined with high thermal conductivity, such as Cu/C composites.

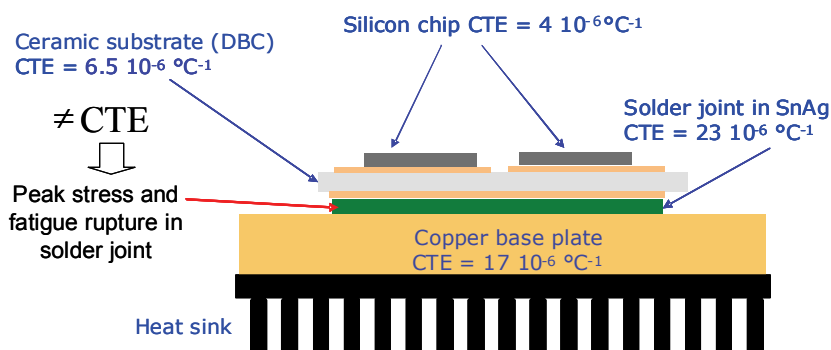


Fig. 1. Design of microelectronic devices with peak stress in solder joint.

Aluminium and copper are good candidate materials for the heat dissipation due to their thermal conductivity, but they have high values of CTE. Materials with low CTE and high

thermal conductivity, such as Al/SiC or Cu/W composites, have improved the reliability of electronic devices [Luedkte, 2004]. However, these composites are often too expensive for many applications. In addition, their machinability and the elaboration of thin sheets remain still very difficult and expensive.

Carbon fibres reinforced copper matrix composites corresponds to a good compromise between thermo mechanical properties and thermal conductivity [Korb et al., 1998]. Their main advantages are the following properties (Table 1):

- i. lower density than copper,
- ii. very good thermal conductivity,
- iii. low coefficient of thermal expansion,
- iv. good machinability.

Other advantages of copper/carbon fibre composites are adaptive thermal properties, which can be adjusted with the nature and the volume ratio of carbon fibres.

Function	Materials	CTE $10^{-6} \text{ }^{\circ}\text{C}^{-1}$ (RT- 250°C)	Thermal conductivity $\text{W.m}^{-1}.\text{K}^{-1}$ at 25°C	Density
Chips	Si	4.2	150	2.3
	GaAs	5.9	45	5.32
Heat sinks	Copper	17	400	8.95
	Aluminum	23	230	2.7
	Aluminum /63 % SiC	8	165	3
	Copper /85 % W	6	180	17
	Copper /40 % Carbon fibres (Pitch)	17 \perp 9-12 //	140-160 \perp > 210 //	6.11
Substrates	Al_2O_3	6.7	20-35	3.9
	AlN	4.5	170-250	3.26

Table 1. Properties of different electronic device materials (/ /: in plane properties; \perp : through-thickness properties).

The purpose of this chapter is to present the main research results during this last decade on the elaboration and properties of Cu/C composites. First, the different elaboration route of Cu/C composites is presented in this chapter. Then, the main physical properties of Cu/C composites are discussed, and a particular attention is given on the improvement of interface copper/carbon and thermal properties of Cu/C composites. Finally, the main potential applications of Cu/C composites are introduced, and their performances in focused applications are discussed at the end of the chapter.

2. Elaboration of Cu/ C composites

Several processes have been developed to elaborate copper carbon composites through hot pressing or squeeze casting [Praksan et al., 1997][Koráb et al., 2002]. However, all processes are difficultly perfecting and too expensive for elaboration of thin sheet materials. Besides, the poor wettability of carbon fibres with copper lead to low interfacial strength of composites obtained with casting or liquid process routes. This low wettability results often by large angle of the copper drop on graphite substrate (fig 2.). Then, one solution is the improvement of this wettability between copper and graphite with alloying element with

copper melt, such as Cr or Ti, in order to create a carbide layer to the copper/carbon interface [Goñi, 1998]. Then, the wetting angle decreases from 137° for the pure copper to 46° for the alloy Cu-1%wt Cr. This alloy has a good wettability with a final wetting angle lower than 90° because of the formation of chromium carbide (Cr_3C_2) layer in the copper/carbon interface.

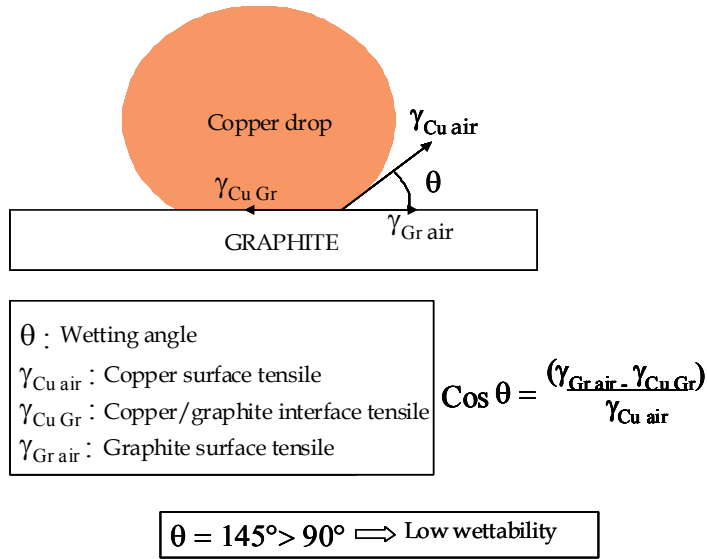


Fig. 2. Wetting angle of copper on graphite substrate.

Currently, the elaboration processes of Cu/C composites are based on powder metallurgy technology that offers many advantages such as the decrease of the machining cost (economical aspect), of power consumption (environmental aspect), and the better interfacial properties between copper matrix and carbon fibres. In opposite, the squeeze casting or liquid process route involves the low melting of matrix, low reactivity of metal liquid with carbon reinforced, and good wettability of metal liquid with carbon fibres.

Indeed, the no reactivity between carbon and copper leads to very low mechanical resistance of the interface and poor mechanical properties of composite. In order to improve the mechanical properties of interface, the carbon fibres require a previous surface treatment. These surface chemical treatments (in different acid solutions) of the carbon fibres, which may be used in order to create chemical bonding at the C-Cu interfaces, will be presented in more details in the following sections.

2.1 Starting copper powders and carbon fibres

The elaboration processes of Cu/C composites based on powder metallurgy technology require the starting copper powder, typically from 10 and 30 μm , and short carbon fibres, typically from 1 to 10 mm of length. In opposite, the squeeze casting process does not require the short carbon fibres or copper powders, but continuous carbon fibres can be used in this route process.

The characteristics of copper powder and short carbon fibres have strong impact on the final structure and properties of composites. These characteristics can be listed as following points:

- Ratio size between copper particles and diameter of carbon fibres. High ratio is favourable to better distributions of carbon fibres in copper matrix, and a ratio higher than one is usually recommended.
- The electrolytic copper powders (dendritic shape) lead to better mixing with short carbon fibres that copper powders obtained by atomisation (spherical shape).
- The length of carbon fibres must be 100 times greater than their diameter in order to obtain the optimal thermo-mechanical properties.

The following figures (fig.3) show two main types of copper powder, the spherical copper particles obtained by atomisation and dendrite copper particles obtained by electrolytic route.

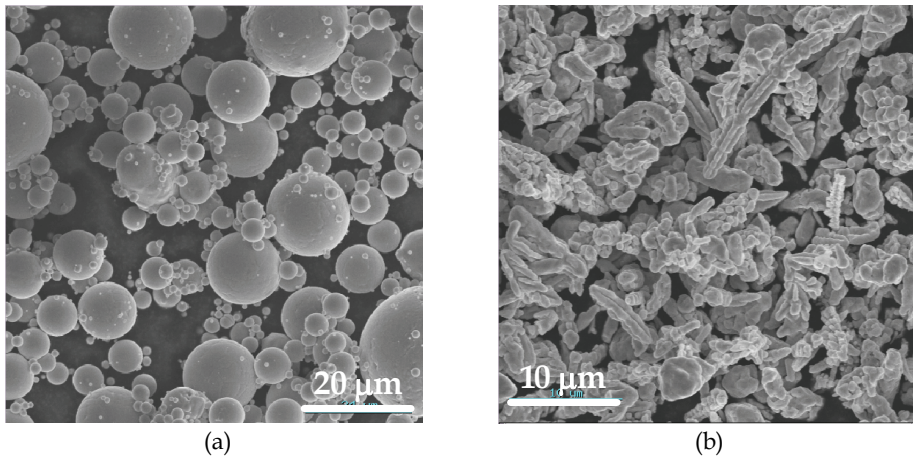


Fig. 3. (a) Copper powders obtained by atomisation from Nanoval, Germany (b) Copper powders obtained by electrolytic route (CH-UF 10) from Eckart Poudmet, Germany

Two main types of carbon fibres are usually used for industrial applications: polyacrylonitrile (PAN) and Pitch. Most of the carbon fibres currently produced in the world is based on PAN. Pitch fibres are produced using existing hydrocarbon resources (petroleum and/or coal) as the raw material to derive high performance carbon materials and product with a textile manufacturing approach.

In comparison to PAN, pitch carbon fibres have higher modulus capability, (equivalent) negative CTE, and higher thermal and electrical conductivity. These properties come from higher crystallisation of carbon fibre after graphitization step at high temperature. However, the Pitch carbon fibres are often more expensive than the PAN carbon fibres. Then, the Pitch carbon fibres are more appropriated for the thermal management applications.

Recently, Vapor Growth Carbon Nano Fibres (VGCNF) have been developed for potential thermal applications with theoretical thermal conductivity close to one of the diamond (1200 W/m.K). The VGCNF can be considered as an intermediate structure between carbon nanotubes and vapor growth carbon fibres. However, the properties of VGCNF have still been some controversy, since the strategy to measure their mechanical properties relies on non-conventional measurement techniques or inverse calculations from models.

The copper particles have dendrite shape with a range size from 25 to 30 µm (Fig. 3b). Starting chopped carbon fibres have diameter ranging from 9 to 10 µm and mean length of 6

mm. After milling, using planetary mill in alumina jar and alumina balls, the mean length of carbon fibres is decreasing down to 100 to 200 μm (Fig. a, b and c). In fact, for carbon fibre length greater than 200 microns, the flowability of slurry decreases strongly leading to the impossibility of slurry casted thin film.

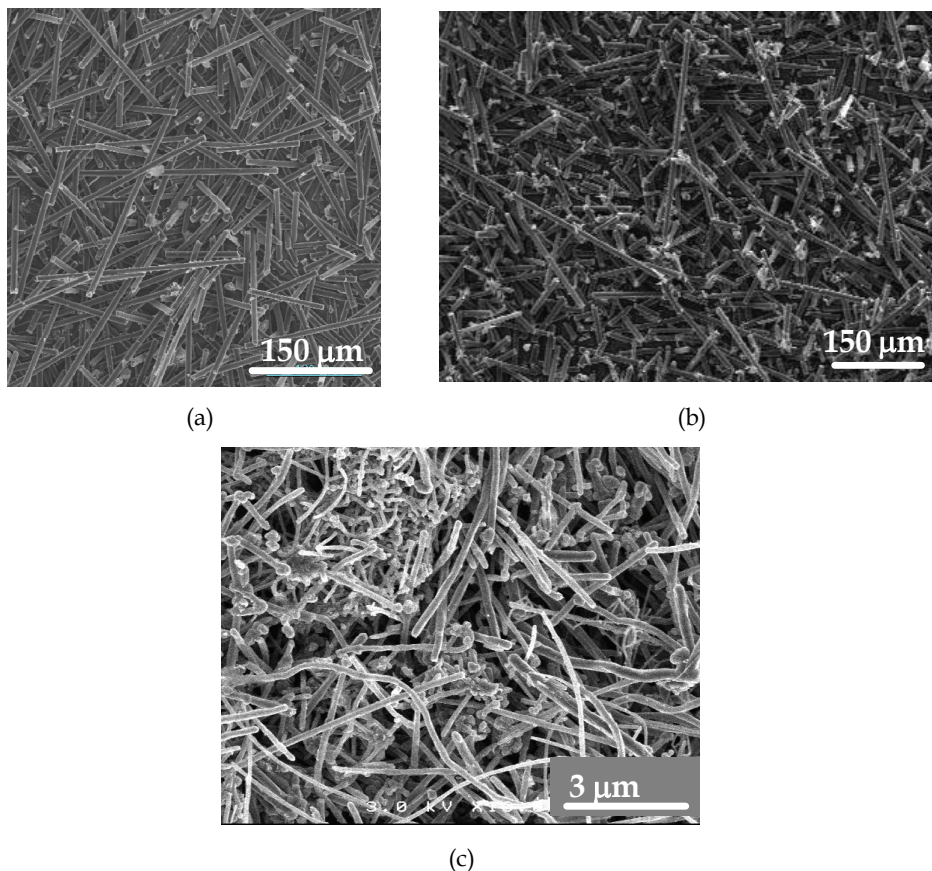


Fig. 4. Short carbon fibres, a) type PAN (T300), b) type Pitch (CN80C) and c) type VGCNF (Showa Denko)

The main physical characteristics of powders are given in Table 2.

2.2 Preparation of short carbon fibres or vapour growth carbon nanofibres (VGCNF)

After acid and ultrasonic treatments, the VGCNF are subjected to 3 consecutive steps (fig. 5). The sensitization (Sn absorption), activation (Pd absorption), and plating (Cu deposition) stages consist in the successive immersion of the VGCNF into the following baths:

- Sensitization bath: 10g/l SnCl_2 , 40ml/l HCl 37%, distilled water;
- Activation bath: 0.25 g/l PdCl_2 , 2.5 ml/l HCl 37%, distilled water;
- Plating bath: 10g/l CuSO_4 , 50g/l $\text{KNaC}_4\text{H}_4\text{O}_6 \cdot 4\text{H}_2\text{O}$, 10 g/l NaOH, 15 ml/l CHOH distilled water

Materials	Specific surface area (m ² .g ⁻¹)	Mean particle diameter (μm)	Apparent density (g.cm ⁻³)	Density (g.cm ⁻³)	CTE (10 ⁻⁶ /°C)	Thermal conductivity (W.m ⁻¹ .K ⁻¹)	Young's modulus (GPa)
Spherical copper powder (Nanoval)	0.05-0.06	10-15	5.1	8.9	17	400	120
Electrolytic Copper powder (CH-UF 10)	0.3	5-10	1.8	8.9	17	400	120
Picht carbon fibres (KT120)	0.4	10 in diameter	(<1) Not applicable	2.12	-1,2 //	1-5 ⊥ 140 //	5-20 ⊥ 640 //
PAN carbon fibre (T300)	0.4	10 in diameter	(<1) Not applicable	2.10	-1,2 //	1-5 ⊥ 70 //	1-5 ⊥ 220 //
Vapour growth carbon nano fibres	13	0.06-0.15 in diameter	(<1) Not applicable	2.12	-1,2 //	1200 //	-

Table 2. Main characteristics of copper powders and carbon fibres.

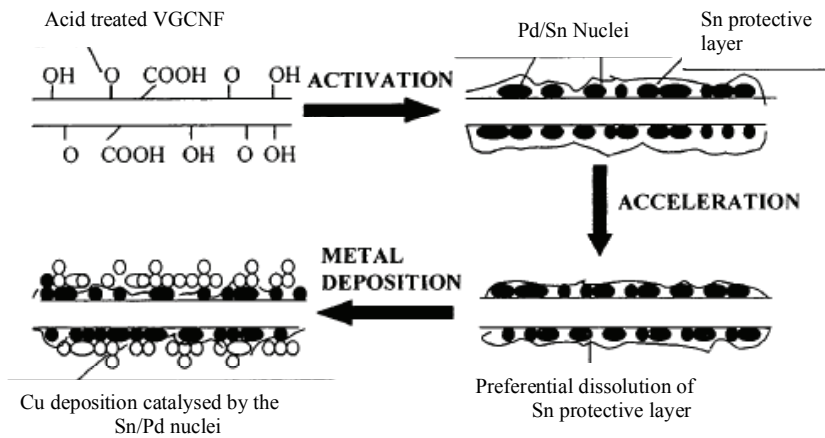
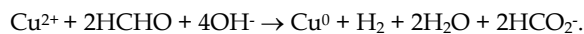


Fig. 5. General principles of electroless coating [Lang et al., 1999]

CHOH initiates the coating deposition by reducing the CuSO₄ according to the following reaction:



The main parameters, which have to be controlled, are: 1) the pH of the solution should be between 9 and 12 (the sodium hydroxide (NaOH) amount is adjusted in order to obtain the

desired pH), 2) the deposition time, 3) the temperature of the different baths and 4) the reaction rates.

After each immersion, the VGCNF are immediately rinsed with distilled water to stop the deposition process and, after the last step, the samples are carefully left dry.

Figures 6 and 7 show the evolution of the VGCNF Cu coating with different conditions. It has to be mentioned that the VGCNF have been treated with an acid solution (VGCNF + ($\text{HNO}_3 + \text{H}_2\text{SO}_4$ 2/3 vol.) during 6 hours, before electroless coating.

Several points can be noticed from this study:

1. The pH of the solution is one of the key factors in order to obtain a homogeneous copper coating around each VGCNF. Homogeneous coating is obtained for pH greater or equal to 12 (fig. 6). For that pH value the VGCNF are mostly covered with homogeneous coating and the coating thickness can easily be controlled with parameters as Cu sulfate concentration, deposition time and VGCNF content.
2. Copper coating is more homogeneous when i) the reducer concentration (HCHO) is increased and ii) the water content of the solution is increased (fig. 7). Both conditions lead to a decrease of the coating speed (see for example fig. 7a and 7b for two water content 100 ml and 200 ml). The diagrams linked with these 2 water contents (fig. 7d and 7f) show the evolution of the bath temperature and Ph with the deposition time. For each diagram, the diagram background color (gray to white) shows the evolution of the color of the solution (non transparent from Ph going to 13 to 10 and transparent when all the Cu salt has reacted and therefore for a pH lower than 10) with reaction time. Whatever the starting point and solution the advancement of the reaction is linked with a decrease of the Ph and an increase of the solution temperature (the exothermicity of the reaction is linked with the VGCNF concentration within the bath)
3. Whatever the starting conditions, an increase of the bath temperature is always observed and linked with the decrease of the pH of the solution.

2.3 Squeeze casting

The squeeze casting is likely one of the most usual manufacturing processes for elaboration of metal matrix composites (MMC). This process consists in the production of rigid porous structures with reinforcement, in our cases carbon fibre structure, that are further infiltrated by metal molten under pressure (fig. 8). The molten copper is poured (1180°C) into the bottom half of the pre-heated die (close to 1000°C).

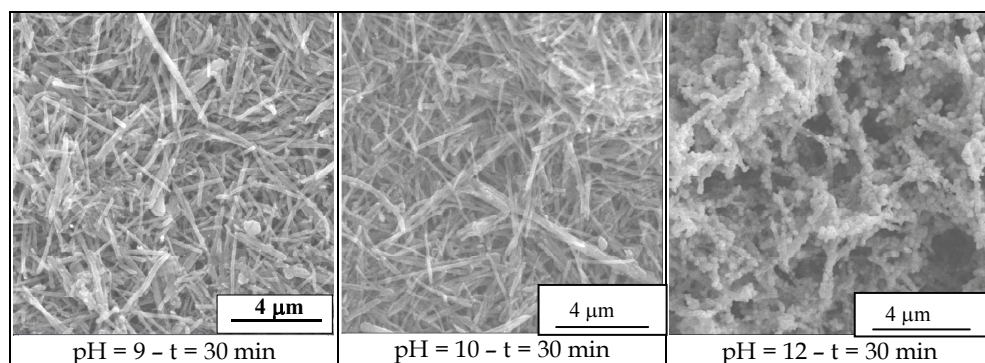


Fig. 6. Evolution of the coating behaviour with the pH of the solution

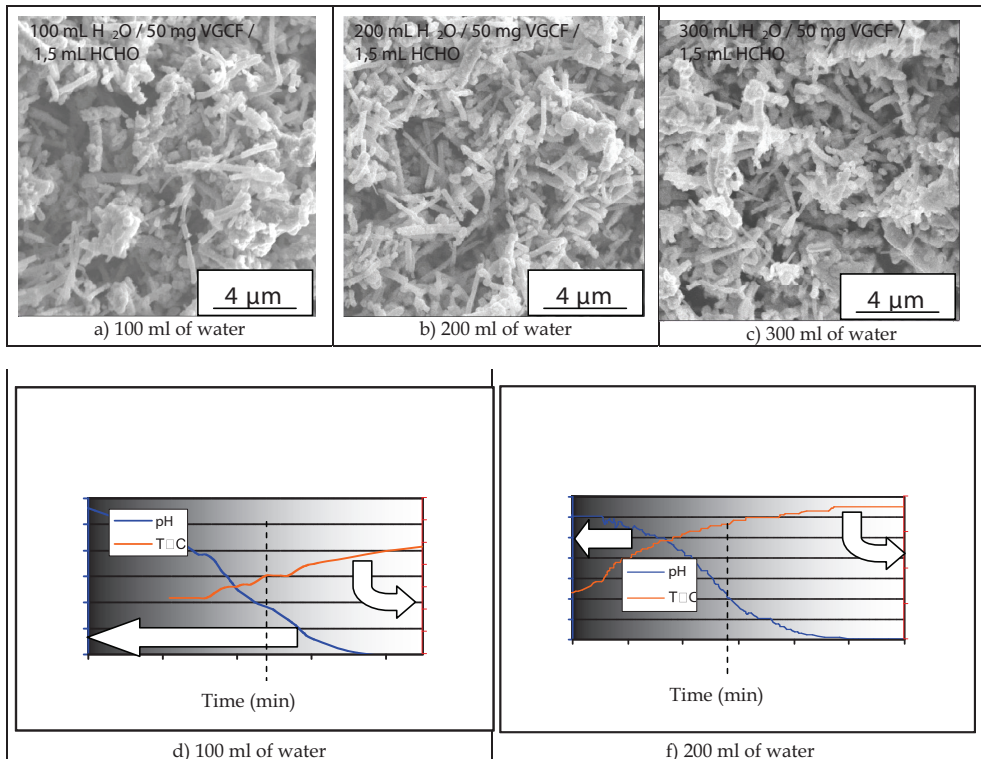


Fig. 7. Evolution of the coating behaviour with the water concentration

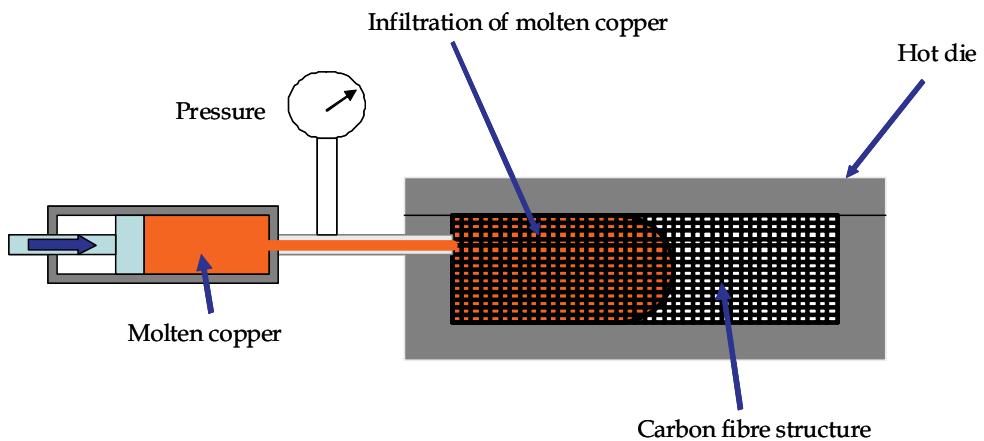


Fig. 8. Squeeze casting process

During the infiltration step, the carbon fibre structure is placed in the die. The main inconvenient of this technique is to keep steady the metal liquid during the infiltration step

because of the high melting point of copper (1083°C). Other inconvenient is linked to low wettability of copper with carbon, which involves the high infiltration pressure. This low wettability can lead to carbon fibre agglomerates and the presence of micro porosity in composites. Then, the squeeze casting is not the best process route for the elaboration of Cu/C composites.

2.4 Tape casting process

The powder metallurgy process are mainly hot press for 3D design or thick substrate (3 mm of thickness) and tape casting process for thin film (from 100 to 500 microns of thickness). Tape casting process offers an original solution for the elaboration of thin sheets of metal matrix composites [Corbin et al., 1997] or, in our case, carbon fibre reinforced copper matrix composites. Tape casting process is currently used on the large scale to produce thin ceramic or multilayer structures of various materials for different applications, [Roosen, 1999] such as Al_2O_3 and AlN substrates for electronic devices, BaTiO_3 for multilayer capacitors, solid electrolytes for sensors or energy conversion, piezoelectric ceramics for actuators or transducers, etc.

The main characteristics of this process are low cost, accurate control of the thickness from 25 to 1000 μm , good surface finish and high quality of laminated materials [Geffroy et al., 2007], (fig. 9).

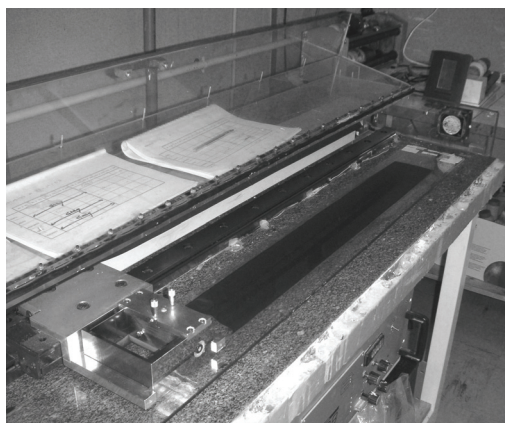


Fig. 9. Picture of discontinuous tape caster in SPCTS lab of Limoges, France.

One of the key points of tape casting process for the elaboration of the copper/carbon composite sheets is the elaboration of stable slurry with copper particles and short carbon fibres. Then, tape casting process (fig. 10) consists of the preparation of a suspension of the inorganic powder(s) in an aqueous or non-aqueous system. This slurry is a complex multicomponent system typically containing the following components: powder (ceramic and/or metallic), solvent, dispersant, binder, and plasticizer. The suspension must be stable, homogeneous and with a suitable rheological behaviour according to the tape casting process. The slurry is spread onto a support by means of a moving doctor blade. After evaporation of the solvent, the obtained dried tape, or green tape, was cut to the desired shape.

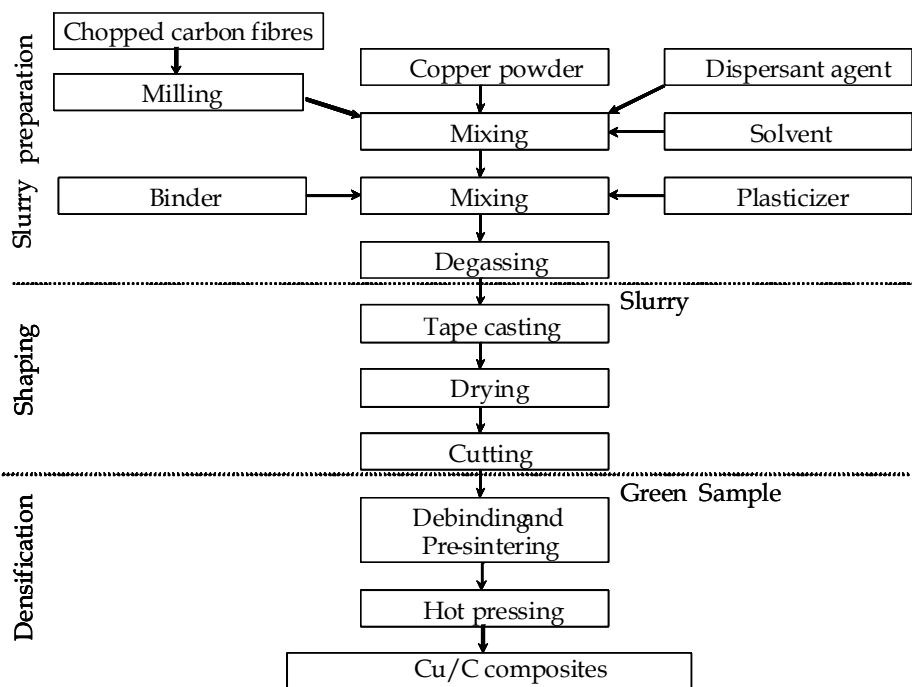


Fig. 10. Processing flow sheet of tape casting process

The main key points of tape casting process are discussed in the following sections.

a. Choice of organic components for tape casting

The solvent must wet the carbon fibres and the copper powder and should have a low temperature of vaporization. The solvent is the azeotropic mixture of ethanol and 2-butanone (40/60). Indeed, it offers a low boiling point (74.8°C) and a low dielectric constant that is favourable for a good wettability of carbon fibre [Johnson et al., 1987]. The nature of the solvent and of the powder determines the choice of organic additives, such as dispersant, binder and plasticizer [Moreno, 1992]. According to sedimentation tests in the azeotropic mixture of ethanol/2-butanone (40/60), one phosphate ester (CP213, Cerampilot, France) corresponds to the best desagglomeration and dispersion of copper and carbon particles. The optimum concentration of dispersing agent can be determined by rheological measurements or sedimentation tests. The minimum viscosity, then the best state of dispersion, is usually obtained for a dispersant concentration of 0.5 wt% on the dry powders basis.

The binder ensures the cohesion of the green sheet to avoid cracking during drying and for handling. After evaporation, the binder molecules form organic bridges between copper particles and carbon fibres, resulting in high mechanical properties of the green tape [Böhnlein-Mauß et al., 1992]. The binder must be easily removed at low temperature without residues. The binder is commonly a PolyMethyl MethAcrylate (PMMA) with a molecular weight ranging between 100 000 and 200 000 g.mol⁻¹.

The plasticizer, which confers the flexibility to the green tape for easy handling, induces a decrease of the T_g of the organic phase. An efficient plasticizer of the PMMA is usually the

dibutyl phthalate or polyethylene glycol with a low molecular weight close to 300 g.mol^{-1} . A good compromise between the flexibility and the mechanical strength of the green tape was obtained for a binder/plasticizer ratio close from 1 to 1.5.

b. Slurry preparation and tape casting

The tape casting suspension is prepared in two steps. The first one consists in dispersing, by planetary milling, the copper powder and carbon chopped fibres in 2-butanone/ethanol solvent with phosphate ester as dispersant. The binder and the plasticizer are added to the suspension in a second step and the complete slurry was homogenised, also by planetary milling, but at a lower rotating velocity. After homogenization, the slurry is degassed and directly casted onto a siliconed Mylar carrier film with a doctor blade. The doctor blade speed is fixed at 0.5 m.min^{-1} with a gap of 0.5 mm. The solvent evaporation is carried out at room temperature under air.

c. Green tape

The geometrical density of the green tapes varying from 2 to 2.5 g.cm^{-3} corresponds to a relative density ranging from 0.55 to 0.65 of TD (theoretical density), that suggests a rather good arrangement of particles, whereas the particle shapes, like short fibres or dendrite copper particles, are not favourable to a good compaction. However, the carbon fibres are oriented in the casting plan due to shear imposed during tape casting.

d. Thermal treatments

The organic components are removed during a thermal treatment at low temperature, i.e. debinding. The composites are then pre-sintering at higher temperature. The resulting composite structures have sufficient strength and flexibility for handling, but still present an important porosity. The thin sheets are then subsequently fully sintered by hot pressing (fig. 11?). In this densification step, 5 or 10 sheets (with thickness equal to $200 \mu\text{m}$) can be pressed together for the elaboration of thick systems.

e. Debinding and pre-sintering

In the first step of firing, the organic additives, i.e. the binder, plasticizer and dispersant are burned out carefully. The removal of plasticizer and binder occurs, under air, between 120°C and 350°C , whereas the extraction, under nitrogen, is performed between 140 and 400°C .

Due to copper oxidation starting at 150°C under air, debinding of copper/carbon composite green sheets are performed at 350°C under nitrogen. In the second step of firing, the copper matrix is pre-sintered at 750°C during 30 mn in nitrogen. The resulting composite has a sufficient strength and flexibility for handling, but still presents an important porosity (20-30 % in volume), which results from the presence of carbon fibres. The densification of the copper/carbon composites starts at about 650°C .

f. Densification by hot pressing

The pre-sintered individual tapes or multilayers are introduced between the two pistons of the steel mould which were heated, under vacuum (0.66 Pa), by induction system and regulation monitor. The usual conditions of hot pressing correspond to 650°C with a heating rate of $25^\circ\text{C.min}^{-1}$ under 50 MPa during 1 min. This last step of densification by hot pressing is presented in more details in the next section.

2.5 Hot pressing

Hot pressing process consists firstly in the preparation of powders mixing. This mixing, which contains ceramic, metallic powders and lubricant agents, must be stable and homogeneous.

The bad wettability of the carbon fibres by copper and the non reactivity between carbon and copper led to the formation of a stable porosity between the copper matrix and the carbon fibres during the densification stage. Thus, the full densification of copper/carbon composites is not possible by conventional sintering. Hot pressing technique, [Evans and McColvin, 1976][Jha and Kumar, 1997], under controlled atmosphere, is finally used in order to obtain fully dense materials.

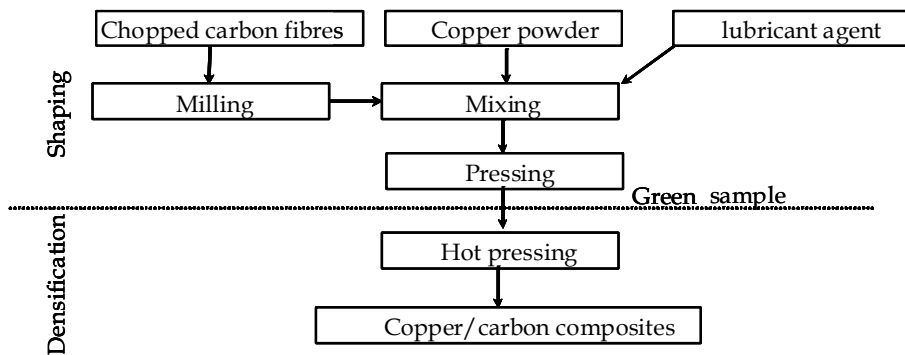


Fig. 11. Processing flow sheet of hot pressing

In a first step, powders are desagglomerated and mixed in ball milling with lubricant agent during 6 hours. Elaboration conditions, such as mixing conditions of the short carbon fibres and the copper powder, dimension and shape of the two powders must be optimized. The powders mixing is pressed to desired shape under 200 MPa, and the green sample obtained have finally sufficient strength and flexibility for handling but still shows important porosity close to 15-25%. Up to 200 MPa, the pressure can lead to the rupture of carbon fibres in green sample and the deterioration of final properties of composites.

In a second step, the green sample is heated and forged up to 600°C under 50 MPa. Figure 12 shows the hot press apparatus with the inducting heating system. The mould can be in steel or in tungsten carbide for higher temperature and pressure. To prevent copper oxidation or steel mould, the atmosphere of hot pressing chamber is usually inert atmosphere (nitrogen or argon) or primary vacuum. The temperature can be controlled with a thermocouple placed into the steel mould.

The temperature and pressure of hot pressing is adjusted in order to obtain full dense composite and to avoid the deterioration of carbon fibres. In the figure 13, the density of hot pressed sample increases with the pressure and the temperature of hot pressing. However, a high pressure can lead to breaks the carbon fibres if the copper is not enough soft. Then, the high temperature leads to a softening of copper matrix and to improving the copper flow around the carbon fibres during the hot pressing step. Finally, the optimal conditions correspond to a moderate temperature, 600-700°C, (which is a low sintering temperature of copper particles) with pressure between 50-100 MPa. The pressure must be higher than 20 MPa, which corresponds likely to the limit of elasticity deformation of copper particles before ductile deformation and copper flow step in composite materials.

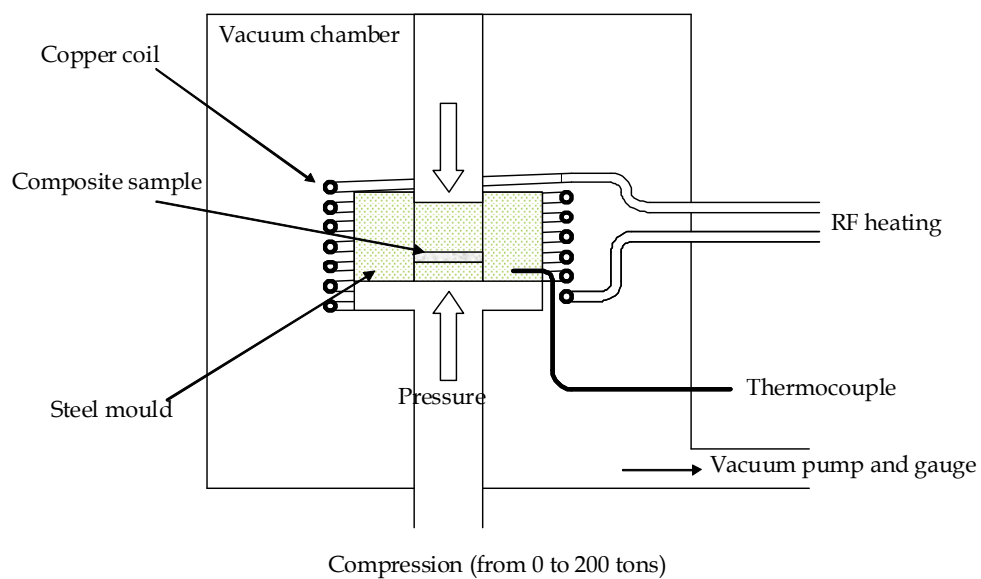


Fig. 12. Scheme of hot pressing facilities

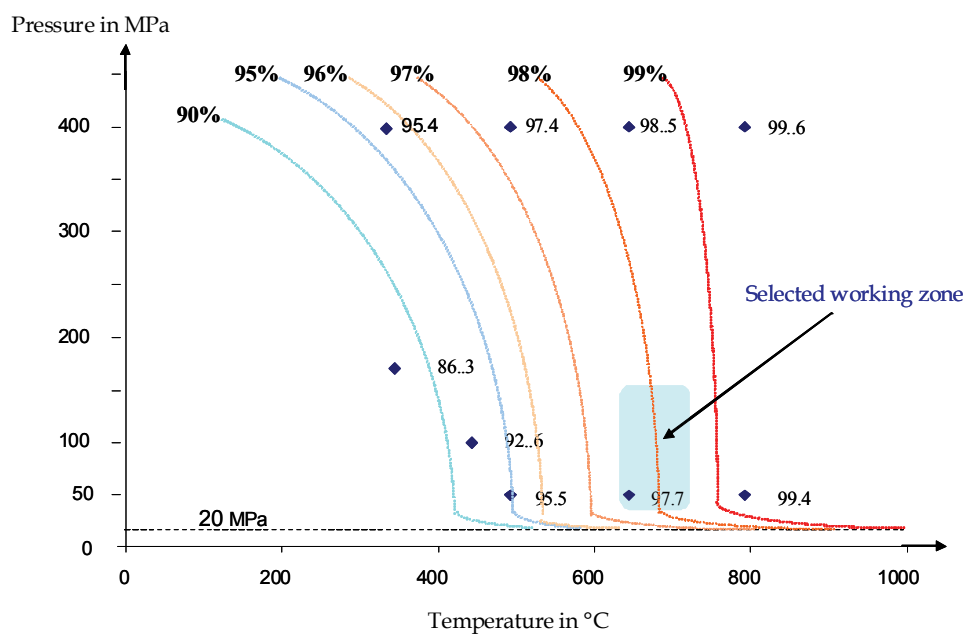


Fig. 13. Relative density of Cu/C composites in relation with temperature and pressure of hot pressing conditions

Besides, a high temperature of hot pressure involves the important technological cost, and it can lead the pre-sinterisation of copper particles, which is prejudicial to suitable softening of copper matrix during the hot pressing. Then, the optimal conditions of hot pressing correspond usually to the best compromise between optimal properties of Cu/C composites and process cost.

Finally, the main parameters of hot pressing, such as temperature, time and atmosphere in the thermal properties of the Cu/C composite materials must be adjusted in relation with the optimal mechanical and thermal properties of Cu/C composites.

2.6 Reporting of Cu/C composites

Composite heat-sink family shows the highest potential for application in heat sinks for electronic applications. The great advantage of this kind of materials is that they can combine metal, polymer and ceramics in a broad range of different products to tailor the final properties sought. Nevertheless, final properties of composites greatly depends on manufacturing processes.

Among the huge amount of different composites, the most efficient and so the most commonly developed for heat dissipation purposes, are metal matrix composites, and most specifically those based on copper and aluminum matrices with a broad range of different reinforcements.

Recently, some investigations in epoxy based composites reinforced with an extremely interesting new kind of carbon fibres (Vapour Grown Carbon Fibres, VGCFs) have shown outstanding thermal conductivities, near 650W/mK. These newly developed kinds of micro/nanofibres (commercially available since the nineties) exhibit the highest thermal conductivity of all materials known. Their special structure based on its manufacturing process (they are produced from gases) gives them a high potential to achieve a highly graphitic structure by a proper heat treatment, not achievable in other carbon fibres, thus leading to outstanding physical and mechanical properties. But the main problem encountered with epoxy based composites is their low highest temperature of use. Nevertheless, in any case, these composites could be applied up to a temperature near 120°C, where polymers can start degrading.

Undoubtedly, the most efficient composites for heat sinks are those based on Cu and Al with a number of different reinforcements. In general, metal matrix composites (MMCs) show several improvements in comparison with currently used materials in electronic packaging, among them the following can be underlined:

- Lower and tailorable CTE (the higher the volume fraction of reinforcement used, the lower the CTE is) to be as similar as possible to ceramic substrates. In the present development, in which a suitable electronic packaging component for GaN semiconductor device will be developed, the coefficient of thermal expansion must be as similar as possible to that of the electronic substrate. This reduction of the CTE mismatch supposes, therefore, a reduction of stresses between the components and their substrates during thermal cycling;
- High heat dissipation capability;
- Lightweight, suitable for space applications;
- High stiffness at high temperatures, being an useful characteristic in order to assure dimensional stability of electronic components working at high temperatures.

Due to their high conductivity, low CTE and lightweight, Al/SiC_p (50-70%SiC_p) composites represent one of the MMC kinds of materials that have found an easier way to be introduced

into real industrial applications [Luedkte, 2004]. Some manufacturing processes for this type of composites have been developed along the last years (infiltration and squeeze casting) for these materials, so they are already available (it depends very much on size, shape, etc...). Unfortunately, they are extremely difficult to machine, therefore, manufacturing processes must be net or near-net shape, in order to get a really profitable manufacturing process. Another interesting kind of MMCs for heat sinks is Cu/diamond composites. But their main problem, again, is that they are expensive because diamond is expensive and difficult to machine.

Looking, at the previous table 1, it can be said that copper based materials are the most promising among MMCs. Most of the composites based on this matrix are reinforced by ceramics (particles, short fibres, and long fibres) in order to reduce their extremely high CTE and match it with those of the semiconductor or other ceramic substrates. Nevertheless, carbon fibres also offer the big advantage of high heat and electrical conductivity. So, MMCs reinforced with long C fibres show excellent thermal conductivity along the fibre direction. Unfortunately, these types of composites are not usable in a broad range of heat sinks, as the excellent thermal conductivity is achieved in surface but not across the thickness. Of major interest are those composites reinforced with short fibres, as although in general terms thermal conductivity is more modest than those reinforced with continuous fibres, they have isotropic properties. In addition, their manufacturing processes are less sophisticated and expensive.

3. Properties of Cu/ C composites

The main properties of Cu/C composites depend strongly of process conditions. One of key points is the improvement of interfacial strength between copper and carbon during process. These main properties obtained by hot pressing and tape casting are discussed and presented in the following parts.

3.1 Microstructure of Cu/C composites

The final density of materials is close to 94-98 %, and no specific degradation of carbon fibres is observed in the Cu/C composites materials microstructures.

Microstructure characterization (fig. 14) shows strong anisotropy structure between the perpendicular and parallel pressing directions. Carbon fibres are oriented in perpendicular plan of pressing direction due to the strains and stresses imposed by pressing conditions and geometry. It can be expected that carbon fibre orientation leads to anisotropic properties of the Cu/C composites.

3.2 Coefficient of thermal expansion (CTE)

The CTE is measured using a differential dilatometer with a heating rate of $10^{\circ}\text{C}.\text{mn}^{-1}$ from room temperature to 250°C under nitrogen to prevent eventual oxidation of copper. Tested samples have typical size of $5 \times 5 \times 20$ mm of length.

The CTE measured in parallel pressing direction of composite is close to $17 \cdot 10^{-6} \text{ }^{\circ}\text{C}^{-1}$ (CTE of copper) for the different volume fractions of fibres. In opposite, CTE values in the perpendicular pressing direction decrease with carbon fibre volume fractions (fig. 15). These anisotropic properties are due to the strong anisotropy of carbon fibre properties (CTE = $-1 \cdot 10^{-6} \text{ }^{\circ}\text{C}^{-1}$ in parallel axis and $12 \cdot 10^{-6} \text{ }^{\circ}\text{C}^{-1}$ in perpendicular axis) and the orientation of the fibres in the perpendicular pressing direction. It has to be noticed that CTE values parallel and perpendicular to the fibre axis have same values whatever the carbon fibre type.

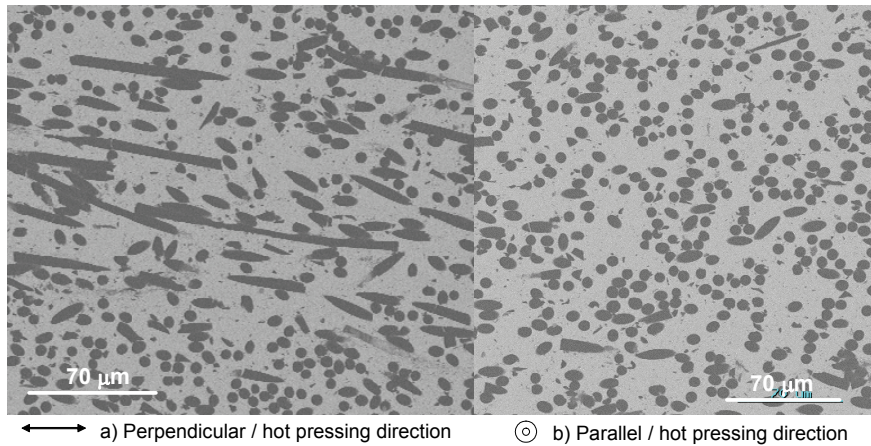


Fig. 14. SEM micrograph of hot pressed C/Cu composite material

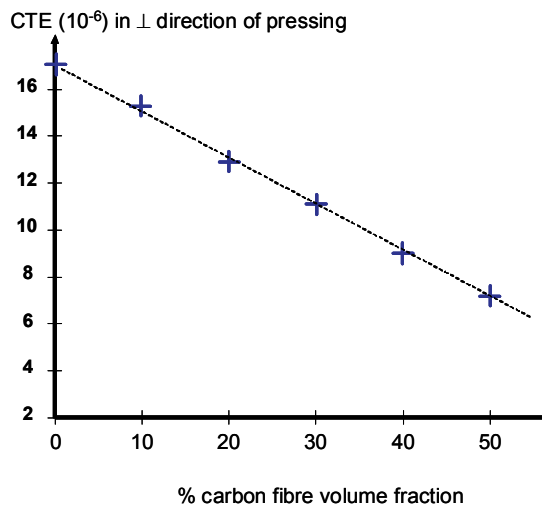


Fig. 15. CTE of Cu/C composites in perpendicular direction of pressing in relation with carbon fibre volume fraction.

3.3 Thermal conductivity (TC)

The thermal conductivity is commonly measured by flash laser method in axial direction of small cylinders, typically 6-15 mm diameter and 2-5 mm high. The small cylinders are machined in both parallel and perpendicular pressing directions in order to measure the thermal conductivity in parallel and perpendicular directions of pressing.

In opposite to CTE properties, TC of C/Cu composite materials is strongly linked with the thermal properties of the carbon fibres (CF) or vapor grown carbon nanofibres (VGCNF). Indeed, TC of CF along their main axis can go from 10 to 900 W/mK whereas TC are

constant perpendicular to CF main axis (close from 5 to 10 W/mK). Table 3 shows the evolution of CTE, TC and density of C/Cu composite materials for one type of CF (with TC = 140 W/mK in parallel to main axis). It can be seen that the thermal conductivity of composites materials decreases with volume fractions of fibres. However, the TC is strongly anisotropic, with 150 and 170 W.m⁻¹.K⁻¹ in perpendicular direction, and 210 and 250 W.m⁻¹.K⁻¹ in parallel and perpendicular direction of multilayer samples for 40 and 30 vol. % fibres, respectively (table 3). Also, the strong anisotropy of carbon fibre properties ($\lambda_{//} = -1 \cdot 10^{-6} \text{ }^{\circ}\text{C}^{-1}$ in axis and $\lambda_{\perp} = 12 \cdot 10^{-6} \text{ }^{\circ}\text{C}^{-1}$ in perpendicular axis of fibre) and orientation of fibres lead to strong anisotropic behaviour of thermal conductivity of Cu/C composite materials (table 3).

Material with %C	CTE 10 ⁻⁶ °C ⁻¹	Thermal Conductivity W.m ⁻¹ .K ⁻¹	Density
Cu /10% C	15-16 \perp	270 //	8.1
Cu /20% C	13 \perp	230 //	7.5
Cu /30% C	11 \perp	260 \perp 180 //	6.8
Cu /40% C	9 \perp	220 \perp 160 //	6.1
Cu /50% C	7 \perp	180 \perp 120 //	5.5
Cu/5% carbon nanofibre (VGCNF)	17 \perp	450 //	8.5

Table 3. CTE and TC measures in parallel (//) and perpendicular (\perp) pressing direction on the copper carbon composites with pitch based carbon fibre (TC = 140 W/mK) [Geffroy et al., 2008] and with carbon nanofibre [Silvain et al., 2009].

The thermal conductivity obtained with Cu/C carbon composite is lower than one expected by inferior limit of Hashin and Shtrikman model [Hashin and Shtrikman, 1962]. This is likely due to the important thermal resistance of copper/carbon interface. Then, the thermal conductivity decreases strongly with an increase of carbon volume fraction. The thermal resistance of interface Cu/C decreases usually with an improvement of mechanical properties of interface copper/carbon by previous surface treatment of carbon fibre, as described in previous section. Indeed, the origin of thermal conduction in copper is electronic, while the one of carbon fibres is due to phonons. These different mechanisms of thermal conduction between copper matrix and carbon fibres explain likely that the interface carbon/copper has a large influence on thermal properties of composites, and is always one of the critical points of thermal properties of Cu/C composites.

Recent research results show that the TC of these composites materials can be improved with a higher thermal conductivity than copper (450 W.m⁻¹.K⁻¹) using a low amount (5% in volume) of carbon nanofibres [Silvain et al., 2009]. However, the elaboration of these composites requires, on the one hand, the previous surface treatment of short carbon fibres in order to improve the Cu/C interface properties, on the other hand, the excellent dispersion of carbon nanofibres in copper matrix.

3.4 Electrical properties

The electrical resistivity of composites is often measured by using conventional four points method. The electrical resistivity is increasing with carbon fibre content (fig. 16). The experimental values are close to those predicted by lower limit of Hashin and Shtrikman model, [Hashin and Shtrikman, 1962], taking $\rho_{Cu} = 1.7 \mu\Omega.cm^{-1}$ and $\rho_{fibre} = 1000 \mu\Omega.cm^{-1}$.

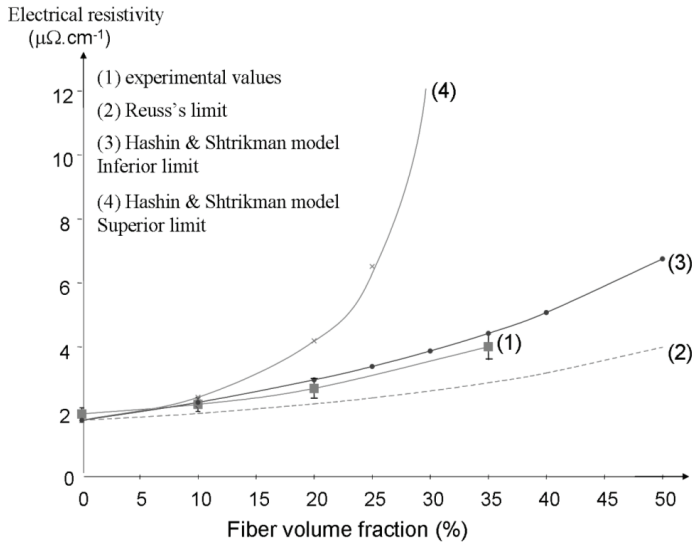


Fig. 16. Electrical resistivity of Cu/C composites in relation to fibre volume fraction [Geffroy and Silvain, 2007].

These models have been described as follow:

Reuss's model:

$$\rho_{composite} = \frac{1}{\frac{1-V_f}{\rho_m} + \frac{V_f}{\rho_f}}$$

upper limit of Hashin and Shtrikman model:

$$\rho_{composite}^+ = \rho_m + \frac{V_f}{\frac{1}{\rho_f - \rho_m} + \frac{V_m}{3\rho_m}}$$

and lower limit of Hashon and Shtrikman model:

$$\rho_{composite}^- = \rho_p + \frac{V_m}{\frac{1}{\rho_m - \rho_f} + \frac{V_f}{3\rho_f}}$$

$\rho_{composite}$: Electrical resistivity of composite V_m : Volume fraction of matrix

ρ_m : Electrical resistivity of matrix V_f : Volume fraction of fibres

ρ_f : Electrical resistivity of fibres

This behaviour is linked to a good electrical contact between carbon fibres and copper matrix and to a low porosity at matrix/copper interfaces. Indeed, the both copper and fibres present a similar mechanism of electrical conduction with free electrons. This involves that the electrical resistance of interface copper / carbon has a low impact on electrical resistivity of composite.

4. Potential applications of Cu/C composites

The electronic industry is involved in an endless search of new materials that enable electronic systems with increasing density of components, through higher heat dissipation capability, lower density, higher reliability while matching the CTE of materials currently used in electronic packaging components, ceramic substrates, Si, SiC and other semiconductors, etc. In fact, reliability appears nowadays as is one of the major problems that affect the electronics, microelectronics, telecom, automotive, and aeronautic industries. Especially, thermal management is an increasingly critical part of achieving competitive functionality in these industries since it impacts speed, size, weight and reliability of components, mainly for future components which will need to dissipate heating from electric currents and packaging densities in order of magnitude higher than those in use today. Due to the high power dissipation capability of the current and future electronic semiconductors and high reliability demand, it is mandatory to develop a new electrical conductive layer based on Cu/C functionally graded materials with adapted CTE in order to adjust the thermal stresses between the FGM ceramic and the Si wafer.

Cu/C composites are so attractive materials for thermal conduction because of its high thermal conductivity and low CTE. Their potential primary applications are heat sinks, thermal planes, and substrates (fig. 17).

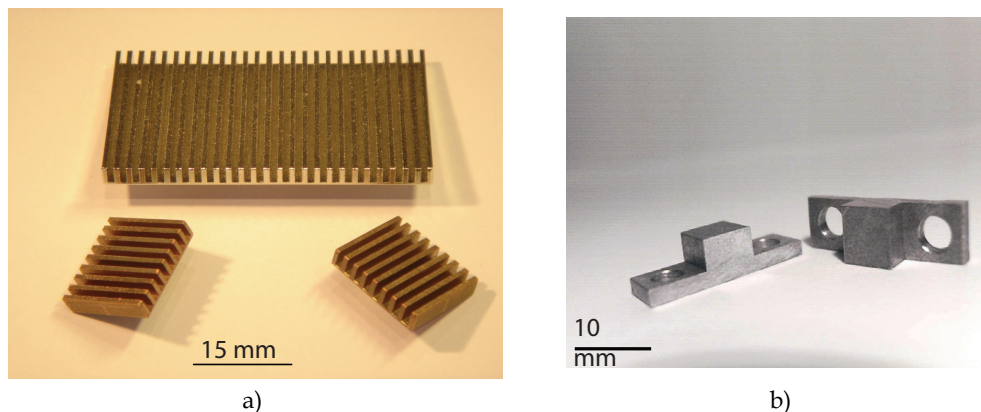


Fig. 17. Two examples of machined C/Cu composite materials for a) railroad application and b) aeronautic application

5. Conclusion and outlooks

The properties of Cu/C composites depend mainly on conditions and routes process. Today, the powder metallurgy processes offer Cu/C composites with a low cost of elaboration, a low CTE and excellent thermal conductivity properties. However, physical properties obtained by power metallurgy process such as CTE and thermal conductivity are

strongly anisotropic. In addition, the lack of interfacial strength between copper and carbon requires a previous surface treatment of short carbon fibres in order to improve the interface properties between copper matrix and carbon fibres. Recent research developments suggest that the thermal conductivity of these composites materials should be largely improved by using nanofibres with a higher thermal conductivity than copper (up to $400 \text{ W.m}^{-1}\text{.K}^{-1}$).

6. References

- Ang L.M. et al; (1999). Electroless plating of metals onto carbon nanotubes activated by a single-step activation method, *Chemistry of Materials*, vol. 11, 2115-2118.
- Böhnlein-Mauß J.; Sigmund W.; Wegner G.; Meyer W.H.; Heßel F.; Seitz K.; Roosen A., (1992). The function of polymers in the tape casting of alumina, *Advan. Mater.*, n°2, 73-81.
- Corbin S.F.; Zhao-jie X.; Henien H.; Apte P.S., (1999), Functionally graded metal /ceramic composites by tape casting, lamination and infiltration, *Mater. Sci. and Eng.*, 192-203.
- Evans R.W; McColvin M., (1976). Hot forged copper powder compacts, *Powder Metall.*, n°4, 202-209.
- Geffroy, P.M.; Chartier T.; Silvain J.F., (2007). Preparation by tape casting and hot pressing of copper carbon composites films, *Journal of the European Ceramic Society*, 27(1): 291-299.
- Geffroy, P.M.; Silvain J.F., (2007). Structural and thermal properties of hot pressed Cu/C matrix composites materials used for the thermal management of high power electronic devices, *Materials Science Forum* 534-536 (PART 2), 1505-1508.
- Geffroy, P.M.; Mathias J.-D.; Silvain J.F., (2008). Heat sink material selection in electronic devices by computational approach, *Advanced Engineering Materials* 10 (4), 400-405.
- Goñi, (1998), Elaboration de composites cuivre carbone, PhD, University of Bordeaux.
- Hashin Z. and Shtrikman S., (1962). On some variational principles in anisotropic and nonhomogeneous elasticity, *J. Mechan. Phys. Solids*, vol. 10, 335-342.
- Jha A.K.; Kumar S., (1997). Investigations into the high-speed forging of sintered copper powder strips, *Journal of Materials Processing Technology*, 1997, 71, 394-401.
- Johnson R. E.; Morrison J.; Morrison W.H., (1987). Ceramic Powder dispersion in nonaqueous systems, *Advances in ceramics*, vol. 21: Ceramic Powder Science, *The Am. ceram. Soc. Inc.*, 173-197.
- Koráb J.; Stefánik P.; Kavecký S.; Sebo P.; Korb G., (2002). Thermal expansion of cross-ply and woven carbon fibre-copper matrix composites, *Composites Part A*, 33, 133-136.
- Korb G.; Buchgrader W.; Schubert T., (1998). Thermophysical properties and microstructure of short carbon fibre reinforced Cu-matrix composites made by electroless copper coating or powder metallurgical route respectively, IEEE/CPMT Berlin, Int'l Electronics Manufacturing Technology Symposium, 27-28 April, 1998.
- Luedkte A., (2004). Thermal management materials for high-performance applications, *Advan. Eng. Mater.*, vol 6, n°3, 142-144.
- Moreno R., (1992). The role of slip additives in tape-casting technology: Part I- Solvents and Dispersants, *Am. Ceram. Soc. Bull.*, vol. 71, N°10, 1521-1530.
- Praksan K.; Palaniappan S.; Seshan S. (1997). Thermal expansion characteristics of cast Cu based metal matrix composites, *Composites Part A*, 28, 1019-1022.
- Roosen A., (1998). Basic requirements for tape casting of ceramic powders, *Ceramic Powder Science*, vol. 1, Part B, 675-692.
- Silvain J.-F.; Vincent C; Heintz J.-M.; Chandra N., (2009). Novel processing and characterization of Cu/CNF nanocomposite for high thermal conductivity applications, *Composites Science and Technology*, vol. 69, 2474-2484.

Engineering, Modeling and Testing of Composite Absorbing Materials for EMC Applications

Marina Koledintseva¹, Konstantin N. Rozanov² and James Drewniak¹

¹*Missouri University of Science and Technology, Missouri,*

²*Institute for Theoretical and Applied Electromagnetics,
Russian Academy of Sciences, Moscow,*

¹*U.S.A.*

²*Russia*

1. Introduction

Non-conducting wideband absorbing materials are important for improving immunity of electronic equipment and solving various problems of electromagnetic compatibility (Celozzi et al., 2008). Application of absorbing materials for the design of shielding enclosures, coatings, gaskets, or filtering patches is preferable compared to metal structures for several reasons. Typically enclosures of electronic equipment are made of highly-conducting metal to achieve the required shielding levels (Neelakanta, 1995). However, requirements to make electronic devices of smaller size and weight necessitate substitution of metal by electrically conducting composites (Sichel, 1982) and polymers (Fox et al., 2008; Wang & Jing, 2005). Moreover, if a conducting surface has sharp edges, slots, and apertures, currents on this surface may drive unintentional antennas and enhance noise coupling paths as culprits of undesirable emissions (Paul, 2006). One of the ways to eliminate this problem is to use absorbing materials, including applications of magneto-dielectric composite materials for electromagnetic shielding purposes.

Engineering of absorbing materials with desirable frequency responses and advanced physical properties is of great importance. These materials can be either bulk or sheet, and, depending on a particular application, they may be shaped as needed. Frequency characteristics of composite absorbing materials may be either wideband, or frequency selective. The materials of interest should provide the required attenuation of surface currents on the extended conducting surfaces, and/or satisfy requirements on damping electromagnetic near-fields of the sources, or far-field electromagnetic waves of the given configuration, direction of incidence, and polarization. Advanced physical, chemical, and mechanical properties of absorbing materials are of great importance as well. The materials must comply with requirements on thermal, chemical, and mechanical stability and durability, incombustibility, non-toxicity, environmental friendliness, and adhesion with surfaces on which they will be placed.

It is important that when applied to electronic products, the engineered absorbing materials would allow for compliance with requirements and regulations from the point of view of

electromagnetic compatibility (EMC), electromagnetic immunity (EMI), signal integrity (SI), and power integrity (PI) over frequency ranges of interest. For applications in high-speed digital electronic designs, the materials that would absorb electromagnetic energy in RF, microwave, and potentially mm-wave bands, are of special interest. The necessity of using absorbing materials becomes more and more important, since operating frequencies of electronic devices increase, package density grows dramatically, and the number of electronic equipment and devices of mass production continues to increase. Thin absorbing noise-suppressing composite sheets and coats are of special interest for such applications, especially because of microminiaturization trends and of convenience to apply directly on the surfaces to be protected, as well as their broadband performance. Some examples of applying thin sheet absorbing materials are shown in Fig. 1. Thin sheet absorbers can wrap cables, or be applied directly on the sources of noise, or at some optimal distance from the source. They can be put directly on the electronic module enclosure, around or over vents, holes, sharp edges, and wedges, or may be placed as patches inside cavities to damp unwanted resonances.

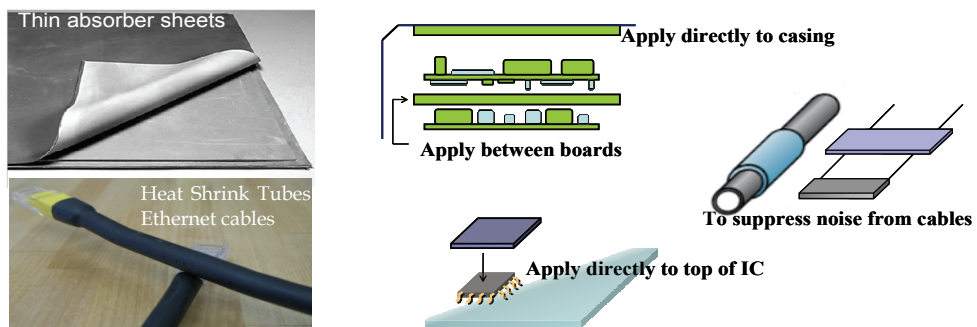


Fig. 1. Some examples of applying thin sheet absorbing materials

Also, electronic composites, whose properties can be controlled by thermal or electromagnetic means, play an important part in modern micro- and nano-electromechanical systems such as sensors, filters, switches, and actuators (Taya, 2005). However, they will not be considered herein, since the specific topic of the present work is absorbing composites for electromagnetic waves and fields.

An absorbing, non-conducting composite material may contain conducting non-magnetic inclusions (e.g., carbon or non-magnetic metal particles) at concentrations below the percolation threshold as fillers in a dielectric host (matrix, base) material (Lagarkov & Sarychev, 1996; Sihvola, 1999; Tretyakov, 2003). Electromagnetic wideband radar absorbing materials may include conducting magnetic (e.g., iron or permalloy) powders (Birks, 1948; Merrill et al., 1999; Absinova et al., 2007) or combinations of granular ferrite and conducting particles, e.g., carbonyl-iron powders (Park, et al., 2000). Electromagnetic wave absorbers also widely use non-conducting soft ferrites with spinel structure, e.g., Ni-Zn, Ni-Zn-Co, or Mn-Zn ferrites (Naito & Suetake, 1971; Shin & Oh, 1993; Kazantseva et al., 2004; Lisjak et al., 2006), or hexagonal ferrites (Mikhailovsky et al., 1965; Ota et al., 1999; Iijima et al., 2000). Combining inclusions of different types (dielectric, conducting, and magnetic) in a multi-phase composite material may yield substantial increase in the absorption level in the

desired frequency range. The absorbers can form either thick or thin films (paint) placed on the surfaces to be protected from unwanted radiation or coupling paths, or foam, as in anechoic chambers. The absorbing materials may form multilayered resonant structures, such as a Jaumann absorber or a Salisbury screen (Knott et al., 2004).

A current objective is to develop a methodology to efficiently design and evaluate novel products based on absorbing magneto-dielectric composite materials primarily for EMC/EMI purposes. Fig. 2 shows a flowchart for engineering design of noise-suppressing materials and electromagnetic filtering structures.

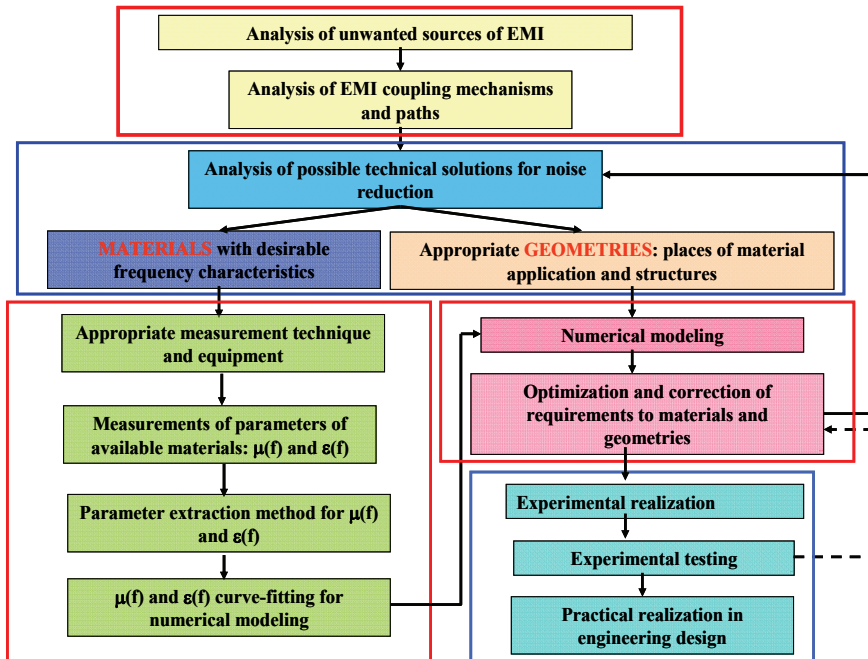


Fig. 2. Flowchart for engineering design of EMI noise-suppressing materials and structures

The analysis starts from diagnosing and characterizing sources of unwanted radiation and/or undesirable electromagnetic interference coupling paths and mechanisms. Then possible technical solutions to eliminate or minimize those noise effects are proposed and analyzed. Any technical solution is based on a combination of proper material (or materials) and geometry. This means deciding, where the chosen materials should be placed, and what their configuration should be to achieve the required noise reduction in the intended frequency and dynamic (power or field amplitude) ranges. If choosing an appropriate material among already existing – either available commercially, or specially synthesized in laboratory conditions, it is important to measure their electromagnetic properties. These are the complex frequency-dependent dielectric susceptibility $\chi_e(\omega)$ or permittivity $\varepsilon(\omega) = \varepsilon_\infty + \chi_e(\omega)$, and complex magnetic susceptibility $\chi_m(\omega)$ or permeability $\mu(\omega) = 1 + \chi_m(\omega)$ in the frequency range of interest. Alternatively, a material is characterized by its dielectric and magnetic susceptibility kernels $\xi_e(t)$ and $\xi_m(t)$, which are the impulse responses corresponding to $\chi_e(\omega)$ and $\chi_m(\omega)$. There are different measurement techniques for

evaluating electromagnetic properties of materials (Chen, 2004;). The choice of a specific measurement technique depends on the frequency range of interest, material type (dielectric, magneto-dielectric, or conductive; isotropic or anisotropic; linear or nonlinear; exhibiting narrowband resonances, or having comparatively flat frequency dependence in the frequency range of interest); instrument availability; required accuracy and repeatability. There are some other factors, for example, how time-consuming and resource-consuming those measurements are. Different methods of characterization of dielectric materials are summarized in (Von Hippel, 1995; Chen, 2004), and various approaches to extract parameters of ferrite materials over different frequency ranges are described in (Polder, 1950; Rado, 1953; Mullen & Carlson, 1956; Lax & Button, 1963; Korolev et al., 2008).

Currently there are numerous automated methods for wideband characterization of dielectric and magnetic bulk materials (Nicholson & Ross, 1970; Weir, 1974; Barry, 1986), as well as of thin films (Bekker et al, 2004; Booth et al., 1994). The existing techniques are typically based on various transmission/reflection measurements, either in the frequency domain, or in time domain, in transmission lines, cavities, open space, or using special probes terminated with material samples under test. The literature is replete with various measurement techniques (Nicholson & Ross, 1970; Fellner-Feldegg, 1972; Weir, 1974; Baker-Jarvis, et al., 1993, 2001; Musil & Zacek, 1986; Ghodgaonkar et al., 1990; Zheng & Smith, 1991; Ganchev et al., 1995; Jargon & Janezic, 1996; Wang et al., 1998; Roussy et al. 2004; Ledieu & Acher, 2003; Bekker et al., 2004).

For practical EMC purposes, it is convenient to have systematic methodology to help EMC engineers to design and evaluate effectiveness of EMI noise-suppressing materials and structures based on their measured dielectric and magnetic responses. An overview of this methodology is presented in Fig. 3, corresponding to the flowchart in Fig. 2.

The dielectric and magnetic properties of the samples, depending on the measurement technique, are extracted either discrete frequency points, or over selected continuous frequency bands. Then the continuous frequency characteristics over the entire frequency range of interest can be restored. This is done using an appropriate curve-fitting technique. For further analytical and/or numerical modeling of structures containing dispersive materials, it is important that the resultant continuous material frequency dependencies would satisfy passivity and causality requirements over the entire frequency range of interest. Passivity means that the initially measured transmission and reflection coefficients in a passive system is in a physically meaningful range between 0 and 1 in unitless system, or fall below 0 in logarithmic units. Causality means that real and imaginary parts of complex permittivity $\varepsilon(\omega) = \varepsilon'(\omega) - j\varepsilon''(\omega)$ and complex permeability $\mu(\omega) = \mu'(\omega) - j\mu''(\omega)$ related through the Kramers-Krönig relations (Landau & Lifshitz, 1960; Lucarini et al., 2005), and, hence, no response could be obtained before a passive linear system has been excited by an external source. After the continuous causal complex functions $\varepsilon(\omega)$ and $\mu(\omega)$ are obtained, they can be used in building either an analytical, or numerical electromagnetic model to predict effects of the absorbing material upon characteristics of the particular noise radiation and coupling scenario under study.

Validation of theoretically predicted or numerically simulated results is an important stage of the methodology. Creating an experimental test vehicle, which is suitable and comparatively simple for modeling, and at the same time captures the main features of noise generation, coupling physics, and attenuation by an absorbing material, is probably the most difficult and time-consuming task. Mutual correction and fine tuning of the experimental setup and a modeling prototype are always required at this stage.

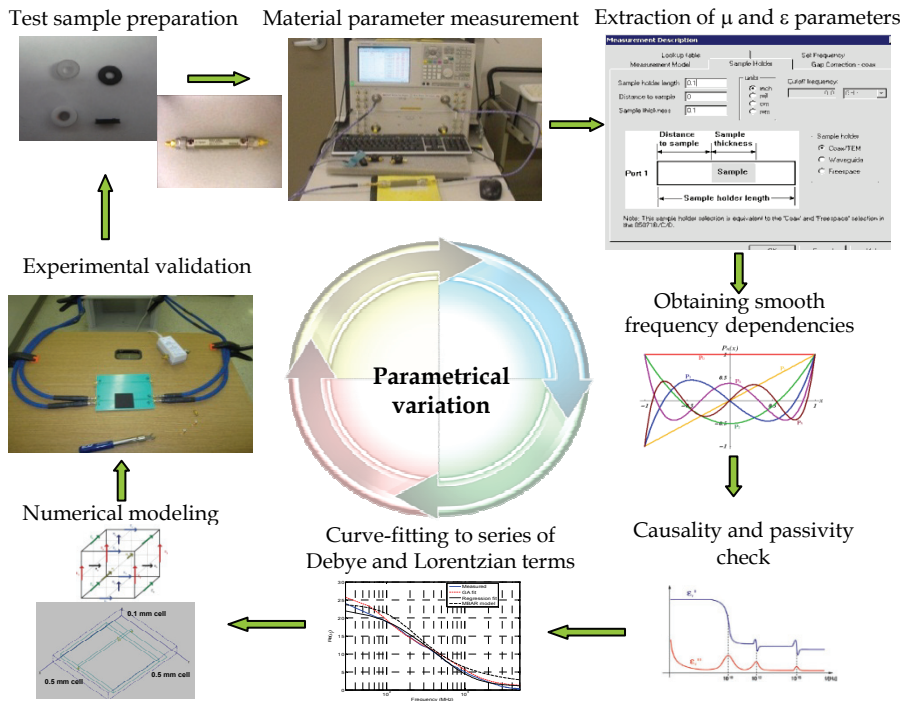


Fig. 3. An EMC absorbing material design methodology

As soon as the agreement between measured and modeled results over the entire frequency range under consideration is achieved, the model and experimental setup may be subjected to some parametrical variations for developing practically useful design curves. Based on those design curves, applicability of the specific absorbing material in the particular practical scenario can be predicted. Different kinds of commercially available or new laboratory-synthesized materials could be compared with each other from the point of view of noise reduction effectiveness according to the imposed criteria, and the optimal solutions could be chosen.

2. Analytical model to predict frequency characteristics of a composite

Prediction of wideband frequency responses of effective electromagnetic parameters (permittivity and permeability), as well as concentration dependencies of composites, are important for engineering new electromagnetic absorbing materials. Herein, the general case of a magneto-dielectric composite material with either non-conducting ferrite, or conducting magnetic alloy inclusions in a dielectric polymer host, is considered. In addition, the composite may contain some fractions of non-magnetic conducting or dielectric inclusions. In the general case, each material phase may have its own frequency-dependent

permittivity and permeability, and the resultant homogenized material would also have a frequency dispersion of its effective dielectric and magnetic properties.

2.1 Background for developing a new mixing rule

A composite material is a medium comprised of at least two different material phases: a matrix (host, bond) material and inclusions. A matrix is typically a polymer dielectric, while inclusions may be either conducting or non-conducting, and may have their own dielectric and magnetic intrinsic properties. Depending on how many phases there are in the mixture, composites can be biphasic or multiphase. The material phases may be intrinsically isotropic or anisotropic, depending on their crystallographic structure or morphology. The latter is determined by synthesis or manufacturing process specifics, such as temperature and pressure regimes, presence of catalysts, doping ions, and the kind of mechanical processing that was applied (milling, extruding, moulding, or pressing). Inclusions may be of identical or different sizes and shapes, and may possess the shape (form) anisotropy. In the general case, the axes of shape anisotropy do not necessarily coincide with crystal or texture axes of their constituent material. Inclusions inside the host matrix may be arranged in a regular periodic 3D or 2D structure, or may be randomly dispersed. They may either be homogeneously distributed over the space, in a the plane, or forming clusters. As for orientations of non-spherical or intrinsically anisotropic inclusions, their main axes may be all aligned, or dispersed statistically according to some distribution law. Inclusions may have any orientation with equal probability in 3D or 2D space, or may fall within some spatial angle, forming a structure with a certain rate of order.

A composite is an inhomogeneous structure. However, it can be characterized by effective electromagnetic parameters, obtained through averaging, or homogenization (Von Hippel, 1995), if sizes of inhomogeneities are much smaller than the wavelength. Any existing homogenization theory tries to ascribe effective parameters to a mixture of different phases, providing mixing rules (Sihvola, 1999). A mixing rule is an analytical formulation that describes an effective parameter as a function of frequency and concentration. Hence, it is very desirable that effective permittivity and permeability of a composite would be governed by the same mixing rule. For example, it has been recently experimentally observed that μ and ϵ of composites with multi-domain magnetic inclusions may be governed by analogous (dual) mixing rules (Rozañov et al., 2009).

There is currently a multitude of mixing rules in the literature based on different homogenization theories and approaches. They are applicable to different types of mixtures, rate of generalization, and depend on which parameters are homogenized, and what their limits are. This is not aimed at a review of all existing homogenization theories and models. A good review of existing mixing rules can be found in the current literature (Landauer, 1978; Sihvola, 1999; Diaz et al., 1998) and references therein.

There are a few most widely used mixing rules, which are briefly reviewed herein. The first is the Maxwell Garnett (MG) formulation (Maxwell Garnett, 1904, 1906), which results in the lowest estimate of the effective parameter. The MG rule in terms of the relative dielectric or magnetic susceptibilities, expressed through the corresponding dielectric and magnetic contrasts between inclusion and host materials

$$\alpha = \begin{cases} \epsilon_{incl} / \epsilon_{host} - 1 \\ \mu_{incl} - 1 \end{cases} \quad (1)$$

and effective parameters of the mixture and the host

$$\beta = \left\{ \begin{array}{c} \varepsilon_{eff} / \varepsilon_{host} - 1 \\ \mu_{eff} - 1 \end{array} \right\}, \quad (2)$$

can be written as

$$\frac{\beta}{1 + n\beta} = \frac{p\alpha}{1 + n\alpha}. \quad (3)$$

The parameter p is the volume concentration of inclusions in the composite. The parameter n describes effective depolarization or demagnetization factors, often called „form factors“ of inclusions (Landau & Lifshitz, 1960). The form factor for calculating permittivity and permeability should be the same. This shape factor is $n=1/3$ for the particular case of spherical inclusions.

The second widely used theory is the Bruggeman symmetric rule (BSR), which is also known as the effective medium approximation (EMA) (Bruggeman, 1935, 1936), as is

$$\frac{p(\alpha - \beta)}{\beta + 1 + n(\alpha - \beta)} - (1 - p) \frac{\beta}{\beta + 1 - n\beta} = 0. \quad (4)$$

For the permittivity of a metal-dielectric mixture, the BSR is conventionally considered the most suitable theory, because it allows for predicting the percolation threshold p_c (McLachlan, 1990). The latter is the concentration at which the composite turns from a non-conducting to a conducting state, and where the real part of effective permittivity of the mixture tends to infinity. As follows from (4), the percolation threshold should be equal to the average form factor, $p_c = n$. However, even for a mixture of spherical particles with $n=1/3$, p_c may vary over a wide range, since the percolation threshold is associated with interactions between inclusions and matrix. It has been experimentally shown, for example, that in composites filled with carbon black inclusions of almost identical spherical shape, but with different polymer host materials, the percolation threshold varied from about 5 to 50% volume fraction of inclusions (Miyasaka et al., 1982). The experimental data do not agree with the BSR prediction of $p_c \approx 30\%$. Moreover, even for a composite containing carbonyl iron powder (CIP) with almost perfect spherical inclusions, the experimentally obtained effective form factor both for permittivity and permeability may significantly deviate from $1/3$ (Osipov et al., 2002). This means that the BSR may not be applicable for predicting properties of magnetic composites.

The third important mixing rule is the the Bruggeman asymmetric rule (BAR), or $1/3$ -power rule (Bruggeman, 1935; Hanai, 1960; Neelakanta, 1995)

$$(\beta + 1)^{\frac{1}{3}} \cdot (1 - p) = \frac{\alpha - \beta}{\alpha}. \quad (5)$$

This rule is fit to the composites of randomly distributed spherical inclusions, and can be applied to both dilute and dense mixtures.

The Landau-Lifshitz-Looyenga (LLL) formula (Landau & Lifshitz, 1960; Looyenga, 1965; Dube, 1970),

$$(\beta + 1)^{1/3} - 1 = p \left\{ (\alpha + 1)^{\frac{1}{3}} - 1 \right\}, \quad (6)$$

plays a special part among the mixing rules. The LLL formula is rigorous at low inclusion-matrix contrast $\alpha \ll 1$, and, hence, at high frequencies ($\omega \rightarrow \infty$). Thus any mixing rule should converge to the LLL limit at the high frequencies. This is important, because predicting frequency dependences of the material parameters must include the high-frequency region. For example, it can be shown that at $n = p_c = 1/3$, the BSR satisfies the LLL high-frequency limit. However, the parameters p_c and n are of a different physical nature: the percolation concentration p_c describes collective properties of inclusions, while shape factor n is an individual characteristic of an inclusion related to its depolarization or demagnetization at the boundary surface. This means that in a physically meaningful mixing formula these two parameters should be uncorrelated “free” fitting parameters for any particular composite. Such splitting of p_c and n as two independent physical properties can be found in a formulation proposed by Odelevsky (Odelevsky, 1951) for calculating static effective permittivity of a metal-dielectric mixture,

$$\varepsilon_{static} = 1 + \frac{p \cdot p_c}{n(p_c - p)} . \quad (7)$$

The formula to describe static magnetic properties of composites containing ferromagnetic inclusions in a dielectric host is analogous to (7)

$$\mu_{static} = 1 + \frac{p \cdot p_c \cdot (\mu_i - 1)}{n(p_c - p)(\mu_i - 1) + p_c} . \quad (8)$$

Odelevsky's formulas (7) and (8) fit experimentally obtained static data (Rozaanov et al., 2009), and it can be used for finding intrinsic permeability and permittivity of inclusions (without any host material). This is very important, since in majority of cases these values are not known and cannot be found by any other methods, especially, intrinsic permeability of magnetic inclusions, which is different from the bulk materials. The latter significantly depends on the way of crushing the bulk magnetic material and the crush parameter ξ , which is a ratio of an average gap between magnetic particles in the crushed bulk material to an average size of a magnetic particle, or grain (Tsutaoka, 2003). At low frequencies ($\omega \rightarrow 0$), Odelevsky's formulas (7) and (8) converge to the corresponding MG formula (3) for $p_c = 1$. When $n = p_c = 1/3$, formula (7) for effective permittivity becomes equivalent to the BSR (4), but formula (8) for effective permeability never turns to (4). Moreover, both (7) and (8) do not satisfy the LLL limit at high frequencies ($\omega \rightarrow \infty$). For this reason, Odelevsky's theory is applicable only for static parameters.

The mixing rules (7) and (8) are formulated for a quasi-static assumption, which means that the inclusion size is much less than the shortest wavelength in the composite. Hence the frequency dependence of the effective material parameters of the mixture is associated with frequency dispersion in its ingredients. If the host matrix is almost non-dispersive, the frequency dependence of the mixture will be totally determined by the frequency responses of the inclusions.

There are also complex mixing rules, which are based on cluster theories, e.g., (Sheng, 1980; Hui & Stroud, 1986; Musal et al., 1988; Doyle & Jacobs, 1990). They describe different groups of inclusions (clusters), using different mixing rules depending on their applicability. Then separate clusters are mixed using some other mixing rule at the higher level of homogenization. In some cases, these cluster theories provide good agreement with

experiment, but due to their complexity, choice of partial mixing rules is a matter of art rather than science, and there are no general recommendations that could work for any type of a composite.

Any mixing rule should describe effective permittivity and permeability using the same mathematical formulation due to the duality of ε and μ . However, existence of numerous mixing rules in the present-day literature indicates that there is no unique rule that is applicable for describing simultaneously dielectric and magnetic properties of magneto-dielectric composites over a wide frequency range. Researchers make attempts to model effective properties for particular cases of mixtures, and any mixing theory has its applicability limitations. Thus, for an important case of composites filled with ferromagnetic metal powders, currently there is no standard unified and experimentally validated mixing rule to calculate dependences both of frequency and concentration.

2.2 A new mixing rule based on a spectral function approach

Alternative to mixing rules, properties of composites can be considered in terms of the Bergman-Milton (BM) *spectral function theory* (Bergman, 1978; Stroud et al., 1986; Bergman & Stroud, 1992; Milton, 2001). A spectral function is an unambiguous and universal characteristic of a composite (Bergman & Stroud, 1992). It describes the statistical distribution of inclusions with respect to their form factors. The spectral function can take into account variations of the effective form factor due to interactions within the mixture, as well as the spread of inclusion form factors. This is an important and favorable feature of the BM theory, as opposed to the existing mixing rules and effective medium theory. The effective normalized susceptibility of the composite can be found as

$$\beta = \int_0^1 \frac{\alpha B(n)}{1 + n\alpha} dn, \quad (9)$$

where $B(n)$ is the spectral function. The sums rules for a spectral function (Bergman, 1978; Fuchs, 1978),

$$\int_0^1 B(n) dn = 1 \quad \text{and} \quad \int_0^1 n B(n) dn = \frac{p(1-p)}{D}, \quad (10)$$

provide an agreement with the LLL theory. The parameter D is the dimensionality of the composite, e.g., $D=2$ for the case of infinite cylinders, and $D=3$ for arbitrary-shaped inclusions of a bulk isotropic composite.

All the known mixing rules are particular cases of the general BM theory with their own spectral functions. Examples of spectral functions for a few different mixing theories are presented in Fig. 4. For convenience of plotting, the functions $nB(n)$ are presented instead of just $B(n)$. The calculations are made for the mean form factor of $\hat{n}=1/3$, and the volume concentration of inclusions of $p=0.25$. Each spectral function “peak”, or continuous region, corresponds to some frequency dispersion range.

The spectral function of the MG theory is the δ -function, concentrated at the average form factor \hat{n} , which is around $1/3$,

$$B(n) = p \cdot \delta\{n - (1-p)\hat{n}\}. \quad (11)$$

The spectral function for the effective medium BSR is

$$B(n) = \begin{cases} \frac{D\sqrt{(n-n_1)(n_2-n)}}{4\pi}, & \text{for } n_1 < n < n_2. \\ 0, & \text{otherwise} \end{cases} \quad (12)$$

In (12), n_1 and n_2 are the range of the possible form factors of inclusions, and D is the composite dimensionality. The BSR spectral function is a semi-circle in terms of $nB(n)$. It can be seen that the BAR has an asymmetric spectral function $nB(n)$ with a higher spectral density at a lower form factors n . Sheng's cluster theory (Sheng, 1980) results in a few separate regions of the $nB(n)$ function. However, there is no physically meaningful explanation, why the distribution with respect to form factors is not continuous in the cluster theory.

Though the BM spectral function approach is general for taking into account physically existing spread of inclusion parameters, it is not widely applied to analyze actual experimental data. The main reason for this is that obtaining the spectral function is not a straightforward procedure. Equation (9) is the integral relation for the intrinsic and effective parameters, and a simple algebraic representation is not always possible.

One of the most practically useful approaches that apply the notion of the BM spectral function is the Ghosh-Fuchs formulation (Ghosh & Fuchs, 1988),

$$B(n) = \begin{cases} C(n-n_1)^{1-A}(n_2-n)^B, & \text{for } n_1 < n < n_2. \\ 0, & \text{otherwise} \end{cases} \quad (13)$$

In this theory, the spectral function is taken the same as in the BSR, but with five fitting parameters: A , B , C , n_1 , and n_2 . C , n_1 , and n_2 determine the amplitude, position, and the "peak" width of the spectral function. As a result, the width of the spectral function may vary over some range to take into account the actual spread of the inclusion form factors. The critical exponents A and B are introduced to get agreement with percolation theory. If $A=B=1/2$ in (13), and $C = D/(4\pi)$, then the spectral function will be the same as in the BSR (12).

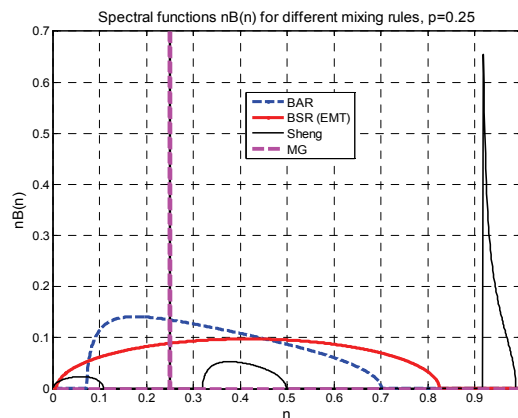


Fig. 4. Spectral functions $nB(n)$ for the BAR, BSR, Sheng's theory and MG mixing rule

The formulation (13), in contrast to the other mixing rules, agrees very well with experiments for both permittivity and permeability of composites containing ferromagnetic inclusions (Rozanov et al., 2009). However, (13) is not convenient for practical use because of cumbersome integral representation for the spectral function, and the necessity of using many (five) fitting parameters. Hence, it is appealing to have a simplified formalism dealing with algebraic operations.

The first step in the development of a simplified model is to set the critical exponents $A=B=1/2$ in the spectral function (13). This assumption is consistent with the BSR, but is different from the classical percolation theory. The reason is that the classical percolation behavior of material parameters is observed only in soot-filled (carbon black) polymers. As for the other materials, it is difficult to make them with concentration close to percolation, and even if it is possible, frequency dependence of permittivity may differ significantly from predicted by the percolation theory. One of the reasons may be imperfect contacts between particles in conducting clusters, since cluster conductivity depends mainly on these contacts, but not geometry of clusters, as the percolation theory assumes. Hence, it is reasonable to exclude the critical indices different from $1/2$ from further consideration. This assumption would allow for further representing the formulation (13) in a simple algebraic form, analogous to the BSR. Also, the scaling coefficient is set $C=1$, as follows from the sums rule (10). It is also important that two limits - the LLL at high frequencies

$$\omega \rightarrow \infty, \alpha \ll 1: \beta = p\alpha + \frac{p(1-p)\alpha^2}{D}, \quad (14)$$

and Odelevsky's static case will be satisfied,

$$\omega \rightarrow 0, \alpha \gg 1: \beta = 1 + \frac{p}{n} \cdot \frac{p_c}{p_c - p}. \quad (15)$$

Since the spectral function chosen is a particular case of the BSR formulation, which is basically a quadratic equation, as follows from (4), the effective medium solution can be written as

$$\beta = Q \left(R + \alpha \pm \sqrt{(\alpha - S)^2 - T} \right), \quad (16)$$

where Q, R, S , and T are unknown coefficients, but they can be found uniquely using the limits (14) and (15). These coefficients depend on the physical parameters: composite dimensionality, inclusion concentration, average form factor, and the percolation threshold. In the BSR and in (16), the percolation threshold is determined by switching the sign (\pm) in the solution of the quadratic equation for α_n effective parameter. This is a consequence of the material passivity, *i.e.*, energy can dissipate, but not generate in the material.

Then the resultant equation corresponding to the new mixing rule can be written as

$$(1-p)p_c\beta^2 - D(p\alpha - \beta)[p(p_c + n\beta) - np_c\beta] = 0. \quad (17)$$

A consequence of this new formulation is that only two fitting parameters ($n = \hat{n}$ and p_c) are used to approximate the spectral function, as opposed to five fitting parameters in the formulation (13). These fitting parameters can be found from the concentration dependence

of permittivity of the composite. The limiting case for this formulation coincides with the LLL mixing rule, and provides a unique equation for the effective material constant (either magnetic or dielectric susceptibility) as a function of inclusion concentration, percolation threshold, and dimensionality.

The correctness of (16) can be checked for a few particular cases. If concentration of inclusions $p=1$, then (16) leads to the result $\beta = \alpha$. If the average form factor is taken as $\hat{n} = 1/3$, and the percolation threshold is not taken into account, *i.e.*, allowed to be $p_c=1$, then (16) converts to the MG formulation (3). If $\hat{n} = 1/3$, but the percolation threshold is $p_c=1/3$, then (16) transforms to (4), which is the Bruggeman effective medium theory, or the BSR. The proposed above formulation is valid for only crumb-like inclusions in the composite, since it should satisfy the inequalities

$$1/4 < p_c < 1 \quad \text{and} \quad \sqrt{4/3} - 1 \approx 0.154 < n < 1/3. \quad (18)$$

The results of applying the above simplified algebraic formulation to reconstruct the experimentally obtained permeability of a polymer-based CIP composite with different volume concentrations of CIP are shown in Fig. 5 (Rozanov et al., 2009). As is seen from Fig. 5, the reconstruction of experimental results well achieved over the frequency range from 10 MHz to 3 GHz. The CIP inclusions had arbitrary crumb-like shape with a mean size of inclusions around 60 μm . Fitting according to the proposed model is provided at each frequency point.

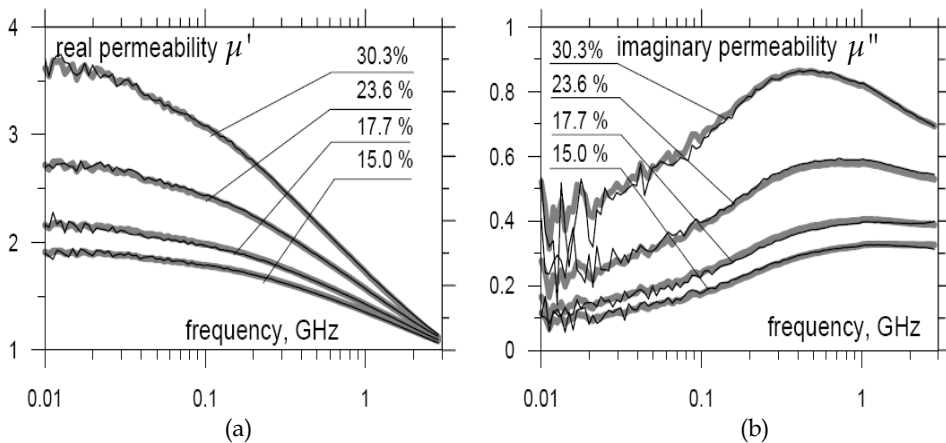


Fig. 5. Experimental (heavy grey) and modeled (thin black) curves for (a) real part of the permeability μ' and (b) imaginary part of permeability μ'' of polymer-based CIP composite with different volume concentrations of CIP (Rozanov et al, 2009)

To reconstruct the experimental data, it is important to retrieve the intrinsic permeability of inclusions. The spectral function as the distribution of inclusions with respect to varying form factor is presented in Fig. 6 (a). As the volume concentration of inclusions increases, the spectral function broadens, and this is evidence of strong cooperative phenomena, such as cluster formation. On the other hand, the spectral function has a significant width even at

the lowest volume fraction under study (15%), which means that the spread in the shapes of powder particles significantly impacts the measured permeability.

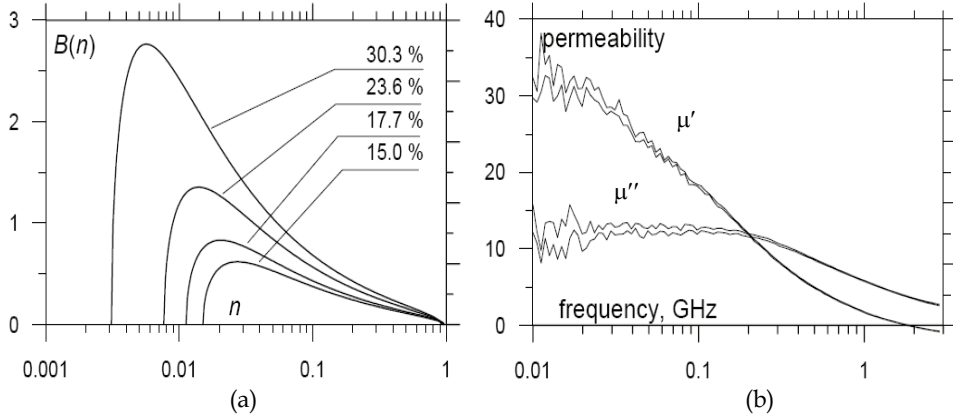


Fig. 6. Restoration of (a) spectral functions for different concentrations of CIP inclusions in the mixture (Rozanov et al, 2009), and (b) intrinsic permeability of CIP inclusions

Fig. 6 (b) shows the frequency dependence of the intrinsic permeability obtained from different concentrations. It is seen that the intrinsic permeability obtained from different concentrations is almost identical. The reconstructed static permeability value for inclusions is $\mu_{static} \approx 30$, while the Odelevsky formula results in about $\mu_{static} \approx 17$. An additional check for the obtained result is made based on Snoek's constant of the inclusions (Snoek, 1948). This value is known to depend on the composition only, basically, on the magnetic saturation $4\pi M_s$, according to Snoek's law (Snoek, 1948; Liu, Y. et al., 2006),

$$(\mu_{static} - 1) \cdot f_{res} = \frac{2}{3} \cdot \gamma \cdot 4\pi M_s, \quad (19)$$

where the gyromagnetic ratio $\gamma \approx 2.8$ GHz/kOe for iron and the majority of ferromagnetics, and f_{res} is the resonance frequency. From the microwave performance, Snoek's constant is estimated as the product of the static permeability and the ferromagnetic resonance frequency ($S = \mu_{static} \cdot f_{res}$). At the ferromagnetic resonance frequency, the real part of permeability is unity, and the imaginary goes through zero. As is seen in Fig. 6(b), it is approximately 1.3 GHz, so Snoek's constant is about $S \approx 39$ GHz, which is in a good agreement with the reference value for iron ($4\pi M_s = 21.5$ kG=2.15 T), so $S \approx 40$ GHz (Liu, Y. et al., 2006). This confirms that the static permeability of inclusions is predicted correctly, while Odelevsky's formula underestimates this value.

2.3 New mixing rule based on modified Bruggeman asymmetric rule

The proposed above theory predicts the behavior of composites containing nearly spherical inclusions. However, composites filled with magnetic needles or flakes are of great practical interest due to the possibility of achieving much higher permeability than the composites containing crumb-like particles with the same inclusion filling factor. A scanning electron microscope (SEM) picture for a powder with iron-type flakes is shown in Fig. 7.

Also, magnetic needles or flakes are favorable for the design of thin sheet materials. The formulation proposed herein is based on the Modified Bruggeman Asymmetric Rule (MBAR), which in terms of permeability is written as (Bruggeman, 1935)

$$\frac{\mu_i - \mu_{eff}}{\mu_i - \mu_{host}} = (1 - p) \left(\frac{\mu_{eff}}{\mu_{host}} \right)^{\frac{1}{3}}. \quad (20)$$

However, demagnetization factors in this formulation are missing. At the same time, it is known that the Polder-van Santen (PVS) formula, which is a consequence of the Bruggeman effective medium theory, or BSR, may account for shape factors (n_k , $k = 1, 2, 3$) of ellipsoidal inclusions (Polder & van Santen, 1946),

$$\mu_{eff} = \mu_{host} + \frac{p(\mu_i - \mu_{host})}{3} \sum_{k=1}^3 \frac{\mu_{eff}}{\mu_{eff} + n_k(\mu_i - \mu_{eff})}. \quad (21)$$

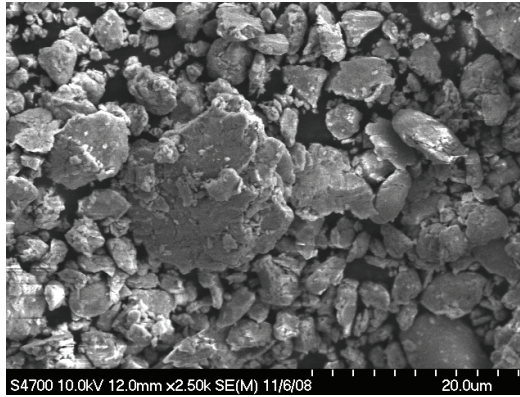


Fig. 7. SEM picture of the magnetic powder

A flake with the disk-like shape, whose aspect ratio is $u = d/h$, where d is the diameter and h is the height of the disk, can be approximated as an oblate spheroid with the axial form factor being approximately (Landau & Lifshitz, 1960)

$$n_3 \approx 1 - \frac{1}{\sqrt{1 + u^2}}, \quad (22)$$

while the other two depolarization factors are assumed to be equal, $n_1 = n_2 = 0.5(1 - n_3)$. For high inclusion-host permeability contrast $\mu_i/\mu_{host} \gg 10$, and for volume loading of inclusions greater than ~30%, the resultant μ_{eff} , calculated using (21), is significantly higher than the values predicted by (20), especially for the low-frequency region. This happens even for an aspect ratio of inclusions close to 1 and the corresponding form factors close to 1/3, as in the spherical case. The reason is the high-frequency nature of the BSR, analogous to the LLL, and not taking into account form factors in the BAR.

The objective is to modify the BAR for permeability (20) in such a way that it would be possible to apply it to flakes. It is appealing to retrieve the correction factor which depends

on both concentration p and aspect ratio u of inclusions from (21), as a coefficient of proportionality between spherical inclusions and flakes as

$$\mu_{flake}^{PVS}(p, u) = F(p, u) \cdot \mu_{sphere}^{PVS}(u). \quad (23)$$

and then apply the same correction coefficient $F(p, u)$ to (20) as

$$\mu_{flake}^{BAR}(p, u) = F(p, u) \cdot \mu_{sphere}^{BAR}(u). \quad (24)$$

Effective permeability curves $\mu_{flake}^{PVS}(u)$ as functions of the aspect ratio u for varying inclusion concentration p are shown in Fig. 8. These curves are calculated for magnetic inclusions with intrinsic static permeability of inclusions $\mu_i = 630$.

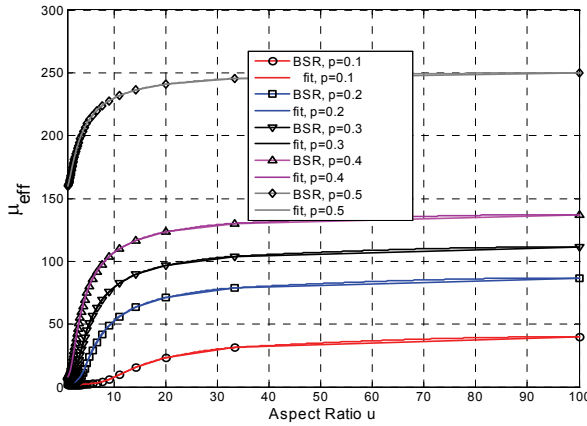


Fig. 8. Effective permeability calculated using BSR (EMT – effective medium theory) and corresponding curve-fitting to retrieve the function (p, u)

The closed-form expression for the correction factor $F(p, u)$ is obtained by analyzing numerous dependencies as those in Fig. 8, and can be well approximated by the function

$$F(p, u) = 1 + \left\{ G \cdot \tanh^2(u) (1 - H \cdot \text{sech}^2(u)) / \mu_{sphere}^{PVS}(p) \right\}, \quad (25)$$

where G and H are the fitting parameters.

Fig. 9 shows the effective permeability of the mixture calculated using the modified BAR when the static permeability of inclusions is $\mu_i = 630$, the resonance frequency in the magnetic Debye curve $f_{res} = 880$ MHz, and $p = 0.25$. As aspect ratio of the plate lets increases, static permeability increases, and the loss peak shifts slightly to lower frequencies.

Fig. 10 shows an example of reconstruction of experimentally obtained and curve-fitted with a sum of Debye terms (this curve-fitting will be discussed in the next Section) permeability and permittivity data for a composite containing magnetic alloy flakes with an average aspect ratio $u = 25$, volume fraction $p = 0.5$, $4\pi M_s = 4000$ G, $\mu_{static}^{bulk} = 2100$, and the crush parameter $\xi = \frac{\langle \delta \rangle_{gap}}{\langle d \rangle_{grain}} = 10^{-3}$. The frequency characteristic of the permeability, modeled using the MBAR, is approximated by the skewed Cole-Davidson dependence with exponents $s = 1.01$ and $t = 0.6$ as

$$\mu = 1 + \frac{\mu_{static} - 1}{(1 + (j\omega\tau)^t)^s} \quad (26)$$

rather than a single-term Debye dielectric curve. The similar formula is used for the permittivity,

$$\varepsilon = \varepsilon_\infty + \frac{\varepsilon_{static} - \varepsilon_\infty}{(1 + (j\omega\tau)^t)^s} - \frac{j\sigma_e}{\omega\varepsilon_0} \quad (27)$$

It is important to mention that μ_{static} in (26) is different from μ_{static}^{bulk} . μ_{static} is for the crushed magnetic material,

$$\mu_{static} = \frac{\mu_{static}^{bulk}}{1 + \xi \mu_{static}^{bulk}} \quad (28)$$

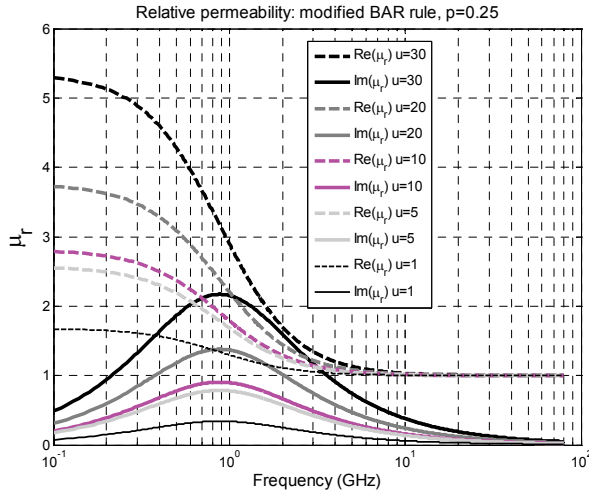


Fig. 9. Effective permeability calculated using the modified BAR, $p=0.25$

When modeling permittivity using the PVS equation (21), the conductivity of inclusions is $\sigma_i = 10^4$ S/m; the parameters of the silicon-based polymer are taken as $\varepsilon_{static}^{host} = 3.32$, $\varepsilon_\infty^{host} = 2.82$, and $\sigma_{host} = 5.5 \cdot 10^{-4}$ S/m. Cole-Davidson dependence exponents are $s=1.01$ and $t=0.6$. This input data gives the closest approximation to the measured results.

Another example is the reconstruction of the complex permeability function for two given volume loadings of flake-like magnetic alloy inclusions (15% and 25%), and prediction of frequency behavior of a composite with 30% volume fraction of the same inclusions. The results are shown in Fig. 11. In this case, the aspect ratio of flakes is $u=110$, $4\pi M_s=9179$ G, $\mu_{static}^{bulk}=2000$, and the crush parameter $\xi = 10^{-3}$. The Cole-Davidson exponents are $s=1.01$ and $t=0.65$.

The proposed modified Bruggeman asymmetric rule allows for realistic predicting the frequency behavior of composites, if intrinsic constitutive parameters of inclusion and host

materials, their volume fractions, and morphology of the composite (shape and size of inclusions, their orientation, including statistical distribution of orientations, homogeneity and formation of clusters, *etc.*) are known *a priori*.

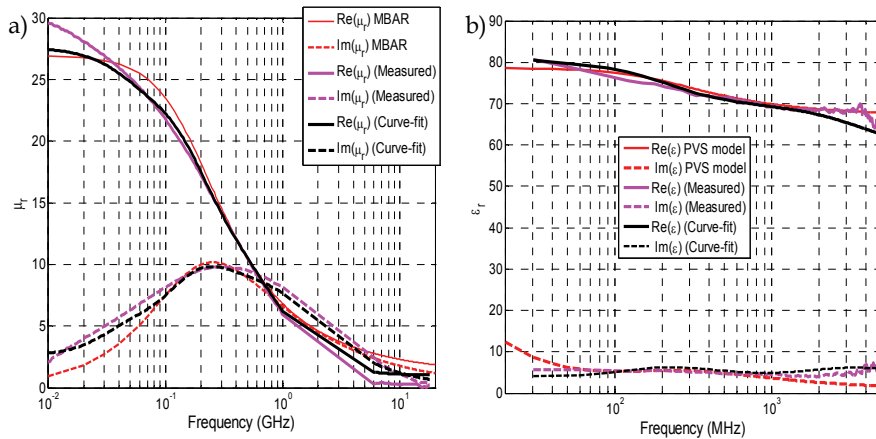


Fig. 10. Measured, curve-fitted (28), (29), and modeled (27), (28) data for (a) permeability and (b) permittivity for the test composite material

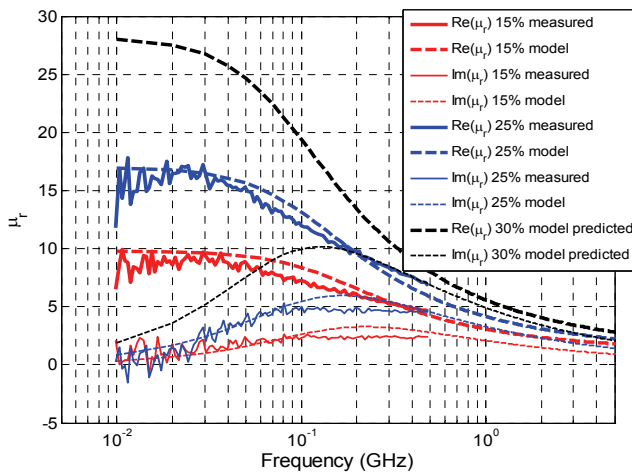


Fig. 11. Measured and reconstructed permeability for two test materials and predicted data for the third material with the different volume loading of inclusions

3. Material extraction procedure and curve-fitting for numerical modelling

A procedure for extracting complex permittivity and permeability of materials from measurements based on a travelling-wave transmission-line technique (single-ended and differential microstrip and stripline) has been applied. It includes an accurate and efficient

curve-fitting for approximating frequency dependencies of both permittivity and permeability by a series of rational-fractional functions. RF and microwave material frequency characteristics in the majority of cases can be accurately approximated by a series of non-resonance Debye and resonant Lorentzian terms, which have poles of the first and the second order, respectively, as

$$\varepsilon(\omega) = \varepsilon_\infty + \sum_{k=1}^N \frac{\chi_{ek}}{1 + j\omega\tau_{ek}} + \sum_{i=1}^M \frac{\chi_{ei}\omega_{0i}^2}{\omega^2 - \omega_{vi}^2 + j\omega\Delta\omega_{ei}} - j \frac{\sigma_e}{\omega\varepsilon_0}, \quad (29)$$

$$\mu(\omega) = 1 + \sum_{k=1}^N \frac{\chi_{mk}}{1 + j\omega\tau_{mk}} + \sum_{i=1}^M \frac{\chi_{mi}\omega_{0i}^2}{\omega^2 - \omega_{vi}^2 + j\omega\Delta\omega_{mi}}. \quad (30)$$

The last term in equation (29) allows for taking into account the d.c. (ohmic) conductivity. The curve-fitting procedure employs Legendre polynomials and regression analysis. The flowchart of this curve-fitting procedure is shown in Fig. 12. The measured data is interpolated to smooth curves using Legendre polynomials. Then a non-linear least-mean-square regression optimization procedure is used to approximate these curves to the series (25) and (26). For $\mu(\omega)$ and $\varepsilon(\omega)$, only Debye terms are sufficient to realize the curves, as is shown herein.

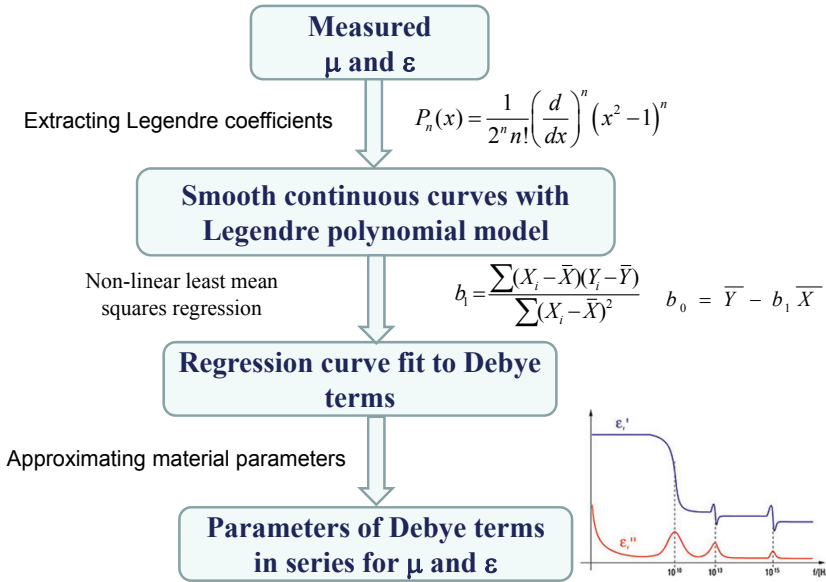


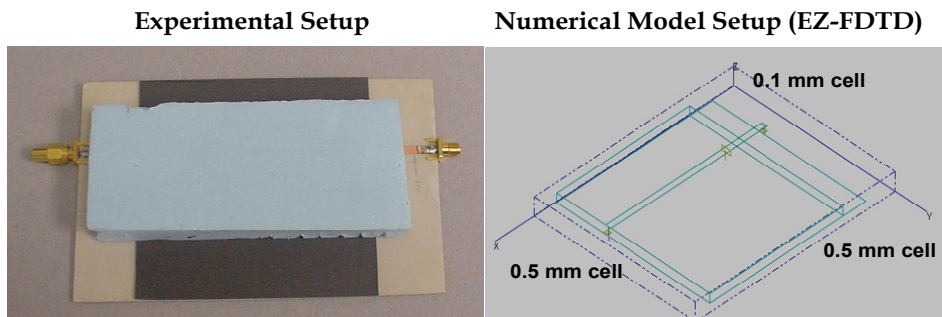
Fig. 12. Flowchart of the curve-fitting procedure

It is important that the curve-fitting procedure ensures satisfying the Kramers-Krönig causality relations, which is necessary for using these characteristics in further numerical and analytical modeling. Moreover, the proposed curve-fitting allows for restoration of the missing measurement data in some frequency intervals. For example, Fig. 10 shows the curve-fitted frequency dependences along with the measured permittivity and permeability

of the test composite material. The curve-fitting algorithm based on the Legendre polynomials and non-linear regression optimization is friendly and converges rapidly. Curve-fitting corrects non-causality of the measured responses. However, as all optimization procedures, it needs some initial guess about the Debye data to start search for the actual Debye parameters, fitting the continuous functions. These continuous functions are obtained from the series of interpolating the measured data at the discrete frequency points and smoothening using the series of the Legendre polynomials.

The curve-fitted frequency dependences of permittivity and permeability are convenient for time-domain electromagnetic numerical simulations, in particular, finite-difference time-domain method (FDTD). The advantage of time-domain techniques is that they efficiently provide broadband responses of the modeled structures. FDTD code can be used for wideband simulations of complex geometries containing frequency-dispersive materials, including a subcellular feature for modeling thin layers of absorbing materials. Both bulk cells and thin-layer sub-cells in this algorithm can include curve-fitted frequency characteristics for both permittivity and permeability.

The numerical simulations have been experimentally tested for a number of structures, such as a single-ended microstrip line, a differential microstrip line, a monopole antenna comprised of a cable driven against a ground plane, and a rectangular cavity. An example with the microstrip line covered with the test absorbing sheet is presented herein. The experimental and the FDTD model setups are shown in Fig. 13. Measured and FDTD modeled amplitude and phase of the input impedance of the open-circuited microstrip line covered with a thin sheet of absorbing material with the modeled frequency characteristics as shown in Fig. 10, is presented in Fig. 14. Good agreement with experiment validates the modeling approach.



Parameters of the structure

- Length of the board is 14.7 cm.
- Trace width is 3.5 mm. FR-4-type dielectric ($\epsilon_r=3.53$; $\tan\delta=0.001$), height = 1 mm.
- Characteristic impedance = 50 Ω . Absorbing sheet: 10 mm x 10 mm x 0.5 mm.

Fig. 13. Single-ended microstrip line on a printed circuit board coated with an absorbing composite layer. The thick top overlay material with $\epsilon_r \approx 1$ is used for pressing the absorbing sheet flat

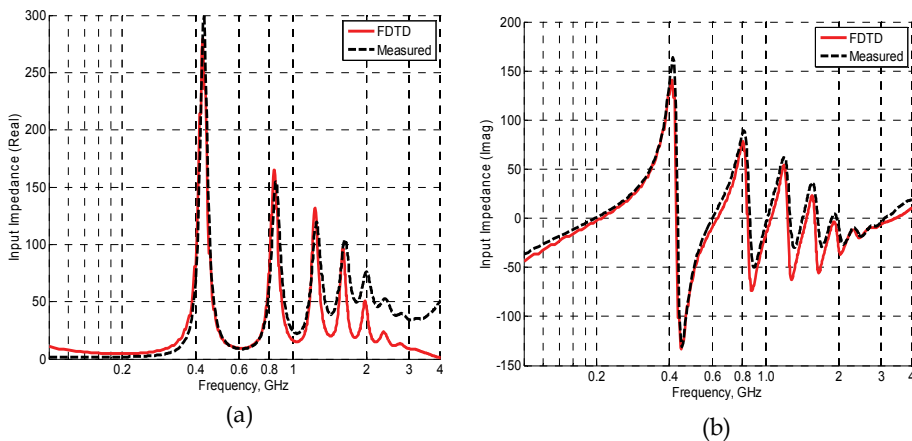


Fig. 14. Measured and FDTD modeled input impedance (in Ohms) of an open-circuit single-ended microstrip transmission line: (a) real part; (b) imaginary part

4. Conclusion

A methodology for engineering of new materials with desirable frequency characteristics and other physical, mechanical, and environmental properties, and their analytical and numerical modeling and experimental testing in different practical scenarios is presented in this work. The proposed methodology may be applied to design absorbers that would mitigate radiation from heatsinks, spurious radiation from chips and other active circuit components, suppress parasitic resonances within enclosures, and reduce radiation from cable structures. It is an effective approach for evaluating whether a material could be a successful candidate for mitigating unwanted radiation and coupling, and to optimize dielectric and magnetic properties of materials and their ingredients in composites, as well as geometries for particular practical problems.

5. Acknowledgment

M. Koledintseva and J. Drewniak would like to acknowledge the support of the research by the Missouri S&T Center for Electromagnetic Compatibility (U.S. NSF grant No. 0855878), and by Laird Technologies and ARC Technologies. The authors are also grateful to Mrs. Clarissa Wisner and Dr. Elizabeth Kulp (Materials Research Center of Missouri S&T) for SEM analysis of samples. K. Rozanov acknowledges the support of the study from the Russian Foundation for Basic Research (RFBR), grant No. 09-08-00158. He also is grateful to Prof. E.P. Yelsukov for providing the iron powders.

6. References

- Abshinova, M.A.; Lopatin, A.V.; Kazantseva, N.E.; Vilcakova, J. & Saha, P. (2007). Correlation Between the Microstructure and the Electromagnetic Properties of

- Carbonyl Iron Filled Polymer Composites. *Composites, Part A: Applied Science and Manufacturing*, Vol. 38, No. 12 (December 2007), pp. 2471-2485, ISSN 1359-835X.
- Backer-Jarvis, J., Janezic, M.D., Grosvenor, J.H. Jr. & Geyer, R.G. (1993). *Transmission/Reflection and Short-circuit Line Methods for Measuring Permittivity & Permeability*, National Institute of Standards and Technology (NIST) Technical Note 1355 (December 1993), U.S. Department of Commerce, USA.
- Baker-Jarvis, J.; Janezic, M.D.; Riddle, B. & Holloway, C.L. (2001), *Dielectric and Conductor-Loss Characterization and Measurements on Electronic Packaging Materials*, National Institute of Standards and Technology (NIST) Technical Note 1520 (July 2001), U.S. Department of Commerce, USA.
- Barry, W. (1986). A Broadband Automated Stripline Technique for Simultaneous Measurement of Complex Permittivity and Permeability, *IEEE Transactions on Microwave Theory and Techniques*, Vol. 34, No. 1, (January 1986), pp. 80-84, ISSN 0018-9480.
- Bekker, V.; Seemann, K. & Leise, H. (2004). A New Strip Line Broad-band Measurement Evaluation for Determining the Complex Permeability of Thin Ferromagnetic Films, *Journal of Magnetism and Magnetic Materials (JMMM)*, Vol. 270 (April 2004), pp. 327-332, Elsevier, ISSN 0304-8853.
- Booth, J.C.; Wu, D.H. & Anlage, S.M. (1994). A Broadband Method for the Measurement of the Surface Resistance of Thin Films at Microwave Frequencies, *Review of Scientific Instruments*, Vol. 65, 2082-2090, ISSN 0196-8092.
- Bergman, D.J. (1978). Analytical Properties of the Complex Effective Dielectric Constant of a Composite Medium with Applications to the Derivation of Rigorous Bounds and to Percolation Problems, *Electrical Transport and Optical Properties of Inhomogeneous Media*, AIP Conference Proceedings, Vol. 40, No.1 (April 1978), pp. 46-62, ISBN 088318-1398.
- Bergman, D.J. & Stroud, D. (1992). Physical Properties of Macroscopically Inhomogeneous Media, *Solid State Physics*, Vol. 46 (1992), pp. 147-269, ISBN 0-12-607746-0.
- Bhattacharya, S.K. (1986). *Metal-filled Polymers: Properties and Applications* (1st edition) , CRC Press, ISBN 0824775554, Boca Raton, FL, USA.
- Birks, J.B. (1948). Microwave Magnetic Dispersion in Carbonyl Iron Powder, *Physical Review*, Series II, Vol. 74, No. 7 (October 1948), pp. 843-844, PROLA.
- Bruggeman, D.A.G. (1935). Berechnung Verschiedener Physikalischer Konstanten von Heterogenen Substanzen, I. Dielektrizitätskonstanten und Leitfähigkeiten der Mischkörper aus isotropen Substanzen, *Annalen der Physik*, Vol. 416, No. 7 (1935), pp. 636-664, Germany, ISSN 0003-3804.
- Bruggeman, D.A.G. (1936). Berechnung Verschiedener Physikalischer Konstanten von Heterogenen Substanzen, II. Dielektrizitätskonstanten und Leitfähigkeiten von Vielkristallen der Nichtregulären Systeme, *Annalen der Physik*, Vol. 417, No. 7 (1936), pp. 654-672, Germany, ISSN 0003-3804.
- Celozzi, S.; Araneo, R. & Lovat, G. (2008). *Electromagnetic Shielding*, Wiley, ISBN 978-0-470-05536-6, Hoboken, NJ, USA.

- Chen, L.F.; Ong, C.K.; Neo, C.P.; Varadan, V.V. & Varadan, V.K. (2004). *Microwave Electronics: Measurement and Materials Characterization*, Wiley, ISBN 0-470-88492-2, Hoboken, NJ, USA.
- Davidson, D.W. & Cole, R.H. (1951). Dielectric Relaxation in Glycerol, Propylene Glycol, and n-Propanol, *The Journal of Chemical Physics*, Vol. 19, No. 12 (December 1951), pp. 1484-1490, ISSN 0021-9606.
- Diaz, R.E.; Merrill, W.M. & Alexopoulos, N.G. (1998). Analytical Framework for the Modeling of Effective Media, *Journal of Applied Physics*, Vol. 84, No.12 (Dec. 1998), pp. 8615-6826, ISSN 0021-8979.
- Doyle, W.T. & Jacobs, I.S. (1990). Effective Cluster Model of Dielectric Enhancement in Metal-Insulator Composites, *Physical Review B: Condensed Matter and Materials Physics*, Vol. 42, No. 15 (November 1990), pp. 9319-9327, ISSN 1098-0121.
- Dube, D.C. (1970). Study of Landau-Lifshitz-Looyenga's Formula for Dielectric Correlation between Powder and Bulk, *Journal of Physics D: Applied Physics*, Vol. 3, No. 11 (November 1970), pp. 1648-1652, ISSN 0022-3727.
- Fellner-Feldegg, H. (1972). A Thin-Sample Method for the Measurement of Permeability, Permittivity, and Conductivity in the Frequency and Time Domain. *The Journal of Physical Chemistry*, Vol. 76, No. 15 (1972), pp. 2116-2122, ISSN 1089-5639.
- Fox, R.T.; Wani, V.; Howard, K.E.; Bogle, A. & Kempel, L. (2008). Conductive Polymer Composite Materials and Their Utility in Electromagnetic Shielding Applications. *Journal of Applied Polymer Science*, Vol. 107, No. 4 (February 2008), pp. 2558-2566, Wiley, ISSN 0021-8995.
- Fuchs, R. (1978). Optical Properties of Small-particle Composites, *Electrical Transport and Optical Properties of Inhomogeneous Media*, AIP Conference Proceedings, Vol. 40, No.1 (April 1978), pp. 276-281, ISBN 0-88318-139-8.
- Ganchev, S.I.; Qaddoummi, N.; Bakhtiari, S. & Zoughi, R. (1995). Calibration and Measurement of Dielectric Properties of Finite Thickness Composite Sheets with Open-ended Coaxial Sensors, *IEEE Transactions on Instrumentation and Measurement*, Vol. 44, No. 6 (December 1995), pp. 1023-1029, ISSN 0018-9456.
- Ghodgaonkar, D.K.; Varadan, V.V. & Varadan, V.K. (1990). Free-space Measurement of Complex Permittivity and Complex Permeability of Magnetic Materials at Microwave Frequencies, *IEEE Transactions on Instrumentation and Measurement*, Vol. 39, No. 2 (April 1990), pp. 387-394, ISSN 0018-9456.
- Ghosh K. & Fuchs, R. (1988). Spectral Theory for Two-component Porous Media. *Physical Review B: Condensed Matter and Materials Physics*, Vol. 38, No. 8 (September 1988-I), pp. 5222-5236, The American Physical Society, ISSN 1098-0121, The American Physical Society.
- Hanai, T. (1960). The Theory of Dielectric Dispersion due to the Interfacial Polarization and Its Applications to Emulsions, *Kolloid-Zeitschrift*, Vol. 171, no. 1 (January 1960), pp. 23-31. ISSN 0368-6590.
- Hui, P.M. & Stroud, D. (1986). Complex Dielectric Response of Metal-Particle Clusters. *Physical Review B: Condensed Matter and Materials Physics*, Vol. 33, No. 4 (February 1986), pp. 2163-2169, ISSN 1098-0121, The American Physical Society.

- Iijima, Y.; Houjou, Y. & Sato, R. (2000). Millimeter Wave Absorber Using M-type Hexagonal Ferrite. *IEEE International Symposium on Electromagnetic Compatibility*, pp. 547-549, ISBN 0-7803-5677-2, Washington, DC, USA, August 21-25, 2000.
- Jargon, J.A. & Janezic, M.A. (1996). Measuring Complex Permittivity and Permeability Using Time Domain Network Analyzers, *1996 IEEE MTT-S Digest*, Vol. 3, pp. 1407-1410, ISBN 0-7803-3246-6.
- Kazantseva, N.E.; Vilcakova, J.; Kresalek, V.; Saha, P.; Sapurina, I.; & Stejskal, J. (2004). Magnetic Behavior of Composites Containing Polyaniline-coated Manganese-Zinc Ferrite. *Journal of Magnetism and Magnetic Materials (JMMM)*, Vol. 269, No. 1 (February 2004), pp. 30-37, ISSN 0304-8853.
- Knott, E.; Shaeffer, J.; Tulley, M. (2004). *Radar Cross Section* (2nd edition), SciTech Publishing, ISBN-10: 1891121251, ISBN-13: 978-1891121258, New York, NY, USA.
- Korolev, K.A.; Chen, S. & Asfar, M.N. (2008). Complex Magnetic Permeability and Dielectric Permittivity of Ferrites in Millimeter Waves, *IEEE Transactions on Magnetics*, Vol. 44, No. 4 (April 2008), pp. 435-437, ISSN 0018-9464.
- Lagarkov, A.N. & Sarychev, A.K. (1996). Electromagnetic Properties of Composites Containing Elongated Conducting Inclusions. *Physical Review B*, Vol. 53, No. 10 (March 1996), pp. 6318- 6336, ISSN 1098-0121.
- Landau, L.D. & Lifshitz, E.M. (1960). *Electrodynamics of Continuous Media: Landau and Lifshitz Course of Theoretical Physics*, Vol. 8, ISBN 0080091059. Pergamon Press, Addison-Wesley, Oxford, UK.
- Landauer, R. (1978), Electrical Conductivity in Inhomogeneous Media, *Electrical Transport and Optical Properties of Inhomogeneous Media*, AIP Conference Proceedings, Vol. 40, No. 1 (April 1978), pp. 2-45.
- Lax, B. & Button, K.J. (1962). *Microwave Ferrites and Ferrimagnetics*, McGraw-Hill, ASIN B000K6650I, New York, San Francisco, Toronto, London.
- Ledieu M. & Acher, O. (2003). New Achievements in High-frequency Permeability Measurements of Magnetic Materials, *Journal of Magnetism and Magnetic Materials (JMMM)*, Vol. 258-259 (March 2003), pp. 144-150, ISSN 0304-8853, Elsevier.
- Levy, O. & Stroud, D. (1997). Maxwell Garnett Theory for Mixtures of Anisotropic Inclusions: Application to Conducting Polymers. *Physical Review B: Condensed Matter and Materials Physics*, Vol. 56, No. 13 (October 1997), pp. 8035-8046, ISSN 1098-0121.
- Lisjak, D.; Bregar, V.B.; Znizarsic, A. & Drofenik, M. (2006). Microwave Behaviour of Ferrite Composites. *Journal of Optoelectronics and Advanced Materials*, Vol. 8, No. 1 (February 2006), 60-65, ISSN 1454-4164.
- Liu, Y., Silmyer, D.J. & Shindo, D. (2006). *Handbook of Advanced Magnetic Materials. Vol. 1: Nanostructural Effects*, ISBN-10: 1-4020-7983-4; ISBN-13: 978-1402-07983-2, Springer.
- Looyenga, H. (1965), Dielectric Constants of Heterogeneous Mixtures. *Physica*, Vol. 31, No. 3 (March 1965), pp. 401-406, Elsevier/North-Holland, Netherlands.
- Lucarini, V.; Saarinen, J.J.; Peiponen, K.-E. & Vartiainen, E.M. (2005). *Kramers-Kronig Relations in Optical Materials Research*. Springer Series in Optical Sciences 110

- (2005), Springer-Verlag, Berlin, Heidelberg, Germany, ISSN 0342-4111, ISBN-10: 3-540-23673-2, ISBN-13: 978-3-540-23673-2.
- McLachlan, D. S., Blaszkiewicz, M. & Newnham, R. E. (1990), Electrical Resistivity of Composites. *Journal of the American Ceramic Society*, Vol. 73, No. 8 (August 1990), pp. 2187-2203, ISSN 0002-7820.
- Maxwell Garnett, J.C. (1904). Colours in Metal Glasses and Metallic Films. *Philosophical Transactions of Royal Society of London, Series A, Containing Papers of a Mathematical of Physical Character*, Vol. 203 (January 1904), pp. 385-420, The Royal Society, London, UK, ISSN 02643952.
- Maxwell Garnett, J.C. (1906). Colours in Metal Glasses, in Metallic Films, and in Metallic Solutions - II. *Philosophical Transactions of Royal Society of London, Series A, Containing Papers of a Mathematical of Physical Character*, Vol. 205 (August 1906), pp. 237-288, The Royal Society, London, UK, ISSN 02643952.
- Merrill, W.M., Diaz, R.E., LoRe, M.M., Squires, M.C. & Alexopoulos, N.G. (1999). Effective Medium Theories for Artificial Materials Composed of Multiple Sizes of Spherical Inclusions in a Host Continuum, *IEEE Transactions on Antennas and Propagation*, Vol. 47, No. 1 (January 1999), pp. 142-148, ISSN 0018-926X.
- Mikhailovsky, L.K., Pollak, B.P., Balakov, V.F. & Hanamirov, A.E. (1965). Properties and Application of Magneto-Uniaxial Ferrites at Millimeter Waves, *Radiotekhnika i Elektronika (Radio Engineering and Electronics)*, Vol. 10, No. 10, October 1965), pp. 1739-1752, ISSN 0033-8494, Moscow, Russia (in Russian).
- Milton, G.W. (2001). *The Theory of Composites* (1st edition), ISBN-10: 0521781256, ISBN-13: 978-0-521-781251-6, Cambridge University Press, UK.
- Miyasaka, K., Watanabe, K., Jojima, E., Aida, H., Sumita, M. & Ishikawa, K. (1982). Electrical Conductivity of Carbon-polymer Composites as Function of Carbon Content, *Journal of Materials Science*, Vol. 17, No. 6 (June 1982), pp. 1610-1616, ISSN 0022-2461, Springer.
- Mullen, E.B. & Carlson E.R. (1956). Permeability Tensor Values from Waveguide Measurements, *Proceedings of the Institute of Radio Engineers*, Vol. 44, No. 10 (October 1956), pp. 1318-1323, 0096-8390.
- Musil, J. & Zacek, F. (1986). *Microwave Measurements of Complex Permittivity and Permeability by Free Space Methods and their Applications*, Elsevier, Amsterdam, ISBN-10: 0444995366, ISBN-13: 978-0444995360.
- Musal, H.M., Jr.; Hahn, H.T. & Bush, G.G. (1988). Validation of Mixture Equations for Dielectric-Magnetic Composites, *Journal of Applied Physics*, Vol. 63, No. 8 (April 1988) pp. 3768-3770, ISSN 0021-8979.
- Naito, Y. & Suetake, K. (1971). Application of Ferrite to Electromagnetic Wave Absorber and its Characterization. *IEEE Transactions on Microwave Theory and Techniques*, Vol. 19 (January 1971), 65-72, ISSN 0018-9480.
- Neelakanta, P.S. (1995). *Handbook of Electromagnetic Materials: Monolithic and Composite Versions and their Applications*, CRC Press, ISBN 0-8493-2500-5, Boca Raton, Florida.

- Nicholson, A.M. & Ross, G.F. (1970). Measurement of the Intrinsic Properties of Materials by Time-domain Techniques, *IEEE Trans. on Instrumentation and Measurements*, Vol. 19, No. 4 (Nov. 1970), pp. 377-382, ISSN 0018-9456.
- Odelevsky, V.I. (1951), Calculation of Generalized Conductivity of Heterogeneous Systems, *Zhurnal Tekhnicheskoi Fiziki (Journal of Technical Physics)*, Vol. 21, No. 6 (June 1951), pp. 667-685 (in Russian).
- Osipov, A.V.; Rozanov, K.N.; Simonov, N.A. & Starostenko, S.N. (2002). Reconstruction of Intrinsic Parameters of a Composite from the Measured Frequency Dependence of Permeability, *Journal of Physics: Condensed Matter*, Vol. 14, No. 41 (October 2002), pp. 9507-9523, ISSN 0953-8984.
- Ota, H.; Kimura, M.; Sato, R.; Okayama, K.; Kondo, S.; and Homma, M. (1999). *Proceedings of IEEE International Symposium on Electromagnetic Compatibility*, pp. 590-593, ISBN 0-7803-5057-X, Seattle, WA, USA, August 2-6, 1999.
- Park, M.-J.; Choi, J. & Kim, S.-S. (2000). Wide Bandwidth Pyramidal Absorbers of Granular Ferrite and Carbonyl Iron Powders. *IEEE Transactions on Magnetics*, Vol. 36, No. 5, September 2000, 3272-3274, ISSN 0018-9464.
- Paul, C.R. (2006). *Introduction to Electromagnetic Compatibility* (2nd edition), Wiley-Interscience, ISBN-10: 0471755001, ISBN-13: 978-0471755005, Hoboken, NJ, USA.
- Polder, D. (1950). Ferrite Materials. *Proceedings of the IEE – Institution of Electrical Engineers, Part II: Power Engineering*, Vol. 97, No. 56 (April 1950), pp. 246-256.
- Polder, D. & van Santen, J.H. (1946), The Effective Permeability of Mixtures of Solids, *Physica*, Vol. 12, No. 5 (August 1946), pp. 257-271.
- Rado, G.T. (1953). Magnetic Spectra of Ferrites. *Reviews of Modern Physics*, Vol. 25, No. 1 (January 1953), pp. 81-89, ISSN 0034-6861.
- Roussy, G.; Chaabane, H. & Esteban, H. (2004). Permittivity and Permeability Measurement of Microwave Packaging Materials, *IEEE Transactions on Microwave Theory and Techniques*, Vol. 52, No. 3 (March 2004), pp. 903-907, ISSN 0018-9480.
- Rozanov, K.N.; Osipov, A.V.; Petrov, D.A.; Starostenko, S.N. & Yelsukov, E.P. (2009). The Effect of Shape Distribution of Inclusions on the Frequency Dependence of Permeability in Composites, *Journal of Magnetism and Magnetic Materials*, Vol. 321 (November 2009), pp. 738-741, ISSN 0304-8853, Elsevier.
- Sheng, P. (1980). Pair-cluster Theory for the Dielectric Constant of Composite Media. *Physical Review B: Condensed Matter and Materials Physics*, Vol. 22, No. 12 (December 1980), pp. 6364-6368, ISSN 1098-0121, The American Physical Society.
- Shin, J.Y. & Oh, J.H. (1993), The Microwave Absorbing Phenomena of Ferrite Microwave Absorbers, *IEEE Transactions on Magnetics*, Vol. 29, No. 6 (November 1993), 3437-3439, ISSN 0018-9464.
- Sichel, E.K. (1982). *Carbon Black-Polymer Composites: The Physics of Electrically Conducting Composites (Plastics Engineering)*, Marcel Dekker Inc, ISBN-10: 0824716736, ISBN-13: 978-0824716738, New York, New York, USA.
- Sihvola, A. (1999). *Electromagnetic Mixing Formulas and Applications*, IEE Electromagnetic Waves Series 47, The Institution of Electrical Engineers, ISBN 0-85296-772-1, London, UK.

- Snoek, J.L. (1948), Dispersion and Absorption in Magnetic Ferrites at Frequencies Above One Mc/s, *Physica*, Vol. 14, No. 4 (May 1948), pp. 207-217, Amsterdam, Netherlands.
- Stroud, D.; Milton, G.W. & De, B.R. (1986). Dielectric Response of Brine-Saturated Porous Rocks, *Physical Review B: Condensed Matter and Materials Physics*, Vol. 34, No. 8 (October 1986), pp. 5145-5153, ISSN 1098-0121, The American Physical Society.
- Tretyakov, S. (2003). *Analytical Modeling in Applied Electromagnetics*, Artech House, ISBN 1-58053-367-1, Norwood, MA, USA.
- Tsutaoka, T. (2003). Frequency Dispersion of Complex Permeability in Mn-Zn and Ni-Zn Spinel Ferrites and Their Composite Materials, *Journal of Applied Physics*, Vol. 93, No. 5 (March, 2003), pp. 2789-2796, ISSN 0021-8979.
- Taya, M. (2005). *Electronic Composites*, Cambridge University Press, ISBN 0-521-84174-7, Cambridge, UK.
- Von Hippel, A.R. (1995). *Dielectric Materials and Applications*, Artech House, ISBN-10: 1-58053-1229, Boston, MA, USA.
- Wang, Y. & X. Jing (2005). Intrinsically Conducting Polymers for Electromagnetic Interference Shielding, *Polymers for Advanced Technologies*, Vol. 16, 2005, pp. 344-351, Wiley, ISSN 1042-7147.
- Wang, S.J.; Niu, M.D. & Xu, D.M. (1998). A Frequency-varying Method for Simultaneous Measurement of Complex Permittivity and Permeability with an Open-Ended Coaxial Probe, *IEEE Transactions on Microwave Theory and Techniques*, Vol. 46, No. 12 (December 1998), pp. 2145-2147, ISSN 0018-9480.
- Weir, W. (1974). Automated Measurement of Complex Dielectric Constant and Permeability at Microwave Frequencies, *Proceedings of IEEE*, Vol. 62, No. 1 (January 1974), pp. 33-36.
- Zheng, H.M. & Smith, C.E. (1991). Permittivity Measurements Using a Short Open-Ended Coaxial Line Probe, *IEEE Microwave and Guided Wave Letters*, Vol. 1, No. 11 (November 1991), pp. 337-339, ISSN 1051-8207.

Radioactivity Control of Composite Materials Using Low Energy Photon Radiation

Konstantinos N. Athanassiadis

Alexander Technological and Educational Institute of Thessaloniki

Department of Automation, Laboratory of Metrology

Greece

1. Introduction

Composite materials (CM), often shortened to **composites**, are engineered materials made from two or more constituent materials functioning as matrix and reinforcement (Hull and Clyne 1996; Milton 2001; Strong 2007; Chung 2010). A composite material is characterized by a complex structure. Composite Materials are successfully used in various sectors of science (naval, aerospace, automotive industry and technology), replacing traditional materials such as timbers, metals and ceramic (Carlsson, Donald F. Adams et al. 2002; Strong 2007; Chung 2010). This is due to their unique attributes, such as non-existence of erosion, rust and also the fact that they demonstrate great resistibility in high temperatures. All the advantages mentioned before have made CM popular in industrial applications.

The continuously wider use of Composite Materials (CM) in various sectors of human activities imposes the growth of new methods and the construction of new appliances in order to study their physical and chemical attributes, such as density and effective atomic number, in high temperatures. The effective atomic number Z_{eff} and the density ρ are among the parameters which characterize the technological, and exploitation attributes of materials and their derivatives (Plotnikov and Pschenicniji 1973; Chudakov and Anshakov 1982; Celi 1992; Athanassiadis 1994).

Existing instruments for measuring and control of the physical and chemical properties of CM, the parameters of the technological processes don't satisfy fully the needs of research institutions and industrial enterprises. In many industrial enterprises definition of density of various materials during production is inherently confusing. The problem is particularly pronounced in developing and manufacturing of composite materials for which the density is one of the most important characteristics, directly or indirectly defines the quality composites and products from them.

The effective atomic number Z_{eff} and density ρ , parameters that play fundamental role in the behavior of materials under high temperatures are determined with the State-of-the-art techniques. These techniques determine these quantities by the average value in the total volume of the measured sample and in particular, statically after the effect of high temperature (Chudakov and Anshakov 1982).

Thus, it is expected that the creation of methods for no-contact, non-destructive control of Z_{eff} and density ρ of local parts of the material samples will allow the clarification of the

physical and mathematical models of degradation of the composite materials under conditions of high temperatures. In addition, it will assist in the improvement of the technical characteristics of parts and elements of CM, due to utilization under conditions of high temperature (up to 3000 K), and make the better possible selection of the material based on its thermal and physical properties, at the stage of product creation (Celi 1992; Athanassiadis 1994).

Radioisotope methods and appliances constitute effective means of non-destructive testing – NDT of many CM attributes. Particular characteristics, like the no-contact measurements, the high productivity, the conformity, and the relatively simple instrumentation needed, have extended the use of methods based on photon radiation transmission to the radioactive control of materials (Athanassiadis 1994). Use of low-energy sources of ionizing radiation (with an energy $E_\gamma < 100$ keV) is appropriate to improve the measurement sensitivity in controlling light environments with low thickness sensed layer (Chudakov and Anshakov 1982). Although in this case we need to take into account variations of element composition of samples.

Radiation γ -methods have comparative simplicity of implementation while providing satisfactory direction of monochromatic radiant flux. Selecting composition and energy radiation can ensure the prevalence of that kind of interaction, which contributes to maximizing information about controlled sample (Athanassiadis 1994). Depending on the effects of interaction of γ -quant with matter and scattering geometry there are resonance and non-resonance absorption methods of scattered radiation, as well as combined methods of γ -control (multi-beam methods) (Athanassiadis, Anshakov et al. 1993; Athanassiadis 2007; Athanassiadis, Chudakov et al. 2008).

2. Theory

2.1 Mass attenuation coefficient (MAC)

Mass attenuation coefficient serves as a measure of absorbing properties of the matter, characterized the interaction γ -rays with substance, and depends on its element composition and energy photons. In other words MAC is a measurement of how strongly a substance absorbs the radiation. Is a measure of the average number of interactions between incident photons and matter that occur in a given mass-per-unit area thickness of material encountered (Hubbell 1982).

A narrow beam of mono-energetic photons is attenuated to an intensity I from an incident intensity I_0 in passing through a layer of material with thickness x according to the exponential absorption law (Hubbell 1982) or Lambert–Beer law:

$$I_{(x)} = I_0 e^{-\mu \rho x} \quad (1)$$

where:

μ – mass attenuation coefficient (MAC),

ρ – density of the material of thickness x

Equation (1) can be rewritten as:

$$\mu = \frac{\ln(I_{(x)} / I_0)}{-\rho x} \quad (2)$$

For materials composed of multi elements the total MAC- μ is the sum of the μ_i values of each constituent element by the following mixture rule (Han, Demir et al. 2009):

$$\bar{\mu} = \sum c_i \bar{\mu}_i \quad (3)$$

where:

c_i - is the concentration of individual chemical element in the sample or in other words is the proportion by weight and $\bar{\mu}_i$ is mass attenuation coefficient of the i -th element.

For materials composed of multi elements, the fraction by weight is given by (Hubbell 1982; Gigante, Pedraza et al. 1985)

$$\mu = m_A \sigma, \quad m_A = \frac{\rho Z N_A}{A} \quad (4)$$

where:

σ - the total atomic cross section, N_A - is the Avogadro's number, Z - the atomic number and A - the atomic number of element.

Considering three main mechanisms of interaction, mass attenuation coefficient μ of low energy γ -radiation in matter is the sum of (Perumallu, Rao et al. 1985; Bhandal and Singh 1993; Manohara and Hanagodimath 2007)

$$\mu = \mu_{phot} + \mu_{Coh} + \mu_{Com} \quad (5)$$

where:

μ_{phot} - mass attenuation coefficient for photo effect;

μ_{Coh} , μ_{Com} - coefficients for coherent and Compton attenuations, respectively.

2.2 Effective atomic number, Z_{eff}

The atomic number, Z , is a ubiquitous parameter in atomic and nuclear physics where it occurs in almost any formula. In Composites Materials for photon interactions, the atomic number cannot be represented uniquely across the entire energy region, as in the case of elements, by a single number. For CM this number is called "effective atomic number" - Z_{eff} , and it varies with energy (İçelli, Erzeneoglu et al. 2005; Manohara, Hanagodimath et al. 2008). Z_{eff} has a physical meaning and allows many characteristics of a material to be visualized with a number (Singh, Kaur et al. 1996). This number is a very useful parameter for technology, and in many fields of scientific applications. In such applications the concept of effective atomic numbers Z_{eff} is introduced to describe the properties of these composite materials in terms of an equivalent element (İçelli, Erzeneoglu et al. 2005). The Z_{eff} is a convenient parameter for representing the attenuation of γ -rays in a complex medium and particularly in CM (Han, Demir et al. 2009). Higher values ($Z_{eff} > 20$) correspond to inorganic compounds and metals, and lower values ($Z_{eff} < 10$) correspond to organic substances. Analysis of Z_{eff} is of a great importance for geological studies of ore and mineral composition, searching for new sources of fossil fuels, structure monitoring of composite materials, separate diagnostics of soft and bone tissues, determination of calcium content in tests for osteoporosis, etc. Study of Z_{eff} provides conclusive information about the target with which the radiation interacts (El-Kateb, Rizk et al. 2000). Z_{eff} can be determined also from the plots of atomic cross-sections versus atomic numbers of the individual elements (Mudahar, Singh et al. 1991; Parthasaradhi, Esposito et al. 1992).

The effective atomic number of a composite sample is equal (Duvauchelle, Peix et al. 1999) with the sum of equation (6). It should be mentioned, however, that the theoretical determination of Z_{eff} does not always coincide with the experimental results (Manninen, Pitkänen et al. 1984; Duvauchelle, Peix et al. 1999; Manohara, Hanagodimath et al. 2008).

$$Z_{eff} = \sum_i a_i^{at} Z_i \quad (6)$$

where:

$$a_i^{at} = \frac{m_i / A_i}{\sum_{i=1}^n m_i / A_i} - \text{is the gram mole fraction that is defined by the per cent of mass } m_i \text{ and}$$

the atomic mass A_i of i element.

2.3 Density measurements

γ -radiation, as mentioned, is fast, low cost, nondestructive, and easily automated. The principle used to measure density with γ -radiation is simply to pass radiation through a material attenuating the radiation, in this case gamma particles. This principle is described by the Lambert-Beer law in eq. (1) (Tiitta, Olkkonen et al. 1996)

$$I_{(x)} = I_0 e^{-\mu \rho x} \quad (1)$$

where:

$I_{(x)}$ = radiation intensity after attenuation (counts/s.)

I_0 = unattenuated radiation intensity (counts/s.)

μ = mass attenuation coefficient (cm²/g)

ρ = density (g/cm³)

x = absorber thickness (cm)

With known values of μ and x , and acknowledging the existence of some amount of background radiation, I_n , Equation (1) may be rearranged as (Tiitta, Olkkonen et al. 1996; Athanassiadis 2009)

$$\rho = \frac{\ln \left[\frac{I_0 - I_n}{I_{(x)} - I_n} \right]}{-\mu x} \quad (7)$$

The weakening of radiation depends on the thickness of a γ -rayed object and is also connected with the density of examined materials. Registering the interaction of low-energy γ -radiation with CM, we can get information about its structure and physical and chemical characteristics. Selecting composition and energy of radiation we can ensure the dominance of a particular type of interaction, to maximize the taken information of the controlled object.

Knowing the MAC of each element and element composition of analyzing object from the measured values of I and I_0 , we can determine the surface density P of object (Athanassiadis 1994):

$$P = \rho l = \frac{1}{\mu_{eff}} \ln(I_0 / I) \quad (8)$$

The knowledge of natural minerals' physical parameters such as the mass attenuation coefficients M , the effective atomic number Z_{eff} is useful for understanding their physical properties. (Han, Demir et al. 2009).

It is important for densitometry of CM (Chudakov and Anshakov 1982), to define the effective parameters of γ -radiation interaction with samples of complex chemical composition. (Plotnikov and Pschenicniji 1973) proposed replacement parameters conditionally substance consisting of one element, and use expressions:

$$\frac{\rho_{eff} A_0}{A_{eff}} \psi(Z_{eff}, E) = \rho A_0 \sum_i \frac{q_i}{A_i} \psi(Z_i, E) \quad (9)$$

where q_i – content of i -th-element

$\psi(Z_{eff}, E)$ – It is accordingly:

$d\sigma^{Phot}(Z_{eff}, E)$ – for a photo effect

$d\sigma^{Coh}(Z_{eff}, E)$ – for coherent scattering and

$d\sigma^{Com}(Z_{eff}, E)$ – for Compton scattering

In the case of incoherent scattering (Plotnikov and Pschenicniji 1973):

$$Z_{eff} = \sqrt[3]{\sum_i q_i Z_i^3} \quad (10)$$

and for coherent scattering (Plotnikov and Pschenicniji 1973):

$$Z_{eff} = \sqrt{\sum_i q_i Z_i^2} \quad (11)$$

3. Non-resonance methods

3.1 Single beam γ -method

The determination of the samples density from the registration system is based on the measurement of γ -radiation beam's intensity attenuation. The beam is transmitted from a constant thickness sample. In collimated beam geometry, the intensity of γ -ray beam is given by the exponential law Eq. (1). Consequently, the density of CM is given by the relation, for samples with known values of μ and x .

$$\rho = \frac{1}{\mu x} \ln(I_0/I) \quad (12)$$

A typical set up of the radioisotope systems to study the low energy γ -rays that transmitted through CM is given in Figure 1.

The γ -ray coming from a source S is registered by the detector D. Collimator K1 is outside of detector. Inside the detector's main body, the collimator K2, the scintillator of NaI(Tl) crystal, the photomultiplier (PMT) and the electronic block are being placed. The electronic block of radiometric data processing information, separates the informative pulses from the signal of the detector's exit. Furthermore, it stabilizes the energy scale of the signals converter and measures the pulses containing information, on a given duration time. Finally, measurements' results are presented on the PC's screen.

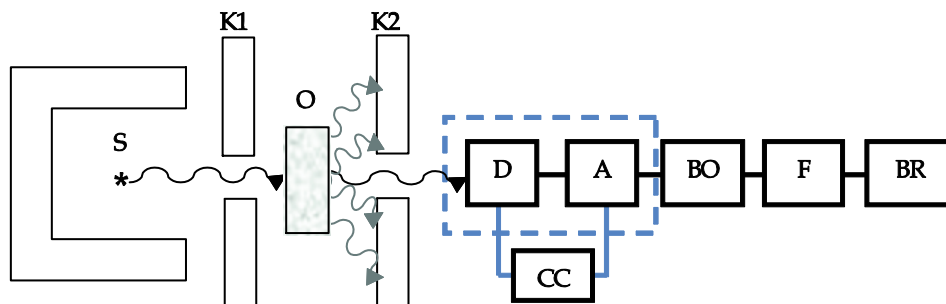


Fig. 1. A common block diagram of the single beam radioisotope measuring schemes

Ratio and system characteristics of collimators K1 and K2 or their absence, determines the required geometry measurements, which depends on the task and provides the most additive signal on detectors output of parameters variation of the sample.

The detector is meant to realize the required measurement geometry. Additionally, it is used to achieve the registration of γ -quanta, which are transmitted from the absorber. The radiation source and the detector have been placed in specific positions in order to ensure personnel's safety. Furthermore, placing the radiation source and the detector in those positions provides the essential collimated geometry.

Density (volume density) ρ is for an object with a known thickness. In technical annexes Single beam γ -method (SBGM) received adequate development (Chudakov and Anshakov 1982; Athanassiadis 1994). SBGM in static measurements are relatively simple in his mathematical description. Single-beam γ -method is appropriate to apply when the sample thickness is $x < 200$ mm (Chudakov and Anshakov 1982). Optimal thickness of layer sample must, estimated on criterion of minimal statistical errors at a fixed measurement time, satisfy the condition (Chudakov and Anshakov 1982; Celi 1992):

$$l = \frac{2}{\mu P} \quad (13)$$

where:

μ – is the MAC and

$P = \rho \cdot l$ – is the surface density of a sample of thickness l and volume density ρ

(Chudakov and Anshakov 1982; Celi 1992) concludes that SBGM allows us to control a change of surface density $P = \rho \cdot l$ in the direction of the heat axis. The conclusion is based on the fact that for the control of homogeneous flat samples of CM which have been high heated from one side and as a result of that heating affected changes in all three characteristics (μ , ρ , l) that are responsible for transmission of γ -rays from an object, while the homogeneity of μ and ρ distribution characteristics is disturb in the direction of the heat. At the same time in the field of $E_\gamma > 100$ keV of CM MAC does not depend of elemental composition. We assume that decomposition of CM impact only, on reducing its density while maintaining or slight change the thickness of sample.

(Chudakov and Anshakov 1982) report that by making use of γ -densitometry methods along with the use of a single beam's radiation technology, the researcher is allowed to check the surface density's change in the address of light's combustion of Composite Materials (CM). This is due to γ -densitometry methods' great simplicity. It holds true that the CM suffers high temperature effects. The development of a system providing the

possibility to dynamically control the measurement, allows the researcher to acquire data concerning the speed of mass' loss in the unit of his heated surface. Furthermore, it offers the change to registrate the internal sample's change of density and to construct its' "behavioral" profile (Athanassiadis, Chudakov et al. 2008).

3.2 Determination of the effective atomic number Z_{eff} for composites materials

3.2.1 Theoretical aspects

The effective atomic number Z_{eff} and the density ρ are among the parameters which characterize the technological, and exploitation attributes of materials and their derivatives. Particular characteristics, like the no-contact measurements, the high productivity, the conformity, and the relatively simple instrumentation needed, have extended the use of methods based on photon radiation transmission to the radioactive control of materials (Athanassiadis 1994).

The creation of methods for no-contact, non destructive control of Z_{eff} and density ρ of localized areas of the material samples will allow the clarification of the physical and mathematical models of degradation of the composite materials under conditions of high temperatures. For the determination of Z_{eff} it is necessary to use detectors with high energy resolution, due to the need to distinguish between spectrum lines of coherent and incoherent scattering of γ -rays (Athanassiadis 2009).

The analysis of physical and chemical characteristics of materials via the determination of change in the effective atomic number Z_{eff} can be performed by measuring the ratio of elastically N_R (Rayleigh) to the in-elastically N_C (Compton) scattered γ -rays intensities.

The total effective atomic cross-section σ_R for Rayleigh scattering approximately is:

$$\sigma_R \cong c_1 \frac{Z^n}{E^m} \quad (14)$$

where:

c_1 – constant for the particular scattering angle;

Z – atomic number;

E – energy of incident photon;

n, m – certain constant numbers.

The effective atomic number and the other parameters are independent from energy (Perumallu, Rao et al. 1985). The values of numbers n, m depend from the type of process.

Total effective atomic cross-section σ_C for Compton scattering approximately is:

$$\sigma_C \cong c_2 \frac{Z}{E^m} \quad (15)$$

Dividing the total atomic cross-section σ_R for the Rayleigh scattering (14) with the total atomic cross-section σ_C for the Compton scattering relation (15) we have the relation between the scattering cross-sections that is (Manninen, Pitkänen et al. 1984):

$$\frac{\sigma_R}{\sigma_C} = c_3 Z^{n-1} \quad (16)$$

where c_3 is a constant for the particular photon energy.

The probability of the processes of coherent and inelastic scattering and their factors are related to the atomic form factor F and the function of inelastic scattering S .

The angle dependence for differential effective cross-section $d_a\sigma_R/d\Omega$ in the unit of solid angle can be calculated multiplying the distribution function for the classic Thompson scattering in the electron and the square of atomic form factor $F(X, Z)$, where X - the transfer momentum due to the change of trajectory of moved photon (Manninen, Pitkänen et al. 1984):

$$\frac{d_a\sigma_R}{d\Omega} = \frac{r_0^2}{2} (1 + \cos^2\theta) \cdot [F(X, Z)]^2 \quad (17)$$

r_0 - the classical radius of electron.

In the coherent scattering, the transfer of momentum in the atom or in electron is performed by the change of direction of trajectory of the moving photon without change of the magnitude of the photon momentum (Karellas, Leichter et al. 1983).

The function of angle distribution for the incoherent Compton scattering is defined by the Klein-Nishina relation multiplied by the incoherent function $S(X, Z)$ (Manninen, Pitkänen et al. 1984):

$$\frac{d_e\sigma_c}{d\Omega} = \frac{r_0^2}{2} \left[\frac{1}{1 + a(1 - \cos\theta)} \right]^2 \cdot \left[1 + \cos^2\theta + \frac{\alpha^2(1 - \cos\theta)^2}{1 + \alpha(1 - \cos\theta)} \right] \cdot S(X, Z) \quad (18)$$

Dividing (17) with (18), we obtain the relation between the cross-sections of coherent and Compton scattering as function of the photon energy, scattering angles and the scatterer's atomic number (Duvauchelle, Peix et al. 1999):

$$\frac{d_a\sigma_R/d\Omega}{d_e\sigma_c/d\Omega} = \frac{[1 + a(1 - \cos\theta)]^2 \cdot (1 + \cos^2\theta) \cdot [F(X, Z)]^2}{\left[1 + \cos^2\theta + \frac{\alpha^2(1 - \cos\theta)^2}{1 + \alpha(1 - \cos\theta)} \right] \cdot S(X, Z)} \quad (19)$$

This relation is important for the measurement of the atomic number with the method of Rayleigh and Compton scattering.

The exponential dependence of coherent to incoherent effective cross-sections scattering ratio from the Z^{n-1} is not obvious consequence of eq. (19), however it is expressed in functions $F(Z)$ and $S(Z)$ (Leichter, Karellas et al. 1985).

The values of index n depend on the value of the given scattering angle (the transfer of momentum during scattering is higher for larger values of the scattering angle). Thus, it is clear that the inner electrons, with higher binding energy, play a decisive role during the scattering process, while at lower energy levels only the outer electrons play a significant role.

More than 75% of scattering actions occur at angles smaller than the so-called "characteristic" angle:

$$\theta_0 = 2\arcsin \left[0,026 \cdot Z^{1/3} \left(\frac{m_0 c^2}{h\nu} \right) \right] \quad (20)$$

If an angle θ is smaller than the "characteristic" angle ($\theta < \theta_0$), then if the "characteristic" angle θ_0 approaches 0, the scattering ratio is proportional to Z^2 and does not depend on the energy E . It is important to note that the ratio σ_R/σ_C increases with increasing atomic number Z and decreasing energy E .

Taking the Thomas-Fermi approach into consideration, for the distribution of electron, the differential cross-section of the coherent scattering can be written as (Manninen, Pitkänen et al. 1984):

$$\frac{d\sigma_R}{d\Omega} = \left(\frac{d\sigma}{d\Omega} \right)_{Th} \cdot \frac{\pi Z^3}{2u^3} \quad (21)$$

$$\text{where: } u = a \frac{4\pi}{\lambda} \sin \frac{\theta}{2}, \alpha = \left(\frac{3}{32\pi^2} \right)^{2/3} \cdot \frac{h^2}{2mc^2}$$

In this approach the differential cross-section $d\sigma_R/d\Omega$ is proportional to Z^3 , however, this is only correct for scattering angles bigger than the characteristic angle (Manninen and Koikkalainen 1984; Leichter, Karellas et al. 1985).

Based on the angular frequencies of incident photons ω_1 and scattered photons ω_2^0 the Klein-Nishina formula is approximated by the relation (Manninen, Pitkänen et al. 1984; Perumallu, Rao et al. 1985):

$$\frac{d\sigma_{KN}}{d\Omega} = \left(\frac{d\sigma}{d\Omega} \right)_{Th} \cdot \left(\frac{\omega_2^0}{\omega_1} \right)^2 \quad (22)$$

and for the incoherent scattering:

$$\frac{d\sigma_C}{d\Omega} = \left(\frac{d\sigma}{d\Omega} \right)_{Th} \cdot \left(\frac{\omega_2^0}{\omega_1} \right)^2 \cdot Z \quad (23)$$

Assuming that the scattering angle is not smaller than:

$$\sin \frac{\theta}{2} \geq 20 \text{ nm}^{-1} \text{ or } \geq 2 \text{ \AA}^{-1} \quad (24)$$

Dividing (21) with (23):

$$\frac{d\sigma_R/d\Omega}{d\sigma_C/d\Omega} = kZ^2 \quad (25)$$

where k –numerical factor.

Equation (25) is acceptable only for specific values of energies $E \leq 100$ keV, scattering angles smaller than θ_0 and elements with $6 < Z < 83$ (Manninen, Pitkänen et al. 1984; Athanassiadis 1994).

From this relation, one can deduce the parabolic dependence of the Rayleigh to Compton scattering ratio (R/C) from the atomic number of the scatterer (Manninen and Koikkalainen 1984; Duvauchelle, Peix et al. 1999; Manohara, Hanagodimath et al. 2008; Athanassiadis 2009).

3.2.2 Method

The atomic number of a composite sample is equal (Duvauchelle, Peix et al. 1999) with the sum of equation (6). It should be mentioned, however, that the theoretical determination of Z_{eff} does not always coincide with the experimental results (Manninen, Pitkänen et al. 1984; Duvauchelle, Peix et al. 1999).

$$Z_{eff} = \sum_i a_i^{at} Z_i \quad (6)$$

where:

$a_i^{at} = \frac{m_i / A_i}{\sum_{i=1}^n m_i / A_i}$ - is the gram mole fraction that is defined by the per cent of mass m_i and the

atomic mass A_i of i element.

The dependence of the coherent and incoherent scattering ratio N_R/N_C of the γ -radiation beams on the atomic number Z of the element, the scattering angles and the energy E_γ of radiation in the sample, can be obtained from relation (26), (Karellas, Leichter et al. 1983; Manninen, Pitkänen et al. 1984; Perumallu, Rao et al. 1985; Duvauchelle, Peix et al. 1999).

$$\frac{N_R}{N_C} \cong \frac{\sigma_R}{\sigma_C} = \frac{C_1 Z_{eff}^n / E_\gamma}{C_2 Z_{eff} / E_\gamma} \Rightarrow \frac{N_R}{N_C} = C_3 Z_{eff}^{n-1} \quad (26)$$

where C_1 , C_2 and C_3 coefficients which are not varied for the particular energy.

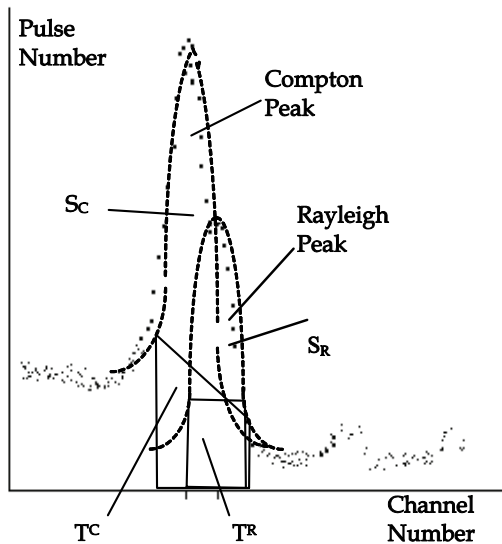


Fig. 2. Scattering Spectra for *Fe* obtained at scattering angle $\theta=75^\circ$

The theoretical determination of the values of coefficients is difficult due to the dependence of these coefficients on the model that describes the atomic shell. However, the experimental

determination of coefficients C_3 in equation (26) is straightforward. It is known (Karellas, Leichter et al. 1983; Manninen and Koikkalainen 1984; Gigante, Pedraza et al. 1985; Leichter, Karellas et al. 1985; Perumallu, Rao et al. 1985; Duvauchelle, Peix et al. 1999), that the value of exponent n for large scattering angles is: $n=3$.

The determination of Z_{eff} from the ratio N_R/N_C depends on the separation of the spectrum lines of the coherently and incoherently scattered γ -quanta. For the basic peaks of the spectrum lines of the coherent and incoherent scattering events, the variation of ratio N_R/N_C appears mainly at the distribution maximum and does not significantly influence the shape of the spectrum lines (Plotnikov and Pschenicniji 1973). However, the separation of the peaks of the spectrum lines of Rayleigh and Compton scattering is not always possible (Fig. 2). It is common to observe an overlap of the peaks. For this reason, various methods are employed for the determination of the area under the peak. This complication imposes the use of detectors with high energy resolution.

3.2.3 Other measurements

Measurements of the Rayleigh to Compton scattering ratio (Singh and et al. 2007) were used also for the evaluation of bone mineral contents and bone mineral density in a number of experimental investigations: (Puumalainen, Sikanen et al. 1979; Kerr and et al. 1980; Karellas, Leichter et al. 1983; Webster and Lillicrap 1985; Parthasaradhi, Esposito et al. 1992; Manohara and et al. 2008). These measurements have been made with radioactive sources at various scattering angles with samples of tissue or bone equivalent materials. (Speller and Horrocks 1991) and (Shakeshaft and et al. 1997) have introduced applications of this technique in the fields of medicine and biology. This technique has also been tested for some elements with atomic number satisfying, $26 \leq Z \leq 82$, by (Içelli and Erzeneoglu 2002) and (Içelli 2006).

Duvauchelle in (Duvauchelle, Peix et al. 1999; Duvauchelle, Peix et al. 2000) have concluded that the Rayleigh to Compton scattering intensity ratio depends only on the mixture under study and provides a non-destructive technique to measure the Z_{eff} of composite materials and the Z -number of unknown elements (Singh and et al. 2007). They suggested that a given Z_{eff} must define a mixture on the basis of the intensity ratio of Rayleigh to Compton scattering, as a single atom is characterized by its atomic number. This technique utilizes the strong dependence of the Rayleigh to Compton scattering intensity ratio on the effective atomic number of the scattering medium. One of the major advantages of this method is that by taking the ratio of the Rayleigh to Compton scattered photons, a number of parameters such as absolute source strength, solid angles subtended by source and the detector at the target are eliminated in the expression of the ratio technique, otherwise these parameters introduce a large amount of error in the measured results (Singh and et al. 2007).

4. Resonance methods

4.1 Theoretical aspects

In fig. 3. is shown a block diagram of Mossbauer-transmission and scattering experiments. Doppler shifted γ radiation is emitted from a source moving with a velocity v . A certain fraction of this radiation is absorbed resonantly in an absorber. The transmitted radiation is detected in a γ detector. The resonance absorption probability and thus the count rate in the detector depend on the relative velocity between the source and the absorber (Weyer 1981). By measuring the count rate at different velocities we can record a transmission spectrum.

For ideal source and absorber materials the lines in the transmission spectrum have approximately Lorentzian shapes for not too thick absorbers (Weyer 1981).

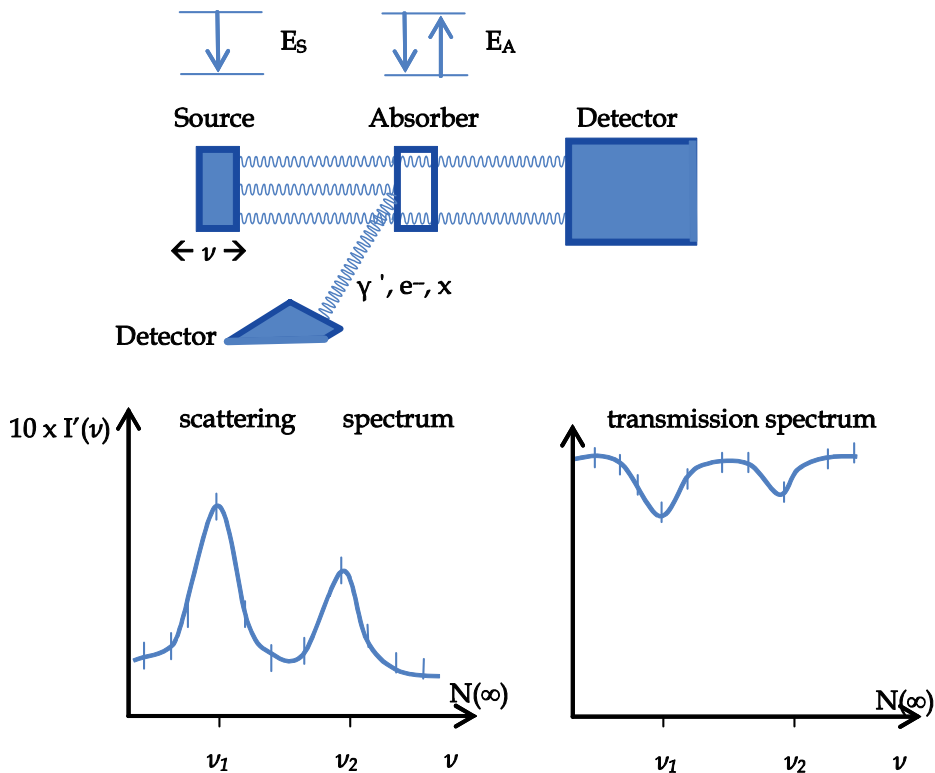


Fig. 3. Schematic illustration of a scattering and a transmission Mossbauer experiment

Mossbauer absorption spectroscopy or nuclear γ -Resonance method (NGR) in its most common form applies only to materials that contain resonance Mossbauer nucleus (such as Fe, Sn, Co) in the samples that we investigate, and this limits the usage field of the method. The problem concerning the study of physical and chemical attributes and processes in the CM and condensed matter is resolved with the method according to which the Rayleigh Scattering of Mossbauer Radiation (RSMR) is registered and in which Mossbauer radiation interacts with electrons of matter (Zolotoyabko and Iolin 1986; Mossop, Kerr et al. 1987).

4.2 Resonance detector

In 1963 Mitrofanov K.P. suggested a resonant detector which is sensitive only for recoilless gamma-quanta (Mitrofanov, Gor'kov et al. 1978). A resonant detector is a special instrument for Mossbauer spectroscopy whose principle of operation is also based on the Mossbauer Effect. The Scintillation Resonant Detector - SRD that are used in Mossbauer spectroscopy, are intended for the selective registration of resonance radiation and allows us to increase resolution and sensitivity and thus to expand the information potential of this method. The operation of resonant detectors is based on the registration of secondary radiation, primarily

secondary electrons (Belyaev, Volodin et al. 2010). In this type of detector, a resonant substance (a converter) is placed inside the working volume of the detector.

The principle of operation of SRD is illustrated in fig. 4 (Maltsev, Mehner et al. 2002). The resonant γ -quanta excite the nuclei of the grains of the resonant substance. In the case that the nucleus deexcites by emission of a conversion electron, this electron will excite along its path a number of atoms of the scintillator, which surrounds the resonant substance grain. The excited atoms of the scintillator produce photons. The photons produce photoelectrons in the photocathode of the photoelectronic multiplier tube.

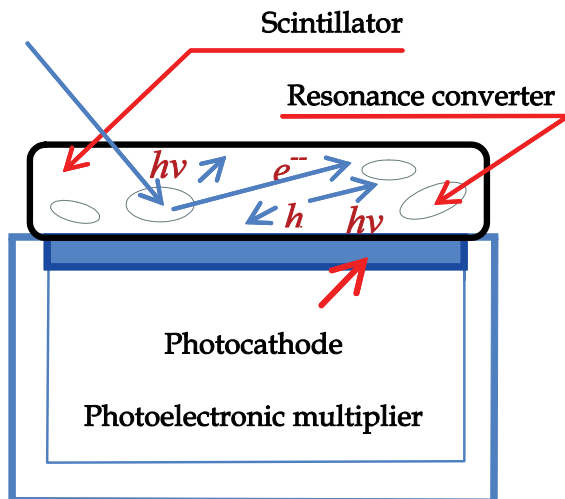


Fig. 4. Principle of operation of the Scintillation Resonance Detector - SRD

The recoilless resonant absorption of γ -rays is followed by a variety of deexcitation processes involving reemission of γ -ray, internal conversion electrons, Auger electrons and X-rays (Sawicki and Tyliczszak 1983). As a matter of fact, only the high-energy part of these deexcitation processes is utilized in Mossbauer scattering experiments, see (Bonchev, Jordanov et al. 1969; Liljequist 1981; Sawicki, Sawicka et al. 1991), whereas low-energy events represented by UV- and optical photons (Lichtenwalner, Guggenheim et al. 1976) or secondary electrons have hardly been investigated. (Sawicki and Tyliczszak 1983).

The method of resonance detection is based on the energy modulation, with moving absorber of Mossbauer radiation placed between the radioactive source (which is in resonance) and the resonance detector.

In γ -resonance spectroscopy with the use of SRD the source and the resonance detector create a resonance pair.

Basic characteristics of these pairs constitute:

- the selectivity,
- the efficiency of registration of recoilless γ -quanta,
- the permissible loading ability.

The selectivity is determined as the ratio of output of registration of γ -beams when $E = E_0$ and $E = \infty$, in case we have resonance and not, respectively. The SRD with plastic Scintillator ensure possibility of loading more than 10^6 cm^{-1} . The value of the resonant effect can be as

high as several hundred percent, when investigating the aftereffects of nuclear transformations in the emission mode (Belyaev, Volodin et al. 2010).

The substance inside the resonant detector must have (Belyaev, Volodin et al. 2010):

- a spectral absorption line width that is close to the natural width;
- a large value of the Lamb-Mössbauer factor (the f -factor);
- a large number of resonant atoms;
- a spectral line coinciding in the energy scale with the position of the source's spectral line. Even a small isomeric shift leads to distortion of the shape of the experimental spectrum with a loss of sensitivity and large isomeric shifts that considerably exceed the line width, leading to the disappearance of the effect.

Mössbauer spectroscopy represents one of the most informative methods for an investigation of a structure of the matter. It is well known that, an essential disadvantage of Mössbauer spectroscopy is a long time of the spectrum recording, usually of about 10 h in transmission geometry, and few tens of hours in the scattering geometry. The use of resonance detectors in Mössbauer spectroscopy allows a reliable determination of the non-resonant background level, which should be taken into account when the absolute value of the Mössbauer fraction (f) is needed. Simple formulae for finding the factors f from the areas of the experimental spectra have been derived in (Mitrofanov, Gor'kov et al. 1978). Also, the use of resonance detectors is promising way to increase a productivity of Mössbauer measurements (Mashlan, Kholmetskii et al. 2006).

4.3 Mössbauer spectrometer for the registration of rayleigh scattering of mossbauer radiation

The 75% of Rayleigh scattering actions is concentrated at angles smaller than the so-called "characteristic" angle (eq. 20) ($\theta \leq 16^\circ$) (Manninen and Koikkalainen 1984; Duvauchelle, Peix et al. 1999). More prospects for the registration of RSMR seem to have the Scintillation Resonance Detectors – SRD (Mitrofanov, Gor'kov et al. 1978; Athanassiadis 1994; Semenov, Irkaev et al. 1995), which allow us to register relatively very small changes in energy during the Doppler modulation of energy.

Therefore, the application of the RSMR method allows us to ignore the necessity of resonance nucleus existence in the samples such as to have the ability to investigate materials, free from Mössbauer resonance nucleus, with precision that is achieved with methods of NGR ($\sim 10^{-8}$ - 10^{-9} eV) (Zolotoyabko and Iolin 1986; Athanassiadis 1994).

The methods that are based on the registration of RSMR are characterized by the relatively low intensity of the beam of secondary radiation that carries the information. Therefore, use of radiation sources of big energy or bigger duration of measurement time, is required (Semenov, Irkaev et al. 1995). These restrictions can be overridden with the creation of new types of high sensitivity detectors, among which the Combined Scintillation Resonance Detectors are distinguished, that unify the positives of various types of scintillation detectors and allow us to avoid the difficulties of multi-detector systems, difficulties that are related to their problem of inter-stabilization (Athanassiadis, Chudakov et al. 2008).

The interest for the detection techniques of secondary radiation led to new methods and detection techniques of Mössbauer radiation with the construction of new types of detectors which have the ability of registering relatively minor changes in the energy of γ -beams.

The construction of the Mössbauer spectrometer for RSMR measurement in small angles requires the study of its basic metrological characteristics such as the determination of the discrimination velocity, the peak asymmetry and the area under peak.

For SRD with radioactive isotope ^{119}Sn , dioxide of tin (SnO_2) is used as converter. This converter satisfies the basic requirements for converters (to have good solubility in the scintillator, in order not to decrease transparency of scintillator and so that there would be no isomeric shift in the converters spectrum relative to the Mossbauer source spectrum). The registration efficiency of Mossbauer radiation from the source $^{119\text{m}}\text{SnO}_2$ is about 30% until 40%, while the registration efficiency of non-resonance radiation – is less than 1 %.

The spectrometer is based on the Combined Resonance Detector (Athanassiadis, Anshakov et al. 1993; Athanassiadis, Chudakov et al. 2008), which is constituted by the coaxial organic scintillation detector of 31 mm diameter and the inorganic one of CsI(Tl) of 10 mm diameter. The resonant scintillation detector consists of a thin organic film in the form of a ring, where the converter material is enriched by up to 90 % by dissolution of $^{119\text{m}}\text{Sn}$ Mossbauer isotope. The spectrometer includes the movement system with constant acceleration of Mossbauer source $^{119\text{m}}\text{Sn}$, the stabilization system of Combined Resonance Detector energy scale and the interface for the connection to computer PC. The system ensures the simultaneous accumulation and treatment of two spectra, which correspond in the registration of resonance radiation from the inorganic and organic scintillation detector. The signals division in the detectors' output from the two scintillators (organic and inorganic) is realized by the difference of scintillation time in the two scintillators (Athanassiadis, Anshakov et al. 1993).

For the study of CM which does not contain Mossbauer nucleus, was created an experimental system, constituted of the SRD and the automated Mossbauer spectrometer, which is given in fig. 5. The spectrometer's technical characteristics are given in table I.

The SRD measures the intensity of resonance γ - radiation which is scattered from the controlled sample. The scattered beam after its transmission from the sample was registered from resonance SRD (5). The SRD is sensitive to register only the coherent scattering of γ -radiation. The biggest of resonance absorption is observed with null velocity of γ -source movement.

The registration of Rayleigh scattering of Mossbauer Radiation (RSMR) allows a researcher to study the physical and chemical attributes along with the processes taking place inside the CM, which is free from Mossbauer resonance nucleus. This is accomplished with a remarkably high precision, by using methods of Nuclear Gamma Resonance ($\sim 10^{-8}$ - 10^{-9} eV).

The Combined Scintillation Resonance Detector CSRD is proposed for the determination of the density ρ , the effective atomic number Z_{eff} and other parameters that characterize the technological attributes of materials. These types of detectors are ideal for registering events that occur in adjacent points in space. The two scintillators are connected through the optical window with a photomultiplier.

Devices of this type are commonly known as "Phoswich detectors". The identification of the registration events in devices of this type depends on the difference between the conversion efficiency or/and the scintillations decay time constants of the scintillators that constitute the combined detector.

A phoswich detector is composed of several independent scintillation crystals coupled to a single photomultiplier tube. Generally, phoswich detectors are designed either for simultaneous detection of different radiation types or for minimizing the background radiation in a radiation field of interest. In both cases scintillation layers are considered to be a unique choice because of their relative sensitivity to the particular radiation type.

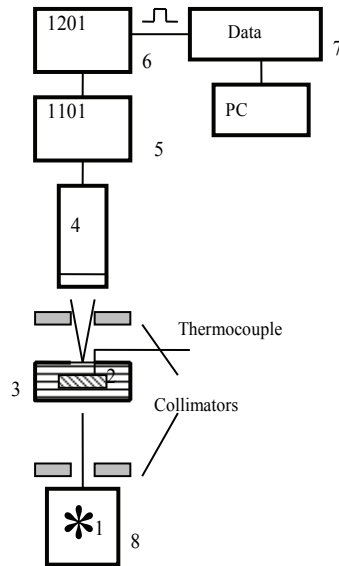


Fig. 5. Mossbauer spectrometer with Scintillation Resonant Detector

Time Stability for 24 hours of continuous work:	< 1 %
Scintillation time of NaI(Tl) scintillator:	$3 \cdot 10^{-9}$ sec
Scintillation time of Resonance scintillator:	$0.6 \cdot 10^{-6}$ sec
Amplitude ratio of Organic Resonance Scintillator to the inorganic NaI(Tl)	1 : 0.75
Discrimination Coefficient of Separation circuit:	$\sim 10^{-3}$
Peak amplitude resolution of the inner conversion electrons:	47 %
Activity of $^{119}\text{mSnO}_2$, Bq:	$8 \cdot 10^8$
Modulation Frequency, of γ -source motion system:	145 Hz

Table 1. Technical Characteristics of Small Angle Spectrometer of Rayleigh scattering of Mossbauer Radiation

Among other things, the scintillators are chosen to have different decay times so that the shape of the output pulse from the photomultiplier tube is dependent on the relative contribution of scintillation light from the two scintillators. The basic characteristics of the combined system are determined by the signals' separation efficiency.

5. Conclusion

By using γ - resonance and non-resonance methods for the radioactivity control of Composite Materials, we can determinate the effective atomic number Z_{eff} and density ρ . These parameters play fundamental role in the behavior of CM.

Making use of γ -densitometry methods along with the use of a single beam's radiation technology, the researcher is allowed to check the surface density's change in the address of light's combustion of Composite Materials (CM). This is due to γ -densitometry methods' great simplicity. It holds true that the CM suffers high temperature effects. The development of a system providing the possibility to dynamically control the measurement, allows the researcher to acquire data concerning the speed of mass' loss in the unit of his heated surface. Furthermore, it offers the change to registrate the internal sample's change of density and to construct its' "behavioral" profile.

These results prove the ability of the use of Mossbauer Effect, via measurements of intensity of Rayleigh scattering, for the study of dynamic physical processes in the condensed matter, which does not contain resonance nucleus, the determination of effective atomic number and the measurement of density in condensed matter (Chudakov and Anshakov 1982).

6. References

- Athanassiadis, K. N. (1994). Transmission methods for the radioactivity control of composite materials using low energy photon radiation. Faculty of Nuclear Physics and Electronics. Minsk, Belarussian State University. Ph.D. Thesis: p. 183.
- Athanassiadis, K. N. (2007). Metrological Characteristics of Small Angle Mossbauer Spectrometer for the Investigation of Condensed Matter. *Instrumentation and Measurement Technology Conference Proceedings*, 2007. IMTC 2007. IEEE.
- Athanassiadis, K. N. (2009). Determination of the effective atomic numbers of light composite materials. *Instrumentation and Measurement Technology Conference*, 2009. I2MTC '09. IEEE.
- Athanassiadis, K. N., O. M. Anshakov, et al. (1993). Combined Resonance Detection System. *Vestnik of Bellarussian State University Serial 1: Physics, Mathematics, Chemistry* (No 3): 31-34.
- Athanassiadis, K. N., A. V. Chudakov, et al. (2008). Automated Registration System of the Density Change at the Depth of Composite Materials, in High Temperature Conditions. *Instrumentation and Measurement Technology Conference Proceedings*, 2008. IMTC 2008. IEEE.
- Athanassiadis, K. N., V. A. Chudakov, et al. (2008). Radiometric Transmitter with Combined Resonance Scintillation Detection System. *Instrumentation and Measurement Technology Conference Proceedings*, 2008. IMTC 2008. IEEE.
- Belyaev, A. A., V. S. Volodin, et al. (2010). "Application of resonant detectors in Mössbauer spectroscopy. *Bulletin of the Russian Academy of Sciences: Physics* 74(3): 412-415.
- Bhandal, G. S. and K. Singh (1993). Study of the mass attenuation coefficients and effective atomic numbers in some multielement materials. *Applied Radiation and Isotopes* 44(6): 929-939.
- Bonchev, Z. W., A. Jordanov, et al. (1969). Method of analysis of thin surface layers by the Mössbauer effect. *Nuclear Instruments and Methods* 70(1): 36-40.

- Carlsson, L., Donald F. Adams, et al. (2002). *Experimental Characterization of Advanced Composite Materials*, CRC Press.
- Celi, J. C. (1992). Transmission gamma-methods of radio-isotope control with resonant detectors. Faculty of Nuclear Physics and Electronics. Minsk, Belarussian State University. PhD Thesis: p. 180.
- Chudakov, A. V. and M. O. Anshakov (1982). Radio-isotope Measurements of light matters density. Minsk, Belarussian State University.
- Chung, D. D. L. (2010). *Composite Materials: Science and Applications (Engineering Materials and Processes)*, Springer.
- Duvauchelle, P., G. Peix, et al. (1999). Effective atomic number in the Rayleigh to Compton scattering ratio. *Nuclear Instruments and Methods in Physics Research Section B: Beam Interactions with Materials and Atoms* 155(3): 221-228.
- Duvauchelle, P., G. Peix, et al. (2000). Rayleigh to Compton ratio computed tomography using synchrotron radiation. *NDT & E International* 33(1): 23-31.
- El-Kateb, A. H., R. A. M. Rizk, et al. (2000). Determination of atomic cross-sections and effective atomic numbers for some alloys. *Annals of Nuclear Energy* 27(14): 1333-1343.
- Gigante, G. E., L. J. Pedraza, et al. (1985). Analysis of metal alloys by Rayleigh to Compton ratios and X-ray fluorescence peaks in the 50 to 122 keV energy range. *Nuclear Instruments and Methods in Physics Research Section B: Beam Interactions with Materials and Atoms* 12(2): 229-234.
- Han, I., L. Demir, et al. (2009). Determination of mass attenuation coefficients, effective atomic and electron numbers for some natural minerals. *Radiation Physics and Chemistry* 78(9): 760-764.
- Hubbell, J. H. (1982). Photon mass attenuation and energy-absorption coefficients. *The International Journal of Applied Radiation and Isotopes* 33(11): 1269-1290.
- Hull, D. and T. W. Clyne (1996). *An Introduction to Composite Materials*, Cambridge University Press.
- Içelli, O. (2006). Practical method for experimental effective atomic number in the coherent to Compton scattering ratio. *Journal of Quantitative Spectroscopy and Radiative Transfer* 101(1): 151-158.
- Içelli, O. and S. Erzeneoglu (2002). Experimental study on ratios of coherent scattering to Compton scattering for elements with atomic numbers 26[less-than-or-equals, slant]82 in 59.5 keV for 55° and 115°. *Spectrochimica Acta Part B: Atomic Spectroscopy* 57(8): 1317-1323.
- Içelli, O., S. Erzeneoglu, et al. (2005). Effective atomic numbers for CoCuNi alloys using transmission experiments. *Journal of Quantitative Spectroscopy and Radiative Transfer* 91(4): 485-491.
- Karellas, A., I. Leichter, et al. (1983). Characterization of tissue via coherent-to-Compton scattering ratio: Sensitivity considerations. *Medical Physics* 10(5): 605-609.
- Kerr, S. A. and et al. (1980). Coherent scattering and the assessment of mineral concentration in trabecular bone. *Physics in Medicine and Biology* 25(6): 1037.
- Leichter, I., A. Karellas, et al. (1985). "Quantitative assessment of bone mineral by photon scattering: Calibration considerations. *Medical Physics* 12(4): 466-468.

- Lichtenwalner, C. P., H. J. Guggenheim, et al. (1976). Enhanced optical fluorescence by resonant Mössbauer excitation. *Physics Letters A* 56(2): 117-118.
- Liljequist, D. (1981). The analysis of natural ^{57}Fe abundance absorbers in conversion electron Mössbauer spectroscopy. *Nuclear Instruments and Methods* 179(3): 617-620.
- Maltsev, Y., H. Mehner, et al. (2002). Precision in Mössbauer spectroscopy. *Hyperfine Interactions* 139-140(1-4): 679-684.
- Manninen, S. and S. Koikkalainen (1984). Determination of the effective atomic number using elastic and inelastic scattering of $[\gamma]$ -rays. *The International Journal of Applied Radiation and Isotopes* 35(10): 965-968.
- Manninen, S., T. Pitkänen, et al. (1984). Study of the ratio of elastic to inelastic scattering of photons. *The International Journal of Applied Radiation and Isotopes* 35(2): 93-98.
- Manohara, S. R. and et al. (2008). Studies on effective atomic number, electron density and kerma for some fatty acids and carbohydrates. *Physics in Medicine and Biology* 53(20): N377.
- Manohara, S. R. and S. M. Hanagodimath (2007). Studies on effective atomic numbers and electron densities of essential amino acids in the energy range 1 keV-100 GeV. *Nuclear Instruments and Methods in Physics Research Section B: Beam Interactions with Materials and Atoms* 258(2): 321-328.
- Manohara, S. R., S. M. Hanagodimath, et al. (2008). On the effective atomic number and electron density: A comprehensive set of formulas for all types of materials and energies above 1 keV. *Nuclear Instruments and Methods in Physics Research Section B: Beam Interactions with Materials and Atoms* 266(18): 3906-3912.
- Mashlan, M., A. Kholmetskii, et al. (2006). Mössbauer spectrometer with resonant detector. *Nuclear Instruments and Methods in Physics Research Section B: Beam Interactions with Materials and Atoms* 243(1): 241-246.
- Milton, G. W. (2001). *The Theory of Composites*, Cambridge University Press.
- Mitrofanov, K. P., V. P. Gor'kov, et al. (1978). Determination of the Mössbauer effect probability using resonance detectors. *Nuclear Instruments and Methods* 155(3): 539-542.
- Mossop, J. R., S. A. Kerr, et al. (1987). The use of coherent gamma-ray scattering for the characterisation of materials. *Nuclear Instruments and Methods in Physics Research Section A: Accelerators, Spectrometers, Detectors and Associated Equipment* 255(1-2): 419-422.
- Mudahar, G. S., M. Singh, et al. (1991). Energy dependence of the effective atomic number of alloys. *International Journal of Radiation Applications and Instrumentation. Part A. Applied Radiation and Isotopes* 42(6): 509-512.
- Parthasaradhi, K., A. Esposito, et al. (1992). Photon attenuation coefficients in tissue equivalent compounds. *International Journal of Radiation Applications and Instrumentation. Part A. Applied Radiation and Isotopes* 43(12): 1481-1484.
- Perumallu, A., A. S. N. Rao, et al. (1985). Z-dependence of photon interactions in multi-element materials. *Physica B+C* 132(3): 388-394.
- Plotnikov, R. I. and G. A. Pschenicniji, Eds. (1973). *Fluorescence Röntgen-radiometric analysis* Moscow.

- Puumalainen, P., P. Sikanen, et al. (1979). Measurement of stable iodine content of tissue by coherently and Compton scattered photons. *Nuclear Instruments and Methods* 163(1): 261-263.
- Sawicki, J. A., B. D. Sawicka, et al. (1991). "Conversion electron Mössbauer spectroscopy of the 73.0 keV ^{193}Ir resonance. *Nuclear Instruments and Methods in Physics Research Section B: Beam Interactions with Materials and Atoms* 62(2): 253-258.
- Sawicki, J. A. and T. Tyliczszak (1983). Resonant emission of secondary electrons associated with recoilless nuclear absorption of gamma rays in solids. *Nuclear Instruments and Methods in Physics Research* 216(3): 501-504.
- Semenov, V. G., S. M. Irkaev, et al. (1995). Highly sensitive Mössbauer spectrometer for SEDM and RSMR investigations. *Nuclear Instruments and Methods in Physics Research Section B: Beam Interactions with Materials and Atoms* 95(2): 253-259.
- Shakeshaft, J. and et al. (1997). Gamma-ray scattering for fat fraction measurement. *Physics in Medicine and Biology* 42(7): 1403.
- Singh, K., R. Kaur, et al. (1996). Study of effective atomic numbers and mass attenuation coefficients in some compounds. *Radiation Physics and Chemistry* 47(4): 535-541.
- Singh, M. P. and et al. (2007). Measurement of the effective atomic number of composite materials using Rayleigh to Compton scattering of 279 keV gamma rays. *Physica Scripta* 76(4): 281.
- Speller, R. D. and J. A. Horrocks (1991). Photon scattering-a 'new' source of information in medicine and biology? *Physics in Medicine and Biology* 36(1): 1.
- Strong, A. B. (2007). Fundamentals of Composites Manufacturing: Materials, Methods and Applications, *Society of Manufacturing Engineers*.
- Tiitta, M., H. Olkkonen, et al. (1996). Veneer sheet density measurement by the ^{55}Fe gamma attenuation method. *European Journal of Wood and Wood Products* 54(2): 81-84.
- Webster, D. J. and S. C. Lillicrap (1985). Coherent-Compton scattering for the assessment of bone mineral content using heavily filtered X-ray beams. *Physics in Medicine and Biology* 30(6): 531.
- Weyer, G. (1981). Mössbauer resonance-scattering techniques for emission spectroscopy on gamma radiation from short-lived radioactive isotopes. *Nuclear Instruments and Methods in Physics Research* 186(1-2): 201-209.
- Zolotoyabko, E. V. and E. M. Iolin (1986). Coherent Rayleigh Scattering of Mössbauer Radiation. Riga, Zinatne Press.

Dynamic Responses of Composite Structures with Fluid-Structure Interaction

Young W. Kwon and Angela C. Owens

Naval Postgraduate School

USA

1. Introduction

As composite materials have been used for marine structures such as boats, ships, offshore structures, etc., the effect of FSI should be understood. In particular, FSI effect is expected to be significant for polymer composites because the water density is very comparable to the composites' densities. For example, the density of a carbon composite is approximately 50% greater than the water density. Sandwich composites consisting of very low densities of core materials have lower densities than that of water. As a result, the hydrodynamic mass associated with FSI would be very critical to composite structures under water. The growing use of composites in ship masts, superstructures, deck grates, piping, ducting, rudders, propellers, stacks, and various submarine structures requires extensive modeling and testing to help designers, builders and operators better understand composite response [Mouritz, et al., 2001].

These materials are subjected to a wide spectrum of loads during manufacturing and service life. Dynamic loadings, in particular, impact type event, represent a serious design concern for use of composite. Composite structures are more susceptible to impact damage than similar metallic structures which are more ductile in nature and can absorb typically large amounts of energy without failure. Furthermore, the damage in composites from impact can go undetected even when the mechanical properties may be drastically reduced from an impact. For these reasons, numerous experimental and analytical studies have been conducted to study the dynamic response of composites subjected to impact loading [Abrate, 1994; Aslan, et al., 2003; Kwon & Wojcik, 1998].

According to the review of past works, most of the research effort has been focused on low velocity impact damage, specifically, the damage predictions, and the evaluation and prediction of residual properties of damaged laminates. All of the research completed thus far has focused on damage in composites under impact loading in dry environments to support development of composites in aircraft structures.

As far as dynamic response of structures under water is concerned, a great deal amount of analytical and experimental studies have been conducted on the effect of fluid force on the natural frequencies, damping ratios and mode shapes of vibrating structures in contact with fluid. This is commonly known as the Fluid Structure Interaction (FSI) problem. FSI investigations have supported many problems in submarine signaling, offshore oil structure stability, and ship structure vibrations. Through these studies, many numerical and analytical methods have been developed in order to predict the added mass and the

resulting changes in natural frequency of a structure in contact with fluid. It has been determined and widely proven that the effect of fluid surrounding a structure decreases the natural frequency of a structure due to the increase in total kinetic energy of the vibrating structure and fluid from the addition of kinetic energy of the fluid. This effect can be interpreted as an added mass to the vibrating structure in the analysis of the dynamic response. Essentially as the structure vibrates, its mass is increased by the mass of the vibrating fluid with which it is in contact, consequently decreasing its natural frequency. Studies of fluid structure interaction and the added mass effect, also known as virtual mass effect, hydrodynamic mass, and hydroelastic vibration of structures, started with Lamb [Lamb, 1921] who calculated the first bending mode of a submerged circular plate. In response to a problem of submarine signaling, Lamb investigated the vibrations of a thin elastic circular plate in contact with water. In his investigation he discovered that the natural frequencies for structures in contact with fluid are lower than the frequencies in air, based on the assumption that the modes shapes are virtually the same in water as in a vacuum. The resonant frequency was determined using Rayleigh's method. Lamb's theoretical results were verified experimentally [Powell & Roberts, 1923]. Much later, more research was conducted for measuring and calculating natural frequencies of free vibrations of beams and plates under water [Lindholm, et al., 1965; Fu & Price, 1979; Kwak, 1996]. Another branch of FSI studies is underwater explosion. Both experimental and numerical studies have been conducted for metallic structures [Kwon & Fox, 1993; Kwon, et al., 1994; Kwon & McDermott, 2001]. On the other hand, a much limited studies were undertaken for composite structures subjected to underwater explosion [Rasmussen, 1992; Rousseau, 1993; Mouritz, 1995, 1996; McCoy & Sun, 1997; Gong & Lam, 1998; and Lam, et al., 2003]. As far as impact loading on composite structures under water is concerned, the author's research team conducted the research for the first time, to our best knowledge [Kwon, 2009; Kwon & Kendall, 2009; Owen, et al., 2010]. This chapter presents both experimental work and numerical modeling and simulation of dynamics responses of composites subjected to impact loading as well as under water. The next section describes the fabrication of composite samples and the testing setup and procedure. Subsequently, experimental results are presented and discussed, followed by computational modeling and simulation of FSI to explain the experimental findings as well as to provide a series of parametric studies so that any important property or parameter can be identified in terms of the FSI effect. Conclusions are provided at the end.

2. Composite specimens and testing equipment

Three carbon fiber laminate samples are constructed for this study. Each sample is fabricated from TORAY T700CF carbon fiber bidirectional weave and DERAKANE 510-A vinyl-ester matrix resin. Each plate is fabricated through the Vacuum Assisted Resin Transfer Molding (VARTM) process, which consists of pulling resin through layers of carbon fibers using a vacuum pump. The plates consisted of eight plies oriented $[0/90/0/90]_s$ at 2.38 mm nominal thickness with dimensions of 457 x 457 mm. The DERAKANE resin is mixed with three hardeners, Methyl Ethyl Ketone Peroxide (MEKP), Cobalt Napthenate (CoNAP), and N-Dimethylaniline (DMA) to achieve a nominal 60 minute curing time. The hardeners are added solely to achieve proper gel time and do not affect composite strength. All resin components are mixed based on a percent weight for a nominal cure time per manufacturer's directions at

a temperature of less than 70°F. The DERAKANE 510-A is measured by volume and the MEKP, CoNAP, and DMA are measured by weight.

Impact tests are conducted using a specially designed drop weight testing system, as shown in Fig. 1. This instrumented apparatus consists of a drop weight impactor, a load transducer, strain gages, high speed data analyzer, and an air box. The sample supporting fixture at the bottom of the drop tower is made of aluminum and facilitated square clamped conditions with a clear span of 305 x 305 mm. The composite plates are then clamped to the impactor frame using c-clamps to represent clamped boundary conditions. The transient response measurement of the sample includes force and strains as a function of time.

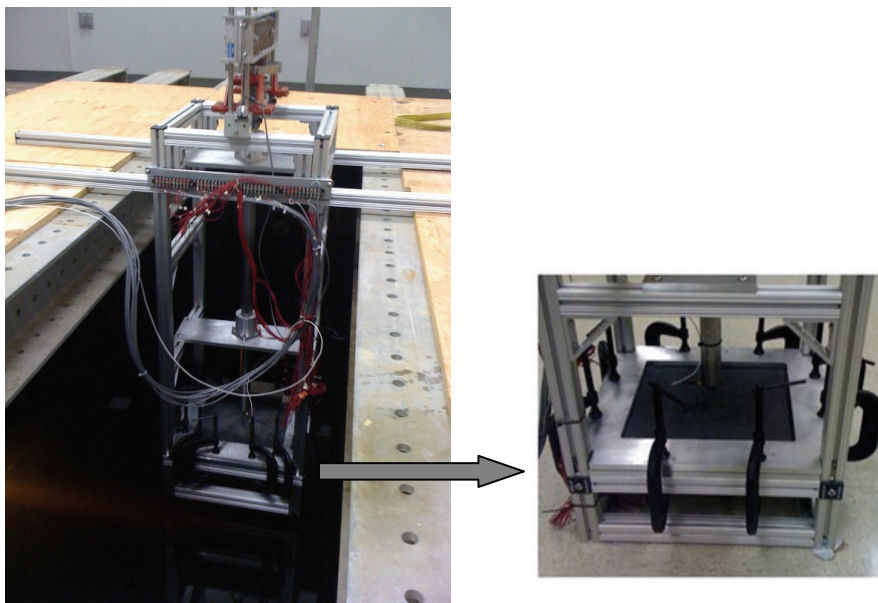


Fig. 1. Drop weight testing system in anechoic water tank

The drop weight impactor consists of a drop weight and an impact rod. The drop weight is supported by 4 steel guide rods, and the impact rod is supported by an aluminum frame base and a linear spring of spring constant 7508 N/m. The dimensions of the guide rods are 1.219 m high with a 6.35 mm diameter, and the dimensions of the base frame are 1.168 m high x 0.457 m wide x 0.457 m deep. The aluminum framing pieces and fasteners are designed and assembled for this research. The falling weight is guided by four small linear bearings. The impact rod is guided with two plain brushing aluminum linear bearings of 38.1 mm diameter enclosed in a casing for support. The top of the impact rod stays above the water surface so that the drop weight does not go into the water as it hits the impact rod on its top. It is important not to disturb the water during the impact testing so that a composite plate interacts with still water. The other end of the impact rod, which strikes a composite plate during impact, is located initially very close to the specimen surface inside the water such that the disturbance of water due to the impact rod is negligible. Therefore, FSI occurs only resulting from dynamic motion of composite plates.

A trigger at the base of the falling weight is used to measure data collection. The drop weight is kept constant at 12.0 kg. The impact rod is made of steel and has a mass of 12.7 kg. Impact energy can be varied by changing the drop height. The maximum height is 1.06 m, which can produce approximately 4.6 m/s initial velocity upon impact. The impact location is at the center of the composite sample. The selection of impact mass and height is made not to cause any damage to the composite plates so that transient dynamic response of the plates can be focused in the study.

The load cell used is an ICP® force sensor manufactured by PCB Piezotronics, Inc. which converts force into a measurable electrical output. The load transducer is mounted on the end of the impactor rod. The gage has an impact diameter of 15.88 mm. In the case of wet testing, the gages and cable connection are coated. The strain gages are three-element 45° single-plane rosettes, model CEA-00-250UR-350, by Vishay Micro-Measurements. There are four rosette strain gages bonded to each composite sample. The gages are bonded to the underside of the laminate samples, opposite side of impact, and waterproofed. Fig. 2 illustrates the orientation, location and designated x-y axis. Gage location #1 is directly at the center on the underside of the sample opposite the impact location. Gages #3 and #4 are placed along a diagonal line of the composite plate with Gage #4 at the quarter distance of the diagonal length. Gage #2 is located close to the vertical symmetric line of the center.

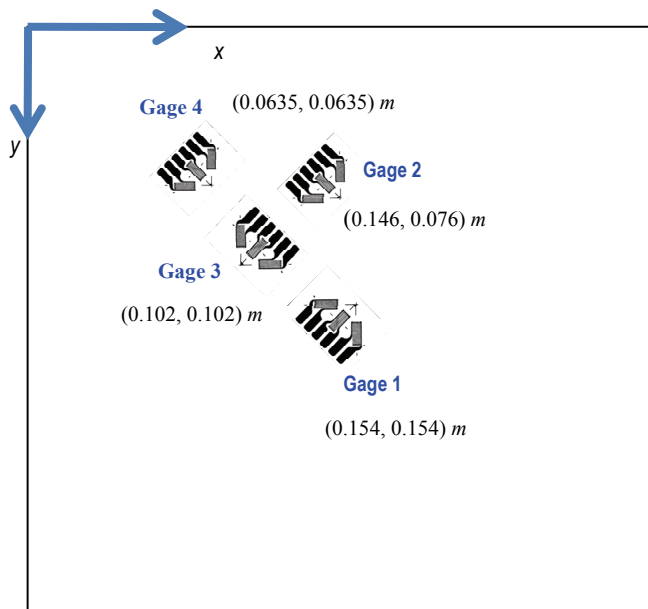


Fig. 2. Strain gage rosette locations opposite the side of impact.

Data acquisition is carried out using an acquisition system specifically developed for this project, that consists of a Pentium™ 4, 2.4 GHz, 512-MB RAM system, National Instruments™ simultaneous sampling multifunction DAQ, and five Vishay™ 2120 multi-channel strain signal conditioners. The system has a 16 bit analog-to-digital conversion resolution and is capable of reading a total of 16 channels at a throughput rate of up to 250 kS/s per channel, which is appropriate for the rate of testing used in this study. The data-

acquisition process is controlled using the NI-DAQmx driver software and LabVIEW™ interactive data-logging software that is specifically formatted for this research. A trigger located at the top of the impact rod is used to initiate data acquisition. Strain readings from four signal conditioners are multiplexed in order to accommodate all strain gages within the available number of channels. Errors due to instrumentation noise do not appear to cause problems in the data capture so no filtering is used.

An air box is specifically constructed to facilitate testing for air-backed wet environments. The box is made of 12.7 mm thick plexi-glass with dimensions 330 mm wide x 330 mm long x 127 mm deep. This box is then secured to the bottom aluminum support plate for the composite sample using 8 c-clamps of dimensions 76 mm jaw x 60 mm throat, and sealed with putty tape to prevent water leakage. The box completely covers the sample so that the bottom side of the plate is not exposed to water. A 19 mm diameter hole is cut out from the side to feed the wiring from the strain gages to the data analyzer, which is filled with putty to prevent water leakage during testing.

An anechoic water tank used for underwater surroundings testing is measured 2.75 m wide x 2.75 m long x 2.75 m deep. The anechoic tank is used to minimize the influence of the wave reflection from the boundary walls. The tank is filled with fresh water. A standing platform is constructed across the top of the tank made with aluminum I-beams and plywood, leaving a 0.635 m x 0.914 m square opening for suspension of the drop weight impactor.

3. Impact testing

Three different impact cases are studied in order to examine the effects of FSI on composite structures under dynamic loading. These cases are shown in Fig. 3. First, the dry impact is conducted as the baseline. For the dry impact test, the composite plates are impacted without having any contact with the water. This is shown in Fig. 3(a). Subsequent wet impact tests are undertaken for the same composite plates. In order to avoid any moisture effect on the composite materials, the wet impact testing is performed as soon as the composite plates are submerged into the anechoic water tank. Furthermore, once the wet impact testing is completed, dry impact of the plate is conducted just following the wet impact. The responses of the dry impact tests before and after the wet impact testing are compared. Their results are consistent. By doing so, it can be verified that the composite plates did not absorb any moisture to affect their material properties.

Two different wet impact conditions are considered. The first case has an air-containing rigid box attached to the bottom of the composite plates. The box is completely sealed so that no water permeates into the box when the composite plate with the attached box is submerged into the water of the anechoic water tank. Then, impact loading is applied to the composite plate submerged in water. This is called the air-backed wet impact and is shown in Fig. 3(b). The air-backed composite plate is only in contact with water at the top side where the impact occurs. The other wet impact case is very similar to the previous one except that the air-box is no longer sealed so that water fills the box when the plate and the box are put into the water tank. This is sketched in Fig. 3(c) and called the water-backed wet impact. The water-backed plate is exposed to water on both sides in this case. The same impact conditions, i.e. the same drop weight and height, are applied to the three impact loading cases. The wet impact responses are compared to the dry impact data in order to evaluate the FSI effects.

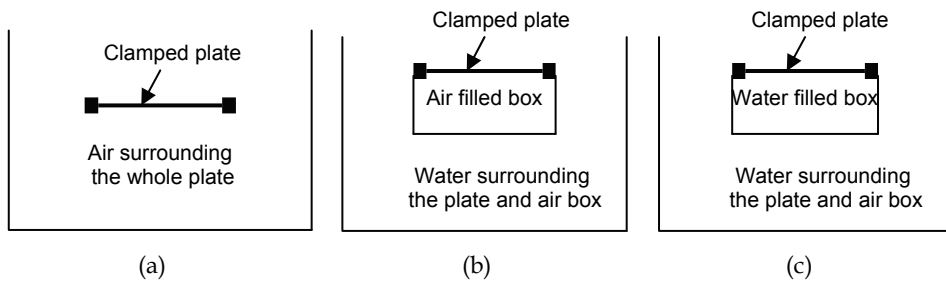


Fig. 3. Three different impact conditions with composite plates held in place: (a) dry impact, (b) air-backed wet impact, (c) water-backed wet impact

4. Experimental results

The impact test is conducted for the dry and wet composite plates. The mass of the free falling object is 12 Kg which is dropped from the height 1.06 m. In order to confirm the repeatability of the impact test data, every test condition is repeated several times for the same composite plate. The measured force and strain data are very close to one another. This fact confirms not only repeatability but also confirms there is no damage in the specimen. If damage occurred and accumulated in the composite plate, repeated testing would show different results with the damage. Figure 4 compares the two force data under the same dry impact condition. Other force data, which are not plotted here to avoid crowding, are very close to the graphs shown in the figure. In all figures unless otherwise mentioned, the force or strain plots are normalized in terms of the dry impact data so that the effects of FSI can be better represented in the plots.

The impact force is compared in Fig. 5 for the dry impact as well as the water-backed and air-backed wet impact cases. As shown in this figure, the air-backed and water-backed wet impacts yield 55% and 50% greater impact force than the dry case, respectively. The larger

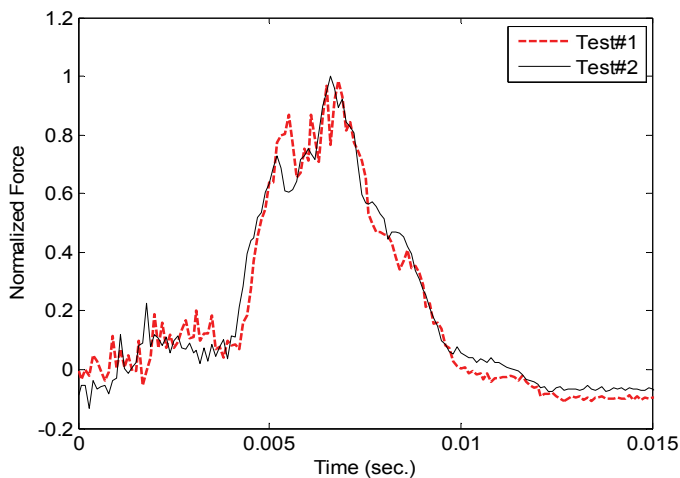


Fig. 4. Comparison of dry impact forces under the same impact condition

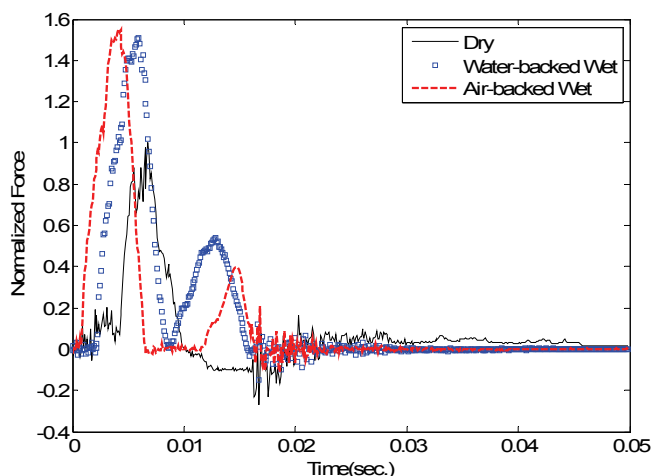


Fig. 5. Comparison of impact forces among dry, water-backed and air-backed wet impact cases

wet impact forces are caused by the hydrodynamic added mass effect. Because the mass of the composite plate is only 1.6 times greater than that of water, the plate with the added mass moves with a much slower velocity. As the plate moves more slowly, the contact force between the impactor and the plate becomes larger, which is recorded to the force gage. In order to support this argument, a series of finite element analyses is conducted in the next section.

Both wet impact forces have steep monotonic increases to their peak values just after the impactor hit the plates while the dry impact force shows an initial low plateau before it moves steeply to its peak value. Because the impactor is not held after the initial impact, it rebounds and lands again. As a result, both wet impacts show secondary peak forces. However, the dry impact does not have the secondary contact. In particular, the air-backed wet impact case gives a quite a delay between the initial and secondary impact forces while the water-backed wet impact case shows the secondary force occurring just after the initial one.

The reason that the air impact test does not produce the secondary impact is due to the spring in the impact test machine. The spring supports the impact rod which is supposed to hit the composite plate from a small distance above the plate before the impact loading. As the impact weight drops and hits the impact rod, the latter moves down with compression of the spring to strike the composite plate. For the air impact case, the initial impact force is lower than that for wet impact cases. Therefore, the rebounding and landing force from the air impact is not large enough to overcome the spring force so that the rod cannot strike the plate again.

Because strain gage location #1 lies right underneath the impact site of the composite plate, the strains contain many higher frequency components compared to strains at other locations. A comparison of Fig. 5 to Fig. 6 shows that the peak values of impact forces and strains at position #1 occur simultaneously. Strains under wet impacts are more than double the dry impact strain at location #1. This ratio of peak strains between the wet and dry impacts is even greater than that of the impact forces.

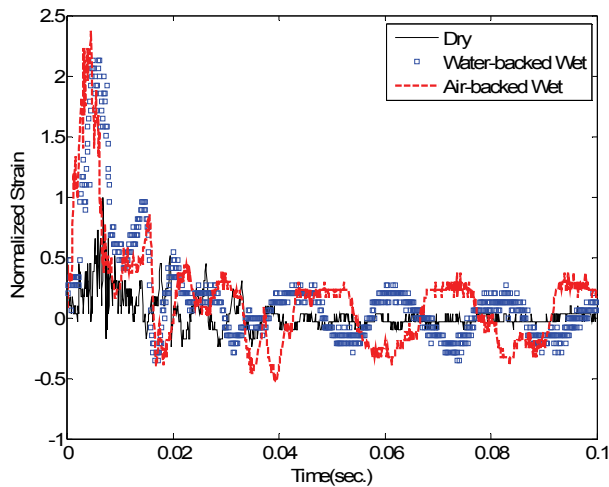
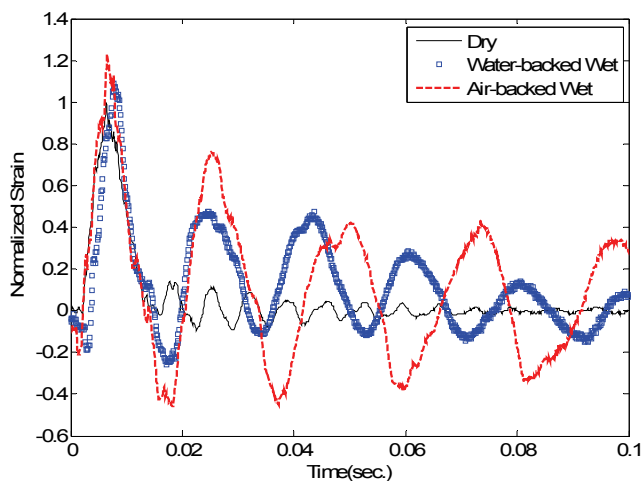


Fig. 6. Comparison of strains along x -axis at position #1 among dry, water-backed and air-backed wet impact cases

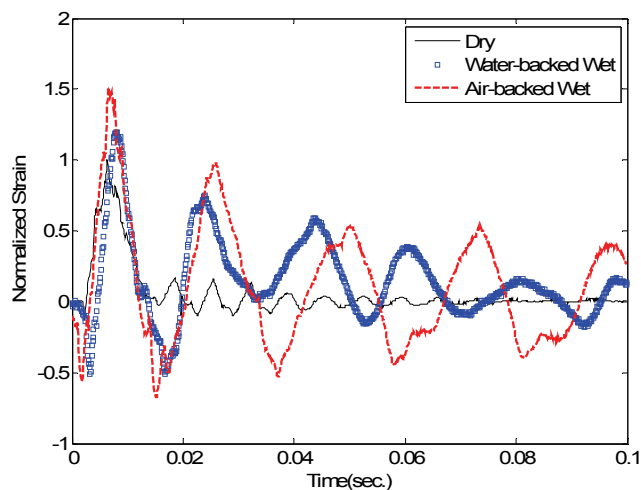
The differences between the wet and dry impact strains are smaller at the gage location #2 than those at the location #1. The strains under the air-backed wet impact are 20% and 50% greater than the dry impact strains along the x -axis and y -axis, respectively, as shown in Fig. 7. On the other hand, the water-backed impact results in 10% and 20% greater strains in the x -axis and y -axis, respectively, than the dry impact. The gage location #2 is closer to the clamped boundary in the y -axis direction. Thus, this suggests that the clamped boundary results in a greater FSI effect on the composite plate. Both wet impact strains show initial compressive strains before much larger tensile strains. Furthermore, these strain measurements show a clear difference among the response frequencies due to the added mass effect. Comparing the wet impact responses to the dry impact response, the response frequencies under the wet impacts are less than a half of the dry impact response frequency. Such a drastic reduction is caused by the light composite structure which is only about 1.6 times as heavy as the water. The response frequency is higher for the water-backed wet impact case than for the air-backed wet impact case by approximately 20%. This is an interesting result because the water-backed wet structure is expected to have a greater added mass effect with a lower response frequency. However, as expected, the decay of the strain peak values is greater for the water-backed wet impact case than the air-backed case. For example, the average damping ratio is 0.053, 0.062, and 0.11 for the dry, air-backed, and water-backed impact cases, respectively. This means the damping effect is the greatest for the water-backed case.

Calculation of the Added Virtual Mass Incremental Factor (AVMIF), β from Eq. (1) given below, yields approximately 6.5 and 11.5 for the water-backed and air-backed wet composite plates, respectively.

$$\frac{\omega_w}{\omega_d} = \frac{1}{\sqrt{1 + \beta}} \quad (1)$$



(a) Strain along x-axis



(b) Strain along y-axis

Fig. 7. Comparison of strains at position #2 among dry, water-backed and air-backed wet impact cases

where ω is the frequency and subscripts w and d denote the wet and dry cases, respectively. AVMIF represents the ratio of the kinetic energy of the water to that of the composite plate. The AVMIF for steel submerged in water ranges from 1.4 to 2.4 depending on the boundary conditions [Fu & Price, 1987; Haddara & Cao, 1996]. Comparison of AVMIF between the composite and steel shows clearly a much larger effect of FSI on the composite than steel.

The strain gage readings at gage location #3 have similar response characteristics as observed in the gage at location #2. Both air-backed and water-backed wet impacts resulted in 30% greater strains in x -axis than the dry impact. Because the gage location #3 is on the diagonal direction, strains in the y -axis were very close to those in the x -axis.

The effect of FSI is very significant for the strain gage reading at location #4, as shown in Fig. 8, and the strain readings are much less harmonic with more constraint effects from the clamped boundaries of the plate. First of all, both wet impact cases result in very large initial compressive strains compared to the dry impact case. The initial compressive strains are due to the clamped boundary conditions. After following the initial large compression, the air-backed wet impact case shows another large tensile strain while the water-backed case has a modest magnitude of tensile strain. The water on the backside of the water-backed composite plate seems to prevent further tensile strain at this gage location. The magnitudes of the strains at the gage location #4 are 4 to 5 times higher for the wet impact cases.

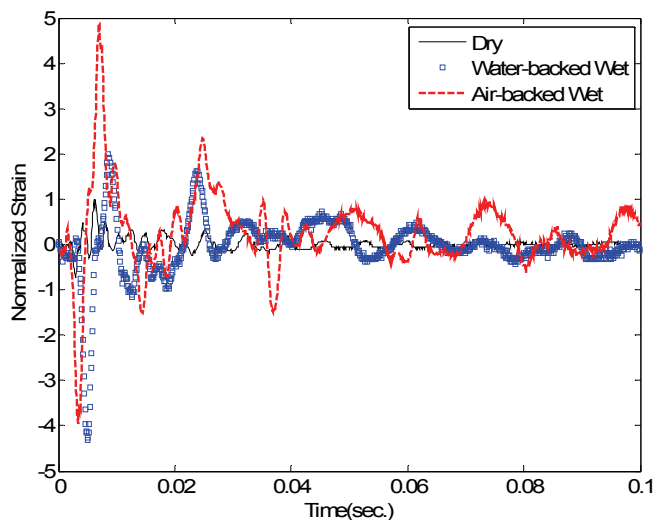


Fig. 8. Comparison of x -strains at position #4 among dry, water-backed and air-backed wet impact cases

In the next set of studies, the impact height is reduced to 0.76 m while the impact mass remains the same. This represents the impact energy reduction by 29%. Both dry and wet impact tests are undertaken with the reduced impact energy. Interestingly, as the impact energy is reduced, the peak forces under the dry and wet impacts are almost the same even though the force-time histories are different as shown in Fig. 9. However, comparison of strain responses between the dry and wet impact cases is similar between the two different impact energy conditions. For example, Figs. 10 and 11 are the strains at the gage locations #2 and #4.

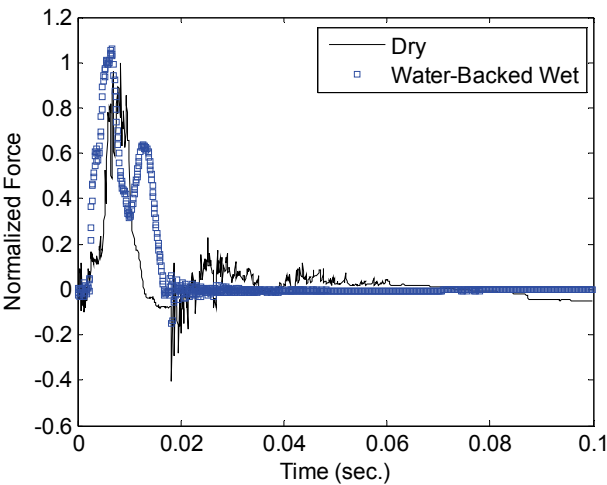


Fig. 9. Comparison of impact forces among dry and water-backed wet impact cases with a 29% reduced impact energy

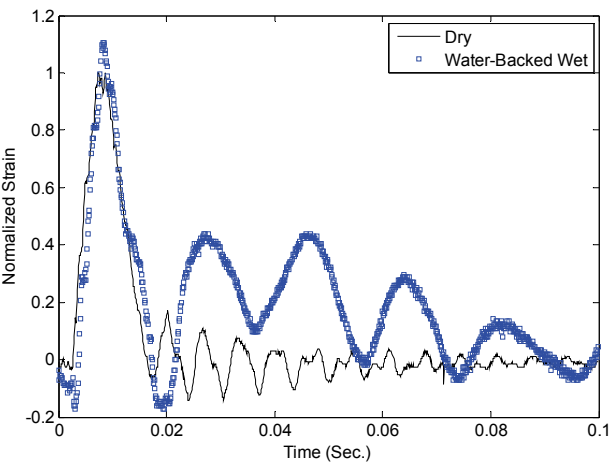


Fig. 10. Comparison of x -strains at position #2 among dry and water-backed wet impact cases with a 29% reduced impact energy

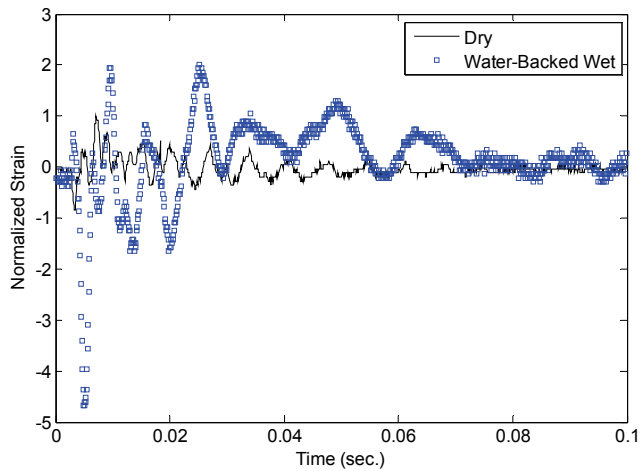


Fig. 11. Comparison of x -strains at position #4 among dry and water-backed wet impact cases with a 29% reduced impact energy

5. Computational modelling

A numerical study is conducted to confirm the experimental results at least qualitatively and to assess the effects of various parameters on FSI and impact loading. For the numerical study, 2-D modeling and analysis is conducted. Even though the experiments are 3-D, it is not believed the qualitative behavior would differ between 2-D and 3-D cases. The 2-D analysis is computationally much less time-consuming, especially with the FSI model containing a large domain of fluid.

The numerical model has a composite beam which has density 2000 Kg/m^3 and elastic modulus 50 GPa . The beam is 400 mm long, 20 mm wide, and 2 mm thick. Therefore, the composite has approximately twice density of water and is 40% lighter than aluminum and one quarter of steel. On the other hand, the elastic modulus is about 70% and 25% of those of aluminum and steel, common structural metals. As a parametric study, both density and elastic modulus of the beam are changed.

The computational model consists of both structure and fluid. Finite element formulations are developed for the FSI study. The beam is modeled using the Euler-Bernoulli beam theory. Because the beam is assumed to be very thin, the transverse shear deformation energy is negligible. The finite element matrix equation for the beam as well as for any general structure is expressed below:

$$[M_s]\{\ddot{d}\} + [C_s]\{\dot{d}\} + [K_s]\{d\} = \{F_e\} + \{F_{fs}\} \quad (2)$$

where $[M_s]$, $[C_s]$, and $[K_s]$ are the mass, damping and stiffness matrices of the structure, $\{d\}$ is the nodal displacement vector, $\{F_e\}$ and $\{F_{fs}\}$ are the force vectors from external loading and the fluid loading, respectively. In other words, the fluid loading comes from the FSI. Superimposed dot denotes the temporal derivative.

For the fluid medium, fluid viscosity was neglected and it was modeled as an acoustic medium. The velocity potential formulation was utilized for the acoustic medium, and it is derived here. The continuity equation is

$$\frac{\partial \rho}{\partial t} + \vec{\nabla} \cdot \rho \vec{u} = 0 \quad (3)$$

where ρ is the density, \vec{u} is the velocity vector, $\vec{\nabla}$ is the gradient operator, and t indicates time. The change of density is expressed as

$$\rho = \rho_0(1 + s) \quad (4)$$

in which s is called condensation and ρ_0 is an ambient fluid density. Substitution of Eq. (4) into Eq. (3) with an assumption of $s \ll 1$ yields

$$\frac{\partial s}{\partial t} + \vec{\nabla} \cdot \vec{u} = 0 \quad (5)$$

The force-balance equation is

$$\rho_0 \frac{\partial \vec{u}}{\partial t} = -\vec{\nabla} p \quad (6)$$

where p is the pressure. A scalar field called the velocity potential is defined as follows:

$$-\vec{u} = \vec{\nabla} \phi \quad (7)$$

Replacing the velocity by the velocity potential in Eq. (6) results in

$$\vec{\nabla} \left(-\rho_0 \frac{\partial \phi}{\partial t} + p \right) = 0 \quad (8)$$

The relationship $p = Bs$ as well as Eq. (7) are substituted into Eq. (5) to give

$$\frac{I}{B} \frac{\partial p}{\partial t} - \nabla^2 \phi = 0 \quad (9)$$

where B is the fluid bulk modulus. Elimination of pressure from Eqs. (8) and (9) yields the final wave equation in terms of the velocity potential.

$$\frac{1}{c^2} \ddot{\phi} - \nabla^2 \phi = 0 \quad (10)$$

in which $c^2 = B / \rho_0$ and c is the speed of sound. In order to apply Eq. (10) to FSI problems, the velocity at the FSI interface boundary is computed from the structural dynamics, i.e. Eq. (2), and it is applied to the wave equation through Eq. (7). On the other hand, the fluid pressure is computed from the wave equation using

$$p = \rho_0 \frac{\partial \phi}{\partial t} \quad (11)$$

The acoustic wave equation is processed using the Galerkin method to formulate the finite element matrix equation. The resulting matrix equation for the wave equation is expressed as

$$\frac{1}{C^2} [M_f] \{\ddot{\varnothing}\} + [K_f] \{\varnothing\} = \{F_f\} \quad (12)$$

where

$$[M_f] = \int_{\Omega^f} [H]^T [H] d\Omega \quad (13)$$

$$[K_f] = \int_{\Omega^f} [\bar{\nabla} H]^T [\bar{\nabla} H] d\Omega \quad (14)$$

$$\{F_f\} = \int_{\Gamma^f} [H]^T u_n d\Gamma \quad (15)$$

Here, $[H]$ the a vector of shape functions. For the present analysis, four-node quadrilateral elements are used for the fluid acoustic model. In addition, Ω^f and Γ^f are the fluid domain and boundary, respectively, and u_n is the fluid velocity normal to the boundary. For an FSI application, Eqs. (2) and (12) are solved in a staggered matter. For example, the structural analysis is conducted using Eq. (2). Then, the structural velocity at the FSI boundary is computed. From the velocity compatibility condition, both structural and fluid velocities must be the same at the FSI boundary. For an inviscid flow, only the normal velocity components are considered for the compatibility condition. As a result, Eq. (15) is computed from the fluid velocity at the FSI interface and the fluid analysis is performed from Eq. (12). From the fluid analysis, fluid pressure is computed at the FSI interface. From the force equilibrium, the fluid pressure is used as an applied force to the structure. This completes one cycle and the whole process continues as the time increases. For an efficient computation, the explicit time integration technique was used for both structural and fluid analyses. For example, time integration of fluid analysis is conducted as below and similarly for structural analysis.

$$\{\ddot{\varnothing}\}^t = [K_f] \{\varnothing\} = [M_f]^{-1} \{\{F_f\}^t - [K_f] \{\varnothing\}^t\} \quad (16)$$

$$\{\dot{\varnothing}\}^{t+\frac{\Delta t}{2}} = \{\dot{\varnothing}\}^{t-\frac{\Delta t}{2}} + \Delta t \{\ddot{\varnothing}\}^t \quad (17)$$

$$\{\varnothing\}^{t+\Delta t} = \{\varnothing\}^t + \Delta t \{\dot{\varnothing}\}^{t+\frac{\Delta t}{2}} \quad (18)$$

6. Numerical results

First of all, the impact force is computed from the models described in the previous section and compared between dry and wet impact cases in Fig. 12. The computer modeling and simulation with an impact energy of 0.5J produced a result qualitatively agreeing with the experimental observation as plotted in Fig. 5. Because of FSI, the wet impact results in a

higher impact force than the dry impact. The FSI produces an added mass effect, which makes the structure under water move slower than the same structure in air. Such a slower movement yields a higher contact force between the impactor and the structure.

A parametric study is conducted to study the effect of different material properties on the peak impact force ratios between the wet and dry impacts. The first parameter is the structural mass density. As shown in Fig. 13, the structural density significantly affects the wet impact force. As the structural mass density becomes smaller and more comparable to the water density, the added mass effect gets greater. Therefore, the peak of the wet impact

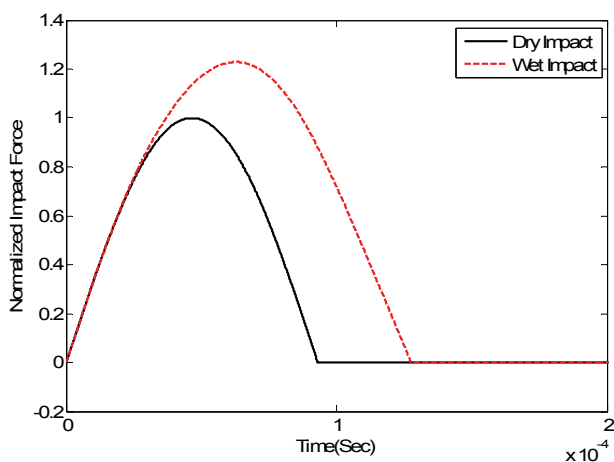


Fig. 12. Comparison of normalized impact forces between dry and wet impact modeling of a composite beam

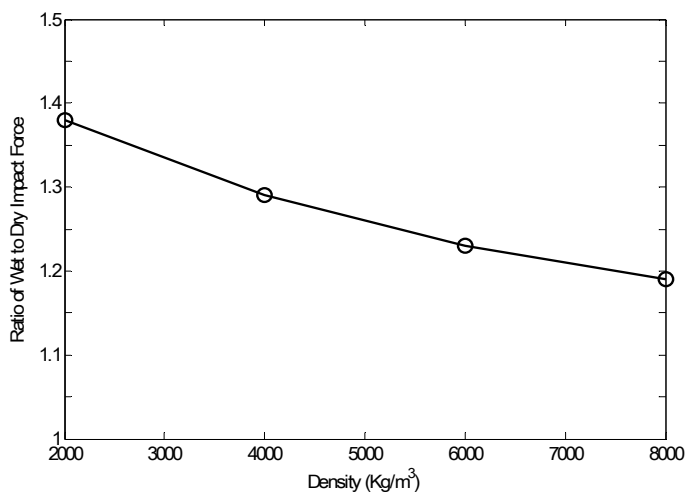


Fig. 13. Plot of effects of beam density on ratios of peak impact forces between wet and dry impact models

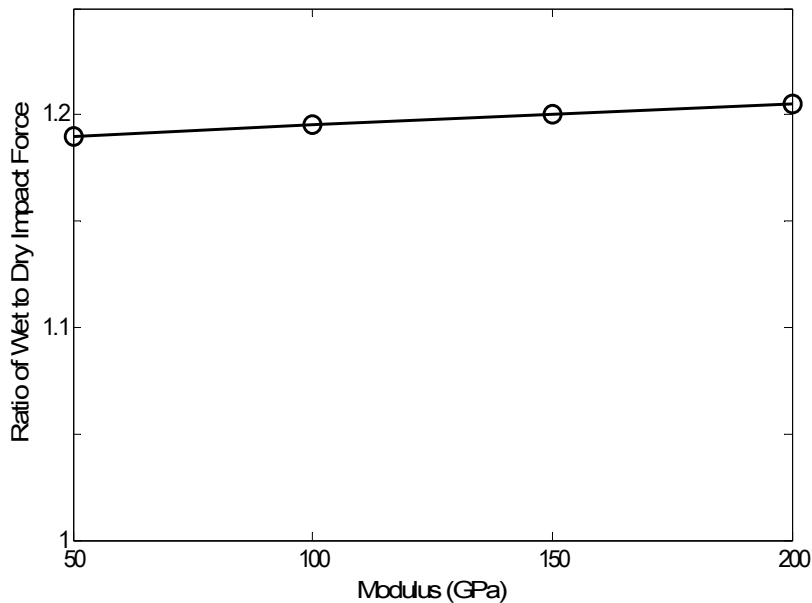


Fig. 14. Plot of effects of beam elastic modulus on ratios of peak impact forces between wet and dry impact models

becomes much greater than that of the dry impact for a lighter structure. This suggests that wet impact is more critical for polymer composite structures than metallic structures because polymer composites have much lower mass densities than conventional metals. On the other hand, a change of elastic modulus of the structure has only a minor effect on the wet impact force as shown in Fig. 15. In other words, the ratio of the wet to dry peak impact forces does not vary much with respect to the change of structural modulus.

Because the previous experimental study also indicates the ratio of the peak impact force between the wet and dry impacts is affected by the impact energy, as the impact energy becomes smaller, the FSI effect also becomes lower so that the impact force ratio approaches unity. This fact is also supported from the numerical study. In the numerical simulation, the impact mass is varied in the finite element model in order to change the impact energy. The maximum contact force under wet impact loading is computed for different impact energy (i.e. impact mass) and the value is normalized in terms of the maximum contact force under dry impact with the same impact energy. The results are plotted in Fig. 16. As shown in the figure, the impact force ratio approaches to unity as the impact mass becomes 0.001.

Another application of the computer model is to investigate the effect of FSI under impact loading on the strain histories of the structure. Because the FSI effect is not uniform, the experimental study indicates that the strain near to the boundary is more influenced by the FSI effect. This fact is also investigated using the numerical model. Fig. 16 shows the locations of the beam where the strains are computed. Figures 17 though 20 plot the strain histories of the wet and dry impacts, respectively. The plots are normalized with respect to

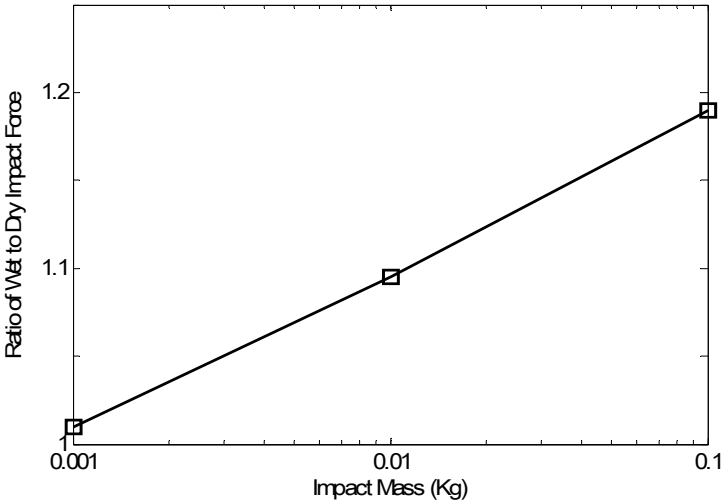


Fig. 15. Plot of effects of impact mass on ratios of peak impact forces between wet and dry impact models

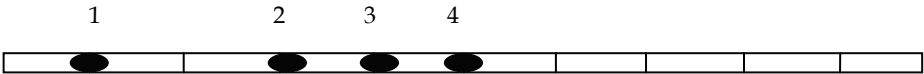


Fig. 16. Location of strain calculations along the clamped beam model

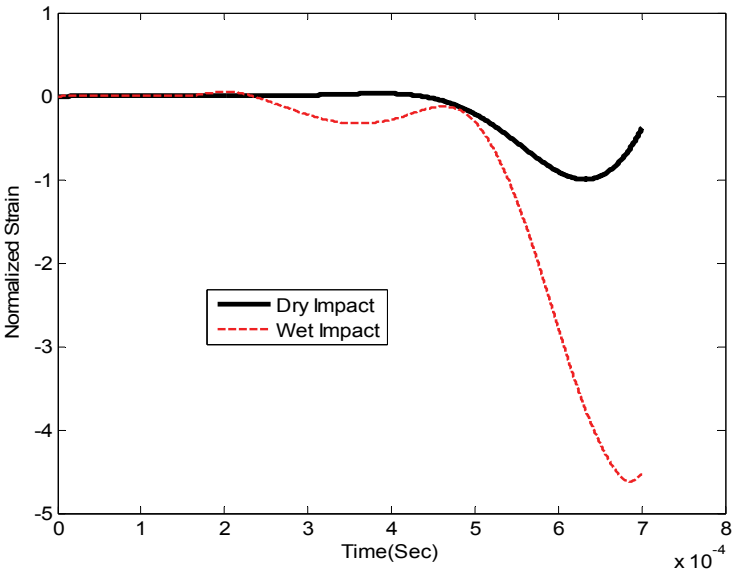


Fig. 17. Strain time history at Location 1 of Fig. 16 (beam model)

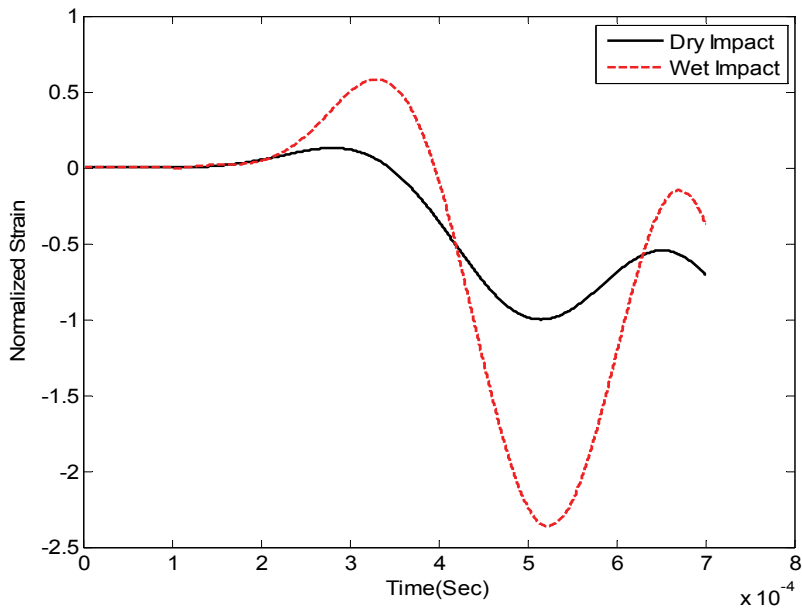


Fig. 18. Strain time history at Location 2 of Fig. 16 (beam model)

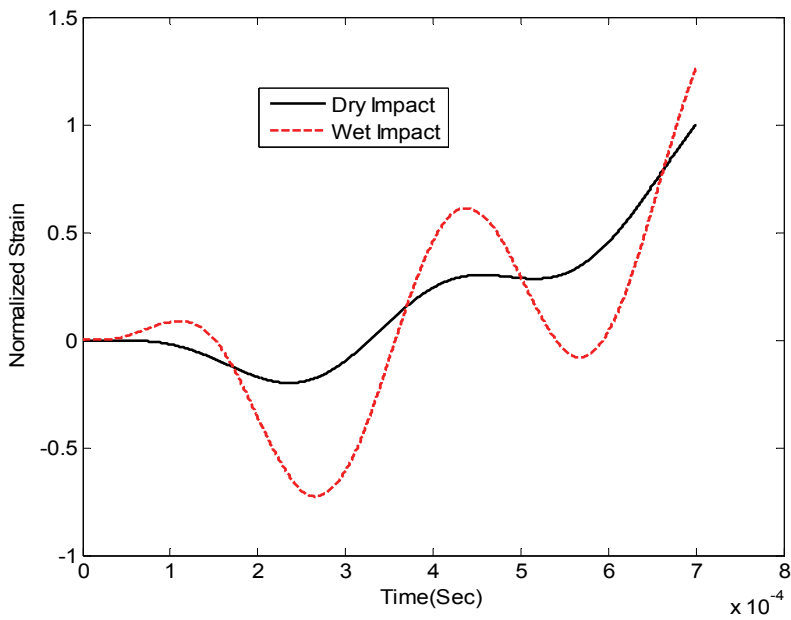


Fig. 19. Strain time history at Location 3 of Fig. 16 (beam model)

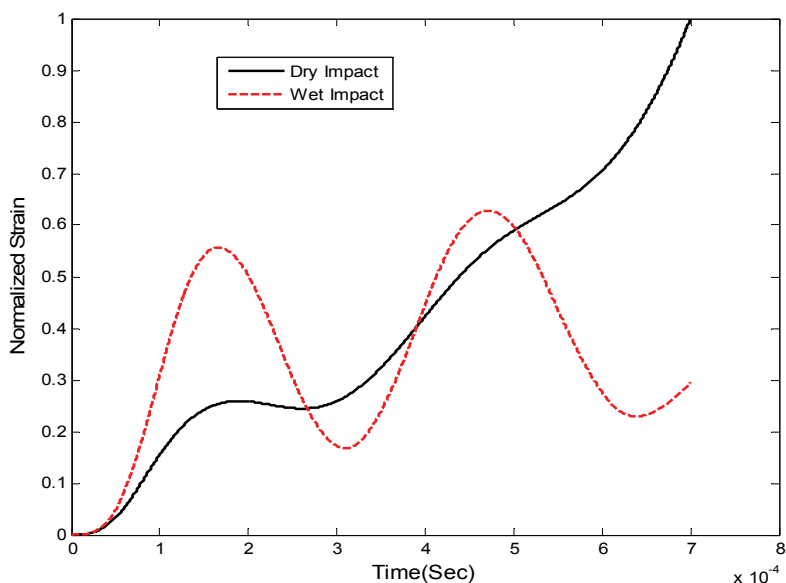


Fig. 20. Strain time history at Location 4 of Fig. 16 (beam model)

the respective dry impact strain. Comparing those strains tells clearly Location 1 has the greatest difference of strain histories between the wet and dry impacts. In other words, the FSI effect with impact loading is greater at the location near to the clamped boundary.

7. Conclusion

Both experimental and numerical studies are conducted to understand the effect of FSI with impact loading on polymer composite structures. For an experimental study, an experimental set-up is designed and fabricated for impact testing on composite plates submerged in water. In order to investigate the transient dynamic response of composite plates with FSI effects under impact loading; three impact conditions, dry, air-backed wet, and water-backed wet impact conditions are considered, respectively. In order to focus on the FSI effects on the transient dynamic responses, impact loading is controlled not to cause any damage to the composite plates. Since the composite material has a very comparable density to water, the FSI effects are very significant on the impact force and transient responses of the plates. Due to the added mass effect of water, the impact force is much greater for the wet impact cases than for the dry impact. Similarly, wet impact produces much greater transient strains on the composite plates. As a result, the wet impact is more detrimental to the structure than the dry impact. However, the increase of magnitude of transient strain responses resulting from the FSI with wet impacts varies significantly. The transient strain responses depend on the location of the composite plate because the added mass effect is not uniform over the plate. The location near to the clamped boundary corner has generally a greater FSI effect on the transient strain response. Comparison of AVMIF

between the composite and steel shows approximately 3 to 5 time greater values for composites than steel, which indicates a much greater effect of FSI on the composite than steel.

The numerical modeling and simulation confirms the experimental observation. Wet Impact loading on a composite structure produces a much greater impact force than dry impact. However, as the impact energy becomes smaller, the peak wet impact force becomes closer to that of the dry impact force. A numerical parametric study also indicates that density of the structure significantly influences the FSI effect of the wet impact. If an impacted structure has a low density like a polymer composite, the FSI effect on impact loading is larger while the effect is less for a structure made of a conventional metal. On the other hand, the elastic modulus of the structure has a negligible change in the FSI effect with impact loading. Furthermore, both experimental and computational studies show that the FSI effect with impact loading is not uniform and greater near to the clamped boundary.

8. Acknowledgement

The authors acknowledge the assistances from T. Christian and J. Mobley for preparing the impact testing equipment; and P. K. Kendall, A. S. Kwon, S. Blair, J. M. Didoszak for assisting with the computational work. They also express sincere thanks to the sponsorship by ONR and NSWC-CD.

9. References

- Abrate, S., (1994). Impact on laminated composites; recent advances, *Applied Mechanics Reviews*, Vol. 47, No. 11, pp. 517-544.
- Aslan, Z.; Karakuzu, R. & Okutan, B., (2003). The response of laminated composite plates under low-velocity impact loading, *Composites Structures*, Vol. 59, pp. 119-127.
- Fu, Y. & Price, W. G., (1987). Interactions between a partially or totally immersed vibrating cantilever plate and the surrounding fluid, *Journal of Sound and Vibration*, Vol. 118, No. 3, pp. 495-513.
- Gong, S. W. & Lam, K. Y., (1998). Transient response of stiffened composite submersible hull subjected to underwater explosive shock,, *Composite Structures*, Vol. 41, No. 1, pp. 27-37.
- Haddara, M. R. & Cao, S., (1996). A study of the dynamic response of submerged rectangular flat plates, *Marine Structures*, Vol. 9, pp. 913-933.
- Kwak, M. K., (1996). Hydroelastic vibration of rectangular plates, *Journal of Applied Mechanics*, Vol. 63, pp. 110-115.
- Kwak, M. K. & Kim, K. C., (1991). Axisymmetric vibration of circular plates in contact with fluid, *Journal of Sound and Vibration*, Vol. 146, pp. 381-389.
- Kwon, Y. W., (2009). Study of fluid effects on dynamics of composite structures, (PVP2009-77982), 2009 ASME Pressure Vessel and Piping Conference, Prague, Czech Republic, July.

- Kwon, Y. W.; Bergensen, J. K. & Shin, Y. S., (1994). Effect of surface coatings on cylinders exposed to underwater shock, *Journal of Shock and Vibration*, Vol. 1, No. 3, pp. 637-646.
- Kwon Y. W. & Cunningham, R. E., (1998). Comparison of USA-DYNA finite element models for a stiffened shell subject to underwater shock", *Computers and Structures*, Vol. 66, No. 1, pp. 127-144.
- Kwon Y. W. & Fox, P. K., (1993). Underwater shock response of a cylinder subjected to a side on explosion, *Computers and Structures*, Vol. 48, No. 4, pp. 637-646.
- Kwon Y. W. & Kendall, P. K., (2009). Fluid-structure interaction of composite structures subjected to dynamic loading", *First Joint ASC and CACSMA Conference*, September 15-17, Newark, Delaware.
- Kwon, Y. W. & McDermott, P. M., (2001). Effects of void growth and nucleation on plastic deformation of plates subjected to fluid-structure interaction", *ASME Journal of Pressure Vessel Technology*, Vol. 123, November, pp. 480-485
- Kwon, Y. W. & Wojcik, G. W., (1998). Impact Study of Sandwich Composite Structures with Delamination, *Journal of Composite Materials*, Vol. 32, No. 5, pp. 407-430.
- Lam, K. Y.; Zong, Z. & Wang, Q. X., (2003). Dynamic Response of a Laminated Pipeline on the Seabed Subjected to Underwater Shock, *Composites Part B: Engineering*, Vol. 34, pp. 59-66.
- Lamb, H., (1921). On the vibrations of an elastic plate in contact with water, *Proceeding of the Royal Society (London)*, Vol. A 98, pp. 205-216.
- Lindholm, U. S.; Kana, D. D. & Chu, W. H., (1965). Elastic vibration characteristics of cantilever plates in water, *Journal Ship Research*, Vol. 9, No. 1, pp. 11-22.
- McCoy, W. & Sun, C. T., (1997). Fluid-structure interaction analysis of a thick-section composite cylinder subjected to underwater blast loading, *Composite Structures*, Vol. 37, No. 1, pp. 45-55.
- Mouritz, A. P., (1995). The damage to stitched GRP laminated by underwater explosion shock loading", *Composite Science and Technology*, Vol. 55, pp. 365-373.
- Mouritz, A. P., (1996). The effect of underwater explosion shock loading of the flexural properties of GRP laminates, *Int. J. Impact Engng*, Vol. 18, No. 2 pp. 129-139.
- Mouritz, A. P.; Gellert, E.; Burchill, P. & Challis, K., (2001). Review of advanced composite structures for naval ships and submarines, *Composite Structures*, Vol. 53, pp. 21-41.
- Owens, A.C.; Didoszak, J. M.; Kwon, A. S. & Kwon, Y. W., (2010). Underwater impact of composite structures, (PVP2010-25065) *2010 ASME Pressure Vessel and Piping Conference*, Bellevue, Washington, July.
- Powell, J. H. & Roberts, J. H. T., (1923). On the frequency of vibration of circular diaphragms, *Proceeding of the Royal Society (London)*, Vol. 35, pp. 170-182.
- Rasmussen, E. A., (1992). Underwater Shock Testing and Analysis of Composite Cylinders, *Shock and Vibration Symposium*, 1992.
- Rousseau, M. P.; Kwon, Y. W. & Shin, Y. S., (1993). Modeling the effects of shock on an underwater composite cylinder", *64th Shock & Vibration Symposium*, Ft. Walton Beach, FL, Oct.

Volcy, G. C.; Morel, P. & Bureau, M., (1979). Some studies and research related to the hydro-elasticity of steel work, *Proceedings of the 122nd Euromech Colloquium on numerical analysis of the dynamics of ship structures*, pp. 403-406.

Experimental Investigation of Dynamic Compression and Damage Kinetics of Glass/Epoxy Laminated Composites under High Strain Rate Compression

Tarfaoui Mostapha

*ENSIETA / MSN, 2, rue François Verny, 29806 Brest cedex 9
France*

1. Introduction

The choice of composite materials as a substitute for metallic materials in high technological applications such as in the marine field is becoming more pronounced especially due to the great weight-savings these materials offer. In many of these practical situations, the structures are subjected to high impact loads like slamming, impact, underwater explosions or blast effects. Material and structural response vary significantly under impact loading conditions compared to static loading. The mechanical characteristics of these materials are well known for static loading; however, with the strain rate they are likely to evolve (Goldsmith et al., 1995; Shi et al., 1993; Tsai & Sun, 2004; Tsai & Sun, 2005; Gillespie et al., 2005; Brara & Klepaczeko, 2007). The behaviour of structures subjected to impact has been of interest to many scientists for design purposes as well as for the purpose of developing constitutive models of the materials tested [7-8]. The study of the composite materials behaviour at high strain rates is still relatively new and reliable data on strain rate effects is very scarce. Even though the problem of obtaining reliable data is accentuated by difficulties encountered in design and conducting impact tests on composites [9], the qualitative relationship between the dynamic constitutive response and the dynamic damage evolution for composites at high strain rates is still far from being fully understood. To investigate the rate-dependent constitutive relations of materials at high strain rates, the Split Hopkinson Pressure Bar (SHPB) technique has been extensively accepted [10]. Experience of the use of SHPB for the investigation of metals has led to the adaptation of this technique for the characterization of laminated polymer composites at medium strain rates. Significant efforts have been made to examine the high strain rate behaviour of more brittle materials such as composites and ceramics using the split Hopkinson bar to measure dynamic response of materials under varying loading conditions (Kumar et al., 1986); (El-Habak, 1991), (Harding, 1993), (Sierakowski & Nevill, 1971). Ochola et al. (2004) studied the strain rate sensitivity of both carbon fibre reinforced polymer (CFRP) and glass fibre reinforced polymer (GFRP). The results show that the dynamic material strength for GFRP increases with increasing strain rates and the failure strain for both CFRP and GFRP is seen to decrease with increasing strain rates. Vinson & Woldensenbet's (2001) results show that the ultimate stress

increases with increasing strain rate. Most recently, the study conducted by Hosur et al. (2004) presents the effect of in-plane off-axis testing of an 8-harness satin weave carbon fabric/SC15 composite specimen. The specimens were tested in the in-plane direction of 0° , 15° , 30° , 45° , 60° , 75° , and 90° in a range of strain rates from 1092 to 2425 s^{-1} . From this study it was noted that the high strain rate-tested specimens showed a considerable increase in the stress to failure and stiffness of the composite compared with the quasistatic loaded specimens. Depending on the fibre orientation of the specimens, the ultimate strength and strain varied considerably and exhibited a nonlinear stress-strain response that increased with angles up to 45° . Gary & Zhao (2000) employed the use of low impedance materials such as nylon, for the incident and output bars of the split Hopkinson bar, to test the strain rate behaviour of glass epoxy composite panels. The failure strength of the glass epoxy panel tested by Gary and Zhao is reported to be strain rate sensitive. Fibre orientation effects on high strain rate properties were considered recently for a carbon epoxy system. Tsai & Sun (2002) have reported the difference between tensile and compressive behaviours in a unidirectional glass fibre-reinforced composite, and developed a nonlinear rate-dependent viscoplasticity model to characterize its compressive stress-strain relationship. Many different models (Gama et al., 2001), (Haque & Ali, 2005), (Vinson. & Woldesenbet, 2001) have been developed to predict failure stress and modes in composites subjected to quasi-static loading. However, few criteria have been developed and experimentally validated for high strain rate loading.

In this study, specimens of glass/epoxy composite were subjected to static and dynamic compression loading. Quasi-static tests were conducted on an Instron universal machine to evaluate the elastic properties and quasi-static response, while the split-Hopkinson pressure bar (SHPB) is used for dynamic tests. Samples were tested in-plane and out of plane direction. The fibre orientations of the samples were 0° , $\pm 20^\circ$, $\pm 30^\circ$, $\pm 45^\circ$, $\pm 60^\circ$, $\pm 70^\circ$ and 90° . Stress-strain curves at increasing strain rates were obtained for different cases. However, no experimental data for the intermediate range of strain rates between ($80s^{-1}$ to $300s^{-1}$) was obtained, because the Instron universal testing machine and the SHPB employed in the experimental tests are designed respectively for low and high strain rates. Off-axis composites and angle-ply laminates exhibited significant nonlinear and strain-dependent behaviour. Finally, experimental observations enable us to draw up a history of dynamic damage in the specimens according to fibre orientation and load direction.

2. Materials

The material used in this study consists of 2400 Tex E-glass fibres impregnated with an epoxy matrix. The resin is an EPOLAM pre-polymer, EPOLAM 2020 hardener and 2020 accelerator from Axson. Glass fibres are commonly used for naval applications because of their high strength/mass ratio and their low cost compared to other reinforcements. The reinforcement consists of a plain weave fabric with 90% warp yarns and 10% weft yarns. Panels are made by an infusion process and seven orientations are studied: 0° , $\pm 20^\circ$, $\pm 30^\circ$, $\pm 45^\circ$, $\pm 60^\circ$, $\pm 70^\circ$ and 90° . The square panels, 500×500 mm, were cut into cubic samples of the geometry dimensions as shown in Table 1. The standard deviations are indicated in brackets.

Panel	Thickness, (mm)	Surface (mm ²)	Void fraction (%)	Stacking sequence	Fibre volume Fraction (%)
A	13.00 (0.1)	13×13 (0.2)	2.26	[0] ₄₀	53.5 (0.5)
B	12.52 (0.3)	13×13 (0.2)	2.00	[±20] ₂₀	54.0 (0.5)
C	13.00 (0.1)	13×13 (0.2)	1.78	[±30] ₂₀	55.0 (0.5)
D	12.78 (0.2)	13×13 (0.2)	1.69	[±45] ₂₀	54.3 (0.5)

Table 1. Geometry and fibre mass fraction of the samples, standard deviation in brackets

Two types of static compression tests are used to obtain the elastic properties of the lamina. In-plane loading (IP), parallel to the plies plane; plane (1,2), and out-of-plane loading (OP), according to the thickness; direction 3 (Figure 1). Table 2 compares the elastic values of the characteristics drawn from relations of micromechanics (Chamis, 1984) with those resulting from experimental work.

Characteristics	E ₁ (MPa)	E ₂ (MPa)	E ₃ (MPa)	ν_{12}	ν_{13}	ν_{23}	G ₁₂ (MPa)	G ₁₃ (MPa)	G ₂₃ (MPa)
Experimental	46217	16086	9062	0.28	0.41	0.097	2224	3500	4540
Rules law	42030	14524	9130	0.31	-	0.01	3441	3273	4508

Table 2. Elastic properties of E-glass/epoxy lamina

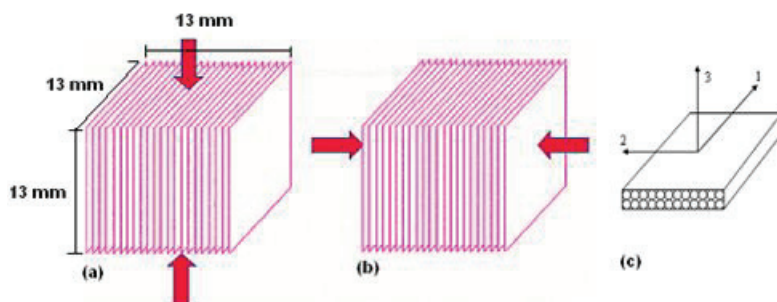


Fig. 1. Sample loadings and coordinates of axis

3. Dynamic compression loading

The split Hopkinson bar test is the most commonly used method for determining material properties at high strain rates, Figure 2. This technique of characterization, based on the response of material to wave propagation for high strain rate, was improved by Kolsky (1949).

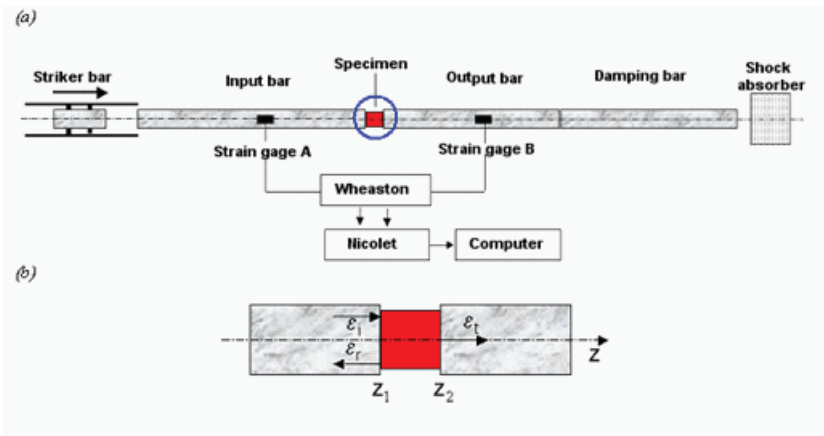


Fig. 2. Typical compressive split Hopkinson bar apparatus

3.1 Assumption for description of material deformation

We assume for the mathematical description of material deformation under dynamic impact (Zukas et al., 1992):

1. The state of the stress over the cross-sectional area is one-dimensional and uniaxial.
2. The state of the stress at any instant is homogenous and in equilibrium over the entire composite specimen.
3. Transverse strain, lateral inertia, and body forces are negligible.
4. Frictions with the interfaces bar-sample are negligible.

A wave is dispersive if it changes shape (through components which travel at different velocities). Issues related to the effect of dispersion in a SHPB at a high strain rate are worthy of verification because composite materials undergo elastic deformation under dynamic or non-uniform loading conditions, making it possible for the pulse to change in amplitude and duration during transmission through the specimen. Since the calculated axial stress in the specimen depends linearly on the axial strain on the output bar, wave dispersion would result in underestimating the strength of the specimen.

Using longer bars and a short specimen minimizes the effect of non-uniform stress and non-equilibrium within the specimen used in this study. Since the time to traverse the specimen is short compared to the duration of the wave, equilibrium within the specimen is satisfied by the possible multiple reflections, (Ravichandran & Subbash, 1994). Thus, stress will be homogenous within the specimen, satisfying assumption (3). Transverse strain, lateral inertia, and body forces are all negligible since the rise time condition is satisfied and the impact is parallel to the longitudinal direction. Validity of the SHPB for application to the dynamic behaviour of materials is well documented (Zhao & Gary, 1996), (Follansbee & Frantz, 1983).

3.2 Stress, strain and strain rate in the specimen

Dynamic loading of the composite panels is provided by a SHPB for compression tests. The longitudinal impact load F_0 of the striker generates the uniaxial stress pulse transmitted to the input bar as:

$$\sigma(t) = \frac{F_0}{S_b} = (\rho c_0) V_p(t) \quad (1)$$

c_0 is the velocity of the wave pulse, bars of S_b is the bars cross-section area, $V_p(t)$ the particle velocity, and ρ the density of the striker material. Accurate measurements of the wave pulse and particle velocity in dynamic impact studies are important since the wave pulse is in fact the propagation of the disturbance or vibration of the particles. The amplitude of the incident wave pulse depends on the impact velocity (a function of the applied air pressure) and material properties of the striker.

$$\frac{\partial^2 u}{\partial t^2} - c_0 \frac{\partial^2 u}{\partial z^2} = 0 \quad (2)$$

$c_0 = \sqrt{E_0 / \rho}$, E_0 is the Young modulus and $u(z, t)$ the longitudinal displacement. The solution yields:

$$\frac{\partial u}{\partial z} = \frac{\alpha}{c_0} \cdot \frac{\partial u}{\partial t} \quad (3)$$

$\alpha = -1$ for wave propagation in the positive direction, $\alpha = 1$ for the wave propagation in the negative direction. It leads to solutions: $u = u(z - c_0 t)$ for $\alpha = -1$ and $u = u(z + c_0 t)$ for $\alpha = 1$.

The particle velocity is as follow:

$$V_p(z, t) = \frac{\partial u(z, t)}{\partial t} \quad (4)$$

Velocities with the interfaces specimen/bars are: $V_1 = dZ_1/dt$ and $V_2 = dZ_2/dt$.

where $Z_1 = z_1 + u(z_1, t)$ and $Z_2 = z_2 + u(z_2, t)$

With the deformation, the length of the specimen is $L = Z_2 - Z_1 = u(z_2, t) - u(z_1, t) + L_0$

where $L_0 = z_2 - z_1$. Then:

$$L = L_0 - \int_0^t (V_2 - V_1) dt \quad (5)$$

Equations (6) and (7) give respectively, the strain, the stress and the strain rate in the sample. ϵ_i , ϵ_r , ϵ_t being respectively the incidental and reflected deformations pulse at the input bar/specimen interface and that transmitted by the interface specimen/output bar interface, Figure 1b. Those are determined by transport formulas of the signals of the gauges towards the interfaces specimen/bars. This transport takes into account the correction of the dispersive character of the propagation, of the deformations pulse in the bars, by optimization of the decomposition coefficients, in series of Fourier, of the signals. The particles in the input bar will propagate to the right at a relative velocity of V_b in the longitudinal direction of the wave pulse. With a specimen of cross-sectional area S_0 ,

sandwiched between the input and output bars, equilibrium at the interfaces is satisfied by the continuities of forces and velocities at the interfaces such that the particle velocities, sample stress, strain and strain rate for a thin sample are derived as:

$$V_s = V_t - (V_i + V_r) \text{ with } \begin{cases} V_i = -c_0 \cdot \epsilon_i \\ V_r = c_0 \cdot \epsilon_r \\ V_t = -c_0 \cdot \epsilon_t \end{cases} \rightarrow V_s = -c_0 [\epsilon_t + \epsilon_r - \epsilon_i] = -2c_0 \epsilon_r \quad (6)$$

Assuming equilibrium in short specimen, $\epsilon_t = \epsilon_i + \epsilon_r$; the strain, strain rate and stress is:

$$\begin{aligned} \epsilon_s &= -\frac{2c_0}{L_0} \int_0^t \epsilon_r(t) dt \\ \frac{d\epsilon_s}{dt} &= -\frac{2c_0}{L_0} \epsilon_r(t) \\ \sigma_s &= \frac{S_b}{S_0} E_0 \epsilon_t(t) \end{aligned} \quad (7)$$

3.3 Data processing procedure

The dynamic compression test conducted in this study consists in placing a cubic sample (13mm in length) between two bars with a high elastic limit, called input bar and output bar. The bar diameter was 20mm. The striker bar was 0.8m long, while the incident bar length was 3m and the transmission bar 2m. These bars are correctly aligned and are able to slide freely on their support. The composite specimen is not attached to the bar in order to prevent the perturbations of measurements due to additional interfaces. The experimental set-up consists of (1) a stress generating system which is comprised of a split Hopkinson bar and the striker, (2) a specimen, (3) a stress measuring system made up of sensors (typically, resistance strain gauges), and (4) a data acquisition and analysis system. The signals are treated with Maple Software using Fast Fourier Transformation to obtain the evolution of the dynamic parameters: stress vs. strain, strain rate vs. time, incident and transmitted load and velocity at the interfaces input bar/sample and output bar/sample vs. time.

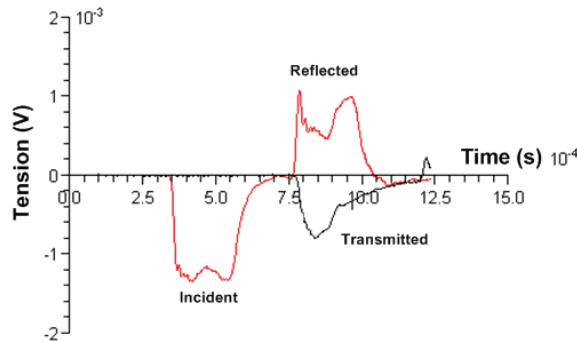


Fig. 3. Typical incident, reflected and transmitted pulse, $[\pm 60]_{20}$ IP test, $P=0.9$ bar

The specimens $[0]_{40}$, $[\pm 20]_{20}$, $[\pm 30]_{20}$, $[\pm 45]_{20}$, $[\pm 60]_{20}$, $[\pm 70]_{20}$ and $[90]_{40}$ were subjected to the in-plane (IP) and out of plane (OP) loading with nine different impact pressures of the striker bar on the input bar: 0.5, 0.6, 0.7, 0.8, 0.9, 1.0, 1.2, 1.4 and 1.6 bar. A typical set of incident, reflected, and transmitted signals resulting from gauges A and B recorded by the digital oscilloscope from a SHPB experiment on the composite at the strain rate of 831 s^{-1} for 60° IP test is shown in figure 3.

4. Dynamic response

Before launching the experimental study for a dynamic case, it is necessary to ensure that the tests can be reproduced. With this objective in mind, for each fibre orientation, a minimum of three tests were carried out at the same impact pressure in order to analyze the tests reproducibility. As figure 4a shows, it is noted that the tests are repeatable and a fact that was checked for each test. Figures 4b and 4c show the velocities and the loads at two faces of specimen. For in-plane and out of plane tests, results for compressive strain rates between 200 s^{-1} and 2000 s^{-1} are obtained using SHPB. Figure 4d shows the evolution of the strain rate versus time. The maximum value is taken into account for the analysis of the experimental results.

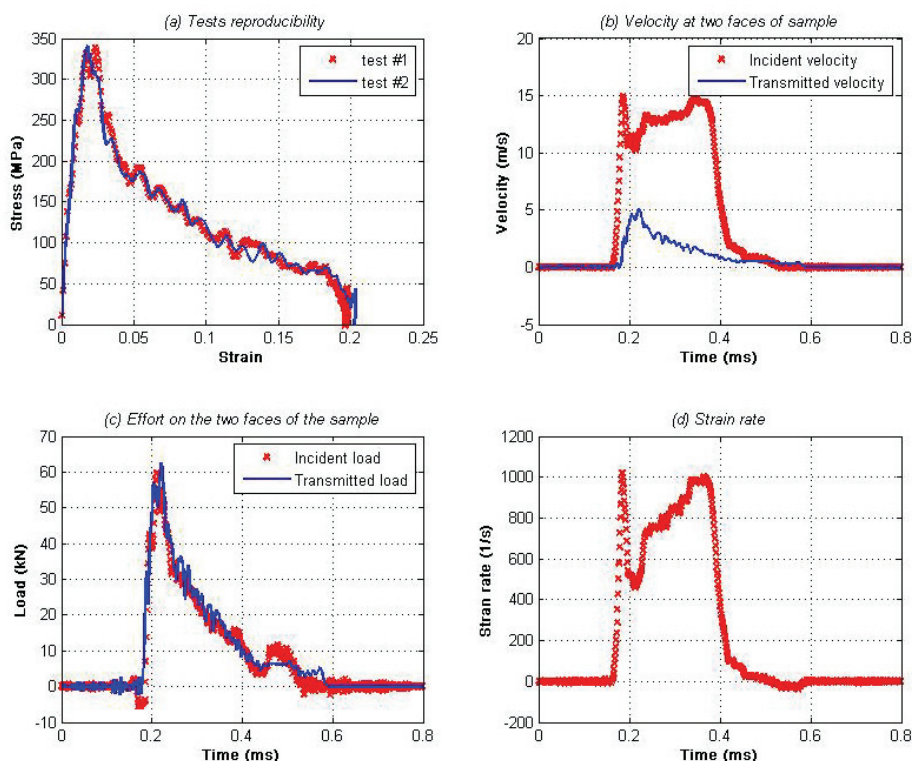


Fig. 4. Test reproducibility, IP test for $[\pm 30]_{20}$, $P=1.2$ bar

4.1 For in-plane tests

The strain rate evolution is sensitive to the entry pressure P in the chamber of compressed air (impact pressure of the striker on the input bar), the loading direction and the sample lay-up (angle θ). The fibre orientation has an effect on the strain rate evolution. Figure 5 gives an example of the evolution of the strain rate vs. time of $[0^\circ]_{40}$, $[\pm 20^\circ]_{20}$, $[\pm 30^\circ]_{20}$, $[\pm 45^\circ]_{20}$, $[\pm 60^\circ]_{20}$, $[\pm 70^\circ]_{20}$ and $[90^\circ]_{40}$. The presence of a second peak is the principal characteristic of these curves, which characterizes the onset of macroscopic damage, which we will see in detail in section 5. The critical pressure P_c responsible for the appearance of a second peak is shown in table 3. The appearance of a second peak is around 1.4bar for $[0^\circ]_{40}$ and between 0.6-0.9bar for the other orientations.

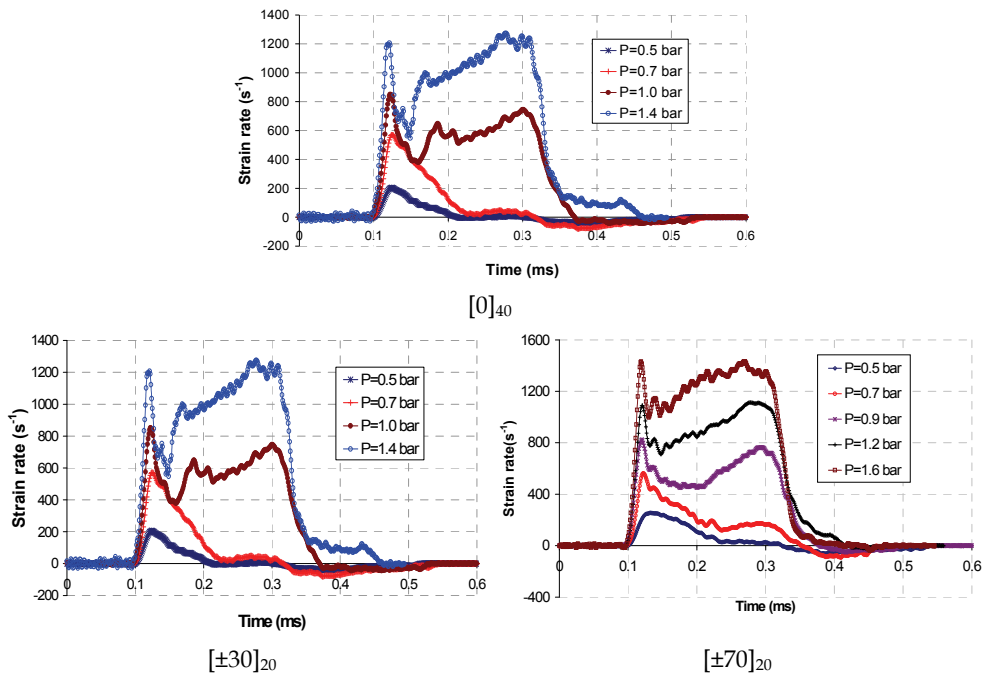


Fig. 5. Strain rate versus impact pressure and stress-strain curve evolution, IP test

IP Tests	0°	$\pm 20^\circ$	$\pm 30^\circ$	$\pm 45^\circ$	$\pm 60^\circ$	$\pm 70^\circ$	90°
P_c (bar)	1.2-1.4	0.9	0.8-0.9	0.8	0.7-0.8	0.7	0.6

Table 3. Critical impact pressure for appearance of second peak

The dynamic behaviour for IP tests is dominated by compressive properties of the polymeric matrix and the damage kinetics is affected by fibre orientation. For non damaging tests, the fall of strain rate reaches negative values, which correspond to the springback in the sample. The combination of $\dot{\epsilon} = f(t)$ and $\sigma = f(t)$ curves, which will be discussed in the next paragraph, reveals that the second peak corresponds to the fall of stress in the

sample. The glass/epoxy composite materials present a high strength on compressive dynamic loading for out-of-plane tests (Bancroft, 1941).

Figure 6 shows the dynamic behaviour of the laminates for the 9-impact pressure. One can note that couple $[\pm 20^\circ]_{20}$ - $[\pm 30^\circ]_{20}$ and $[\pm 60^\circ]_{20}$ - $[\pm 70^\circ]_{20}$ have similar tendencies. For the $[90^\circ]_{40}$ laminate, a brittle behaviour is noted, which is controlled by matrix failure. According to the various orientations, the nonlinear part of the $\sigma = f(\epsilon)$ curves is different and corresponds to different damaging modes.

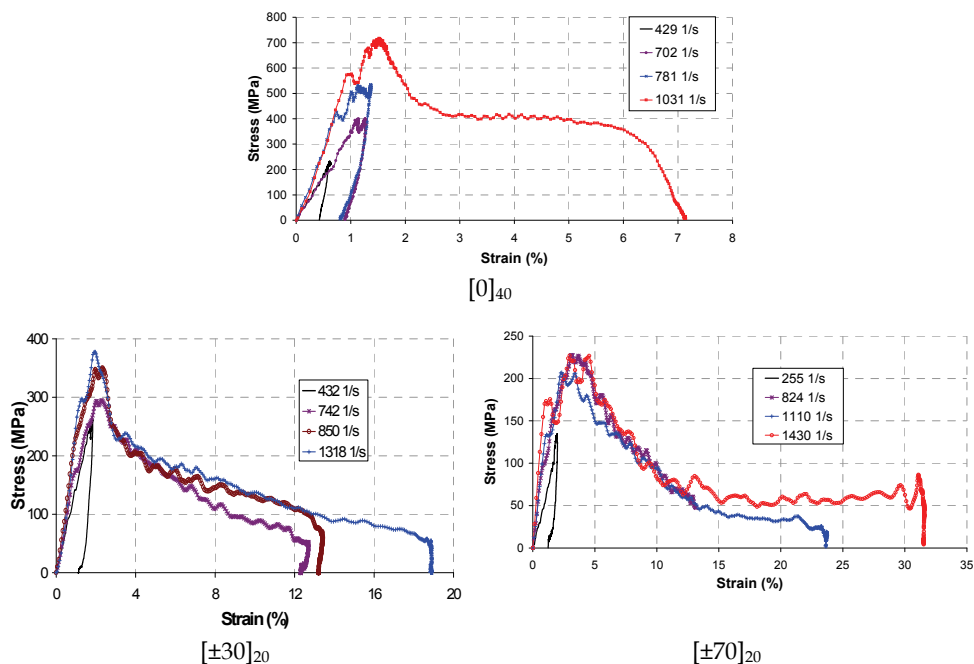


Fig. 6. Strain rate versus impact pressure and stress-strain curve evolution, IP test

With a view to simplifying the graphic representations, the analyzed parameters $E_{dynamic}$ and σ_{max} will be given according to the impact pressure (P) and the fibre orientation θ (Teta). Figure 7 shows the detailed trends of dependencies of $E_{dynamic}$ and σ_{max} on both fibre orientation and impact pressure. At a given impact pressure, the origin stiffness evolution with fibre orientation presents a minimum around 55° - 65° . This tendency is not encountered in quasi-static loading for which a monotonic decrease associated with the fibre orientation increase of 0° to 90° can be analytically proved. This tendency can be explain by the fact that strain rate is not constant at a given impact pressure, as shown in Figure 8, and viscoelastic effects cannot be neglected. For the various orientations, the laminate stiffness $E_{dynamic}$ and the maximum stress σ_{max} increase with the impact pressure until a pressure threshold is reached from which the tendency is reversed; i.e. they decrease with the increase of impact pressure. Table 3 gives the pressure thresholds. The thermal softening due to inelastic heat dissipation and damage may explain this behaviour.

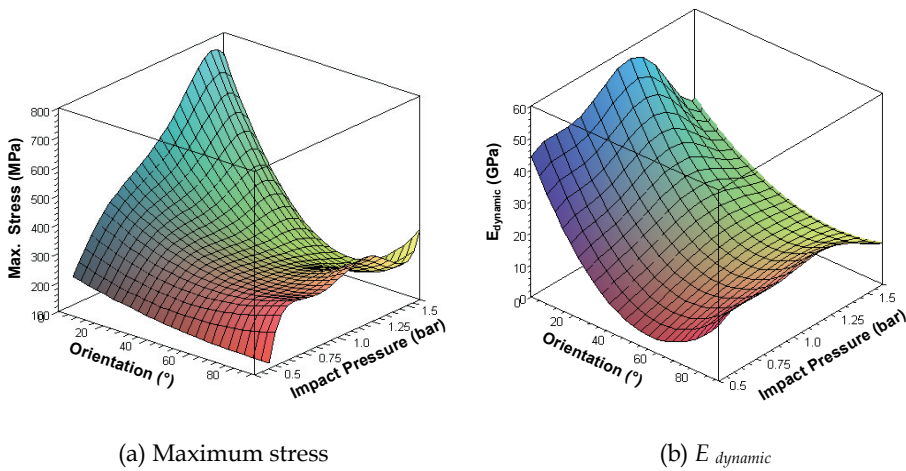


Fig. 7. σ_{max} and $E_{dynamic}$ versus P and θ

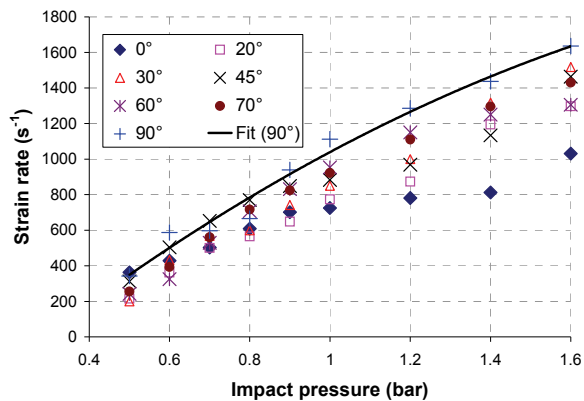


Fig. 8. Strain rate versus impact pressure for different fibre orientations

4.2 For out-of-plane tests

For out-of-plane (OP) tests, figure 8 give the evolution of the strain rate of $[0^\circ]_{40}$, $[\pm 20^\circ]_{20}$, $[\pm 30^\circ]_{20}$ and $[\pm 45^\circ]_{20}$ samples for 9 impact pressures. The appearance of a second peak is around 0.9bar for $[0^\circ]_{40}$ and 1.4bar for the other orientation, Table 4. The dynamic behaviour is dominated by compressive properties of the polymeric matrix and the damage is created for high impact pressure. The fibres orientation affects the initiation and propagation of damage. For undamaging tests, the fall of strain rate passes by negative values, which correspond to the springback in the sample. The glass/epoxy composite materials present a high strength on compressive dynamic loading for OP tests.

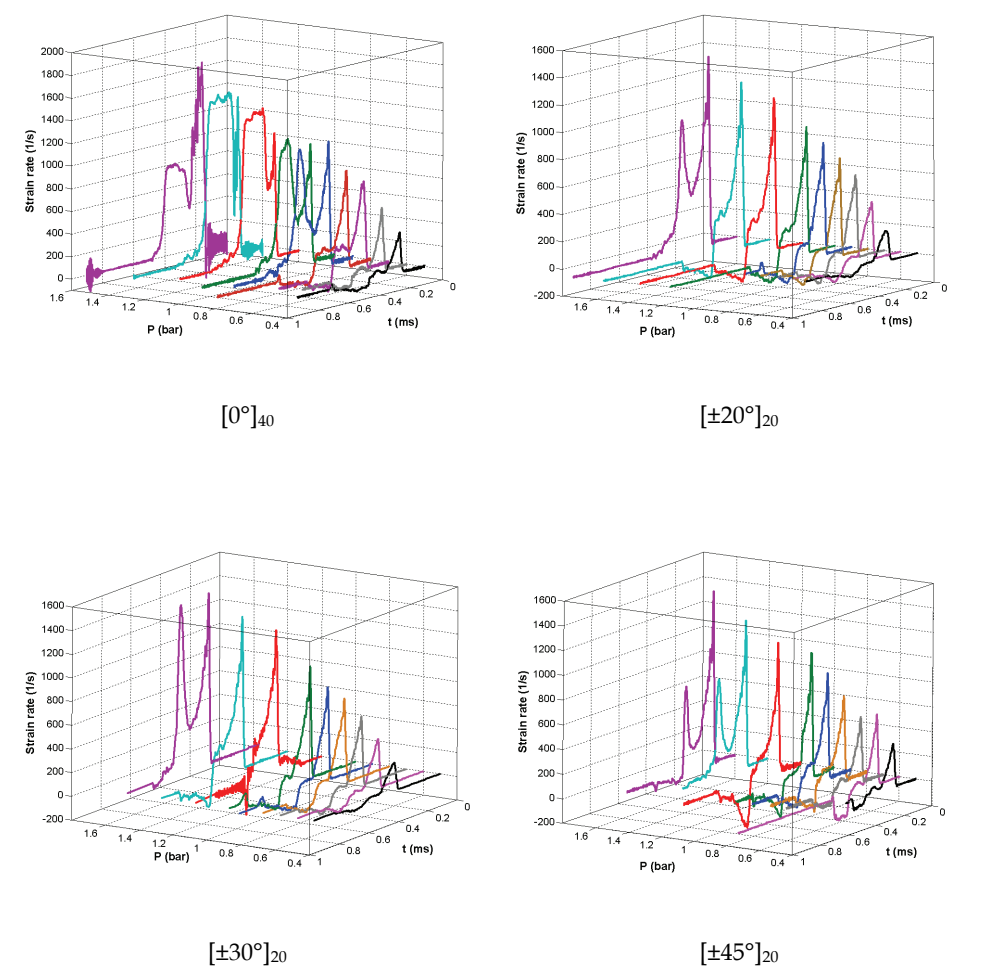


Fig. 9. Strain rate evolution versus impact pressure

OP Tests	$[0^\circ]_{40}$	$[\pm 20^\circ]_{20}$	$[\pm 30^\circ]_{20}$	$[\pm 45^\circ]_{20}$
P_c (bar)	0.9	1.6	1.6	1.4

Table 4. Critical impact pressure for appearance of second peak

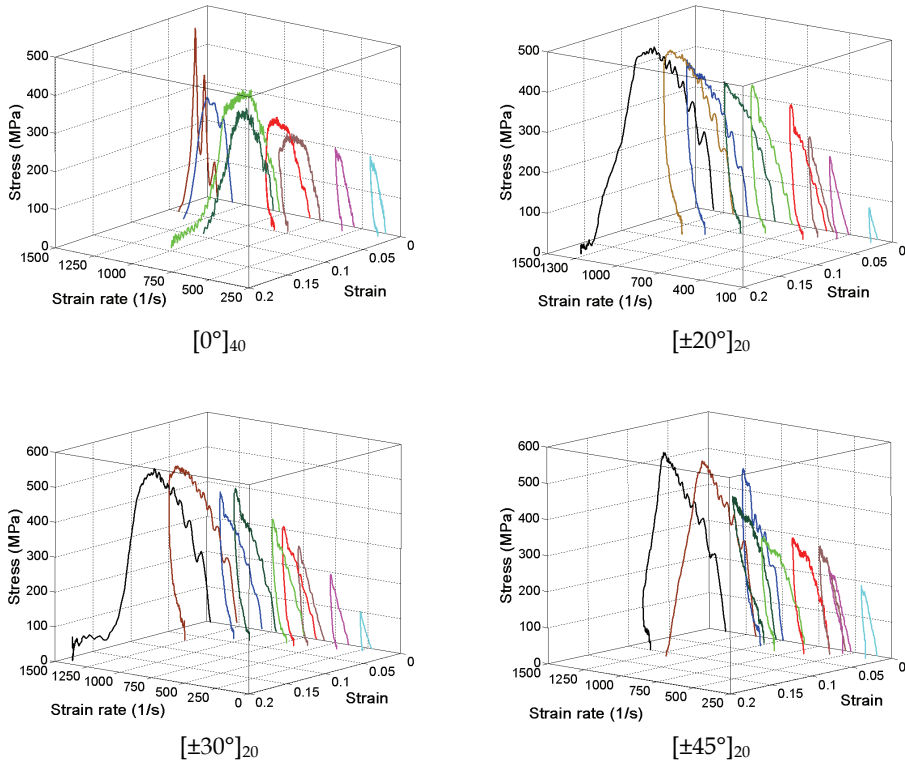


Fig. 10. Stress - Strain curves evolution versus strain rate

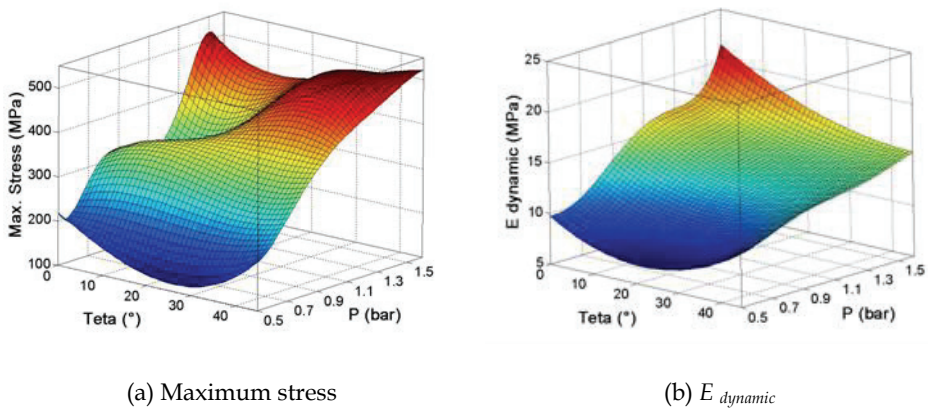


Fig. 11. σ_{max} and $E_{dynamic}$ versus P and θ

One can note that [20/70] and [30/60] have similar dynamic response, Figure 10. The unloading part of $\sigma = f(\epsilon)$ curves indicates if there is plasticity or other damaging modes. The second peak of $\dot{\epsilon} = f(t)$ curves corresponds to the fall of stress in the sample. The dynamic behaviour of the various laminates is strongly affected by the strain rate and fibres orientation, Figure 11. For OP tests, there is always an increase in $E_{dynamic}$ and σ_{max} with the increase in the impact pressure. There is not threshold effect for OP loading; the transitional pressure does not exist.

5. Kinetics of macroscopic damage

Damage tolerance is an important parameter for the use of composite materials in technologically advanced sectors and in particular for military naval applications. This characterization involves drawing up a history of the damage kinetics of the specimens from initiation to complete failure. Several techniques are used to examine the extent of damage. First, during the dynamic compression high-speed photography and infrared cameras are used to follow the damage in the samples. Frames taken in real time are used to illustrate the evolution of the damage. Impacted samples are inspected by optical techniques and fluorescent dye is applied to improve damage visualization. The onset of macroscopic damage can also be located by the presence of a second peak on the $\dot{\epsilon} = f(t)$ curve. These various techniques make it possible to follow the macroscopic and microscopic damage. The failure modes preserved in the specimens after mechanical loading at various impact pressures thus well define damage and failure loading history at high impact pressure. According to the results stated previously, it can be concluded that the damaging mode mainly depends on the fibre orientation and the loading direction without significant strain rate effect.

5.1 For in-plane tests

Based on the results obtained five damaging modes for 0° , 20° - 30° , 45° , 60° - 70° and 90° were determined. Figures 12 to 20 summarize the damaging modes for the various laminates. Each figure outlines the specimen's history of damage initiation up to final failure.

In this section we will discuss the damage that occurs in dynamic compression for the various orientations. Through this analysis, we will establish a history of defect development in the samples until final failure.

a) For $[0^\circ]_{40}$ laminates

The damage for the $[0]_{40}$ laminate occurs for an impact pressure higher than 1.4bar ($\dot{\epsilon} = 845s^{-1}$). The damage is initiated by matrix plasticity, which can be detected on the $\sigma = f(\epsilon)$ curves, Figure 6. It is followed by cracks crossing the layers of the laminate and forming the letter V. The branches of the letter V are due to layer shearing. The shearing mode generates buckling of local layers and matrix cracks. After that, a delamination is initiated with the point of V followed by dilation in the transverse direction that involves a buckling of the external layers. At the end of dynamic compression, this buckling involves a delamination and a separation of several layer blocks. Figure 12 illustrates the evolution of damage.

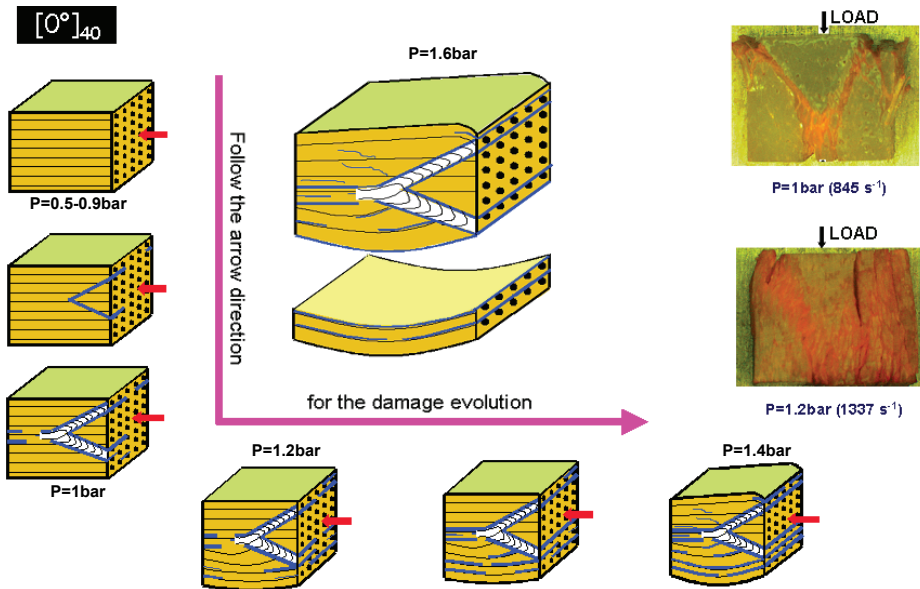


Fig. 12. Damage history of $[0^\circ]_{40}$ for IP tests at high pressure

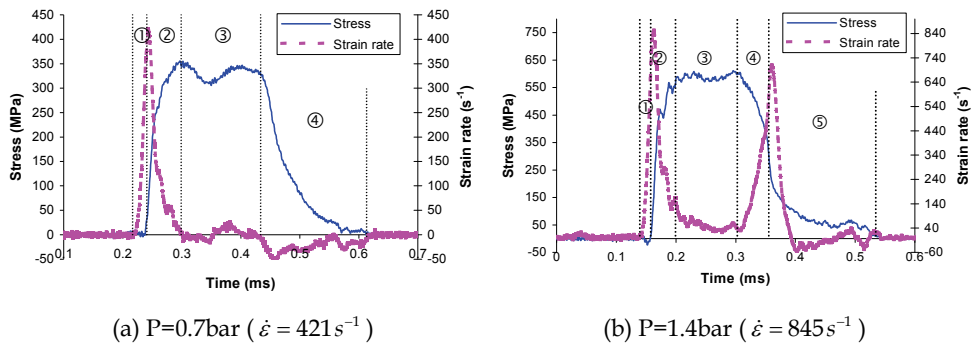


Fig. 13. Strain rate and stress curves for $[0^\circ]_{40}$

The macroscopic damage can also be detected by the presence of a second peak on the $\dot{\epsilon} = f(t)$ curve. As shown in figure 13, a fall in stress occurs at the appearance of this peak, which is associated to the formation of the letter V and delamination on the external layers. In the curves describing the strain rate and stress evolution during the test, one can distinguish various zones, which can be summarized as follows:

- i. For non damaging tests, Figure 13a
 - Zone ①: fast evolution of $\dot{\epsilon}$, which can be interpreted by the self-installation of the sample between the bars. Indeed, the parallelism of the sample facets in contact with the bars is not 100% guaranteed, which accounts for clearance and zero stress in this zone.

- Zone ②: Once perfect contact is ensured, the strength of material generates a drop in $\dot{\epsilon}$ and an increase in σ .
- Zone ③: evolution of σ translates the incidental signal evolving around an average value with $\dot{\epsilon}$ tending towards a zero value. When $\dot{\epsilon}$ tends towards zero, the sample reaches maximum compression under maximum stress.
- Zone ④: in this zone, $\dot{\epsilon}$ changes sign whereas σ starts to decrease; the specimen began to relax. This behaviour can be interpreted by the specimen springback, which is carrying out by an analysis of stereotypes taken by high-speed photography. At the end of this zone, the two signals are cancelled at the same time.
- ii. For damaging tests, Figure 13b
 - Zone ① : same observations as for zone 1 of the non damaging tests.
 - Zone ② : Once perfect contact is ensured, material strength generates a drop in $\dot{\epsilon}$ and an increase in σ .
 - Zone ③ : the stress evolution represents dynamic compression with a constant average value of σ and $\dot{\epsilon}$. In this zone, where σ reaches its maximum value, more marked fluctuations compared to the non damaging test. One can explain this phenomenon by the appearance of the damage on a microscopic scale.
 - Zone ④ : the accumulation of microscopic damage involves the appearance of a macroscopic defects. Inherent damage in the specimen generates a rapid fall in the stress with a rapid increase in $\dot{\epsilon}$.
 - Zone ⑤: the damaged specimen becomes more compact, which causes a sharp drop in $\dot{\epsilon}$. In this zone, σ always decreases but in a way less marked than in zone 4. One can note that the appearance of the damage brings about the disappearance of the springback behaviour.

b) For $[\pm 20^\circ]_{20}$ and $[\pm 30^\circ]_{20}$ laminates

The impact pressure 0.8bar corresponds to a critical phase where the kinetics of damage evolves differently; this is why the analysis for each laminate will comprise two parts:

i. Pressures lower than 0.8-0.9bar

For this range of pressures, $[\pm 20^\circ]_{20}$ and $[\pm 30^\circ]_{20}$ laminates undergo only "plastic deformations" which can be quantified in the same way as for the other laminates by analyzing $\sigma = f(\epsilon)$ curves. The damage for $[\pm 30^\circ]_{20}$ laminate appears for lower impact pressures.

ii. Pressures higher or equal to 0.8-0.9bar

• In-plane view

At the beginning, the compression wave generates a deformation on the entire sample. As compression evolves, one can see delamination, which occurs in the opposite sides of the sample. The size and the incidence of this damage become increasingly significant as a result of increasing pressures and they start to cross the sample starting from pressure 1 bar, Figure 14.

• Out-of-plane view

The first damage occurs in the layers plane. Indeed compression generates a crack along the diagonal of the external layers and can sometimes occur along the two diagonals. These cracks can cause the failure of the weft or warp yarns. Figure 14 illustrates the stages of the crack formation along the diagonal.

The same damage history occurs for $[\pm 20^\circ]_{20}$ and $[\pm 30^\circ]_{20}$ but the initiation is generated at a high impact pressure for $[\pm 20^\circ]_{20}$.

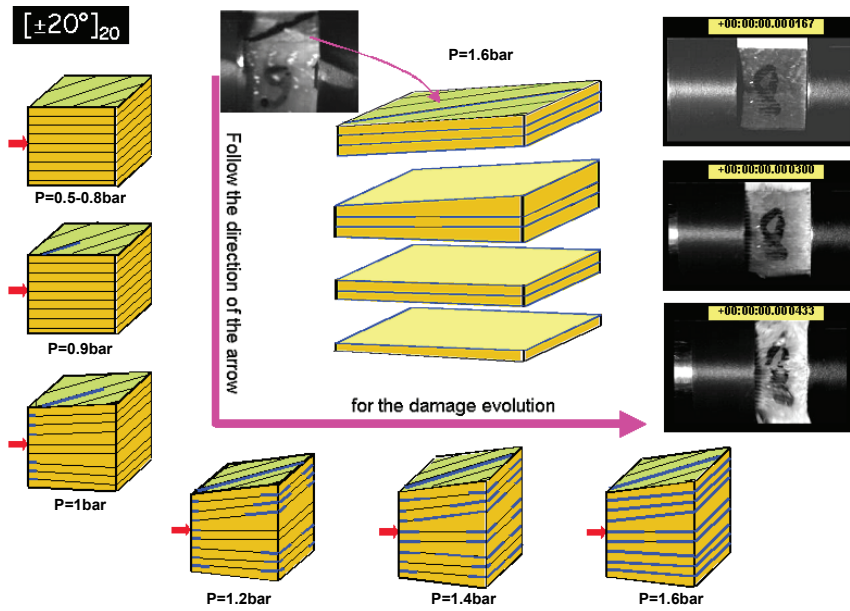


Fig. 14. Damage history of $[\pm 20^\circ]_{20}$ (and $[\pm 30^\circ]_{20}$) for IP tests at high impact pressure

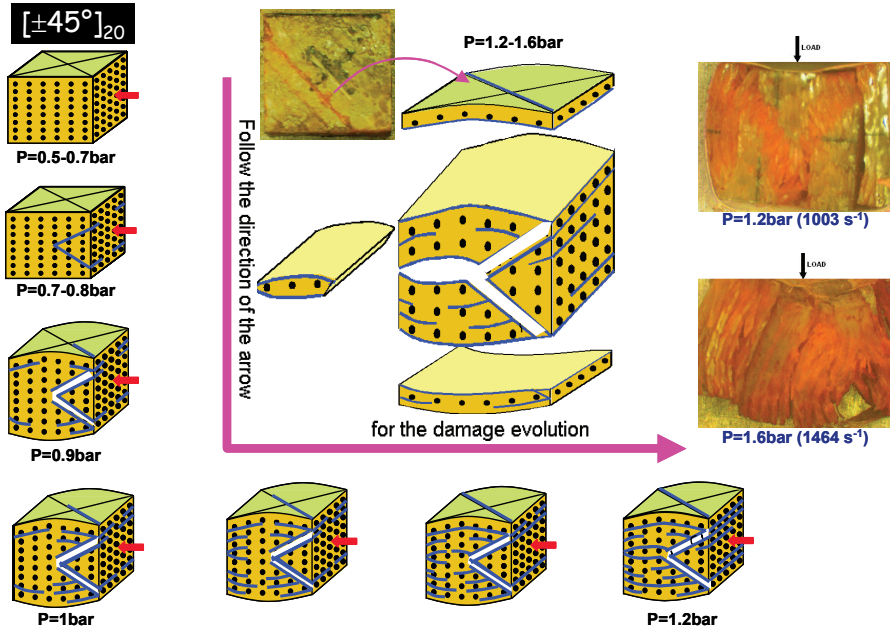
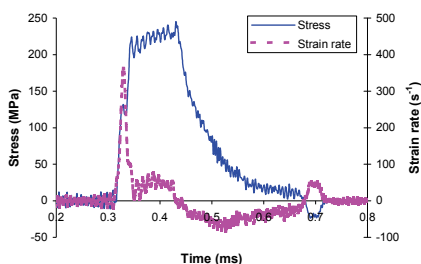


Fig. 15. Damage history of $[\pm 45^\circ]_{20}$ for IP tests at high impact pressure

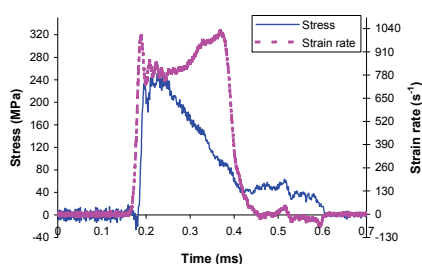
c) For $[\pm 45^\circ]_{20}$ laminates

The damage for $[\pm 45^\circ]_{20}$ laminates occurs for an impact pressure below 0.8bar. The damage is initiated by a crack forming the letter V. This shearing generates local layer buckling and cracks. Compression also generates a crack according to the diagonal of the external layers. The evolution of this compression generates substantial displacement in the thickness direction with a buckling of the external layers. This involves delamination and the final failure is caused by a separation of several layers block, Figure 15.

Figure 16 shows that stress falls with the appearance of a second peak. A comparison of figure 13 and 16 illustrates the difference between $[0^\circ]_{40}$ and $[\pm 45^\circ]_{20}$ on dynamic behaviour and damage kinetics. The macroscopic failure is more brittle for $[0^\circ]_{40}$ than for $[\pm 45^\circ]_{20}$ since the buckling effect is stronger (higher longitudinal stiffness) for $[0^\circ]_{40}$ laminates than for $[\pm 45^\circ]_{20}$ laminates.



(a) $P=0.6\text{bar}$ ($\dot{\epsilon} = 369\text{s}^{-1}$)



(a) $P=1.2\text{bar}$ ($\dot{\epsilon} = 1003\text{s}^{-1}$)

Fig. 16. Strain rate and stress curves for $[\pm 45^\circ]_{20}$

d) For $[\pm 60^\circ]_{20}$ and $[\pm 70^\circ]_{20}$ laminates

The damage for $[\pm 60^\circ]_{20}$ and $[\pm 70^\circ]_{20}$ laminates occurs for an impact pressure between 0.7 and 0.8 bar.

i. Pressures lower than 0.7-0.8bar

For this impact pressure, slight plastic strain is detected by analyzing the stress-strain curves.

ii. Pressures higher or equal to 0.7-0.8bar

By analyzing the videos and frames it is of note that the dynamic compression of the samples can create three damaging modes independent of the strain rate.

- First damaging mode

The sample undergoes plastic deformation at the beginning of the shock, then compression of the sample generates a damaged zone which has the shape of the letter V on the incidental bar side. The evolution of damage in this zone generates a shearing mode between the V zone and the rest of the specimen. Under the compression wave effect, there is a buckling mode of the external layers, which leads to local delamination at pressures between 0.8 and 1bar. This leads to a delamination of packages of layers for pressures from 1.2 to 1.6bar. At the same time, the penetration of the angular point of V generates delamination of the specimen in the transmitted bar side. Figure 17 shows the stages of damage.

- Second damaging mode

This mode begins with local plasticity followed by the generation of a V zone but on the transmitted bar side. The shearing mode propagates at the tip of the V domain along the two directions formed by the letter V. At the end of this propagation, a large deformation occurs transversally and generates layer buckling under the effect of the compression wave, which causes delamination, and separation of packages of n layers. Figure 18 illustrates the three stages of the evolution of the damage.

- Third damaging mode

This damaging mode seldom occurs, it begins with a local plasticity, as for the first two previous modes, followed by the formation of two V zones, one on the incidental bar side and the other on the transmitted bar side. This mode is the most severe of the three modes, this is why it can cause extensive damage even at relatively low impact pressures, Figure 19.

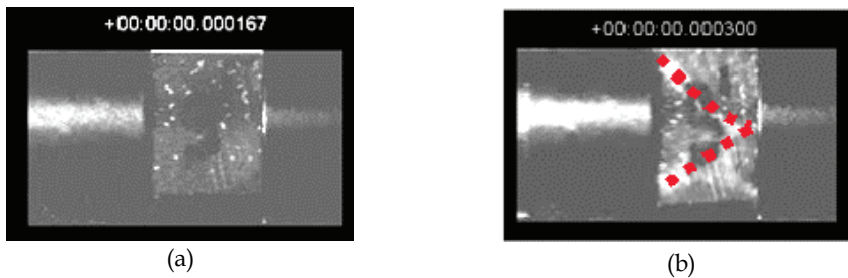


Fig. 17. First damaging mode of $[\pm 60^\circ]_{20}$ for in-plane tests

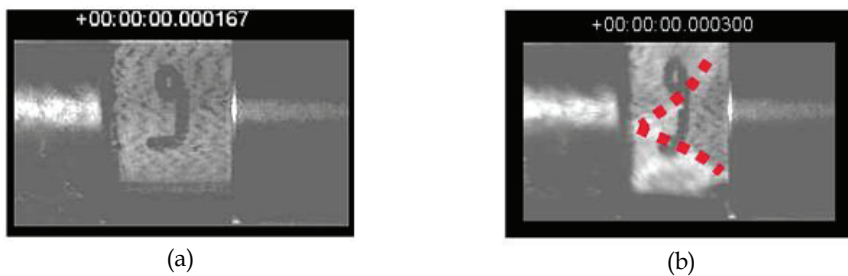


Fig. 18. Second damaging mode of $[\pm 60^\circ]_{20}$ for in-plane tests

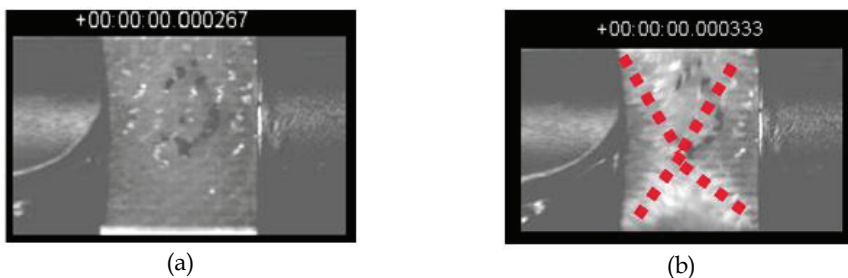


Fig. 19. Third damaging mode of $[\pm 60^\circ]_{20}$ for in-plane tests

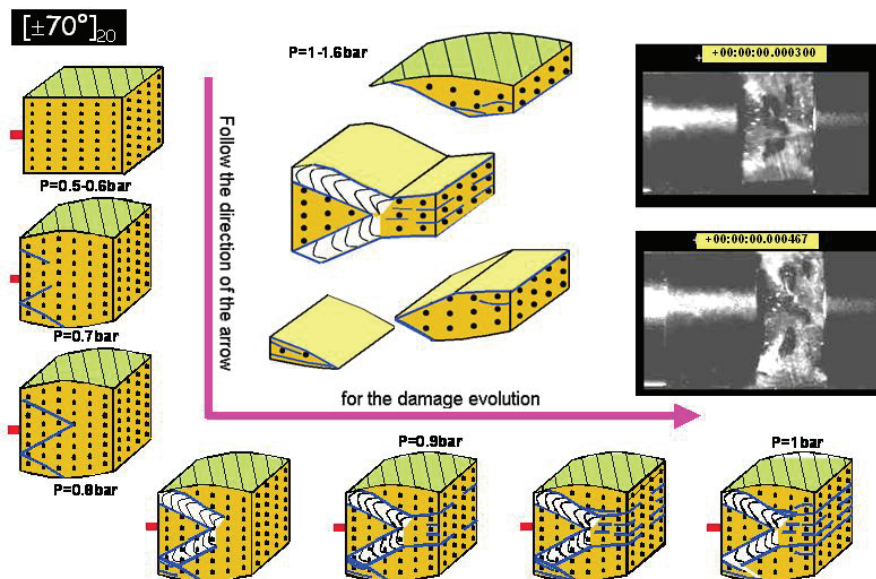


Fig. 20. Damage history of $[\pm 70^\circ]_{20}$ for IP tests at high impact pressure

The same damage history occurs for $[\pm 60^\circ]_{20}$ and $[\pm 70^\circ]_{20}$ but the fragments of the $[\pm 70^\circ]_{20}$ laminates are larger and there are few delamination modes, Figure 20.

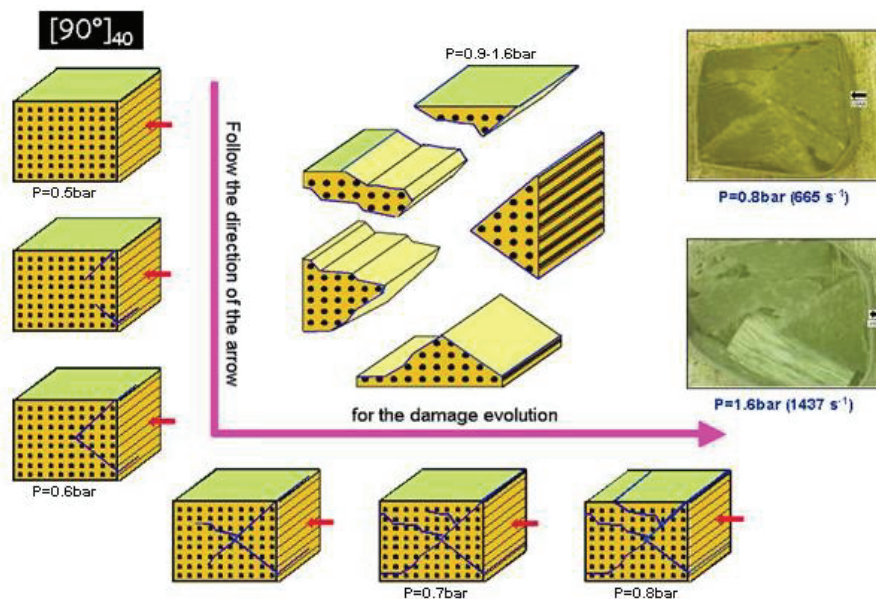


Fig. 21. Damaging modes for IP tests at high impact pressure for $[90^\circ]_{40}$

e) For $[90^\circ]_{40}$ laminates

The damage for $[90^\circ]_{40}$ specimens occurs for an impact pressure higher than 0.6bar ($\dot{\epsilon} = 587\text{s}^{-1}$). The damage is initiated by a crack crossing the laminate layers and forming the letter V. The branches of the letter V represent macro cracks, which continue to propagate through the layers. The final failure of the laminate is generated by these cracks. This failure involves the formation of several pieces of various dimensions, Figure 21. There exists a great difference between the damaging modes of $[0^\circ]_{40}$ and $[90^\circ]_{40}$. The failure of $[90^\circ]_{40}$ is abrupt without delamination or local buckling. The fall in stress is instantaneous.

5.2 For out of plane tests

The first observation that one can make, for out-of-plane tests, is that material shows a greater strength. The damage appears only for the great impact pressures: 0.8bar for $[0^\circ]_{40}$, 1.4 -1.6bar for $([20^\circ]_{20}$ and $[30^\circ]_{20})$ and 1.4bar for $[45^\circ]_{20}$. For this lower range of impact pressure there were only residual "plastic" deformations due to matrix cracks. One can also notice that the nature of the damage is strongly affected by the laminates orientation, which stills a parameter in improving also out of plane dynamic compressive strength. The multiplication of the microscopic cracks involves the catastrophic failure. The high strength recorded for 20° and 30° can be correlated with damaging modes observed and reported in figure 22. In fact for these specimens multiple mode fracture is depicted. As the strain rate increase more damage mechanism is involved; from matrix cracking to delamination with multiple paths to final fracture. For 0° and 45° specimens a dominant path is observed along the weakest link, respectively across weft yarns and plies interfaces, which may explain the lower strength. The kinetics of damage for this direction of loading is strongly conditioned by the specimen's fibre orientations. Figures 23 and 24 summarize the history of damaging modes for the various laminates.

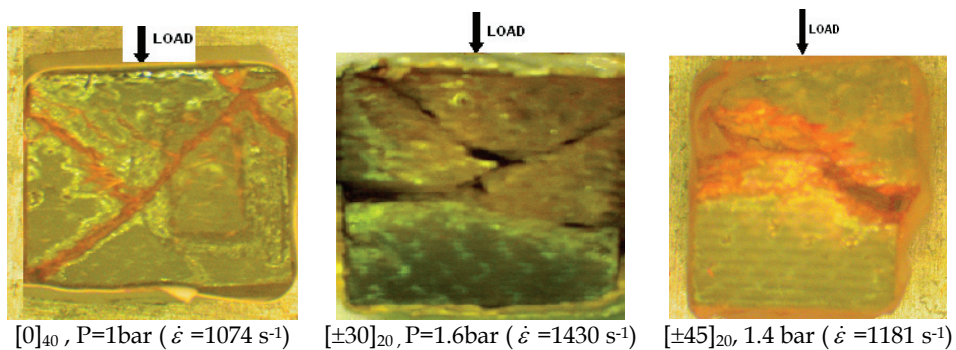


Fig. 22. Damage specimens for out-of-plane tests

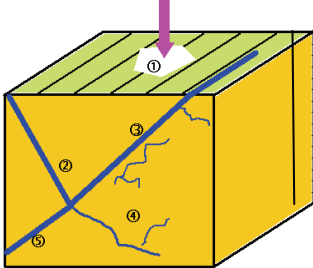
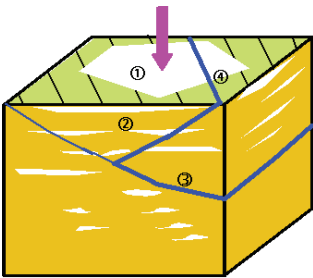
<p>$[0]_{40}$ $[90]_{40}$</p>		<p>① : Crushing of the resin in contact with the incidental bar ② : Formation of damaged zone (V shape) ③ : "Macro"-cracks ④ : "Micro"-cracks ⑤ : Propagation of ② and ③ → Failure</p>
<p>$[\pm 20]_{20}$ $[\pm 70]_{20}$</p>		<p>① : Crushing of the resin in contact with the incidental bar ② : Layers crushing with plasticity (important crushing in the direction of the incidental bar - matrix cracks) ③ : Shearing through the layers - Macro cracks ④ : Cracks in the external layers → Failure</p>

Fig. 23. Damage specimens for out-of-plane tests

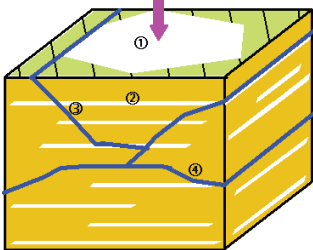
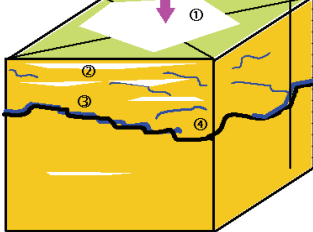
<p>$[\pm 30]_{20}$ $[\pm 60]_{20}$</p>		<p>① : Crushing of the resin in contact with the incidental bar ② : Layers crushing with plasticity (important crushing in the direction of the incidental bar - matrix cracks) ③ : Shearing through the layers - Macro cracks ④ : Cracks in the external layers → Failure</p>
<p>$[\pm 45]_{20}$</p>		<p>① : Layers crushing with plasticity ② : Micro cracks ③ : Macro cracks ④ : Propagation of ③ → Failure</p>

Fig. 24. Damaging modes for OP tests

6. Conclusions

In this work, the high strain rate material response of $[0]_{40}$, $[\pm 20]_{20}$, $[\pm 30]_{20}$, $[\pm 45]_{20}$, $[\pm 60]_{20}$, $[\pm 70]_{20}$ and $[90]_{40}$ E-glass/epoxy composite material systems was investigated. A Split Hopkinson pressure bar was used to conduct high strain rate experiments. Maximum strain rates around 2000s^{-1} were achieved. Samples were subjected to IP and OP tests. The first observation can be made, for in-plane tests, is that materials show a strength dependency on fibre orientation and impact pressure. Damage appears only for specific impact pressures: 1.2bar for $[0]_{40}$, 0.9-1bar for $([\pm 20]_{20} - [\pm 30]_{20})$, 0.9bar for $[\pm 45]_{20}$, 0.7-0.8bar for $([\pm 60]_{20} - [\pm 70]_{20})$ and 0.6bar for $[90]_{40}$. For this lower range of impact pressure there was no macroscopic damage but the existence of microscopic damage remains a possibility. It can also be noticed that the nature of the damage is strongly affected by the orientation of the laminates, a major parameter in improving dynamic compressive strength. The multiplication of the microscopic and macroscopic damage involves catastrophic failure. For these specimens a multiple fracture mode is determined and described. As the strain rate increases more damage mechanisms are involved; from matrix cracks to delamination with multiple paths to final fracture. The damage kinetics for in-plane loading is strongly conditioned by the specimen's fibre orientations. The initiation and propagation of failure mechanisms at different strain rates have been examined. Specimens fail due to fibre kinking at low strain rates, with delamination and interfacial separation dominating the high strain rate failure regime.

For OP tests, the stress-strain curves of the composite materials show that the material is strongly sensitive to fibre orientation at the same impact pressure: the initial modulus of elasticity and maximum failure stress, strain at maximum stress and the maximum strain are all dependent on fibre orientation and strain rates. The initiation and propagation of failure mechanisms at different strain rates have been examined. The most pronounced effect of increasing the strain rate results in changes in the failure modes. Off-axis composites and angle ply laminates exhibited significant nonlinear and strain dependent behaviour. The glass/epoxy composite material is more resistant for OP loading. Indeed, the damage appears for high pressure.

7. References

- Bancroft, D. (1941). The velocity of longitudinal waves in cylindrical bars. *Physical Review*, Volume 59, N° 59, 1941, 588-593.
- Brara, A. & Klepaczko, J.R. (2007). Fracture energy of concrete at high loading rates in tension. *International Journal of Impact Engineering*, Volume 34, Issue 3, March 2007, 424-435.
- Chamis, C.C. Simplified micromechanics equations for hygral, thermal, and mechanical properties. SAMPE Quarterly, 1984.
- El-Habak A.M.A. (1991). Mechanical behavior of woven glass fiber-reinforced composites under impact compression load. *Composites*, Volume 22, Issue 2, 1991, 129-134.
- Follansbee, P.S. & Frantz, C., (1983). Wave Propagation in the Split Hopkinson Pressure Bar. *Journal of Engineering Materials and Technology*, Volume 105, Issue 1, 61-66.
- Gama, B.A., Gillespie, J.W., Mahfuz, H., Raines, R.P., Haque, A., Jeelani, S., Bogetti, T.A. & Fink, B.K. (2001). High Strain-Rate Behavior of Plain-Weave S-2 Glass/Vinyl Ester Composite. *Journal of Composite Materials*. 2001; 35: 1201-1228.

- Gary, G. & Zhao H. (2000). Dynamic testing of fiber polymer matrix composite plates under in-plane compression. *Composites Part A: Applied Science and Manufacturing*, Vol. 31, Issue 8, 2000, 835-840.
- Gilat, A.; Golberg, R.K. & Roberts, G.D. (2002). Experimental study of strain rate dependent behavior of carbon/epoxy composite. *Composite Science and Technology*, 62, 1469-1476 (2002).
- Gillespie, J.W.; Gama B.A.; Cichanowski, C.E. & Xiao, J.R. (2005). Interlaminar shear strength of plain weave S2-glass/SC79 composites subjected to out-of-plane high strain rate compressive loadings. *Composites Science and Technology*, Volume 65, Issues 11-12, September 2005, 1891-1908.
- Goldsmith, W., Dharan, C.K.H. & Chang, H. (1995). Quasi-static and ballistic perforation of carbon fiber laminates. *International Journal of Solids and Structures*, Volume 32, Issue 1, January 1995, 89-103.
- Haque, A. & Ali, M. (2005). High Strain Rate Responses and Failure Analysis in Polymer Matrix Composites - An Experimental and Finite Element Study. *Journal of Composite Materials*, 3 2005; vol. 39: pp. 423 - 450.
- Harding J. (1987). The Effect of High Strain Rate on Material Properties. Materials at High Strain Rate, chapter 4, Ed. T. Z. Blazynski. *Elsevier Applied Science*, London & New York, 1987, 130-173.
- Harding J. (1993). Effect of strain rate and specimen geometry on the compressive strength of woven glass-reinforced epoxy laminates. *Composites*, Volume 24, Issue 4, 1993, 323-332.
- Hosur, M.V.; Alexander, J.; Vaidya, UK.; Jeslani, S. & Mayer A. (2004). Studies on the o-axis high strain rate compression loading of satin weave carbon/epoxy composites. *Computer and Structure* 2004; 63: 75-85.
- Hou, J. P. & Ruiz, C. (2000). Measurement of the properties of woven CFRP T300/914 at different strain rates. *Composites Science and Technology*, Volume 60, Issue 15, November 2000, Pages 2829-2834.
- Kolsky H. (1949). An investigation of the mechanical properties of materials at very high rates of loading. *Proc. Phys. Soc.*, 1949, Vol. 62B, 676-700.
- Kumar P., A. Garg. & Argawal, B.D. (1986). Dynamic compressive behavior of unidirectional GFRP for various fiber orientations. *Material letters*, 1986, Volume 4, Issue 2, 111-116.
- Ochola R. O.; Marcus K.; Nurick G. N. & Franz T. (2004). Mechanical behavior of glass and carbon fiber reinforced composites at varying strain rates. *Composite Structures*, Volume 63, Issues 3-4, February-March 2004, Pages 455-467.
- Ravichandran, G. & Subhash, G. (1994). Critical Appraisal of Limiting Strain Rates for Compression Testing of Ceramics in a Split Hopkinson Pressure Bar. *Journal of the American Ceramic Society*, Volume 77, Issue 1, pages 263-267, January 1994.
- Shi, Y. B.; Hull, D. & Price, J. N (1993). Mode II fracture of $+0/-0$ angled laminate interfaces. *Composites Science and Technology*, Volume 47, Issue 2, 1993, 173-184.
- Sierakowski R.L. & Nevill G.E. (1971). Dynamic compressive strength and failure of steel reinforced epoxy composites. *Journal of Composite Materials*. 1971, Vol. 5, 362-377.
- Tsai, J.L. & Sun, C.T. (2002). Constitutive model for high strain rate response of polymeric composites. *Composite Science and Technology* 2002;62:1289-97.

- Tsai, J.L. & Sun, C.T. (2004). Dynamic compressive strengths of polymeric composites. *International Journal of Solids and Structures*, Volume 41, Issues 11-12, June 2004, 3211-3224.
- Tsai, J.L. & Sun, C.T. (2005). Strain rate effect on in-plane shear strength of unidirectional polymeric composites. *Composites Science and Technology*, Volume 65, Issue 13, October 2005, 1941-1947.
- Vinson, J.R. & Woldesenbet, E. (2001). Fiber orientation effects on high strain rate properties of graphite/epoxy composites. *Journal of Composite Materials*, 2001, Vol. 35, 509-521.
- Vinson, J.R. & Woldesenbet, E. (2001). Fiber Orientation Effects on High Strain Rate Properties of Graphite/Epoxy Composites. *Journal of Composite Materials*, 3 2001; vol. 35: pp. 509 - 521.
- Zhao, H. & Gary, G., (1996). On the use of SHPB techniques to determine the dynamic behavior of materials in the range of small strains. *International Journal of Solids and structures*, 1996.
- Zukas, J.A., Nicholas, T., Greszczuk, L.B., Swift, H.F., Curran, D.R., (1992). *Impact Dynamics*, Wiley, New York (republished by Krieger, Malabar, FL, 1992).

Buckling and Post-buckling Analysis of Composite Plates

Elena-Felicia Beznea and Ionel Chirica
*University Dunarea de Jos of Galati
Romania*

1. Introduction

Thin walled stiffened composite panels are among the most utilized structural elements in ship structures. The composite layered panels with fibers are the most usually used in shipbuilding, aerospace industry and in engineering constructions as well. These structures possess the unfortunate property of being highly sensitive to geometrical and mechanical imperfections. These panels, unfortunately, have one important characteristic connected to big sensitivity on geometrical imperfections (different dimensions comparative with the design ones). The defects are of following types: different directions of fibers design, variations in thickness, inclusions, delaminations or initial transversal deformations.

Ship structure plates are subjected to any combination of in plane, out of plane and shear loads during application. Due to the geometry and general load of the ship hull, buckling is one of the most important failure criteria of these structures.

This is why it is necessary to develop the appropriate methodologies able to correctly predict the behavior of a laminated composite plate in the deep postbuckling region, at the collapse load, which is characterized by separation between the skin and the stiffeners, delaminations, crack propagations and matrix failure, as well as to understand its behavior under repeated buckling.

During its normal service life, a ship hull, which is composed of many curved laminated composite stringer stiffened panels, may experience a few hundreds of buckling-postbuckling cycles. Although it is well recognized that CFRP stiffened structures are capable of withstanding very deep post-buckling, yielding collapse loads equal to three - four times their buckling load (Bisagni & Cordisco, 2004, Knight & Starnes, 1988), there exists scarce knowledge in the literature about the effects of repeated buckling on the global behavior of the laminated composite panels under combined loading influences.

According to the studies, it is possible to predict on how far into the post-buckling region it is possible to increase loading without loosing structural safety.

Buckling failure mode of a stiffened plate can further be subdivided into global buckling, local skin buckling and stiffener crippling. Global buckling is collapse of the whole structure, i.e. collapse of the stiffeners and the shell as one unit.

Local plate buckling and stiffeners crippling on the other hand are localized failure modes involving local failure of only the skin in the first case and the stiffener in the second case. A grid stiffened panel will fail in any of these failure modes depending on the stiffener configuration, plate thickness, shell winding angle and type of applied load.

Over the past four decades, a lot of research has been focused on the buckling, collapse and post buckling behavior of composite shells. The simplest stiffened panel consists of only orthogonal stiffeners (stiffened orthogrid) such as longitudinal and transversal girders.

Another type of stiffener arrangement is the transversal framing system.

Different analytical tools have so far been developed by researches to successfully predict the three buckling failure modes associated with stiffened panels subjected to different loading conditions.

The use of finite-elements analysis for investigation of buckling problem of composite panels is becoming popular due to the improvement in computational hardware and emergence of highly specialized software. Depending on the degree of accuracy desired and limit of computational cost, three types of buckling analysis can be carried out. Linear bifurcation analysis is the basic analysis type which does not take into consideration the pre-buckling deformation and stresses. This analysis can accurately predict the buckling load of a geometrically perfect compression loaded panel, and the pre-buckling deformation and stress in the panel have an insignificant effect on the predicted bifurcation buckling load of the shell. The second kind of bifurcation analysis takes into consideration the nonlinear pre-buckling deformation and stresses and results in a much more accurate buckling load.

The third analysis, the nonlinear buckling analysis, allows for large nonlinear geometric deflections. Unlike the previous two bifurcation analyses that are eigenvalue problems, the nonlinear analysis is iterative in nature. In this analysis the load is steadily increased until the solution starts to diverge.

In this chapter, layered composite plates with imperfections are analysed.

1.1 Plates with initial imperfection

The composite layered panels with fibers are the most usually used in shipbuilding industry and in engineering constructions as well. Taking into account that fabrication technologies of composite materials are hand made based, the probabilistic occurrence of defects is quite too high. These panels, unfortunately, have one important characteristic connected to big sensitivity on geometrical imperfections (initial transversal deformation).

In this chapter is analyzing the buckling behavior of the plates placed between two pairs of stiffeners of the ship hull structure. Objective is to present the results obtained after buckling analysis of ship hull plates made of composite materials taking into account the transversal imperfection (spatial cosine form) due to fabrication. Due to the special behavior of the layered composite plates, the nonlinear analysis of the buckling behavior of the plates is to do. In certain cases, to determine the buckling load (ultimate strength), the failure criterion is applied. The buckling load is determined when the first failure occurs in an element, based on the Tsai-Wu failure criterion, who provides the mathematical relation for the strength under combined stresses.

1.2 Plates with delaminations

Delamination in composite structures can be a serious threat to the safety of the structure.

Delamination leads to loss of stiffness and strength of laminates under some conditions. This is particularly so in the case of compressively loaded structures as the loss of stiffness may lead to buckling, the consequences of which can be catastrophic.

Causes of delamination are many. In shipbuilding and aerospace applications, this includes manufacturing defects, as well as operationally induced defects such as bird strikes hits due

to runway debris and tool drops (aerospace), or cargo operating and slamming loading (shipbuilding).

The type of delamination that is dealt with in this report is the one that is already initiated by one of the above causes.

When a laminate is subjected to in-plane compression, the effects of delamination on the stiffness and strength may be characterised by three sets of analytical results:

- a. Buckling load;
 - b. Post-buckling solutions under increased load;
 - c. Results concerning the onset of delamination growth and its subsequent development.
- Many of the analytical treatments deal with a thin near surface delamination. Such approaches are known as "thin-film" analysis in the literature. The thin-film analytical approach may involve significant errors in the post-buckling solutions.

2. Theory, finite element and experimental modeling of perfect composite plates

The buckling of composite plates is treated with specific methods applied to each particular case. This part deals with classical bifurcation and FEM buckling analysis, discusses the relevant plate equations and their solutions and edge conditions for perfect plates. The buckling phenomena mean collapse of the structure at the maximum point in a load versus deflection curve and bifurcation buckling. The way in which buckling occurs depends on how the structure is loaded and on its geometrical and material properties. The prebuckling process is often nonlinear if there is a large bending energy being stored in the structure throughout the loading history. According to the level of bending energy, the buckling of plates can occur in two ways: the first is bifurcation buckling and the second is limit point buckling. Bifurcation buckling is an instability in which there is a sudden change of shape of the structure. A bifurcation point is a point in a load-deflection space where two equilibrium paths intersect. On a load-frequency curve, a bifurcation point can be characterized by the load-frequency curve passing through a frequency of zero with a non-zero slope.

Limit point buckling is an instability in which the load-displacement curve reaches a maximum and then exhibits negative stiffness and releases strain energy. During limit point buckling there are no sudden changes in the equilibrium path; however, if load is continuously increased then the structure may jump or "snap" to another point on the load-deflection curve. For this reason, this type of instability is often called "snap-through" buckling, because the structure snaps to a new equilibrium position. A limit point is characterized by the load-frequency curve passing through a frequency of zero with a zero slope. The load-deflection curve also has a zero slope at the point of maximum load (limit point).

Buckling analysis of a plate may be divided into three parts:

- Classical buckling analysis;
- Difficult classical effects;
- Non classical phenomena.

The classical buckling theory may be described by the curve 1-3, from the Fig. AA1 where is plotted the in-plane loading force (N) versus the transversal displacement (w) of a representative point of the plate. By supposing that the loading is applied in the median plane of the plate, no transversal displacement will occur, and in the conditions of perfect symmetry the loading may increase up to the yield point, according to the curve 1-2. At a

value over the N_{cr} , the instability may occur. At $N=N_{cr}$ one bifurcation point does exist. This means that on the curve loading-displacement, on the path 4, other way, much stable for buckling occurring does exist. At the value N_{cr} a little perturbation will generate a transversal displacement.

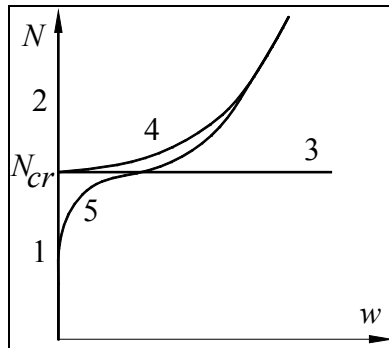


Fig. 17.1. Variation of transversal displacement, w , of a plate's point versus in-plane load N

The classical linear analysis, which is a generalization of the Euler buckling for beams, should indicate the fact that w increases to infinite at $N=N_{cr}$ (curve 3). Really, the nonlinear effects started to act and after an initial finite displacement, the in-plane loading N is increasing since the displacement is increasing. In this case the plate is able to carry loads far in excess of N_{cr} before it collapse. The latest curve (4) is so called a "postbuckling curve" because it depicts the behaviour of the plate after the buckling load N_{cr} is reached.

The difficult effects in classical buckling analysis are in connection with vibrations, shear deformations, springs, non homogeneities and variable thicknesses, nonlinear relations between stresses and strains. Non classical buckling analysis involves considerations such as imperfections, non-elastic behaviour of the material, dynamic effects of the loading, the fact that the in-plane loading is not in the initial point of the plate.

Finally, it may point out that no plate is initially perfect (perfectly flat or perfectly symmetry) and if initial deviation (from flatness or symmetry) exists, the behaviour of the plate will follow the path similar with curve 1-5. In this case, no clear buckling phenomenon may be identifying. The deviations of the plate from the flatness and symmetry are usually called imperfections (initial transversal imperfections, delaminations) as it will be treated in the following chapters.

The following cases (in numerical and experimental ways) are presented: compressive buckling, shear buckling, mixed compressive and shear buckling. The results (for linear and nonlinear model) are presented as variation of the buckling loads function of maximum transversal displacement (buckling and post-buckling behaviour).

The state of equilibrium of a plate deformed by forces acting in the plane of the middle surface is unique and the equilibrium is stable if the forces are sufficiently small. If, while maintaining the distribution of forces constant at the edge of the plate, the forces are increased in magnitude, there may arise a time when the basic form of equilibrium ceases to be unique and stable and other forms become possible, which are characterized by the curvatures of the middle surface.

The equation of the deflected surface of symmetrically laminated plates is

$$\begin{aligned}
& D_{11} \frac{\partial^4 w}{\partial x^4} + 4D_{16} \frac{\partial^4 w}{\partial x^3 \partial y} + 2(D_{12} + D_{66}) \frac{\partial^4 w}{\partial x^2 \partial y^2} + 4D_{26} \frac{\partial^4 w}{\partial x \partial y^3} + D_{22} \frac{\partial^4 w}{\partial y^4} - \\
& -N_x \frac{\partial^2 w}{\partial x^2} - 2N_{xy} \frac{\partial^2 w}{\partial x \partial y} - N_y \frac{\partial^2 w}{\partial y^2} = 0
\end{aligned} \quad (\text{AA1})$$

For symmetrically laminated cross-ply plates there is no coupling between bending and twisting. So, $D_{16}=D_{26}=0$. In this case, the equation (AA1) will have the form as the buckling equation for a homogeneous, orthotropic plate

$$D_{11} \frac{\partial^4 w}{\partial x^4} + 2(D_{12} + D_{66}) \frac{\partial^4 w}{\partial x^2 \partial y^2} + D_{22} \frac{\partial^4 w}{\partial y^4} - N_x \frac{\partial^2 w}{\partial x^2} - 2N_{xy} \frac{\partial^2 w}{\partial x \partial y} - N_y \frac{\partial^2 w}{\partial y^2} = 0 \quad (\text{AA2})$$

where D_{11} , D_{22} , D_{66} , D_{16} , D_{26} are the orthotropic plate stiffnesses, calculated according to the equation

$$D_{ij} = \frac{1}{3} \sum_{k=1}^N \bar{Q}_{ij}^k (\bar{z}_k^3 - \bar{z}_{k-1}^3) \quad (\text{AA3})$$

The thickness and position of every ply can be calculated from the equation

$$t_k = z_k - z_{k-1} \quad (\text{AA4})$$

and

$$\bar{z}_k = z_{k-1} + \frac{t_k}{2} \quad (\text{AA5})$$

The second and fourth terms from equation (AA2) are the measure of the orthotropic coupling, resulting from the fact that the principal orthotropic axes are not orthogonal with the plate geometry axes.

Linear buckling of beams, membranes and plates has since been studied extensively. A linearized stability analysis is convenient from a mathematical viewpoint but quite restrictive in practical applications. What is needed is a capability for determining the nonlinear load-deflection behaviour of a structure. Considerable effort has also been expended on this problem and two approaches have evolved: class-I methods, which are incremental in nature and do not necessarily satisfy equilibrium; and class-II methods, which are self-correcting and tend to stay on the true equilibrium path (Thurley & Marshal, 1995).

Historically, class-I was the first finite element approach to solving geometrically non-linear problems (Ambarcumyan, 1991). In this method the load is applied as a sequence of sufficiently small increments so that the structure can be assumed to respond linearly during each increment.

To solving of geometrically and material nonlinear problems, the load is applied as a sequence of sufficiently small increments so that the structure can be assumed to respond linearly during each increment.

For each increment of load, increments of displacements and corresponding increments of stress and strain are computed. These incremental quantities are used to compute various corrective stiffness matrices (variously termed geometric, initial stress, and initial strain

matrices) which serve to take into account the deformed geometry of the structure. A subsequent increment of load is applied and the process is continued until the desired number of load increments has been applied. The net effect is to solve a sequence of linear problems wherein the stiffness properties are recomputed based on the current geometry prior to each load increment. The solution procedure takes the following mathematical form

$$(K + K_i)_{i-1} \Delta d_i = \Delta Q \quad (\text{AA6})$$

where

K is the linear stiffness matrix,

K_i is an incremental stiffness matrix based upon displacements at load step $i-1$,

Δd_i is the increment of displacement due to the i -th load increment,

ΔQ is the increment of load applied.

The correct form of the incremental stiffness matrix has been a point of some controversy. The incremental approach is quite popular (this is the procedure applied in all studies in this chapter). This is due to the ease with which the procedure may be applied and the almost guaranteed convergences if small enough load increments are used.

The plate material is damaged according to a specific criterion.

For various materials classes three dimensional failure criteria are developed. These include both isotropic and anisotropic material symmetries, and are applicable for macroscopic homogeneity. In the isotropic materials form, the properly calibrated failure criteria can distinguish ductile from brittle failure for specific stress states. Although most of the results are relevant to quasi-static failure, some are for time dependent failure conditions as well as for fatigue conditions.

The buckling load determination may use the Tsai-Wu failure criterion in the case if the general buckling does not occurred till the first-ply failure occurring. In this case, the buckling load is considered as the in-plane load corresponding to the first-ply failure occurring.

The Tsai-Wu failure criterion provides the mathematical relation for strength under combined stresses. Unlike the conventional isotropic materials where one constant will suffice for failure stress level and location, laminated composite materials require more elaborate methods to establish failure stresses. The strength of the laminated composite can be based on the strength of individual plies within the laminate. In addition, the failure of plies can be successive as the applied load increases. There may be a first ply failure followed by other ply failures until the last ply fails, denoting the ultimate failure of the laminate. Progressive failure description is therefore quite complex for laminated composite structures. A simpler approach for establishing failure consists of determining the structural integrity which depends on the definition of an allowable stress field. This stress field is usually characterized by a set of allowable stresses in the material principal directions.

The failure criterion is used to calculate a failure index (F.I.) from the computed stresses and user-supplied material strengths. A failure index of 1 denotes the onset of failure, and a value less than 1 denotes no failure. The failure indices are computed for all layers in each element of your model. During postprocessing, it is possible to plot failure indices of the mesh for any layer.

The Tsai-Wu failure criterion (also known as the Tsai-Wu tensor polynomial theory) is commonly used for orthotropic materials with unequal tensile and compressive strengths. The failure index according to this theory is computed using the following equation (Altenbach & all, 2004, Ambarcumyan, 1991).

$$F.I. = F_1 \cdot \sigma_1 + F_2 \cdot \sigma_2 + F_{11} \cdot \sigma_1^2 + F_{22} \cdot \sigma_2^2 + F_{66} \cdot \sigma_6^2 + 2F_{12} \cdot \sigma_1 \cdot \sigma_2 \quad (AA7)$$

where

$$F_1 = \frac{1}{R_1^T} - \frac{1}{R_1^C}; F_{11} = \frac{1}{R_1^T \cdot R_1^C}; F_2 = \frac{1}{R_2^T} - \frac{1}{R_2^C}; F_{22} = \frac{1}{R_2^T \cdot R_2^C}; F_{66} = \frac{1}{R_{12}^2}. \quad (AA8)$$

The coefficient F_{12} , which represents the parameter of interaction between σ_1 and σ_2 , is to be obtained by a mechanical biaxial test. In the equations (AA8), the parameters R_i^C , R_i^T are the compressive strength and tensile strength in the material in longitudinal direction ($i=1$) and transversal direction ($i=2$). The parameter R_{12} is in-plane shear strength in the material 1-2 plane.

According to the Tsai-Wu failure criterion, the failure of a lamina occurs if

$$F.I. > 1. \quad (AA9)$$

The failure index is calculated in each ply of each element. In the ply where failure index is greater than 1, the first-ply failure occurs, according to the Tsai-Wu criterion. In the next steps, the tensile and compressive properties of this element are reduced by the failure index. If the buckling did not appeared until the moment of the first-ply failure occurring, the in-plane load corresponding to this moment is considered as the buckling load.

3. Finite element and experimental modeling of composite plates with initial transversal imperfection

3.1 Presentation

In this part, the buckling behavior of the plates with initial transversal deformation, placed between two pairs of stiffeners of the ship hull structure is analyzing. The results obtained on buckling analysis of ship hull plates made of composite materials taking into account the imperfection due to fabrication, are presented. Due to the special behavior of the layered composite plates, the nonlinear analysis of the buckling behavior of the plates is done. The buckling load is determined according to the first failure occurring in an element, based on the Tsai-Wu failure criterion.

The most used framing construction types for the ship deck plates made of composite materials are transversal or mixed. So, the following case of plate placed in the ship deck structure is analyzed: the plate placed between two pairs of parallel stiffeners (two transversal web frames and two longitudinal frames - longitudinal framing construction system).

The geometry of the plate is square one, having the side length of 320mm, and total thickness of 4.96mm. The layers were grouped into the macro-layers (group of layers having the same characteristics: thickness (t), direction of fibers (α) and type of material).

The imperfections of plates are considered the initial transversal deformations. The shape of the deformation is just the first form of the buckling of perfect plate clamped on the sides. The analysis presented in this part is done for the most usual magnitudes of the transversal deformation of the imperfections (versus side length of the plate) occurred in the ship deck plates after fabrication.

The following cases (in numerical and experimental ways) are presented: compressive buckling, shear buckling, mixed compressive and shear buckling. The results (for linear and

nonlinear model) are presented as variation of the buckling loads function of maximum transversal displacement (buckling and post-buckling behaviour).

The simplest stiffened plate consists of only orthogonal stiffeners (stiffened orthogrid) such as longitudinal and transversal girders. Other type of stiffener arrangement is the transversal framing system.

The characteristics of the material used in this chapter are:

$E_x=46$ GPa, $E_y=13$ GPa, $E_z=13$ GPa, $G_{xy}=5$ GPa, $G_{xz}=5$ GPa, $G_{yz} = 4.6$ GPa, $\mu_{xy}=0.3$, $\mu_{yz}=0.42$, $\mu_{xz}=0.3$,

- traction strengths $R_x=1.062$ GPa, $R_y=0.031$ GPa,
- compression strength $R_y=0.118$ GPa,
- shear strength $R_{xy}=0.72$ GPa.

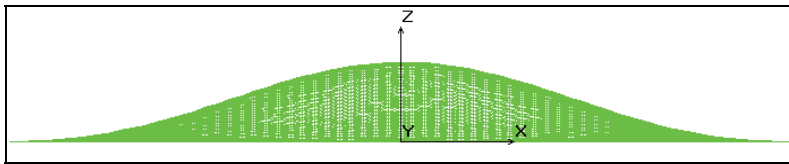


Fig. 17.2. Plate cross section in plane xz

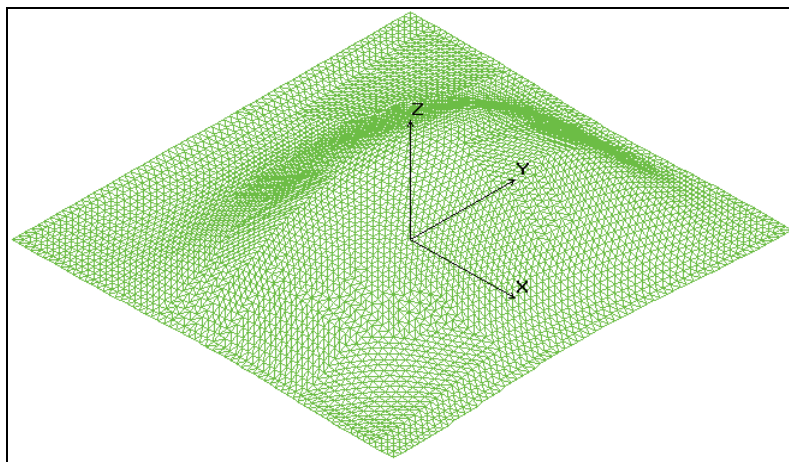


Fig. 17.3. Imperfect plate

Different analytical tools have so far been developed by researches to successfully predict the three buckling failure modes associated with stiffened panels subjected to different loading conditions. These analytical tools developed are divided into three major categories. The use of finite-elements analysis for investigation of buckling problem of composite panels is becoming popular due to the improvement in computational hardware and emergence of highly specialized software. Depending on the degree of accuracy desired and limit of computational cost, three types of buckling analysis can be carried out. Linear bifurcation analysis is the basic analysis type which does not take into consideration the pre-buckling deformation and stresses. This analysis can accurately predict the buckling load of a geometrically perfect compression loaded plate, and the pre-buckling deformation and

stress in the plate have an insignificant effect on the predicted bifurcation buckling load of the shell (Ambarcumyan, 1991, Thurley & Marshall, 1995). The second kind of bifurcation analysis takes into consideration the nonlinear pre-buckling deformation and stresses and results in a much more accurate buckling load (Adams & all, 2003, Chirica & all, 2008).

The third analysis, the nonlinear buckling analysis, allows for large nonlinear geometric deflections. Unlike the previous two bifurcation analyses that are eigenvalue problems, the nonlinear analysis is iterative in nature. In this analysis the load is steadily increased until the solution starts to diverge (Adams & all, 2003). A lot of work has been done in finite elements analysis pertaining to the investigation of buckling of stiffened panels (Beznea, 2008, Chirica & all, 2008). One of the major drawbacks associated with this tool is the tedious model-building phase involved and the subsequent inconvenient parametric study.

Following to these considerations, in this chapter the results of the buckling behavior analysing of the plates placed between two pairs of stiffeners of the ship hull structure are analysed. In the following pages only the results obtained after buckling analysis of ship hull plates made of composite materials taking into account the imperfection due to fabrication will be presented. Due to the special behavior of the layered composite plates, the nonlinear analysis of the buckling behavior of the plates is to do (Altenbach, 2004, Hilburger, 2001).

3.2 Numerical studies on compression buckling

The most used framing construction types for the ship deck panels made of composite materials are transversal or mixed. So, in this chapter the following case is presented (case of plates placed in the ship deck structure): plate placed between two pairs of parallel stiffeners (2 transversal web frames and 2 longitudinal frames, in the case of longitudinal framing construction system);

The geometry of the plates is square one, having the side length of 320mm, and total thickness of 4.96mm respectively. The orthotropic directions (a), thickness of the macro-layers (t) and plate lay-up are presented in Table AA1. The layers were grouped into the macro-layers (group of layers having the same characteristics: thickness (t), direction of fibers (a) and type of material).

The constrains are considered according to each plate. The degrees of freedom (displacements u and rotations r), considered to be zero are:

- on the sides parallel with x axis: u_z , r_x , r_y ;
 - on the sides parallel with y axis: all d.o.f. (clamped side); u_y , u_z , r_x , r_y , r_z (charged side).
- The shape of the initial transversal deformation is considered as just the first form of the buckling of perfect plate clamped on the sides (Figures AA2 and AA3).

The analysis presented in this chapter is done for the most usual magnitudes (w_0) of the transversal deformation of the imperfections (versus side length of the plate) occurred in the ship deck plates after fabrication. The following three cases are considered: $w_0=1.06\text{mm}$ (symbol 12); $w_0=3.2\text{mm}$ (symbol 32); $w_0=9.6\text{mm}$ (symbol 92).

In figures AA2 and AA3 the FEM model using shell composite elements is presented. In figure AA4, the variation of the transversal displacement of the middle point of the plate versus in-plane loading magnitude for the plate is plotted.

Since the plates have initial transversal deformation, as it is seen in the figure AA4 the increasing of the transversal deformation is starting from the beginning, which is so named buckling is starting as the in-plane load is starting to increase from 0.

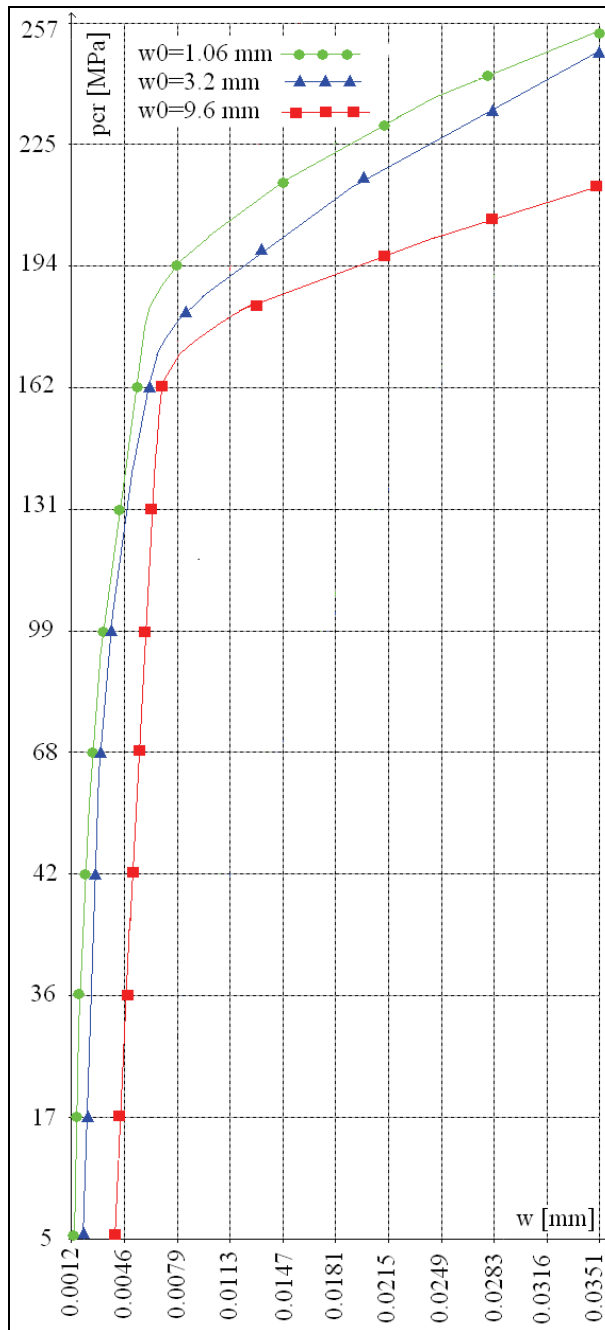


Fig. 17.4. Buckling and post buckling behaviour of compression buckling of plate with transversal imperfection

Macro-layer	α	t [mm]
1	2x0°	0.62
	45°	0.31
	2x90°	0.62
	45°	0.31
	2x0°	0.62
2	2x0°	0.62
	45°	0.31
	2x90°	0.62
	45°	0.31
	2x0°	0.62

Table 17.1. Plate lay-up

The explanation is that due to the initial deformation, the in-plane loading produces the compression in the plate and also bending in the area of imperfection. Therefore it is difficult to determine the buckling load by numerical way.

This is why we have chosen the graphical method, by drawing the asymptote to the curve in the area where the slope is changing almost suddenly.

The intersection of the asymptote with the loading axis can be considered as buckling load. Anyway the asymptote is not an unique one and we may determine the buckling loading in a range of values. Also, according to the curves the buckling load is decreasing since the amplitude of the imperfection is increasing.

So, as it is seen in figure AA4, according to the plotted asymptotes, the buckling loads of the pates are placed in the domain

$$140 \text{ MPa} < p_{cr} < 175 \text{ MPa}.$$

On the other part, we can determine the behaviour of the plate after the buckling (so name post-buckling behaviour), to estimate the ultimate capacity (ultimate strength) using one of the failure criteria. So, the in-plane loading value of first fail occurring in the material may be considered as the ultimate strength of the plate.

In the studies described in this chapter, the occurring of the first fail was done according to the Tsai-Wu failure criterion. Due to the elasticity of the thin plate, no any fail occurs for the in-plane pressure increasing up to the 260 MPa.

3.3 Experimental studies on compression buckling

The experiments were performed on plates having an initial transversal deformation with magnitude of 9.6 mm to determine the results obtained by numerical tests, such as:

- variation of the transversal displacement (w) of the point placed in the middle of the plate, on the surface, function of in-plane loading magnitude (p);
- variation of the strains in the certain point placed so on the concave face and on the convex face of the plate.

The measurements were done with the stretching machine, displacement transducer, strain gauge measurement system. In figure AA5, the plate and equipment used for experiments are shown.

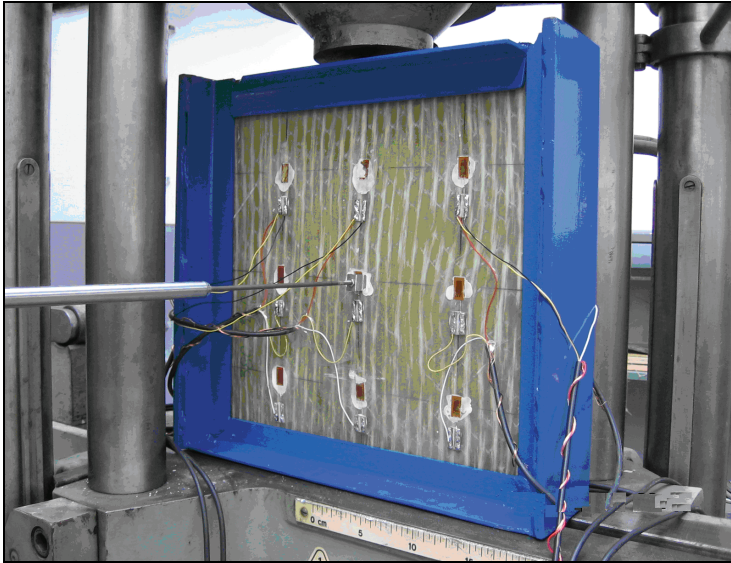


Fig. 17.5. Test rig and imperfect composite plate

To assure the boundary condition on the plate sides a special very rigid frame was made. So, the plate is clamped on three sides and simple supported on the side where the pressure is acting.

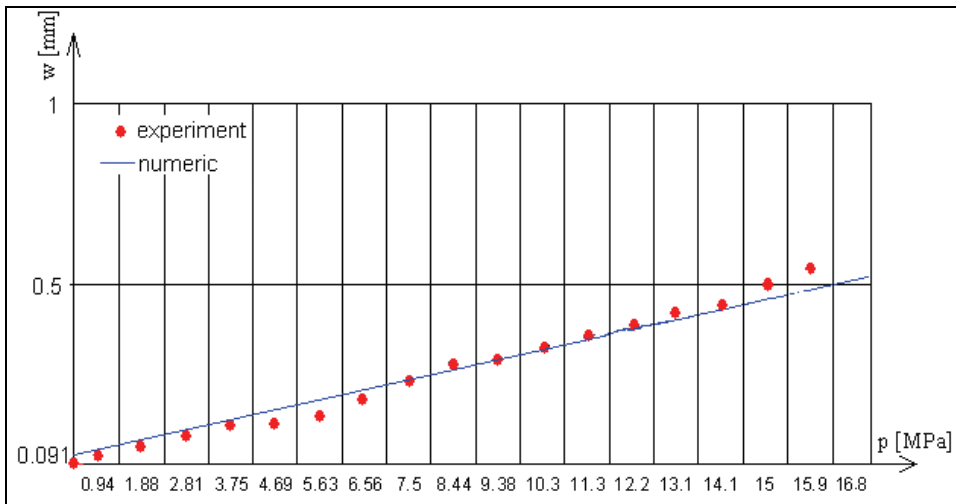


Fig. 17.6. Variation of compression load versus displacement of the point placed in the middle of the plate

In the figure AA6, the results obtained from experiments are plotted with dots. Acceptable deviations between numerical and experimental results, for the transversal displacement of the point placed in the middle of the plate, are observed. In the figures only the elastic range of the curve is presented, because the experiment was made in this domain. In the abscise, a gap for pression corresponds to a force $\Delta F = 1 \text{ kN}$.

3.4 Numerical studies on shearing buckling

The geometry of the plates is square one, having the side length of 320mm, and total thickness of 4.96mm. The orthotropic directions (α), thickness of the macro-layers (t) and plate lay-up are presented in Table AA1. The layers were grouped into the macro-layers (group of layers having the same characteristics: thickness (t), direction of fibers (α) and type of material).

The constrains are considered according to plate presented in the previous chapter. The loading acting on the plate is according to figure AA7.

The all types of amplitude of initial transversal deformation have been analysis.

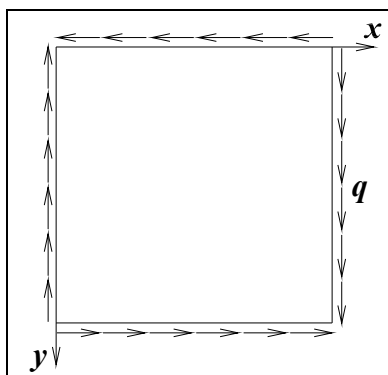


Fig. 17.7. Plate in shearing

In the table AA2 the buckling loads so for perfect and for imperfect plates are presented.

As it is seen, according to the graphical method, the buckling loads for the all three imperfect plates are in the range $104 \text{ MPa} < p_{cr} < 275.78 \text{ MPa}$. As it is seen in figure AA8, the buckling load is decreasing since the magnitude of the transversal imperfection is increasing. In this case, the load capacity of the plate is decreasing since the transversal deformation of the plate is increasing.

But, after the nonlinear calculus according to Tsai-Wu criterion, the ultimate strength, presented in table AA2, may be considered as buckling load, due to the fact the values of the ultimate strength are almost constant for all plates (15 MPa).

Failure type	Perfect plate	$w_0=1.06 \text{ mm}$	$w_0=3.2 \text{ mm}$	$w_0=9.6 \text{ mm}$
FAIL 1 (tension)	20	15	15	15

Table 17.2. Shear buckling load (ultimate strength) in [MPa]

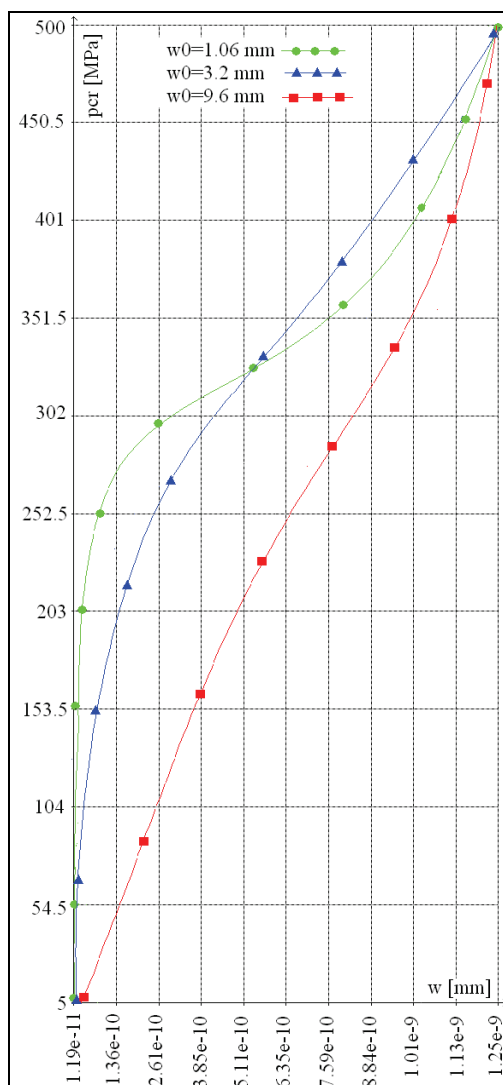


Fig. 17.8. Shear buckling and post buckling behaviour of the imperfect plate

3.5 Numerical studies on combined (compression and shear) buckling

The compression and shear buckling analysis is made only for thin plates (with material characteristics presented in previous chapter). The geometry of the plates is square one, having the side length of 320mm, and total thickness of 4.96mm. The orthotropic directions (a), thickness of the macro-layers (t) and plate lay-up are presented in Table AA1.

The constraints are considered according to plates type b from the previous chapter. The loading acting on the plate is according to figure AA9. For analysis the parametric calculus was done for various ratios $a=q/p$, that is {0.2; 0.4; 0.6; 0.8; 1}.

The all types of amplitude of initial transversal deformation are analysed.

In the table AA3 the buckling loads so for perfect and for imperfect plates are presented.

Only the cases of $a=0.2$ and $a=0.4$ are presented in figure AA10. As it is seen in figure AA10, according to the graphical method, the buckling loads for the all three imperfect plates are in the range $0.134\text{MPa} < p_{cr} < 0.288\text{MPa}$.

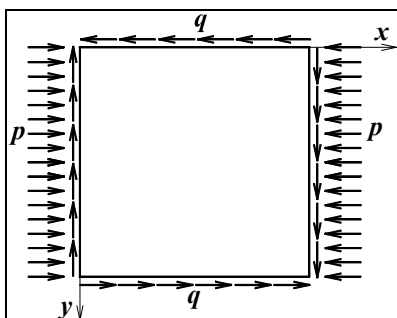


Fig. 17.9. Plate in shearing and compression

$a=q/p$	$w_0=0$	$w_0=1.06\text{ mm}$	$w_0=3.2\text{ mm}$	$w_0=9.6\text{mm}$
0.2	41.765	0.288	0.222	0.134
0.4	41.561	0.266	0.111	0.087
0.6	41.007	0.288	0.088	0.071
0.8	40.167	0.277	0.111	0.071
1	39.119	0.305	0.124	0.081

Table 17.3. Buckling load in [MPa] for shearing and compression loading of plate

$a=q/p$	Failure mode	Perfect plate	$w_0=1.06\text{ mm}$	$w_0=3.2\text{ mm}$	$w_0=9.6\text{mm}$
0.2	Tension	2.499	0.706	0.605	0.403
	Compression	-	1.413	1.312	1.211
0.4	Tension	2.499	0.706	0.504	0.403
	Compression	-	1.311	1.211	0.999
0.6	Tension	1.874	0.504	0.504	0.302
	Compression	-	0.908	0.876	0.802
0.8	Tension	1.562	0.403	0.403	0.302
	Compression	-	0.806	0.706	0.706
1	Tension	1.249	0.302	0.302	0.302
	Compression	-	0.706	0.563	0.563

Table 17.4. Buckling load (ultimate strength) in [MPa] for shearing and compression loading of plate

As it is seen in figure AA10, the buckling load is decreasing since the magnitude of the transversal imperfection is increasing for all cases of loading ratios (see also table AA3).

In this case, the load capacity of the plate is decreasing since the transversal deformation of the plate is increasing. According to the nonlinear calculus (according to Tsai-Wu criterion), the ultimate strength is presented in table AA4.

The ultimate strength (pression corresponding to the first fail occurring) for perfect plates is greater than the ultimate strength of the plate with transversal imperfection.

In the central area, in the layers the compression fails occurs at an in-plane pression greater than the pression corresponding to tension fails.

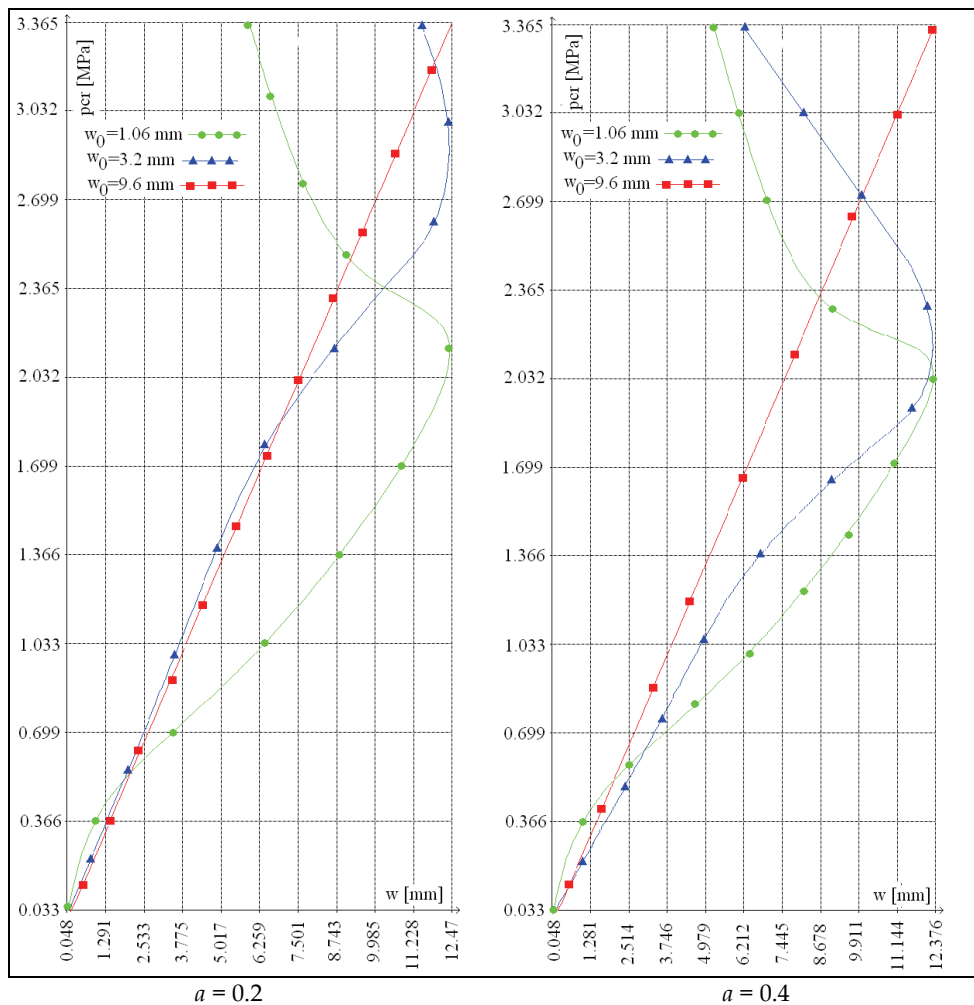


Fig. 17.10. Shear and compression behaviour of the plate

The ultimate strength decreases since the transversal imperfection is increasing.

The tension fails occur in a corner of the plate. On the other part, the compression fails occur in the central part (imperfection area) of the plate.

3.6 Conclusions for buckling of plates with transversal imperfections

The FEM based methodology and the experimental test program were successfully developed for the investigation of buckling problems of composite plates. The FEM model is robust in that it can be used to predict the global buckling loads of composite plates either on one side or both sides. Finite-elements analysis and experimentation were carried out to assess the reliability of the methodology. The buckling behaviour of the orthotropic composite plates is different than the buckling behaviour of the isotropic plates. A special remark is to do for the plates having initial transversal deformation: the transversal deformation is increasing since the in-plane load starts to increase.

The buckling load determination is too difficult without applying a graphical method, or applying the Tsai-Wu failure criterion.

So, for a plate with transversal imperfection, since the magnitude of the initial transversal deformation is increasing, the value of the force for compression failure or tension failure of an element is decreasing.

The lack of the criterion is referring to the anticipation of the real mode to occurring the cracking.

Taking into account the mathematical formulation, the Tsai-Wu failure criterion is easy to be applied. Additionally, this criterion offers advantages concerning the real prediction of the strength at variable loadings. It is to remark that by applying linear terms, it is possible to take into account the differences between the tension and compression strengths of the material.

A good correlation between the numerical and experimental results is concluded.

4. Finite element modelling of delaminated composite plates

4.1 Presentation

Due to the anisotropy of composite laminates and non-uniform distribution of stresses in lamina under flexural bending as well as other types of static/dynamic loading, the failure process of laminates is very complex.

Large differences in strength and stiffness values of the fiber and the matrix lead to various forms of defect/damage caused during manufacturing process as well as service conditions.

In shipbuilding, many structures made of composite laminates are situated such that they are susceptible to foreign object impacts which can result in barely visible impact damage. Often, in the form of a complicated array of matrix cracks and interlaminar delaminations, these barely visible impact damages can be quite extensive and can significantly reduce a structure's load bearing capability.

Delamination or separation of two adjacent plies in a composite laminate is one of the most common modes of damage. The presence of delamination may reduce the overall stiffness as well as the residual strength leading to structural failure. A clear understanding of the influence of delamination on the performance of the laminates is very essential to use them efficiently in structural design applications.

Since such damage is in general difficult to detect, structures must be able to function safely with delamination present.

Although several studies are available in the literature in the field of delamination prediction and growth, effect of delamination on buckling, post-buckling deformation and delamination propagation under fatigue loading, etc. the work on the effect of delamination on the first ply failure of the laminate is scarce.

However, there clearly exists the need to be able to predict the tolerance of structures to damage forms which are not readily detectable (Chirica & al, 2006).

(Ambarcumyan, 1991, Adams & al, 2003) have analysed experimental characterization of advanced composite materials. When a laminate is subjected to in-plane compression, the effects of delamination on the stiffness and strength may be characterized by three sets of results, (Finn & Springer, 1993):

- a. Buckling load;
- b. Postbuckling solutions under increased load;
- c. Results concerning the onset of delamination growth and its subsequent development.

Many of the analytical treatments deal with a thin near surface delamination. Such approaches are known as "thin-film" analysis in the literature (Kim & al, 1999, Thurley & al, 1995). The thin-film analytical approach may involve significant errors in the post-buckling solutions.

(Naganarayana & Atluri, 1995) have analysed the buckling behaviour of laminated composite plates with elliptical delaminations at the centre of the plates using finite element method. They propose a multi-plate model using 3-noded quasi-conforming shell element, and use J-integral technique for computing point wise energy release rate along the delamination crack front.

(Pietropaoli & al, 2008) studied delamination growth phenomena in composite plates under compression by taking into account also the matrix and fibers breakages until the structural collapse condition is reached.

The aim of the work presented in this chapter is to present the studies on the influence of elliptical delamination on the changes in the buckling behaviour of ship deck plates made of composite materials. This problem has been solved by using the finite element method, in (Beznea, 2008). An orthotropic delamination model, describing mixed mode delaminating, by using FEM analysis, was applied. So, the damaged part of the structures and the undamaged part have been represented by well-known finite elements (layered shell elements). The influence of the position and the ellipse's diameters ratio of delaminated zone on the critical buckling force was investigated.

If an initial delamination exists, this delamination may close under the applied load. To prevent the two adjacent plies from penetrating, a simple numerical contact model is used.

Taking into account the thickness symmetry of the plates, only cases of position of delamination on one side of symmetry axis are presented. The variations of the transversal displacement of the point placed in the middle of the plate versus the in-plane applied pressure are plotted for each position of delamination. Buckling load determination for the general buckling of the plate has been done by graphical method. The post-buckling calculus has been performed to explain the complete behaviour of the plate.

Only cases with one delamination placed between two laminas is presented here.

There are several ways in which the panel can be modeled for the delamination analysis. For the present study, a 3-D model with 4-node shell composite elements is used. The plate is divided into two sub-laminates by a hypothetical plane containing the delamination. For this reason, the present finite element model would be referred to as two sub-laminates

model. The two sub-laminates are modeled separately with shell composite elements, and then joined face to face with appropriate interfacial constraint conditions for the corresponding nodes on the sub-laminates, depending on whether the nodes lie in the delaminated or undelaminated region.

The delamination model has been developed by using the surface-to-surface contact option (Fig. AA11). In case of surface-to-surface contact, the FE meshes of adjacent plies do not need to be identically. The contact algorithm used in the FEM analysis has possibility to determine which node of the so-called master surface is in contact with a given node on the slave surface. Hence, the user can define the interaction between the two surfaces.

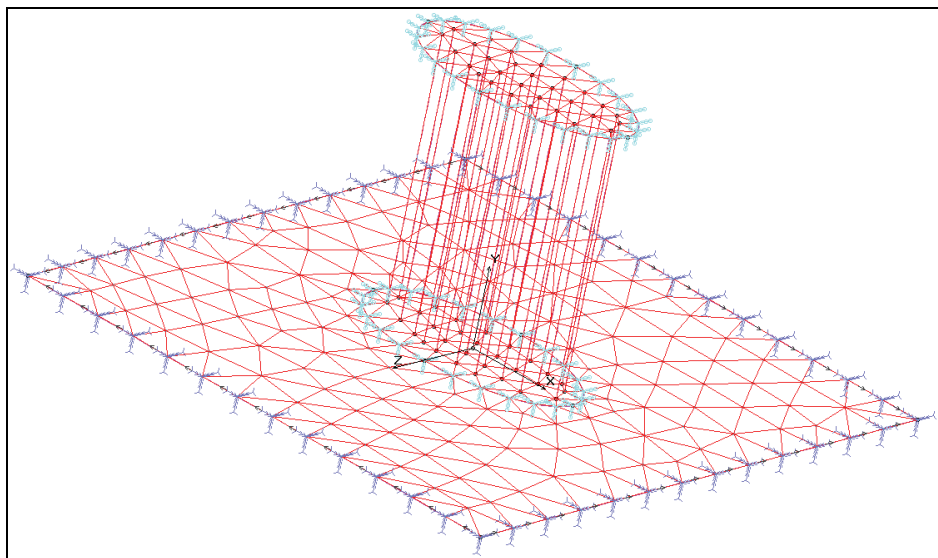


Fig. 17.11. The FEM delamination model

The condition is that the delaminated region does not grow. These regions were modeled by two layers of elements with coincident but separate nodes and section definitions to model offsets from the common reference plane. Thus their deformations are independent. At the boundary of the delamination zones the nodes of one row are connected to the corresponding nodes of the regular region by master slave node system.

Typically, a node in the underlaminated region of bottom sub-laminate and a corresponding node on the top sub-laminate are declared to be coupled nodes using master-slave nodes facility. The nodes in the delaminated region, whether in the top or bottom laminate, are connected by contact elements. This would mean that the two sublaminates are free to move away from each other in the delaminated region, and constrained to move as a single laminate in the undelaminated region.

The material characteristics presented in previous chapter are used.

Two material models were used: quasi-nonlinear model and non linear model.

A quasi-nonlinear model means that the material behaviour is not according to a failure criterion.

The non-linear model is the material fulfilling Tsai-Wu failure Criterion.

The ellipse's diameters of the delamination area placed in the middle of the plate are considered from the condition of the same area for all cases. In the parametric calculus, the following diameters ratios were considered:

- Case 1 ($D_x/D_y=0.5$): transversal diameter $D_y=141\text{mm}$, longitudinal diameter $D_x=70.5\text{mm}$;
- Case 2 ($D_x/D_y=1$): transversal diameter $D_y=100\text{ mm}$; longitudinal diameter $D_x=100\text{mm}$;
- Case 3 ($D_x/D_y=2$): transversal diameter $D_y=70.5\text{ mm}$; longitudinal diameter $D_x=141\text{mm}$.

In this chapter the following cases (in numerical and experimental ways) are presented: compressive buckling, shear buckling, mixed compressive and shear buckling. The results (for linear, and nonlinear model) are presented as variation of the buckling loads function of maximum transversal displacement (buckling and post-buckling behaviour).

The buckling analysis of delaminated plates was done on square plates ($320\times 320\text{mm}$), made of E-glass/epoxy (biaxial layers having the thickness $t=0.32\text{mm}$).

These layers are grouped into macro-layers as are presented in table AA1. The position of the delamination is considered between two neighbors layers i and $i+1$, ($i=1,10$). The calculus was done for the all 9 cases. Only results obtained for a specific case of position of delamination ($i=4$) are presented in the chapter.

4.2 Numerical studies on compression buckling

The plate is considered as clamped on the sides. The in-plane loading was applied as an uniform compressive pressure in the x direction (Fig. AA12). The force was increased step by step (with and certain increment). In the figure AA13, the variation of the transversal displacements of the central point, versus applied loading is drawn. Each curve corresponds to one diameters ratio.

Buckling load has been determined by the graphical method. On each curve that corresponds to a delamination type, an asymptote on curve after the bifurcation has been plotted. Critical value for the buckling load was obtained in the range:

$$43.41\text{ MPa} < p_{cr} < 59.5\text{ MPa}$$

In the case of nonlinear model of the material behaviour the buckling load (ultimate strength) was determined by Tsai Wu criterion. So, the degradation index (failure index) for tension and compression of the delaminated plates was determined (Table AA7). Only the plate global buckling was examined.

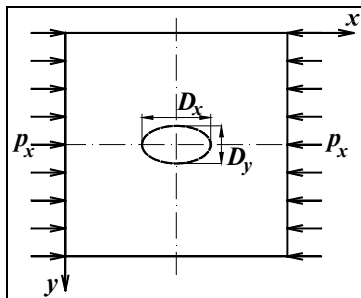


Fig. 17.12. Delaminated plate with in-plane loading

Failure mode	Fail 1 (Tension)	Fail 2 (Compression)
$D_x/D_y=0.5$	35	74
$D_x/D_y=1$	37	78
$D_x/D_y=2$	39	82

Table 17.5. Buckling load (ultimate strength) in [MPa] for compression loading

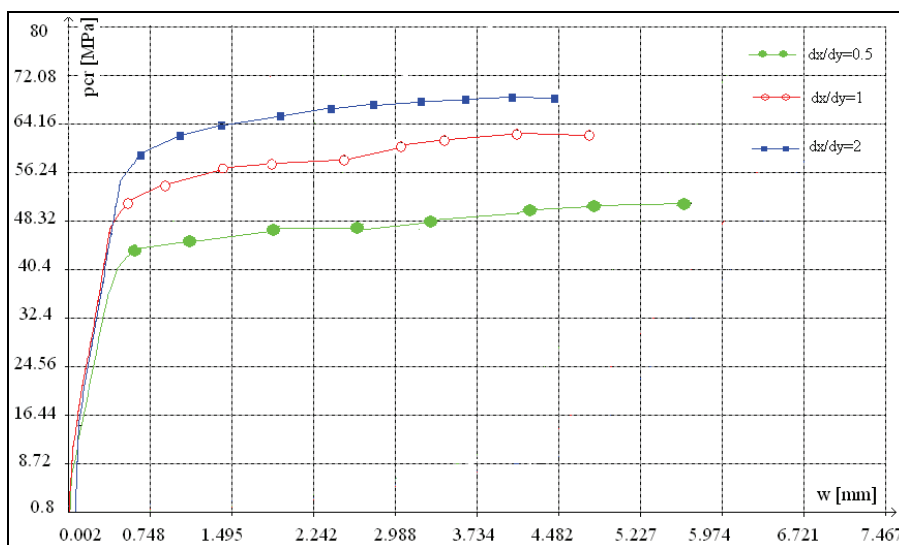


Fig. 17.13. Compression buckling and post buckling behaviour of the plates with central delamination placed between macro-layers 4 and 5

4.3 Numerical studies on shearing buckling

4.3.1 Shearing buckling of thin plates

In this chapter, the thickness and the lay-up of the plate are according to Table AA1. The plate, considered as clamped on the sides, was loaded with an uniform shear pressure on the sides (Fig. AA14). The force was increased step by step (with a certain increment).

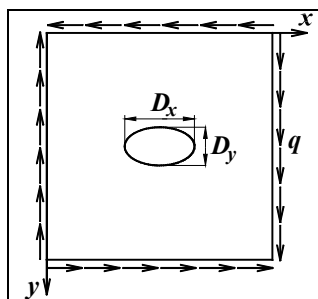


Fig. 17.14. Shear loaded plate with central delamination

In the figure AA15, the variation of the transversal displacements of the central point, versus applied loading is drawn, for delamination placed between macro-layers 4 and 5. Each curve corresponds to one diameters ratio.

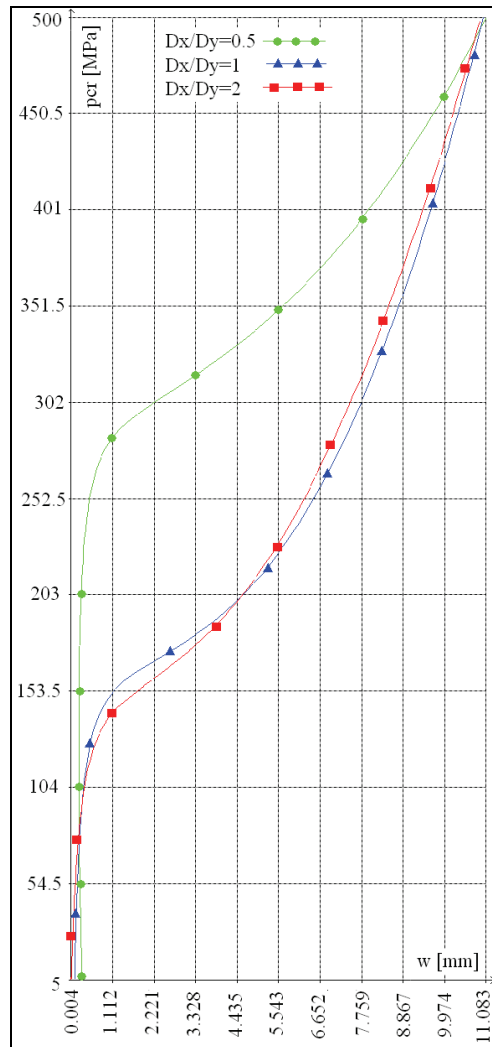


Fig. 17.15. Shear buckling and post buckling behaviour of the plates with central delamination placed between macro-layers 4 and 5

Buckling load has been determined by the graphical method (an asymptote on curve after the bifurcation has been plotted).

Critical value for the buckling load was obtained in the range $109 \text{ MPa} < p_{cr} < 289 \text{ MPa}$.

In the case of nonlinear model of the material behaviour the buckling load (ultimate strength) was determined by Tsai Wu criterion. So, the degradation index (failure index) for

tension and compression of the delaminated plates was determined (Table AA6). Only the plate global buckling was examined.

Dx/Dy		0.5	1	2
Position of delamination	Fail type			
Macro-layer 1	Traction	25	20	20
Macro-layer 2	Compression	90	-	-
Macro-layer 2	Traction	25	20	20
Macro-layer 3	Compression	90	-	-
Macro-layer 3	Traction	25	20	20
Macro-layer 4	Compression	90	-	-
Macro-layer 4	Traction	25	20	20
Macro-layer 5	Compression	90	-	-

Table 17.6. Buckling load (ultimate strength) in [MPa] for shear loading of the plates

4.4 Numerical studies on combined (compression and shear) buckling

The discussions and results on compression and shear buckling analysis will be done only for plate presented in figure AA9, having the same geometry and the orthotropic directions (α), thickness of the macro-layers (t) and plate lay-up according to Table AA1.

For analysis the calculus was done for various ratios $a=q/p$, that is $\{0.2; 0.4; 0.6; 0.8; 1\}$.

In figure AA16 the combined loading (shear and compression) buckling and post buckling behaviour of the plates with central delamination placed between macro-layers 1 and 2, for $a=0.2$ is presented.

$a=q/p$	Failure mode	Perfect plate	Dx/Dy=0.5	Dx/Dy=1	Dx/Dy=2
0.2	Tension	3962	3.962	3.962	4.239
	Compression	8.879	8.059	7.649	6.147
0.4	Tension	3.688	3.688	3.688	4.098
	Compression	7.649	6.966	6.966	5.874
0.6	Tension	3.142	3.005	2.868	2.868
	Compression	6.966	6.693	5.601	5.191
0.8	Tension	2.868	2.322	2.049	2.049
	Compression	6.693	6.425	6.425	5.327
1	Tension	1.912	1.912	1.639	1.639
	Compression	6.147	4.508	4.508	4.508

Table 17.7. Buckling load in [MPa] for shearing and compression loading

According to the curves presented in figure AA16 the buckling load is decreasing since the value of the diameters ratio is increasing.

So, as it is seen in figure AA16, according to the plotted asymptotes, the buckling loads of the thin plates are placed in the domain

$$0.368 \text{ MPa} < p_{cr} < 2.634 \text{ MPa}.$$

In the case of nonlinear model of the material behaviour, the buckling load (ultimate strength) was determined by Tsai Wu criterion, so that the degradation index (failure index) for tension and compression of the delaminated plates may be shown in Table AA7.

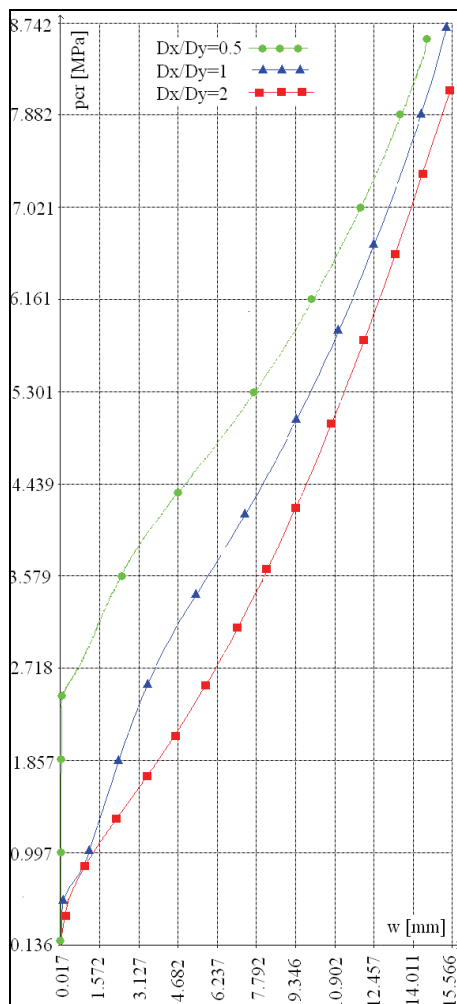


Fig. 17.16. Buckling and post buckling behaviour of the plate

4.5 Conclusions for buckling of plates with delaminations

Delamination is a phenomenon of critical importance for the composite industry. It involves a breakdown in the bond between the reinforcement and the matrix material of the composite. Understanding delamination is essential for preventing catastrophic failures. Due to the geometry and general load of the ship deck, buckling is one of the most important failure criteria. The FEM based methodology was successfully developed for the investigation of buckling problems of composite plates having a central delamination. Two hypotheses regarding the type of material modeling were used: linear and nonlinear model. In the chapter, a convenient methodology to model delaminated composite plates was presented. The FEM modeling can be used to predict the global buckling loads of composite plates with delaminations.

In the case of linear model used for material, the following conclusions can be formulated:

- For the values of in-plane loads lower than 40 MPa, the displacement values are increasing since the diameters ratio is increasing. This trend is due to the fact the transversal diameter is decreasing (since the delaminated area remains constant). Smaller transversal diameter means increasing of shear stiffness.
- In the case of the in-plane loading values bigger than 40 MPa, the displacement values are decreasing since the diameters ratio is increasing. This trend is due to the contact pressure between the layers in contact in the delamination, which is increasing since the loading force is increasing.

In the case of nonlinear material model (Figure AA13) the trend of the curves is so that the transversal displacement is increasing since the diameters ratio is increasing for the same in-plane loading, for a in-plane loading value under 25-40 MPa. For an in-plane loading value between 40 and 65 MPa in each case, a small instant jumping of transversal displacement is observed. This means that what is recover in plate stiffness after the increasing of contact pression in the delamination area, is lost due to the lamina damage occurring.

The buckling load determination is too difficult without the applying a graphical method, or the applying the Tsai-Wu failure criterion in the case of the general buckling not occurred till the first-ply failure occurring.

The first failure occurring in an element is based on the Tsai-Wu failure criterion, which provides the mathematical relation for strength under combined stresses was used.

The failure index is calculated in each ply of each element. In the ply where failure index is greater than 1, the first-ply failure occurs, according to the Tsai-Wu criterion. In the next steps, the tensile and compressive properties of this element are reduced by the failure index. If the buckling did not appeared until the moment of the first-ply failure occurring, the in-plane load corresponding to this moment is considered as the buckling load.

The lack of the criterion is referring to the anticipation of the real mode to occurring the cracking.

Taking into account the mathematical formulation, the Tsai-Wu failure criterion is easy to be applied. Additionally, this criterion offers advantages concerning the real prediction of the strength at variable loadings. In the case of shear buckling of thin plates, the ultimate strength of the delaminated plate is not depending on the position of delamination. For diameters ratio greater than 1, the ultimate strength in shear loading occurs only for traction fail.

Final remarks may be done. A very good postbuckling load carrying ability specific to light weight structures can be exploited to obtain high performance. Finite element analysis can offer more accurate analyses with a high degree of fidelity.

Since the plates included in the ship hull structure (so perfect or imperfect) are subjected to in-plane forces combined with transverse pressure, the buckling response of such plates is a basic concern in the design process. Furthermore, the presence of imperfections may weaken the load-carrying capacity of structures due to stiffness loss and cause an increase in stress concentrations in the imperfection area.

After the buckling, the composite plates, so perfect or imperfect, have a great capacity to be overloaded, so that the plate and finally the structure is not collapsed immediately.

5. Acknowledgement

The results presented in this chapter are based on the work supported by CNCSIS-UEFISCSU, project number PNII - IDEI, code 512/2008.

6. References

- Adams, D.F., Carlsson, L.A. & Pipes, R.B. (2003). *Experimental Characterization of Advanced Composite materials*, Ed. Taylor & Francis Group.
- Altenbach, H., Altenbach, J. & Kissing, W. (2004). *Mechanics of Composite Structural Elements*, Ed. Springer, Berlin.
- Ambarcumyan, S.A: (1991). *Theory of Anisotropic Plates: Strength, Stability, and Vibrations*, Hemisphere Publishing, Washington.
- Beznea, E.F., (2008). *Studies and Researches on the Buckling Behaviour of the Composite Panels*, Doctoral Thesis, University Dunarea de Jos of Galati.
- Beznea, E.F., & Chirica, I.,(2009). Studies on buckling behaviour of the composite plates with delamination, *Proceedings of the 26-th DAS-2009: Danubia-Adria Symposium on Development in Experimental Mechanics*, Leoben, Austria, pp.13-14, ISBN 978-3-902544-02-5
- Bisagni, C. & Cordisco, P., (2004). Testing of Stiffened Composite Cylindrical Shells in the Postbuckling Range until Failure, *AIAA Journal*, Vol. 42, No. 9, pp. 1808- 1817
- Chirica, I., Beznea, E.F., Chirica, R., Boazu, D., Chirica, A. & Berggreen C.C., (2008). *Journal of Material Testers Magazine*, www.anyagvizsgaloklapja.hu, Vol. 18/1, p. 24.
- Chirica, I., Beznea, E.F., & Chirica, R., (2009). Studies on buckling of the ship deck panels with imperfections made of composite materials, *Materiale Plastice*, vol. 46, nr.3, , pp. 243-248, ISSN0025/5289
- Engelstad, S. P., Reddy, J. N. & Knight, N. F., Jr. (1992). Postbuckling Response and Failure Prediction of Graphite-Epoxy Plates Loaded in Compression, *AIAA Journal*, 30(8), 2106-2113
- Finn, S.C. & Springer, G.S. (1993). Delamination in Composites Plates under Transverse Static or Impact Loads—a model, *Composite Structures*, vol. 23
- Hilburger, M.F. (2001). Nonlinear and Buckling Behavior of Compression-loaded Composite Shells, *Proceedings of the 6th Annual Technical Conference of the American Society for Composites*, Virginia.
- Kawai, T. & Ohtsubo, H. (1968). A Method of Solution for the Complicated Buckling Problems of Elastic Plates With Combined Use of Rayleigh-Ritz's Procedure in the Finite Element Method, *AFFDLTR*-68-150
- Kim, H. & Kedward, K.T., (1999). A Method for Modeling the Local and Global Buckling of Delaminated Composite Plates. *Composite Structures* 44: 43-53
- Knight N. F. Jr. & Starnes J. H. Jr., (1988). Postbuckling Behavior of Selected Curved Stiffened Graphite Epoxy Panels Loaded in Axial Compression, *AIAA Journal*, Vol. 26, No. 3, pp.344-352.
- Naganarayana, B.P. & Atluri, S.N. (1995). Strength Reduction and Delamination Growth in Thin and Thick Composite Plates under Compressive Loading, *Computational Mechanics*, 16: 170-189.
- Pietropaoli, E., Riccio, A. & Zarrelli, M., (2008). Delamination Growth and Fibre/Matrix Progressive Damage in Composite Plates under Compression. ECCM13, *The 13-th European Conference on Composite Materials*, June 2-5, Stockholm, Sweden
- Schlack, A.L., Jr. (1964). Elastic Stability of Pierced Square Plates. *Experimental Mechanics*, June 167-172.
- Thurley, G.J. & Marshall, I.H. (1995). *Buckling and Postbuckling of Composite Plates*, Ed. Chapman & Hall, London.

Finite Element Analysis of Delamination Growth in Composite Materials using LS-DYNA: Formulation and Implementation of New Cohesive Elements

Ahmed Elmarakbi

*Faculty of Applied Sciences, University of Sunderland
United Kingdom*

1. Introduction

This chapter provides an overview of the delamination growth in composite materials, cohesive interface models and finite element techniques used to simulate the interface elements. For completeness, the development and implementation of a new constitutive formula that stabilize the simulations and overcome numerical instabilities will be discussed in this chapter.

Delamination is a mode of failure of laminated composite materials when subjected to transverse loads. It can cause a significant reduction in the compressive load-carrying capacity of a structure. Cohesive elements are widely used, in both forms of continuous interface elements and point cohesive elements, (Cui & Wisnom, 1993; De Moura et al., 1997; Reddy et al., 1997; Petrossian & Wisnom, 1998; Shahwan & Waas, 1997; Chen et al., 1999; Camanho et al., 2001) at the interface between solid finite elements to predict and to understand the damage behaviour in the interfaces of different layers in composite laminates. Many models have been introduced including: perfectly plastic, linear softening, progressive softening, and regressive softening (Camanho & Davila, 2004). Several rate-dependent models have also been introduced (Glennie, 1971; Xu et al., 1991; Tvergaard & Hutchinson, 1996; Costanzo & Walton, 1997; Kubair et al., 2003). A rate-dependent cohesive zone model was first introduced by Glennie (Glennie, 1971), where the traction in the cohesive zone is a function of the crack opening displacement time derivative. Xu et al. (Xu et al., 1991) extended this model by adding a linearly decaying damage law. In each model the viscosity parameter (η) is used to vary the degree of rate dependence. Kubair et al. (Kubair et al., 2003) thoroughly summarized the evolution of these rate-dependant models and provided the solution to the mode III steady-state crack growth problem as well as spontaneous propagation conditions.

A main advantage of the use of cohesive elements is the capability to predict both onset and propagation of delamination without previous knowledge of the crack location and propagation direction. However, when using cohesive elements to simulate interface damage propagations, such as delamination propagation, there are two main problems. The first one is the numerical instability problem as pointed out by Mi et al. (Mi et al., 1998), Goncalves et al. (Goncalves et al., 2000), Gao and Bower (Gao & Bower, 2004) and Hu et al.

(Hu et al., 2007). This problem is caused by a well-known elastic snap-back instability, which occurs just after the stress reaches the peak strength of the interface. Especially for those interfaces with high strength and high initial stiffness, this problem becomes more obvious when using comparatively coarse meshes (Hu et al., 2007). Traditionally, this problem can be controlled using some direct techniques. For instance, a very fine mesh can alleviate this numerical instability, however, which leads to very high computational cost. Also, very low interface strength and the initial interface stiffness in the whole cohesive area can partially remove this convergence problem, which, however, lead to the lower slope of loading history in the loading stage before the happening of damages. Furthermore, various generally oriented methodologies can be used to remove this numerical instability, e.g. Riks method (Riks, 1979) which can follow the equilibrium path after instability. Also, Gustafson and Waas (Gustafson & Waas, 2008) have used a discrete cohesive zone method finite element to evaluate traction law efficiency and robustness in predicting decohesion in a finite element model. They provided a sinusoidal traction law which found to be robust and efficient due to the elimination of the stiffness discontinuities associated with the generalized trapezoidal traction law.

Recently, the artificial damping method with additional energy dissipations has been proposed by Gao and Bower (Gao & Bower, 2004). Also, Hu et al. proposed a kind of move-limit method (Hu et al., 2007) to remove the numerical instability using cohesive model for delamination propagation. In this technique, the move-limit in the cohesive zone provided by artificial rigid walls is built up to restrict the displacement increments of nodes in the cohesive zone of laminates after delaminations occurred. Therefore, similar to the artificial damping method (Gao & Bower, 2004), the move-limit method introduces the artificial external work to stabilize the computational process. As shown later, although these methods (Gao & Bower, 2004; Hu et al., 2007) can remove the numerical instability when using comparatively coarse meshes, the second problem occurs, which is the error of peak load in the load-displacement curve. The numerical peak load is usually higher than the real one as observed by Goncalves et al. (Goncalves et al., 2000) and Hu et al. (Hu et al., 2007).

Similar work has also been conducted by De Xie and Waas (De Xie & Waas, 2006). They have implemented discrete cohesive zone model (DCZM) using the finite element (FE) method to simulate fracture initiation and subsequent growth when material non-linear effects are significant. In their work, they used the nodal forces of the rod elements to remove the mesh size effect, dealt with a 2D study and did not consider viscosity parameter. However, in the presented Chapter, the author used the interface stiffness and strength in a continuum element, tackled a full 3D study and considered the viscosity parameter in their model.

With the previous background in mind, the objective of this Chapter is to propose a new cohesive model named as adaptive cohesive model (ACM), for stably and accurately simulating delamination propagations in composite laminates under transverse loads. In this model, a pre-softening zone is proposed ahead of the existing softening zone. In this pre-softening zone, with the increase of effective relative displacements at the integration points of cohesive elements on interfaces, the initial stiffnesses and interface strengths at these points are reduced gradually. However, the onset displacement for starting the real softening process is not changed in this model. The critical energy release rate or fracture toughness of materials for determining the final displacement of complete decohesion is kept constant. Also, the traction based model includes a cohesive zone viscosity parameter (η) to vary the degree of rate dependence and to adjust the peak or maximum traction.

In this Chapter, this cohesive model is formulated and implemented in LS-DYNA (Livermore Software Technology Corporation, 2005) as a user defined materials (UMAT). LS-DYNA is one of the explicit FE codes most widely used by the automobile and aerospace industries. It has a large library of material options; however, continuous cohesive elements are not available within the code. The formulation of this model is fully three dimensional and can simulate mixed-mode delamination. However, the objective of this study is to develop new adaptive cohesive elements able to capture delamination onset and growth under quasi-static and dynamic Mode-I loading conditions. The capabilities of the proposed elements are proven by comparing the numerical simulations and the experimental results of DCB in Mode-I.

2. The constitutive model

Cohesive elements are used to model the interface between sublaminae. The element consists of a near zero-thickness volumetric element in which the interpolation shape functions for the top and bottom faces are compatible with the kinematics of the elements that are being connected to it (Davila et al., 2001). Cohesive elements are typically formulated in terms of traction vs. relative displacement relationship. In order to predict the initiation and growth of delamination, an 8-node cohesive element shown in figure 1 is developed to overcome the numerical instabilities.

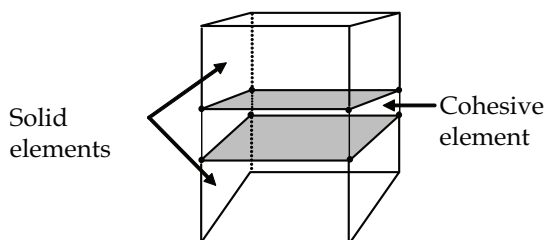


Fig. 1. Eight-node cohesive element

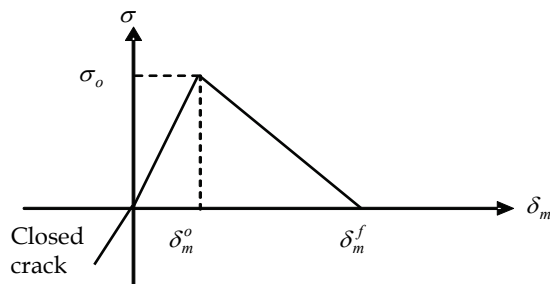


Fig. 2. Normal (bilinear) constitutive model

The need for an appropriate constitutive equation in the formulation of the interface element is fundamental for an accurate simulation of the interlaminar cracking process. A constitutive equation is used to relate the traction to the relative displacement at the

interface. The bilinear model, as shown in figure 2, is the simplest model to be used among many strain softening models. Moreover, it has been successfully used by several authors in implicit analyses (De Moura et al., 2000; Camanho et al., 2003; Pinho et al., 2004; Pinho et al., 2006).

However, using the bilinear model leads to numerical instabilities in an explicit implementation. To overcome this numerical instability, a new adaptive model is proposed by Hu et al. (Hu et al., 2008) and presented in this Chapter as shown in figure 3. The adaptive interfacial constitutive response shown in figure 3 is implemented as follows:

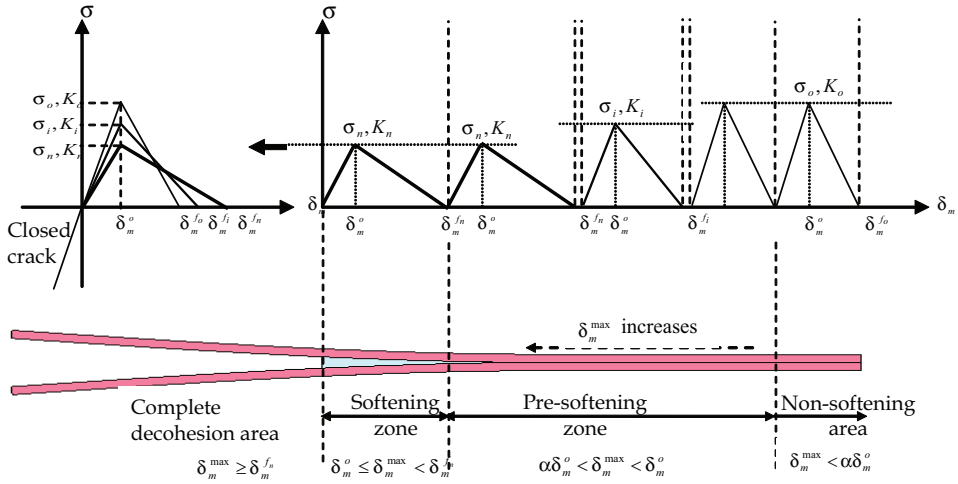


Fig. 3. Adaptive constitutive model for Mode-I (Hu et.al, 2008)

In pre-softening zone, $\alpha\delta_m^o < \delta_m^{\max} < \delta_m^o$, the constitutive equation is given by

$$\sigma = (\sigma_m + \eta \dot{\delta}_m) \frac{\delta_m}{\delta_m^o} \quad (1)$$

and

$$\sigma_m = K\delta_m^o \quad (2)$$

where σ is the traction, K is the penalty stiffness and can be written as

$$K = \begin{cases} K_o & \delta_m \leq 0 \\ K_i & \delta_m^{\max} < \delta_m^o \\ K_n & \delta_m^o \leq \delta_m^{\max} < \delta_m^f \end{cases} \quad (3)$$

δ_m is the relative displacement in the interface between the top and bottom surfaces (in this study, it equals the normal relative displacement for Mode-I), δ_m^o is the onset displacement and it is remained constant in the simulation and can be determined as follows:

$$\delta_m^o = \frac{\sigma_o}{K_o} = \frac{\sigma_i}{K_i} = \frac{\sigma_{\min}}{K_{\min}} \quad (4)$$

where σ_o is the initial interface strength, σ_i is the updated interface strength in the pre-softening zone, σ_{\min} is the minimum limit of the interface strength, K_o is the initial stiffness, K_i is the updated stiffness in the pre-softening zone, and K_{\min} is the minimum value of the stiffness. For each increment and for time $t+1$, δ_m is updated as follows:

$$\delta_m^{t+1} = t_c \varepsilon^{t+1} - t_c \quad (5)$$

where t_c is the thickness of the cohesive element and ε^{t+1} is the normal strain of the cohesive element for time $t+1$, $\varepsilon^{t+1} = \varepsilon^t + \Delta\varepsilon$, where $\Delta\varepsilon$ is the normal strain increment. The $(\delta_m^{\max})^t$ is the max relative displacement of the cohesive element occurs in the deformation history. For each increment and for time $t+1$, δ_m^{\max} is updated as follows:

$$(\delta_m^{\max})^{t+1} = \delta_m^{t+1} \quad \text{if } \delta_m^{t+1} \geq (\delta_m^{\max})^t \text{ and,} \quad (6)$$

$$(\delta_m^{\max})^{t+1} = (\delta_m^{\max})^t \quad \text{if } \delta_m^{t+1} < (\delta_m^{\max})^t \quad (7)$$

Using the max value of the relative displacement δ_m^{\max} rather than the current value δ_m prevents healing of the interface. The updated stiffness and interface strength are determined in the following forms:

$$\sigma_i = \frac{\delta_m^{\max}}{\delta_m^o} (\sigma_{\min} - \sigma_o) + \sigma_o, \quad \sigma_o > \sigma_{\min} \text{ and } (\alpha \delta_m^o < \delta_m^{\max} < \delta_m^o) \quad (8)$$

$$K_i = \frac{\delta_m^{\max}}{\delta_m^o} (K_{\min} - K_o) + K_o, \quad K_o > K_{\min} \text{ and } (\alpha \delta_m^o < \delta_m^{\max} < \delta_m^o) \quad (9)$$

It should be noted that α in equations (8) and (9) is a parameter to define the size of pre-softening zone. When $\alpha = 1$, the present adaptive cohesive mode degenerates into the traditional cohesive model. In these computations, α was set to zero. From our numerical experiences, the size of pre-softening zone has some influences on the initial stiffness of loading-displacement curves, but not so significant. The reason is that for the region far always from the crack tip, the interface decrease or update according to equations (8) and (9) is not obvious since δ_m^{\max} is very small. The energy release rate for Mode-I G_{IC} also remains constant. Therefore, the final displacements associated to the complete decohesion δ_m^{fi} are adjusted as shown in figure 3 as

$$\delta_m^{fi} = \frac{2G_{IC}}{\sigma_i} \quad (10)$$

Once the max relative displacement of an element located at the crack front satisfies the following conditions; $\delta_m^{\max} > \delta_m^o$, this element enters into the real softening process. Where, as shown in figure 3, the real softening process denotes a stiffness decreasing process caused by accumulated damages. Then, the current strength σ_n and stiffness K_n , which are almost equal to σ_{\min} and K_{\min} , respectively, will be used in the softening zone.

2. In softening zone, $\delta_m^o \leq \delta_m^{\max} < \delta_m^f$, the constitutive equation is given by

$$\sigma = (1 - d)(\sigma_m + \eta \dot{\delta}_m) \frac{\delta_m}{\delta_m^o} \quad (11)$$

where d is the damage variable and can be defined as

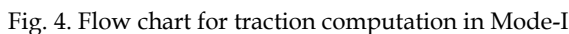
$$d = \frac{\delta_m^f(\delta_m^{\max} - \delta_m^o)}{\delta_m^{\max}(\delta_m^f - \delta_m^o)}, \quad d \in [0, 1] \quad (12)$$

The above adaptive cohesive mode is of the engineering meaning when using coarse meshes for complex composite structures, which is, in fact, an 'artificial' means for achieving the stable numerical simulation process. A reasonable explanation is that all numerical techniques are artificial, whose accuracy strongly depends on their mesh sizes, especially at the front of crack tip. To remove the factitious errors in the simulation results caused by the coarse mesh sizes in the numerical techniques, some material properties are artificially adjusted in order to partially alleviate or remove the numerical errors. Otherwise, very fine meshes need to be used, which may be computationally impractical for very complex problems from the capabilities of most current computers. Of course, the modified material parameters should be those which do not have the dominant influences on the physical phenomena. For example, the interface strength usually controls the initiation of interface cracks. However, it is not crucial for determining the crack propagation process and final crack size from the viewpoint of fracture mechanics. Moreover, there has been almost no clear rule to exactly determine the interface stiffness, which is a parameter determined with a high degree of freedom in practical cases. Therefore, the effect of the modifications of interface strength and stiffness can be very small since the practically used onset displacement δ_m^o for delamination initiation is remained constant in our model. For the parameters, which dominate the fracture phenomena, should be unchanged. For instance, in our model, the fracture toughness dominating the behaviors of interface damages is kept constant.

3. Information finite element implementation

The proposed cohesive element is implemented in LS-DYNA finite element code as a user defined material (UMAT) using the standard library 8-node solid brick element and *MAT_USER_DEFINED_MATERIAL_MODELS. The keyword input has to be used for the user interface with data. The following cards are used (LS-DYNA User's Manual; LSTC, 2005) as shown in table 1.

This approach for the implementation requires modelling the resin rich layer as a non-zero thickness medium. In fact, this layer has a finite thickness and the volume associated with the cohesive element can in fact set to be very small by using a very small thickness (e.g. 0.01 mm). To verify these procedures, the crack growth along the interface of a double cantilever beam (DCB) is studied. The two arms are modelled using standard LS-DYNA 8-node solid brick elements and the interface elements are developed in a FORTRAN subroutine using the algorithm shown in figure 4.



The LS-DYNA code calculates the strain increments for a time step and passes them to the UMAT subroutine at the beginning of each time step. The material constants, such as the stiffness and strength, are read from the LS-DYNA input file by the subroutine. The current and maximum relative displacements are saved as history variables which can be read in by

the subroutine. Using the history variables, material constants, and strain increments, the subroutine is able to calculate the stresses at the end of the time step by using the constitutive equations. The subroutine then updates and saves the history variables for use in the next time step and outputs the calculated stresses. Note that the *DATABASE _ EXTENT _ BINARY command is required to specify the storage of history variables in the output file.

Variable	MID	RO	MT	LMC	NHV	IORTHO	IBULK	IG
Type	I	F	I	I	I	I	I	I
Variable	IVECT	IFAIL	ITHERM	IHYPER	IEOS			
Type	I	I	I	I	I			
Variable	AOPT	MAXC	XP	YP	ZP	A1	A2	A3
Type	F	F	F	F	F	F	F	F
Variable	V1	V2	V3	D1	D2	D3	BETA	
Type	F	F	F	F	F	F	F	
Variable	P1	P2	P3	P4	P5	P6	P7	P8
Type	F	F	F	F	F	F	F	F

where

MID: Material identification; RO: Mass density; MT: User material type (41-50 inclusive); LMC: Length of material constant array which is equal to the number of material constant to be input; NHV: Number of history variables to be stored; IORTHO: Set to 1 if the material is orthotropic; IBULK: Address of bulk modulus in material constants array; IG: Address of shear modulus in material constants array; IVECT: Vectorization flag (on=1), a vectorized user subroutine must be supplied; IFAIL: Failure flag (on=1, allows failure of shell elements due to a material failure criterion; ITHERM: Temperature flag (on=1), compute element temperature; AOPT: Material axes option; MAXC: Material axes change flag for brick elements; XP,YP,ZP: Coordinates of point p for AOPT=1; A1,A2,A3: Components of vector a AOPT=2; V1,V2,V3: Components of vector v AOPT=3; D1,D2,D3: Components of vector d AOPT=2; BETA: Material angle in degrees for AOPT=3; P1..P8.: Material parameter (LSDYNA User's Manual; LSTC, 2005).

Table 1. Keyword cards for UMAT (LSDYNA User's Manual; LSTC, 2005)

It is worth noting that the stable explicit time step is inversely proportional to the maximum natural frequency in the analysis. The small thickness elements drive up the highest natural frequency, therefore, it drives down the stable time step. Hence, mass scaling is used to obtain faster solutions by achieving a larger explicit time step when applying the cohesive element to quasi-static situations. Note that the volume associated with the cohesive element would be small by using a small thickness and the element's kinetic energy arising from this be still several orders of magnitude below its internal energy, which is an important consideration for quasi-static analyses to minimize the inertial effects.

4. Numerical simulations

4.1 Quasi-static analysis

The DCB specimen is made of a unidirectional fibre-reinforced laminate containing a thin insert at the mid-plane near the loaded end. A 150 mm long specimen (L), 20 mm wide (w)

and composed of two thick plies of unidirectional material ($2h = 2\times1.98\text{ mm}$) shown in figure 5 was tested by Morais (Morais et al., 2000). The initial crack length (l_c) is 55 mm. A displacement rate of 10 mm/sec is applied to the appropriate points of the model. The properties of both carbon fiber-reinforced epoxy material and the interface are given in table 2.

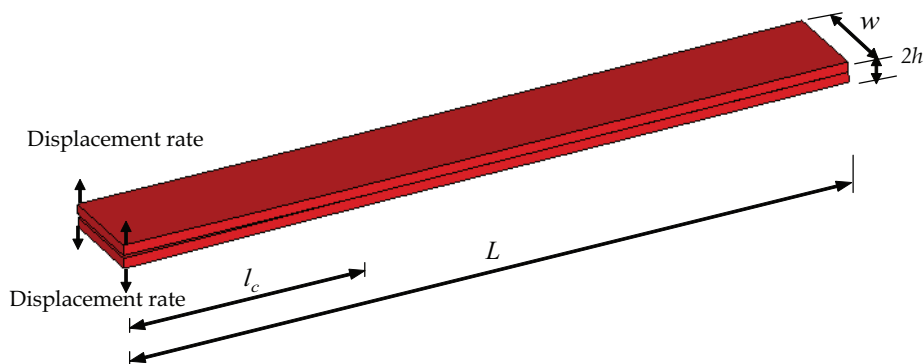


Fig. 5. Model of DCB specimen

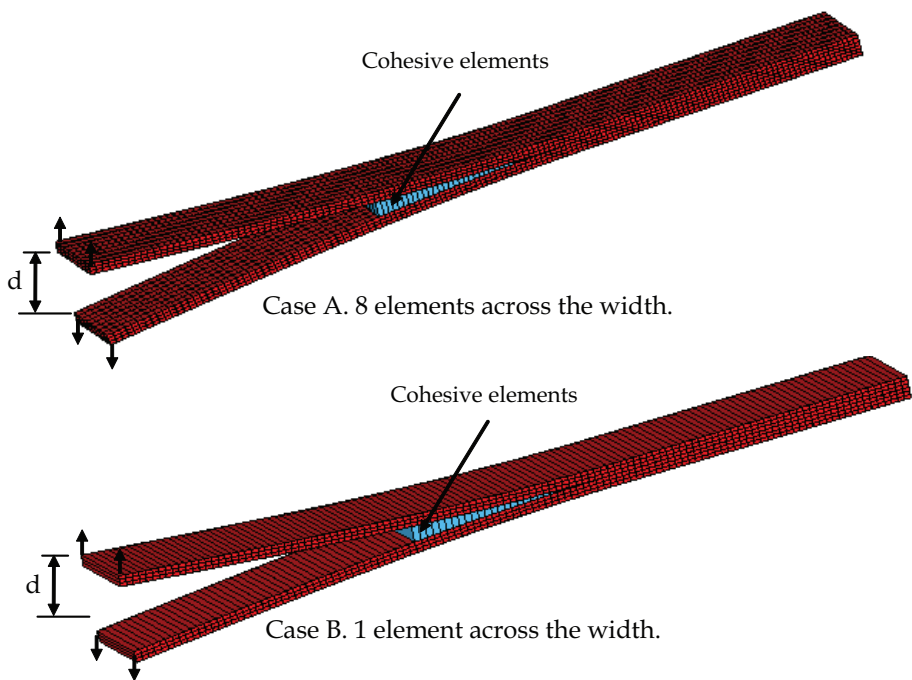


Fig. 6. LS-DYNA finite element model of the deformed DCB specimen

Carbon fiber- reinforced epoxy material	DCB specimen interface
$\rho = 1444 \text{ kg/m}^3$	$G_{IC} = 0.378 \text{ kJ/m}^2$
$E_{11} = 150 \text{ GPa}, E_{22} = E_{33} = 11 \text{ GPa}$	$K_o = 3 \times 10^4 \text{ N/mm}^3$
$\nu_{12} = \nu_{13} = 0.25, \nu_{23} = 0.45$	$\sigma_o = 45 \text{ MPa}$ case I
$G_{12} = G_{13} = 6.0 \text{ MPa}, G_{23} = 3.7 \text{ MPa}$	$\sigma_o = 60 \text{ MPa}$ case II

Table 2. Properties of both carbon fiber-reinforced epoxy material and specimen interface

The LS-DYNA finite element model, which is shown deformed in figure 6, consists of two layers of fully integrated S/R 8-noded solid elements, with 3 elements across the thickness. Two cases with different mesh sizes are used in the initial analysis, namely: case A, which includes eight elements across the width, and case B, which includes one element across the width, respectively. The two cases are compared using the new cohesive elements with mesh size of 1 mm to figure out the anticlastic effects.

A plot of a reaction force as a function of the applied end displacement is shown in figure 7. It is clearly shown that both cases bring similar results with peak load value of 64 N. Therefore, the anticlastic effects are neglected and only one element (case B) is used across the width in the following analyses.

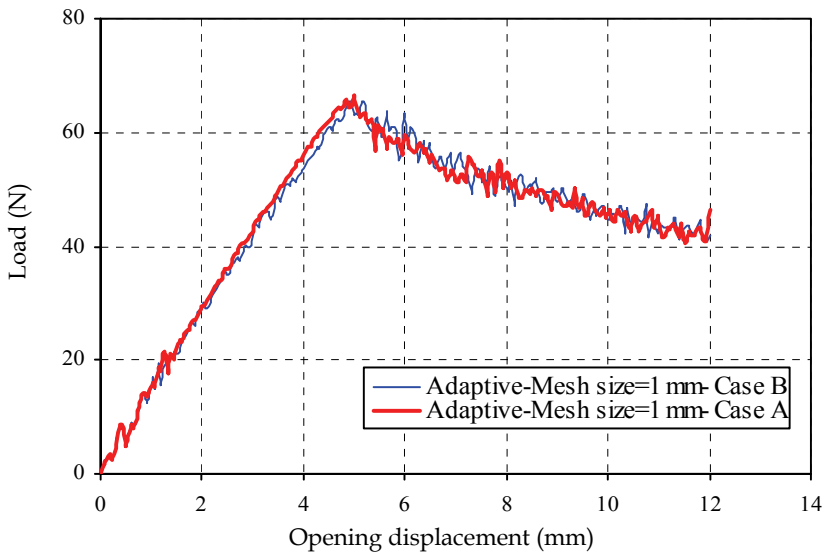


Fig. 7. Load-displacement curves for a DCB specimen in both cases A and B

Different cases are considered in this study and given in table 3 to investigate the influence of the new adaptive cohesive element using different mesh sizes. The aim of the first five cases is to study the effect of the element size with constant values of interface strength and stiffness on the load-displacement relationship. Different element sizes are used along the interface spanning from very small size of 0.5 mm to coarse mesh of 2 mm. Moreover, cases 3, 6, and 7 are to study the effect of the value of minimum interface strength on the results. Finally, Cases 6 and 8 are to find out the effect of the high interfacial strength.

Case 1	Mesh size = 2 mm	$\sigma_o = 45 \text{ MPa}$, $\sigma_{\min} = 15 \text{ MPa}$	$K_o = 3 \times 10^4 \text{ N/mm}^3$, $K_{\min} = 1 \times 10^4 \text{ N/mm}^3$
Case 2	Mesh size = 1.25 mm	$\sigma_o = 45 \text{ MPa}$, $\sigma_{\min} = 15 \text{ MPa}$	$K_o = 3 \times 10^4 \text{ N/mm}^3$, $K_{\min} = 1 \times 10^4 \text{ N/mm}^3$
Case 3	Mesh size = 1 mm	$\sigma_o = 45 \text{ MPa}$, $\sigma_{\min} = 15 \text{ MPa}$	$K_o = 3 \times 10^4 \text{ N/mm}^3$, $K_{\min} = 1 \times 10^4 \text{ N/mm}^3$
Case 4	Mesh size = 0.75 mm	$\sigma_o = 45 \text{ MPa}$, $\sigma_{\min} = 15 \text{ MPa}$	$K_o = 3 \times 10^4 \text{ N/mm}^3$, $K_{\min} = 1 \times 10^4 \text{ N/mm}^3$
Case 5	Mesh size = 0.5 mm	$\sigma_o = 45 \text{ MPa}$, $\sigma_{\min} = 15 \text{ MPa}$	$K_o = 3 \times 10^4 \text{ N/mm}^3$, $K_{\min} = 1 \times 10^4 \text{ N/mm}^3$
Case 6	Mesh size = 1 mm	$\sigma_o = 45 \text{ MPa}$, $\sigma_{\min} = 22.5 \text{ MPa}$	$K_o = 3 \times 10^4 \text{ N/mm}^3$, $K_{\min} = 1.5 \times 10^4 \text{ N/mm}^3$
Case 7	Mesh size = 1 mm	$\sigma_o = 45 \text{ MPa}$, $\sigma_{\min} = 10 \text{ MPa}$	$K_o = 3 \times 10^4 \text{ N/mm}^3$, $K_{\min} = 0.667 \times 10^4 \text{ N/mm}^3$
Case 8	Mesh size = 1 mm	$\sigma_o = 60 \text{ MPa}$, $\sigma_{\min} = 30 \text{ MPa}$	$K_o = 3 \times 10^4 \text{ N/mm}^3$, $K_{\min} = 1.5 \times 10^4 \text{ N/mm}^3$

Table 3. Different cases of analyses

Figures 8 and 9 show the load-displacement curves for both normal (bilinear) and adaptive cohesive elements in cases 1 and 5, respectively, with different element sizes.

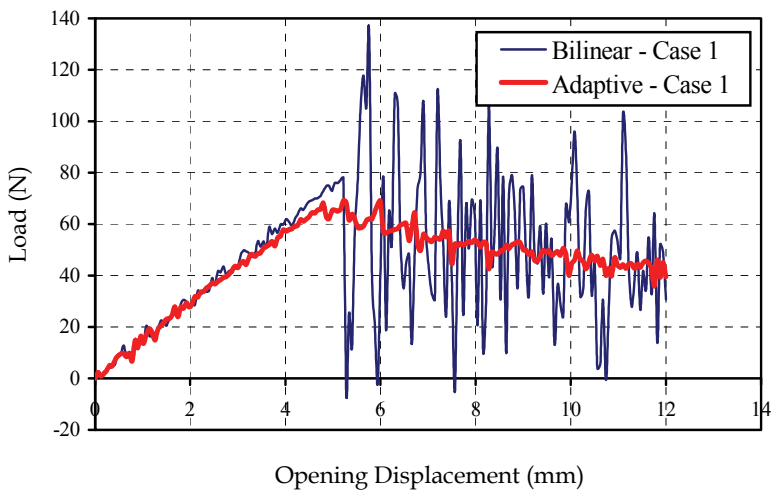


Fig. 8. Load-displacement curves obtained using both bilinear and adaptive formulations- case 1

Figure 8 clearly shows that the bilinear formulation results in a severe instability once the crack starts propagating. However, the adaptive constitutive law is able to model the

smooth, progressive crack propagation. It is worth mentioning that the bilinear formulation brings smooth results by decreasing the element size. And it is clearly noticeable from figure 9 that both bilinear and adaptive formulations are found to be stable in case 5 with very small element size. This indicates that elements with very small sizes need to be used in the softening zone to obtain high accuracy using bilinear formulation. However, this leads to large computational costs compare to case 1. On the other hand, figure 10, which presents the load-displacement curves, obtained with the use of the adaptive formulation in the first five cases, show a great agreement of the results regardless the mesh size. Adaptive cohesive model (ACM) can yield very good results from the aspects of the peak load and the slope of loading curve if σ_{\min} is properly defined. From this figure, it can be found that the different mesh sizes result in almost the same loading curves. Even, with 2 mm mesh size, which considerable large size, although the oscillation is higher compared with those of fine mesh size, ACM still models the propagation in stable manner. The oscillation of the curve once the crack starts propagates became less by decreasing the mesh size. Therefore, the new adaptive model can be used with considerably larger mesh size and the computational cost will be greatly minimized.

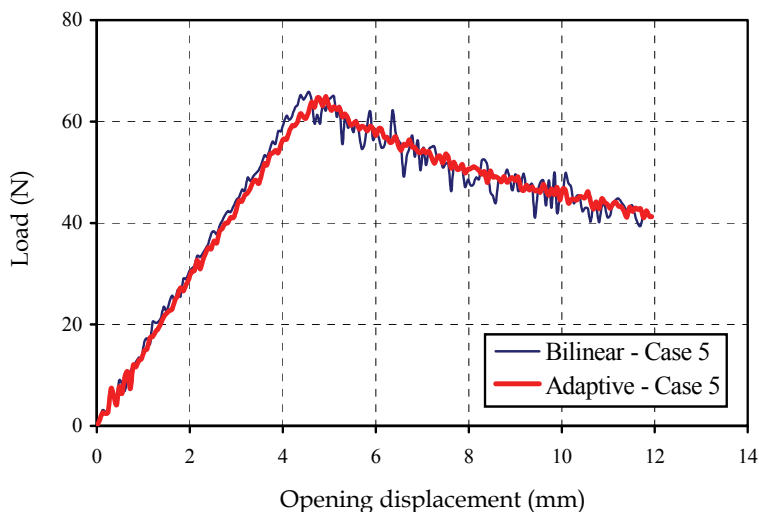


Fig. 9. Load-displacement curves obtained using both bilinear and adaptive formulations- case 5

The load-displacement curves obtained from the numerical simulation of cases 3, 6 and 7 are presented in figure 11 together with experimental data (Camanho & Davila, 2002). It can be seen that the average maximum load obtained in the experiments is 62.5 N, whereas the average maximum load predicted from the three cases is 65 N. It can be observed that numerical curves slightly overestimate the load. It is worth noting that with the decrease of interface strength, the result is stable, very good result can be obtained by comparing with the experimental ones, however, the slope of loading curve before the peak load is obviously lower than those of experimental ones (case 7; $\sigma_{\min}=10.0$ MPa). In case 6 ($\sigma_{\min}=22.5$ MPa) and case 3 ($\sigma_{\min}=15$ MPa), excellent agreements between the experimental data and the

numerical predictions is obtained although the oscillation in case 6 is higher compared with those of case 3. Also, the slope of loading curve in case 3 is closer to the experimental results compared with that in case 6.

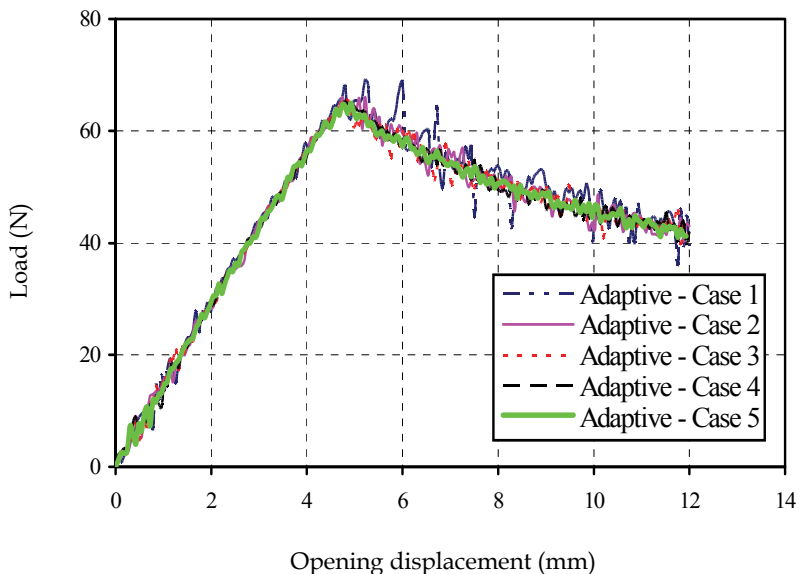


Fig. 10. Load-displacement curves obtained using the adaptive formulation-cases 1-5

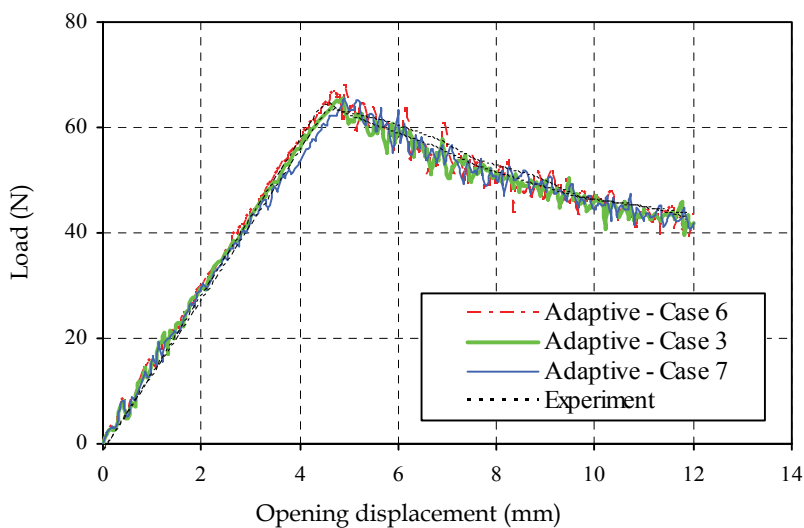


Fig. 11. Comparison of experimental and numerical simulations using the adaptive formulation - cases 3, 6 and 7

Figure 12 show the load-displacement curves of the numerical simulations obtained using the bilinear formulation in both cases, i.e., cases 6 and 8.

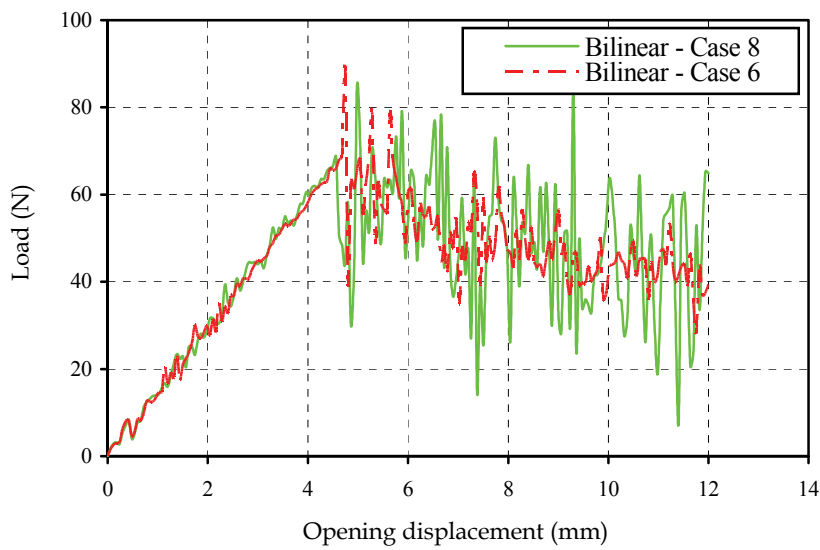


Fig. 12. Load-displacement curves obtained using the bilinear formulation- cases 6 and 8

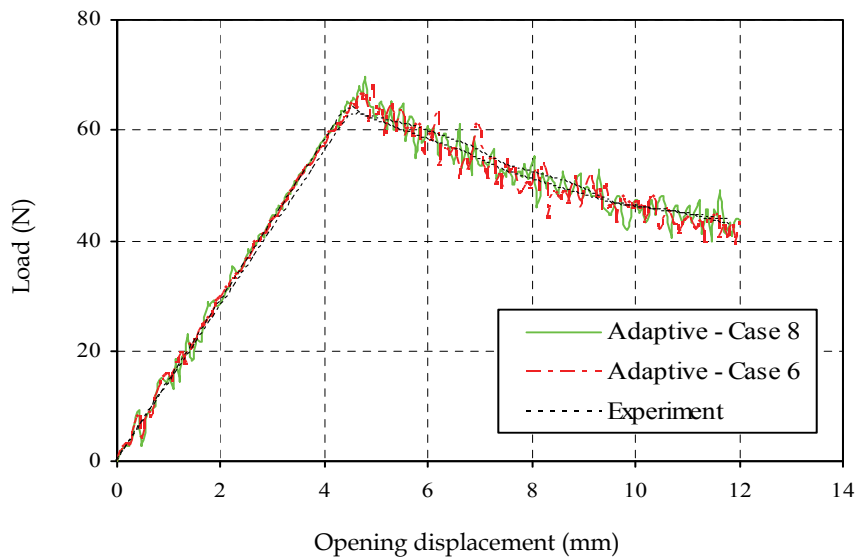


Fig. 13. Comparison of experimental and numerical simulations using the adaptive formulation-cases 6 and 8

The bilinear formulations results in a severe instabilities once the crack starts propagation. It is also shown that a higher maximum traction (case 8) resulted in a more severe instability compared to a lower maximum traction (case 6). However, as shown in figure 13, the load-displacement curves of the numerical simulations obtained using the adaptive formulations are very similar in both cases. The maximum load obtained from case 8 is found to be 69 N while in case 6, the maximum load obtained is 66 N. The adaptive formulation is able to model the smooth, progressive crack propagation and also to produce close results compared with the experimental ones.

4.2 Dynamic analysis

The DCB specimen, as shown in figure 5, is made of an isotropic fibre-reinforced laminate containing a thin insert at the mid-plane near the loaded end, $L=250$ mm, $w=25$ mm and $h=1.5$ mm, was analyzed by Moshier (Moshier, 2006). The initial crack length (l_c) is 34 mm. A displacement rate of 650 mm/sec is applied to the appropriate points of the model. Young's modulus, density and Poisson's ratio of carbon fibre-reinforced epoxy material are given as $E=115$ GPa, $\rho=1566$ Kg/m³, and $\nu=0.27$, respectively. The properties of the DCB specimen interface are given as following: $G_{IC}=0.7$ kJ/m², $K_o=1 \times 10^5$ N/mm³, $K_{min}=0.333 \times 10^5$ N/mm³, $\sigma_o=50$ MPa, and $\sigma_{min}=16.67$ MPa

Similarly, the LS-DYNA finite element model consists of two layers of fully integrated S/R 8-noded solid elements, with 3 elements across the thickness. The adaptive rate-dependent cohesive zone model is implemented using a user defined cohesive material model in LS-DYNA. Two different values of viscosity parameter are used in the simulations; $\eta=0.01$ and 1.0 N-sec/mm³, respectively. Note that η is a material parameter depending on deformation rate, which appears in equations (1) and (11). When $\eta=0$, it would be a traditional model without rate dependence. By observing equation (1), η determines the ratio between viscosity stress $\eta\dot{\sigma}_m$ and interface strength σ_m since $\sigma_m=\sigma_i$ if equations (1) and (4) are considered by setting $K=K_i$. For example, if $\dot{\sigma}_m=6.5$ mm/sec is assumed on the interface here (i.e. 1% of loading rate). $\eta=0.01$ N-sec/mm³ corresponds to a low viscosity stress of 0.065 MPa, which is much lower than the initial interface strength of 50 MPa. However, $\eta=1.0$ N-sec/mm³ corresponds to a viscosity stress of 6.5 MPa, which is around 13% of the interface strength, and denotes a higher rate dependence. In addition, two sets of simulations are performed here. The first set involves simulations of normal (bilinear) cohesive model. The second set involves simulations of the new adaptive rate-dependent model.

A plot of a reaction force as a function of the applied end displacement of the DCB specimen using cohesive elements with viscosity value of 0.01 N-sec/mm³ is shown in figure 14. It is clearly shown from figure 14 that the bilinear formulation results in a severe instability once the crack starts propagating. However, the adaptive constitutive law is able to model the smooth, progressive crack propagation. It is worth mentioning that the bilinear formulation might bring smooth results by decreasing the element size.

The load-displacement curves obtained from the numerical simulation of both bilinear and adaptive cohesive model using viscosity parameter of 1.0 N-sec/mm³ is presented in figure 15. It can be seen that, again, the adaptive constitutive law is able to model the smooth, progressive crack propagation while the bilinear formulation results in a severe instability once the crack starts propagating. The average maximum load obtained using the adaptive

rate dependent model is 110 N, whereas the average maximum load predicted form the bilinear model is 120 N.

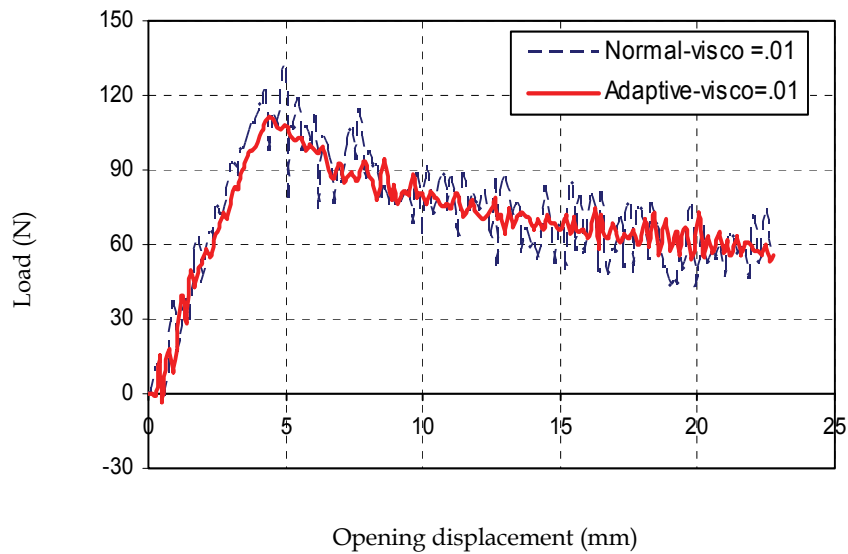


Fig. 14. Load-displacement curves obtained using both bilinear and adaptive formulations ($\eta = 0.01$)

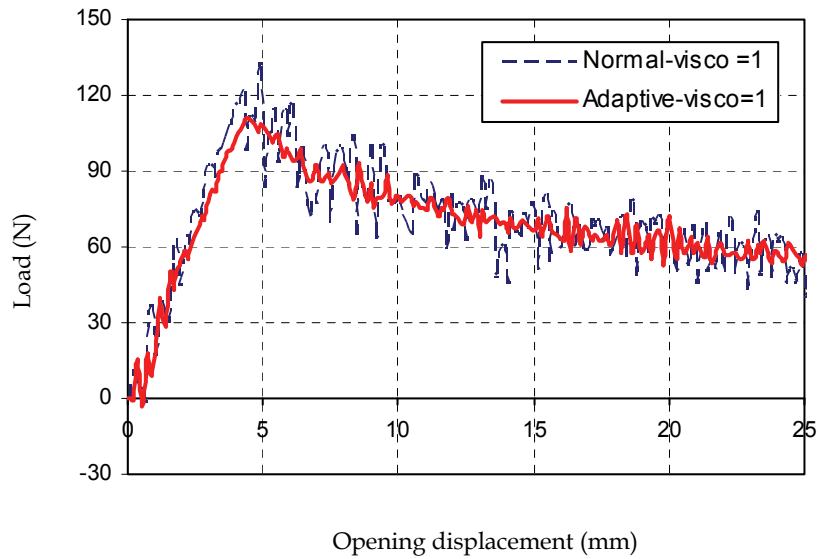


Fig. 15. Load-displacement curves obtained using both bilinear and adaptive formulations ($\eta =1$)

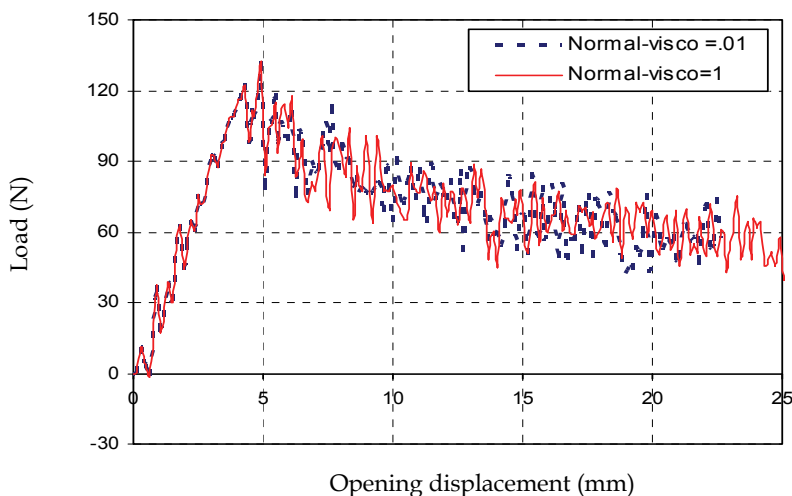


Fig. 16. Load-displacement curves obtained using bilinear formulations ($\eta = 0.01, 1$)

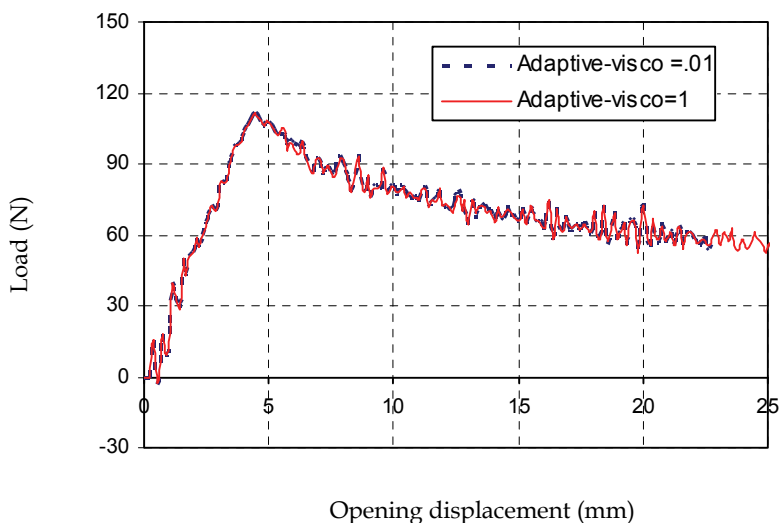


Fig. 17. Load-displacement curves obtained using adaptive formulations ($\eta = 0.01, 1$)

Figure 16 shows the load-displacement curves of the numerical simulations obtained using the bilinear formulation with two different viscosity parameters, 0.01 and 1.0 N-sec/mm³, respectively. It is noticed from figure 16 that, in both cases, the bilinear formulation results in severe instabilities once the crack starts propagation. There is a very slight improvement to model the smooth, progressive crack propagation using bilinear formulations with a high viscosity parameter. On the other hand, the load-displacement curves of the numerical simulations obtained using the new adaptive formulation with two different viscosity

parameters, 0.01 and 1.0 N-sec/mm³, respectively, is depicted in figure 17. It is clear from figure 17 that the adaptive formulation able to model the smooth, progressive crack propagation irrespective the value of the viscosity parameter. More parametric studies will be performed in the ongoing research to accurately predict the effect of very high value of viscosity parameter on the results using both bilinear and adaptive cohesive element formulations.

5. Conclusions

A new adaptive cohesive element is developed and implemented in LS-DYNA to overcome the numerical insatiability occurred using the bilinear cohesive model. The formulation is fully three dimensional, and can be simulating mixed-mode delamination, however, in this study, only DCB test in Mode-I is used as a reference to validate the numerical simulations. Quasi-static and dynamic analyses are carried out in this research to study the effect of the new constitutive model. Numerical simulations showed that the new model is able to model the smooth, progressive crack propagation. Furthermore, the new model can be effectively used in a range of different element size (reasonably coarse mesh) and can save a large amount of computation. The capability of the new mode is proved by the great agreement obtained between the numerical simulations and the experimental results.

6. Acknowledgement

The author wishes to acknowledge the research support and constitutive models provided for this ongoing research by Professor Ning Hu.

7. References

- Camanho, P. & Davila, C. (2004). Fracture analysis of composite co-cured structural joints using decohesion elements. *Journal of Fatigue & Fracture of Engineering Materials & Structures*, Vol. 27, 745-757
- Camanho, P.; Da'vila, C. & De Moura, M. (2003). Numerical simulation of mixed-mode progressive delamination in composite materials. *Journal of Composite Materials*, Vol. 37, No. 16, 1415-38
- Camanho, P. & Davila C. (2002). Mixed-mode decohesion finite elements for the simulation of delamination in composite materials. NASA/TM-2002-211737, 1-37
- Camanho, P.; Davila, C. & Ambur, D. (2001). Numerical simulation of delamination growth in composite materials. NASA-TP-211041, 1-19
- Chen, J.; Crisfield, M.; Kinloch, A.; Busso, E.; Matthews, F. & Qiu, Y. (1999). Predicting progressive delamination of composite material specimens via interface elements. *Mechanics of Composite Material and structures*, Vol. 6, No. 4, 301-317
- Costanzo, F. & Walton, J. (1997). A study of dynamic crack growth in elastic materials using a cohesive zone model. *International Journal of Engineering Science*, Vol. 35, No. 12/13, 1085-1114
- Cui, W. & Wisnom, M. (1993). A combined stress-based and fracture mechanics-based model for predicting delamination in composites. *Composites*, Vol. 24, 467-474

- Davila, C.; Camanho, P. & De Moura M. (2001). Mixed-mode decohesion elements for analyses of progressive delamination. *42nd AIAA/ASME/ASCE/AHS/ASC Structures, Structural Dynamics and Material Conference*, pp. 1-12, April 2001, Washington, USA
- De Moura, M.; Gonçalves, J.; Marques, A. & De Castro, P. (2000). Prediction of compressive strength of carbon-epoxy laminates containing delaminations by using a mixed-mode damage model. *Composite Structure*, Vol. 50, No. 2, 151-157
- De Moura, M.; Goncalves, J.; Marques, A. & De Castro, P. (1997). Modeling compression failure after low velocity impact on laminated composites using interface elements. *Journal of Composite Materials*, Vol. 31, No. 15, 1462-1479
- De Xie, A. & Waas, A. (2006). Discrete cohesive zone model for mixed-mode fracture using finite element analysis. *Engineering Fracture Mechanics*, Vol. 73, No. 13, 1783-1796
- Gao, Y. & Bower, A. (2004). A simple technique for avoiding convergence problems in finite element simulations of crack nucleation and growth on cohesive interfaces. *Modelling and Simulation in Materials Science and Engineering*, Vol. 12, No. 3, 453-463
- Glennie, E. (1971). A strain-rate dependent crack model. *Journal of the Mechanics and Physics of Solids*, Vol. 19, No. 5, 255-272
- Goncalves, J.; De Moura, M.; De Castro, P. & Marques, A. (2000). Interface element including point-to-surface constraints for three-dimensional problems with damage propagation. *Engineering Computations*, Vol. 17, No. 1, 28-47
- Gustafson, P. & Waas, A. (2008). Efficient and robust traction laws for the modeling of adhesively bonded joints. *49th AIAA/ASME/ASCE/AHS/ASC Structures, Structural Dynamics, and Materials Conference*, pp. 1-16, April 2008, Schaumburg, IL, USA
- Hu, N.; Zemba, Y.; Okabe, T.; Yan, C.; Fukunaga, H. & Elmarakbi, A. (2008). A new cohesive model for simulating delamination propagation in composite laminates under transverse loads. *Mechanics of Materials*, Vol. 40, No. 11, 920-935
- Hu, N.; Zemba, Y.; Fukunaga, H.; Wang, H. & Elmarakbi, A. (2007). Stable numerical simulations of propagations of complex damages in composite structures under transverse loads. *Composite Science and Technology*, Vol. 67, No. 3-4, 752-765
- Kubair, D.; Geubelle, P. & Huang, Y. (2003). Analysis of a rate dependent cohesive model for dynamic crack propagation. *Engineering Fracture Mechanics*, Vol. 70, No. 5, 685-704
- LSTC, Livermore Software Technology Corporation, California, USA, LS-DYNA 970, 2005
- Mi, Y.; Crisfield, M. & Davis, G. (1998). Progressive delamination using interface element. *Journal of Composite Materials*, Vol. 32, No. 14, 1246-1272
- Morais, A.; Marques, A. & De Castro, P. (2000). Estudo da aplicacao de ensaios de fractura interlaminar de mode I a laminados compositos multidireccionais. *Proceedings of the 7as jornadas de fractura, Sociedade Portuguesa de Materiais*, p. 90-95, 2000, Portugal
- Moshier, M. (2006). Ram load simulation of wing skin-spar joints: new rate-dependent cohesive model. RHAMM Technologies LLC, USA, Report No. R-05-01
- Petrossian, Z. & Wisnom, M. (1998). Prediction of delamination initiation and growth from discontinues plies using interface elements. *Composite A*, Vol. 29, 503-515
- Pinho, S.; Iannucci, L. & Robinson, P. (2006). Formulation and implementation of decohesion elements in an explicit finite element code. *Composite A*, Vol. 37, 778-789
- Pinho, S.; Camanho, P. & De Moura, M. (2004). Numerical simulation of the crushing process of composite materials. *International Journal of Crashworthiness*, Vol. 9, No. 3, 263-76

- Reddy, E.; Mello, F. & Guess, T. (1997). Modeling the initiation and growth of delaminations in composite structures. *Journal of Composite Materials*, Vo. 31, No. 8, 812-831
- Riks, E. (1979). An incremental approach to the solution of snapping and buckling problems. *International Journal of Solid and Structures*, Vo. 15, 529-551
- Shahwan, K. & Waas, A. (1997). Non-self-similar decohesion along a finite interface of unilaterally constrained delaminations. *Proceeding of the Royal Society of London A*, Vol. 453, No. 1958, 515-550
- Tvergaard, V. & Hutchinson, J. (1996). Effect of strain-dependent cohesive zone model on predictions of crack growth resistance. *International Journal of Solid and Structures*, Vol. 33, No. 20-22, 3297-3308
- Xu, D.; Hui, E.; Kramer, E. & Creton, C. (1991). A micromechanical model of crack growth along polymer interfaces. *Mechanics of Materials*, Vol. 11, No. 3, 257-268

Finite Element Analysis of Progressive Degradation versus Failure Stress Criteria on Composite Damage Mechanics

J.L. Curiel Sosa

*Materials and Engineering Research Institute, Sheffield Hallam University
United Kingdom*

1. Introduction

It is well known that the engineering applications using composite materials is in constant growth, mainly because of the large strength/weight ratio that they provide. The modelling of these materials has been of interest for a long time, due to the experimental costs that can be saved by means of computer simulations. However, the mixed mode of failure in composite materials makes it a complicated task to deal with, resulting often in sophisticated damage models.

There have been numerous techniques proposed for the simulation or prediction of the failure of composites. Many of these techniques were integrated on analytical methods that were subsequently implemented on major simulation software packages or in-house finite element method programs. This is the case in failure models based on stress quadratic functionals, such as those by Tsai & Wu (1971), and implemented within ANSYS (Swanson, 2007) or by Hoffman (1967) and included within ABAQUS (Hibbit et al., 2007). Such functionals imply the disappearing of bearing capability to outstanding loads once the stress criteria are satisfied. From a strict numerical point of view, a finite element satisfying the criteria may potentially be removed from the mesh as it does not experience further loading. This possibility is available in major software packages such as LS-DYNA. The removal of a finite element frequently causes certain numerical oscillations when using explicit solvers. This may degenerate into instabilities and, hence, in divergence of the numerical procedure. A significant number of these criteria have been proposed in the last decades. For instance, the models by Tsai & Wu (1971), Hoffman (1967), Yamada and Sun (1978) or Puck and Schurmann (1998) amongst many others have been very popular. A worldwide assessment failure exercise (WWFE) of a number of these criteria is described in references (Hinton and Soden, 1998; Hinton et al., 2004). Also, Soden et al. (1998a) presented the result for fibre-reinforced composite laminates and their correlation to a set of shared-by-participants experimental data (Soden et al., 1998b). It is clear that considerable efforts have been done in the searching of a general criteria that may be applied in a wide range of problems. However, Daniel (2007) reveals discrepancies of up to 200-300% in the WWFE results shown by Soden et al. (1998a). Unawareness of the numerical consequences that carry the use of these criteria within a finite element method, such as instability and, finally, divergence of the numerical procedure, result in unrealistic solutions. On the other hand, different

computational techniques for modelling damage progressively were developed to adapt to the finite element methodology. The progressive damage causes the degradation of the stiffness in the damaged zone. Thus, a damaged finite element does not lose completely its loading bearing capacity but the latter is decreased inversely proportional to the degree of damage. The progressive damage models derive from the thermodynamical approaches proposed by Kachanov (1958) initially and, most famously acknowledged by Lemaitre (1992); Lemaitre and Chaboche (1990) and Chaboche (1981). Proposals in this field by Matzenmiller et al. (1995), Maimi et al. (2007a;b), Barbero & De Vivo (2001) or Schipperen (2001) have contributed to extend the number of techniques available for damage evolution on composite materials.

The progressive damage models are attractive as they are readily implemented either in major codes or in-house finite element programs. Nevertheless, these models have the uncertainty on when the onset of damage is reproduced. Some authors coupled it to stress criteria as initiation criteria for developing damage to solve this drawback. For instance, Lapczyk & Hurtado (2007) combined a progressive damage model with the stress criteria proposed by Hashin (1980) as a damage initiation criteria. The formulation is based on the fracture energy for representation of fibre failure and matrix failure. Hufenbach et al. (2004) have successfully shown how interactive criteria –combining progression and failure criteria– may be applied for the prediction of failure in textile reinforced composites assuming that they are formed by unidirectional layers. However, Cuntze & Freund (2004) state that the conditions of initiation of failure are not as relevant as the evolution of the stiffness degradation, due to the fact that its influence is decreasing with the damage progression. This is in agreement with other theories that defend the inelastic behaviour of a range of composite materials, (Barbero & Lonetti, 2002). Chow and Yang (1998) developed an inelastic model for the description of damage in composite laminates and its implementation into an incremental displacement-based Finite Element Method (FEM). The stress strain relationship is incorporated into a modified Newton-Raphson iterative method. More recently, Zobeiry et al. (Camanho et al., 2008) presented a progressive damage model with special attention to the nonlocal regularisation of the damage computations. A significant number of these last approaches are limited to plane stress models, such as those by, for example, Allen et al. (1987); Edlun and Volgers (2004); Harris et al. (1995); Hochard et al. (2001); Talreja (1987); Tan (1991) and McCartney (2003). In the best of knowledge, pioneering works on nonlinear behaviour of composites were developed by Chang and Chang (1987) and by Shahid and Chang (1995). Both works are dedicated to the analysis of composite plates. Lessard and Shokrieh (1995) state that two-dimensional analysis may produce sensibly different results as a consequence of the anisotropy induced by distinct modes of damage in the originally orthotropic composite. Nowadays, three dimensional models for laminates are readily implemented in computational techniques due to advances in computer power and programming facilities.

New techniques have been explored for assessing damage and, in some cases, healing on composite laminates. Such are the cases of the Virtual Crack Closure Technique (VCCT) or the use of cohesive elements –(interface elements)– on finite element procedures. Both of these techniques have links to the *Fracture Mechanics* field. VCCT was proposed by Rybicki and Kanninen (1977) and Rybicki et al. (1977) derived from the Irwin's theory (Irwin, 1948) for crack analysis. Xie & Biggers (2006) and Leski (2007) coded successfully VCCT within a finite element program. VCCT relies on the calculation of the J-integral without the restriction

of having excessive refinement of the mesh in the proximities of the crack tip which is also an advantage for computational saving. VCCT has the problem, like progressive damage models based in thermodynamical theory, of not having an initiation criteria for propagation of the fracture. The use of cohesive elements has been recently boosted. An excellent works by Camanho & Mathews (1999); Camanho et al. (2003) or Iannucci and Willows (2006) show a damage progression scheme combined with interface elements to couple the damage evolution with the mechanics of the fracture. An excellent review of these technique is provided by Wisnom (2010). Cohesive models are preferred to VCCT technique for a growing number of authors, such as Dugdale (1960), Xie & Waas (2006), Turon et al. (2007)), Tvergaard & Hutchinson (1996), Allen & Searcy (2000), or Cox & Yang (2006). Camanho et al. (2008) and also Hallet (1997) have used interface elements for the prediction of delamination on laminates.

In this chapter, finite element analysis is applied to laminates, and the formulation of the model is developed at lamina scale. The laminate is a stack of laminae of different, in general, fibre orientations. An explicit integration strategy for the finite element analysis is used due to the simplicity and robust convergence that provide¹. The model is adapted in order to be included into an explicit *FEM* (see explicit formulation in Curiel Sosa et al. (2006) for implementation details) whereby the transient response may be conveniently simulated. This chapter is outlined as follows: firstly, a general discussion over damage modes is performed; secondly, the main theoretical aspects of the model are shown; thirdly, the computational algorithm, for implementation of the damage model as an individual module into an in-house *FEM* program as well as in major commercial software packages such as Abaqus or Ansys, is provided; and finally, a set of numerical examples including the low velocity impact on a composite laminate $[0, 90]_a$.

2. Composite damage modes

The damage in composites is generally represented by several modes: matrix cracking, matrix crushing, fibre kinking, fibre rupture or breakage. From a modelling point of view, one may find in the literature different choices of mixed modes of damage in composites. Hashin (1980) considered in his stress criteria four modes:

- matrix failure in tension and compression represented by a criterion that includes transverse-to-fibres stress and a combination of shear stresses.
- fibre-matrix disbonding as a function of the longitudinal stress and shear stresses.
- fibre failure in compression or tension, depending upon the limit values of the axial stresses.
- delamination.

Similar mixed modes criteria were used by Chang and Lessard (1991) which were coded by Ambur et al. (2004) as an *Abaqus* user subroutine for the reader interested in this type of computer implementations. They modelled the progression of the damage modes proposed by Hashin (1980) and applied it to the simulation of composite shells. No implementations to 3D solid elements were shown. Some authors, for example Curiel Sosa et al. (2008a); Curiel Sosa (2008b); Matzenmiller et al. (1995), take into account the following damage modes for modelling:

¹ Stability must be satisfied, i.e. step-time can not trespass on the critical time step

- fibre rupture.
- fibre kinking.
- matrix cracking.
- matrix crushing.

In the progressive damage model presented in Section 3 a three dimensional element is used rather than shells and, hence, a general description of the modes is more appropriate under these premises. Delamination is in an upper material scale and is implicitly implemented in the general flow of the procedure as matrix cracking may eventually result in delamination. In this manner, inelasticity is integrated straightforward within the model. It is well-known from experimental evidence that the idealisation of composite behaviour as linear elastic is inadequate (Chang and Lessard, 1991; Xu, 1994) as inelastic deformations evolve not only due to micro-cracks at the micro-scale but also due to complex damage modes occurring at the macroscale, leading, eventually, to the total failure. Contrary to purely brittle materials, the fibre-reinforced composite material exhibits at some extent a softening behaviour preceding the total failure. This phenomenon, from a strictly thermodynamical point of view, is related to the dissipative (irreversible) process that rearranges the distribution of material properties due to the presence of damage.

3. Progressive damage modelling (PDM)

In this section, a progressive damage model for composites (PDM) is presented (Curiel Sosa et al., 2008a; Curiel Sosa, 2008b), the results of this model are then compared with the outcome of some stress failure criteria. The formulation concerning the implementation of the damage model is also presented below. In PDM, it is assumed that different damage modes develop simultaneously on the failed composite structure and that they can interact directly influencing each other. The approach presented may be framed within the continuum damage mechanics field. The damage variables represent the state of damage at any stage of deterioration. They are implicitly defined for what they may be considered internal state variables that can provide a quantifiable magnitude of the degradation of the composite material. In PDM, damage variables are referred to damage modes via superposition. Thus, a damage mode is represented for one or more than one damage variables with distinct weights as explained below. The adopted damage modes, generically denoted as γ , are modelled by means of a linear combination of growth functions Φ^γ and damage directors \mathbf{v}^γ (Curiel Sosa et al., 2008a). In summary, PDM admits the modelling of different damage modes that can be integrated directly in the description of damage through Equation (6) which is explained on Section (4).

Thus, the damage state may be defined by a series of internal variables ω_{kj} , filling the diagonal damage tensor \mathbf{D} (see Equation (1)) that represents the state of damage in the composite.

$$\hat{\sigma} = \mathbf{D} \cdot \sigma \quad (1)$$

where $\sigma^T = [\sigma_{11}, \sigma_{22}, \sigma_{33}, \sigma_{12}, \sigma_{23}, \sigma_{31}]$ is an array formed by the stress components and $\hat{\sigma}$ is the so-called effective stress array (Chaboche, 1981). The definition of tensors and properties is conducted in a local system of reference for the lamina. Variables and parameters numeric subscripts refer to the local lamina system of reference. Thus, axis 1 is pointed

in the longitudinal direction to the fibres whereas the other two axes, i.e. 2 and 3, are in perpendicular direction to fibres.

The damage tensor is built as a diagonal tensor and contains the damage internal variables ω_{kj} , see Equation (2). These are responsible for the degradation of the stiffness components.

$$diag(\mathbf{D}) = \left[\frac{1}{1-\omega_{11}}, \frac{1}{1-\omega_{22}}, \frac{1}{1-\omega_{33}}, \frac{1}{1-\omega_{12}}, \frac{1}{1-\omega_{23}}, \frac{1}{1-\omega_{31}} \right] \quad (2)$$

The effective stresses $\hat{\sigma}$ are assumed to fulfil the strain equivalence principle (Lemaitre and Chaboche, 1990) resulting, eventually, in Equation (3).

$$\hat{\sigma} = \mathbf{C}_0 \cdot \varepsilon \quad (3)$$

Inverting the damage tensor \mathbf{D} and substituting Equation (1) into Equation (3), renders the stress-strain constitutive law, Equation (4).

$$\sigma = \mathbf{D}^{-1} \cdot \mathbf{C}_0 \cdot \varepsilon = \mathbf{C}(\omega) \cdot \varepsilon \quad (4)$$

where \mathbf{C}_0 is the stiffness matrix. It should be noticed that the introduction of the degradation internal variables ω_{ij} yields a non-symmetric tensor $\mathbf{C}(\omega)$ (see Equation (5)). The matrices \mathbf{A} and \mathbf{B} , defined in a local system of reference, are introduced in order to read \mathbf{C} in a more compact manner.

$$\mathbf{A}(\omega) = \begin{bmatrix} \frac{(1-\omega_{11})(1-\nu_{23}\nu_{32})}{E_{22}E_{33}\Delta} & \frac{(1-\omega_{11})(\nu_{12}+\nu_{32}\nu_{13})}{E_{11}E_{33}\Delta} & \frac{(1-\omega_{11})(\nu_{13}+\nu_{12}\nu_{23})}{E_{11}E_{22}\Delta} \\ \frac{(1-\omega_{22})(\nu_{12}+\nu_{32}\nu_{13})}{E_{11}E_{33}\Delta} & \frac{(1-\omega_{22})(1-\nu_{13}\nu_{31})}{E_{11}E_{33}\Delta} & \frac{(1-\omega_{22})(\nu_{23}+\nu_{21}\nu_{13})}{E_{11}E_{22}\Delta} \\ \frac{(1-\omega_{33})(\nu_{13}+\nu_{12}\nu_{23})}{E_{11}E_{22}\Delta} & \frac{(1-\omega_{33})(\nu_{23}+\nu_{21}\nu_{13})}{E_{11}E_{22}\Delta} & \frac{(1-\omega_{33})(1-\nu_{12}\nu_{21})}{E_{11}E_{22}\Delta} \end{bmatrix}$$

where Δ is a determinant that depends upon the elastic properties,

$$\Delta = \frac{(1 - \nu_{12}\nu_{21} - \nu_{23}\nu_{32} - \nu_{31}\nu_{13} - 2\nu_{21}\nu_{32}\nu_{13})}{E_{11}E_{22}E_{33}}$$

$$\mathbf{B}(\omega) = \begin{bmatrix} (1-\omega_{12})G_{12} & 0 & 0 \\ 0 & (1-\omega_{23})G_{23} & 0 \\ 0 & 0 & (1-\omega_{31})G_{31} \end{bmatrix}$$

Note that the 'damaged' stiffness tensor $\mathbf{C} \in \mathcal{R}^{6 \times 6}$ is built as follows,

$$\mathbf{C}(\omega) = \left[\begin{array}{c|c} \mathbf{A}(\omega) & \mathbf{O} \\ \hline \mathbf{O} & \mathbf{B}(\omega) \end{array} \right] \quad (5)$$

where $\mathbf{O} \in \mathcal{R}^{3 \times 3}$ is a matrix filled with zeros.

4. Definition of damage internal variables

The time variation of damage internal variables is defined as a linear combination of the Φ^γ growth functions and the damage directors (Equation (6)).

$$\dot{\omega} = \sum_{\gamma=1}^{nmodes} \Phi^\gamma \mathbf{v}^\gamma \quad (6)$$

In the above, γ denotes a mode of damage and n_{modes} denotes the total number of failure modes. The growth functions for each damage mode γ are computed through Equation (7).

$$\Phi^\gamma = \langle \nabla_\epsilon g^\gamma, \dot{\epsilon} \rangle_+ \quad (7)$$

where ∇_ϵ is the strain gradient $\frac{\partial}{\partial \epsilon}$ and $\dot{\epsilon}$ the strain rate. $\langle \cdot \rangle_+$ denotes the non-negative inner product accounting for the trespassing on the damage surface. The subscript $+$ indicates that the inner product vanishes for negative values. This ensures that there is no growth of damage if the damage surface is not reached. If the strain increment vector is pointing to the interior of the surface (for a generic damage mode γ) there is no progression of that particular damage mode. So a simple way to effectively computing this is to perform the nonnegative scalar product as represented in equation (7). In Equation (8), g^γ are the evolving damage surfaces in the strain space.

$$g^\gamma = \epsilon^T \cdot \mathbf{G}^\gamma \cdot \epsilon - c^\gamma \quad (8)$$

where c^γ is an empirical parameter defining the damage surface. The variations of these surfaces on the strain space result in Equation (9). It should be noticed that c^γ are not needed in the numerical scheme as Equation (9) is the one necessary for the computational procedure. In this manner, the number of experimental data, which are difficult, or even impossible with the current techniques to obtain, are sensibly reduced.

$$\nabla_\epsilon g^\gamma = \epsilon^T \cdot (\mathbf{G}^{\gamma T} + \mathbf{G}^\gamma) \quad (9)$$

After some algebra, \mathbf{G}^γ second-order tensors are derived from Equation (3) and from the equivalence of the quadratic forms in stress and strain spaces given by Equation (10) (Curiel Sosa et al., 2008a).

$$\sigma^T \cdot \mathbf{F}^\gamma \cdot \sigma = \epsilon^T \cdot \mathbf{G}^\gamma \cdot \epsilon \quad (10)$$

\mathbf{F}^γ are second-order tensors are derived from damage surfaces defined on the stress space. The modelling of the unitary damage directors \mathbf{v}^γ is based upon the stiffness components that are degraded when a particular mode of damage occurs. For instance, fibre rupture $\mathbf{v}^{(1)}$ affects to the stiffness degradation in (11), (12) and (31) directions,

$$\mathbf{v}^{(1)} = \left[\lambda_{11}^{(1)} \ 0 \ 0 \ \lambda_{12}^{(1)} \ 0 \ \lambda_{31}^{(1)} \right]^T$$

The weights λ_{ij}^γ may be estimated from experimental observations in a qualitative manner for the corresponding damage mode. This technique is still being researched to provide a more straightforward computational strategy that allows to update \mathbf{v}^γ at every time step of the numerical procedure. Techniques such as *Inverse Modelling* or *Optimization* are also possible for a more efficient modelling of \mathbf{v}^γ . However, at present, no attempt of using these techniques is being made.

5. PDM algorithm

The PDM algorithm has been implemented into an in-house *FEM*. Additionally, it was coded within AbaqusTM as a *vumat* subroutine. It is adapted for the majority of the commercial software packages based in the *explicit FEM*. The computation of stresses, performed by numerical integration, includes the constitutive law expressed by the model described (see the algorithm below). A loop over damage modes is performed for the computation of stress

at each quadrature point. This is gathered in step (I) below. The computational algorithm is briefly outlined as follows,

- I. Loop over damage modes, for $\gamma = 1$ to $\gamma = nmodes$ do:
 - i. Compute the 'damaged' stiffness tensor: $\mathbf{C}(\omega)$.
 - ii. Generate \mathbf{F}^γ . Note that the γ superscript may be treated as a third index which may provide clarity to the code.
 - iii. Calculate: $\mathbf{G}^\gamma = \mathbf{C}^T \cdot \mathbf{F}^\gamma \cdot \mathbf{C}$. Each γ gives place to a distinct damage surface in the strain space g^γ , i.e. one for every damage mode (see Equation (8)). Calculation of g^γ is not required as \mathbf{G}^γ is the only entity needed for the following steps.
 - iv. Strain gradient of damage in strain space: $\nabla_\varepsilon g^\gamma = \varepsilon^T \cdot (\mathbf{G}^{\gamma T} + \mathbf{G}^\gamma)$.
 - v. Growth of damage γ : $\Phi^\gamma = \langle \nabla_\varepsilon g^\gamma, \dot{\varepsilon} \rangle_+$
 - vi. Directional damage vector: \mathbf{v}^γ
- II. For current gauss point, compute the damage internal variables array as a linear combination of damage directors and damage mode growth: $\dot{\omega} = \sum_{k=1}^{nmodes} \Phi^\gamma \mathbf{v}^\gamma$.

6. Numerical examples

6.1 Tension and compression tests

In this section, tension and compression tests on a fibre reinforced composite are presented using the PDM algorithm. The lamina is formed by longitudinal glass fibres embedded firmly within an epoxy matrix. The material parameters for the tests are: Young's modulus $E_1 = 126\text{GPa}$, $E_2 = E_3 = 11\text{GPa}$, Poisson ratios $\nu_{12} = \nu_{13} = 0.28$, $\nu_{23} = \nu_{32} = 0.4$, $\nu_{21} = \nu_{31} = 0.024$ normal strengths $X_{11} = 1950\text{MPa}$, $X_{22} = X_{33} = 48\text{MPa}$, and shear strengths $S_{12} = S_{31} = 79\text{MPa}$. The load is a distributed force applied incrementally in parallel direction to the fibres up to complete failure, i.e. until the lamina can not withstand the load any longer. The load is applied over one of the sides of dimension $1\text{ m} \times 0.1\text{ m}$, whilst the opposite side is constrained in motion.

Charts represent the evolution of variables and parameters at the interior central point, i.e. centre of mass. Figure (1) displays the stress vs. strain relationship from the numerical simulation and comparison with the experimental data for the tension test. A misplacement can be observed in the slope corresponding to the linear elastic behaviour. However, this is not sensibly affecting the overall response and, in particular, the softening response in the nonlinear inelastic regime in which the proposed model is focused. A numerical quantification of each damage mode are the internal variables Φ^γ which represent the evolution of each damage mode. In other words, the evolution of Φ^γ is a numerical quantifiable representation of the damage mode γ allowing to know what are the magnitude of a particular damage mode and its relation to the remaining damage mode evolutions to be determined. It should be expected that the damage modes in tension would be fibre rupture and matrix cracking and, on the contrary, the damage modes that should evolve in compression would be fibre kinking and matrix crushing. This is what PDM detects efficiently as proved in Figure (2) for the tension test and, in Figure (3) for the compression test. This is an excellent characteristic of PDM as it permits the detection of the correct damage mode depending upon the stress state in corresponding region or domain. Thus, for example, Φ_2 corresponding to fibre kinking damage mode should be zero as this type of failure is not possible in a tension test. Fibre

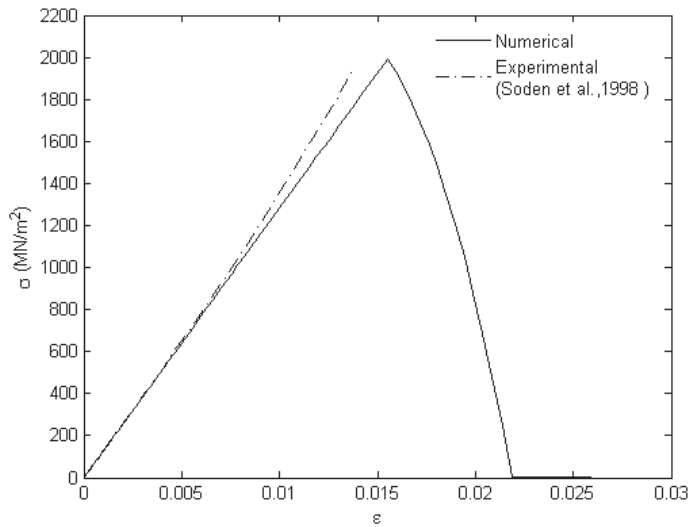


Fig. 1. Stress vs strain relationship in fibre direction for the tension test.

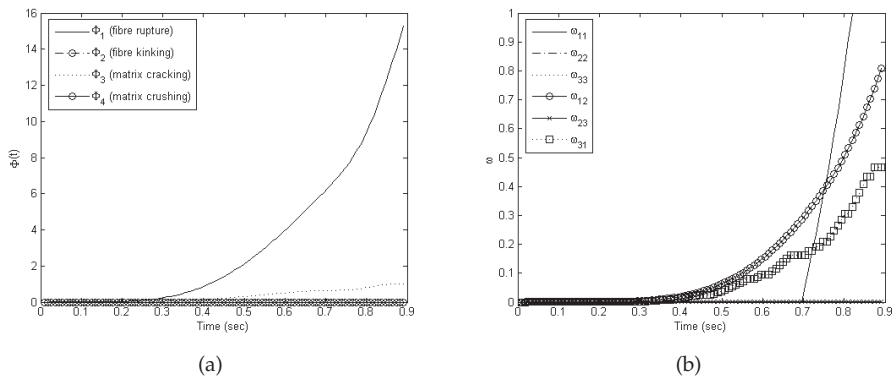


Fig. 2. Tension test –longitudinal direction to the fibres:(a) Evolution of each damage mode growth parameter. (b) Damage internal variables time evolution.

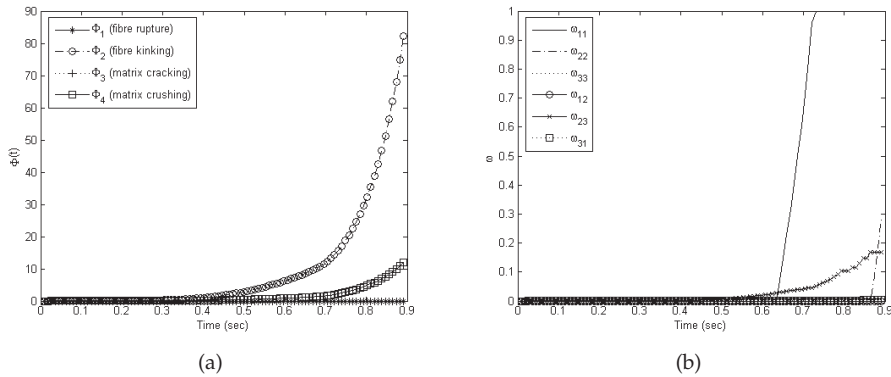


Fig. 3. Compression test –longitudinal direction to the fibres:(a) Evolution of each damage mode growth parameter. (b) Damage internal variables time evolution.

rupture or breakage and matrix cracking are the only modes expected in a tension test. This is in agreement with the computational model output, see Figure (2a). Also, the internal variables ω_{ij} shows how the different damage modes affect the degradation of the stiffness components (see Equation (4)). In Figure (2b), it is observed, as expected, that ω_{11} increases in an exponential manner. Eventually, it reached the maximum of 1 which is equivalent to complete failure.

In the compression test, the modes of damage obtained are fibre kinking and matrix crushing. This is in agreement with the mechanics of the composite as no other sort of damage should be observed in the centre of the sample in this test. As the failure is significantly affecting the longitudinal direction, again, the internal variable subjected to a higher rate of increment is ω_{11} , see Figure (3b).

6.2 Impact on $[0/90]_a$ laminate

In this section, the proposed model is tested by means of a well known three-dimensional example with clear matrix crushing and matrix cracking damage developments. This test consists of a low velocity impact -7.08 ms^{-1} on a laminate $[0/90]_a$ formed by 21 alternate laminae, see Figure 4, made of carbon fibres and epoxy resin. The composite obtained is a transversally isotropic fibre reinforced composite material with a volume fraction of 60%. Experimental tests were conducted by Hallet (1997) using a Hopkinson bar apparatus, see (Hou et al., 2000) for more details of the set-up of this experiment. Basically, the projectile is a titanium alloy rod with a diameter of 9.55 mm and a total length of 500 mm and its head is rounded in order to damp the vibrations. The mass of the projectile was calibrated to 260 g to strictly replicate the experiment.

The dimensions of the laminate were $2.6 \times 85 \times 85 \text{ mm}^3$ and it is supported by a steel ring with an inner diameter of 45 mm . In the experiments performed by Hallet (1997), the impact velocity was measured by infra-red timing gates just before the laminate was struck. C-scan and dye contrasts were used to detect damage after impact. The results of dye contrast test showed that the projectile impacted with an initial velocity of 7.08 ms^{-1} and, hence, this is the impact velocity that has been used in these numerical tests. In the experiments by Hallet (1997) as

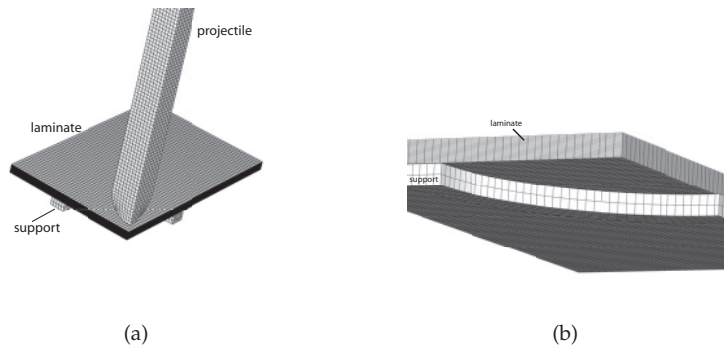


Fig. 4. Initial setup: (a) A quarter of the real configuration is used in the numerical tests thanks to the symmetry. (b) A closer snapshot of the laminate and the support.

well as in the numerical tests conducted by Hou et al. (2000), a matrix crushing zone was observed just beneath the contact region, i.e. in the through-thickness compression region under the projectile. The numerical result for matrix crushing region from the proposed model is depicted in Figure 5. It may be observed that the matrix crushing zones are located in agreement with the experimental results by Hallet (1997); Hou et al. (2000). The progressive development of those regions is more realistic than the result obtained using just stress failure criteria as depicted in Figure (6) which provides Boolean values for the damage variables without considering any progression of the damage. In the computational results using PDM, neither fibre rupture nor fibre kinking were developed as expected with that impact velocity. To turn off the damage modes according to physical reality is an excellent characteristic of PDM.

7. Conclusion

This chapter has provided an overview of the different techniques used for modelling damage in composites briefly showing the current state-of-art of the topic. Basically, from a computational point of view, there are two main trends:

- failure criteria which generally use a stress quadratic form.
- a progressive evolution of the damage.

The author's choice is the second one for two main reasons. Firstly, because failure criteria is creating Boolean values for deciding when a finite element is deleted or split which, in turn, cause numerical instabilities and, eventually, divergence in explicit finite element simulations. Secondly, the progression of damage, even if it is sudden, evolves sequentially in a microscopic scale which reasonably makes the progressive damage models more realistic. Following this second tendency, the author has presented a progressive damage model (PDM) for fibre reinforced composites. The approach is based in a directional computation and a progressive growth of of damage modes depending upon the stress state and strain rate amongst other variables. Moreover, the constitutive law is implicitly relying upon the strain rate, which makes the model suitable for a wide range of strain rate values including impact. The computation is, in general, intended for time stepping numerical methods and, in particular, for the *explicit FEM*. The PDM algorithm is offered for straightforward

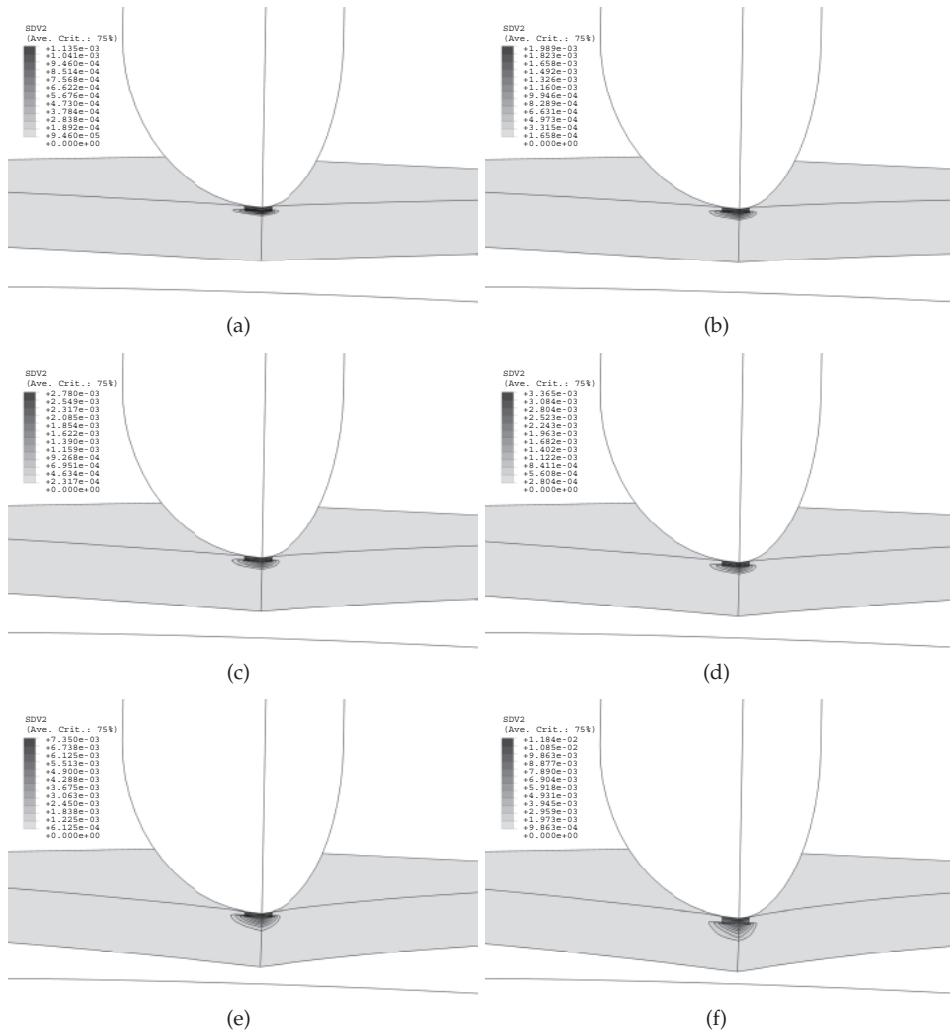


Fig. 5. Development of matrix crushing damaged zone and grades in the laminate when impacted at 7.08 m s^{-1} .

implementation in an explicit FEM code either commercial software package or in-house code. The outcome obtained by using PDM for tension and compression tests provide the expected progression of the damage variables, being able to determine the corresponding damage modes associated with each stress state and rate of strain, eventually leading to the expected behaviour. Furthermore, the computational results by using PDM for the low velocity impact on a laminate were in an excellent agreement with the experimental observations of matrix cracking and matrix crushing which, eventually, caused the delamination in those damaged regions of the laminate.

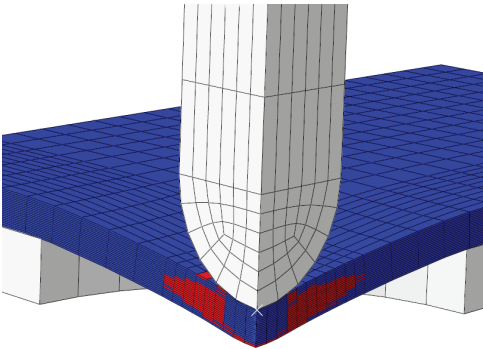


Fig. 6. Matrix cracking pattern using a classical failure criterion based on stress components. The elements in red fulfilled the criterion which means that they are not withstanding loads any longer.

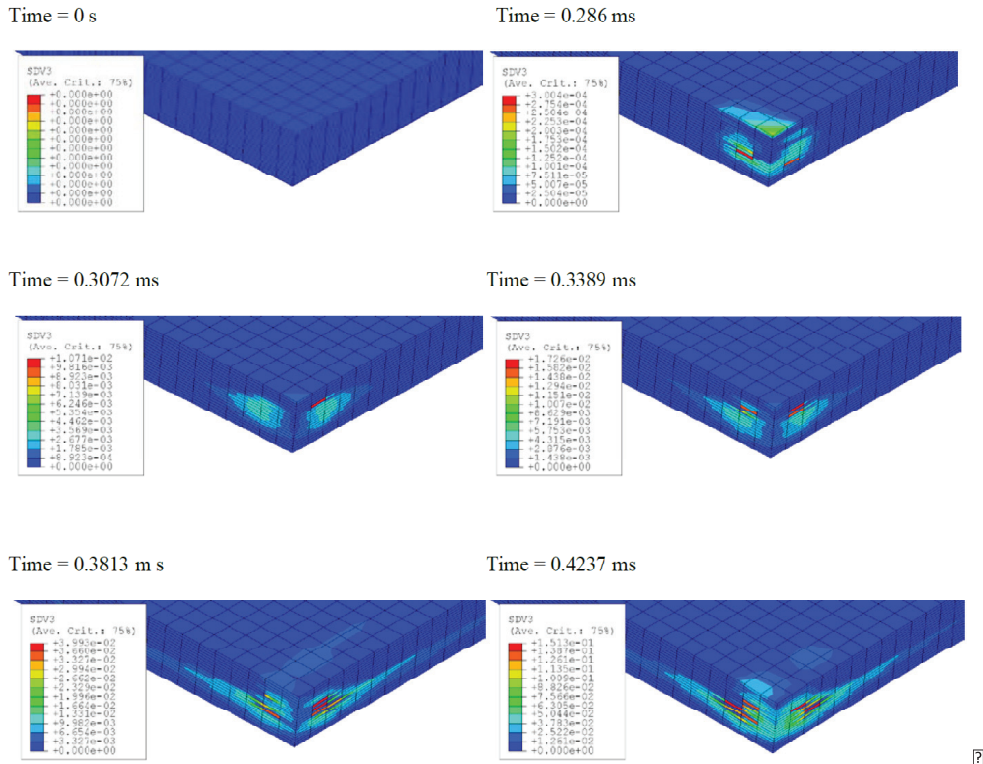


Fig. 7. Sequential matrix cracking pattern observed during simulation by explicit FEM using PDM. A time progressive evolution of this damage mode, which eventually turned into delamination, is observed in an excellent agreement with the experimental observations.

8. References

- Allen, D.H., Harris, C., & Groves, S.E. (1987). A thermomechanical constitutive theory for elastic composites with distributed damage. Part I: theoretical development. *Int. J. Solids Struct.* **Vol.** 23(No. 9):1301-1318.
- Allen, D.H. & Searcy, C.R. (2000). Numerical aspects of a micromechanical model of a cohesive zone. *Journal of Reinforced Plastics and Composites*, **Vol.** 19(No. 3):240–248.
- Ambur, D.R., Jaunky, N., Hilburger M. & Dávila C.G. (2004). Progressive failure analyses of compression-loaded composite curved panels with and without cutouts. *Composite Structures* **Vol.** 65:143-155.
- Barbero, E.J. & De Vivo, L. (2001). Constitutive model for elastic damage in fiber-reinforced pmc laminae. *International Journal of Damage Mechanics*, **Vol.** 10(No. 1):73–93.
- Barbero, E.J. & Lonetti, P. (2002) An inelastic damage model for fiber reinforced laminates. *Journal of Composite Materials*, **Vol.** 36(No. 8):941–962.
- Boso, D., Pellegrino, C., Galvaneto, U. & Schrefler, B.A. (2000). Macroscopic damage in periodic composite materials. *Commun. Numer. Meth. Engng.* **Vol.** 16:615-623.
- Camanho, P.P. & Mathews, F.L. (1999). A progressive damage model for mechanically fastened joints in composite laminates. *J. Composite Mater.* **Vol.** 33(24):2248-2280.
- Camanho, P.P., Dávila, C.G. & de Moura, M.F. (2003) Numerical simulation of mixed-modes progressive delamination in composite materials. *J. Composite Mater.* **Vol.** 37 (No. 16):1415-1438.
- Camanho, P.P., Dávila, C.G., Pinho, S.T. & Remmers, J.J.C. (2008). *Mechanical Response of Composites: Preliminary Entry 10 (Computational Methods in Applied Sciences)*. Springer.
- Cox, B. & Yang, Q. (2006). In quest of virtual tests for structural composites. *Science*, **Vol.** 314 (No. 5802):1102–1107, 2006.
- Chaboche, J-L. (1981). Continuous Damage Mechanics—a tool to describe phenomena before crack initiation. *Nucl. Engng. Des.* **Vol.** 64:233-247.
- Chang, F-K. & Chang, K.Y. (1987). A progressive damage model for laminated composites containing stress concentration. *J. Composite Mater.* **Vol.** 21:834-855.
- Chang F.K. & Lessard L.B. (1991). Damage Tolerance of Laminated Composites Containing an Open Hole and Subjected to Compressive Loadings: 1 Analysis. *J. Composite Mater.* **Vol.** 25:2-43.
- Chow C.L. & Yang F. (1998). Inelastic finite element analysis of fibre-reinforced composite laminates with damage. *Proc Instn Mech Engrs Part C* **Vol.** 212:717-729.
- Cuntze, R.G. & Freund, A. (2004). The predictive capability of failure mode concept-based strength criteria for multidirectional laminates. *Composites Science and Technology*, **Vol.** 64(3-4):343–377.
- Curiel Sosa, J.L., de Souza Neto, E.A. & Owen D.R.J. (2006). A combined implicit-explicit algorithm in time for non-linear finite element analysis. *Commun. Numer. Meth. Engng.* **Vol.** 22:63-75.
- Curiel Sosa, J.L., Petrinic, N. & Wiegand, J. (2008). A three-dimensional progressive damage model for fibre-composite materials. *Mechanics Research Communications* **Vol.** 35 (No. 4):219-221.
- Curiel Sosa, J.L. (2008). A Novel Directional Damage Model for Composites. *Proceedings of the Ninth International Conference on Computational Structures Technology*. Topping, B. H. V. and Papadrakakis, M. Civil-Comp Press, Athens, Greece. Paper 307.

- Daniel, I.M. (2007). Failure of composite materials. *Strain* **Vol.** 43:4-12.
- Dugdale, D.S. (1960). Yielding of steel sheets containing slits. *Journal of the Mechanics and Physics of Solids*, **Vol.** 8(No. 2):100-104.
- Edlund, U. & Volgers, P. (2004). A composite ply failure model based on continuum damage mechanics. *Composite Structures* **Vol.** 65:347-355.
- Hallet, S.R. (1997). *Small specimen impact testing and modelling of carbon fibre T300/914*. PhD thesis, University of Oxford.
- Harris, C.E., Coats, T.W., Allen, D.H. & Lo, D.C. (1995). A progressive damage model and analysis methodology for predicting the residual strength of composite laminates. *J. Compos. Technol. Res.* **Vol.** 29:926-981.
- Hashin, Z. (1980). Failure criteria for unidirectional fiber composites. *J. App. Mech.* **Vol.** 47:329-334.
- Hibbit, Karlsson, & Sorensen (2007). *Abaqus. User Manual*.
- Hinton, M.J. & Soden, P.D. (1998). Predicting failure in composite laminates: the background to the exercise. *Compos. Sci. Technol.* **Vol.** 58:1001-1010.
- Hinton, K.J., Kaddour, A.S. & Soden, P.D. (2004). A further assessment of the predictive capabilities of current failure theories for composite laminates: Comparison with experimental evidence. *Compos. Sci. Technol.* **Vol.** 64 (No. 3-4):549-588.
- Hochard, C., Auburg, P.A. & Charles, J.P. (2001). Modelling of the mechanical behaviour of woven fabric CFRP laminates up to failure. *Compos. Sci. Technol.* **Vol.** 61:221-230, 2001.
- Hoffman, O. (1967). The brittle strength of orthotropic materials. *Journal of Composite Materials*, **Vol.** 1(No. 2):200-206.
- Hou, J.P., Petrinic, N., Ruiz, C. & Hallet, S.R. (2000). Prediction of impact damage in composite plates. *Compos. Sci. Technol.* **Vol.** 60:273-281.
- Hufenbach, W., Bohm, R., Kroll, L. & Langkamp, A. (2004). Theoretical and experimental investigation of anisotropic damage in textile-reinforced composite structures. *Mechs. Compos. Mater.* **Vol.** 40(6):519-532.
- Iannucci, L. & Willows, M.L. (2006). An energy based damage mechanics approach to modelling impact onto woven composite materials. Part I: Numerical models. *Composites: Part A* **Vol.** 37:2041-2056.
- Irwin G.R. (1948). *Fracture dynamics, fracturing of metals*, **Vol.** 8:147-66.
- Kachanov L.M. (1958). Time of the rupture process under creep conditions. *Izv. Akad. Nauk. SSR*, **Vol.** 8(No. 8):26-31.
- Lapczyk, I. & Hurtado, J.A. (2007). Progressive damage modeling in fiber-reinforced materials. *Composites Part A: Applied Science and Manufacturing*, **Vol.** 38(No. 11):2333-2341.
- Lemaitre J. (1992). *A Course on Damage Mechanics*.
- Lemaitre J, Chaboche J-L. 1990. *Mechanics of Solids Materials*. Cambridge University Press.
- Leski, A. (2007). Implementation of the virtual crack closure technique in engineering fe calculations. *Finite Elements in Analysis and Design*, **Vol.** 43(No. 3):261-268.
- Lessard, L.B. & Shokrieh, M.M. (1995). 2-D modelling of composite pinned-joint failure. *J. Composite Mater.* **Vol.** 29(No. 5):671-697.
- McCartney, L.N. (2003). Physically based damage models for laminated composites. *Proc. Instn. Mech. Engrs. - J. Mater. Design and Application* **Vol.** 217 (No. L3):163-199.
- Maimi, P., Camanho, P.P., Mayugo, J.A. & Dávila, C.G. (2007a). A continuum damage model for composite laminates: Part i - constitutive model. *Mechanics of Materials*, **Vol.** 39 (No. 10):897-908.

- Maimi, P., Camanho, P.P., Mayugo, J.A. & Dávila, C.G. (2007b). A continuum damage model for composite laminates: Part ii - computational implementation and validation. *Mechanics of Materials*, **Vol.** 39(10):909–919.
- Matzenmiller, A., Lubliner, J. & Taylor, R.L. (1995). A constitutive model for anisotropic damage in fiber-composites. *Mechs. Mater.* **Vol.** 20:125-152.
- Puck, A. & Schurmann, H. (1998). Failure analysis of FRP laminates by means of physically based phenomenological models. *Compos. Sci. Technol.* **Vol.** 58:1045-1067.
- Rybicki, E.F. & Kanninen, M.F. (1977). A finite element calculation of stress intensity factors by a modified crack closure integral. *Engineering Fracture Mechanics*, **Vol.** 9(No. 4): 931–938.
- Rybicki, E.F., Schmueser, D.W. & Fox, J. (1977). Energy release rate approach for stable crack growth in the free-edge delamination problem. *Journal of Composite Materials*, **Vol.** 11: 470–487, 1977.
- Shahid, I. & Chang, F.-K. (1995). An accumulative damage model for tensile and shear failure of laminated composite plate. *J. Compos. Mater.* **Vol.** 29:926-981.
- Schipperen J.H.A. (2001). An anisotropic damage model for the description of transverse matrix cracking in a graphite-epoxy laminate. *Composite Structures*, **Vol.** 53(No. 3):295–299.
- Soden, P.D., Hinton, M.J. & Kaddour, A.S. (1998a). A comparison of the predictive capabilities of current failure theories for composite laminates. *Compos. Sci. Technol.* **Vol.** 58 (No. 7):1225-1254.
- Soden, P.D., Hinton, M.J. & Kaddour, A.S. (1998b). Lamina properties, lay-up configurations and loading conditions for a range of fibre-reinforced composite laminates. *Compos. Sci. Technol.* **Vol.** 58 (7):1011-1022.
- Swanson, J. (2007). *Ansys. User Manual*.
- Talreja, R. (1987). Modelling of damage development in composites using internal variables concepts. *Proceedings of the ASME, Damage Mechanics in Composites, AD* **Vol.** 12:11-16.
- Tan, S.C. (1991). A progressive failure model for composite laminates containing openings. *J. Composite Mater.* **Vol.** 25 (No. 5):556-577.
- Tsai, S.W. & Wu, E.M. (1971). General theory of strength for anisotropic materials. *Journal of Composite Materials*, **Vol.** 5:58–80.
- Turon, A., Davila, C.G., Camanho, P.P. & Costa, J. (2007). An engineering solution for mesh size effects in the simulation of delamination using cohesive zone models. *Engineering Fracture Mechanics*, **Vol.** 74(No. 10):1665–1682.
- Tvergaard, V. & Hutchinson, J.W. (1996). Effect of strain-dependent cohesive zone model on predictions of crack growth resistance. *International Journal of Solids and Structures*, **Vol.** 33(No. 20-22):3297–3308.
- Wisnom, M.R. (2010). Modelling discrete failures in composites with interface elements. *Composites Part A: Applied Science and Manufacturing*, **Vol.** 41(7):795–805.
- Xie, D. & Biggers Jr, S.B. (2006). Progressive crack growth analysis using interface element based on the virtual crack closure technique. *Finite Elements in Analysis and Design* **Vol.** 42(No. 11):977–984.
- Xie, D. & Waas, A.M. (2006). Discrete cohesive zone model for mixed-mode fracture using finite element analysis. *Engineering Fracture Mechanics* **Vol.** 73(13):1783–1796.
- Xu, L.Y. (1994). Interaction between matrix cracking and delamination in composite laminates. *Compos. Sci. Technol.* **Vol.** 50 (No. 4):469-478.

- Yamada, S.E. & Sun, C.T. (1978). Analysis of laminate strength and its distribution. *Journal of Composite Materials* **Vol.** 12:275–284.
- Zohdi, T., Feucht, M., Gross, D. & Wriggers, P. (1998). A description of macroscopic damage through microstructural relaxation. *Int. J. Numer. Meth. Engn.* **Vol.** 43:493-506.

Bonded Composite Patch Repairs on Cracked Aluminum Plates: Theory, Modeling and Experiments

Fabrizio Ricci, Francesco Franco and Nicola Montefusco
*University of Naples "Federico II", Department of Aerospace Engineering
Italy*

1. Introduction

Composite patches, bonded on cracked or corroded metallic aircraft structures, have shown to be a highly cost effective method for extending the service life and maintaining high structural efficiency (Baker & Jones, 1988; Baker, 1993; Molent et al., 1989; Baker et al., 1984; Torkington, 1991; Bartholomeus, 1991).

Damage tolerant and fail-safe design of aircraft, aerospace and civil structures requires a substantial amount of inspection and defects-monitoring at regular intervals. There is a large number of high-cost inventory of aircraft structures in operation throughout Europe and the world, that are undergoing continuous degradation through aging. Moreover, this number is increasing by around 5% every year, resulting in significant negative impact on the economy of many nations. The degradation of defects critical structures is controlled through careful and expensive regularly scheduled inspections in an effort to reduce their risk of failure.

The replacement of a damaged structural component has a relevant impact on the life cycle cost of an airplane. Bonded composite patches for repairing cracks and defects in aircraft structures have been widely used in the last years. This technology offers many advantages over mechanical fastening or riveting, including improved fatigue behavior, restored stiffness and strength, reduced corrosion and readily formed into complex shapes. The repair of metal structures with composite materials is a technology that was first introduced in Australia in the early 1970s and later in USA in early 1980s. It is now estimated that over 10 000 flying patch repairs, for corrosion and fatigue damages, have been performed on Australian and US military aircraft (Christian et al., 1992; Umamaheswar & Singh, 1999; Roach, 1995). This technology was first used for the repair of military aircraft and then applied also to civil aircraft. The success of a bonding repair depends on the properties of both the adhesive and the patch. The quality of the repair depends upon bonding process and surface treatment as well. Carbon-epoxy composites have been mostly used in aeronautics due to their high stiffness and strength to weight ratios. The performance of the adhesive plays a key role in the successful utilization of bonded composite patch repairs.

The role of a bonded composite patch is to restore the stress state modified by the presence of the crack. The stress intensity factor is then reduced by the presence of the patch. Many authors have already investigated the behavior of metallic structures repaired by composite

patches. Baker and Jones (Baker & Jones, 1988) studied an aluminum panel repaired with composite patches. For a repaired cracked plate they showed that the stress intensity factor does not increase indefinitely with the crack length, as it asymptotically reaches a limit value. According to Baker's results, Rose (Rose, 1981 and 1982) showed that the stress intensity factor range of a repaired structure does not depend on the crack length if the crack grows up below the repair. As a result, the crack growth rate does not depend on of crack length according to the Paris law. Klug (Klug et al., 1999) investigated the fatigue behaviour of pre-cracked 2024-T3 aluminum plates repaired with a bonded carbon/epoxy patch. Single sided repairs were found to provide about a 4-5 times improvement in the fatigue life.

After these early works many authors have addressed many numerical and experimental aspects. Naboulsi, Schubbe and Mall (Nabulosi & Mall, 1996; Schubbe & Mall, 1999) have analyzed the modeling of the composite and adhesive layers, using the three layer technique in comparison with the high computational cost of the three dimensional Finite Element models. Naboulsi and Mall (Nabulosi & Mall, 1998) have successively adopted the three layer technique for the nonlinear analysis of the repaired structure in order to take in account large displacements and material nonlinearities. Chung and Yang (Chung & Yang, 2002) and Jones, Whittingham and Marshall (Jones et al., 2002) have investigated the fracture and the crack growth behavior in a more complex structure, such as stiffened panel, deriving some design formulas. Tong and Sun (Tong and Sun, 2003) have presented a novel finite element formulation for developing adhesive elements and conducting a simplified nonlinear stress analysis of bonded repairs in curved structures. Some other authors have focused their attention on the optimal design of the bonded patches, by finite element models, in terms of edge taper (Wang et al., 2005) and in-plane shape (Mahadesh & Hakeem, 2000). Some of the above mentioned numerical activities have been compared with experimental data measured with reference to the stress intensity factor and fatigue life of the repaired structural elements (Schubbe & Mall, 1999; Wang et al., 2005;).

The aim of this work is to review the capability of finite element models in estimating the mechanical behavior of metallic panels repaired by composite patches. The attention has been focused on those commercial codes implementing the "quarter-point location" formulation. The interest in commercial finite element codes is due to their use in most of the industrial applications. Furthermore the validation of the finite element procedures for a metallic panel with a composite patch repair is a promising result for the analysis of composite structures to be repaired with composite patches.

The numerical analyses, limited to the case of mode I (opening crack), have been strongly supported by well known theoretical formulations and several experimental tests. Moreover, the experimental data allowed a comparison among different patches, adhesives and surface preparation properties.

In this work a repair with a single patch - single sided configuration - (i.e. bonded only on one side of the panel) has been considered. This configuration could avoid the removal of the damaged component and in general could lead to a significant reduction of time and costs of repair operations.

Section 2 of the paper presents the geometry of the panel used as test-case. Section 3 reviews the mechanical behavior of the cracked panel. The mechanical behavior of the repaired panel, estimated by the numerical models, is presented in Section 4 and the comparison with the experimental data is discussed in Section 5. Finally, Section 6 summarizes the work conclusions and outlines some final considerations.

1.1 List of symbols

a	Half crack length – total crack length: $2a$
BC	correction term
C	material constants
E	Young's modulus
G	shear modulus
G_I	energy release rate
H	Patch length
K_I	stress intensity factor, elastic
I	moment of inertia
K_I^*	stress intensity factor, elasto-plastic
K_{IC}	fracture toughness
K_R	stress intensity factor for a one sided repair
K_{th}	threshold value
m	material constants
N	number of cycles
r_y	plastic radius
t	Thickness
U	elastic strain energy
W	plate width
Y	geometry factor
y_{max}	distance of the extreme fiber ply from the neutral axis

Greek symbols

β	shear stress transfer length
ν	Poisson's ratio
σ	asymptotic stress
σ_s	yield strength
σ_{max}	asymptotic stress max
σ_{min}	asymptotic stress min
σ_0	nominal stress
$\Delta K = K_{max} - K_{min}$	Stress intensity range
$\Delta \sigma = \sigma_{max} - \sigma_{min}$	Stress range

Notations

a	adhesive subscript
p	plate subscript
r	patch subscript

2. Panel geometry

The geometry of the cracked structure in the present work is shown in Fig. 1. It was considered a 6061-T6 aluminum alloy plate; a through thickness crack is used to simulate the defect in the structural components.

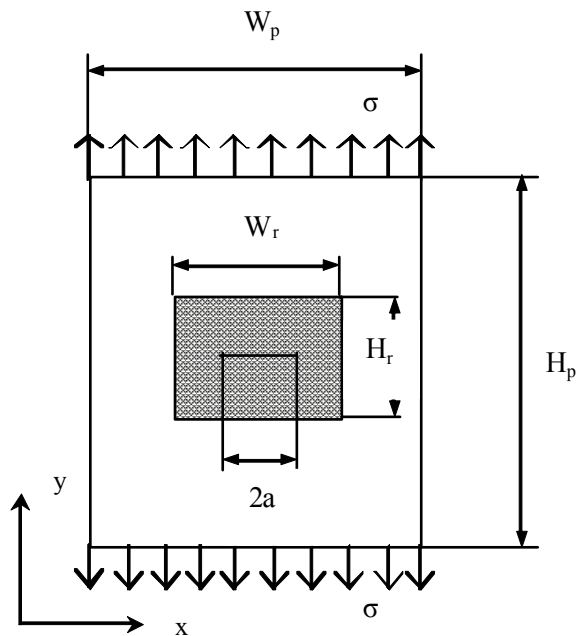


Fig. 1. The geometry of panel with the patch

The fracture is made with the technique of Electrical Discharge Machining (EDM), based on the erosion of metals by spark discharges. This technique allows an accurate control of the crack size and tips shape. The size of the panel is: $H_p = 180$ [mm], $W_p = 180$ [mm] and thickness $t_p = 1.5$ [mm]. The central crack has a length $2a = 40$ [mm] repaired by carbon-epoxy composite patch bonded with adhesive having an estimated thickness $t_a = 0.1$ [mm]. Tables 1 and 2 show the mechanical properties of the patch and adhesives used. The height and width of the patch are $H_r = 40$ [mm] and $W_r = 60$ [mm], respectively. It is well known (Mahadesh & Hakeem, 2000) that the rectangular shape of the patch is not the best choice; nevertheless the rectangular shape is a good compromise between mechanical performances and manufacturing aspects. The patch size is the result of various numerical tests not reported here for the sake of brevity. It represents the minimum patch size, covering integrally the crack length, that leads to a significant improvement of the mechanical behavior under the considered loading conditions as shown in the next Sections.

	Type 1	Type 2
E_r [GPa]	18.00	12.73
G_r [Gpa]	34.90	24.76
ν_r	0.68	0.7
ply orientation	[45/-45]	[(45)]Fabric
t_r [mm]	0.6	0.3

Table 1. Patch properties

Two types of carbon-epoxy patches were used. Type 1 is a two unidirectional layers $+45^\circ/-45^\circ$ patch, and Type 2 is a single fabric layer patch with the fibers oriented along the $\pm 45^\circ$ directions.

	Loctite Hysol EA95	Cytec FM73	AF163-2K
E_a [GPa]	2.48	1.43	1.10
G_a [Gpa]	0.905	0.53	0.44
ν_a	0.37	0.35	0.34
t_a [mm]	0.1	0.1	0.1

Table 2. Adhesive properties

E [GPa]	68.00
G [GPa]	26.20
ν_r	0.33
σ_s [MPa]	276
K_{IC} [MPa \sqrt{m}]	28.57
K_{IC} [MPa \sqrt{m}]	3.85

Table 3. Material properties of the aluminum alloy plate

The panel is subjected to various tests with a sinusoidal uniaxial load at 1 Hz. Tables 3 and 4 report the mechanical properties of the aluminium alloy panel and the loading conditions, respectively.

Tests	Load [kN]	σ_{max} [MPa]	σ_{min} [MPa]
Test 1	14.71	54.50	0
Test 2	22.07	81.75	0
Test 3	29.43	109.01	0

Table 4. Load conditions applied in the tests

3. Panel without patch

3.1 Analytical procedure

In the present analysis, the Irwin - Westergaard model (Pook, 2000) is used to calculate SIF in the panels without patch. The basic relationships are herein reported. The linear elastic fracture mechanics (LEFM) for a plate of infinite size and central crack (opening mode I) is given by the following expression:

$$K_I = \sigma\sqrt{\pi a} \quad (1)$$

The stress intensity factor, K_I , completely characterizes the stress distribution at the crack tip in a linear elastic material where σ is the asymptotic tensile stress perpendicular to the crack plane and a is the crack half-length. Since the plate is of finite size, the boundary conditions introduce an higher stress intensification at the crack tip. The mode I stress intensity factor is given by (Jukes & Vogwell, 1995; Feddersen, 1996):

$$K_I = \Delta\sigma\sqrt{\pi a} \left[\sec\left(\frac{\pi a}{wp}\right) \right]^{\frac{1}{2}} \quad (2)$$

The elastic stress analysis becomes highly inaccurate as the inelastic region at the crack tip grows up. Simple corrections to the linear elastic fracture mechanics are available when moderate crack tip yielding occurs (Tada et al., 1985; Burdekin & Stone; McClintock & Irwin, 1965). The size of the crack tip yielding zone can be estimated by the Irwin approach, where the elastic stress analysis is used to estimate the elastic plastic boundary. A first order estimation of the plastic zone size, r_y , is

$$r_y = \frac{1}{2\pi} \left(\frac{K_I}{\sigma_s} \right)^2 \quad (3)$$

The stress intensity factor with plasticity correction is given by:

$$K_I^* = \Delta\sigma\sqrt{\pi(a - r_y)} \left[\sec\left(\frac{\pi a}{wp}\right) \right]^{\frac{1}{2}} \quad (4)$$

The estimation of K_I^* , in Eq.(4), needs an iterative approach.

If this plastic zone is small compared to the crack size, then the linear elastic assumptions are correct. If not, the linear elastic fracture mechanics (LEFM) is not applicable and the elasto-plastic fracture mechanics (EPFM) should be used. The value of K_I^* can be related to G_I , the energy release rate for similar crack growth, in the usual way:

$$K_I^* = \sqrt{G_I E'} \quad (5)$$

Where, from the results of Griffith (Griffith, 1924) the energy released normalized with respect to the new crack surface created during the crack extension, namely the strain energy release rate, is given by

$$G_I = -\frac{1}{t_p} \cdot \frac{dU}{da} \quad (6)$$

An increase in the crack length leads to a decrease of the stored elastic strain energy ΔU .

3.2 Numerical procedure

A finite element analysis of the configuration in Fig.1 is carried out, using the finite element code Franc2D/L developed at Kansas University (Swenson & James, 1998).

The plate, without patch, was meshed using standard six node-isoparametric elements with triangular shape, as showed in Fig.2. These elements perform well for elastic analysis and have the advantage that the stress singularity at the crack tip can be incorporated in the solution adopting the quarter-point location method (Henshel & Shaw, 1975). The strain energy release rate is calculated using the modified crack closure method and then the stress intensity factor from the Eq. (5). The values are reported in the Table 5.

For the loading condition #3 the value of K_I^* is close to the fracture toughness. The numerical values are in good agreement with the analytical ones but they are always higher. Fig. 3 presents the comparison between analytical and numerical evaluation of the stress intensity factor as function of the crack length.

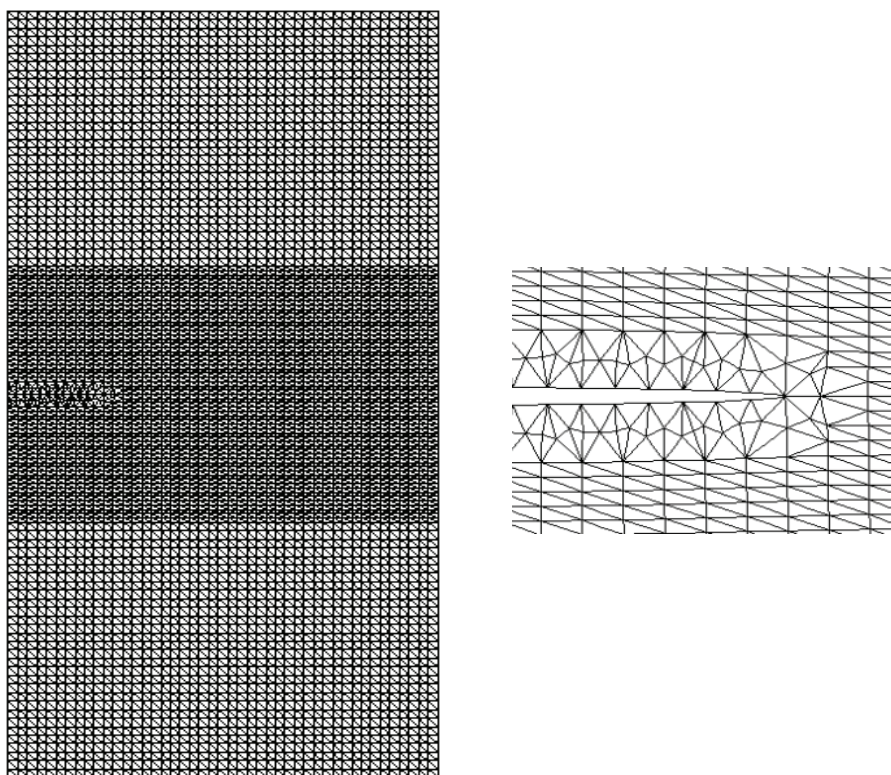


Fig. 2. The finite element model of the half plate geometry: detail of crack tip in pure mode I
The Fig. 3 shows that the good agreement between analytical and numerical results does not depend on the crack length.

	Analytical	Numerical (FEM)	Difference [%]
Strain Energy Release Rate: G_I [MPa m]			
Test 1	$2.919 \cdot 10^{-3}$	$3.030 \cdot 10^{-3}$	3.80
Test 2	$6.567 \cdot 10^{-3}$	$6.817 \cdot 10^{-3}$	3.81
Test 3	$1.167 \cdot 10^{-2}$	$1.212 \cdot 10^{-2}$	3.86
SIF: K_I^* [MPa \sqrt{m}]			
Test 1	14.23	14.45	1.54
Test 2	21.61	21.68	0.32
Test 3	29.37	28.91	1.57

Table 5. Analytical and numerical values

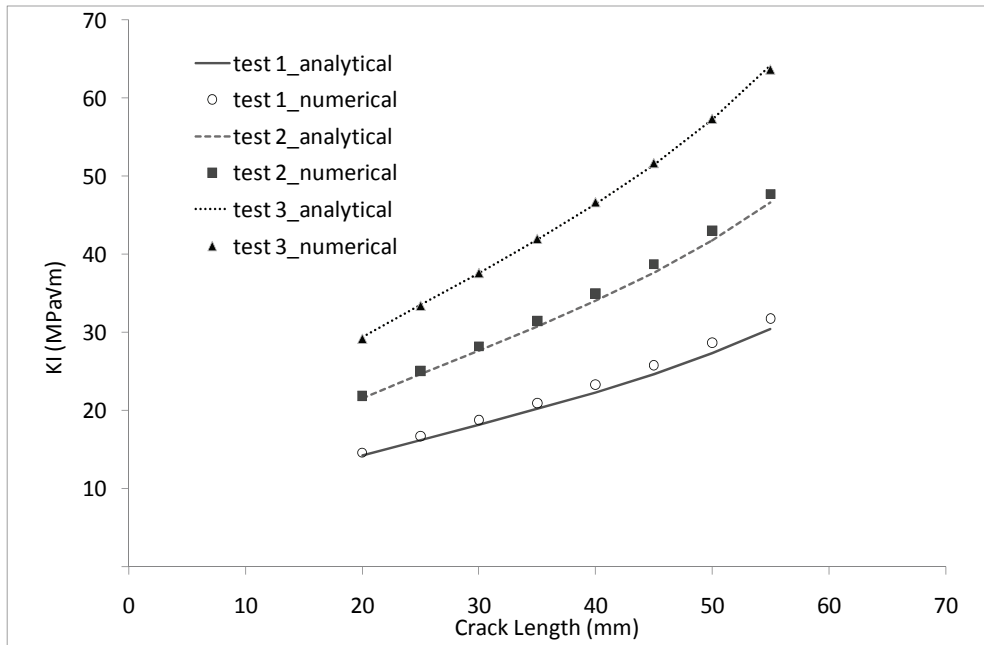


Fig. 3. Analytical and numerical evaluation of the SIF vs. crack length

3.3 Fatigue life prediction

The fatigue-crack growth prediction models usually employ the following Paris power law due to its simplicity (Pook, 2000). In this work, Paris law is used to study the fatigue behaviors of cracked plates:

$$\frac{da}{dN} = C(\Delta K)^m \quad (7)$$

The so-called material constants, C and m , for 6061-T6 aluminum alloy, are $C=1.8404 \cdot 10^{-9}$, $m=2.3$. The quantity ΔK is the stress intensity range. Predictions of the fatigue life of plate without patch can be made by numerical solution of the Paris law:

$$\Delta N_i = \frac{\Delta a_i}{C(\Delta K_i)^m} \quad (8)$$

where Δa_i is the crack length increment.

The crack grows up in a stable way until the SIF reaches the fracture toughness, i.e. $K_I \geq K_{IC}$. At each calculation step the value of ΔK_i varies due to the crack growth which determines the transformation of the tension state at the crack tip. The loading condition, considered in this study, is characterized by $\sigma_{min} = 0$, with tension ratio $R = 0$, then ΔK_i is simply equal to K_{max} : namely the SIF value corresponding to the K_I^* analytically or numerically calculated.

The value of ΔK_i is then corrected to take into account two phenomena that affect the rate of the crack growth: the closure of the crack and the static fracture (Pook, 2000).

As a crack cannot grow up when it is closed, ΔK becomes:

$$\Delta K_{eff} = K_I^* - K_{th} \quad (9)$$

where K_{th} is the material threshold value.

The crack growth rate depends on the value of ΔK_i which is function itself of the crack length. But the rate of the crack growth increases more rapidly when the critical condition of fracture is reached. In order to model the contribution of the static fracture the Eq. (9) is modified by the term K_{fs} :

$$\Delta K_{eff}^* = \Delta K_{eff} + K_{fs} \quad (10)$$

where

$$K_{fs} = \frac{\Delta K_{eff}}{K_{IC} - \Delta K_{eff}} \quad (11)$$

Obviously the added term K_{fs} becomes more and more dominant as ΔK_{eff} reaches the fracture toughness value.

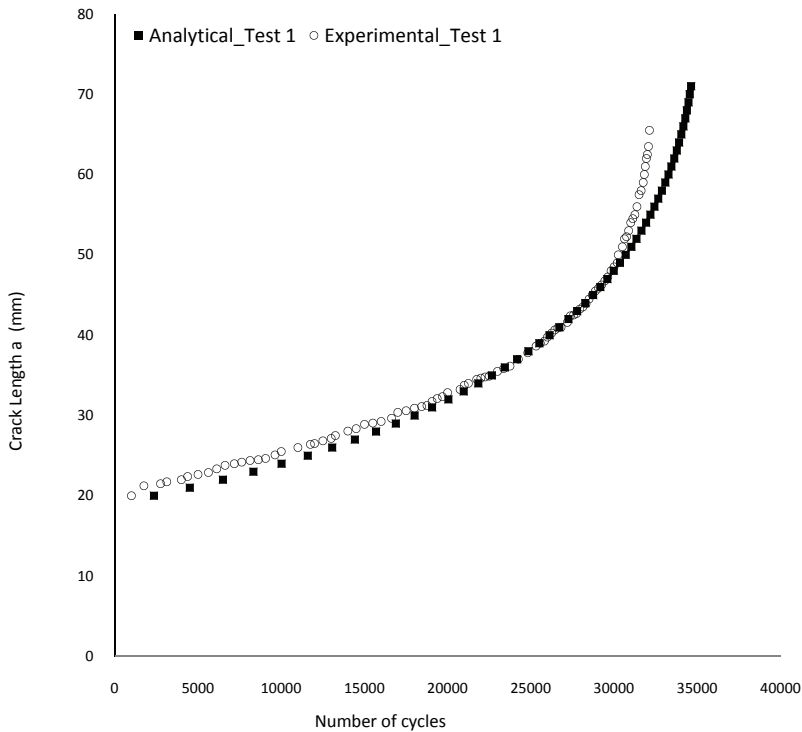


Fig. 3. The experimental and numerical fatigue life for the loading condition “Test 1”

Table 6 shows the analytical results of fatigue tests carried out for the three loading conditions. The number of cycles to failure is based on the K_{max} criterion, i.e. when the K_{max} reaches the fracture toughness K_{IC}

	Load [kN]	Number of cycles to failure
Test 1	14.71	34622
Test 2	22.07	9658
Test 3	29.43	2267

Table 6. Fatigue life prediction of the cracked un-patched panel

The Fig. 3 shows a comparison of the crack growth between the numerical model (Eqns. 7-11) and the experimental results for the cracked panel (without patch) under the loading condition #1. The details of the experimental measurements are reported in Section 5. The higher experimental crack growth rate at the number of cycles close to the failure is due to an asymmetric growth of the crack experienced during the tests.

4. Panel with patch

4.1 Analytical procedure

Rose's analytical model (Rose, 1981 and 1982) is used to compute the SIF for the repaired plates by single patch,

$$K_R = Y \cdot \sigma_0 / \sqrt{k} \quad (12)$$

where Y is a geometric factor, which accounts for repairs to center or edge cracks; $Y=1$ for a repair to a centre crack; σ_0 is the nominal stress that would exist in an uncracked plate after the application of a patch:

$$\sigma_0 = \frac{\Delta\sigma}{1 + S} \quad (13)$$

where $S = E_r t_r / E_p t_p$, k represents a spring constant given by:

$$k = \frac{\beta S}{(1 + S)(1 - \nu_p)} \quad (14)$$

where β is a shear stress transfer length in a representative bonded joint:

$$\beta = \left[\frac{G_a}{t_a} \left(\frac{1}{E_p t_p} + \frac{1}{E_r t_r} \right) \right]^{\frac{1}{2}} \quad (15)$$

In the case of one sided repairs, Ratwani (Ratwani, 1979) provided a bending correction factor:

$$K_R^* = (1 + BC) K_R \quad (16)$$

where K_R^* is the stress intensity factor for a one sided repair, the correction term BC is given by:

$$BC = a y_{max} \left(1 - \frac{K_R}{K_R^*} \right) \frac{t_p(t_p + t_r)}{l} \quad (17)$$

where y_{max} is the distance of the extreme fiber ply from the neutral axis of the cracked plate:

$$y_{max} = t_p + Z \quad (18)$$

with

$$Z = \frac{S(t_p + t_r + 2t_a)}{2(1+S)} \quad (19)$$

and I is the total moment of inertia of the plate repair:

$$I = I_p + nI_r \quad \text{and} \quad n = \frac{E_r}{E_p} \quad (20)$$

where

$$I_p = w_p \frac{t_p^3}{12} + w_p t_p Z^2 \quad (21)$$

$$I_r = w_r \frac{t_r^3}{12} + w_r t_r \frac{\left[\frac{t_r}{2} + t_a + \left(\frac{t_p}{2} - Z \right) \right]^2}{4} \quad (22)$$

The stress intensity factors, computed with the above mentioned analytical procedure, for the different patch configurations (i.e. fiber lay-up and adhesive type) are shown in the Tables 7.

Specimen Configuration	Analytical K^*_R [MPa√m]	FEM K^*_R [MPa√m]	Difference [%]
Test 1 - repaired plate:			
patch type 1 + ad. EA956	8.62	8.32	-3.6
patch type 1 + ad. FM73	8.97	9.22	2.6
patch type 1 + ad. AF163-2K	9.12	9.54	4.4
patch type 2 + ad. EA956	10.15	9.95	-2.0
patch type 2 + ad. FM73	10.4	10.91	4.7
patch type 2 + ad. AF163-2K	10.5	11.24	6.6

Table 7.1. Analytical and numerical SIF for the repaired plate in Test 1

Test 2 - repaired plate:			
patch type 1 + ad. EA956	12.92	12.51	-3.3
patch type 1 + ad. FM73	13.46	13.87	2.9
patch type 1 + ad. AF163-2K	13.67	14.35	4.7
patch type 2 + ad. EA956	15.23	14.98	-1.7
patch type 2 + ad. FM73	15.59	16.43	5.1
patch type 2 + ad. AF163-2K	15.75	16.94	7.0

Table 7.2. Analytical and numerical SIF for the repaired plate in Test 2

Test 3 - repaired plate:			
patch type 1 + ad. EA956	17.23	16.75	-2.9
patch type 1 + ad. FM73	17.95	18.58	3.4
patch type 1 + ad. AF163-2K	18.23	19.23	5.2
patch type 2 + ad. EA956	20.3	20.08	-1.1
patch type 2 + ad. FM73	20.8	22.15	6.1
patch type 2 + ad. AF163-2K	21.0	22.74	7.6

Table 7.3. Analytical and numerical SIF for the repaired plate in Test 3

4.2 Numerical procedure

A finite element analysis of the configurations of Fig. 4 is carried out using the finite element code Franc2D/L for the total structure (plate and patch).

The patched plate is meshed using standard two-dimensional six node isoparametric elements with triangular shape.

The repaired structure is modeled as three layer structure (plate, patch and adhesive). Due to the symmetry of the problem, only half plate is modeled using 29373 nodes and 14578 elements. Tables from 7.1 to 7.3 report the SIF obtained with the finite element models and the comparison with the previous analytical results. The configuration with the adhesive AF163-2K usually demonstrates the highest difference between numerical and analytical values. This performance is due to improved atomic bond of the glue. The adhesive AF163-2K has the lowest elastic and shear moduli. The patch type 2 always provides a higher SIF and among these configurations those using the adhesive AF163-2K are the highest.

5. Experimental procedure

5.1 Testing procedure

In order to verify the effectiveness of analytical and numerical analyses some experimental measurements, for the damaged and repaired panels, are carried out. The tests are performed at room temperature in a 100 kN Metrocom Engineering SpA servo-hydraulic test machine. The tests are focused to evaluate the fatigue life of the structures under cycling loads at $R=0$ as described in Section 2 - Table 4. Each test is performed up to the complete fracture of the panel. In each test the number of the cycles, the crack growth and the SIF are evaluated. In particular the SIF is measured at the crack tip using three measurement grids strain-gauges. A National Instrument data acquisition system is used to acquire the load and strain measurements during the tests.

In all the experimental tests the panel surface is treated with a solvent to clean and remove any impurities and / or contamination from the surface and subjected to a local mechanical abrasion to increase and activate the contact surfaces between the metal panel and the composite patch. In the configuration A4 reported in the Table 8, the surface is subjected to a treatment of pickling sulfur chromium for aluminum alloys according to UNI EN 2334:1998 - Aerospace Division.

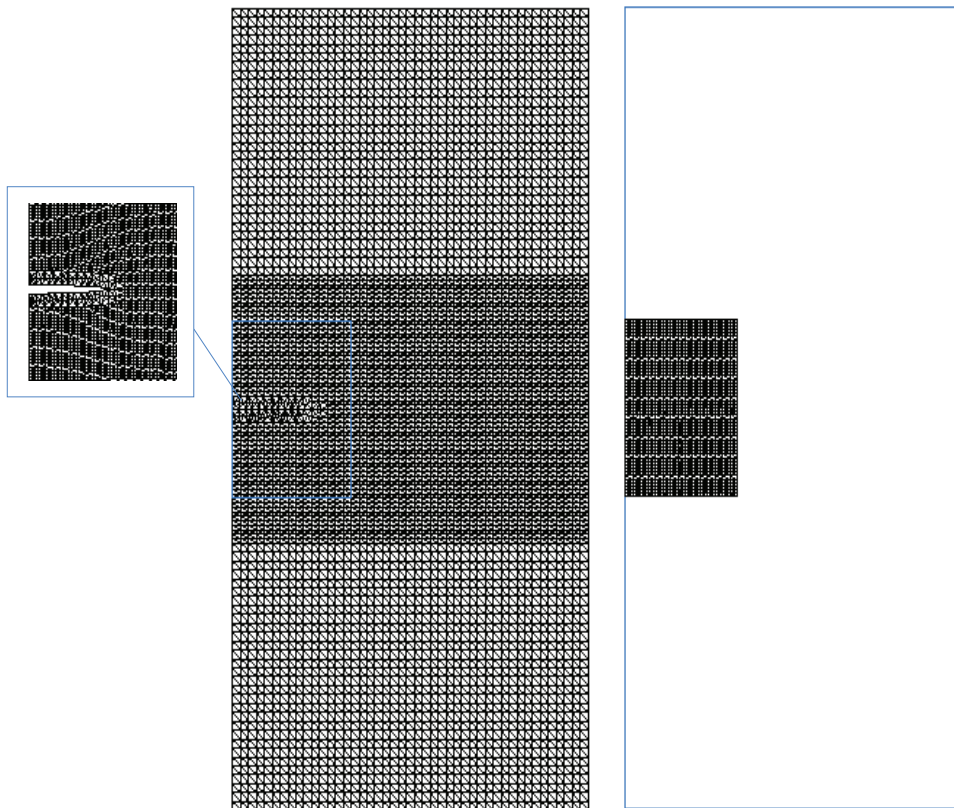


Fig. 4. Finite element model of the plate repaired with the composite patch

5.2 Experimental results

Among all the possible combinations of patch and adhesive types and loading conditions, a subset of tests is carried out. The experimental configurations, discussed in the present work, are summarized in Table 8:

Configuration Name	Patch Type	Adhesive Type	Loading Condition	Surface Treatment
A1	Type 1	EA956	Test 2	Yes
A2	Type 2	FM 73	Test 2	Yes
A3	Type 2	AF163-2K	Test 2	Yes
A4	Type 2	AF163-2K	Test 2	Yes
B1	Type 1	EA956	Test 3	Yes
B2	Type 1	EA956	Test 3	Yes

Table 8. Experimental configurations

A good repeatability is found for the configurations A1÷A4 as the load amplitude is a moderate percentage of the ultimate static load. The configurations B1 e B2 are characterized by an higher load amplitudes. Moreover for the configuration B1 the patch is bonded using the technique of mechanical compression; on the contrary for the configuration B2 it is bonded using the vacuum bag technique. Therefore the results of the configurations B1 and B2 are presented separately in order to show the scatter of the experimental results, summarized in the Tables 9 and 10. The configurations A1 showed the best performances in terms of stress level and fatigue life. The configuration A1 is repaired with a patch "Type 1" that is thicker and therefore introduces a higher stiffness by increasing the fatigue life, but amplifies the bending in the panel. The configurations A2÷A4, with the same type of bonded patch, show the role of both the adhesive layer and the surface treatment. In particular the configuration A4 provides a fatigue life comparable with configuration A1 although the measured SIF for A4 is the highest among the configurations A. In Fig. 5 it is shown how for the configuration A4 the crack propagates through the composite patch leading to the simultaneous fracture of the metal panel and of the patch.

In other configurations the crack propagates in the adhesive layer and the patch slid over the panel surface as showed in Fig. 6.

Configuration Name	Experimental	Numerical	Difference [%]
A1	13.61	12.92	5.1
A2	14.85	15.59	-5.0
A3	15.11	15.75	-4.3
A4	16.83	15.75	6.4
B1	17.89	17.36	3.0
B2	18.02	17.36	3.7

Table 9. SIF - K_I [MPa \sqrt{m}]: Experimental and numerical results

Configuration Name	Experimental	Numerical	Difference [%]
A1	21770	23188	-6.51
A2	18843	21207	-12.50
A3	19375	21268	-9.77
A4	21450	21268	0.85
B1	4425	5235	-18.30
B2	4926	5235	-6.27

Table 10. Fatigue cycles: Experimental and numerical results

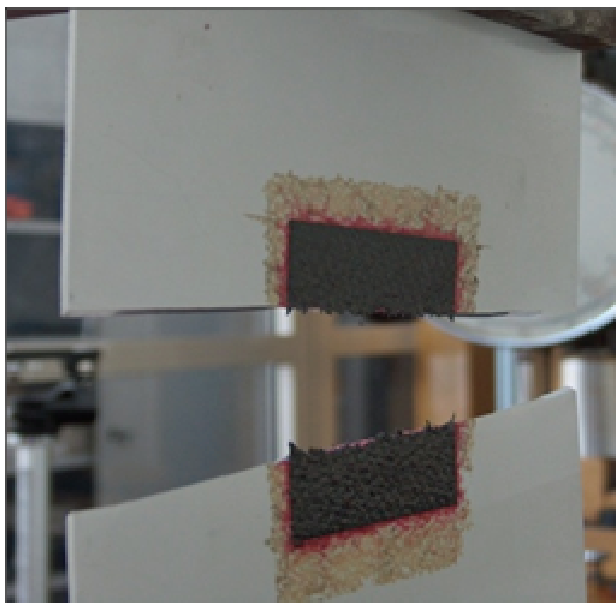


Fig. 5. The configuration A4: the crack propagated through the composite patch



Fig. 6. The crack propagated in the adhesive layer that leads to the sliding of the full patch
The configurations B demonstrate again the role of the curing procedure and a small variation in the SIF provided a larger difference in the fatigue life.

5.3 Comparison of numerical and experimental results

The developed finite element models are not able to take account of the difference between the configurations A3, A4 and B1, B2. Therefore the same numerical value is reported in the Tables 9 and 10. The comparison of the SIF shows a good agreement between experimental and numerical results. On the contrary, the numerical results, in general, overestimated the experimental fatigue life. The small differences in terms of SIF values lead to a larger overestimation of the fatigue life. The curing procedure of the patch on the metallic panel introduces random factors that cannot be easily accounted for in the finite element model reducing its predictive capabilities.

6. Final considerations and conclusions

The main purpose of this study has been the determination of the effectiveness of bonded composite patches to repair cracked thin aluminum panels. The repair is realized by patching only one side of the panel in order to reduce the associated costs and time required. In most of the cases, in fact, the other side of the panels is not easily accessible. Moreover, this type of repair might be applied locally without the need of disassembling a complex structure.

Several experimental tests are carried out to obtain a set of data useful to estimate the state of stress and the fatigue behavior of cracked and bonded repaired panels and to define the effectiveness of the repairing patch. The comparison of the data obtained from the cracked and patch repaired panels have pointed out a significative reduction of the stress intensity factor at the crack tips in the repaired configurations. The experimental tests demonstrate a reduction of the average stress of about 30% due to the patch that turns out in an increase of about 50% of the fatigue life. To support the experimental activities and reduce the associated costs, theoretical and numerical models have been developed and the mechanisms of the damage propagation by using fracture mechanics and fatigue strength analyzed.

The capabilities of numerical and analytical methods are compared with a set of experimental results. In particular the analytical model, based on Rose's analytical solution and Paris' law, are developed to predict the stress intensity factor and the fatigue life of the panel with and without repair.

The numerical and experimental results show that the bonded patch highly reduces the stress intensity factor and increases the fatigue life. Moreover, it has been shown that the effectiveness of the repair strongly depends on the patch stiffness, adhesive characteristics, surface treatments and in general curing procedure. The effectiveness of the composite patches is shown in the next results.

The SIF values, evaluated with the Franc2D/L finite element code and reported in Table 12, show the benefits of the patch repair due to a decrease of about 30% of the stress amplitude near the crack tips.

Specimen Configuration	Load [kN]	$K_I(\text{MPa}\sqrt{\text{m}})$ (Average Value Experimental)		Difference [%]
		Without Patch	With Patch	
Test 1	14.71	14.23	9.61	32.5
Test 2	22.07	21.62	14.46	33.1
Test 3	29.43	29.37	19.38	34.0

Table 12. Comparison of the panel with and without patch

The Fig. 7 shows how the SIF as function of the crack length is attenuated when the through thickness cracked plate is repaired with a bonded patch (Test 2). The finite element model takes into account a progressive patch cracking as far as the crack grows up in the plate, even though the effect of the patch, including the SIF growth rate, might be different as explained in the Section 5.2. When the crack tips overtake the edges of the patch, the crack growth rate quickly increases as showed in Fig. 8. In this figure the crack length is plotted as function of the number of loading cycles for the patched and unpatched aluminum cracked plate used in the experiments (Test 2). For the patched panel, it is evident as the growth rate increases when the crack becomes larger than the patch width. Table 13 summarizes the fatigue lives for various specimen configurations.

The fatigue life of the repaired plate increases of about 110%. The bonded patch can significantly increase the fatigue life of the cracked panel, depending on the stiffness of the patch, the adhesive characteristics, the surface treatments and, in general, the procedure used to apply the patch.

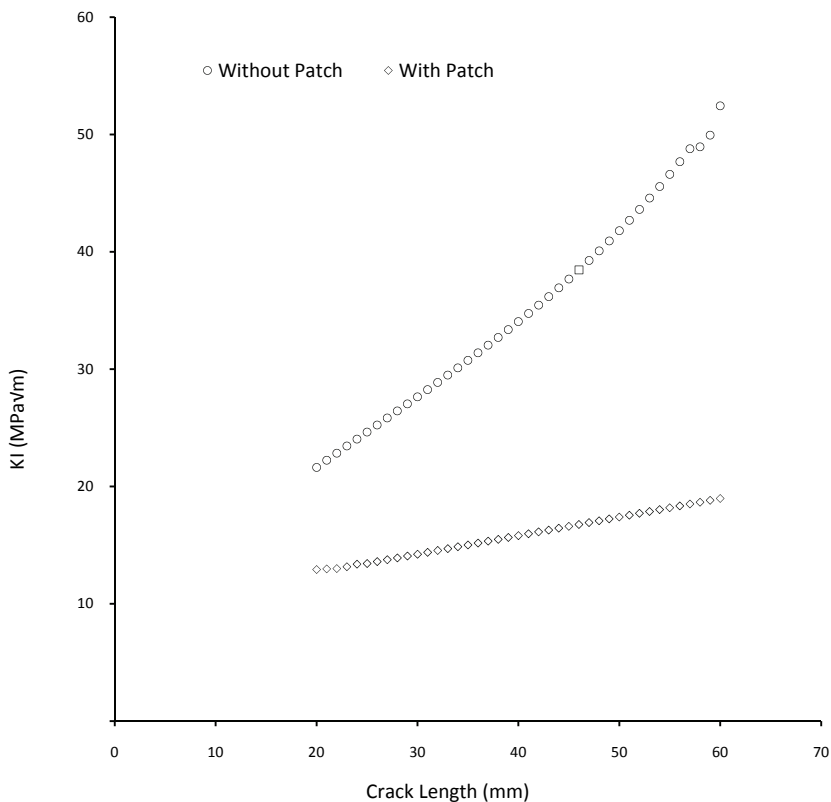


Fig. 7. Comparison of the SIF between patched (test 2 plate repaired A1) and unpatched cracks

Specimen Configuration	Load [kN]	Fatigue life Cycles (Average Value Experimental)		Difference [%]
		Without Patch	With Patch	
Test 1	14.71	34622	72628	-109
Test 2	22.07	9658	20354	-110
Test 3	29.43	2267	4675	-106

Table 13. Comparison of the fatigue life of the panel with and without patch

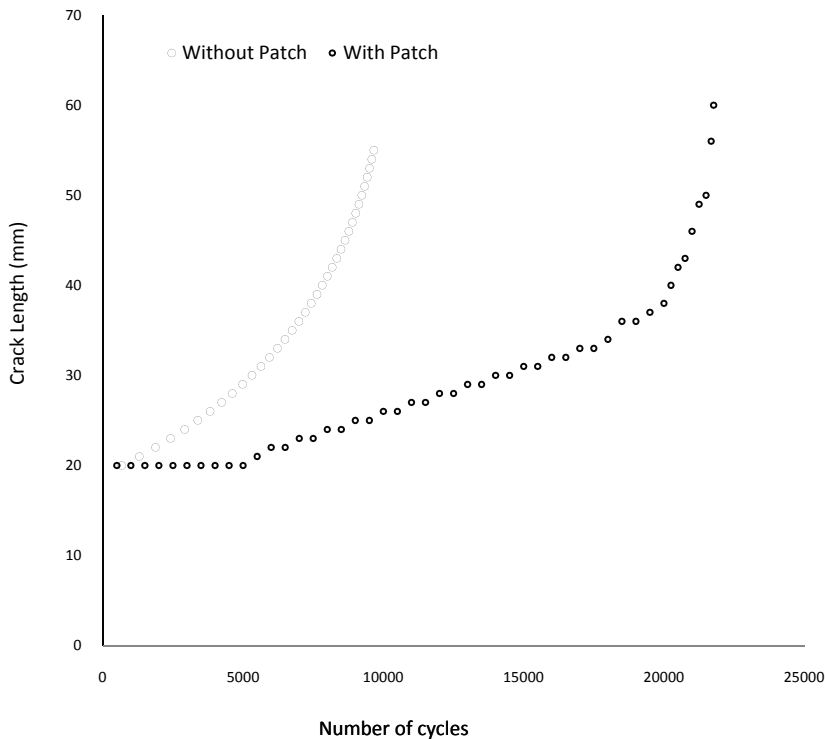


Fig. 8. Comparison the crack length vs. loading cycles

7. References

Baker A.A. & Jones R. (1987). *Bonded repair of aircraft structures*, Martinus Nijhoff, ISBN: 90-247-3606-4, The Netherlands

Pook L.P. (2000). *Linear Elastic Fracture Mechanics for Engineers: Theory and Applications*. WITPRESS, ISBN:1 8531 2703 5, Computational Mechanics Inc.

Swenson D. & James M. (1997). *FRANC2D/L: A crack propagation simulator for plane layered structures*. Version 1.4, User's Guide, University of Kansas, USA

- Tada H., Paris P.C., Irwin G.R. (1985). *Handbook of the stress analysis of cracks*, Paris Productions Incorporated, St. Louis, Missouri, USA
- Roach D. (1995). Performance analysis of bonded composite doublers on aircraft structures, *International Conference on Composite repair of aircraft*, (08/1995), Vancouver, Canada
- Tong L. & Sun X. (2003). Nonlinear stress analysis for bonded patch to curved thin-walled structures, *International Journal of Adhesion & Adhesives*, Vol. 23, No. 5, pp. 349-364
- Baker A.A.; Callinan R.J.; Davis M.J.; Jones R. & Williams J.G. (1984). Repair of Mirage III aircraft using BFRP crack patching technology, *Theoretical and Applied Fracture Mechanics*, Vol. 2, No.1, (10/1984), page numbers (1-16)
- Baker A.A. (1993). Repair efficiency in fatigued-cracked aluminum components reinforced with boron/epoxy patches. *Fatigue and Fracture of Engineering Materials and Structures*, Vol. 16, No. 7, (07/1993), page numbers (753-765), ISSN: 8756-758X
- Burdekin F.M. & Stone D.E.W. (1966). The crack opening displacement approach to fracture mechanics in yielding materials. *Journal of Strain Analysis*, Vol. 1, page numbers (145-153)
- Christian T.F. Jr.; Hammond D.O. & Cochran J.B.(1992). Composite material repairs to metallic airframe components, *Journal Aircraft*, Vol. 29, page numbers (470-476)
- Chung H.K. & Yang W.H. (2002). Fracture mechanics analysis on the bonded repair of a skin/stiffener with an inclined central crack, *Composite Structures*, Vol. 55, No. 3, (02/2002), page numbers (269-276)
- Griffith A.A. (1921). The phenomenon of rupture and flow in solids. *Philosophical Transactions of the Royal Society of London*, Series A, Vol.221, page numbers (163-198)
- Henshel R.D. & Shaw K.G. (1975). Crack tip finite elements are unnecessary. *International Journal for Numerical Methods in Engineering*, Vol.9, No.3, page numbers (495-507)
- Jones R.; Whittingham B. & Marshall I.H. (2002). Bonded repairs to rib stiffened wing skins, *Composite Structures*, Vol.57, No. 1, page numbers (453-458)
- Jukes R. & Vogwell J. (1995). A method for establishing geometry correction factors by ratio of finite element stresses, *Engineering fracture mechanics*, Vol. 50, No. 4, page numbers (581-589)
- Klug J.C.; Maley S. & Sun C.T. (1999). Characterization of fatigue behavior of bonded composite repairs, *Journal Aircraft*, Vol. 36, No. 6, page numbers (1016-1022)
- Mahadesh Kumar A. & Hakeem S.A. (2000). Optimum design of symmetric composite patch repair to centre cracked metallic sheet, *Composite Structures*, Vol. 49, No. 3, (07/2000), page numbers (285-292)
- Molent L.;Callinan R.J. & Jones R. (1989). Structural aspects of the design of an all boron/epoxy reinforcement for the F-111C wing pivot fitting, *Composite Structures*, Vol. 11, page numbers (57-83)
- Naboulsi S. & Mall S. (1996). Modeling of a cracked metallic structure with bonded composite patch using the three layer technique, *Composite Structures*, Vol. 35, page numbers (295-308)
- Naboulsi S. & Mall S. (1998). Nonlinear analysis of bonded composite patch repair of cracked aluminum panels, *Composite Structures*, Vol. 41, page numbers (303-313)

- Ratwani M.M. (1979). Analysis of Cracked, Adhesively Bonded Laminated Structures. *AIAA Journal*, Vol. 17, No. 9, (09/1979), page numbers (988-994)
- Rose L.R.F. (1981). An application of the inclusion analogy for bonded reinforcements. *International Journal Solid Structure*, Vol. 17, No. 8, page numbers (827-838)
- Rose L.R.F. (1982). A cracked plate repaired with bonded reinforcements, *International Journal of Fracture*, Vol. 18, No. 2, (02/1982), page numbers (135-144)
- Schubbe J.J. & Mall S. (1999). Modeling of cracked thick metallic structure with bonded composite patch repair using three-layer technique, *Composite Structures*, Vol. 45, No.3, (06/1999), page numbers (185-193)
- Schubbe J.J. & Mall S. (1999). Investigation of cracked aluminium panel repaired with bonded composite patch, *Engineering Fracture Mechanics*, Vol. 63, No. 3, (06/1999), page numbers (305-323)
- Umamaheswar T.V.R.S. & Singh R. (1999). Modeling of a patch repair to a thin cracked sheet. *Engineering Fracture Mechanics*, Vol. 62, page numbers (267-289)
- Wang J.; Rider A. N.; Heller M. & Kaye M. (2005). Theoretical and experimental research into optimal edge taper of bonded repair patches subject to fatigue loadings. *International of Adhesion & Adhesives*, Vol. 25, page numbers (410-426)
- Bartholomeus R.A.; Paul J.J. & Roberts J.D. (1991). Application of bonded composite repair technology to Civilian Aircraft - 747 Demonstrator Program, In: *National Conference Publication on Aircraft Damage Assessment and Repair*, Institution of Engineers, (91 pt 17), page numbers (216-220), ISBN 85825 537 5, Australia
- Feddersen C.E (1966). Plane strain crack toughness testing of high strength metallic materials, In: *W.F. Brown and J.E. Srawley*, ASTM STP 410, page numbers (77-79)
- McClintock F.A. & Irwin G.R. (1965). Plasticity Aspects of Fracture Mechanics, In: *Fracture toughness testing and its applications*, ASTM STP 381, page numbers (84-113), ISBN-EB: 978-0-8031-4569-6
- Torkington C. (1991). The regulatory aspects of the repair of civil aircraft metal structures, In: *International Conference on Aircraft Damage Assessment and Repair*, Institution of Engineers, page numbers (1-5), ISBN: 0858255375, Melbourne Victoria, Australia

Part 4

Stress-strength Analysis of Adhesive Joints

Strength of Composite Scarf Joints

Young W. Kwon
Naval Postgraduate School
 USA

1. Introduction

In recent years, large composite structures have been used increasingly in the aerospace and naval industries. Such a large composite structure is mostly fabricated using the scarf joining technique so that multiple substructures can be connected together. Figure 1 shows three commonly used scarf joint configuration. Among the three, the step/overlap joint is considered as the strongest because it has the largest joint surface area. As a result, this chapter addresses the step/overlap joint. The scarf joint is typically constructed as sketched in Fig. 2. The Vacuum Assisted Resin Transfer Molding (VARTM) technique is frequently used for the joint fabrication process because the technique can be applied to a large size of structure. Furthermore, the scarf joint can be also used for repair of a damaged section.

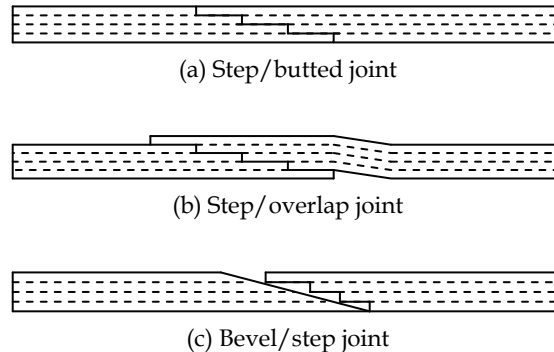


Fig. 1. Different kinds of scarf joints

Because there is a discontinuity of reinforcing fibers at the joint interfaces as shown in Fig. 2, the scarf joint becomes usually the weakest part of the structure. Therefore, it is important to be able to predict the failure strength of the scarf joint, to enhance the joint strength, and to monitor the progress of failure at the joint before any catastrophic failure. The next section discusses experimental testing of scarf joints as well as Mode I and Mode II fracture testing, which is followed by the computer modeling and simulation section. Subsequently, a technique is described to enhance the strength of the scarf joint interface using Carbon NanoTubes (CNT). After that, a section discusses how to monitor crack growth at the joint interface using CNT. Finally, summaries and conclusions are provided.

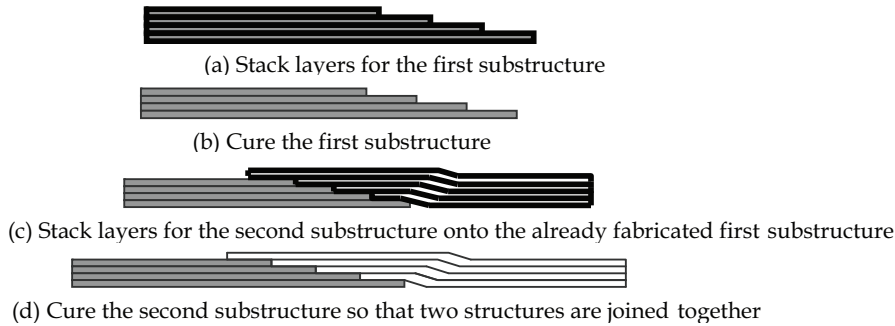


Fig. 2. Construction of composite scarf joint

2. Experimental study of joint strength

Scarf joints are fabricated using carbon-fiber and fibreglass plain weave composites. Carbon-fiber is T700 while fibreglass is E-glass. The Derakane 510A ester resin is used as the binding matrix material. The scarf joint specimens are fabricated using the VARTM technique. After the base plate is fabricated using VARTM, it is cured for 72 hours before the joint surface is sanded down and then cleaned with acetone in preparation for creating the patch part using VARTM again. Four different combinations of scarf joints are fabricated and their strengths are compared. The constructed scarf joints are carbon base/carbon patch composite joints, glass base/glass patch composite joints, carbon base/glass patch composite joints, and glass base/carbon patch composite joints. The difference between the last two joints is illustrated in Fig. 3. In addition, scarf joints are fabricated either using the piece by piece as shown in Fig. 2 (called two-step cured process) or all together (called co-cured process). The latter case is not practically common but used to compare the scarf joint strength between the two fabrication processes. Because fracture of the scarf joint is a mixed mode fracture, specimens are also fabricated to test Mode I and Mode II fracture strength, respectively. To this end, single edge crack beams are made and tested. The Mode I fracture is tested as the double cantilever beam as shown in Fig. 4 while Mode II fracture is tested as the three-point bending beam as seen in Fig. 5.

The critical energy release rate for Mode I fracture is computed using

$$G_{Ic} = \frac{3P\delta}{2b(a + |\Delta|)} \quad (1)$$

where P is the load when the crack propagates, δ is the tip displacement, b is the sample width, a is the crack length, and Δ is the horizontal axis intercept from a vs. $C^{1/3}$ curve. Here C is the compliance of the double cantilever beam (ASTM, 2002). No applicable ASTM Standard exists for pure Mode II fracture toughness testing. Mode II testing consists of a three point bending test as shown in Fig. 5. Because the crack lies in the midplane of the beam, only shear stress is applied to the crack. The following equation is used to determine Mode II critical energy release rate, G_{IIc} (Todo et al., 2000):

$$G_{IIc} = \frac{9P^2a^2C}{2b(2L^3 + 3a^3)} \quad (2)$$

where P is the critical load when the crack propagates, C is compliance, a is the initial crack length, b is the sample width, and L is a half of the span length.

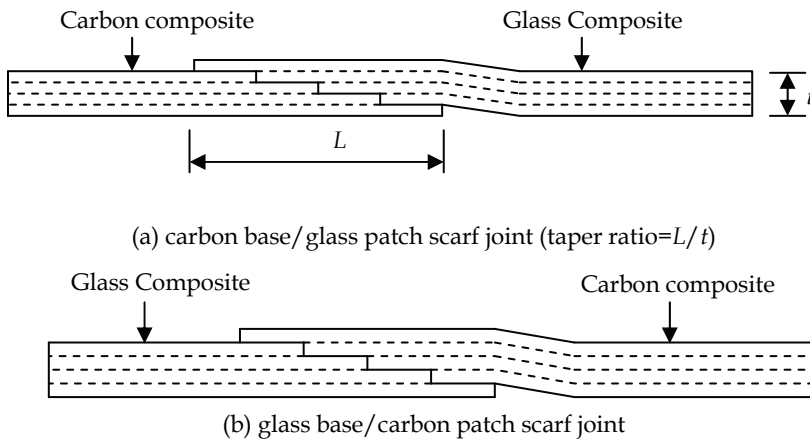


Fig. 3. Difference between carbon base/glass patch and glass base/carbon patch scarf joints

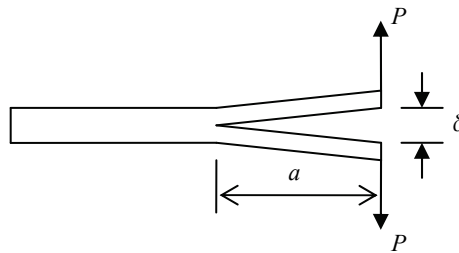


Fig. 4. Double cantilever beam test for Mode I (i.e., crack opening) fracture

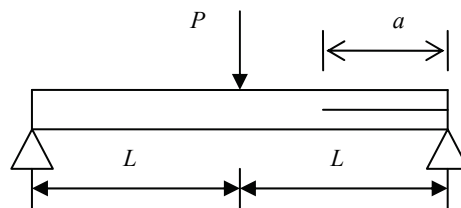


Fig. 5. Three point bending test for Mode II (i.e., shearing mode) fracture

The experiment is conducted using Instron 4507. The specimens are measured and placed under an axial load until failure. In order to avoid buckling of the specimen without using any anti-buckling guide under compression, the unsupported length to thickness ratio is between 15 and 20. Both force and displacement are recorded. Scarf joint specimens fail at the interface. Some specimens fail through the joint interface as shown in Fig. 6(a), and others start the failure at a tip of the joint interface and are fractured across the cross-section of the joint as seen in Fig. 6(b).

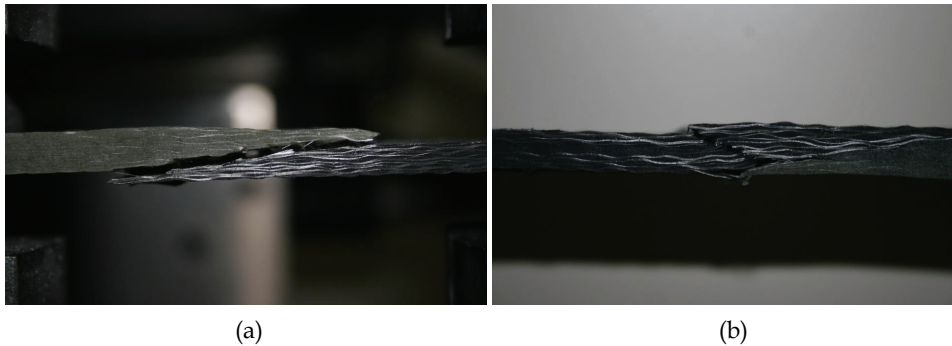


Fig. 6. Joint failure (a) through interface (b) across the joint cross-section

The compressive joint strength of the four different scarf joints is compared in Fig. 7. As expected, carbon base/carbon patch composite joint is strongest. Furthermore, the homogeneous scarf joints made of the same materials are stronger than the hybrid scarf joints made of two different materials. Especially, the glass base/carbon patch composite joint is the weakest.

Another comparison of compressive failure strength is made between the two-step (or called 2-stage) cured and co-cured (or called 1-stage cured) scarf joints. Figure 8 shows that the 2-stage cured joint is stronger than the 1-stage cured joint made of carbon base and glass patch. It is believed that the preparation of interface surface for the 2-stage cured specimens (i.e. sanding and cleaning with acetone) contributes to the enhancement of the joint strength compared to the 1-stage cured specimens. Another study compares the Mode II critical energy release rates between the two-step cured and co-cured interface of carbon/carbon composites using the three point bending test as shown in Fig. 5. The results also show that the two-step cured samples have a larger critical energy release rate than the co-cured samples, which is plotted in Fig. 9.

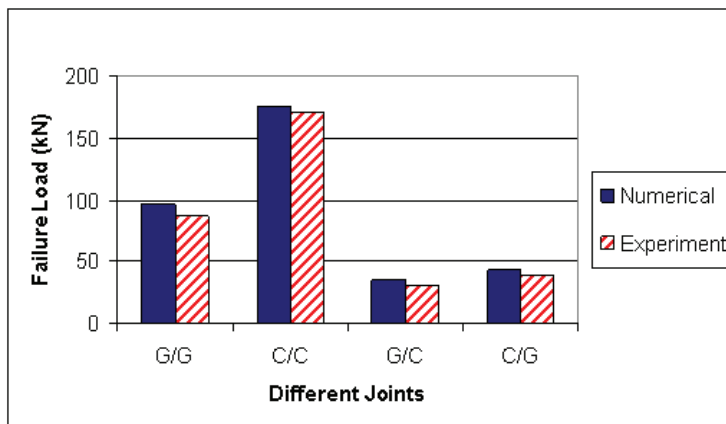


Fig. 7. Comparison of failure loads of scarf joints made of different combinations of composite materials under compressive load (G: Glass-fiber, C: Carbon-fiber)

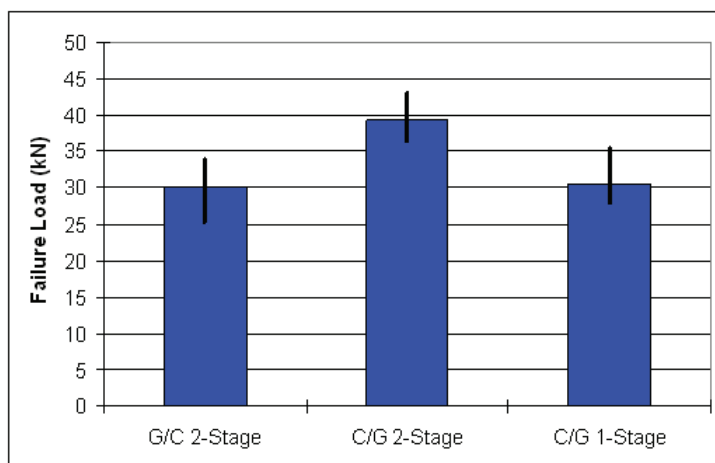


Fig. 8. Experimental compressive strength for hybrid joints (Glass/Carbon and Carbon/Glass)

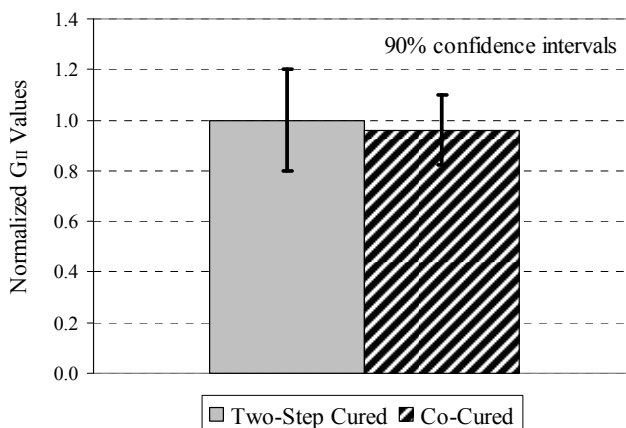


Fig. 9. Comparison of normalized average values of G_{II} for carbon fiber composites.

3. Numerical modelling and prediction

In order to predict the strength of composite scarf joints, finite element based computer models are developed and assessed against the experimental data. Fracture mechanics based models are selected to predict the joint strength. A small size of crack is assumed at the critical location of the joint interface. The critical location is found using the finite element analysis without incorporating any crack. The critical location is located at a tip of the scarf joint interface, especially at the tip of the base material. A small crack is then considered at the critical location. The size of the crack is selected such that it is smaller than the minimum detectable size using the nondestructive technique. The “undetectable” crack length is generally considered as 0.254 mm or less. Therefore, the present computational models assume a crack no longer than 0.254 mm.

Because the size of crack is much smaller than the size of the specimen, a multiscale technique is adopted. The large scale analysis considers the whole scarf joint specimen as shown in Fig. 10 without a crack. Proper boundary and loading conditions are applied to the analysis model. The next small scale model considers only the region containing the critical location as indicated by lines in Fig. 10 and zoomed in Fig. 11. The size of the small scale model should be sufficiently greater than the size of the crack so that the boundary displacements of the small scale model are not affected by inclusion of the small crack. By doing so, the boundary displacements of the small scale model are obtained from the large scale model which does not include the small crack. Besides, the resin layer may be modeled discretely in the small scale model as shown in Fig. 11. Because the large scale model does not consider the resin layer, the resin layer vanishes at the boundary of the small scale model. A crack is embedded in the resin layer.



Fig. 10. Large scale finite element model without considering a crack

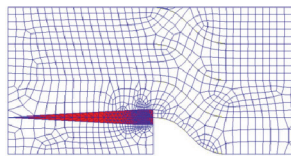


Fig. 11. Small scale finite element model including the resin layer at the critical location and a small size of a crack (the triangular zone is the resin layer)

In modeling the crack, different kinds of crack models are considered and evaluated to determine what kind of crack model produces the results matching the experimental data [Kwon & Marron, 2009]. The first crack model assumes a crack at the critical joint interface without an explicit resin layer as sketched in Fig. 12(a). The second crack model includes a very thin explicit resin layer at the critical joint interface and assumes a horizontal crack in the resin as seen in Fig. 12(b). Finally, the third crack model is similar to the second model except that the crack is angled in the resin at the same slope of the scarf joint taper ratio L/t as shown in Fig. 12(c). The taper ratio is shown in Fig. 3. In Fig. 12(b) and (c), the resin layer thickness is exaggerated to show the crack clearly. The actual resin thickness in the model is 0.05 mm. For the second crack model, the crack is located in three separate places, respectively; at the resin bottom/composite interface, inside the resin, and at the resin top/composite interface. Figure 12(b) only shows the crack inside the resin. For the third crack model, only one crack is modeled. This crack is assumed to originate at the interface of the resin bottom/composite, as shown in Fig. 12(c). The angle of the slanted crack is 14.0° for the taper ratio of 4, and 7.13° for the taper ratio 8.

The Virtual Crack Closure (VCC) technique is used to extract Mode I and Mode II components of energy release rates from finite element fracture models. Two techniques have been explored for this study, the traditional VCC technique and the modified VCC technique. The modified technique gives results very comparable to the traditional technique, and saves significant amount of time while running the models. For this reason, the modified VCC technique is adopted for this study.

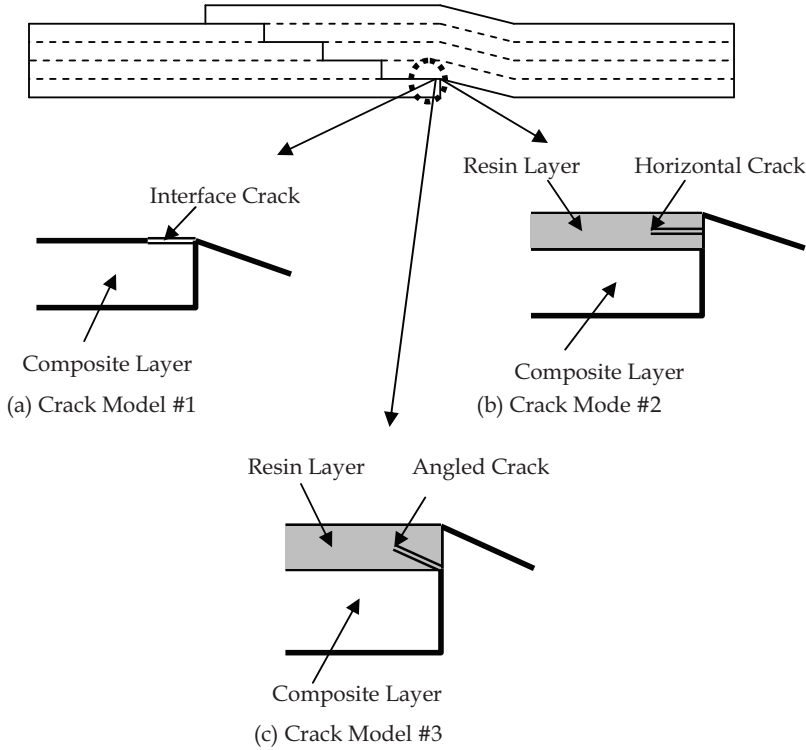


Fig. 12. Three different crack models at the critical location of scarf joint

The modified VCC approach uses the same information from a finite element analysis (i.e., nodal forces and displacements) as the traditional VCC method does. The former has its advantage over the latter because only one finite element solution has to be generated for the former while two finite element analyses are necessary for the latter technique. This can save an ample amount of time. When using the modified VCC technique, the elements at the crack tips must be equal in size to the virtual crack extension length Δa , as sketched in Fig. 13. The size Δa is usually assumed to be less than 5% of the assumed crack length. Furthermore, when using this method, it is assumed that this extension will not considerably change or alter the crack tip as the elements deform [Krueger, 2002]. Since the deformation is small, this is satisfied throughout the analysis.

In calculating the energy release rates for Modes I and II, G_I and G_{II} , the following formulas are used for the modified VCC method following Fig. 13 notations:

$$G_I = \frac{\left[Y_i \left(w_k^t - w_k^b \right) + Y_j \left(w_l^t - w_l^b \right) \right]}{(2\Delta a)} \quad (3)$$

$$G_{II} = \frac{\left[X_i \left(u_k^t - u_k^b \right) + X_j \left(u_l^t - u_l^b \right) \right]}{(2\Delta a)} \quad (4)$$

where u and w are the displacements parallel and normal to the crack orientation, and X and Y are the forces at the nodal points in parallel and normal to the crack direction. Subscripts denote the nodal positions and superscripts t and b indicate the top and bottom nodes at the crack face as shown in Fig. 13. If there is no crack opening, G_I becomes zero.

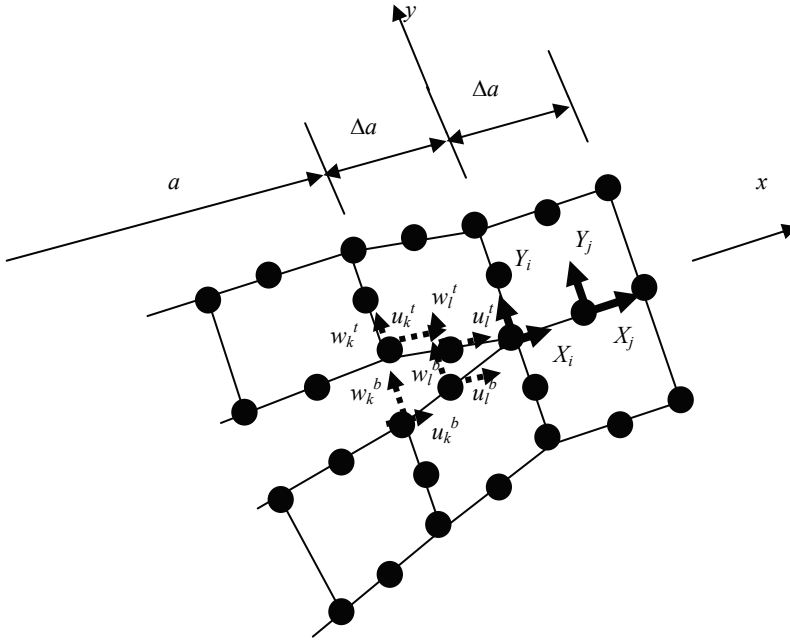


Fig. 13. Modified virtual crack closure technique

Because most cases studied here have both Mode I and Mode II energy release rates, it is necessary to use mixed mode fracture criteria. There are many different mixed mode criteria proposed so far [Reeder, 1992]. This study considers the following mixed mode criteria:

$$\frac{G_I}{G_{Ic}} + \frac{G_{II}}{G_{IIc}} = 1 \quad (5)$$

$$\left(\frac{G_I}{G_{Ic}} \right)^2 + \left(\frac{G_{II}}{G_{IIc}} \right)^2 = 1 \quad (6)$$

$$\left(\frac{G_I}{G_{Ic}} \right)^2 + m \left(\frac{G_I}{G_{Ic}} \right) \left(\frac{G_{II}}{G_{IIc}} \right) + \left(\frac{G_{II}}{G_{IIc}} \right)^2 = 1 \quad (7)$$

in which subscript “c” indicates the critical energy release rate of each fracture mode. Equation (5) is called the mixed linear criterion, Eq. (6) the mixed quadratic criterion, and Eq. (7) the mixed biquadratic criterion which contains the interactive term, i.e. the second term. If the interactive parameter m is set to zero, it is the same as the mixed quadratic criterion. For linear fracture mechanics, the failure load for mixed fracture is computed as below for the three criteria. For the mixed linear criterion, the failure load is

$$P_{fail} = P_{applied} \sqrt{\frac{G_{Ic}G_{IIc}}{G_{Ic}G_{II} + G_{IIc}G_I}} \quad (8)$$

Where P_{fail} and $P_{applied}$ are the failure and applied forces, respectively. For the mixed quadratic and biquadratic criteria, the failure loads are computed from the following equations, respectively.

$$P_{fail} = P_{applied} \sqrt[4]{\frac{G_{Ic}^2 G_{IIc}^2}{G_{Ic}^2 G_{II}^2 + G_{IIc}^2 G_I^2}} \quad (9)$$

$$P_{fail} = P_{applied} \sqrt[4]{\frac{G_{Ic}^2 G_{IIc}^2}{G_{IIc}^2 G_I^2 + m G_{Ic} G_{IIc} G_I G_{II} + G_{Ic}^2 G_{II}^2}} \quad (10)$$

All three equations are explored in order to find the best result for the model. These results are provided later. In this study, the critical energy release rates were determined from pure Mode I or Mode II coupon testing, respectively. Their values are 307 N/m and 1280 N/m for Mode I and II, respectively.

In order to validate computational models, the models' geometries are based on the test specimens. Those specimens consist of laminate plates with a scarf joint of length L at the center as shown in Fig. 3. A longer joint length yields a greater joint strength because of the larger joint surface area. Therefore, any general repair uses a large scarf joint taper ratio such as 10 to 20. However, such a large scarf taper ratio results in a large size of specimen which is not practical at the laboratory environment. As a result, a smaller taper ratio is adopted in this study for experimental testing in order to validate the computational models. One set of specimens are 227 mm long and 37 mm wide for the taper ratio $L/t = 4$ as shown in Fig.3. The glass composites are 7 mm thick and carbon composite are 5 mm thick with the overlap joint of four-steps. Another set of specimens have the taper ratio 8. In this case, the total specimen length is twice as long as the previous specimens with $L/t = 4$. Because of computational efficiency, 2-D plain strain models are considered instead of 3-D models.

The models consist of E-glass-fiber and carbon-fiber composites along with the vinyl ester resin. A previous study showed that either isotropic or orthotropic material modeling of the 2-D scarf joint produced almost the same results because the longitudinal modulus is the major load-carrying direction. Therefore, an isotropic material modeling is used in this study with the following material properties. Carbon composites have elastic modulus 52.4 GPa and Poisson's ratio 0.34 while glass composites have elastic modulus 17.2 GPa and Poisson's ratio 0.24. In particular, for a discrete resin layer modeling, the resin has elastic modulus of 8.34 GPa and Poisson's ratio 0.28.

Each specimen is fixed at the left end while a tensile or compressive loading is applied at the right end. The axial loading is applied using a uniform displacement as conducted for the experiments. As a result, the axial displacement is applied uniformly to the right end of the specimen while its transverse displacement is constrained from any movement.

Results from various computer models are compared to experimental data for model validation. While tensile loading produces mixed mode of fractures (i.e. existence of both Mode I and Mode II) at the critical location where virtual cracks are considered, compressive loading yields only Mode II fracture because of crack closure. Therefore, the tensile load results are compared for mixed mode criteria as expressed in Eq. (5) through (7). The computer models are validated with the glass/glass scarf joint with a taper ratio of 4 as shown in Fig. 14. In the figure, five different crack models and three different mixed mode criteria are compared to the experimental data. Among the five cracks models, Model #1 in Fig. 12 does not include a discrete resin layer while the remaining four models consider a discrete resin layer only at the critical location as in Ref. [Kwon & Craugh, 2001]. Among the four models, three cases (Model #2a, 2b and 2c) consider a horizontal crack while one case (Model #3) uses an angled crack. The horizontal crack is located at the lower side interface of the resin layer called Model #2a, in the middle of the resin layer (#2b), or at the upper side of the resin layer (#2c). As shown in Fig. 12, the angled crack with the biquadratic mixed mode criterion is closest to the experimental data. In the biquadratic model, the interaction parameter m is selected -1.3.

In order to further validate the selected model, i.e. the angled crack with a discrete resin layer along with the biquadratic mixed mode criterion with $m = -1.3$; glass/glass scarf joint with a taper ratio 8 is also analyzed and compared to the experimental data as shown in Fig. 15. The selected model produces the almost same failure load as the experimental data. The higher taper ratio yields a much closer result for the selected computer model. Because the angled crack has the same angle as the joint taper ratio, this crack orientation is considered to represent the actual crack growth direction well in the resin layer. That is why the angled cracks consistently predict joint strengths well.

The next set of validation is conducted for different composite materials under compression. As stated previously, compressive loading results in only Mode II fracture. Therefore, different mixed mode criteria cannot be evaluated for these cases. Instead, the selected crack model, i.e. the angled crack in a resin layer, can be assessed against the experimental data. The scarf joints are constructed using glass-fiber and carbon-fiber composites. The four different joints assessed against the experimental data are glass/glass (G/G), carbon/carbon (C/C), carbon/glass (C/G), and glass/carbon (G/C). As stated previously, the first material is the base and the second material is the patch added to the base material. Figure 7 shows comparisons of four different joints. The angled crack model in a resin layer produces consistently excellent predictions for the failure loads. The computer model slightly over-predicts the experimental results for all four joints.

In predicting the failure loads in all previous results, the same critical energy release rates for Mode I and Mode II have been used regardless of the fiber materials because the same resin material has been utilized. This means the failure at the joint interface depends on the fracture toughness of the resin materials. Therefore, modeling a resin layer at the critical location of the failure is essential to an accurate prediction of the failure load. In addition, the crack growth direction is affected by the taper ratio of the scarf joint. It is necessary to reflect the taper ratio in the crack orientation.

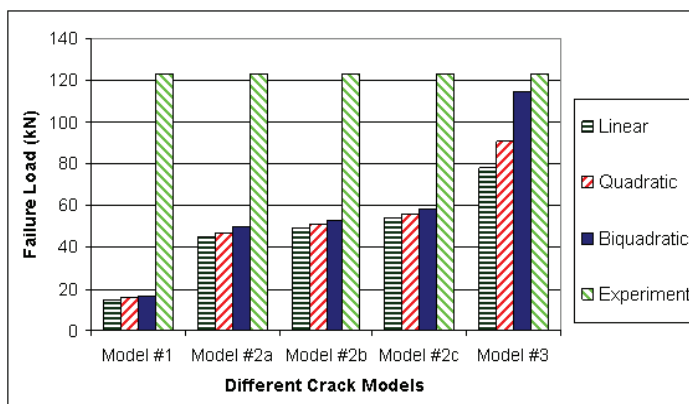


Fig. 14. Comparison of failure loads of glass/glass scarf joints with taper ratio of 4 under tensile load (Model #1: crack with no resin layer; Model #2a: horizontal crack at the lower resin layer interface; Model #2b: horizontal crack in the middle of the resin layer; Model #2c: horizontal crack at the upper resin layer interface; Model #3: angled crack in the resin layer)

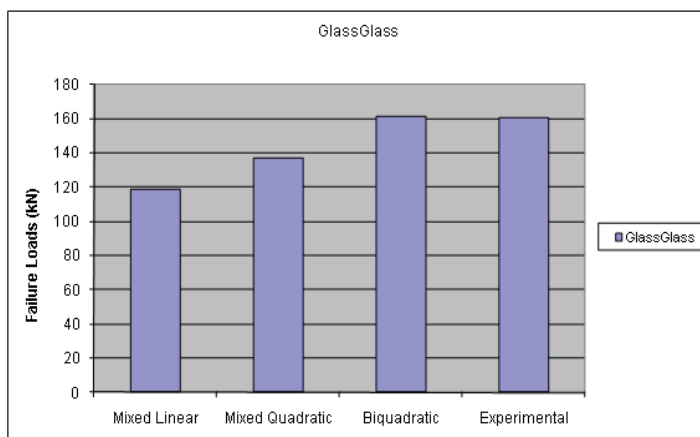


Fig. 15. Comparison of failure loads of glass/glass scarf joints with taper ratio of 8 under tensile load using angled crack model in resin layer

4. Enhancement of interface strength

Many studies have been conducted to determine the type of bonds formed between CNT and epoxy. The general conclusion is that CNT bond in three main ways: micromechanical interlocking, chemical bonding, and van der Waals bonding. While the CNT surface is quite smooth, it has been proposed that there are local non-uniformities in the CNT such as kinks, bends, and changes in diameter. It is at these local non-uniformities where micromechanical interlocking occurs [Wong, et al., 2003]. Chemical bonding is possible, but it is not guaranteed [Shadler, et al., 1998]. Finally, van der Waals bonding certainly occurs, but a relatively weak bond forms. One study also proposes the effects of thermal properties. The

coefficient of thermal expansion of CNT is much higher than that of the polymer matrix. As a result, residual compressive thermal stress is present after the polymer matrix hardens. This thermal stress results in closer contact between the CNT and polymer, which in turn increases micromechanical interlocking and non-bond interactions [Wong, et al., 2003].

In an attempt to improve the joint interface strength, CNTs are introduced at the interface. Since the scarf joint is constructed using the two-step process, CNTs are applied to the joint surface area after the base portion is cured, sanded, and cleaned, i.e. after Fig. 2(b). The CNTs are mixed with acetone and the solution is stirred until the CNTs are dispersed in the solution. The CNT solution is manually spread out over the joint interface area and acetone evaporates completely leaving CNTs behind. Therefore, it is not possible to have very uniform distribution of CNTs over the joint surface area. First, two different surface concentrations of CNTs are used. For this part, 95% pure Multi-Wall Caron NanoTubes (MWCNTs) with a length of 1-5 microns and a diameter of 15 ± 5 nm are selected. The tested surface concentration levels are 11.5 g/m^2 and 7.5 g/m^2 , respectively. Compressive strength tests are conducted for the specimens without CNTs as well as specimens with two different surface concentrations of MWCNTs. The result is plotted in Fig. 16. The data shows CNTs improve the joint strength when compared to the no CNT case. In addition, the CNT surface concentration of 7.5 g/m^2 yields a greater strength than the higher concentration case.

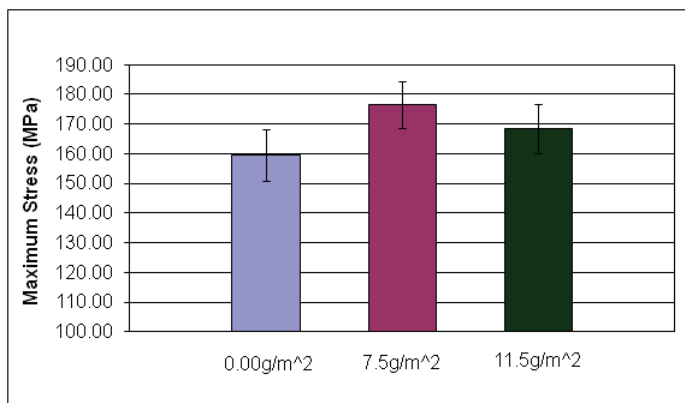


Fig. 16. Comparison of failure strength with two different surface concentrations of CNTs

For subsequent studies, the surface concentration of 7.5 g/m^2 is selected. The next study uses various kinds of CNTs at the joint interface. Single-Wall Carbon NanoTubes (SWCNTs), MWCNTs with two different diameters and two different lengths, and bamboo-structure MWCNTs with two different lengths are considered as listed in Table 1. Figure 17 compares the strength of scarf joints made of different CNTs.

Each CNT group provides a joint strength increase, compared to the non-reinforced specimens, with the exception of group C. The CNTs from Group C is the economical one which has less quality control. The greatest strength increase is observed by Groups D, E, and F. All three of those groups demonstrate an average strength increase of greater than 11 percent. Of these three groups, it appears that Group D possesses the best strength enhancement characteristics. It has greater than an 11 percent increase in strength and possesses the most consistent data of the three top reinforcements. This consistency can be seen by observing the standard deviations shown in Fig. 17.

Groups E and F are bamboo-type CNTs. They have regularly occurring compartment-like graphitic structures inside the nanotubes similar to the bamboo plant [Ding, et al., 2006]. These types of CNTs are used with the notion that the compartment-like graphitic structures may provide additional support when used for reinforcement. The open ended molecular structure of the multi-walled bamboo CNT may increase wettability and functionalization as well. This may allow for increased interfacial bonding which in turn increases the load transfer between the resin and the CNT so that the joint interface strength of the composite structure may be improved. The strength increase confirms that the bamboo structure has better strength characteristics compared to conventional CNTs of similar size and purity. Group B, the economic option, has some samples that provide strong reinforcement and others that are actually weaker than the non-reinforced specimens. As a result, the average strength is greater than the non-reinforced samples, but the standard deviation is quite large. The standard deviation of group B is almost 30 percent larger than any other group. All MWCNT groups are 95% pure, but perhaps the economic option encounters a higher frequency of defects.

	Description
MWCNT-A	Multiwall carbon nanotubes, outer diameter 30 +/-15nm, Length 1-5 microns, Purity > 95%
MWCNT-B	Multiwall carbon nanotubes, outer diameter 25 +/-5nm, Length 10-30 microns, Purity > 95%
MWCNT-C	Multiwall carbon nanotubes, outer diameter 15 +/-5nm, Length 5-20 microns, Purity > 95%
MWCNT-D	Multiwall carbon nanotubes, outer diameter 30 +/-15nm, Length 5-20 microns, Purity > 95%
MWCNT-E	Bamboo structure multiwall carbon nanotubes, outer diameter 30 +/-15nm, Length 1-5 microns, Purity > 95%
MWCNT-F	Bamboo structure multiwall carbon nanotubes, outer diameter 30 +/-15nm, Length 5-20 microns, Purity > 95%

Table 1. Different types of multi-wall carbon nanotubes

The majority of test samples fracture at the expected location along the diagonal step interface of the joint as shown in Fig. 6(a). Those test joints initiates cracks at either the base of the bottom step or at the center of the joint and propagate diagonally along the joint interface. There is another type of fracture that rarely occurs, where the crack propagation does not follow the path of the joint interface. The crack initiate at the base but instead of propagating along the interface, it propagates at a 45 degree angle away from the interface as shown in Fig. 6(b).

Figure 18 shows another line of fracture under compression. In this case the fracture follows the path of the undulated fiber section instead of the scarf interface. Figure 18 shows a test specimen that failed along the alternative fracture line. Only one group has consistently these types of fractures. Group D has every test joint failed along this line of fracture. This group also happens to have the most consistent strength enhancement and the highest elastic modulus of the three top CNT reinforcements.

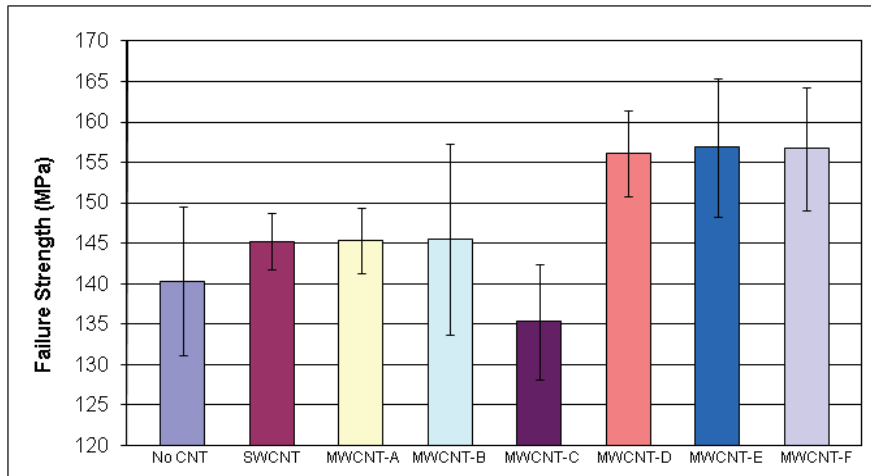


Fig. 17. Comparison of failure strength with different CNTs

A potential explanation for the consistency of this failure in Group D is that the CNTs provide enough enhancements in strength along the joint interface that the interface ceases to be the weakest portion of the specimen. Instead the samples fail along second weakest portion of the joint, the undulated section of the overlap construction. The mode of this type of failure is localized fiber buckling. Normally this type of failure is intermittent. The consistency in Group D suggests the joint may be reinforced enough to make it stronger than the stress required to cause the localized buckling failure at the location of the fabric down step.

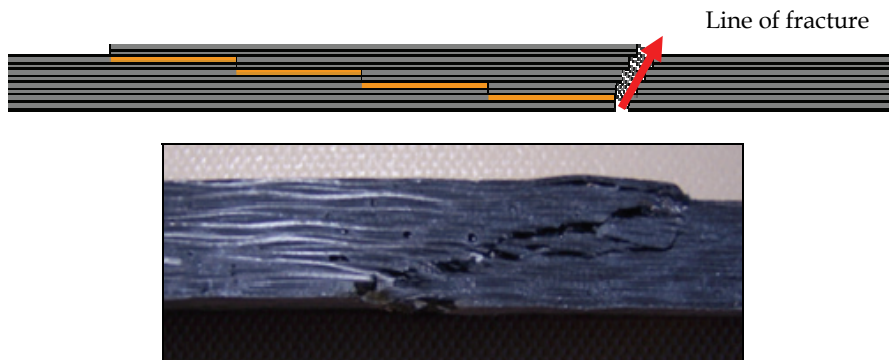


Fig. 18. Another failure mode under compression

In order to further understand the effect of CNTs on the strength of the scarf joints, individual fracture testing of Mode I and Mode II, as shown in Figs. 4 and 5, is conducted, respectively. This set of tests explains on what fracture mode the CNTs affects to improve the interface joint strength [Faulkner, et al., 2009].

Crack opening mode (i.e. Mode I) testing results shows a modest improvement in the critical energy release rate G_I when the joint interface is reinforced with CNT. Figure 19 compares

the average values of normalized G_I for resin only samples (i.e. without CNT reinforcement) and CNT reinforced samples. Standard deviation is also shown in the figure. The average G_I value increases about 10% with CNT reinforcement. However, Mode I crack propagation characteristics were observed with no discernable difference between the CNT reinforced and non-reinforced samples. The Digital Image Correlation (DIC) System was used to observe the crack growth in both CNT reinforced and non-reinforced specimens and their images are very similar. After testing, the samples are fully broken to inspect the cracked surface. Mode I samples reveal little difference between CNT reinforced and non-reinforced samples. Both CNT reinforced and non-reinforced samples have crack growth through the resin layers where the initial cracks are located.

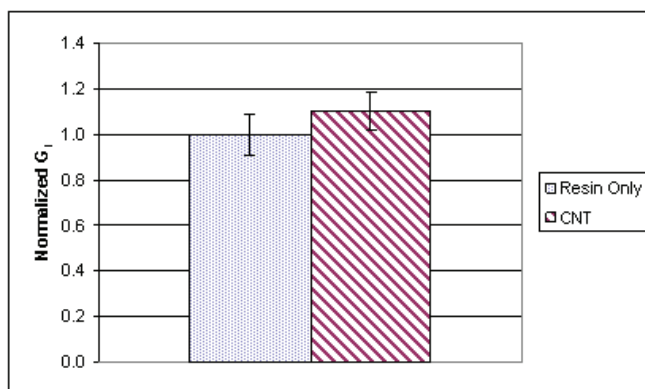


Fig. 19. Normalized G_I values for Mode I

Mode II (i.e. shearing mode) testing results in a significant increase in the critical energy release rate G_{II} for the samples reinforced with CNT. Figure 20 shows the normalized average values of G_{II} for the specimens. Again, standard deviation is also shown in the figure. As shown by the standard deviation, the lowest CNT reinforced value is higher than the highest non-reinforced value. The average CNT reinforced G_{II} value is 32% higher than the average resin only G_{II} value. The G_{II} values are computed from the compliance of the load vs. displacement curves. Representative plots of load-displacement are shown in Figs. 21 and 22. The point of crack propagation is marked with an X.

Qualitatively, the observed crack propagation for Mode II is significantly different between the CNT reinforced and non-reinforced samples. For the non-reinforced samples, crack propagation begins at the tip of the initial crack and continues through the interface resin material. However, for CNT reinforced samples, a crack begins to nucleate away from the initial crack tip, perhaps in an area of lower CNT concentration, i.e., a weaker strength zone. Eventually, this newly formed crack grows to be connected to the initial crack. This result is widely observed in the CNT reinforced samples.

After testing, the samples are fully broken to inspect the cracked surface. For the non-reinforced samples, the joint interface bond is broken through the resin while in others the resin is pulled away from the fibers. However, the CNT reinforced samples fail much differently. The CNTs reinforce the resin at the interface, making it stronger. The CNTs themselves do not fracture. The CNTs bond to the resin, blocking crack propagation. As a result, at some locations, the crack propagates through the fibers rather than through the

resin. The critical energy release rate for CNT reinforced samples become higher because the crack propagates through the carbon fibers vice resin.

Representative images from the DIC system are shown in Fig. 23. Without CNT reinforcement at the joint interface, the initial crack propagates through the interface all the way as shown in Fig. 23(a). On the other hand, CNT reinforcement resulted in a tougher joint interface so that the crack path deviates away from the joint interface as seen in Fig. 23(b).

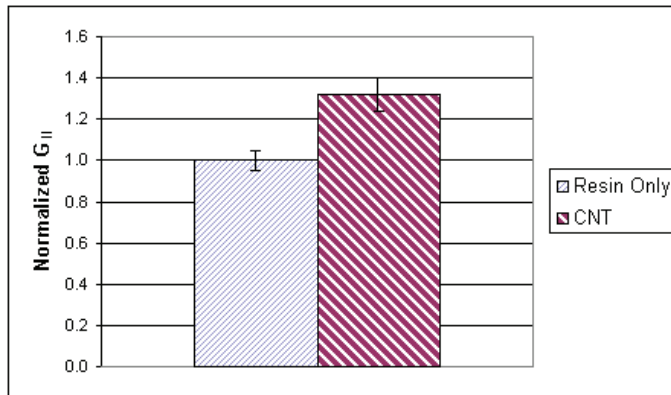


Fig. 20. Mode II Normalized G_{II} Values

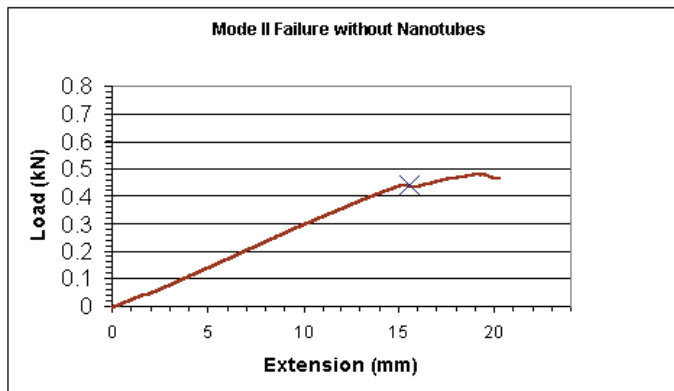


Fig. 21. Representative load versus extension plot for Mode II testing of non-reinforced sample (The point of crack propagation is marked with an X.)

CNT reinforcement is more significant for Mode II fracture than for Mode I. A possible explanation is given below. The CNTs are not believed to have a strong chemical bond with the resin material. Instead, CNTs are considered to be entangled with resin polymer chains, called a mechanical interlocking. Such a mechanical interlocking is more effective to resist the shearing force of Mode II than the normal force of Mode I. Therefore, the fracture toughness of Mode II becomes much higher with CNT reinforcement.

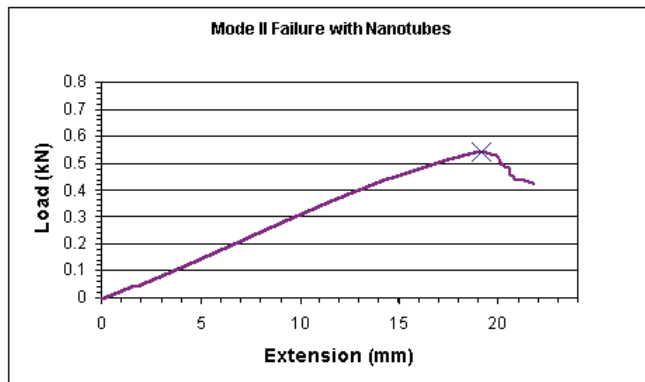
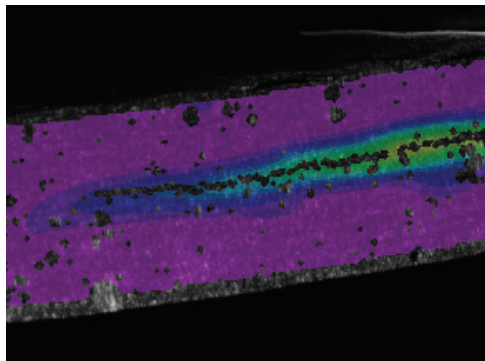
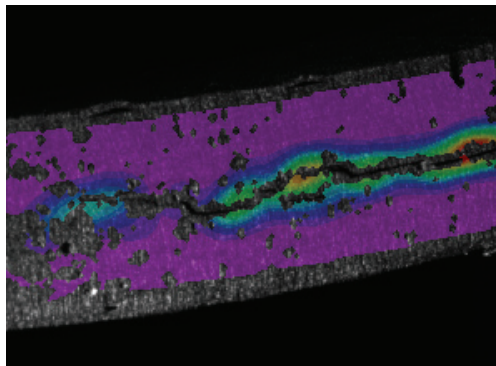


Fig. 22. Representative load versus extension plot for Mode II testing of CNT reinforced sample (The point of crack propagation is marked with an X.)



(a) Without CNT reinforcement



(b) With CNT reinforcement

Fig. 23. Images of crack growth: (a) Without CNT reinforcement, the crack propagated through the joint interface plane. (b) With CNT reinforcement, the crack path showed deviation away from the joint interface.

Another purpose of testing is to optimize the surface concentration of CNT, i.e. the mass of CNT per unit CNT-reinforced surface area of interface. To achieve this goal, three concentrations of CNT are used: 5 g/m², 7.5 g/m², and 10 g/m². As with all sample sets, non-reinforced samples are constructed and tested as a reference point. Mode II testing is completed since prior phases determined CNT reinforcement significantly affected Mode II fracture toughness. The results of Mode II testing are shown in Fig. 24 along with standard deviation. As shown in the figure, 7.5 g/m² of CNT is the optimal concentration, which is consistent with the previous study [Kwon, et al., 2008]. Again, the lowest value of G_{II} for samples reinforced with 7.5 g/m² CNT is higher than the highest value of non-reinforced samples.

The higher concentration of 10 g/m² results in slightly lower critical energy release rate than the 7.5 g/m² concentration. On the other hand, interface toughness with the CNT concentration of 5 g/m² is even lower than that of non-reinforced specimens. This result suggested that a lower amount of CNT at the interface does not provide proper mechanical interlocking while serving as a localized defect because of a lower bonding between CNT and polymers.

The additional purpose of testing is to determine the effect of “banding” CNT. “Banding” refers to only reinforcing a part of the interface area on the sample. All other sample sets involved using CNT to reinforce the entire secondary bond between the top and bottom plates. However, samples for the present tests are only reinforced in the area extending 6 cm from the initial crack tip. “Banding” CNT may be applicable to repair of carbon fiber composite components when only a localized area requires reinforcement. The Mode II critical energy release rate results in 19% increase due to CNT reinforcement with 7.5 g/m² CNT concentration. The drop from roughly 30% found in previous sample sets is due to “banding” the CNT vice reinforcing the entire secondary bond.

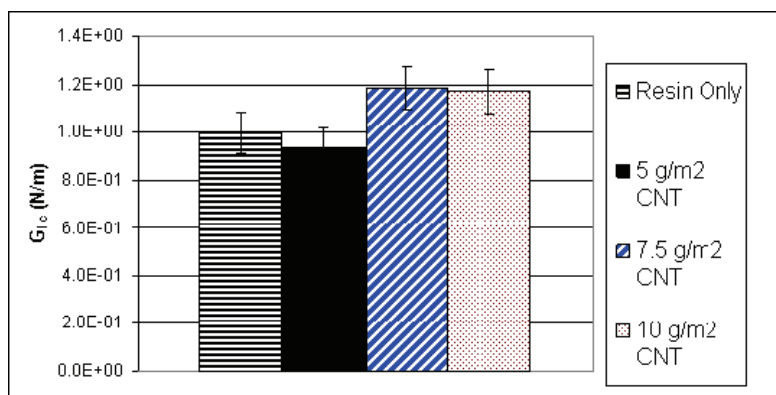


Fig. 24. Normalized G_{II} values for different concentration of CNT

5. Interface crack growth monitoring

Many different studies have been conducted to determine the feasibility of damage detection in composite materials through the use of CNTs. In one study, a polymer with CNTs was used in a piezoresistive strain sensor for structural health monitoring [Kang, et

al., 2006]. This sensor proved to have a linear symmetric strain response under static and dynamic loading. However, the CNTs were only included within the sensor itself. A similar study showed that multidirectional strains could be measured using an isotropic film of CNTs placed on a four point probe [Dharap, et al., 2004]. This probe then could be used at different locations sensing a linear strain response in all locations. Another more recent study investigated the use of CNTs as a replacement for strain gauges [Nofar, et al., 2009]. This study placed semi-conductive multiwall CNT-fiberglass-epoxy polymer composites under both tensile and cyclic loading to detect failure. It was shown that the multiwall CNTs were able to outperform regular strain gauges in sensing different types of failures. This outcome was due to their ability to be interspersed within the composite and, as a result, react more sensitively to the changing stress fields around them.

Although much work has been done using CNTs as strain gages, more limited research has been focused on the inclusion of CNTs to monitor crack propagation. In one study, CNTs were first dispersed into a polymer matrix and then infiltrated into layers and bundles of conventional fibers [Thostenson & Chou, 2006]. This technique created a percolating network which was then used as a sensor to detect the onset, nature, and evolution of damage in advanced-polymer-based composites. A similar study demonstrated that a network of CNTs throughout the composite material was an effective way to monitor fatigue-induced damage, as well as opportunities for damage repair [Zhang, 2007]. Yet another study showed that if a high aspect ratio could be maintained throughout the entire network of CNTs, they could be highly conductive within the structure allowing for damage detection [Chou & Thostenson, 2008].

Each of these studies, however, used a network of CNTs dispersed throughout the composite base material to enable damage detection. These methods, although successful in the detection of damage, may not isolate the interfacial damage and may be impractical for large composite sections. In order to detect the interface damage, this study focuses on a layer of CNTs percolated along the interface layers. [Bily, et al., 2010].

Because CNTs have high electrical conductivity, CNTs at the joint interface are used for potential crack detection. As a crack propagates through the interface containing CNTs, the electric conducting paths through CNTs are disrupted. As a result, the electric conductivity through the interface is lowered. By measuring the electric conductivity or resistivity, the crack growth is monitored.

Figure 25 shows that two metal sheets are used at both ends of the specimens so that they can be used as the leads for measuring electrical conductivity or resistivity through the interface. A Teflon film is used to represent the initial crack. CNTs are spread to connect between the two metal sheets. The upper layers are laid on the bottom layers using the VARTM process and the final plate is cut into strips for the Mode II fracture testing. Both carbon fiber composites and fiberglass composites are studied for crack monitoring.

Mode II testing of ten carbon composite coupons containing CNTs at the interface layers are tested. Based on initial test results, the ratio of initial crack length (a) to span length ($2L$) needs to be greater than 0.2 to ensure failure by Mode II crack propagation. Hence, the initial crack length is set at 40 mm for a full span length of 160 mm and coupon width of 24 mm. Test speed is 1 mm/min displacement at the point of load application.

Prior to the start of testing, each coupon's resistance through the interface is measured for baseline comparisons. Starting resistance readings shows a high degree of scatter (26.5 to 1081.0 ohms) across coupons. This scatter is due to the non-uniform distribution of CNTs, directly resulting from the dispersion technique and VARTM process. However, each

particular coupon's resistance is essentially constant (within a tenth of an ohm) based on multiple measurements.

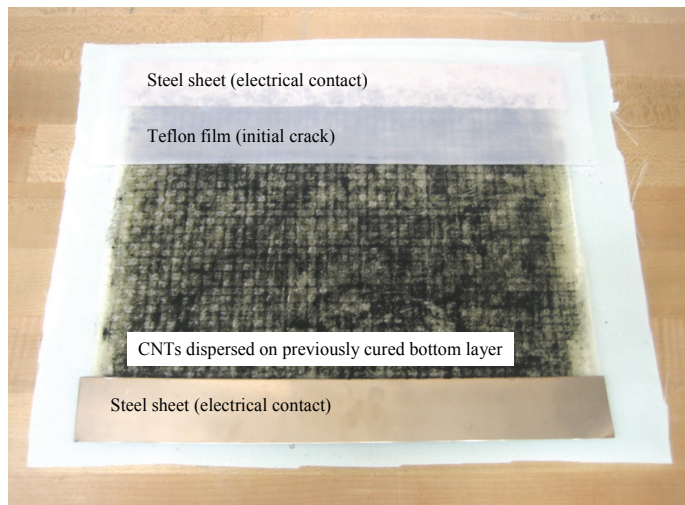


Fig. 25. Bottom layer of two-step cure sample covered with CNTs, stainless steel sheets, and Teflon film

During the three-point bending tests, resistance across each coupon is recorded at 30 second intervals. These values generally vary little from the initial readings throughout the test. Once additional cracking takes place, the sample is left in the bent position under load. The readings taken in the bent position are again constant, only fluctuating to the tenth of an ohm, and within $\pm 4\%$ of the initial resistance values for 8 of the 10 samples. However, when the coupons are released from this bent position, the resistances increase an average of 16%. The variance in the percentage increase can be attributed to the non-uniform CNT dispersion. It is important to note that the resistance changes due to crack growth are generally observed only after the cracked specimens are unloaded.

After unloading, the CNT-reinforced carbon fiber samples are subsequently tested with loading and unloading cycles using a force of just 100 N – a small load enough not to cause any further interface crack growth. During each loading cycle, the resistance is measured before loading and after unloading. The measured resistances show consistency in the reading, varying 0.3% to 2.2% from sample to sample. Thus, despite continued load cycles, the resistances do not significantly increase as the crack does not grow any further.

With resistance change shown to be dependent on crack growth, the CNT-reinforced carbon fiber coupons are then further cracked under additional loading. Once the crack propagates (determined by both sight and sound), the load is removed and the new crack length and the corresponding resistance are both measured. This process is repeated until the crack tip eventually reaches the point of load application, at which point it is no longer possible to further crack the coupons under three-point bending load. The resulting data are plotted to determine a relationship between change of crack length and change in resistance.

Figure 26 shows the plots for three different samples, which have low (5.85 ohms/mm), medium (34.1 ohms/mm), or high (164.7 ohms/mm) values of resistance change versus crack

growth length. Because each sample has different (non-uniform) dispersion of CNTs at the interface, the resistance readings are different. However, the resistance change is very linear in terms of crack growth for any individual sample, albeit with different slope for each sample. This trend can be useful to predict the crack length for a given sample if the slope is determined from a couple of initial measurements. This increase in resistance is related to the fact that the cracks for the carbon fiber composites with CNTs propagate through the layer of CNTs. Thus, as the crack continues to propagate, the CNTs are separated from each other, and their ability to conduct electricity along the interface is decreased.

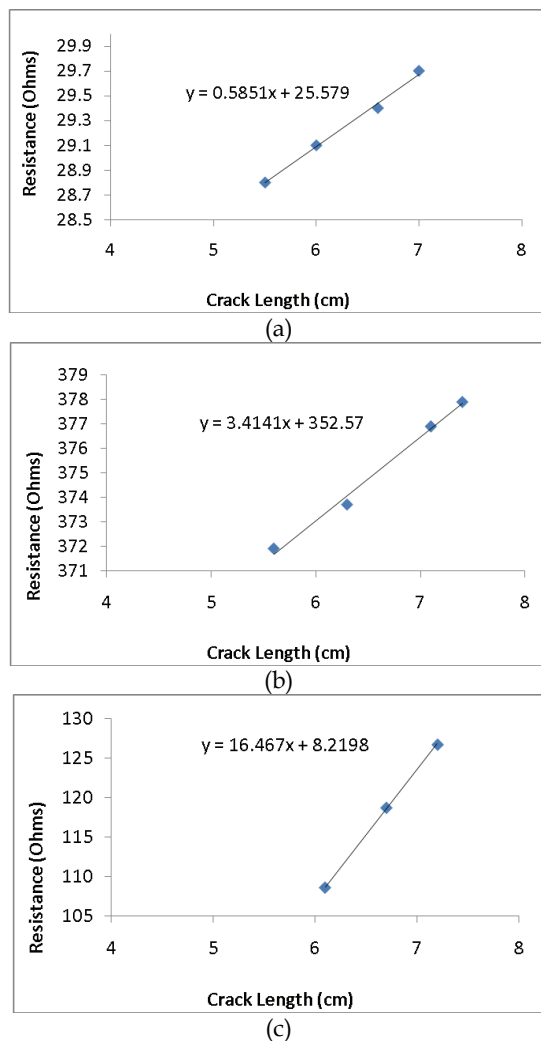


Fig. 26. Plots of resistance vs. interface crack length of CNT-reinforced carbon fiber composites: specimen with (a) a smaller change of resistance, (b) an average change of resistance, and (c) a higher change of resistance.

E-glass fiber composite coupons containing CNTs are also tested. Fiberglass samples have an initial crack length 40 mm, a span length 160 mm, and a width 24 mm. These geometric parameters along with a Mode II test speed of 1 mm deflection per minute result in coupon failure through crack propagation.

Prior to loading, resistance is measured for ten coupons containing CNTs along the interface for baseline comparisons. An advantage to using fiberglass for testing is that the CNTs inside the composite can easily be seen. Some coupons do not conduct as areas within the coupons are observed to be void of CNTs. Each of the coupons that conduct electricity has a dark visual path of CNTs that are continuous throughout the length of the coupon. This result shows that for CNTs to be effective, the network must be contiguous, as expected. It also shows that CNTs can be effective even in non-conductive composite materials. In order to ensure that CNTs are contiguous in non-conductive media, reliable means for more uniform dispersion during the VARTM process should be developed and employed.

Even though only four of the coupons constructed are conductive, all coupons containing CNTs are put through Mode II testing and values of the resistance readings are recorded at 30 second intervals. As expected, the six coupons that initially do not conduct registered no readings throughout the test. The resistance values for the four conducting fiberglass coupons, although much higher than those obtained for the carbon fiber composite coupons, show the same trends. During the loading, the resistance readings vary little from the initial readings (within 6%). After the sample cracks and continues to crack, the resistance readings are steady (varying only a few ohms at a time), again consistent with carbon fiber composite coupons with CNTs.

When the initial loading is completed, the sample is left in the bent position as was done previously. The readings in the bent position are constant, but all readings have increased from the initial values, with an average increase of 24%. When the coupons are released from this bent position, the resistances increase further. Although each coupon shows an increase in resistance, there is a scatter due to the non-uniform distribution of CNTs. The four conductive samples have resistance increases of 17, 27, 28, and 100% (for an average of 43%) compared to the initial values. This increase is qualitatively consistent with carbon fiber composites.

As before, subsequent additional loads are applied such that additional crack growth would not occur. Corresponding resistance readings are taken both before loading and after unloading. This cycling is done at least three times for each sample. The readings are consistent for each sample, only varying by at most 6.4%. Again the difference can be attributed to the uneven distribution of CNTs across the coupons. Thus, the resistance readings are not significantly altered by loads which do not produce crack growth. After taking the consistency readings, the fiberglass coupons are again loaded for crack growth using the Instron machine. Unfortunately, no useful information is gathered from this step. Upon further crack propagation, resistance readings jump to over 1 M Ω . These high readings are indications that the CNTs are no longer touching and the samples are acting as open circuits.

When testing the carbon fiber composites, the way in which they failed is expected based on previous research. Fiberglass, however, is a bit surprising in its behavior both with and without CNTs. During testing of fiberglass coupons with CNTs, a loud cracking sound is heard upon failure followed by a quick decrease in the loading. This loud cracking sound is not observed during testing of fiberglass composites without CNTs. Instead, a soft crackling sound is heard. Furthermore with the fiberglass coupons without CNTs, after the crack is visually and audibly verified, additional loading is still possible.

Differences in both the sound of failure, and crack propagation can be attributed to the CNTs. In the non-reinforced samples, crack propagation begins at the tip of the initial crack, and continues to propagate through the interface. This crack without CNT-reinforcement occurs

early in the loading process and slowly propagates while still maintaining an increasing load. For the fiberglass composites reinforced with CNTs, the crack also initially propagates from the initial tip through the interface. However, at a certain point the crack takes a path of least resistance outside the layer of CNTs, as shown in Fig. 27. This result is observed in the CNT-reinforced fiberglass samples and is the source for the loud cracking sound.

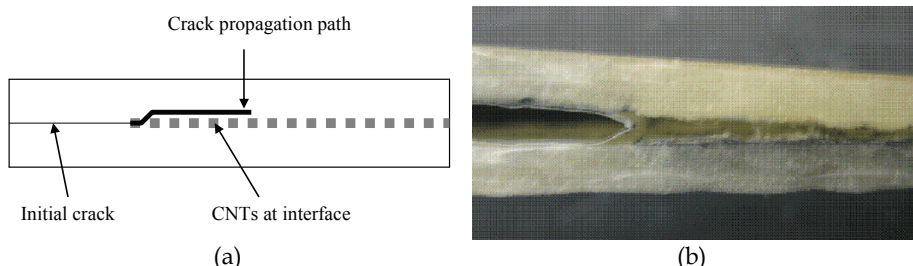


Fig. 27. Path of crack propagation for fiberglass composites with CNT application: (a) schematic sketch, and (b) picture of actual specimen.

6. Conclusions

This chapter studied the strength of composite scarf joints. First of all, a modelling technique was developed to accurately predict the joint strength. The technique is based on fracture mechanics with a very small initial crack at the most critical interface location. The crack is embedded in a resin layer with an orientation equal to the taper ratio of the scarf joint. For the mixed mode fracture, the interactive quadratic criterion is selected. This technique resulted in predicted joint strength very comparable to experimental data under different loading conditions and different taper ratios of the scarf joints.

Furthermore, CNTs were used to enhance the joint strength as well as to monitor crack growth along the interface. The introduction of CNTs along the interface especially improved the Mode II fracture strength much more than the Mode I fracture strength. The study also selected an optimal surface density of CNTs as well as the type of CNTs. The surface density of 7.5 g/m^2 was optimal and the MWCNTs with a larger diameter produced a greater strength. When the joint strength was improved enough with CNTs, the failure occurred under compression along the undulated section rather than the joint interface. That is, the joint interface was not the weakest joint any more.

High electric conductivity of contiguous CNTs at the interface yields a low resistivity. However, crack growth disrupts the conductivity thereby increasing the resistivity. Such a significant change in resistivity is only observed when the specimen is unloaded. The change of resistivity is very linearly proportional to the crack growth length. However, the proportional constant is different from sample to sample because the CNT distributions are non-uniform. The knowledge in the chapter aids to better design and analysis of scarf joints with integrity.

7. Acknowledgements

The author acknowledges the contribution of his graduate students and colleagues including, but not limited to, A. Marron, G. Burkholder, J. Klopfer, M. Bily, R. Slaff, S. Faulkner, T. Greene, W. Shultz, and R. Pollak. Furthermore, financial and technical support from the NSWC-Carderock Division, ONR, and AFOSR are greatly appreciated.

8. References

- ASTM Standard D 5528-01, (2002). Mode I Interlaminar Fracture Toughness of Unidirectional Fiber-Reinforced Polymer Matrix Composites, March.
- Bily, M. A.; Kwon, Y. W. & Pollak, R. D., (2010). Study of Composite Interface Fracture and Crack Growth Monitoring Using Carbon Nanotubes", *Applied Composite Materials*, (doi: 10.1007/s10443-009-9124-4).
- Chou, T. W. and Thostenson, E. T., (2008). Carbon Nanotube/Vinyl Ester Nanocomposites for in Situ Sensing," September 17-29, University of Maryland University College, Adelphia, MD. *Office of Naval Research Solid Mechanics Program Review Meeting: Marine Composites and Sandwich Structures*: pp. 42-49.
- Dharap, P.; Li, Z.; Nagarajaiah, S. & Barrera, E. V., (2004). Nanotube Film Based on Single-Wall Carbon Nanotubes for Strain Sensing, *Nanotechnology*, Vol. 15, pp. 379-382.
- Ding, F.; Bolton, K. & Rosén, A., (2006). Molecular Dynamics Study of Bamboo-Like Carbon Nanotube Nucleation, *Journal of Electronic Materials*, February.
- Faulkner, S. D.; Kwon, Y. W.; Bartlett, S. & E. A. Rasmussen, E. A., (2009). Study of Composite Joint Strength with Carbon Nanotube Reinforcement, *Journal of Materials Science*, Vol. 44, Issue 11 pp. 2858-2864.
- Kang, I; Schulz, M. J.; Kim, J. H.; Shanov, V. & Shi, D., (2006). A Carbon Nanotube Strain Sensor for Structural Health Monitoring, *Smart Materials and Structures*, Vol. 15, pp. 737-748.
- Krueger, R. (2002). The Virtual Crack Closure Technique: History, Approach, and Applications, NASA/CR-2002-211628, April 2002. Hampton, VA: ICASE, NASA Langley Research Center.
- Kwon, Y. W. & Craugh, L. E., (2001), Progressive Failure Modeling in Notched Cross-Ply Fibrous Composites, *Applied Composite Materials*, Vol. 8, No. 1, January, pp. 63-74.
- Kwon, Y. W. & Marron, A., (2009). Scarf Joints of Composite Materials: Testing and Analysis, *Applied Composite Materials*, Vol. 16, No. 6, pp. 365-378.
- Kwon, Y. W.; Slaff, R.; Bartlett, S. & Greene, T., (2008). Enhancement of Composite Scarf Joint Interface Strength through Carbon Nanotube Reinforcement, *Journal of Materials Science*, Vol. 43, pp. 6695-6703.
- Nofar, M.; Hoa, S. V. & Pugh, M. D., (2009). Failure Detection and Monitoring in Polymer Matrix Composites Subjected to Static and Dynamic Loads Using Carbon Nanotube Networks, *Composites Science and Technology*, Vol. 69, No. 10, pp.1-22.
- Reeder, J. R., (1992). An evaluation of mixed-mode delamination failure criteria, NASA Technical Memorandum 104210, February.
- Schadler, L. S.; Giannaris, S. C. & Ajayan, P. M., (1998). Load Transfer in Carbon Nanotube Epoxy Composites, *Applied Physics Letters*, Vol. 73, no. 26, pp. 3842-3844, December.
- Thostenson, E. T. & T. W. Chou, T. W., (2006), Carbon Nanotube Networks: Sensing of Distributed Strain and Damage for Life Prediction and Self Healing, *Advanced Materials*, Vol. 18, pp. 2837-2841.
- Todo, M.; Nakamura, T. & Takahashi, K., (2000). Effects of Moisture Absorption on the Dynamic Interlaminar Fracture Toughness of Carbon/Epoxy Composites, *Journal of Composite Materials*, Vol. 34, pp. 630-648.
- Wong, W.; Paramsothy, M.; Xu, X. J.; Ren, Y.; Li, S. & and K. Liao, K., (2003). Physical Interactions at Carbon Nanotube-Polymer Interface, *Polymer*, Vol. 44, issue 25, pp. 7757-7764, December.
- Zhang, W.; Sakalkar, V. & Koratkar, N., (2007). In Situ Health Monitoring and Repair In Composites Using Carbon Nanotube Additives, *Applied Physics Letters*, Vol. 91.

Design and use of a Fatigue Test Machine in Plane Bending for Composite Specimens and Bonded Joints

G. Di Franco, G. Marannano, A. Pasta and G. Virzì Mariotti
*Università degli Studi di Palermo, Dip. di Meccanica,
Viale Delle Scienze – 90128 Palermo
Italy*

1. Introduction

Polymeric and composites materials are used increasingly as structural parts in industry and therefore many informations on mechanical properties (creep, relaxation, fatigue life) are necessary.

Composite materials behavior subjected to fatigue load is very complex due to non homogeneous and anisotropic properties, and it has been studied for a long time; however, composite materials design is still based on very long fatigue tests and high safety factors are used.

Composites industry uses various types of resin (usually epoxy or polyester resin) and reinforced fibers (usually fiberglass). Many industrial components and consumer goods are made in this way, such as parts for boats, car components, etc.

Composites with polymer matrix are used by the industries with much performed resins and stubborn and rigid reinforced fiber. Composite materials are used primarily in aerospace, military and automotive industries, however, are also utilized in sports such as golf, fishing, skiing (and snowboarding) and in the naval industry (Marannano & Virzì Mariotti 2008).

These materials have very high mechanical properties such as low weight, high strength and stiffness, good formability and high design flexibility. Many theoretical studies (Van Paepegem & Degrieck, (b) 2001; Van Paepegem & Degrieck, 2002 ;Marannano & Pasta 2006; Natarajan et al. 2005) are dedicated to the study of crack propagation, applying the concepts of fracture mechanics. Fatigue failure can be described as a sequence of two phases:

- crack formation;
- crack propagation.

The crack propagation has been studied carefully, ignoring the formation crack, and pre-cracked specimens are used for this purpose; the study requires the development of equipping, methodologies and specialist analysis. Fatigue studies usually require several days (sometimes weeks) of load cycles to obtain an appreciable damage. The tests show inhomogeneous results, so it is necessary to do many repetitions to get a more accurate

estimate of fatigue life. In this case it is very important to develop a specific approach to fatigue tests based on the use of materials testing machines (FTM) to avoid the utilization of expensive hydraulic machines. Some ideal characteristics of FTM machines are:

1. adaptability to different geometries and rigidities of the specimens;
2. facility to perform various conditions of load (alternate or pulsatory load);
3. possibility to develop fatigue studies by recording the obtained data from different tested materials, which can be applied any criterion to predict the fatigue life;
4. possibility to measure strains;
5. low cost of instrumentation to perform several tests simultaneously;
6. adaptability of load frequency.

This chapter presents a FTM materials testing machine and experimental fatigue tests, to study composite materials behavior subjected to fatigue bending plane; the machine is designed to perform specific fatigue tests with different boundary conditions (such as frequency, elastic modulus, etc.). The development of a fatigue testing machine in plane bending starts with the need to perform multi-axial fatigue tests on metallic materials (Frustey & Laserre, 1989) and to make fatigue-corrosion tests (Berchem & Hocking, 2006), on aluminum alloys (Beck et al. 2002; Van Paepegem & Degrieck, (a) 2001) and on α -brass (Sugeta et al. 2006). It is very difficult to find specifics to FTM machines for composite and polymeric materials in the literature (Trotignon, 1995; Caligiana et al. 2003; Marannano et al. 2007), while applications on bonded joints are not frequent. Initially the properties of composite materials under static conditions are evaluated, then fatigue curves are obtained for different loading conditions. Wöhler curve are obtained using N10 criterion, corresponding to the loss of 10% of the initial stiffness. Finally, the model of residual resistance was adopted as a tool to describe the fatigue behaviour.

2. Materials testing machine (FTM)

2.1 General presentation

Fatigue tests on plastics and composite materials must be performed under similar conditions to those operational (frequency, environmental conditions, specimen geometry, etc.). Materials testing machine for dynamic load in alternate plane bending is constituted by three modules:

1. the first module (or control module) generates a sinusoidal movement;
2. the second module can modify loading conditions;
3. the third module (or module data acquisition) measures the stress (load) and analyzes the values through the computer to plot the curves of the load versus the number of cycles.

2.2 The first module (or control module)

Figure 1 shows the built and used structure to perform fatigue tests in plane bending. A three-phase electric motor (1) with inverter (2) (to adjust the frequency of loading from 0.04 to 23 Hz) rotates a pulley (with throat z) that, via a link belt (3), places in rotation an intermediate shaft (4) with transmission ratio equal to one. The transmission ratio is verified by optical tachometer, monitoring the number of rotations of the crankshaft and the corresponding speed of the drive shaft. Power transmission by belt ensures the electrical insulation of the specimen by the engine, with particular advantage if the specimens contain metal or carbon. An eccentric cam system (5) allows to transform the circular motion in a

purely symmetric and oscillating motion of the solicitation rod (6). The specimen to be tested (7) is stuck to a rigid frame at one end (8) and stressed by the rod load at other end.

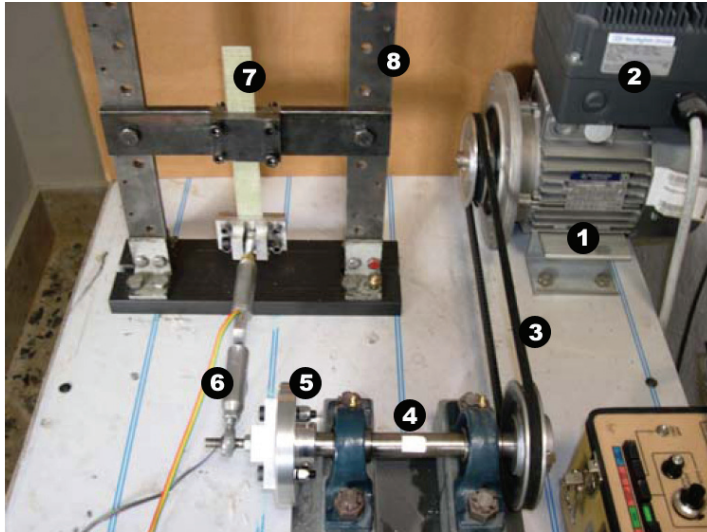


Fig. 1. Materials testing machine

Stress magnitude is determined by the distance between the points P (mobile) and Q (fixed) (Figure 2). It is possible to change load type (alternate or pulsatory) depending on the eccentricity and variable length of the connecting rod. The development of load-number of cycles is monitored at regular intervals or continuously, for all imposed displacement.

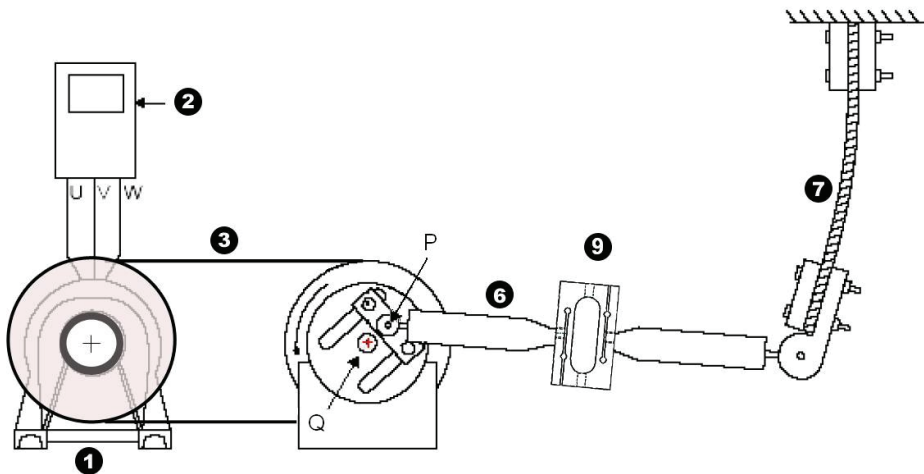


Fig. 2. Schematic representation of materials testing machine

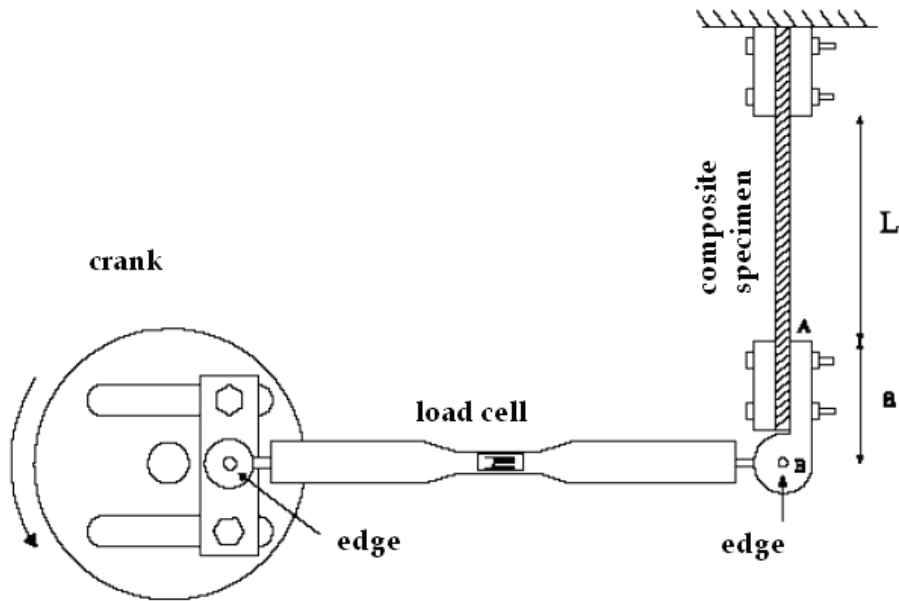


Fig. 3. Schematic representation of the second module

2.3 The second module

The second module (Fig. 3) allows to vary the length of the connecting rod and to modify some geometric values. The extension of the rod can be varied in a micrometer way in order to adjust the scale of imposed displacement and consequently the type of stress (alternate, symmetric or throbbing). In this way the deflection of the specimen can vary from zero up to a maximum value, quite apart from the load type. Moving the crossbar panel, tests on specimens of different lengths can be performed, with the maximum force depending on the power of the engine installed.

2.4 The third module (or data acquisition module)

The load values are monitored and registered by a dedicated acquisition system during the experimental tests. The whole system consists of a strain sensor (load cell), a strain indicator, a digital-analog connector and a computer. Special software, created and developed in LabView room, allows to record and display the values of variation of stiffness of the composite or the bonded joint, thus obtaining in real time the damage versus the time or cycles number. The decrease in stiffness is measured via the stress until specimen failure, operating with constant amplitude strain. Also it is possible to use any criterion of fatigue life of composite materials.

2.5 Setting machine

The device can perform tests under pulsatory or alternating loads with the "flexibility" of some organs. In particular, as shown in figure 4, it is possible to increase the maximum displacement imposed to the test clamped the bar in the back of the two standing by the change in the position of horizontal beam (which allows the grasping of upper specimen).

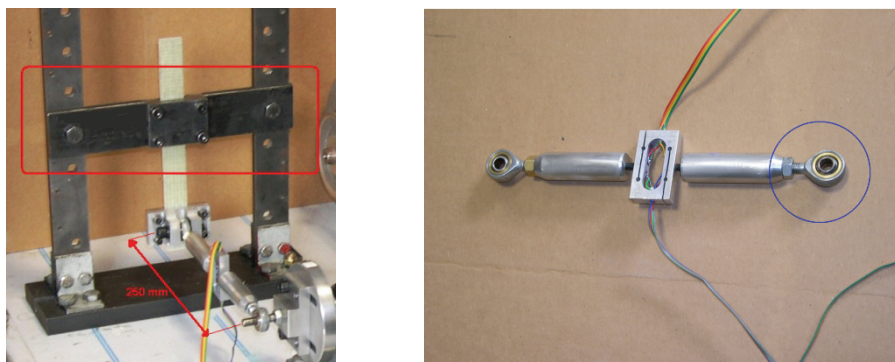


Fig. 4. Control system through horizontal beam (on the left) and joint (on the right)

Another way to change imposed movement is provided by joint (Fig. 4 on the right). One or both of the joints are screwed or unscrewed to adjust the distance between the eccentric and specimen, so it is possible to vary the minimum (u_{\min}) and maximum (u_{\max}) imposed displacement. Also (Fig. 4 on the left) the distance between the eccentric and the system of lower grasping specimen is illustrated, approximately 250 mm. Critical value of possible strain ($u_{\max} - u_{\min}$) is 150 mm theoretically, equal to the sum of twice distance QP (fig. 2), crank radius formed by the eccentric with the elongation imposed at the joints.

3. Load cell

Load cell is constituted by a metal body that takes different forms according to the following requirements: amplitude of measured load; applications type; environmental conditions.

Two cells for two different load values are designed: in aluminum (Fig. 5) for stresses not exceeding 50 N and in steel for stresses not exceeding 200 N. 3D solid modeling was obtained using Solid Edge, and analysis was performed by ANSYS to verify the design and the stress response of the transducer, obtaining the definitive optimized configuration.

Operating with constant amplitude of deformation (strain control), the decrease in stiffness is proportional to the variation of the load recorded by the load cell, from the beginning of the test until the complete damage of the specimen.

Aluminium load cell just weights 25 g and is well suited for monitoring small loads; the demonstration is its resolution: 0.42 g. Four electrical strain gauges having resistance of 350 Ω are placed in the hollow area; the basis of measurement is 3 mm. The transducer also has two holes M5 (top and bottom holes) to connect it to material testing machine and two side holes (radius 4 mm) to pass the cables connecting the strain gauges. Similar geometry to the aluminium transducer is used to realize the load cell in steel. Also in this case four electrical resistance strain gauges of 350 Ω were used and the basis of measurement is 3 mm. Also in this second case the weight remains relatively low and is equal to 59.9 g.

3D solid model obtained by Solid Edge has been imported into the finite element code Ansys. The analysis was performed to verify the size of transducer. Figure 6 shows the longitudinal strain, interesting four strain gauges on the cell subjected to load equal to 200 N and Von Mises stress map obtained by ANSYS, when load cell (steel) is subjected to a load of 200 N.

The maximum strain is obtained in closeness of the fillet radius and therefore the strain gauges are positioned in these areas. Static safety factor are obtained 6.3 for the aluminium load cell and 3.5 for the steel load cell by the numerical study in ANSYS.

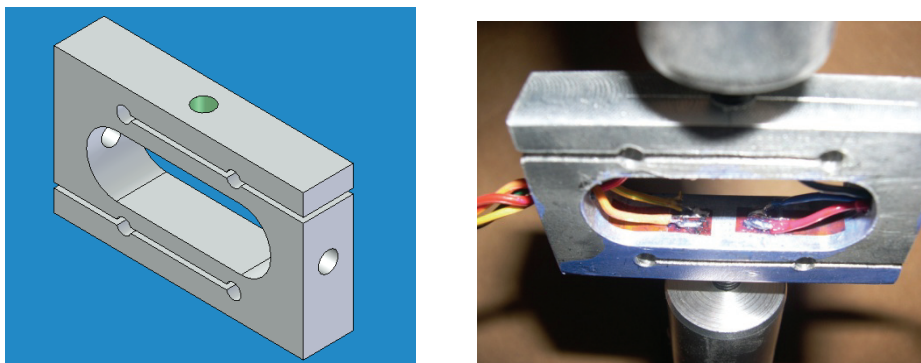


Fig. 5. 3D model of load cell (9) (on the left) and positioning of strain gauges (on the right)

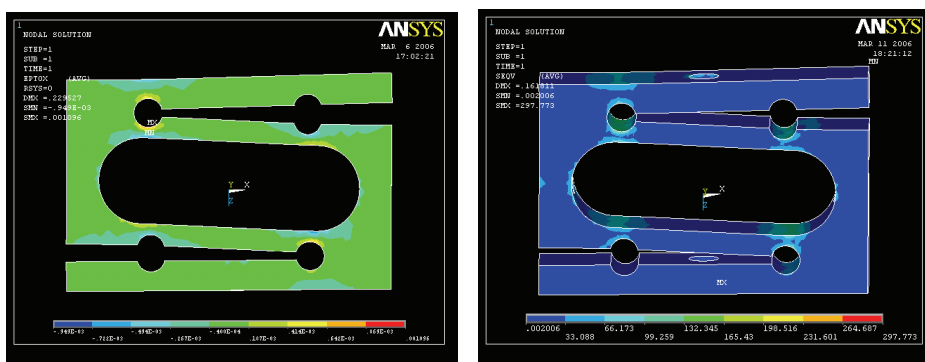


Fig. 6. Map of longitudinal strain (on the left) and of Von Mises stress (on the right)

3.1 Load cell calibration

Calibration involves the recording of output signal by the load cells, when loads are known. The aim is to derive calibration curve, allowing the correction of the output signal by cells, in order to read the exact value of the load acting in every direction. A load varying between a minimum and a maximum is applied at predetermined intervals; the calibration has been performed at least twice to verify measurements repeatability: calibration curve is drawn in the case of correlation of the two tests, otherwise the data are interpolated by Ordinary Least Squares and another test is run to confirm the results. Calibration methodology is shown in the EN 10002/3 and ISO 376 rules, which are international standards of reference.

4. Fatigue behavior of composite materials

Unlike homogeneous materials, composites accumulate the damage in various parts rather than localized way, when subjected to fatigue load. In composite materials the fracture

always does not start with the growth and development of macro-crack at an only point. Also there are good possibilities that cracks formation and propagation are already present within the materials (cracks in the matrix, broken fibres). Under fatigue load, these defects give rise to the formation of cracks and to their propagation. Defects growth is microstructural in these materials and includes the presence of cracks in the matrix, delamination and fibres breakage. Fatigue life prediction of composite materials is very difficult.

In unidirectional composites with not-axial loading (angle between 0° and 90°), the apex of the crack is subjected to two displacement components: an opening normal mode and a sliding parallel mode to the fibres. The effects of two damage types depend on the loading angle. For example, crack propagation is only as opening mode with a load of 90° , while the crack propagation is only as sliding mode with an angle of 0° . Then there is mixed mode crack propagation for angles between 0° and 90° . In multidirectional composite fibres failure is related to transverse fibres; the crack propagates through the interface of the layers, it causes a stress concentration. Multidirectional laminates also create induced stresses in the edges as a result of different elastic properties of layers, often increasing the delamination between planes.

4.1 Failure mode

In some cases the failure is coincident with rupture (brittle behaviour), in other cases it coincides with the deviation from linear elastic behaviour (ductile behaviour). Failure can occur in various modes:

1. broken fibres;
2. fibre-matrix separation (debonding);
3. crack of the matrix (typical of fatigue);
4. separation of the sheets (delamination).

Sometimes these failure modes occur separately, sometimes they coexist.

4.2 Fatigue in composite materials

The growing use of composite materials is mainly due to their high strength and stiffness, coupled with a low density compared with steel. The fatigue load involves the formation of cracks in the matrix and then in the fibres. Composite materials can show different combinations (fibre orientation) and forms, so the fatigue study is particularly complex and demanding.

The fatigue failure occurs first in brittle materials characterized by low values of strain, so the matrix is damaged before the formation of cracks. The fatigue failure can take various forms in composite materials: broken fibres, fibre-matrix interface failure, delamination, presence of cracks in the matrix. Cracks decrease the stiffness and strength of the composite materials. The formation and numbers of cracks depends on fibres orientation. In composite materials with different fibre orientation cracks arise first in the weaker plans and then in other plans until the stronger.

Fibreglass composite materials have a greater versatility of geometry, but laminates offer a lower stiffness and static strength due to the distortion of fibreglass. Another possible reason is the percentage of fibres that is less than 60-65%.

4.3 Fatigue graphs: load-number of cycles curves

The most common method to present fatigue dates is to plot stress (S) versus the number of cycles (N), these graphs are called S-N curves. The ordinate is usually the maximum stress

or stress range. The abscissa is usually the number of cycles to failure for fixed cycle of stress or deformation and it is usually plotted on a logarithmic scale. Stress ratio (R) and test frequency (Hz) are kept constant for all the specimens. All materials have a negative slope, so the number of cycles to failure increases with decreasing load. S-N curves of the composites generally depend on several factors:

- variables of material:
 - material and fibre volume fraction (V_f);
 - matrix (resin);
 - guidance plan;
- test variables:
 - load type (traction or traction-compression);
 - average stress;
 - frequency;
 - environmental conditions.

S-N curves usually are linear for less than one million life cycles and can be expressed by linear equations like this:

$$\frac{\sigma_{app}}{\sigma_{stat}} = A + B \log N \quad (1)$$

σ_{app} and σ_{stat} are applied and static stress respectively, A and B are constants that depend on the material. The fatigue limit depends on many factors such as the reinforcement type, matrix and fibres orientation. Unlike metallic materials, stress-number of cycles curves of composite materials are not characterized by a fatigue limit, in fact, these curves show a continuous gradient (downwards) towards zero as the number of cycles. The criteria for the fatigue life are numerous for composite materials; usually the criterion N_{10} is used, which indicates the number of cycles to have a decrease in stiffness of 10%. In other words, the criterion N_{10} is the number of cycles required for the stress drops to 90% of initial value.

A composite material, in its simplest form, has unidirectional fibres aligned with the direction of stress (load on axis); the fibres bear most of the load in the case of fatigue load. It is easy to think that the fatigue behaviour of a composite depends exclusively on the fibre; in reality the experimental results show that the fatigue behaviour of a composite material depends mainly on the stress in the matrix. The fatigue life increases with increasing angles layers (Marannano & Virzi' Mariotti, 2008) in multidirectional composite materials. The presence of fibres causes damage and delamination among layers in the case of transverse loads and off-axis.

4.4 Composite damage

The damage process has two predominant phases: an initial stage where the development of non-interacting cracks leads to the Characteristic Damage State (CDS), in which a model of stable crack is developed. In the second phase, cracks of different nature interact among them with the increase of the number of cycles, causing an increase in localized cracks and the consequent fracture.

In the first phase, the cracks of matrix are generated in the plane if stresses, orthogonal to the fibres direction, exceed the strength of the matrix. These cracks usually occur in composites with brittle matrix (epoxy resin), but can also occur if the matrix is ductile (metal matrix).

Innate micro defects in the material increase continuously with fatigue loads, and when the size of the defects reaches a characteristic dimension, a first crack (original or primary crack) is formed at the beginning of CDS. First cracks in the matrix are due to consequent development of the damage under fatigue loads, and are a basis for the development of localized defects, buckling and growth of delamination in compressive loads.

The CDS is a property of the laminate, and it depends on the properties of individual layers, thickness and sequence. The CDS is independent of the loading history, boundary conditions, treatments, residual stress and humidity. It is the starting point for those processes that control the strength, stiffness and fatigue life of the laminates. It also represents a state of the damage that can be accurately described.

Characteristic of second phase is the delamination. Primary cracks propagate due to the propagation of the secondary cracks near the interface of the layers. Secondary cracks are usually perpendicular to primary and are due to stress directed along primary axis of the cracks. High interlaminar stresses generate interlaminar cracks that cause the delamination within the laminate, in the region where there are primary and secondary cracks. Then the fibres break heavily (third phase), and cause the final break. In many cases, it was noted that two thirds of the broken fibre occur in the first third of total number of cycles. However, the final failure occurs when the broken fibres are aligned with principal stress. The phases of the damage model do not occupy separate regions within material life; however, the cracks formation in the matrix characterizes the first phase of the damage model while the delamination characterizes the second phase.

5. Experimental procedures

5.1 Realization of the laminates

Quasi-isotropic and reinforced aluminium specimens have been used in experimental tests (Vasek et al., 1997). The vacuum bag technique has been used to implement the laminates (Marannano & Virzi' Mariotti, 2008) with a polyester resin, since this resin is very used in shipbuilding for its low cost.

The catalyst (2-3% in volume) is added to make the resin more viscous and to reach a state where it is not more liquid: this is the *gel point*. The resin hardens to obtain the hardness and final properties; the reaction is accompanied by heat generation that increases reaction time, the process is known as *curing*. The construction of reinforced aluminium laminates is quite similar to quasi-isotropic composite materials, except the curing treatment, that is done at room temperature due to the different coefficients of thermal expansion that characterize the composite and aluminium, with consequent formation of residual stresses and possible cracks inside the specimens.

5.2 Basic concepts

An appropriate acquisition system was made to monitor the parameters of material damage during the experimental tests.

Induced stresses are monitored with an appropriate acquisition system during the tests (continuously or not, as appropriate). This system is made of a load cell, a "strain indicator", a digital-analog connector and a computer. Dedicated software can record and show the values of the material resistance, and so it is possible to have the load-number of cycles curves in real time. The acquisition software (Labview) records input signal and it shows the evolution of signals peak with the number of cycles at regular intervals through the connector, so it is possible to study the yielding of the specimen during the test.

5.3 First campaign of experimental test

5.3.1 Quasi-isotropic laminates

The first campaign of experimental test has the aim to evidence the better quality of the Glare respect to the optimized composite laminates. Table 1 shows the characteristics of composite materials to perform the tests. It shows the calculation performed in Excel to determine the volume fraction of fibres. The value 69.21% was achieved using the vacuum bag technique; in fact it can not get these properties with the normal lay-up at room temperature.

Size laminate	Nr. layers	12
	thickness [mm]	3
	length [mm]	150,6
	width [mm]	259
Weight	layers weight [g]	202,9
	fibres specific weight [g/m ²]	300
	fibres weight [g]	140,42
%	% fibres weight	69,21
	% resin weight	30,79

Table 1. Properties of quasi-isotropic composite materials

Particular laminates are quasi-isotropic, where the stiffness is independent of considered direction. They must have: a total number of laminates n greater or equal to 3 and laminates of the same constitution and thickness; the angle $\Delta\theta$ between the two laminates must be constant (angularly equidistant laminates). The name does not depend on the fact that these laminates can have small variations of the stiffness with the direction, but on the fact that they have isotropic behaviour with respect to traction-compression and not respect to bending and torsion. Quasi-isotropic laminates can be obtained with an appropriated orientation of the fibres, for example a symmetric laminate that has 12 layers positioned according to the scheme $[+30/+90/+30]_s$ (total thickness 3 mm). Half of the laminate is made of 6 layers spaced 60° angularly (Van Paepegem & Degrieck, 2001; Marannano & Virzi' Mariotti, 2008)).

	Preimp. Unidir. Fibers S_2 ($v_f=60\%$)	2024-T3
Young modulus E_1 [GPa]	54,0	72,2
Young modulus E_2 [GPa]	9,4	72,2
Ultimate strength σ_r [MPa]	2640	455
Ultimate strain ε_r [%]	4,7	19
Poisson Ratio ν_{12}	0,33	0,33
Poisson Ratio ν_{21}	0,0575	0,33
Shear modulus [GPa]	5,55	27,6
Density ρ [kg/m ³]	1980	2770

Table 2. Properties of glare constituents

5.3.2 GLARE

The glare is a fibre-metal laminate; it is made of thin aluminium sheets with a thickness of 0.2-0.5 mm and fibreglass embedded in an epoxy matrix with a thickness of 0.125 mm and a nominal fibre volume fraction of 59%.

Fibres direction is related to the lamination direction of aluminium sheets; 0° or *Longitudinal rolling direction* (L) indicates that the fibres are placed in the direction of metal lamination, while 90° or *Longitudinal-Transverse rolling direction* (T) indicates that the fibres are oriented in transverse direction. Composite materials suffer a treatment in autoclave at high pressure and temperature. Mechanical properties of Glare depend on the characteristics of his constituents: aluminium and fibre, the most important properties are reported in table 2.

Mechanical properties of the adhesive are negligible if compared with the characteristics of embedded fibres, but the contribution of the adhesive characterizes the laminate performance strongly (Robinson & Hodgkinson, 2000). It determines the force between metal and fibre layers and its detachment of the adhesive at the metal / fibre layer is one of the most frequent modes of laminate failure. The use of thin layers of aluminium (0.3 - 0.6 mm) can not consider the thickness effects, as regards individual aluminium layers, and the laminate in its entirety. The method called "Metal Volume Fraction" (MVF) and "Theory of mixtures", it can determine the glare properties (Vasek et al., 1997).

5.3.3 Experimental tests

The specimens (Fig. 7) are made of fibreglass in the configuration quasi-isotropic [$\pm 30/\pm 90/\pm 30$]_s but also reinforced with aluminium sheets 6061-T6 [$+30/-30/+90/\text{aluminium}/+90/-30/+30$] (glare). The laminate thickness is 3 mm in the first case, 3.1 mm in the second case, and epoxy resin was used for both specimen types. Composite specimens are made of 12 fibreglass layers, while the glare is composed of 6 fibreglass layers and aluminium sheet in the middle.

Geometric characteristics of the specimens are presented in table. 3. The tests were performed with different values of imposed strain. The following "shift ratio" was used to characterize each tests:

$$R_d = \frac{u_{\min}}{u_{\max}} \quad (2)$$

It is similar to stress ratio R. All experimental parameters are known with knowledge of the value of maximum deflection and the length L between the two attacks.

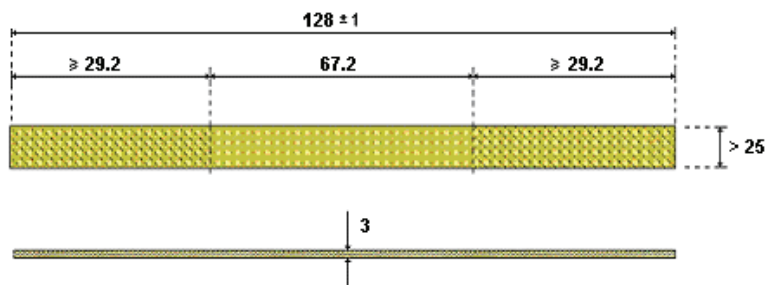


Fig. 7. Specimens geometry

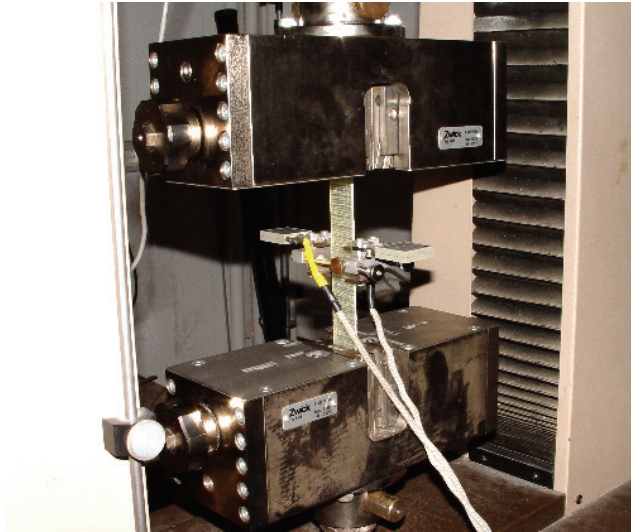


Fig. 8. Tensile test

Tensile tests were made to determine mechanical properties of both materials with Hounsfield material testing machine, equipped with proper grips for tensile test (Fig. 8). An extensometer was installed on the specimen to detect strains, while the load value is supplied by the load cell of 20000 N.

Static and fatigue tests were performed on different types of composite materials. All specimens are made of polyester resin and fibreglass, the vacuum bag technique was used. Table 4 shows the characteristics of the materials.

All specimens were loaded with a sinusoidal signal generated by the machine. It was operated at a frequency 3 Hz and was constant for all experimental tests. Also 10 load cycles were monitored to minimize the influence of any spurious signals for each acquisition. It was calculated the stress magnitude and then the mean is done and any anomalous points is eliminated.

	Composite Materials	Glare
Thickness [mm]	3.00	3.10
Width [mm]	25.60	25.30
Height [mm]	129.1	127
Arm [mm]	67.2	67.2
No. layers	12	7
Weight [g]	17.2	22.6

Table 3. Geometrical characteristics of the specimens

Filtering was done with a low pass filter downstream of the signal acquisition, to cancel the influence of noise, always present, even if of negligible value, obtaining the signal in Figure 9. Finally, the program shows the magnitude of each load cycles, a very important element in the early cycles, where it is possible to have a rapid damage of the material.

Material properties	quasi-isotropic composite	Glare
fiber/resin	Glass/polyester	Glass/polyester
direction fiber	Equidirectional (60°)	Equidirectional (60°)
fiber volume fraction	69.21	-
MVF (Metal Volume Fraction)		51.6
thickness [mm]	3,0	3.1
longitudinal module[MPa]	16357	38401
ultimate strength [MPa]	303	≅ 200

Table 4. Material properties

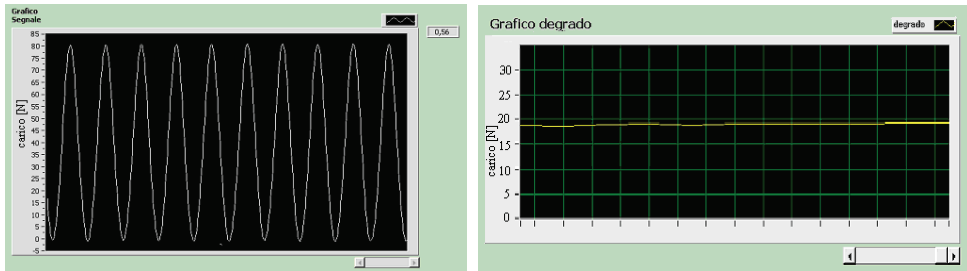


Fig. 9. Filtered signal (on the left) and monitored load (on the right)

Fatigue tests were performed with different values of imposed strain, all characterized by pulse bending. The displacement ratio defined by 2 was zero since the minimum displacement was zero. So the position of minimum displacement is depicted in figure 3. Figure 10 shows load-number of cycles curves for almost-isotropic specimens, subject to pulsatory load with a maximum deflection (u_{max}) from 10 to 27 mm. Figure 11 shows similar results for glare specimens.

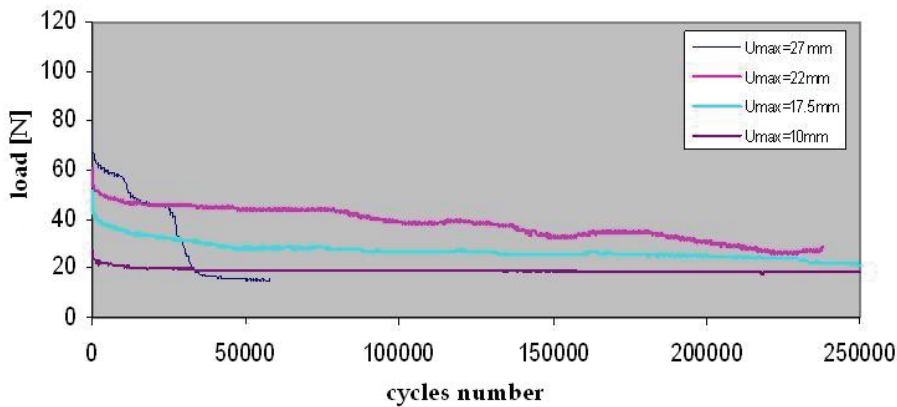


Fig. 10. Degradation in quasi-isotropic specimens

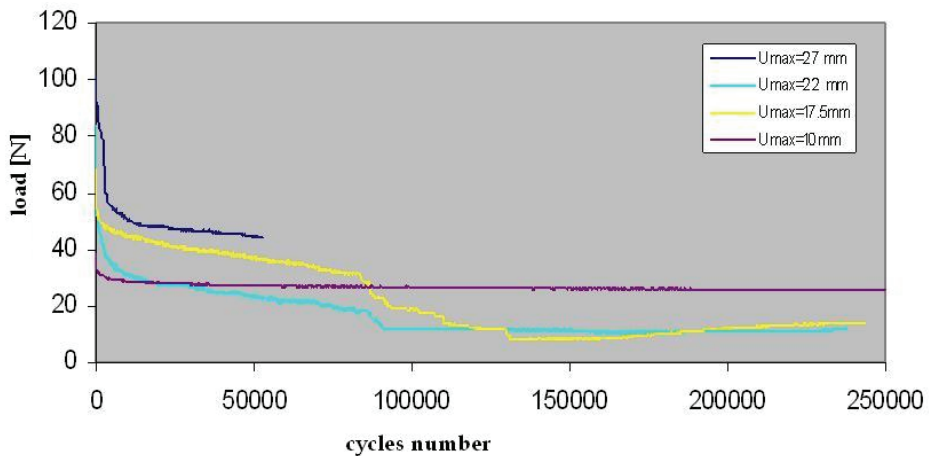


Fig. 11. Degradation in glare specimens

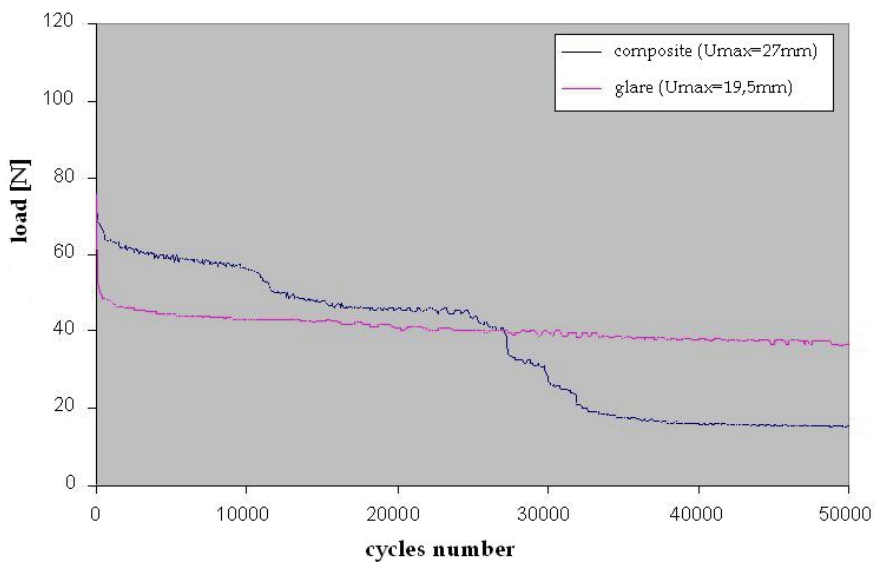


Fig. 12. Degradation of two specimen types for similar initial load

The behaviour of both materials is dependent on load highly. In fact there is a reduction of initial stiffness for small loads, and then a decrease of bearable load, which remains constant subsequently (Van Paepegem & Degrieck, 2002). During experimental test (i.e. for 500,000 cycles) glare specimens support a higher load than that of the quasi-isotropic composite, with a similar trend. Imposing greater displacements, the load trend is more variable than in the case of composite specimens. In composite specimens there is a damage step, indicating a gradual breaking of layers, for loads exceeding a critical value (60 N); while the glare can maintain a larger value of the load for long time, after an initial damage. This is due to the

presence of aluminium, which absorbs much of the load, leaving unstressed the glass fibres and allowing the specimen to maintain a non-negligible stiffness.

Figure 12 shows the degradation of specimens subjected to similar initial load. It shows as the glare presents a significant and unique collapse load, with few significant changes until the break; instead in the composite there is the sequential breaking of compressed fibres, with a step change of supported load. In all performed and analyzed tests there is always a localized damage in compressed fibres.

5.4 Second campaign of experimental test (GLARE)

A further study of glare is done using different specimens, to obtain a material that minimizes construction costs and has required characteristics. Laminates have been designed to study the propagation mode of the crack, and in these specimens the fibres are not in the direction of maximum strength to promote the investigated damage. 12 specimens are built, and are divided into:

- Nr. 6 specimens with configuration $[\pm 30/90/\text{Al}/90/\pm 30]$: 6+1 layers, 6 unidirectional layers (fibreglass) with a quasi-isotropic configuration, 1 aluminium sheet type 6061-T6 (thickness 1mm) and total thickness is 3 ± 0.1 mm.
- Nr. 6 specimens with configuration $[\pm 30/\text{Al}/90]_s$: 6+2 layers, 6 unidirectional layers (fibreglass) with a quasi-isotropic configuration, 1 aluminium sheet type 6061-T6 (each thickness 0.6 mm) and total thickness 3.1 ± 0.1 mm.

Figure 13 shows the detail of frontal view, while the figures 14 and 15 show side views (profile) of the two specimen types, from those it is possible to see the sequence of various packaging types. The aluminium sheet is clearly visible in a central position in fig. 14, while the two aluminium sheets are visible in fig. 15.



Fig. 13. Front view of specimen



Fig. 14. Side view of specimen (type a)

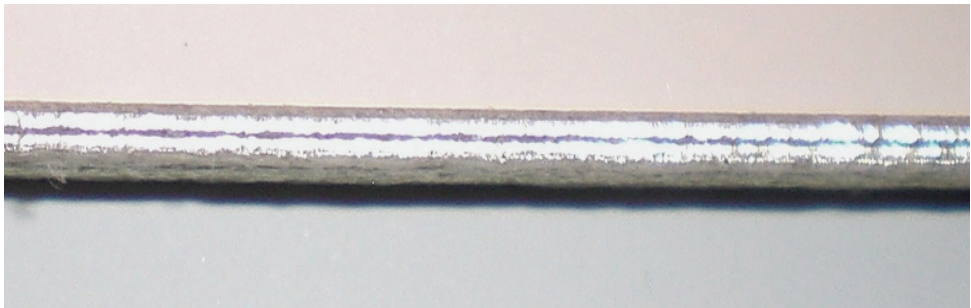


Fig. 15. Side view of specimen (type b)

The choice of these configurations has been made to have the specimens with similar thicknesses. Specimens geometries are shown in figures 16 and 17, and the size are listed in the table 3.

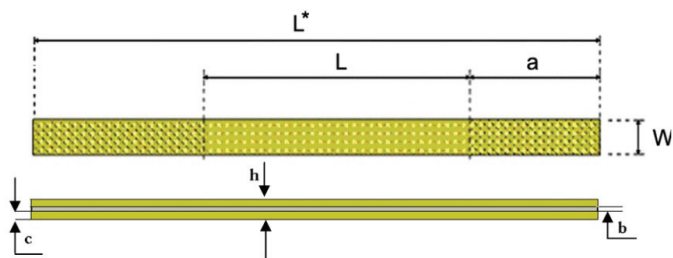


Fig. 16. Specimen geometry (type a)

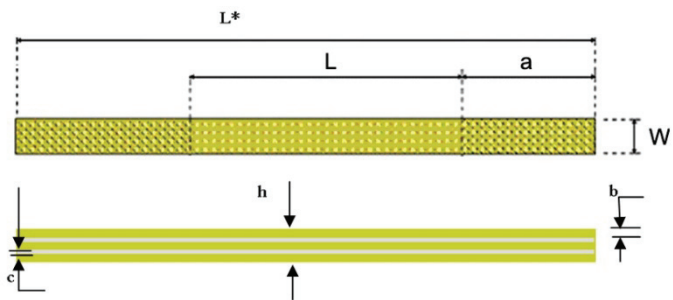


Fig. 17. Specimen geometry (type b)

Specimen types	No. tests	W [mm]	L [mm]	L^* [mm]	a [mm]	b [mm]	c [mm]	h [mm]
(type a)	6	25,5	120	230	37	1	1	3
(type b)	6	25,5	120	230	37	0.6	0.6	3

Table 3. Specimens size

Nr. test	Initial load [N]	
	Glare (type a)	Glare (type b)
1	6,67	8,7
2	17,3	16,1
3	28,8	30,3
4	29,1	40,2
5		83,2

Table 4. Load imposed on Glare specimens (of course some tests are discarded because they are not reliable)

Also fatigue tests in bending were done for specimen types and for different values of imposed displacement as table 4 shows.

Figures 18 and 19 show the load curves versus the number of cycles, for the hybrid specimens with one and two aluminium sheets. It is possible to see as the damage is manifested in the first part of the curve mainly, which follows an asymptotic trend. Graphical comparison of experimental results gives an idea of the different behaviour that the two materials have during a fatigue load. The comparison of obtained results shows that the material type (a) has in initial phase a bigger damage than that of type (b) with similar displacements imposed (Fig. 20).

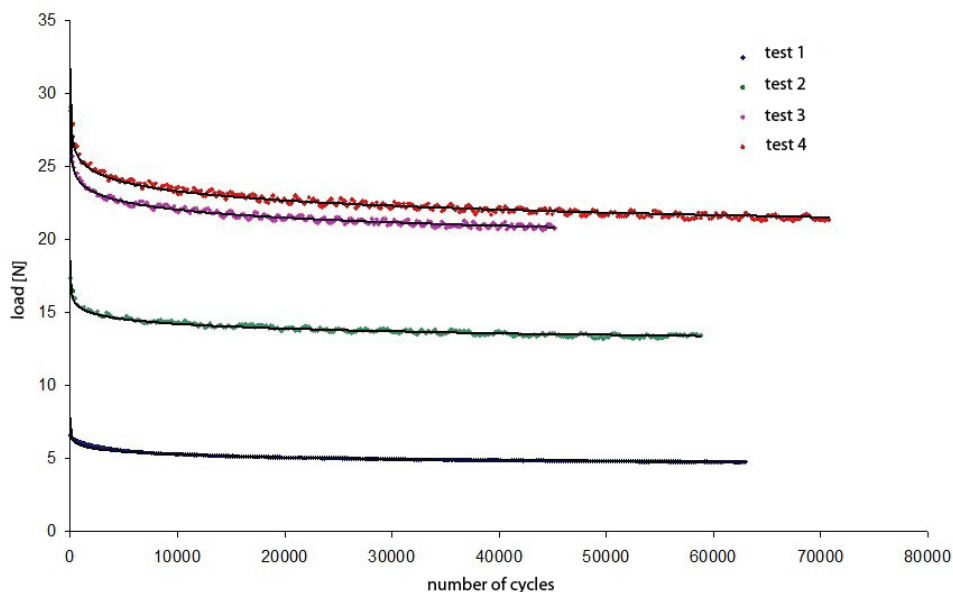


Fig. 18. Load curves versus the number of cycles (type a)

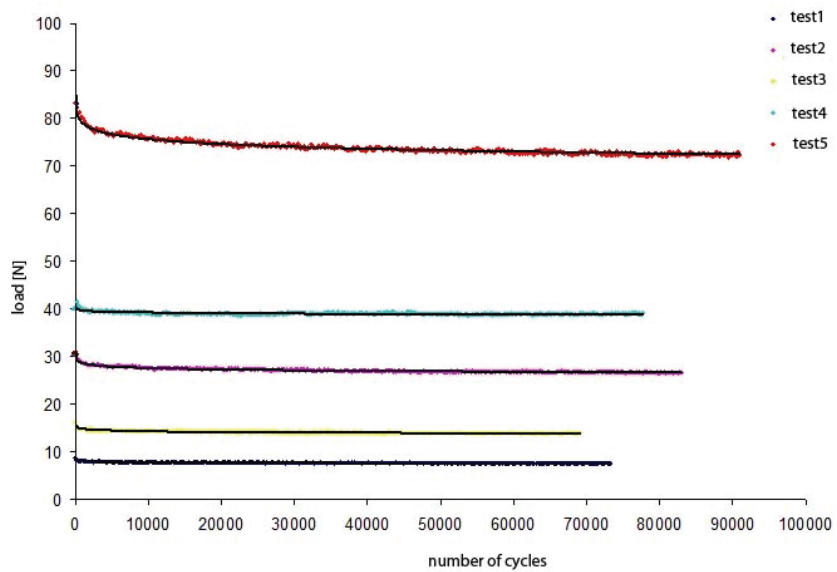


Fig. 19. Load curves versus the number of cycles (type b)

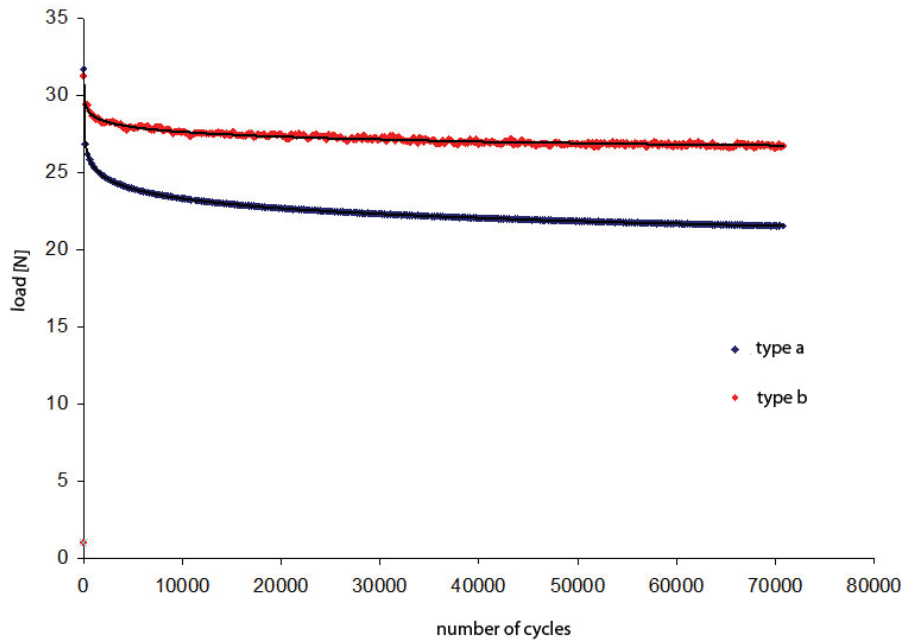


Fig. 20. Comparison of experimental curves for type (a) and type (b) tests under similar initial conditions

5.5 Third campaign of experimental test (bonded joints Al-Al)

Specimens made of two aluminium layers 2024 T3 are used For MMELS tests (Mixed Mode End Load Split) and DP760 3M epoxy adhesive is used (Ducept, Gamby & Davies, 1999; Pirondi & Nicoletto, 2001).

epoxy adhesive		2024 T3 aluminium alloy	
Shear strength [MPa]	28.2	Ultimate strength [MPa]	448
Peel strength [N/cm ²]	61.6	Yield strength [MPa]	310
Compressive strength [MPa]	78.8	Young modulus [MPa]	73100
Young modulus [MPa]	5972	Poisson Ratio	0.33
Poisson Ratio	0.4		

Table 5. Mechanical and elastic properties

Epoxy adhesive is a bi-component product: the base (epoxy) and the accelerant (modified amine), it cures at room temperature and it has high temperature resistance (Higgins, 2000). The mixing ratio in volume of the two constituents is 2:1 and it is obtained through the use of 3M EPX applicator (Fig. 21). Table 5 shows the values of elastic properties and mechanical properties of the adhesive and of 2024 T3 aluminium alloy: The yield strength is the stress causing a permanent deformation 0.2%.

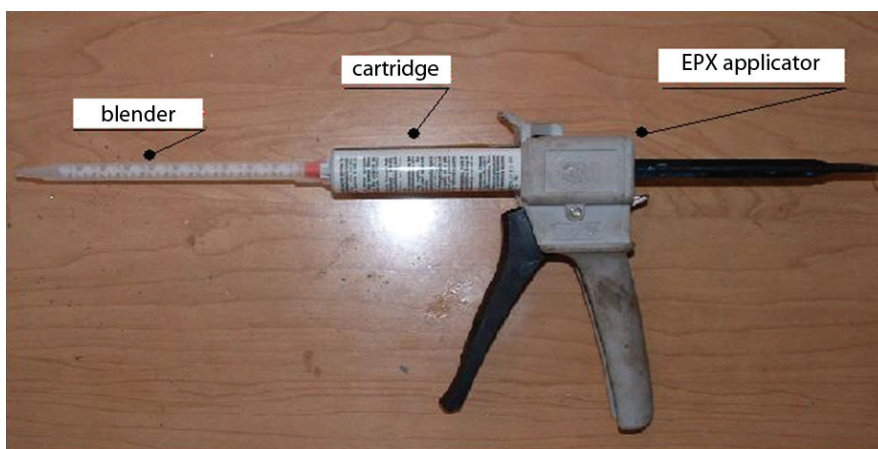


Fig. 21. EPX Applicator

The curing time is influenced by temperature and air humidity greatly, and decreases with increasing temperature and humidity. The minimum time recommended by 3M is 24 hours at room temperature followed by treatment in the oven for 1 hour at $80 \pm 2^\circ\text{C}$ with subsequent slow cooling. The thickness of aluminium sheet is 3 mm.

Tensile test is performed with a testing machine (Hounsfield) to determine elastic properties and 20 kN load cell is used. Studied model is MMELS; all the same changes of geometric nature are done on the model for workshop necessity.

The first change is done to transmit the displacement to the model: loaded sheet is longer than discharged sheet. Figure 22 shows the detail of the grasping between the specimen and the lever that applies the displacement. The second change is imposed by the full-scale load cell. The length of the specimen is increased to avoid the plasticization both of the load cell and of the model in the joint and to avoid to impose very small displacements. Figure 23 shows optimal size of model, obtained applying the beam theory. Total thickness is $B=20$ mm, the thickness of loaded sheet is $h_1=1.6$ mm, while the thickness of discharged sheet is $h_2=3$ mm.

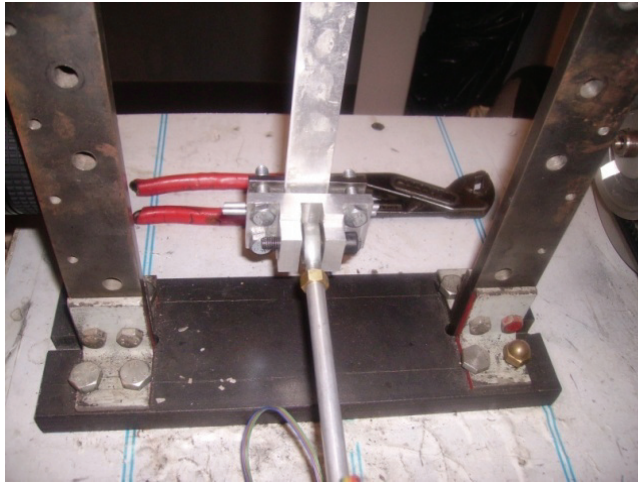


Fig. 22. System grasping between specimen and machine

Initial crack was created by interposing a Teflon layer between the two adherents (Figure 24). The thickness of Teflon is $50\text{ }\mu\text{m}$, and then 4 Teflon layers are interposed to have desired thickness of adhesive layer (200 micron).

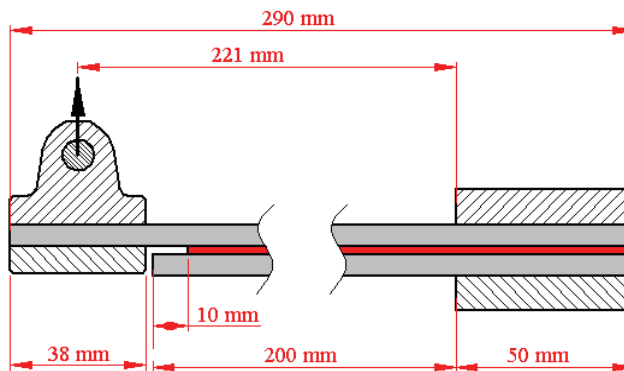


Fig. 23. Experimental model, loading and constraint system used for experimental tests

Fatigue tests were conducted on specimens that have different initial crack lengths a_0 and different imposed displacement (Table 6) (Blanco Villaverde, 2004).

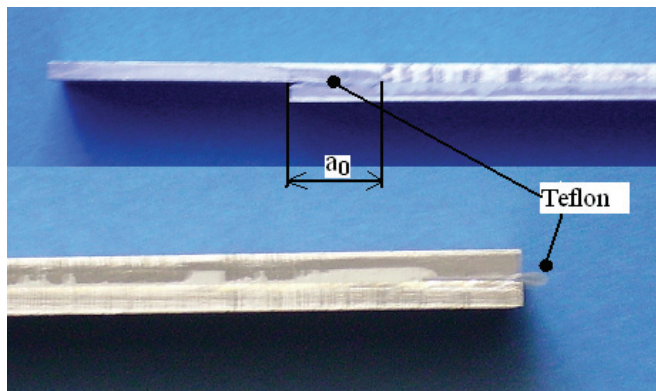


Fig. 24. Teflon layer interposed between adherents to create desired thickness and initial crack

Figure 25 shows that the load evolution can be divided into three zones. In the first area the load has a decreasing trend with increasing number of cycles; the specimen accumulates a small damage at the apex of the crack. The second area shows a sharp drop in the load due to rapid damage to the area near the apex of the crack (unstable defect propagation). In the third phase there is a very slow crack growth, which continues until complete delamination. The study of different curves shows that the specimen accumulates damage up to the break during load cycles (Sun & Jih, 1987; Boniface & Simha, 1999).

a_0 [mm]		Imposed displacement [mm]	Initial load [N]
30	A	11	29,5
	B	8,5	21.8
	C	7	17.9
35	D	12,5	29,8
	E	12	27
40	F	17	32,4
	G	13,5	25,4
	H	9,5	17.9
50	I	7	9.2

Table 6. Experimental tests

Load-number of cycles curves were obtained (Fig. 25).

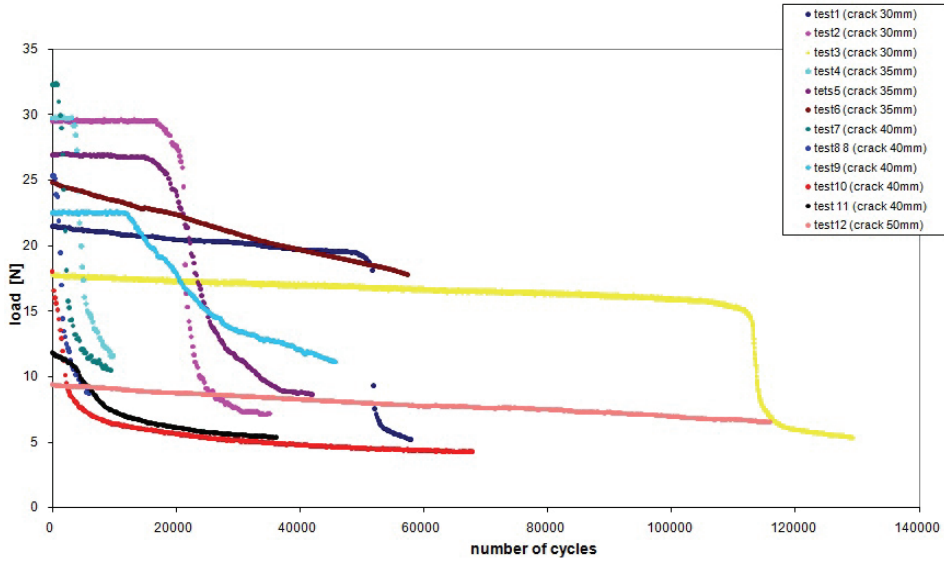


Fig. 25. Load-number of cycles curves of the bonded joints for different crack lengths

6. Numerical results

Experimental results are compared with those obtained by numerical simulations. The damage criterion has been implemented inside ANSYS code to evaluate current dimension of the defect varying the number of cycles; the mesh is implemented by square elements. External load is applied at the top of loaded layer; the constraints are placed in appropriate way to avoid axial tensions that change the ratio of mixed-mode failure.

Classic model (Sidoroff & Subagio, 1987; Van Paepegem & Degrieck, (a) 2001) for unidirectional composite fiberglass and epoxy resin (GLARE) subject to fatigue loads is applied, introducing the value of applied load instead of amplitude strain.

$$\frac{dD}{dN} = \begin{cases} A \cdot \left(\frac{\Delta\sigma}{\sigma_{TS}} \right)^c & \text{in traction} \\ 0 & \text{in compression} \end{cases} \quad (3)$$

Stress and strain are linked together by the relationship:

$$\sigma = E_0 \cdot (1 - D) \cdot \varepsilon \quad (4)$$

Where E_0 is the elastic modulus of non stressed material.

The parameter D is the variable of local damage, N the number of cycles, $\Delta\sigma$ is the amplitude of cyclic load applied, σ_{TS} is ultimate tensile strength of the material, A , b and c are three coefficients depending on experimental material. Material constants are obtained by an optimization process applied to numerical simulation and the values are shown in table 7.

Glare (type a)	A=0.1809 E (-1)	b=0.7166	c=4.9896
Glare (type b)	A=0. 28010 E (-2)	b=1.5631	c=11.125

Table 7. Material constants for GLARE specimens

The analysis of damage propagation in hybrid composite specimens is carried out considering only the degradation of composite laminates and neglecting the damage of aluminum sheet. Below some experimental-numerical comparisons are showed for specimens with one and two aluminum alloy sheets (Fig. 26).

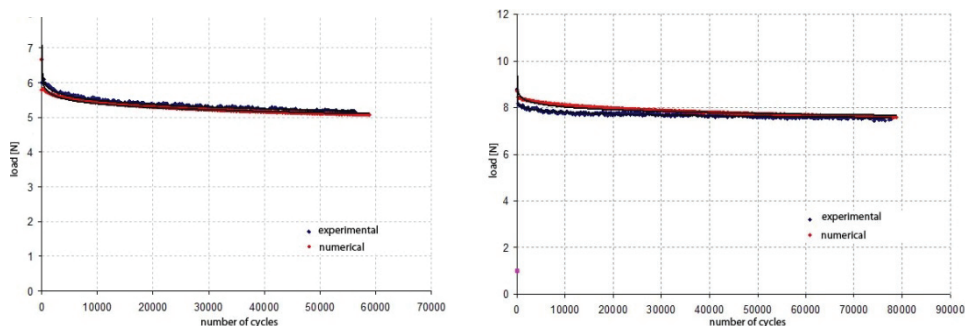


Fig. 26. Experimental-numerical results for GLARE specimens for one (on the left) and two (on the right) aluminium sheet

Propagation under conditions of mixed mode of opening (MMELS), as widely described in literature (Blanco et al., 2006), is modeled by a power law type:

$$\frac{da}{dN} = C \Delta G^m \quad (5)$$

The following damage model is used in numerical analysis:

$$\frac{da}{dN} = \frac{c_1 \left(e^{c_2 \left(\frac{\Delta G}{G_{crit}} \right)^{c_3}} - 1 \right)}{c_2} \left(\frac{\Delta G}{G_{crit}} \right)^{c_3} \quad (6)$$

The parameter a is the crack length, N the number of cycles, ΔG is available energy at the peak of the defect, G_{crit} is the critical energy of the crack. The constants c_1 , c_2 , c_3 are obtained numerically by an extrapolation process according to the performance of G-a (energy-crack length) that are assumed a pattern of exponential growth. It is then used a classic pattern (Model Stirling) to hypothesize the evolution of the crack growth.

$$c_1 = 0,18 \text{ E } (-2) \quad c_2 = 0,21 \quad c_3 = 1,29 \quad (7)$$

Fig. 27 shows some experimental-numerical comparisons.

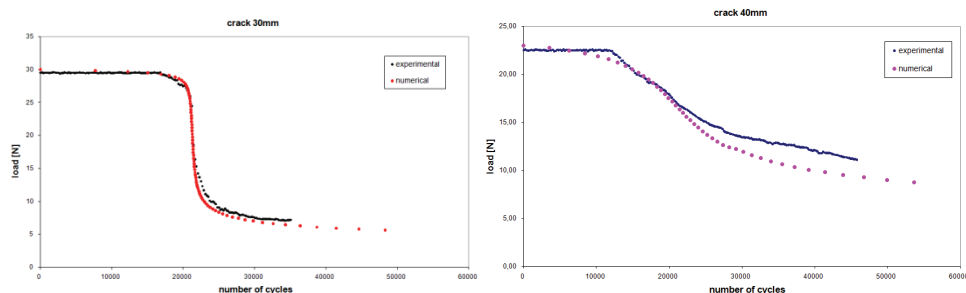


Fig. 27. Experimental-numerical results comparison for MMELS tests

7. Conclusions

During the project the machine is designed in very flexible way, choosing the load type, its size, its frequency, etc. So that fatigue tests on composite materials can be performed in operating conditions close to those of component in function. Analyzed specimens do not show subsidence or deformations after an initial visual inspection, but subsequent accurate observations show the presence (frequently) of the damage at interface between aluminium and composite layers.

Damage causes of a composite structure can be due to the application of fatigue loads (which determine the birth and propagation of cracks in sensitive areas) and the nucleation and propagation of interlaminar defects. These two types of damage can also coexist within structural element. Specimen damage after the initial phase of rapid growth tends to stop, this is due to the ability of redistribution of matrix-fibres composites to support stresses.

Then it is essential to analyze the degradation mechanisms because the stresses that are created near a geometrical discontinuity could promote the delamination propagation or break of the layer of matrix. A severe obstacle to the spread of composites is their high sensitivity to defects and the degradation. The tests have allowed to study very well the damage evolution and so to estimate operating conditions of structural element after applying a certain number of fatigue cycles.

Experimental study of MMELS model for bonded joints is conducted to determine the damage before the phase of unstable crack propagation and shows that defect propagation occurs at the interface between adhesive and loaded layer (adhesive fracture) in MMELS model. The damage accumulated in adhesive coat during the loading history was marked. Load-number of cycles curve has a slight negative slope during fatigue load. Adhesive coat downstream from the apex of the defect accumulate some damage that alter the bending stiffness of the specimen. Unstable phase of crack growth follows at stable phase which rapidly spreads within a few cycles until final break of the component. A good correspondence between experimental and numerical results is found in all the analyzed cases both to composite laminates and to bonded joints.

The results show that the machine FTM setup is able to carry out its task with testing costs quite content. The extension to the bonded joints is particularly interesting.

Future developments: the optimization of the machine can be done by replacing the base with a more rigid and larger in order to have a second engine, more powerful, to perform tests that require higher loads, with an appropriate load cell. Also it is appropriate to

consider the creation of a load cell for lower loads than 10 N, while eccentricity adjustment can be performed with micrometer spindle.

8. References

- Beck, T., Lohe, D., Baumgartner, F., 2002, The Fatigue Behaviour of an Aluminium Foam Sandwich Beam Under Alternating Bending – *Advanced Engineering Materials*, vol. 4, n. 10, pp 787-790
- Berchem, K., Hocking, M. G., 2006, A simple plane bending fatigue and corrosion testing machine, Design Note, *Measurement Science and Technology* 17 (10), art. no. N05, pp. N60-N66
- Blanco Villaverde, N., 2005, Variable mixed-mode delamination in composite laminates under fatigue conditions : testing & analysis [dirigida per Josep Costa Balanzat] Publicació Universitat de Girona, DL, ISBN 8468909904.
- Blanco N., Gamstedt E. K., Costa J., Trias D., 2006, Analysis of the mixed-mode end load split delamination test, *Composite Structures*, vol. 76, 14-20
- Boniface, V., Simha, K. R. Y. , 1999, Re-examination of crack opening model of interface fracture, *Engineering Fracture Mechanics* vol. 64, pp 677-691.
- Caligiana, G., Minak, G., Ghezzi, F., Cicchetti, M., 2003, "Dispositivo per prove di fatica su materiali compositi: progetto, messa a punto e risultati sperimentali", XXXII *Convegno Nazionale AIAS*, Salerno 3-6 Settembre 2003, AIAS 2003
- Ducept, F., Gamby, D., Davies P., 1999, A mixed-mode failure criterion derived from tests on symmetric and asymmetric specimens, *Elsevier Composites Science and Technology*, Vol. 59, pp. 609-619.
- Froustey, C., Lasserre, S. 1989, Multiaxial fatigue endurance of 30NCD16 steel, *International Journal of Fatigue* 11 (3), pp. 169-175
- Higgins, A., 2000 Adhesive bonding of aircraft structures, *International Journal of Adhesion & Adhesives* Vol. 20, pp. 367-376.
- Marannano, G. V., Pasta, A., Virzì Mariotti, G., 2007 Progetto e messa a punto di una macchina prova materiali a fatica a flessione piana per provini in composito - XXXVI *Convegno Nazionale AIAS*, ISBN 978-88-87 998-75-7, 4-8 Settembre 2007, Ischia (Na), Italy
- Marannano, G. V; Pasta, A., 2006. An analysis of interface delamination mechanisms in orthotropic and hybrid fibre-metal composites laminates - *Engineering Fracture Mechanics*. Vol. 74 (4). Pp. 612-626. ISSN: 0013-7944.
- Marannano, G., Virzì Mariotti, G., 2008. Structural Optimization and Structural Analysis of Composite Material Panel for Naval Use – *Meccanica*, vol. 43, 2008, pp. 251-262 -. DOI: 10.1007/s11012-008-9120-z. ISSN: 0025-6455.
- Natarajan, V., GangaRao, H.V.S., Shekar, V. 2005. Fatigue response of fabric-reinforced polymeric composites. *Journal of Composite Materials* Vol. 39 (17), pp. 1541-1559
- Pirondi A., Nicoletto G., 2001, Tenacità a frattura in Modo Misto I/II di giunti incollati- XXX *Convegno Nazionale AIAS-Alghero (SS)* 12-15 settembre 2001.
- Robinson, P., Hodgkinson, J. M. , 2000, Interlaminar fracture toughness, in: *Mechanical Testing of Advanced Fibre Composites*, Editor(s): Hodgkinson, Cambridge, Woodhead Publishing Ltd., Pages: 170-210, ISBN:9780849308451
- Sideroff, F., Subagio, B. (1987), Fatigue damage modelling of composite materials from bending test. Sixth International Conference on Composite Materials (ICCM-VI) &

- Second European Conference on Composite Materials (ECCM-II): Volume 4. Proceedings*, 20-24 July 1987, London, UK, Elsevier, pp. 4.32-4.39.
- Sugeta, A., Uematsu, Y., Tomita, K., Hirose, K., Jono, M., 2006, Development of Fatigue Testing System for in-situ Observation by an Atomic Force Microscope and Small Fatigue Crack Growth Behavior in α -Brass, *JSME International Journal, Series A*, vol. 49, no.3, pp. 382-389
- Sun, C. T., Jih, C. J., 1987, On strain energy release rates for interfacial cracks in bi-material media, *Engineering Fracture Mechanics* -Vol. 28, No.1, pp 13-20,.
- Trotignon J. P. (1995). A New Universal Fatigue Machine for Plastics and Composites. *Polymer Testing* Volume: 14, Issue: 2, pp. 129-147.
- Van Paepegem, W., Degrieck, J. (a) 2001. Fatigue degradation modelling of plain woven glass/epoxy composites, *Composites - Part A: Applied Science and Manufacturing* 32 (10), pp. 1433-1441.
- Van Paepegem, W., Degrieck, J. (b) 2001. Experimental set-up for and numerical modelling of bending fatigue experiments on plain woven glass/epoxy composites. *Composite Structures* 51 (1), pp. 1-8
- Van Paepegem, W., Degrieck, J. 2002. Coupled Residual Stiffness and Strength Model for Fatigue of Fibre-reinforced Composite Materials. *Composites Science and Technology*, 62(5), 687-696 (SCI-IF: 1.320).
- Vasek, A., Polák, J., Kozák, V. 1997. Fatigue crack initiation in fibre-metal laminate GLARE 2. *Materials Science and Engineering A* 234-236, pp. 621-624.

On the Behavior of FRP-to-concrete Adhesive Interface: Theoretical Models and Experimental Results

Enzo Martinelli, Antonio Bilotta, Ciro Faella and Emidio Nigro

Department of Civil Engineering, University of Salerno, Fisciano (SA),

*Department of Structural Engineering, University of Naples "Federico II", Naples
Italy*

1. Introduction

Fiber-reinforced polymers (FRP) are more and more commonly employed for strengthening existing structures of both reinforced concrete (RC) and masonry. Since FRP sheets (cured in situ) or plates (preformed) are externally bonded on a concrete or masonry substrate, the issue of adhesion on those materials generally controls the effectiveness of strengthening in members stressed either in bending or shear (Motavalli & Czaderski, 2007).

The use of composite materials for structural strengthening of civil structures and infrastructures began with some pioneering application at the middle of the '80s (Meier, 1987) of the past century.

Plenty of experimental work and theoretical investigations have been carried out in the following years with the aim of demonstrating the feasibility of strengthening civil structures by means of composite materials (Swamy et al., 1987; Meier, 1995). However, composite materials were already widely used in other fields of structural engineering, such as aerospace (Hart-Smith, 1973), aeronautics and, later, automotive. Thus, the initial research activities about the possible use of composites in civil structures were not mainly focused on the behavior of composites themselves. They were rather intended at addressing two main issues regarding, on the one hand, the different behavior of composites with respect to more traditional materials (basically, steel) commonly used as a reinforcement in civil structures (Arduini & Nanni, 1997; Naaman et al., 2001; Triantafillou et al., 2001) and, on the other hand, the aspects related to the adhesive connection of the FRP laminates to the concrete (or masonry) substrate (Täljsten, 1997; Neubauer & Rostasy, 1997).

The main findings of the research activities carried out in the '90s contributed to guidelines (fib, 2001; CNR-DT200, 2004; ACI 440-2R-08) for designing FRP-based strengthening intervention of RC and masonry members.

Bonding between FRP laminates (sheets or plates) and concrete emerged as a cutting-edge issue from the first decade of research activities on composite materials for civil structures. In particular, several failure modes due to loss of adhesion between the externally bonded FRP element and the concrete substrate have been observed experimentally and recognized as specific features of this kind of members (Meier, 1995; Bonacci, 1996).

As a matter of principle, the following seven failure modes have been defined in the scientific literature (Teng et al., 2002):

- a. flexural failure by FRP rupture;
- b. flexural failure by crushing of compressive concrete;
- c. shear failure;
- d. concrete cover separation;
- e. plate end interfacial debonding;
- f. intermediate flexural crack induced interfacial debonding;
- g. intermediate flexural-shear crack induced interfacial debonding.

The last three failure modes are actually related to debonding failure of the FRP laminate from the concrete substrate. Local failure possibly induced by irregularities in the substrate surface can be also observed. Fig. 1 represents those failure modes pointing their typical position throughout the FRP-to-composite adhesive interface.

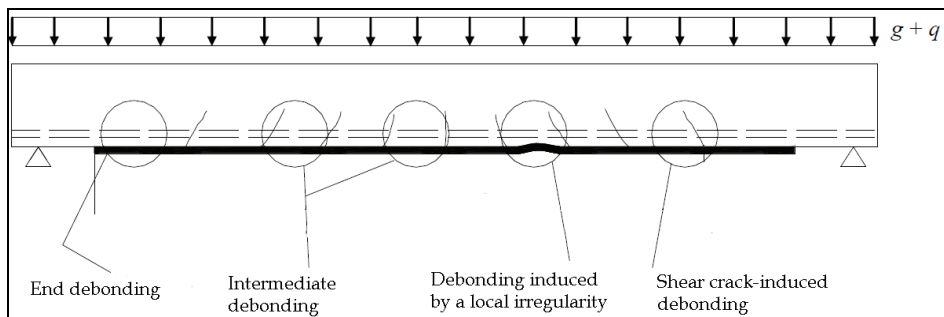


Fig. 1. Possible failure modes due to debonding in RC beams externally strengthened by FRP

Analytical studies have been carried out for determining the actual distribution of stresses throughout the adhesive interface. In particular, well-established elastic models, already used within the framework of structural mechanics, have been proposed as simplified practical methods for determining both shear and normal (peeling) stresses at the FRP-to-concrete interface (Roberts, 1989; Malek et al., 1998; Rabinovich & Frostig, 2000). However, those simplified methods were generally based on the assumption of an elastic behaviour of the above mentioned interface. Although this assumption can be considered under service loads, it cannot be generally accepted for the load values close to the onset of debonding. Micro-cracking phenomena develop as the levels of the interface stresses cannot be resisted by concrete, resulting in a highly nonlinear behaviour for the FRP-to-concrete interface which can be modelled by means of several possible relationships between interface stresses and displacements (Lu et al, 2005). Consequently, more advanced numerical models have been also proposed for simulating the actual distribution of stresses looking after the various fracture phenomena developing in concrete beneath the adhesive interface (Rabinovich & Frostig, 2000; Faella et al., 2008).

More recently, several models have been proposed in the scientific literature for predicting the strength of beams against both plate end-debonding and intermediate-debonding (Smith & Teng, 2001; Teng et al., 2003). They generally derive by mechanical observations carried out on the behaviour of FRP laminates glued on concrete blocks (Täljsten, 1996) and tested in pullout with the aim of measuring some relevant quantities, such as the ultimate strength

at debonding and the axial strain distribution throughout the FRP bonded length (Chajes et al., 1996).

Understanding the behaviour of FRP-to-concrete joints tested under pull-out actions is of paramount importance for describing the key mechanical properties of the adhesive interface between FRP and concrete, which plays a key role in the possible debonding failure of externally strengthened beams. Thus, advanced testing and monitoring techniques have been also used for a deeper investigation of the behaviour of those joints (Czaderski et al., 2010). The experimental results obtained by the mentioned pull-out tests can be considered for identifying the non-linear relationships connecting interface stresses and displacements (Faella et al., 2009). In particular, a bilinear elastic-softening relationship between the interface shear stress and the corresponding displacements is often used for the FRP-to-concrete interface. The elastic branch of that stress-strain relationship results from the elastic behaviour of both the adhesive layer and the concrete substrate, mainly stressed in shear. The slope of such an elastic branch (namely, the “slip modulus” according to Lee et al, 1999) is generally much smaller than the value corresponding to the ration between the shear modulus of the resin and its thickness, as it would be determined by assuming a fully stiff behaviour of the concrete block (Faella et al., 2002).

A closed-form analytical solution has been derived in Faella et al. (2002) for the distribution of both shear stresses and relative slips in FRP-to-concrete joints with a bilinear adhesive interface. Further advances have been proposed by Lu et al. (2005), while the influence of different assumptions on the shape of the stress-slip relationship (i.e. bilinear, linearly softening, rigid-plastic, and so on) is discussed in both Chen & Teng (2001) and Wu et al. (2002). However, the fracture energy G_F (Täljsten, 1996) is the key parameter characterizing any various shear-stress-interface-slip relationship. The ultimate pull-out strength of the FRP-to-concrete joints is controlled by that parameter as well as the axial stiffness of the laminate and the bonding length. A limit value of the bonding length beyond which no further increases of the ultimate pull-out force can be observed; it is generally referred as “transfer length” (Bizindavyi & Neale, 1999). Some concepts of Fracture Mechanics are more and more employed in modelling the overall behaviour of both FRP laminates connected to concrete blocks (Yuan et al., 2007) and RC beams externally strengthened by FRP (Rabinovitch & Frostig, 2001; Achintha & Burgoyne, 2008).

The present chapter deals with the mechanical behaviour of the adhesive interface between FRP and concrete, proposing a wide overview of some theoretical models and experimental results which can be useful for understanding such a behaviour.

In the second section, an analytical model will be firstly presented for determining both shear and normal stresses throughout the adhesive interface in the linear range. The nonlinear behaviour of the FRP-to-concrete interface will be also addressed by discussing the ultimate bearing capacity of FRP laminates bonded on concrete members.

The third section will present the features of the most well-established testing techniques for investigating the mechanical behaviour of FRP-to-concrete interface, from the early loading stages up to failure. A series of experimental results of pull-out tests on FRP laminates will be also presented for pointing out the most important behavioural characteristics of the FRP-to-concrete interface in the case of both sheets and plates.

Finally, the fourth section will present some of the most recent design formulae which can be derived by the above mentioned theoretical models and calibrated on the available experimental results, partly reported in the present chapter.

2. Theoretical models

An analytical formulation for modelling the behaviour of the FRP-to-concrete adhesive interfaces is presented and discussed in the present section. The behaviour of FRP-to-concrete joints in the linear range is examined in the first subsection. Then, the aspects more directly related at the ultimate behaviour are addressed in the second one.

2.1 A general analytical model: formulation in the linear range

A simplified model is formulated in the present section with the aim of simulating the behaviour of FRP laminates bonded on concrete and tested in pull-out, simulating how both the in-plane (namely, "slip") and out-of-plane displacement components develop throughout the FRP length. It is based on the following assumptions:

- the FRP strip is simulated as a Bernoulli beam;
- the adhesive layer is modelled as a bi-dimensional elastic domain in plane deformations.

The generalized forces N , V , M applied on the transverse section of the strip at the abscissa z and the interface stresses (shear τ and normal σ , respectively) are represented in Fig. 2. The following equilibrium equations can be stated between those force and stress components:

$$\frac{dN}{dz} + \tau_f b_f = 0 \quad , \quad (1)$$

$$\frac{dV}{dz} = -b_f \sigma_y \quad , \quad (2)$$

$$\frac{dM}{dz} + \tau_f \frac{b_f t_f}{2} - V = 0 \quad . \quad (3)$$

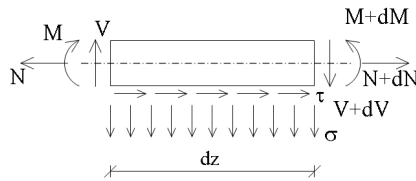


Fig. 2. Forces on the segmental FRP strip element

The parameters v , w and φ completely describe the displacement field of the strip and the following compatibility equations relate them to the axial strain ε and the curvature χ (Fig. 3):

$$\varepsilon = \frac{dw}{dz} \quad , \quad (4)$$

$$\chi = \frac{d\varphi}{dz} \quad , \quad (5)$$

$$\varphi = -\frac{dv}{dz} \quad . \quad (6)$$

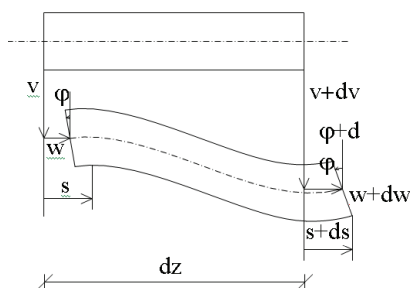


Fig. 3. Displacements components of the segmental element

The interface slip s , namely the axial displacement at the bottom chord of the strip transverse section, can be also related to the displacement components represented in Fig. 3:

$$s = w + \frac{t_f}{2} \cdot \phi . \quad (7)$$

Finally, the usual (generalized) stress-strain relationships can be introduced for the strip modelled as a Bernoulli beam:

$$N = EA_f \varepsilon = E_f b_f t_f \varepsilon , \quad (8)$$

$$M = EI_f \chi = E_f \frac{b_f t_f^3}{12} \chi , \quad (9)$$

where EA_f and EI_f are respectively the axial and flexural stiffnesses which can be assumed for the strip transverse section. Based on the second assumptions reported at the beginning of section 2.1, The following equilibrium equations can be written for the infinitesimal 2D element of resin within the adhesive layer (Fig. 4):

$$\left\{ \begin{array}{l} \frac{\partial \sigma_{yy}}{\partial y_a} + \frac{\partial \tau_{yz}}{\partial z_a} = 0 \\ \frac{\partial \tau_{yz}}{\partial y_a} + \frac{\partial \sigma_{zz}}{\partial z_a} = 0 \end{array} \right. , \quad (10)$$

where y_a and z_a are the Cartesian coordinates of the infinitesimal areal element of resin.

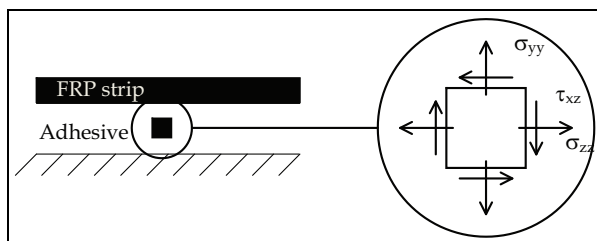


Fig. 4. General plane stress-state for an infinitesimal element of the adhesive layer

The corresponding strain measures can be expressed as functions of the displacement field $v_a(y_a, z_a)$ e $w_a(y_a, z_a)$ within the adhesive layer:

$$\left\{ \begin{array}{l} \varepsilon_{yy} = \frac{\partial v_a}{\partial y_a} \\ \varepsilon_{zz} = \frac{\partial w_a}{\partial z_a} \\ \gamma_{yz} = \frac{\partial v_a}{\partial z_a} + \frac{\partial w_a}{\partial y_a} \end{array} \right. , \quad (11)$$

where y_a and z_a are the Cartesian coordinates of the infinitesimal areal element of resin. Finally, the following elastic relationships can be stated between stresses and strains:

$$\left\{ \begin{array}{l} \varepsilon_{yy} = \frac{1}{E_a} \cdot [\sigma_{yy} - \nu_a \cdot \sigma_{zz}] \\ \varepsilon_{zz} = \frac{1}{E_a} \cdot [\sigma_{zz} - \nu_a \cdot \sigma_{yy}] \\ \gamma_{yz} = \frac{\tau_{xy}}{G_a} = 2 \cdot (1 + \nu_a) \cdot \frac{\tau_{xy}}{E_a} \end{array} \right. , \quad (12)$$

where E_a and G_a are the elastic properties of the adhesive layer. In this formulation, it connects the FRP laminates to a stiff substrate representing the concrete element. The upper bound of this layer is connected to that strip and some compatibility equations should be written for introducing this physical constraint into the mathematical model. Thus, the three equations (10)-(12) can be worked out for deriving a relationship between the displacement components $v_a(0, z_a)$ and $w_a(0, z_a)$ and the corresponding stress components $\sigma_{yy}(0, z_a)$ and $\tau_{xy}(0, z_a)$. A key assumption can be introduced for simplifying the analytical expressions of the interface stresses, considering a constant value of the shear stress throughout the adhesive thickness (Rabinovich & Frostig, 2000):

$$\tau_{yz} = \tau_a(z_a) = \tau_a(z) . \quad (13)$$

Consequently, the second one of the two equations in (10) leads to the following simplification in terms of the normal stress in longitudinal direction:

$$\frac{\partial \sigma_{zz}}{\partial z_a} = 0 \Rightarrow \sigma_{zz} = f_1(y_a) \Rightarrow \sigma_{zz} = 0 . \quad (14)$$

The last implication derives by the assumption of zero axial stress on the initial section of the layer adhesive.

Further simplifications can be introduced looking after the first equations in (10) and introducing therein the stress-strain relationship and the compatibility equation within the adhesive layer:

$$\sigma_{yy}(y_a, z_a) = - \int \frac{d\tau_a}{dz} dy + g_1(z_a) = - \frac{d\tau_a}{dz} y_a + g_1(z_a) , \quad (15)$$

and

$$\varepsilon_{yy}(y_a, z_a) = \frac{\sigma_{yy}(y_a, z_a)}{E_a} = -\frac{1}{E_a} \cdot \frac{d\tau_a}{dz} y_a + \frac{g_1(z_a)}{E_a}. \quad (16)$$

The transverse component of the displacement field can be derived by further integration:

$$\begin{aligned} v_a(y_a, z_a) &= v(z_a) + \int \varepsilon_{yy} dy = v(z_a) + \int \left(-\frac{1}{E_a} \cdot \frac{d\tau_a}{dz} y_a + \frac{g_1(z_a)}{E_a} \right) dy = \\ &= v(z_a) - \frac{1}{E_a} \cdot \frac{d\tau_a}{dz} \frac{y_a^2}{2} + \frac{g_1(z_a)}{E_a} y_a \end{aligned} \quad (17)$$

and the value of the unknown function g_1 can be finally derived by imposing zero value to the displacement at the bottom interface ($y_a = t_a$):

$$v(z_a) - \frac{1}{E_a} \cdot \frac{d\tau_a}{dz} \frac{t_a^2}{2} + \frac{g_1(z_a)}{E_a} t_a = 0, \quad (18)$$

$$g_1(z_a) = -\frac{E_a}{t_a} \cdot v(z_a) + \frac{d\tau_a}{dz} \frac{t_a}{2}. \quad (19)$$

Consequently, the following explicit expressions can be written for σ_{yy} , ε_{yy} and v_a described in (15), (16) and (17), by introducing the expression of g_1 given by equation (19):

$$\varepsilon_{yy}(y_a, z_a) = \frac{d\tau_a}{dz} \cdot \left(\frac{t_a - 2y_a}{2 \cdot E_a} \right) - \frac{v(z_a)}{t_a}, \quad (20)$$

$$\sigma_{yy}(y_a, z_a) = E_a \cdot \varepsilon_{yy}(y_a, z_a) = \frac{d\tau_a}{dz} \cdot \left(\frac{t_a - 2y_a}{2} \right) - \frac{E_a}{t_a} v(z_a), \quad (21)$$

$$v_a(y_a, z_a) = v(z_a) \cdot \left(1 - \frac{y_a}{t_a} \right) + \frac{d\tau_a}{dz} \cdot \left(\frac{t_a - y_a}{2E_a} \right) y_a. \quad (22)$$

Shear strain and stress can be related according to the following relationship:

$$\gamma_{yz}(z_a) = \frac{\tau_a(z_a)}{G_a}, \quad (23)$$

and, considering the compatibility equation involving shear strains, further transformations can be carried out by introducing the compatibility equation in (11):

$$\gamma_{yz}(z_a) = \frac{\partial v_a}{\partial z_a} + \frac{\partial w_a}{\partial y_a}. \quad (24)$$

The first derivative of the longitudinal displacement w_a inside the adhesive layer can be written as follows:

$$\frac{\partial w_a}{\partial y_a} = \gamma_{yz}(z_a) - \frac{\partial v_a}{\partial z_a} = \frac{\tau_a(z_a)}{G_a} - \frac{dv}{dz} \cdot \left(1 - \frac{y_a}{t_a}\right) - \frac{d^2 \tau_a}{dz^2} \cdot \left(\frac{t_a - y_a}{2E_a}\right) y_a, \quad (25)$$

and the corresponding function w_a can be derived by integrating eq. (25) and introducing a zero-displacement condition for $y_a = t_a$ (namely, at the bottom of the adhesive layer):

$$w_a(y_a, z_a) = -\frac{\tau_a(z_a)}{G_a} (t_a - y_a) + \frac{dv}{dz} \cdot \left(\frac{t_a}{2} - y_a + \frac{y_a^2}{2t_a}\right) + \frac{d^2 \tau_a}{dz^2} \cdot \left(\frac{t_a^3}{12E_a} - \frac{t_a y_a^2}{4E_a} + \frac{y_a^3}{6E_a}\right), \quad (26)$$

The above relationship can be utilized for deriving the expression of the axial displacements beneath the laminate ($y_a = 0$), corresponding to the slip at the interface $s(z)$:

$$w_a(0, z_a) = s(z) = -\frac{t_a}{G_a} \cdot \tau_a + \frac{t_a^3}{12E_a} \cdot \frac{d^2 \tau_a}{dz^2} + \frac{t_a}{2} \cdot \frac{dv}{dz}, \quad (27)$$

as well as equation (22) can be utilized for recognizing that the corresponding transverse component $v_a(0, z_a = z)$ is equal to $v(z)$:

$$\sigma_{yy}(y_a, z_a) = E_a \cdot \varepsilon_{yy}(y_a, z_a) = E_a \cdot \left[\frac{d\tau_a}{dz} \cdot \left(\frac{t_a - 2y_a}{2 \cdot E_a}\right) - \frac{v(z_a)}{t_a} \right], \quad (28)$$

$$\sigma_y(z) = \sigma_{yy}(0, z_a) = -v(z_a) \cdot \frac{E_a}{t_a} + \frac{t_a}{2} \cdot \frac{d\tau_a}{dz}. \quad (29)$$

Thus, the rotation field $\varphi(z)$ of the laminate element can be easily defined through equation (6) and the generalized strain fields can be determined by means of equation (4) and (5).

The above equations can be finally combined for deriving a unique differential equation in terms of interface shear stresses. A first equation can be obtained by differentiating eq. (7) and introducing (4), (6) and (8). After a further differentiation and introducing the definition of interface slip provided by eq. (27), the following differential relationship between the shear stress and the transverse displacements can be obtained:

$$\frac{G_a}{E_f t_f t_a} \cdot \tau_a - \frac{d^2 \tau_a}{dz^2} + \frac{G_a}{2} \cdot \frac{d^3 v}{dz^3} + \frac{G_a}{12E_a} \cdot t_a^2 \cdot \frac{d^4 \tau_a}{dz^4} = 0. \quad (30)$$

Another relationship is obtained by differentiating equation (3) and introducing equation (2), (5), (6) and (9) for expressing both the bending moment and the shear force in terms of transverse displacements and interface (shear and normal) stresses. The final expression of an equation in terms of t_f and v (and their derivatives) can be obtained introducing equation (29):

$$\frac{b_f(t_f + t_a)}{2} \cdot \frac{d\tau_a}{dz} - \frac{E_f b_f t_f^3}{12} \cdot \frac{d^4 v}{dz^4} - \frac{E_a b_f}{t_a} \cdot v = 0. \quad (31)$$

The two equations (30) and (31) can be easily combined for deriving the following eighth-order differential equation in terms of interface shear stresses:

$$\frac{G_a}{E_f t_f t_a} \cdot \tau_a - \frac{d^2 \tau_a}{dz^2} + \left(\frac{t_a^2}{3} + \frac{t_a t_f}{6} + \frac{t_f^2}{12} \right) \cdot \frac{G_a}{E_a} \cdot \frac{d^4 \tau_a}{dz^4} - \frac{E_f t_a t_f^3}{12 \cdot E_a} \cdot \frac{d^6 \tau_a}{dz^6} + \frac{E_f G_a t_a^3 t_f^3}{144 \cdot E_a^2} \cdot \frac{d^8 \tau_a}{dz^8} = 0. \quad (32)$$

Finally, an expression of the displacement function v as a function of the interface shear stresses can be derived by solving equation (31) and introducing the (30):

$$v = \frac{3 \cdot t_a^2 + 3 \cdot t_a t_f + t_f^2}{6 E_a} \cdot \frac{d \tau_a}{dz} - \frac{E_f t_a t_f^3}{6 E_a G_a} \cdot \frac{d^3 \tau_a}{dz^3} + \frac{E_f t_a^3 t_f^3}{72 \cdot E_a^2} \cdot \frac{d^5 \tau_a}{dz^5}. \quad (33)$$

Eight boundary conditions are needed for the problem at hand and they can be symbolically written as follows:

$$\tau_a|_{z=0} = 0, \quad \tau_a|_{z=L} = 0, \quad (34)$$

$$\varepsilon|_{z=0} = -\frac{N(0)}{E_f A_f}, \quad \varepsilon|_{z=L} = \frac{N(L)}{E_f A_f}, \quad (35)$$

$$M|_{z=0} = 0, \quad M|_{z=L} = 0, \quad (36)$$

$$V|_{z=0} = 0, \quad V|_{z=L} = 0. \quad (37)$$

Typical solutions of the problem described by equation (32) and the boundary conditions (34)-(37) are represented in figures 5 and 6, in terms of shear and normal stresses respectively. In both graphs, the interface stress components are divided by the average shear stress $\tau_m = F/b_f L$ and the abscissa are reported in non-dimensional form as $\bar{z} = \omega z$.

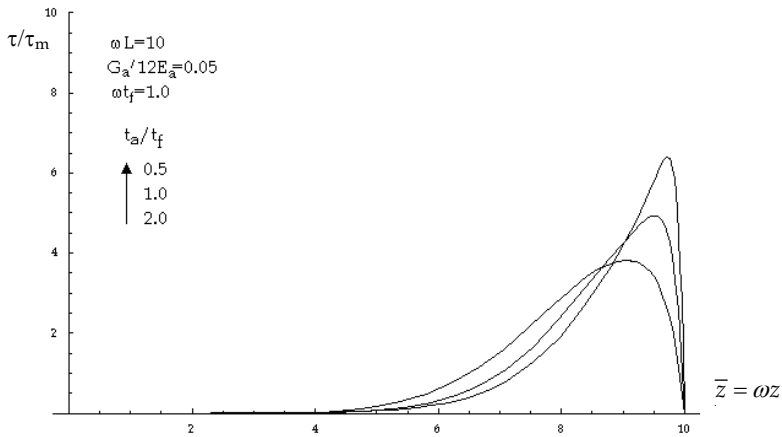


Fig. 5. Possible distributions of interface shear stresses throughout the adhesive interface

The results of the analysis carried out by means of this model are completely controlled by the following non-dimensional parameters:

$$\omega L, \quad (38)$$

$$\omega t_f = \sqrt{\frac{G_a t_f}{E_f t_a}} = \sqrt{\frac{k_{s,a} t_f}{E_a}} , \quad (39)$$

$$\frac{G_a}{E_a} = \frac{k_{s,a}}{k_{v,a}} , \quad (40)$$

$$\frac{t_a}{t_f} . \quad (41)$$

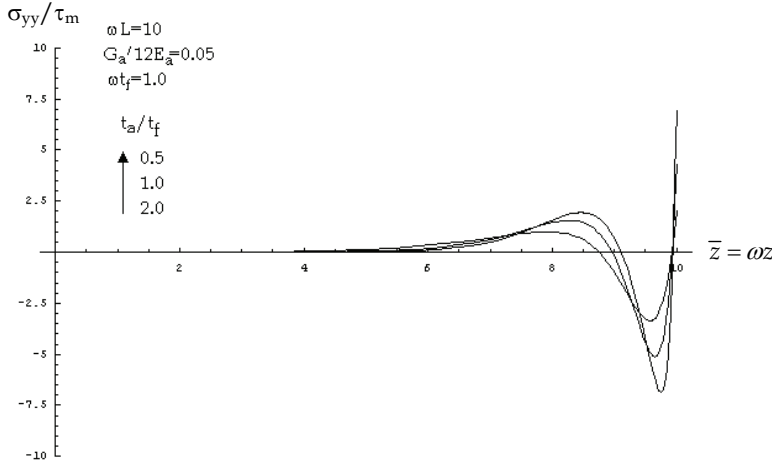


Fig. 6. Possible distributions of interface normal stresses throughout the adhesive interface

2.2 Possible simplifications of the general model

The general model formulated in the previous section can be simplified by introducing further assumptions about the geometric and mechanical assumptions.

In particular, a key simplification derives in the case of negligible thickness t_f of the FRP laminate, if compared, for instance, with a suitable reference value of the length. In particular, it is possible to demonstrate that the height-order equation (32) can be reduced by uncoupling the equations (30) and (31):

$$\frac{d^2 \tau_a}{dz^2} + \omega^2 \tau_a = 0 , \quad (42)$$

$$\frac{d^4 v}{dz^4} + 12 \cdot \frac{E_a}{t_a t_f^3} v = 0 , \quad (43)$$

Under the mathematical point of view, the above simplification derives from the condition $\omega t_f \rightarrow 0$ for whichever value of the non dimensional parameters listed at the end of section 2.1. It means that the thickness of the FRP laminate is much smaller than the characteristic length of the problem ω , which is the main argument of the solutions of the general equation (32). The uncoupled boundary conditions for eq. (42) simplify as a consequence of the condition $\omega t_f \rightarrow 0$, turning in a completely uncoupled expressions:

$$\varepsilon|_{z=0} = -\frac{N(0)}{E_f b_f t_f} = \frac{ds}{dz}\bigg|_{z=0} \quad \varepsilon|_{z=L} = \frac{N(L)}{E_f b_f t_f} = \frac{ds}{dz}\bigg|_{z=L} . \quad (44)$$

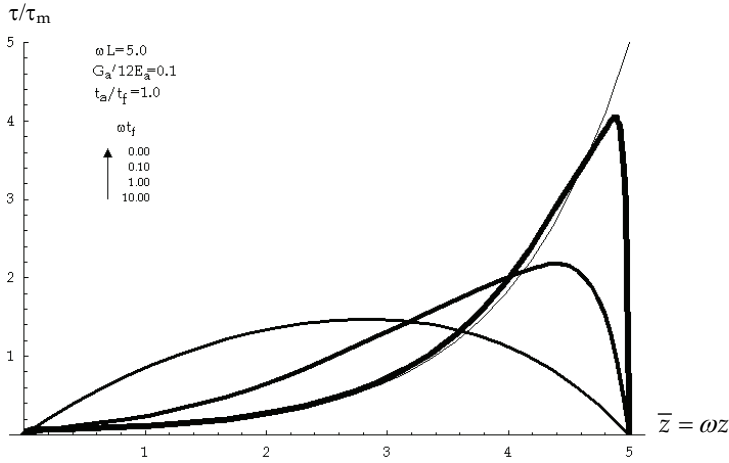


Fig. 7. Interface shear stress for a thin FRP strip

A sound demonstration about how equation (32) reduces to (42)-(43) in the case of $\omega t_f \rightarrow 0$, can be obtained by means of some mathematical transformations of both the equation (32) and the boundary conditions (34)-(37) in dimensionless form. These transformations, as well as the discussion about the slight modifications in the out-of-plane stress regime, are omitted herein for the sake of brevity.

2.3 Solutions in the nonlinear range

The assumption introduced in the subsection 2.2 for simplifying the general eighth-order equation formulated in subsection 2.1 can be generally assumed as a reasonable trade-off between the (good) accuracy of the obtained model and the (higher) simplicity of its equations. The approximation introduced by the supplementary assumption is generally accepted especially in the nonlinear range, as further uncertainties are introduced by the fracture behaviour of concrete which cannot be covered by the complex assumptions leading to equation (32).

Thus, the nonlinear response of FRP-to-concrete joints under pull-out actions can be analyzed by assuming the problem described by equation (42) with the boundary conditions in (44). Since the nonlinear response is now of interest, equation (42) can be slightly modified for considering the possibility of a nonlinear relationship $\tau_a = \tau(s)$. Moreover, eq. (1) can be written in terms of axial strains ε in the FRP strip by introducing equation (8):

$$\frac{d\varepsilon}{dz} + \frac{\tau(s)}{E_f t_f} = 0 . \quad (45)$$

and, considering the relationship between axial strains and interface slip derived at the end of the subsection 2.2, the following relationship can be written for generalizing eq. (42) to the nonlinear range:

$$\frac{d^2s}{dz^2} + \frac{\tau(s)}{E_f t_f} = 0 . \quad (46)$$

The bilinear shear-stress-interface-slip relationship is considered herein as a general relationship for the nonlinear response of the interface between FRP and concrete:

$$\tau(s) = \begin{cases} -k_{el} \cdot s & |s| \leq s_{el} \\ -k_u \cdot (s_u - |s|) \cdot \text{sign}(s) & s_{el} < |s| \leq s_u \\ 0 & |s| > s_u \end{cases} , \quad (47)$$

where all symbols are represented in Fig. 8. For the sake of simplicity, only the monotonic behaviour with $s \geq 0$ will be considered in the following elaborations.

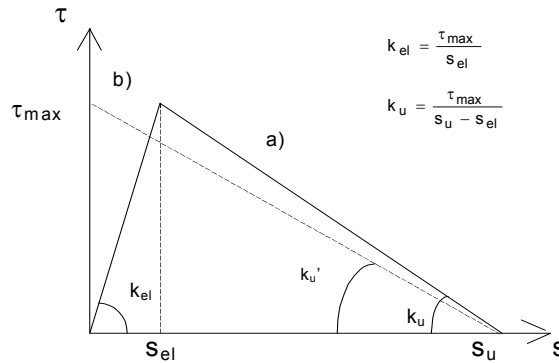


Fig. 8. Bilinear shear-stress-interface-slip relationship (fib - bulletin 14, 2001)

Consequently, two second order differential equations can be obtained by introducing the two nonzero branches of the relationship (47) within the general equation (46). In particular, under low load levels, the condition $0 \leq s \leq s_{el}$ yields throughout all the bonding length and the equation (46) can be written in the following form in terms of interface slips s :

$$\frac{d^2s}{dz^2} - \omega^2 \cdot s = 0 . \quad (48)$$

Considering a pull-out force P applied at the end ($z=L$) of the bonding length, the following boundary conditions can be written after eq. (44):

$$\varepsilon \Big|_{z=0} = \frac{ds}{dz} \Big|_{z=0} = 0 \quad \varepsilon \Big|_{z=L} = \frac{ds}{dz} \Big|_{z=L} = \frac{P}{E_f b_f t_f} . \quad (49)$$

Simple mathematical transformations (whose details are omitted herein) lead to the following solution in terms of interface shear stresses

$$\tau = -\omega \cdot \frac{P}{b_f} \cdot \frac{\cosh(\omega \cdot z)}{\sinh(\omega L)} , \quad (50)$$

which can be easily turned in terms of interface slips s considering the expression describing the linear elastic branch in eq. (47). This solution can be accepted for values of the shear strength $|\tau| \leq \tau_{\max}$ or, in order words, for pull-out forces lower than P_{el} :

$$F_{el} = \frac{\tau_{\max}}{\omega} \cdot b_f \cdot . \quad (51)$$

leading to an interface slip $s=s_{el}$ in $z=L$. As $P>P_{el}$, two different parts of the adhesive interface can be recognized. In the first part, namely for $0 \leq z \leq z_{el} < L$, the values of the interface slips s keep smaller than the elastic threshold s_{el} . In the second part, for $z_{el} < z \leq L$, the interface slips s are in the range (s_{el}, s_u) , and the following solution can be derived by integrating the two differential equations:

$$\frac{d^2 s_1}{dz^2} - \omega \cdot s_1 = 0 \quad \text{for} \quad 0 \leq z \leq z_{el} < L, \quad (52)$$

$$\frac{d^2 s_2}{dz^2} + \frac{k_{in}}{E_f t_f} \cdot s_2 = \frac{k_{in}}{E_f t_f} \cdot s_u \quad \text{for} \quad z_{el} < z \leq L. \quad (53)$$

with the following boundary conditions:

$$\varepsilon|_{z=0} = \frac{ds_1}{dz} \Big|_{z=0} = 0 \quad s_1|_{z=z_{el}} = s_{el} \quad (54)$$

$$s_1|_{z=z_{el}} = s_1|_{z=z_{el}} \quad \frac{ds_1}{dz} \Big|_{z=z_{el}} = \frac{ds_2}{dz} \Big|_{z=z_{el}} \quad (55)$$

The following solution in terms of interface shear stress τ involves the parameter $z_{el} < L$, describing the length of the elastic part of the bonding length:

$$|\tau| = \begin{cases} \tau_{\max} \frac{\cosh(\omega \cdot z)}{\cosh(\omega \cdot z_{el})} & 0 \leq z \leq z_{el} \\ \tau_{\max} \left\{ \cos[\omega_{in}(z - z_{el})] - \frac{\omega_{in}}{\omega} \cdot \sin[\omega_{in}(z - z_{el})] \cdot \tanh(\omega z_{el}) \right\} & z_{el} < z \leq L \end{cases} \quad (56)$$

where

$$\omega_{in} = \sqrt{\frac{\tau_{\max}/(s_u - s_{el})}{E_f t_f}} = \sqrt{\frac{k_{in}}{E_f t_f}} \quad (57)$$

Fig. 9 shows two typical distributions of shear stresses in the a) linear and b) nonlinear range of the behaviour of the adhesive interface described by the bilinear relationship in eq. (47). It is worth noting that z_{el} can actually range in the interval $[z_{el,min}, L)$:

$$z_{el,min} = \max\{0; z_{el,deb}\} \quad (58)$$

in which $z_{el,deb}$ is the value of z_{el} leading to $\tau(L)=0$ (or $s(L)=s_u$):

$$\cos[\omega_{in}(L - z_{el,deb})] - \sqrt{\frac{k_{in}}{k}} \cdot \sin[\omega_{in}(L - z_{el,deb})] \cdot \tanh(\omega \cdot z_{el,deb}) = 0. \quad (59)$$

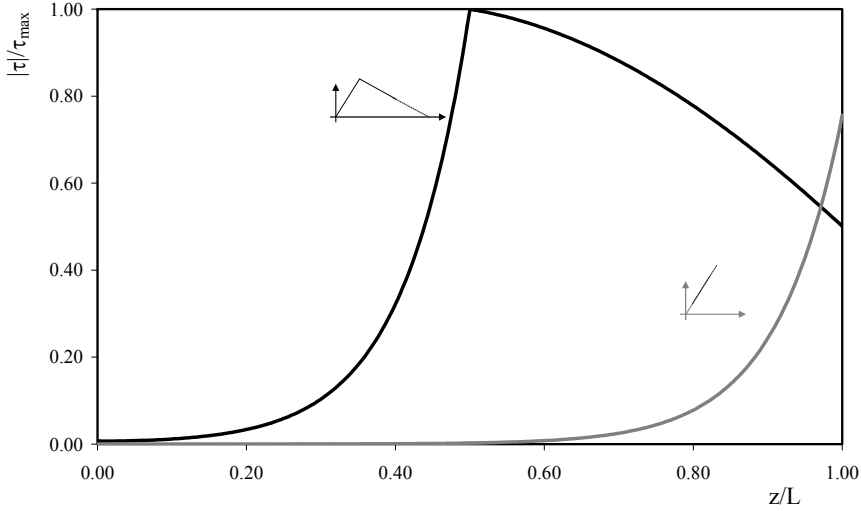


Fig. 9. Typical distribution of interface shear-strength in the linear and nonlinear range

2.4 Key parameters related to the ultimate strength

The case of $z_{el,deb}=0$ is of particular relevance, as it represents the condition of debonding initiation (namely, $s(L)=s_u$) with $\tau(0)=\tau_{max}$. A characteristic length L_{eff} can be defined in that case by means of equation (59):

$$\cos[\omega_{in}L_{eff}] = 0 \Rightarrow L_{eff} = \frac{\pi}{2} \cdot \sqrt{\frac{E_f t_f}{k_{in}}}. \quad (60)$$

Under the mechanical standpoint, this characteristic value has a paramount conceptual meaning. It represents the border between “short” and “long” anchorage length. In particular, the general expression of the force $F > F_{el}$ corresponding to a given position of z_{el} can be derived by integrating the shear stresses in equation (56):

$$F = \tau_{max} b_f \cdot \left\{ \frac{\sin \omega_{in}(L - z_{el})}{\omega_{in}} + \frac{\cos \omega_{in}(L - z_{el}) \cdot \tanh \omega z_{el}}{\omega} \right\}. \quad (61)$$

It can be applied if and only if $z_{el} \in [z_{el,min}, L)$ (namely, the interface slip s is $s_{el} \leq s \leq s_u$). In the case of $z_{el}=L$ equation (61) reduces to (51). On the contrary, when $z_{el}=z_{el,deb}=0$ the following expression can be derived for the pull-out force:

$$F_{deb} = \tau_{max} b_f \cdot \frac{\sin \omega_{in} L_{eff}}{\omega_{in}} = \frac{\tau_{max} b_f}{\omega_{in}} = b_f \cdot \sqrt{\tau_{max} \cdot (s_u - s_{el}) \cdot E_f t_f}. \quad (62)$$

Since generally $s_u \gg s_e$ the value F_{deb} is only slightly lower than the maximum strength F_{max} which can be evaluated by applying the theory of Fracture Mechanics (Täljsten, 1996) (or either as a maximum on z_{el} of the for F in eq. (61)):

$$F_{max} = b_f \cdot \sqrt{2G_F \cdot E_f t_f} = b_f \cdot \sqrt{\tau_{max} \cdot s_u \cdot E_f t_f} . \quad (63)$$

They can be assumed as coincident in the approximation of rigid-softening behaviour in considered Fig. 9.

Note that equation (63) can be applied only if $L_b \geq L_{eff}$ being L_{eff} , the effective transfer length. If $L_b < L_{eff}$ a smaller value of the ultimate force has to be expected according to the following relationship:

$$F_{max} = \sqrt{2G_F E_f t_f} \cdot b_f \cdot \left[\frac{L_b}{L_{eff}} \cdot \left(2 - \frac{L_b}{L_{eff}} \right) \right] . \quad (64)$$

3. Experimental testing techniques and results

As stated above, the effectiveness of FRP externally bonded on RC members is strongly related to the interface behaviour that depends on the mechanical and geometrical properties of materials. Thus an FRP-to-concrete bond strength model is the key to the accurate prediction of debonding failures in FRP-strengthened RC beams, including plate end debonding failures and shear crack-induced debonding failures, as well as intermediate flexural or flexural-shear crack-induced debonding failures (Teng et al., 2002).

Plenty of pull-out tests have been carried out by researchers during last years in order to experimentally investigate the influence of FRP and concrete mechanical properties on the bonding behaviour.

An overview of most common bond test techniques is reported in the first subsection. Then, the most significant results achieved by such bond tests are showed in the second one.

3.1 Overview of testing techniques

Yao et al. (2005) classified the existing test setups into the following types: (a) double-shear pull tests; (b) double-shear push tests; (c) single-shear pull tests; (d) single-shear push tests; and (e) beam (or bending) tests. These arrangements are based on the definition of the loading condition of the element and on the symmetry of the system (a double or single test refers to the contemporaneous loading of two or one FRP reinforcement applied on the specimen sides). Collectively, the first four test methods, may also be referred to as pull tests, as the plate is always directly pulled by a tensile force. Pull-pull (a) and push-pull (d) test setup are the most popular test methods. In end debonding failures in FRP flexural- strengthened RC beams with longitudinal laminates as well as debonding failures in FRP shear-strengthened RC beams with transverse laminates, the bond strength model developed from pull tests is directly applicable. Furthermore, in intermediate crack-induced debonding failures in FRP flexural- strengthened RC beams with longitudinal laminates, the stress state in the critical region of the beam is also closely similar to that of the concrete prism in a single-shear pull test. In order to extend the results of bond tests to various types of strengthening (flexural, shear, torsion), the pull-pull test setup (a and c) are probably the configuration giving the loading condition more similar to the actual one in RC elements, but it is also the most difficult to realize with a reliable setup. Furthermore the test setup (a), as well as (b) could lead to

underestimate the bond strength due to the influence of detailing (Blontrock et al., 2002; Ceroni et al., 2008). On the contrary, the push-pull test (d), where the concrete is partially in compression, is easier to be realized but it gives comparable predictions of the bond strength, if the pushing force is applied on the concrete block sufficiently far from the external reinforcement (Yao et al., 2005). Indeed, if the compressed area of concrete is too extended, the volume of material involved in the debonding failure can be lower and, thus, the related fracture energy decreases.

Asymmetrical schemes (c and d) are, in general, preferable to the symmetrical ones (a and b) mainly because the latter are more influenced by the alignment detailing of the two strengthened sides. Moreover the specimen symmetry is however lost when the debonding starts on one side and prevents from following correctly the post-peak behaviour.

As concerns the asymmetrical push-pull test setups (d), they are commonly realized by positioning a single concrete block in a stiff steel frame with an upper plate compressing the specimen, while the end of the FRP reinforcement, glued on one side, is clamped in the grips of a tensile machine (Nigro et al., 2008; Savoia et al. 2009; Ceroni and Pecce, 2010). An alternative configuration can be also realized by fixing the end of the concrete block, placed horizontally, and applying tension to the FRP reinforcement with an hydraulic jack (Yao et al., 2005; Mazzotti et al., 2009). As concerns the asymmetrical pull-pull test setups (c), they can be realized by installing metallic threaded rods inside the concrete specimen which can be clamped in the testing machine grips (Bilotta et al. 2011).

Asymmetrical single-shear test setup (c or d) appear to be promising candidate as a standard setup for determining the FRP-to-concrete bond strength; hence they were adopted to perform the tests showed in the following section.

3.2 Experimental results

A total of 58 SST tests in four sets (i.e. I-12 tests, II-16 tests, III-12 tests, IV-18 tests) were performed on CFRP plates (38) and sheets (20) applied on two opposite longitudinal faces of 29 concrete prisms. Concrete mix was specifically designed to obtain low compressive concrete strength to simulate the FRP application on existing concrete. Compressive tests were performed at 28 days after casting: the cylinder mean strength, f_{cm} , was equal to 23.82 MPa, 21.46 MPa, 26.00 MPa and 19.00 MPa for set I, II, III and IV respectively. CFRP Young's moduli, E_f , were obtained by means of tensile flat coupon tests: their mean values were between 110-220 GPa for plates and 170-240 GPa for sheets. Prior to FRP installation, the concrete surface was treated by sand paper (sets I, II, III) or by bush hammering (set IV), in order to eliminate the mortar till the aggregate became clear. Primer was always used to consolidate the concrete surface except for specimens of set VI. Further details related to experimental tests of each set can be founded in (Nigro et al. 2008, Savoia et al. 2009, Bilotta et al. 2009, Bilotta et al. 2011).

Note that several strain gauges were applied along the FRP laminates in order to measure axial strains during the bond test (see Fig. 10b,c). Experimental readings allow theoretical models of the adhesion laws to be verified or calibrated.

The behaviour of the FRP-to-concrete interface was analyzed by plotting the experimental axial strains $\varepsilon_i(z)$ measured by means of strain gauges during the test along the FRP reinforcement. Strains recorded along FRP plates at different load level are plotted in Fig. 12a,b for sheets and plates respectively. The first debonding load, P_{fd} , identified the beginning of debonding.

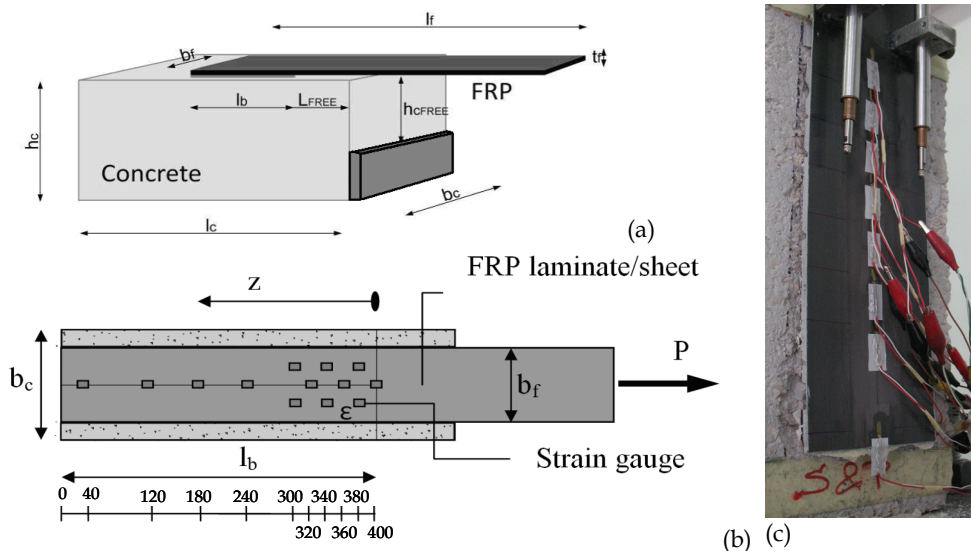


Fig. 10. Test setup scheme (a) – strain gauges distributions: scheme (b) and photo (c)



Fig. 11. Specimen after test and typical failure mode

Note that the maximum strain recorded at the loaded ends of FRP sheets was $\epsilon_{\text{sheets}} \approx 0.6\%$; for plates it was significantly lower ($\epsilon_{\text{plates}} \approx 0.2\%$), even if, for both types of reinforcement, the bond length was higher than the theoretical effective one, $L_{\text{eff}} = \sqrt{(E_f \cdot t_f) / (2 \cdot f_{\text{ctm}})}$, evaluated according to *fib* bulletin 14 (2001) and CNR-DT200/2004 (2004), where f_{ctm} is the mean tensile strength. Such result is mainly due to the higher stiffness of plates; indeed, as showed above by (63), the FRP stiffness, $E_f t_f$, is the main parameter affecting the debonding strain, being maximum strain at debonding phenomenon being the maximum strain due to debonding proportional to the factor $\sqrt{1 / (E_f t_f)}$. In particular, the ratio $(\sqrt{1 / (E_f t_f)})_{\text{sheets}} / (\sqrt{1 / (E_f t_f)})_{\text{plates}}$ of FRP reinforcements investigated in Fig. 12 is 2.5

similar to $\varepsilon_{\text{sheets}} / \varepsilon_{\text{plates}} \approx 3$. Moreover, since plates are about eight times thicker than sheets while the ratio between Young moduli is very close to unity (i.e. $E_{f,s}/E_{f,p}=1.35$), this result seems to confirm that the reinforcement thickness particularly affects debonding behaviour. Indeed, the greater the thickness, the higher the increase in the normal and shear stresses at FRP to concrete interface and consequently the probability of premature debonding occurrence (Oehlers and Moran, 1990; Tounsi et al., 2009).

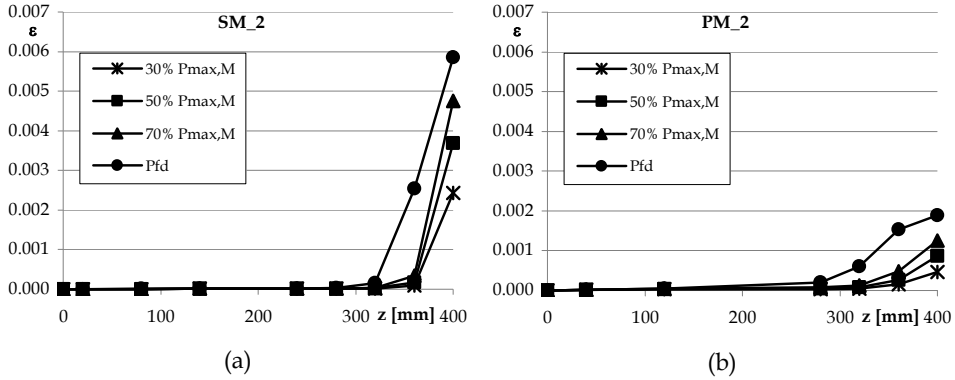


Fig. 12. Strain recorded on sheet (a) and plate (b) reinforced specimens

The interface shear stresses $\tau_i(z)$ were obtained by the variation of axial stress and, hence, strain throughout the FRP by the following relationship between two strain gauges at distance $\Delta z_{i,i+1}$

$$\tau_{i,i+1} = \frac{\varepsilon_{i+1} - \varepsilon_i}{\Delta z_{i,i+1}} \cdot E_f \cdot t_f \quad (65)$$

where E_f and t_f are FRP Young's modulus and thickness, respectively. Typical shear stress profiles assessed for sheets and plates, respectively, are reported in Fig. 13a,b.

Note that, at the loaded end of the reinforcement, the shear stresses assessed for loads close to the debonding of the reinforcement are lower than those assessed for lower loads. This indicates that in this zone of the reinforcement the shear-stress-slip law is in the softening stage typical of a post-elastic behaviour.

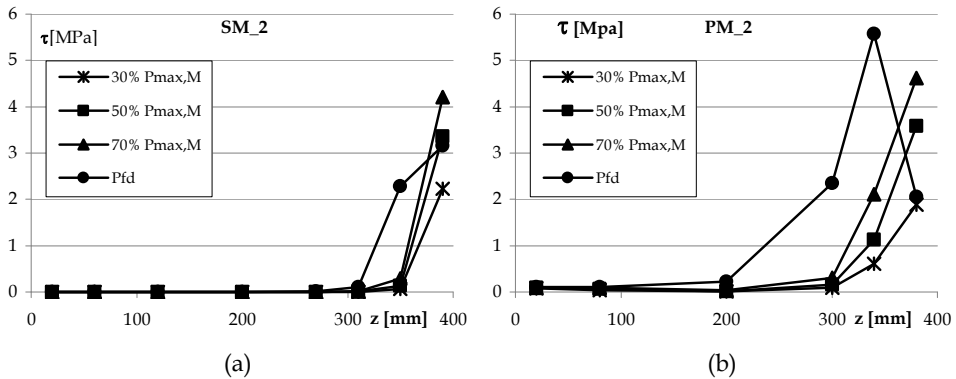


Fig. 13. Shear stresses assessed on sheet (a) and plate (b) reinforced specimens

The shear-stress-slip relationship, describing the FRP-to-concrete interface law, can be identified starting from the experimental results of pull-out tests; the distribution of shear stresses could be, in fact, obtained by Eq. (65) and the corresponding slips values by integrating the axial strains measured during the test by the following relationship

$$s_{i,i+1} = \sum_{k=0}^i \frac{(\varepsilon_{k+1} + \varepsilon_k)}{2} \cdot (x_{k+1} - x_k) \quad (66)$$

In particular the bond law at the FRP-to-concrete interface (see Fig. 14) can be obtained by calculating the shear stresses using Eq. (65) (considering the strains recorded by two gauges nearest the loaded end of FRP, see Fig. 10) and the corresponding slips using Eq. (66) (considering all the strain gauges applied on the FRP reinforcement).

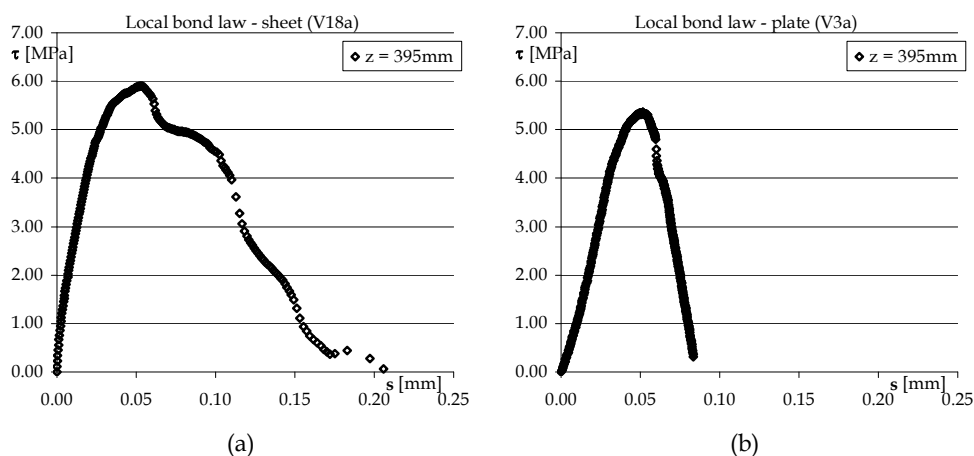


Fig. 14. Experimental bond law at the FRP-to-concrete interface: sheet (a) and plate (b)

In this way a direct identification method (DirIM) is put in place since the interface law is obtained directly with respect to experimental values of shear stresses and relative slips.

As stated above, according to the study made by Taljsten (1996), derived by linear fracture mechanics, the maximum value F_{max} of the force applied to the FRP-to-concrete joint can be obtained by (63) where G_F is the specific fracture energy of the interface depending on the mechanical properties of the adhesive FRP-to-concrete interface.

Although plenty of alternative models are available in the literature (i.e. Savoia et al., 2003) to describe FRP-to-concrete interface interaction, a simplified bi-linear relationship can reproduce the key aspects of the interface behaviour as pointed out by the comparative study carried out by Lu et al. (2005). Elasto-softening bilinear relationship is one of the most widely accepted expressions for the interface relationship and fracture energy; three mechanical parameters completely identifies such relationship (maximum shear stress τ_{max} , ultimate slip s_u , and elastic stiffness k_e), but obviously the knowledge of G_F by solving equations (63) and (64), is not sufficient for determining such parameters.

As widely discussed in Faella et al. (2009), two approaches are mainly possible to calibrate an interface relationship: the first approach (Direct Identification Method - DirIM) starts

from the experimental strains measured during the test: the distribution of shear stresses can be roughly evaluated through equilibrium of the axial stresses depending on the axial strain by (65); the corresponding slip values can be obtained by integrating throughout the FRP the axial strains by (66). The couples of values $(\bar{s}_i, \bar{\tau}_i)$ can be “directly” used to calibrate the τ - s relationship through a numerical regression, such as the least square method. Although the DirIM is very easy under the analytical standpoint, the drawback of the method is that the distribution of shear stresses cannot be directly compared with data provided by the pull out tests, because both interface shear stresses and local displacements cannot be directly measured during the usual pull-out tests. In order to overcome such problem, the indirect identification procedure (IndIM) can be pursued to calibrate an interface relationship starting from the availability of axial strain evolution in FRP plate at different load levels up to debonding failure: once a bi-linear interface relationship has been assigned, the corresponding theoretical strain distributions can be evaluated and compared with experimental data; the procedure is iterative and ends when the difference between theoretical and experimental strains is less than a prefixed tolerance (Faella et al., 2003). With reference to some experimental data (Nigro et al., 2008) both DirIM and IndIM have been applied in order to plot the τ - s relationship and derive the corresponding specific fracture energy G_F , computed by totalling up the area under the bi-linear curve. Table 1 shows that IndIM leads to specific fracture energy G_F larger than those computed by DirIM in almost all analyzed cases. Moreover, in the case of experimental tests carried out by the authors, values of G_F obtained with IndIM are as stable as the measured failure loads P_{test} , confirming the superior accuracy of IndIM with respect to DirIM. Some of the most representative bi-linear interface relationships obtained by applying both DirIM and IndIM are reported in Fig. 15.

Label		PM_1	PM_2	PM_3	SM_1	SM_2	SM_3
G_F	(DirIM)	0.45	1.20	0.86	0.66	0.86	0.48
G_F	(IndIM)	0.73	1.75	1.03	0.66	0.67	0.72
$G_{F(IndIM)}/G_{F(DirIM)}$		1.61	1.46	1.20	0.99	0.78	1.50

Table 1. Specific fracture energy G_F : (DirIM) Vs (IndIM)

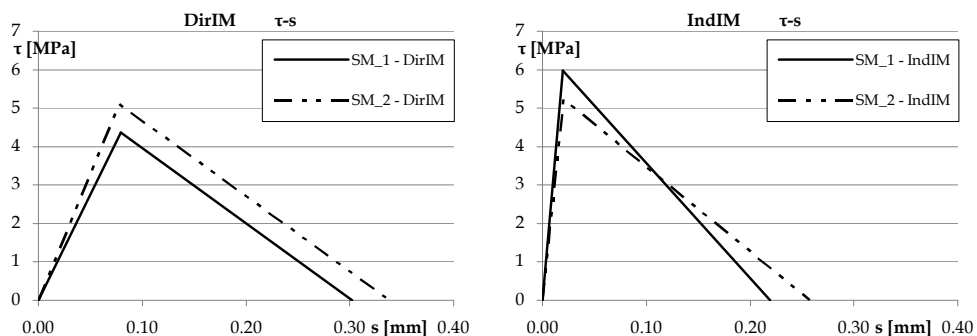


Fig. 15. Bi-linear interface relationship: (DirIM) Vs (IndIM)

Two methods lead to results that could be even significantly different, especially in terms of ultimate slips. Furthermore, the ascending branches of DirIM curves are characterized by a lower slope with respect to IndIM.

Comparisons between the theoretical and experimental values of the axial strains throughout the FRP plate are reported, for different values of load test, in Fig. 16. The results are referred to test SM_3. The theoretical strain values have been obtained by closed-form solutions reported in Faella et al. (2003).

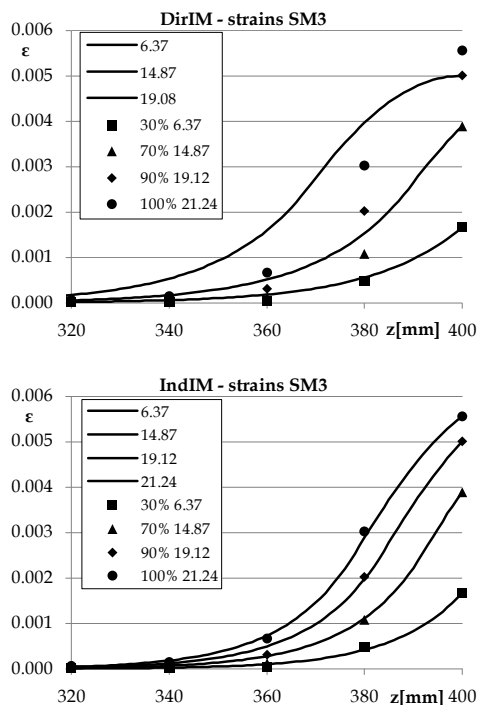


Fig. 16. Theoretical and experimental strains: (DirIM) Vs (IndIM)

The theoretical values of strains obtained assuming the interface relationship identified through IndIM are much closer to the observed ones than the values which can be derived assuming the τ -s relationship calibrated by means of DirIM. Finally it is worth observing that the experimental data can be simulated with good accuracy even if a simplified adhesion law (i.e. a bilinear adhesion law) is assumed.

4. Design formulae

The fracture energy, Γ_F , depends on both the strength properties of adherents, concrete and adhesive, and the properties of the concrete surface. When the reinforcement is correctly applied, the detachment of the reinforcement occurs with debonding in the concrete layer and the specific fracture energy of the interface law can be written in a form similar to that

used for the shear fracture (mode I). Therefore, in order to obtain design formulae, the fracture energy can be expressed as a function of the shear strength in the concrete: $\Gamma_F(\tau_{b,\max})$, where $\tau_{b,\max}$ depends on the tensile and compressive strength of concrete.

4.1 Theoretical formulations of debonding load

In most formulations the fracture energy is directly expressed as function of the tensile and/or compressive strength of concrete and it is also function of a shape factor depending on the FRP to concrete width (b_f/b_c).

Based on experimental tests, many theoretical formulations have been proposed in the past (Taljsten, 1994; Neubauer and Rostasy, 1997; Brosens and Van Gemert, 1997; fib bulletin, 2001; Chen and Teng, 2001; Smith and Teng, 2002; CNR-DT200, 2004; Lu et al., 2005; Seracino et al., 2007) to evaluate bond strength at the end of R.C. beams externally strengthened with FRP.

The lay out of the existing formulations is often similar; the differences are essentially related to the numerical coefficients calibrated on experimental results and to the eventual presence of safety factors. This last point is an important issue in using these formulations for design when the safety level (mean, characteristic or design provisions) has to be chosen. Some of these formulas are used to predict the bond strength at the intermediate crack too, through the exchange of some factors (Teng et al., 2003; Chen et al., 2006; CNR-DT200, 2004). For illustrative purposes an example of a calibration procedure of a simplified design relationship based on experimental data is reported in the following section. The example was made with reference to the theoretical relationship (67) suggested in CNR DT200-2004 but the procedure can be used to calibrate also different formulations.

$$N_{f,\max} = \frac{1}{\gamma_{f,d}\sqrt{\gamma_c}} \cdot \beta_L \cdot b_f \cdot \sqrt{k_G \cdot k_b} \sqrt{2 \cdot E_f \cdot t_f \cdot \sqrt{f_{ck} \cdot f_{ctm}}} \quad (67)$$

$$L_e = \sqrt{\frac{E_f \cdot t_f}{2 \cdot f_{ctm}}} \quad (68)$$

$$k_b = \sqrt{\frac{2 - b_f/b_c}{1 + b_f/400}} \quad (69)$$

$$\beta_L = \frac{L_b}{L_e} \cdot \left(2 - \frac{L_b}{L_e} \right) \quad \text{if} \quad L_b \leq L_e; \quad \beta_L = 1 \quad \text{otherwise} \quad (70)$$

f_{ck} being the characteristic value of cylindrical compressive strength of concrete, k_G a coefficient regarding the experimentally calibrated fracture energy and equal to 0.064 for mean value provision or 0.03 for design value. The safety factor for debonding failure, $\gamma_{f,d}$, is usually assumed equal to 1.2 or 1.5 (non-controlled or controlled gluing application); γ_c is the safety factor for concrete (equal to 1.5, EC2, 2004).

4.2 Simplified calibrating procedure

The mean value of the maximum axial strain in FRP corresponding to debonding failure can be expressed by means of a relationship obtained by a deterministic model and fine-tuned

on experimental data through a probabilistic approach, as suggested in (EN1990 – Annex D) and applied by Monti et Al. (2009).

By assuming a simplified formulation similar to the design relationship (67), taking into account no safety partial factors, the debonding strain can be expressed as:

$$\varepsilon_{fd}(k_{bf}, f_c, f_{ct}, E_f, t_f, b_f, k_b) = k_{bf} \cdot \sqrt{\frac{2 \cdot k_b \cdot \sqrt{f_c \cdot f_{ct}}}{E_f t_f}} \quad (71)$$

where the coefficient k_{bf} can be calibrated based on experimental results using a least-square procedure consisting in the resolution of the following minimum problem (Bilotta et al. 2011):

$$k_{bf} = \arg \min_{k_{bf}} \sum_{i=1}^n \left[\varepsilon_{fd}(k_{bf}, f_c^{(i)}, f_{ct}^{(i)}, E_f^{(i)}, t_f^{(i)}, b_f^{(i)}, k_b^{(i)}) - \varepsilon_{exp}^{(i)} \right]^2 \quad (72)$$

Furthermore, a random variable δ can be defined, for each i^{th} test, as the ratio of the experimental debonding strain, $\varepsilon_{exp,i}$ to the theoretical one, $\varepsilon_{fd,i}$ evaluated by considering the geometric and mechanical data characterizing that test:

$$\delta_i = \frac{\varepsilon_{exp,i}}{\varepsilon_{fd,i}} \quad (73)$$

The error function, δ , can cover the uncertainties of the simplified model considered as follows:

$$\varepsilon_{fd} = \varepsilon_{fd}(k_{bf}, f_c, f_{ct}, E_f, t_f, b_f, k_b) \cdot \delta \quad (74)$$

therefore, the mean value of the intermediate debonding strain can be obtained by a coefficient k_m , starting from k_{bf} adjusted by means of the mean value of the error parameter $\bar{\delta}$, being in general $\bar{\delta} \neq 1$ because the regression line is imposed to intercept the origin:

$$k_m = k_{bf} \cdot \bar{\delta} \quad (75)$$

Obviously, this strain is proportional to the debonding stress, being linear elastic the FRP constitutive law.

If the random variable represents a strength, its characteristic value is often defined for design purposes as the 0.05 percentile of the frequency distribution associated to the examined variable. Gauss distribution is the most generally considered for describing the errors. Assuming that the Young modulus of the FRP reinforcement, E_f , and the concrete tensile and compressive strengths, f_{ctm} and f_{cm} , are the only mechanical parameters influencing the value of the maximum axial strain developed in FRP at debonding, the expressions for the both general model and the calibrated one involving the coefficient k_{bf} as well as $\bar{\delta}$ are:

$$\varepsilon_{th} = \varepsilon_{th}(E_f, f_{cm}, f_{ctm}) \quad (76)$$

$$\varepsilon_{th,m} = \varepsilon_{th,m}(E_f, f_{cm}, f_{ctm}, \bar{\delta}, k_{bf}). \quad (77)$$

E_f , f_c and f_{ct} are assumed normally and independently distributed random variables, with a priori values of the coefficients of variation according to the design relationships provided by codes and literature information (Bilotta et al. 2011). Also the variable δ can be assumed as normally distributed. However, the hypothesis of normal distribution is required to be checked at least by comparing the experimental curve of the cumulative frequency to the theoretical one corresponding to a Gaussian distribution having the same mean value and standard deviation. Hence, under the hypothesis of normal distribution for the variable δ , the strain provision corresponding to the 0.05 percentile of the Gaussian distribution is:

$$\varepsilon_{th,k} = \varepsilon_{th,m} - 1.64 \cdot [\text{Var}(\varepsilon_{th,m})]^{0.5} \quad (78)$$

where the variance of $\varepsilon_{th,m}$ can be expressed as:

$$\text{Var}(\varepsilon_{th,m}) = C_{Efm}^2 \cdot \text{Var}(E_f) + C_{fcm}^2 \cdot \text{Var}(f_{cm}) + C_{fctm}^2 \cdot \text{Var}(f_{ctm}) + C_{\delta m}^2 \cdot \text{Var}(\delta_m) \quad (79)$$

$$C_{Efm} = \left| \frac{\partial \varepsilon_{th,m}}{\partial E_f} \right|_{\bar{E}_f}, C_{fcm} = \left| \frac{\partial \varepsilon_{th,m}}{\partial f_{cm}} \right|_{\bar{f}_{cm}}, C_{fctm} = \left| \frac{\partial \varepsilon_{th,m}}{\partial f_{ctm}} \right|_{\bar{f}_{ctm}}, C_{\delta m} = \left| \frac{\partial \varepsilon_{th,m}}{\partial \delta_m} \right|_{\bar{\delta}_m} \quad (80)$$

If the Eqs. (80) and (79) are substituted in the Eq. (78), the following general expression is obtained, providing the 0.05 percentile of the debonding load:

$$\varepsilon_{th,k} = \varepsilon_{th,m} - 1.64 \cdot \varepsilon_{th,m} \cdot [a \cdot \text{CoV}_{E_f}^2 + b \cdot \text{CoV}_{f_{cm}}^2 + c \cdot \text{CoV}_{f_{ctm}}^2 + \text{CoV}_{\delta_m}^2]^{0.5} \quad (81)$$

where the coefficient a , b , c depend on the functional relationship of E_f , f_{cm} and f_{ctm} in the expression of ε_{th} ; moreover the coefficients of variation are defined for each parameter as the ratio of the mean value to its standard deviation:

$$\text{CoV}_{E_f} = \frac{\bar{E}_f}{S_{E_f}}, \text{CoV}_{f_{ctm}} = \frac{\bar{f}_{ctm}}{S_{f_{ctm}}}, \text{CoV}_{f_{cm}} = \frac{\bar{f}_{cm}}{S_{f_{cm}}}, \text{CoV}_{\delta_m} = \frac{\bar{\delta}_m}{S_{\delta_m}} \quad (82)$$

Clearly the coefficient of variation of the variable δ_m , CoV_{δ_m} , depends on the data distribution. The Eq. (81) can be written as:

$$\varepsilon_{th,k} = k_k \cdot \varepsilon_{th} \quad (83)$$

assuming:

$$k_k = k_m \cdot \left(1 - 1.64 \cdot [a \cdot \text{CoV}_{E_f}^2 + b \cdot \text{CoV}_{f_{cm}}^2 + c \cdot \text{CoV}_{f_{ctm}}^2 + \text{CoV}_{\delta_m}^2]^{0.5} \right). \quad (84)$$

Lower percentiles can be obtained by substituting in the Eq. (78) the coefficient 1.64, related to the 0.05 percentile of the frequency distribution, with the coefficients 2.58 and 3.08 corresponding to the 0.005 and 0.001 percentiles, respectively.

The use of percentiles lower than 0.05 can be alternative to the use of safety factors that usually have to be additionally applied to characteristic provision to take into account the model uncertainty (EN1990 - Annex D).

In Table 2 the coefficient k_m and the R^2 , that is a measure of the reliability of the regression, are reported: two different experimental samples were considered for sheets and plates respectively. Note that for the cured-in-situ FRP systems (sheet) the R^2 value is quite high (0.855); on the contrary for the preformed systems (plate) the R^2 value is quite low (0.349), mainly due to a higher scattering of the experimental data.

In addition the mean value of the variable δ_m and its CoV are reported. In both cases the CoV, that represents a measure of the model significance, is lower than the threshold value of 40% (Monti et al., 2009) so that all the models can be considered reliable.

Finally, Table 2 shows that different scattering of experimental data leads to very different 0.05, 0.005 and 0.001 percentile of the calibrating coefficient k , for sheet and plate respectively.

FRP type	k_m	R^2	$\bar{\delta}_m$	CoV_{δ_m}	$k_m \cdot \bar{\delta}_m$	$k_{k,5\%}$	$k_{k,0.5\%}$	$k_{k,0.1\%}$
Sheet	0.270	0.855	1.027	17.7%	0.278	0.192	0.143	0.117
Plate	0.236	0.349	1.064	23.2%	0.251	0.152	0.095	0.064

Table 2. Statistical data

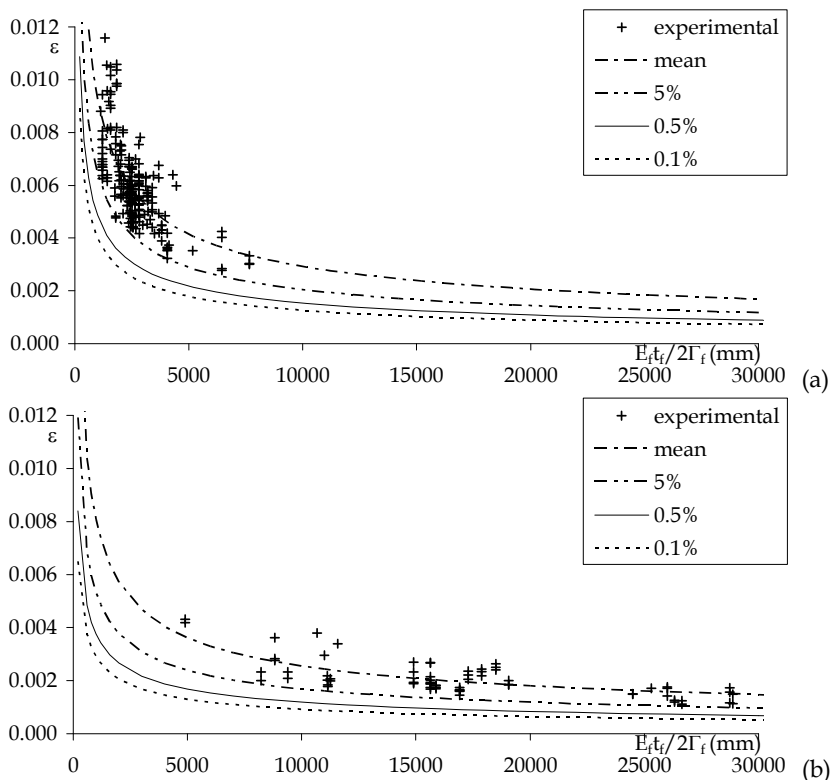


Fig. 17. Theoretical and experimental strains: sheets (a) and plates (b)

Theoretical debonding strain (71) are plotted in Fig. 17a,b versus the parameter $E_f t_f / k_b \sqrt{f_{cm} f_{ctm}}$, for sheets and plates respectively. Each curve is obtained with reference to each percentile of the k coefficient reported in Table 2. Theoretical debonding strains, obtained by means the calibrating procedure showed above, can be easily compared with experimental ones (singular point).

5. Conclusions

A wide overview of the key contributions in understanding the mechanical behavior of FRP laminates bonded on a concrete substrate has been reported in this chapter. Several original contributions have been also proposed.

First of all, a general analytical model has been formulated for describing the distribution of shear and normal stresses within the adhesive layer connecting the FRP laminate to the substrate. The key dimensionless parameters governing such distributions have been clearly pointed out and their influence has been showed in numerical application. The possible simplification of that general analytical model in a simpler one based on the assumption of a layer of elastic springs connecting the FRP laminate to the substrate has been also proposed. This model leads to much simpler differential equations with a reasonable reduction of accuracy. Moreover, it can be easily extended to the nonlinear branch, especially in the case of a supposed bi-linear (namely, elastic-softening) behaviour of the interface in terms of relationship between shear stresses and interface slip. Closed-form solutions of the stress and strain distribution throughout the FRP laminate can be derived under this assumption.

Those closed-form solutions can be employed for identifying the actual properties of the interface relationship. The numerical stability of an indirect-identification procedure based on those solutions has been demonstrated in the section 3 of this chapter. Moreover, it has been showed that the experimental data can be simulated with good accuracy even if a simplified adhesion law (i.e. a bilinear adhesion law) is assumed.

The values of the mechanical properties of the adhesive FRP-to-concrete interface obtained by some experimental tests available in the scientific literature have been finally utilized for calibrating simplified design-oriented formulae for determining the values of the maximum axial strains which can be developed in the FRP laminate before the onset of the debonding phenomenon. The effect of both the material randomness and the model uncertainties in defining the characteristic value of the axial strain in FRP at debonding have been handled by means of a well-established statistical procedure.

6. References

- Achintha P. M. M. & Burgoyne C. J. (2008). Fracture Mechanics of Plate Debonding, *ASCE Journal for Composites for Construction*, Vol. 12, No. 4, July/August 2009, 396-404, ISSN 1090-0268
- ACI 440.2R-08 (2008). Guide for the Design and Construction of Externally Bonded FRP Systems for Strengthening Concrete Structures. *ACI440.2R-08* American Concrete Institute, Farmington Hills, MI, 2008, 76 pp.

- Arduini M. & Nanni A. (1997). Behavior of precracked RC beams strengthened with carbon FRP sheets, *ASCE Journal for Composites for Construction*, Vol. 1, No. 2, 63-70, ISSN 1090-0268
- Bilotta A., Ceroni F., Di Ludovico M., Nigro E. & Pecce M. (2011). Bond Tests on concrete elements strengthened with EBR and NSM FRP systems, *Proceedings of FRP RCS 10*, Tampa, Florida, April 2011, accepted.
- Bilotta A., Ceroni F., Nigro E. & Pecce M. (2011). Design by testing of debonding load in RC element strengthened with EBR FRP materials, *Proceedings of FRP RCS 10*, Tampa, Florida, April 2011, accepted.
- Bilotta A, Di Ludovico M. & Nigro E. (2009). Influence of effective bond length on FRP-concrete debonding under monotonic and cyclic actions. *Proceedings of 9th International Symposium on Fiber Reinforced Polymer Reinforcement for Concrete Structures*, Sydney (Australia), July 2009 (CD ROM).
- Bizindavyi L. & Neale K. W. (1999). Transfer lengths and bond strengths for composites bonded to concrete, *ASCE Journal for Composites for Construction*, Vol. 3, No. 4, July/ August 1999, 153-160, ISSN 1090-0268
- Blontrock, H., Taerwe, L. & Vanwalleghem, H. (2002). Bond testing of externally glued FRP laminates at elevated temperature, *Proceedings of the International Symposium "Bond in Concrete: from research to standards"*, 648-654, ISBN 963-420-714-6, Budapest, November 2002, Publisher, City
- Bonacci J.F. (1996). Strength, Failure Mode and Deformability of Concrete Beams Strengthened Externally with Advanced Composites, *Proceedings of the 2nd International Symposium on Advanced Composite Materials in Bridges and Structures*, ISBN, Montreal (Canada), 419-426, Publisher, City
- Ceroni, F., Pecce, M., Matthys, S. & Taerwe, L. (2008). Bond tests on concrete elements with CFRP and anchorage systems, *Composites: Part B - Elsevier*, Vol. 39, No.3, April 2008, 429-441, ISSN 1359-8368
- Ceroni F. & Pecce M. (2010). Evaluation of bond strength and anchorage systems in concrete elements strengthened with CFRP sheets, *ASCE Journal of Composites in Construction*, in press, ISSN 1090-0268
- Chajes M.J., Finch W.W., Januszka T.F. & Thomson T.A. (1996). Bond and force transfer of composite-material plates adhered to concrete, *ACI Structural Journal*, Vol. 93, No. 2, February 1996, 208-217, ISSN 0889-3241
- Chen J.F. & Teng J.G. (2001): Anchorage Strength Models for FRP and Plates Bonded to Concrete, *ASCE Journal of Structural Engineering*, Vol. 127, No. 7, July 2001, 784-791, ISSN 0733-9445
- CNR-National Council for Research (2004), *Guide for the Design and Construction of Externally Bonded FRP Systems for Strengthening Existing Structures-Materials, RC and PC structures, masonry structures*
- Czaderski C., Soudki K. & Motavalli M. (2010). Front and Side View Image Correlation Measurements on FRP to Concrete Pull-Off Bond Tests, *ASCE Journal for Composites for Construction*, Vol. 14, No. 4, July/ August 2010, 451-463, ISSN 1090-0268
- European Committee for Standardization. *EN 1990 - Eurocode - Basic of Structural Design*. 2002.
- Faella C., Martinelli E. & Nigro E. (2002). Aderenza tra calcestruzzo e Lamine di FRP utilizzate come placcaggio di elementi inflessi. Parte II: modelli teorici ed

- elaborazioni numeriche, Proceedings of the XIV C.T.E. Conference, Mantua (Italy), 7-8 November 2002, 237-245, (in Italian);
- Faella C., Martinelli E. & Nigro E. (2008). Formulation and Validation of a Theoretical Model for Intermediate Debonding in FRP Strengthened RC Beams, *Composites Part B*, Vol. 39, No. 4, 645-655, June 2008, ISSN 1359-8368
- Faella C., Martinelli E. & Nigro E. (2009). Direct versus Indirect Method for Identifying FRP-to-Concrete Interface Relationships, *ASCE Journal for Composites for Construction*, Vol. 13, No. 3, May/June 2009, 226-233, ISSN 1090-0268
- fib Bulletin No. 14 (2001). *Externally bonded FRP reinforcement for RC structures*, Technical report, ISBN 978-2-88394-054-3, Lausanne (CH)
- Hart-Smith, L. J. (1973). Adhesive-bonded double-lap joints, NASA Technical Report, CR-112235, Hampton, Va. (USA)
- Lee Y. J., Boothby T. E., Bakis C. E. & Nanni A. (1999). Slip Modulus of FRP Sheets Bonded to Concrete, *ASCE Journal of Composites for Construction*, Vol. 3, No. 4, November 1999, 161-167, ISSN 1090-0268
- Lu X.Z., Teng J.G., Ye L.P. & Jiang J.J. (2005). Bond-slip models for FRP sheets/plates bonded to concrete, *Engineering Structures*, Vol. 27, No. 6, May 2005, 920-937, ISSN 0141-0296
- Mazzotti C., Savoia M. & Ferracuti B. (2009). A new single-shear set-up for stable debonding of FRP-concrete joints, *Construction and Building Materials - Elsevier*, Vol. 23, No.4, April 2009, pp. 1529-1537. ISSN 0950-0618
- Malek A. M., Saadatmanesh H. & Ehsani M. R. (1998). Prediction of failure load of R/C beams strengthened with FRP plate due to stress concentration at the plate end, *ACI Structural Journal*, Vol. 95, No. 2, March/April 1998, 142-152, ISSN 1090-0268
- Meier U. (1987). Brückensanierungen mit Hochleistungs-Faserverbundwerkstoffen, *Material und Technik*, Vol. 15, No 4, 125-128 ISSN
- Meier U. (1995). Strengthening of structures using carbon fibre/epoxy composites, *Construction and Building Materials*, Vol. 9, No. 6, June 1995, 341-351, ISSN 0950-0618
- Monti G., Alessandri S. & Santini S. (2009). Design by Testing: A Procedure for the Statistical Determination of Capacity Models, *Journal of Construction and Building Materials, Special Issue on FRP Composites Elsevier*, Vol. 23, 1487-1494. ISSN 0950-0618
- Motavalli M. & Czaderski C. (2007). FRP Composites for Retrofitting of Existing Civil Structures in Europe: State-of-the-Art Review, *Proceedings of the American Composites Manufacturers Association 2007*, ISBN, Tampa, FL (USA), October 2007, Publisher, City
- Naaman A.E., Park S.Y., Lopez M.M. & Till R.D. (2001). Parameters Influencing the Flexural Response of RC Beams Strengthened Using CFRP Sheets, *Proceedings of the Conference FRPRCS-5*, Cambridge (UK), 117-125, ISBN 0727730290
- Neubauer, U. & Rostasy, F.S. (1997). Design Aspects of Concrete Structures Strengthened with Externally Bonded CFRP Plates, Concrete and Composites, *Proceedings of 7th International Conference On Structural Faults and Repair*, Vol. 2, 109-118, ISBN, ECS Pub. Edinburgh, Scotland.

- Nigro E., Di Ludovico M. & Bilotta A. (2008). FRP- Concrete Debonding: experimental Tests under Cyclic Actions, *Proceedings of 14th World Conference on Earthquake Engineering*, ISBN, Beijing (China), October 2008, Publisher, City
- Oehlers D.J., Moran J.P. (1990). Premature failure of externally plated reinforced-concrete beams, *Journal of Structural Engineering - ASCE*, Vol. 116, No.4, April, 1990, 978-995. ISSN 0733-9445
- Rabinovich O. & Frostig, Y. (2000). Closed-form High-order Analysis of RC Beams Strengthened with FRP Strips, *ASCE Journal of Composites for Construction*, Vol. 4, No. 2, March-April 2000, 65-74, ISSN 1090-0268
- Rabinovich O. & Frostig, Y. (2001). Delamination Failure of RC Beams Strengthened with FRP Strips—A Closed-Form High-Order and Fracture Mechanics Approach, *Journal of Engineering Mechanics*, Vol. 127, No. 8, August 2001, ISSN 0733-9399
- Roberts T.M. (1989). Approximate analysis of shear and normal stress concentrations in the adhesive layer of plated RC beams, *The Structural Engineer*, Vol. 67, No. 12, December 1989, 229-233, ISSN 0039-2553
- Savoia M., Bilotta A., Ceroni F., Di Ludovico M., Fava G., Ferracuti B., Mazzotti C., Nigro E., Olivito R., Pecce M. & Poggi C., (2009). Experimental round robin test on FRP concrete bonding, *Proceedings of FRPRCS9*, Sydney (Australia), July, 2009 (CD ROM).
- Smith S.T. & Teng J.G. (2001), Strength Models for Plate End Debonding in FRP-Strengthened RC Beams, *Proceedings of the Conference FRPRCS-5*, ISBN 0727730290, Cambridge (UK), 419-428, 2001, Publisher, City
- Smith S. T. & Teng J. G. (2002). FRP-strengthened RC beams. I: review of debonding strength models, *Engineering Structures*, Vol. 24, No. 4, April 2002, 385-395, ISSN 0141-0296
- Swamy R.N., Jones R. & Bloxham J.W. (1987). Structural behaviour of reinforced concrete beams strengthened by epoxy-bonded steel plates, *The Structural Engineer*, Vol. 65A, No. 2 February 1987, 59-68, ISSN 0039-2553
- Taljsten B. (1996). Strengthening of concrete prisms using the plate bonding technique, *International Journal of Fracture*, Vol. 82, No., 253-266, ISSN 0376-9429
- Taljsten B. (1997). Strengthening of beams by plate bonding, *ASCE Journal of Materials in Civil Engineering*, Vol. 9, No. 4, November 1997, 206-211, ISSN 1943-5533
- Teng J.G., Chen J.F., Smith S.T. & Lam L. (2002). *FRP Strengthened RC Structures*, John Wiley & Sons Ltd., ISBN 0-471-48706-6, 245pp. Chichester (UK)
- Teng J. G., Smith S. T., Yao J. & Chen J. F. (2003). Intermediate crack-induced debonding in RC beams and slabs, *Construction and Building Materials*, Vol. 17, No. 6-7, September-October 2003, 447-462, ISSN 0950-0618
- Tounsi A., Hassaine Daouadji T., Benyoucef S. & Addabedia E.A. (2009). Interfacial stresses in FRP-plated RC beams: Effect of adherend shear deformations, *International Journal of Adhesion & Adhesives - Elsevier*, Vol. 29, No. 4, June, 2009, 343-351, ISSN 0143-7496
- Triantafillou T., Matthys S. & Taerwe L. (2001). Design of Concrete Members Strengthened with Externally Bonded FRP Reinforcement, *Proceedings of the Conference FRPRCS-5*, Cambridge (UK), 157-166, ISBN 0727730290, Publisher, City

- Wu, Z., Yuan, H. & Niu, H. (2002). Stress transfer and fracture propagation in different kinds of adhesive joints, *ASCE Journal of Engineering Mechanics*, Vol. 128, No. 5, May 2002, 562-573, ISSN: 0733-9399
- Yao J., Teng J.G. & Chen J.F. (2005). Experimental study on FRP-to-concrete bonded joints, *Composites: Part B*, Elsevier, Vol. 36, No. 2, March, 2005, 99-113, ISSN 1359-8368
- Yuan H., Chen J.F., Teng J.G., Lu X.Z. (2007). Interfacial stress analysis of a thin plate bonded to a rigid substrate and subjected to inclined loading, *International Journal of Solids and Structures*, Vol. 44, No. 16, August 2007, ISSN 0020-7683

Part 5

Characterization and Thermal Behaviour

Estimation of the Degree of Anisotropy and Overall Elastic Stiffness of Advanced Anisotropic Materials

Mohamed S. Gaith and Imad Alhayek

*Department of Mechanical Engineering, Al-Balqa Applied University, Amman,
Department of Applied Sciences, Al-Balqa Applied University, Amman,
Jordan*

1. Introduction

Most of the elastic materials in engineering are, with acceptable accuracy, considered as anisotropic materials; metal crystals (due to the symmetries of the lattice), fiber-reinforced composites, polycrystalline textured materials, biological tissues, rock structure etc. can be considered as orthotropic materials. In recent years fiber reinforced composite materials have been paid considerable attentions due to the search for materials of light weight, great strength and stiffness. Consequently the determination of their mechanical properties, i.e. stiffness effect, becomes important.

Piezoelectric materials nowadays have been widely used to manufacture various sensors, conductors, actuators, and have been, extensively, applied in electronics, laser, ultrasonics, naval and space navigation as well as biologics, smart structures and many other high-tech areas.

The wide-gap II-VI semiconductors, well known anisotropic materials used in high technology, have received much attention in the past decades since they have important applications in short-wavelength light-emitting diodes (LEDs), laser diodes and optical detectors (Okuyama, 1992). Moreover, semiconductor materials constitute today basic components of emitters and receivers in cellular, satellite, fiberglass communication, solar cells, and photovoltaic systems. Their electronic and structural properties of such systems are subject of considerable interest in nanotechnology as well. For the semiconductor compounds ZnX and CdX ($X=S, Se, \text{ and } Te$), the zinc-blend structure (ZB) has the lowest minimum total energy. With respect to classical II-VI semiconductors, these semiconductor compounds have attracted much attention in recent years for their great potential in technological applications (Reich, 2005). They have a high melting point, high thermal conductivity, and large bulk modulus. The hardness and large bulk modulus of these anisotropic materials make them ideal protective coating materials in photovoltaic applications and in machine tools (Reich, 2005). These materials can, therefore, be used for optoelectric devices in which the availability of light sources in the mid-infrared spectral region is crucial for many applications, i. e., molecular spectroscopy and gas-sensor systems for environmental monitoring or medical diagnostics (Leitsmann et al., 2006). Being stable to high temperatures and can be made of sufficiently insulating allows precise measurements

of piezoelectric, elastic, and dielectric constants. For such data eventually a fully quantum-mechanical description is essential in order to serve to verify a quantitative theory of piezoelectricity and elasticity in these structures. The window layer compounds CuInSe_2 , CuInS_2 , AgGaSe_2 , and AgGaS_2 have a chalcopyrite structure that is closely related those of zinc blend and wurtzite structures. These compounds are found in many applications such as fiberglass communication, thin film solar cells, and photovoltaic systems. Thin film solar cells made from ternary chalcopyrite compounds, such as the aforementioned heterojunction layers, are characterized by low-cost and clean energy sources. Their high absorption and resistance to deterioration make them good candidate materials for solar cell absorbers. Moreover, due to their flexible optical properties and good stabilities, they are promising compounds for fabricating polycrystalline thin film heterojunction solar cells (Ramesh et al., 1999; Ramesh et al., 1998; Murthy et al.; 1991). Yet, the significant discrepancy in the efficiency of solar cells between the laboratory scale, over 19% (Murthy et al.; 1991), and the commercial one, around 13 %, is due to the lack of fundamental understanding of interface and junction properties in the film.

Historically, the study of anisotropic elastic materials has been synonymous with study of crystals. For a deep understanding of the physical properties of these anisotropic materials use of tensors is inevitable. Tensors are the most apt mathematical entities to describe direction-dependent-physical properties of solids, and the tensor components characterize physical properties which must be specified without reference to any coordinate system. When all the directions in the material can be considered as equivalent the physical property is isotropic, and consequently, the choice of the reference frame is of no real importance. More often the medium is anisotropic and tensor notation can not be avoided. Specifying the values of the tensor components which represent physical properties of crystals, as Nowacki(Nowacki, 1962) points out, do not determine the material constants directly since their values vary with the direction of the coordinate axes. It is, therefore, natural to seek to characterize physical properties of crystals by constants whose values do not depend upon the choice of the coordinate system, i.e. constants which are invariant under all coordinate transformations. Some of such invariants have been obtained using different decomposition methods in the case of photoelastic coefficients ((Srinivasan & Nigam, 1968)), piezoelectric coefficients (Srinivasan, 1970) and elastic stiffness coefficients (Srinivasan et al. (Srinivasan & Nigam, 1968; Srinivasan, 1969; Srinivasan, 1985). A physical property is characterized by a rank tensor that has two kinds of symmetry properties. The first kind is due to an intrinsic symmetry derives from the nature of the physical property itself, and this can be established by the thermodynamical arguments or from the indispensability of some of the quantities involved. The second kind of symmetry is due to the geometric or crystallographic symmetry of the system described.

The purpose of this chapter, hence, is to develop the existing methods of decomposing Cartesian tensors into orthonormal basis using invariant-form to decompose some well-known tensors into orthonormal tensor basis. Next, as an outcome of these decompositions, to investigate the contributions to the formulation of the physical properties of elastic stress, strain, piezoelectric and elastic stiffness anisotropic materials. Finally, the concept of norm and norm ratios is introduced to measure the overall effect of material properties and to measure the degree of anisotropy. Numerical engineering applications are introduced for several engineering materials like semiconductor compounds, piezoelectric ceramics and fiber reinforced composites.

2. Form invariants and orthonormal basis elements

The decomposition methods of tensors have many applications in different subjects of engineering. In the mechanics of continuous media i.e. in elasticity studies; so far, the stress and strain tensors are decomposed into spherical (hydrostatic) and deviatoric parts, the hydrostatic pressure is connected to the change of volume without change of shape, whereas the change of shape is connected to the deviatoric part of the stress.

The anisotropic elastic properties represented by the fourth rank tensor of elastic coefficients is designated as the elasticity tensor. The constitutive relation for linear anisotropic elasticity is the generalized Hooke's law

$$\sigma_{ij} = C_{ijkl} \varepsilon_{kl} \quad (1)$$

which is the most general linear relation between the stress tensor whose components are σ_{ij} and the strain tensor whose components are ε_{kl} . The coefficients of linearity, namely C_{ijkl} , are the components of the fourth rank elastic stiffness tensor. The elastic properties of crystals appear to be well described in terms of symmetry planes. Symmetry planes (i.e. planes of mirror symmetry) were defined, for example, by Spencer (Spencer, 1983). Cowin et al. (Cowin & Mehrabadi, 1987) classified the known elastic symmetries of materials and ordered materials on the basis of symmetry planes. Cowin et al. (Cowin & Mehrabadi, 1987), and Hue and Del Piero (Hue & Del Piero, 1991) listed ten symmetry classes. There are three important symmetry restrictions on C_{ijkl} that are independent of those imposed by material symmetry:

$$C_{ijkl} = C_{jikl}, \quad C_{ijkl} = C_{ijlk}, \quad C_{ijkl} = C_{klij} \quad (2)$$

which follow from the symmetry of the stress tensor, the symmetry of the strain tensor, and the thermodynamic requirement that no work be produced by the elastic material in a closed loading cycle, respectively (Srinivasan, 1998; Blinowski, A. & Rychlewski, 1998). The number of independent components of a fourth rank tensor in three dimensions is 81, but the restrictions in (2) reduce the number of independents of C_{ijkl} to 21, which corresponds to the most asymmetric elastic solid, namely triclinic media. Since it has 21 independent components, there is considerable information on the material properties apparent a decomposition of C_{ijkl} into orthonormal tensor basis would be of interest.

The determination of the class system of an elastic medium from its elastic constants in an arbitrary coordinate is not a trivial matter. The problem has been studied thoroughly by several authors (Srinivasan, 1969; Srinivasan, 1985; Spencer, 1983; Cowin & Mehrabadi, 1987; Hue & Del Piero, 1991; Srinivasan, 1998; Blinowski & Rychlewski, 1998; Tu, 1968).

Another interesting material property in anisotropic solids is the direct piezoelectric effect that comprises a group of phenomena in which the mechanical stresses or strains induce in crystals an electric polarization (electric field) proportional to those factors. Besides, the mechanical and electrical quantities are found to be linearly related as following (Srinivasan, 1998).

$$P_i = d_{ijk} \sigma_{jk} \quad (3)$$

where P_i and σ_{jk} denote the components of the electric polarization vector and the components of the mechanical stress tensor, respectively, and d_{ijk} are the piezoelectric coefficients forming a third rank tensor. The piezoelectric tensor is a third rank tensor symmetric with respect to the last two indices

$$d_{ijk} = d_{ikj} \quad (4)$$

with 18 coefficients for the noncentrosymmetric triclinic case. Considerable information on the material properties apparent a decomposition of d_{ijk} into orthonormal tensor basis would be of interest, as well.

In writing out tensors which represent physical properties of solid materials, it is customary to choose a Cartesian frame reference which has a specific orientation with respect to the material coordinate axes. A physical property is characterized by n rank tensor that has two kinds of symmetry properties. The first kind is due to an intrinsic symmetry derives from the nature of the physical property itself, and this can be established by the thermodynamical arguments or from the indispensability of some of the quantities involved. The second kind of symmetry is due to the geometric or crystallographic symmetry of the system described.

The symmetry properties of the material may be defined by the group of orthonormal transformations which transform any of these triads into its equivalent positions. For each of the symmetry classes, we will choose as reference system a rectangular Cartesian coordinate system $Oxyz$, so related to the material directions v_1, v_2, v_3 in the material under consideration that the symmetry of the material may be described by one or more of the transformations. Transformations in which the coefficients satisfy the orthogonality relations are called linear orthogonal transformations. In this formulation, the number of elastic constants and their values do not depend on the choice of the coordinate system.

The form-invariant expressions for the electrical susceptibility components, the piezoelectric coefficients and the elastic stiffness coefficients are, respectively

$$\chi_{ij} = v_{ai} v_{bj} A_{ab} \quad (5)$$

$$d_{ijk} = v_{ai} v_{bj} v_{ck} A_{abc} \quad (6)$$

$$C_{ijklm} = v_{ai} v_{bj} v_{ck} v_{dm} A_{abcd} \quad (7)$$

Where summation is implied by repeated indices, v_{ai} are the components of the unit vectors v_a ($a=1,2,3$) along the material directions axes. The quantities A_{ab} , A_{abc} , A_{abcd} are invariants in the sense that when the Cartesian system is rotated around $Ox'y'z'$, where v_1, v_2, v_3 form a linearly independent basis in three dimensions but are not necessarily always orthogonal. Their relative orientations in the seven crystal systems are well known (Ikeda, 1990). The corresponding reciprocal triads satisfy the relations

$$v_{aj}^{ai} v_{aj} = \delta_{ij} \quad (8)$$

2.1 Second rank tensors

In the theory of linear elasticity, the relation between the stress and strain in a solid body is usually described by Hooke's law which postulates a linear relation between the two. The stress-strain relations for elastic anisotropic material have not been very well established as compared to those of the isotropic material in the classical theory of elasticity. The symmetry properties of the material, due to the geometric or crystallographic symmetry, may be defined by the group of orthonormal transformations which transform any of its triads v_a into its equivalent positions. For the monoclinic symmetric second rank tensor, for instance, the basis elements can be found depending on the form invariant for the monoclinic system. Its form invariant expression, with v_2 normal to the $v_1 v_3$ plane, can be written as

$$\sigma_{ij} = A_{11} v_{1i} v_{1j} + A_{22} v_{2i} v_{2j} + A_{33} v_{3i} v_{3j} + A_{31} (v_{3i} v_{1j} + v_{1i} v_{3j}) \quad (9)$$

where v_{ai} are the components of the unit vectors v_a ($a = 1, 2, 3$) along the material directions axes. The corresponding reciprocal triads satisfy the relations (Srinivasan, 1998)

$$v_{aj}^{ai} v_{aj} = \delta_{ij}$$

using (8) and orthonormalization by the well known Gram-Schmidt scheme, the four basis elements of the monoclinic system are obtained (Srinivasan, 1998):

$$\begin{aligned} T_{ij}^I &= \frac{1}{\sqrt{4}} \delta_{ij} \\ T_{ij}^{II} &= \frac{1}{\sqrt{2}} (2\delta_{ij} \delta_{1i} \delta_{1j} + \delta_{3i} \delta_{3j} - \delta_{ij}) \\ T_{ij}^{III} &= -\frac{1}{\sqrt{6}} (3\delta_{3i} \delta_{3j} - \delta_{ij}) \\ T_{ij}^{IV} &= \frac{1}{\sqrt{2}} (\delta_{3i} \delta_{1j} + \delta_{1i} \delta_{3j}) \end{aligned} \quad (10)$$

It is well known that for a symmetric second order tensor is of dimension six; an orthonormal basis set of six elements can be constructed. By taking cyclic permutation of {1, 2, 3}; the elements V and VI can be generated from IV in (10) as

$$\begin{aligned} T_{ij}^V &= \frac{1}{\sqrt{2}} [\delta_{1i} \delta_{2j} + \delta_{2i} \delta_{1j}] \\ T_{ij}^{VI} &= \frac{1}{\sqrt{2}} [\delta_{2i} \delta_{3j} + \delta_{3i} \delta_{2j}] \end{aligned} \quad (11)$$

A complete orthonormal basis for the second rank symmetric tensor will be the set {I, II, ..., VI}. The decomposition of σ_{ij} is given in terms of these basis elements as

$$\sigma_{ij} = \sum_k (\sigma, T_{ij}^k) T_{ij}^k, \quad (k = I, II, \dots, VI) \quad (12)$$

where (σ, T_{ij}^k) represents the inner product of and the k^{th} elements, T_{ij}^k , of the basis. Hence, the second rank symmetric tensor is decomposed into six orthonormal terms expressed in matrix form:

$$\begin{aligned} \sigma_{ij} = & \begin{bmatrix} \frac{1}{3}\sigma_{pp} & 0 & 0 \\ 0 & \frac{1}{3}\sigma_{pp} & 0 \\ 0 & 0 & \frac{1}{3}\sigma_{pp} \end{bmatrix} + \begin{bmatrix} \frac{1}{2}(2\sigma_{11} + \sigma_{33} - \sigma_{pp}) & 0 & 0 \\ 0 & \frac{1}{2}(-2\sigma_{11} - \sigma_{33} + \sigma_{pp}) & 0 \\ 0 & 0 & 0 \end{bmatrix} + \\ & + \begin{bmatrix} \frac{1}{6}(-3\sigma_{33} - \sigma_{pp}) & 0 & 0 \\ 0 & \frac{1}{6}(-3\sigma_{33} - \sigma_{pp}) & 0 \\ 0 & 0 & \frac{1}{6}(6\sigma_{33} - 2\sigma_{pp}) \end{bmatrix} + \begin{bmatrix} 0 & 0 & \sigma_{13} \\ 0 & 0 & 0 \\ \sigma_{13} & 0 & 0 \end{bmatrix} + \\ & + \begin{bmatrix} 0 & \sigma_{12} & 0 \\ \sigma_{12} & 0 & 0 \\ 0 & 0 & 0 \end{bmatrix} + \begin{bmatrix} 0 & 0 & 0 \\ 0 & 0 & \sigma_{23} \\ 0 & \sigma_{23} & 0 \end{bmatrix} \quad (13) \end{aligned}$$

From (13), the second rank symmetric tensor, σ_{ij} , is decomposed into six terms, each of which has a physical meaning. Also, the second rank symmetric tensor is virtually decomposed into two parts:

$$\sigma_{ij} = \frac{1}{3}\sigma_{pp}\delta_{ij} + (\sigma_{ij} - \frac{1}{3}\sigma_{pp}\delta_{ij}) \quad (14)$$

From (14), it is clear that the symmetric second rank stress tensor is decomposed into spherical (hydrostatic pressure) part, $\frac{1}{3}\sigma_{pp}\delta_{ij}$, which is the first term of (13), and the

deviatoric part, $(\sigma_{ij} - \frac{1}{3}\sigma_{pp}\delta_{ij})$, which is the sum of the other five terms of (13). Hence, it is

shown that the method is able to decompose the symmetric second rank stress (and strain, in a similar manner) tensors into the spherical part which is connected to the change of volume without change of shape, and into deviatoric part, which is connected to the change of shape. This result is very well known in the literature. On the other hand, this method is introducing a new form of decomposition, which has a more featured and transparent

physical information. It is easily verified that the sum of the six decomposed tensors is the symmetric second rank tensor, σ_{ij} . Physically, each of the six tensor parts is associated with a distinct type of deformation; the first part of (13) represents the spherical (hydrostatic pressure) effect, the second and third parts represent combined simple extension or contraction along the various symmetry axes. The second term could be, for example, stress of a non-uniform distribution of pure shear stress, which occurs in a long rod subjected to pure torsion, while the last three parts represent simple shearing in the symmetry planes. Besides, the deviatoric part of the stress tensor is decomposed into traceless tensors each of them is related to shearing which represents a general symmetric second rank tensor (stress and strain tensors). The results agree with previous studies considered as special cases of this general case, for instance, Blinowski et al. (Blinowski & Rychlewski, 1998) have decomposed a tensor of only shear into exactly identical forms to the last three terms of (13) for this specific case.

2.2 Third rank tensors

In the continuum approach to the study of anisotropic solids it is well known that certain physical properties can be represented by tensors. The polarization of a crystal produced by an electric field is an example of an anisotropic material property that is represented by tensors. If a stress is applied to certain crystals they develop an electric moment whose magnitude is proportional to the applied stress; known as piezoelectric effect. The piezoelectric effect in materials has not attracted much attention until after the Second World War, since when the applications and the research of piezoelectric materials have advanced greatly. Piezoelectric materials nowadays have been widely used to manufacture various sensors, conductors, actuators, resonators, oscillators and monitors. They also play an important role in the so-called smart structures. In fact, piezoelectric materials have been applied extensively in electronics, laser, ultrasonics, microsonics, naval and space navigation as well as biologies and many other high-tech areas. The piezoelectric coefficients appear in the equation $P_i = d_{ijk} \sigma_{jk}$, where P_i are the components of the electrical polarization vector and σ_{jk} , the components of the stress tensor. The form invariant expressions are derived for many classes of piezomagnetic (Srinivasan, 1970), and piezoelectric coefficients (Tsai, 1992). Although such constitutive equations are form invariant with respect to arbitrary orthogonal coordinate transformations, the coefficients, d_{ijk} , do not determine directly the material constants since their values vary with the direction of the coordinate axes. The piezoelectric coefficients with the following symmetry $d_{ijk} = d_{ikj}$ the number of non-vanishing independent coefficients is reduced from 27 to 18 independent coefficients for the triclinic system. For the monoclinic system, for example, of class 2, the number of independent coefficients is reduced to 8, for the orthotropic system of class mm2 is reduced to five coefficients, and for the hexagonal system of class 6mm is reduced to three independent coefficients. The form invariant expression for the hexagonal system class 6mm is (Srinivasan, 1970)

$$d_{ijk} = d_1 \delta_{3i} \delta_{3j} \delta_{3k} + d_2 (\delta_{3k} \delta_{ij} + \delta_{3j} \delta_{ik}) + d_3 \delta_{3i} \delta_{jk} \quad (15)$$

Following the same procedure used for second rank tensor, the basis elements are

$$\begin{aligned}
 T_{ijk}^I &= \delta_{3i} \delta_{3j} \delta_{3k} \\
 T_{ijk}^{II} &= \frac{1}{\sqrt{2}} (\delta_{3i} \delta_{jk} - \delta_{3i} \delta_{3j} \delta_{3k}) \\
 T_{ijk}^{III} &= \frac{1}{2} (\delta_{3k} \delta_{ij} + \delta_{3j} \delta_{ik} - 2\delta_{3i} \delta_{3j} \delta_{3k})
 \end{aligned} \tag{16}$$

The decomposition of d_{ijk} is given in terms of this basis elements as

$$\begin{aligned}
 d_{ijk} &= \sum_k (d_{ijk}^q) T_{ijk}^q, \quad (q = I, II, III) \\
 &= (d_{ijk}^I) T_{ijk}^I + (d_{ijk}^{II}) T_{ijk}^{II} + (d_{ijk}^{III}) T_{ijk}^{III}
 \end{aligned} \tag{17}$$

where (d_{ijk}^q) represents the inner product of d_{ijk} and q_{th} elements, T_{ijk}^q of the basis.

$$\begin{aligned}
 d_{ijk} &= \begin{bmatrix} 0 & 0 & 0 & 0 & 0 & 0 \\ 0 & 0 & 0 & 0 & 0 & 0 \\ 0 & 0 & d_{33} & 0 & 0 & 0 \end{bmatrix} + \begin{bmatrix} 0 & 0 & 0 & 0 & 0 & 0 \\ 0 & 0 & 0 & 0 & 0 & 0 \\ \frac{1}{2}(d_{31} + d_{32}) & \frac{1}{2}(d_{31} + d_{32}) & 0 & 0 & 0 & 0 \end{bmatrix} + \\
 &+ \begin{bmatrix} 0 & 0 & 0 & \frac{1}{2}(d_{24} + d_{15}) & 0 & 0 \\ 0 & 0 & \frac{1}{2}(d_{24} + d_{15}) & 0 & 0 & 0 \\ 0 & 0 & 0 & 0 & 0 & 0 \end{bmatrix}
 \end{aligned} \tag{18}$$

Physically, we have decomposed the tensor d_{ijk} into three independent tensors, each has an independent piezoelectric coefficient. If a tensile stress σ_3 is applied parallel to x_3 which is a diad axis of the crystal, the first matrix in (18) shows that the components of polarization are given by the moduli in the third column of the first matrix. Thus, the decomposition that we present is decomposing the polarization along orthogonal axes into three parts; the first part is the polarization along the diad axes due to normal stress, the second part, the polarization along the nondiad orthogonal axes due to normal stress, and the third part, is the polarization due to the shear stresses.

2.3 Fourth rank tensors

Fourth rank tensors were introduced in specification of physical properties for several anisotropic media. A decomposition of these tensors into independent elementary tensors is undertaken, to offer valuable insight into the tensor structure. In an anisotropic material, the

elasticity symmetric tensor generally contains twenty-one non-zero distinct constants. When the material has some kind of symmetry, the number of these coefficients is reduced if the coordinate axes coincide with symmetry axes for the material.

In analyzing the mechanical properties of anisotropic linear elastic medium, a tensor of fourth rank is required to make up a linear constitutive relation between two symmetric second-rank tensors, each of which represents some directly detectable and measurable effect in the medium. The constitutive relation characterizing linear elastic anisotropic solids is the generalized Hook's law as expressed in (1). Due to the symmetries in (2), the number of elastic coefficients is reduced from 81 to 21 which correspond to the most asymmetric elastic solid, namely, triclinic medium. The presence of symmetry in a medium reduces still further the number of independent elastic coefficients. For example, monoclinic symmetry medium (Tu. 1968) reduces the number of the non-vanishing independent elastic coefficients to 13, similarly, orthotropic to 9, hexagonal to 5, cubic to 3 and isotropic medium (the most symmetry) to 2 elastic coefficients.

The isotropic system has the well defined form invariant as following (Srinivasan, 1968):

$$C_{ijkl} = A_1 \delta_{ij} \delta_{km} + A_2 \delta_{ik} \delta_{jm} + A_3 \delta_{im} \delta_{jk} \quad (19)$$

where A_1, A_2 and A_3 are constants, and later, Tu (Tu. 1968) has reduced the three tensors into two basis elements. Following the same procedure presented in previous sections, the decomposition of C_{ijkl} for the isotropic system is given in terms of the basis elements as:

$$\begin{aligned} C_{ijkl} &= \sum_k (C, T_{ijkl}^k) T_{ijkl}^k, \quad (k = I, II) \\ &= (C, T_{ijkl}^I) T_{ijkl}^I + (C, T_{ijkl}^{II}) T_{ijkl}^{II} \end{aligned} \quad (20)$$

where (C, T_{ijkl}^k) represents the inner product of C_{ijkl} and the k th elements, T_{ijkl}^k , of the basis, and

$$T_{ijkl}^I = \frac{1}{3} \delta_{ij} \delta_{km} \quad (21)$$

$$T_{ijkl}^{II} = \frac{1}{6\sqrt{5}} \delta_{ij} \delta_{km} (3(\delta_{ik} \delta_{jm} + \delta_{im} \delta_{jk}) - 2\delta_{ij} \delta_{km})$$

substituting these elements, then

$$\begin{aligned} C_{ijkl} &= \frac{1}{9} C_{ppqq} \delta_{ij} \delta_{km} + \\ &\quad \frac{1}{36(5)} (6C_{ppqq} - 2C_{ppqq}) (3(\delta_{ik} \delta_{jm} + \delta_{im} \delta_{jk}) - 2\delta_{ij} \delta_{km}) \end{aligned} \quad (22)$$

and in matrix form as:

$$C_{pq} = K_v \begin{bmatrix} 1 & 1 & 1 & 0 & 0 & 0 \\ 1 & 1 & 1 & 0 & 0 & 0 \\ 1 & 1 & 1 & 0 & 0 & 0 \\ 0 & 0 & 0 & 0 & 0 & 0 \\ 0 & 0 & 0 & 0 & 0 & 0 \\ 0 & 0 & 0 & 0 & 0 & 0 \end{bmatrix} + 2G_v \begin{bmatrix} \frac{2}{3} & -\frac{1}{3} & -\frac{1}{3} & 0 & 0 & 0 \\ -\frac{1}{3} & \frac{2}{3} & -\frac{1}{3} & 0 & 0 & 0 \\ -\frac{1}{3} & -\frac{1}{3} & \frac{2}{3} & 0 & 0 & 0 \\ 0 & 0 & 0 & \frac{1}{2} & 0 & 0 \\ 0 & 0 & 0 & 0 & \frac{1}{2} & 0 \\ 0 & 0 & 0 & 0 & 0 & \frac{1}{2} \end{bmatrix} \quad (23)$$

with

$$K_v = \frac{1}{9} C_{ppqq}$$

$$G_v = \frac{1}{10} (C_{pqpq} - \frac{1}{3} C_{ppqq})$$

K_v and G_v are the well known Voigt average polycrystalline bulk and shear modulus, respectively. Hence, the symmetric fourth rank elastic tensor of isotropic media is decomposed into two orthogonal terms. Equation (23) indicates that the isotropic symmetric fourth rank tensor, C_{ijkl} , is a subset of the general symmetric fourth rank elastic tensor, and decomposed into two terms, each of which has a distinct physical meaning, and the two terms are the same terms consisting the isotropic case. It is easily verified that the decomposed tensors form an orthogonal set, and their sum is the isotropic symmetric fourth rank tensor, C_{ijkl} , which is identical to those found by Nye (Nye, 1959).

In fact, the above results are the same as those given in (Tu, 1968; Nye, 1959; Voigt, 1889; Radwan, 1991; Ikeda, 1990). Thus, it has been established that macroscopically isotropic elastic coefficients, which were obtained by W. Voigt, can be obtained directly from the procedure developed. Moreover, this procedure is valid for the most anisotropic triclinic elastic tensor.

3. The concept of norm

The comparison of magnitudes of the norms can give valuable information about the origin of the physical property under examination. Since the norm is invariant in the material, the norm of a Cartesian tensor may be used as the most suitable representing and comparing the overall effect of a certain property of anisotropic materials of the same or different symmetry or the same material with different phases based on the crystallographic level (Spencer, 1983; Srinivasan, 1998; Tu, 1968; Nye, 1959; Voigt, 1889; Radwan, 1991; Ikeda, 1990). The larger the norm value, the more effective the property is. Generalizing the

concept of the modulus of a vector, a norm of a Cartesian tensor is defined as the square root of the contracted product over all the indices with itself (Srinivasan, 1998; Tu, 1968; Radwan, 1991). Since the constructed basis in this method is orthonormal and C_{ijklm} is in the space spanned by that orthonormal basis, the norm for the elastic stiffness, for example, is given by:

$$N = \|C\| = \left\{ C_{ij} \cdot C_{ij} \right\}^{1/2} \quad (24)$$

3.1 A proposed relation between the norm ratio and the anisotropy degree

It is known that the anisotropy of the material, i.e., the symmetry group of the material and the anisotropy of the measured property depicted in the same material may be quite different. Obviously, the property tensor must show, at least, the symmetry of the material. For example, a property which is measured in a material can almost be isotropic but the material symmetry group itself may have very few symmetry elements.

In the elastic stiffness tensors, the isotropic symmetry material is decomposed into two parts, the decomposition of the cubic symmetry material is consisted of the same two isotropic decomposed parts and a third part, and the decomposition of the hexagonal symmetry material is consisted of the same two isotropic decomposed parts and another three parts. Consequently, the Norm Ratio Criteria (NRC) proposed in this chapter is close to that proposed in (Gaith & Alhayek, 2009; Gaith & Akgoz, 2005). For isotropic materials, the elastic stiffness tensor has two parts, so the norm of the elastic stiffness tensor for isotropic materials is equal to the norm of these two parts, i.e., $N = N_{iso}$. Hence, the ratio

($\frac{N_{iso}}{N} = 1$) for isotropic materials. For cubic symmetry materials the elastic stiffness tensor

has the same two parts that consisting the isotropic symmetry materials and a third, will be designated as the other than isotropic or the anisotropic part, so two ratios are defined:

$\frac{N_{iso}}{N}$ for the isotropic parts and $\frac{N_{anis}}{N}$ for the anisotropic part. For more anisotropic

materials, the elastic stiffness tensor additionally contains more anisotropic parts, so $\frac{N_{anis}}{N}$

is defined for all the anisotropic parts.

Although the norm ratios of different parts represent the anisotropy of that particular part, they can also be used to asses the anisotropy degree of a material property as a whole, in this chapter the following criteria are proposed:

1. When N_{iso} is dominating among norms of the decomposed parts, the closer the norm ratio $\frac{N_{iso}}{N}$ is to one, the closer the material property is isotropic.
2. When N_{iso} is not dominating or not present, norms of the other parts can be used as a criterion. But in this case the situation is reverse; the larger the norm ratio value, the more anisotropic the material property is.

4. Applications

4.1 Piezoelectric semiconductors and ceramics

Among semiconductor crystals, a family of wurtzite- type belongs to the 6mm class, which is piezoelectric active. The material properties (Tsai, 1992) and the norm calculations are in Table 1. From the table, the most piezoelectric effective among the five materials is CdS which has a very important feature in the thin films of semiconductors. For piezoelectric ceramics, the most potential piezoelectric material because of its higher strength, high rigidity and more importantly the better piezoelectricity, Table 2 includes the piezoelectric coefficients (Temple, 1960) and calculated norms. From the table, the most effective piezoelectric among the seven ceramics is PZT-5H.

Material	d_{11}	d_{33}	d_{15}	N
BeO	-0.12	0.24		0.29
ZnO	-5.0	12.4	-8.3	18.48
CdS	-5.2	10.3	-14.0	23.50
CdSe	-3.9	7.8	-10.0	17.07

Table 1. The Constants and Norms of Piezoelectric Semiconductors [$10^{-12} \text{ C N}^{-1}$]

Material	d_{11}	d_{33}	d_{15}	N
PZT-4	-5.2	15.1	12.7	24.59
PZT-5	-5.4	15.8	12.3	24.71
BaTi O3	-4.35	17.5	11.4	18.82
PZT-5H	-6.5	23.3	17	34.72
PZT-6B	-0.9	7.1	4.6	9.71
PZT-8	-4.0	23.3	10.4	28.13
C-24	1.51	8.53	3.89	10.37

Table 2. The Constants and Norms of Piezoelectric Ceramics [$10^{-12} \text{ C N}^{-1}$]

4.2 Fiber reinforced composite materials

Under specific couplings of the elastic constants of orthotropic media, a very important family of orthotropic materials degenerates into the class of either transversely isotropic or isotropic media. Most of the engineering composites, especially fiber-reinforced, are of transversely isotropic media. Hence, for different composites, the norms are calculated for each material (Radwan, 1991) in Table 3. From the table, it can be clearly concluded that B(4)/N5505 has the strongest stiffness effect among the five composites. From Table 4, the most isotropic composite is E-glass/epoxy, and the most anisotropic composite is T300/5208. From the latter table, it was possible to measure the degree of anisotropy for several composites.

Materials	C_{11}	C_{22}	C_{12}	C_{23}	C_{44}	C_{55}	Norm
T300/5208	184.60	13.94	5.88	7.06	3.44	7.17	174.06
B(4)/N5505	208.08	25.04	95.72	12.70	6.17	5.59	284.62
AS/H3501	141.80	12.20	85.08	6.21	3.00	7.10	222.11
E-lass/Epoxy	41.12	11.57	21.38	6.04	2.77	4.14	62.58
Kev 9/Epoxy	78.66	7.53	53.49	3.86	1.83	2.30	132.92

Table 3. Elastic constants and norms for transversely isotropic materials, GPa

Material	N_{iso}	N_{aniso}	N	$\frac{N_{iso}}{N}$	$\frac{N_{anis}}{N}$
T300/5208	99.67	142.64	174.06	0.56	0.82
B(4)/N5505	223.39	176.37	284.62	0.78	0.62
AS/H3501	173.04	139.24	222.11	0.78	0.63
E-glass/Epoxy	55.01	29.84	62.58	0.88	0.48
Kev 49/Epoxy	105.13	81.34	132.92	0.79	0.61

Table 4. The Norm ratios for transversely isotropic materials, GPa

4.3 II-IV semiconductor compounds ZnX ($X=S, Se, Te$)

Covalent materials such as II-IV semiconductor compounds ZnX ($X=S, Se, Te$) have been extensively studied for their intrinsic structural, optical, and elastic properties such as energy gap, charge density, lattice constants and bulk modulus. However, bulk modulus has been found to correlate well with strength and hardness in many materials and those with largest bulk moduli are usually expected to be the hardest materials. Therefore, one of the important parameters that characterize the physical property of a material system is the material stiffness and its corresponding bulk modulus which measures the degree of stiffness or the energy required to produce a given volume deformation. The bulk modulus reflects important bonding characters in the material and, for many applications, is used as an indicator for material strength and hardness. Early experimental and theoretical investigations for bulk modulus were reported in (Cohen, 1985; Lam et al., 1987). Cohen (Cohen, 1985) obtained an empirical expression for the bulk modulus based on the nearest-neighbour distance. His theoretical and experimental results were in agreement. Lam et al. (Lam, 1987) obtained an expression for bulk modulus using the total energy method with acceptable results. The bulk modulus for the semiconductor compounds was found to be inverse proportionally correlated to the lattice constants (Lam et al., 1987; Al-Douri et al., 2004).

Physical properties are intrinsic characteristics of matter that are not affected by any change of the coordinate system. Therefore, tensors are necessary to define the intrinsic properties of the medium that relate an intensive quantity (i.e. an externally applied stimulus) to an extensive thermodynamically conjugated one (i.e. the response of the medium). Such intrinsic properties are the dielectric susceptibility, piezoelectric, and the elasticity tensors. An interesting feature of the decompositions is that it simply and fully takes into account the symmetry properties when relating macroscopic effects to microscopic phenomena. One can directly show the influence of the crystal structure on physical properties, for instance,

when discussing macroscopic properties in terms of the sum of the contributions from microscopic building units (chemical bond, coordination polyhedron, etc). A significant advantage of such decompositions is to give a direct display of the bearings of the crystal structure on the physical property.

The proposed procedure in this chapter has introduced a method to measure the stiffness and piezoelectricity in fiber reinforced composite and piezoelectric materials using the norm criterion on the crystal scale. In this method, norm ratios proposed to measure the degree of anisotropy in an anisotropic material, and compare it with other materials of different symmetries. It was able to segregate the anisotropic material property into two parts: isotropic and anisotropic parts. Of the new insights provided by invariance considerations, the most important is providing a complete comparison of the magnitude of a given property in different crystals. Such a comparison could be obvious for average refractive index, even birefringence, piezoelectricity, electro-optic effects, elasticity, etc. From a device point of view, the new insights facilitate the comparison of materials; one is interested in maximizing the fig. of merit by choosing the optimum configuration (crystal cut, wave propagation direction and polarization, etc); and one wants to be able to state that a particular material is better than another for making a transducer or modulator (Jerphagnon, 1978). It is most suitable for a complete quantitative comparison of the strength or the magnitude of any property in different materials belonging to the same crystal class, or different phases of the same material. The norm concept is very effective for selecting suitable materials for electro-optic devices, transducers, modulators, acousto-optic devices.

Therefore, using the elastic constant for anisotropic material, an elastic stiffness scale for such anisotropic material, and a scale to measure the isotropic elasticity within the material will be discussed. Besides, the microscopic origin of the overall elastic stiffness and bulk modulus calculation will be correlated with the structural properties parameter, i.e. lattice constant a , which represents some fundamental length scale for the chemical bond of the unit cell.

The elastic stiffness matrix representation for the isotropic system can be decomposed in a contracted form as:

$$C_{ij} = \begin{bmatrix} 2C_{44} + C_{12} & C_{12} & C_{12} & 0 & 0 & 0 \\ C_{12} & 2C_{44} + C_{12} & C_{12} & 0 & 0 & 0 \\ C_{12} & C_{12} & 2C_{44} + C_{12} & 0 & 0 & 0 \\ 0 & 0 & 0 & C_{44} & 0 & 0 \\ 0 & 0 & 0 & 0 & C_{44} & 0 \\ 0 & 0 & 0 & 0 & 0 & C_{44} \end{bmatrix} \quad (25)$$

$$= A_1 \begin{bmatrix} 1 & 1 & 1 & 0 & 0 & 0 \\ 1 & 1 & 1 & 0 & 0 & 0 \\ 1 & 1 & 1 & 0 & 0 & 0 \\ 0 & 0 & 0 & 0 & 0 & 0 \\ 0 & 0 & 0 & 0 & 0 & 0 \\ 0 & 0 & 0 & 0 & 0 & 0 \end{bmatrix} + A_2 \begin{bmatrix} 4 & -2 & -2 & 0 & 0 & 0 \\ -2 & 4 & -2 & 0 & 0 & 0 \\ -2 & -2 & 4 & 0 & 0 & 0 \\ 0 & 0 & 0 & 3 & 0 & 0 \\ 0 & 0 & 0 & 0 & 3 & 0 \\ 0 & 0 & 0 & 0 & 0 & 3 \end{bmatrix}$$

where

$$A_1 = \frac{1}{3}(C_{11} + 2C_{12}), \quad C_{11} = 2C_{44} + C_{12} \quad (26)$$

$$A_2 = \frac{1}{15}(C_{11} - C_{12} + 3C_{44})$$

where A_1 and A_2 are the Voigt average polycrystalline bulk B and shear G modulus, respectively. The decomposed parts of Eq. (25) designated as bulk and shear modulus are identical to those found in literature (Voigt, 1889; Hearmon, 1961; Pantea et al., 2009). For cubic crystals such as the II-VI semiconductor compounds, there are only three independent elastic stiffness coefficients C_{11} , C_{12} , and C_{44} that can describe the mechanical elastic stiffness for these materials. The elastic coefficient C_{11} is the measure of resistance to deformation by a stress applied on the (100) plane, while C_{44} represents the measure of resistance to deformation with respect to a shearing stress applied across the (100) plane. These elastic coefficients are function of elastic material parameters, namely, Young's modulus, shear modulus, and Poisson's ratio. Thus, using the orthonormal decomposition procedure (Gaith & Akgox, 2005), the elastic stiffness matrix representation for cubic system can be decomposed in a contracted form as:

$$C_{ij} = \begin{bmatrix} C_{11} & C_{12} & C_{12} & 0 & 0 & 0 \\ C_{12} & C_{11} & C_{12} & 0 & 0 & 0 \\ C_{12} & C_{12} & C_{11} & 0 & 0 & 0 \\ 0 & 0 & 0 & C_{44} & 0 & 0 \\ 0 & 0 & 0 & 0 & C_{44} & 0 \\ 0 & 0 & 0 & 0 & 0 & C_{44} \end{bmatrix} = A_1 \begin{bmatrix} 1 & 1 & 1 & 0 & 0 & 0 \\ 1 & 1 & 1 & 0 & 0 & 0 \\ 1 & 1 & 1 & 0 & 0 & 0 \\ 0 & 0 & 0 & 0 & 0 & 0 \\ 0 & 0 & 0 & 0 & 0 & 0 \\ 0 & 0 & 0 & 0 & 0 & 0 \end{bmatrix} \quad (27)$$

$$+ A_2 \begin{bmatrix} 4 & -2 & -2 & 0 & 0 & 0 \\ -2 & 4 & -2 & 0 & 0 & 0 \\ -2 & -2 & 4 & 0 & 0 & 0 \\ 0 & 0 & 0 & 3 & 0 & 0 \\ 0 & 0 & 0 & 0 & 3 & 0 \\ 0 & 0 & 0 & 0 & 0 & 3 \end{bmatrix} + A_3 \begin{bmatrix} -4 & 2 & 2 & 0 & 0 & 0 \\ 2 & 4 & -2 & 0 & 0 & 0 \\ 2 & 2 & -4 & 0 & 0 & 0 \\ 0 & 0 & 0 & 2 & 0 & 0 \\ 0 & 0 & 0 & 0 & 2 & 0 \\ 0 & 0 & 0 & 0 & 0 & 2 \end{bmatrix}$$

where

$$A_1 = \frac{1}{3}(C_{11} + 2C_{12})$$

$$A_2 = \frac{1}{15}(C_{11} - C_{12} + 3C_{44}) \quad (28)$$

$$A_3 = \frac{1}{10}(C_{12} - C_{11} + 2C_{44})$$

It can be shown that the sum of the three orthonormal parts on the right hand side of Eq. (27) is apparently the main matrix of cubic system (Hearmon, 1961). Also, the first two terms on the right hand side are identical to the corresponding two terms obtained in Eq. (23) for the isotropic system (Hearmon, 1961). Hence, it can be stated that the cubic system is discriminated into the sum of two parts: isotropic part (first two terms), and anisotropic part (third term). The latter term resembles the contribution of the anisotropy on elastic stiffness in the cubic system. On the other hand, the first term on the right hand side of Eqs (23) and (27), designated as the bulk modulus, is identical to Voigt bulk modulus (Hearmon, 1961).

Nowadays, the necessity of alternative energy use is widely accepted. In solar energy technology, thin film solar technology based on the II-IV semiconductor compounds, is very promising due to lower production costs and shorter energy pay back times (Fischer, 2006). For these compounds, a successful interface between absorber and buffer layers with alternative and promising non-toxic materials requires compositional and electronic material characterization as a prerequisite for understanding and intentionally generating interfaces in photovoltaic devices (Fischer, 2006). On the other hand, stability of ZnTe/ZnS solar cells is of concern for their application in space, where the cells have to withstand high energy particles, mainly electrons and protons that can cause severe damage in solar cells up to a complete failure. Therefore, the radiation hardness and damage mechanism of the ZnTe solar cells is associated with the overall elastic stiffness and bulk modulus (Bätzner, 2004). Table 5 presents the materials elastic stiffness coefficients, calculated bulk B and overall elastic stiffness N moduli for the II-VI semiconductor ZnX ($X=S, Se, \text{ and } Te$) compounds. Fig. 1 shows clearly the correlation between overall elastic stiffness N and bulk modulus B . Quantitatively, the overall elastic stiffness increases as the calculated bulk modulus B increases. Besides, the calculated bulk moduli are identical to those found by theory of anisotropy (Hearmon, 1961), and are in agreement with experimental values (Cohen, 1985) with maximum error of 8.5 % for ZnTe. The calculated bulk moduli obey the cubic stability conditions, meaning that $C_{12} \leq B \leq C_{11}$. Fig. 2 shows that the bulk modulus is inversely proportional to lattice

constants a which was confirmed in several studies (Lam et al., 1987; Al-Douri et al., 2004). Consequently, from Fig. 3 the overall elastic stiffness N is inversely proportional to lattice constants a , as well. Fig. 1-3 indicate that among the three compounds under examination, ZnS has the largest elastic stiffness, largest bulk modulus (lowest compressibility), and lowest lattice constant, while ZnTe, in contrary, has the smallest elastic stiffness, smallest bulk modulus, and largest lattice constant. Therefore, the overall elastic stiffness and bulk modulus, the only elastic moduli possessed by all states of matter, reveal much about interatomic bonding strength. The bulk modulus also is the most often cited elastic constant to compare interatomic bonding strength among various materials (Pantea, 2009), and thereafter the overall elastic stiffness can be cited as well.

For the isotropic symmetry material, the elastic stiffness tensor is decomposed into two parts as shown in Eq. (23), meanwhile, the decomposition of the cubic symmetry material, from Eq. (27), is consisted of the same two isotropic decomposed parts and a third part. It can be verified the validity of this trend for higher anisotropy, i.e., any anisotropic

	C11	C12,	C44	N	B	Bexp (Cohen, 1985)	a (Chelikowsky, 1987)
ZnS	104	65	46.2	266.5	78	77	0.54
ZnSe	95.9	53.6	48.9	244.0	67.7	64.7	0.57
ZnTe	82	42	55	224.0	55.3	51	0.61

Table 5. Elastic coefficients (GPa) (Cohen, 1985), overall stiffness N (GPa), bulk modulus B (GPa), and lattice constants a (nm)

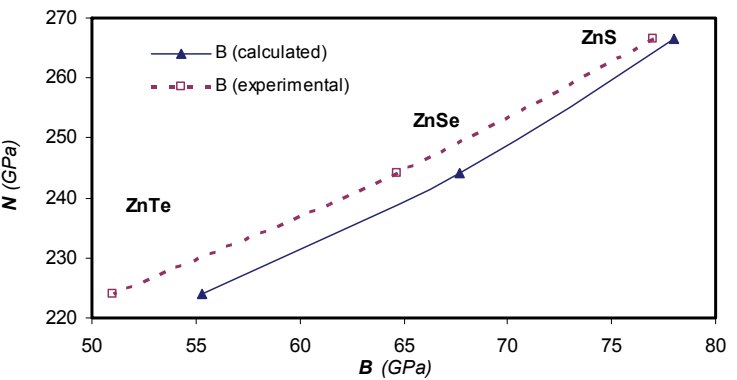


Fig. 1. The overall elastic stiffness N versus bulk modulus B for ZnX (X=S, Se, Te)

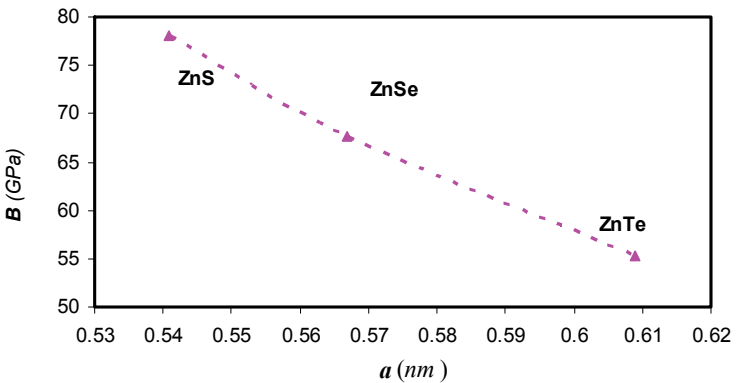


Fig. 2. The bulk modulus B versus the lattice constants a for ZnX (X=S, Se, Te)

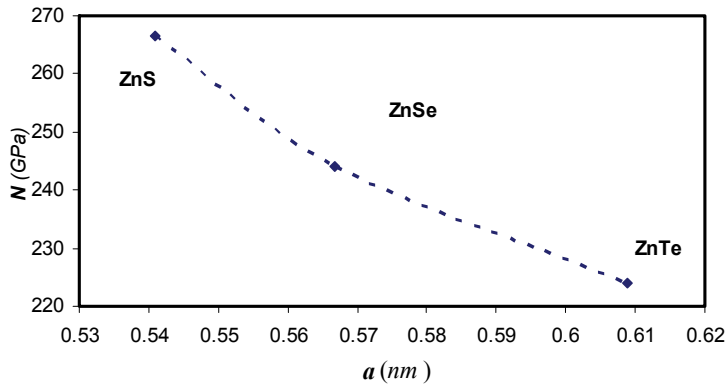


Fig. 3. The overall stiffness N versus the lattice constants a for ZnX ($X=\text{S, Se, Te}$)

	Niso	Naniso	N	$\frac{N_{\text{iso}}}{N}$	$\frac{N_{\text{anis}}}{N}$	B	A
ZnS	262	49	266.5	0.9830	0.1836	78	0.54
ZnSe	238.7	50.9	244.0	0.9780	0.2084	67.7	0.57
ZnTe	214.6	64.2	224.0	0.9581	0.2865	55.3	0.61

Table 6. The overall elastic stiffness N (GPa) and norm ratios for the II-IV semiconductor compounds ZnS, ZnSe, and ZnTe

The norms and norm ratios for ZnS, ZnSe, and ZnTe are calculated and presented in Table 6.

From the table, interesting phenomena are observed; as the isotropic ratio $\frac{N_{\text{iso}}}{N}$ increases,

the anisotropic ratio $\frac{N_{\text{anis}}}{N}$ decreases, which confirms the definitions of these two ratios, and the bulk modulus increases at the same time. Therefore, the nearest material to isotropy (or least anisotropy) is ZnS, with $\frac{N_{\text{iso}}}{N} = 0.9830$, in which corresponds to the largest bulk

modulus $B = 78$ GPa. The least isotropic (or nearest to anisotropy) is ZnTe, with $\frac{N_{\text{iso}}}{N} = 0.9581$, in which corresponds to the smallest bulk modulus $B = 55.3$ GPa. Since the cubic system is the nearest to isotropy among the anisotropic systems, the calculated values of isotropic norm ratio, $\frac{N_{\text{iso}}}{N}$, in Table 2 are very close to one (i.e., 0.9581 - 0.9830). Hence, it can be concluded that the closer the material is to isotropy, the larger the bulk modulus for

the material is. A reverse trend correlating the norm ratios and lattice constants can be seen from the table; the closer the material is to isotropy, the smaller the lattice constant for the material is.

The overall elastic stiffness of II-IV semiconductor compounds ZnS, ZnSe, and ZnTe is calculated and found to be directly proportional to bulk modulus and inversely proportional to lattice constants. Among these compounds, ZnS has the largest overall elastic stiffness and bulk modulus and the smallest lattice constant. Meanwhile, ZnTe has the smallest overall elastic stiffness and bulk modulus and the largest lattice constant. The Norm Ratio Criteria (NRC) is introduced to scale and measure the isotropy in the cubic system material among the semiconductor compounds ZnS, ZnSe, and ZnTe. Hence, a scale quantitative comparison of the contribution of the anisotropy to the elastic stiffness and to measure the degree of anisotropy in an anisotropic material is proposed. ZnS is the nearest to isotropy (or least anisotropic) while ZnTe is the least isotropic (or nearest to anisotropic) among these compounds. These conclusions can be investigated on the II-IV semiconductor compounds CdX (X=S, Se, Te) in similar manner.

4.3 The hetrojunction layers compounds in solar photovoltaic cells: CuInSe₂, CuInS₂, AgGaSe₂, and AgGaS₂

Various attempts have been made to correlate the bulk modulus of compound semiconductors and chalcopyrite compounds with many other physical parameters. Nevertheless, it is found that bulk modulus interconnected well with strength and hardness in many materials (Choi & Yu, 1996). Therefore, the material stiffness and its corresponding bulk modulus is one of the important factors that characterize the physical property of a material system which quantifies the degree of stiffness or the energy required to produce a given volume deformation. With a good agreement result, an empirical expression for the bulk modulus was obtained by Cohen (Cohen, 1985) based on the nearest-neighbour distance. Using the total energy method Lam et al. (Lam et al., 1987) obtained an expression for bulk modulus with acceptable results. The bulk modulus for the semiconductor compounds was found to be inverse proportionally correlated to the lattice constants (Lam et al., 1987 & Al-Douri, 2004). Gaith et al (Gaith & Alhayek, 2009) have studied the correlation between the bulk modulus and the over all stiffness and lattice constants for CdX and ZnX (X=S, Se, and Te) using orthonormal decomposition method (ODM) (Gaith & Alhayek, 2009) from continuum mechanics point of view.

The purpose of this section is to understand how qualitative ground state concepts of the hetrojunction layer compounds, CuInSe₂, CuInS₂, AgGaSe₂, and AgGaS₂, such as overall elastic stiffness, can be related to bulk modulus and lattice constants. Therefore, using the elastic coefficients for anisotropic material, an elastic stiffness scale for such anisotropic material, and a scale to quantify the isotropic elasticity within the material will be discussed. The number of elements of the decomposed stiffness tensor should be equal to the number of non-vanishing distinct stiffness coefficients, i.e., six constants for tetragonal materials, that can completely describe the elastic stiffness in that medium. Thus, using Orthonormal Decomposition Method (ODM), namely, Orthonormal Tensor Basis Method (OTBM) (Gaith & Alhayek, 2009; Gaith & Akgöz, 2005), the matrix representation for the elastic stiffness with tetragonal symmetry system is decomposed into a contracted form as shown in Eq. (29):

$$\begin{aligned}
 C_{ij} = & \begin{bmatrix} C_{11} & C_{12} & C_{13} & 0 & 0 & 0 \\ C_{12} & C_{11} & C_{13} & 0 & 0 & 0 \\ C_{13} & C_{13} & C_{33} & 0 & 0 & 0 \\ 0 & 0 & 0 & C_{44} & 0 & 0 \\ 0 & 0 & 0 & 0 & C_{44} & 0 \\ 0 & 0 & 0 & 0 & 0 & C_{66} \end{bmatrix} = A_1 \begin{bmatrix} 1 & 1 & 1 & 0 & 0 & 0 \\ 1 & 1 & 1 & 0 & 0 & 0 \\ 1 & 1 & 1 & 0 & 0 & 0 \\ 0 & 0 & 0 & 0 & 0 & 0 \\ 0 & 0 & 0 & 0 & 0 & 0 \\ 0 & 0 & 0 & 0 & 0 & 0 \end{bmatrix} + \\
 & +A_2 \begin{bmatrix} 4 & -2 & -2 & 0 & 0 & 0 \\ -2 & 4 & -2 & 0 & 0 & 0 \\ -2 & -2 & 4 & 0 & 0 & 0 \\ 0 & 0 & 0 & 3 & 0 & 0 \\ 0 & 0 & 0 & 0 & 3 & 0 \\ 0 & 0 & 0 & 0 & 0 & 3 \end{bmatrix} + A_3 \begin{bmatrix} -3 & -1 & -1 & 0 & 0 & 0 \\ -1 & -3 & -1 & 0 & 0 & 0 \\ -1 & -1 & 12 & 0 & 0 & 0 \\ 0 & 0 & 0 & -1 & 0 & 0 \\ 0 & 0 & 0 & 0 & -1 & 0 \\ 0 & 0 & 0 & 0 & 0 & -1 \end{bmatrix} + \\
 & +A_4 \begin{bmatrix} -3 & -5 & 4 & 0 & 0 & 0 \\ -5 & -3 & 4 & 0 & 0 & 0 \\ 4 & 4 & 0 & 0 & 0 & 0 \\ 0 & 0 & 0 & 1 & 0 & 0 \\ 0 & 0 & 0 & 0 & 1 & 0 \\ 0 & 0 & 0 & 0 & 0 & 1 \end{bmatrix} + A_5 \begin{bmatrix} -1 & 1 & 0 & 0 & 0 & 0 \\ 1 & -1 & 0 & 0 & 0 & 0 \\ 0 & 0 & 0 & 0 & 0 & 0 \\ 0 & 0 & 0 & 1 & 0 & 0 \\ 0 & 0 & 0 & 0 & 1 & 0 \\ 0 & 0 & 0 & 0 & 0 & -1 \end{bmatrix} + \\
 & +A_6 \begin{bmatrix} -1 & 1 & 0 & 0 & 0 & 0 \\ 1 & -1 & 0 & 0 & 0 & 0 \\ 0 & 0 & 0 & 0 & 0 & 0 \\ 0 & 0 & 0 & 0 & 0 & 0 \\ 0 & 0 & 0 & 0 & 0 & 0 \\ 0 & 0 & 0 & 0 & 0 & 1 \end{bmatrix} \quad (29)
 \end{aligned}$$

where

$$\begin{aligned}
 A_1 &= \frac{1}{90}(2C_{11} + 2C_{12} + C_{33} + 4C_{13}) \\
 A_2 &= \frac{1}{45}(2C_{11} - C_{12} + 6C_{44} + 3C_{66} + C_{33} - 2C_{13}) \\
 A_3 &= \frac{1}{90}(-3C_{11} - C_{12} - 4C_{44} - 2C_{66} + 6C_{33} - 2C_{13}) \\
 A_4 &= \frac{1}{144}(-6C_{11} - 10C_{12} + 8C_{44} + 4C_{66} + 16C_{13}) \\
 A_5 &= \frac{1}{16}(-2C_{11} + 2C_{12} + 8C_{44} - 4C_{66}) \\
 A_6 &= \frac{1}{8}(-2C_{11} + 2C_{12} + 4C_{66})
 \end{aligned} \quad (30)$$

Where A_1 to A_6 are constants in terms of elastic stiffness coefficients expressed as in Eq. (30). It can be observed clearly that the first two terms on the right hand side are identical to the corresponding well known two terms namely bulk and shear (Gaith & Akgöz, 2005) which are identical to those found in literature (Voigt, 1889) for the isotropic system (Hearmon, 1961). Here, A_1 and A_2 defined in Eq. (2), are the Voigt average polycrystalline bulk B and shear modulus G , respectively. Hence, it can be stated that the tetragonal system is discriminated into the sum of two parts: isotropic part (first two terms), and anisotropic part (other four terms). The latter part resembles the contribution of the anisotropy on elastic stiffness in the tetragonal system.

In solar energy technology, thin film solar technology based on the heterojunction layer compounds CuInSe_2 , CuInS_2 , AgGaSe_2 , and AgGaS_2 , is very promising due to lower production costs and shorter energy pay back times (Fischer et al., 2006). For these compounds, the successful interface between absorber and buffer layers with alternative materials requires structural and optical material characterization as a prerequisite for understanding interfaces in photovoltaic devices (Fischer et al., 2006). On the other hand, stability of these compounds in solar cells is of concern due to their application in space, where the cells have to withstand high energy particles, mainly electrons and protons that can cause severe damage in solar cells up to a complete failure. Therefore, the radiation hardness and damage mechanism of the heterojunction layer compounds solar cells is associated with the overall elastic stiffness and bulk modulus (Bätzner et al., 2004). The materials elastic stiffness coefficients and lattice constants for CuInSe_2 , CuInS_2 , AgGaSe_2 , and AgGaS_2 are presented in Table 7. The correlation trend between overall elastic stiffness N and bulk modulus B for each group, i.e. (CuInS_2 , CuInSe_2) and (AgGaS_2 , AgGaSe_2) is clearly shown in Fig. 4; the overall elastic stiffness increases as the calculated bulk modulus B increases. Besides, the calculated bulk moduli are in good agreement with those found by theory of anisotropy (Hearmon, 1961) and experimental values (Cohen, 1985). Also, the bulk modulus for each group is inversely proportional to lattice constants a , as shown in Fig. 5, which was confirmed in several studies (Lam et al., 1987; Al-Douri et al., 2004; (Christensen & Christensen, 1986; Al-Douri et al., 2001). Consequently, the overall elastic stiffness N is inversely proportional to lattice constants a , as shown in fig. 3. CuInS_2 and AgGaS_2 have larger elastic stiffness, largest bulk modulus, and lower lattice constant than those for CuInSe_2 and AgGaSe_2 , respectively. Therefore, the overall elastic stiffness and bulk modulus, the only elastic moduli possessed by all states of matter, reveal much about interatomic bonding strength. The bulk modulus also is the most often cited elastic constant to compare interatomic bonding strength among various materials (Pantea et al., 2009), and thereafter the overall elastic stiffness can be cited as well (Gaith & Alhayek, 2009).

For the isotropic symmetry material, the elastic stiffness tensor is decomposed into two parts (Kim & Chen, 2004; Spencer, 1983; Voigt, 1889; Hearmon, 1961); meanwhile, the decomposition of the tetragonal symmetry material, from Eq. (29) is consisted of the same two isotropic decomposed parts and other four terms. The Norm Ratio Criteria (NRC) used in here is similar to that proposed in (Gaith & Alhayek, 2009; Gaith & Akgöz, 2005). For tetragonal symmetry materials, the elastic stiffness tensor has the same two parts that consisting the isotropic symmetry materials and the other four terms, will be designated as

the other than isotropic or the anisotropic part. Hence, two ratios are defined as: $\frac{N_{iso}}{N}$ for the isotropic parts and $\frac{N_{anis}}{N}$ for the anisotropic parts. The norm ratios can also be used to assess the degree of anisotropy of a material property as a whole. The norms and norm ratios for the hetrojunction layer compounds CuInS₂, CuInSe₂, AgGaSe₂, and AgGaS₂ are calculated and shown in Fig. 7 and 8; as the isotropic ratio $\frac{N_{iso}}{N}$ increases, the anisotropic ratio $\frac{N_{anis}}{N}$ decreases and this confirms the definitions of these two ratios, and the bulk modulus increases at the same time.

Therefore, CuInS₂ is a closer material to isotropy (or less anisotropy), with $\frac{N_{iso}}{N} = 0.9859$, and larger bulk modulus $B = 64.43$ GPa than those for CuInSe₂. Similarly, AgGaS₂ possesses a closer material structure to isotropy and larger bulk modulus B than those for AgGaSe₂.

	C11	C12	C44	C13	C33	C66	a
CuInS ₂ (Pantea et al., 2009)	83.7	54.4	34.5	54.8	84.5	33.9	0.5532 (Krustok et al., 2001)
CuInSe ₂ (Pantea et al., 2009)	71.0	45.3	45.5	45.3	63.3	47.4	0.5782 (Kannan et al., 2004)
AgGaS ₂ (Grimsditch & Holah, 1975)	87.9	58.4	24.1	59.2	84.5	30.8	0.5759 (Chahed et al., 2005)
AgGaSe ₂ (Eimerl et al., 1991)	89.8	65.7	21.7	45.1	63.3	13.3	0.5993 (Chahed et al., 2005)

Table 7. Elastic coefficients (GPa) and lattice constants a (nm) for the hetrojunction layers compounds

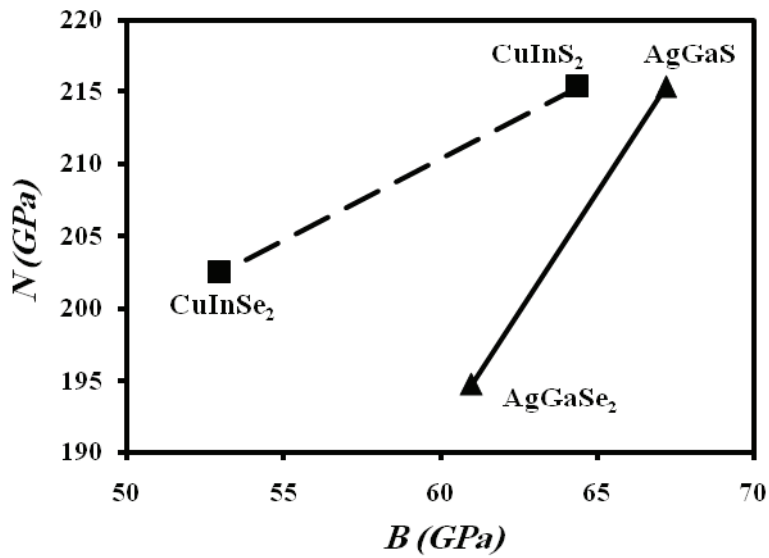


Fig. 4. The relation between the overall elastic constant N and bulk modulus B for the hetrojunction layer compounds

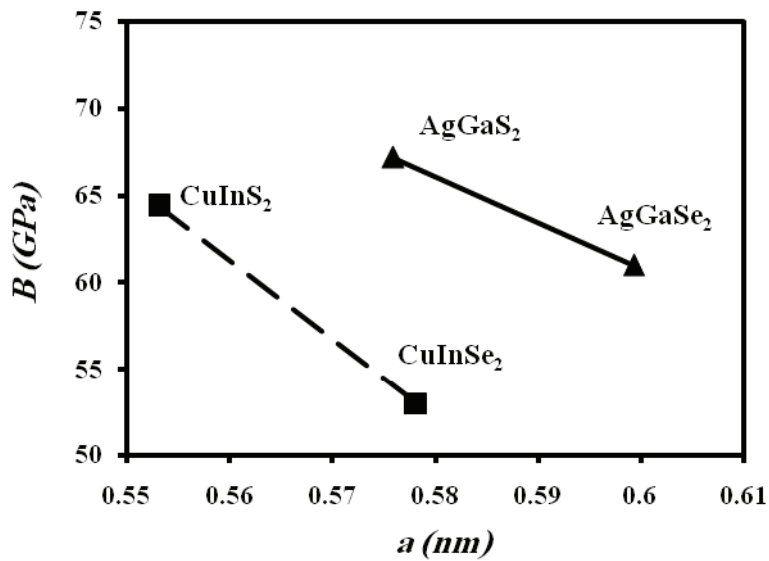


Fig. 5. The relation between the bulk modulus B and lattice constant a for the hetrojunction layer compounds

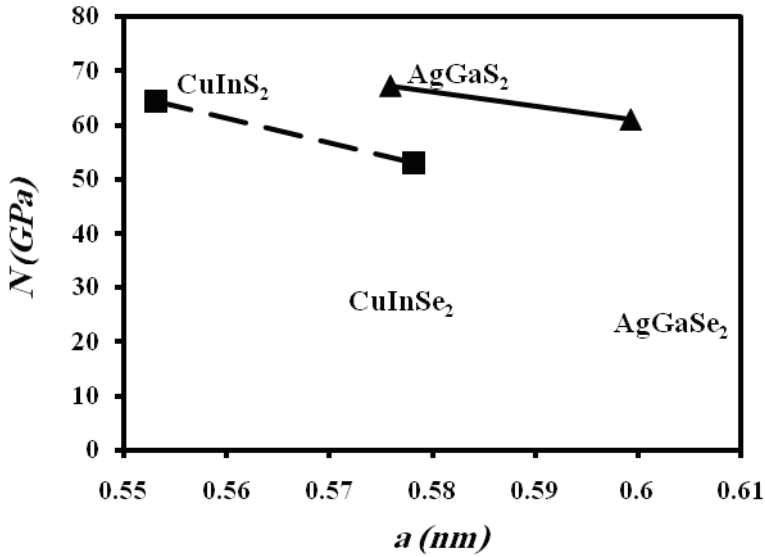


Fig. 6. The relation between the overall elastic constant N and lattice constant a for the hetrojunction layer compounds

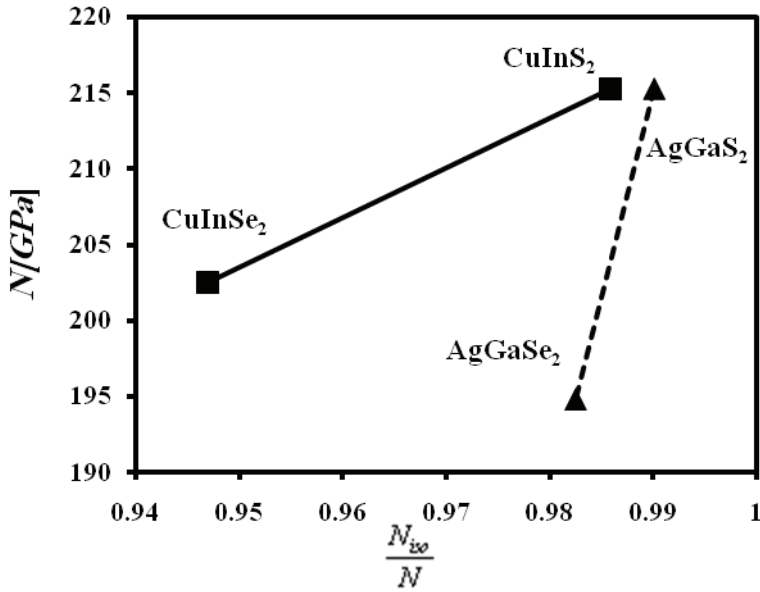


Fig. 7. The relation between the overall elastic constant N and isotropy ratio $\frac{N_{iso}}{N}$ for the hetrojunction layer compounds

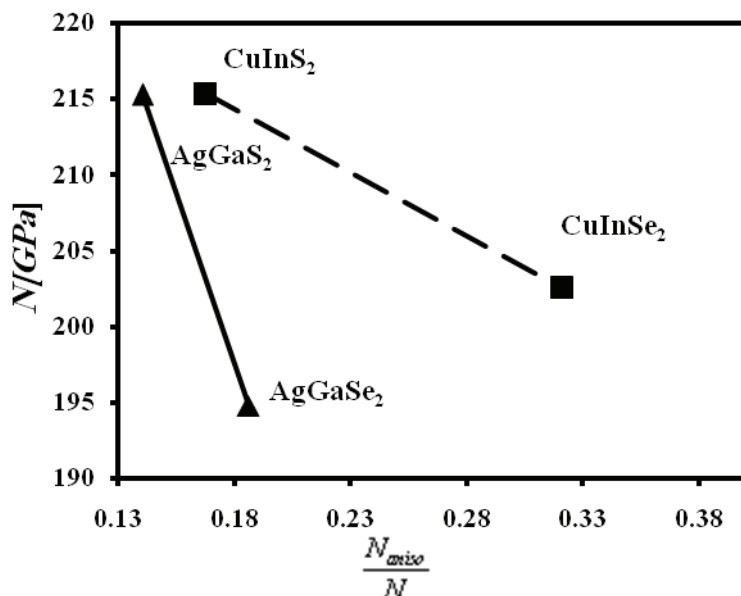


Fig. 8. The relation between the overall elastic constant N and anisotropy ratio $\frac{N_{aniso}}{N}$ for the hetrojunction layer compounds

A significant contribution of this decomposition method is the direct correlation between the macroscopic and microscopic features of a material by means of symmetry properties. Based on the Orthonormal Tensor Basis Method (OTBM), the elastic stiffness for tetragonal system materials into two parts; isotropic (two terms) and anisotropic (four parts) is presented. The overall elastic stiffness is calculated and correlated with lattice constants and calculated bulk modulus for the hetrojunction layer compounds CuInS₂, CuInSe₂, AgGaS₂, and AgGaSe₂. The overall elastic stiffness is quantified and correlated to bulk modulus and inversely proportional to lattice constants. CuInS₂ and AgGaS₂ have larger overall elastic stiffness and bulk modulus and the smaller lattice constant than CuInSe₂ and AgGaSe₂, respectively. Based on the Norm Ratio Criteria (NRC), the hetrojunction layer compounds CuInS₂ and AgGaS₂ are closer to isotropy (or less anisotropic) than CuInSe₂ and AgGaSe₂.

5. Conclusion

Any physical property is characterized by n rank tensors, and this method is capable for decomposing these tensors with intrinsic symmetry, which is derived from the nature of the physical property itself, of any rank into orthonormal tensor basis. This method is capable to decompose tensors with non-intrinsic symmetry of rank n by generating an orthonormal basis using the well Known Gram-Schmidt process for the corresponding symmetry media of that tensor, and the number of basis elements should be equal to the number of non-vanishing distinct coefficients in that media. The decomposition procedure developed in this work has many engineering applications in anisotropic elastic materials which are, both

qualitatively and quantitatively, different from isotropic materials. A new innovational decomposition of general and more explicit physical property for the symmetric second rank stress and strain tensors is introduced. The results are compared and found to be identical for special cases available in literature (Spencer, 1983; Cowin & Mehrabadi, 1987; Hue & Del Piero, 1991; Srinivasan, 1998; Blinowski & Rychlewski, 1998; Tu, 1968; Nye, 1959; Ikeda, 1990). Nevertheless, this method is introducing a new form of decomposition that has a more featured and transparent physical information. The Criteria to measure the overall effect of the material properties proposed using the norms to represent the piezoelectricity and stiffness effect in the material like piezoceramics and fiber-reinforced composites, respectively. Through this method it is possible to study the effect of angle orientation of fibers and the material properties of fiber and matrix on the stiffness of the composite. A new proposed norm ratios criterion is introduced to measure the anisotropy degree and compare it with other materials of different symmetries. These ratios can be used to study the linear and non-linear damage parameters using total energy for fiber reinforced composite structures (will be published soon).

6. References

- Al-Douri, Y.; Abid, H. & Aourag, H. (2004). Empirical Formula Relating the Bulk Modulus to the Lattice Constant in Tetrahedral Semiconductors. *Materials Chemistry and Physics*, Vol. 87, pp. 14-17
- Bätzner, D.L.; Romeo, A.; Terheggen, M.; Döbeli, M.; Zogg, H. & Tiwari, A. N. (2004). Stability Aspects in CdTe/CdS Solar Cells. *Thin Solid Films*, Vol. 451, pp. 536-543
- Blinowski, A. & Rychlewski, J. (1998). Pure Shears in the Mechanics of Materials. *Mathematics and Mechanics of Solids*, Vol. 4, pp. 471-503
- Chahed, A.; Benhelal, O.; Laksari, S.; Abbar, B.; Bouhafs, B.; Amrane, N. (2005). *First-Principles Calculations of the Structural, Electronic and Optical Properties of AgGaS₂ and AgGaSe₂*. *Physica B*, Vol. 367, pp.142-151
- Chelikowsky, J.R. (1987). High-Pressure Phase Transitions in Diamond and Zinc-Blende Semiconductors. *Physical Review B*, Vol. 35, pp. 1174-1180
- Choi, In-Hwan, Yu, P.Y. (1996). Optical investigation of defects in AgGaS₂ and CuGaS₂. *Journal of Chemistry and Physics of Solids*, Vol. 57, pp.1695-1704
- Cohen M.L. (1985) . Calculation of Bulk Moduli of Diamond and Zinc-Blende Solids. *Physical Review B*, Vol. 32, pp. 7988-7991
- Cowin, S.C. & Mehrabadi, M.M. (1987). On Eigentensors of Orthotropic Materials. *Quarterly Journal of Mechanics and Applied Mathematics*, Vol. 40, pp. 451-476
- Eimerl, D.; Marion, J.; Graham, E. K.; McKinstry, H. A.; Haussuhl, S. (1991). Elastic Constants and Thermal Fracture of AgGaSe₂ and d-Lap. *IEEE Journal of Quantum Electronics*, Vol. 27, pp.142-145
- Fischer, C.H.; Batzer, M.; Glatzel, T.; Lauermann, I., M. C.; Lux-Steiner, M. C. (2006). Interface Engineering in Chalcopyrite Thin Film Solar Devices. *Solar Energy Materials & Solar Cells*, Vol. 90, pp. 1471-1585
- Gaith, M. & Akgoz, C.Y. (2005). A new Representation for the Properties of Anisotropic Elastic Fiber Reinforced Composite Materials. *Review of Advance Material Sciences*, Vol. 10, pp. 138-142

- Gaith, M. & Alhayek, I. (2009). Correlation Between Overall Elastic Stiffness, Bulk Modulus and Interatomic Distance in Anisotropic Materials: Semiconductors. *Review of Advance Material Sciences*, Vol. 21, pp. 183-191
- Grimsditch, N.S. & Holah, G.D. (1975). Brillouin Scattering and Elastic Moduli of Silver Thiogallate (AgGaS_2). *Physical Review B*, Vol. 12, pp. 4377-4382
- Hearmon, R.F.S. (1961). *An Introduction to Applied Anisotropic Elasticity*. Oxford University Press
- Hue, Y.Z. & Del Piero, G. (1991). *Journal elasticity*. Vol. 21, pp. 203-246
- Ikeda, T. (1990). *Fundamentals of Piezoelectricity*. Oxford University Press
- Jerphagnon, J.; Chemla, D.S. & Bonneville, R. (1978). The Decomposition of Condensed Matter Using Irreducible Tensors. *Advances in Physics*, Vol. 27, pp. 609-650
- Kannan, M.D.; Balasundaraprabhu, R.; Jayakumar, S. & Ramanathaswamy, P. (2004). Preparation and Study of Structural and Optical Properties of CSVT deposited CuInSe_2 thin films. *Solar Energy Materials & Solar Cells*, Vol. 81, pp. 379-395
- Kim E. & Chen C. (2004). Calculation of Bulk Modulus for Highly Anisotropic Materials. *Physics Letters A*, Vol. 326, pp. 442-448
- Krustok, J.; Raudija, J. & Collan, H. (2001). Photoluminescence and the Tetragonal Distortion in CuInS_2 . *Thin Solid Films*, Vol. 387, pp. 195-197
- Lam, P.K.; Cohen, M.L. & Martinez, G. (1987). Analytic relation between bulk moduli and lattice constants. *Physical Review B*, Vol.35, pp. 9190
- Leitsmann, R.L.; Ramos, L.E. & Bechstedt, F. (2006). Structural Properties of PbTe/CdTe Interfaces from First Principles. *Physical Review B*, Vol. 74, pp. 085309
- Murthy, Y.S.; Hussain O.M.; Naidu, S.B. & Reddy, P.J. (1991). Characterization of p- $\text{AgInSe}_2/\text{n-Zn}_{0.35}\text{Cd}_{0.65}\text{S}$ Polycrystalline Thin Film Hetrojunction. *Materials Letters*, Vol.10, pp. 504-508
- Nowacki, W. (1962). *Thermoelasticity*. Oxford:Pergamon press
- Nye, J.F. (1959). *Physical Properties of Crystals; their Representation by Tensors and Matrices*. Oxford: Clarendon Press
- Nowacki, W. (1962). *Thermoelasticity*. Oxford:Pergamon press
- Okuyama, H.; Miyajima, T.; Moringa, Y.; Hiei, F.; Ozawa, M. & Akimot, K. (1992). *Electronics Letters*, Vol. 28, pp. 1798
- Pantea, C.; Mihut, I.; Ledbetter, H.; Betts, J.B.; Zhao, Y.; Daemen, L.L.; Cynn, H. & Miglori, A. (2009). Bulk Modulus of Osmium. *Acta Materialia*, Vol. 57, pp. 544-548
- Radwan, F.A. (1991). *Irreducible Cartesian Tensors in Anisotropic Continua*. Ph.D. Thesis, METU, Turkey
- Ramesh, P.P.; Hussain, O.M.; Uthanna, S.S.; Naidu, P. & Reddy, P.J. (1998). Photovoltaic Performance of p- $\text{AgInSe}_2/\text{n-CdS}$ Thin Film Hetrojunction. *Materials Letters*, Vol. 34, pp. 217-221
- Ramesh, P.P.; Hussain, O.M.; Uthanna, S.; Naidu, P.S. & Reddy, P.J. (1999). Characterization of p- $\text{AgInSe}_2/\text{n-Zn}_{0.35}\text{Cd}_{0.65}\text{S}$ Polycrystalline Thin Film Hetrojunction. *Materials Science and Engineering B*, Vol. 49, pp.27-30
- Reich, S.; Ferrari, A.C.; Arenal, R.; Loiseau, A.; Bellom, I. & Robertson, J. (2005). Resonant Raman Scattering in Cubic and Hexagonal Boron Nitride. *Physical Review B*, Vol. 71, pp. 205201
- Spencer, A.T.M. (1983). *Continuum Mechanics*, Longmans: London

- Srinivasan, T.P. & Nigam, S.D. (1968). Invariant forms. *Journal of Mathematical and Physical Sciences*, Vol. 2, pp. 311-320
- Srinivasan, T.P. (1969). Invariant Elastic Constants for Crystals. *Journal of Mathematics and Mechanics*, Vol. 19, pp. 411-420
- Srinivasan, T.P. (1970). Invariant Piezoelectric Coefficients for Crystals. *Physica Status Solidi*, Vol. 41, pp. 615-620
- Srinivasan, T.P. (1998). Decomposition of Tensors Representing Physical Properties of Crystals. *Journal of Physics: Condensed Matter*, Vol. 10, pp. 3489-3496
- Tsai, S.C. (1992). *Theory of Composite Design*, Academic Press
- Tu, Y.O. (1968). The Decomposition of Anisotropic Elastic Tensor. *Acta Crystallographica A*, Vol. 24, pp. 273-282
- Voigt, W. (1889). The Relation Between the Two Elastic Moduli of Isotropic Materials. *Annals of Physics*, (Leipzig) Vol. 33, pp. 573

Lightweight Unfolded Composite Materials Acquiring Stability of the Shape due to Factors of Space Environment

Laricheva V.P.

*Branch of FSUE "Karpov Institute of Physical Chemistry"
Obninsk, Kaluga Region,
Russia*

1. Introduction

In this article it is discussed the compact-packed materials, which acquire rigidity under the exposure to ionizing radiation. The prepreg materials, additionally curable under the irradiation exposure, can be used for the fabrication of large-size products (for example, supporting constructions of the large space antennas of space transport vehicles and aircrafts, protective shields of spacecraft and shielding constructions on the lunar surface); they can be transformed in the space environment and acquire rigidity (stability of form) under the influence of space factors (UV radiation, vacuum). The materials, additionally cured under the irradiation exposure, can be obtained with the use of specially developed complex binders, that include the components of different sensitivity to ionizing radiation and curable by different mechanisms.

One of the problems, that space researchers are facing, is the creation of easy and at the same time rigid structures transformed at a space environment to suit desirable applications in the specific conditions of the outer space. In particular, it can be structures for lunar settlements, bearing constructions of solar batteries, auxiliary or constructional materials for assembly or repair of constructions at space conditions.

The polymeric structures compactly packed on the Earth, transported in space, transformed at space conditions in the necessary configurations and acquiring desirable stability of shape under influence of space factors are most acceptable to these purposes. Such factors are the space vacuum, fluxes of radiation of the exoatmospheric Sun and the ionizing radiation of the outer space. It is important to note that radiation conditions on the moon surface coincide with those on spacecraft on the near-earth orbits.

The first researches in this direction were aimed at development of foldable metallic structures [1]. Use of metals in such structures made them heavy and, thus, unsuitable for large-size constructions. Also it is known that rigid foldable structures were obtained by impregnation of tight-sealed synthetic fabrics in water solution of gelatin. Rigidity of structure was got due to evaporation of water. Another procedure of increase of structure rigidity was accomplished by formation of hard foam hardening due to the effect of the space factors on the binders impregnating "sandwich". This method was used on the American satellite ECHO-2. However, it was not possible to obtain the structure of exact configuration, and the method was not acceptable for large-size products [2].

Interest in the unfolded constructions which can be used for the solution of problem in the generation of electricity at space and its transfer to earth by solar batteries has intensified recently again [3-5].

Use of film-type solar batteries for these purposes is especially effective. The absence of the effective constructions of unfolding and maintenance of the form of solar batteries in flight is obstacle on the way of the effective realization of the film-type solar batteries technology. These problems are solved due to the use of the frameless centrifugal space constructions [5].

For these purposes it is offered to create the non-sticky intermediates of products made of the prepregs, received on the basis of specially created complex binders. Such binders consist of the components, which are polymerized by different mechanisms, such as polycondensation (or step-by-step addition) and radical polymerization. In this case it is possible to separate these reactions in the time and to obtain the non-sticky pre-fabricated compact-packed products, which can be additionally hardened by ionizing radiation and other space environment factors even after long storage at 40 °C [6-7].

The experiments were executed to obtain binders for the prepregs, based on the components, which are polymerized by the radical mechanism. For it unsaturated compounds (mostly polyester oligomers) were selected as binder components. Polymerization of polyester oligomers can be initiated at the exposure to UV radiation, γ -quanta and accelerated electrons. In the absence of radiation initiators these compounds are not polymerized and, thus, they can serve as plasticizers at the obtaining of prepregs due to other components of complex binder.

The components, polymerizing by step-by-step addition or polycondensation, can be selected from a wide group of substances. It can be epoxy oligomers with different hardeners, epoxy novolac, phenol formaldehyde, silicon-organic and other oligomers depending on the desirable polymerization rate and properties of the finished product. As a rule, polymerization of such compounds is initiated by high doses of the ionizing radiation. Our research focuses on the compositions of epoxy oligomers with different hardeners. This selection is not random. According to our papers [8-10], radiation resistance of epoxy compositions, both hardened and non-hardened, depends on the type of the used hardener and, therefore, the process can be controlled to the desirable way.

The prepregs were prepared by immersion of different fabrics into binder compositions. The excess of binder was removed by the rollers. Then the impregnated fabrics were stretched on the mandrels. The mandrels, intended for shaping of samples, were first protected by polyethylene to avoid the sticking of binder.

The following fabrics were used: capron, phenylone, arimide, fiberglass fabric grade EZ-100 P, sulphone, CVM-4, and carbon fabric T10-XO. To obtain better wettability, capron underwent preliminary washing. However, even after washing capron poorly was impregnated, but the other fabrics showed the good impregnating properties.

Depending on composition, the prepregs were prepared by three ways: 1) cold hardening; 2) hot hardening; and 3) radiation hardening (exposure to low-dose electron radiation in the accelerator «Electron 3M», 400-700 keV energy).

The samples of the prepregs were additionally hardened by accelerated electrons in the energy range from 300 keV to 3 MeV on different accelerator facilities, by fluxes of radiative energy from the lamp SVD-120A (at 100 mm from the lens, i.e., 0.05 W/cm² full flux intensity, and UV radiation at < 384 nm, ~ 0.025 W/cm²) and from the lamp DKcR-3000 (UV intensity in 200 - 400 nm is ~3 Suns, that is in 3 times higher than UV radiation intensity of the exoatmospheric

Sun on the Earth orbit) in vacuum (about 10^{-5} mmHg) on the facility IC-600/300. This facility was designed for the UV exposure of the large lots of the samples of materials at different temperatures (from 30 to 200 °C and above) in high vacuum. On this facility the samples can be exposed to UV irradiation separately or simultaneously in two working chambers with a capacity of 300 liters and 600 liters by fluxes of irradiative energy from the xenon arc lamps of ultrahigh pressure of the type DKcR-3000, DKcShRB-3000 or DKcShRB-5000 at different intensities. Special target devices were developed to expose material samples of various types by different UV energies. At low doses of UV radiation (to 5 ~ 7 equivalent solar days) plated targets were used for film-type, textile and flat samples for the construction materials.

On Figures 1 and 2 the IR spectra are presented for epoxypolyester complex binder used in the formation of prepregs. Spectroscopy investigations make it possible to understand the mechanisms of the processes taken place at the creation of such materials, both at the stage of obtaining and at further radiation hardening. It is observed on Figure 1 that at the stage of formation of prepreg the changes occur only in the epoxy components of the complex binder. In this case the chemical hardening of prepregs (with amine hardener) is accompanied by decrease of epoxy group content during the time (at 910 cm^{-1} band) and simultaneous increase of hydroxyl group content (at 3450 cm^{-1} band). Radiation additional hardening (Fig. 2) of prepregs occurs due to opening double bonds (decrease of bands intensity and even disappearance at 1650 cm^{-1} and 760 cm^{-1}) in the polyester component of complex binder. In this case is observed also that additional hardening of prepregs can proceed with participation of residual epoxy groups in the epoxy components of complex binders. Therefore, the band of intensity of hydroxyl groups increases at 3450 cm^{-1} , while intensity of epoxy groups decreases, according to the IR spectral data of the UV exposed binder. The efficiency of this process depends on the type of hardener.

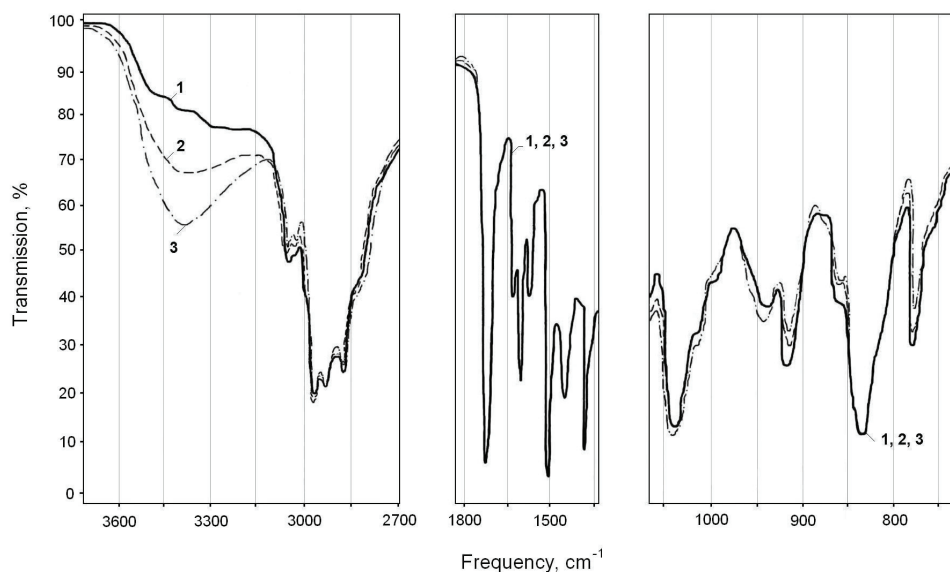


Fig. 1. Kinetics of hardening (IR-spectra) of epoxypolyester binder:

1 – right after preparation; 2 – in a day after preparation; 3 – in 10 days

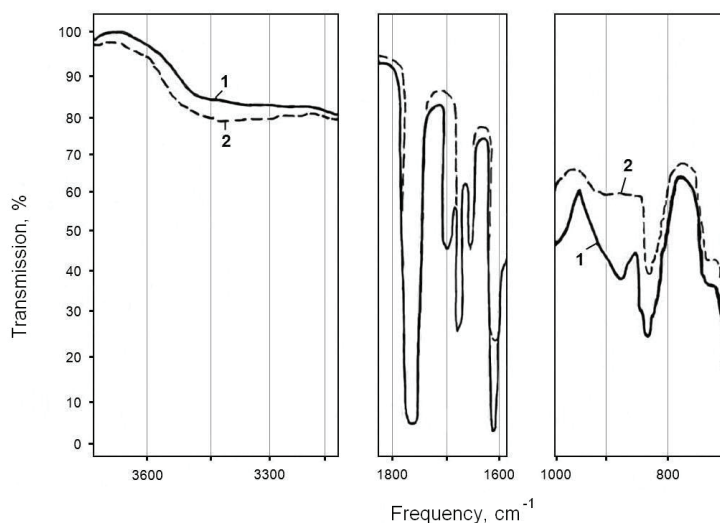


Fig. 2. IR-spectra of epoxypolyester binder:

1 – non-irradiated; 2 – irradiated by electrons, dose 0.05 MGy

№	Composition	Exposure energy, e.s.h.*	Gel-fraction, %
1	Epoxypolyester binder, aliphatic amine as hardener, fabric SVM-4	0	71.82
		1	95.76
		10	98.3
2	Epoxypolyester binder, aliphatic amine as hardener, fiberglass fabric	0	69.2
		10	90.2
3	Epoxypolyester binder, aliphatic amine as hardener, Capron fabric (hot hardening)	0	66.1
		10	90.4
4	Epoxypolyester binder, aliphatic amine as hardener, Phenylone fabric (hot hardening)	0	70.8
		1	77.44
		10	97.9
5	Epoxypolyester binder, aromatic amine as hardener, fabric SVM-4	0	72.2
		1	90.1
		10	97.9
6	Epoxysilicoorganic polyester binder, aliphatic amine as hardener, fabric SVM-4	0	56.9
		1	87.9
		10	93
7	Epoxypolyesterstyrene binder, aliphatic amine as hardener, fabric SVM-4	0	79.48
		1	95.22
		10	100
8	Epoxyacrylamide binder, aliphatic amine as hardener, fabric SVM-4	0	80
		1	76.37
		10	30

*e.s.h. – equivalent solar hours

Table 1. Content of gel fraction in the prepreps additionally hardened in the UV facility IC-600/300

Additional hardening of the binder lead to the increase gel-fraction, and the most intensive crosslinking occurs during the first hour of radiation exposure as follows from Table 1. The process of additional hardening completely concludes in polyester on double-bonds at energy exposition of about 10 equivalent solar hours as proved by disappearance of the band at 1650 cm^{-1} and $\sim 100\%$ of gel-fraction (Fig. 2, Table 1). The finished cross-linked product has the higher heat resistance (315°C), than initial polyesters (280°C). Therefore, as a whole new composite material will have higher values of heat resistance as compared to the initial prepreg, this is clearly shown by the differential thermal analysis (Fig. 3). It should be noted that additional hardening of the prepreps depends on the binder composition and is practically independent of the fabric type (Tables 1-3). However, the properties of the prepreps and additionally hardening composites and, consequently, products on their base depend on fabric characteristics. After long storage of the fiberglass prepreps it is easy to identify bending lines on the samples. At the place of bending the sealing properties become low. It looks like fiberglass fabric cuts a hardened binder. Therefore, this fabric was not used in further experiments.

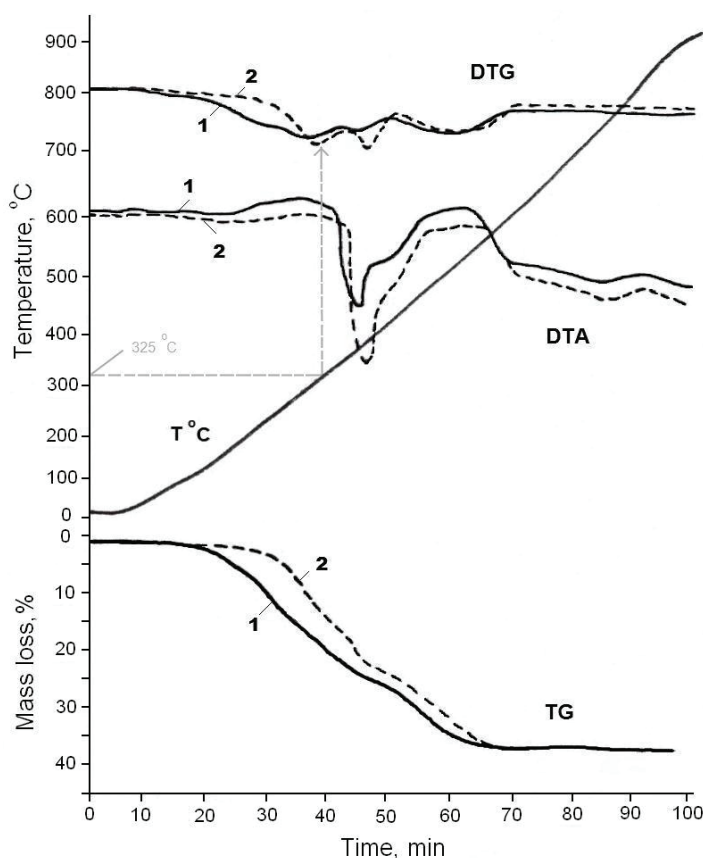


Fig. 3. Differential thermal analysis of hot-hardened prepreps based on epoxypolyester binder: 1 - non-irradiated binder; 2 - 10 hours after UV irradiation

According to Table 2, the strength of both the prepregs and the finished compositional materials (or products) is defined also by binder composition. In the process in all cases during additional hardening by UV radiation the mechanical strength very strongly increases, while the relative elongation decreases. These dependences are valid for all fabrics used in the research (Table 3). It should be noted, that the strength of the compositional materials (and therefore, products on their base), additional hardened by space-simulated factors (UV exposure about 10 equivalent solar hours or electron radiation about 0.03 MGy), decreases only by 40 % and for sulphone fabric even by 20 % at thermal tests of 200 °C.

After additional hardening by the UV-radiation or by the accelerated electrons the composite materials, based on the carbon fabric of grade T-10-X0 (GOST 15170-73), acquire the highest strength, i.e. 1177 MPa in comparison with ~ 147 MPa for the samples, based on the other fabrics. However, this fabric is unsuitable for fabrication the prepregs, since finished products badly roll up into rolls. Most probably the fabric samples required for this objective should be much thinner.

It is significant that after radiation processing the characteristics of the prepregs, in particular rigidity, and of the finished products on their base noticeably depend on the properties of the initial fabrics (Fig. 4). On this Figure the initial rigidity of prepregs on the fabrics of grade TPR-2MU-1 on SVM fiber is 3 times higher than on the fabric TPR-2MU-2 on arimide filament, though the same binder and the same regime were used to obtain both prepregs. Moreover, these prepregs have different vacuum resistance that is obvious on Fig. 5. The initial rigidity of prepregs can be increased, without change of characteristics of tightness and capability to compact packing, due to the irradiation by the low doses of

№	Prepreg composition	Before irradiation		After irradiation - 10 e.s.h.*	
		Tensile strength, MPa	Relative elongation, %	Tensile strength, MPa	Relative elongation, %
1	Epoxy polyester styrene binder, aliphatic amine as hardener, fabric - Phenylone	73.3±6.9	40±4	134.1±4.1	19±2
2	Epoxy polyester binder, aliphatic amine as hardener, fabric - Phenylone	39.8±2.9	38±3	67.8±1.7	29±7
3	Epoxy polyester binder, aromatic amine as hardener, fabric - Phenylone	61.8±3.4	25	127.7±6.9	13±2
4	Epoxy silicoorganic polyester binder, aliphatic amine as hardener, fabric - Phenylone	28.0±1.9	33±2	118.0±1.3	6±1

*e.s.h. – equivalent solar hours

Table 2. Change of physico-mechanical properties of the prepregs after UV irradiation

Fabric type	Before irradiation					After irradiation – 10 e.s.h.*				
	Gel, %	Temperature of testing, °C				Gel, %	Temperature of testing, °C			
		σ, MPa		ε, %			σ, MPa		ε, %	
		20°	200°	20°	200°		20°	200°	20°	200°
Phenylone (analog: Nomex, Konex)	73	80.4	51.0	26	29	98.2	92.2	58.8	15	27
SVM-4 (analog: Technor)	72	147.4	103.4	9	14	95.4	169.2	123.5	6	9
Arimide (analog: P-84)	72	88.3	52.8	23	26	97.6	106.2	63.7	14	25
Carbon fabric		806.7	523.7	9	12		1176. 7	823.7	4	8
Sulphone	71.8	41.2	31.6	35	27	95.7	53.9	36.3	28	30

*e.s.h. – equivalent solar hours

σ – tensile strength

ε – relative elongation

Table 3. Physico-mechanical properties of the preregs based on different fabrics (more than a year storage life)

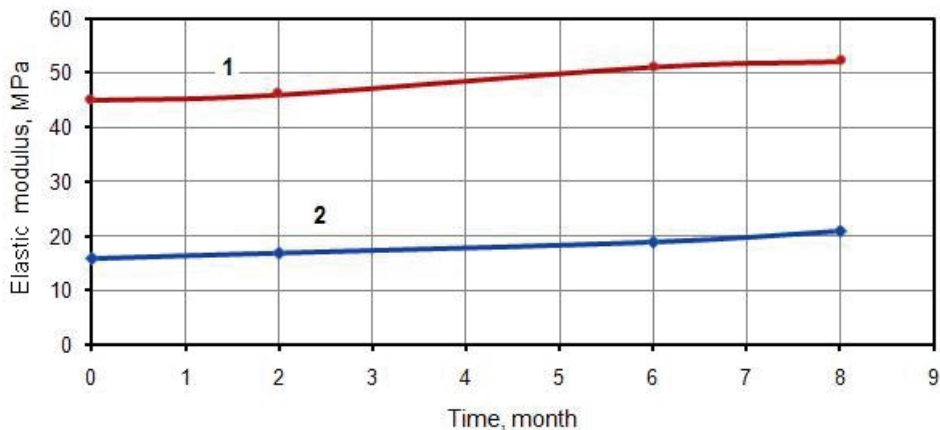


Fig. 4. Change of elastic modulus during storage of preregs depending on the initial fabric structure: 1 – prepeg on fabric TPR-2MU-1 and epoxypolyester binder; 2 – prepeg on fabric TPR-2MU-2 and epoxypolyester binder

0.0025 or 0.005 MGy (Fig.6). In conditions of vacuum the values of mass loss decrease from 4 % to 0.5 % (Fig. 7). The pre-fabricated products, based on the special compositions of binder, acquire the shape stability at exposure to electron irradiation about 0.03 MGy and above and to UV irradiation not less than 10 equivalent suns. In this case the rigidity values (estimated by the elasticity modulus at bending on the sample based on fabric TPR-2MU-1) of the non-

irradiated prepreg and irradiated by dose 0.0025 MGy are 12.2 MPa and 12.8 MPa respectively. Accordingly, the products based on these prepregs acquire rigidity of 160 MPa and 174 MPa after additional UV hardening by 10 equivalent suns. At the same time a factor of thermal expansion do not change. The products obtained by such procedure have resistance to dose of 1 MGy. On exposure to space factors the heat resistance of the cured composite materials is 105 °C.

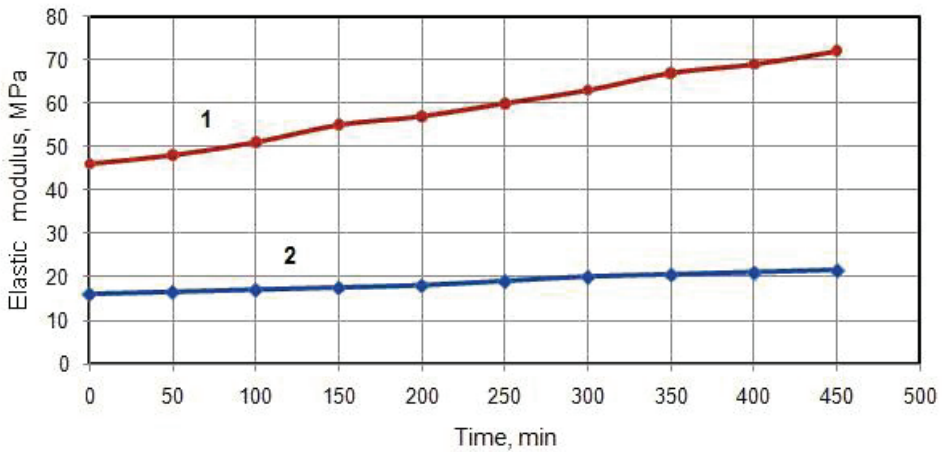


Fig. 5. Change of elastic modulus of prepregs on various fabrics in vacuum:
1 - TPR-2MU-1; 2 - TPR-2MU-2

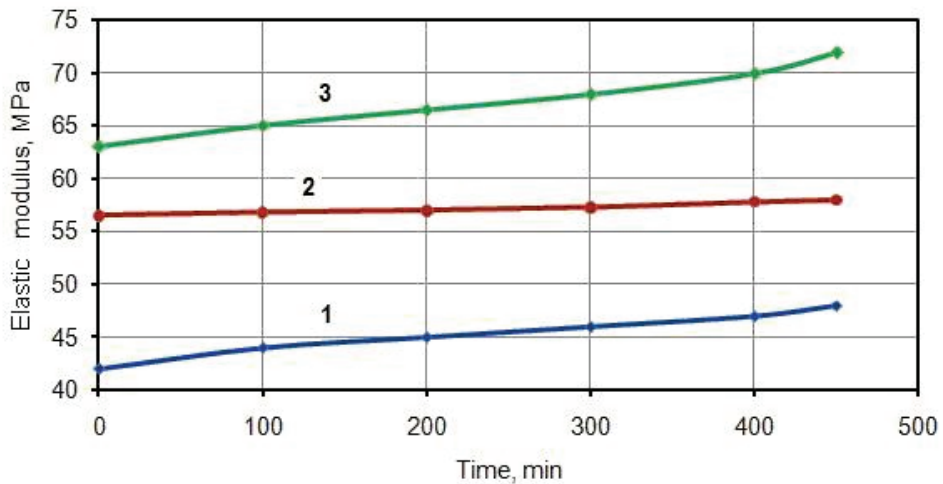


Fig. 6. Influence of electron radiation and vacuum on elastic modulus of prepregs on fabric TPR-2MU-1: 1 - non-irradiated; 2 - radiation dose 0.0025 MGy; 3 - radiation dose 0.005 MGy

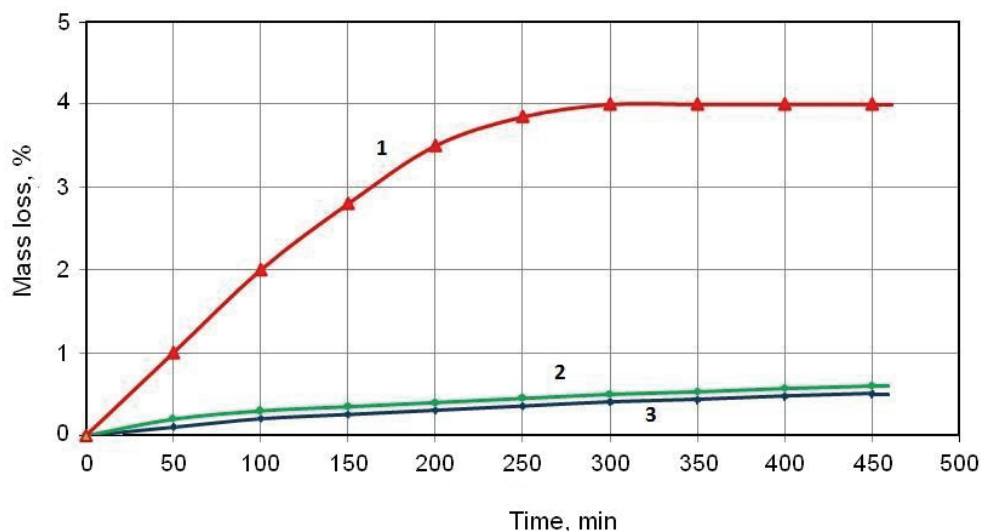


Fig. 7. Egress of volatile substances of the prepreps formed by different methods (on one binder) at irradiation in vacuum: 1 – non-irradiated; 2 – radiation dose 0.0025 MGy; 3 – radiation dose 0.005 MGy

2. Conclusions

1. It is shown that the non-sticky intermediate products (prepreps), which can be compactly packed on the Earth and be opened in the space conditions, can be prepared by three ways depending on composition: 1) cold hardening; 2) hot hardening; 3) radiation hardening (hardening by low doses of electrons, at such doses the samples are soft and can be compact packed).
2. It is possible to carry out the additional hardening of the intermediate products (prepreps) by accelerated electrons with the energies from 300 keV to 3 MeV on different installations by doses of the order of 0.03 MGy and by UV-radiation in the field of 200-400 nanometers at an exposition of the order of 5-10 e.s.h. also. Thus the samples acquire the shape stability.
3. It is shown that on the basis of the combinations of special complex binders, polymerizing by different mechanisms, and high-strength fabrics, it is possible to develop the pre-fabricated products, which can be compact packed on the Earth and in the sequel be unfolded in the space conditions. Under exposure of space environment these products can acquire shape stability and sufficient strength and, thus, they become suitable for assembling or repairing the constructions in the space conditions.
4. The products received thus stand the irradiation doses more than 1 MGy.

3. References

- [1] US Patent № 4089004.
- [2] Materials and Processes. 15-th National Symposium and Exhibition, April 29 – May 1. 1969. Los Angeles, California. Vol. 15. pp. 1073-1089.

- [3] Semenov Yu.P., Sokolov B.A., Senkevich V.P., Komkov V.A., Mel'nikov V.M., Kagan M.B. Perspektivy bol'shoi kosmicheskoi energetiki. Konversiya v mashinostroenii. 2002. № 6. s.11-16.
- [4] Mel'nikov V.M., Komkov V.A., Rembeza A.I., Ivanov N.N., Harlov B.N. Solnechnye plenki. Novosti kosmonavтики. 2006. № 10. s. 38-39.
- [5] Tsentrobezhnnye beskarkasnye krupnogabaritnye kosmicheskie konstruksii. M. FIZMATLIT. 2009. s. 447.
- [6] USSR Author's Certificate № 253063.
- [7] USSR Author's Certificate № 196880.
- [8] Laricheva V.P., Kalgashkina G.V. Radiation Impact on Polymerization Rate of Epoxy Resins with Hardener Content. In Proc.: Radiation Resistance of Polymers and Polymer-Containing Materials in Space Conditions. Moscow. 1982. pp. 50-55.
- [9] Laricheva V. Effect of ionizing radiation on epoxy oligomers of different structures and manufacture of new promising materials on their base. Radiation Physics and Chemistry. 2008. V. 77. Issue 1. pp. 29-33 (doi:10.1016/j.radphyschem.2007.02.033).
- [10] Laricheva V.P., Korotkii A.F. Himiya vysokih energii. 2008. T. 42. № 1. s. 27.

G40-800/5260 Carbon Fiber/Bismaleimide Composite Material: High Temperature Characteristics of Static and Fatigue Strengths

Toshiyuki Shimokawa¹, Yoshiaki Kakuta² and Takenori Aiyama³

¹*Formerly Tokyo Metropolitan Institute of Technology,*

²*Japan Aerospace Exploration Agency,*

³*Toyota Motor Corporation
Japan*

1. Introduction

A lot of polymer composite materials are being used in the structures of civil transport aircraft currently under development, such as the Boeing 787, Airbus A350, and Bombardier C Series. Their percentages of structural weight are announced at 50%, 53% and 46%, respectively. However, mostly carbon fiber/epoxy (CF/Ep) systems are being introduced into their primary structures and they are only being introduced in environments where they are not expected to encounter high temperature. On the other hand, application of carbon fiber/bismaleimide (CF/BMI) composite materials is being expanded, especially for military aircraft structures such as the airframes of the F-22 Raptor and the F-35 Lightning II Joint Strike Fighter, the jet engine nacelle skins of the F-35 as well as the thrust reverser structure of the Gulfstream G450 business jet in civil aircraft (McConnell, 2009), and is expected for structures of the next-generation supersonic transport (SST).

There are several reasons for CF/BMI system application for the structures described above. As for epoxy system composite materials, about 70°C is usually set as the design limit temperature for long term use (Brandecker & Hilgert, 1988, Fawcett et al., 1997). Meanwhile, carbon fiber/polyimide (CF/PI) system composite materials can be used for hotter structures, although they are very expensive and involve complicated processes. CF/BMI composite materials offer temperature performance and costs between those of epoxy and polyimide systems. Moreover, CF/BMI systems can be easily handled in an airframe parts manufacturing process in a way that is equivalent to that for epoxy systems.

The design limit temperature of CF/BMI composite materials for aircraft structures is supposed to be around 120°C on the basis of actual application to the mechanically loaded structures described above. If the design limit temperature is set as 120°C, it is necessary to know the detailed characteristics of static and fatigue strengths at about 150°C from the view point of the safety margin; moreover, 150°C is considered to be close to the service-limit temperature for CF/BMI composite materials. Therefore, in order to apply CF/BMI composite materials for aircraft structures that encounter medium high temperatures,

knowledge of their static and fatigue properties at 150°C is very important in comparison with that at RT.

The following reports presented the static strength of a CF/BMI composite material, G40-800/5260, with a quasi-isotropic layup. As part of the investigation of the potential of high temperature composite materials for the next-generation SST, the authors' group assessed open-hole (OH) tensile and compressive static strengths at RT and 120°C (Shimokawa et al., 1999-a). Hirano reported OH tensile and compressive static strengths at RT only (Hirano, 2001). Johnston and Gates investigated OH tensile static strength at from 23°C to 218°C (Johnston and Gates, 1998).

Meanwhile, the following investigations were carried out on fatigue strength or *S-N* relationships of CF/BMI composite materials with a quasi-isotropic stacking sequence at RT. Hirano conducted axial tension, compression, and tension-compression fatigue tests for OH specimens of a G40-800/5260 CF/BMI laminate along with CF/PI composite materials based on a small number of specimens and presented a rough estimate of *S-N* relationships (Hirano, 2001). For materials with a non quasi-isotropic stacking sequence, Gathercole et al. fatigue tested unnotched specimens of a T800/5245 CF/BMI laminate with $[(\pm 45, 0_2)_2]_S$ layup under constant amplitude loading over a wide range of stress ratio *R* (=minimum stress/maximum stress), and discussed Weibull life-distributions, *S-N* relationships, and Goodman's diagram based on an analysis of test results (Gathercole et al., 1994). Following this paper, Adam et al. reported the results of programmed fatigue tests of block variable loading, provided the cumulative damage fraction to failure, and discussed the applicability of a nonlinear cumulative damage rule (Adam et al., 1994). On the other hand, Tyahla and McClellan reported various kinds of test results on the durability and damage tolerance of IM6/3100 and IM6/F650 CF/BMI composite materials, including results of fatigue testing of OH specimens (Tyahla and McClellan, 1988). The layup of OH specimens was $[0^\circ(50\%)/\pm 45^\circ(40\%)/90^\circ(10\%)]$ and fatigue tests were carried out at only two or three stress levels for *R*=-1 and 10 under cold temperature dry (CTD), room temperature dry (RTD), and elevated temperature wet (ETW) conditions.

Although as described above many reports about the static and fatigue strengths of CF/BMI composite materials have been published, this chapter discusses only test results obtained for specimens with a quasi-isotropic layup, because such test results can be used for the reference or comparison data. Moreover, this chapter focuses on the high-temperature characteristics of the static and fatigue strengths.

For OH static strength at high temperatures, only data at 120°C by the authors and those of OH tensile strength by Johnston and Gates were reported. As for fatigue strength, Hirano only discussed rough *S-N* relationships of fatigue characteristics at RT as determined by axial tension, compression and tension-compression fatigue tests using a small number of test specimens. Under these circumstances, the authors systematically conducted static tests on NH and OH specimens and fatigue tests on OH specimens for a CF/BMI composite material with a quasi-isotropic layup at RT and high temperatures and discussed test results and the high-temperature practicality of this material (Shimokawa et al., 2008).

In this chapter the authors introduce the major contents of their previous paper from a practical viewpoint. The material used was a G40-800/5260 CF/BMI composite material selected from popular CF/BMI composite materials. The objective of this study was to systematically clarify static and fatigue strength at RT and 150°C. In addition, solely static compressive tests on NH specimens were conducted at several high temperatures up to

215°C. Static tests provided static tensile and compressive strengths of NH and OH specimens. Fatigue tests under constant amplitude loading provided S - N relationships for just the OH specimens, i.e., tension, compression, and tension-compression fatigue tests. Visual and CCD microscope observation showed the fracture behavior of static and fatigue failure.

The major subjects of this chapter are as follows. (1) An offer of reference data with respect to the static and fatigue strengths at RT and high temperatures. (2) Fiber dominant and matrix (resin) dominant properties in static and fatigue strengths. (3) Open-hole and temperature dependence on static strength. (4) The dependence of the stress ratio R (R =minimum stress/maximum stress in fatigue loading) and temperature on fatigue strength and S - N relationships. (5) The strength ratio (=compression strength/tension strength) for static and fatigue strengths. (6) The influence of load components on fatigue strength degradation, i.e., the influence of tension, compression, and tension-compression load cycles. (7) Practicality evaluation of static and fatigue strengths in the marginal high temperature region for long-term use.

2. Material, specimens and testing procedures

The prepreg system used is a combination of G40-800 CF and 5260 toughened BMI resin made by CYTEC Co. The lamination has a quasi-isotropic (QI) stacking sequence, 32 plies $[45/0/-45/90]_{4S}$. The nominal thickness of 4.29 mm ($0.134 \text{ mm} \times 32$) was used in calculating stress on specimens. Laminate panels were cured in an autoclave at 190°C for two hours at a pressure of 6.0 kgf/cm² and post-cured at 215°C for four hours in an air-circulating oven. All panels were cured at the same time.

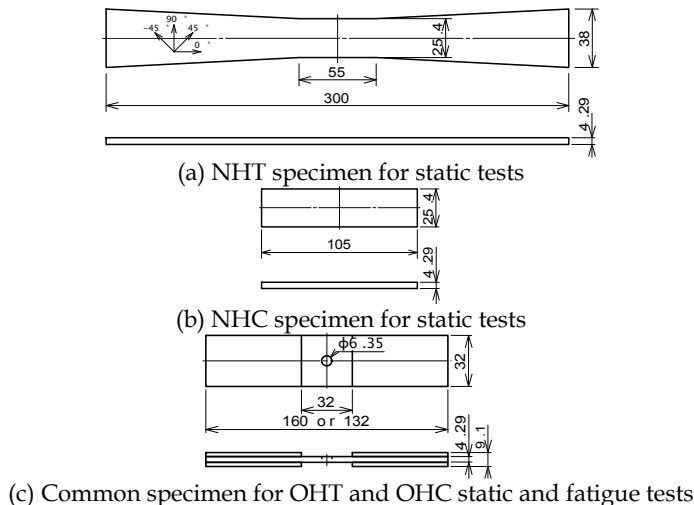


Fig. 1. Specimen configurations for static and fatigue tests (mm)

Fig. 1 (a) and (b) illustrate specimen configurations for NH tensile and compressive static tests. Fig. 1 (c) shows the configuration of OH specimens used for both static and fatigue tests. To avoid the complex stress state of coupon-type fatigue leading to failure in the vicinity of the clamping location, only OH specimens were used for fatigue tests. The

clamping parts of OH specimens were bonded with tubs made of the same material as the specimens. In the static tensile and tension fatigue tests, a longer clamp was used, while the static compressive tests, and compression fatigue and tension-compression fatigue tests used the shorter grip size shown in Fig. 1 (c). Laminate processing and specimen manufacturing were carried out at Kawasaki Heavy Industries, Ltd.

For generality, specimen configurations conform to ASTM standards or SACMA recommendations. Since the objectives of this study included the direct comparison of NH static and OH static strengths, the use of common OH specimens for comparing OH static and fatigue strengths, and specimen cost reduction, the specimen configuration shown in Fig. 1 (c) was employed. In particular, the cross-sectional area was equal for both NH and OH specimens. The hole diameter of OH specimens in this study was that from SACMA recommended methods, and other dimensions were smaller than those in the SACMA methods. Table 1 shows the number of specimens tested, with the number of run-out specimens for which the fatigue test was suspended given in parentheses.

Temperature (°C)	Static test specimen				Fatigue test, OH specimen		
	NHT	NHC	OHT	OHC	R=0.1	R=10	R=-1
RT	4	3	2	4	10(2)	8	7
120	-	1	-	-	-	-	-
150	3	3	2	4	5	7	5
180, 215	-	1 each	-	-	-	-	-

Number in () represents run-out specimens

Table 1. Number of specimens used for static and fatigue tests

An INSTRON 8500 digitally-controlled servo-hydraulic material testing machine with an environmental chamber was used for static and fatigue tests. Static tensile tests for NH and OH specimens and static compressive tests for OH specimens were conducted using hydraulic grips. Static compressive tests for NH specimens were conducted using the NAL (National Aerospace Laboratory) type compression test fixture (Shimokawa et al., 1999-a, 1999-b, 2002) shown in Fig. 2. A supporting guide for both clamps seen in Fig. 2(a), which has a fine clearance to the top clamp, prevents moving of the clamps in the out of plane direction of the specimen. The test part of the specimen is not supported against out of plane bending. The compression load is given from both end-sections of the specimen. The actuator speed of the testing machine for all static tests was 1 mm/min.

Fatigue tests were conducted under sinusoidal constant amplitude loading with a repetition frequency of 1 Hz or 5 Hz. Three kinds of stress ratio, R =minimum stress/maximum stress, were selected, i.e., R =0.1 for tension fatigue tests, R =10 for compression fatigue tests, and R =-1 for tension-compression fatigue tests.

The temperature in the laboratory was controlled by an air conditioner at around 23°C throughout the year. Static and fatigue tests at high temperatures used an air-circulating environmental chamber (Shimokawa et al., 2007). Elevated temperature tests were mainly conducted at 150°C, as indicated in Table 1. For the static NH compressive tests only, several temperatures were chosen up to 215°C in order to estimate the effect of the heat-resistance of the BMI resin with respect to compressive strength. Stress in OH specimens in this study is represented by the net section stress,

$$S = \frac{P}{(W-d)t} \quad (1)$$

where P is applied load, W specimen width, d open hole diameter, and t the nominal thickness of a specimen. Failed specimens were inspected visually and with a CCD microscope to determine the failure mode: fiber dominant or matrix dominant.

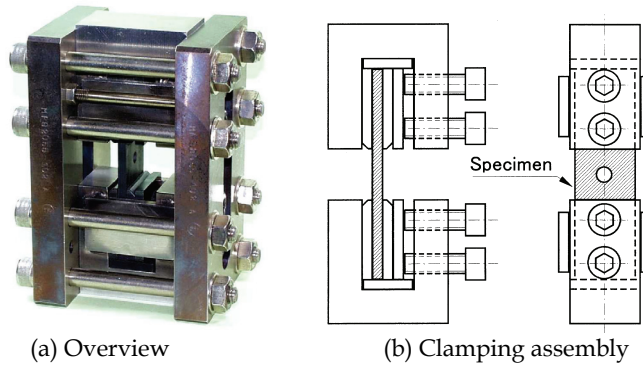


Fig. 2. NAL type compression test fixture

3. Test results

Table 2 presents the numerical data of static strength S_u and its mean \bar{S}_u , while Table 3 presents fatigue life data. These data were systematically obtained as described above and are expected to be used for the reference or comparison data for conventional CF/BMI composite materials and new CF/BMI materials recently developed for low-cost and out-of-autoclave manufacturing such as those produced by a VaRTM (Vacuum assisted Resin Transfer Molding) method.

Specimen	Load	Temp. (°C)	Strength S_u (MPa)	Mean \bar{S}_u (MPa)
NH	Tens.	RT (23)	1016, 1060, 1116, 1126	1079
		150	871, 1000, 1033	968
	Comp.	RT (23)	834, 884, 899	872
		120	751	751
		150	651, 652, 659	654
		180	586	586
OH	Tens.	215	246	246
		RT (23)	704, 724	714
	Comp.	150	672, 708	690
		RT (23)	409, 446, 476, 514	461
		150	376, 377, 391, 408	388

Table 2. Static strength data

Fat. Load (R)	T (°C)	S-N relationship: $S=S_{\max}$ or S_{\min} (MPa), N =Number of cycles to failure								
		S	S_{\max}	S_{\min}	S_{\max}	S_{\min}	S_{\max}	S_{\min}	S_{\max}	S_{\min}
Tens. (0.1)	RT (23)	S	688	688	652	652	651	616	614	580
		N	5	134	553	8,960	338,223	211,916	*89,000	4,313,329
	150	S	674	639	638	602	567		580	579
		N	8	62,283	3,469	67,000	445,500		*1,000,000	5,760,765
Comp. (10)	RT (23)	S	-410	-387	-387	-364	-364	-364	-319	-318
		N	3,150	7,771	8,891	16,294	38,871	47,191	836,882	2,112,567
	150	S	-356	-356	-336	-336	-316	-316	-277	
		N	807	1,734	2,428	13,558	225,944	261,779	6,726,000	
Tens.-Comp. (-1.0)	RT (23)	S	387	387	364	341	319	318	273	
		N	460	5,583	11,197	24,210	81,004	76,457	851,768	
	150	S	336	316	277	277	240			
		N	892	15,114	132,437	239,397	1,182,763			

R=stress ratio, T=temperature, * indicates no failure

Table 3. Fatigue life data

3.1 Static strength of NH and OH specimens

Fig. 3 shows non-hole tensile (NHT) strength, non-hole compressive (NHC) strength, open-hole tensile (OHT) strength, and open-hole compressive (OHC) strength at RT and high temperatures, where OH strength is represented by net section stress, as described above. Since these tests were carried out to determine their temperature dependence, only a few specimens were tested for each case, as shown in Table 1. The relationship between static strength and temperature is represented by a solid line, which connects the mean strength at every test temperature. When there is only one test result, this value is taken as the mean.

NHT strength at 150°C is slightly lower than that at RT. Although this fact is strongly influenced by the lowest value measured at 150°C (Fig. 3), this tendency is considered to be reasonable if referred to the tendency that appeared in OHT static strength (Fig. 3) and OHT fatigue strength, as described later. When the mean values are compared, the NHT strength at 150°C is 10% lower than that at RT. Since the usual allowable temperature limit of carbon fibers is about 538°C (1000°F) (Niu, 1996), the strength of carbon fibers in the material tested is considered unchanged between RT and 150°C. Furthermore, since all 0° fibers need to be broken for the final failure of the material tested, the tensile strength is dominated by the fiber strength, i.e., it is considered to be a fiber-dominant property. However, the small decrease in tensile strength found at 150°C means that the matrix binding the fibers also has a small effect on tensile strength, so this is not entirely a fiber-dominant property. This aspect will be discussed in detail later on the basis of careful examination of failed specimens. On the other hand, the mean OHT strength at 150°C is only 3% lower than that at RT. Although this reduction is quite small in comparison with that of NHT strength, this tendency to decrease with increasing temperature is common for NHT and OHT strengths.

NHC strength decreases considerably with increasing temperature and the mean NHC strength at 150°C is 25% lower than that at RT. Furthermore, although NHC strength drops gently up to 180°C, it drops heavily at 215°C. The compressive strength of both NH and OH specimens is considered to be a matrix-dominated property. Although this study did not measure the glass transition temperature of the material tested, Johnston and Gates reported

that the glass transition temperature of a G40-800/5260 CF/BMI composite was about 228°C after the material was left in a laboratory environment for several days (Johnston and Gates, 1998). Therefore, this heavy drop of the compressive strength of NH specimens is understandable. The decrease in NHC strength with temperature rise is considered to be a reflection of the decrease in matrix strength in that the specimen failure mechanism is not changed. The mean OHC strength at 150°C is 16% lower than that at RT and this drop is not very large, though it is larger than that of the mean OHT strength. The above results indicate that high temperatures have a large effect on NHC strength, but have a comparatively small effect on other strengths, i.e. NHT, OHT, and OHC strengths. The favorable test results mentioned above are considered to have appeared due to the effectiveness of using heat-resistant polymer as the matrix.

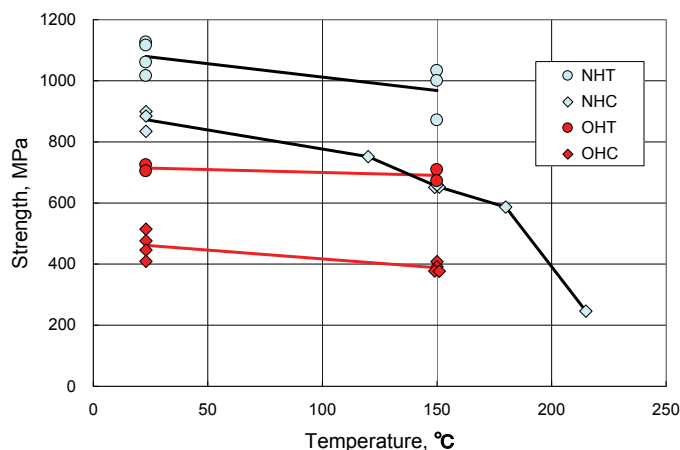


Fig. 3. Static tensile and compressive strengths of NH and OH specimens as a function of temperature

3.2 Fatigue strength of OH specimens

Let us examine S - N (stress-life) relationships on semi-logarithmic graph paper based on net section stress, placing the maximum stress S_{\max} on the ordinate and the logarithm of fatigue life $\log N$ on the abscissa, where N is the number of load cycles to failure. In compression fatigue, the minimum stress S_{\min} is used instead of S_{\max} on the ordinate. If N is assumed to be an independent variable on the S - N diagram, S_{\max} will be a dependent variable and can be regarded as fatigue strength. OH static strength is plotted as S_{\max} at $N=1$ to compare it with fatigue strength. An S - N relationship is assumed to be linear on semi-logarithmic graph paper. The S - N line approximating only S - N data is determined by the least-squares method.

The S - N equation is represented by

$$S_{\max} = a - b \cdot \log N \quad (2)$$

where a and b are constants and treated as parameters, i.e., intersection and slope. Since the slope of the S - N relationship in this study is quite small, N is dealt with as an independent variable and S_{\max} as a dependent variable to aid intuitive understanding. Table 4 shows the

parameters of S - N equations for three kinds of R . In order to discuss tension-compression fatigue-test results later, the $S_{\text{range}}-N$ relationship for compression fatigue is also shown in Table 4, where $S_{\text{range}} (=S_{\text{min}}-S_{\text{max}})$ is the compression repeated stress range.

Fatigue test & S - N relationship	Temp.	Parameters	
		a (MPa)	b (MPa)
Tension, $S_{\text{max}}-N$, ($R=0.1$)	RT	714	18.9
	150°C	698	18.9
Compression, $S_{\text{min}}-N$, ($R=10$)	RT	-510	-31.4
	150°C	-410	-18.6
Tension-compression, $S_{\text{max}}-N$, ($R=-1$)	RT	508	38.2
	150°C	433	30.4
Compression, $S_{\text{range}}-N$, ($R=10$)	RT	459	28.3
	150°C	369	16.7

Table 4. Parameters of S - N equations

3.2.1 Tension fatigue strength

Fig. 4 shows the static OHT strength and S - N relationships from tension fatigue tests for $R=0.1$ at RT and 150°C. In the RT fatigue tests, an arrow shows those run-out specimens whose fatigue tests were terminated without specimen failure; however, these points were included in the S - N data when approximated by an S - N line. Therefore, the S - N line at RT provides a conservative estimate. From the two S - N lines in this figure and the b values in Table 4, the S - N relationships at RT and 150°C have equal slopes and are considered to be parallel. Moreover, the difference between fatigue strength at RT and 150°C is close to the difference of the mean static strength at $N=1$ regardless of N . That is, the test results showed that the difference in static strength in the two environments appeared in the difference in fatigue strength. This fact points out that a difference between the S - N lines at RT and 150°C exists but it is very small. Furthermore, since the slope of the S - N line is small, the decrease in S_{max} is small with an increase in N at either RT or 150°C.

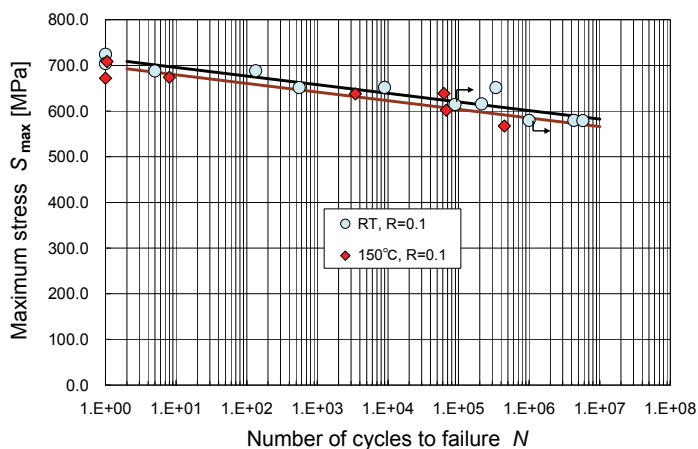


Fig. 4. S - N diagram of OH specimens from tension fatigue tests, $R=0.1$, at RT and 150°C

The mean tensile static strength is 714 MPa at RT and 690 MPa at 150°C in Table 2. Meanwhile, the intersection a in Table 4 is 714 MPa at RT and 698 MPa at 150°C. Although there is a slight difference between the static strength and the intersection of the S - N line at 150°C, static strength can be treated as a part of the S - N relationship for $R=0.1$ in both environments.

The fact that tension fatigue strength is slightly influenced by temperature and load repetition means that it is strongly fiber-dominated. However, since these small effects are real, the fiber dominance is not total.

3.2.2 Compression fatigue strength

Fig. 5 presents the static OHC strength and S - N relationships obtained from compression fatigue tests for $R=10$ at RT and 150°C. From the two S - N lines in this figure and the b or b/a values in Table 4, compression fatigue strength S_{\min} at RT and 150°C drops considerably with the increase in the number of load cycles N . Moreover, there is a clear difference between the two S - N lines at RT and 150°C. However, as N becomes larger, the difference between the lines tends to decrease.

The values of intersection a in Table 4 are very close to the highest values of static compressive strength plotted at $N=1$ for the RT and 150°C conditions, and higher than their mean in Table 2. Since the scatter of static compressive strength at RT is fairly large, the difference between the highest and mean values is fairly large. The static compressive strength is judged not suitable for regarding as a part of the S - N relationship. In contrast, at 150°C the static compressive strength has a small scatter and may be regarded as a part of the S - N relationship. However, generally including the data on static compressive strength in the compression fatigue data cannot be recommended.

As mentioned above, since the compression fatigue strength is greatly influenced by temperature and the number of load cycles, it becomes apparent that compression fatigue strength is a matrix-dominated property.

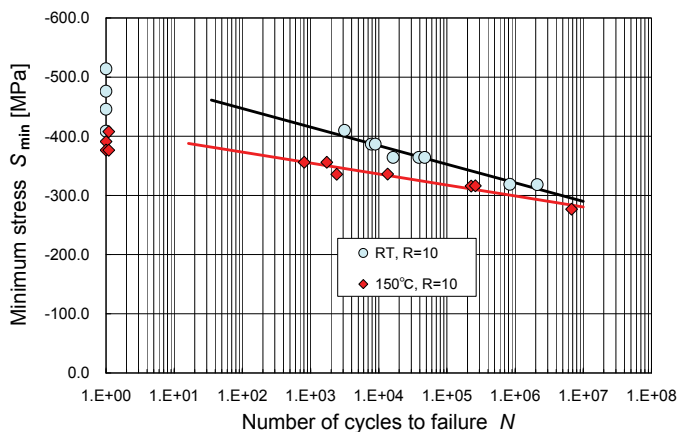


Fig. 5. S - N diagram of OH specimens from compression fatigue tests, $R=10$, at RT and 150°C

3.2.3 Tension-compression fatigue strength

Fig. 6 shows the static OHC strength and S - N relationship obtained from tension-compression fatigue tests for $R=-1$ at RT and 150°C. Since compression load repetition

greatly influences fatigue life in tension-compression fatigue tests, as described later, static OHC strength was plotted at $N=1$ as in the case of compression fatigue. According to the $S-N$ lines at RT and 150°C and the b values in Table 4, S_{\max} apparently decreases with increasing N . Moreover, there is an apparent difference between the two $S-N$ relationships at RT and 150°C, as was the case in the compression fatigue tests. The tension-compression fatigue strength is strongly dependent on temperature and the number of load cycles, as in the compression fatigue tests.

Furthermore, these $S-N$ lines pass fairly above their mean compressive strengths given by compressive \bar{S}_u in Table 2. Generally, \bar{S}_u is considered to be not included in the $S-N$ lines in Fig. 6 at both RT and 150°C.

As mentioned above, since the tension-compression fatigue strength is strongly influenced by temperature and the number of load cycles, it is also judged to be a matrix-dominant property.

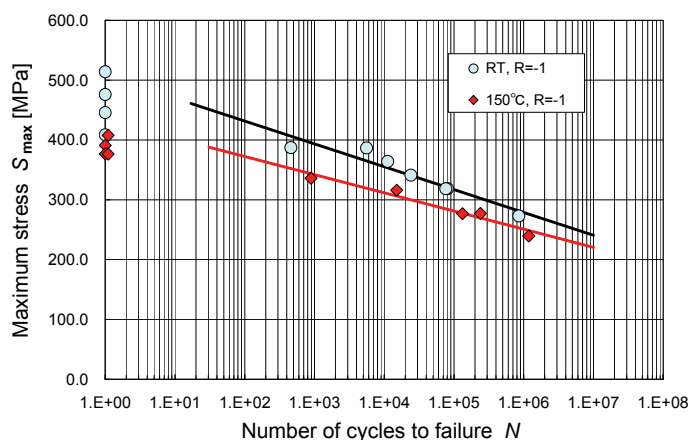


Fig. 6. $S-N$ diagram of OH specimens from tension-compression fatigue tests, $R=-1$, at RT and 150°C

4. Detailed discussion of test results

4.1 Fiber-dominant strength, matrix-dominant strength, and failure modes

As described above, static tensile strength and tension fatigue strength are predominantly fiber-dominant, and static compressive strength and compression and tension-compression fatigue strengths are matrix-dominant. This section discusses the fiber-dominant and matrix-dominant characteristics of static and fatigue strengths based on observations of specimen failure and failure modes. The mechanical properties of carbon fibers are considered to be constant over the range from RT to 215°C. Moreover, since no signs of fatigue damage were found in the fibers themselves, any fatigue strength reduction of carbon fibers can be left out of consideration. Therefore, matrix damage influenced by temperature and load repetition is considered to generate the temperature dependence of the static and fatigue strengths, and also the load cycle dependence of fatigue strength.

Initially, we will consider static NHT strength. In order to generate tensile failure in an NH specimen, fibers in the 0° fiber layers that directly bridge both end regions where the load is

introduced must finally be broken. If static tensile strength is determined only by 0° fiber fracture, temperature dependence will not appear and perfect fiber dominance will be seen. However, both the static NHT and OHT strengths in Fig. 2 indicate small temperature dependence. This means that the matrix has a small effect on static tensile strength. This aspect can be clarified by examining the failure mode of a specimen. The load-displacement diagram observed in a static tensile test of an NH specimen was considered to be linear up to final failure. In addition, fibers in the 45° fiber layers did not bridge both ends where the load was introduced. Thus geometry tells us that if 45° fiber layers also share internal load via the matrix until the fracture of 0° fiber layers, the final strength of the laminate will become higher than if only 0° fiber layers share internal load. This phenomenon can be evaluated by inspecting whether fiber fracture exists in the 45° layers after final specimen failure.

Fig. 7 shows surface and side views of static tensile failure in NH and OH specimens. A surface view of static tensile fracture in an NH specimen at RT is shown in Fig. 7(a). The front line of the surface 45° -fiber-layer fracture intersects with the 45° fiber direction at 90° . In addition, the 45° fiber layer was also cut at the load-axis orientation. This is evidence that the $\pm 45^\circ$ fiber layers shared the axial load via the matrix until just before the final specimen fracture. Since the fiber binding strength of the matrix will decrease with increasing temperature, the load sharing rate of the $\pm 45^\circ$ fiber layers will decrease at the same time. Fig. 7(b) shows the static tensile fracture of an OH specimen at RT, with surface and side views from the same specimen. As shown in the left-hand figure, only a small number of surface $+45^\circ$ fibers failed. The right-hand figure displays small slits in a comb pattern produced by fiber separation in the -45° fiber layers in the upper part of the side face. Such slits extended even to the lower part of the opposite face. In the lower part of the slits in the right-hand figure, delaminations produced by the pull-out of 0° fibers can be seen. These facts mean that $+45^\circ$ fibers fractured inside the specimen. Static OHT strength dropped slightly with increasing temperature similarly to static NHT strength, as shown in Fig. 3. However, the matrix binding strength decreases at elevated temperatures in comparison with that at RT, and stress concentration around the open hole is considered to drop at elevated temperatures. Therefore, this is a possible reason why OHT strength has small temperature dependence but does not fall in the same way as NHT strength at 150°C .

Next, we consider static compressive failure. The compressive strength of a composite material is considered to reflect the temperature dependence of the matrix strength. Fig. 8 shows the appearance of static NHC failure, which formed a rhombus shape in the side view. The main failure mechanism is considered to be compressive buckling failure generated by delamination progressing from micro-buckling. Partial shear fracture in the side view is also confirmed. This macroscopic shear fracture can be considered to have progressed from kinking initiation. Since these mechanisms of compression failure initiation depend on matrix strength (Pilato & Michno, 1994), the compressive strength is directly related to the temperature-dependent matrix strength. Fig. 9(a) and (b) show side views of static compression failure of different OH specimens at 150°C . Around the cross section having an open hole, macroscopic rhombus-shaped failure and shear failure in the thickness direction can be seen. Figure 9(a) shows typical rhombus-shape failure and the fracture mode in Fig. 9(b) seems to be shear-dominant; however, the fracture mode around the hole has a rhombus shape. Though the compressive fracture mechanism in an OH specimen is similar to that in an NH specimen, the drop of compressive strength at 150°C from RT is smaller than that of an NH specimen. This phenomenon is considered to originate in the relaxation of stress concentration around the hole at 150°C .

In the case of tension fatigue, matrix damage such as transverse micro-cracking and small delamination occurs in the open-hole wall and grows with the increase in the number of load cycles, and the 0° fiber layers gradually charge themselves with the load that $\pm 45^\circ$ fiber layers shared. Specimen failure will occur when the 0° fiber layers are loaded up to the limit load or the limit strain to failure. This means that although fatigue strength is influenced by high temperature and load repetition, there is a compensating effect as high temperature and load repetition reduce stress concentration around the open hole. Therefore, the tension fatigue strength is strongly fiber-dominant; however, it is slightly influenced by high temperature and the number of load cycles.

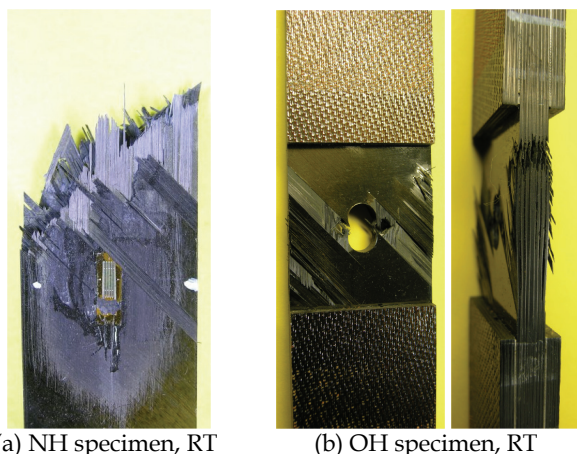


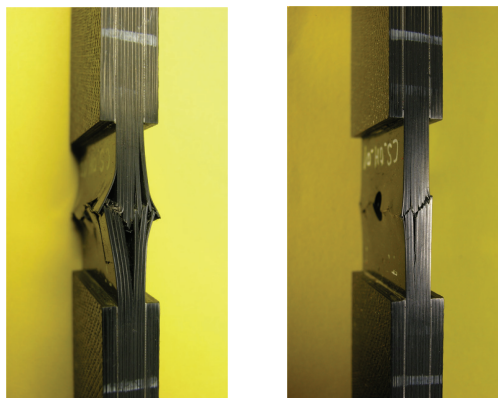
Fig. 7. Surface and side views of static tensile failure of NH and OH specimens



Fig. 8. External view of static compressive failure of an NH specimen at RT

In the case of compression fatigue, fatigue damage such as transverse micro-cracking and small delamination occurs in the open-hole wall and delamination and local buckling progress, finally resulting in compression buckling failure. Inspection also showed partial shear fracture in the thickness direction. Thus, compression fatigue strength is governed by matrix failure and dependent on temperature and the number of load cycles. Additionally, the relaxation effect of stress concentration around the hole on compression fatigue strength is superimposed, producing the $S-N$ relationships shown in Fig. 5. Rosenfeld and Gause also

pointed out that compression fatigue strength is matrix-dominated for a CF/epoxy composite material (Rosenfeld & Gause, 1981).



(a) OH specimen, 150°C (b) OH specimen, 150°C

Fig. 9. Side views of static compressive failure of OH specimens

In tension-compression fatigue, the final failure mode was similar to that of compression fatigue, i.e. delamination buckling. This fact suggests the important role of compression load repetition promoting delamination growth. The tension load component is also thought to contribute to delamination buckling by accelerating the initiation and growth of matrix damage. That is, the fatigue failure mode in tension-compression fatigue can be considered to be matrix-dominant and the tension-compression fatigue strength is dependent on temperature and the number of load cycles.

As mentioned above, since static compressive strength, compression fatigue strength, and tension-compression fatigue strength can be classified as matrix-dominant properties, the effectiveness of using a high-temperature resin as a matrix in an elevated temperature environment can be established. This viewpoint is very important and discussed again later.

4.2 Effect of an open hole on static strength and its temperature dependence

This section discusses the ratio of static OH strength to static NH strength and its temperature dependence, where this ratio is calculated from the mean strength based on the test results in Table 2 or Fig. 3. Since the cross section of OH specimens was equal to that of NH specimens and the static strength was represented by the net section stress in this study, the experimental results are directly comparable.

Table 5 shows the ratios of the mean OH strength \bar{S}_{UO} to the mean NH strength \bar{S}_{UN} , where \bar{S}_{UO} is represented by the net section stress, calculated from the data at RT and 150°C.

$$r_{notch} = \frac{\bar{S}_{UO}}{\bar{S}_{UN}} \quad (3)$$

This table indicates that an open hole greatly reduces static strength for both tensile and compressive loading. The effect of stress concentration produced by the open hole is clearly apparent. Moreover, comparison of the reduction in tensile strength and compressive

strength shows that compressive strength decreases more than tensile strength does at either RT or 150°C. Furthermore, the strength reduction ratio due to the open hole at RT is larger than that at 150°C. This fact is explained by the relaxation of stress concentration around the open hole due to resin softening at 150°C, as described above.

Comparison	Temp.	r_{notch} (%)
Tensile strength ratio, OHT/NHT	RT	66
	150°C	71
Compressive strength ratio, OHC/NHC	RT	53
	150°C	59

Table 5. Effect of an open-hole on static strength represented by the ratio of the mean static strength of OH specimens to that of NH specimens

The following published data obtained at only RT were found. OHT/NHT strength ratios are 57% for T650-35/Radel 8320 CF/thermoplastic resin (Pilato & Michno, 1994), 58% for T800S/3900-2B and 56% for T800H/3900-2 CF/epoxy (JAXA, 2007). OHC/NHC strength ratios are 52% for T800H/F655-2 CF/BMI (Marais et al., 2001) and 51%-53% for T800S/3900-2B and T800H/3900-2 CF/epoxy (Nagao et al., 2007). Therefore, the numerical values presented in Table 3 are considered reasonable. The authors discussed the effect of an open hole on the static strength of CFRPs in detail based on theoretical formulae and test results (Shimokawa et al., 2008).

4.3 Comparison of RT and 150°C strengths subjected to static or fatigue loading

To examine the high-temperature performance of the material tested, we will discuss the ratio of 150°C strength to RT strength when the specimens are subjected to either static or fatigue loading. This strength ratio, $r_{150}(N)$, is defined as

$$r_{150}(N) \equiv \frac{150^\circ\text{C strength}(N)}{\text{RT strength}(N)} \quad (4)$$

where static strength is given for $N=1$.

Table 6 indicates $r_{150}(N)$ values calculated by Eq. (4) for NH and OH specimens. Since the static strength ratio was described in Section 3.1, this section gives only numerical values in Table 6 for the sake of comparison. In the case of fatigue strength, the ratio was calculated by the S - N equation, Eq. (2), and the parameters in Table 4. For OH specimens the 150°C fatigue strength is adequately high in comparison with RT fatigue strength. In addition, the ratio of OHT fatigue strength agrees with that of OHT static strength. Furthermore, the ratio for OHC fatigue strength is larger than that for OHC static strength, i.e., the reduction in fatigue strength is smaller than that in static strength. This result is remarkable. Moreover, the tension-compression fatigue strength of OH specimens was adequately high at 150°C in comparison with that at RT.

As mentioned above, a high ratio listed in Table 6 for static and fatigue strengths indicates the high temperature performance of the material tested, and can be evaluated to demonstrate sufficient practical utility from the viewpoint of static and fatigue strength at 150°C.

Specimen and loading	Static strength ratio, $r_{150}(1)$	Fatigue strength ratio, $r_{150}(N)$			
		$N=10^4$	$N=10^5$	$N=10^6$	$N=10^7$
NH tension	90 %	-	-	-	-
NH compression	75 %	-	-	-	-
OH tension	97 %	97 %	97 %	97 %	97 %
OH compression	84 %	88 %	90 %	93 %	97 %
OH tension-compression	-	88 %	89 %	90 %	92 %

Table 6. The ratio of strength at 150°C to that at RT, $r_{150}(N)$, for NH and OH specimens given by the mean static strength and the fatigue strength calculated from the S_{\max} - N equation

4.4 Ratio of compression strength to tension strength in static and fatigue strengths

We now discuss the ratio of static compressive strength to static tensile strength in NH and OH specimens, and the ratio of compression fatigue strength ($R=10$) to tension fatigue strength ($R=0.1$) in OH specimens. That is, this section evaluates the weakness of the material tested for compression loading on the basis of the ratio of compression strength to tension strength.

The fatigue strength ratio for arbitrary N is defined by

$$r_{CT}(N) = \frac{S_{comp,min}(N)}{S_{tens,max}(N)} \quad (5)$$

where $S_{comp,min}(N)$ is compression fatigue strength ($R=10$), and $S_{tens,max}(N)$ tension fatigue strength ($R=0.1$). The static strength ratio is defined for $N=1$, $r_{CT}(1)$, where $S_{comp,min}(1)$ is the mean compressive strength and $S_{tens,max}(1)$ the mean tensile strength. Fatigue strength is calculated by Eq. (2) and the parameters given in Table 4.

Table 7 indicates the calculated strength ratio, $r_{CT}(N)$. The static strength ratio of NH specimens is 81% at RT and 68% at 150°C. As described below, this ratio at RT is considered reasonable; however, it is fairly small at 150°C. This tendency is reflected in the compressive strength reduction presented in Fig. 3. On the other hand, the static strength ratio of OH specimens is 65% at RT and 56% at 150°C. That is, an open hole reduces this ratio further.

Moreover, the following published examples obtained at RT were found for the static strength ratio. For NH specimens of CF/epoxy composites, the static NHC/NHT strength ratio was 77% (JAXA, 2007) and 84% (Nagao et al., 2007) for two cases of T800S/3900-2B, and 83% for T800H/3900-2 (JAXA, 2007). For OH specimens, the static OHC/OHT strength ratio was 57% and 66% for T800S/3900-2B and T800H/3900-2 CF/epoxy composites, respectively (JAXA, 2007), and 67% (Shimokawa et al., 1999-a) and 68% (Hirano, 2001) for G40-800/5260 CF/BMI composites. Therefore, the numerical values of the static strength ratio in Table 7 are considered reasonable as compared with other test results.

As shown in Table 7, the fatigue OHC/OHT strength ratio is in the range of 50% to 60% at RT and 150°C. It is lower than that of static strength and has a tendency to decrease with the increase in the number of load cycles. Moreover, there is a tendency for the ratio at 150°C to be slightly lower than that at RT. Since compression strength is expected to be lower than

tension strength because of being a matrix-dominant property, these quantitative values are very important from an engineering perspective. This property should be fully taken into account in the design of composite structures.

Comparison	Temp.	Static strength ratio	Fatigue strength ratio			
			$N=10^4$	$N=10^5$	$N=10^6$	$N=10^7$
NHC/NHT	RT	81 %	-	-	-	-
	150°C	68 %	-	-	-	-
OHC/OHT	RT	65 %	60 %	57 %	53 %	50 %
	150°C	56 %	54 %	53 %	51 %	50 %

Table 7. The ratio of compression strength to tension strength, $r_{CT}(N)$, for NH and OH specimens: static strength ratio=mean compressive strength/mean tensile strength, and fatigue strength ratio=compression fatigue strength ($R=10$)/tension fatigue strength ($R=0.1$)

4.5 Effect of compression load cycles on tension-compression fatigue strength

The repeated stress range, S_{range} , of compression fatigue tests ($R=10$) in this study is calculated by $S_{range}=-0.9 \times S_{min}$. If the $S_{range}-N$ relationships in Fig. 5 are noticed, it can be understood intuitively that they are very close to the tension-compression $S_{max}-N$ relationships in Fig. 6. These relationships are discussed in detail below.

S_{max} in tension-compression fatigue tests ($R=-1$) is the stress amplitude and indicates the tension stress range or compression stress range. Fig. 10 shows Fig. 6 itself together with the $S_{range}-N$ relationships converted from the compression $S_{min}-N$ relationships in Fig. 5. Thick lines are the tension-compression $S_{max}-N$ relationships and fine lines represent the compression $S_{range}-N$ relationships, whose parameters are given in Table 4. Fig. 10 indicates that two $S-N$ relationships at RT broadly overlap over a wide range. When the parameters of two $S-N$ lines at RT in Table 2 are compared, the $S_{range}-N$ line of compression fatigue has a lower intersection and a lower slope than those of the tension-compression $S_{max}-N$ line, respectively. It turns out that the two $S-N$ lines at RT gradually intersect. Moreover, Fig. 10 means that compression load cycles contribute primarily to tension-compression fatigue strength and most tension-load cycles have little influence on tension-compression fatigue strength in the range for which fatigue data exists.

Two $S-N$ lines at 150°C in Fig. 10 clearly intersect. However, the slopes of the two straight lines are not very different. Therefore, it is obvious that the repeated application of a compression load mainly affects tension-compression fatigue strength. In addition, the compression fatigue strength expressed by S_{range} is lower than the tension-compression fatigue strength in the life region shorter than where the two lines intersect. This tendency is explained as follows. With regard to the mean stress in a compression fatigue test ($R=10$), the mean stress and stress amplitude constitute the maximum compression stress, which generates the final fatigue failure due to delamination buckling. Next, since the tension-compression fatigue strength is equal to the compression fatigue strength expressed by S_{range} in the vicinity of the intersection, this means that the tension-load repetition in tension-compression fatigue tests did not affect the tension-compression fatigue strength, as in the case of the tension-compression $S_{max}-N$ relationship at RT. Simultaneously, the mean compression stress in the compression fatigue test becomes smaller, and this is considered to not have any influence on fatigue strength. In the life range larger than the intersection, the

tension-compression fatigue strength becomes smaller than the compression fatigue strength expressed by S_{range} in Fig. 10, and this means that the tension-load repetition in a tension-compression fatigue test has an effect on delamination growth. The concept described above provides a coherent explanation for the S - N relationship at 150°C. Moreover, this kind of concept is also qualitatively applicable to S - N relationships at RT.

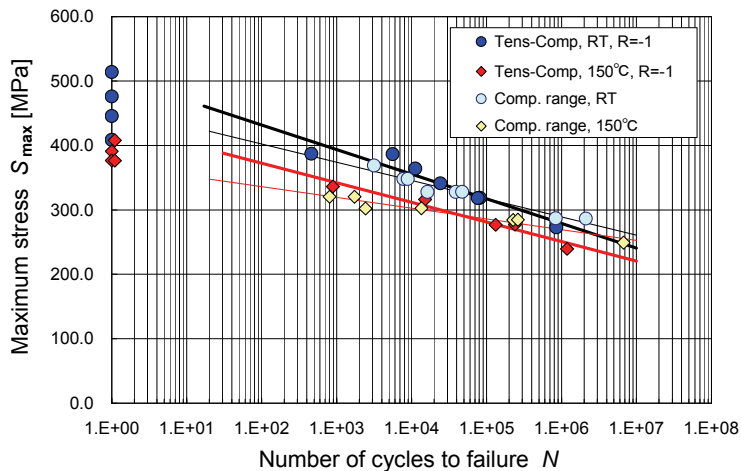


Fig. 10. S - N relationships from tension-compression fatigue tests and those showing the compression stress range from compression fatigue test results

The authors derived an $S_{\text{range}}-N$ relationship from the compression $S_{\text{min}}-N$ data ($R=10$) of NH specimens of a T800/5250 CF/BMI laminate with $[(\pm 45, 0_2)_2]_S$ layup given by Gathercole et al. (Gathercole et al., 1994) and compared it with the tension-compression $S_{\text{max}}-N$ data ($R=-1$). This comparison showed that the $S_{\text{range}}-N$ relationship ($R=-1$) was very close to the $S_{\text{max}}-N$ relationship ($R=-1$) and the two S - N lines gradually intersected in almost the same manner as those at RT in Fig. 10. On the other hand, Tyahla and McClellan reported fatigue test results of OH specimens of IM6/3100 and IM6/F650 CF/BMI composite materials with $[0^\circ(50\%)/\pm 45^\circ(40\%)/90^\circ(10\%)]$ layup for $R=-1$ and 10 (Tyahla & McClellan, 1988). Though IM6/3100 experienced longer lives during compression-only cycling ($R=10$) than reversed cycling ($R=-1$) on the basis of $S_{\text{max}}-N$ diagrams under CTD and RTD conditions, IM6/F650 showed no extension of life during compression-only cycling compared to reversal cycling. They described that perhaps fatigue life in the case of IM6/F650 was controlled by delamination growth with compression loading and failure would occur when delaminations grew to a critical size.

The test results and discussion described above show that the repeated compression-load component of a tension-compression fatigue test has a large effect on fatigue strength over the entire life region, together with the maximum compression stress in the short life region. The repeated tension-stress component has an effect only in the long-life region. This phenomenon is explained delamination growth in tension-compression fatigue being mainly driven by compression load repetition while final failure is generated by delamination buckling. This phenomenon and its interpretation are particularly noteworthy.

4.6 Comparison of fatigue data at room temperature obtained by the authors and Hirano

As stated in the introduction, Hirano reported S - N test results at RT for a G40-800/5260 CF/BMI composite material using a small number of specimens (Hirano, 2001). This section will compare his data with those obtained in the present study. He used OH specimens 38.1 mm wide, and with other dimensions such as the hole diameter, stacking sequence, and thickness the same as those in this study. The loading conditions of the fatigue tests were $R=0.05$ for tension fatigue, $R=20$ for compression fatigue, and $R=-1$ for tension-compression fatigue. The combination of R and the number of specimens tested, n , are $\{R=0.05, n=4(1)\}$, $\{R=20, n=3(1)\}$, and $\{R=-1, n=5\}$, where the figure in () is the number of unbroken specimens. Since there are several differences between his and the authors' investigations, the sets of data are compared in the following way: (1) Net section stress is used. (2) Stress range is used, because R values are different in tension fatigue and compression fatigue tests. (3) Only Hirano's failure data are used. The results compared are as follows: (1) Both tension fatigue strength and compression fatigue strength in the present study are slightly higher than those given by Hirano; however, the difference is regarded as falling within the scatter band of data in the present study. (2) The tension-compression fatigue strength was equivalent in both investigations. Therefore, (3) it can be considered that the tension-compression fatigue strength was in agreement with the compression fatigue strength expressed by S_{range} as in the case of the present investigation. The results mentioned above are considered to indicate that the fatigue test results obtained by both investigations are effective and can be used as reference data. Moreover, the use of net section stress and stress range was effective in comparing the fatigue test results obtained for the different specimen width and R .

5. Conclusions

This study determined the static strength of NH (non-hole) and OH (open-hole) specimens and the fatigue strength of OH specimens made of a G40-800/5260 CF/BMI high-temperature polymer composite material with a quasi-isotropic layup at RT (room temperature) and high temperatures, mainly 150°C, where OH static and fatigue strengths were represented by net section stress. Major conclusions are as follows:

1. This study generated systematic test results of the static and fatigue strengths at RT and high temperatures and presented the original data in mathematical tables available for reference data.
2. NHT (non-hole tension) static strength, OHT (open-hole tension) static strength, and OHT fatigue strength ($R=0.1$) are classified as fiber-dominated properties; however, they have some weak matrix-dependence and are slightly influenced by temperature. Furthermore, due to its slight matrix dependence, OHT fatigue strength is weakly dependent on the number of load cycles.
3. NHC (non-hole compression) static strength, OHC (open-hole compression) static strength, OHC fatigue strength ($R=10$), and OHTC (open-hole tension-compression) fatigue strength ($R=-1$) are classified as matrix-dominated properties and are temperature-dependent. Because of the matrix dependence, OHC and OHTC fatigue strengths are fairly dependent on the number of load cycles.
4. The fiber fracture of 45° plies was also observed in the static tensile failure of an NH specimen, though the static tensile strength was considered to be a strongly fiber-

- dominated property. In the static compressive failure of NH and OH specimens, the rhombus shaped fracture and partial shear failure were observed on the side face. These failure modes were regarded as indicative of matrix-dominated fracturing.
5. An open hole greatly reduced static strength and this effect was larger for compressive strength than for tensile strength. The strength reduction due to the hole either for tension load or compression load was smaller at 150°C than at RT.
 6. The static strength ratio (=compressive strength/tensile strength) was fairly low for both NH and OH specimens, except for the comparatively high ratio for NH static strength at RT. The fatigue strength ratio (=OHC fatigue strength/OHT fatigue strength) was generally lower than the static strength ratio, and it decreased to 50% at both RT and 150°C.
 7. The $S_{\text{range}}-N$ line of compression fatigue ($R=10$) and the $S_{\text{max}}-N$ line of tension-compression fatigue ($R=-1$) gradually intersected each other at either RT or 150°C. Especially at RT the two $S-N$ lines broadly overlapped. This fact indicates that the compression stress range mostly controlled fatigue lives in tension-compression fatigue tests at RT and 150°C.
 8. The use of net section stress and stress range was effective in comparing the fatigue test results obtained for the different specimen width and R .
 9. The static and fatigue strengths showed relatively small reduction from RT to 150°C except for NHC static strength. This is due to the use of a BMI resin for the material tested and demonstrates its practical utility at 150°C. However, structural designers should be careful about strength reduction when a structure has open holes and encounters compression loads in a high temperature environment.

6. References

- Adam, T.; Gathercole, N., Reiter, H. & Harris, B. (1994). Life prediction for fatigue of T800/5245 carbon-fiber composites: II. Variable-amplitude loading. *International Journal of Fatigue*, Vol. 16, pp. 533-547. ISSN: 01421123.
- Brandecker, B. & Hilgert, R. (1988). A320 full scale structural testing for fatigue and damage tolerance certification of metallic and composite structure. ICAS-88-5.8.1, pp. 1244-1256.
- Fawcett, A.; Trostle, J. & Ward, S. (1997). 777 empennage certification approach. *Proc. 11th International Conference on Composite Materials*, Gold Coast, pp. I-178/I-199.
- Gathercole, N.; Reiter, H., Adam, T., & Harris, B. (1994). Life prediction for fatigue of T800/5245 Carbon-Fiber Composites: I. Constant-Amplitude Loading. *International Journal of Fatigue*, Vol. 16, pp. 523-532. ISSN: 01421123.
- Hirano, K. (2001). Long-term durability performance for advanced high temperature polymer matrix composites. *Proc. 13th International Conference on Composite Materials*, ID-1299 (CD-ROM), Beijing.
- JAXA (Japan Aerospace Exploration Agency). (2007). *Advanced Composites Database System: JAXA-ACDB*, Ver. 06-1. <http://www.jaxa-acdb.com/>.
- Johnston, W.M. & Gates, T.S. (1998). The effects of stress and temperature on the open-hole tension fatigue behavior of a graphite/bismaleimide composite. *Composite Materials: Fatigue and Fracture*, ASTM STP 1330, pp. 179-198, American Society for Testing and Materials. ISSN: 0066-0558.

- Marais, C.; Shimokawa, T. & Katoh, H. (2001). Compressive strength degradation relationship of carbon/BMI composites after thermal cycling and aging for the second generation SST structures. *Proc. 13th International Conference on Composite Materials*, ID-1024 (CD-ROM), Beijing.
- McConnell, V.P. (2009). Resins for the hot zone, Part II: BMIs, CEs, benzoxazines and phthalonitriles. *High Performance Composites*, Sept. 2009. <http://www.compositesworld.com/articles/resins-for-the-hot-zone-part-ii-bmis-ces-benzoxazines-and-phthalonitriles>.
- Nagao, Y.; Iwahori, Y., Hirano, Y. & Aoki, Y. (2007). Low cost composite wing structure manufacturing technology development program in JAXA, *Proc. 16th International Conference on Composite Materials*, Kyoto (CD-ROM).
- Niu, M.C.Y. (1996). *Composite Airframe Structures - Practical Information and Data* -, Hong Kong Conmilit Press Ltd., p. 75. ISBN: 9627128066.
- Pilato, L.A. & Michno, M.J. (1994). *Advanced Composite Materials*, Springer-Verlag, p. 129 & p. 151. ISBN/ISSN: 3540575634/0387575634.
- Rosenfeld, M.S. & Gause, L.W. (1981). Compression fatigue behavior of graphite/epoxy in the presence of stress raisers. *Fatigue of Fibrous Composite Materials*, ASTM STP 723, American Society for Testing and Materials, pp. 174-196. ISSN: 0066-0558.
- Shimokawa, T.; Hamaguchi, Y., Kakuta, Y., & Katoh, H. (1999-a). Effect of isothermal aging on ultimate strength of high temperature composite materials for SST structures. *Journal of Composite Materials*, Vol. 33, No. 12, pp. 1104-1118. ISSN 0021-9983.
- Shimokawa, T.; Hamaguchi, Y. & Katoh, H. (1999-b). Effect of moisture absorption on hot/wet compressive strength of T800H/PMR-15 carbon polyimide. *Journal of Composite Materials*, Vol. 33, No. 18, pp. 1685-1698. ISSN 0021-9983.
- Shimokawa, T.; Katoh, H., Hamaguchi, Y., Sanbongi, S., Mizuno, H., Nakamura, H., Asagumo, R., & Tamura, H. (2002). Effect of thermal cycling on microcracking and strength degradation of high-temperature polymer composite materials for use in next-generation SST structures. *Journal of Composite Materials*, Vol. 36, No. 7, pp. 85-895. ISSN 0021-9983.
- Shimokawa, T.; Kakuta, Y., Saeki, D. & Kogo, Y. (2007). Carbon plain-weave fabric low-temperature vacuum cure epoxy composite: static and fatigue strength at room and high temperatures and practicality evaluation. *Journal of Composite Materials*, Vol. 41, No. 18, pp. 2245-2265. ISSN 0021-9983.
- Shimokawa, T.; Kakuta, Y., Hamaguchi, Y. & Aiyama, T. (2008). Static and fatigue strengths of a G40-800/5260 carbon fiber/bismaleimide composite material at room temperature and 150°C. *Journal of Composite Materials*, Vol. 42, No. 7, pp. 655-679. ISSN 0021-9983.
- Tyahla, S.T. & McClellan, P.S., Jr. (1988). Durability and damage tolerance of bismaleimide composites - Volume I: Technical Report. AFWAL-TR-88-3026, Wright-Patterson Air Force Base.

Self-Consistent Micromechanical Enhancement of Continuous Fiber Composites

Andrew Ritchey¹, Joshua Dustin¹, Jonathan Gosse² and R. Byron Pipes¹

¹*Purdue University*

²*The Boeing Company*
USA

1. Introduction

Much of the previous work in developing analytical models for high performance composite materials has focused on representations of the heterogeneous medium as a homogenous, anisotropic continuum. The development of the equivalent properties of the homogenous medium from the geometry of the microstructure and the fiber and matrix properties has been come to be known as “micromechanics” (Daniel & Ishai, 2006). The term “homogenization” has been applied to the process of determining the effective properties of the homogenous medium and for much of the past half century homogenization was the only task of micromechanics. However, increases in computational capability has allowed for the use of micromechanics as a “de-homogenization” tool as well. The de-homogenization method that is the focus of the current study has been come to be known as “micromechanical enhancement” (Gosse & Christensen, 2001; Buchanan et al., 2009). Here the deformation of the homogeneous medium is enhanced by influence functions derived from unit cell micromechanical models representing extremes in the packing efficiencies of fiber arrangements. The motivation for development of the de-homogenization step is the need for an increase in the robustness and fidelity of failure theories used for these material systems wherein the deformation fields within the homogenized solutions are enhanced to reflect the actual strain field topologies within the fiber and matrix constituents. It is these enhanced strain fields that are used to determine the onset of damage initiation within the medium.

There are several categories of models which have been proposed to perform the homogenization step of micromechanics including: mechanics of materials (Voigt, 1887; Reuss, 1929); self-consistent field (Hill, 1965); bounding methods based on variation principals (Paul, 1960; Hashin & Rosen 1964); semi-empirical (Halpin & Tsai, 1967); numerical finite element methods (Sun & Vaidya, 1996) and experimental methods such as uniaxial coupon tests. A significant amount of work has been devoted to this topic and more complete reviews are found elsewhere (Christensen 1979; Pindera et al., 2009). Although any analysis method used should be vetted against a rigorous testing program, accurate micromechanics models can provide a cost effective method for a priori material evaluation and ranking of composite systems. In the traditional composite analysis workflow, homogenized material properties are used in a laminate analysis of a structural

member to determine lamina level stresses and strains. Stresses and strains at the lamina level are then used directly in a failure criterion to determine the ultimate performance of the member. Some success has been achieved with this approach but the analysis fails to take into account the actual state of stress and strain within the constituent phases. In addition, residual thermal stresses resulting from a mismatch in the coefficient of thermal expansion between the fiber and matrix phases are usually neglected. Others have noted that non-physical singularities may arise in homogenized solutions containing free-edges (Pagano & Rybicki, 1974; Pagano & Yuan, 2000).

Several methods for recovery of the state of stress/strain from a homogenized solution have been proposed as well. Analytic methods have been proposed based on phase averaging methods (Hill, 1963; Hashin 1972). More recently, numerical methods have been employed. One method is to perform a global-local finite element analysis. In this approach the forces or displacements obtained from a homogenized solution are applied to a domain in which the fiber and matrix phases are modelled explicitly (Wang et al., 2002). With this method one must first determine an appropriate size for the local region, typically containing several fibers, using the so-called "local domain test." It has been suggested that a single fiber local region is feasible for determining fiber-matrix interface stresses if the continuum is modelled using the micro-polar theory of elasticity (Hutapea et al., 2003). Others have suggested the use of a multilevel analysis that models a homogenized region, a transition region and a region containing the explicit microstructure in a single finite element analysis (Raghavan et al., 2001). A more computationally efficient method for recovering the stress and strain in the fiber and matrix phases is to use an influence function formulation (Gosse & Christensen, 2001). In this method, also referred to as micromechanical enhancement, a set of six canonical states of deformation and a separate thermal load are applied to a unit cell prior to performing an analysis of the homogeneous medium. The influence functions extracted from the unit cells are then used to relate the state of homogeneous strain in each lamina to the state of strain within the representative volume element through the use of the enhancement matrix. Microscopic residual thermal strains can also be recovered with a superposition vector (Buchanan et al., 2009).

In a previous study (Gosse & Christensen, 2001), the homogenization step was an experimental one wherein the effective properties of the homogeneous medium employed in the analysis were determined by experiments while the de-homogenization (micromechanical enhancement) step was carried out by a finite element analysis of a representative volume element. In addition to this procedure, an alternative method has been developed to utilize the derived effective elastic and thermal lamina properties from the same micromechanical models developed to assess the strain fields within the unit cells. In this paper the latter approach is investigated exclusively in order to provide the consistency of utilizing the same method for both homogenization and de-homogenization. In the current chapter, the micromechanical enhancement method is investigated in more detail and a self-consistent method for determining the microscopic strain field is presented. By using a self-consistent analysis, the inherent approximations of the method are present in both steps while no new uncertain quantities, such as experimental test variables, are introduced. Self-consistency is assured by utilizing the same micromechanical models for both the homogenization and de-homogenization steps in the method. The goal is to provide an efficient link in a multi-scale analysis of a composite structure and to elucidate the analysis steps used in the current method.

2. Homogenization

The homogenization process seeks to obtain equivalent homogenous continuum properties for a medium composed of multiple phases of varying constitutive properties. For the current discussion, we will limit ourselves to a heterogeneous medium consisting of collimated, continuous fibers within an isotropic matrix. Many methods and closed-form expressions have been developed to achieve this goal (Pindera et al., 2009). Among these, the most accurate in predicting the average response of an orthotropic medium is the finite element method (Daniel & Ishai, 2006). In the finite element approach, one would like to determine the relationship between the average stress and average strain as expressed in Equation 1.

$$\bar{\sigma}_i = \bar{C}_{ij} (\bar{\varepsilon}_j - \bar{\alpha}_j \Delta T) \quad (i, j = 1-6) \quad (1)$$

The overbar indicates an average or homogenized quantity. From the homogenous stiffness matrix (\bar{C}_{ij}), the effective lamina engineering constants (E_1 , E_2 , ν_{12} , G_{12} , etc.) can be calculated. Alternatively, the engineering constants can be determined directly by systematically performing finite element analysis corresponding to the definitions of the engineering constants (Sun & Vaidya, 1996). In this approach, the average stress is related to the average strain through the strain energy density. Typically, a representative volume element, as shown in Figure 1, is used to simplify the analysis. Equation 2 gives the stress-strain relation for the case when $\Delta T = 0$.

$$\bar{\sigma}_i = \bar{C}_{ij} \bar{\varepsilon}_j \quad (i, j = 1-6) \quad (2)$$

Where "1" coincides with the fiber direction, "2" is transverse to the fiber direction and "3" is normal to the 1 and 2 directions. Also, note the use of a contracted notation such that $i=1-3$ are the three normal components of stress and strain, 11, 22, and 33, respectively, while $i=4-6$ are the three *engineering* shear components, 23, 13 and 12, respectively. The average stress is shown in Equation 3 for the case when a canonical state of deformation is applied so that the only active strain component is $\bar{\varepsilon}_1$. The superscript indicates the isolated average mechanical strain component. As shown, the relationship of can be rearranged to determine the first column of the homogenous stiffness matrix.

$$\bar{\sigma}_i^{(\bar{\varepsilon}_1)} = \bar{C}_{i1}^k \bar{\varepsilon}_1 \quad \text{or} \quad \bar{C}_{i1}^k = \bar{\sigma}_i^{(\bar{\varepsilon}_1)} / \bar{\varepsilon}_1 \quad (i = 1-6) \quad (3)$$

The other five columns of the effective homogenous stiffness matrix are determined by applying the remaining five other states of canonical deformation such that each strain component is isolated. A total of six finite element analyses are required to fully determine the effective homogenous stiffness matrix for the general anisotropic solid. A seventh finite element analysis is required to determine the thermal response of the effective medium. For this case, the domain is subjected to a thermal loading of ΔT with the average mechanical strain, $\{\bar{\varepsilon} - \bar{\alpha} \Delta T\}$, constrained to be zero. Equation 4 gives the calculation of the average coefficients of thermal expansion. As seen from Equation 1, constraining the average mechanical strain to be zero requires that the average stress be zero. This condition can be used to check the validity of the boundary conditions.

$$\{\bar{\alpha}_i\} = \bar{\varepsilon}_i / \Delta T \quad (i = 1-6) \quad (4)$$

Equation 5 shows the average strain in a unit cell determined from the surface displacement, u_i and u_j with $i, j = 1-3$, by using Gauss' theorem and written in index notation (Sun & Vaidya, 1996).

$$\bar{\varepsilon}_{ij} = \frac{1}{2V} \int_S (u_i n_j + u_j n_i) dS \quad (5)$$

Where S is the boundary surface of the representative volume element and n_i is the unit surface normal in the i^{th} direction. Thus, the average strain in the unit cell can be calculated for a set of displacement boundary conditions.

Specifying the components of deformation on the surface of the representative volume element will, in general, induce average stress components. The average stress is calculated in Equation 6 using the reaction forces obtained on the boundaries of the unit cell and the definition of stress.

$$\bar{\sigma}_{ij} = F_j n_i / A \quad (i, j = 1-3) \quad (6)$$

Where index notation is used with F_j the j^{th} component of the total force applied to a face with a total area of A oriented in the i^{th} direction. In this way, all six components of the stress tensor that may result for a state of deformation applied to the representative volume element are determined.

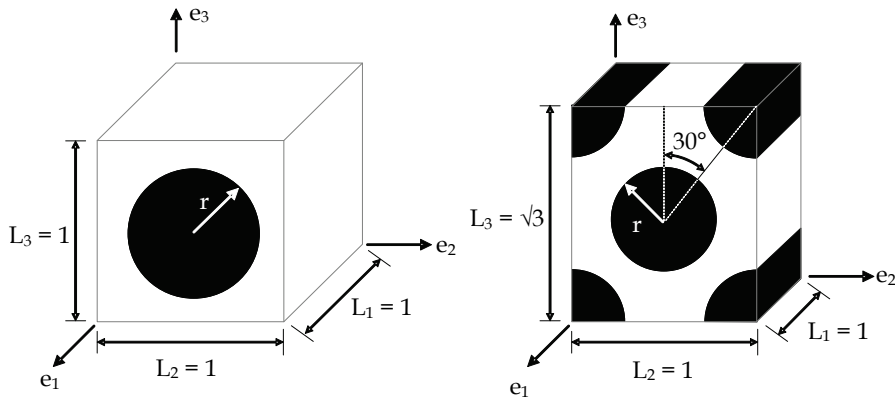


Fig. 1. Schematics of the square and hexagonal representative volume elements (Buchanan et al., 2009)

3. De-homogenization

Utilizing classical laminate theory in the analysis of a composite laminate represented as a homogenous, anisotropic solid provides accurate predictions of structural deformations resulting from applied forces and moments. Although analysts have successfully used this

approach, there are several shortcomings, which, if overcome, may provide increasingly accurate predictions of ultimate properties. The most apparent shortcomings of a homogenized analysis are: the modeling of fictitious interfaces; stresses and strains in the homogenized continuum exist in neither the fiber phase nor the matrix phase and the loss of the residual micromechanical thermal stress field due to a temperature change. The current chapter will focus on the latter two shortcomings by predicting the strain state within the fiber and matrix phases using a process referred to as micromechanical enhancement (Gosse & Christensen, 2001; Buchanan et al., 2009).

The role of micromechanical enhancement is to provide a computationally efficient micromechanics analysis that includes congruent homogenization and de-homogenization steps. The current approach uses a single finite element model subjected to canonical states of deformation to provide the information needed for both homogenization (micromechanics) and de-homogenization (micromechanical enhancement) and is thus considered to be a self-consistent approach. This chapter is primarily focused on building a general framework required to obtain self-consistent results and transferring information between micro and macro scale composite models. Through the use of a simple example problem we will address the process used to recover strains at the micro-scale resulting from both mechanical loading and residual thermal stresses.

First, consider a representative volume element subjected to an arbitrary state of average mechanical strain, $\{\bar{\varepsilon} - \bar{\alpha}\Delta T\}$, where $\bar{\varepsilon}$ is the average total strain and $\bar{\alpha}$, the vector of effective coefficients of thermal expansion for the homogenized medium. As shown in Equation 7, the state of strain at a prescribed point within the representative volume element is calculated using an influence function formulation.

$$\varepsilon_i^k - \alpha_i^k \Delta T = M_{ij}^k (\bar{\varepsilon}_j - \bar{\alpha}_j \Delta T) + A_i^k \Delta T \quad (i, j = 1-6) \quad (7)$$

The matrix M_{ij}^k and the vector A_i^k are the influence function matrix and the thermal superposition vector of strain for the k^{th} point in the representative volume element, respectively (Gosse & Christensen, 2001; Buchanan et al., 2009).

The components of the influence function matrix can be determined uniquely, in a fashion similar to determining the stiffness matrix for the effective homogeneous medium, by prescribing a canonical state of deformation in the representative volume element and carrying out three-dimensional finite element analyses to determine the components of the strain tensor at the specified point, k . For example, let $\bar{\varepsilon}_1 \neq 0$, in the absence of the other five strain components and with no thermal loading. Shown in Equation 8, the first column of the influence matrix can be determined by relating the local strain to the average axial strain by using Equation 7.

$$\varepsilon_i^{k(\bar{\varepsilon}_1)} = M_{i1}^k \bar{\varepsilon}_1 \text{ or } M_{i1}^k = \varepsilon_i^{k(\bar{\varepsilon}_1)} / \bar{\varepsilon}_1 \quad (i = 1-6) \quad (8)$$

Note that a single finite-element analysis with boundary conditions that meet the condition, $\bar{\varepsilon}_1 \neq 0$ with $\bar{\varepsilon}_{2-6} = 0$, yields six of the 36 coefficients in the influence function matrix at any point within the representative volume element. A total of six finite-element analyses are required to completely determine terms of M_{ij}^k at any point within the domain for a given representative volume element geometry.

Calculation of the thermal superposition vector requires an additional finite element analysis in which the unit cell is subjected to a temperature change with the constraint that the average mechanical strain vanishes, i.e. $\{\bar{\varepsilon} - \bar{\alpha}\Delta T\} = 0$. Equation 9 gives the thermal superposition vector obtained by inserting this constraint into Equation 7.

$$A_i^k = \frac{\varepsilon_i^k - \alpha_i^k \Delta T}{\Delta T} \quad (i = 1-6) \quad (9)$$

4. Representative volume element boundary conditions

The imposition of canonical states of strain upon the representative volume element utilizing finite-element analyses requires the development of a corresponding set of displacement boundary conditions. The representative volume element principal directions, (e_1, e_2, e_3) are shown in Figure 1. Equation 10 defines the appropriate displacement boundary conditions for the prescribed extensional strain in the "1" direction with u_i representing the displacement vector and x_i the position vector.

$$u(0, x_2, x_3) = \tau_{xy}(0, x_2, x_3) = \tau_{xz}(0, x_2, x_3) = 0 \quad (10a)$$

$$u(L_1, x_2, x_3) = \bar{\varepsilon}_1 L_1; \quad \tau_{xy}(L_1, x_2, x_3) = \tau_{xz}(L_1, x_2, x_3) = 0 \quad (10b)$$

$$v(x_1, 0, x_3) = \tau_{yx}(x_1, 0, x_3) = \tau_{yz}(x_1, 0, x_3) = 0 \quad (10c)$$

$$v(x_1, L_2, x_3) = \tau_{yx}(x_1, L_2, x_3) = \tau_{yz}(x_1, L_2, x_3) = 0 \quad (10d)$$

$$w(x_1, x_2, 0) = \tau_{zx}(x_1, x_2, 0) = \tau_{zy}(x_1, x_2, 0) = 0 \quad (10e)$$

$$w(x_1, x_2, L_3) = \tau_{zx}(x_1, x_2, L_3) = \tau_{zy}(x_1, x_2, L_3) = 0 \quad (10f)$$

As an example, Equation 11 gives the canonical shearing displacements for shearing in the 2-3 plane.

$$u(0, x_2, x_3) = \tau_{xy}(0, x_2, x_3) = \tau_{xz}(0, x_2, x_3) = 0 \quad (11a)$$

$$u(L_1, x_2, x_3) = \tau_{xy}(L_1, x_2, x_3) = \tau_{xz}(L_1, x_2, x_3) = 0 \quad (11b)$$

$$w(x_1, 0, x_3) = \sigma_{yy}(x_1, 0, x_3) = \tau_{yx}(x_1, 0, x_3) = 0 \quad (11c)$$

$$w(x_1, L_2, x_3) = \bar{\gamma}_{23} L_2 / 2; \quad \sigma_{yy}(x_1, L_2, x_3) = \tau_{yx}(x_1, L_2, x_3) = 0 \quad (11d)$$

$$v(x_1, x_2, 0) = \sigma_{zz}(x_1, x_2, 0) = \tau_{zx}(x_1, x_2, 0) = 0 \quad (11e)$$

$$v(x_1, x_2, L_3) = \bar{\gamma}_{23} L_3 / 2; \quad \sigma_{zz}(x_1, x_2, L_3) = \tau_{zx}(x_1, x_2, L_3) = 0 \quad (11f)$$

This simple set of displacement boundary conditions are only valid for doubly periodic representative volume elements. In general, further constraints are required on the displacement field to maintain periodicity between adjacent unit cells. However, periodicity is satisfied automatically in the symmetric unit cells studied here. The desired average strain is recovered by inserting the boundary conditions shown in Equations 10 and 11 into Equation 6. The nodal forces taken from each face of the representative volume element can then be used in Equation 6 to determine the average stress and thereby provide the homogenized material properties as discussed in Section 2.

For the case of a uniform temperature change of the representative volume element, boundary conditions are imposed to allow for free expansion of the representative volume element with the constraint that all faces must remain planar. This condition results from Equation 8 that requires the representative volume element to exhibit the free thermal deformation $\bar{\alpha}\Delta T$ in order that the homogenized mechanical strains vanish. In this case, free thermal deformation of representative volume element is equal to that defined by the coefficients of thermal expansion of the homogenized unidirectional lamina, $\bar{\alpha}\Delta T$. The planar constraint is required to maintain periodicity between adjacent volume elements. Procedures to implement these constraints are implemented in both Abaqus (© Dassault Systèmes) and StressCheck® (ESRD). For StressCheck® when the analysis is performed for any given load, the program will create constraint equations for all the degrees of freedom associated with the selected faces. The internal degrees of freedom (faces and edges) are eliminated at the element level (local constraint equations), while the equation for the nodal variables are written in compact form at the global level.

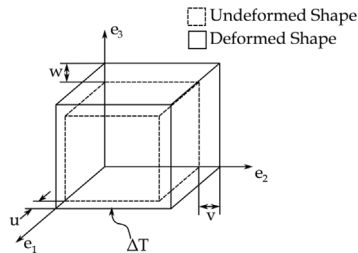


Fig. 2. Constrained deformation due to thermal loading. All faces remain planar to maintain periodicity

Since each face is constrained to remain planar, no average shearing strain will be obtained. The normal strain components are given in Equation 12. Using the normal strain components, the homogenized coefficients of thermal expansion can be determined with Equation 4, where U , V and W are the displacement components shown in Figure 2. It should be noted that these displacements are unknown prior to performing the analysis.

$$\bar{\epsilon}_1 = \frac{U}{L_1}, \quad \bar{\epsilon}_2 = \frac{V}{L_2}, \quad \bar{\epsilon}_3 = \frac{W}{L_3} \quad (12)$$

5. Example

First, consider a general laminate to be analysed using a self-consistent micromechanics method. Presented graphically in Figure 3 is the self-consistent micromechanics method

used herein. A complete set of material properties for both the fiber and matrix phase are required. Six canonical states of deformation, extending from Equations 10 and 11, are applied as boundary conditions to two representative volume elements, a square array and a hexagonal array shown in Figure 1. The fiber volume fraction of the representative volume elements is 60 percent. For this step the finite element program Abaqus is utilized. Six canonical states of deformation provide both the homogenized stiffness matrix (\bar{C}_{ij}) and the enhancement matrix (M_{ij}) for the two micro-geometries.

Both domains are subjected to a uniform change in temperature in a seventh finite element analysis. This thermal loading case provides the homogenized coefficients of thermal expansion ($\bar{\alpha}_i$) and the thermal superposition vector (A_i). In total, seven finite element analyses are required for each representative volume element of interest.

The homogenized material properties become the input for the laminate level analysis. For illustration, the boundary conditions are limited to in-plane force resultants and a uniform change in temperature ΔT applied to symmetric, balanced laminates. The laminate level calculation is performed twice, once for both sets of homogenized material properties corresponding to the representative volume elements modelled.

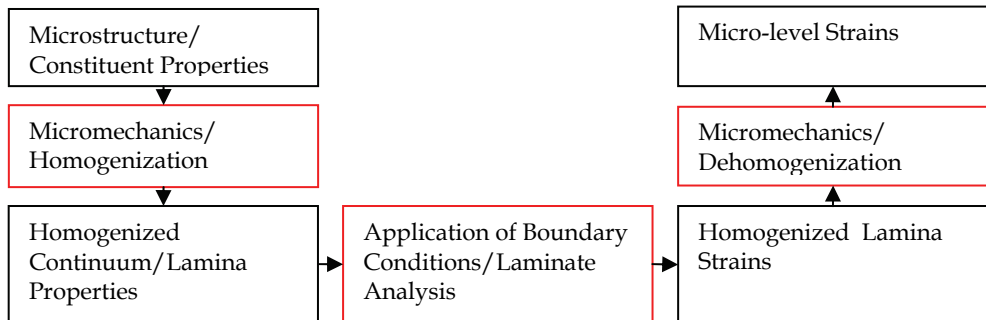


Fig. 3. Flow chart of self-consistent micromechanical enhancement. The analysis steps are boxed in red while the inputs and outputs to each step are boxed in black

The strains in each lamina of the laminate are calculated with a classical laminated plate theory analysis and become inputs to Equation 7. From this step, we obtain two sets of self-consistent states of strain at the micro-level, i.e. in the fiber and matrix phases. This method is considered to be a highly efficient way to obtain micro-level information because laminate geometry and loading conditions can be changed independently of the micromechanics step. Therefore, the initial set of seven finite element analyses only need to be carried out once for each representative volume element. This decoupling of micro and macro level analysis is the characteristic that is responsible for the flexibility and computational efficiency of the method described herein. The alternative approaches described in the introduction require explicit modelling of the fiber and matrix phases for each loading condition and laminate geometry.

5.1 Prediction of homogenized properties

In the current example, two representative volume elements are considered, the square and hexagonal arrays. However the self-consistent micromechanics method can be applied to other representative volume element geometries that meet the doubly periodic condition. A

schematic of each geometry is given in Figure 1. The first two columns in Table 1 are the input constituent material properties for an IM7/8552 carbon fiber, epoxy matrix composite. The final two columns in Table 1 give the predicted homogenized composite properties for the two representative volume elements.

Property	Matrix	Fiber	Square Cell	Hex Cell
E_1 (GPa)	4.76	276.0	167.5	167.5
E_2 (GPa)	4.76	19.5	11.5	10.7
E_3 (GPa)	4.76	19.5	11.5	10.7
G_{12} (GPa)	1.74	70.0	6.78	6.30
G_{13} (GPa)	1.74	70.0	6.78	6.30
G_{23} (GPa)	1.74	5.74	3.10	3.34
ν_{12}	0.37	0.28	0.31	0.31
ν_{13}	0.37	0.28	0.31	0.31
ν_{23}	0.37	0.70	0.57	0.60
α_1 ($10^{-6}/^{\circ}\text{C}$)	64.8	-0.4	0.41	0.41
α_2 ($10^{-6}/^{\circ}\text{C}$)	64.8	5.6	34.7	35.1
α_3 ($10^{-6}/^{\circ}\text{C}$)	64.8	5.6	34.7	35.1

Table 1. Fiber, matrix and equivalent homogenized medium material properties

The homogenized stiffness matrix (\bar{C}_{ij}) is first calculated from Equation 3. Equation 13 shows the calculations used to determine the homogenized engineering elastic constants from the homogenized stiffness matrix. Shown in Tables 2 and 3 are the homogenized stiffness matrix and the homogenized compliance matrix (\bar{S}_{ij}), respectively. The predicted engineering constants are used as inputs in the laminate level analysis.

$$[\bar{S}] = [\bar{C}]^{-1} \quad (13a)$$

$$\bar{E}_1 = 1/\bar{S}_{11}, \bar{E}_2 = 1/\bar{S}_{22}, \bar{E}_3 = 1/\bar{S}_{33} \quad (13b)$$

$$\bar{\nu}_{23} = -\bar{S}_{32}/\bar{S}_{22}, \bar{\nu}_{13} = -\bar{S}_{31}/\bar{S}_{11}, \bar{\nu}_{12} = -\bar{S}_{21}/\bar{S}_{11} \quad (13c)$$

$$\bar{G}_{23} = 1/\bar{S}_{44}, \bar{G}_{13} = 1/\bar{S}_{55}, \bar{G}_{12} = 1/\bar{S}_{66} \quad (13d)$$

Square Array, \bar{C}_{ij} (GPa)						Hexagonal Array, \bar{C}_{ij} (GPa)					
172.8	8.7	8.7	0.0	0.0	0.0	172.8	8.6	8.6	0.0	0.0	0.0
8.7	17.6	10.3	0.0	0.0	0.0	8.6	17.1	10.5	0.0	0.0	0.0
8.7	10.3	17.6	0.0	0.0	0.0	8.6	10.5	17.1	0.0	0.0	0.0
0.0	0.0	0.0	3.1	0.0	0.0	0.0	0.0	0.0	3.3	0.0	0.0
0.0	0.0	0.0	0.0	6.8	0.0	0.0	0.0	0.0	0.0	6.3	0.0
0.0	0.0	0.0	0.0	0.0	6.8	0.0	0.0	0.0	0.0	0.0	6.3

Table 2. Homogenized stiffness matrix representative volume elements

Square Array, \bar{S}_{ij} (1/GPa 10^{-3})						Hexagonal Array, \bar{S}_{ij} (1/GPa 10^{-3})					
5.97	-1.86	-1.86	0.00	0.00	0.00	5.97	-1.86	-1.86	0.00	0.00	0.00
-1.86	87.24	-50.16	0.00	0.00	0.00	-1.86	93.48	-56.07	0.00	0.00	0.00
-1.86	-50.16	87.24	0.00	0.00	0.00	-1.86	-56.07	93.48	0.00	0.00	0.00
0.00	0.00	0.00	322.27	0.00	0.00	0.00	0.00	0.00	299.00	0.00	0.00
0.00	0.00	0.00	0.00	147.54	0.00	0.00	0.00	0.00	0.00	158.69	0.00
0.00	0.00	0.00	0.00	0.00	147.54	0.00	0.00	0.00	0.00	0.00	158.69

Table 3. Homogenized compliance matrix representative volume elements

5.2 Determination of influence matrix and thermal superposition vector

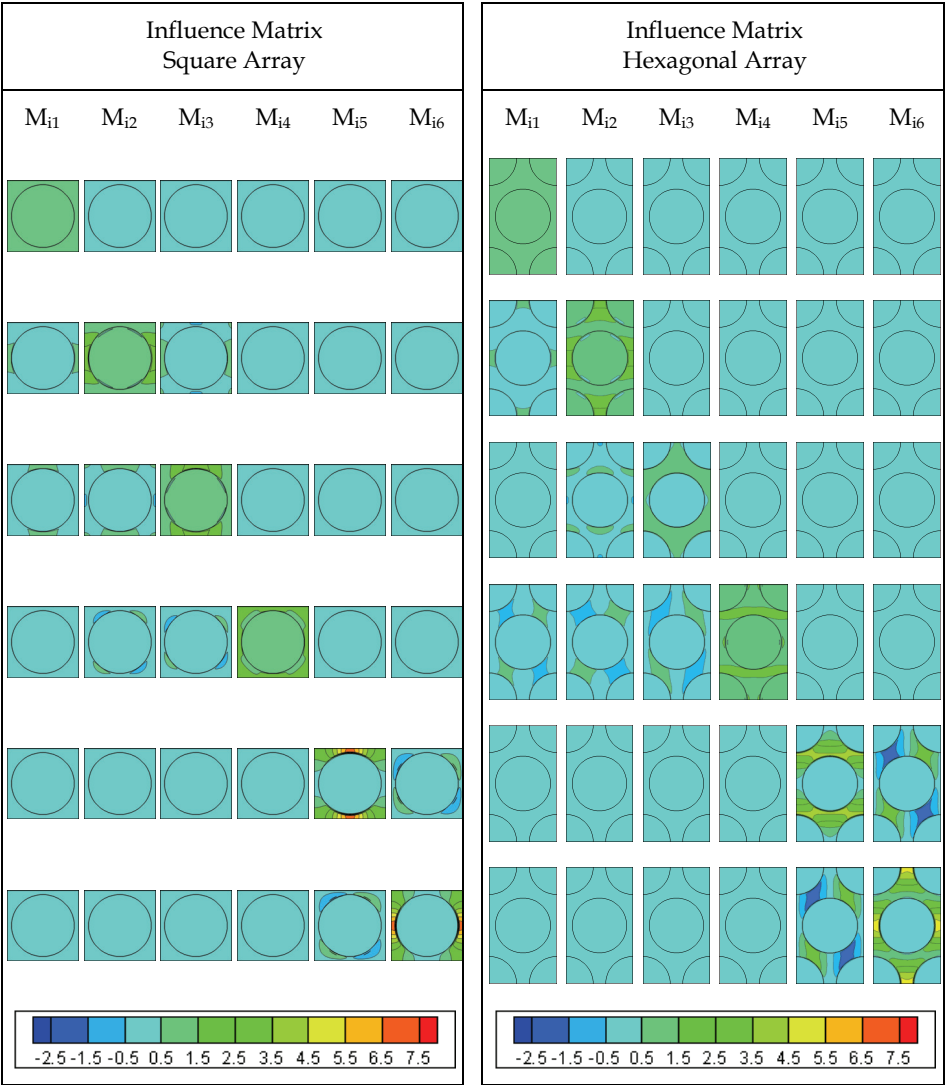
The influence matrix and thermal superposition vector can be extracted from the same set finite element analyses used to determine the effective lamina properties. It should be noted that both the influence matrix and the thermal superposition vector are field variables. That is, each specific geometric point within a representative volume element yields a unique influence matrix. Presented as field variables, the terms of the influence matrices and thermal superposition vectors are illustrated graphically in Figures 4 and 5, respectively.

The micro-strain field can be extracted at every node or integration point within the representative volume element. The enhanced strain field at every point within a volume element can be used in a point failure criteria. Alternatively, a smaller set of points can be selected for examination in order to increase computational efficiency. The same method is applicable for a stress based criteria whereby the stress state at a point is determined from the strain state through the appropriate constitutive relationships.

In the current example, a single point is used to provide a numerical illustration of the micromechanical enhancement process. Tables 4 and 5 contain the influence matrix and thermal superposition vectors respectively. The data is extracted for both the square and hexagonal representative volume elements at the point $(e_1, e_2, e_3) = (L_1/2, L_2, L_3/2)$. Although both points represent locations that are midway between two fiber centers, the influence matrix and thermal superposition vectors are different for the two representative volume elements. This shows the effect of packing geometry on the local strain fields and the need for a comprehensive understanding of the underlying geometry contained in the composite material.

Square Array, M_{ij} $(x, y, z) = (0.5, 1.0, 0.5)$						Hexagonal Array, M_{ij} $(x, y, z) = (0.5, 1.0, \sqrt{3}/2)$					
1.0	0.0	0.0	0.0	0.0	0.0	1.0	0.0	0.0	0.0	0.0	0.0
0.8	3.2	1.0	0.0	0.0	0.0	0.6	2.8	0.3	0.0	0.0	0.0
-0.3	-0.6	0.5	0.0	0.0	0.0	-0.2	-0.5	0.6	0.0	0.0	0.0
0.0	0.0	0.0	2.0	0.0	0.0	0.0	0.0	0.0	1.4	0.0	0.0
0.0	0.0	0.0	0.0	0.1	0.0	0.0	0.0	0.0	0.0	0.3	0.0
0.0	0.0	0.0	0.0	0.0	6.8	0.0	0.0	0.0	0.0	0.0	4.7

Table 4. Influence matrix for both representative volume elements at the selected location



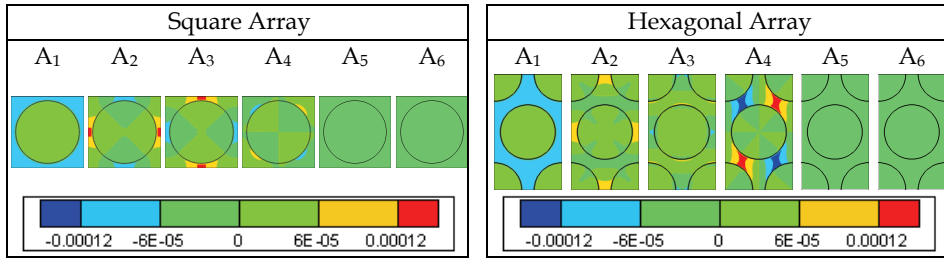


Fig. 5. Thermal superposition vector fields for both representative volume elements, square and hexagonal

5.3 Review of classical laminated plate theory

To illustrate the full process of using the self-consistent micromechanics method described herein, two laminate stacking sequences are investigated, the $[0/90/90/0]$ cross-ply laminate and the $[45/-45/-45/45]$ angle-ply laminate. For this example, the laminate level analysis is preformed using classical laminate plate theory but, finite element methods can also be used for more complex geometries and loading conditions.

Consider only the in-plane resultant forces, $[N_x, N_y, N_{xy}]$ as defined in Figure 6, and thermal loading. Under these conditions, Equation 14 gives relationship between the lamina stresses and strains referenced to the principal material axis (1,2).

$$\bar{\sigma}_i = \bar{Q}_{ij} \varepsilon_j \quad (i, j = 1, 2, 6) \quad (14)$$

Here, \bar{Q}_{ij} is the reduced stiffness matrix in the material principal coordinate system. Equation 15 shows the entries in the reduced stiffness matrix written in terms of the homogenized stiffness matrix.

$$\bar{Q}_{ij} = \bar{C}_{ij} - \frac{\bar{C}_{i3}\bar{C}_{j3}}{\bar{C}_{33}} \quad (i, j = 1, 2, 6) \quad (15)$$

The stresses and strains can be written in the laminate coordinate system (x,y) obtained by rotating the material coordinate system through an angle, θ , about the material 3 axis, see Figure 6. Equation 16 gives the stress strain relation of Equation 14 written in the transformed coordinate system.

$$\bar{\sigma}_i = \bar{Q}'_{ij} (\varepsilon_j - \alpha_j \Delta T) \quad (i, j = 1, 2, 6) \quad (16)$$

A primed quantity is referenced to the laminate coordinate system (x,y). As given in Equation 17, the reduced stiffness matrix referenced to the laminate coordinate system (x,y) is obtained by applying a transformation to the reduced stiffness matrix of Equation 14.

$$[\bar{Q}'] = [T]^T [\bar{Q}] [T] \quad \text{with} \quad [T] = \begin{bmatrix} c^2 & s^2 & sc \\ s^2 & c^2 & -sc \\ -2sc & 2sc & c^2 - s^2 \end{bmatrix} \quad (17a, b)$$

$$s = \sin \theta \quad \text{and} \quad c = \cos \theta \quad (17c, d)$$

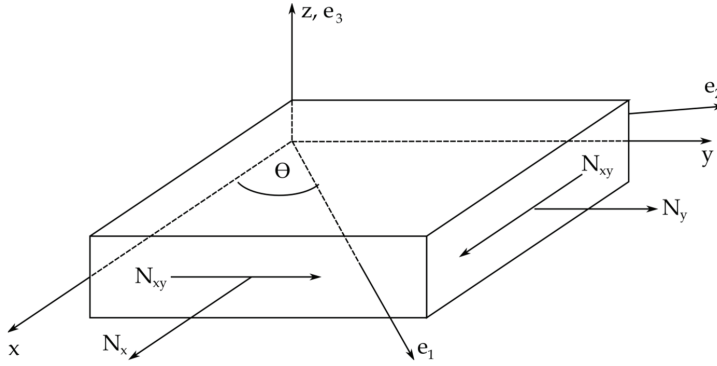


Fig. 6. Definition of laminate resultant forces

For both the cross-ply and the angle-ply laminates being considered, the in-plane loading is decoupled from any out of plane curvatures. As shown in Equation 18, the laminate strains are related to the force resultants, $[N_x, N_y, N_{xy}]$, through the extensional stiffness matrix A_{ij} .

$$\{N\} = A_{ij} \bar{\epsilon}_j - \{N^T\} \quad (18a)$$

$$A_{ij} = \sum_{l=1}^L (\bar{Q}_{ij}^{(l)}) t^{(l)} \text{ and } \{N^T\} = \Delta T \sum_{l=1}^L [\bar{Q}]^{(l)} \{\bar{\alpha}\}^{(l)} t^{(l)} \quad (18b,c)$$

Where the l index sums over the total number of lamina in the laminate and t is the thickness of each lamina. The laminate strains are determined in Equation 19 by rearranging Equation 18a.

$$\bar{\epsilon}_i = A_{ij}^{-1} [\{N\} + \{N^T\}] \quad (19)$$

For the de-homogenization step, the components of homogenized strain field must be referenced to the principal material axis. This is accomplished by applying the transformation matrix of Equation 17b to the laminate strain in Equation 19. The transformation is applied for each lamina within the laminate. The plane stress condition is then inserted into Equation 2 to determine the out-of-plane strain component, $\bar{\epsilon}_3$. Equation 20 gives the relationships obtained for an orthotropic material system. The homogenized strain state is now fully specified and the strain state within each representative volume element can be determined.

$$\bar{\epsilon}_3 = -\frac{\bar{C}_{13}\bar{\epsilon}_1 + \bar{C}_{23}\bar{\epsilon}_2}{\bar{C}_{33}} \quad (20)$$

5.4 Application of uniaxial force resultant, N_x

First, a purely mechanical loading is considered. The lamina level homogenized material properties calculated in Section 5.3 are used to determine the macroscopic state of strain in a

both laminates subjected an axial force resultant, N_x , in the absence of other two force resultants, N_y and N_{xy} . The laminate resultants are defined in Figure 4.

Consider the cross-ply and angle-ply laminates under a loading case in which the resulting edge forces are $[N_x, N_y, N_{xy}] = [100 \text{ kN/m}, 0, 0]$ without a temperature change. The macroscopic strain state in each lamina is determined using the process described in Section 5.3 with a lamina thickness, t , of 0.2 mm. The homogenized mechanical strains in the cross-ply and angle-ply laminates are given in Tables 6 and 7 respectively. From these homogenized states of strain, the state of strain within both representative volume elements is found by applying the influence matrices according to Equation 8. For this example, the influence matrices shown in Table 4 are used to determine the strain in the matrix phase at the location $(e_1, e_2, e_3) = (L_1/2, L_2, L_3/2)$. Tables 8 and 9 list the strains within the matrix at the selected point for the cross-ply and angle-ply laminates, respectively. The results show that the state of strain at the point of inquiry in each representative volume element can be very different from the homogenized state of strain in each lamina.

5.5 Application of uniform temperature change, ΔT

Next, consider the cross-ply and angle-ply laminates subjected to a uniform temperature change of $\Delta T = -100^\circ\text{C}$. The macroscopic strain state in each lamina is determined using the classical laminate theory analysis outlined in Section 5.3 with a lamina thickness, t , of 0.2 millimetres. The homogenized mechanical strains in the cross-ply and angle-ply laminates are given in Tables 10 and 11 respectively. The strain within both representative volume element is found from the homogenized states of strain by applying the influence matrices and thermal superposition vectors according to Equation 8. Mechanical strains are present at the lamina level and at the micro-level for the thermal loading case. This is due to a mismatch in the homogenized coefficients of thermal expansion of the lamina and a mismatch in the coefficients of thermal expansion of the constituents. Again, the influence matrices shown in Table 4 and the thermal superposition vectors of Table 5 are used to determine the strain in the matrix phase at the location $(x, y, z) = (L_x/2, L_y, L_z/2)$ for both representative volume elements. Tables 12 and 13 list the strain state at the selected location within the matrix for the cross-ply and angle-ply laminates, respectively. It is obvious that identical results are obtained for the $[0/90/90/0]$ and $[45/-45/-45/45]$ laminates because the two laminates thermally identical after a rotation of 45° . As such, both laminates have identical states of strain in the material principal coordinates.

	Square Array, 10^{-6}		Hexagonal Array, 10^{-6}	
	0° Ply	90° Ply	0° Ply	90° Ply
$\bar{\epsilon}_1 - \bar{\alpha}_1 \Delta T$	1,390	-55	1,396	-52
$\bar{\epsilon}_2 - \bar{\alpha}_2 \Delta T$	-55	1,390	-52	1,396
$\bar{\epsilon}_3 - \bar{\alpha}_3 \Delta T$	-655	-786	-670	-825

Table 6. Homogenized mechanical strains due to a force resultant, $N_x = 100 \text{ k N/m}$ in the $[0/90/90/0]$ laminate

	Square Array, 10^{-6}		Hexagonal Array, 10^{-6}	
	45° Ply	-45° Ply	45° Ply	-45° Ply
$\bar{\varepsilon}_1 - \bar{\alpha}_1 \Delta T$	667	667	672	672
$\bar{\varepsilon}_2 - \bar{\alpha}_2 \Delta T$	667	667	672	672
$\bar{\varepsilon}_3 - \bar{\alpha}_3 \Delta T$	-720	-720	-748	-748
$\bar{\varepsilon}_6 - \bar{\alpha}_6 \Delta T$	-9221	9221	-9921	9921

Table 7. Homogenized mechanical strains due to a force resultant, $N_x = 100 \text{ kN/m}$ in the [45/-45/-45/45] laminate

	Square Array, 10^{-6} $(x, y, z) = (0.5, 1.0, 0.5)$		Hexagonal Array, 10^{-6} $(x, y, z) = (0.5, 1.0, \sqrt{3}/2)$	
	0° Ply	90° Ply	0° Ply	90° Ply
$\varepsilon_1 - \alpha_1 \Delta T$	1,390	-55	1,396	-52
$\varepsilon_2 - \alpha_2 \Delta T$	281	3618	491	3,630
$\varepsilon_3 - \alpha_3 \Delta T$	-712	-1211	-655	-1,183

Table 8. Micro-level mechanical strain due to a force resultant, $N_x = 100 \text{ kN/m}$ at the selected location in the [0/90/90/0] laminate

	Square Array, 10^{-6} $(x, y, z) = (0.5, 1.0, 0.5)$		Hexagonal Array, 10^{-6} $(x, y, z) = (0.5, 1.0, \sqrt{3}/2)$	
	45° Ply	-45° Ply	45° Ply	-45° Ply
$\varepsilon_1 - \alpha_1 \Delta T$	667	667	672	672
$\varepsilon_2 - \alpha_2 \Delta T$	1,948	1,948	2060	2060
$\varepsilon_3 - \alpha_3 \Delta T$	-960	-960	-919	-919
$\varepsilon_6 - \alpha_6 \Delta T$	-62,703	62,703	-46,629	46,629

Table 9. Micro-level mechanical strain due to a shell edge traction, $N_x = 100 \text{ kN/m}$ at the selected location in the [45/-45/-45/45] laminate

	Square Array, 10^{-6}		Hexagonal Array, 10^{-6}	
	0° Ply	90° Ply	0° Ply	90° Ply
$\bar{\varepsilon}_1 - \bar{\alpha}_1 \Delta T$	-277	-277	-263	-263
$\bar{\varepsilon}_2 - \bar{\alpha}_2 \Delta T$	3,152	3,152	3,206	3,206
$\bar{\varepsilon}_3 - \bar{\alpha}_3 \Delta T$	-1,708	-1,708	-1,823	-1,823

Table 10. Homogenized mechanical strains due to thermal loading, $\Delta T = -100^\circ \text{C}$ in the [0/90/90/0] laminate

	Square Array, 10^{-6}		Hexagonal Array, 10^{-6}	
	45° Ply	-45° Ply	45° Ply	-45° Ply
$\bar{\varepsilon}_1 - \bar{\alpha}_1 \Delta T$	-277	-277	-263	-263
$\bar{\varepsilon}_2 - \bar{\alpha}_2 \Delta T$	3,152	3,152	3,206	3,206
$\bar{\varepsilon}_3 - \bar{\alpha}_3 \Delta T$	-1,708	-1,708	-1,823	-1,823

Table 11. Homogenized mechanical strains due to thermal loading, $\Delta T = -100^\circ \text{C}$ in the [45/-45/-45/45] laminate

	Square Array, 10^{-6} $(x, y, z) = (0.5, 1.0, 0.5)$		Hexagonal Array, 10^{-6} $(x, y, z) = (0.5, 1.0, \sqrt{3}/2)$	
	0° Ply	90° Ply	0° Ply	90° Ply
$\varepsilon_1 - \alpha_1 \Delta T$	6123	6123	6137	6137
$\varepsilon_2 - \alpha_2 \Delta T$	-4743	-4743	-728	-728
$\varepsilon_3 - \alpha_3 \Delta T$	5638	5638	3356	3356

Table 12. Micro-level mechanical strain due to thermal loading, $\Delta T = -100^\circ \text{C}$ at the selected location in the [0/90/90/0] laminate

	Square Array, 10^{-6} $(x, y, z) = (0.5, 1.0, 0.5)$		Hexagonal Array, 10^{-6} $(x, y, z) = (0.5, 1.0, \sqrt{3}/2)$	
	45° Ply	-45° Ply	45° Ply	-45° Ply
$\varepsilon_1 - \alpha_1 \Delta T$	6123	6123	6137	6137
$\varepsilon_2 - \alpha_2 \Delta T$	-4743	-4743	-728	-728
$\varepsilon_3 - \alpha_3 \Delta T$	5638	5638	3356	3356

Table 13. Micro-level mechanical strain due to thermal loading, $\Delta T = -100^\circ \text{C}$ at the selected location in the [45/-45/-45/45] laminate

6. Conclusions

A computationally efficient method for estimating the microscopic strain field within the discrete phases of a heterogeneous medium consisting of collimated, continuous fibers within an isotropic matrix has been developed. The goal of the development has been to provide an essential link in a multi-scale analysis of a composite structure. The structural loading and deformations at the macro-scale can be related to the state of strain within the fiber and matrix phases at the micro scale by using the self-consistent micromechanics method. The model utilizes a conventional influence function formulation and considers thermo-mechanical deformations. Results have been presented that illustrate the utility of the approach in determining microscopic state of strain in the [0/90/90/0] and [45/-45/-

45/45] laminates. Enhanced strain components within each of the lamina were calculated for both uniaxial loading and a uniform change in temperature.

The present example showed results extracted for a single point within the representative volume element. As shown in Figure 3, the influence matrix and thermal superposition vector are field values. Therefore, the state of strain within the representative volume element can also be represented as a field value. As such, the analysis is not limited to analysis of the state of strain at a single point. However, the reader may choose as many interrogation points as are required in order to address de-homogenization of all of the phases or to meet a specific need with a minimum computational cost.

Microstructures found in fiber reinforced composites typically consist of an irregular array of fibers which differ from the representative volume elements analysed herein. An efficient method for dealing with variability is through the use of a statistically equivalent periodic unit cell. With this approach, a computational step is used to generate an equivalent representative volume element that replaces the actual complex geometry. This method has been applied at several length scales including a unidirectional fiber tow (Zeman and Sejnoha, 2007).

The main assumption implicit in the analysis is that the representative volume element is subjected to a uniform state of strain. Certainly, this is not true at all locations within a laminate. Examples include areas with large strain gradients or locations with discontinuities in the assumed periodicity such as ply interfaces. In light of these limitations, the described method provides a reasonable first order approximation of the state of strain within the constitutive phases of an ordered heterogeneous medium.

7. References

- Buchanan, D. L.; Gosse, J. H.; Wollschlager, J. A.; Ritchey, A. & Pipes, R. B. (2009). Micromechanical enhancement of the macroscopic strain state for advanced composite materials. *Composites Science and Technology*, Vol. 69, (month and year of the edition) page numbers (1974–1978), 0266-3538
- Christensen, R. M. (1979). *Mechanics of Composite Materials*, John Wiley & Sons, 0-471-05167-5, New York, New York.
- Daniel, I. M. & Ishai, O. (2006). *Engineering Mechanics of Composite Materials*, Oxford University Press, 0-19-515097, New York, New York.
- Gosse, J.H. & Christensen, S. (2001). Strain Invariant Failure Criteria for Polymers in Composites. *Proceedings of 42nd AIAA/ASME/ASCE/AHS/ASC Structures, Structural Dynamics, and Materials Conference and Exhibit*, Seattle WA, April 2001
- Halpin, J. C. & Tsai, S. W. (1967). Effects of Environmental Factors on Composite Materials. *Air Force Technical Report AFML-TR-67-423*, Wright Aeronautical Labs, Dayton, OH
- Hashin, Z. & Rosen, B. W. (1964). The Elastic Moduli of Fiber-Reinforced Materials. *Journal of Applied Mechanics*, Vol. 21 (1964) page numbers (233-242), 0021-8936
- Hashin, Z. (1972). *Theory of Fiber Reinforced Materials*. NASA CR-1974, Langley Research Center
- Hill, R. (1963). Elastic Properties of Reinforced Solids: Some Theoretical Principles. *Journal of Mechanics and Physics of Solids*, Vol. 11, No. 5, (September 1963) page numbers (357-372), 0022-5096

- Hill, R. (1965). Theory of Mechanical Properties of Fibre-Strengthened Materials: III, Self-Consistent Model. *Journal of the Mechanics and Physics of Solids*, Vol. 13, No. 4, (August 1965) page numbers (189-198), 0022-5096
- Hutapea, P.; Yuan, F.G.; Pagano, N.J. (2003) Micro-stress prediction in composite laminates with high stress gradients. *International Journal of Solids and Structures*, Vol. 40, No. 9, (May 2003) page numbers (2215-2248), 0020-7683
- Pagano, N. J. & Rybicki, E. F. (1974). On the significance of effective modulus solutions for fibrous composites. *Journal of Composite Materials*, Vol. 8, No. 3, (July 1974) page numbers (214-228), 0021-9983
- Pagano, N. J. & Yuan, F. G. (2000). The significance of effective modulus theory (homogenization) in composite laminate mechanics. *Composites Science and Technology*, Vol. 60, No. 12-13, (September 2000) page numbers (2471-2488), 0266-3538
- Paul, B. (1960). Prediction of Elastic Constants of Multiphase Materials. *Transactions of AIME*, Vol. 218, page numbers (36-41), 0096-4778
- Pindera, M. J.; Khatam, H.; Drago, A. S. & Bansal, Y. (2009). Micromechanics of spatially uniform heterogeneous media: A critical review and emerging approaches. *Composites Part B: Engineering*, Vol. 40, No. 5, (July 2009) page numbers (349-378), 1359-8368
- Raghavan, P.; Moorthy, S.; Ghosh, S. & Pagano, N. J. (2001). Revisiting the composite laminate problem with and an adaptive multi-level computational model. *Composite Science and Technology*, Vol. 61, 2001, (June 2001) page numbers (1017-1040), 0266-3538
- Reuss, A. (1929). "Berechnung der Fließgrenze von Mischkristallen auf Grund der Plastizitätsbedingung für Einkristalle". *Zeitschrift für Angewandte Mathematik und Mechanik*, Vol. 9 No. 1 (February 1929) page numbers (49-58), 1521-4001
- Sun, C. T. & Vaidya, R. S. (1996). Prediction of composite properties from a representative volume element. *Composites Science and Technology*, Vol. 56, No. 2, (1996) page numbers (171-179), 0266-3538
- Voigt, W. (1887). Theoretische Studien über die Elastizitätsverhältnisse der Krystalle. *Abhandlungen der Gesellschaft der Wissenschaften zu Göttingen*, Vol. 34, (August 1887) page numbers (3-51)
- Wang, Y.; Sun, C.; Sun, X. & Pagano, N. J. (2002). Principles for Recovering Micro-Stress in Multi-Level Analysis, In: *Composite Materials: Testing, Design and Acceptance Criteria*, ASTM STP 1416, A. Zureick and A. T. Nettles, (Ed.), page numbers (200-211), American Society for Testing and Materials International, 0-8031-2893-2, West Conshohocken, PA
- Zeman, J; Sejnoha, M. (2007). From random microstructures to representative volume elements. *Modeling and Simulation in Materials Science and Engineering*, Vol. 15, No. 4, (2007) page numbers (S325-S335), 0965-0393

The Effective Thermal Transport in Composite Materials

Bashir M. Suleiman

*Department of Applied Physics, College of Sciences,
University of Sharjah, P.O. Box 27272, Sharjah,
United Arab Emirates*

1. Introduction

Composite materials are promising materials, which should exhibit an improve on several aspects of the physical properties such as mechanical, thermal, electrical etc.. A composite material is a system of materials composed of two or more components randomly mixed and bonded on a macroscopic scale. For example, metal-alloys Silicon carbides such as Aluminum Silicon Carbide (AlSiC) is made up of Aluminum, Silicon and Carbone on a microscopic scale. It is a metal matrix composite (MMC) packages that have a unique set of material properties. It is ideally suited to thermal management performance, and a functionality that supports high-density interconnection microelectronic packaging applications (Hollecka et al., 1988) & (Zhang et al., 2004). This example is one of the concrete evidences that thermal conduction is an important feature of composites' application for electronic packaging, which are associated with thermal insulation, and heat spreader. General speaking, we should have different composite materials which are suitable for different applications (Xu, & Yagi, 2004), and this can be achieved because of the unique character of the detailed microstructure of the composites.

In particular, a composite material is composed of strengthening items (reinforcement) such as particles, flakes, fibers, etc., embedded in a matrix of metals, ceramics, or polymers. The matrix holds these items to form the desired shape while the items improve the overall physical properties of the matrix. When designed properly, the new combined material exhibits better physical property than would each individual material. When composites are selected over traditional materials such as metal alloys or plastics, it is usually because of one or more desired properties regarding cost, weight, size, surface condition, strength, thermal and electrical conduction etc...

For example, Silicon Carbide SiC/SiC composites, which are relatively cheap, have upper limit for thermal conductivity that exceeds the corresponds obtained in single crystal and high-purity chemically vapor deposited CVD SiC. Effective thermal conductivity (λ_{eff}) of such composites reaches maximum values of $\sim 320 \text{ W/m } ^\circ\text{C}$ at room temperature (Zinkle & Snead, 1999). This value is comparable if not higher than the thermal conductivity of some precious expensive metals such gold and silver.

A new generation of functionally graded fibrous composites called functionally graded materials (FGMs) (Suresh, 1998), (Koizumi, 1993) and (Fung & Hu, 2008). FGMs have dynamic effective thermal properties and the volume fraction of the materials changes

gradiently. It is the non-homogeneous microstructures in these materials that produce continuous graded macroscopic properties, such as the thermal conductivity, specific heat, mass density and elastic modulus. FGMs have been developed as the super-resistant materials for propulsion systems and airframe of the space planes in order to decrease thermal stresses and to increase the effect of protection from heat (Gray et al., 2003) and (Kuo & Chen, 2005). FGMs can reduce the thermal stress in such structures working in high temperature environment. All the effective thermal properties of FGMs can provide great help in predicting the overall behavior under various loading conditions. The least to say is that the theoretical and experimental investigation of the effective thermal properties of all composites including FGMs is an area which has received great interest in recent years.

2. Historical background of theoretical models

Estimation of the effective thermal conductivity of composite material has been subject of many theoretical and experimental investigations. The earliest model was proposed by Maxwell (Maxwell, 1892). He derived an expression for the simplest kind of two-phase dispersion consisting of spherical particles suspended or imbedded into a continuous medium of another material neglecting the interactions between the particles. The derived expression was valid only for very low concentrations of the dispersed phase i.e. for dilute volume fraction.

For non-dilute volume fractions, The interaction between the spherical particles has a significant effect and cannot be neglected, the work of Maxwell was later followed by the work of Rayleigh in 1892 to account for these interactions. By considering a form of a simple cubic lattice of spheres in a homogeneous material and using a series expansion, Rayleigh assumed that the spherical particles as inclusions that form a cubical array, and included the interaction effect of a number of nearby spheres.

Other proposed works for non-spherical inclusions developed by other researchers such as the work of (Polder & Van Santen, 1946), (Reynolds & Hough, 1957), (Hamilton & Crosser 1962), (Rocha & Acrivos, 1974) and others. Extension of these previous works was also carried out by (McPhedran & McKenzie, 1978), and (Sangani & Acrivos, 1983). In the course of models developments Hashin, 1968 proposed a general self-consistent treatment. The treatment provides a physically realistic model of particle to particle interaction for two phase system covering the full range of the volume fraction. The self-consistent field concept is extended to include the contact resistance in the composite reinforced with coated spheres. Benveniste & Miloh (1991) and Felske et. al. (2004) employed effective medium theories to predict the effective thermal conductivity of coated short-fiber composites. Later, Samantray and co-workers (Samantray et al, 2006) proposed the correlations between the inclusions to estimate the effective thermal conductivity of two-phase materials. Recently in 2009, (Fang et. al, 2009) applied the thermal wave method to investigate the unsteady effective thermal conductivity of particular composites with a functionally graded interface. The scattering and refraction of thermal waves by a spherical particle with an inhomogeneous interface layer in the matrix are analyzed, and the results of the single scattering problem are applied to the composite medium.

2.1 Determination of bounds and estimation of λ_{eff}

In general, using a theoretical model to estimate the effective thermal conductivity (λ_{eff}) of a multiphase medium requires the previous knowledge of the thermal conductivity of each

phase, the volume concentrations of the phases, the phase morphology (distribution), the shape of inclusions of the different phases in the solid matrix, and the fractional porosity if the medium is porous.

In this chapter, the problem of determining the bounds and/or estimating the effective thermal conductivity (λ_{eff}) of a composite (multiphase) system has been examined. A comparison between the measured data and the results predicted by theoretical models has been made. Two different categories of composite materials have been investigated, namely wood and ceramics. In particular we investigate the effect of morphology in woods and mineralogy in ceramics.

Wood is a heterogeneous porous material with known anisotropy due to its intrinsic distribution of phase morphology (inter layers arrangement). It should be mentioned that measurements of the thermal conductivity as a function of phase morphology (grain size and orientation) indicate preferential heat conduction along the conducting chain of grains. Its low for random distribution of grains and high for layered (parallel) grains.

The phenomena of heat transfer in wood depend on the geometry of the wood, as well as porosity. Such heterogeneous medium containing the three phases, its thermal conductivity is only an apparent conductivity because it results from complex exchanges concerning simultaneous conduction in solids, and fluids (gases and/or liquids). Regarding the theoretical models to estimate wood conductivity, there are various models of heat conductivity are given in the literature, for example, see references given by Gronli (1996). In this study, we will use one of these models which given by (Kollmann & Cote, 1968). The influences of density, porosity and anisotropy on thermal transport in wood are investigated. To estimate the effective thermal conductivity (λ_{eff}) in a fibrous wood like structure, a model (Kollmann, & Cote, 1968) based on a weighting bridge-factor (ξ) between two limiting parallel and serial conduction cases have been used. The model indicates an increase in the effective conductivity as the density/porosity increases/decreases which was in agreement with our investigation regarding the influence of microstructure on the heat conduction in wood. Moreover, indicates significant difference between the longitudinal and the transverse directions.

At this point, it is worth mentioning that a worldwide research and development efforts are underway to examine the potential use of a wide range of non-destructive testing (NDT) and non-destructive evaluation (NDE) technologies for evaluating wood and wood-based materials as fiber-based materials or multiphase composites—from the assessment of standing trees to in-place structures (Brashaw et al., 2009).

Ceramics on the other hand are multiphase mechanically strong, relatively non-porous material with unknown anisotropy but with known volume fractions and conductivities of phases. The thermal transport in such material depends mainly on its mineralogy (microstructure details) of its constituents. Seven heterogeneous samples of Ceramics marbles and glasses have been selected. The tested models include those of the effective medium theory (EMT) (Noh et. al 19), Hashin and Shtrikman (HS) bounds (Hashin & Shtrikman, 1962) and Wiener bounds, (Wiener, 1912). These models can be used to characterize macroscopic homogeneous and isotropic multiphase composite materials either by determining the bounds for the effective thermal conductivity and/or by estimating the overall conductivity of the random mixture. It turns out that the most suitable one of these models to estimate λ_{eff} is the EMT model. This model can be used to characterize macroscopic homogeneous and isotropic multiphase composite materials after determining the parallel and serial bounds (Wigner bounds) of the overall conductivity of the random

mixture. We used Wiener bounds, as a preliminary indicator to validate the homogeneity condition of the investigated samples, i.e. the measured values for the conductivity should be within the limits of the Wigner bounds. After a comparison between the experimental data of the effective thermal conductivity with the corresponding theoretical estimation, it turns out that the EMT model is a suitable one to estimate λ_{eff} . This model is a mathematical model based on the homogeneity condition, which satisfies the existence of a statistically homogeneous medium that encloses inclusions of different phases. Numerical values of thermal conductivity for the samples that satisfy the homogeneity condition imposed by the effective medium theory are in best agreement with the experimentally measured ones.

3. Experimental techniques

The reliability of a specific technique to measure thermal properties is determined by several factors, such as the speed of operation, the required accuracy and performance under various environmental conditions, the physical nature of material, and the geometry of the available sample. However, in most techniques the main concern is to obtain a controlled heat flow in a prescribed direction, such that the actual boundary and initial conditions in the experiment agree with those assumed in the theory. There are several methods (techniques) used to measure the effective thermal conductivity of composites. Indeed, the choice of technique depends on the type of application, size of the sample and the available sample geometry; however they are divided into two groups, the steady state and the non-steady state (transient) methods.

3.1 Steady state techniques

In the 1st group, the sample is subjected to a constant heat flow. In the past, much attention has been focused on the problems of this group. Examples of steady state are the well-known guarded hot plate and heat flow meter techniques for thermal conductivity (ISO 8302, 1991), (Gawin et al., 2004) and (Sombatsompop, 1997) which are typically suited for bulk applications that require large and thick samples. For these methods, testing times can be long due to the need for thermal equilibrium, which can be of the order of 24 hours, and temperature gradients across the sample can be large. The principle of the heat flow meter method is based on mounting the test-sample between two plates, a 'hot' and a 'cold' plate, then a heat flux transducer is used to measure the heat flow through the sample. Using measurements of the heat flux, temperature difference across the sample and sample thickness the thermal conductivity can be found. The method is a quasi-steady state method and is a variant of the guarded hot plate technique thus the instrument and sample must be allowed to reach isothermal condition (thermal equilibrium) before measurements are made. It should be mentioned that this method is a comparative method and thus the instrument must be calibrated using a specimen of known thermal conductivity. More details and analysis can be found in ASTM E1530.

On other hand, these steady state methods may not be suited to testing molten composites which include soft materials such as plastics and polymers. In this type of composites, in addition to other practical factors related to the molten state of the soft materials, they are vulnerable to degradation during performing the measurements and before the required thermal equilibrium is attained. The thermal properties of such composites are influenced by the level of crystalline and molecular structure of the molten which are directly related to its thermal history (Sombatsompop, 1997).

3.2 Non-steady state(transient) techniques

In the 2nd group, a periodic or transient heat flow is established in the sample. In comparison with the first group, the transient or non-steady state techniques for thermal conductivity are appealing in that the test time is comparatively short, small specimens can be measured, and formed products can be tested (e.g. films, sheets and mouldings). Two Examples of this group are the transient plane source (TPS)(Gustafsson , 1991) to determine the thermal conductivity, thermal diffusivity and their anisotropy (Suleiman et al. 1999) & (Fan et al.,2006), and the transient line-source probe method (Dawson et al., 2006).

The transient line-source probe technique, also known as the needle probe method, is a development of the hot wire method but is suited for testing molten composites in both their molten and solid states (Dawson et al., 2006). A thermocouple and linear heating element are enclosed and casted in a form of a needle, which is typically 50-100 mm in length and 1.5 - 2 mm in diameter. The heater is positioned along the length of the needle and the thermocouple is anchored at the middle position. The needle is immersed and held in the sample until temperature equilibrium is achieved at the desired temperature. Then, by applying a voltage across the resistance heater during a specified time period a heat wave propagates through the sample in the radial direction. The thermal conductivity is determined from the temperature-time profile of the probe. It should be noted that the temperature-time profile (the rate of temperature rise) is sensitive to and depended on the magnitude of the thermal conductivity of the test-sample. It is low profile for higher conductivity and visa versa. Due to this sensitivity and other factors such as the finite probe dimensions and end effects, the technique requires the probe to be calibrated using a reference material with known thermal conductivity (ASTM D5930-01).

More attention will be given to the TPS technique due the fact that most of the experimental data and results discussed in this work are obtained using the TPS technique.

The principle of this technique is simple. The sample is initially kept at thermal equilibrium, and then a small disturbance is applied to the sample in a form of a short heating pulse through the heater/sensor. The temperature profile is characterized by a transient temperature rise of a plane heat source/sensor, known as Hot Disk (Gustafsson, 1991). The hot disk is a thin resistive element, in the form of a bifilar spiral, which acts as both a heat source and a temperature sensor, a schematic drawing is depicted in fig 1. Measurements are simply performed by recording the voltage (resistance/temperature) variations across the sensor during the passage of a heating current in a form of a constant electrical pulse. Figure 1 shows actual recordings of low conductivity ceramic and relatively high conductivity steel samples. These recordings correspond to relatively low temperature rises (around one degree) across the samples. Using this type of sensor, it is possible to measure both the heat input and the temperature increase, from which both the thermal conductivity and thermal diffusivity are simultaneously determined. The theory of the TPS method is based on a three-dimensional heat flow inside the sample, which can be regarded as an infinite medium, if the time of the transient recording is ended before the thermal wave reaches the boundaries of the sample. To validate the theory of the method, the diameter of the sample should be larger than the diameter of the disk as shown schematically in figure 1. In other words; the sample is large enough so that it can be regarded as infinite medium provided that the time of the transient recording is ended before the thermal wave reaches the boundaries of the sample and produces edge effects. Edge effects can be prevented by satisfying a criterion concerning the probing (penetration) depth. The criterion is associated

with the total time of the transient event which is proportional to the square of the overall dimension of the conduction pattern or the distance from the conducting pattern to the nearest free surface of the sample. This is evident from the expression for the probing depth (Gustafsson, 1991) $\Delta_p = \beta (t_{\max} \kappa)^{1/2}$, where t_{\max} is the total time of the recording, κ is the thermal diffusivity of the specimen and β is an adjustable parameter that is related to the relative sizes of the sensor and the specimen, and indirectly correlated with the experimental accuracy. The probing depth and the specimen size are intimately connected in the sense that the shortest distance from any point on the sensor element to the nearest point on any of the free surface of the specimen must always exceed Δ_p to avoid edge effects. Edge effects due to the reflected thermal wave at the boundaries disturb the measurements and affect the accuracy. To achieve high accuracy in our measurements, a β -value of 1.42 seems to define reasonably well the probing depth. The assessment of the temperature increase $\Delta T(t)$ in the heater depends on several factors such as the power output in the sensor element, the design parameters of the sensor, and the thermal transport properties of the surrounding specimen. For the disk-shaped sensor, the thermal conductivity and diffusivity can be obtained from $\Delta T(t)$ that is given by the following equation:

$$\Delta T(t) = P_o (\pi^{3/2} a \lambda)^{-1} D(t) \quad (1)$$

Here P_o is the total output power, λ is the thermal conductivity of the test-sample, and a is the radius of the sensor. $D(\tau)$ is the theoretical expression (Suleiman, 1994) of the time dependent temperature increase, which describes the conducting pattern of a disk-shaped sensor, assuming that the disk consists of a number m of concentric ring sources.

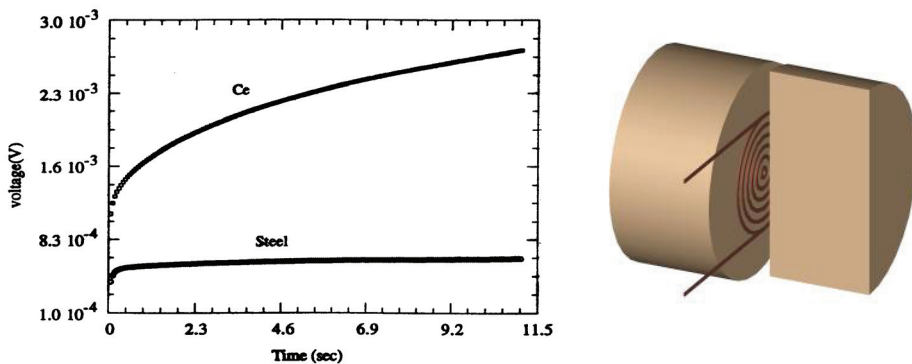


Fig. 1. A typical voltage recordings and a schematic drawing of sample/sensor experimental set-up

This technique has an additional advantage of using a flat thin sensor, which makes it more suitable to substantially, reduce the contact resistance between the specimen and the sensor. This technique has been used several times to report thermal conductivity measurements over a wide range of temperatures (Gustafsson, 1991) & (Suleiman et al, 1996) including the

data presented in next section. A full complete description of the experimental capability regarding precision/accuracy and reproducibility of the measured data of various applications is given elsewhere (Suleiman, 1994).

4. Results and discussion

Two types of multiphase composite materials have been selected, namely; wood and ceramics. As it was mentioned in section 2, in particular we investigate the effect on thermal conduction due to structural morphology in woods and structural mineralogy in ceramics.

4.1 Woods

It is known that wood is a fiber-based ligno-cellulosic material (Avramidis & Lau, 1992). In this type of materials, the crystalline structure of cellulose chains may be altered, due to temperature variations, leading to a permanent loss in strength and considerable changes in physical behaviour including its ability to conduct heat. The purpose of this study is to investigate the relation between the thermal conductivity of wood and the various factors affecting this property. The transient hot-disk method was used at 20 degree Celsius to perform measurements of the thermal conductivity (λ).

The investigated wood samples were hardwood from birch trees used for energy conversion purposes (approximate age of 10-15 years) with a stem diameter of approximately 100 mm. The samples were cut from the stem at a distance of one meter above the ground level. The samples were prepared from different stems, each sample consisting of two disks. Six samples were selected so that sufficient uniformity of density, grain size and orientation, and other physical characteristics could be obtained. The measurements were performed on this six samples on oven-dry basis at room temperature. To insure good thermal contact, in the experimental arrangement the sensor was clamped between the sample halves that consist of two identical cylinder-shaped pieces, each having a diameter of 30 mm and a thickness of 10 mm, see figure 1. The two disks that are required for each test sample were cut from successive portions of the same stem to obtain as much as possible identical and uniform characteristics. To study the influence of fiber direction on thermal conduction the disks were cut parallel (three samples) or perpendicular (three samples) to the fiber direction. Their surfaces were smoothened with sandpaper and equilibrated to the same testing laboratory conditions and then the measurements were performed along the prescribed directions. Although the theory of the TPS method is based on a three-dimensional heat flow inside the sample, however, the samples were cut in a specified direction to maintain a unidirectional-measured property and to minimize any additional contribution of heat flow from the perpendicular directions to the assigned direction of measurement. By cutting the sample in a specified direction, it can be regarded as a unidirectional infinite medium if the time of the transient recording is ended before the thermal wave reaches the boundaries of the sample and produces edge effects. These measurements were done on the longitudinal (along the grain) direction and on the transverse direction (a combination of both radial and tangential directions to the annual rings), the arrows in figure 2 illustrate the measurements directions. Fan and his co-workers (Fan et al, 2006) proposed a fractal model based on SEM images to predict both the tangential and the radial effective thermal conductivities of wood. They used improved TPS method to validate the model, obtaining credible and precise results.

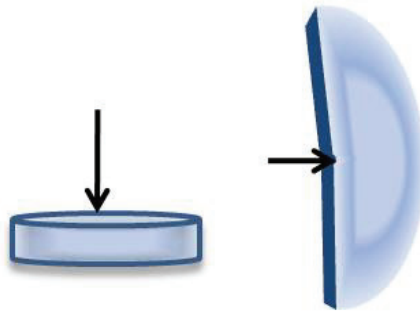


Fig. 2. Schematic drawing; the arrows indicate the longitudinal and transverse measurements directions, respectively

All samples were oven-dried at a temperature of 120 °C until they reached a moisture free condition at constant mass. At a temperature of 120 °C both the free water and the bound water in wood are released, and thus the samples were completely dry. To prevent presence of any moisture, the samples were wrapped by Al-foil during the measurements and kept in plastic containers at all other times. Based on oven-dry masses and volumes, the average values of the apparent densities were calculated at the time of measurements for each sample.

Wood is a porous material and porosity is a parameter, which is likely to affect the magnitude as well as the temperature dependence of the thermal conductivity. This porosity r can be estimated using

$$\rho = 1 - (\rho_{ave}/\rho_{th}) \quad (2)$$

where ρ_{ave} is the average apparent density of the sample, ρ_{th} is the assumed theoretical density of a compact solid wood free from voids. Its value is taken to be 1500 kg/m³ (Kollmann & Cote, 1968). The accuracy of the thermal conductivity data has been estimated to be better than 5%. Care was taken not to increase the temperature in the samples more than one degree Celsius. A larger temperature difference will mask any changes that occur in a narrow interval around a phase transition (Suleiman et. al, 1996). The mean values of five runs of λ at 20 °C, are represented in Fig. 3 for both longitudinal (filled circles) and transverse (open circles) directions. The variations of the thermal conductivity λ as a function of density and porosity are given by the lower and upper axis, respectively. The accuracy was within 3-5% for the conductivity measurements. According to the estimated porosity given in the figure, and considering the fact that the samples have similar thermal conductivity behavior in terms of their thermal profiles, the longitudinal /axial samples would be expected to have somewhat higher λ -values than the transverse samples as shown in the figure. They exhibit the same behavior that of the density but with negative slopes as given by Eq.(2); the conductivity decreases as porosity increases. Although the few data points in the figure show the expected general trend for the conductivity, the figure does not explain why, at fixed temperature (20 °C), there is a difference in the slope as density increases or porosity decreases. Our discussion will be focused on λ and its relation to microstructure (density and/or porosity) and anisotropy. The porosity is typically in the range from 0.5 to 0.8. Voids due to the porosity serve as scattering centers for phonons, and they take up a fraction of the heat conduction volume of the material leading to a lower thermal conductivity. From the

present data related to density and porosity, the following can be deduced: Firstly, a density variation of 20% could alter the conduction by 15% as it is the case for the longitudinal direction at 20 °C. Secondly, the presence of other heat conduction obstacles in addition to voids, such as rays and cell boundaries could also affect the conduction process.

However, it seems that conduction through voids is the dominant factor influencing heat conduction in this type of wood samples. Peculiarities in bulk structure or inherent chemical composition of the different samples appear to have no influence upon thermal conduction, other than that due to the unique microstructure of each sample.

Regarding the anisotropic nature of wood there is no dispute about direction dependency of thermal conductivity in both hard and soft woods, see for example the review by Steinhagen (1977). Thermal conductivity in the longitudinal direction (parallel to the grain) is greater than conductivity in the transverse direction. This may be attributed to orientation of the molecular chains within the cell wall. The long-chain linear polymers (cellulose) that comprise the cell wall, are arranged in bundles called microfibrils. These microfibrils are most closely aligned with the longitudinal axis of the cell. Obviously, the thermal conduction is higher along the length of a microfibril (parallel direction) than across a series of microfibrils (series direction), (Parrott & Stuckes, 1975).

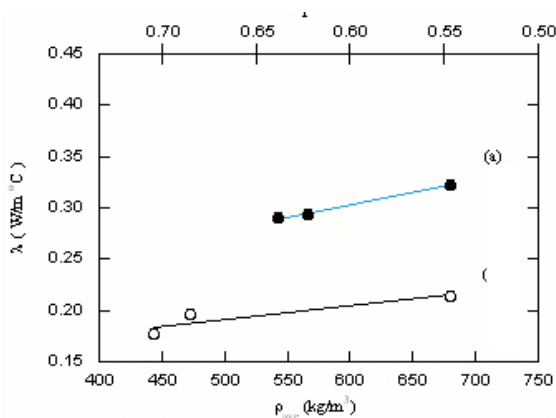


Fig. 3. Thermal conductivity as a function of density (lower axis) and porosity (upper axis) in the longitudinal (solid circles) and the transverse (open circles) directions, respectively

There might be some debate about the direction dependence of the transverse conductivity (the difference in conductivity between the tangential and radial directions with respect to the annual rings). Radial conductivity may be higher than the tangential conductivity and this may be attributed to the influence of the radially oriented wood rays. According to Steinhagen (Steinhagen, 1977), it appears that the ratio of the tangential versus radial conductivity is primarily determined by the volume of the ray cell in hardwoods and by latewood volume in softwoods. However, in our case, no appreciable difference would be expected between the radial and the tangential conductivities, since our samples have a uniform structure throughout the annual rings. Furthermore, our samples are cut from young trees, i.e. the samples are mostly free from latewood.

On the other hand, our data show a significant difference between the longitudinal and the transverse directions. This difference is expected to be larger than what we have measured. The reason for this is that, in order to satisfy the theoretical principle of the Hot-Disk

method and to maintain unidirectional measured properties, we have cut the samples in a specified direction, and this will not eliminate any contribution of heat flow from the perpendicular directions to the assigned direction of measurement. Thus, the resultant measured thermal conductivity in our case is an averaged value, which is lower than the actual value in the direction of measurement.

Kollmann & Cote 1969 model gives the effective thermal conductivity of a wood-like fibrous structure by using a weighting bridge-factor (ξ) between the two limiting cases of Wiener bounds. Namely: conduction in parallel layers (λ_{\parallel}) of gas, liquid and solid phases and serial layers (λ_{\perp}) in relation to the heat transfer direction. Furthermore, the model includes the influence of the radiation in the gas phase. According to this model, the effective thermal conductivity (λ_{eff}) for pre-dried wood can be written as:

$$\begin{aligned}\lambda_{\text{eff}} &= \xi \lambda_{\parallel} + (1 - \xi) \lambda_{\perp} \\ \lambda_{\parallel} &= (1 - r) \cdot \lambda_{\text{fiber}} + r(\lambda_g + \lambda_{\text{rad}}) \\ \lambda_{\perp} &= \frac{1}{\frac{(1-r)}{\lambda_{\text{fiber}\perp}} + \frac{r}{(\lambda_g + \lambda_{\text{rad}})}}\end{aligned}\quad (3)$$

where r is the porosity, $\lambda_{\text{fiber}\parallel}$ is the thermal conductivity of the cell-wall substance/fibers along the grain, $\lambda_{\text{fiber}\perp}$ is the corresponding conductivity perpendicular to the grain, and λ_g is the gas(air) conductivity. The irradiative thermal conductivity λ_{rad} , at 20 °C, is very small and can be neglected.

A plot of the effective thermal conductivity (λ_{eff}) for various values of the bridge-factor is shown in Fig. 4. This plot was generated by applying Eq. (2) and using $\lambda_g = 0.0258 \text{ W/m } ^\circ\text{C}$ for dry air, $\lambda_{\text{fiber}\parallel} = 0.766 \text{ W/m } ^\circ\text{C}$ and $\lambda_{\text{fiber}\perp} = 0.430 \text{ W/m } ^\circ\text{C}$ for the wood fibers at a density of 1500 kg/m^3 . The values of $\lambda_{\text{fiber}\parallel}$ and $\lambda_{\text{fiber}\perp}$ have been used by Gronli, (Gronli, 1996) and were taken from mean values at room temperature reported by Maku, (Maku, 1954) and by Siau, (Siau, 1984).

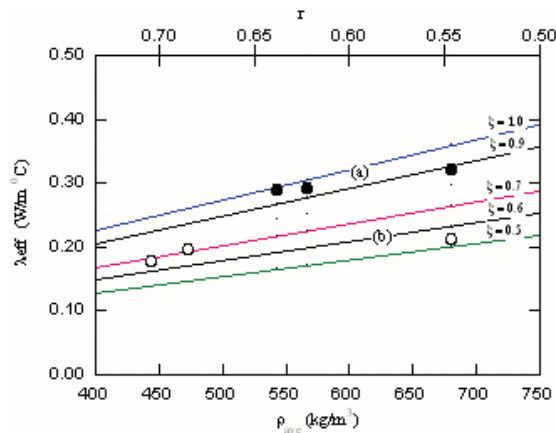


Fig. 4. The effective thermal conductivity according to eq (3) for different ξ values as a function of density(lower axis) and/or porosity (upper axis). The symbols of the data points are the same as the corresponding ones in Fig. 3

Our data in the longitudinal direction at 20 °C lie in the range $\xi = 0.8$ -1.0. The data in the transverse direction are in the range $\xi = 0.5$ -0.7. At 20 °C, our values for both directions are in agreement with literature data. Gronli (1996) obtained ξ in the range from 0.8 to 1.0 for the longitudinal direction and in the range from 0.35 to 0.6 for the transverse direction. Kollmann et al. (1968) found $\xi = 1$ for the longitudinal direction and $\xi = 0.58$ for the transverse direction.

Furthermore, the model indicates an increase in the effective conductivity as the density increases or porosity decreases, which agrees with our interpretation regarding the influence of microstructure on the heat conduction in wood. Therefore, such measurements can be used to probe the effect of anisotropy (morphology) in wood samples.

It should be noted that there are some constraints imposed upon using this model, such as a limited number of samples, using mean values for $\lambda_{\text{fiber}\parallel}$ and $\lambda_{\text{fiber}\perp}$, and limiting the analysis to room temperature data. Such constraints may introduce a degree of uncertainty in the conclusions. However, there is a tendency of a good agreement between the measured and calculated thermal conductivities and the results are supported by prediction of the model proposed by Kollmann and Cote (Kollmann & Cote, 1968) in spite of the various assumptions involved. Furthermore, in this attempt the purpose of using this model for these six samples, just to examine the possibilities of determining the bounds for estimating the effective thermal conductivity.

4.2 Ceramics

Seven samples of ceramic materials; glasses and marbles with different mineralogy and effective conductivities were selected. These samples were labelled from P1 to P7. These materials are classified into two types of samples, rock marbles and ceramic glasses. The rocks were two grey-red gneissic granite samples labelled P1 & P2 and the other five were either provided through a private communication with Dr. Vlastimil Boháč from the Institute of Physics, Slovak Academy of Sciences (SAS) or selected from the A-Z materials database within the www.amazon.com website. The effective thermal conductivity (λ_{eff}) of such composite multiphase samples with unknown isotropy requires the previous knowledge of the thermal conductivity of each phase, the volume concentrations of the phases, and the shape of inclusions of the different phases in the solid matrix.

Table 1 shows the volumetric fractions of constituents of the seven samples which were determined either by the point-counting method for the marbles or using X-ray (XRF) analysis for the ceramic glasses. The effective thermal conductivity of these samples depends on its mineralogy and the microstructure details of its constituents. Moreover, it appears that for these samples, the major influence on the effective conductivity is due to the magnitude of different conductivities of the constituents and their volumetric composition.

For these homogeneous and isotropic (with unknown morphology) multiphase composite materials, we have used the EMT Model mentioned in sec 2.1 to estimate the overall conductivity of the random mixture after determining the serial and parallel conduction (Wiener) bounds. Wiener was the first one to introduce these two bounds.

According to the definitions of Wiener bounds, a dry rock sample consisting of a mixed orientation of mineral layers (parallel and serial distributions of phases), is expected to have an effective conductivity value within these two bounds (homogeneity condition). Hashin & Shtrikman, 1962, introduced a model narrowing the range between Wiener bounds by imposing requirements on the isotropy of the medium. They derived new

bounds for an effective magnetic permeability of a composite material by means of variational theorems. The HS model can be directly applied to different transport properties including thermal conductivity (Helsing & Grimvall, 1991). The corresponding equations of HS bounds for three dimension multiphase media can be expressed in terms of Upper (λ_U) and Lower (λ_L) bounds which are functions of the highest and lowest values of λ_i 's of the different phases and their volume fractions P_i 's. (Porfiri et. al 2008) & (Suleiman, 2010).

Marble Samples	Density (g cm ⁻³)	Quartz	Alkali-felds	Plagioclase	Bio-tite	Chlorite	Muscovite	Epidote	Zircon	Sphene
		%								
P1	2.79	27.20	24.00	35.20	9.00	0.80	0.80	2.60	0.00	0.40
P2	2.53	22.20	64.10	0.00	1.70	0.00	10.20	1.40	0.40	0.00
Ceramic Samples	Density (g cm ⁻³)	Al ₂ O ₃	SiO ₂	Fe ₂ O ₃	TiO ₂	CaO	MgO	K ₂ O	Na ₂ O	Impurity
		%								
P3	2.76	57.83	36.14	0.68	0.27	0.12	0.25	3.45	0.38	0.41
P4	2.51	47.50	46.30	0.90	0.29	0.23	0.25	3.36	0.56	0.61
P5	2.75	59.98	34.48	0.65	0.25	0.16	0.25	3.32	0.50	0.41
P6	2.50	41.90	55.20	0.80	0.50	0.30	0.20	0.50	0.40	0.00
P7	2.52	46.00	16.00	0.00	0.00	0.00	17.00	10.00	0.00	7 (B ₂ O ₃)

Table 1. The volume fractions of the samples components

Using the more confined limits of Hashin and Shtrikman, it is reasonable to estimate the effective thermal conductivity of the multiphase isotropic medium by taking the mean value of the upper and lower limits (Horai et al., 1972), i.e.,

$$\lambda_{\text{eff(HS)}} = \frac{\lambda_U - \lambda_L}{2} \quad (3)$$

It should be mentioned that according to Chen (Chen et al, 1977) at the outset because of boundary resistance, the Hashin & Shtrikman (1962) bounds, derived under the assumption of temperature continuity between the two phases, are no longer valid in case of relatively large temperature variations at the boundaries.

Tables 2 shows the thermal conductivities λ 's of the marbles and glasses samples components, respectively. These values of λ_i 's for the rocks were taken from Landolt-Börnstein, Numerical Data and Functional Relationships in Science and Technology (1994). The corresponding λ 's values of the individual components for the classes samples were collected from the 88th edition of CRC hand book of chemistry and physics (Lide ed, 2008). The conductivity range for the impurities were estimated from the weighted average value of the other components conductivities using the limits of the upper and lower bonds defined by the above mentioned bounds.

Component	Quartz	Alkali-felds	Plagioclase	Biotite	Chlorite	Muscovite	Epidote	Zircon	Sphene
λ [W/m °C]	7.69	2.15*	1.84*	1.17	5.14	2.32	2.82	4.45	2.33
Component	Al ₂ O ₃	SiO ₂	Fe ₂ O ₃	TiO ₂	CaO	MgO	K ₂ O	Na ₂ O	Impurity
λ [W/m °C]	3	1.45	12.5	12	14	42	2*	0.5*	1.6-2.0
*The thermal conductivity of these components slightly varies with the chemical composition - a mean value was therefore used. The range of values for impurity was obtained from the weighted average value, for more details see the text.									

Table 2. The thermal conductivity λ [W/m °C] of the components of the marbles and glasses samples, respectively

In general, the utility of bounds gives a narrower range to predict a good match to the real value of the effective conductivity only if the conductivities of the components are not too different in magnitude. It is possible to evaluate λ_{eff} using the EMT model which is dependent on the existence of statistically homogeneous medium surrounding inclusions of different phases. As it was stated in sec 2.1, in this model, it is assumed that the phases with λ_i 's are distributed in such a way that the material can be considered isotropic and homogeneous, then according to EMT, the effective conductivity $\lambda_{\text{eff(EMT)}}$ is determined self consistently from the formula:

$$\sum_i P_i \left(\frac{\lambda_{\text{eff(EMT)}} - \lambda_i}{\lambda_{\text{eff(EMT)}} + \lambda_i} \right) = 0 \quad (4)$$

This formula has been derived from the solution to the problem of dilute spherical inclusions of one phase embedded in a matrix of a second phase (Noh et al. 1991). However, equation (4) designates a symmetric representation to all phases without singling out a certain phase as dilute. The solution of this equation will have a physical meaning under certain imposed conditions such as considering $\lambda_{\text{eff(EMT)}}$ as continuous function of the volume fraction P .

Table 3 shows the values of the calculated thermal conductivities at room temperature using effective medium theory (EMT), Hashin & Shtrikman, and Wiener bounds. The calculated values indicate that there are four out of the seven samples namely; P3, P5, P6, and P7 do not satisfy the theoretical necessary rule imposed by the parallel and serial bounds. According to this rule and by definition, the measured values should be within the limits of the parallel and serial bounds. This can be seen from the obtained values of the parallel and serial bounds. In other words, these samples they will not satisfy the validity condition (homogeneity condition) and therefore, have been exempted from our discussion regarding the models' validities. The average deviations of $\lambda_{\text{eff(EMT)}}$ from the measured values of these four samples are within 28-29%. Therefore, for the samples P3, P5, P6, and P7 the mismatch between the theoretical models and the measured values should not be attributed to models' validities. The most proper reason is that the distribution of phases within these samples is not uniform within the composite matrix.

Further work should be done to investigate the uniformity of different phases within these samples in order to estimate the values of λ 's and draw any affirmative results. However,

for the other three samples namely; P1, P2 and P4 the average deviations of $\lambda_{eff(EMT)}$ from λ_{meas} did not exceeding 3%. It is also obvious that, the mean value of HS bounds $\lambda_{eff(HS)}$ for these samples is rather good estimation to the measured (λ_{meas}) value at room temperature; The best approximation in this context, were obtained from the effective medium approach represented by the solution of equation (4). The self-consistent solutions of this equation for the three samples yielded nine roots. Each solution resulted in only one positive root that has a physical meaning. The deviation of $\lambda_{eff(EMT)}$ from the experimental values is less than 3.3%. Thus, of all of the calculated approximations, the EMT method appears to be the best for estimating the effective value of thermal conductivity only for samples that satisfy the homogeneity condition.

sample	The number of components	Parallel & Serial Wiener bounds		H S mean of U & L bounds	The E. M. T Model	Measured Value
	n	λ_P	λ_S	$\lambda_{eff(HS)}$	$\lambda_{eff(EMT)}$	λ_{meas}
P1	9	3.50	2.32	2.94	2.93	2.85
P2	9	3.40	2.56	3.02	2.97	2.97
P3	9	2.59	2.12	2.38	2.36	3.32
P4	9	2.46	1.96	2.21	2.19	2.27
P5	9	2.61	2.14	2.39	2.39	3.32
P6	8	2.56	2.06	2.33	2.31	5.00
P7	6	8.66	2.00	2.56	3.12	1.50

Table 3. The estimated λ 's [W/m °C] calculated using the corresponding models

At this point, it should be noted that for these ceramic composites there are some constrains imposed upon using these models such as limiting the number of samples, limiting the analysis to room temperature data, and neglecting the anisotropy of the thermal conductivity of the samples or the components that constitute the samples. In these circumstances such constrains may introduce a degree of uncertainty in the results. However, regards of all that, it seems that assuming isotropic and homogeneous conditions for ceramic samples, may still lead to a good agreement between the values of the measured and calculated thermal conductivities of such heterogeneous samples. Furthermore, in this attempt, the purpose of applied the models for these samples, just to examine the possibilities of determining the bounds and/or estimating the effective thermal conductivity of a multi-phase composite system given the volume fractions and the conductivities of the components.

In some cases where structure phase morphology (interlayer structure) details are very important an accurate knowledge of the thermal conductivity of composites could only be obtained experimentally. The experimental measurements can then be used as a probe to monitor microstructure changes.

Finally, these theoretical models can only be utilized provided the investigated samples satisfy the necessary condition that the measured values for the conductivity should be within the limits of the Wigner bounds. According to our calculations for the selected samples, the effective medium approach produced calculated values that agreed best with the measured values.

5. Conclusions

Four different models are tested to investigate the problem of determining the bounds and/or estimating the effective thermal conductivity (λ_{eff}) of composite (multiphase) systems given the volume fractions, the conductivities of the components and porosity (for woods). Three of the tested models namely; the effective medium theory (EMT), Hashin and Shtrikman (HS) bounds, Wiener bounds were applied on the ceramic samples and the fourth weighted bridge-factor model based on Wiener bounds was applied on wood as fiber-based materials or multiphase composites samples.

The effective thermal conductivity of wood at 20 °C slightly increases in both longitudinal and transverse directions. The effect of density and porosity on the thermal conductivity may be attributed to the presence of other scattering mechanisms such as voids, and cell boundaries. It seems that the porosity (conduction through voids) is the dominant influencing factor on the heat conduction in wood. Regarding the anisotropic nature of wood our results indicate that the thermal conductivity in the longitudinal direction (parallel to the grain) is greater than conductivity in the transverse direction. This may be attributed to orientation of the molecular chains within the cell wall. The long-chain linear polymers (cellulose) that comprise the cell wall, are arranged in bundles called microfibrils. These microfibrils are most closely aligned with the longitudinal axis of the cell. Our data in the longitudinal direction at 20 °C lie in the range $\xi = 0.8$ –1.0. The data in the transverse direction are in the range $\xi = 0.5$ –0.7. At 20 °C, our values for both directions are in agreement with literature data.

Although we did not take into account the possibility of anisotropy of thermal conductivity in the ceramic samples, it seems that, assuming isotropic and homogeneous conditions, the thermal conductivity of such samples may be calculated from their contents with rather good accuracy. The deviation of $\lambda_{\text{eff(EMT)}}$ from the experimental values is less than 3.3%. However, the possible consequences of a large anisotropy in their thermal conductivities may not be disregarded and further investigations are needed. These theoretical models can only be utilized provided that the investigated samples satisfy the necessary condition that the measured values for the conductivity should be within the limits of the parallel and serial bounds. According to our investigations for the selected samples, the effective conductivity can be used as a probe to monitor microstructure changes in both morphological and mineralogical aspects. An extended version of this work is planned to be published in the University of Sharjah international press.

6. Acknowledgement

The author would like to thank Dr Vlastimil Boháč for supplying the XRF data. The financial support from the University of Sharjah for the project is gratefully acknowledged.

7. References

- Angenheister G. (ed.), (1982) Landolt-Börnstein, *Numerical Data and Functional Relationships in Science and Technology*, vol. 1/a (Springer, Berlin), p. 341
- ASTM D5930-01, *Standard test method for thermal conductivity of plastics by means of a transient line-source technique*.

- ASTM E1530-06, Standard test method for evaluating the resistance to thermal transmission of materials by guarded heat flow meter technique.
- Avramidis, S. and Lau, P. (1992): Thermal coefficients of Wood Particles by Transient Heat-Flow Method. *Holzforschung* 46(5): 449-453
- B. Hay, J.R. Filtz, J. Hameury, L. Rongione, (2005), Uncertainty of thermal diffusivity measurements by laser flash method, *Int. J. Thermophys.* 26 (6) 1883-1898.
- Benveniste Y. & Miloh T. (1991) *Journal of Applied Physics* 69 1337-1344
- Brashaw Brian K., Voichita Bucur, Ferenc Divos, Raquel Gonçalves Jianxiong Lu, Roger Meder, Roy F. Pellerin, Simon Potter, Robert J. Ross, Xiping Wang, and Yafang Yin, (2010). Nondestructive Testing and Evaluation of Wood: *Forest Products Journal* Vol. 59, No. 3, page 7-14
- Chen F C, Choy C L & Young K. (1977) A theory of the thermal conductivity of composite materials *J. Phys. D: Appl. Phys.* Vol. 9, 10 571-586
- Dawson, M. Rides, J. Nottay, (2006) The effect of pressure on the thermal conductivity of polymer melts, *Polymer Testing* 25 (2) 268-275.
- Fan Li-Wu, Hu Ya-Cai *, Tian Tian & Zi-Tao Yul. (2006) The prediction of effective thermal conductivities perpendicular to the fibers of Wood using a fractal model and an Improved transient measurement technique, *International Journal of Heat and Mass Transfer* 49 4116-4123
- Fang X.-Q., LIU J.-X & T. Zhang (2009) *Journal of Composite Materials* Vol. 43, No. 21 2351-2369
- Fang, X.-Q. & Hu, C. (2008), Dynamic effective thermal properties of functionally graded fibrous composites using non-Fourier heat conduction *Computational Materials Science* 42 194-202.
- Felske J.D. (2004) Effective thermal conductivity of composite spheres in a continuous medium with contact resistance, *Int. Heat Mass Transfer* 47 3453-3461
- Gawin D., Kosny J., and Wilkes K. Thermal Conductivity of Moist Cellular Concrete- Experimental and Numerical Study *ASHRAE Buildings IX*, 2004, 1-10
- Gray L.J., Kaplan T. & Richardson J.D. (2003) *ASME J. Appl. Mech.* 70 -543
- Gronli, M. G. (1996) A Theoretical and Experimental Study of The Thermal Degradation of Biomass, PhD Theses, Department of Thermal Energy and Hydropower, The Norwegian University of Science and Technology.
- Gustafsson S.E. (1991) Transient plane source techniques for thermal conductivity and thermal diffusivity measurements of solid materials, *Rev. Sci. Instrum.* 62 (3) 797-804.
- Hamilton RL & Crosser OK (1962) *Ind. Engng Fundament.* 1 187-91
- Hashimoto T. (1994), *Data Book of Thermal Diffusivity of Polymers*, Youtes, Tokyo
- Hashin Z. & Shtrikman S. (1962) A variational approach to the theory of the effective magnetic permeability materials *Journal of Applied Physics* 33 3125-3131
- Hashin Z. (1968) Assessment of the self consistent scheme approximation: conductivity of particulate composites *Journal of Composite Materials* 2 284-300
- Helsing J. & Grimvall G. (1991) Thermal conductivity of cast iron: Models and analysis of experiments: *J. Appl. Phys.* 70: 1198-1206.
- Hollecka H., Leiste H., Nolda E., Schulza H., & Skokana A. (1988). Multiphase ceramic materials and coatings for fusion reactor applications. *Journal of Nuclear Materials* Volumes 155-157, Part 1, 2 July issue, Pages 221-224

- Horai K. & Baldrige S. (1972b) Thermal conductivity of nineteen igneous rocks. II Estimation of the thermal conductivity of rock from the mineral and chemical composition: *Phys. Earth Planet. Interiors* 5.
- Hu C., Fang X.Q., Huang W.H., *Archive of Applied Mechanics* 78 (2008) 177-190.
- ISO 8302:1991, Thermal insulation – Determination of steady-state thermal resistance and related properties – Guarded hot plate apparatus.
- ISO/DIS 22007-1, Plastics – *Determination of thermal conductivity and thermal diffusivity* – Part 1: General principles.
- ISO/DIS 22007-3, Plastics – *Determination of thermal conductivity and thermal diffusivity* – Part 3: Temperature wave analysis method.
- ISO/DIS 22007-4, Plastics – *Determination of thermal conductivity and thermal diffusivity* – Part 4: Laser flash method.
- Koizumi M.(1993), *The concept of FGM*, in: J.B. Holt, M. Koizumi, T.Hirai, Z.A. Munir (Eds.), *Ceramic Transactions, Functionally Graded Materials*, vol. 34, The American Ceramic Society.
- Kollmann, F. and Cote, W. A. (1968). —*Principles of Wood Science and Technology*, Solid Wood. Springer-Verlag, NewYork: 246 – 250
- Kuo H.-Y.& Chen T. (2005) *Int. J. Solids Struct.* 42 1111
- Lide D.R. (ed.) (2008), *CRC Handbook of Chemistry and Physics*, 88th edn. (CRC Press, Boca Raton)
- Lobo H., Cohen C., (1990) *Polym. Eng. Sci.* 30 65.
- Maku, T. (1954) Studies on Heat Conduction in Wood Kyoto University, *Bulletin of the Wood Research Institute* No. 13 :1-80
- Maxwell J.C. (1892), *A Treatise on Electricity and Magnetism*, third ed., vol. 1, Dover, New York, 1954. Oxford: Clarendon pp 435-41
- McPhedran R. & McKenzie D. (1978) The conductivity of lattices of spheres. in the simple cubic lattice, *Proceeding of the Royal Society of London*: A 359 45-63
- Morikawa J., Leong C. & Hashimoto, T. (2008) *J. Appl. Phys.* 103 063522
- Morikawa J., Tan,J. Hashimoto T. (1995), *Polymer* 36 4439
- Noh T W, Song P H & Sievers A J (1991) Self-consistency conditions for the effective-medium approximation in composite materials: *Phys. Rev. B* 44 123-165
- Parrott, J. E. & Stuckes A. D. (1975) *Thermal conductivity of solids*. Pion Limited, London.
- Polder D & Van Santen J H (1946) *Physicu* 12 257-71
- Porfiri M, Gupta N. & Nguyen N. Q. (2008) thermal conductivity of multi-phase particulate composite materials, 1-13
- Rayleigh, L. (1892) On the influence of obstacles arranged in rectangular order upon the properties of the medium. *Philosophical Magazines* 34 481-502
- Reynolds J A & Hough J M (1957) *Proc. Phys. Soc. B* 70 769-75
- Rocha A & Acrivos A (1974) *Proc. R. Soc. A* 337 123-33
- Rocha, A. and Cruz, M.E. (2001). Computation of the Effective Conductivity of Unidirectional Fibrous Composites with an Interfacial Thermal Resistance, *Numerical Heat Transfer A _ Applications*, 39: 179-203.
- Salazar A. Terrón J.M., Sánchez-Lavega A., & Celorrio R. (2002), *Applied Physics Letter* 80 1903-1905.
- Samantray P.K., Karthikeyan P.& Reddy K.S. (2006) *International Journal of Heat and Mass Transfer* 49 4209-4219

- Sangani A. & Acrivos A. (1983) Proceeding of the Royal Society of London: A 386 263–275
- Siau, J. F. (1984) *Transport Processes in Wood*, Springer-Verlag, New York
- Sombatsompop, N. & Wood A.K. (1997), Measurement of thermal conductivity of polymers using an improved Lee's disc apparatus, *Polymer Test* 16 (3) 203–223.
- Steinhagen, H. P. (1977) Thermal properties of wood, green or dry, from -40° to +100° C: A literature review. *USDA Forest Service General Technical Report FPL-9*, Forest Products Laboratory, Madison, WI.
- Suleiman B M (1994) Ph. D. Thesis: Chapter 4, *Transient Plane Source Method*, Physics Department, Chalmers University of Technology, Gothenburg, Sweden, 37-58.
- Suleiman B M, Börjesson L. and Berastegui P, (1996), Effect of cobalt doping on thermal conductivity of YBa₂Cu₃O_{7-δ} superconductor, *Phys. Rev. B* 53 (9), 5901-5906.
- Suleiman B. M. (2010) Effective thermal conduction in composite materials *Appl Phys A* 99: 223–228
- Suleiman B. M., Larfeldt J., Leckner B., (1999), Thermal conductivity and diffusivity of Wood, *Wood Sci. Technol.* 33 465–473.
- Suresh S. & Mortensen A. (1998), *Fundamentals of Functionally Graded Materials* IOM Communication Ltd., London.
- Wiener O. (1912) *Abh. Math.-Phys. Kl. König. Sächs. Ges. Wiss. (Leipz.)* 32, 509
- Xu Y. & Yagi K. (2004). Automatic FEM model generation for evaluating thermal conductivity of composite with random materials arrangement, *Comput. Mater. Sci.* 30 242–252.
- Zhang, H. W., Zhang, S., Bi, J. Y., & Schrefler, B. A., (200) Thermo-mechanical analysis of periodic multiphase materials by a multiscale asymptotic homogenization approach, *International Journal for Numerical Methods in Engineering* Volume 69 Issue 1, 87 – 113
- Zinkle S.J. & Snead L.L. (1999). Thermophysical and Mechanical Properties of SiC/SiC Composites an upcoming version of the fusion *Materials Properties Handbook* (MPH) J.W. Davis ed. (Boeing, St. Louis). Oak Ridge National Laboratory